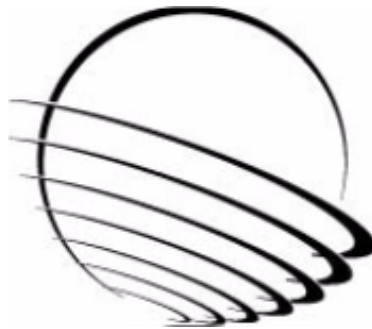




47th Aerospace Mechanisms Symposium

Compiled/Edited by: Edward A. Boesiger & Jonathan P. Wood



Proceedings of a Symposium
Hosted by the NASA Langley Research Center and
Lockheed Martin Space
Sponsored and Organized by the Mechanisms Education Association

May 15-17, 2024

2024

PREFACE

The Aerospace Mechanisms Symposium (AMS) provides a unique forum for those active in the design, production and use of aerospace mechanisms. A major focus is the reporting of problems and solutions associated with the development and flight certification of new mechanisms. Sponsored and organized by the Mechanisms Education Association, responsibility for hosting the AMS is shared by the National Aeronautics and Space Administration and Lockheed Martin Space.

The 47th AMS was held in Virginia Beach, Virginia from May 15 to May 17. These proceedings are published to provide these lessons learned and mechanism design information to the mechanism community. Topics included instrument mechanisms, gimbals, release devices, tribology, materials issues, deployment, on-orbit performance, actuators and cubesat mechanisms.

The high quality of this symposium is a result of the work of many people, and their efforts are gratefully acknowledged. This extends to the voluntary members of the symposium organizing committee representing the eight NASA field centers, Lockheed Martin Space, and the European Space Agency. Appreciation is also extended to the session chairs, the authors, and particularly the personnel at NASA Langley responsible for the symposium arrangements and the publication of these proceedings. A sincere thank you also goes to the symposium executive committee who is responsible for the year-to-year management of the AMS, including paper processing.

The use of trade names of manufacturers in this publication does not constitute an official endorsement of such products or manufacturers, either expressed or implied, by the National Aeronautics and Space Administration.

CONTENTS

Symposium Schedule	viii
Symposium Organizing and Advisory Committees.....	xiv
Caging and Release Mechanism Design for the Simplified Gravitational Reference Sensor	1
Joseph Footdale, Chad Sypolt, Joseph Mackin , Stephen Bennett, John Conklin & Peter Wass	
Development Plan of the Upgraded Release Mechanism for the LISA Space Mission	15
Carlo Zanoni, Daniele Bortoluzzi, Davide Vignotto, Matteo Tomasi, Edoardo Dala Ricca, Abraham Ayele Gelan, Francesco Marzan, Paolo Radaelli, Riccardo Freddi & Alessandro Paolo Moroni	
FD04 Frangibolt Actuator Performance Test: Measuring Force and Stroke Margin	29
Ingie Baho & Kim Aaron	
Development of an Ejectable Data Recorder Ejection Mechanism for the Low-Earth Orbit Flight Test of an Inflatable Decelerator	39
Brian Saulman & Robert Wagner	
LARES2 Mission: Retention and Separation Subsystem	53
Matteo Spinelli, Alessandro Bursi, Simone Pirrotta & Roberto Bertacin	
Design and Qualification of the Low-Earth Orbit Flight Test of an Inflatable Decelerator (LOFTID) Payload Adapter Separation System (PASS).....	67
Sean Hancock, Jacob Montgomery, Ben Nickless & Matt Realsen	
Development and Testing of a Novel Solenoid Launch Lock for a Lunar Lander Thrust Vector Control Actuator	81
Joseph Plunkett	
Testing Frangibolts for Extended Space Mission Durations	91
Brian Gore, Ryan Hill & Timothy Woodard	
Development of a Bulk Metallic Glass Planetary Gearmotor for Unheated Actuation in Cryogenic Environments	107
Andrew Kennett & Robert Dillon	
Extreme Benefits of Visual Inspection under Magnification of Mechanical Components.....	121
Duval Johnson	
Motor Stator (Fluidize) Insulation Material Options and Testing Summary	133
Jonathan Wood, Emmett Donnelley-Power, Jessica Hamm & Recarda Schmitz	
Ti Beta-C Spring Development Testing for Low Cycle, Cold Deep Space Applications.....	151
Pavlina Karafillis & Grady Lynch	
Lessons Learned in Building and Testing the Regolith and Ice Drill for Exploring New Terrain (TRIDENT).....	163
Philip Chu, Samuel Goldman, Carter Fortuin, Vincent Vendiola, Helen Xu, Jaqueline Stamboltsian, Raymond Lin, Anchal Jain, Jack Wilson & Kris Zacny	

Micro-Sampler: A Kilogram Class Drill for Planetary Sampling and Powder Collection.....	177
Nick Traeden, Honeybee Robotics LLC, Altadena, CA	
Development of the DrACO Drill: A Rotary Percussive Drill for Cryogenic Operation.....	191
Grayson Adams, Matthew Dottinger & Patrick Corrigan	
Government Reference Design of the Vertical Solar Array Technology Demonstrator.....	207
Scott Belbin, Carl Mills & Ryan Chan	
Bearings for Extreme Environments – NiTi-Hf as a Premium Material for Miniature Radial Ball Bearings Intended for the use in Extreme Environments in Space and Healthcare Applications.....	223
Christoph Bayer, Thomas Kreis and David Nufer	
Magnetic Fast Steering Mirrors for High Power Optical Communication.....	229
Etienne Betsch, Gérald Aigouy, Clément Cote, Augustin Bedek, Arnaud Barnique, Nicolas Bourgeot, Hugo Gardel, Pierre Personnat, Patrick Meneroud, Théo Simon, Marc Fournier, Sylvain Chardon, Frank Claeysen & François Barillot	
Lessons Learned on Synchronization System Modelling for Solar Array Wing Deployment Predictions.....	241
Héloïse Boross & Philipp Schmidheiny	
Testbed for Lunar Extreme Environment Wear Tolerant Applications.....	249
Valerie L. Wiesner, Glen C. King, Christopher S. Domack, Brandon M. Widener, Keith L. Gordon & Christopher J. Wohl	
Development and Qualification of a New SADM for Small Satellites.....	257
Adrien Guignabert, Flavien Deschaux, Luc Herrero, Etienne Magnin-Robert & Jean-Bernard Mondier	
Development of a Shape Memory Alloy Thermostat.....	263
Alai Lopez & Kerri Cahoy	
On the Internal Loading Distribution in a Radial Load Rolling Element Bearing.....	269
Mário C. Ricci	
Programable Lead Screw Actuated Self-Leveling Platform.....	275
Iok Wong	
Aerocapture Technology Demonstration Risk Reduction Activity.....	283
Scott Belbin & Nicholas Vitullo	
Listening into the JUICE Deployments with the On-Board High Accuracy Accelerometer.....	289
Ronan Le Letty, Christian Erd, Alessandro Atzei, Massimiliano Pecora & Luciano Less	
Bricard Mechanism-Based Engulfing Gripper for Space Debris Removal.....	301
Abhijith Prakash, Sankalp Vishnoi, Sandeep & Biju Prasad	
DIABLO – Deployable Interlocking Actuated Bands for Linear Operations; Design, Development, Testing, and Applications.....	311
Vishnu Sanigepalli, Robert Van Ness, Brian Vogel & Kris Zacny	

A Modular Ready-to-Use Active Gravity Offloading System.....	325
Frederik Doll, Stefan Oechslein & Benjamin Krolitzki	
Origami-Inspired, Re-Deployable, Compact Lunar Solar Array System.....	339
Alexander Gendell	
Design and Testing of a Deployment Mechanism for NASA's 1653-m2 Solar Cruiser Sail.....	345
Zachary McConnel & Mark S. Lake	
Advanced Composite Solar Sail System (ACS3): Mechanisms and Lessons Learned from a CubeSat Solar Sail Deployer.....	355
Nigel Schneider, Gregory Dean, Olive Stohman, Jerry Warren, Juan Fernandez, W. Keats Wilkie & Todd Denkins	
Design and Test of the Orion Crew Module Launch Abort System Hatch.....	369
Jeff Heyne & Aaron Larson	
Precision Actuation in the Flight Design of the Roman-CGI Focus Control Mechanism.....	389
Mineh Badalian, Johnathan W. Carson & Dalia Raafat	
A Dust-Resilient Thermal Shutter Mechanism for Lunar Radiators.....	397
Andrew S. Gibson, Olly Poyntz-Wright, Angus Bishop, Matthew Oldfield, Angel Iglesias, Fabrice Rottmeier, Martin Humphries & Philipp B Hager	
An Introduction to Flexure Design.....	413
Johnathan Carson & Gary Y. Wang	
Design and Test of Retention Mechanism to Apply Direction-Dependent Axial Force to Mars Returnable Sample Tube Assemblies.....	429
Jay Marion	
Tough Precision Piezoelectric Motors for Space Applications.....	445
Francois Barillot, Jocelyn Rebufa, Etienne Betsch, Jolan Gauthier, Alexandre Pagès & Nabil Bencheikh	
VenSpec-H Filter Wheel Mechanism Breadboard Development and Test.....	459
Gerhard Székely, Robert Eberli , Marco Grossmann, Samuel Tenisch, Hans-Peter Gröbelbauer, Florian Wirz, Pascal Seiler, Paola Kögl, Stefan Kögl, Paul J. Tackley, Taras Gerya, Ann-Carine Vandaele & Eddy Neefs	
Development of an Advanced 2-Axis Electrical Propulsion Pointing Mechanism.....	473
Paul Janu, Daniel Ruckser, Jarmila Suhajdova, Zoran Ignjatov & Mario Toso	
MPCV SADA for Artemis Program: A Story of Increasing Demands and Continuous Improvement.....	487
Josef Viktor Zemann, Paul Joachim Schüngel & Matthias Schmalbach	
Development and Qualification of an Electrical Thruster Two Axis Pointing Mechanism.....	497
Richard Horth, Stéphane St-André, Xavier Marcotte, Marc-André Verreault & Etienne Desrosiers	

Dry-Film Lubricated Ball Bearing Tests for High-Speed, Moderate-to-Long Life, Cryogenic Operation.....	505
Robert Wei, Gale Paulsen, Andrew Bocklund, Nate Jensen, Zach Begland & Tim Newbold	
Cold Welding under Space and Launch Conditions.....	519
Roland Holzbauer, Andreas Merstallinger, Lionel Gaillard & Nathan Bamsey	
Qualification of RHEOLUBE 3000-3Pb for the BABAR-ERI Chopper Mechanism.....	529
Darren Erickson & Bob Hoffman	
Development of Strain Wave Gearing Lubrication for the Steering Unit for The Manned Pressurized Rover.....	541
Jun'ichi Kurogi, Yoshihide Kiyosawa, Masaru Kobayashi, Takuya Akasaka, Hiroyuki Toyoda, Shoichi Shono, Shingo Obara, Koji Matsumoto & Nobuo Kenmochi	
On the Potential of Orthoborate Ionic Liquids to Meet Lubrication Challenges in Space Mechanisms.....	555
Román de la Presilla, Oleg N. Antzutkin & Sergei Glavatskih	
Design and Test of Bearings Used in Electromechanical Systems under High Vibration Environments.....	566
Kyle Gotthelf, Javier Becerra & Andrew Maurer	
Development and Qualification of an Extreme Mechanical Live Antenna Pointing Mechanism, part of the Inter Satellite Link of an ESA Mission Spacecraft.....	579
Richard Horth, Stéphane St-André, Nicolas Sturkenboom & William Dumberry	

SYMPOSIUM SCHEDULE

WEDNESDAY, 15 May 2024

7:00 **Wednesday Presenters' Breakfast** - Meeting Room 2A

8:00 **CHECK-IN**- Meeting Room 2B

8:15 **INTRODUCTORY REMARKS**

Edward Boesiger, General Chairman, Lockheed Martin Space, Sunnyvale, CA
Benjamin Nickless, Host Chairman, NASA Langley Research Center, Hampton, VA
Clayton Turner, Center Director, NASA Langley Research Center, Hampton, VA

8:30 **SESSION I - RELEASE MECHANISMS**

Session Chair: David Eddleman, NASA Marshall Space Flight Center, Huntsville, AL

- Caging and Release Mechanism Design for the Simplified Gravitational Reference Sensor
Joseph Footdale, Chad Sypolt, Joseph Mackin & Stephen Bennett, BAE Systems, Inc., Boulder, CO; John Conklin & Peter Wass, University of Florida, Gainesville, FL
- Development Plan of the Upgraded Release Mechanism for the LISA Space Mission
Carlo Zanoni, National Institute for Nuclear Physics, Italy; Daniele Bortoluzzi, Davide Vignotto, Matteo Tomasi, Edoardo Dala Ricca, Abraham Ayele Gelan & Francesco Marzan, University of Trento, Trento, Italy; Paolo Radaelli, Riccardo Freddi & Alessandro Paolo Moroni, OHB Italia SpA, Italy
- FD04 Frangibolt Actuator Performance Test: Measuring Force and Stroke Margin
Ingie Baho & Kim Aaron, Jet Propulsion Laboratory, Pasadena, CA
- Development of an Ejectable Data Recorder Ejection Mechanism for the Low-Earth Orbit Flight Test of an Inflatable Decelerator
Brian Saulman & Robert Wagner, NASA Langley Research Center, Hampton, VA

10:10 **BREAK**

- LARES2 Mission: Retention and Separation Subsystem
Matteo Spinelli & Alessandro Bursi, OHB Italia, Milan, Italy; Simone Pirrotta & Roberto Bertacin, Italian Space Agency, Rome, Italy
- Design and Qualification of the Low-Earth Flight Test of an Inflatable Decelerator (LOFTID) Payload Adapter Separation System (PASS)
Sean Hancock, Jacob Montgomery & Ben Nickless, NASA Langley Research Center, Hampton, VA; Matt Realsen, United Launch Alliance, Centennial, CO
- Development and Testing of a Novel Solenoid Launch Lock for a Lunar Lander Thrust Vector Control Actuator
Joseph Plunkett, Honeybee Robotics, Longmont, CO
- Testing Frangibolts for Extended Space Mission Durations

Brian Gore, Ryan Hill & Timothy Woodard, The Aerospace Corporation, El Segundo, CA

12:20 **LUNCH**

Lunch for AMS Attendees in Ballroom One

1:20 **SESSION II - MATERIALS MEET MECHANISMS**

Session Chair: Gilles Feusier, École Polytechnique Fédérale de Lausanne, Lausanne, Switzerland

- Development of a Bulk Metallic Glass Planetary Gearmotor for Unheated Actuation in Cryogenic Environments
Andrew Kennett & Robert Dillon, Jet Propulsion Laboratory, Pasadena, CA
- Extreme Benefits of Visual Inspection under Magnification of Mechanical Components
Duval Johnson, Jet Propulsion Laboratory, Pasadena, CA
- Motor Stator (Fluidize) Insulation Material Options and Testing Summary
Jonathan Wood & Emmett Donnelley-Power, Lockheed Martin Space, Sunnyvale, CA; Jessica Hamm, Sierra Space, Durham, NC; Recarda Schmitz, Windings, Inc., New Ulm, MN
- Ti Beta-C Spring Development Testing for Low Cycle, Cold Deep Space Applications
Pavlina Karafillis & Grady Lynch, Lockheed Martin Space, Denver, CO

3:00 **BREAK**

3:30 **SESSION III - DRILLING MACHINES**

Session Chair: Terry Nienaber, NASA Langley Research Center, Hampton, VA

- Lessons Learned in Building and Testing the Regolith and Ice Drill for Exploring New Terrain (TRIDENT)
Philip Chu, Samuel Goldman, Carter Fortuin, Vincent Vendiola, Helen Xu, Jaqueline Stamboltsian, Raymond Lin, Anchal Jain, Jack Wilson & Kris Zacny, Honeybee Robotics LLC, Altadena, CA
- Micro-Sampler: A Kilogram Class Drill for Planetary Sampling and Powder Collection
Nicklaus Traeden, Kathryn Bywaters, Damien Hackett, Gabriel Zwilinger, Christian Sipe, Peter Pulai & Kris Zacny, Honeybee Robotics LLC, Altadena, CA; Philippe Sarrazin & Maite Diez, SETI Institute, Mountain View, CA
- Development of the DrACO Drill: A Rotary Percussive Drill for Cryogenic Operation
Grayson Adams, Matthew Dottinger & Patrick Corrigan, Honeybee Robotics LLC, Altadena, CA

4:45 **BREAK**

5:00 **SESSION IV - POSTER SESSION PREVIEW**- *A rapid fire session of poster papers. Each presenter will give their best 5-minute pitch and attendees can follow up at the reception or other time.*

Session Chair: Mark Balzer, NASA Jet Propulsion Laboratory, Pasadena, CA

- Government Reference Design of the Vertical Solar Array Technology Demonstrator
Scott Belbin, Carl Mills & Ryan Chan, NASA Langley Research Center, Hampton, VA
- Bearings for Extreme Environments - NiTi-Hf as a Premium Material for Miniature Radial Ball Bearings Intended for the use in Extreme Environments in Space and Healthcare Applications
Christoph Bayer & Thomas Kreis, GRW, Rimpar, Germany; David Nufer, GRW, Bloomfield, CT
- Magnetic Fast Steering Mirrors for High Power Optical Communication
Etienne Betsch, Gérald Aigouy, Clément Cote, Augustin Bedek, Arnaud Barnique, Nicolas Bourgeot, Hugo Grardel, Pierre Personnat, Patrick Meneroud, Théo Simon, Marc Fournier, Sylvain Chardon, Frank Claeysen & François Barillot, Cedrat Technologies, Meylan, France
- Lessons Learned on Synchronization System Modelling for Solar Array Wing Deployment Predictions
Héloïse Boross & Philipp Schmidheiny, Beyond Gravity, Zurich, Switzerland
- Testbed for Lunar Extreme Environment Wear Tolerant Applications
Valerie Wiesner, Glen King, Keith Gordon & Christopher Wohl, NASA Langley Research Center, Hampton, VA; Christopher Domack & Brandon Widener, Analytical Mechanics Associates, Inc., Hampton, VA
- Development and Qualification of a New SADM for Small Satellites
Adrien Guignabert, Flavien Deschaux, Luc Herrero, Etienne Magnin-Robert, Comat Aerospace, Flourens, France; Jean-Bernard Mondier, CNES, Toulouse, France
- Development of a Shape Memory Alloy Thermostat
Alai Lopez, MIT Lincoln Laboratory, Lexington, MA; Kerri Cahoy, Massachusetts Institute of Technology, Cambridge, MA, USA
- Programable Lead Screw Actuated Self-Leveling Platform
Iok Wong, NASA Langley Research Center, Hampton, VA
- Aerocapture Technology Demonstration Risk Reduction Activity
Scott Belbin & Nicholas Vitullo, NASA Langley Research Center, Hampton, VA

6:00-10:00 **RECEPTION** - Ballroom One

Component suppliers display current products and provide tutorials, Poster Papers are displayed, Robotics Team demonstrations, and a buffet meal.

THURSDAY, 16 May 2024

7:00 **Thursday Presenters' Breakfast** - Meeting Room 2A

8:00 **SESSION V - DEPLOYMENT MECHANISMS**

Session Chair: Matthew Zwack, NASA Marshall Space Flight Center, Huntsville, AL

- Listening into the JUICE Deployments with the On-Board High Accuracy Accelerometer
Ronan Le Letty, Christian Erdl & Alessandro Atzeil, ESA/ESTeC, Noordwijk, The Netherlands; Massimiliano Pecora, THALES Alenia Space Italia, Gorgonzola, Italy; Luciano Iess, Sapienza University of Rome, Rome, Italy
- Bricard Mechanism Based Engulfing Gripper for Space Debris Removal
Abhijith Prakash, Sankalp Vishnoi, Sandeep R & Biju Prasad B, Vikram Sarabhai Space Centre, Thiruvananthapuram, India
- DIABLO - Deployable Interlocking Actuated Bands for Linear Operations; Design, Development, Testing, and Applications
Vishnu Sanigepalli, Robert Van Ness, Brian Vogel & Kris Zacny, Honeybee Robotics LLC, Longmont, CO
- A Modular Ready-to-Use Active Gravity Offloading System
Frederik Doll, Stefan Oechslein & Benjamin Krolitzki, CarboSpaceTech GmbH, Immenstaad am Bodensee, Germany

9:40 **BREAK**

- Origami-Inspired, Re-Deployable, Compact Lunar Solar Array System
Alexander Gendell, Folditure, Hoboken, NJ
- Design and Testing of a Deployment Mechanism for NASA's 1653-m² Solar Cruiser Sail
Zachary McConnel & Mark S. Lake, Redwire Space, Longmont, CO
- Advanced Composite Solar Sail System (ACS3): Mechanisms and Lessons Learned from a CubeSat Solar Sail Deployer
Nigel Schneider, Analytical Services & Materials Inc., Hampton, VA; Gregory Dean, Olive Stohlman, Jerry Warren, Juan Fernandez, W. Keats Wilkie, Todd Denkins, NASA Langley Research Center, Hampton, VA
- Design and Test of the Orion Crew Module Launch Abort System Hatch
Jeff Heyne, Aaron Larson, Ryan Dardar, Lance Lininger & Evan Siracki, Lockheed Martin Space, Houston, TX & Littleton, Co; Brian Emmett, NASA Langley Research Center, Hampton, VA

11:50 **LUNCH**

Lunch for AMS Attendees in Ballroom One

12:50 **SESSION VI - INSTRUMENTS**

Session Chair: Justin Scheidler, NASA Glenn Research Center, Cleveland, OH

- Precision Actuation in the Flight Design of the Roman-CGI Focus Control Mechanism

Mineh Badalian, Johnathan W. Carson & Dalia Raafat, Jet Propulsion Laboratory, Pasadena, CA

- A Dust-Resilient Thermal Shutter Mechanism for Lunar Radiators
Andrew Gibson, Olly Poyntz-Wright, Angus Bishop & Matthew Oldfield, ESR Technology Ltd. - European Space Tribology Laboratory, Warrington, UK; Angel Iglesias & Fabrice Rottmeier, Almatech, Lausanne, Switzerland; Martin Humphries, Spacemech Limited, Bristol, UK; Philipp B Hager, European Space Agency (ESA/ESTEC), Noordwijk, The Netherlands
- An Introduction to Flexure Design
Johnathan Carson & Gary Y. Wang, Jet Propulsion Laboratory, Pasadena, CA
- Design and Test of Retention Mechanism to Apply Direction-Dependent Axial Force to Mars Returnable Sample Tube Assemblies
Jay Marion, Jet Propulsion Laboratory, Pasadena, CA
- Tough Precision Piezoelectric Motors for Space Applications
Francois Barillot, Jocelyn Rebufa, Etienne Betsch, Jolan Gauthier, Alexandre Pagès & Nabil Bencheikh, Cedrat Technologies, Meylan, France
- VenSpec-H Filter Wheel Mechanism Breadboard Development and Test
Gerhard S. Székely, Robert Eberli, Marco Grossmann & Samuel Tenisch, Lucern University of Applied Sciences & Arts, Horw, Switzerland; Hans-Peter Gröbelbauer, Florian Wirz & Pascal Seiler, University of Applied Sciences and Arts Northwestern Switzerland, Windisch, Switzerland; Paola Kögl & Stefan Kögl, KOEGL Space GmbH, Dielsdorf, Switzerland; Paul Tackley & Taras Gerya, Zürich, Switzerland; Ann-Carine Vandaele & Eddy Neefs, Royal Belgian Institute for Space Aeronomy, Brussels, Belgium

3:20 **BREAK**

3:50 **SESSION VII - GIMBALS**

Session Chair: Jason Schuler, NASA Kennedy Space Center, Kennedy Space Center, FL

- Development of an Advanced 2-Axis Electrical Propulsion Pointing Mechanism
Paul Janu, Daniel Ruckser, Jarmila Suhajdova & Zoran Ignjatov, Beyond Gravity, Wien, Austria; Mario Toso, ESA/ESTeC, Noordwijk, The Netherlands
- MPCV SADA for Artemis Program: A Story of Increasing Demands and Continuous Improvement
Josef Viktor Zemann, Paul Joachim Schüngel & Matthias Schmalbach, Beyond Gravity, Zurich, Switzerland
- Development and Qualification of an Electrical Thruster Two Axis Pointing Mechanism
Richard Horth, Stéphane St-André, Xavier Marcotte, Marc-André Verreault & Etienne Desrosiers, MDA, Quebec, Canada

5:05 **SPECIAL PRESENTATION** - Astronaut and F-22 Pilot, Major Nicole Ayers
Nichole Ayers was selected by NASA to join the 2021 Astronaut Candidate Class. She graduated from the U.S. Air Force Academy with a bachelor's degree

in mathematics and later earned a master's degree in computational and applied mathematics from Rice University. She became an instructor pilot in the T-38, leading adversary missions that provided combat training for the F-22 Raptors at Langley AFB. As one of the few women to have flown the F-22 Raptor, Ayers led the first-ever all-woman F-22 formation in combat in 2019 with more than 200 combat hours in Operation Inherent Resolve over Iraq and Syria.

7:00-11:00 **BANQUET** - Military Aviation Museum
Dinner and entertainment amongst World War II vintage airplanes.

FRIDAY, 17 May 2024

7:00 **Friday Presenters' Breakfast** - Meeting Room 2A

8:00 **SESSION VIII - THE STU LOEWENTHAL TRIBOLOGY SESSION**

Session Chair: Stu Loewenthal, Lockheed Martin Space (Retired), Sunnyvale, CA

- Dry-Film Lubricated Ball Bearing Tests for High-Speed, Moderate-to-Long Life, Cryogenic Operation
Robert Wei, Gale Paulsen, Andrew Bocklund, Nate Jensen, Zach Begland & Tim Newbold, Honeybee Robotics LLC, Altadena, CA
- Cold Welding under Space and Launch Conditions
Roland Holzbauer & Andreas Merstallinger, Aerospace & Advanced Composites GmbH, Wiener Neustadt, Austria; Lionel Gaillard & Nathan Bamsey, European Space Agency, Noordwijk, The Netherlands
- Qualification of Rheolube 3000-3Pb for the BABAR-ERI Chopper Mechanism
Darren Erickson, Laboratory for Atmospheric and Space Physics, University of Colorado, Boulder, CO; Bob Hoffman, NYE Lubricants (Member of the FUCHS Group), Inc., Fairhaven, MA

9:15 **BREAK**

- Development of Strain Wave Gearing Lubrication for the Steering Unit for The Manned Pressurized Rover
Jun'ichi Kurogi, Yoshihide Kiyosawa, Masaru Kobayashi & Takuya Akasaka, Harmonic Drive Systems Inc, Nagano-ken, Japan; Hiroyuki Toyoda & Shoichi Shono, Toyota Motor Corporation, Japan; Shingo Obara, Koji Matsumoto & Nobuo Kenmochi, Japan Exploration Agency, Japan
- On the Potential of Orthoborate Ionic Liquids to Meet Lubrication Challenges in Space Mechanisms
Roman de la Presilla, KTH Royal Institute of Technology, Stockholm, Sweden; Oleg Antzutkin, Luleå University of Technology, Luleå, Sweden; Sergei Glavatskih, University of New South Wales, Sydney, Australia and Ghent University, Ghent, Belgium
- Design and Test of Bearings Used in Electromechanical Systems under High Vibration Environments
Kyle Gotthelf, Javier Becerra & Andrew Maurer, Honeybee Robotics LLC, Longmont, CO
- Development and Qualification of an Extreme Mechanical Live Antenna Pointing Mechanism, part of the Inter Satellite Link of an ESA Mission Spacecraft
Richard Horth, MDA, Quebec, Canada

11:10 **SPECIAL PRESENTATION - SHOCK QUALIFICATION OF AIRCRAFT CARRIERS**

Michael Reilly and Michael Talley

Huntington Ingalls Industries, Newport News Shipbuilding

This area of Virginia is a key shipbuilding area for the United States. Satellites have to design for shock from release devices all the time and this presentation will give you another perspective!

11:40 **TECHNICAL SESSIONS CONCLUSION**

Jonathan Wood, Lockheed Martin Space, Sunnyvale, CA
- Herzl Award Presentation

12:00 **LUNCH**

Lunch for AMS Attendees in Ballroom One

1:00-5:00 **TOUR**

1:00 Buses depart Convention Center for NASA Langley or USS Wisconsin
5:00 Approximate time buses return to Convention Center

SYMPOSIUM ORGANIZING COMMITTEE

Host Chairs

James Wells, NASA LaRC

Benjamin J. Nickless, NASA LaRC

General Chairman - Edward A. Boesiger, Lockheed Martin Space

Deputy Chairman - Jonathan P. Wood, Lockheed Martin Space

Mark A. Balzer, JPL

Torin L. Bowman, NASA ARC

Earl Daley, NASA ARC

Adam G. Dokos, NASA KSC

Michael J. Dube, NASA NESC

David E. Eddleman, NASA MSFC

Carlton L. Foster, NASA MSFC (retired)

Lionel Gaillard, ESA/ESTeC

Nicolas E. Haddad, JPL

Claef F. Hakun, NASA GSFC

Louise Jandura, JPL

Timothy L. Krantz, NASA GRC

Lance R. Lininger, Lockheed Martin Space

Alan C. Littlefield, NASA KSC (retired)

Stuart H. Loewenthal, Lockheed Martin Space (retired)

Ronald E. Mancini, NASA ARC (retired)

Fred G. Martwick, NASA ARC

Donald H. McQueen, Jr., NASA MSFC (retired)

Landon Moore, NASA JSC

Brandan Robertson, NASA JSC

Justin J. Scheidler, NASA GRC

Joseph P. Schepis, NASA GSFC

Jason M. Schuler, NASA KSC

Donald R. Sevilla, JPL (retired)

Mathew R. Zwack, NASA MSFC

Caging and Release Mechanism Design for the Simplified Gravitational Reference Sensor

Joseph Footdale^{*}, Chad Sypolt^{*}, Joseph Mackin^{*}, Stephen Bennett^{*}, John Conklin^{**} and Peter Wass^{**}

Abstract

The Simplified Gravitational Reference Sensor (S-GRS) is an ultra-precise inertial sensor for future Earth geodesy missions. These sensors are used to measure or compensate for all non-gravitational accelerations of the host spacecraft so that they can be removed in the data analysis to recover spacecraft motion due to Earth's gravity field, which is the main science observable. In the on-orbit operational state, the GRS functions by sensing the state of a precision cubic Test Mass (TM) with respect to the surrounding Electrode Housing (EH) via non-contacting electrostatic distance sensing and actuation electrodes. The S-GRS Instrument approach consists of two opposing Caging Mechanism (CM) assemblies that constrain the TM for launch and release into pure freefall on-orbit such that the residual velocity is within the non-contact actuation system control authority. This paper focuses on the novel mechanism design and initial functional testing of the S-GRS CM.

Introduction

The gravity recovery missions, GRACE [1] and GRACE Follow-On [2], have provided a more than 20-year climate data record of the Earth system mass changes. These missions use interferometers to measure the separation of two satellites orbiting the Earth. GRACE uses a microwave interferometer, while GRACE FO adds a laser interferometer, improving the potential measurement sensitivity by three orders of magnitude. The current data products are limited in their quality by temporal aliasing errors. Improved mission parameters for the upcoming GRACE-C mission and its ESA partner mission, Next-Generation Gravity Mission (NGGM), may improve the aliasing problem. The main error source will then be imperfect corrections of non-inertial forces on the spacecraft measured with on-board accelerometers. To realize the precision allowed by the laser interferometer, an improved accelerometer is needed.

Figure 1 shows the total error and various contributions for the GRACE-FO mission, along with the predicted error contribution of the S-GRS [3].

The S-GRS sensor design follows that of the flight-proven LISA Pathfinder (LPF) Gravitational Reference Sensor (GRS) that represents the state-of-the-art in precision inertial sensors [4,5]. The S-GRS instrument (Figure 2) presented in this paper is essentially a scaled-down version of the LPF GRS fundamental architecture, where opposing linearly actuated grabbing fingers (GF) constraining the TM within the Electrode Housing cavity are simultaneously retracted, releasing the TM to a non-contact freefall state (Figure 3). The S-GRS Caging Mechanism mechanical design deviates from that of LPF in two primary different manners: 1) S-GRS eliminates the secondary TM launch restraint mechanism, utilizing the GF interface in a dual role of constraining the TM during launch as well as releasing the TM into the freefall state, and 2) S-GRS replaces the piezo stack actuator that controls the Release Tip (RT) internal to the GF with a passive spring. The residual translational and rotational velocities of the TM imparted by the release process need to be sufficiently low, on the order of $<4.5 \mu\text{m/s}$ and $<300 \mu\text{rad/s}$ respectively, for the non-contact electrostatic actuators to stabilize the TM. Details of the S-GRS EH design, TM sizing, and retraction release dynamic analysis utilized to support the passive spring approach were previously presented in Ref. [3].

^{*} BAE Systems, Inc., Boulder, CO; joseph.footdale@ballaerospace.com

^{**} University of Florida, Gainesville, FL

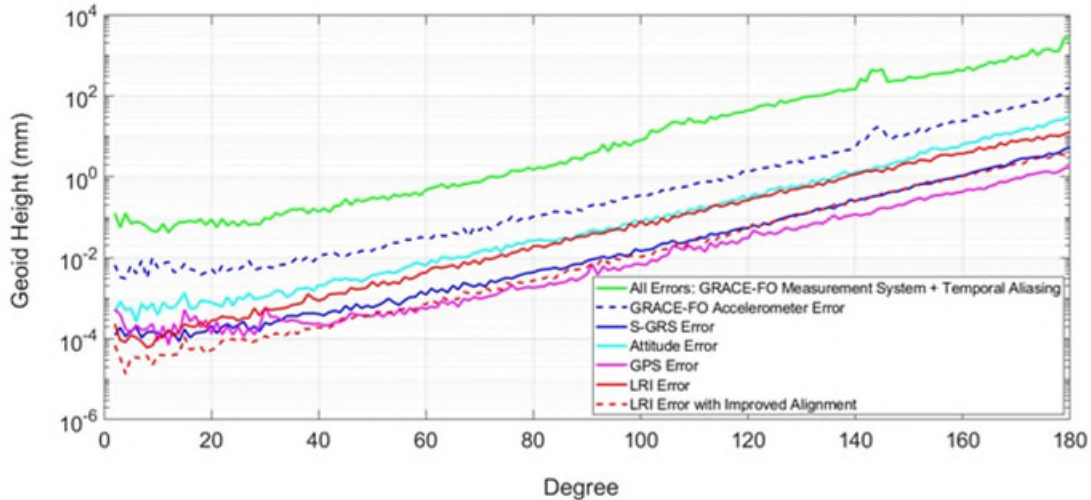


Figure 1. Various noise sources in the GRACE-FO mission. The x axis is error contribution, while the y axis is an esoteric unit: degree of the spherical harmonic of the gravity solution. This translates roughly to spatial resolution = 20,000 km/degree. Thus, $2^\circ = 10,000$ km, and $60^\circ = 333$ km. The overall uncertainty of the gravity measurement is shown in green and the driving error from the current accelerometers is shown in dashed blue. The S-GRS would reduce the accelerometer uncertainty to that shown in solid blue, bringing the mission closer to realizing the full capability of the LRI, shown in red.

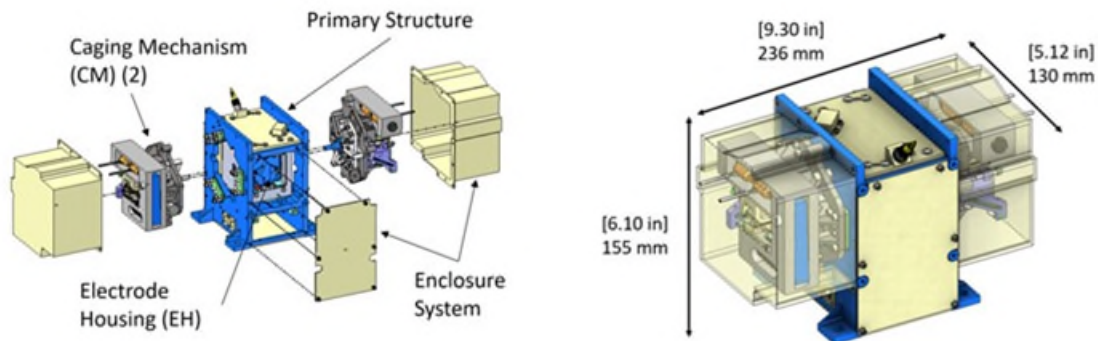


Figure 2. S-GRS Instrument primary subsystems includes Electrode Housing assembly and the opposing Caging Mechanisms.

The decision to utilize the GF for both the launch constraint and subsequent release operations was primarily motivated by the desire to minimize overall sensor volume and mass to be compatible with future geodesy missions implementing small satellite platforms. Integration of S-GRS into the space vehicle cannot deviate substantially from current solutions [6] to be prohibitive despite its superior noise performance potential. Preliminary structural analyses of the instrument with the 54-gram, 30-mm cubic TM supports using the GF for the launch restraint is feasible. Analytically predicting this adhesion force is expected to be highly uncertain due to the material and geometric nonlinearities that are estimated to have significant contributions. It is the plan of this effort to characterize the forces required to separate the GF from the TM by test.

The adhesion forces from the combined launch preload and inertial forces are anticipated to be excessive where it is not conducive to releasing the TM within the residual velocity requirements. There is also the potential for the TM to remain affixed to one of the GF after separation of the opposing since the force from the internal RT is also not anticipated to overcome the adhesion force. To eliminate these potentially high post-launch adhesion forces, the instrument will initially go through a series of maneuvers utilizing the EH

frame as a reaction structure to individually separate the respective GF from the TM, and then re-engage with a desired low-level constraining force. After both sides complete this process, the TM is centered within the EH volume and the release procedure is initiated. This process is illustrated in Figure 4.

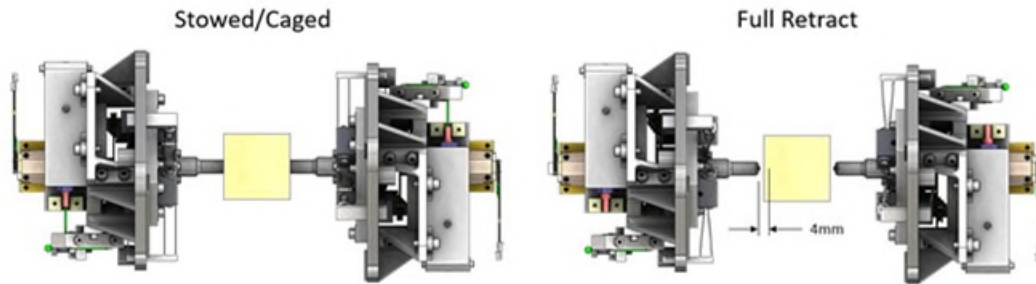


Figure 3. Opposing caging mechanisms retract 4 mm to release the TM into freefall within the EH (not shown for clarity).

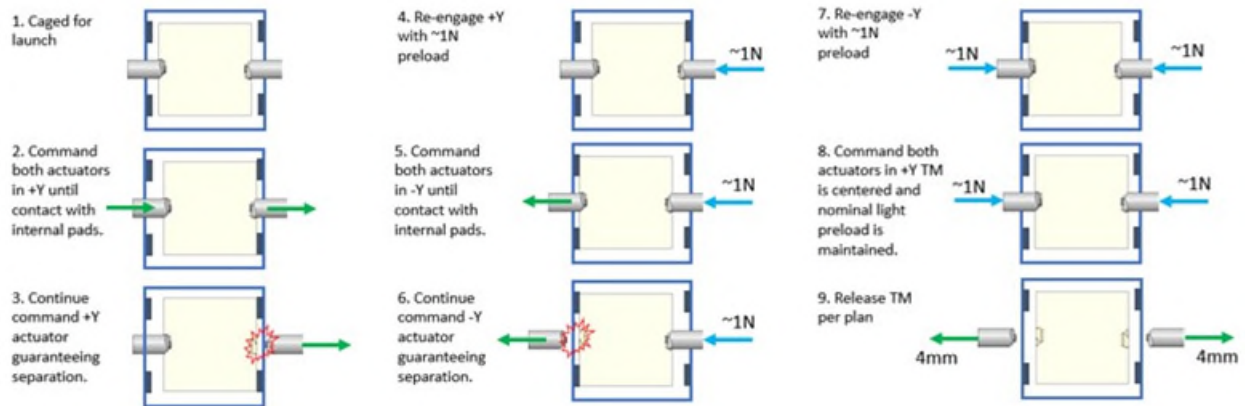


Figure 4. Baseline plan utilizes the EH interior wall as reaction structure to overcome suspected elevated adhesion forces due to launch constrain preload forces.

The identified key driving mechanism-level requirements are listed in Table 1. Top sensor-level performance requirements, such as TM linear and angular release velocities, are not included here since verification is not part of the scope for the mechanism development effort. The scope of this funded effort is to develop the design to Technology Readiness Level (TRL) 6, System/subsystem model or prototype demonstration in a relevant environment (ground or space) [7]. The full sensor shown in Figure 2 was designed and fabricated to be a flight-like prototype unit, including an electrically functional EH, with several known detailed design exceptions that are not anticipated to affect assessing the architecture design. It is planned to subject the prototype sensor to random vibration and thermal vacuum testing. TM dynamic release characterization testing with the actuator assembly components will supplement the sensor-level testing to support TRL 6 status. This paper focuses on the caging mechanism assembly mechanical design and functional testing.

Table 1. The S-GRS design meets the key driving requirements for the caging mechanism.

Requirement	Value	Compliant
Test Mass Enclosure Access	Access hole in electrode housing diameter shall be ≤ 7 mm	Yes, single 7-mm access hole per GF.
Materials	Shall not use ferromagnetic materials, lubricants	Yes, prototype uses CRES fasteners.
Launch TM preload	$820 \text{ N} \pm 80 \text{ N}$	Yes, per analysis. Test pending.
GF Retraction Stroke	$\geq 4 \text{ mm}$	Yes.
Pre-release TM preload	$1 - 5 \text{ N}$	Yes.
Pre-release TM preload accuracy	$\pm 0.2 \text{ N}$	Yes.
Release Tip Stroke	$\geq 0.05 \text{ mm}$	Yes, 1 mm.
GF Path Accuracy	$< 1400 \text{ mrad}$ [0.08 deg], tip stays within 0.01 mm of primary actuation axis	Yes, per analysis. Test pending.
Exported Shock	$< 200 \text{ g SRS}$	Expect to comply.
Capture	CM shall be able to capture TM in any location and orientation within the volume	Yes, per analysis.
Sensor Mass	$< 10 \text{ kg}$ [Goal]	8.5 kg
Sensor Volume	$< 150 \text{ mm} \times 150 \text{ mm} \times 205 \text{ mm}$ [Goal]	$130 \text{ mm} \times 155 \text{ mm} \times 236 \text{ mm}$

Detailed Mechanical Design Description

Linear Actuation Stage

A PiezoMotor LEGS® [8] actuator was selected for its precise open-loop motion, large stroke, non-magnetic material construction, and unpowered holding force capability. The actuator features a rectangular ceramic drive rod that is articulated via synchronized control of piezo elements (or legs) on opposing sides of the drive rod. Friction between the legs and drive rod enables the actuator to operate without backlash or mechanical play. This friction and the construction of the actuator are not sufficient to constrain the TM in a vibrating launch environment if directly coupled, even if the unpowered holding force capability exceeds the launch loads. There is also potential for the drive rod to exhibit excessive transverse motions that may re-contact the TM when retracting [5,9]. A flexure stage was designed to have relatively high stiffness in 5 degrees of freedom (DOF) to achieve the linear path accuracy requirement and compliant in the axial translation such that the piezo actuator can articulate greater than 4 mm with sufficient motorization force, currently calculated margin of 180%. The piezo actuator is coupled to the path flexure via a coupling flexure, such that transverse loads and moments are minimized. These drive components are shown in Figure 5 and Figure 6. The sectioned view of Figure 5 also shows the in-line force sensor used as the primary feedback mechanism to apply the desired low-level preload to the TM prior to the on-orbit release operations. It can also be utilized to infer gross actuator position with calibration to the flexure reaction force versus displacement relationship. The planned concept of operations currently does not rely on precise (sub-micron) absolute position knowledge. If it is found that the positional hysteresis and drift inherent to piezo-based actuators poses operational issues with the achievable resolution and accuracy of the load cell, then an additional displacement sensor such as a linear encoder can be added.

Radial Clamp Assemblies

As mentioned above, the primary linear guide flexure was designed to yield stable and precise linear motion of the GF body over the full 4-mm retraction stroke. For the GF/flexure body to function as the launch restraint mechanism, it needs to be capable of reacting the loads in all 6-DOF. Ideally only the compliant axial translation DOF would need to be constrained, relying on the relatively high stiffness of the remaining 5-DOF to yield acceptable system-level structural performance. This was not achievable with the selected

flexure architecture subject to the stroke and force margin requirements. A radial arrangement of three clamping subassemblies (Figure 5) were integrated to constrain the GF body, providing the primary load path from the GF interface with the TM through the primary instrument structure.

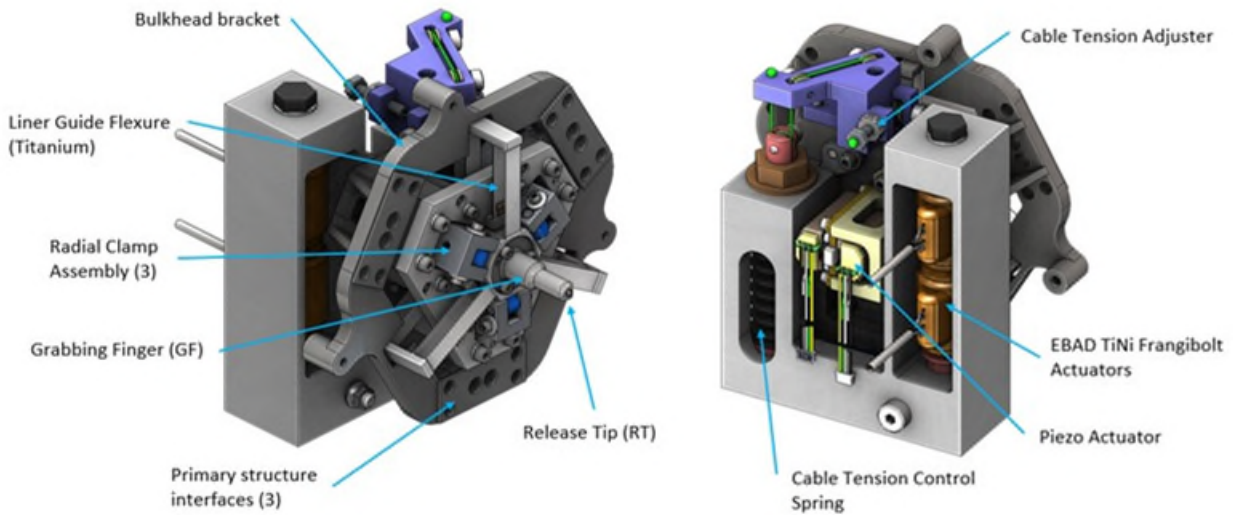


Figure 5. Caging Mechanism assembly component identifications.

The function of the radial clamp assembly is illustrated in the sequence shown in Figure 6. Each clamp assembly consists of an independent bracket with a pivoting arm passively driven to the open/released state by an internal compression spring. The pivot arm has a machined cylindrical feature that interfaces with a grooved feature machined into the central GF body. The pivot arms are preloaded against the GF body using a tensioned Vectran™[10] braid routed circumferentially. Post launch, the Radial Clamp Release Mechanism, shown in Figure 5 and described further below, releases the tension in a slow and controlled fashion with sufficient stroke to allow the radial clamp pivot arms to fully articulate away from the GF body. In this state, the piezo actuator now has position control authority of the GF body.

The machined groove feature on the GF body varies from one CM assembly to the opposing. On one side of the mechanism, the launch lock arms engage v-grooves on the GF body. When the locks are engaged, that GF body is fully fixed in all 6-DOF. On the opposing side, the arms engage with one-sided ramps such that they try to force the GF body to translate towards the test mass. A comprehensive assembly and preload application plan has been developed, only briefly summarized here. The CM with the v-groove features and radial clamps engaged (designated CM1) is mounted within the instrument structure. The TM is held in nominal contact on the GF tip of CM1. CM2, with the one-sided ramp features, is then carefully positioned to nominally engage the opposing side of the TM. The preload cable of CM2 is tensioned to the pre-determined level, where the load path translates to the desired preload on the TM.

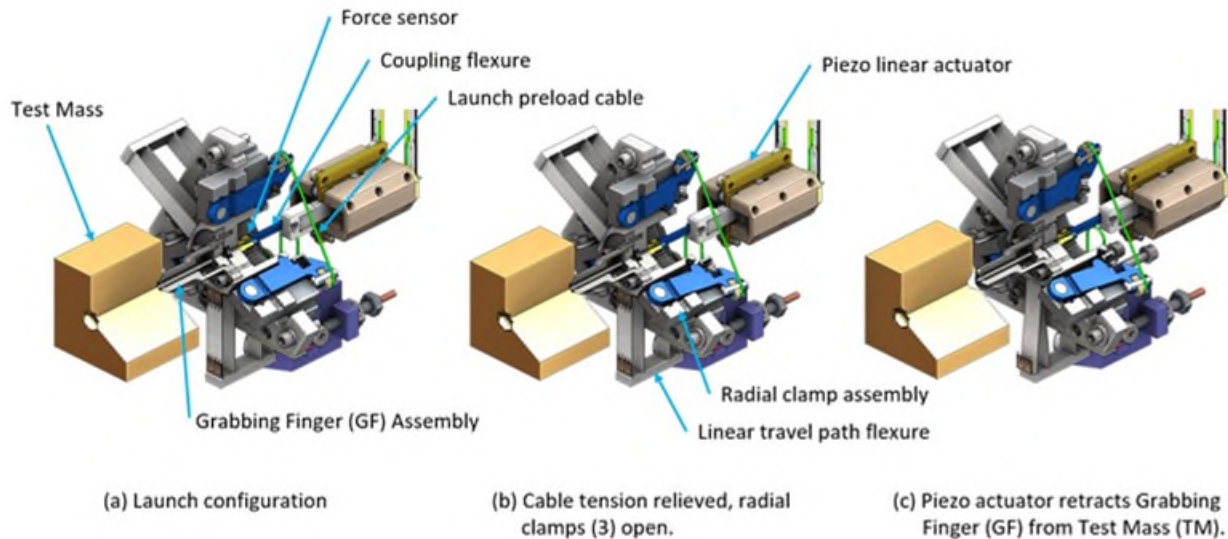


Figure 6. Partial sectional view of caging mechanism subassembly tensions a circumferential cable to constrain the GF body for launch. The cable tension is released with sufficient stroke for radial clamps to open, allowing the piezo actuator to articulate the GF body.

Radial Clamp Release Mechanism

The axial preload between the GF and TM must be controlled to a stable constant value. To achieve this, the launch lock cable tension is maintained by a compression spring. The relatively low stiffness of the spring compared to the rest of the mechanism components results in a cable tension that is insensitive to thermal deformations and cable creep effects. The release mechanism subassembly in the tensioned/stowed state and actuated/released state is shown in Figure 7.

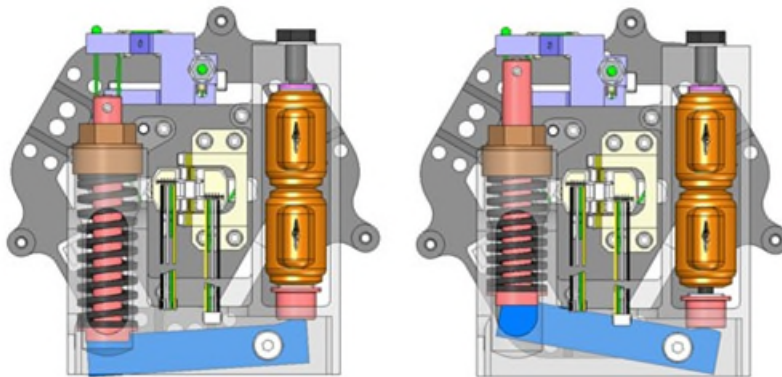


Figure 7. Radial Clamp Release Mechanism in the stowed and actuated/released states.

The magnetic cleanliness requirement precluded the use of electromagnetic actuators such as motors to control the release of the launch lock cable. The need for a “shock-free” release and the desire to avoid a loose cable after release precluded the use of a cable cutter actuator or similar device that would instantaneously eliminate cable tension. It was desired to slowly remove cable tension in a controlled manner, and further articulate creating sufficient slack to allow the radial clamp arms clear the GF body. High Output Paraffin (HOP) actuators were an attractive solution for this mechanism; however, a survey of available HOP actuators concluded that a HOP actuator with the necessary work output would be too large to fit in the S-GRS envelope. Therefore, another solution had to be developed. It was found that the most “work-dense” actuators readily available that met the magnetism goals were EBAD TiNi Frangibolt actuators

[11]. These high-force output actuators are typically used to break metallic fastener coupling the deploying structure to the static via tensile elongation. The high force is achieved through expansion of the internal shape memory alloy material going through phase transformation when power is applied, which occurs over timeframe on the order of 30-60 seconds. The actuator expansion (stroke) is orders of magnitude less than what is required to release the radial clamps. After some design iteration, the selected configuration consisted of two Frangibolt FC3 actuators in series. This provided approximately 1.8 mm [.072 in] total linear travel (0.9 mm [.036 in] from each actuator) and approximately 1260 N [5600 lbf] of force output. A lever arm with a 5.7:1 ratio is utilized to amplify the actuator stroke to achieve the needed articulation. A pulley arrangement yields an additional 2:1 mechanical advantage resulting in total cable travel of 21 mm [0.82 in].

Mechanism Functional Testing

Path Flexure and Grabbing Finger Release Tip Characterization

The following section shows the methods and results of the characterization of the guide flexure spring force over the travel extent of the actuator, and the release tip spring force relative to the displacement of the release tip. The details of the force curve resulting from the mating of the grabbing finger into the test mass detents during recapture operations will be explored in future testing campaign at a forthcoming phase of the program.

The guide flexure characterization testing was performed at the subassembly level, with the actuator, guide flexure, load cell, integrated into mechanism frame. The guide flexure characterization data is of interest as a calibration table to convert load cell data to position of the actuator, so actuator position knowledge can be found without the use of a position encoder. The mechanism inline load cell was monitored, and actuator displacement was observed using a dial indicator. The test configuration is shown in Figure 8. The actuator travel zero location was defined as where the load cell value was zero when the mechanism was in the horizontal, or gravity offload, orientation. The mechanism was returned to the vertical orientation, and the actuator was moved over the extent of 1-mm [0.04-in] inboard, and 4-mm [0.16-in] outboard.

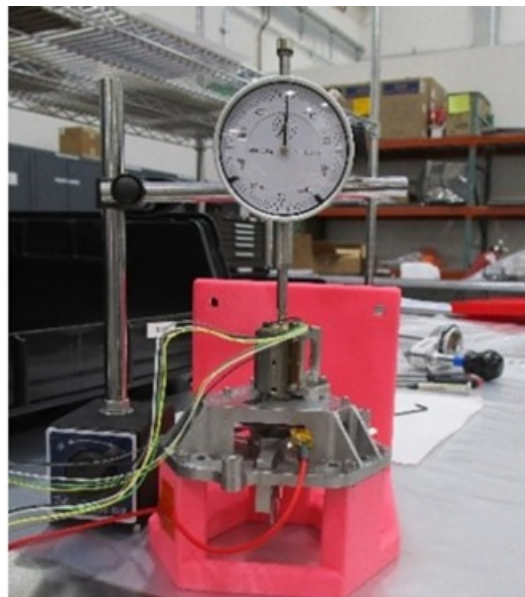


Figure 8. Guide flexure characterization test configuration.

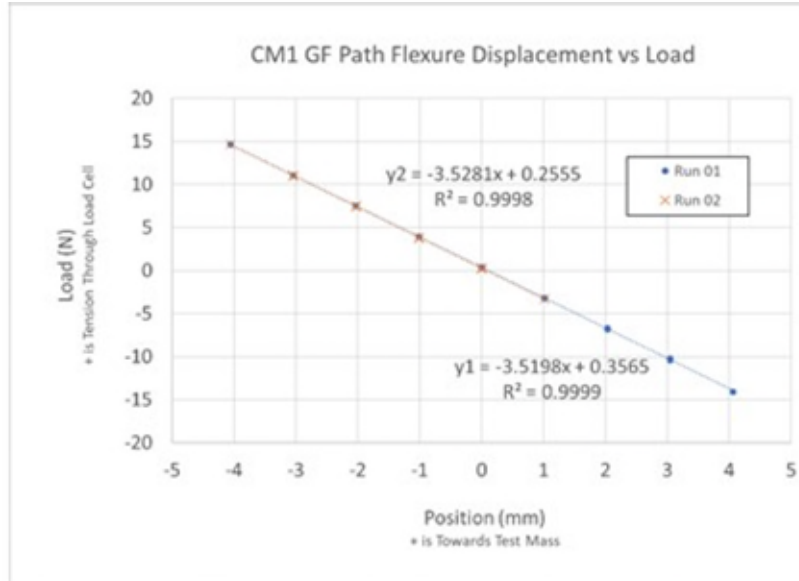


Figure 9. Guide flexure force vs displacement characterization results.

Test results from the guide flexure characterization, shown in Figure 9, show a linear spring rate over the travel distance of interest with a calculated spring rate of 3.52 N/mm [20.1 lbf/in] from linear regression. An offset at the zero location is due to gravity loading of the suspended mass of the guide flexure and grabbing finger. The guide flexure characterization test data was repeatable to within the accuracy of the manual dial indicator. Future characterization of the GF tip path profile to assess compliance with the path accuracy requirement will implement a displacement transducer with suitable accuracy, such as a laser displacement sensor.

The release tip flexure characterization testing was performed at the subassembly level with the same mechanism components used in the guide flexure testing. The release tip characterization test was set up to use the load cell and the guide flexure calibration table to calculate the displacement of the actuator. The release tip was compressed by pressing the grabbing finger and release tip assembly into a hard stop while recording the mechanism inline load cell value. The test configuration is shown in Figure 10. Engagement of the release tip onto the hard stop was clearly observable by a change in the slope of the displacement vs load curve. Spring force of the release tip was calculated from the difference in force between the extrapolated force curve due to the guide flexure, and the observed force curve of the release tip plus guide flexure.

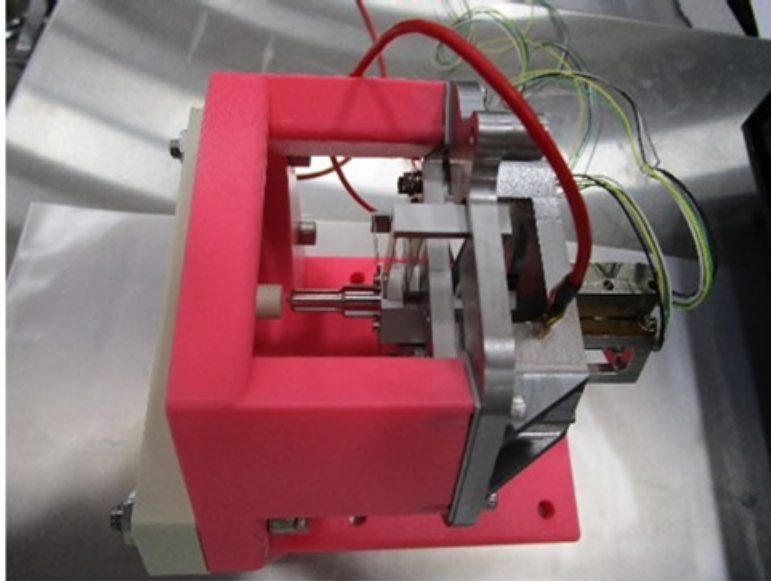


Figure 10. Release tip characterization test setup.

The RT stiffness characterization test was performed five times. A representative plot of the load versus calculated actuator travel is shown in Figure 11. Testing results show the release tip flexure spring rate ranged from 1.38 N/mm to 1.69 N/mm. Taking the minimum observed stiffness value translates to an available force of 0.32 N from the release tip at a compression of 0.23 mm [0.009 in]. The release tip spring force is designed to overcome the adhesion force between the test mass and the grabbing finger mating surfaces. If future adhesion testing between the grabbing finger and the test mass show adhesion levels are greater than the available 0.32 N generated by the release tip, the release tip can be redesigned with additional flexures placed in parallel to the original two as a way to increase force margins.

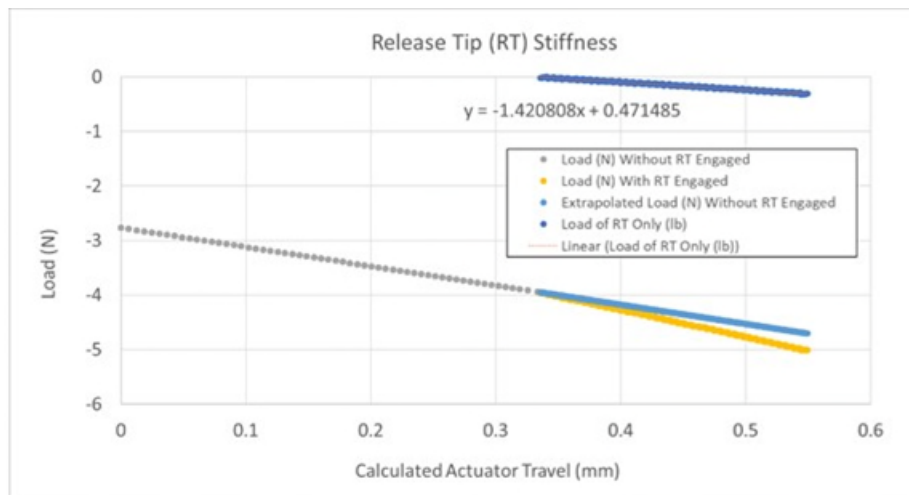


Figure 11. Test data from release tip characterization run. The bottom plots show measured test data, and extrapolated force data without the release tip engaged. The top plot shows the calculated release tip spring force data.

Release Cable Development and Lessons Learned

The Vectran cable used in the mechanism as part of the cable clamp assembly required development of a cable stop technology. The low resistance of cutting of the fiber cable material proved that an original knotted cable end was insufficient to carry the working load required and the cable failed at the base of the

knot in testing. Three different copper cable stops were designed and evaluated to replace the knot. The three copper cable stop designs were built and evaluated for strength are: a partially crimped thick wall stop with epoxy bonding, a fully crimped thick wall stop with epoxy bonding, and a thin-walled stop with epoxy bonding and integrated mounting surface. The copper cable stop hardware is shown in Figure 12.

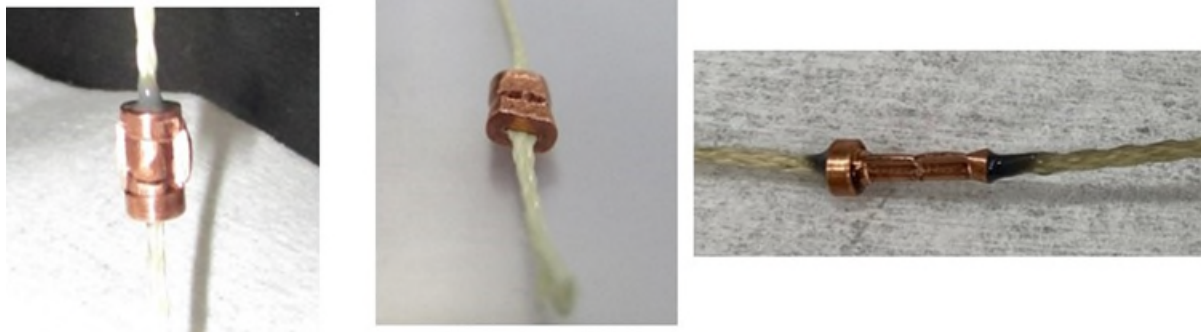


Figure 12. Copper cable stops evaluated for the CRM cable assembly. The thick, lightly crimped and bonding cable stop shown to the left, the thick fully crimped and bonded cable stop shown in the center, and the thin-walled stop with epoxy bonding and integrated mounting surface shown to the right.

The three cable stop designs were integrated into a cable assembly, installed into a tension testing station that represents the EDU cable mounting and tensioning device, then pulled to failure. Results from the testing are shown in Table 2.

Table 2. Ultimate strength and failure mode of the three different cable assembly designs.

Cable stop configuration	Minimum Cable Breaking Strength (N)	Failure mode
Thick walled, crimped and epoxy bonded	151	Cable pull through, adhesion failure of epoxy to copper stop
Thick walled, crimped to flat, and epoxy bonded	222	Cable cut at end of fitting
Thin wall with receded mounting head, epoxy bonded	386	Cable break on tension side near epoxy joint.

The thick and lightly crimped stop failed via an adhesion failure between the epoxy, and the copper stop, resulting in the epoxy being pulled out of the stop in full as a cylinder, indicating the ID of the copper stop was not deformed during the crimping process.

The second copper stop design used the thick-wall stop with an epoxy bonded joint, but increased clamping force on the crimp to pull the ID of the stop against the cable. Testing of this crimping approach showed that the end of the stop creates a significant stress concentration of the cable where it enters the stop, likely due to the sharp edge of the stop. This design is highly process dependent as the crimping effort and significantly impacts the stress concentrating at the end of the stop depending on the axial position of the crimp.

The third stop design, the thin-walled third design with the mounting surface and epoxy bond, was designed to eliminate the incomplete crimp of the first stop design, and the stress concentration that occurs at the end of the second stop design. The new stop design has a reduced OD in the crimp section that can accommodate two crimps with a small uncrimped section in between to key lock in the epoxy joint, and a full diameter mounting flange with an epoxy filled counter bore to eliminate contact of the cable to the edge of the stop at the mounting surface. The updated cable stop geometry proved to be the strongest design

with the most repeatable assembly process, providing a minimum of 53% of the filament ultimate strength. Design details are showing in Figure 13.

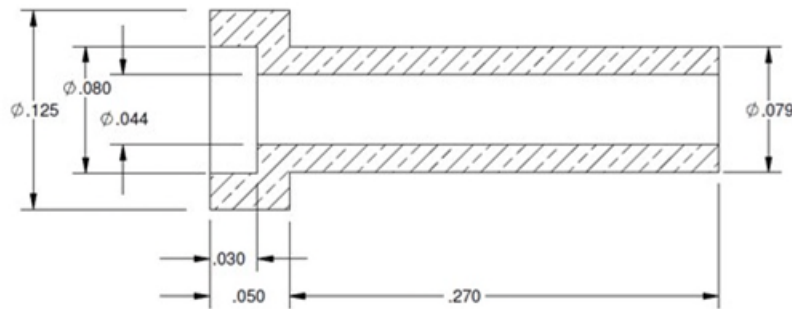


Figure 13. Cable stop design details. Cable stop mounting surface shown to the left with counterbore to prevent contact with the cable; crimping area shown to the right. Assembly has the cable passing through the stop, epoxy filling the free space and the counter bore, and two crimps placed into the thin section with a small gap between the crimp location to provide a keyway fit of the epoxy inside the stop.

Release Cable Material Creep Mitigation

The Vectran cable material is subject to elongation of up to 2% at the max working load. The mechanism architecture can overcome settling of the cable system due to the spring in the design, maintaining cable tension if slight lengthening of the cable occurs over time. To minimize risk of the cable stretch inducing large enough stretch that the spring tension plunger can exceed the travel allocated for creep, set at 0.33 mm [0.013 in], the cable was pre-stretched to cause the cable to reach the full stretched length before installation into the mechanism.

A small testing campaign was executed to identify the correct cable tension and duration to apply to the cables to pre-stretch the cable. A test fixture comprising of a short, 20-cm (8-inch) cable assembly with two cable stops, a load cell, and a cable tension screw was assembled in line. Testing showed that pre-stretching the cable with a tension of 177.9 N [40 lbf] for 15 minutes resulted in negligible additional creep when subsequently tensioned to the nominal design load of 142 N [32 lbf] over a 24-hour observation period. The test was repeated at 266.9 N [60 lbf] of tension for 15 minutes, also showing zero measurable deflection of the tension spring when the tension was dropped to the 142 N [32 lbf] operating cable tension for the mechanism and allowed to dwell for 24 hours. Qualitatively, the cable was observed to become slightly stiffer after the pre-stretching operation. From the test results, a pre-stretch tension of 200 N [45 lbf] for a duration of 30 minutes was selected to be applied to the EDU cable assemblies to reduce risk of the Cable Release Mechanism exceeding the 0.33-mm (0.013") allowable travel spring plunger travel allocated for settling of the cable and mechanism; test results suggest that zero settling should occur due to cable creep.

Future Planned Testing

At the time of writing this paper, two additional testing efforts are planned to characterize the operation of the mechanism. A launch preload characterization effort that confirms the calculated axial force generated to the grabbing finger from the cable release assembly, and a cable release functional test that verifies full release of the grabbing finger assembly from the launch lock device.

Launch Preload Characterization Testing

The launch preload characterization testing effort will evaluate the effectiveness and stability of the cable release mechanism to convert string tension into axial force at the grabbing finger, identify the creep in the mechanism over time, and to observe the mechanism response axial loads equal to those expected from the test mass under future vibration testing. The test will be conducted using an Instron tensile and

compression testing machine which provides calibrated axial compression load and precision displacement knowledge.

The fully assembled mechanism will be prepared for testing by ensuring the cable tension device, used to tighten the clamping bars against the ramps in the guide flexure, is at the full relaxed position. The mechanism will be installed into the test fixture, shown in Figure 14, and installed into the Instron machine.

Cable release mechanism string tension will be calibrated to axial force first by bringing the Instron load cell into contact with the grabbing finger and secured in place. The cable tension mechanism will be tightened to exert force on the Instron load cell. Cable tension and the resultant applied load will be increased until applied load reaches 898.5 N [202 lbf] as measured by Instron machine. The UUT will then be evaluated for creep of the applied load by dwelling for 24 hours and recording the final applied load values.

The displacement response of the mechanism to predicted inertial load generated by the test mass on the grabbing finger during vibration loading will occur after creep testing is complete. The 822-N [185-lbf] predicted initial load will be applied to the UUT by the Instron machine and the displacement of the load cell, and resulting mechanism, will be recorded. Near zero deflection is expected to be observed in response to the application of the predicted internal load.

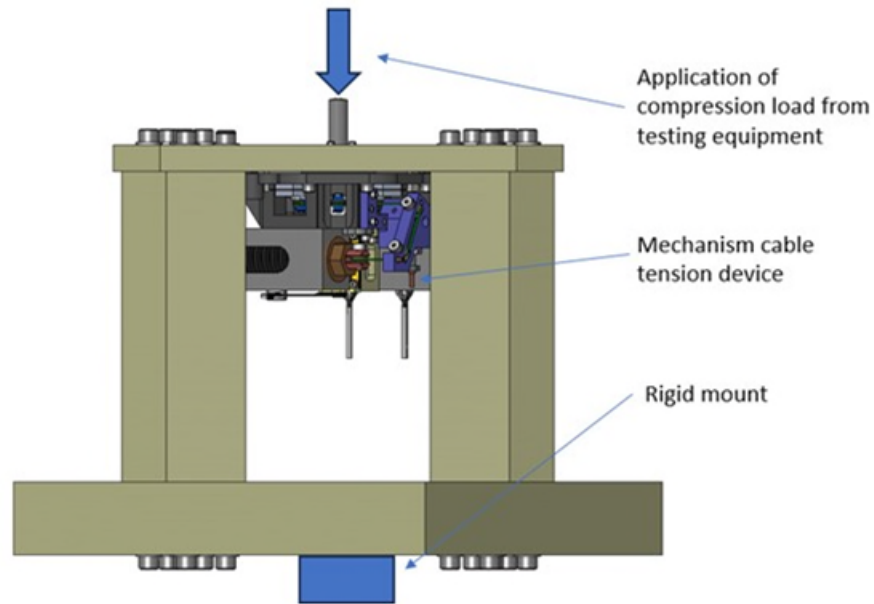


Figure 14. Launch preload characterization testing fixture with mechanism installed.

Cable Release Functional Test

The cable release testing is designed to verify the launch restraint system can be released while under operational loads. The test will consist of installing the mechanism into a test fixture with the cable tension device in the relaxed position, tightening the cable to the operational cable tension, then exercising the Frangibolt actuators to release the restraint mechanism. This setup is shown in Figure 15. The load cell internal to the mechanism will be observed for force response before, during, and after exercising the restraint release operation; the actuator will then be retracted to ensure unrestrained travel of the grabbing finger over the operational range.

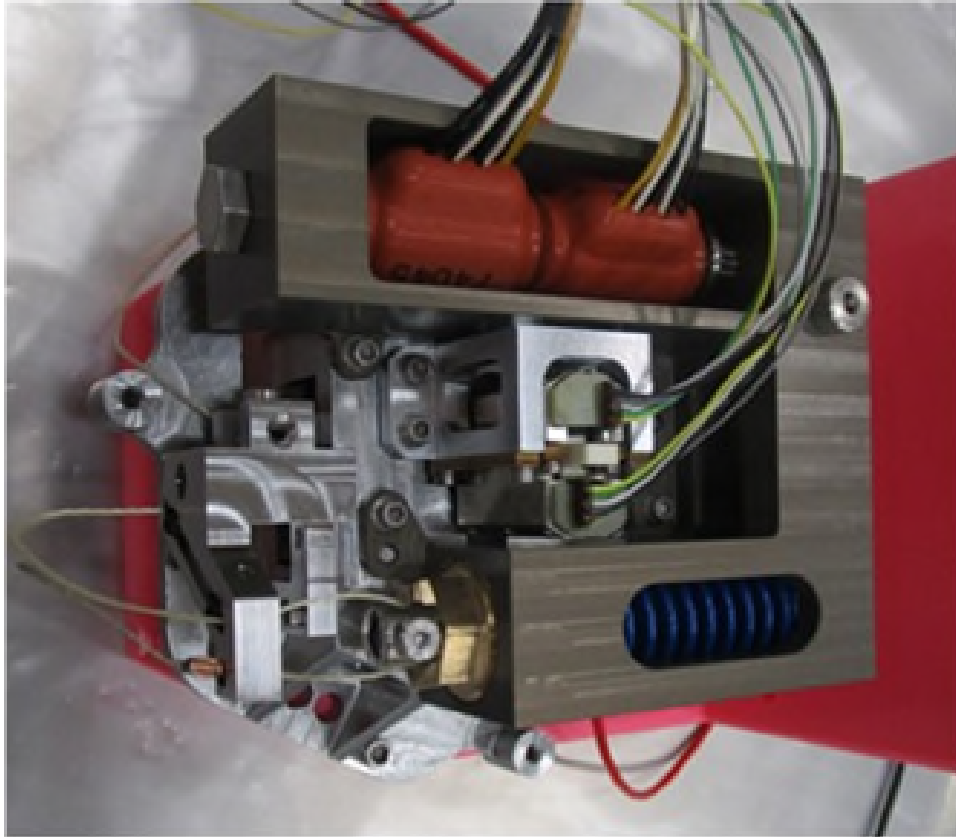


Figure 15. Fully assembled CM during integration of radial clamp tensioned cable.

Conclusions

The current S-GRS development effort designed and fabricated a novel flight-like mechanism prototype to support achieving a Technology Readiness Level of 6 for the full sensor system shown in Figure 2. This is expected to be achieved through future planned testing and analysis upon completion of the functional testing described in this paper. Key aspects that remain to be verified include the utilization of the GF body as the primary launch load restraint and the passive spring release tip. Previous extensive experience of precision mechanism design, coupled with the preliminary structural analyses performed during the mechanism conceptual design trade and architecture selection, support the mechanism will achieve the primary objectives. It was concluded from a technical and schedule risk assessment that fundamental architecture could not be confidentially verified through focused component-level testing, rather should be conducted with the major subassemblies and integrated system. In the event testing shows the test mass cannot be adequately restrained by the opposing grabbing fingers, it is envisioned that the guide flexure driven by the piezo actuator would remain relatively unchanged, and the cable release mechanism could be adapted to control the release of spatially separate constraints on the test mass.

References

1. Tapley B.D., Bettadpur S., Watkins M., Reigber C., "The gravity recovery and climate experiment: Mission overview and early results.", *Geophysical Research Letters* 31(9), DOI <https://doi.org/10.1029/2004GL019920>, 2004.
2. Sheard B., Heinzl G., Danzmann K., Shaddock D., Klipstein W., Folkner W., "Intersatellite laser ranging instrument for the grace follow-on mission." *Journal of Geodesy* 86, DOI 10.1007/s00190-012-0566-3, 2012.
3. Dávila Álvarez, A., Knudtson, A., Patel, U. et al. "A simplified gravitational reference sensor for satellite geodesy." *J Geod* 96, 70 (2022).
4. Bortoluzzi, D., Vignotto, D., Zambotti, A., et al. "In-flight testing of the injection of the LISA Pathfinder test mass into a geodesic." *Advances in Space Research*, Vol. 67, 2021.
5. Bortoluzzi, D., Vignotto, D., Dalla Ricca, E., Mendes, J.. "Investigation of the in-flight anomalies of the LISA Pathfinder Test Mass release mechanism." *Advances in Space Research*, Vol. 68, 2021.
6. Christophe, B., Boulanger, D., Foulon, B., Huynh, P.-A., Lebat, V., Liorzou, F., and Perrot, F., "A new generation of ultra-sensitive electrostatic accelerometers for GRACE Follow-on and towards the next generation gravity missions," *Acta Astronautic*, Vol. 117, 2015.
7. NASA Technology Readiness Levels, <https://www.nasa.gov/directorates/somd/space-communications-navigation-program/technology-readiness-levels/>, Last Checked 02/27/2024.
8. PiezoMotor LEGS® Linear Actuators, <https://piezomotor.com/technology/>, Last Checked 03/05/2024.
9. Tomasi, M., Dalla Ricca, E., Vignotto, D., and Bortoluzzi, D., "Development of a dynamical model of a release mechanism for in-flight performance prediction," *Advances in Space Research*, Vol. 72, 2023.
10. Vectran™ <https://www.vectranfiber.com/>
11. Ensign-Bigford Aerospace and Defense (EBAD) TiNi™ Frangibolt® Actuator, <https://www.ebad.com/tini-frangibolt/>, Last Checked 02/19/2024.

Development Plan of the Upgraded Release Mechanism for the LISA Space Mission

Carlo Zanoni^{*}, Daniele Bortoluzzi[†], Davide Vignotto[†], Matteo Tomasi[†], Edoardo Dalla Ricca[†], Abraham Ayele Gelan[†], Francesco Marzari[†], Paolo Radaelli[‡], Riccardo Freddi[‡] and Alessandro Paolo Moroni[‡]

Abstract

One of the single point of failures of the LISA mission, the first gravitational observatory in space, is the transition phase of the instrument between the launch-lock configuration and science operations. This phase relies on dedicated mechanisms that inject the observatory end-mirrors, 1.92-kg gold-platinum alloy test masses, in a geodesic trajectory.

Several technologies of LISA were tested between 2015 and 2017 in the LISA-Pathfinder space mission. This latter project highlighted anomalies in the injection phase of the test masses. These anomalies are the focus of a delta-design phase relying on flight data analyses and on-ground tests, as described in this paper.

Introduction

Release mechanisms are crucial devices for the success of space missions. In LISA, the first gravitational-waves observatory in space [1] [2], the grabbing positioning and release mechanism (GPRM) is responsible for setting all the test masses (TMs) in the free fall condition necessary for starting science observations. This mechanism is considered a key equipment for the success of the entire space mission since it is a single point of failure.

The measurement approach of LISA involves three pairs of 1.92-kg AuPt cubic test masses subjected almost exclusively to planetary gravitational forces. These TMs are housed within three spacecraft forming a triangular configuration with sides approximately 2.5 million kilometers in length. The relative distances between TM pairs, housed in different spacecraft, are affected, among other modeled effects, by the passage of gravitational waves.

Each TM is the core of a payload known as the gravitational reference system (GRS) [3]. The GRS provides the TM with a low-noise vacuum environment and performs actuation and sensing functions in all its degrees of freedom. The TM is enclosed within an electrode housing (EH). Due to the substantial gaps between the TM and the EH walls (ranging from 3 to 4 mm) and the TM's significant mass, leaving the TM unrestricted during launch is not feasible. To prevent damage, a caging launch-lock mechanism is employed. However, this mechanism, while exerting high force on the TM at launch, cannot re-lock and re-release the TM in a manner compatible with the stringent requirements of the spacecraft-TM position and attitude control system.

A dedicated release mechanism, the GPRM, was thus developed. This device, Figure 1, actuates two opposed plungers that grab the TM and center it within the EH, thanks to a form fit between the plunger

^{*} National Institute for Nuclear Physics (INFN) and Department of Industrial Engineering, University of Trento, Italy

[†] Department of Industrial Engineering, University of Trento, and the National Institute for Nuclear Physics (INFN), Italy

[‡] OHB Italia SpA, Italy

heads and two indents machined on the TM faces. Two smaller tip-shaped end effectors (0.8 mm in diameter), actuated independently inside the plungers, are adopted to perform the final TM release into free-fall. Thanks to the mechanism symmetry, the TM is ideally set free with a velocity relative to the spacecraft that approaches zero.



Figure 1. Rendered view of the LPF GPRM.

The GPRM underwent intense testing both on-ground and in LISA-Pathfinder (LPF), a space mission conducted between 2015 and 2017. During these operations, an anomaly was detected in the TM velocity after release, leading to some failures.

The anomalies have been analyzed, identifying the role of various contributions such as:

- Cold welding (or adhesion) between the TM and the release-dedicated GPRM end effectors (tips)
- Actuation delay between the two nominally symmetrical halves of the GPRM at the release
- Electrostatic attraction between the TM and the plungers
- Anomalous motion of the GPRM plungers, due to internal friction.
- Mechanism vibrations at the quick actuation of the release tips
- Fabrication, alignment and integration tolerances

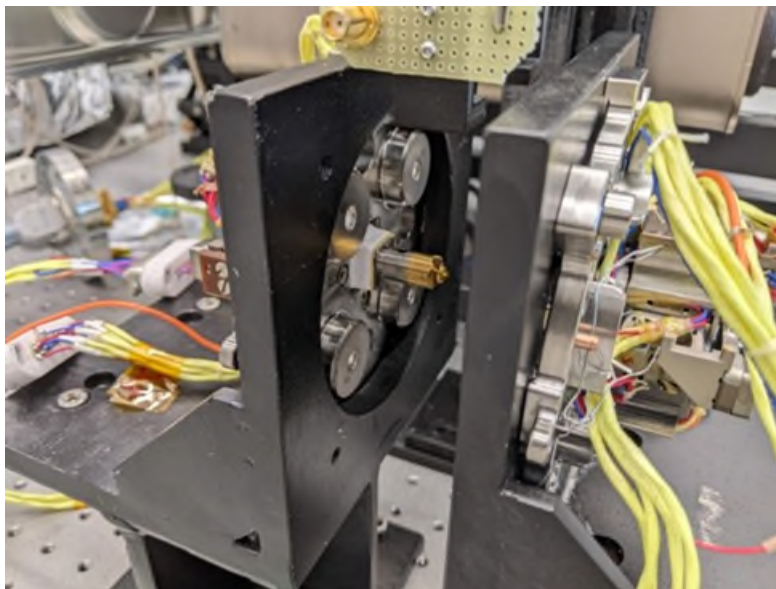


Figure 2. View of the EQM of the LISA-Pathfinder GPRM used for preliminary on-ground tests for LISA.

The unexpected behavior encountered in LISA-Pathfinder has been thoroughly studied [4] [5] and is the basis of the delta-development of the GPRM, funded by ESA and ASI, in the perspective of the LISA mission. The activities are under the responsibility of OHB Italia SpA with the support of the University of Trento and the Istituto Nazionale di Fisica Nucleare (National Institute for Nuclear Physics, INFN).

In the framework of the LISA mission project, a crucial constraint is that the exceptional science performance of LISA-Pathfinder needs to be replicated. To do so, there is a heritage requirement that calls for a design of all the systems hosted inside the GRS that is as close as possible to the one flown in LISA-Pathfinder. For this reason, on one side a nominal in-flight behavior is requested for the GPRM release function, on the other side the design freedom for the updated GPRM is very limited and requires motivated and carefully tested delta-developments.

To explore some possible improvements, we are running breadboard tests that guide us in implementing some design updates that we have identified. The GPRM is a rather unique mechanism, with tight requirements and micrometric precision goals. The development of the LISA's GPRM is presented in this work and requires us to perform detailed analysis and tests, strictly based on the lessons learnt from LISA Pathfinder.

The presentation starts from the mechanism performance in LISA-Pathfinder, summarizing the criticalities and the proposed design improvements. The mechanism development philosophy is then discussed, in the current status of the LISA design, based on GPRM breadboard and engineering models and related testing activities.

The GPRM in LISA Pathfinder

The GPRM is designed to perform the following functions:

- hold and center the TM once the one-shot launch-lock mechanism is retracted or when operational needs arise (i.e., system transition to safe mode).
- re-position the TM inside the EH.
- remove any mechanical constraint and leave the TM free, with position, attitude and velocities that are controllable by the EH electrostatic actuators, that exert forces/torques in the order of $\mu\text{N}/\text{pNm}$.

In LPF the maximum velocities set by requirements were $5 \mu\text{m/s}$ linear and $100 \mu\text{rad/s}$ rotational, for all the axes.

The GPRM is a pair of linear actuators that engage the TM on the +z and -z faces, where two pyramidal indentations are machined, Figure 3. The GPRM plungers are slightly different: one of them has a pyramidal-shaped head and the other one has a conical-shaped head, which is axial-symmetrical. This asymmetry allows the mechanism to align rotationally the TM on the pyramidal plunger reference surfaces. Most of the GPRM is made of titanium alloy, with some components in aluminum. The parts that enter the EH are either made of gold or gold coated, to comply with specific LISA requirements.

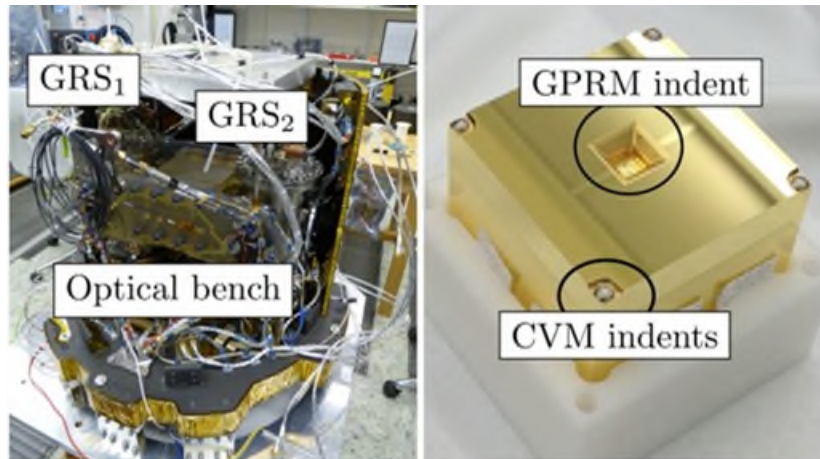


Figure 3. Left: view of the LISA-Pathfinder payload during assembly integration and testing. Two GRSs, each one with a TM inside, are located on opposite sides of a Zerodur structure hosting an optical bench. Right: LPF TM. The indentations are the interfaces with the caging mechanisms.

The plunger is attached via flexures to a titanium component called linear runner, whose motion is commanded by a customized piezo-electric PI NEXLINE walking actuator. The off-axis (or “lateral”) motion of the linear runner/plunger is constrained on the x-z plane, Figure 5, by a set of side-guides, with sliders on the -x side and a pair of rollers on the +x side. On the y-z plane the constraint is provided by the legs of the piezo-walker.

The rollers are installed on a cart which is connected to the frame through a washer spring, with a nominal 55-N force that keeps the linear runner attached to the sliders on the opposite side.

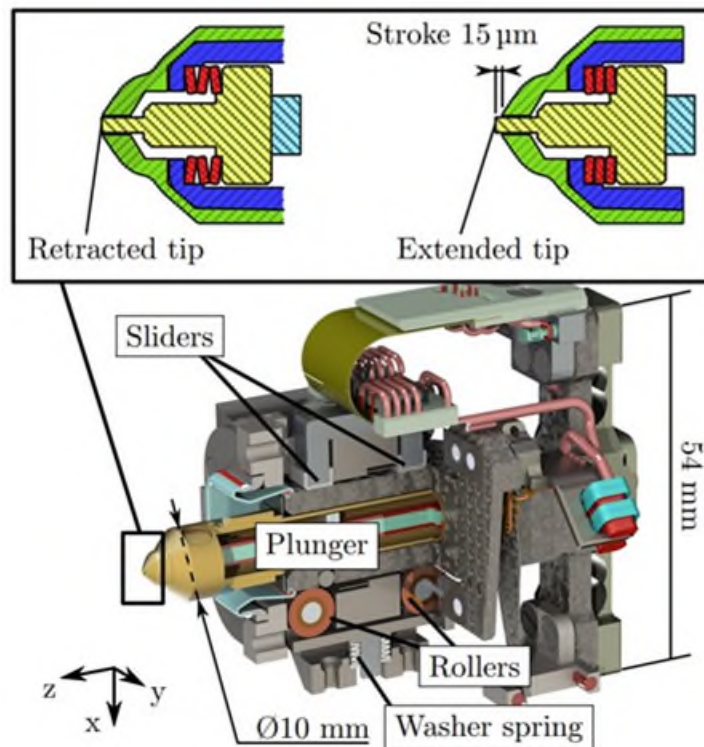


Figure 4. Open CAD view of the conical side of the GPRM.

The release-dedicated tip, coaxial to the plunger, is actuated separately by means of two cold-redundant piezo-stacks with a nominal extension of 15 μm . The function of the movable tip is to detach the plunger head from the TM prior to release, minimizing the residual mechanical contact at the release. The residual preload before the release is about 0.3 N. The GPRM CAD model is visible in Figure 4.

The requirement on the release velocities is challenging. For LPF the main concern was the adhesion between the TM and the tips' gold surfaces. This phenomenon has been widely studied and is now considered to be under control, [6]. Electrostatic effects have been also investigated and identified as contributing to less than 10% of the release velocities [7].

The LPF in-flight anomaly

During the nominal mission period of LPF, the release procedure did not produce controllable TM states in any of the releases performed (6 for TM1 and 5 for TM2). This means that not only the velocity was above the requirement (5 $\mu\text{m/s}$), but also that the control system was not able to capture the TM and bring it to a quiet condition in the EH center. In fact, these high velocities were exacerbated by an undesired actuation crosstalk effect when the TM was far from the EH center.

Table 1. TM releases performed in LPF.

Number of releases		
Date	TM1	TM2
May 2016	2	1
Sept. 2016	1	1
Oct. 2016	1	1
Jan. 2017	1	1
April 2017	1	1

A back-up release strategy, involving manual operations, was then adopted for the releases. This strategy consisted of not actuating the release tips but rather releasing the TM by retracting the plungers. This strategy still produced high TM velocities, but this time the TM kinetic energy was damped by impacts with the plungers that remained close to the TM (few hundred microns). Besides, the electrostatic control forces were activated, via dedicated commands from ground, only when the TM was in a region close to the center of the EH to avoid the undesired crosstalk.

Such a procedure relied on a handmade sequence, and it is not practical in LISA, due to the larger time-delay in the commands exchange. For this reason, at the end of the LPF, during the extended mission phase, a campaign of tests dedicated to the GPRM was executed. In this campaign, the main tests focused on finding an automated release procedure that worked reliably by:

- adding the “hammering”, which consists in improving the fitting of the tips into the TM indents by moving one plunger back-and-forth by few microns prior to the release;
- slowly moving back the plungers once the tips are retracted, leaving them nearby the TM for a longer time;
- reducing the preload force on the TM at the release to 0.1 N (in the nominal procedure it was 0.3 N).

These modifications were implemented to execute the automated releases, 64 for each TM. The set of releases is divided into two subsets: releases with nominal tip retraction (quick) and releases with slow tip retraction.

Table 2 summarizes the results of the release campaign. In the table, a compliant release is a release where the TM has a state within the limits set by the requirements. The TM is defined captured if, after a time interval shorter than 30 minutes from the tip retraction, it is successfully controlled by the electrostatic force. The reliability of the automated release (percentage of captured TM) procedure is below 90% and unequal between the two mechanisms.

Table 2. Result of the automated releases of LPF, performed during the extended mission.

	Fast tip		Slow tip	
	Compliant	Captured	Compliant	Captured
TM1	77%	91%	100%	100%
TM2	0%	78%	87%	43%

Further analyses [5] performed after the mission showed that the non-compliant TM state at the release is caused by an impact with the plungers, that are close to the TM when the tips are retracted (nominal distance of approximately 9 μm) and are vibrating after the quick motion of the tips. In an on-going analysis we demonstrate that the momentum transferred during in-flight releases is consistent with the on-ground estimations if the effect of the impacts is subtracted. The impacts are thus crucial in the LPF anomaly and shall be avoided in LISA.

Delta-Development for LISA

The GRS design for LISA is specified to be an LPF rebuild, when compatible with the LISA requirements. Small incremental design changes are being considered for the GPRM to guarantee sufficient margin for an autonomous release for LISA.

The trade-offs are rather complex. On one side, we need to replicate the exceptional LPF science performance, which can be affected by changes in the design (e.g., different materials can affect the outgassing behavior of the GRS). On the other side, we need to guarantee a reliable release of the TM, considering that LISA will host six TMs and may need to perform the release also during the science phase, in a failure scenario in which the Charge Management System does not work, a re-grab and release is performed every couple of weeks to discharge the TM.

In this framework, a delta development plan was conceived as part of the LISA’s GRS work. The plan is structured as follows:

1. Technology transfer (2022 – 2023). The LPF GPRM was built by RUAG (Switzerland). To transfer the ownership, both from a technical and formal point of view, ESA issued a dedicated contract to OHB Italia SpA.
2. Bread-board tests (2023 – 2024). As part of the technology transfer, possible improvements to the GPRM design were envisioned. The feasibility of two of such changes have been tested with a dedicated breadboard model.
3. Engineering model (EM) tests (2024). Following the technology transfer, the breadboard tests and the decision on the LISA baseline design, a dedicated engineering model will be built and tested towards the end of 2024. In line with the ECSS, the EM is a “flight representative model in terms of form, fit and function used for functional and failure effect verification”. The EM is not equipped with space-grade components and redundancy.

Key tools throughout the abovementioned phases have been two numerical models, described in the next sub-sections.

Numerical models of the GPRM

The model of the GPRM was built in Ansys 2022R2. It is worth noting that some geometries and materials have changed between the qualifying model (QM) and flight model (FM) of LPF. At the University of Trento/INFN we use an LPF QM, available on ground to validate the FE model. In this description we thus refer to that. The differences between the QM and the FMs are outlined at the end of this Section. The mesh of the model is shown in Figure 5, with about 200k nodes for 150k elements.

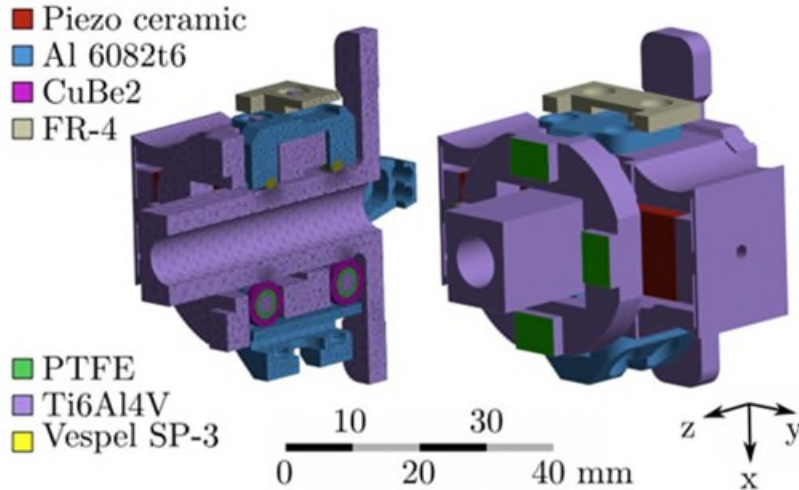


Figure 5. View of the mesh and the materials assigned on the parts of a GPRM actuator. The interface with the GRS is a flange attached at the four surfaces highlighted in green.

The interfaces indicated in Figure 6 are the external constraints of the GPRM. Internally, most of the contacts are provided with the bonded option (i.e., the nodes of both sides are mutually constrained). The interface between the sliders and the LR as well as the interfaces with and within the rollers have a dry friction behavior, with constant static and dynamic behavior. For the friction coefficients we have identified reasonable values. Concerning the sliders-to-runner interface, the following information is available:

- Vespel SP3 to steel in air: 0.17 – 0.25, according to the datasheets.
- Vespel SP3 to steel in vacuum: 0.03, according to the datasheets.
- Vespel SP3 to titanium in air and vacuum: 0.3, according to unpublished tests run during the LPF campaign.

We include the friction against steel because it is the only reliable information we had on a Vespel SP3 to metal interface and because it explains why this material was used initially in LPF.

Material	Density	Young modulus	Poisson ratio
Al 6082t6	2700	73	0.33
Caro Bronze	8750	115	0.33
CuBe2	8300	135	0.34
Ti6Al4V	4620	115	0.34
Vespel SP3	1605	3.2	0.36

Concerning the roller side, we have these pairs of materials:

1. Titanium to beryllium-copper (linear runner to wheels).
2. Beryllium-copper to Teflon (wheels to bearing).
3. Titanium to Teflon (bearing to shaft).
4. Titanium to aluminum (shaft to structure).

The actuation provided by the NEXLINE is modeled by including the geometry of the piezos with a reasonable value of the elastic properties, which are then tuned to match the experimental data. The interface between the piezo and the LR is modelled as an internal joint that constrains the motion along y, the rotation around y and the motion along z, where the commanded actuation is imposed. The other degrees of freedom are free.

A crucial parameter in the model is the internal preload. We identified two sources of preload on the guides. The first is the force applied via the washer spring connecting the rollers. This force is nominally 55 N and was applied through a 200- μ m shim calibrated independently. We speculate that this value is affected by

significant uncertainty. On top of this load, the NEXLINE actuators may push the LR along x due to misalignments. i.e., the two walking piezo stages have a small angle around z that forms a V configuration. During the LPF flight campaigns it was observed that the LR was occasionally drifting towards the rollers side. This happens if the NEXLINE spurious preload is pointing towards that side and is higher than the washer spring preload. The flight models have been tested to avoid this effect, to make sure that either the NEXLINE preload points towards the sliders or is lower than the spring preload. We consider both loads in our analysis.

The main difference between the QM and the FM model is the material of the sliding pads, see Table 3, which is Vespel SP-3 in the QM, instead of the Teflon of the FM. This affects the friction coefficient, which was discovered to be high for Vespel in vacuum. The geometry of the component holding the sliding pads in the FM is also different.

Table 3. Differences between LPF QM and FM

Component	Material	
	QM	FM
Frame	Titanium	Titanium
Linear runner	Titanium	Titanium
Rollers	AA7075	CuBe2
Bearings	Vespel	PTFE
Pins	Bronze	ZrO2
Washer	PTFE	PTFE
Sliders	Vespel	PTFE

The FE model is effective in understanding spurious behavior due to friction and elasticity of the parts. In particular we were able to replicate the undesired lateral motion of the tip of the plungers when the commanded motion is inverted (as it is for a release operation), [8]. Having validated the model, we plan to use it for analyzing the updated design.

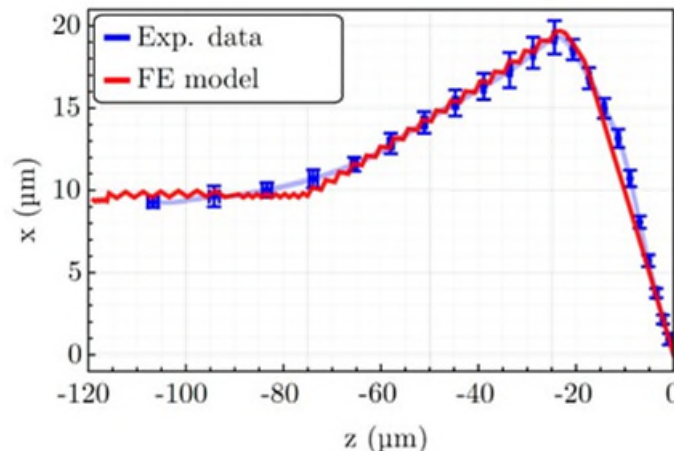


Figure 6. The results obtained with the FE compared to the experimental data for the pyramidal unit. Experimental data are plotted with the 1σ uncertainty.

Gap-model as a tool for systems engineering budgeting

In the development phase for LISA, we proposed a model approach to keep control of the critical quantities which may produce unwanted contacts between the TM and plunger upon release, as one of the relevant root causes of the LPF anomaly.

In nominal conditions, i.e., with ideal geometries of the parts and perfect alignment of the GPRM components, the extraction of the release tip and the consequent retraction of the plunger leaves a gap between the plunger head and the TM indent. The nominal gaps are reported in Table 1, where the axes are referred to the displacement and rotation of the plungers with respect to the TM in the indent local reference frame, Figure 7.

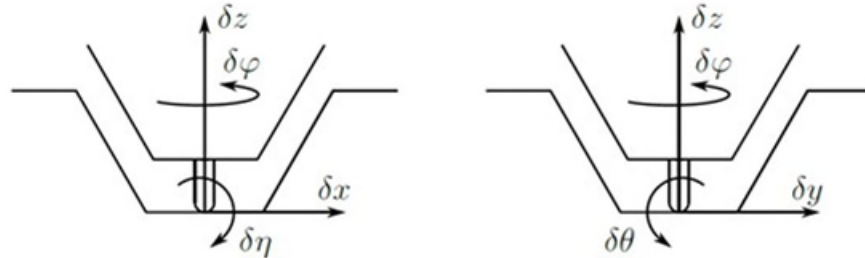


Figure 7. View of the TM indent local reference frame in the x-z and y-z planes.

The gap model is defined as a normalized formula:

$$G = \frac{\delta x_{eq}}{\delta x_{max}} + \frac{\delta z_{eq}}{\delta z_{max}}$$

Where δx_{eq} is the equivalent displacement of the Plunger head (equivalent because it sums lateral displacements and rotations) and δx_{max} is the available gap. Each deviation from ideality, in the fabrication (tolerances), assembly (alignment) and operations (lateral motion, friction, vibrations) will reduce the gap. Once the gap is 0 (i.e., the parameter G is above 1), the Plunger head is in contact with the TM and will transfer a significant momentum due to vibrations, Figure 8.

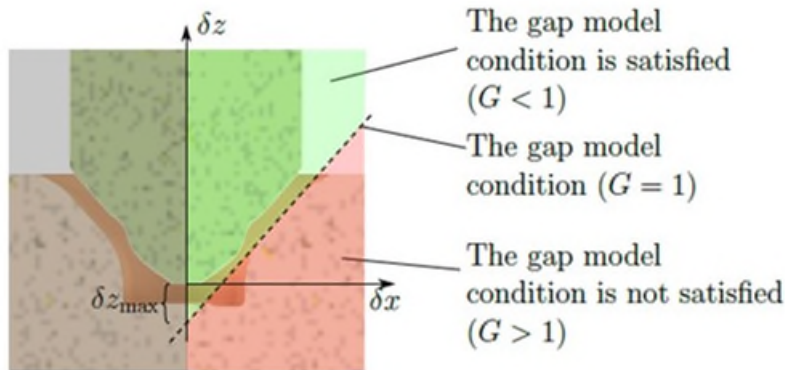


Figure 8. Visualization of the concept behind the gap model.

The gap model is a kinematic approximation of the TM and GPRM plunger relative position in various phases of the grabbing and release procedure. For instance, if one of the plungers is misaligned laterally, when the TM is grabbed, it will rotate to touch both plungers. We assume that the TM-plunger contacts are a rotational joint. This relative rotation between the TM and the plunger translates into a reduction of the ideal gap length that we account for in the model.

A thorough description of the model is too specific for this paper. The take-home message is that with such a tool we can focus the delta development efforts on aspects of the design that have the highest impact on the probability of an unwanted contact between plunger and TM. The results point to a crucial importance of:

- the piezo stack elongation (i.e., the available gap size);
- the lateral motion of the plunger when it is retracted away from the TM;

- the fabrication and alignment tolerances;
- the vibrations at the time of the release.

This motivated the breadboard tests, described in more detail in the next Section. We use this model also in a statistical fashion, Figure 9. With a Monte Carlo analysis we understand that in LPF spurious contacts were rather likely. However, we estimate that, with carefully chosen changes, the undesired contact and momentum transfer can be avoided.

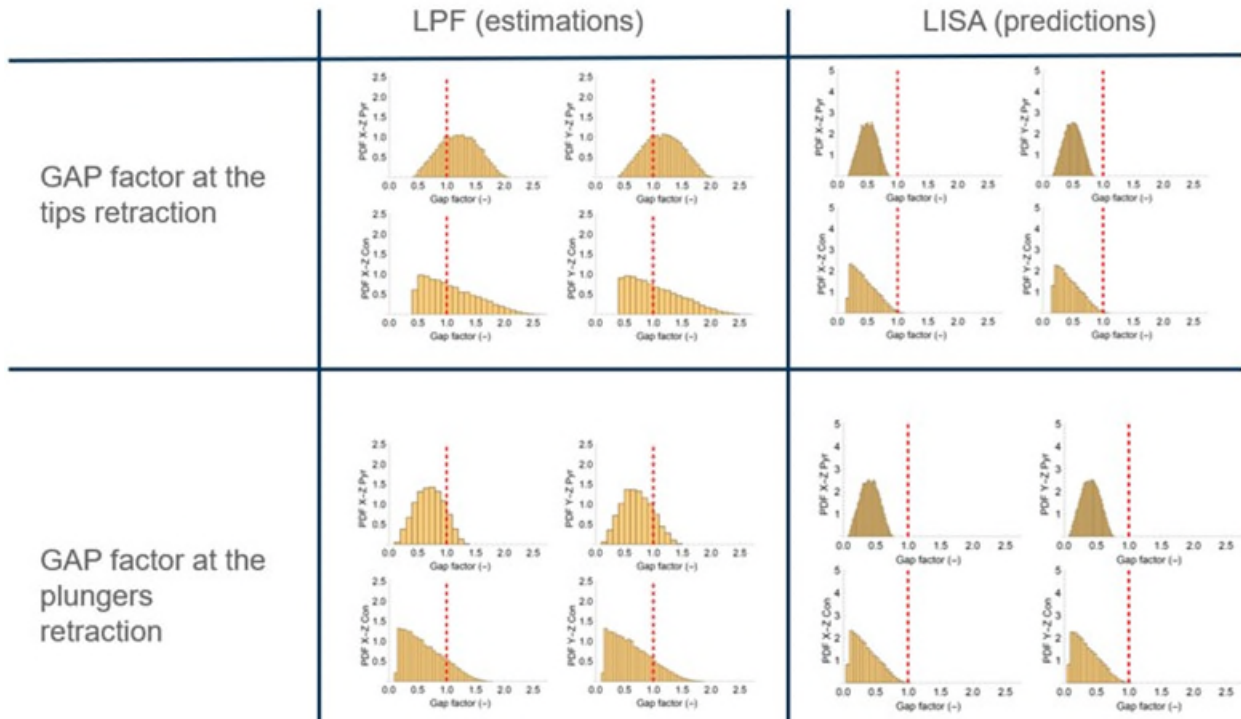


Figure 9. Monte Carlo simulations of the model forecasting the probability of plunger-to-TM impact

Improvements under Investigation and Breadboard Tests

The breadboard mechanism (BBM) of the LISA GPRM is designed in collaboration with OHB Italia SpA. The BBM had the main goal to test two of the main modifications proposed for the GPRM of LISA, namely a longer piezo-stack and an improved side-guiding for the linear runner.

The two modifications are implemented on a dummy linear runner, which also includes the plunger in a single component (the force sensor is not present, since it is not of interest for the tests).

Inside the BBM linear runner we insert a long piezo-stack (36 mm), in series with a short piezo-stack (18 mm, LPF baseline), that extends a release tip with the same dimensions of the LPF release tips. The series of piezo stacks is preloaded to 100 N thanks to a disk spring, reproducing the internal components layout of the GPRM of LPF.

The BBM linear runner is free to move along its main axis (z) thanks to a side guide. The side guide acts only on plane x-z, while on plane y-z only the friction forces maintain the linear runner in position. The external structure that holds the side guiding system is designed to guarantee access to the guide fixtures. In this way, the side guide configuration can be changed from the LPF baseline (fixed sliders on one side, flexible rollers support on the other side) to the update design (fixed rollers on one side, flexible rollers support on the other side), Figure 10.

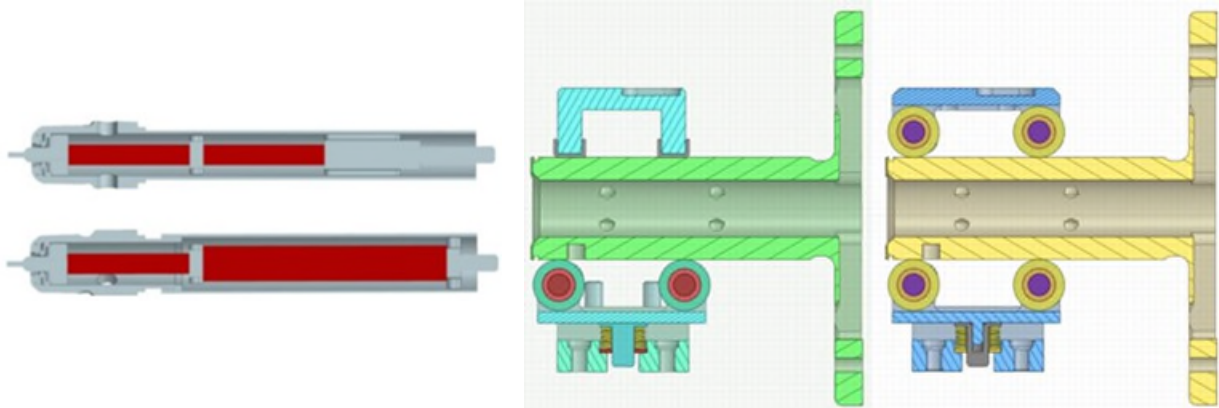


Figure 10. On the left panel, configuration of the piezo stacks inside the LPF GPRM (top) and the BBM plunger (bottom). On the right panel, different side-guiding systems tested with the BBM. On the left, slider-roller (LPF baseline); on the right, roller-roller.

To minimize the y displacement, since along that direction the linear runner is not constrained except by the friction forces developing on the side guiding, the BBM is tested in a vertical position (z axis pointing downwards, see Figure 11).

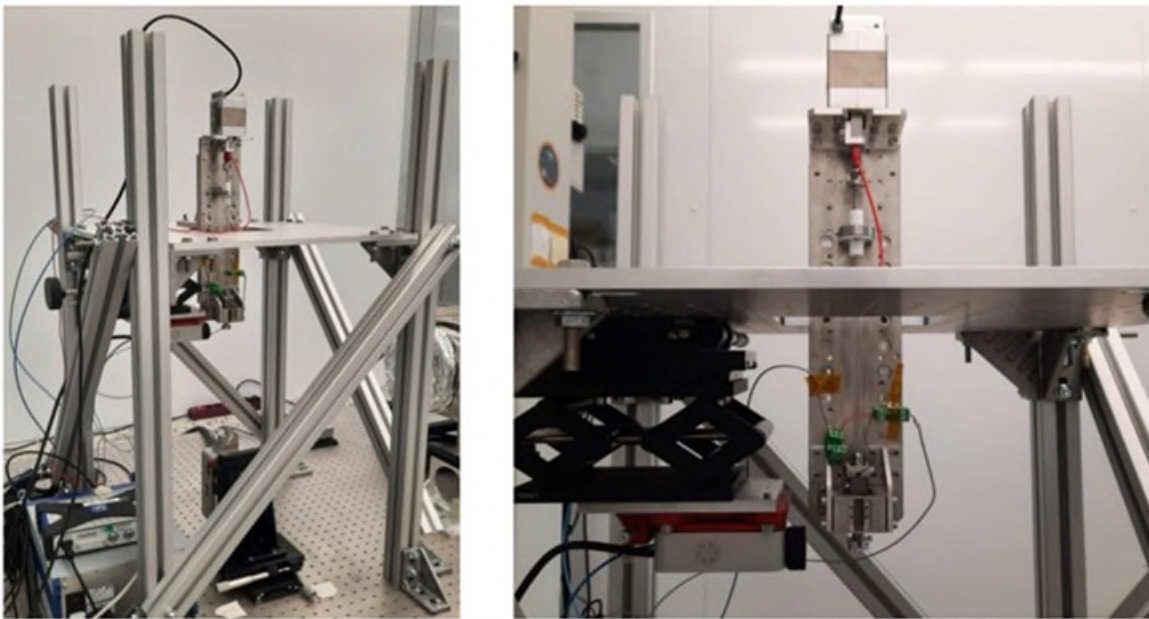


Figure 11. BBM mounted in its test configuration at the Laboratory of Space Applications. The NEXLINE (top) is used to move the linear runner (bottom) through a slender steel beam.

The linear runner is actuated with a commercial NEXLINE unit by Physick Instrumante, that is located approximately 30 cm away from the back of the linear runner, to which it is connected by a slender steel beam. A commercial load cell is mounted between the NEXLINE end effector and the beam, to measure the force required to move the BBM linear runner.

The location of the NEXLINE far away from the linear runner is another difference between the BBM and the nominal GPRM design. Albeit this limits the analysis of the dynamics of the mechanism (oscillations are not comparable with the ones of the nominal GPRM design), it is not affecting the two aspects under investigation with the BBM:

- extension and retraction of the tip with the longer piezo stack

- lateral motion (x) of the plunger/linear runner at the inversion of motion on the plane of the side-guide (x-z)

The desired displacements are measured with two laser interferometers instruments from SIOS manufacturer. One is a single beam LSV120NG, the other is a three beams SP5000TR. The setup allows measuring 4 channels simultaneously, one along direction x and three along z, with an accuracy better than 0.05 μm . Such an accuracy is more than sufficient for the purpose of the tests, given the expected displacements are in the order of 1 μm to tens of microns. The maximum sampling frequency is 2 MHz. The testing of the BBM was carried out at the Laboratory of Space Applications of the University of Trento and INFN, and the results agree with the expectations.

Release-tip tests

Concerning the release tip tests, both the baseline (short) and the upgraded (longer) piezo stacks are capable of extending the piezo by the desired amount. When 100 V are applied to the piezo-stack, the tip extends by approximately 13 μm with the short piezo-stack and 30 μm with the long piezo-stack.

Thanks to the commercial electronics used to command the BBM, it was possible to perform a set of measurements of the double extension (both the piezo stacks extended in rapid sequence). The total extension of the tip in those tests sums up to approximately 42 μm .

Plunger lateral motion tests

The lateral motion tests aimed at comparing the baseline sided guiding (slider-roller) with the updated side guiding (roller-roller). The experiments results are in accordance with the expectations, generated from accurate finite element models of the linear runner motion inside the BBM supporting structure. The tests are divided into two subsets: short stroke (z displacement of few hundred microns) and long stroke (z displacement of few millimeters).

In the short stroke tests, Figure 12, the slider-roller exhibits a large lateral motion of the plunger head near the TM (approximately 14 μm along x) in the first 100 μm of retraction. Close to the TM, the roller-roller has far superior performance, generating a lateral displacement below 1 μm along x in the first 100 μm of retraction along z.

In the long stroke tests, Figure 13, the slider-roller shows the same lateral deviation as the short stroke test. In other words, the linear runner displacement along x reaches its maximum (14 μm) value in the first 100 μm of z retraction and then it stays at the same x for the rest of the stroke.

The roller-roller instead behaves differently: the lateral displacement of the linear runner during the full stroke of the mechanism is affected by the run-out of the rollers and any deviation from the roundness of the rollers translates into a lateral motion.

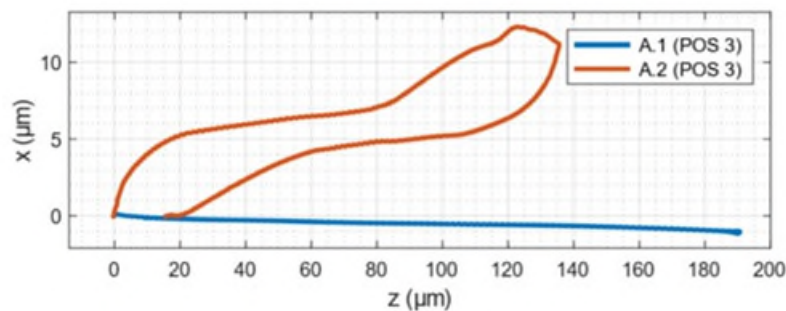


Figure 12. Short stroke tests results. The trajectory of the plunger head to the TM on the x-z plane for the slider-roller (orange) and the roller-roller (blue) configurations.

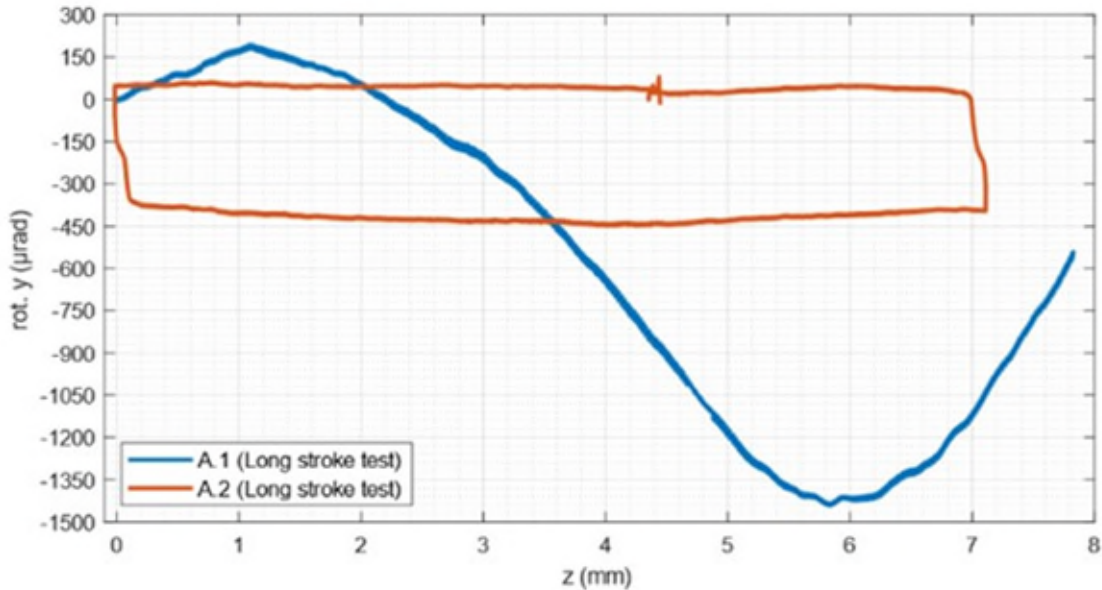


Figure 13. Long stroke tests results. Rotation of the plunger in the x-z plane (about y) during half of the in-flight stroke. Results are shown for the slider-roller (orange) and the roller-roller (blue) configurations.

Baseline Proposal

Following the results of the breadboard test and with the guidance of the numerical models, the GPRM team proposed a baseline design that includes a longer custom-built piezo stack and the roller-roller guiding system along with a more sensitive force sensor. The proposal is being evaluated internally through a review process. The final baseline will be implemented for EM tests foreseen between 2024 and 2025 and aimed at verifying the nominal functionality of the GPRM. The construction of the EM will also address outstanding questions concerning manufacturing and assembling.

Conclusions

The Grabbing Positioning and Release Mechanism (GPRM) is one of the technologies enabling the construction of LISA, the first gravitational wave observatory in space. In LISA Pathfinder the GPRM exhibited an anomaly that hindered the release according to the nominal procedure. LISA will not allow a backup manual commanding solution from the ground and needs a reliable function of the GPRM. With several studies of the LPF data, ground tests, and numerical analyses, the main causes of the LPF anomaly were identified and are being resolved with a delta development process. More specifically, among possible design changes, the change in extension length of the piezo stack will mitigate the probability of a spurious impact occurring at the release.

With an internal review, we are assessing all the proposed changes and defining our baseline in view of engineering model tests between 2024 and 2025.

References

1. G. Wanner, "Space-based gravitational wave detection and how LISA Pathfinder successfully paved the way," *Nature Physics*, vol. 15, no. 3, pp. 200–202, 2019.
2. T. E. Bell, "Hearing the heavens", *Nature*, vol. 452, no. 7183, pp. 18–22, 2008.
3. R. Dolesi, D. Bortoluzzi, P. Bosetti, L. Carbone, A. Cavalleri, I. Cristofolini, M. Da Lio, G. Fontana, V. Fontanari, B. Foulon et al., "Gravitational sensor for LISA and its technology demonstration mission," *Classical and Quantum Gravity*, vol. 20, no. 10, p. S99, 2003.
4. D. Bortoluzzi, D. Vignotto, A. Zambotti, M. Armano, H. Audley, J. Baird, P. Binetruy, M. Born, E. Castelli, A. Cavalleri et al., "In-flight testing of the injection of the LISA pathfinder test mass into a geodesic," *Advances in Space Research*, vol. 67, no. 1, pp. 504–520, 2021.
5. D. Bortoluzzi, D. Vignotto, E. Dalla Ricca, and J. Mendes, "Investigation of the in-flight anomalies of the LISA Pathfinder test mass release mechanism," *Advances in Space Research*, vol. 68, no. 6, pp. 2600–2615, 2021.
6. C. Zanoni, D. Bortoluzzi, "Experimental-Analytical Qualification of a Piezoelectric Mechanism for a Critical Space Application". *IEEE/ASME Transactions on Mechatronics*, 2015.
7. C. Zanoni, D. Bortoluzzi, "Estimation of the electrostatic effects in the LISA-Pathfinder critical test mass dynamics via the method of moments". *IEEE/ASME Transactions on Mechatronics*, 2021.
8. D. Vignotto, C. Zanoni et al. "The Role of Friction in the LISA-Pathfinder Release Mechanism Anomaly". *AIAA Journal*, 2023.

FD04 Frangibolt Actuator Performance Test: Measuring Force and Stroke Margin

Ingie Baho* and Kim Aaron**

Abstract

A new approach for measuring force and stroke margins for Frangibolt actuators has been developed and is described in this paper. Frangibolt actuators, which are sold by Ensign-Bickford Aerospace & Defense Company (EBAD), are widely used across the Aerospace industry as hold-down and release mechanisms. They are comprised of a resistance heater which warms a piece of shape memory alloy (SMA). Elevated temperature induces a crystalline phase change (martensite to austenite) in the SMA, which grows in length enough to break a notched fastener, thereby releasing the bolted joint. The SMA alloy in the FD series actuators is formed from a single crystal of Copper, Nickel, and Aluminum. The FD family is smaller and exhibits greater expansion relative to its size than the multi-crystalline Titanium-Nickel alloy used in the FC series actuators. Due to the difference in crystallinity between the FC and FD series, we discovered that the standard FC test approach typically used to measure the force and stroke (expansion) of the actuator, would not be appropriate to test the FD series actuators. Testing of the FC family can be accomplished by applying the intended demonstration load using an Instron machine in compression with the actuator; however, this approach is not applicable due to the single crystal nature of the FD family. The novelty of this FD test procedure is that an initial preload is applied through a stack of Belleville springs to the Frangibolt actuator, simulating the load and stiffness of a torqued bolt in a flight assembly. After the preload is applied, our FD04 Frangibolt actuator is energized and the load it experiences linearly increases to the test load as it compressed the stack of Belleville springs. The stroke of the Frangibolt actuator was measured at each test load using an extensometer. The force and stroke needed to break the notched Frangibolt fastener are 2860 N and 201 μm , respectively, which were calculated from data provided by EBAD. In this paper, we explain the novel features of our test method and the differences between our new method and that which was used for the FC series Frangibolt actuators. Details of our test results are also provided which ultimately verify that the FD04 Frangibolt demonstrates more than enough force and stroke to break the notched Frangibolt fastener: 5720 N and 490 μm on average, respectively.

Introduction

This report describes force and stroke performance tests of FD04-4457 Frangibolt actuators that were conducted for SunRISE project [1]. The SunRISE mission aims to launch an array of six CubeSats to collectively monitor solar activity to better understand solar particle storms [2]. A key payload of each CubeSat is a set of Spiral Tube Actuators for Controlled Extension / Retraction (STACER) antennas, which are booms restrained and deployed using Frangibolt actuators. A Frangibolt actuator is a form of hold-down and release mechanism which consists of a shape memory alloy (SMA) cylinder with redundant heater elements and a resistance temperature detector (RTD). The SMA is encapsulated in silicone rubber insulation, as shown in Figure 1.

An electric current is passed through the heater circuit, which heats the SMA to its phase transition temperature. The SMA material's crystal structure changes from martensite to austenite, which causes the SMA to expand, thereby breaking the notched Frangibolt fastener in the assembly. In this report, we refer to this as the "actuated state". After actuation, the SMA must be reset to its shorter length at room temperature by applying the appropriate force (6670 N for FD04 model) using the reset tool provided by Ensign-Bickford Aerospace & Defense Company (EBAD).

* Jet Propulsion Laboratory, California Institute of Technology, Pasadena, CA at time of this work; currently Massachusetts Institute of Technology, Cambridge, MA

** Jet Propulsion Laboratory, California Institute of Technology, Pasadena, CA



Figure 1. FD04 Frangibolt Actuator.

Historically, a performance test has been developed and performed on the FC series Frangibolt actuators. When the same test method was applied to the FD series Frangibolt actuators, the test was unsuccessful. This is because the FC series Frangibolt actuators utilize a multi-crystalline SMA whereas the Frangibolt actuator in the FD04 is comprised of a single crystal SMA. In the FC series Frangibolt actuator testing, a compressive load greater than the ultimate tensile strength of a Frangibolt fastener was applied to the Frangibolt actuator before actuation. This was appropriate for the FC series due to the relative insensitivity of the multi-crystalline SMA's phase transformation to applied load. To initiate the phase transition during actuation, a nucleation site is needed. The grain boundaries between the crystals in FC series provide many nucleation sites, even at high loads. The SMA in the FD04, however, is a single crystal, and does not have any grain boundaries to facilitate nucleation. Since compressive load suppresses nucleation and growth of the higher-volume austenite phase, there is a limit to the value of compressive load that can be applied and still have the Frangibolt actuator function as desired. In practice, this means that the magnitude of the largest compressive load that should be applied to the Frangibolt actuator at the start of a performance test is the maximum Frangibolt fastener preload. Once the austenite phase nucleates and starts to grow, then the load applied to the Frangibolt can ramp up. This is where the novelty in our test approach lies, and it is presented in further detail in the following sections.

This test campaign used two spare FD04-4457 Frangibolt actuators: serial numbers (SN) F1942 and F1943 drawn from the SunRISE flight lot. The force and stroke performance of the Frangibolt actuators were quantified in terms of force and stroke margins, which must meet the SunRISE requirements of 100% and 10%, respectively. Force and stroke margins measure the amount of additional force and stroke available in the Frangibolt actuator beyond what is needed to break the notched Frangibolt fastener. A 100% force margin means that the force produced by the Frangibolt actuator is 100% more than the ultimate tensile strength (UTS) of the notched Frangibolt fastener. Similarly, a 10% stroke margin means the Frangibolt actuator must demonstrate 10% more stroke than required to break the notched Frangibolt fastener. Our measurements are presented in this paper and compared to these requirements. For conservatism, the voltage applied to the Frangibolt actuator's resistive heater was initially set to the lowest voltage expected during flight: 5.5 VDC. A more typical flight voltage would be in the range of 6-7 VDC. For one of the test units, the applied voltage was ramped up to 5.9 VDC during actuation to test stroke performance under a higher applied voltage (further discussed in later sections).

A few key operating parameters for the actuators used in this test are provided in Table 1. The B-basis high and B-basis low force and stroke values were calculated by conducting a B-basis analysis on a notched Frangibolt fastener dataset provided by EBAD. The bolt pre-load and not-to-exceed temperature values were provided as recommendations by EBAD.

Table 1. Key Frangibolt fastener breaking characteristics and Frangibolt actuator usage conditions provided by EBAD.

Key Parameters	Value
B-Basis Low Bolt Breaking Force	2770 N
B-Basis High Bolt Breaking Force	2860 N
B-Basis High Bolt Breaking Stroke	201 μm
Bolt Nominal Pre-Load	667 N
Not-to-exceed Temperature	180°C

Materials

1. 2 FD04-4457 Frangibolts [1] (SN F1942, SN F1943)
2. 2 FR-4 thermal insulation washers [1]
3. Frangibolt Reset Tool (EBAD PN: F83549-1) [1]
4. Instron 8801 Servo-hydraulic Fatigue Testing System (with 25 kN load cell) [3]
5. Epsilon Axial Extensometer (Model 3542) [4]
6. Caliper
7. Electrical ground support equipment (EGSE):
 - Agilent 34980 data acquisition system (DAQ) [5]
 - Keysight N5765A power supply [6]
 - Digital multimeter (DMM):
8. Mechanical ground support equipment (MGSE):
 - 2 McMaster-Carr Belleville spring washers (9712K459) [7]
 - Belleville washer cup
 - Top and bottom Frangibolt fixtures
 - 3 stabilizing posts
 - 3 McMaster-Carr spring plunger tips (3126A2) [8]
 - Spacer blocks
 - Clamps
 - Shim material

Test Configuration

Mechanical Ground Support Equipment (MGSE)

Most of the MGSE was designed specifically for this test, although some components, such as the Belleville spring washers and spring plungers were purchased from McMaster-Carr. Figures 2 and 3 illustrate all the GSE that was used to conduct this test as well as the overall configuration of the parts in the assembly. The Frangibolt actuator is inserted between two FR-4 thermally insulating washers to simulate the flight assembly. Instead of a Frangibolt fastener, the top and bottom Frangibolt fixtures have short alignment pins that fit into the through hole in the ends of the Frangibolt actuator.

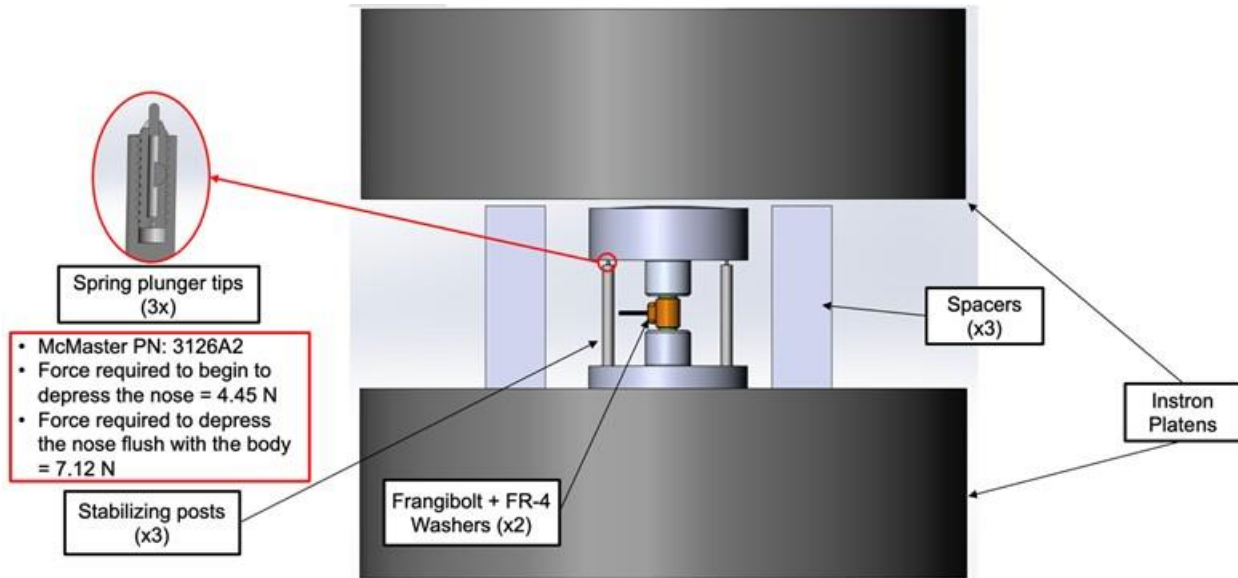


Figure 2. GSE and test configuration.

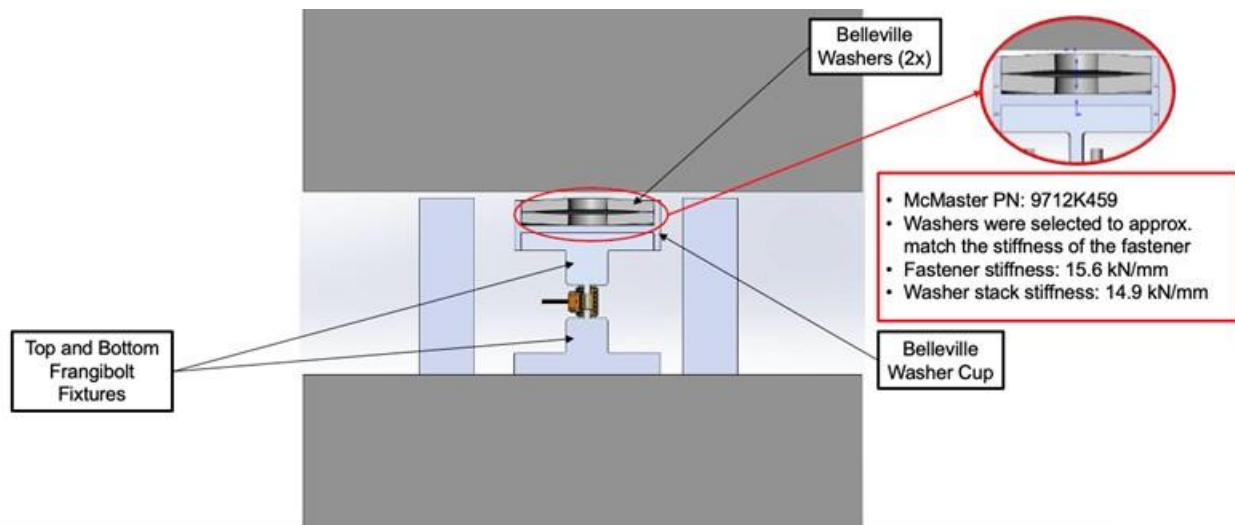


Figure 3. Cross section of GSE and test configuration.

Stabilizing posts with spring plunger tips at the top were attached to the lower Frangibolt fixture. The top Frangibolt fixture was levelled horizontally by resting on these three spring tips. A 4.45 N load is needed to depress a single spring plunger, and the combined 13.3 N is greater than the weight of the top assembly, so it was easy to adjust the lengths of the three supports to ensure they were of equal length to keep the top assembly parallel to the bottom assembly. The stroke to fully depress the spring plungers is greater than the distance they were compressed during the test, and their maximum force at full depression would be 21.3 N. This force was considered insignificant in relation to the applied forces by the Instron.

A cup which held a stack of two Belleville spring washers in series rested on the top Frangibolt fixture. The Belleville washers were selected based on their stiffness value to closely match the stiffness of the Frangibolt fastener. The spring constant of the Frangibolt fastener was calculated from 13 data points (provided by EBAD) of the tension load applied to the fastener and the extension at that load. Force divided by displacement was used to determine the Frangibolt fastener spring constant of 15.6 kN/mm. The stiffness of the Belleville washers was similarly calculated by dividing load and deflection values using data taken from the McMaster-Carr datasheet. The stiffness value for each Belleville spring washer was

29.7 kN/mm, so the two springs stacked in series have a combined spring constant of half of that value: 14.9 kN/mm. The selected Belleville springs were reasonably linear over the range of force and deflection used in the testing. Finally, spacer blocks were placed around Frangibolt fixture assembly. These spacer blocks were shimmed to ensure that they were the appropriate height. An extensometer was installed which grips the top and bottom Frangibolt fixtures to measure the deflection of the Frangibolt as it strokes. The positioning of the extensometer is shown in Figure 4. There was no contact between the extensometer and the leveling support shown behind it in the diagram.

When setting up the test apparatus, the Belleville washer stack was shimmed to be proud of the spacer blocks by approximately 50.8 μm . This ensured that as the Instron platen was lowered onto the spacers, the Belleville washer stack deflected by approximately 50.8 μm and applied a preload of approximately 667 N onto the Frangibolt actuator. This is the nominal preload applied by the notched fastener in normal use of the FD04 Frangibolt actuator. As the Instron platen load continued to ramp up to the predefined test load, the 667 N preload on the Frangibolt remained constant while the remaining load was carried by the spacer blocks. When the Frangibolt was actuated, it initially compressed the stack of Belleville washers until the force was equal to the constant predefined test load that was being applied by the Instron. As the Frangibolt expanded further, it pushed the stack upward and raised the Instron completely off the spacers. From this point onward, the full predefined test load was experienced by the Frangibolt actuator. The Instron was operated in constant force mode.

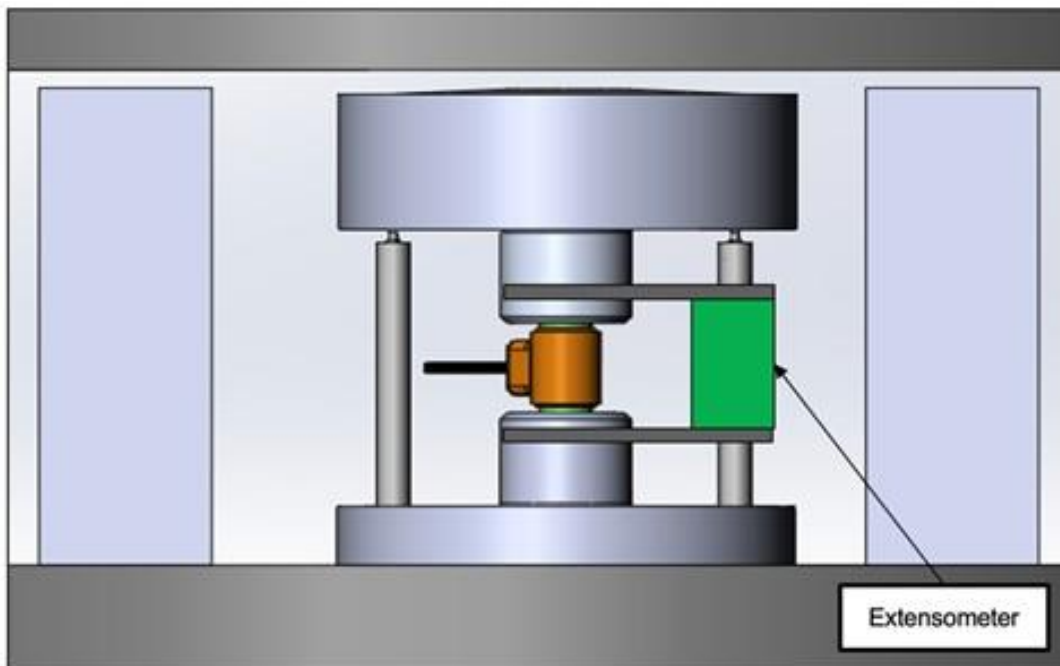


Figure 4. Extensometer to measure Frangibolt Actuator stroke.

Electrical Ground Support Equipment (EGSE)

The EGSE required to support this test primarily consisted of a power supply and DAQ (Data Acquisition) system. A DMM (digital multimeter) was also used to check voltage and resistance values. The power supply used to actuate the Frangibolt was set at 5.5 VDC and was equipped with over-voltage and over-current protection features to safeguard the hardware. The DAQ recorded the applied voltage by the power supply and the electric current. The DAQ also measured the resistance of the RTD and converted the reading to degrees Celsius while displaying it to the operator in real time. In addition, the DAQ recorded two channels from the Instron: applied load and extensometer displacement. These two channels were also recorded in the Instron's own data stream for redundancy. Finally, the DAQ was connected to a laptop computer to run the 34980A Benchlink Data Logger software to collect and compile the data. An illustration of the EGSE and the required connections is provided in Figure 5. Data sets were acquired at about 3 to 4 samples per second.

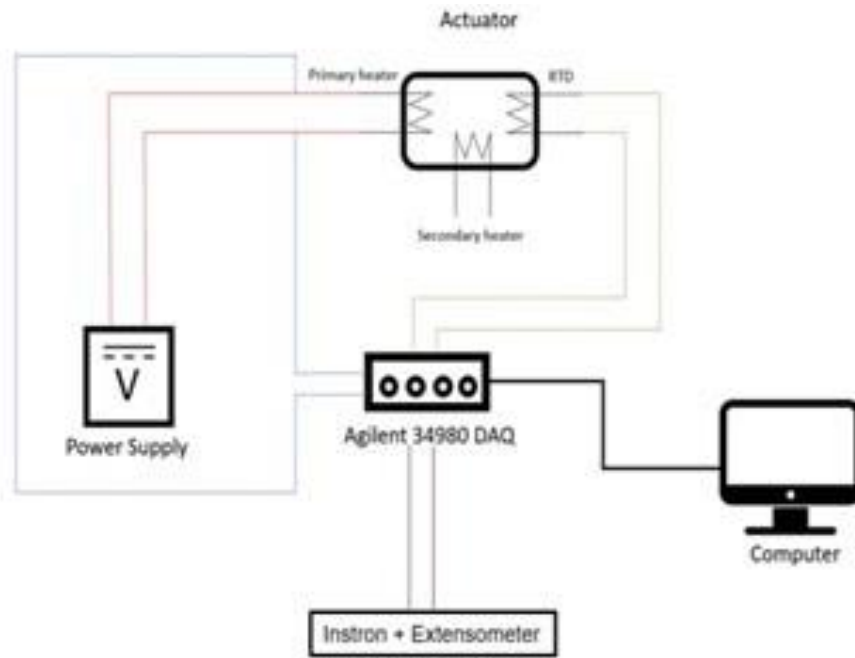


Figure 5. Diagram overview of EGSE connections

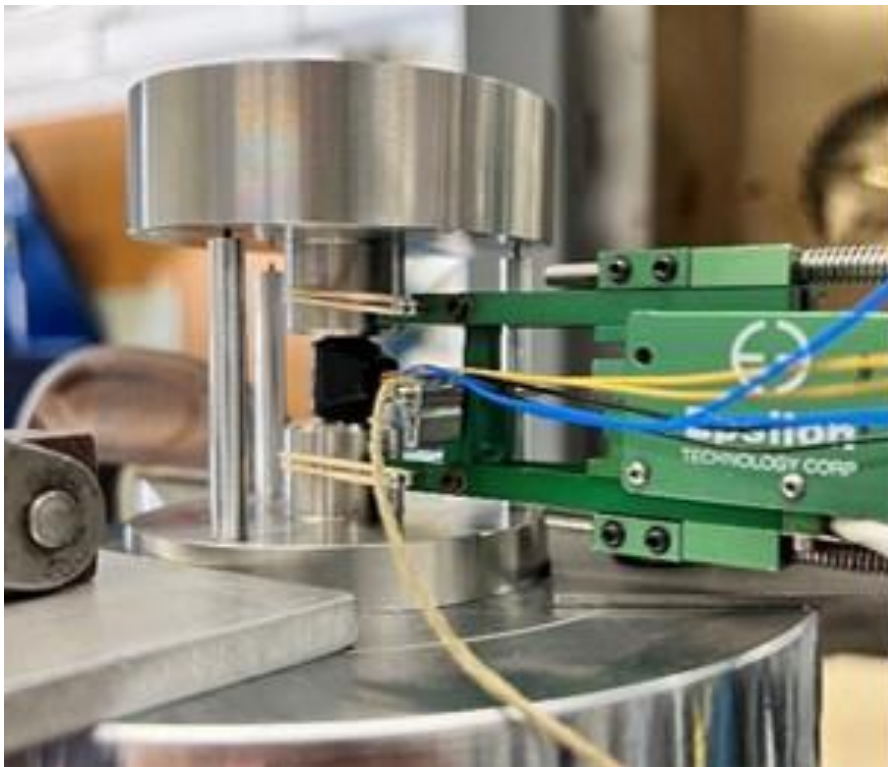


Figure 6. GSE assembly sitting on bottom Instron platen with the extensometer mounted in place (top Instron platen and spacer blocks not pictured)



Figure 7. Instron top platen lowered onto the assembly with spacer blocks (shimmed gauge blocks with holes) and guide plates (metal plates clamped onto Instron to prevent slipping)

Procedure

Since the Frangibolt actuators arrived from EBAD in the actuated state, the two Frangibolt actuators were first compressed using the reset tool following instructions provided in the user manual prepared by EBAD. The Frangibolt actuator was reset by torquing a fastener in the reset tool to apply a force of 6670 N to compress two platens against the Frangibolt actuator. The length of the compressed Frangibolt actuator was measured using calipers and compared against the nominal length provided in the datasheet for each actuator. The compressed Frangibolt actuator along with the extensometer were inserted into the MGSE assembly as described in the previous section (see Figures 6 and 7). Additionally, metal plates which contact the top and bottom Frangibolt fixtures at three points were clamped onto the Instron platens to center the GSE as shown in Figure 7. These plates were used to prevent an instability of the setup observed in an earlier test with a dummy Frangibolt in which the blocks slid laterally, overcoming friction, along the Instron platen surfaces.

The upper Instron platen was first manually lowered until it just barely touched the top Belleville washer. This position was programmed to be the starting position of the test. The Instron was then switched to force control mode and programmed to linearly increase the compressive load to the predetermined test load. The linear load ramp was programmed to go from zero to the full test load in 60 s. As the Instron load increased, the Belleville washers were compressed around 50.8 μm until the Instron platen hit the spacers (applying 667 N of preload on the Frangibolt). Once the predetermined test load was attained and held constant, voltage was applied to the Frangibolt actuator to actuate it. The Frangibolt actuator was allowed to heat up until the maximum allowable temperature of 180°C was reached. During the entirety of the actuation, the extensometer was recording the stroke of the Frangibolt. At 180°C, the power supply was shut off manually. After this, the Instron was unloaded linearly back to zero load over a 60-s period. The Frangibolt actuator was removed from the fixture, and its final extended length was measured using a caliper. The Frangibolt actuator was then reset using the reset tool, and the compressed length was again measured with a caliper. This procedure was repeated for each test load. The test loads defined for this test campaign are presented in Table 2. One small modification was made to this procedure during testing. F1943 was the first unit tested at exactly 5.5 VDC. However, at all test loads except for 2770 N, F1942 was initially actuated with 5.5 VDC then manually increased up to 5.9 VDC during actuation to allow for more stroke. 5.9 VDC is still lower than the expected flight voltage of 6 VDC, and while the voltage was increased, the temperature was still maintained below 180°C.

Table 2. Test loads defined for the Frangibolt stroke and force test.

Test Loads	Force [N]
B-Basis Low Bolt Breaking Load	2770
B-Basis High Bolt Breaking Load	2860
1.3x B-Basis High Bolt Breaking Load	3720
1.5x B-Basis High Bolt Breaking Load	4290
2.0x B-Basis High Bolt Breaking Load	5720

Results

The outputs measured during the test include the applied load of the Instron, the voltage and current applied to the Frangibolt actuator, stroke measured by the extensometer, and RTD temperature. Selected data series were plotted against time, as shown in Figures 8 and 9. Figure 8 includes annotations which indicate the total measured stroke and the obtained stroke margin, which is the additional stroke beyond what is needed to reach the B-Basis bolt breaking stroke of 201 μm . Note that the forces are shown as negative values because Instron machines are more typically used to apply tensile loads rather than compressive loads, and tension is considered a positive load.

Figure 8 shows the B-basis high bolt breaking load needed to break a Frangibolt fastener, 2860 N, as well as the load applied by the Instron against which the Frangibolt actuator is moving. Note that in Figure 8, the test load was equal to the B-basis high bolt breaking load; therefore, the force margin for that case (by definition) is zero.

Figure 9 depicts the highest load applied during the test campaign. During the unloading phase near the end of the test, significant additional stroke occurred (sharp increase in slope at ~400s). This was typical of the higher load cases (3720 N to 5720 N). This extra stroke was not included in the stroke margin computation. Only stroke in the constant load region was used in the stroke margin computation. However, the extra stroke occurred at a load that was still greater than the B-basis high bolt breaking load, so there is significant additional stroke margin here that we are not including in our data processing to be conservative. To calculate the percent stroke margin from the obtained data, the Eq.1 was applied, where *actuator stroke* is the complete stroke the Frangibolt demonstrated under the test load. The *bolt breaking stroke* is the B-basis high bolt breaking stroke value of 201 μm .

$$\% \text{ Stroke Margin} = \left[\frac{\text{Actuator stroke}}{\text{Bolt breaking stroke}} - 1 \right] * 100\% \quad (\text{Eq. 1})$$

Similarly, the percent force margin was calculated using Eq. 2, where *actuator force* is equal to the applied test load against which the Frangibolt was actuating. The *bolt breaking load* is the B-basis high bolt breaking value of 2860 N. We used the *magnitude* of the forces in these calculations of force margin.

$$\% \text{ Force Margin} = \left[\frac{\text{Actuator force}}{\text{Bolt breaking load}} - 1 \right] * 100\% \quad (\text{Eq. 2})$$

The calculated force and stroke margin values are provided for Frangibolt actuator SN F1942 in Table 3 and Frangibolt actuator SN F1943 in Table 4. The test load of 2770 N is the B-basis low bolt breaking load, and therefore the percent force margin formula which utilizes the B-basis high bolt breaking load does not apply. The Frangibolt actuators can only demonstrate positive force margin values at test loads larger than 2860 N. It is worth noting that the low stroke value for the 2770 N test load in the first row of Table 3 is not representative of the stroke capability. This was the first test of the campaign, and the preprogrammed duration for holding the applied constant load was too short. The actuator did not have sufficient time to reach its full transition temperature before the Instron started unloading. Therefore, the Frangibolt actuator did not complete its stroke before the test was terminated. If tested with a longer duration, a much larger stroke value and stroke margin would have been observed for this load case.

As stated in the procedure, the voltage for the F1942 Frangibolt actuator was ramped up to 5.9 VDC for all test loads except the first. This explains some differences between the stroke margins calculated for SN's F1942 and F1943. As expected, the F1942 Frangibolt actuator achieved more stroke than the F1943, excluding 2770 N, as it was supplied with a higher voltage.

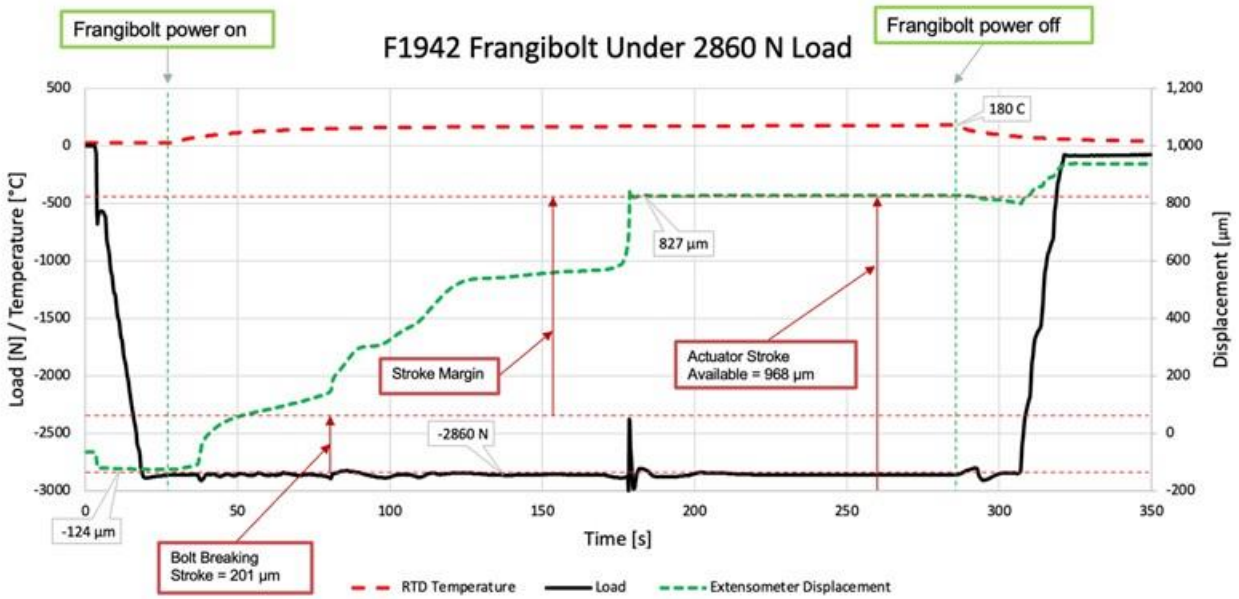


Figure 8. F1942 Frangibolt actuator under 2860-N load, Defining Stroke Margin

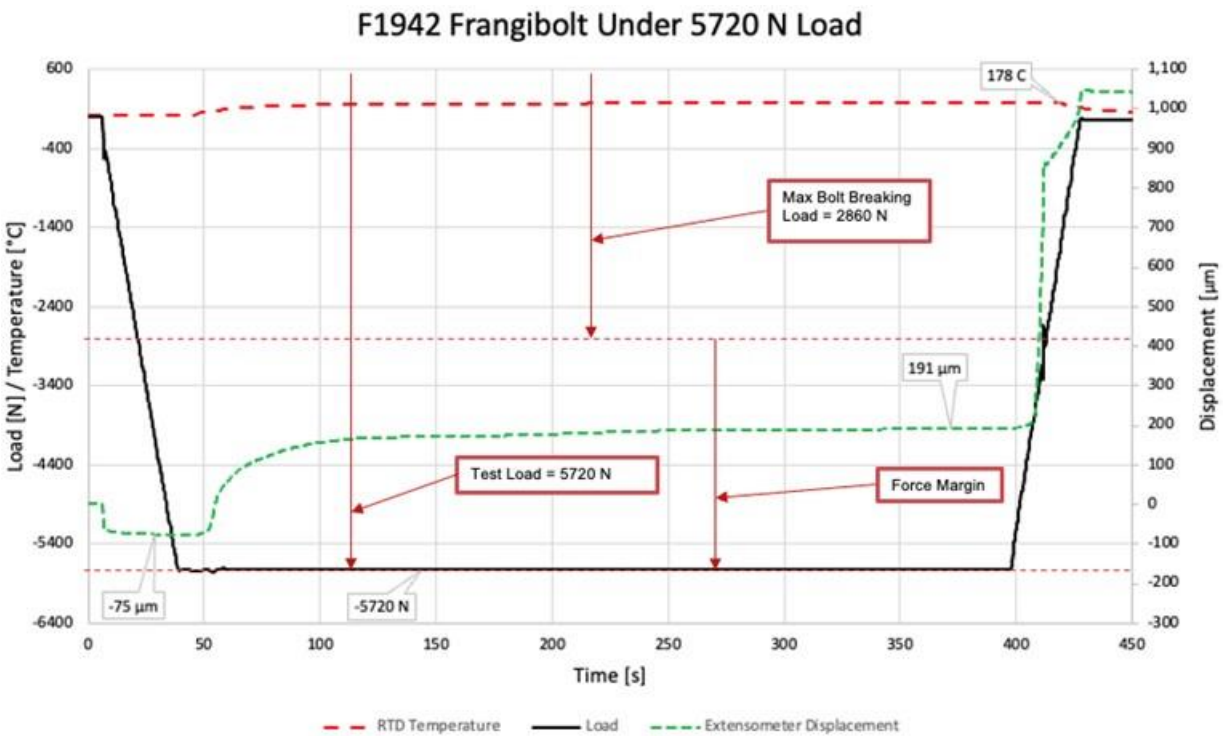


Figure 9. F1943 Frangibolt under 5720 N load, Defining Force Margin

Table 3. Calculated percent force and stroke margin for Frangibolt SN F1942.

Test Load [N]	Stroke [μm]	Force Margin (%)	Stroke Margin (%)
2770	279	NA	43
2860	965	0	380
3720	635	30	210
4290	279	50	44
5720	279	100	33

Table 4. Calculated percent force and stroke margin for Frangibolt SN F1943.

Test Load [N]	Stroke [μm]	Force Margin (%)	Stroke Margin (%)
2770	864	NA	330
2860	787	0	290
3720	279	30	39
4290	279	50	37
5720	254	100	23

Conclusion

Overall, the Frangibolt demonstrates more force and stroke than needed to break the notched Frangibolt fastener with plenty of margin. For the two tests at the maximum force of 5720 N, which corresponds to 100% force margin, the average stroke margin is 28%. This stroke margin was demonstrated simultaneously with 100% force margin. At the nominal worst-case load (B-basis high bolt breaking strength, 2860 N), the demonstrated stroke margin averaged over both Frangibolt actuators was greater than 300%. Results from the performance tests verify that the EBAD FD04-4457 Frangibolt actuators exceed the 100% force and 10% stroke margins required for the SunRISE project. Our test approach has demonstrated robustness and repeatability and may be implemented as an appropriate method for measuring the performance of an FD04 Frangibolt actuator. The MGSE used in this test approach may also be modified and resized to test other Frangibolt models, such as the FC series which are slightly larger.

Acknowledgements

The research was carried out at the Jet Propulsion Laboratory, California Institute of Technology, under a contract with the National Aeronautics and Space Administration (80NM0018D0004). We would like to acknowledge the SunRISE project at the Jet Propulsion Laboratory for funding this work.

References

- [1] "Tini™ mini frangibolt® actuator," Ensign-Bickford Aerospace & Defense, 07-Sep-2022 <https://www.ebad.com/tini-mini-frangibolt/>. [Accessed: 05-Feb-2023].
- [2] "SunRISE," NASA. <https://www.jpl.nasa.gov/missions/sun-radio-interferometer-spa.ce-experiment>. [Accessed: 05-Feb-2023].
- [3] "Floor standing fatigue testing systems - Instron." <https://www.instron.com/en/products/testing-systems/dynamic-and-fatigue-systems/servo-hydraulic-fatigue/8801---8802>. [Accessed: 05-Feb-2023].
- [4] "Axial extensometers - model 3542," *Epsilon Tech*, 28-Apr-2022. <https://www.epsilontech.com/products/axial-extensometer-model-3542/>. [Accessed: 05-Feb-2023].
- [5] Keysight, "34980A multifunction switch / measure unit, modules," *Keysight*, 08-Sep-2020. <https://www.keysight.com/us/en/products/modular/data-acquisition-daq/digital-acquisition-benchtop-system/34980a-multifunction-switch-measure-mainframe-and-modules.html>. [Accessed: 05-Feb-2023].
- [6] Keysight, "Technical support: N5765A power supply, 30 V, 50 A, 1500 W," *Keysight*, 10-Feb-2021. <https://www.keysight.com/us/en/support/N5765A/powersupply-30v-50a-1500w.html>. [Accessed: 05-Feb-2023].
- [7] "Carr," *McMaster*. <https://www.mcmaster.com/9712K459/>. [Accessed: 05-Feb-2023].
- [8] "Carr," *McMaster*. <https://www.mcmaster.com/3126A2/>. [Accessed: 05-Feb-2023].

Development of an Ejectable Data Recorder Ejection Mechanism for the Low-Earth Orbit Flight Test of an Inflatable Decelerator

Brian Saulman* and Robert Wagner**

Abstract

On November 10, 2022, the 1100-kg (2425-lb) Low-Earth Orbit Flight Test of an Inflatable Decelerator (LOFTID) Reentry Vehicle (RV) was launched on a United Launch Alliance (ULA) Atlas V as a secondary payload with the Joint Polar Surveyor System-2. The 6-meter diameter (~20 ft) aeroshell (a type of heat shield) entered the atmosphere at 8 kilometers per second (18,000 miles per hour), flew nominally, enduring the intended heat pulse that saw temperatures exceeding 1371°C (2500°F) on the front side while the payload skin remained only about 38°C (100°F) before landing under parachute in the Pacific Ocean off the coast of Hawaii. The RV exceeded Mach 30 and the heat-affected aeroshell withstood a pressure pulse that exerted 9g's deceleration maintaining stable flight through the hypersonic, supersonic, transonic, and subsonic regimes to the parachute deployment. As part of the Agency's strategic goal "to extend human presence deeper into space and to the moon for sustainable long-term exploration and utilization", the LOFTID inflatable aerodynamic decelerator or aeroshell technology could one day help land humans on Mars.

As with any flight test, data collection is of utmost importance. Without a data downlink from the RV and a possibility of the RV sinking before the recovery crew could get to it, a secondary data collection method was introduced. The RV would eject an ejectable data recorder (EDR) before splashdown, which would have a duplicate copy of the on-board flight data and be retrieved separately. This paper discusses the development of the ejection mechanism used to eject the data recorder from the RV during the test flight.

Introduction

The LOFTID RV was designed such that there was no data downlink to receive flight data in real time. With the very real possibility of the RV sinking after splashdown, a secondary means of retrieving the flight data was conceived. The EDR was developed to accomplish this. While it resides on-board the RV during flight, it received a copy of the flight data along with a similar unit that remained within the vehicle. The EDR is projected out away from the RV during descent and splashdown in the Pacific Ocean to be recovered up to thirty days later after ejection. To project the EDR from the RV, the EDR ejection mechanism was developed. Throughout the development, the mechanism had many constraints and challenges which will be discussed in this paper.

EDR Ejection Mechanism Background

The LOFTID RV consists of an inflatable soft goods structure and a metallic center body structure, Figure 1. The center body consists of three segments: forward, mid, and aft, Figure 2. The aft segment was chosen to house the EDR ejection mechanism due to its location having the most direct path for an object to clear the inflated aeroshell. This location provides its own set of challenges. The aft segment also houses the parachute system, parachute mortar, and various electronics systems, leaving very little space for the ejection mechanism. The location also sits roughly even with the outer torus of the inflatable structure and 2 meters away from it forcing ejection trajectory to be more vertical. Due to space constraints in the aft segment, a 20° off horizontal angle was selected for ejection path, Figure 3.

* NASA Langley Research Center, Hampton, VA

** NASA Langley Research Center, Science and Technology Corporation, Hampton, VA

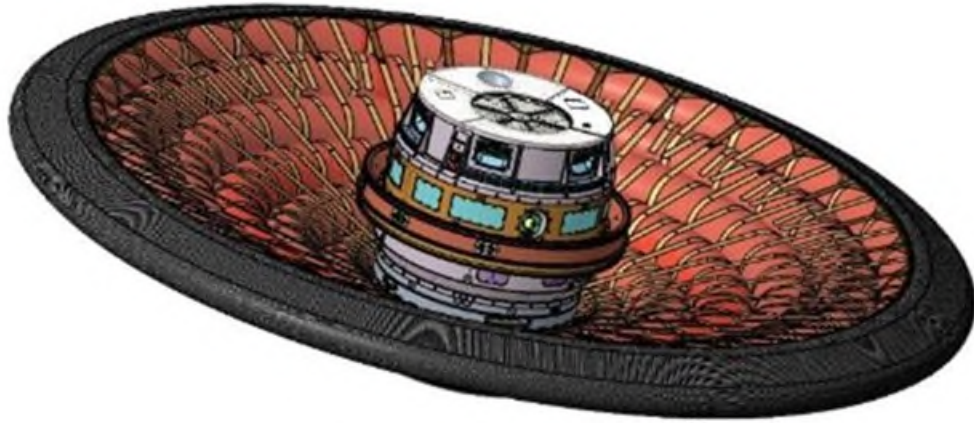


Figure 1. LOFTID RV in Flight Configuration

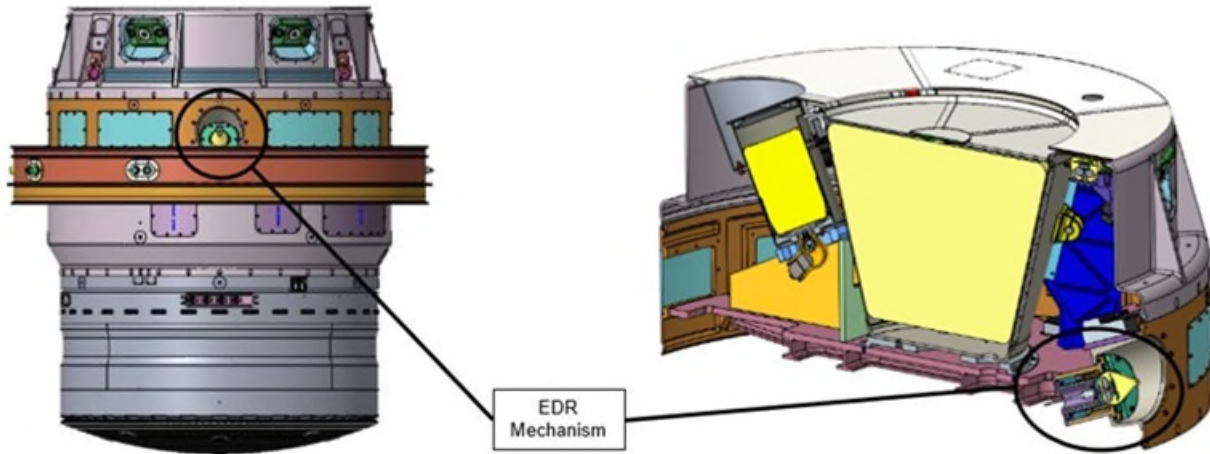


Figure 2. LOFTID Center Body and EDR Mechanism Location

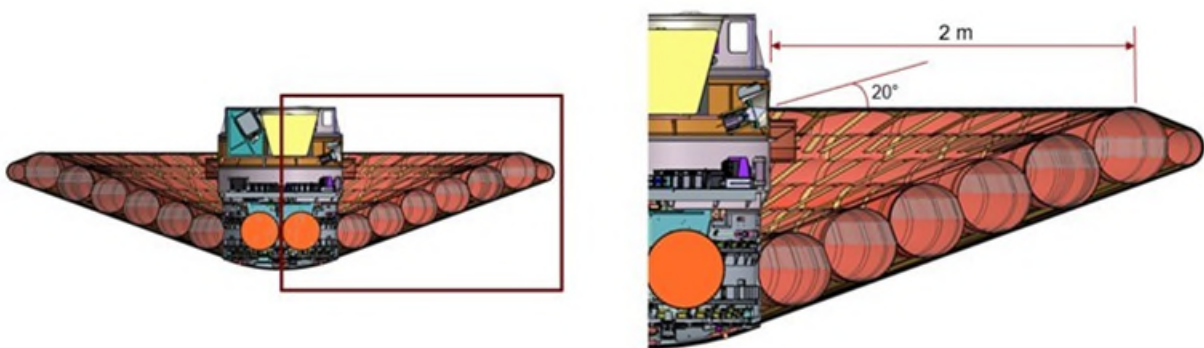


Figure 3. LOFTID RV Flight Configuration and EDR Mechanism Location

The ejection system ejects the Ejectable Data Module (EDM), Figure 4, through the RV boundary layer and clear of the vehicle during decent. The EDM is a pear-shaped polyurethane cast assembly that contains data storage, Iridium and Long Range (LoRA) broadcast networks, and batteries to survive at least thirty days in the ocean. The EDM weighs only 165 grams (0.364 lb) and constrains the ejection system to impart a maximum acceleration of 200g's which limits how much force can be used to eject it.

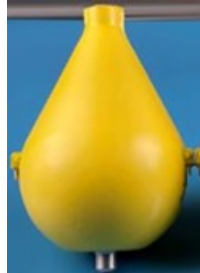


Figure 4. Ejectable Data Module

EDR Ejection Mechanism Design and Analysis Overview

The ejection mechanism is a bolted assembly consisting of housing components, compression spring, EDM pusher with tungsten disulfide dry film lubricant, guide pins, non-explosive actuator (NEA), elastomeric bumper, EDM, EDM interface board, shield, and a flexible thermal protective system (FTPS), Figure 5. A bushing and closeout plates were added later in the design cycle due to test findings that will be discussed later.

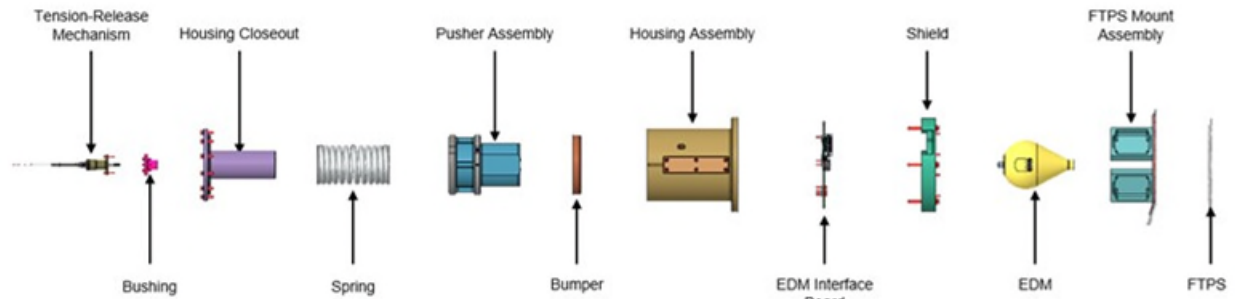


Figure 5. Ejection Mechanism Components

Using MSC.ADAMS, a dynamics model was constructed to account for the relative motion of the RV; this motion is like a spinning top— as the RV spins about the roll axis, the RV tilts in a sinusoidal motion about the pitch and yaw axes from center-of-gravity of the RV. As illustrated in Figure 6, the EDM is located approximately on the same horizontal plane as the top of the RV toroid. As mentioned previously, the housing of the EDR is set to a maximum angle of 20°. In the MSC.ADAMS model, the top of the RV toroid is constructed out of rigid beams; therefore, a clearance marker was added to the model to account for the maximum displacement envelope of the flexible toroid structure. Independent testing was performed on the RV aeroshell to baseline displacements against finite element model results.

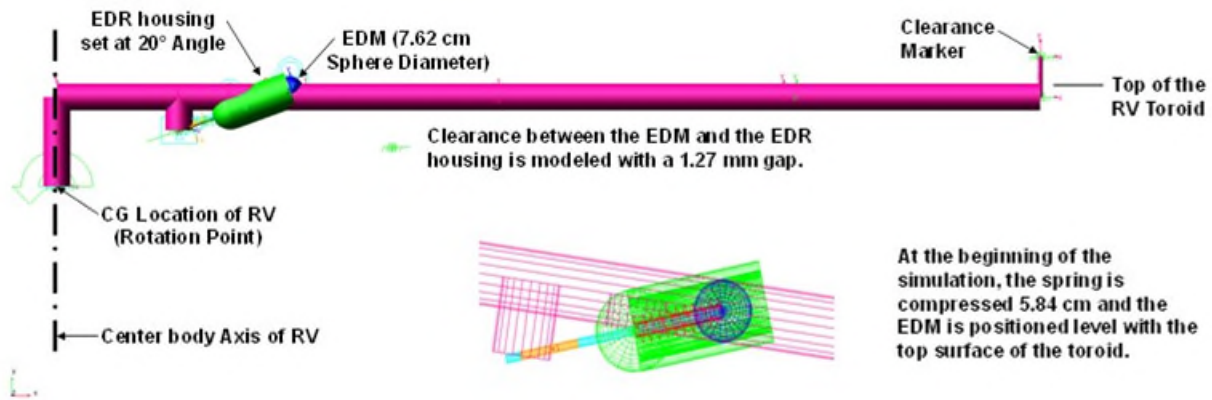


Figure 6. MSC.ADAMS Ejectable Data Recorder Model

Trajectory studies were performed on the RV's reentry. The 2σ pitch and yaw angular velocity and angular acceleration rates were derived and supplied for the analysis. With the EDR ejection planned at 15,240 m (50,000 ft), frequencies were calculated for pitch and yaw orientations at elevations ranging from 13,716 m (45,000 ft) to 16,764 m (55,000 ft). The natural frequency observed averaged nearly 3.485 rad/s and was consistent through 13,716 m to 16,764 m, Figure 7.

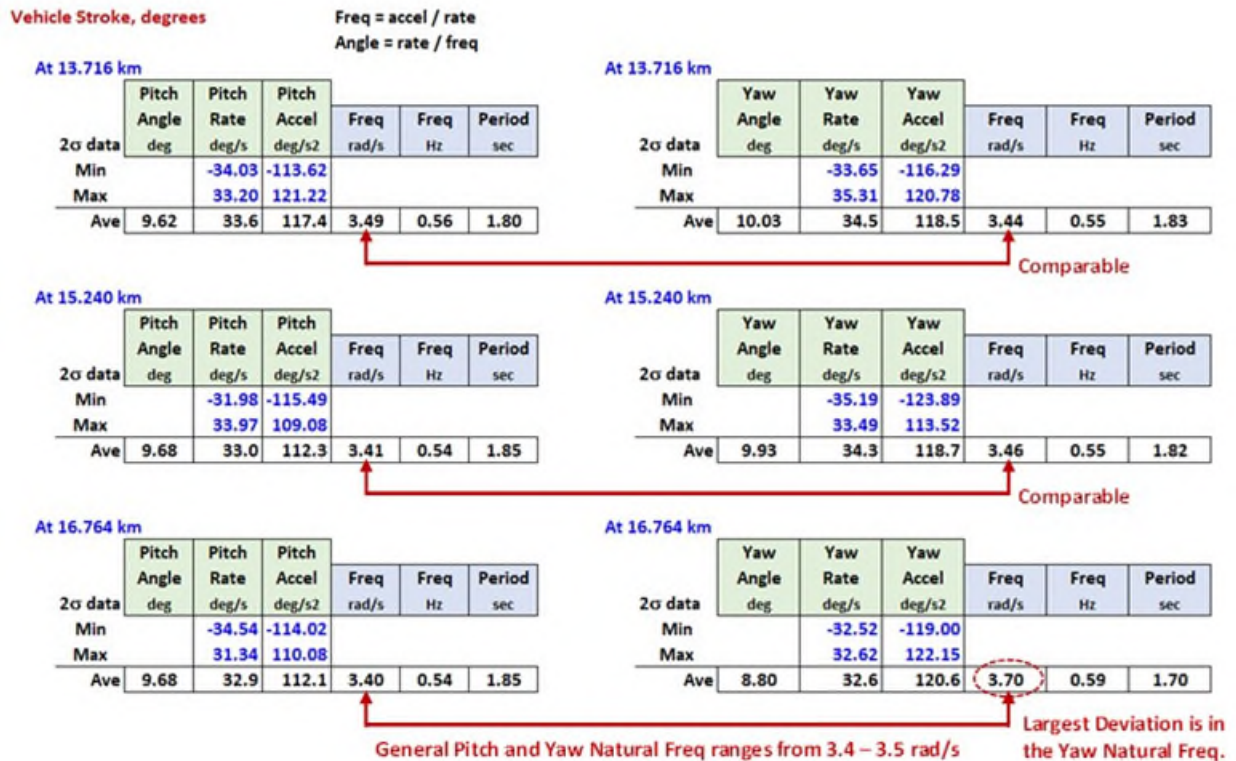


Figure 7. Trajectory Study Data from 13,716 m (45,000 ft) to 16,764 m (55,000 ft)

General motion of the toroid is controlled through the equation for velocity as a function of time. Several simulations were performed by releasing the data module at different time increments with measurements taken from the clearance marker to the EDM as it passes over the edge of the toroid.

In accordance with NASA-STD-5017, a minimum ejection velocity of 9.27 m/s is needed to maintain a positive force margin of safety. As shown in Figure 8, the dots along the oval represent each of the individual simulations. The red curve indicates that the angular velocity of the RV is upward, which is where the smallest clearance was observed.

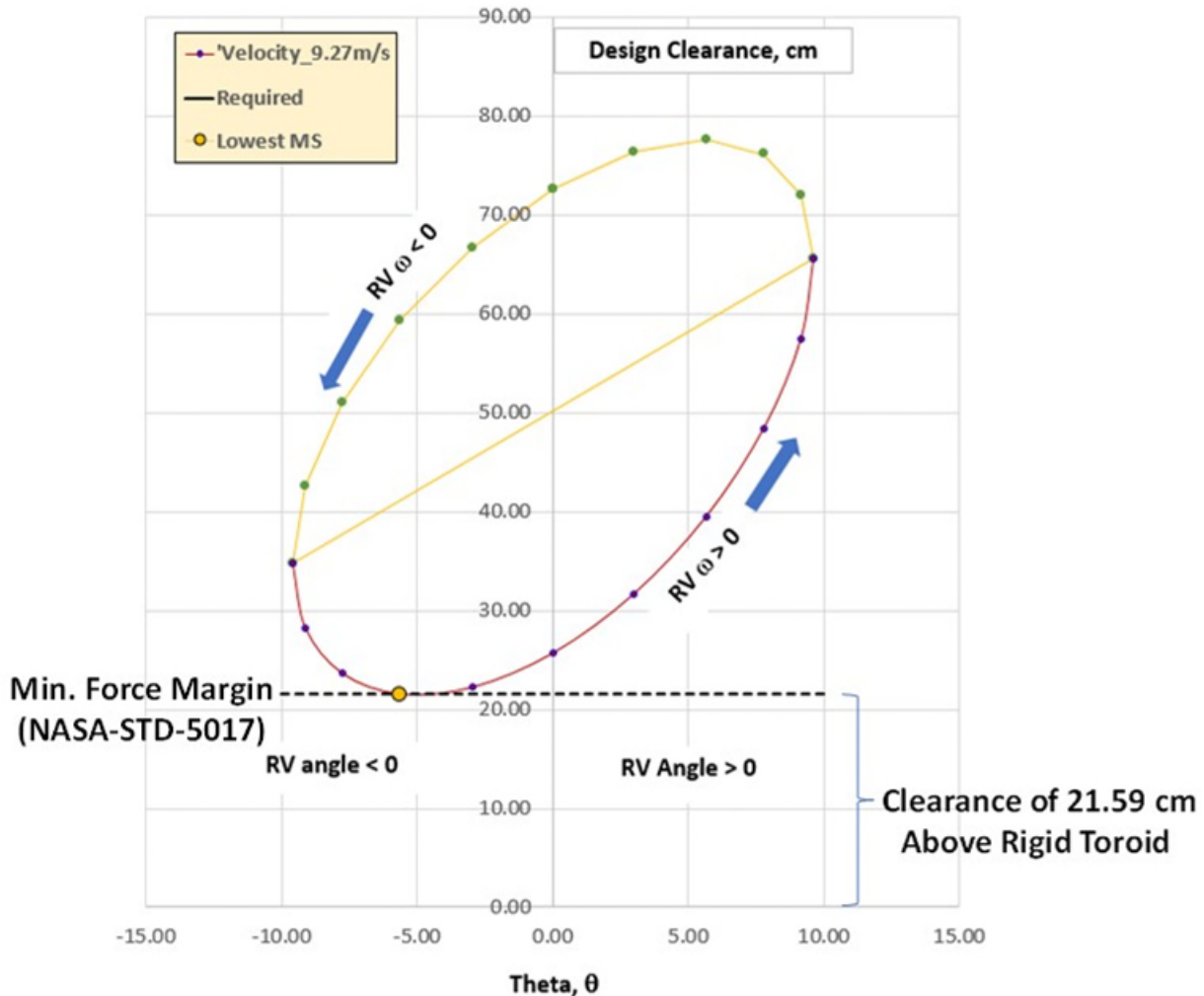


Figure 8. Ejection Velocity at 9.27 m/s

From the minimum ejection velocity needed, the kinetic energy is calculated and then converted into spring energy per Equation 1.

$$0.5 * m * v^2 = 0.5 * k * x^2 \quad (1)$$

EDR Ejection Mechanism Assembly and Function

The mechanism was a standalone assembly and was installed as late as possible into the RV before encapsulation and assembly onto the booster. Assembly was straightforward. With the bumper already bonded to the inside of the housing, the pusher was placed into the housing. Three dowel pins aligned the pusher to the housing with one of the dowel pins smaller than the other two so the pusher could only be assembled in one orientation. The spring was slid over the housing closeout, inserted into the housing, and bolted to the housing. The interface board and EDM were aligned to the pusher. Two dowel pins oriented the EDM to the pusher. Different sized dowel pins were used again so the EDM could only be oriented one

way. Once in place, the interface board was fastened to the housing. All the previous operations only needed to be completed once.

To load the mechanism for ejection, a set of custom retraction screws were threaded through the back of the housing into the pusher. Sprockets and chain were then installed to the retraction screws as this allowed the screws to be turned at the same time with a standard socket wrench, Figure 9. Retraction occurred until the EDM was seated properly into the interface board. Once retracted, safety bolts were installed to prevent inadvertent spring extensions.

A bushing and the NEA, Figure 10, were then installed through the back of the housing. The NEA threaded into the base of the EDM until hand tight and then fastened in place. The retraction screws were then removed, preloading the NEA fastener.



Figure 9. Mechanism Retraction



Figure 10. Non-Explosive Actuator

The shield, FTPS mount, and FTPS were then assembled to the forward end of the housing, completing the assembly, Figure 11.



Figure 11. EDR Mechanism Assembly

There are two ways to operate the EDR mechanism. For flight, a voltage is applied to the NEA and a bridge wire wrapped around a split spool expands releasing the NEA fastener. For testing or quickly repeating operations, the NEA split spool was replaced with a mechanical release device that could be manually operated by turning it, Figure 12.



Figure 12. NEA Split Spool (Top), Mechanical Release (Bottom)

EDR Developmental Testing

The ejection system relies on a single spring. The compression spring was sized by empirical calculations to calculate the stiffness and the available stroke of the spring. As shown in Figure 13, the candidate spring has a stiffness of 23,779 N/m (135.8 lbf/in) and a stroke length of 0.0584 m (2.3 in). A calculated force of 1389.2 N (312.3 lbf) is expected when the spring is compressed 0.0584 m (2.3 in).

Compression testing was performed on the compression spring to vary the theoretical stiffness calculations, Figure 14. The spring slightly exceeded the empirical calculations. In addition to compression testing, creep testing was performed over a 90-day period with negligible loss in measured force; this loss in force was more likely due to a non-controlled temperature environment.

	17-7 PH Material	Metric Units	17-7 PH Material	English Units	Comments
Spring Length,	17.780	cm	7.000	in	per Vendor catalogue
Spring Diameter, D_{outer}	6.190	cm	2.437	in	per Vendor catalogue
Wire Diameter, d	0.792	cm	0.312	in	per Vendor catalogue
Minimum Diameter, D_{min}	4.605	cm	1.813	in	$= D_{outer} - 2 * d$
Mean Diameter, D	5.398	cm	2.125	in	$= D_{outer} - d$
Shear Modulus, G	7.58E+04	MPa	11.0E+06	psi	Material Property Dependent
Number of Total Coils, N	12		12		per Vendor catalogue
Select Type of End	Closed and Ground		Closed and Ground	< <input type="checkbox"/> >	
Number of Active Coils, n	10		10		Ranges for $\{N \text{ to } (N-2)\}$ based on End Type
Spring Stiffness, k	23,779	N/m	135.8	lbs/in	$= G * d^4 / (8 * n * D^3)$
Wahl Curvature Stress Correction Factor, K	1.219		1.219		$= [4 * (D/d) - 1] / [4 * (D/d) - 4] + [0.615 / (D/d)]$
Beginning of Stroke, δ_{begin}	5.84	cm	2.30	in	Mechanical stop used to limit the beginning of stoke.
End of Stroke, δ_{end}	0.00	cm	0.00	in	Mechanical stop used to limit the end of stoke.
Stroke Length, δ	5.84	cm	2.30	in	$= \delta_{begin} - \delta_{end}$
Wire Shear Stress, τ	468	MPa	67,849	psi	$= 8 * k * D * K * \delta / (\pi * d^3)$
Max. Suggested Stroke, δ_{max}	6.35	cm	2.50	in	per Vendor catalogue
Displacement to Reach Solid Height, h	8.270	cm	3.256	in	per Vendor catalogue
Spacing between Coils, x	0.689	cm	0.271	in	Check: Spacing between coil < wire diameter
Max Operating Spring Force, P_{max}	1,389.2	N	312.3	lbs	per Vendor catalogue
Material Specification,	ASTM A313		ASTM A313		
Material Class,	17-7 PH Cond CH		17-7 PH Cond CH		Rockwell hardness ranges from C38-C57
Ultimate Tensile Strength, σ_{ult}	1,324	MPa	192,000	psi	from ASTM A313 Type 631 Table 2 (17-7 PH Stainless)
Ultimate Shear Strength, τ_{ult}	887	MPa	128,640	psi	$= 0.65 * \sigma_{ult}$ (R. L. Norton)
Yield Strength, σ_y	1,125	MPa	163,200	psi	Ranges between $\{0.75 - 0.85\} * \sigma_{ult}$
Shear Yield Strength, τ_y	754	MPa	109,344	psi	$= (\tau_{ult} / \sigma_{ult}) * \sigma_y$
FS for Mission-critical springs, FS_{ult}	1.65		1.65		per NASA-STD-5017a (Table 3) Ultimate Strength
FS for Mission-critical springs, FS_{yield}	1.50		1.50		per NASA-STD-5017a (Table 3) Yield Strength
Margin of Safety on Ultimate, MS_{ult}	0.15		0.15		$= [\tau_{ult} / (FS_{ult} * \tau)] - 1$
Margin of Safety on Yield, MS_{yld}	0.07		0.07		$= [\tau_y / (FS_{yld} * \tau)] - 1$

Please note: δ_{max} is a statistical service-life of 100,000 cycles with infrequent breakage ~ Century Spring Corp.

Figure 13. Compression Spring Calculations



Figure 14. Compression Spring Test Results (Left); Creep Testing Setup (Right)

Developmental functional testing was used to characterize the design and to estimate friction losses in the system. High speed video was utilized to capture the velocity and height of the EDM after 2 meters of travel (the distance to outer surface of the RV aeroshell). The ejection mechanism assembly was mounted to a test stand with white contrasting backdrop setup on partitions. A line was measured and drawn at 2 meters using black tape on the backdrop to mark the end of the aeroshell and a curtain was set up to catch the EDM after ejection at the end of each test, Figure 15.



Figure 15. Functional Test Setup

Velocity and height measurements were derived from the high-speed video captures. Velocities were measured just after ejection exit and at the 2-meter mark. Height was also measured at the 2 meters mark, Figure 16. These numbers were compared to the theoretical numbers and friction loss of the system was derived. An energy loss of around 25% was derived which was a little more than anticipated for the system.

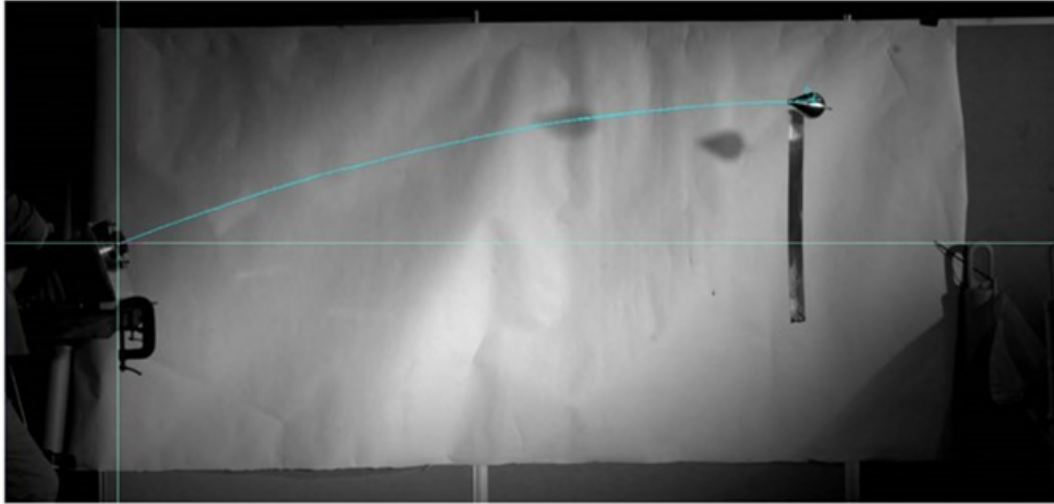


Figure 16. High-Speed Video Clip

After functional testing, the mechanism was subjected to random vibration testing. While testing, an anomaly occurred resulting in a premature release of the mechanism. Immediate findings showed that the NEA threaded stud broke and a guide dowel pin had been liberated from the mechanism assembly, Figure 17.

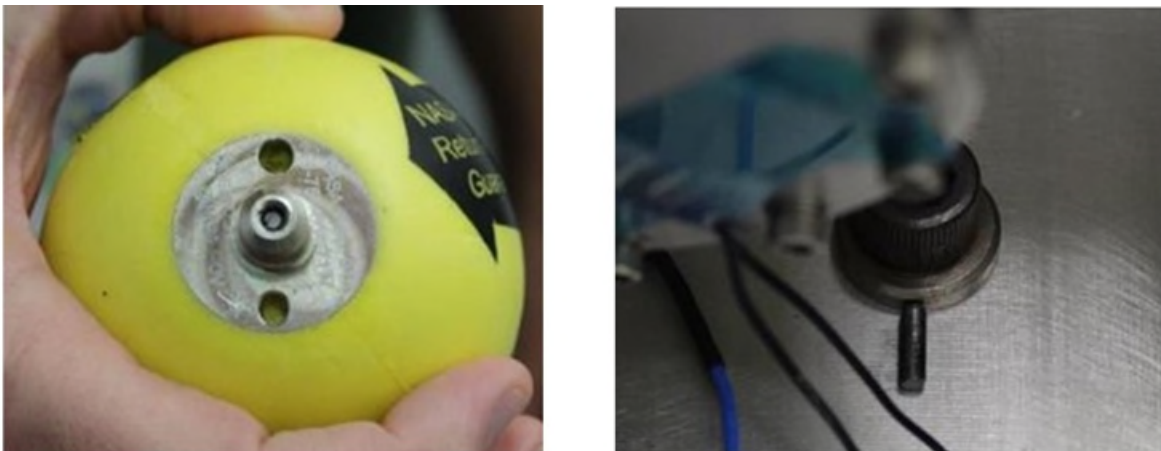


Figure 17. Broken Threaded Stud (Left); Liberated Dowel Pin (Right)

Further investigations showed that the threaded stud failed by fatigue. The fracture started, travelled about 40% of the surface and then the morphology changed. The fracture then travelled another 10% before the stud completely broke. The belief is the morphology change was from the dowel pin liberating itself from the assembly. Investigating the dowel pin revealed the pin and its mating hole were covered in dry film lubricant, Figure 18. It appeared that the dowel pin hole was not thoroughly cleaned before pressing the pin in place.



Figure 18. Lubricant on Pin (Left). Lubricant Wiped (Center). Lubricant in Hole (Right)

From this anomaly, a redesign effort was made to reduce cycling on the threaded stud and to retain the three guide pins. A custom flanged bushing was added between the pusher and the EDM to reduce movement in the NEA threaded stud, Figure 19.

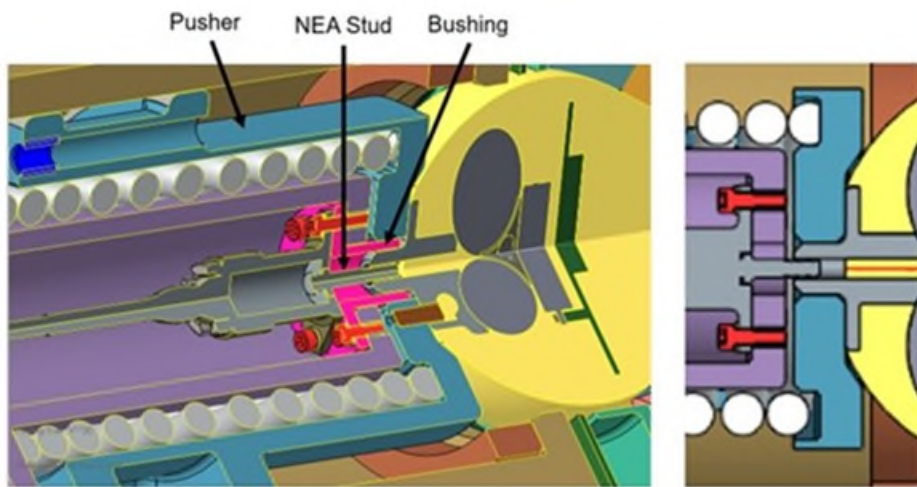


Figure 19. Added Bushing (Left). Previous Design (Right)

Retention plates were also added to keep the three guide pins from backing out of the pusher. Figure 20.

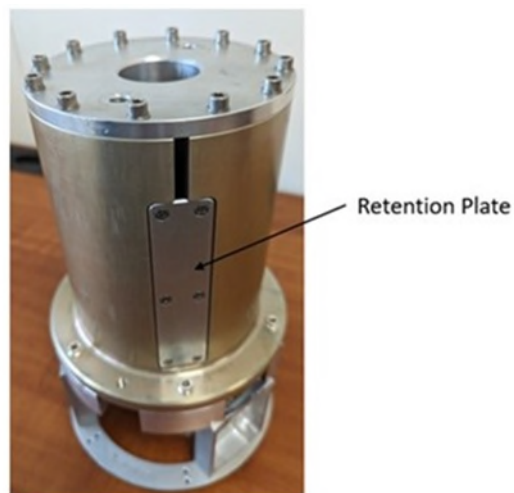


Figure 20. Retention Plate

The addition of the bushing introduced more friction into the system so some mass was machined out of the pusher to compensate.

The updated mechanism design was then run through its qualification tests successfully. These tests included functional and performance, random vibration, thermal vacuum, and maximum/minimum temperature firings. As shown in Figure 21, the velocities were very predictable and consistent at room temperature, so the expected standard deviation is small. In Figure 22, AT-017 was not clamped to the stand, therefore energy was lost in the recoil to the EDR. The resultant velocity was below the minimum needed for a positive force margin forcing a risk to be introduced to the project. The risk would be the EDM not clearing the RV during flight and the risk was deemed low.

Test	Test ID Number	Velocity (ft/sec)	Velocity (m/sec)
1	AT-001	27.30	8.32
2	AT-002	27.30	8.32
3	AT-003	27.30	8.32
4	AT-004	27.30	8.32
5	AT-005	27.50	8.38
6	AT-006	27.30	8.32
7	AT-007	27.50	8.38
8	AT-008	27.30	8.32
9	AT-009	27.30	8.32
10	AT-010	27.50	8.38
11	AT-011	27.20	8.29
12	AT-012	27.50	8.38
13	AT-013	27.50	8.38
14	AT-014	27.40	8.35
15	AT-015	27.40	8.35

Minimum Velocity, v_{min}	27.20	ft/s	= Min(Test 1 through Test 15)
Maximum Velocity, v_{max}	27.50	ft/s	= Max(Test 1 through Test 15)
Average Velocity, v_{avg}	27.37	ft/s	= Sum(Test 1 through Test 15) / No. of Tests
Standard Deviation, σ_{vel}	0.10	ft/s	= stdev.p(Test 1 through Test 15)
2 σ Minimum Velocity, $v_{min\ projected}$	27.17	ft/s	= $v_{avg} - 2 * \sigma_{vel}$

Figure 21. Run-In Testing (Flight Unit)

Test	Test ID Number	Velocity (m/sec)	Velocity (ft/sec)	Comments
1	AT-016	8.93	29.30	Ejection performed after TVAC and Vibing
2	AT-017*	8.02	26.30	Hot-Temperature Ejection
3	AT-018	9.72	31.90	Cold-Temperature Ejection

* AT-017 velocities were low due to recoil (the test fixture was not clamped).

Figure 22. Run-In Testing (Flight Unit)

Flight Ejection

The ejection mechanism successfully ejected the EDM during reentry, clearing the RV, and splashing down in the Pacific Ocean, Figure 23. The EDM landed approximately 6 miles from the recovery ship and was retrieved. Data was successfully extracted from the EDM as well.

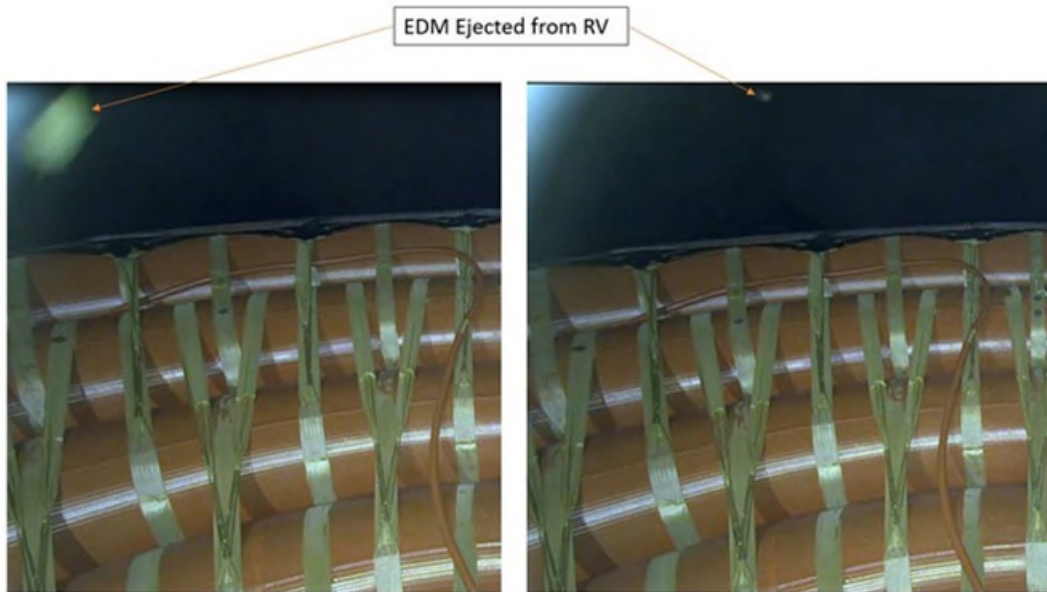


Figure 23. EDM Ejecting from RV

Conclusion

The EDR ejection mechanism had a few challenges throughout its development but ended up being successful. Through development testing, friction was found to be greater than anticipated, which reduced the ejection velocity and forced the team into evaluating the risk of having a negative force margin. In lieu of relying on published data for low-friction coating such as tungsten disulfide, a test program to develop friction coefficients for this configuration would have been invaluable. The EDR ejection mechanism is currently being looked at for future HIAD flights as a secondary data recovery system.

LARES2 Mission: Retention and Separation Subsystem

Matteo Spinelli^{*}, Alessandro Bursi^{*}, Simone Pirrotta^{**} and Roberto Bertacin^{**}

Abstract

During the LARES2 program, successfully launched in July 2022 with the VEGA-C launcher qualification flight, the Retention and Separation subsystem (SSEP) was re-designed and improved by OHB-Italy starting from the previous LARES SSEP to retain the spherical LARES2 satellite during launch and release it in the final orbit. This article describes the design and development of the LARES2 SSEP and summarizes key design drivers and relevant improvements from the first LARES one. Moreover, the article presents the multibody model correlation at elegant breadboard level and the fundamental contribution of flexible-body multibody analysis to predict the SSEP internal dynamic at satellite release. Finally, it also shows the results of the release test on the ground.

Introduction

The LARES2 (LAsER RELativity Satellite 2) is an all-Italian scientific mission, developed for the Italian Space Agency (ASI) and successfully deployed in orbit by the European launch vehicle VEGA-C on its qualification flight on July 13, 2022. This is the second mission of a series: the first LARES mission, founded by ASI, was successfully launched in 2012 with the VEGA maiden flight, as described in [1]. The main aim of the LARES2 mission is to allow higher accuracy measurements with respect to previous missions, of an orbital disturbance predicted by general relativity called frame-dragging or Lense Thirring effect; it is the dragging of inertial frame due to additional space-time curvature produced by the Earth's angular momentum. To reach this purpose, LARES2 satellite shall be as close as possible to a point mass in orbit along with a precise positioning measurement of its orbital position. Two secondary objectives were assigned to the mission: to allow the release of six cubesats (three 3U and three 1U) at the final orbit and support the Launch Vehicle (LV) qualification, hosting a set of sensors. In order to accommodate all the payloads and provide their structural connection with the LV, the LARES2 System has been designed and developed by OHB-Italy. Key technological improvements have been implemented in this second mission that distinguish LARES2 System from the first one: the Retention and Separation subsystem has been upgraded and the supporting structure has been designed to minimize its mass and the elastic energy collaborating to the retention and release functionalities.

LARES2 System Architecture and Subsystems

The LARES2 System, shown in Figure 1, is composed of the following main elements:

- LARES2 satellite: designed by La Sapienza university of Rome and manufactured by the National Institute of Nuclear Physics (INFN), is the scientific satellite, consisting of an Inconel718 sphere of about 430-mm diameter and 300 kg of mass, hosting 303 Cubic Corner Retroreflectors (CCR) on its surface. The CCRs are needed to precisely track the satellite position from ground stations through the laser ranging system.
- Retention and Separation subsystem (SSEP): fully developed by OHB-I, the SSEP, is a complex and non-conventional device which clamps the spherical satellite when subjected to the high launch accelerations and, once in orbit, releases it providing the required separation velocity. These functions are guaranteed by different mechanisms applying a preload directly on the spherical surface with retaining function. The activation signals are provided by the LV.

^{*} OHB Italia, Milan, Italy

^{**} Italian Space Agency, Rome, Italy

- Cubesat secondary payloads: the four 3U cubesat dispensers loaded with the six cubesats.
- Sensors secondary payloads made up by the LV sensors (two microphones and two accelerometers) mounted on the LARES2 System to monitor critical environmental parameters during the launcher ascent and a camera to record the satellite separation.
- Structural support subsystem (SSTR): it is the structural element that connects the SSEP and the secondary payloads to the LV standard V1194 payload adapter (PLA) and it guarantees the fulfilment of static and dynamic structural requirements of LARES2 System.

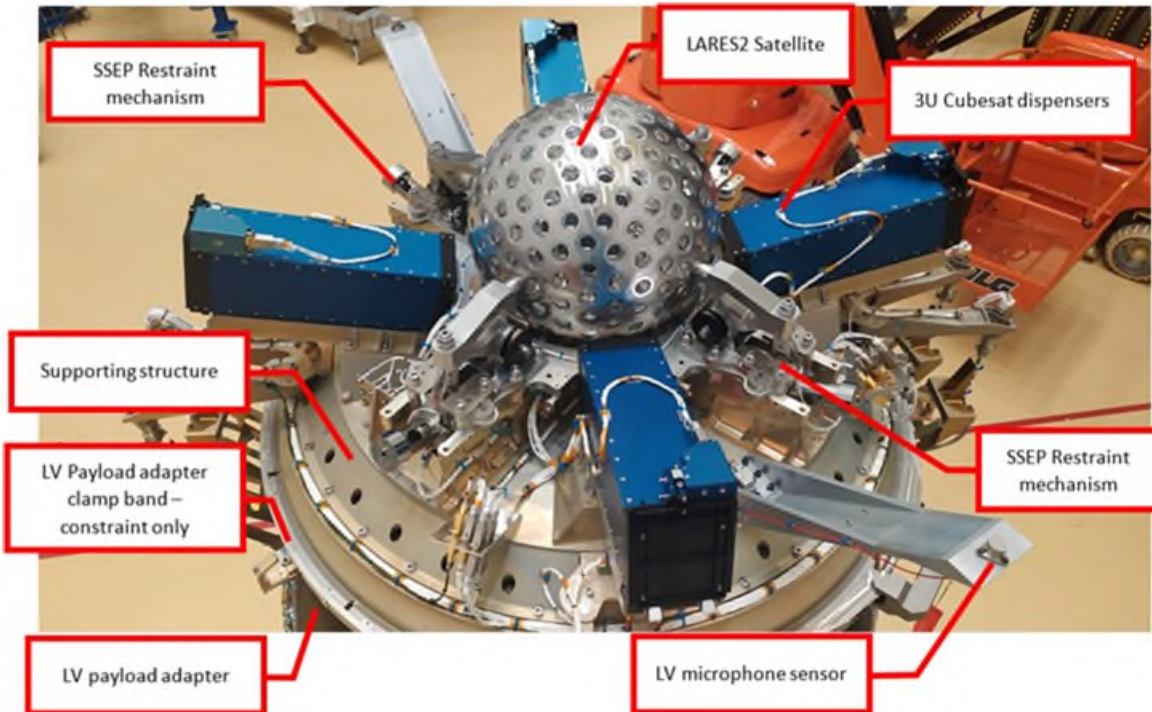


Figure 1. LARES2 System on top the LV payload adapter little before launch

LARES2 SSEP Design Driving Requirements

Main goal of the SSEP was the fulfillment of the following challenging requirements:

- Provide a high stiffness connection to the LARES2 satellite to limit the amplification of the LV sine environment during launch (sine loads of 1.2 g longitudinally and 0.5 g laterally up to 110 Hz).
- Withstand high launch environmental loads (i.e., quasi static load of 15 g in each orthogonal direction applied to the 300-kg Satellite to cover foreseen amplification in sine environment).
- Lock a spherical body by minimizing the contact areas, avoiding damage to the CCR and avoiding any protrusion and unbalance in the satellite spherical shape.
- Release the satellite with 0.5-m/s relative speed and be single point failure tolerant in terms of release function (a degraded kinematical separation condition is acceptable in the latter case).
- Transmit negligible shock to the satellite during the separation to avoid damage to the CCRs.
- Be compact and lightweight, to keep the mass and CoG position of the LARES2 System under 550 kg and 500 mm from the LV PLA plane respectively.

Furthermore, at the start of the development, some of the high-level requirements were not frozen since the launch was the qualification flight of the LV (e.g., between the PDR and the CDR the PLA interface was changed from the V937 to the larger V1194). Hence, the LARES2 SSEP has been designed to be flexible to changes on LV interface requirements. Moreover, according to the development plan, the LARES2 SSEP has to extensively re-use the heritage of LARES SSEP to reduce the development risks and meet the tight schedule constraints.

LARES2 SSEP Design Development and LARES Heritage

The design of the first LARES SSEP, described in [2] and shown in Figure 2, was directly applicable to the LARES2 SSEP for the disposition and shape of the mechanical interfaces to the satellite. In particular, both SSEP are made up by the following mechanisms:

- Four equal Restraint Mechanisms that represent the equatorial mechanical interfaces toward the satellite and include the initiator device which releases the mechanisms. The aim of these mechanisms is to restrain the satellite and once commanded, to retract to release it. The retraction is achieved thanks to the rotation of the restraining pins around a hinge.
- One Pushing Mechanism to structurally support the satellite and absorb part of the loads and, once the restrain mechanisms are retracted, provide correct separation velocity to the satellite.

Furthermore, on the LARES SSEP, a supporting structure was used to provide the mechanical interface to the mechanisms towards the system.

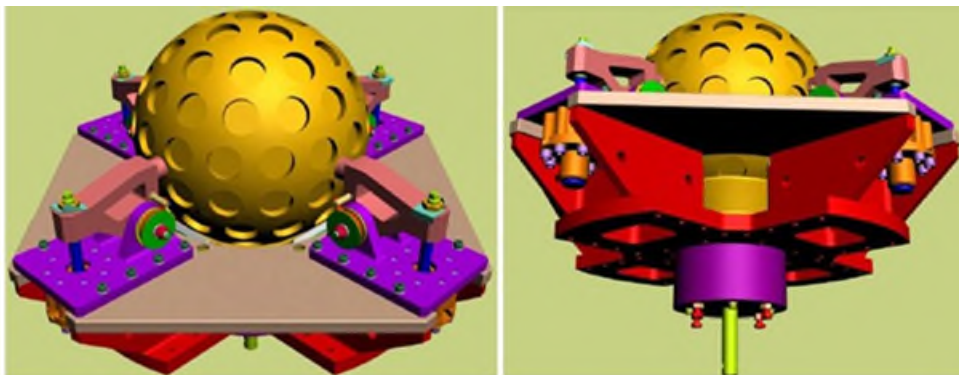


Figure 2. LARES SSEP with LARES satellite installed on it

The contact surfaces between the first LARES SSEP and the satellite were:

- Pushing mechanism: Sphere on cone, the SSEP part is covered by PTFE tape, to avoid LARES surface damage. No criticality due to hertzian stress, well below materials allowable. Furthermore, the cone shape is also covering the satellite CCRs.
- Restrain mechanism: sphere on sphere (cavity on satellite and pin on SSEP). The sphere geometries have been optimized to have an acceptable level of hertzian stress, in addition to avoid cold welding issues Braycote 601 lubricant has been used in between.

The functionality of the first LARES release mechanism is explained in the separation sequence shown in Figure 3, from locked configuration up to the satellite separation.

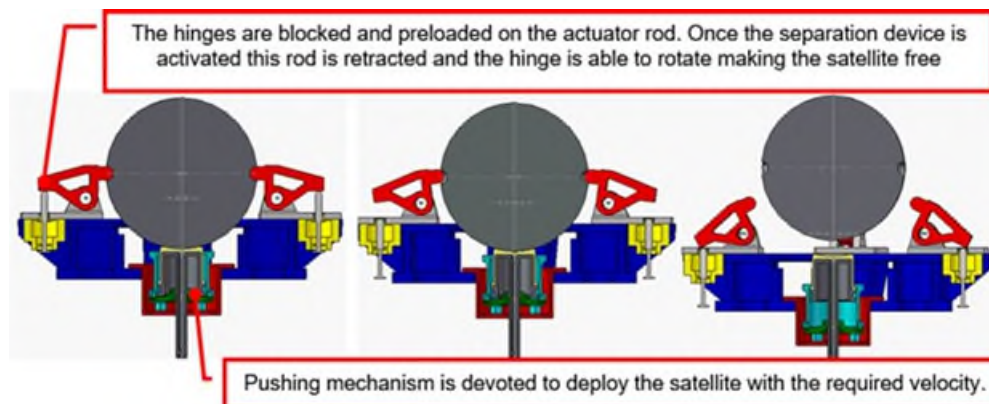


Figure 3. LARES SSEP separation sequence (from left to right) and functional explanation

Applicability of LARES SSEP Heritage to LARES2 SSEP

The LARES heritage was proven to be applicable to LARES2 SSEP except for the following three reasons:

1. The requirement for a smaller mass and lower CoG position for LARES2 System wrt LARES ones.
2. The LARES2 satellite diameter is larger than the LARES satellite one (430 mm vs 360 mm) and its surface is covered by a larger number of CCRs (303 vs 92), leading to a smaller percentage of not covered surface usable by the SSEP to interface with the satellite.
3. The release actuator used in LARES SSEP was an ad hoc customization of an NEA Electronics catalog product and the manufacturer declared that for the LARES2 mission a new qualification was needed. Furthermore, the proposed lead time for actuator qualification and procurement was not compatible with the LARES2 mission schedule.

The first point, along with the larger satellite dimension, leads to a merging of the SSEP supporting structure with the LARES2 System SSTR to reduce the overall mass and lower the System CoG. After this modification, the LARES2 SSEP is composed only by the four equatorial Restraint Mechanisms (RM) and the Pushing Mechanisms (PM), as shown in Figure 4, and it shall be integrated along with the LARES2 System SSTR. The second point leads to a modification of the PM contact surface towards the satellite to avoid contact over the CCR to be safer wrt LARES mission. In particular, the larger diameter of the satellite implies less distance of the CCR surface from the ideal spherical shape, thus, it has been decided to cut the contact line according to the CCR pattern to press only on satellite metallic surface, as shown in Figure 6. The third and last point leads to the change of the release actuator and thus to a large impact on the heritage on Restraint Mechanism design.

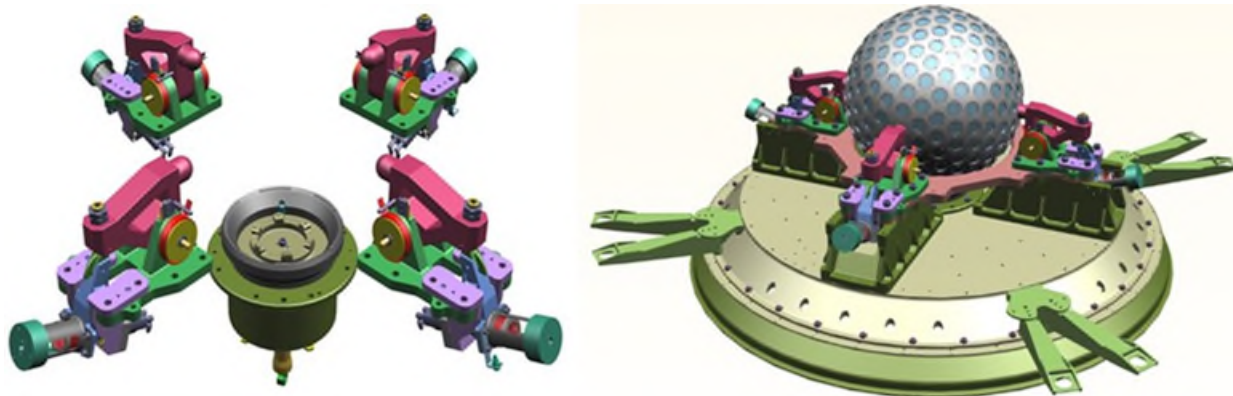


Figure 4. LARES2 SSEP design (left) and SSEP installed on the SSTR (right)

Restraint Mechanism Release Actuator Change

The RM release actuator change has been investigated by considering the following basic requirements:

- The new actuator to be used shall be an off the shelf fully qualified for the LARES2 System application (a Category A according to ECSS standards).
- The electrical interfaces of the new actuator shall be identical to the previous one.
- The lead time shall be compatible with the LARES2 mission schedule.

To fulfill the above requirements, the Separation Nut Actuator (SNA) from Eaton Cooper P/N 9421-1600-001 has been selected. It is a fully qualified off the shelf component and its qualification status covers the LARES2 System requirements. Furthermore, it has been already used by OHB-Italy on two other projects and the electrical interfaces are identical to the old actuator ones. Finally, the lead time is compatible with the schedule. However, the strength of the SNA is much lower (33-kN max preload while the first SSEP actuator was capable of 148-kN max preload) and the functioning of the SNA is the opposite of the old actuator one: the first one is a tension actuator (i.e., the actuator is used as a nut to engage a tensioned bolt and, when commanded, the nut releases the bolt), while the second one is a compression actuator (i.e., a fixed rod protruding from the actuator is pushed to carry the load and, when commanded, this rod

retracts inside the actuator body). For this reason, a major change in the RM kinematic link is needed to use the SNA while preserving the heritage for the RM satellite release. Different solutions were investigated and compared with the LARES RM characteristics in terms of mass and stiffness to design a new RM unlocking feature compatible with the SNA functioning. The resulting LARES2 RM design concept is based on a lever that can rotate around a hinge and at launch is kept in position by the SNA preload. The lever position is kinematically linked with the position of the latch (the component in contact with the satellite). Particular attention has been placed in the component materials chosen to be compatible with the high hertzian contact stresses in the separation surfaces, stresses that have been previously minimized through the evolution of the component's shapes. Each RM is made up of the following main components:

- Latch, to constrain the satellite at launch and to release it by rotating back around the RM hinge
- Hinge, to accommodate the latch pivot and connect the RM to the SSTR
- Lever, to constrain the latch and to release it by rotating around the actuator bracket hinge
- Actuator bracket, to accommodate the lever pivot and the SNA, connecting them to the hinge
- Preloading pin, to preload the latch against the satellite applying a force on the lever
- Bolt catcher, to retract and retain the separation bolt after the SNA actuation thanks to a preloaded spring
- Sphere-Cone separable interface, to join lever and actuator bracket at launch thanks to the preload of the separation bolt tightened into the SNA.

The resulting LARES2 RM design concept is presented in Figure 5. By considering Figure 2, it is possible to compare the design evolution with respect to LARES RM design, presented also in Figure 3.

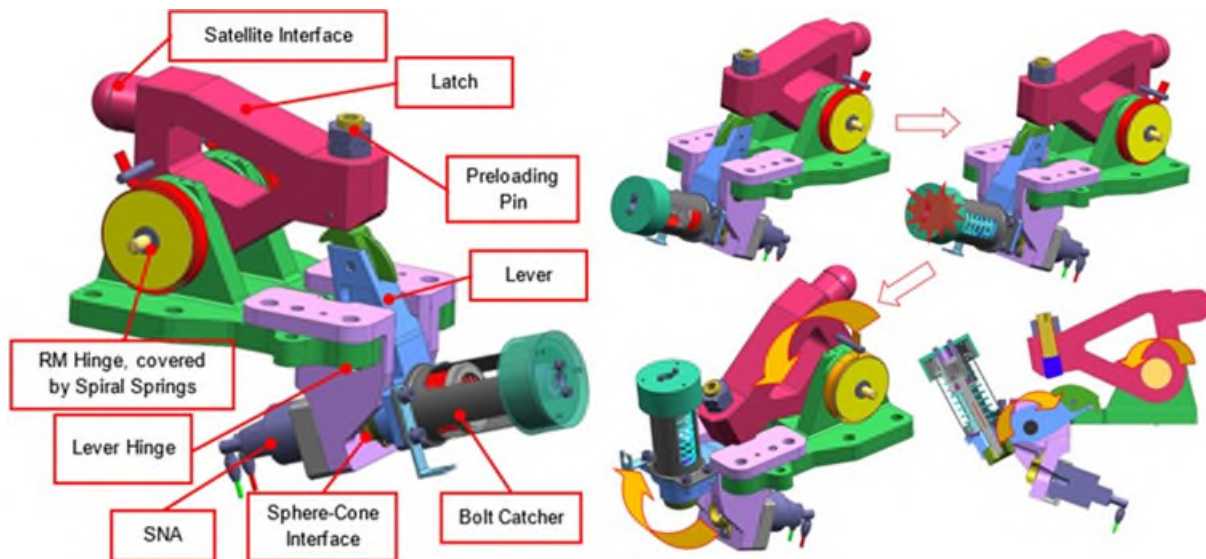


Figure 5. LARES2 RM design concept and release sequence

Pushing Mechanism Design Update

The PM design has been updated to cope with the larger satellite dimensions and the increased number of CCRs. To allow this, a metal to metal contact lubricated with Braycote 601 grease has been selected to be compatible with the resulting hertzian stresses. During this process, the previous PM internal design has been simplified to reduce the overall mass and to ease the manufacturing and the integration. The release functioning heritage is completely maintained by updating the spring stiffness and stroke to the LARES2 satellite mass and separation velocity. The PM is composed of the following items:

- Cup, to accommodate the satellite at launch and absorb part of the launch loads
- Pusher, to eject the satellite after RM releases through a compression spring
- Cup support, which is the connection of the PM with the SSTR and accommodate the switches
- Switches, to communicate the complete extension of the pusher after the satellite separation

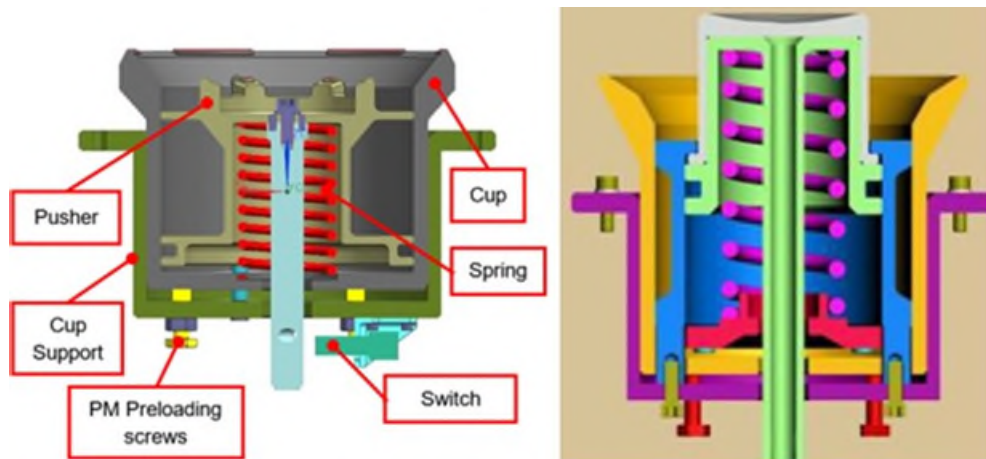


Figure 6. LARES2 PM design concept (left) comparison with LARES PM (right)

LARES2 SSEP Functioning

The SSEP needs to be preloaded against the satellite to perform its restraining function. Both RM and PM have provisions to apply and measure the preload through Strain Gauges (SG), as shown in Figure 7.

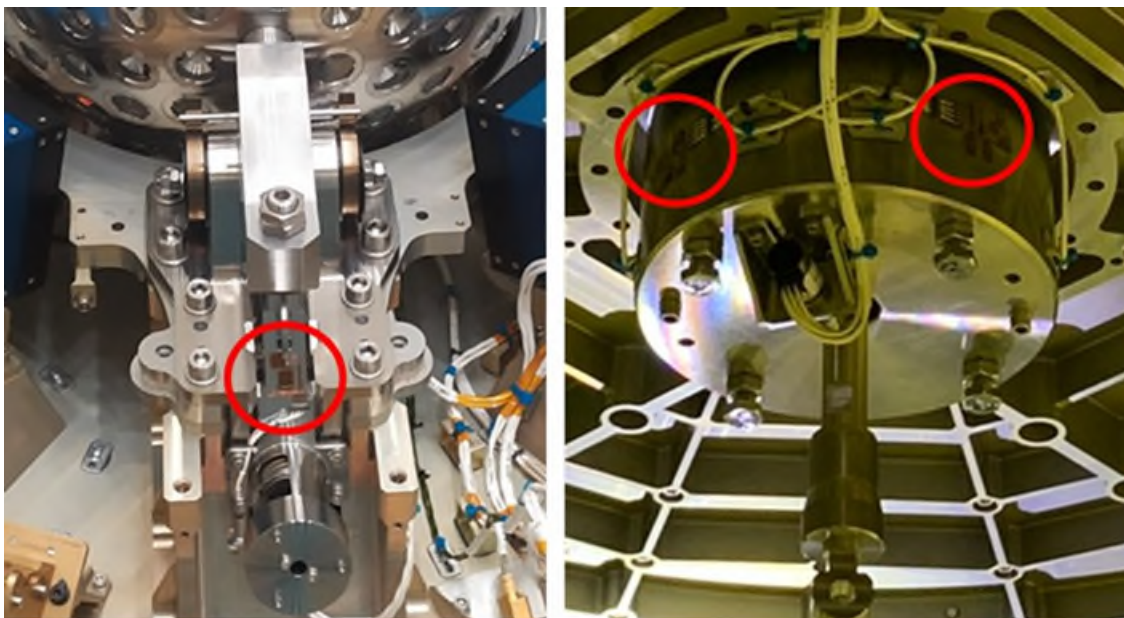


Figure 7. RM strain gauges (left) and PM strain gauges (right)

However, applying the preload on the satellite through the RM or the PM has completely different effectiveness:

- The RM is preloaded in two steps; firstly the lever is locked in position by tightening the separation bolt in the SNA. Then, the latch is preloaded towards the satellite by tightening the preloading pin against the lever. The first step is done without the aid of a measurement system by applying a calibrated torque (i.e., the torque needed to reach the target preload has been measured for each SNA with a new separation bolt prior to mechanism integration) while, during the second step, the applied preload is measured thanks to a SG set in full bridge configuration placed on the lever external side. The preloading pin tightening produces a latch rotation towards the satellite, hence, the preload applied on the satellite has both in-plane and vertical force

components: the in-plane one is directly reacted by the RM placed in the satellite opposite side, while the vertical component is reacted by the PM.

- The PM has four SG sets, each one in full bridge configuration, placed on the cup support lateral cylindrical surface in correspondence of each RM. In this way, it is possible to evaluate the vertical forces balancing applied to the satellite by the four RM. The PM also has the possibility to increase and balance the vertical preload on the satellite by tightening four preloading screws placed on the PM bottom side in correspondence of the four RMs.

The SSEP target preload has been derived from FEM analysis and the mechanisms' SGs target values has been retrieved from correlations performed at mechanism level. The RMs are correlated during their stiffness tests and the PM is correlated during LARES2 System integration, by reading the SG when the satellite is placed on it. To apply a uniform preload as much as possible, the SSEP is integrated by exploiting the heritage of the LARES SSEP satellite integration procedure, which granted a high precision alignment of the mechanisms to the satellite. The resulting LARES2 SSEP functioning sequence is shown and summarized in Figure 8.

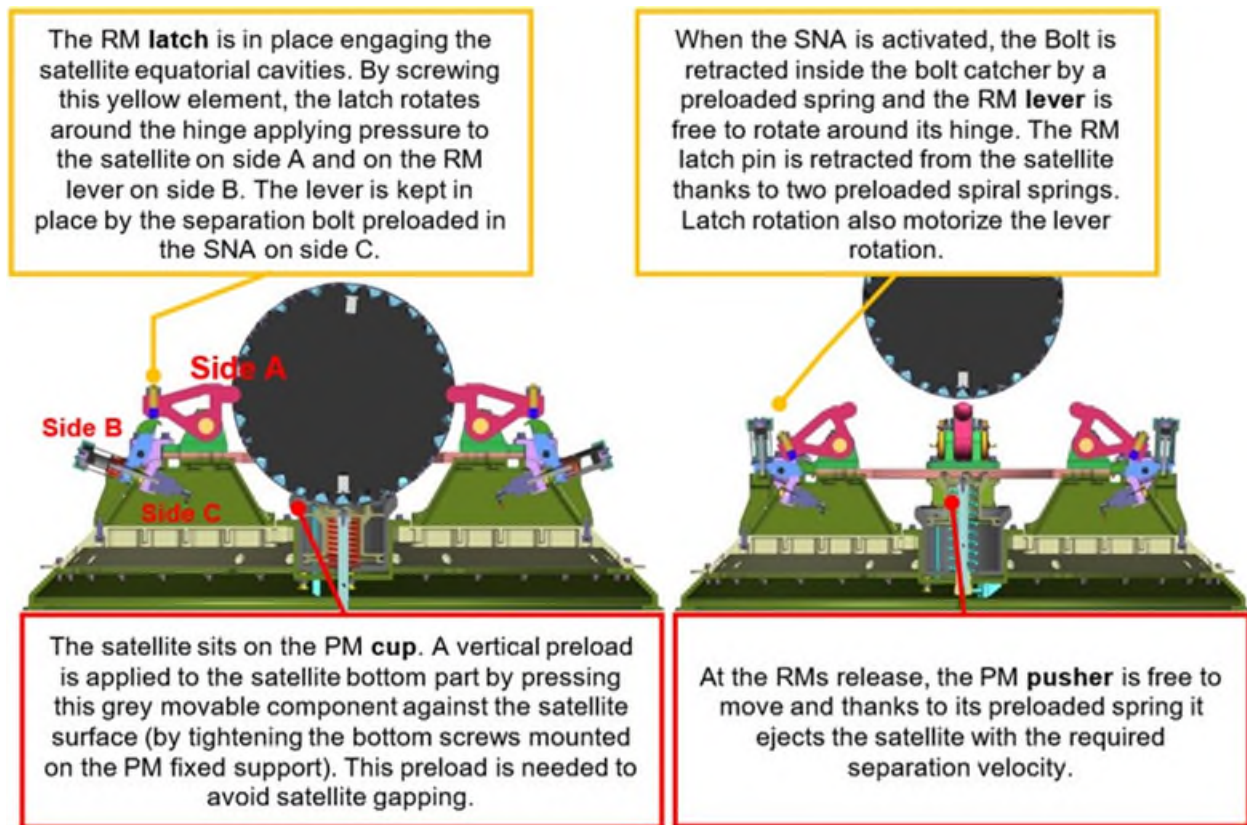


Figure 8. LARES2 SSEP functioning explanation

RM Breadboard Tests and Multibody Model Correlation

Taking into account the criticality of the SSEP and the deviation from the LARES heritage, two breadboards (BB) models have been implemented for the RM. The first one was a fully representative RM and it has been used for structural (stiffness) and functional (torque margin and deployment main parameters) characterization of the new RM design. The second BB was a pin on disk fretting test representative of the RM to satellite interface to measure cold welding behavior of contact materials lubricated with Braycote 601. The fretting test showed that the highest measured adhesion force of all

tests over all environments was 66 mN. This value is below any tendency of cold welding, which is expected in the range of 200 mN or higher, according to STM-279.

RM Breadboard Stiffness Test

The objectives of this test were the measuring of the stiffness along the three principal directions of the RM and thus the stiffness correlation of both structural model and functional multibody (MBD) model. The RM BB has been loaded through interfaces which are representative of the satellite ones to retrieve reliable results as shown in Figure 9. Furthermore, a force of 10 kN has been considered for each direction: it has been applied in ten steps through a screw with a load cell in series to be highly modulable and three loading-unloading cycles have been performed for each test. The displacements of peculiar points of the RM have been measured through Linear Variable Displacement Transducer (LVDT) sensors with precision in the order of microns. The correlation of the RM MBD model has been achieved by setting an equivalent stiffness at the connection of the RM to the SSTR, in order to keep the RM model made by rigid elements with the actual geometry of the RM and constraints between the parts which are ideal or geometrical interaction constraints (i.e., relative motion between parts is driven by direct interaction by means of their modeled geometry, friction, hertzian contact stiffness and damping parameters).

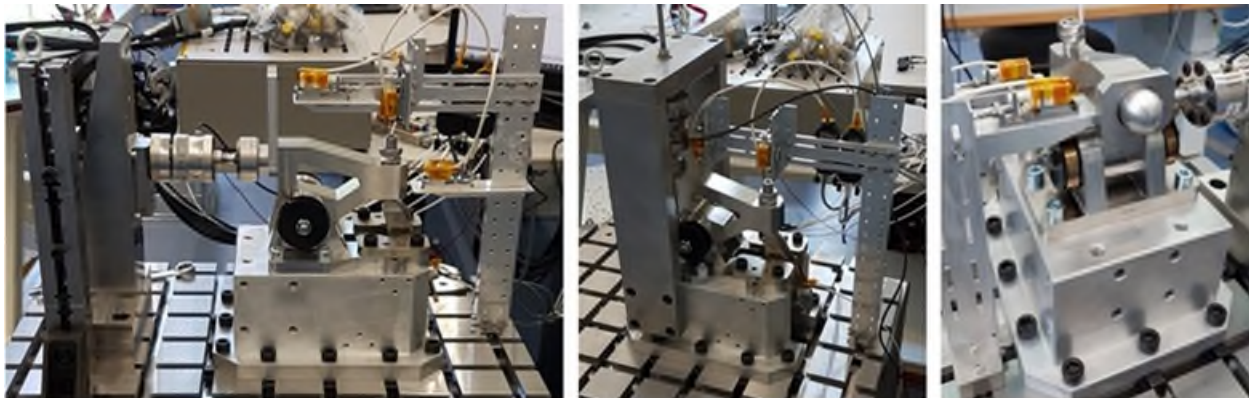


Figure 9. RM BB longitudinal (left), vertical (center) and lateral (right) stiffness tests

RM Breadboard Functional Test

The objectives of this test were the measuring of the friction coefficient of the latch hinge, of the lever hinge and of the latch-lever contact and then, the dynamic correlation of RM functional MBD model. To measure the friction coefficients of the hinges, two “free drop tests” on the latch and on the lever have been performed: the own weight of the components is considered to motorize the motion and their time to drop measured through high-speed camera recording. A set of repetitions per test have been carried out and average values have been employed for correlation: the friction coefficient measured for both hinges is 0.1 with an error less the 1% on MBD correlation. To measure the friction between the latch and the lever in contact, two tests have been performed:

- The static friction coefficient has been measured by increasing the bolt catcher mass (on the back of the lever) to reach the equilibrium and lock the latch-lever motion: the value found is 0.21.
- The dynamic friction coefficient has been obtained by comparing the measured drop time of a free release test and the time predicted by the MBD model correlated with the previous results: the value found is 0.235, with an error less the 6% on MBD correlation.

Finally, the whole RM BB has been tested by performing a release test in both free and preloaded configurations by starting the release with an electrical actuation of the SNA. The setup for the RM functional tests is shown in Figure 10. The bracket on which the RM is preloaded has been modelled as a flexible body starting from its FEM model to consider its deformability in the test.



Figure 10. RM BB release test sequence: SNA actuation (left), bolt impact (center) and latch impact (right)

In this case, the rotation speed of the lever is driven from the force exchanged with the latch and from the impact force of the release bolt at the end of travel against its shock absorber (made by crushable honeycomb). Since the friction was already correlated in previous tests, the energy absorbed from the shock absorber became the reference parameter for the correlation: in order to have the same timing between test and MBD simulation, the energy absorbed by the crushing honeycomb is 30%. The timing difference between the test and the MBD analysis is less than the 7% for each of the main events of the release (i.e., bolt impact, latch impact and lever impact) while the whole release lasts 0.136 s. In Figure 11, the MBD comparison between the release times of the free and preloaded configurations is shown. It is possible to notice that the 11-kN preload effect is negligible and the bolt retraction dynamic is decoupled from the lever one by one order of magnitude in time (i.e., bolt impact reached in 0.013 s wrt lever impact in 0.13 s).

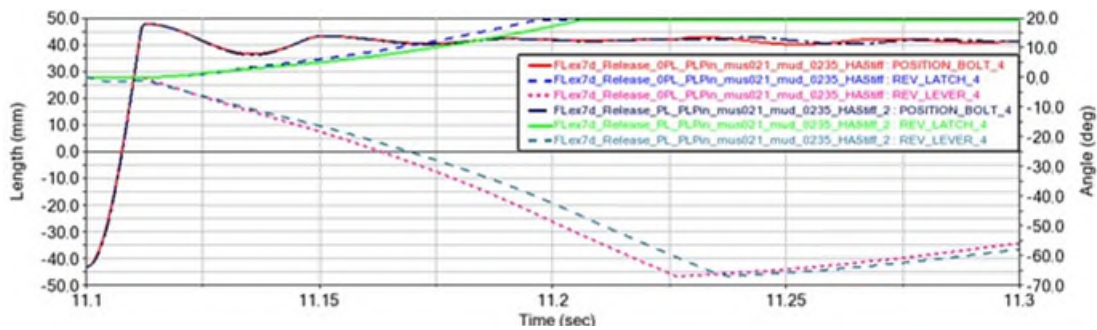


Figure 11. RM breadboard release test events comparison: zero preload (OPL) vs 11-kN preload (PL)

LARES2 SSEP Multibody Model Analyses and Design Updates

The MBD model of the LARES2 System, depicted in Figure 12, consists of the MBD models of the SSEP mechanisms, composed of rigid bodies and one single flexible part, made up by the SSTR, derived directly from the SSTR FEM model. This model has been used to carry out satellite release analysis in both nominal and degraded cases, to investigate the single failure tolerance capabilities of the SSEP. Parts are kinematically connected through appropriate joints and constraints, and their interaction occurs by means of imposed motions, spring actuation forces, surface contacts, and impact events. In particular, the RM model exploits the correlations achieved on the BB MBD model and it is connected to the SSTR with a flexible connection which simulates the RM stiffness measured during the BB stiffness test. Furthermore, the RM preloading phase has been simulated imposing a motion between the preloading pin and the latch, thus pushing against the lever; hence, a very realistic preloading phase has been simulated. The PM has been considered in contact with the satellite from the beginning by relying on the integration procedure of the satellite. The SSTR has been considered in the MBD model as a single flexible part created directly by reducing the SSTR FEM model according to the Component Modes Synthesis technique, by adding 106 dynamic shapes to the reduced model (6 free-free mode shapes & 100 flexible mode shapes): in this way, a good dynamic correlation is obtained with the flexible body. The reduction has been carried out considering the six I/F of the supporting structure as reduction nodes: one PLA interface, considered fixed to ground, one PM interface and four RM interfaces. By considering the

support structure flexibility, the effects of the deformation energy stored in the system structure due to the preloaded status at the release has been evaluated.



Figure 12. SSEP multibody model in preloaded configuration

SSEP Multibody Model Release Analysis in Flight Configuration

The SSEP MBD model was used to perform several release analyses in flight configuration (i.e., no gravity) to investigate the SSEP dynamic behavior and its release capabilities with different release sequences. The analyses performed are presented in Table 1. All analyses performed consider an initial settling phase of 0.1 s to let the solver evaluate all contacts between parts geometries, then the RM are preloaded to their 22.5-kN nominal preload against the satellite in 10 s (i.e., in a quasi-static way) to avoid high frequency disturbance due to solver integration issues. A second settling phase of 1 s is performed by keeping the satellite preloaded to let all the damping forces related to the preloading phase vanish. Finally, the release sequence starts at 11.1 s of simulation time by removing the RM internal constraint which simulates the locked SNA, thus in a fully representative way.

Table 1. SSEP multibody analysis performed

Analysis id	Analysis description	Release sequence	Release delay
An_0	Simultaneous release	RM 1,2,3,4	N/A
An_1	Nominal release	RM 1,3 – 2,4	100 ms between RM pairs
An_2	Delayed release 1	RM 1,3 – 4 – 2	100 ms from RM 1,3 release then 50 ms after RM4 release
An_3	Delayed release 2	RM 1,3 – 4 – 2	100 ms from RM 1,3 release then 100 ms after RM4 release
An_4	Failure release 1 RM2 remains locked	RM 1,3 – 4	100 ms from RM 1,3 release
An_5	Failure release 2 RM3 remains locked	RM 1 – 2,4	100 ms from RM 1 release
An_6	Failure release 3 No PM spring action	RM 1,3 – 2,4	100 ms between RM pairs
An_7	RM1 friction coefficient doubled	RM 1,3 – 2,4	100 ms between RM pairs

In Figure 13 the relative speed of the satellite is shown for all the analysis. It is possible to notice that in all cases the satellite is successfully released (even if, in failure cases, the relative velocity is lower than the required 0.5 m/s and the spin may reach 1.4 rad/s). Hence, it is confirmed that the designed SSEP is single failure tolerant, as requested.

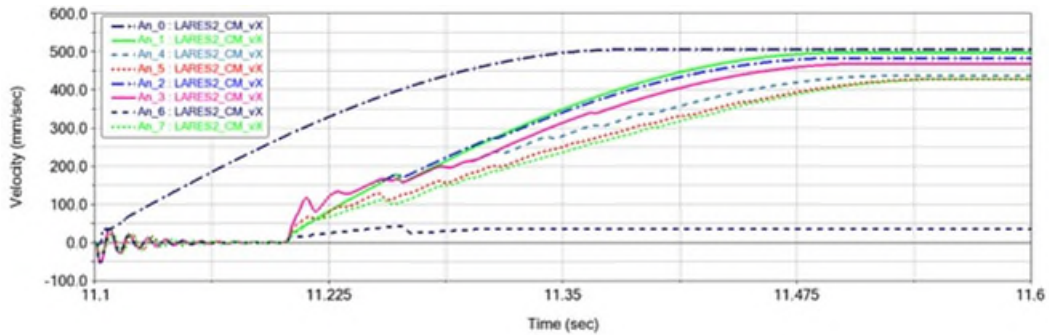


Figure 13. LARES2 satellite longitudinal velocity

However, MDB analysis shows that the RM lever angular velocity at SNA release may reach a staggering 30.5 rad/s, as shown in Figure 14, due to the elastic energy stored in the preloaded SSTR. This lever rotation dynamic (complete rotation time of 0.042 s) was not compatible with the RM separation bolt retraction dynamics at the time of the analyses. Hence, to avoid the possibility of clashing between the rotating lever and the translating separation bolt at the beginning of the RM release, the design of the RM has been improved prior to RM manufacturing for the SSEP qualification model.

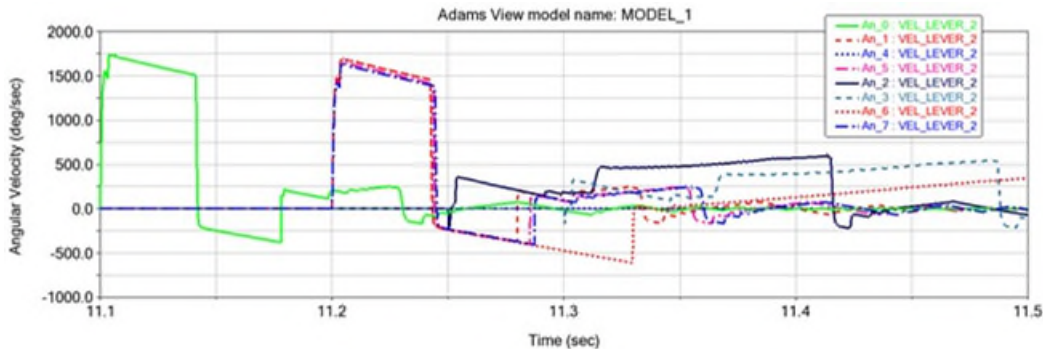


Figure 14. Restraint Mechanism lever angular velocity at release

Restraint Mechanism Design Update after Multibody Analyses

Thanks to the SSEP MBD analyses results, the RM design has been promptly updated to be compatible with the lever rotation dynamic. A disk spring has been added to the bolt catcher while the channel of all components passed through by the bolt has been enlarged to allow a lateral movement of the bolt tip due to a lever rotation. The bolt reaches very high speed at the beginning of the RM release thanks to the disk spring; the bolt is completely extracted in less than 3 ms. All the RM modifications are reported in Figure 15 and have been implemented on the RM manufactured for the Qualification Model (QM) of the SSEP.

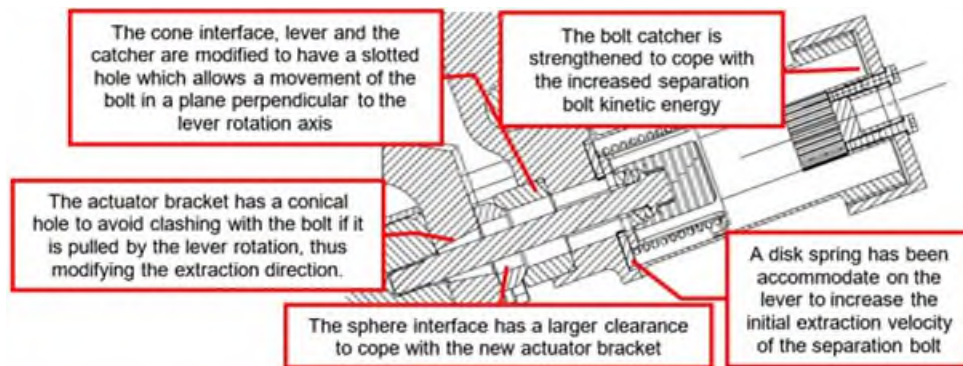


Figure 15. Restraint Mechanism design updates to cope with lever angular velocity at release

LARES2 SSEP Qualification Test Campaign

The SSEP QM, completely equal to the Flight Model (FM), was subjected to a qualification test campaign which comprises a vibration test to verify the strength of the SSEP at 15g along the three directions and then a full release test to verify the release capabilities of the SSEP after the launch preconditioning. The satellite used for the SSEP QM test campaign was a Demonstration Model made of steel instead of Inconel718 alloy, with a ~5% larger mass, only few CCRs mounted, and Inconel718 equatorial inserts to have representative interfaces with the RMs. In Figure 16 the two test setups are shown. The vibration test showed that the SSEP clamping configuration is able to dissipate energy at the main modes due to the sliding of the RM-satellite interfaces when the input is high enough to overcome the friction torque of the interfaces. In particular, the FEM correlation performed after the test, showed that at resonance search input level, the response of the SSEP is characterized by high stiffness and high amplification (estimated damping ~1% critical), while at qualification level, the response is characterized by a frequency shift wrt the resonance search results along with a marked decrease of the amplification (estimated damping ~ 6% critical in vertical direction and ~12% in in-plane directions).

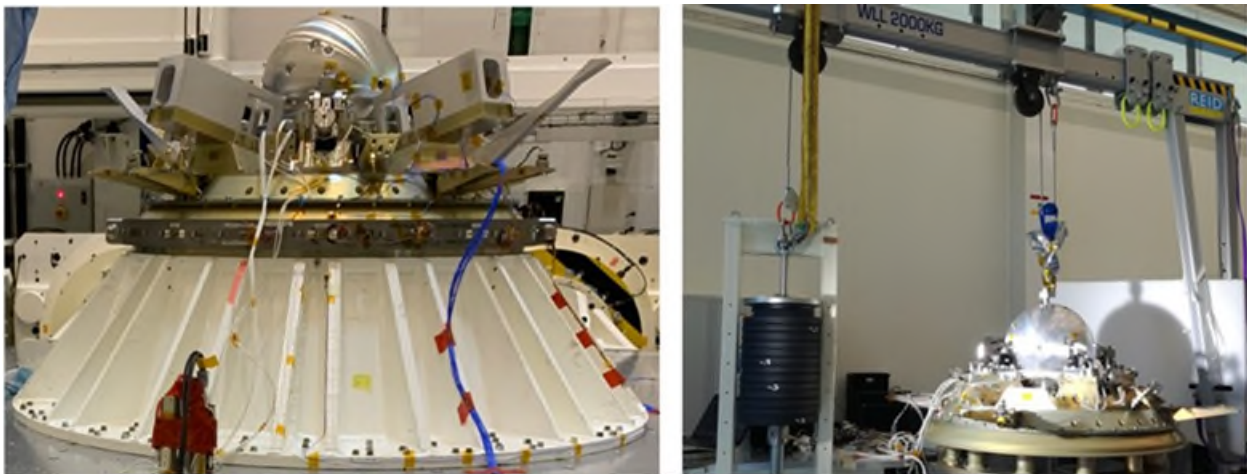


Figure 16. SSEP QM vibration test (left) and release test setups (right)

SSEP Release Test on Ground and Multibody Model Final Correlation

The SSEP release test has been performed thanks to an offloading device based on a ballast mass connected to the satellite north pole through a pulley. To measure the output velocity of the satellite while ejected by the SSEP mechanism, a high-speed camera (>1000 fps) has been used. In Figure 17, the release sequence recorded is shown: from the video, the distance travelled by the satellite is measured by comparing frame by frame the position of the Satellite wrt the release reference system. The MBD model of the SSEP has been inserted in a representation of the release test setup to predict the final speed of the satellite during the test; the predicted speed of 278mm/s (please consider that the offloading device inertia affects the release dynamics, lowering the final satellite velocity wrt the expected 500 mm/s in orbit) is then compared with the satellite computed velocity of 240 mm/s \pm 6%. This difference might be related to a PM Pusher friction higher than the expected and/or an energy dissipation in the offloading device due to impacts/frictions in the ballast mass guide. For the correlation of the MBD model, only the possibility of a PM friction higher than the expected has been considered since it is the worst case for the satellite release velocity in orbit.

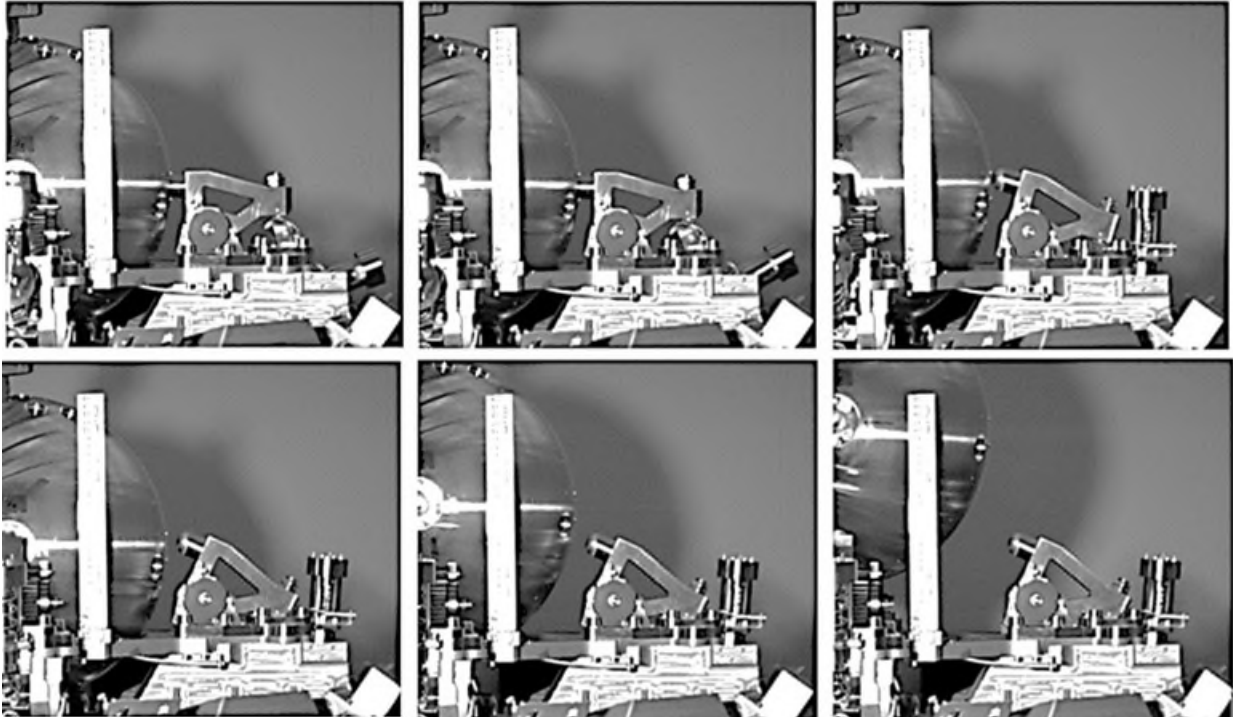


Figure 17. SSEP release test sequence (from left to right): SNA release, bolt impact, lever retraction, latch retraction, satellite in motion and satellite fully released

In Figure 18 the comparison between the measured velocity and the correlated multibody model result is presented. The model correlation has been performed by updating the PM spring stiffness to 75% of the measured spring stiffness. A further validation of the MBD correlation comes from the verification of the time interval between RM release and the switch activation: this time for the correlated MBD is 0.445 second whereas the measured one is 0.46 second.

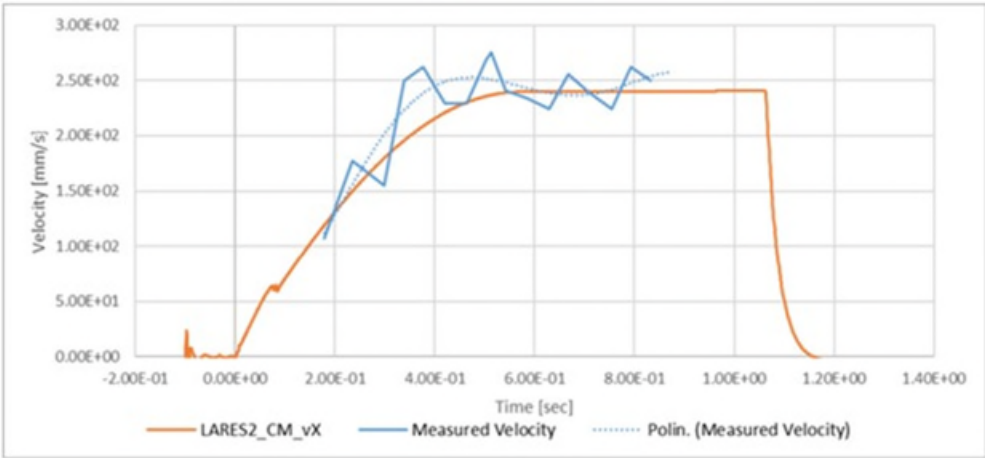


Figure 18. SSEP release test sequence and multibody model correlation

Visual inspections performed after the release test did not identify any damage or physical degradation on the satellite nor on the SSEP (i.e., no damage occurred after vibration test). Furthermore, the analysis of the high-speed video of the release confirmed the MBD model prediction of high speed lever rotation just after the SNA actuation thus confirming the correctness of the RM update to increase the separation bolt extraction velocity. The correlated MBD model shown that the resulting release velocity in orbit is

437 mm/s whereas the design one was 496 mm/s. However, this discrepancy is acceptable for the LARES2 mission since the requirement was $500 \text{ mm/s} \pm 20\%$. After launch, the SSEP performed nominally as shown by the video recorded by the on-board camera. The satellite left the SSEP with negligible spin and negligible lateral velocity, as expected. Furthermore, all visible CCRs were in nominal shape as shown in Figure 19 which depicts one frame of the recorded release video. The integrity of LARES2 satellite has been also confirmed by the high quality of the returned laser signal; in fact, since its first acquisition happened on July 15th by the ASI Matera Laser Ranging Observatory, the mission is regularly generating accurate scientific data, as described in [3].



Figure 19. LARES2 satellite release filmed in orbit

Conclusions

The LARES2 mission was successfully completed in 2022 with the correct release of the LARES2 satellite in the nominal orbit. The SSEP design, based on first LARES SSEP heritage, took benefit from a wide use of multibody analyses to cope with stringent release requirements and the adoption of a completely different release actuator. In particular, the Restraint Mechanism lever high rotational velocity of 30.5 rad/s predicted by the model and recorded during the test, may have jeopardized the mission schedule if not discovered in advance of the SSEP qualification model release test. In conclusion, the LARES2 SSEP experience proved the importance of improving the reliability of mechanisms multibody models by including flexible parts derived from structural models wherever their preloads induce large deformations (i.e., when the elastic energy stored in the system is not negligible).

References

1. A. Paolozzi, and I. Ciufolini, "LARES successfully launched in orbit: satellite and mission description" *Acta Astronautica* 91 (2013): 313-321.
2. A. Bursi, P. Camilli, C. Piredda, G. Babini and E. Mangraviti; "LARES Mission: Separation and Retention Subsystem", *Proceedings of the 42th Aerospace Mechanisms Symposium, NASA Goddard Space Flight Center, May 14-16, 2014*
3. I. Ciufolini, A. Paolozzi, E. Pavlis, J. Ries, ... and R. Penrose, "The LARES2 satellite, general relativity and fundamental physics", *The European Physical Journal C*, 2023 Vol.83/1

Design and Qualification of the Low-Earth Flight Test of an Inflatable Decelerator (LOFTID) Payload Adapter Separation System (PASS)

Sean M. Hancock^{*}, Jacob P. Montgomery^{*}, Ben J. Nickless^{**}, and Matt B. Realsen[†]

Abstract

On November 10, 2022, NASA and United Launch Alliance (ULA) launched Low-Earth Orbit Flight Test of an Inflatable Decelerator (LOFTID) as a secondary payload on an Atlas V Centaur from Vandenberg Space Force Base. After deploying the primary payload, JPSS-2, to a sun-synchronous orbit, the Centaur reoriented LOFTID for reentry, ejecting the Payload Adapter to expose the stowed LOFTID reentry vehicle (RV). The Hypersonic Inflatable Aerodynamic Decelerator (HIAD) was then deployed and inflated, and the Centaur reoriented the RV to the desired entry attitude, spun the vehicle to roughly three rpm, and separated the reentry vehicle. After nearly half an orbit of free flight, LOFTID reentered the atmosphere at >8 km/sec, demonstrating stable flight from hypersonic entry through subsonic parachute deployment. A mission-unique Payload Adapter Separation System (PASS) enabled the successful LOFTID flight demonstration, allowing the launch vehicle to accommodate a superstack of two independent, similarly sized payloads. This paper discusses the design, development, and qualification of the LOFTID PASS along with lessons learned.

Introduction

In November 2022, engineers at NASA Langley Research Center, collaborating with United Launch Alliance (ULA), validated Hypersonic Inflatable Aerodynamic Decelerator (HIAD) technology through the successful execution of the Low-Earth Orbit Flight Test of an Inflatable Decelerator (LOFTID) technology demonstration mission. LOFTID demonstrated the complete operational cycle of deployment, reentry, splashdown, and retrieval of a 6-meter HIAD [1]. HIAD represents a pivotal advancement in aerospace technology, facilitating the controlled atmospheric entry of heavy payloads to celestial bodies with atmospheres. The utilization of a deployable aeroshell effectively circumvents the size constraints inherent in prevailing rigid aeroshell entry systems imposed by the launch vehicle payload fairing. This adaptation enables the utilization of larger aeroshells, thereby yielding reduced ballistic coefficients and heightened entry system performance, manifesting in enhanced payload carrying capacity and/or volume, and elevated landing altitudes (e.g., expanding access to destinations such as southern highlands of Mars) [2].

Leveraging surplus capacity of the ULA's Atlas V launch vehicle, LOFTID was deployed as a secondary payload accompanying NASA-NOAA's Joint Polar Satellite System-2 (JPSS-2) weather observing satellite, launching from the Vandenberg Space Force Base. Following the successful delivery of JPSS-2 into its designated orbit, the ULA Centaur upper stage reoriented the LOFTID reentry vehicle (RV) for reentry. The RV was inflated, positioned, and separated to reenter into Earth's atmosphere at a velocity >8 km/s, culminating in a safe splashdown in the Pacific Ocean [3]. Accommodating the JPSS-2/LOFTID superstack (Figure 1) of two independent, comparably sized payloads, necessitated a unique mission configuration, with LOFTID beneath JPSS-2, housed within the Payload Adapter (PLA).

To separate the PLA from the launch vehicle prior to starting the LOFTID flight demonstration, NASA and ULA developed a mission-unique Payload Adapter Separation System (PASS). Separating flawlessly in

^{*} STC at NASA Langley Research Center, Hampton, VA

^{**} NASA Langley Research Center, Hampton, VA

[†] United Launch Alliance, Centennial, CO

flight, the PASS played a pivotal role in enabling mission success. The following paper provides an in-depth examination of the LOFTID PASS design and qualification, including encountered development challenges.



Figure 1 JPSS-2/LOFTID superstack

Payload Adapter

The LOFTID RV launched stowed inside the JPSS-2 Payload Adapter (Figure 2). This configuration highlights the HIAD's ability to eliminate size constraints of the payload fairing to allow larger aeroshells with lower ballistic coefficients. Because the HIAD can pack down into a small volume for launch, LOFTID was able to fly a 6 m in the Atlas V 4-m Extended Payload Fairing as a secondary payload.

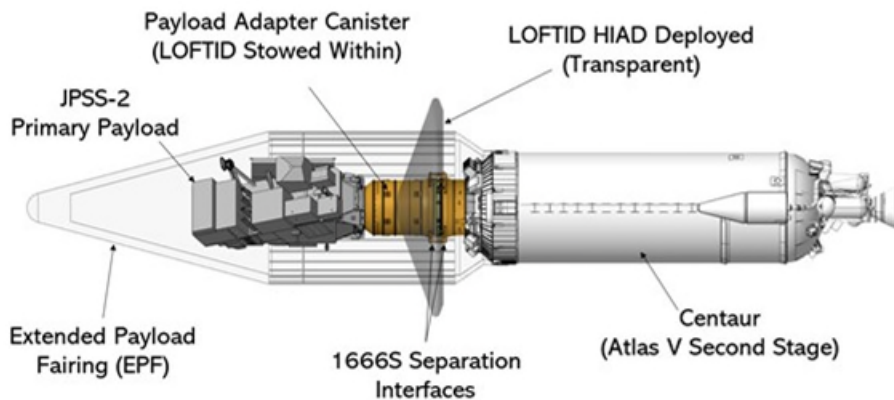


Figure 2 JPSS-2/LOFTID superstack

Figure 3 illustrates the PLA configuration. The PLA utilized a series of three ULA common payload separation systems and NASA's specially designed PASS. The PLA was mated to the Centaur upper stage via a standard ULA C-13 Adapter, mounting onto the Centaur Forward Adapter at the upper stage's forward end. A conical 1666S Payload Separation Ring (PSR) and a custom Reentry Vehicle to Payload Adapter Interface Ring (RVPAIR) facilitated the connection between the RV and the PLA. The PLA Canister comprised a 1666 Forward Separation Ring (FSR), a reversed 1666S PSR, a sequence of ULA C-adapter cylinders, and a B1194 Payload Separation Ring. A Contamination Control Diaphragm sealed the PLA Canister forward of the RV. This assembly separated to unveil the LOFTID payload. A single pneumatic disconnect and eight avionics in-flight disconnects (IFDs) spanned the PLA Canister

separation interface, while two additional avionics IFDs extended across the RV separation interface. The forward 1666S PSR facilitated separation of the PLA Canister from the RV while still attached to the Centaur, while the aft 1666S PSR executed separation of the RV from the Centaur. The PASS mounted internal to the PLA.

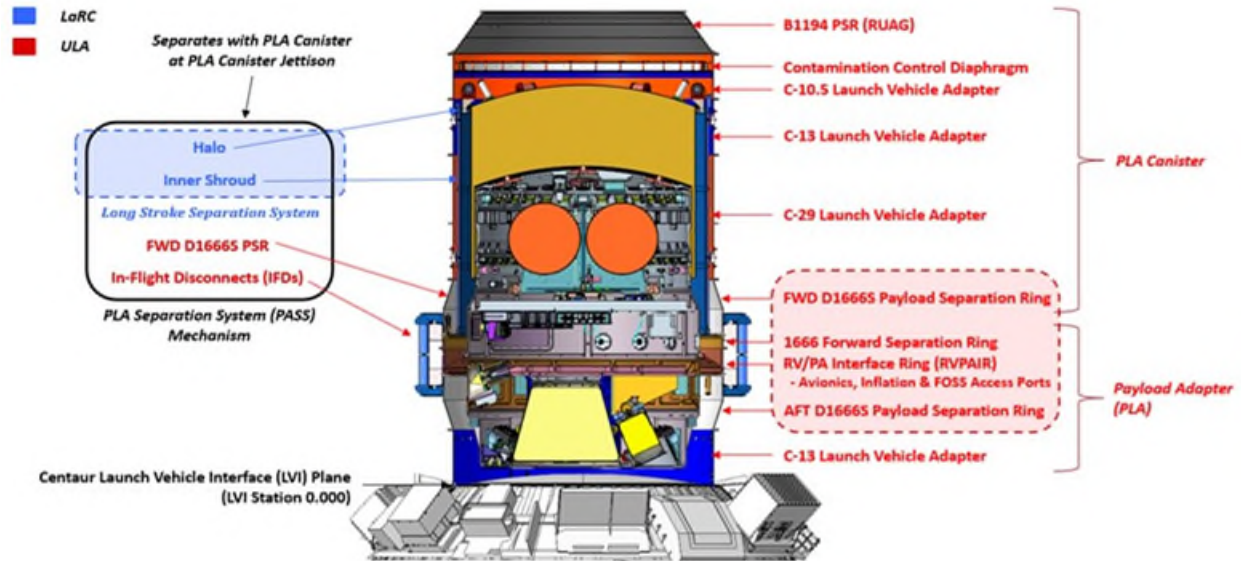


Figure 3 LOFTID Payload Adapter

PASS Design

The process of determining a rideshare configuration, the iterative nature of ULA's PLA design development, and a fixed JPSS-2 launch date resulted in a challenging PASS development timeline. To align with the launch schedule, PASS design and fabrication commenced prior to finalization of the rideshare decision.

Initially, the rideshare configuration included an Evolved Expendable Launch Vehicle Secondary Payload Adapter (ESPA) ring, accommodating up to 544 kg (1200 lbm) of Auxiliary Payloads (APLs), as depicted in Figure 4. In addition to the uncertain APL configuration, the PASS design had to anticipate potential APLs failing to separate from the ESPA, necessitating separation with the PLA Canister. Consequently, a broad spectrum of mass properties had to be factored into the design.

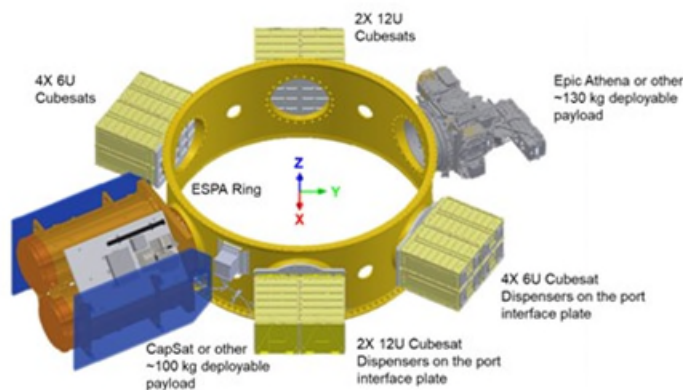


Figure 4 LOFTID Potential Rideshare Payloads

In addition to separating the PLA Canister from the RV, the PASS had a requirement to prevent damage to the stowed aeroshell during PLA Canister separation. To mitigate tip-off during separation, various concepts, including guide rails, were considered. However, due to uncertainties in separation mass and properties, the design eventually accepted potential contact between the separating PLA Canister and the stowed aeroshell. This led to the development of a design aimed at safeguarding the stowed aeroshell. Ultimately, a rideshare configuration eliminating the ESPA and all APLs was adopted, reducing mass by ~635 kg (~1400 lbm) (ESPA: ~91 kg (~200 lbm), APLs: ~544 kg (~1200 lbm)). The PASS design could accommodate this PLA configuration change with minimal impact.

A collaborative effort between ULA and NASA, the PASS comprised an inverted ULA-provided 1666S PSR and a NASA-provided Long Stroke Separation System (LSSS). The 1666S PSR supplied the initial kick-off motive force, while the LSSS ensured a positive separation force margin and protected the stowed LOFTID aeroshell.

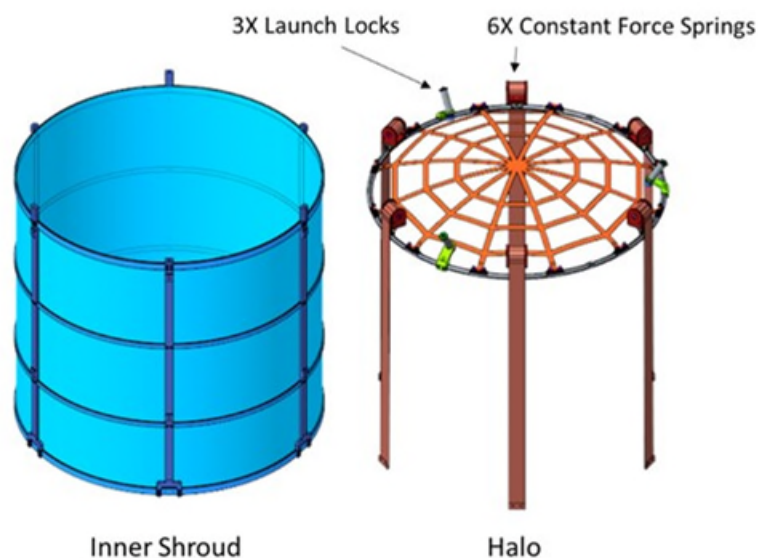


Figure 5 PASS Long Stroke Separation System

The LSSS comprised two primary sub-components: the Inner Shroud and the Halo, depicted in Figure 5. The Inner Shroud, featuring a Teflon-impregnated hardcoat anodized coating liner to provide a low friction surface to protect the stowed aeroshell during PLA Canister separation, attached to the PLA Canister at twelve locations – upper and lower mounts clocked in 60 degree increments. The Inner Shroud alone was not a stiff structure, however bolting it to the interior of the PLA Canister gave it considerable stiffness. The Halo, an aluminum ring hosting six constant force (CF) springs, three launch locks to ensure the Halo remained centered over the stowed aeroshell throughout launch, and custom webbing that provided a conformal interface to the stowed aeroshell. Like the interior of the Inner Shroud, the Halo was coated with a Teflon-impregnated hardcoat anodized coating.

The CF springs, shown in Fig. 6, provided a constant separation force margin during the separation event. The CF springs were pre-stressed flat strips of spring material formed into a constant radius coil around a drum. When extended, the inherent stress resists the loading force at a nearly constant (zero) rate. The springs offer high force output with minimal space requirements, provide long strokes, and store power indefinitely when extended. The springs, clocked 60 degrees apart, were matched to minimize tip-off.

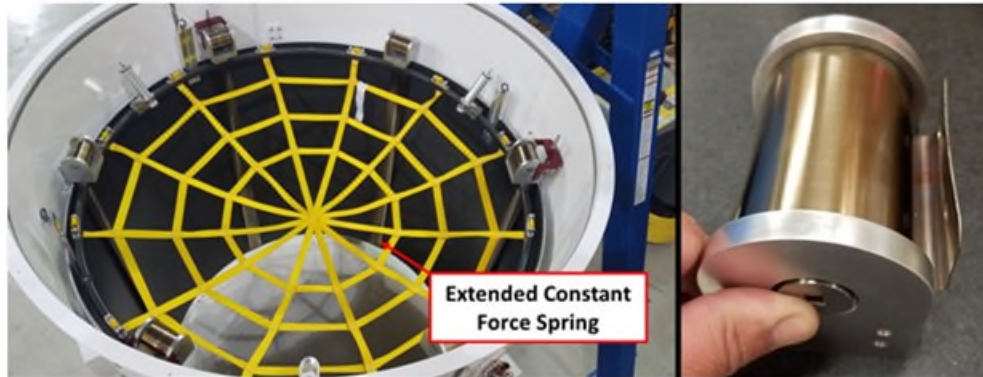


Figure 6 PASS Constant Force Spring

Following the KISS (Keep It Simple, Stupid) principle, the PASS operated akin to a sling shot. Upon command from the ULA Centaur, the 1666S clamp band released, initiating separation. The constant force springs retracted, pulling the Inner Shroud and PLA Canister up while exerting separation force against the stowed aeroshell until the PLA Canister disengaged from the RV. Fig. 7 illustrates this sequence.

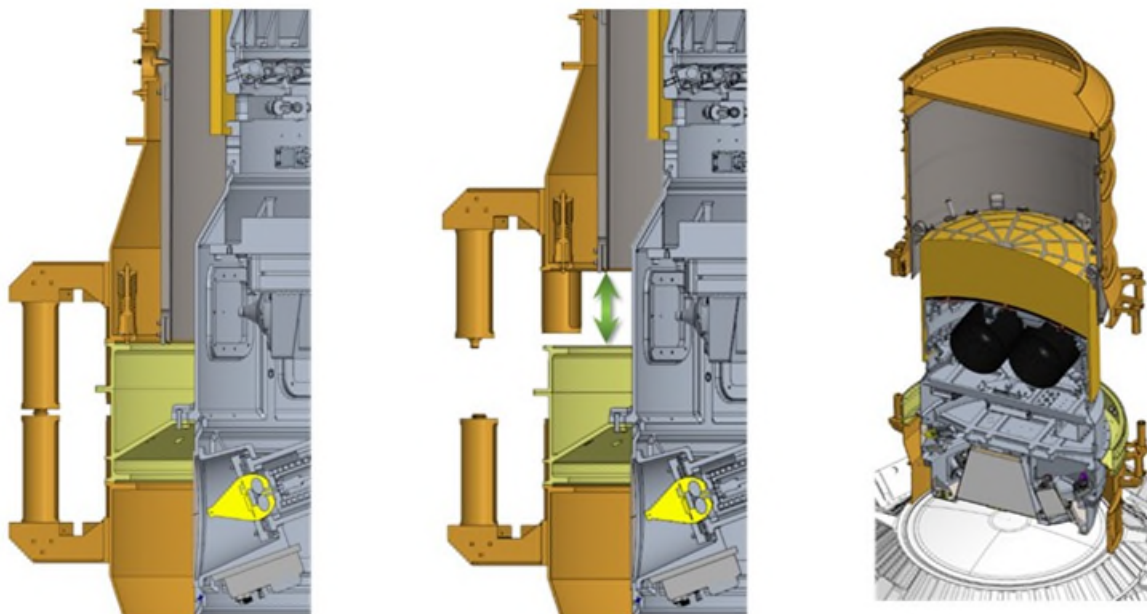


Figure 7 PASS Separation

Development and Qualification Testing

The PASS system's development adhered to the conventional NASA prototype development process, with the fabrication and testing of a qualification unit (Engineering Development Unit (EDU)), followed by a flight unit. NASA-STD-5017A Design and Development Requirements for Mechanisms [4] was tailored to maintain the requisite technical rigor yet align with the project's schedule, budget, and risk posture. Prior to the assembly of the PASS EDU, the CF springs underwent a comprehensive testing regime, encompassing component-level sine vibration testing, characterization testing, run-in testing, and life cycle testing. Concurrently, the PASS Halo assembly underwent static load testing. Subsequently, the fully assembled EDU underwent mechanism testing, including run-in testing, pre-random vibration

performance testing, random vibration performance testing, post-random vibration performance testing, and life cycle testing. Details of the Qualification Test Matrix can be found in Table 1.

Table 1: LOFTID PASS Qualification Test Matrix

Test	Recommended Qual Unit Testing	LOFTID PASS EDU Testing	Comments
Run-In	(1)	Nominal Actuation	Minimum of 3 Cycles at Assembly Level
Performance	Envelopes	Nominal Actuation	
Leak	X	N/A	
Shock	X	No	Analysis Only
Transportation from LaRC to GSFC			
Random Vibration	Qual Level	Qual Level	Post-Test Visual Inspection
Acoustic Vibration	Qual Level	No	Covered by Random Environments
Sinusoidal Vibration	Qual Level	No	Not Required
Transportation from GSFC to LaRC			
Thermal Cycle/Thermal Vacuum	X	No	Thermal characterization of spring sets
Thermal Gradient	X	N/A	
Depressurization/Repressurization	X	N/A	
Climactic	X	N/A	
Electromagnetic Compatibility	X	N/A	
Life	X	Nominal Actuation	Minimum of 5 Cycles
Statis Loads	X	No	Analysis Only
Performance	Envelopes	Nominal Actuation, Envelopes, Off-Nominal	Envelope – Maximum linear acceleration, Minimum linear acceleration Off Nominal – 1666S Spring-out, CF Spring-out, Halo Misalignment

- (1) Run-in testing is not listed in the qualification sequence because it is a workmanship test, and it is assumed that the qualification unit undergoes acceptance testing prior to qualification testing. However, if for some reason acceptance testing is not performed on the qualification unit, the qualification unit should still be run-in prior to qualification testing.

The CF Spring sine vibration test provided invaluable insights into the response of a CF spring in a flight configuration to the launch environment's acceleration input, facilitating a qualitative understanding of the interaction between the spring tape and the inner shroud liner. For this purpose, a dedicated fixture was fabricated to mount the spring fully extended against a liner surrogate, with clearances aligned with those in the PASS assembly, with testing conducted in all three axes.

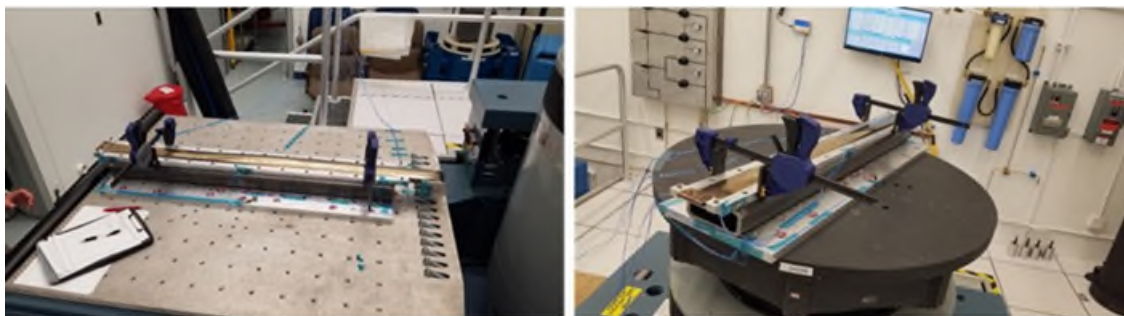


Figure 8 CF Spring Sine Vibe Testing – x and z axis (left), y axis (right)

For qualification testing, twelve constant springs were procured. The sine vibration testing spring was not used further. The remaining eleven springs were subjected to characterization testing. A matched set of six springs was selected post-characterization. Spring characterization testing utilized an MTS testing frame equipped with an integral thermal chamber to measure the spring pull force across its full range of travel. This configuration is shown in Figure 9. Each spring underwent a minimum of 15 cycles for component run-in testing, with deviations allowed during run-in testing provided the average force for the last five cycles did not deviate more than $\pm 10\%$ from the mean. After run-in testing, springs were subjected to additional cycles until each spring had been cycled 48 times. Testing also measured thermal sensitivity of spring force to temperature by testing a hot case and a cold case for each spring. Figure 9 also shows a typical measured spring force profile. It should be noted that the unsmooth nature of the curve was due to twisting of the spring in the load frame as the spring was extended or retracted, however the resolution of measurements was such that this impact was negligible. It should also be noted that the measured force on the spring extension was higher than that for retraction. This was the case for every cycle measurement. Because the pass springs were to retract in flight, the retraction measurements were used for PASS analysis.

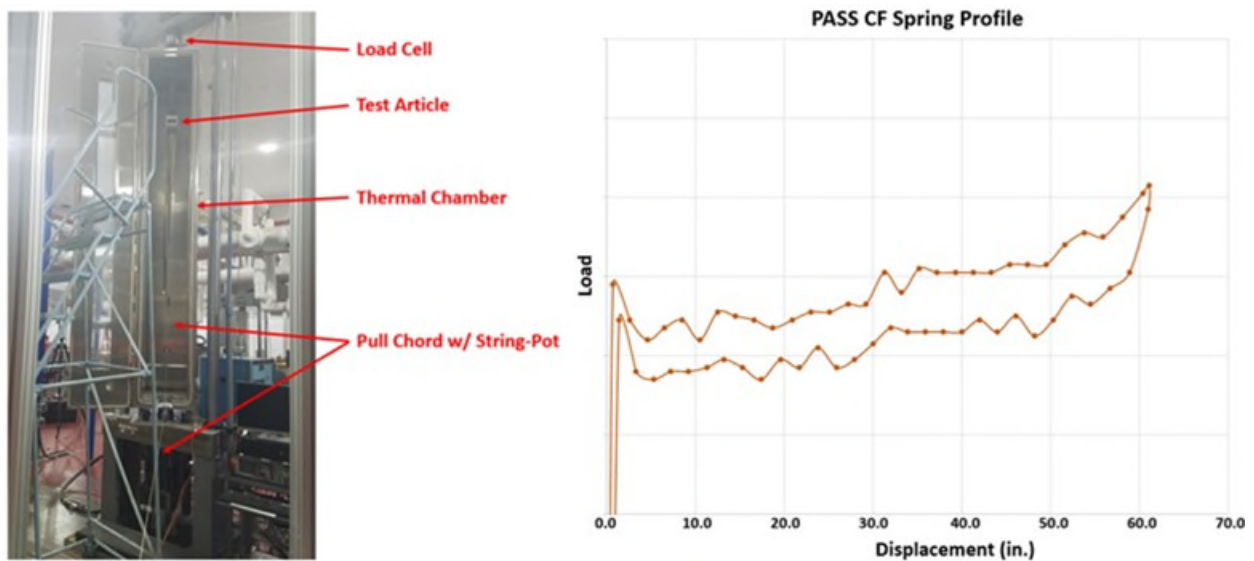


Figure 9 CF Spring characterization - test setup (left), typical spring force profile (right)

The LOFTID project learned a valuable lesson in the use of constant force springs during the first spring characterization test. The springs must be constrained against rotation lateral to the pull direction. If the spring is allowed to twist laterally, it will reach a critical point where the spring will unroll from the spool and re-coil orthogonal to the spool. This failure is shown in Figure 10.



Figure 10 PASS CF Spring Failure



Figure 11 PASS Halo static load testing

Before integrating the Halo to the Inner Shroud, the Halo underwent static load testing to 125% of its design load in a flight-like configuration, with test weights mounted to the CF Spring mounts and the weight pulling the webbing down against a mock-up of the stowed aeroshell. Figure 11 depicts a Halo static load test.

The PASS mechanism underwent testing using a planar air bearing test that allowed for three degrees of freedom in a 1-g environment – 2 translational and 1 rotational. Because this configuration only allowed freedom to rotate in the yaw direction, the mechanism was tested in two planes (two separate tests for each condition) and utilized superposition to qualify its operation in a zero-g environment. The mechanism test configuration is shown in Figure 12.

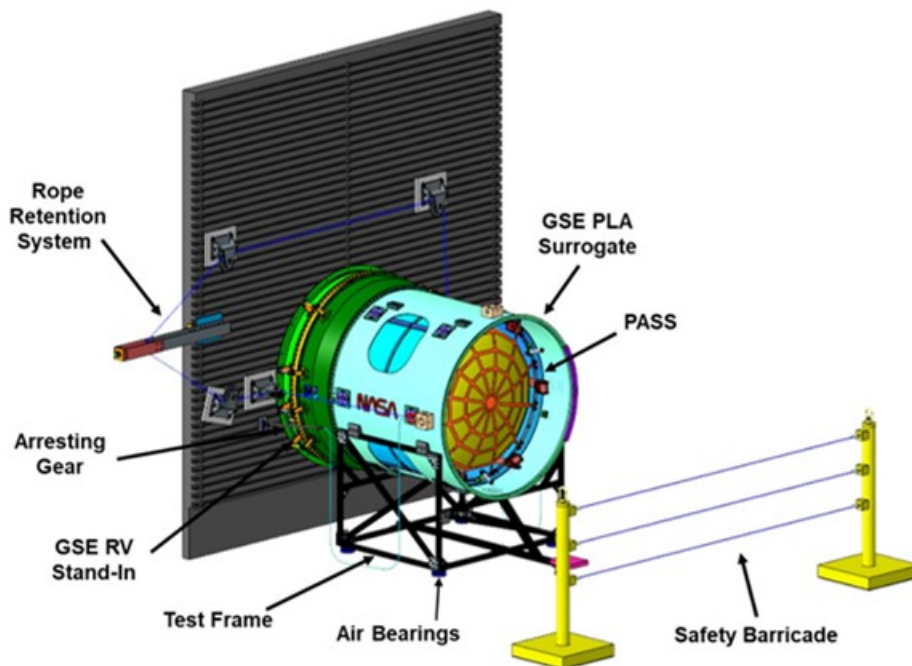


Figure 12 PASS mechanism test setup

PASS mechanism testing utilized an RV Stand-In mounted to a rigid backstop. The PASS EDU was mounted to a PLA Canister Surrogate mounted on a frame supported by planar air bearings. Because the FWD 1666S clamp band would not function properly in a horizontal 1-g configuration, the PLA Canister Surrogate was secured to the RV Stand-In using a series of ropes and pulleys that could be tensioned. When it was time to test separation, the rope was cut, and the PLA Canister, with the PASS EDU installed, could separate freely on the air bearings. A set of dampers secured to the backstop and the PLA Canister slowed and then stopped the PLA Canister after separation was complete. In-case the damper system failed to stop the PLA Canister, a safety barricade was added. Photogrammetry with high-speed cameras was used to measure the PLA canister separation and tip-off rates and to qualitatively inspect PASS performance during separation. Test success criteria required that the mean separation velocity of an individual test fall within $\pm 10\%$ of the overall mean from all tests for a given configuration. Failure of the PASS/PLA Canister to fully separate or cause damage to the aeroshell restraint bag would also constitute a test failure.

Qualification mechanism testing included three run-in cycles, a single performance cycle, and fifteen life-cycle cycles for a total of 18 individual tests, all demonstrating repeatable performance. Two envelope tests were conducted in a single plane. These tests were maximum and minimum linear acceleration. Three off-nominal cases were evaluated, again in a single plane. These included a ULA kick-off spring-out case, a CF spring-out case, and a case that simulated the Halo shifting all the way to one side during launch (launch lock failure). The PASS separated the PLA Canister Surrogate cleanly during each of the off-nominal cases.

Test-as-you-fly requirements necessitated duplicating flight interfaces between the PASS and the RV. An RV Stand-In was fabricated to duplicate the OML of the RV from the RVPAIR ring forward to the stowed aeroshell. Figure 13 provides a comparison of the RV Stand-In with the flight RV and shows the external features incorporated, including access panel fasteners, bulkhead connectors on the RVPAIR, a Fiber Optic Sensing System (FOSS) [5] cover with fasteners, and the packing restraint bag cord cutter blocks and retention groove. Because the stowed aeroshell reacts the load of the PASS CF Springs and the Halo webbing had to be conformal to the stowed aeroshell OML, the RV Stand-In included a surrogate for the stowed aeroshell, shown in Figure 14. The stowed aeroshell surrogate was fabricated from model foam of the same density as the packed HIAD. The OML was machined to match a simple revolution of a section from a laser scan of stowed aeroshell EDU. The stowed aeroshell surrogate was then covered with the packing restraint EDU, providing a completely flight-like interface between the PASS and the RV.

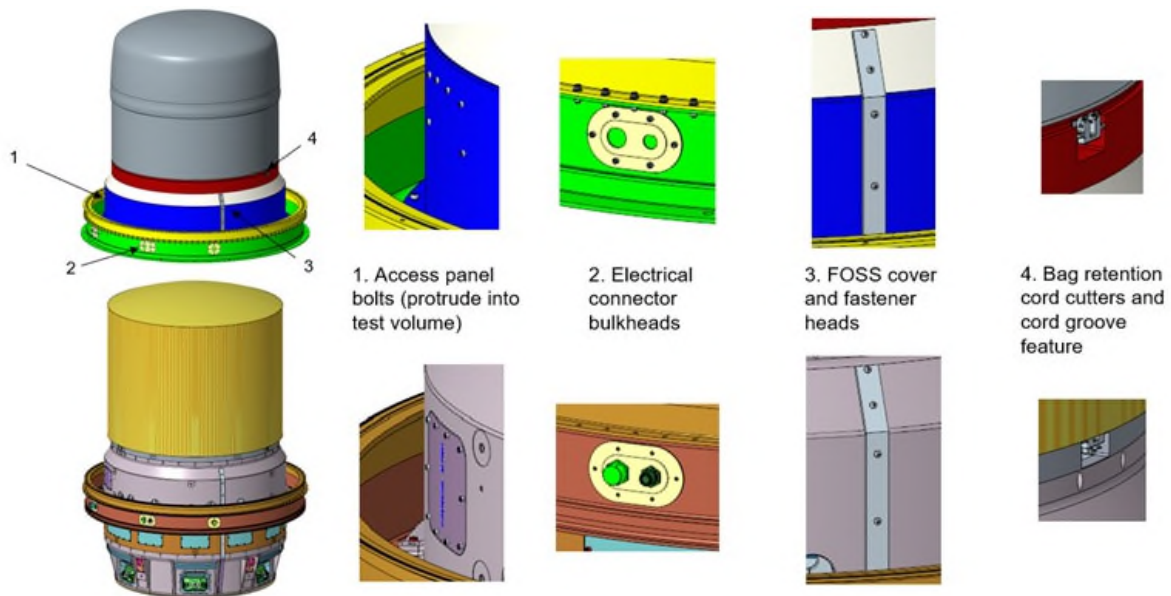


Figure 13 RV Stand-In (top) compared to RV (bottom)



Figure 14 RV Stand-In stowed aeroshell surrogate (left) with packing restraint EDU (right)

To duplicate the PASS and PLA Canister interfaces, a PLA Canister Surrogate was constructed. It incorporated all of the separation mechanism features of the ULA 1666S PSR with the exception of the clamp band. ULA provided kick-off compression springs and the separation surface between the 1666S PSR and 1666 FSR was replicated. IFD surrogates, mimicking JPSS-2 IFDs, were placed in the correct positions across the PLA Canister separation plane. These surrogates matched the nominal pull force of the flight IFDs, and each was subjected to characterization pull testing to ensure the intended force. These data were later utilized in a dynamic model to predict PASS flight performance accurately. Additionally, the PLA Canister Surrogate included twelve PASS to PLA Canister interfaces, built to specified tolerances outlined in the Mechanical Interface Control Drawing. This facilitated early verification of compatibility between the PASS and the PLA Canister. illustrates a comparison between the PLA Canister Surrogate and the flight PLA Canister, highlighting the incorporated features.

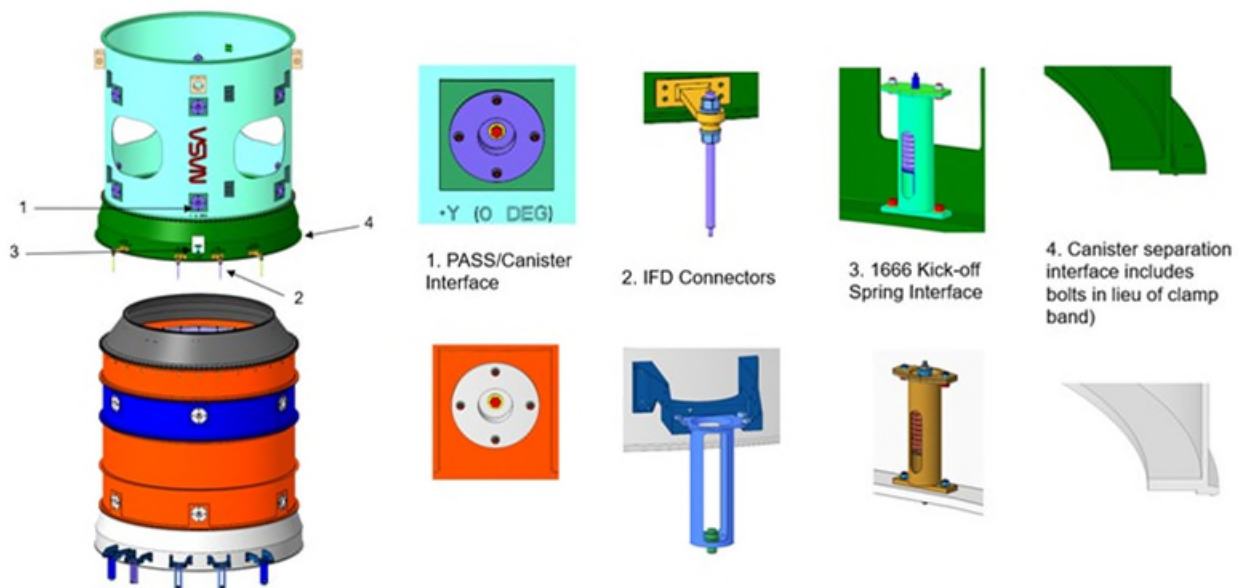


Figure 15 PLA Canister Surrogate (top) compared to PLA Canister (bottom)

Kinematics dictates PASS separation performance is a strong function of PLA Canister mass properties. To ensure ground testing simulated flight conditions accurately, the PLA Canister surrogate was designed so that when placed on the test stand, the test hardware's mass closely matched the predicted mass of

the flight hardware within 1%, and the location of the CG in the two directions of lateral freedom of motion were matched to within 2.54 mm (.10 in) of the predicted CG location of the flight hardware. Ballast was employed in each test setup to achieve this.

In order to match mass properties of the separating ground test element to that of the flight Canister, it was necessary to use small, light-weight air bearings. The air bearings used have very tight tolerances on floor flatness. This resulted in lessons learned in the application of these air bearings over the large spans of the test stand. The initial design called for an air bearing at each of the four corners of the stand. Test demonstrations showed that this would result in some binding and friction between the bearing and floor that would negatively impact test results. It was theorized that adding more air bearings would reduce the weight on any given air bearing and improve the performance, so the frame was modified to use a total of twelve air bearings. This, however, had the opposite effect, and resulted in more binding. So, the frame was again modified to have air bearings at only 3 locations (three points define a plane) – two in the front and one in the center rear without-riggers added at the rear corners to prevent tip-over. This last change resulted in a configuration that minimized impacts of friction between the test stand and the floor.

Due to the large size, required energy levels, and mass of the PASS, PLA Canister and the RV Stand-In, the PASS was random vibration tested at Goddard Space Flight Center (GSFC) vibration test facility 409 and 410. The PASS was tested to prototype qualification levels – limit level + 3 dB for a 2-minute duration in each axis. Figure 16 shows the test configuration. The final run-in mechanism test was used as a pre-random vibration baseline of performance and compared against a post-random vibration mechanism performance test, with no variation in performance.



Figure 16 PASS random vibration testing - lateral (left) and axial (right).

Analysis

A comprehensive ADAMS [6] model of the PASS was constructed to predict relative motion during separation and to delve into the effects of adjusting key parameters identified earlier. Initially, during the inception of the design phase, the model was built emulate in-flight dynamics to predict minimum and maximum separation accelerations, velocities, rotational rates, and other crucial metrics essential for informed design decisions. Subsequently, a ground test model was created from the flight model with constraints to reflect the ground test scenario, so that ground testing could verify the model accuracy and validity.

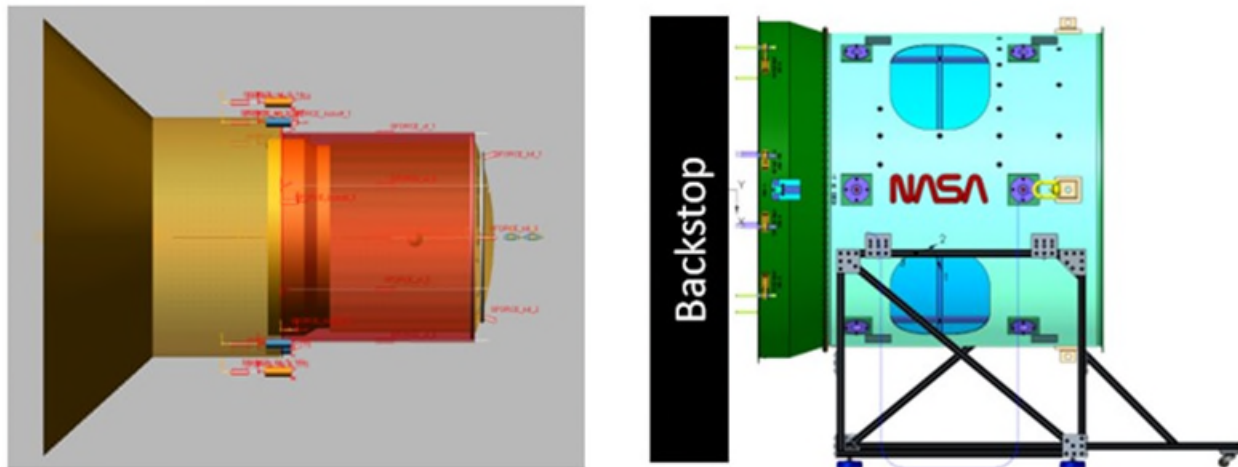


Figure 17 ADAMS model compared to test configuration

The ADAMS model incorporated three separate bodies, each with its associated mass properties: the LOFTID RV and Launch Vehicle (lumped together), the PASS Inner Shroud and PLA Canister, and the Halo. Figure 17 shows the ADAMS model alongside a CAD representation of the ground test configuration.

The various forces contributing to the separation event, including In-Flight Disconnects (IFDs), kick-off springs, and Constant Force (CF) springs, were assigned nominal values and tolerances during the initial stages evaluating the flight model. However, as the modeling transitioned to accommodate the ground test, numerous test article components underwent characterization testing, notably the CF Springs and IFDs. Nonetheless, not all components received comprehensive characterization, and those that were had assessments conducted in test fixturing rather than in their operational configuration. So, for these and other reasons (data noise, environmental factors, etc.) it was expected the ADAMS model would necessitate refinement to align with the actual behavior observed during testing, thus ensuring accurate correlation with the test data. The test data itself served as a guiding benchmark for the tuning process, guiding adjustments to achieve closer alignment between the model and observed behavior.

Figure 18 provides an example of model-test correlation, showcasing the velocity profile of the X-configuration test before and after model tuning. Notably, prior to tuning, the general behavior is captured well, requiring only minor adjustments to specific component behaviors to better align with the observed test performance. The minor adjustments included: decreasing the CF Spring force level, adjustment of the ULA spring hard-stop location, adjustment of IFD force application start and stop points, and increasing IFD force levels. Figure 19 shows the percent difference between the model and test, and that after tuning, the requirement of correlation within 10% was met, excepting values below 3X-noise-floor, as evidenced by the high percent difference for the first 20 milliseconds or so.

There were some lessons learned regarding analysis and model correlation. There is a likelihood the data received for correlation will be noisy or less-than-pristine, and that sorting through it may require some iteration. In this case, that meant a few rounds of low-pass filtering, as we were looking for the DC component of the velocity measurements. This also applies to the component test data used as model inputs, which required filtering and smoothing so as not to cause model instability. In addition, some high-pass filtering was necessary to establish the noise floor. An additional lesson learned for test set-up, is to consider early on how the different outputs to be correlated will respond to the inputs (e.g., the set of inputs vs the variance across the inputs) and let that inform both the test data requested and the methods to be used for correlation. During test planning, consider any test-unique inputs that may have been excluded from modeling based on assumptions, and revisit those assumptions if necessary. Regarding

the lessons learned about the air bearings described previously, for modeling correlation, it would have been helpful to have an in-test measurement of the air bearing drag, since it ended up having a larger effect than anticipated.

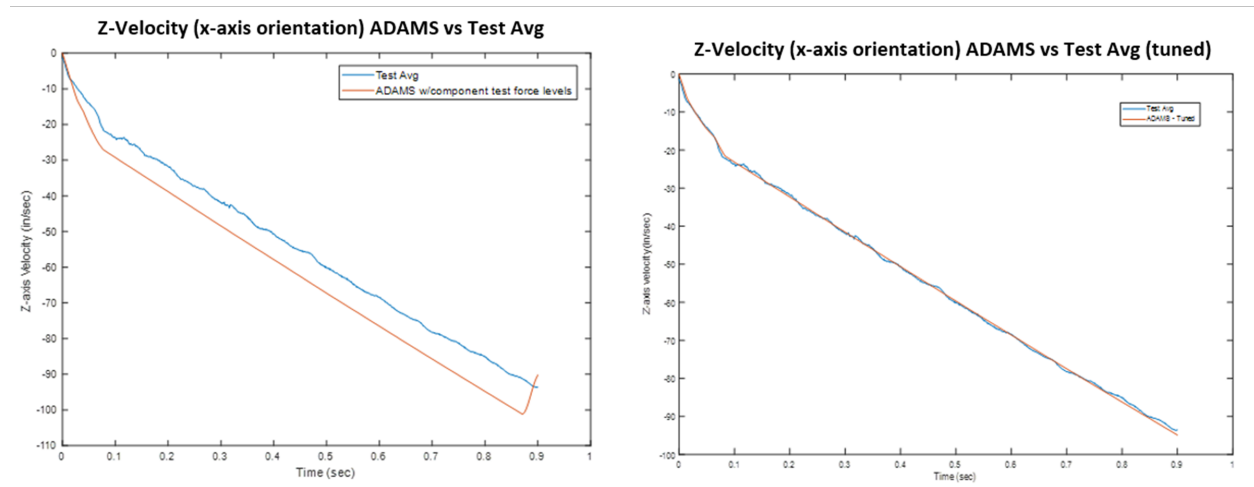


Figure 18 Sample ADAMS model versus Testing comparison – untuned (left) and tuned (right).

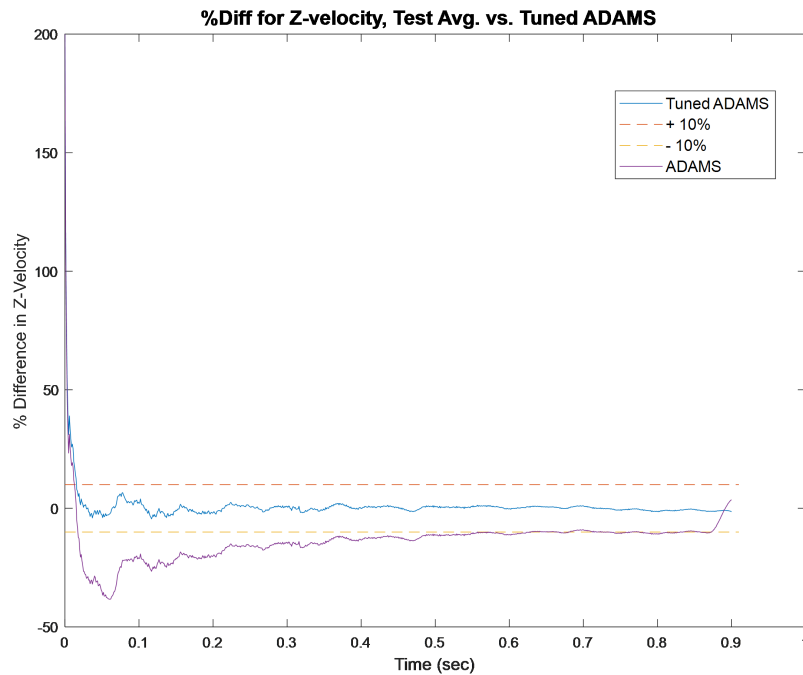


Figure 19 Model velocity versus Test velocity percent difference (tuned & untuned).

Conclusions

The PASS design underwent a rigorous testing regimen, comprising 30 successful ground mechanism tests encompassing various phases of qualification and acceptance – 24 EDU tests and six tests of the flight PASS. Throughout these trials, the PASS consistently executed clean separations of the PLA Canister (or Surrogate), including three off-nominal tests designed to simulate challenging conditions. The PASS demonstrated flawless performance during flight, exhibiting no discernible tip-off behavior. A

qualitative analysis of the flight video verifies that the separation velocity was in kind with outcomes observed during ground testing and predictions generated by the ADAMS model.

References

1. DiNonno, J., and Cheatwood, N. "Low-Earth Orbit Flight Test of an Inflatable Decelerator (LOFTID) Mission Overview and Science Return." AIAA SciTech, 2024.
2. Cheatwood, F.M., et al. " Manufacturing Challenges and Benefits when Scaling the HIAD Stacked-Torus Aeroshell to a 15m-Class System." IEEE Aerospace Conference, 2016.
3. Hughes, S.J., Swanson, G., Cheatwood, N., and DiNonno, J. " Low-Earth Orbit Flight Test of an Inflatable Decelerator (LOFTID) Aeroshell Performance." AIAA SciTech, 2024.
4. NASA-STD-5017A, "Design and Development Requirements for Mechanisms." 2015.
5. Parker, A.R., et al. " Fiber Optics Sensing System (FOSS) deployment on Low-Earth Orbit Flight Test of an Inflatable Decelerator (LOFTID)." AIAA SciTech, 2024.
6. ADAMS, Automated Dynamic Analysis of Mechanical Systems, Software Package, Ver. 2022.2, Hexagon, Stockholm, Sweden, 2022. <https://hexagon.com/products/product-groups/computer-aided-engineering-software/adams>.

Development and Testing of a Novel Solenoid Launch Lock for a Lunar Lander Thrust Vector Control Actuator

Joseph Plunkett*

Abstract

Honeybee Robotics has developed and tested a novel solenoid launch lock mechanism, designed as part of a Thrust Vector Control (TVC) actuator. This electromechanical TVC system provides precise gimbaling for the main engine of a large lunar lander. The launch lock must react significant inertial loads during ground transportation and launch, disengage reliably under load, operate in an extreme vibration environment ($>100 g_{rms}$) during lander engine firings, and fail in a safe (locked) state when unpowered. The final design integrates a spring-return solenoid into the TVC drive motor, which restricts movement of the motor rotor when engaged. The novel design features are shallow castellated teeth which form a positive locking interface between the solenoid armature and the motor rotor, and a tri-lobed prismatic joint which acts as an anti-rotation feature. Extensive prototype testing was performed to characterize the performance of the mechanism under various environmental and load cases. Testing demonstrates that this design can operate reliably at high vibrate loads and react $\sim 30x$ the torque of traditional friction brakes of comparable size and mass, with lower power dissipation.

Mission Requirements

The primary function of the launch lock is to prevent unwanted movement of the engine during ground transportation and launch. The launch lock must be resettable by the flight computer in space, precluding the use of conventional “field resettable” shape memory alloy pin pullers, which require manual operator input to reset. The TVC actuator must react a maximum static load of approximately 14,000 N while locked. The actuator must also be capable of unlocking under an external load of approximately 1300 N, due to compression of the engine fuel bellows. Placing the launch lock on the motor rotor reduces the required load by the ratio of the drivetrain which consists of a ball screw and a planetary gearbox. Resultant derived maximum load at the launch lock is approximately 4.2 N·m while locked, and 0.3 N·m while being disengaged. This configuration also enables the actuator output piston to be locked at any position along its travel in increments of 1/3 of a motor revolution (increments of <1 mm at actuator output).

This mechanism must also operate in an extreme vibration environment during engine firing. Qualification-level vibration input for the TVC actuator system is approximately 15 g_{rms} during launch (actuator locked), and 60 g_{rms} during lander engine firing (actuator unlocked). However, finite element modal analysis predicts significant amplification in the axial direction between the spacecraft mounting interface and the internal motor mounting interface. This results in a derived qualification vibration amplitude for the launch lock of approximately 30 g_{rms} during launch and approximately 120 g_{rms} during engine firing.

Derived load case requirements for the launch lock mechanism are summarized in Table 1. The Launch load case represents ground transportation and terrestrial launch, where the launch lock is engaged (unpowered) and the lander engine is not firing. Transit represents the neutral-engine-position load in space, under which the launch lock must disengage in anticipation of firing the lander main engine. The Engine Burn load case is applicable during main engine firing events, such as trans-lunar injection and powered descent to the surface of the moon, during which the launch lock is powered and must remain disengaged to allow unrestricted movement of the TVC system throughout the burn.

* Honeybee Robotics, Longmont, CO; joplunkett@honeybeerobotics.com

Table 1. Launch Lock Load Case Summary

Load Case	External Load	Vibration Level
Launch	4.2 N·m	30 g _{rms}
Transit	0.3 N·m	0 g _{rms}
Engine Burn	0 N·m	120 g _{rms}

Design Challenges and Limiting Factors

On a conventional spring-loaded friction brake, holding torque in the engaged (unpowered) position is proportional to spring preload force. However, using a stiffer spring to increase capacity increases the current required to hold the armature in the disengaged (powered) position. When a friction brake is exposed to a vibration environment in the engaged position, the inertial force acting on the mass of the armature compresses the spring causing fluctuations in the normal force between the armature and rotor. This can result in a significant loss of holding torque capacity. Friction brakes can also contain exotic surface coatings, are very sensitive to piece part and assembly tolerances, and require precise adjustment of spring preload during assembly. These factors drive up manufacturing time and cost, and lead to high power draw and thermal dissipation for high torque brake designs.

Replacing the friction surfaces with interlocking castellated teeth (Figure 1, Figure 3) largely disconnects holding torque capacity from spring preload force by transmitting torque from the rotor into the armature through the parallel faces of the teeth, providing robust engagement under vibrate and allowing for relaxed machining and assembly tolerances. The mechanism is unlocked by energizing the coil at approximately 200 mA for less than 1 second. After the air gap has been closed, the solenoid becomes dramatically more efficient, and the current can be reduced to approximately 50 mA for powered holding.

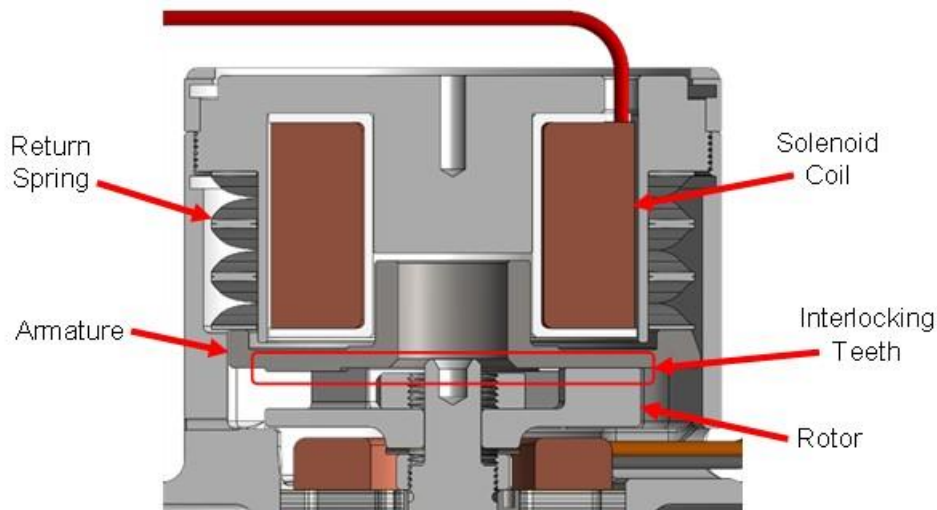


Figure 1. CAD Section View

The electromagnetic and mechanical design of this mechanism was highly optimized to maximize performance and balance several fundamental limitations. The key driving requirements for the design are as follows:

- Spring preload must be high enough to maintain positive tooth interlocking during launch.
- Armature and rotor teeth must be strong enough to react external loads during launch.
- Solenoid must be strong enough to pull in armature at maximum air gap at the end of transit.
- Solenoid must be strong enough to hold armature in disengaged position during engine burn.

The force exerted by the solenoid decreases quadratically with the air gap between the armature and solenoid, limiting the maximum air gap to approximately 0.5 mm for reliable operation. Maximum air gap could be increased with a weaker spring at the expense of armature stability, increasing the likelihood of rocking or gapping of the armature under vibrate when in the locked position. When in the unlocked position positive clearance must be maintained between the stationary armature and the spinning rotor, limiting armature tooth height to approximately 0.25 mm to account for manufacturing tolerances and runout. Caution must be exercised when manufacturing functional features of this size: for example, conventional deburring procedures could damage or eliminate the vertical contact faces of the shallow teeth.

Mass is a primary driver of armature stability under vibrate so armature mass should be minimized. However, sections that are too thin can create flux concentrations, causing premature electromagnetic saturation. ANSYS Maxwell FEA was used to model magnetic flux in the armature and solenoid housing, and to predict the attractive force between the armature and solenoid in both the locked and unlocked armature positions (Figure 2). The design of the cross-sectional profile of the armature was iterated with FEA to optimize mass without sacrificing holding capacity.

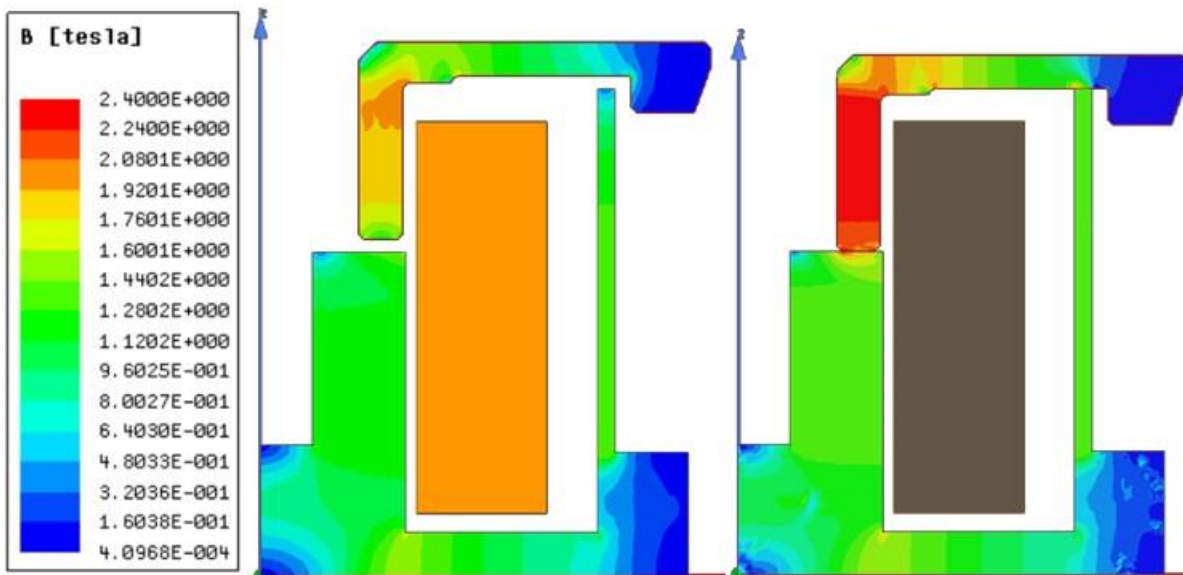


Figure 2. FEA Flux Density in the Locked (Left) and Unlocked (Right) Armature Positions

Material selection is also important. The high-saturation soft magnetic alloy used for the armature significantly increases electromagnetic performance but has lower mechanical strength and is more difficult to machine than conventional stainless-steel alloys. This results in low stress margins, especially on the contact surfaces of the shallow armature teeth. Composite armatures with soft magnetic alloy cores and harder materials on the contact surfaces may be explored for future applications.

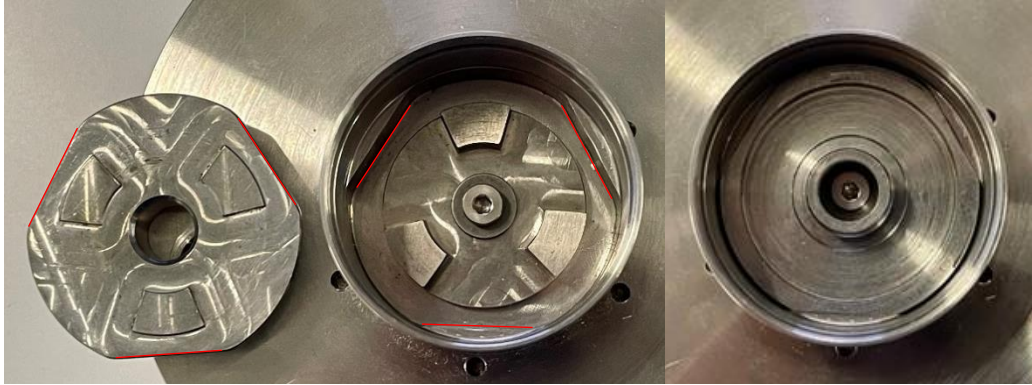


Figure 3. Photos of Anti-rotation Interface

Three flat sides comprise the armature/stator anti-rotation feature (Figure 3), creating a prismatic constraint that prevents the armature, and consequently the rotor, from rotating while still allowing axial movement. This design transmits rotational reaction forces directly into the stator increasing torsional stiffness and allowing the spring to be separated from the armature. One drawback compared to the heritage design is some added backlash due to the clearance fits necessary to allow the sliding motion of the armature. Because this backlash occurs at the prime mover it is divided by gearbox and ball screw reductions and is considered negligible at the TVC output.

The three-sided design of the armature is inherently self-centering and ensures simultaneous contact on all sides. The triradially symmetric arrangement of the teeth matches the three-speed resolver allowing for an operation case in which the motor is used to drive to a known gap in the teeth before locking or to relieve load from the armature before initiating the unlock sequence if the solenoid cannot overcome the external load on its own.

Prototype Characterization and Testing

Given the level of deviation from heritage friction brake designs, a prototype was built as a risk-mitigation measure. The prototype hardware (Figure 4) was made by modifying heritage components and utilizing 3D printed and quick-turn machined GSE where possible. The prototype was tested in three distinct test GSE fixture configurations:

1. Breakaway: characterizes the powered armature holding force envelope.
2. Continuity: uses electrical continuity to detect the position of the armature to characterize pull-in and drop-out behavior under vibe.
3. Dynamic: verifies mechanism functionality and load-holding capability under vibe.



Figure 4. Launch Lock Prototype Components

Table 2 summarizes the combinations of fixture configuration and load case under which the prototype was tested, and what operational state each test sought to represent.

Table 2. Test Case Summary

	Fixture	Load Case	Mechanism State
Test Case 1	Breakaway	Engine Burn	Unlocked
Test Case 2	Continuity	Engine Burn	Unlocked
Test Case 3	Continuity	Launch	Locked
Test Case 4	Dynamic	Launch	Locked
Test Case 5	Dynamic	Transit	Transitional
Test Case 6	Dynamic	Engine burn	Unlocked

Breakaway Testing

The breakaway fixture replaces the armature return spring with a plunger allowing the operator to apply load directly to the back side of the armature with a force gauge (Figure 5).

Test Case 1: during engine burn the solenoid must exert enough force on the armature to react vibration loads and hold it in the unlocked position. This test sought to characterize the force at which the armature breaks away from the solenoid, as a function of applied current. A power supply is used to energize the coil at a constant current level simulating the “unlocked” state of the launch lock. Force applied to the armature is then slowly increased until the armature is forcibly dislodged from the solenoid bobbin. The test is repeated as the current is incrementally increased, until the solenoid “saturates” and increasing current no longer causes a corollary increase in the force required to dislodge the armature. This dataset of breakaway force as a function of applied current established a proxy to estimate the dynamic force being exerted on the armature during vibration testing.

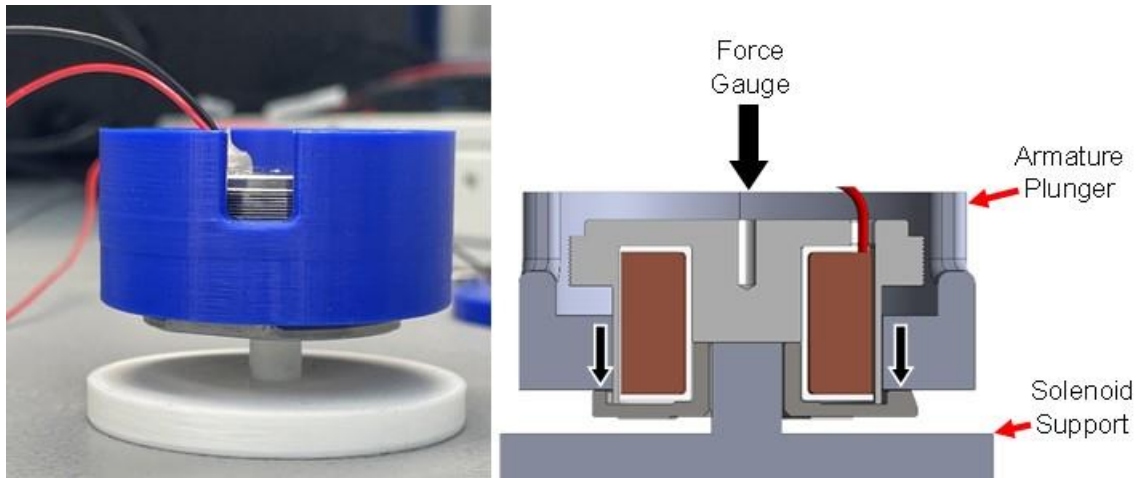


Figure 5. Benchtop Prototype Test Configuration

Figure 6 plots average breakaway force of the armature, across several trials, as a function of solenoid current. The saturation inflection occurs around 100 mA, above which breakaway force remains functionally constant¹.

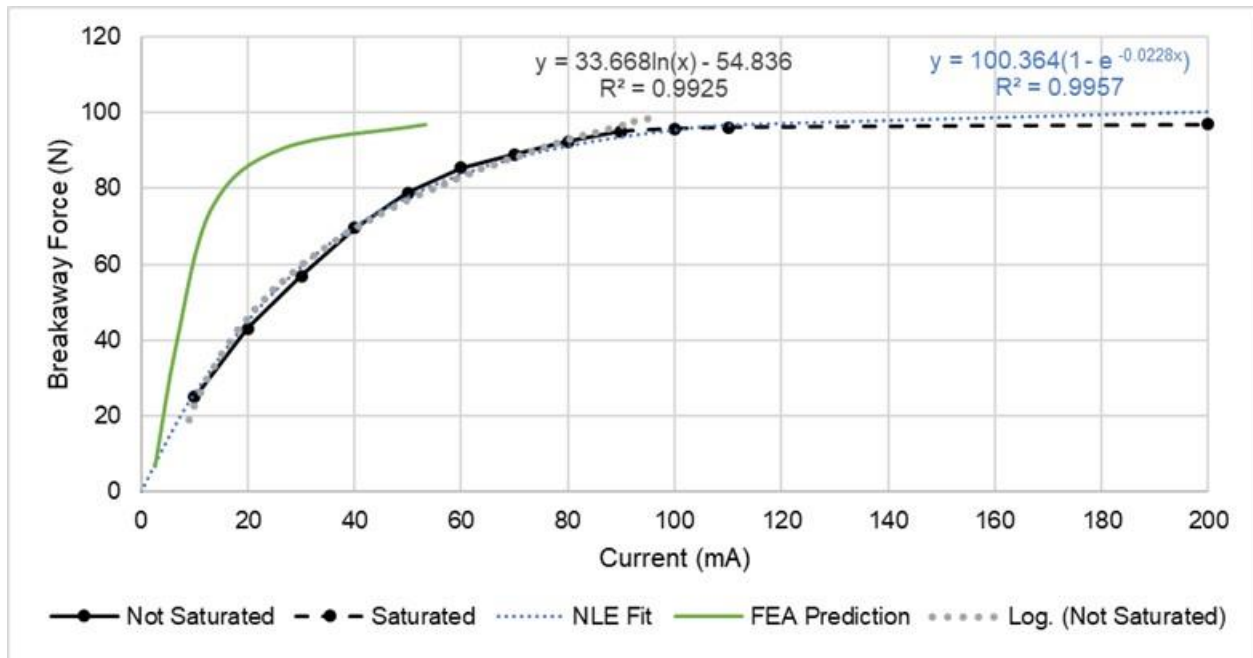


Figure 6. Armature Drop-out force vs. Solenoid Current for Test Case 1

The FEA prediction for maximum armature breakaway force of approximately 100 N was corroborated by the benchtop test data indicating the flux density and saturation estimates were accurate. However, the FEA model significantly overpredicted current sensitivity in the non-saturated regime resulting in lower than predicted power efficiency. This simulation methodology has produced good hardware correlation for brushless electric motors but needs some refinement for analyzing solenoids. One possible explanation for the discrepancy is that the effective air gap between the armature and solenoid is greater on the physical prototype than represented in the model. This could be due to machining tolerances, surface roughness, material inconsistencies, or some other phenomenon that increases the reluctance of the magnetic flux circuit.

Continuity Vibration Testing

In the second prototype test setup the armature is spring-loaded as in the flight configuration, but the rotor is replaced by a facsimile of copper contacts with one contact representing each tooth of the rotor/armature interface (Figure 7). After being installed into the fixture, the contacts were lapped to create a single coplanar and parallel contact surface with the armature. Each contact is connected independently to a high-frequency data acquisition channel, recording and displaying continuity between the armature and the contacts in real-time during vibration testing. A closed circuit indicates that the armature is in the locked position while an open circuit indicates the unlocked position. This setup was designed to test possible failure modes for both the launch case, with the armature in in the locked (unpowered) position, and engine burn, with the armature in the unlocked (powered) position.

¹ The regression found to have the best empirical fit for the full envelope of the solenoid, up to and through saturation, is a non-linear exponential curve of the form $y = A(1 - e^{-kx})$, with a fit of $R^2=0.9957$ from 10 to 200 mA. However, in the non-saturated regime, from 10 to 90 mA, a standard logarithmic regression yields a comparable fit of $R^2=0.9925$. For simplicity, standard logarithmic and exponential fits will be used for analysis in the non-saturated regime going forward.

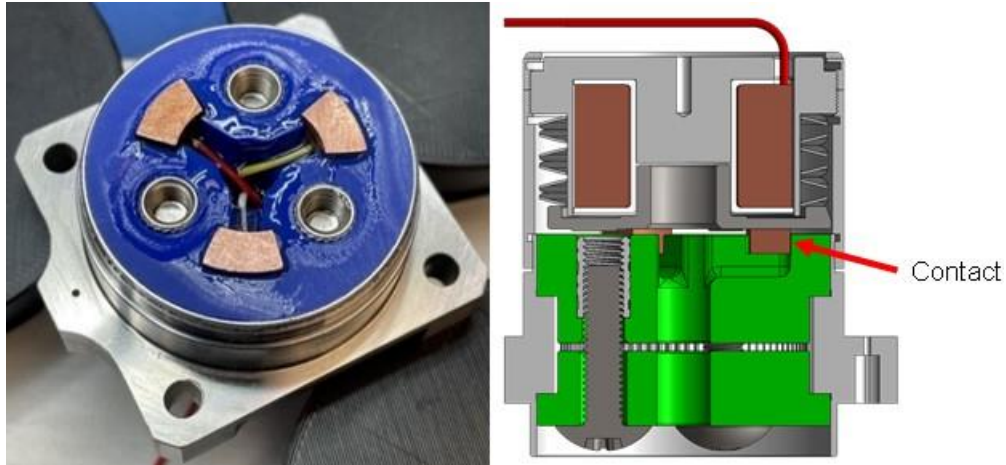


Figure 7. Photo and CAD of Non-operational Vibration Testing Fixture

Test Case 2: during engine burn the armature must remain in the unlocked position at all times otherwise the rotor could be erroneously locked during operation. This test sought to characterize the current at which the armature drops out from the solenoid and contacts the rotor facsimile as a function of vibration level. To find the drop-out point the current is slowly reduced until continuity is detected between the armature and the fixture contacts². This test was repeated three times at each random vibration level, increasing in 10 g_{rms} increments from 0 to 80 g_{rms} to characterize drop out current as a function of vibration amplitude. An exponential relationship was observed between drop-out current and vibration level (Figure 8).

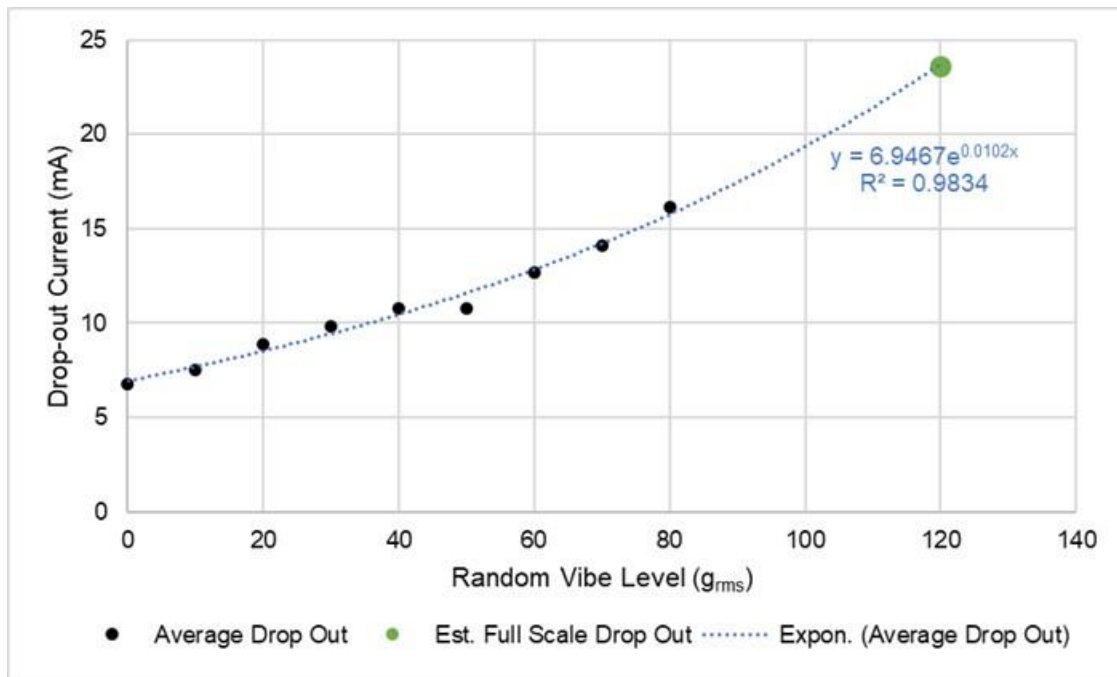


Figure 8. Armature Drop Out Current vs. Vibration Level for Test Case 2

² There is a theoretical failure mode that this setup cannot detect, wherein the armature partially drops out and is displaced more than 0.25 mm, but then is drawn back to the solenoid before reaching the sensor contacts, located at a distance 0.5 mm. However, due to the quadratic relationship between air gap and solenoid force, this is highly unlikely.

The increase in drop-out current is believed to be primarily attributable to inertial forces acting on the armature and spring due to acceleration. The combined mass of the armature and spring is approximately 20 grams, which would predict an inertial force of approximately 16 N at 80 g_{rms}. From 0 to 80 g_{rms}, drop-out current increases from 7 to 16 mA. Using the data from Test Case 1, this corresponds to an estimated increase in breakaway force of 19.2 N. Given that the launch lock has no significant predicted axial modes when in the powered position, inertial force is expected to increase linearly with vibration level. The expected inverse of the logarithmic increase in breakaway force as a function of linearly increasing current seen in Figure 6, would be an exponential increase in current to react linearly increasing inertial force which is borne out in Figure 8.

Even with no head expander and a very lightweight test fixture, the 133-kN (30,000-lbf) shaker table on which this testing was performed was only able to reach 80 g_{rms} with the qualification ASD profile. However, given the consistent and repeatable trend of datapoints from 0 to 80 g_{rms}, it was deemed reasonable to extrapolate a predicted minimum drop-out current for the engine burn vibration level of 120 g_{rms}. The predicted minimum drop-out current of 25 mA at 120 g_{rms} is well within the non-saturated regime characterized during Test Case 1.

The results of Test Case 2, when combined with the data from Test Case 1, provided a high degree of confidence that the armature can be reliably held in an unlocked position at the required vibration levels with ample solenoid force and electromagnetic saturation margin.

Test Case 3: during launch the mechanism is unpowered and the spring must maintain constant positive interlocking between the armature and rotor. This test sought to verify that the armature is held in constant contact with the rotor facsimile while exposed to random vibration. If an interruption in continuity is detected on one or more contacts, this could mean that the armature has lost preload and is tilting or lifting away from the rotor. This could potentially lead to a loss of engagement of the locking interface if displacement is high enough. In this test case, momentary losses in continuity of single contacts began to be detected around 20 g_{rms} with interruptions becoming more frequent across the three contacts as vibration amplitude increased. In a friction brake this loss of preload would be considered a failed condition due to the resulting loss of holding torque, but the interlocking teeth of this lock only allow movement if armature displacement is more than the height of the teeth. The continuity sensors provide only a binary indication of armature position, so displacement could not be accurately determined with the data collected. Thus, Test Case 3 was deemed inconclusive prompting additional prototype testing.

Dynamic Prototype Testing

The third and final prototype test setup integrated the solenoid, spring, and armature with a movable rotor and a flight-like internal housing geometry with anti-rotation features and interfaces (Figure 3). In this configuration the lock is fully operable and precise torque can be applied to the rotor while undergoing vibrate by using a force gauge to pull a cord wrapped around a pulley (Figure 9).

Test Case 4: during launch the mechanism is unpowered, and the spring must maintain constant positive interlocking between the armature and rotor. This test sought to verify that rotation cannot be induced through manipulation of the rotor while the mechanism is exposed to random vibration. For this test the prototype was tested under a full representative load of 4.2 N·m and up to 60 g_{rms}. This test validated the mechanical durability of the armature teeth and the ability of the spring to maintain positive interlocking at approximately double the launch case qualification vibration level. Quick reversing loads were also tested to verify that the rotor teeth cannot “sneak in” under a chattering armature.

Test Case 5: at the end of a transit period, prior to firing the engine, the launch lock must be disengaged while under a load of approximately 0.3 N·m. This test case sought to determine whether the armature can be pulled in under this load. Throughout the prototype testing campaign, the lock was repeatedly successfully disengaged under external loads in excess of 1 N·m. The prototype was also successfully engaged and disengaged under load while being vided, although this is not an expected operational case.

Test Case 6: during engine burn the mechanism must remain unlocked at all times. This test sought to confirm that the rotor can move freely while the launch lock is experiencing vibration loads in the unlocked state. No interference was detected between the armature and rotor the armature at vibration levels up to 60 g_{rms} . However, because the testing facility could not achieve the predicted amplified qualification vibration level of 120 g_{rms} , the results from Test Case 2 remain the strongest supporting evidence for successful operation during engine burn.

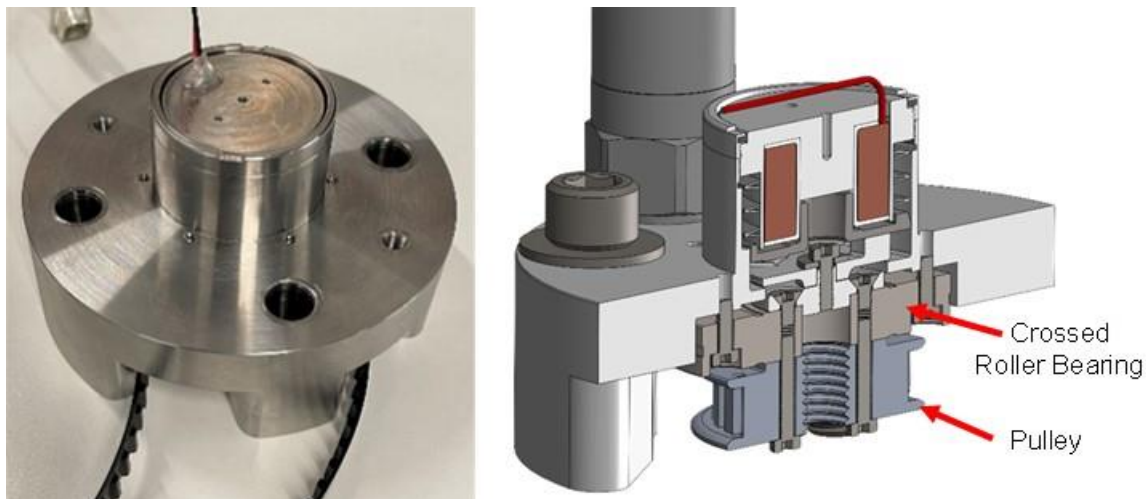


Figure 9. Photo and CAD of the Dynamic Vibration Testing Fixture

Conclusions

This novel launch lock mechanism design represents a significant step forward in capability compared to friction brakes. The lighter armature and less stiff spring result in lower holding power consumption and dissipation under vibrate, and the toothed interface is able to react approximately 30x more torque. The results of the prototype testing campaign provided a high degree of confidence that this design will meet mission requirements.

- **Launch Case:** while exposed to vibrate in Test Case 3, continuity sensors indicated that there may be some movement of the armature while in the unpowered state, however Test Case 4 confirmed in that any displacement is not of sufficient magnitude to permit undesired movement of the rotor or interfere with the load holding capacity.
- **Transit Case:** Test Case 5 demonstrated the ability of the armature to disengage while exposed to significantly greater than the required load, obviating the need for an active load relief scheme as described at the end of the design section.
- **Engine Burn Case:** Extrapolating predicted drop-out current from the vibration testing performed for Test Case 2 and correlating that with data from Test Case 1, indicated that the solenoid can produce ~2x the force required to prevent drop-out at 120 g_{rms} .

Inspecting the soft magnetic alloy armature under magnification after the conclusion of prototype testing showed that all the shallow teeth maintained their sharp vertical edges and showed no signs of significant yielding or deformation on the contact surfaces (Figure 10).

One area of forward work is to better understand the poor correlation between predicted efficiency from FEA and empirical test data. The EDU units and the first four flight/qual units have all been measured and have in-family drop-out force vs. current performance to the prototype unit, so the conclusions of the prototype development testing effort are believed to be applicable to all units that successfully pass acceptance testing (which includes drop-out force vs. current measurement). The model correlation will be reevaluated in the process of developing a next-generation, electrically redundant version of this mechanism in the coming year.



Figure 10. 150X Magnified Image of 0.25-mm Armature Teeth After Testing

After prototype testing, Honeybee Robotics successfully manufactured three Engineering Development Unit (EDU) TVC actuators containing launch locks of this design and subjected them to full-load benchtop testing. The launch lock successfully met system-level requirements demonstrating its reliability and functionality under load. Qualification and flight units are currently in production and expected to undergo environmental acceptance and qualification testing in 2024.

Testing Frangibolts for Extended Space Mission Durations

Brian Gore*, Ryan Hill* and Timothy Woodard*

Abstract

Occasionally, there are space mechanism deployment applications that must wait days, weeks, or years prior to release due to outgassing concerns or other mission CONOPS requirements. In the case of the Ensign Bickford Aerospace and Defense (EBAD) / TiNi™ Frangibolt® actuator, no data was found to support performance predictions for the device after being dormant in a space environment for an extended duration, so The Aerospace Corporation constructed a test to establish some representative data, and to share the findings with the user community.

A set of preloaded joints with Frangibolt actuators underwent a simulated on-orbit aging test which subjected the actuators to radiation and thermal cycling environments replicating multiple (~8) years in both low Earth orbit (LEO) as well as geosynchronous Earth orbit (GEO). The characterization data shows no degradation of Frangibolt actuator performance during or following exposure of up to 8 years in the LEO and/or GEO environments. The baseline and post-test data show consistent actuator behavior.

Introduction

The primary objective of this test series was to determine whether Frangibolts undergo any change in performance or physical characteristics when subjected to radiation and thermal cycling simulating up to 8 years in low Earth orbit (LEO). Any environment which causes either premature actuation or a failure to actuate upon command is not suitable for the use of Frangibolts. The environmental conditions selected to simulate those eight (8) years in LEO consisted of a radiation dose of 76 krad followed by more than 38,000 thermal cycles between 0°C and 40°C. The bulk of this paper details the tests and results of the LEO phase of testing, with the additional conditions and results of the GEO phase presented at the end.

Test Item Description

The Frangibolt is a hold-down and release device made by EBAD, formerly TiNi Aerospace. It primarily consists of a hollow cylindrical nickel-titanium shape-memory alloy (SMA) actuator, a notched bolt which is inserted through the actuator, and a resistance heater and insulating jacket which are wrapped around the actuator as shown in Figure 1. The 7075-T6 aluminum finned washers were designed in-house and included to accelerate the thermal cycling rate for this test; they are not typical in a Frangibolt assembly. The model used for this test series was TiNi's standard FC4 [1], which is sized to accept a 0.25 in (6.35 mm) diameter notched bolt made by EBAD and is approximately 38 mm (1.5 in) in length.

In operation, the molecular structure of the nickel-titanium SMA is hysteretic and exists in either an austenite or martensite phase depending on the temperature and pressure [2]. Each phase manifests with its own characteristic shape or dimensions of the sample piece. The actuators used in this test series were compressed to a martensite phase with a force of 44.5 kN (10,000 lbf) at room temperature. This particular SMA formulation begins to return to its austenitic dimensions at a temperature above 60°C when unrestrained; different ratios of nickel-to-titanium in the alloy result in different transition temperatures. When a notched EBAD bolt is installed through a compressed actuator, the device's heater will cause the SMA to change phase, expand, and eventually break the bolt at the notch location. The units described

* The Aerospace Corporation, El Segundo, CA
Approved for public release. OTR 2024-00430

herein reached a temperature of 73°C before overcoming the bolt-break strength. The SMA is re-compressible and reusable for at least 60 cycles, per EBAD guidelines.

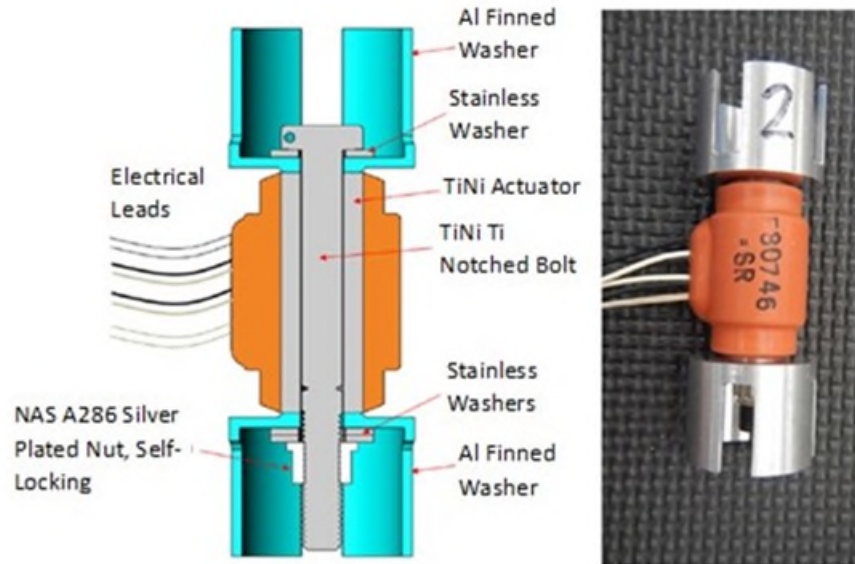


Figure 1. Cross-Section of Frangibolt Test Assembly (Left) and Sample Photograph (Right)

The 0.25 in (6.35 mm) bolts used with the FC4 actuators feature a precisely machined notch resulting in a controlled tensile breaking strength of 21.4 ± 1.8 kN ($4,800 \pm 400$ lbf) [3].

Heat is applied to the actuator via a resistance heater which supplies nominally 80 watts at 28 volts DC. A silicone rubber jacket surrounds the heater so that most of the heat goes into the SMA actuator rather than radiating away from the unit.

EBAD has changed the silicone rubber jacket material due to material obsolescence since the period of this testing. The Aerospace Corporation's Space Materials Laboratory has stated that there is no significant difference in radiation endurance or performance between the old and new materials.

Test Methodology

The most critical performance requirement of the Frangibolt is that it actuates when and only when commanded. Either a failure to release on command or a premature release could be detrimental to a mission. The mechanical failure modes associated with longer-duration space use are thought to be driven by two environmental factors: radiation exposure and thermal cycling.

Radiation exposure can potentially degrade (particularly embrittle) certain components of the actuator such as the silicone rubber jacket, bonding and wire insulation, or the heater substrate. Delamination or other failure of these layers could result in insufficient heating when power is applied to the heaters, leading to a failure to function when commanded. Heat buildup due to environmental exposure could also potentially cause the SMA to prematurely expand and inadvertently break the notched bolt.

Frangibolt actuators in flight would typically be shielded from radiation to some degree. The predominant driver of induced properties change in bulk silicone material is the total ionizing dose (TID), which can be effectively simulated with gamma ray exposure, according to radiation SMEs in Aerospace's Materials Processing Dept. The space environment would subject the actuators to particle impact, which would be most severe at the surface and be attenuated with depth into the material. In an unshielded application, the dose on orbit was calculated to be approximately 3.2 Mrad near the exterior surface of the silicone, 76 krad

near the middle, and 23 krad at inner diameter. The mid-range test value of 76 krad was conservative at the innermost depth of the jacket, but the exterior surface was somewhat undertested. The test was conducted using gamma rays, for which there is minimal attenuation in these materials, so the dose of 76 krad was seen by all the parts to within about 5%.

Thermal cycling causes stress cycles in materials with mismatched coefficients of thermal expansion (CTE), as well as thermal gradients. These could potentially lead to fatigue in the metal parts, embrittled silicone jacket or Kapton heater, result in a buildup of localized phase transitions in the SMA, or change the bolt preload, any or all of which could lead to either failure to release or a premature release.

There are significant differences in CTE between the silicone rubber jacket and the nickel-titanium alloy in the SMA. Radiation-induced embrittlement of the silicone followed by thermal cycling is one example of how the two environments together were postulated to cause the actuator to fail.

A fatigue analysis was performed [4] on the assembled test items with a nominal preload of 6.7 kN (1500 lbf) at room temperature, corresponding to a stress of 331 MPa (48 ksi) at the notch in the bolt. The temperature cycling and CTE mismatch cause changes in preload and stress of only ± 0.3 percent. The expected fatigue life of the bolt at this loading condition is 30 million cycles, nearly three orders of magnitude greater than the length of this test plan. Fatigue was ruled out as a concern for aging in space but was still tested through the nearly 40,000 cycles in this test program.

The temperature limits used in this test were nominally 0°C and 40°C. Spacecraft design must protect the Frangibolt units from extreme temperatures because the SMA will break the bolt if it reaches its actuation temperature, regardless of whether the heater was powered. In this test, one year was represented by 4,745 thermal cycles, corresponding to approximately 13 cycles per day on a 110-minute orbit period. This results in 37,960 cycles over 8 years.

Test Summary

The eight test units were organized into two groups, shown in Table 1, to isolate the effects (if any) of repeated functioning. Four of the units were intended to be functioned and reset after each environment, providing a trend if gradual degradation were to occur, and four were intended to remain undisturbed until the conclusion. Functional tests were performed at the schedules shown in Table 1: initially before any conditioning (“Baseline”), then after radiation, and again after 1, 2, 4, 6, and 8 cumulative years of thermal cycling.

Table 1. Functional Test Matrix

Environment	Test Unit ID							
	Group I				Group II			
	1	2	3	4	5	6	7	8
Baseline	x	x	x	x	x	x	x	x
Post-LEO Radiation	x	x	x	x				
Post-Year 1 Thermal	x	x	x	x				
Post-Year 2 Thermal	x	x	x	x				
Post-Cryogenic Exposure	x					x		
Post-Years 3–4 Thermal	x	x	x	x				
Post-Years 5–6 Thermal	x	x	x	x				
Post-Years 7–8 Thermal	x	x	x	x	x	x	x	x

Shortly after the beginning of the third year of thermal cycling, a test anomaly occurred in which a valve in the thermal chamber failed open, cooling all the units to -196°C , the boiling point of LN_2 ("Cryogenic Exposure" in Table 1). Actuators 1 and 6 were subsequently functioned to assess any damage, but no adverse effects were observed. Thermal cycling was temporarily resumed in an alternate (slower) chamber to continue the progress, and the units were eventually returned to the original chamber partway into year 4 after chamber repairs were made for safety and reliability purposes.

The basic sequence of events for the test items subjected to functional testing (every "x" in Table 1) was as follows:

- 1) Compress actuators and measure length
- 2) Install bolts and perform initial ultrasonic preload measurement
- 3) Wait at least 18 hours and measure preload after relaxation
- 4) Validate actuators' internal resistance temperature detector (RTD) resistance values
 - Done at the beginning of thermal cycling years 1, 2, 3, 4, 5, and at the end of year 8
- 5) Subject items to conditioning environment, namely radiation exposure or thermal cycling
 - No conditioning was performed by Aerospace prior to the initial baseline functional
- 6) Perform post-environment ultrasonic preload measurement
- 7) Measure DC resistance of heaters (checking for open or short failures)
- 8) Perform functional test
- 9) Measure hot length and calculate stroke
- 10) Compress actuators and measure length

Test units that were not repeatedly functioned (the empty cells in Table 1) were only subjected to measurements which did not disturb the bolted joint configuration: RTD resistance validation, post-environment ultrasonic preload measurement, and DC heater resistance.

The metrics used to evaluate the performance and physical characteristics of the test items throughout the test series were as follows:

- 1) Visual appearance
- 2) Actuation time
 - Defined as duration from application of power to heater until bolt breaks
- 3) Length of SMA actuators after compressing
- 4) Stroke
 - Defined as change in length from compressed state to fully expanded state with no load
- 5) Change in bolt preload due to environmental exposure
- 6) DC resistance of primary and secondary heaters at room temperature
- 7) RTD resistance compared with calibrated thermocouples at 0°C and 40°C

Environmental Test Conditions and Equipment

The radiation exposure and thermal cycling were conducted on assembled test units as shown in Figure 1. For the radiation exposure, the units were loosely (so as not to disturb the preloaded joint) threaded onto a female-threaded standoff which connected to an acrylic plate (standard for the radiation chamber) as shown in Figure 2.

The actuators, configured as shown in Figures 1 and 2, were exposed to 76 krad total ionizing dose (TID) measured at the midplane of the actuators, approximately 300 mm (12 in) from a Cobalt-60 source. The actuators were oriented with the bolt head closest to the source. The exposure rate was 5.65 rad/s for approximately 3.5 hours, measured with an ionization chamber type dosimeter. The measurement error is estimated at $\pm 4\%$ and the spatial variation within the chamber is less than 5%.

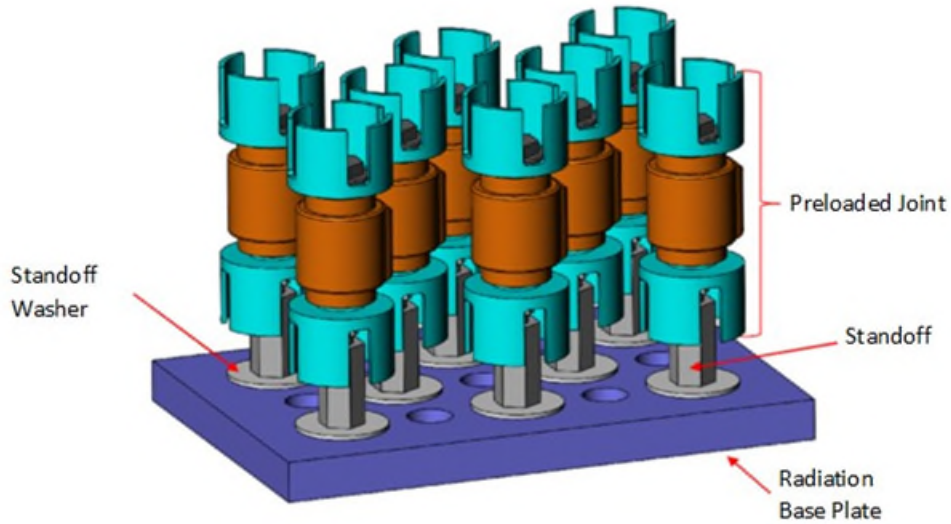


Figure 2. Radiation Exposure Configuration

A lead-aluminum shield was placed in between the source and test units, which is an industry-standard practice for Co-60 exposure. This shield reduces the lower energy X-rays but allows most of the gamma radiation to pass through. The dose rate measurements were performed with the shield in place. RTD temperatures were not recorded during the gamma radiation exposure.

For thermal cycling, a custom Teflon plate was designed which featured circular cavities of a diameter slightly larger than the aluminum finned washers. Four smaller holes were placed around each cavity at 90-degree angles. The test units were placed into the cavities with the threaded end of the bolt facing down toward the plate (Figure 3).

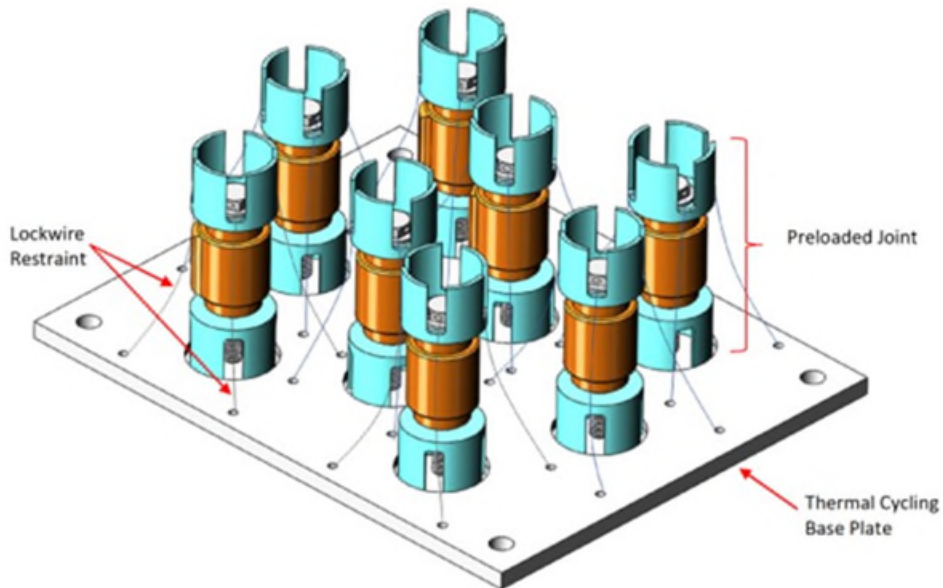


Figure 3. Thermal Cycling Configuration

Lockwire was fed through the adjacent four holes, through holes in the bolts' heads, and tied; the lockwire prevented the bolt head from being ejected during the functional test or accidental actuation in thermal

cycling or handling, and it also served as a guywire to keep the actuators upright during the test. The nut and threaded end were contained within the bottom finned washer and the plate cavity during the functional tests. Enough slack was left in the lockwires to allow the actuator the necessary 1.5 mm (0.060 in) stroke during the test, and the cavities were 3.2 mm (0.125 in) deep. The overall plate was 200 x 150 x 6 mm (8 x 6 x 0.25 in).

The thermal cycle range objective, as measured by the test units' built-in primary RTDs, was 0°C to 40°C. A cycle was counted whenever the primary RTDs on all actuators indicated a round trip past thresholds of less than 3°C and greater than 37°C. The chamber was programmed with temperature extremes of -8°C and +45°C to drive the test units. The ramp-rate between conditions was limited to 36°C per minute (although the actual performance of the chamber was slower and variable, particularly in cooling), and a two- to four-minute dwell was programmed at each extreme to allow the units time to reach their temperature requirements. The cycling was based on the chamber's internal controller; there was no real-time feedback from the test units.

Figure 4 plots the minimum and maximum temperatures extracted from each thermal cycle and illustrates the schedule of events.

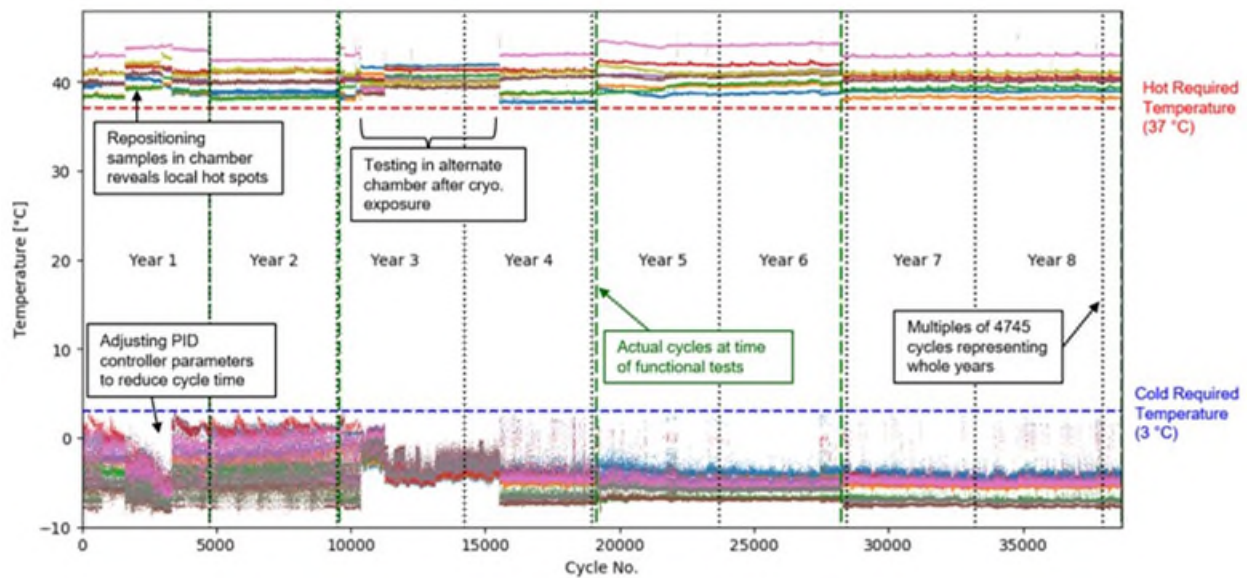


Figure 4. Minimum and Maximum Temperatures Recorded for each Thermal Cycle

Table 2 lists the planned and actual cycles for each block of simulated years between functional tests. The “actual” columns represent the minimum number of cycles obtained by any of the eight actuators. It was not feasible to stop thermal cycling exactly at the planned cycle counts due to lab or staff availability; cycles were counted and verified using post-processing software after the chamber was stopped.

Table 2. Planned and Actual Thermal Cycles

Year(s)	Planned	Actual	Cum. Planned	Cum. Actual
1	4,745	4,765	4,745	4,765
2	4,745	4,829	9,490	9,594
3-4	9,490	9,547	18,980	19,141
5-6	9,490	9,121	28,470	28,262
7-8	9,490	10,397	37,960	38,659

Figure 5 plots a histogram of the round-trip thermal cycle times. The atypical nature of the cycle times in Figure 5 were related to variable performance of the cold nitrogen supply and the chamber's PID (proportional-integral-derivative) controller; the units were brought much closer to the -8°C set point during cycles with slower cooling rates than on the faster cycles. The chamber's heating rate was much more consistent, but variation of a particular cold condition caused some variation in the subsequent hot condition.

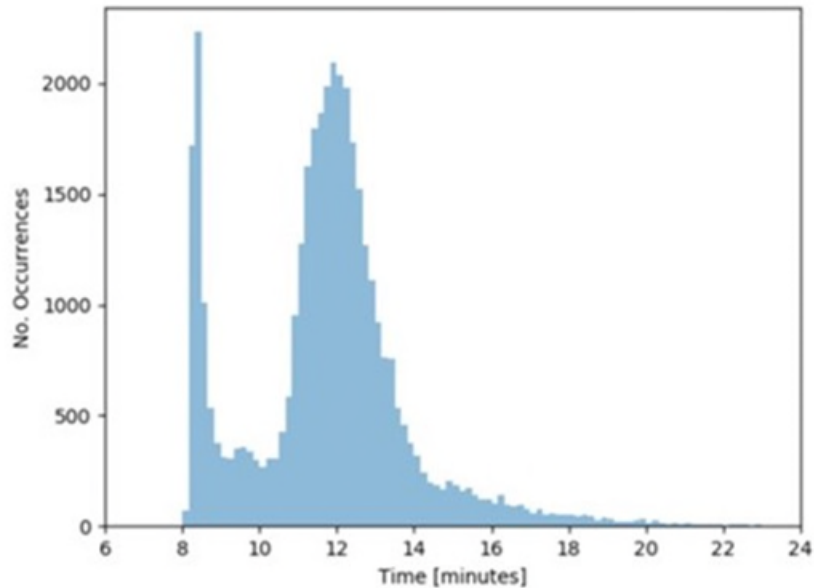


Figure 5. Histogram of Round-Trip Thermal Cycle Times

Functional Test Descriptions

Unless otherwise specified, all functional tests and measurements were performed at room temperature and uncontrolled humidity. The units were often slightly heated during bolt installation and initial preload measurement due to handling. Attempts were made to allow the units to return to room temperature prior to measuring preload, but repeated adjustments of bolt torque to achieve proper preload sometimes made this impractical.

Primary RTD resistance was recorded immediately preceding any measurement or test that was performed on a given test item.

Actuator compression was performed using a TiNi Aerospace FBT-CT2 reset fixture. The unit comprises a hand-operated hydraulic pump, press, and features to center the SMA actuators in the press. After the initial pressurization, the pressure indicated on the dial would slowly decrease by 1-2% over several seconds. Without relieving pressure, the operators would reapply pressure to achieve the recommended value until the gauge stabilized for at least 5 seconds.

The length of the SMA cylinder (excluding the silicone jacket) was measured using a caliper. Each actuator's RTD resistance was recorded simultaneously with the length to indicate temperature. In cases where handling or compressing the actuators caused a change in their temperature, a subsequent length measurement was recorded only after the RTD resistance returned to within 8Ω (about 2°C) of the original value.

After compressing each actuator, the SMA surface was recessed slightly below the silicone jacket. In these cases, extra pressure was applied to the caliper so the jaws would reach the face of the SMA. The SMA

actuators were often bowed (the two ends were not parallel) after functional tests, since the power was switched off before the actuators had reached their full stroke. In order to maintain a consistent measurement, the jaws of the caliper were approximately centered over the hole in the actuator, and the actuator was rotated about its axis until the smallest measurement was obtained. This technique ensured that the caliper jaws were out of plane relative to the bow in the actuator.

Bolt preload was measured using an ultrasonic transducer and oscilloscope (Figure 6). This method is well established and has been presented at the 42nd Aerospace mechanisms Symposium [5].

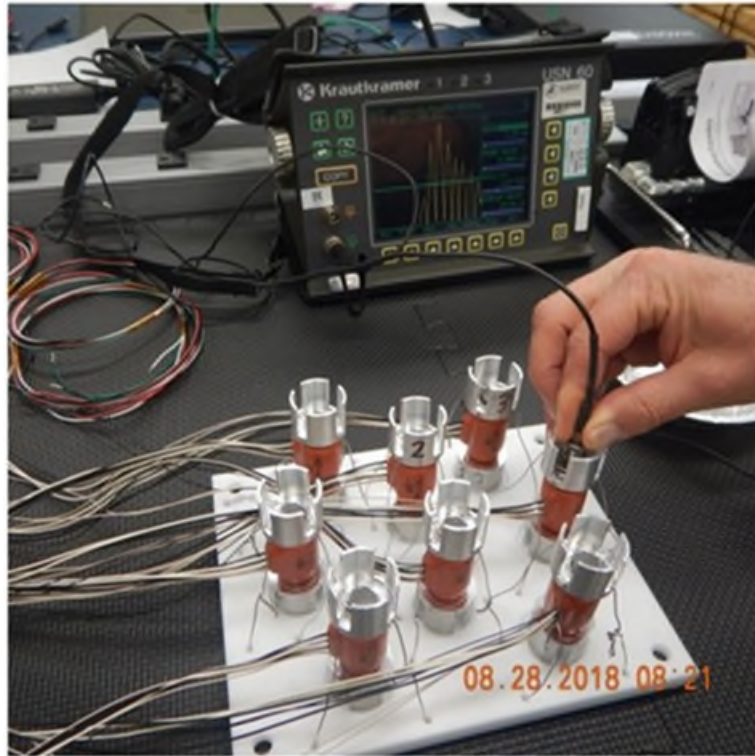


Figure 6. Ultrasound Preload Measurement Setup

Prior to the start of this test series, the ultrasonic preload measurement method was calibrated by placing the first eight bolts (used in the baseline test) in a load cell. The bolts were subjected to preloads up to 6.7 kN (1500 lbf) in 1.1 kN (250 lbf) increments. Linear regressions were developed (and were well-correlated) for changes in ultrasonic wave time of flight and bolt length vs. preload. Bolt length vs. preload is shown in Figure 7 as an example. These pooled regression curves were used for the remainder of the test series; subsequent bolts were not individually calibrated, but all bolts were from the same production lot.

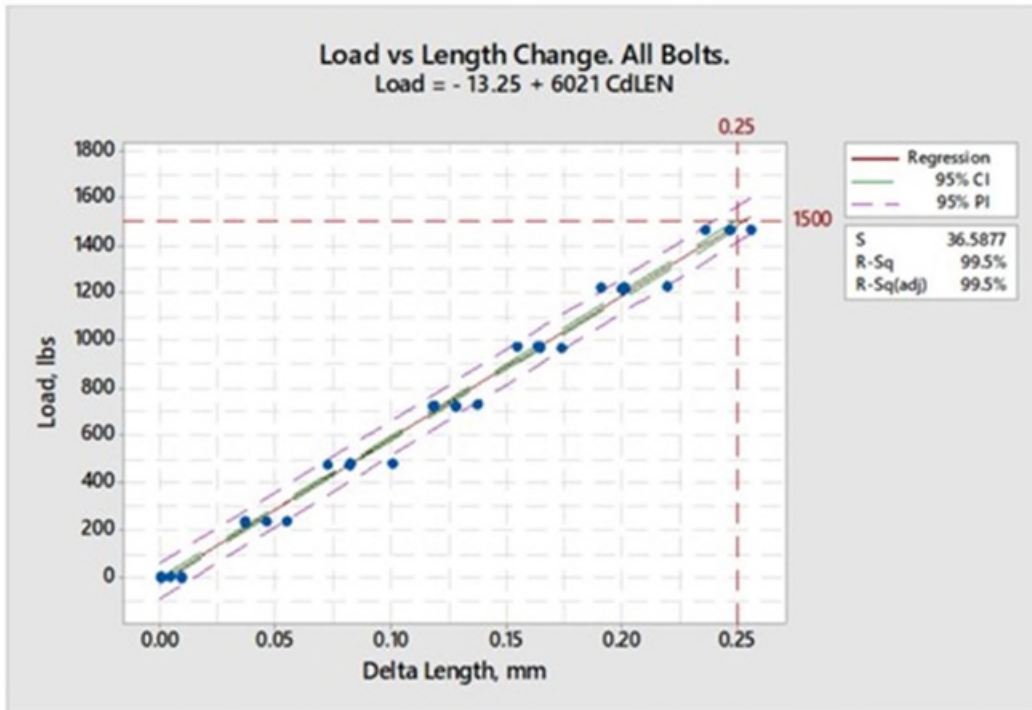


Figure 7. Linear Regression Example for ΔL Calibration Using a Load Cell

The bolt installation procedure encompasses assembling the test units in the configuration shown in Figure 1 and achieving the desired bolt preload. The preload recommendation as stated by EBAD [6] is 6.7 kN (1500 lbf) with a recommended installation torque of 7.3 N•m (65 in•lbf). The orientation of the bolt head, aluminum finned washers, and steel washers was always the same with respect to the actuator for every assembly instance. Also, the washers became slightly concave after the first installation, and their orientation was maintained to prevent reversal of the yielding.

The running torque of each nut-bolt pair was measured immediately prior to installation. With the nut fully engaging the threads, the nut was advanced using a break-over torque wrench. The joint was initially torqued to 5.7 N•m (50 in•lbf) above the running torque. Preload was then verified via ultrasound, and torque was adjusted as necessary.

The units were allowed to relax overnight, and a second ultrasound was performed. Typically, the joints would lose between 5-15% of their initial preload overnight. This change was measured so that it could be excluded from the environmental conditioning effects. Figure 8 shows the preload values after the joints had relaxed and before entering any environmental conditioning stage.

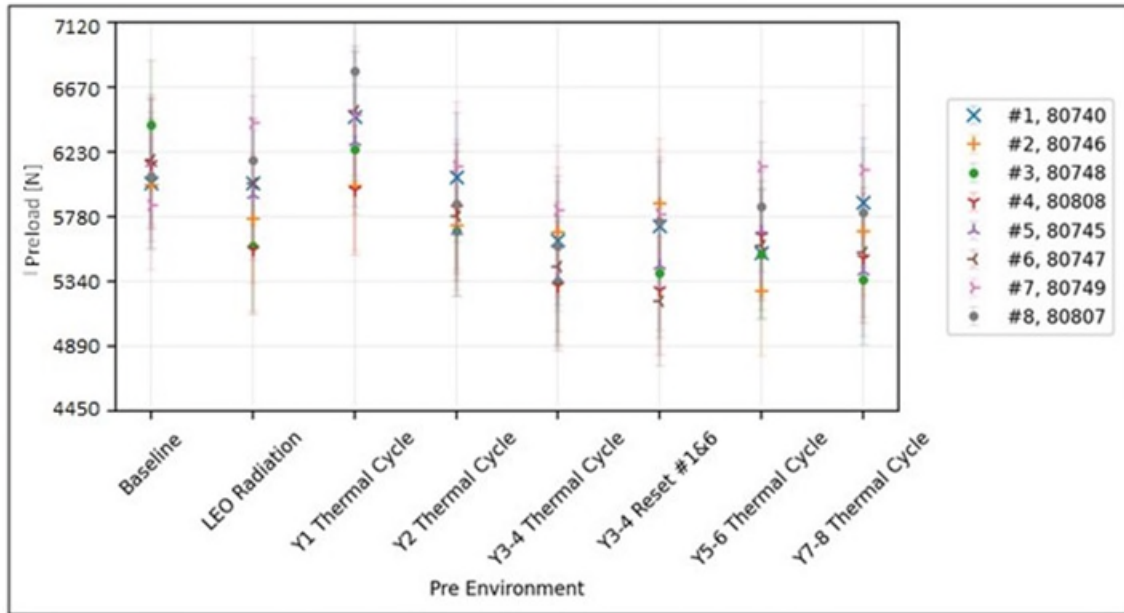


Figure 8. Relaxed Preload Prior to Entering Each Environment

Prior to each unit's functioning, the DC resistance of the primary and redundant heaters was measured along with RTD resistance to verify the ambient temperature. In order to validate the RTD readings, the units under test were soaked together in the thermal chamber for at least 25 minutes at 0°C and 40°C to achieve equilibrium. The Frangibolts' built-in platinum RTD values were compared against Type E and Type K thermocouples, as well as the chamber's internal platinum RTD. All sensors agreed to within 1°C and within 0.2-0.3% in resistance values. Therefore, the RTD resistance values were not corrected for any constant bias.

Functional tests were conducted by applying 28 volts DC to the primary heater in each actuator. The primary data obtained during this test was the actuation time, defined as the duration from initial application of the supply voltage until the notched bolt broke. Actuation times were measured using a handheld stopwatch.

After each functional actuation, that actuator was conditioned in an oven at 85°C for 10 minutes. The length of the SMA cylinder was measured immediately after removal from the oven before the actuators had a chance to return to room temperature. This measurement was referred to as the *hot length* (no load). The stroke was defined as the change in an actuator's length from the compressed state to the hot length.

LEO Test Results

The actuation times were largely stable over the course of the test program as shown in Figure 9. The error estimate of ± 0.50 second is conservative based on the commonly reported uncertainty value of 0.2 second due to human reaction time with handheld stopwatch use.

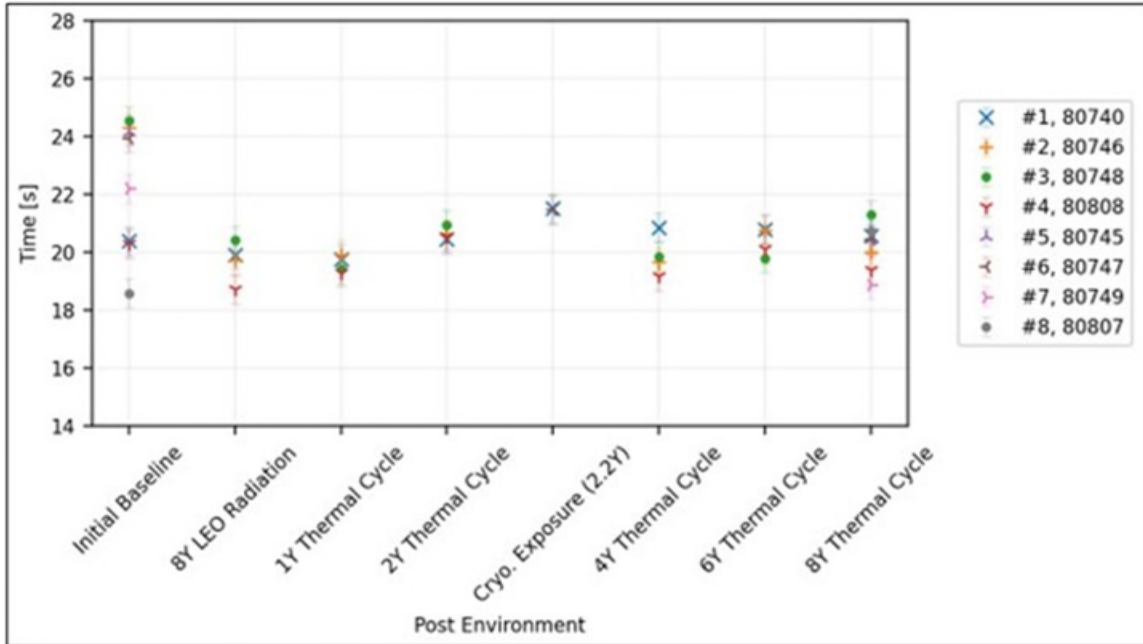


Figure 9. Actuation Time for Each Functional Test

It can be seen in the data that at the baseline functioning, there was a larger distribution among the test units. Upon closer investigation, actuators 2, 3, 5, 6, and 7 took longer than 22 seconds to break their respective bolts; these same five actuators were in their compressed state (without bolts) upon receipt from the donating contractor. Actuators 1, 4, and 8 were in their expanded state upon receipt and functioned in less than 21 seconds at the baseline test. It is unknown whether this correlation is relevant. Another possible cause is that the steel washers used in the test configuration were new at the baseline function and reused throughout the remainder of the test. They became slightly concave due to the forces involved in breaking the bolts, so some of the convergence of actuation times may be due to wearing-in of the test assemblies.

Figure 10 plots the actuators' strokes, which is the difference between a corresponding pair of compressed and hot measurements; the error here is estimated at 0.05 mm (± 0.002 in). Once again, the performance of the test units was remarkably stable over the course of the test series. Nine similar bolts just 6.4 mm (0.25 in) shorter were subjected to tensile testing and broke after an average displacement of 0.43 mm (0.017 in). The stroke capability of the actuators presented in Figure 10 shows significant margin over that required to break the bolts in this test setup.

The bolts' preloads were measured after each environmental exposure and subtracted from their respective pre-exposure values (Figure 8). Any change in preload would be assumed to occur solely due to the environment, since the joints were allowed to relax before entering the conditioning. The results are plotted in Figure 11. The uncertainty due to the subtraction of the two measurements is estimated at ± 0.9 kN (200 lbf). The mean value of the 56 measurements is -0.1 kN (-25 lbf), which is well within the uncertainty and only about a 2% loss from the relaxed preloads. There appears to be no significant change in bolt preload due to these long-life environments.

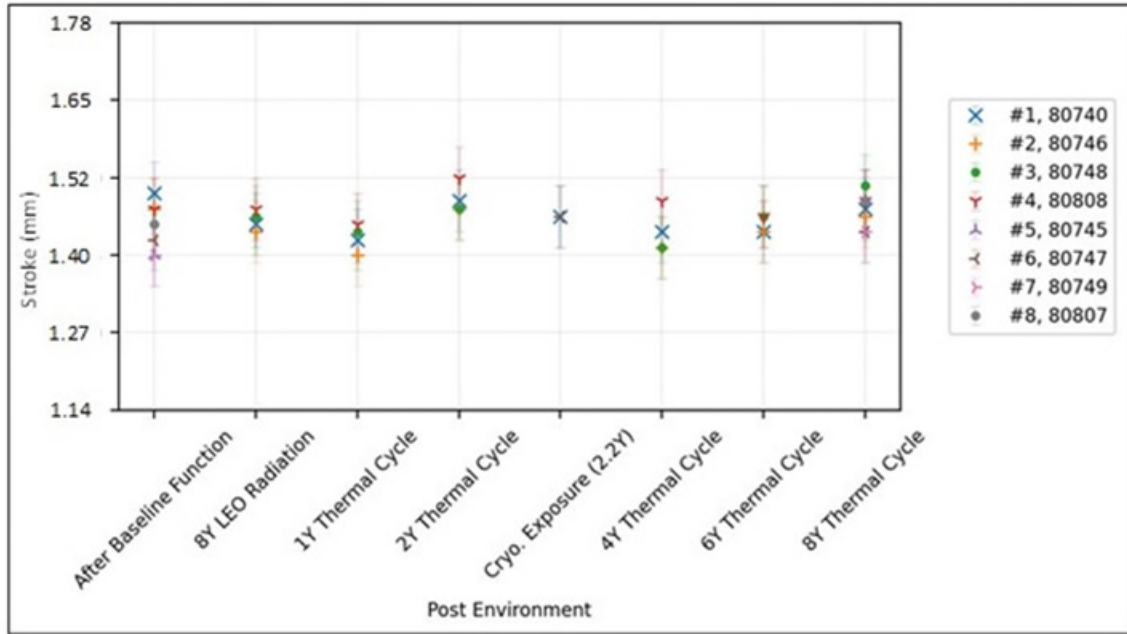


Figure 10. Actuator Stroke Following Environmental Exposure

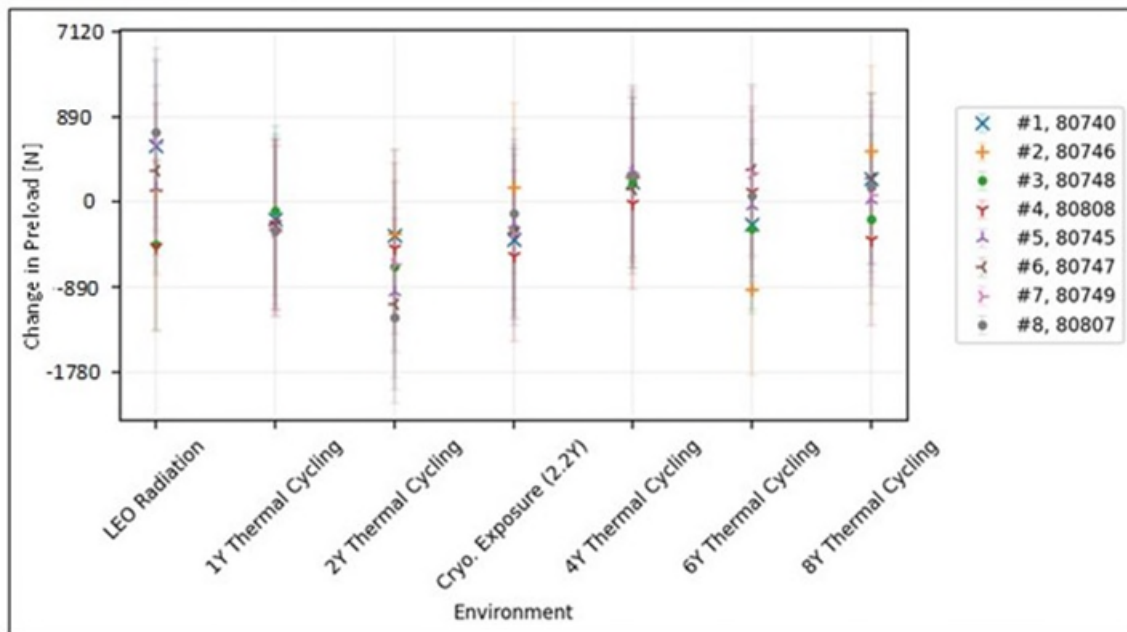


Figure 11. Change in Preload Following Environmental Exposure

Figure 12 also shows that the thermo-electrical performance of the heaters and the RTDs was stable over the course of the test. At baseline, the RTD measurements were recorded to the nearest 1 ohm with a handheld multimeter. Subsequent measurements were recorded digitally once the rest of the data acquisition system was set up. This explains the increase in the resolution after the baseline measurement, and the use of a different instrument may explain the offset in mean value from baseline to the subsequent measurements.

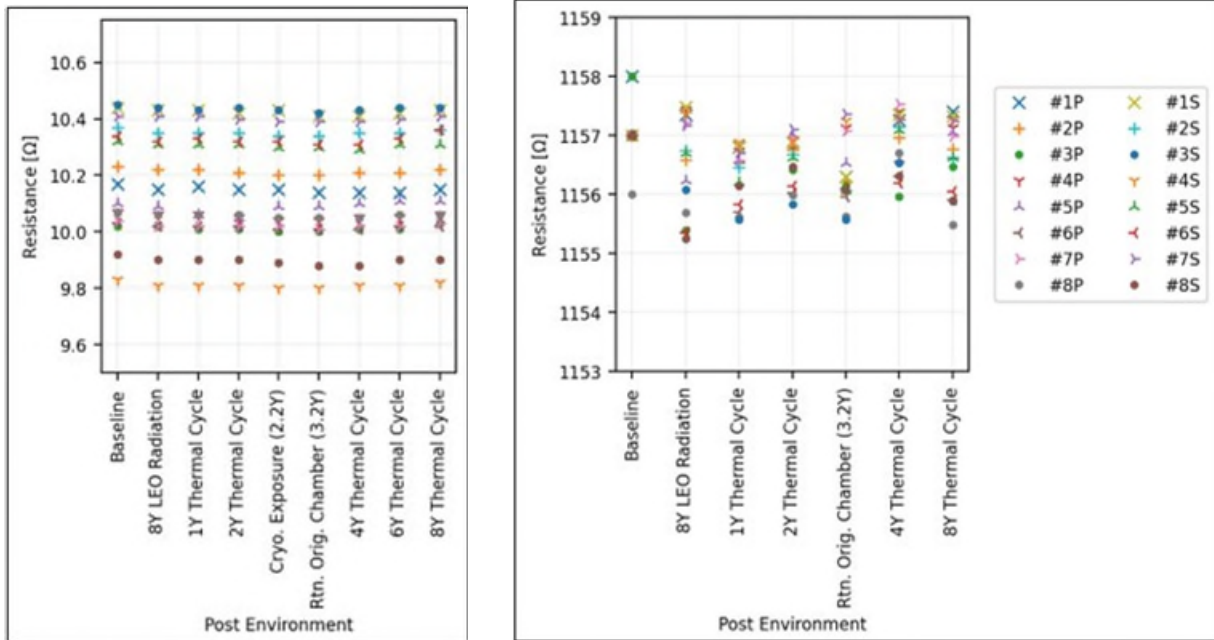


Figure 12. DC Resistance of Heaters (Left) and RTD Measurements at 40°C (Right)

The published value for the RTD reading is 1155.4 ohms at 40°C. An error of ± 1 ohm corresponds to $\pm 0.257^\circ\text{C}$. The variance shown in Figure 12 is less than the $\pm 2^\circ\text{C}$ tolerances for the thermocouples against which they were compared. As such, there appears to be no significant change in heater or RTD performance due to these long-life environments either.

GEO Test Results

The same eight units previously subjected to a simulated eight years of LEO environments were subsequently tested to radiation and thermal cycling environments to represent 8 years in GEO. This time four pairs each were exposed to varying radiation doses from 100 krad to 10 Mrad of gamma ray exposure (see Table 3). The radiation doses were selected in logarithmically spaced intervals of 4-5x per pair, and the maximum dose of 10Mrad was partially schedule-driven, as that single exposure level took nine days to accomplish, given the available test equipment; 10 Mrad corresponds to ~ 8 years GEO exposure assuming ~ 0.5 mm (0.020 in) aluminum shielding.

Table 3. GEO Test Phase Radiation Doses

Actuators	Dose
1, 2	100 krad
3, 4	500 krad
5, 6	2 Mrad
7, 8	10 Mrad

All eight units were also subjected to an additional 776 thermal cycles, this time going a bit colder, between -40°C and $+40^\circ\text{C}$. The calculation assumed that most of the year would be spent in constant sunlight due to the tilt of the Earth's axis, but with approximately six weeks of daily eclipses surrounding the Spring and Fall equinoxes. At ~ 90 cycles per year, that comes to 720 cycles in eight years; the testing was conveniently stopped during the workday after 776 cycles.

Much like during the LEO testing phase, length, stroke, time to break, bolt preload, heater resistance, and RTD validation at various temperatures were all assessed before and after the environmental exposures mentioned above. All of these plots throughout the environmental exposure, measurements, and functioning performed the same as in LEO, namely displaying insignificant change over the entire life. Figure 13 is a typical example of this, showing the fundamental performance parameter, time to break.

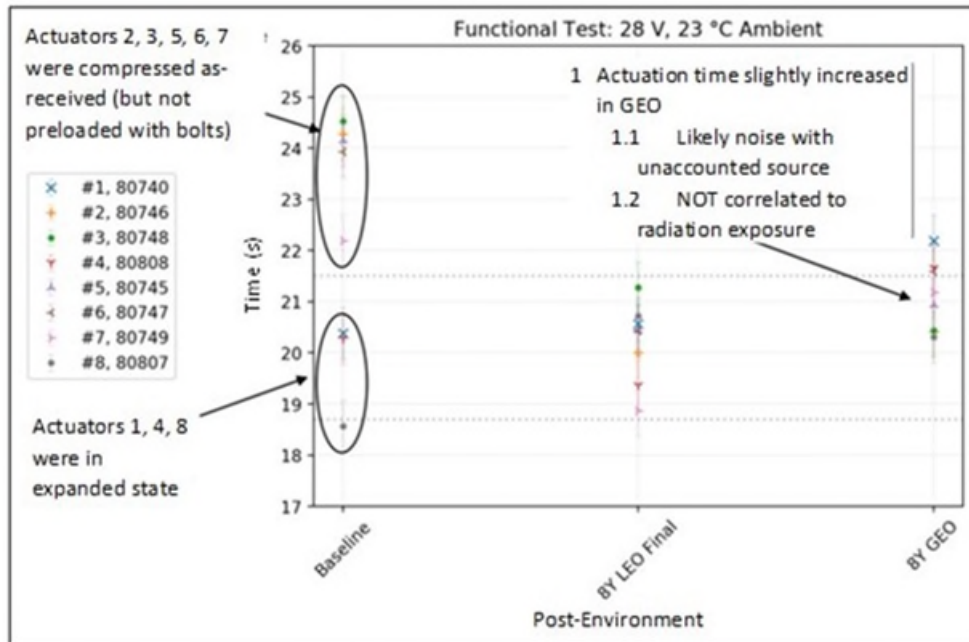


Figure 13. Time to Break for all Actuators Through all Phases of Life Exposure

One might be tempted to look at Figure 13 and conclude that the few additional thermal cycles and higher doses of radiation might cause the bolt breaking time to increase as a result, but a closer look shows that the increase is insignificant. Moreover, when the same eight actuators' time to break was evaluated as a function of increasing radiation it was revealed that the more radiation exposure a unit sees, its time actually decreases slightly. Even this trend is considered insignificant as it was only a 1% reduction in time for an entire order of magnitude increase in radiation dose.

Lessons Learned

Several lessons learned were captured as this study progressed, some more obvious and warranting of a gentle reminder, and others that can hopefully assist others in their future work.

- Never assume a Frangibolt actuator is compressed or uncompressed – always keep a log, and follow EBAD's guidelines about overall dimensions and comparisons to previous measurements
- Use redundant safety shutoff features (or an alarm) for unsupervised testing – especially over weekends and holidays
- One can maximize heat transfer to/from units via aluminum finned washers and use of a very small-volume thermal chamber with high convection rate and over-driving temperatures to conduct 10-12x accelerated age test
- Be knowledgeable about the accuracy of ultrasonic preload measurement – even though it is far better than torque, it still comes with its own uncertainty
 - Trial-and-error still required to obtain precise preload measurements when adjusting torque and iteratively checking with ultrasound
- Handling Frangibolt actuators, including the act of compressing them, raises their temperature slightly, if one is sensitive to that

- Bolts are not reusable; plan ahead and keep ample spares on hand. Nuts may or may not be reusable
 - Herein, silver plated nuts were reused for some of the final tests since there *were* two unplanned extra actuations after the cryogenic exposure mishap

Conclusion

It is critical that space application hold-down and release devices such as the Frangibolt actuate when and only when commanded. An accelerated aging test simulating eight years of low Earth orbit (LEO) was conducted to show that such an environment would not cause either premature actuation or significant degradation to the point of a failure to actuate when commanded. Eight Frangibolt actuators were subjected to 76 krad of gamma radiation followed by more than 38,000 thermal cycles between 0°C and 40°C. Moreover, the units were inadvertently cooled to the liquid nitrogen boiling point (-196°C) for more than 12 hours of cryogenic exposure during a test chamber anomaly.

Overall, the Frangibolts' performance was unaffected by these aggregated environments. There were no premature actuations during exposure, nor were there any failures to release in any functional tests. There was no significant change in the device's primary performance metrics of actuation time, stroke, or actuator length from the baseline test to the final actuation. The resistance of the electric heaters in the units and the accuracy of the internal RTDs were essentially unchanged. There was no significant increase or loss of bolt preload. There was also no apparent change in the color or texture of the silicone jacket (except some cracking which occurred on two of the units during the inadvertent cryogenic exposure). Finally, there was no discernible difference between the units that were repeatedly functioned and reset versus the units which were kept in a preloaded state throughout the entire program and only fired at the conclusion.

The relative simplicity of the Frangibolt leads to few failure modes, which can all be monitored and tested easily. Properly designed and preloaded joints can be expected to survive similar conditions to those tested herein.

References

1. TiNi Aerospace Drawing No. WI-1163. *FC4 STD Frangibolt Actuator ICD, Rev. C*. 7 April 2016.
2. TiNi Aerospace Document No. WI-1339. *Frangibolt Nitinol Characterization Test Report for ST60D118A4-18*. 6 March 2002.
3. TiNi Aerospace Drawing No. WI-4109. *STD Frangibolt Fastener ICD, Rev. D*. 6 December 2016.
4. Woodard, Timothy P. "Frangibolt Aging Test Fatigue Analysis." *Aerospace Technical Memorandum ATM-2020-00839*. 4 March 2020.
5. Johnson, Eric C., et al. "Ultrasonic Method for Deployment Mechanism Bolt Element Preload Verification." *Proceedings of the 42nd Aerospace Mechanisms Symposium* (May 2014), pp. 245-257.
6. TiNi Aerospace Document No. F-1382. *Frangibolt Re-Loading Procedure, Rev. G*. 14 June 2016.

Acknowledgements

The authors would like to formally recognize and thank several individuals and organizations who made this large endeavor possible and successful, without whom this data would never have been collected and shared with the community. Nick Czaplicki of Lockheed Martin provided the Frangibolt actuators – the key elements for all of this. Evgueni Todorov of The Aerospace Corporation's Materials Science Department provided equipment and service in measuring all the bolts' preload throughout the test. Adam Bushmaker of The Aerospace Corporation's Electronics and Photonics Laboratory provided equipment and service toward the radiation exposure test phase on all the units. Michael Benson and Michael Rosado of The Aerospace Corporation's Mechatronics Research Laboratory provided test space and support services throughout the entire mechanical portion of the test phase. Albert Ugarte and Rebecca Lin of The Aerospace Corporation's Parts, Materials, & Processes Department provided thermal chambers and support services throughout the entire thermal cycling portion of the test phase. And of course, Geoff Kaczynski, Luis Macias, and Philip Venti of EBAD provided timely and helpful support for all the Q&A along the way.

Development of a Bulk Metallic Glass Planetary Gearmotor for Unheated Actuation in Cryogenic Environments

Andrew Kennett* and Robert “Peter” Dillon*

Abstract

Bulk Metallic Glasses (BMGs), a class of amorphous metal alloys, were selected for development of gears for unheated actuators that can be used in cryogenic environments such as Mars, the Moon, and outer planetary icy bodies (e.g., Enceladus and Europa). Specifically, an alloy of $\text{Cu}_{43}\text{Zr}_{43}\text{Al}_7\text{Be}_7$ was used to successfully develop a BMG planetary gearbox and prototype and flight gearmotors for operation at $\leq -180^\circ\text{C}$. Components and configurations, testing (including shock and vibration), and qualification for use in the Cold Operable Lunar Deployable (robotic) Arm (COLDArm) system are presented in addition to lessons learned from all phases of development.

Introduction

Bulk metallic glasses (BMGs) are amorphous metal alloys that avoid crystallization when cooled rapidly from the melt. The resulting properties of many of these alloys, e.g., high hardness, high strength, large elastic strain limit, and low modulus of elasticity appear advantageous for gears. In 2011, during a NASA Center Innovation Fund workshop, the connection of BMGs for gear applications was made and a goal established to develop BMGs for reliable, torque-dense, extreme cold environment actuators that do not require the use of heaters.

Actuators for use in extreme cold environments require heating of the gearboxes to maintain adequate operating temperatures ($> -55^\circ\text{C}$) for the lubricant to function and minimize wear to meet mission requirements. It is estimated that up to 30% of the budgeted daily discretionary energy of the Curiosity rover is used for heating actuators. Initial development of BMGs for gear applications was through internal research and development and the NASA Game Changing Development (GCD) program’s Advanced Manufacturing Technology (AMT) portfolio project. Infusion was targeted at the follow-on rover to Curiosity; however, a build-to-print approach for the new rover restricted the use of new technology in the actuator system and development stalled when the project was closed.

BMG gear development quickly restarted as its own project in the GCD program when potential application in a notional Europa Lander mission was identified. The concept had a robotic arm, would likely be severely power constrained, and have limited life requirements. Subsequently, several notional missions from the Decadal Survey [1] and the Moon to Mars initiative would likely benefit from actuators that can operate unheated in similar conditions ($\ll -55^\circ\text{C}$) as they are also expected to be severely power constrained. With unheated actuators, power previously needed for heating gearboxes can be reallocated to accomplishing mission science objectives. Operation during the night becomes feasible and collection of volatile materials that are susceptible to a material state change or loss through sublimation is more viable without heat from the sampling system.

BMG alloy development and selection for gearing applications was previously described by Hofmann et al [2]. This paper discusses the successful development history of BMG planetary gearboxes from the initial proof-of-concept (PoC) design targeting infusion into a notional Europa lander, followed by a pivot to Lunar applications with the design and testing of an Engineering Development Unit (EDU) that integrates the

* Jet Propulsion Laboratory, California Institute of Technology, Pasadena, CA

gearbox with a modified Commercial-Off-The-Shelf (COTS) motor, and finally to an Engineering Model (EM)/Flight Model (FM) configuration that has been qualified and integrated into the COLDArm (Cold Operable Lunar Deployable robotic Arm) EM and FM actuators. Gearbox and gearmotor testing and gearmotor qualification for COLDArm has been completed and performance results from these tests as well as lessons learned from all phases are presented. A description of the COLDArm system is previously published [3].

BMG Planetary Gearbox Proof of Concept (PoC)

The PoC design for a BMG planetary gearbox leveraged requirements for a notional Europa lander robotic sampling arm circa 2016 which would utilize actuators consisting of an encoder/brake/motor driving a planetary gearbox which would drive a Harmonic gearbox, Figure 1.

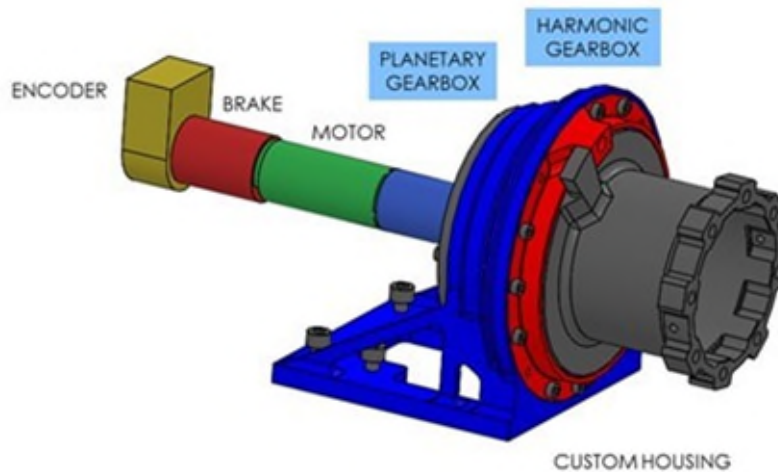


Figure 1. Cartoon of notional (circa 2016) Europa lander robotic sampling arm actuator for which the proof-of-concept BMG planetary gearbox was designed.

An alloy of $\text{Cu}_{43}\text{Zr}_{43}\text{Al}_7\text{Be}_7$ was selected from the BMG alloy development work [2] for its combination of hardness, strength, toughness, comparable spur gear mass loss due to wear in both air and vacuum, and glass formability. Spur gear testing showed an unlubricated wear rate 65% less than C300 Maraging Steel with this BMG alloy. A hybrid (BMG-steel) gearbox consisting of a commercially available single stage steel gearbox modified with replacement (like-for-like) planet gears suction cast from the same BMG alloy and lubricated with doped- MoS_2 dry film showed ambient input cycle life greater than 3x of that required for Curiosity rover's drive and steer actuators (approx. 15 million motor revolutions for 1x life). Additional testing of the hybrid configuration at moderately higher contact stress, and cold cycling achieved 14.9 million motor (input) revolutions (revs) with 3.4 million of those revs at temperature $<-120^\circ\text{C}$. The spur gear and hybrid gearbox test data were combined for a low confidence contact stress v. stress-cycles life model, Figure 2, that was used for the initial design allowables in the design of the planetary gearbox for proof-of-concept.

A 3-stage configuration (Figure 3a) with a gear ratio of 5.5:1 for each stage ($\sim 166:1$ total), an output torque of 3 N-m, and an output speed of 1.5708 rad/s (15 rpm) was selected for the PoC design. Specific attention was paid to maximize rolling contact and minimizing sliding contact for the final gear designs. To reduce development costs, the same gear design and size was used for each of the three planet stages. This resulted in an apparent oversizing of the input and middle stages. A factor of three was held on the target input life to comply with typical JPL mechanism design practice, and an additional minimum margin was held on the system given the immaturity of the initial design allowables. The gear design inputs and resulting outputs are summarized in Tables 1 and 2, respectively. Planet bearings were used, as opposed to bushings, to allow for rolling contact, and caged needle roller bearings were chosen in this case to achieve the lowest practical contact stresses.

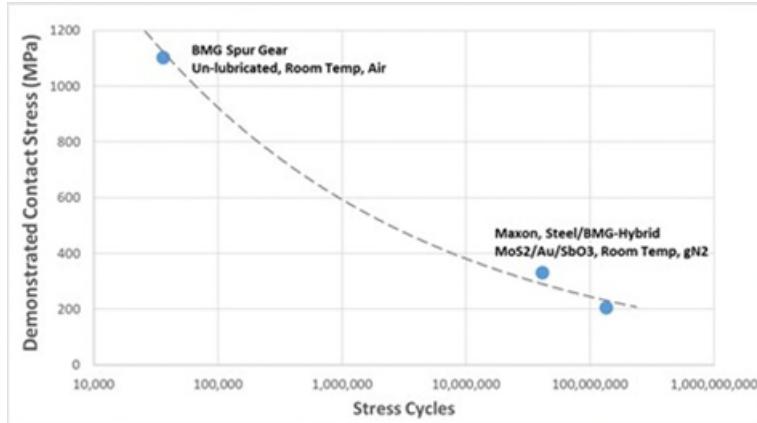


Figure 2. Contact stress v. stress cycles life model that was used in the PoC planetary gearbox design developed from spur gear and BMG-steel hybrid planetary gearbox tests. The contact interfaces in the spur gear test were unlubricated BMG-BMG. In hybrid gearbox testing they were doped-MoS₂ dry film lubricated BMG-Steel.

Table 1: BMG Planetary Gearbox Proof of Concept (PoC) Design Inputs

Design Inputs	Units	Value
Output Torque	N·m (in·lbf)	3 (27)
Assumed Stage Efficiency	-	0.95
Total Gear Ratio	-	166.4
Design Input Life (including 3x life test factor)	Revolutions (revs)	3,000,000
Design Output Life (including 3x life test factor)	Revolutions (revs)	18, 032

Table 2: BMG Planetary Gearbox Proof of Concept (PoC) Design Outputs

Design Outputs	Units	Stage 1	Stage 2	Stage 3
Stage Ratio	-	5.5	5.5	5.5
Input Torque	N·m (in·lbf)	0.0215 (0.19)	0.0644 (0.57)	0.5740 (5.08)
# of Planet Gears	-	4	4	4
Mesh Load Factor	-	1.32	1.32	1.32
Torque per Gear	N·m (in·lbf)	0.0068 (0.06)	0.0362 (0.32)	0.1898 (1.68)
Diametral Pitch	-	96	96	96
# of Ring Teeth	-	108	108	108
# of Sun Teeth	-	24	24	24
# of Planet Teeth	-	41	41	41
Face Width	cm (in)	0.6985 (0.275)	0.6985 (0.275)	0.6985 (0.275)
Pressure Angle	deg	20	20	20
Steel Equivalent Contact Stress (No Additional Rating Factors)	kPa (psi)	134923.5 (19,569)	308409.4 (44,731)	701438.1 (101,735)
Input Cycles	-	3,000,000	545,455	99,174
Sun-Gear Stress Cycles	-	9,818,182	1,785,124	324,568
Expected Stress-Cycle Life Capability	-	252,959,288	51,702,151	1,417,035
Expected Life Margin (at Time of Design)	-	25	28	3

BMG gear components, Figure 3b, were fabricated using a modified injection molding process at Visser Precision (Denver, CO) and subsequently dry film lubricated (DFL) with Ni and Au/Sb doped MoS₂ for comparative performance testing. At the time of fabrication, manufacturing capability limited component mass to <100 g, including gates and runners, and a critical casting thickness (a value related to the size of part that can be produced in the amorphous state) of ~5 mm. In this design, the ring gear was at the edge of existing manufacturing capability. Integration of the gearbox is accomplished with carbon steel needles in a glass reinforced polyimide cage as planet gear bearings. These rotate on 3Y-TZP (zirconia) ceramic axes that are constrained in Ti6Al4V planet carriers with 3M 2216 Gray epoxy adhesive. (The 1st and 2nd stage planet carriers are overmolded with BMG alloy pinions while the 3rd stage (output) is Ti6Al4V.) The input and output housings are also Ti6Al4V while the input shaft is stainless steel. A Si₃N₄ ball is used to limit axial motion between the motor and gearbox while a crowned surface on the face of the 2nd and 3rd stage sun gears achieves a similar function. Input and output bearings are 3Y-TZP ceramic balls and races with PTFE cages and shields. The gearbox assembly (Figure 3c) mass is ~278 g.

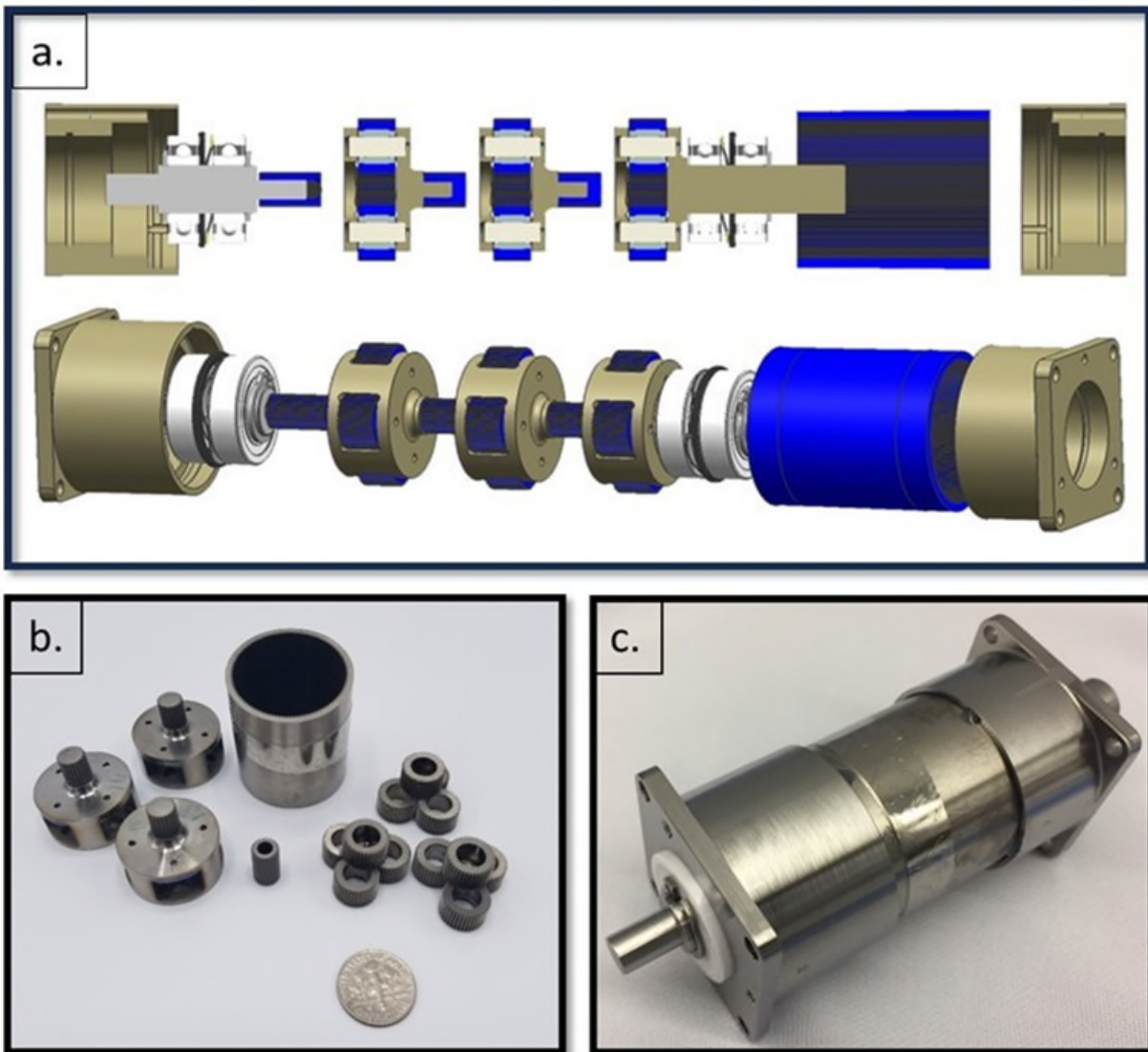


Figure 3. (a) Exploded views of the PoC gearbox design in cross-section and solid body. (b) Commercially fabricated BMG gear components (CW from left): overmolded planet gear carriers, ring gear, planet gears, pinion gear; (c) Assembled 3-stage, dry film lubricated BMG-based ~166:1 planetary gearbox.

Overmolding of the BMG alloy onto the Ti6Al4V planet carrier (Figure 4a) to form the pinion (Figure 4b) does not require in any metallurgical joining of the materials. Instead, the BMG alloy is mechanically locked to the planet carrier using a stub with retention and constraining features. The box shape of the stub minimizes rotational movement and the radial undercut below the stub retains and minimizes axial movement of the overmolded pinion. This design is not without challenges. The overmolding process can produce voids that are readily observable in x-ray computed tomography (CT), Figure 4c. The face of the overmolded pinion is also an axial thrust contact surface that can degrade and be a source of debris, particularly if the surface is decorated with voids from the overmolding process. Fabricating the planet carrier pinion separately from planet carrier and assembling it as a unit is a viable alternative, but care must be taken to account for thermal expansion mismatch, to hold the pinion angularly and axially, and to control the thrust contact surface.

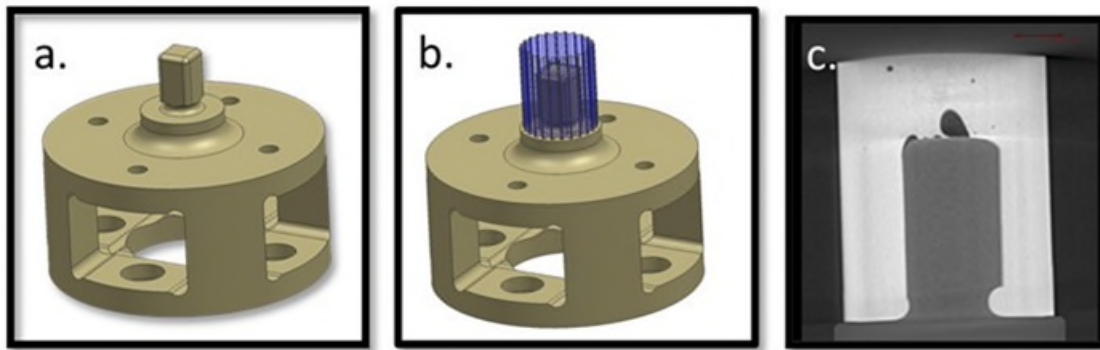


Figure 4. (a) Cartoon of a planet gear carrier showing the box shape of the overmolded pinion gear retention stub constraining rotational movement and the undercut constraining axial movement; (b) Cartoon of overmolded sun gear on machined carrier. (c) X-ray CT image of the BMG pinion gear overmolded on the retention feature of the planet gear carrier. The asymmetry in the image is due to the location from which the CT image slice was taken from the CT image volume.

While direct casting (or injection molding) of the BMG gear components promised advantages of lower cost production and consistent component quality, tooling cost was substantial with significant lead time for tooling and fabrication (~18 months to deliver the ring, planet, and pinion gears and overmolded planet carriers in sufficient quantity to assemble 10 gearboxes). Component quality was reflective of the quality of the tooling and detailed understanding of component shrinkage in processing. Where 12.7 μm tolerance was expected 25.4 to 38.1 μm was commonly observed. With that understanding, test articles of the PoC design were assembled and life tested. Manufacturing improvements such as casting of blanks for subsequent precision gear grinding are introduced later.

Life testing was performed using the Space Environment Dynamometer (SED) at NASA KSC [4]. This test bed allows testing in air, under vacuum, and at various temperatures including cryogenic temperatures. One test article, SN004 (unlubricated) was tested at an output torque of 2.5 N·m in air and vacuum. In air, the test article ran at 104.72 rad/s (1000 rpm) input velocity for ~1.8M clockwise (CW) input revolutions (revs). In vacuum, the test article ran at 31.416 rad/s (300 rpm) input velocity for ~1.4M counterclockwise (CCW) input revs for a total of 3.2M input revs. The rotational direction change from CW to CCW was made when a temperature rise was observed from thermocouples attached to the surface of the ring gear. Operation under vacuum was done to coarsely evaluate performance in air compared to vacuum while the slower speed was selected to minimize self-heating.

Three test articles, SN001 (MoS₂:Au/Sb₂O₃ sputtered DFL), SN002 (MoS₂:Ni sputtered DFL), and SN003 (unlubricated) were tested to failure with ~60k input revs of ambient operation at 104.72 rad/s (1000 rpm) under load followed by cryo (≤ 100 Kelvin) operation at 104.72 rad/s (1000 rpm) for ~400k input revolutions

at ~3.0 N·m (Figure 5), ~315k input revs at ~2.5 N·m, and ~244k input revs at ~3.0 N·m, respectively. Figure 5 shows the input and output torque and temperature data for the BMG planetary gearbox with Au/Sb₂O₃ doped MoS₂ dry film lubricated gears. An increase in input torque can be seen between ambient and cold operation. Both a rise in temperature and further increase in input torque are observed near end of life.

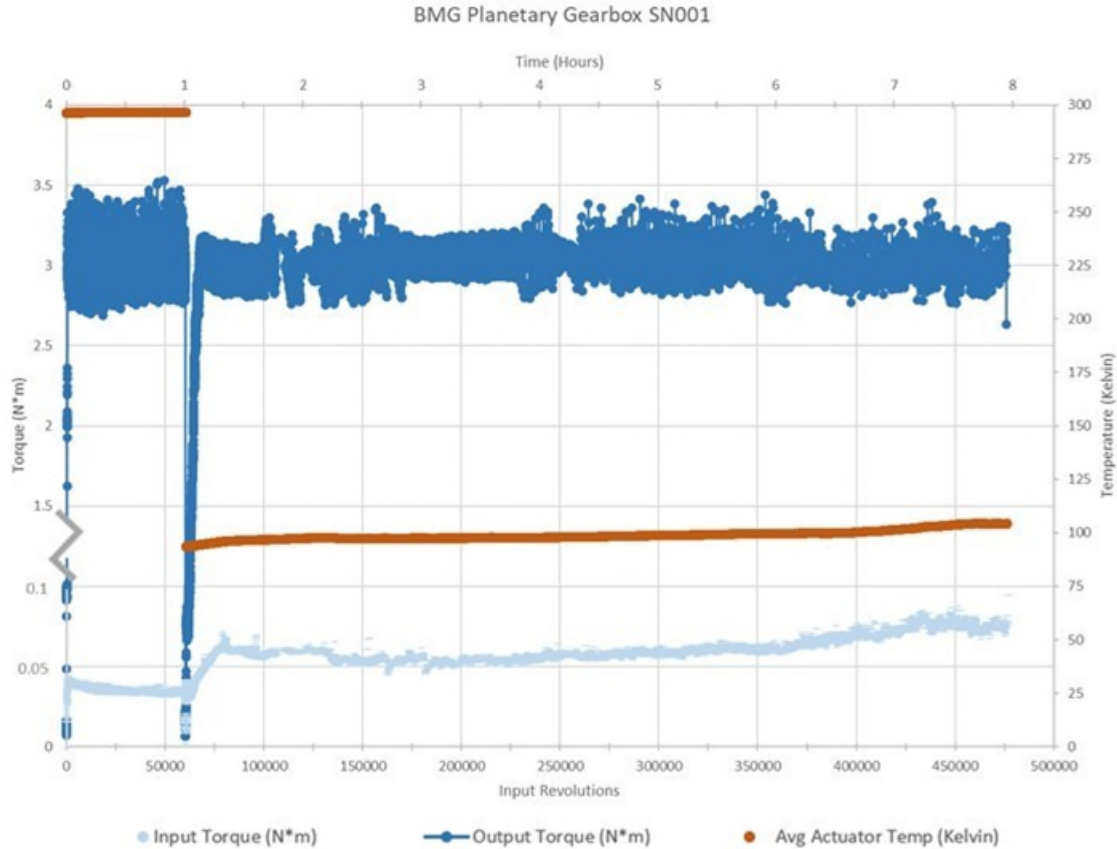


Figure 5. Torque and temperature data a BMG planetary gearbox with Au/Sb₂O₃ doped MoS₂ dry film lubricant run to failure after ~475k input revs.

Disassembly of the tested gearboxes revealed wear through of the DFL and progressive wear of the BMG base material in the gear teeth. Significant debris was present in the gearbox; however, there was no catastrophic failure observed for any of the gear teeth.

BMG Planetary Gearmotor Engineering Development Unit (EDU)

The design of the EDU, Figure 6, swaps out the stainless-steel input shaft for a modified COTS EC 32 flat Maxon motor. Cryo-capability with this motor was demonstrated after modification with dry ceramic bearing bearings similar to those used in the input and output of the gearbox. The DFL used on the gears was also changed from doped MoS₂ to Tribologix iKote. To improve the dimensional quality and surface finish of some of the gear components, the pinion and planet gears were reworked by precision gear grinding at Forest City Gear (Roscoe, IL). The geometry of the ring gear and overmolded planet carrier prohibited similar rework of those components.



Figure 6. BMG Planetary Gearmotor EDU consisting of a COTS size 32 Maxon motor integrated with the 166:1 PoC design BMG planetary gearbox.

BMGs have limited ductility (~1%). To demonstrate sufficient BMG alloy toughness and robustness of the design, the gearmotor was subjected to dynamic testing (shock and random vibration). Pyroshock and launch vibration qualification test levels from Mars 2020's Sample Caching System (SCS) were selected for the EDU shock and random vibration test levels. Testing took place in JPL's Environmental Testing Laboratory using the Tunable Beam for shock (Figure 7a) and a small shaker for random vibration (Figure 7b). For shock testing each of three axes were shocked twice. Functional tests performed before and after shock tests showed no discernable change in performance and no damage was noted. The same test article used for the shock test was used for vibration testing. For vibration testing each of three axes was exposed for two minutes. A low-level signature survey was performed before and after the full-level random vibration tests. Some variation, typical of actuator mechanisms similarly tested, was noted for Y- and Z-axes. No structural or mechanical failure was indicated in the signature survey results. The BMG Actuator was functionally tested initially and after the final axis of full-level random vibration testing. Motor current change from 27 mA prior to testing to 30 mA after testing was deemed acceptable. Subjectively, there was no discernable change in the acoustic characteristics of the operating actuator.

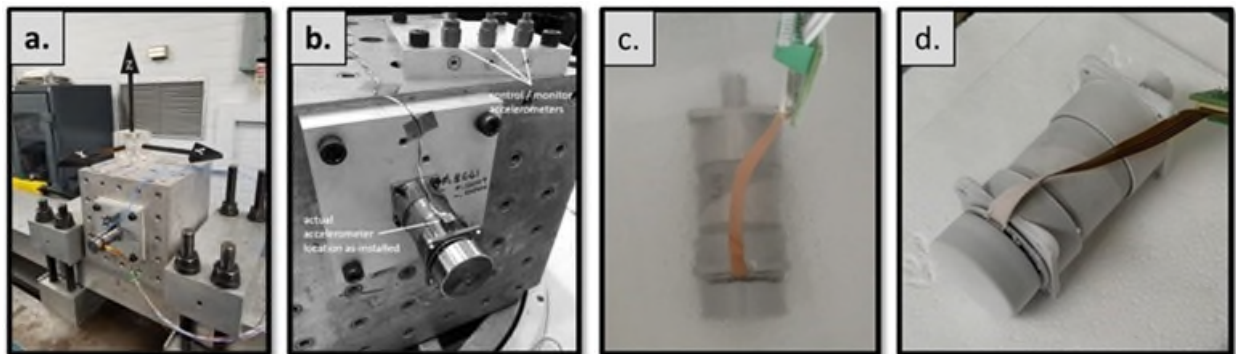


Figure 7. (a) EDU actuator mounted for shock testing on the tunable beam. (b) EDU actuator mounted for random vibration testing on the small shaker. (c) EDU actuator operational in LN2 after dynamic testing. (d) EDU actuator operational after dynamic testing and removal from LN2.

Following shock and vibration testing, cold start capability and operation was demonstrated using the same test article. The gearmotor was submerged in liquid nitrogen (LN2) until all boiling stopped. The motor was reconnected to the controller and the gearmotor operated under no load in LN2 for ~1 minute (Figure 7c). The gearmotor was removed from the LN2 and operated in air under no load while warming to ambient (Figure 7d). There was no noticeable qualitative change in performance.

To further demonstrate robustness and cold capability of the EDU "cryo-shock" testing was also performed using the same test article as used for shock and random vibration testing. Pyroshock qualification test levels from Mars 2020's Sample Caching System (SCS) were again selected and used for the cryo-shock

test levels. Testing took place in JPL's Environmental Testing Laboratory using the Tunable Beam for shock (Figure 8b). The test article was shrouded by a "bucket" (Figure 8a) that allowed the test article to be cooled with LN₂ until the LN₂ stopped boiling (Figure 8c). A plug was removed allowing LN₂ to drain from the bucket and the shock test run while the test article temperature was <-180°C. For shock testing each of three axes were shocked twice. Functional tests performed before and after shock tests showed no discernable change in performance and no damage was noted.

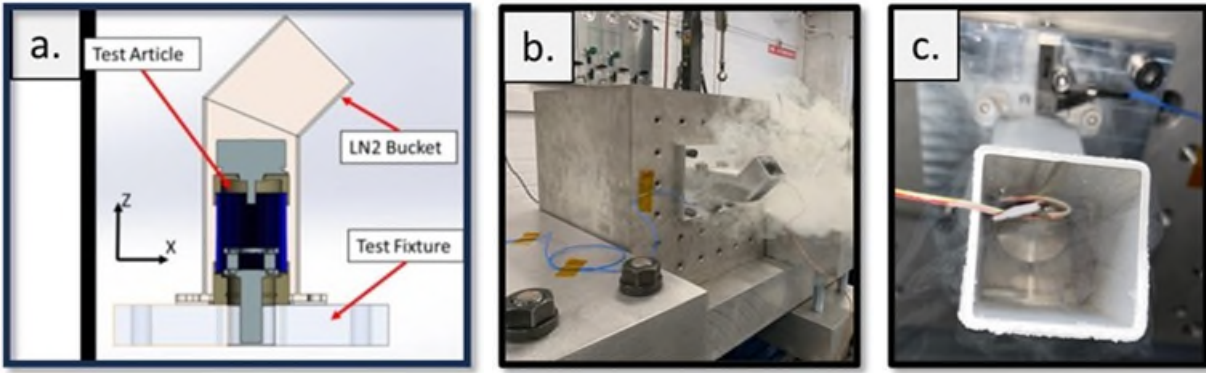


Figure 8. (a) Cryo-shock test fixture design for (b) shock testing on JPL's tunable beam. (c) A "bucket" is mounted over the test article enabling conditioning of the test article with LN₂ to the test temperature (< -180°C) and draining of the LN₂ just prior to a shock test.

Life Testing

The Cold Operable Lunar Deployable (robotic) Arm (COLDArm) [3] was conceived as a technology demonstration mission during preparation for life testing of the EDU. A programmatic pivot was made to focus gearmotor development on infusion into the COLDArm system's actuators. COLDArm's baseline architecture utilizes a 50:1 size 20 strain wave drive at the output of each of the four actuators in the robotic arm. These drives are driven by a BMG planetary gearmotor. Life testing of the EDU utilized a notional input torque to the strain wave drive of 1 N·m as the output torque for both ambient and cold testing.

Life testing of the EDU was performed using the Space Environment Dynamometer (SED) at NASA KSC [4]. Two similarly configured test articles, both with gears dry film lubricated with Tribologix's iKote, were tested to failure. The first test was performed under vacuum at ambient temperature and the second test was performed under cryogenic conditions under vacuum at a temperature of <100K. For both tests the motor speed was 209.44 rad/s (2000 rpm), the output torque was 1 N·m, and forward-reverse duty cycled every 2000 revs. 10M motor revs were achieved at ambient temperature while 1.5M motor revs were achieved at ≤ -180°C. Both tests stopped when motor stalling was observed. The rate of performance degradation is seen in the plot of the moving average efficiency (Figure 9) for both tested gearmotors. Disassembly revealed wear debris and debris migration into the output bearing assembly.

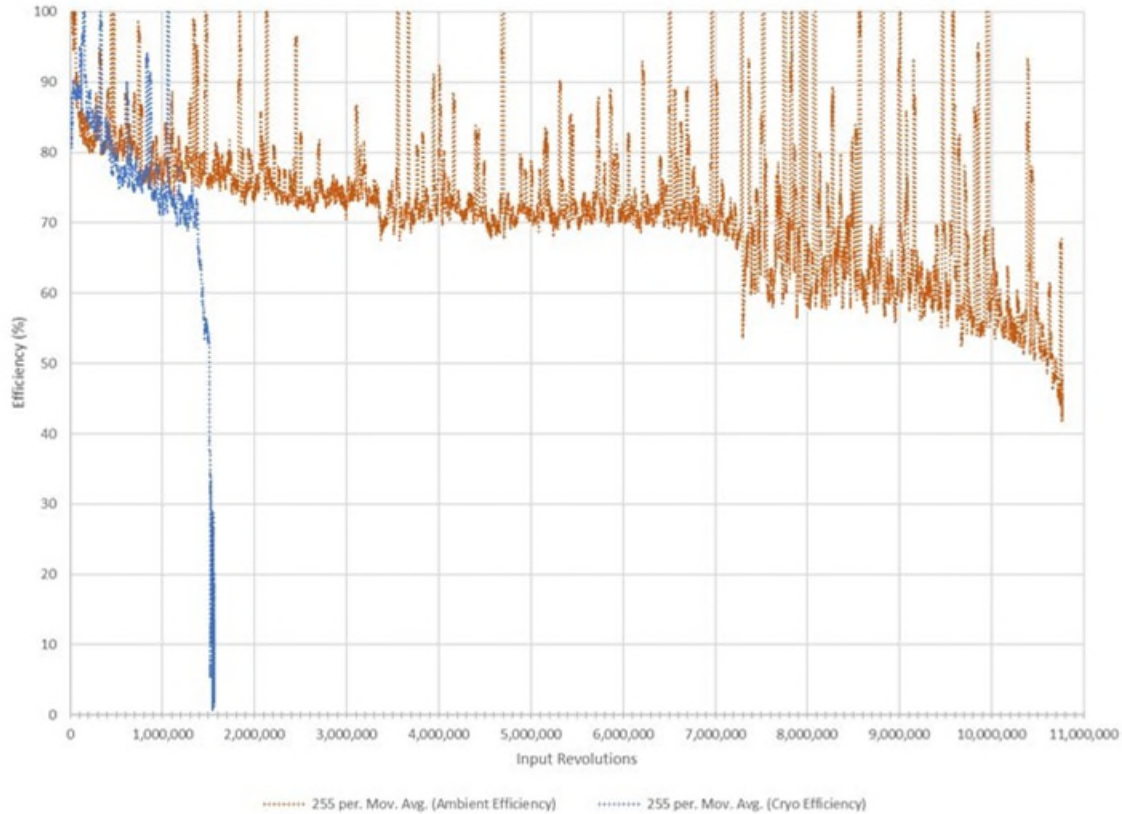


Figure 9. Ambient and cryo (-180°C) test data showing gear efficiency as a function of motor revolutions for EDU planetary gearmotors.

BMG Planetary Gearmotor Engineering Model/Flight Model (EM/FM)

Engineering Model (EM)/Flight Model (FM) BMG planetary gearmotors (Figure 10) were developed from the EDU to further meet COLDArm [3] requirements. This included a ground test demonstration of capability to meet 3x life requirements at ambient (presumed 25°C) and -180°C, and a notional mission operations temperature of -100°C. For the EM/FM units, a flight-qualified Maxon motor with magnetic detents [5] was selected. Testing of the Hall sensors used in these motors revealed a loss of functionality at temperatures <-130°C. Commercially available Infineon Hall sensors were found to function at temperatures <-180°C. These components were selected, parts screened for functionality to -180 °C, and provided for modification of the motor. The motor was also modified by Maxon with dry lubricated motor bearings for cryogenic operation.

Maintaining the necessary precision in the cast/injection molded parts was challenging for the PoC gearboxes and EDU gearmotors. For the EM/FM units, amorphous blanks were fabricated for the ring, planet, and pinion gears at Visser Precision (Denver, CO) from $\text{Cu}_{43}\text{Zr}_{43}\text{Al}_7\text{Be}_7$ feedstock produced by Materion (Elmore, OH). (BMG feedstock manufacturing has since been licensed and transferred by Materion to Eutectix, Tolleson, AZ.) Forest City Gear (Roscoe, IL) ground the planet and pinion gears to specification. The ring gear tooth profile was fabricated by wire electrical discharge machining (EDM). Recast from the wire EDM process was removed using a finishing process at Microtek. The gear teeth of the overmolded pinion are produced to net shape as part of the overmolding process, so it can be challenging to achieve the same precision when compared to directly grinding the gear teeth. Tribologix iKote DFL was applied to the gears.

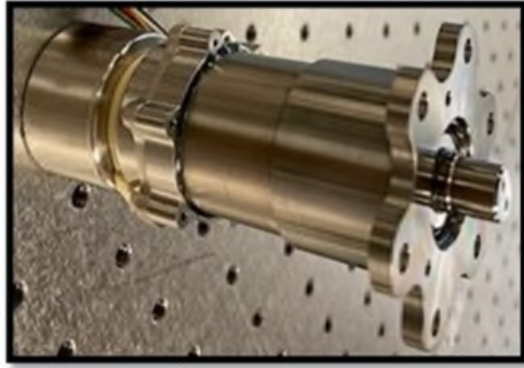


Figure 10. BMG planetary gearmotor in the EM/FM configuration. Note D-shaped output shaft and hexagonal bolt patterns for increasing the robustness of the interfaces.

Initial testing of the EM/FM configuration exhibited anomalous behavior and premature failure during ambient run-in (Figure 11a). A planet gear in the 1st stage was jammed (Figure 11b) by the buildup of material between the planet gear shim and the planet carrier (Figure 11c). Investigations using optical microscopy and x-ray computed tomography (CT) revealed the presence of microscopic burrs on the planet gears (Figure 11d) and planet gear shims as well as small voids in some planet gears in the root near the surface (Figure 11e), all of which could have liberated material and caused the anomaly. Ultimately, the planet gears were deburred and screened for voids using CT, and after changing the shim material, the shims were electropolished and lubricated with Tiolube 1175. Run-in was successful after this rework. No debris was observed after disassembly and inspection. Qualification testing began following reassembly.

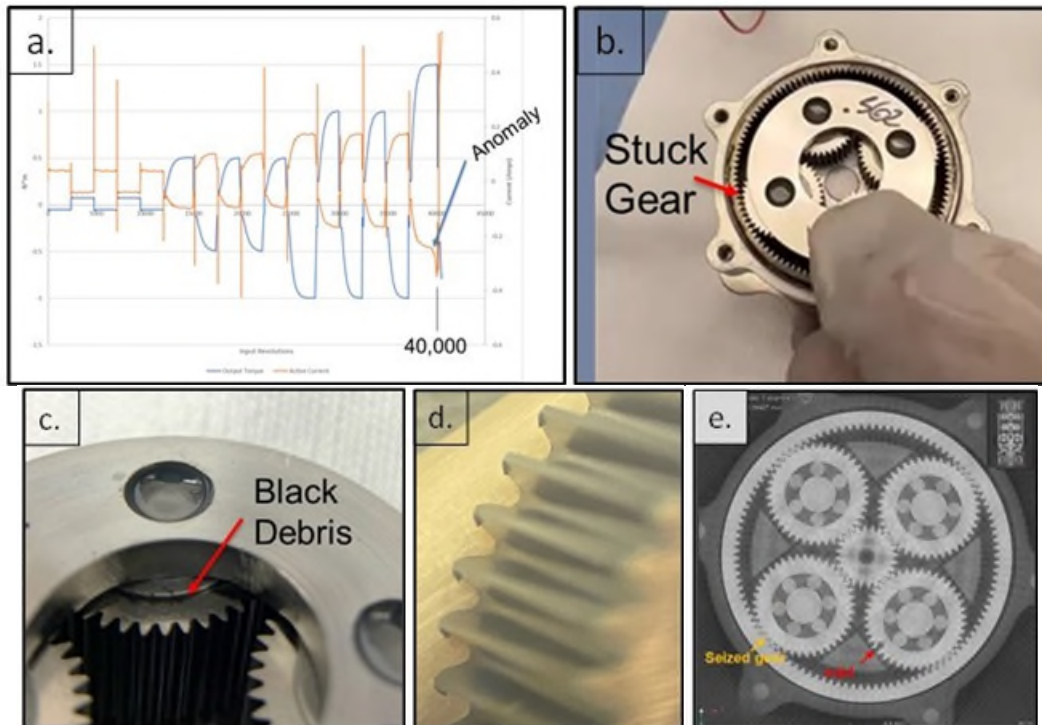


Figure 11. (a) Plot of output torque and motor current from ambient gearmotor run-in at the beginning of testing with occurrence of anomaly indicated after ~40,000 motor revs. (b) Stuck gear in the 1st stage planet carrier assembly. (c) Noticeable debris at the edge of the gear shim. (d) Optical image of burrs on the planet gears prior to use. (e) X-ray CT image of the 1st stage planet gear assembly showing a planet gear with a void just below a tooth root next to the stuck gear.

Qualification Testing

Output torques and cycles in revolutions (revs) for qualification testing (Table 3) of the EM/FM configuration for COLDArm were established from actual input torques measured during strain wave gear life testing. Rotational direction was changed every 50 output revolutions, equivalent to the input for 1 strain wave gear output revolution. Output torque was increased after 3x life through 5x life to represent degradation in strain wave gear efficiency as observed during strain wave gear life testing. After 5x life the gearmotor was operated at 2.2 N·m of output torque until failure.

Table 3. 1x Planetary Gearmotor Output Torque and Life Requirements

Strain Wave Output Torque Bins (N·m)	0-10		10-20		20-30		30-40		40-50		50-60	
	revs	N·m	revs	N·m	revs	N·m	revs	N·m	revs	N·m	revs	N·m
-180°C	125	0.68	0	-	0	-	25	1.95	0	-	0	-
-100°C	241	0.64	70	1.00	5	1.3	0	-	0	-	5	2.5
25°C	2318	0.43	414	0.68	269	0.91	353	1.23	455	1.55	618	1.95

The qualification test article, modified with deburred and screened planet gears and electropolished and lubricated shims, was successfully tested (Figure 12) demonstrating 3x COLDArm life requirements for ambient ground test, -180°C ground chamber test, and -100°C (notional mission), additional cycles demonstrating capability for degraded Harmonic performance, and continuous output to failure at -180°C. This qualified the design for COLDArm with ~5,269,000 total motor revs of flight-like usage.

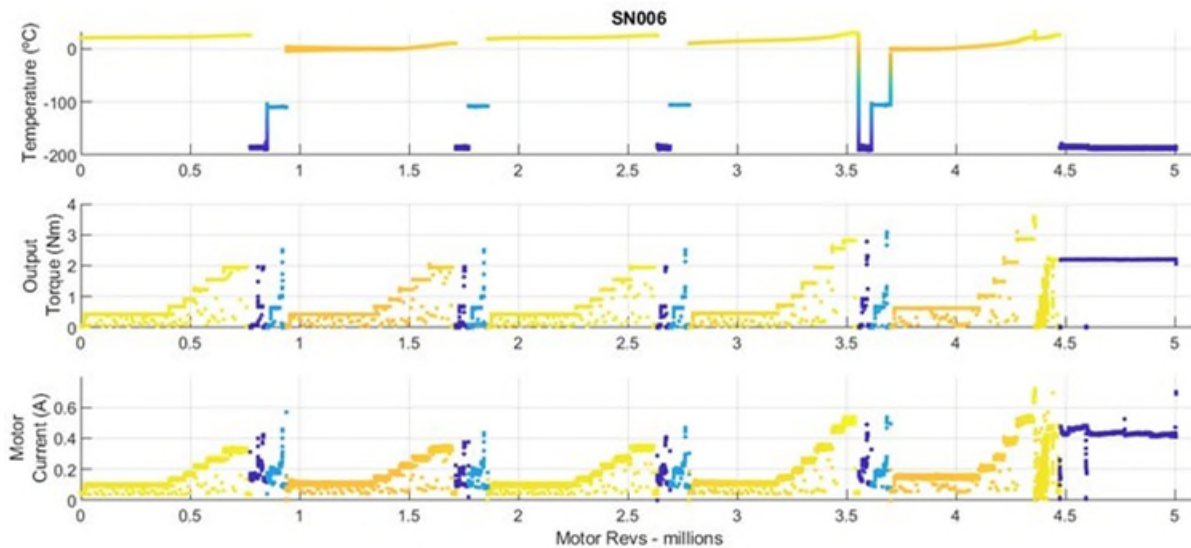


Figure 12. Qualification life test results of the EM/FM planetary gearmotor for COLDArm. plot color scaled with gearbox temperature with yellow being warmer and dark blue being colder. Absolute values shown. Data hidden during velocity transitions.

This unit was disassembled to assess the cause of failure (Figure 13). Fine debris was present in the input stage, and the dry lubricant was discolored and/or removed, but that gearing showed only minor signs of wear. Wear was more prevalent on the 2nd and 3rd (output) stages of the gearbox, as well as gear tooth

fracture in both stages. The causality of the wear & debris v. the tooth fracture is not currently well understood. The initial degradation in performance seems to align with the system being brought to its highest output torque (~3.54 N·m), at around 4.4M revs (during the extended life portion of the test), suggesting that this event may have triggered a fracture that cascaded into other fractures and wear. This is notably different from end-of-life failures seen in early developmental units where planetary gears wore out due to abrasive wear, without signs of fracture. It is theorized that differences in processing and/or the inclusion of foreign elements in the metallic glass may have led to some level of embrittlement in these gears. An activity is being conducted in parallel to this effort to assess manufacturing variability and establish design allowables for mechanical properties.

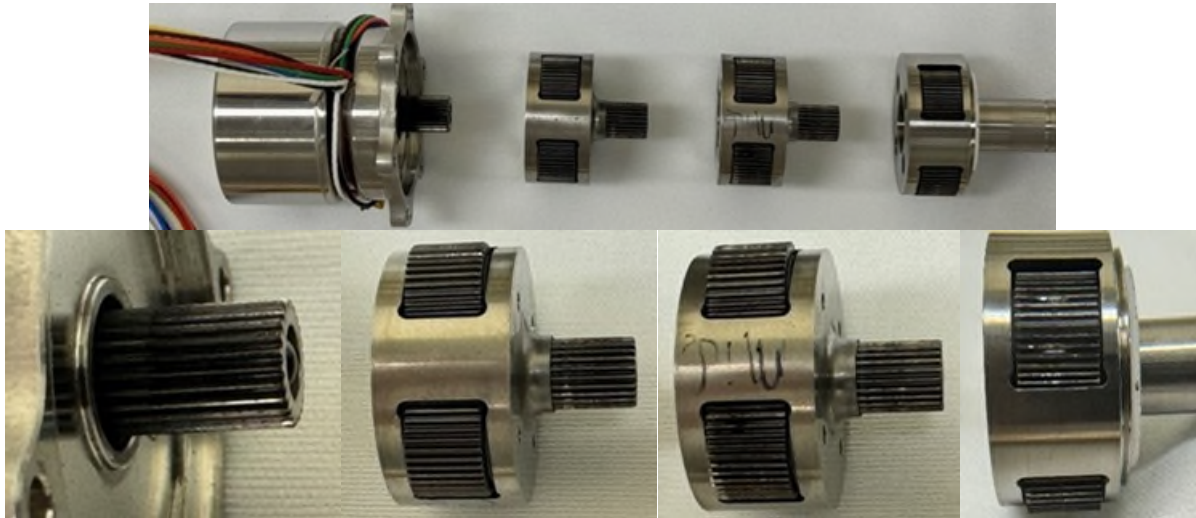


Figure 13. Post-test inspection images of COLDArm life test unit. 1st, 2nd, and 3rd stages are shown left to right. Gear tooth fracture is observable in the 2nd and 3rd stages.

An additional test was conducted on a second developmental/qualification unit, where the resistive torque was held at a semi-constant 1 N·m, while the direction of rotation was alternated, and temperature was cycled between room temperature and -180°C. Rather than following a “flight-like” profile, this constant torque test was seen as a better way to characterize the design capability of the system. This test achieved 9M motor revs before performance began to degrade and the test was ultimately stopped. This test data is shown in Figure 14. A second constant-torque test is planned at a higher level of torque to help inform the change in life as a function of load.

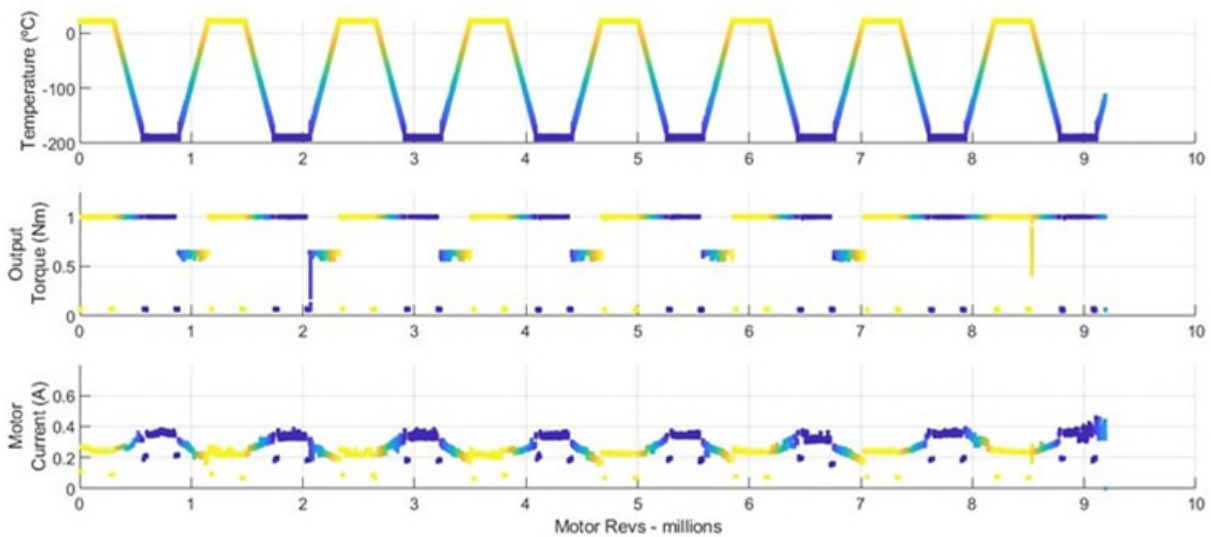


Figure 14. Life test results of the test planetary gearmotor at semi-continuous torque. Plot color scaled with gearbox temperature with yellow being warmer and dark blue being colder. Absolute values shown. Data hidden during velocity transitions.

Lesson Learned and Extensibility to Other Applications

For reliable, torque-dense, extreme cold environment actuators that do not require the use of heaters, BMG gears are not a panacea. They are a solution to one problem in a set of problems that make up the system design challenge. Motors, bearings, seals are just a few of “all the other things” that need to be considered. For the BMG planetary gearmotor presented here, a COTS motor only required limited modification (a bearing swap to a ceramic bearing) to function as required for the EDU. This and the Hall sensor knowledge helped Maxon make informed modifications to the heritage motors for the EM/FM configuration. An increase in motor current at cold was observed. The source of this change is still unclear but could be related to magnetic property change in the motor, over-preloaded bearings, or some other cause. 3Y-TZP ceramic bearings with PTFE cages for the input and output bearing were shown to be capable in shock and vibrate and function without apparent degradation at cryogenic temperature. Especially considering that any debris which is generated within the gearbox is not going to get “trapped” by lube, careful attention should be given to sealing the bearings and/or creating tortuous pathways to protect the bearings from this debris, potentially more so than typical for a wet lubricated system.

Precision component lead time can be substantial and BMG gear components were not immune. Acquisition of master alloy, tool design and fabrication, component fabrication, post processing by grinding or wire EDM, surface prep such as recast removal by microfinishing, and dry film lubricant application all contribute to lead time. Visual and dimensional inspection of components and non-destructive evaluation (NDE) by X-ray CT for internal defects such as voids are also contributors to lead time. Further, it is important that the inspections are performed prior to dry lubrication to most easily allow rework and limit handling of the dry lubricated parts.

Continued maturation of the manufacturing process by commercial suppliers should help improve the lead time and component quality. Similarly, capability to fabricate components larger than those in the BMG planetary gearmotor presented here is expected from the BMG component supplier base. While there is a theoretical limit to BMG component size resulting from the chemistry of the alloy, there is room in the available commercial processes for practical improvements that increase the component size and mass that can be manufactured. That stated, an alternative to an all-BMG gear component gearmotor is a hybrid configuration that utilizes a mix of BMG and steel gears. Such a hybrid configuration was mentioned in the

PoC gearbox development section and is an approach to overcome BMG gear component size manufacturing limitations, particularly when considering the ring gear. There is also some limited evidence that that this configuration of dis-similar materials at the gear interface may improve total life. This hybrid approach was taken by Motiv Space Systems in developing the DEEDS (Distributed Extreme Environments Drive System) actuator developed under the Small Business Innovation Research (SBIR) program [6].

Conclusions

A BMG-based, unheated planetary gearbox was conceived and successfully developed into an EM/FM gearmotor configuration with performance qualified for COLDArm's robotic arm actuators. BMG gear components are long lead items that may require additional processing such as gear grinding to achieve the high precision necessary. BMG gear component sizing, i.e., the largest component size that can be practically produced, is limited not only by the chemistry of the alloy but also by the capability of the manufacturer. Hybrid configurations with steel-BMG gear interfaces can overcome near term process limitations. BMG gear components are not necessarily the most challenging aspect of unheated planetary gearboxes. Motor and bearing selection and designing for debris management, i.e., keeping wear debris out of bearings, are very important. Component quality, including that of seemingly benign parts like shims, can have a profound negative impact on performance.

Acknowledgements

The COLDArm system is developed with industrial partner, Motiv Space Systems, Inc (Pasadena, CA). Research described in this publication was carried out at the Jet Propulsion Laboratory, California Institute of Technology, under a contract with the National Aeronautics and Space Administration (80NM0018D0004). U.S. Government sponsorship acknowledged.

References

1. "Origins, Worlds, and Life: A Decadal Strategy for Planetary Science and Astrobiology 2023-2032.," The National Academies Press, Washington, DC.
2. D. Hofmann e. al., "Optimizing Bulk Metallic Glasses for Robust Highly Wear-Resistant Gears," *Adv.Eng.Mater*, vol. 19, no. 1, p. 1600541, 2017.
3. D. Newill-Smith e. al., "Cold Operable Lunar Deployable Arm (COLDArm) System Development and Test," 2023 IEEE Aerospace Conference, Big Sky, MT, USA, 2023, pp. 1-19
4. C.J. Clark e. al., "Experimental Capabilities and Achievements of the Space Environment Dynamometer (SED)" 2023 IEEE Aerospace Conference, Big Sky, MT, USA, 2023, pp. 1-20
5. M. LoSchiavo e. al., "Mars 2020 maxon Commercial Motor Development from Commercial-Off-the-Shelf to Flight-Qualified Motors, Gearboxes, and Detent Brakes: Overcoming Issues and Lessons Learned," in *Proceedings of the 45th Aerospace Mechanisms Symposium*, 2020.
6. <https://motivss.com/motiv-space-systems-announces-nasa-contract-for-deeds/> (last accessed 3/16/24)

Extreme Benefits of Visual Inspection under Magnification of Mechanical Components

Duval A. Johnson*

Abstract

Microscope inspections are a very valuable tool for identifying features of a mechanism component that do not meet drawing specifications or have damage due to rough handling, high intensity ultrasonic cleaning and a host of other damaging actions. Many examples of the benefits of microscope inspections will be provided in this paper.

Introduction

The world would be a far better place if each mechanism component manufactured conformed to all drawing specifications. Common drawing notes such as “remove burrs and sharp edges” are frequently overlooked and can cause a host of issues in mechanism assembly, testing and operation. All too often mechanism components that have passed either a vendor or onsite machine shop Quality Assurance (QA) and a mechanical inspection dimensional characterization, are found to have burrs and other defects visible to the naked eye and clearly visible under magnification. JPL’s Laboratory for Applied Tribology (LAT) processes many mechanical components that are slated for wet and dry film lubricant application alike. Common process techniques include inspection under magnification, degaussing, cleaning, lubricant application, and a final inspection prior to releasing the component for use. Throughout the years, it has become clear that one of the most powerful tools at our disposal is the visual inspection under magnification. In this paper, common mechanism components will be viewed under magnification to highlight some of the most prevalent issues found. Each example will give an overview of the component and its function and stress the benefits of visual inspection under magnification.

Threads

Roughly 80% of the parts that come through the LAT have at least 1 burr on them. It became so prevalent that a deburring vendor was vetted and brought online to help with a series of mechanism components. Figure 1 shows the backside of a set of threads where it appears that the machinist tried to deburr the holes but managed to leave large hanging burrs anyway. Proper deburring was performed, and the part was released for use.

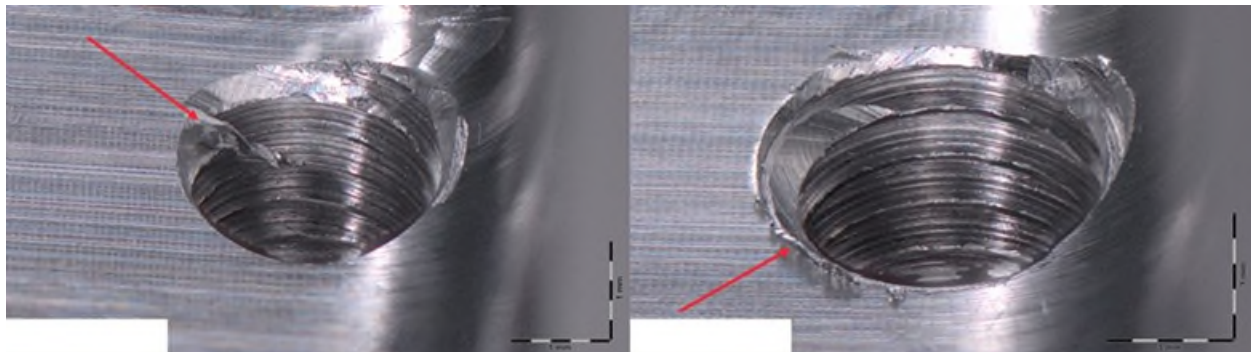


Figure 1 – Burrs on the backside of a threaded feature

* Jet Propulsion Laboratory, California Institute of Technology, Pasadena, CA

Threads come in all shapes and sizes but can have similar problems in their fabrication. Figure 2 highlights this by showing the first partial thread on an ACME lead screw. This thin, ribbon-like, partial thread has been damaged and needs to be removed and blended prior to assembly. If a technician tried to assemble the lead nut onto this lead screw without realizing that the resistance in the threading operation was due to a damaged thread the lead nut could have been damaged during assembly and tested in a damaged state.

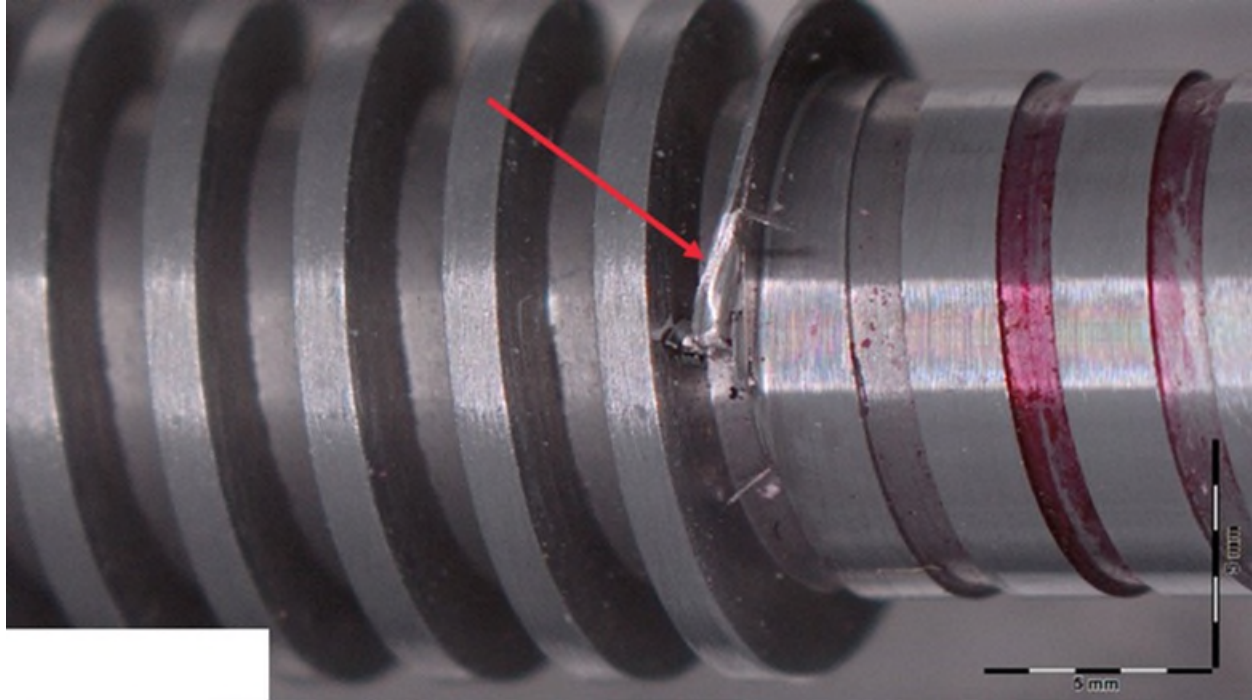


Figure 2 – Damaged thread on ACME lead screw.

Another ACME thread example is shown in Figure 3 where handling issues were observed on a significant number of threads on the major diameter of a lead screw. Constant volume deformation caused dents in the major diameter to become raised surfaces on the flanks of the threads. The raised surface areas increase stress of the contacting surfaces, increase the wear rate, and shed debris into the system starving the grease of its oil.

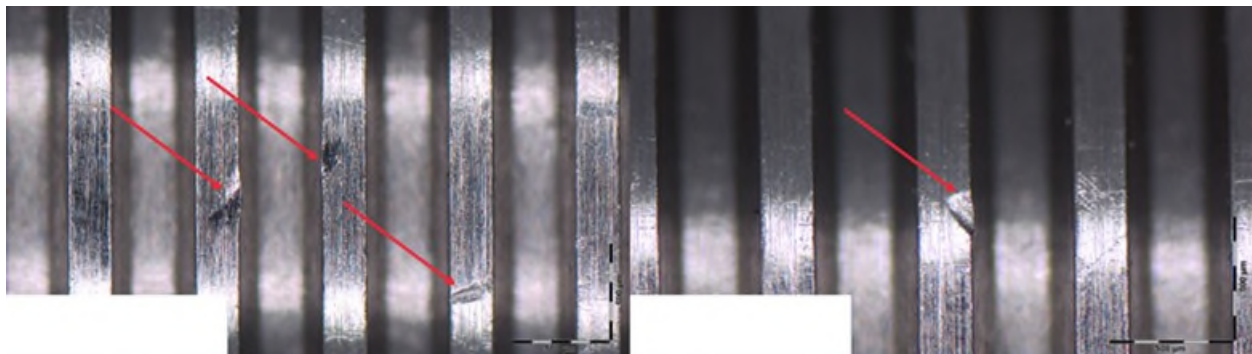


Figure 3 - Major diameter dents and dings

The raised surfaces were filed down with a combination of ruby rods, whet stones and fine sandpaper until the raised areas were not proud of the thread flank. A thorough microscope inspection allowed this issue to be found and handling constraints were introduced throughout the fabrication and shipping process to help alleviate this type of damage.

Internal threads are highly susceptible to fabrication issues and benefit greatly from visual inspection under magnification. Internal threads should be examined visually along with using standard thread gauges and/or other techniques to ensure a thread is formed that meets the referenced specification on the drawing. Figure 4 highlights an internal thread that has two sets of threads formed in a single hole. Using magnification, you can plainly see there is one set of threads on the left of the image and another on the right. This thread was hand-tapped and is most likely the result of shifting the axis of the tap slightly from entry to egress causing the two-thread pattern.

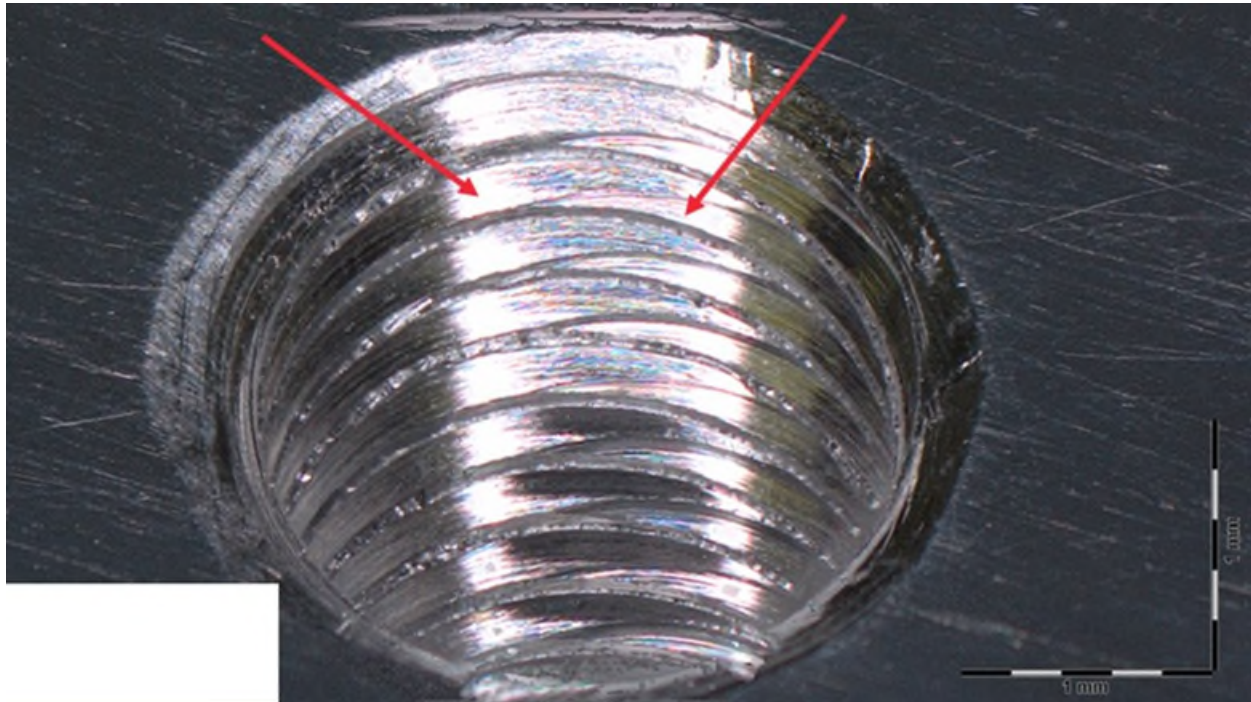


Figure 4 – Dual thread pattern observed under magnification.

This hole passed a QA inspection using standard methods and was only caught as the component progressed through the LAT, for wet lubricant application, using standard microscope inspection procedures. This component was repaired using Heli-Coils and slated for limited-use. Internal thread issues became so common at JPL that a training course was implemented to help Mechanical Inspection personnel perform a visual inspection of threaded holes under magnification prior to characterizing the thread itself using go/no-go gages.

Thread inspections can extend to the tap or tool that will form them as well. In the case of an ACME internal thread a tap was purchased to generate the threads in an aluminum bronze nut. The tap was delivered to the machinist who eventually tapped the threads into the nut. When the nut was assembled onto the lead screw and tested, the wear rate was found to be significantly higher than expected and the system did not reach its life expectancy. The lead nut and screw were brought to the LAT where a visual microscope inspection was performed along with dimensional characterizations. During the inspection, lab personnel asked to see the tap that cut the threads into the nut. Figure 5 left shows the tap as someone might look at it with the naked eye while Figure 5 right is a magnified view of the trailing edges of the tap. It becomes clear that burrs were formed on the trailing edges of the tap and never removed by the manufacturer. One of these burrs came loose while tapping the nut and embedded itself into one of the thread flanks of the lead nut.

When assembled onto the screw and tested, the embedded tap material scratched the lead screw over the axial motion of the system as observed in Figure 6 left. The result was a specific wear rate in the abrasive

regime, which significantly shortened life, caused adhesion of the nut material onto the screw, and generated significant wear debris which starved the lubricant of oil as shown in Figure 6 right.

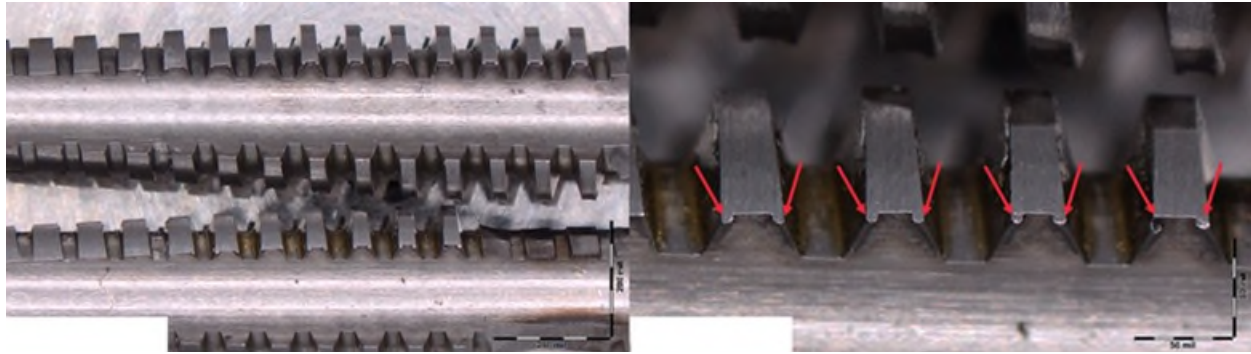


Figure 5 Left – ACME thread tap. Right – Red arrows pointing to burrs on trailing side of tap teeth.

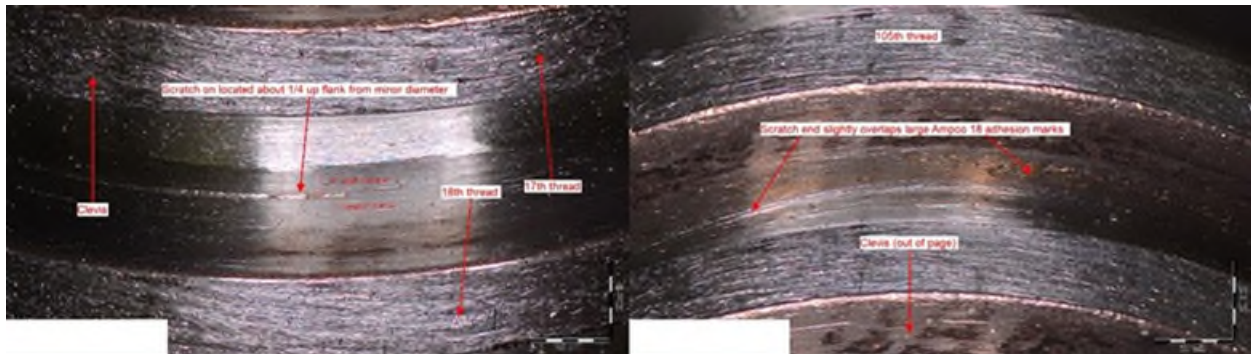


Figure 6 Left – scratch in lead screw. Right – transferred nut material.

Gears

Another class of components that benefit greatly from visual inspection are gears. Even though gears are supposed to pass vendor visual inspections and a check against a master gear it should never be taken for granted that a good gear has arrived at your facility. Figure 7 shows one tooth of a planetary gear that arrived at the LAT for wet lubricant application. Following standard LAT procedures, every gear in the gearbox underwent a visual microscope inspection prior to degaussing, cleaning, and lubrication. It was apparent that all the gears in the assembly exhibited radial lines on the tooth faces and striations across the tooth face as observed in Figure 7. Potential causes include hob radial and axial feed rates along with issues like index, rake, flute lead, surface finish and edge preparation (a class AA finisher can end up a class D rougher by utilizing poor sharpening practices).

When the face of the gear was characterized using the LAT's Mitutoyo AVANT Formtracer it was found that the maximum heights of the radial peaks were greater than $2.5 \mu\text{m}$ as shown in Figure 8. The gears were

in a very low life mechanism and were accepted “as is” but in a longer-life mechanism the gears could have been life limiting.

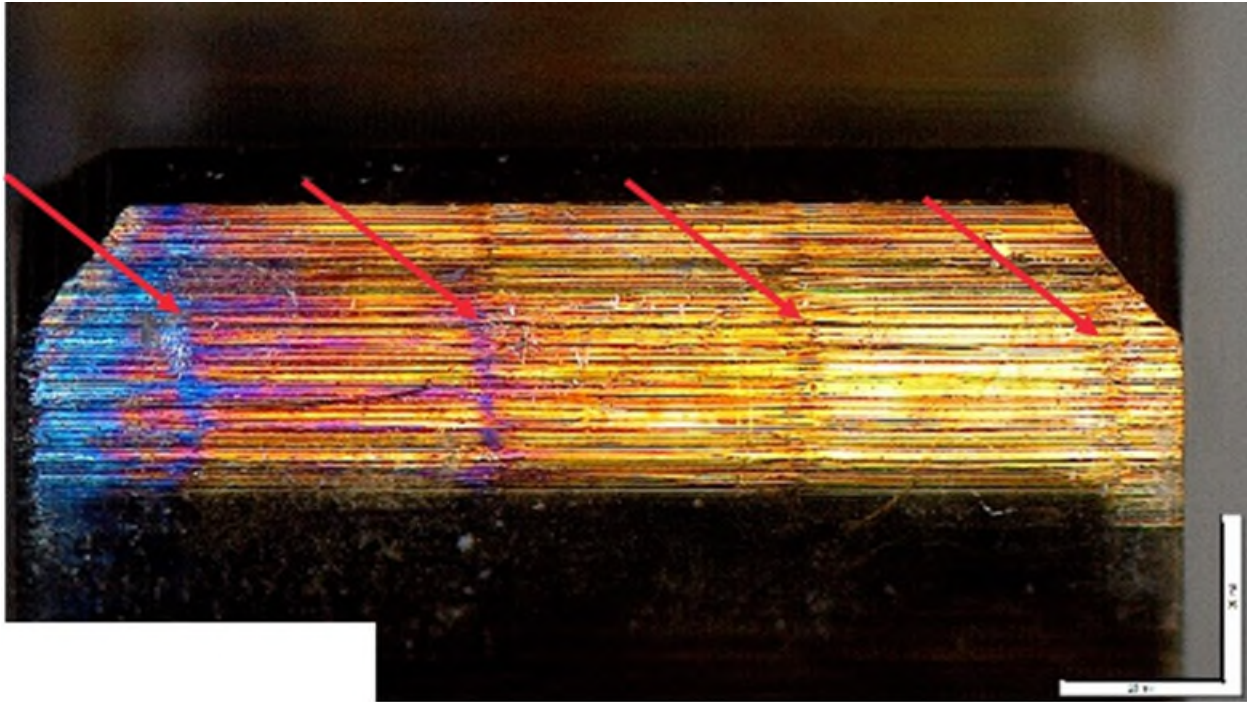


Figure 7 – Radial lines observed on tooth face

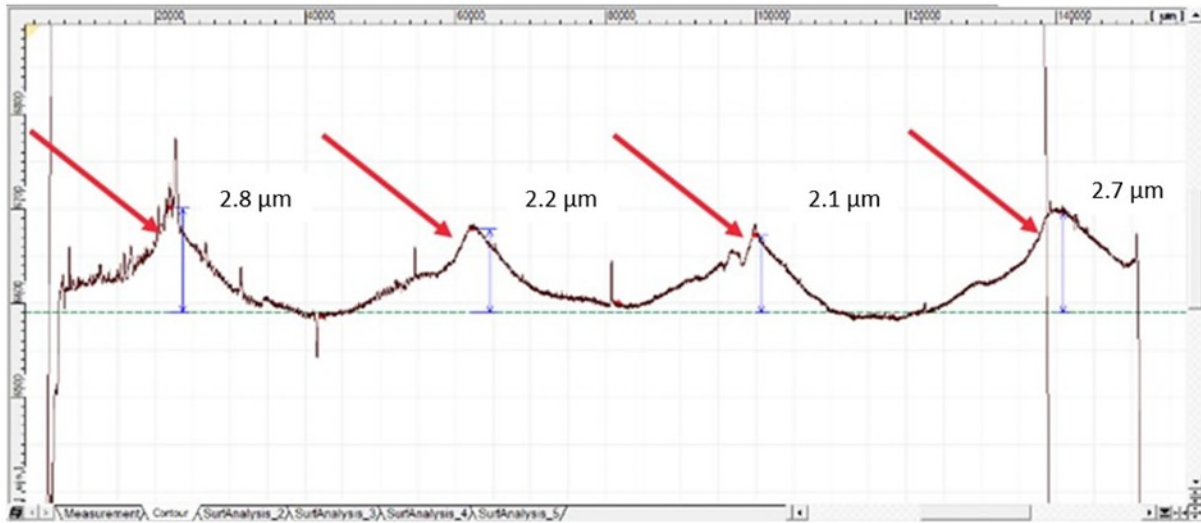


Figure 8 – Dimensional characterization of radial lines observed on tooth face.

Planetary roller screws (PRS) have gears and threads and so fall into both thread and gear classes but are highlighted here because the threads were formed very well while the gears were not. Figure 9 left shows one roller from a planetary roller screw assembly where you can plainly see the large axial burrs running

the length of the geared section of the shaft and ending with large burrs on the ends of the rollers as observed in Figure 9 right.

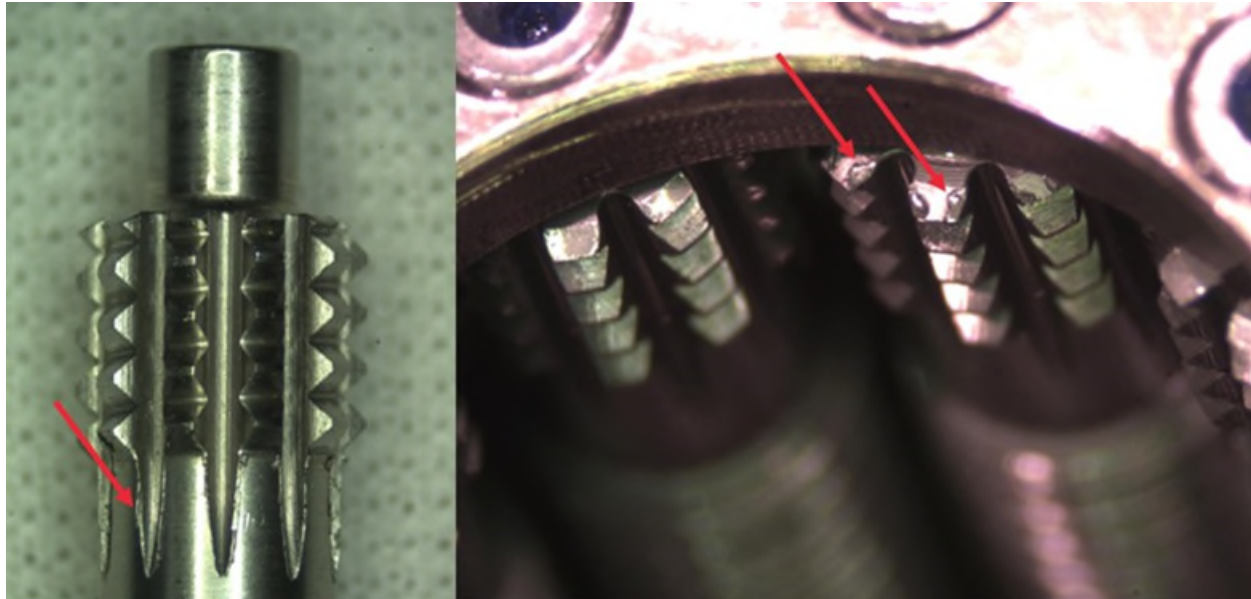


Figure 9: Left – planetary roller screw roller with burrs. Right – assembled PRS showing burrs on roller ends.

The PRS had burrs on the ring gears and every roller along with other issues not shown here. The problems with the PRS were only caught because they were brought to the LAT for wet lubricant application and could have been quite problematic if not caught by visual microscope inspection. This PRS passed the vendor QA and would have been used “as-is” if a microscope inspection was not performed and the issues not caught.

One last gear example is shown in Figure 10. Harmonic drive flex splines, manufactured from a bulk metallic glass (BMG) and intended to be used in very cold temperatures, were brought to the LAT for inspection and Dry Film Lube (DFL) application. Under magnification, it was immediately apparent that the BMG flex spline tooth profiles were not manufactured with tooth profiles that represented the commercial-off-the-shelf (COTS) flex spline. These simple magnified images were enough to show that the tooth profiles were not a close match to the COTS tooth profile. Using the LAT’s Mitutoyo AVANT Formtracer, the COTS tooth profile was characterized, and the data was used to correct errors in the drawing of the BMG flex spline.

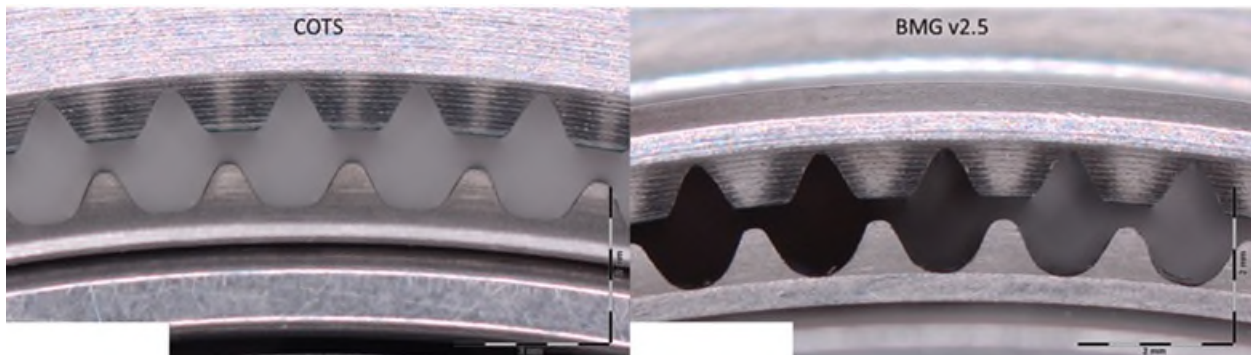


Figure 10 - Comparison between a COTS flex spline and a BMG v2.5 flex spline.

Bushings (Plain Bearings)

Plain bearings come in many flavors ranging from metal-polymer, bi-metallic composite, bronze wrapped, self-lubricating, injection molded, hydrodynamic and babbitted, spherical, and more. Figure 11 is an image of a bronze-backed bushing that has a bonded porous sintered bronze interlayer impregnated with Polytetrafluoroethylene (PTFE) containing a mixture of inorganic fillers and polymer fibers.

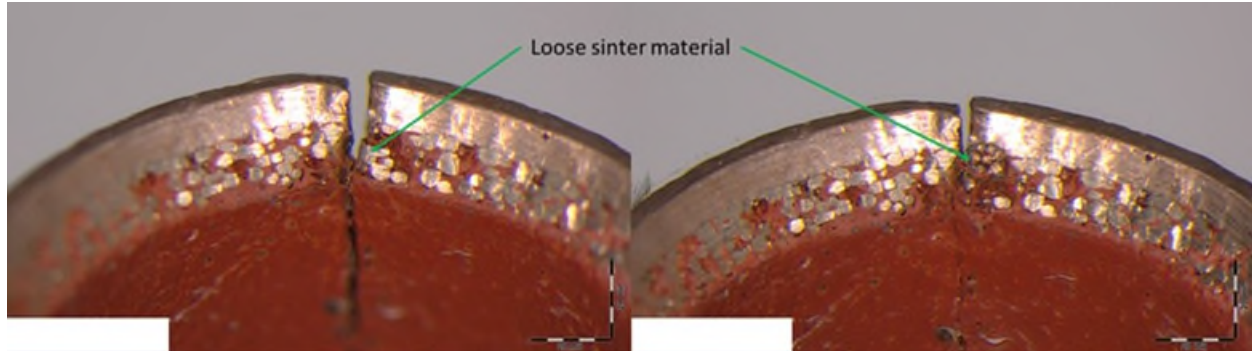


Figure 11: Left – bushing image prior to loose sinter removal. Right - loose sinter moved upwards with pick.

During a microscope inspection, loose sintered material was observed along the split of the bushing with a concentration of loose sintered material on the chamfers on either side of the bushing. This material was easily liberated and has the potential to dislodge during assembly, testing or launch and end up causing problems for the local operation of the shaft/bushing assembly or fall into other sensitive areas of the mechanism. Microscope inspection, once again, caught problems with a component prior to assembly.

Spherical plain bearings (SPB) also benefit from a microscope inspection. Figure 12 shows a spherical plain bearing that had a DFL outer ring and ball. During microscope inspection large metal burrs were observed near the swage that retains the ball. The burrs had been coated with DFL suggesting that the issue was not caught by the manufacturer prior to DFL application. This also suggests that the DFL vendor did not inspect the SPBs prior to DFL application. The burrs were easily liberated using only a stainless-steel pick with minimal force.

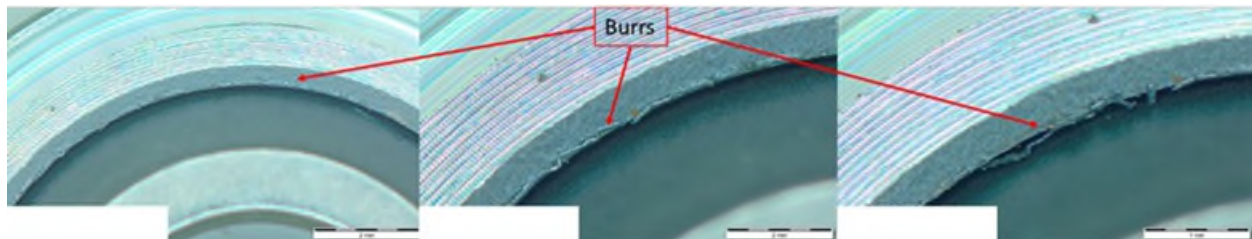


Figure 12: left – SPB as received. Center – magnified image of left. Right – burr easily liberated with pick.

During the inspection of this lot of SPBs it was also found that several balls did not have the required DFL applied. This could pose risk to mechanism function if not found during microscope inspection and removed from use.

Rolling Element Bearings

Bearings come in all shapes and sizes but nonetheless need a microscope inspection to ensure they're ready for mechanism integration. Figure 13 contains images of a harmonic drive (HD) wave generator bearing. When looked at using the naked eye (top left and top center) the bearings look very good and no one would question using one in their mechanism. When viewed under magnification (top right, and bottom left and center), brinelling and corrosion (bottom right) of the balls and raceway grooves was observed.

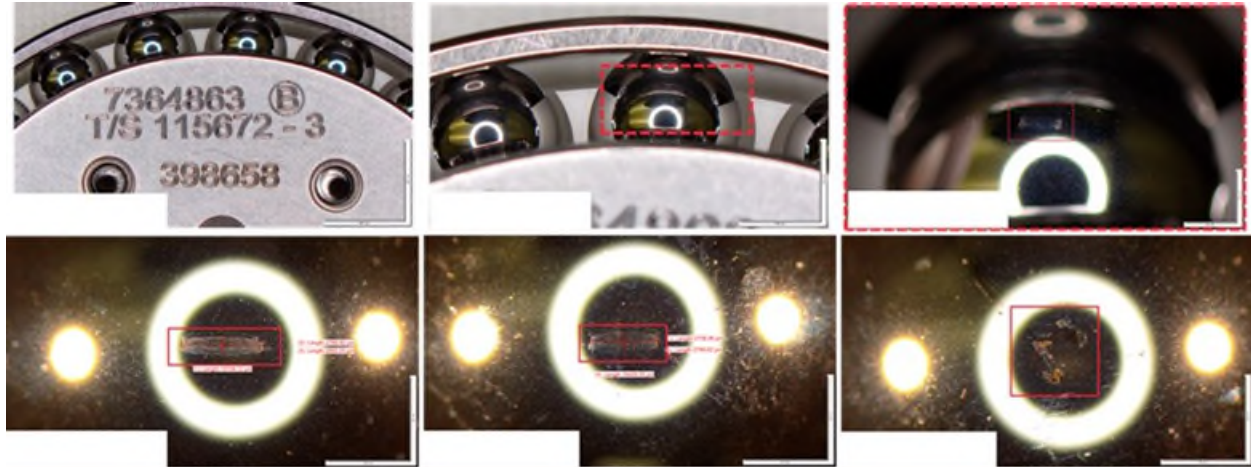


Figure 13: From top row from left to right – various stages of magnification. Bottom row from left to right – different balls under various stages of magnification showing brinelling and corrosion.

Upon further investigation it was found that 60% of the balls had varying degrees of brinelling and corrosion as shown in the bottom images of Figure 13. The balls had brinelling at 180-deg spacing while the race way grooves exhibited brinelling on the order of ball spacing (every 15.7 deg) suggesting that the brinelling occurred in one event, possibly during cleaning or handling of the bearing.

Figure 14 highlights a common issue found in an Oldham connector groove of a wave generator plug that is easily observable under magnification.

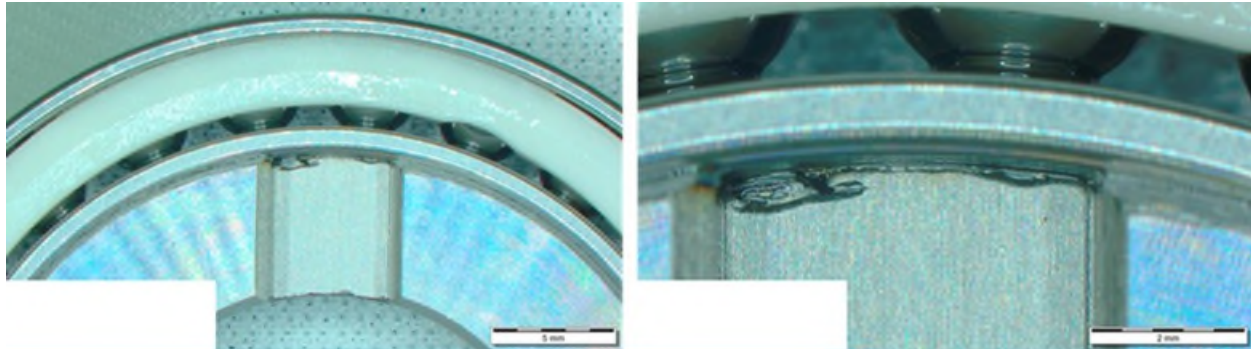


Figure 14 – Burrs on the intersection of wave generator plug and inner ring of bearing.

The wave generator plug seems to have had a burr left on it prior to pressing the plug into the wave generator bearing. When the plug was pressed into the bearing, this burr rolled over the edge of the plug and remained in the Oldham connection groove. This was easily removed, and processing of the harmonic drive assembly continued.

Figure 15 shows PTFE ball spacers that were damaged by the manufacturer during installation. Roughly 30% of the ball spacers were damaged during assembly and needed replacement. There were ball spacers that would fall from their position in the bearing when the axis of the bearing was vertical and even slight hand vibrations were induced. These defects were not visible to the naked eye and were only caught during microscope inspection of the bearings. Ground support equipment was fabricated to facilitate installation of

new spacers and the damaged spacers were replaced allowing the bearings to be used in a Flight application.

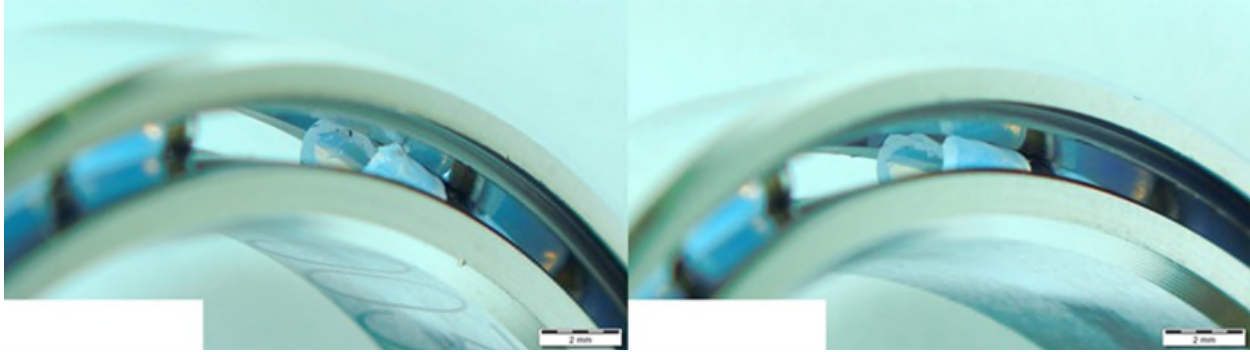


Figure 15 – Damaged PTFE ball spacers in a rolling element bearing.

Ball Lock Mechanism

Ball lock mechanisms are quite common for quick disconnect couplers and a host of other uses. Figure 16 highlights two ball lock cavities that have burrs on the retaining end of the pocket. The ball locks have very tight tolerances and burrs of this size can inhibit function. The surface the burr was generated from, and the burr itself, were both nitrided in the state they're currently in. This suggests that several inspections were performed that missed the burrs entirely including the manufacturer and the mechanical inspection department of the receiving institution. This once again highlights the advantages of diligent microscope inspections.

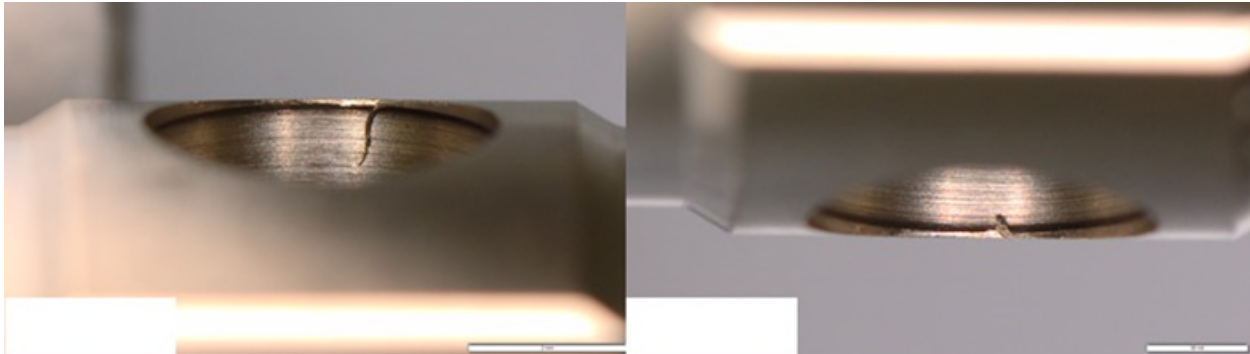


Figure 16 – Ball lock pockets plagued by burrs.

Springs

Figure 17 has 4 images of a wave spring. Wave springs typically have sheared ends and have been formed by imparting the wave profile to the spring material and forcing the material into the required diameter. The sheared ends and the length of one side of the spring are known to shed burrs and should always be checked under magnification prior to use. The LAT specifically degausses ferromagnetic materials prior to

cleaning to ensure metallic particles are removed. Wave springs typically undergo a deburring step using deburring tools, Scotch-Brite, and fine sandpaper to ensure the spring won't shed burrs into the mechanism.

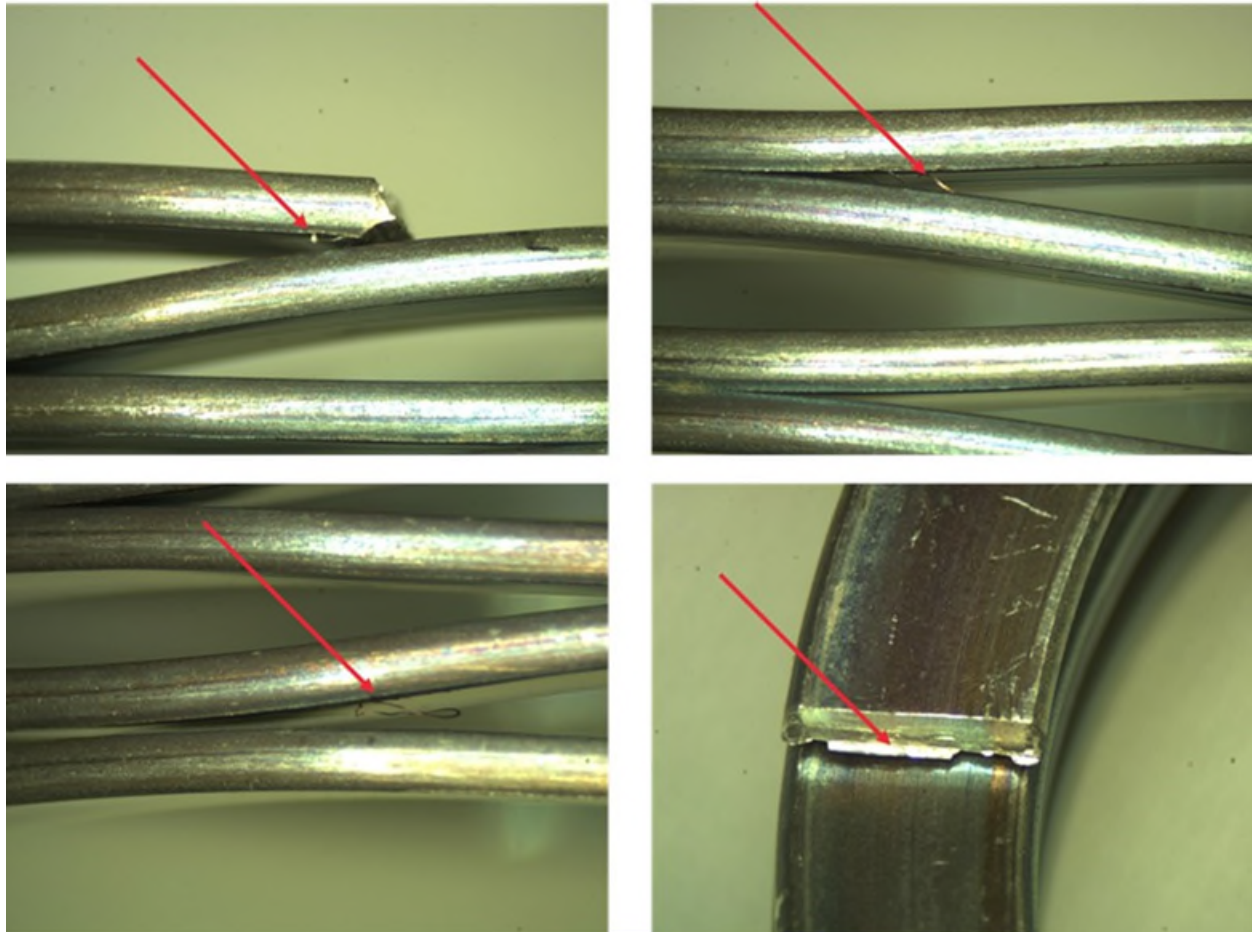


Figure 17 – Wave spring with burrs on the sheared end and along the length of the spring.

Conclusions

Hopefully the advantages of microscope inspections are evident from the examples in this paper but there are a few points that should be mentioned. Generally, a magnification level of 10x to 20x is sufficient to bring to light potential issues a part might have. Magnification levels greater than this tend to highlight more detail than necessary on any given component. The object of the microscope inspection is not to capture every minute detail that might be wrong with a component. Instead, one would like to capture relevant information that would affect mechanism functionality and correct it prior to integration.

The next caveat is that the person using the microscope needs to have enough experience to understand what a part should look like and differentiate between what is acceptable and what isn't. This means the user should understand what the mechanism is tasked with as well as what other mechanisms are nearby. The microscope should have a good camera system coupled with it to allow the user to image potential issues for documentation and presentation to affected parties. It is important to have a trinocular microscope that allows for both binocular viewing and monocular imaging which is very useful. The microscope should allow for a wide range of parts to be held under the objective. This has limited the LAT to using only light microscopes mounted on an adjustable boom that can swing off the table for viewing a wide range of sizes.

There should be a computer and monitor near the microscope to quickly record images and share them in real time with anyone interested in the part.

The system should have multiple light sources such as LED and incandescent. The LED light source should have the ability to turn off sections of the light ring to minimize reflections when needed. A light box is particularly useful to eliminate shadows during viewing and imaging (note the sealed border cleanroom white wipers that are being used for this in Figure 18). An accessible PanaVise and V-blocks will facilitate holding components for imaging. A Z-stacking feature embedded in the software allows for capturing features at different heights in the same image while in focus. These are just some of the considerations when purchasing a microscope for inspection purposes. Figure 18 shows one of the microscopes used in the LAT for part inspections.



Figure 18 – One of the microscopes used in the LAT for component inspections.

This microscope assembly has served the LAT well for over 5 years and has reduced the risk of mechanism anomalous performance and failures by identifying and correcting component issues before integration. Take the time to set one up in your lab and then find someone who knows what to look for. The savings in time and money from forming Tiger Teams alone will be worth it.

Acknowledgements

The research was carried out at the Jet Propulsion Laboratory, California Institute of Technology, under a contract with the National Aeronautics and Space Administration (80NM0018D0004)

© 2024. California Institute of Technology. Government sponsorship acknowledged.

Motor Stator (Fluidize) Insulation Material Options and Testing Summary

Jonathan P Wood *, Emmett Donnelley-Power *, Jessica Hamm ** and Recarda Schmitz †

Abstract

3M 5555 Fluidize powder-coating was a popular choice for motor stator secondary insulation in many space applications. Unfortunately, in 2021, 3M announced they planned to retire the 5XXX product line.

As a result of this announcement, a multi-company task force was assembled, consisting of Lockheed Martin, The Aerospace Corporation, Windings Inc, Sierra Space, and Moog. The task force worked through 2022 to identify candidates to replace the 3M 5555 product, determine a test plan for material screening, and down-select final candidates for an accelerated thermal-cycle life test. In 2023 the final tests were completed, and the resulting data is presented herein.

Introduction

Wire-wound motors rely on an extremely thin “varnish” applied to the stator magnet wire to provide insulation between adjacent turns within the motor windings, between adjacent coils that make physical contact, and in the cases where an electrically conductive stator core material is used, between the windings and the stator core. A typical stator core is made from laminated “electrical iron” or a wire-cut billet of electrical iron. Regardless of whether a solid wire-cut core or a laminated core is used, the stator core has sharp corners that would quickly cut through the thin varnish insulation during the inserting process (or if not during inserting, during operation due to temperature swings).



Figure 1: Typical motor stator with 3M 5555 Fluidize Coating

* Lockheed Martin Space, Sunnyvale, CA; jonathan.p.wood@lmco.com;
emmett.donnelley-power@lmco.com

** Sierra Space, Durham, NC; jessica.hamm@sierraspace.com

† Windings Inc, New Ulm, MN; recarda.schmitz@gmail.com

© 2024 Lockheed Martin Corporation. All Rights Reserved

Proceedings of the 47th Aerospace Mechanisms Symposium, NASA Langley Research Center, May 15-17, 2024

Due to this reality, a “secondary insulation” material is used to provide a radius at the corners that contact the magnet wires and additional insulation strength wherever the magnet wires contact the stator core. In other words, the secondary insulation protects the magnet wire from damage, via the radius it creates, and protects the motor from a phase-to-chassis short via the high insulation resistance and robust thickness of the secondary insulation.

In the world of non-ironless, wire-wound motors, the two most common methods used to provide secondary insulation are: Applying an insulating powder-coating to the stator core prior to insertion, and the combination of non-conductive (plastic) end-laminations with slot-liners. Generally speaking, slot-liners can be more labor-intensive to install but are less process-dependent. Slot-liners usually result in lower thermal conductivity between the motor winding coils and the stator core, which can preclude their use in high current-density applications. However, slot-liners are generally less sensitive to extreme cold temperatures, and therefore more common in cryogenic applications. On the other hand, the powder-coating method is less labor-intensive, but is more process dependent. Due to its superior thermal conductivity, this insulation method is more common in motors that have a high current density.

Within the US space motor industry, 3M 5555 was the most commonly used material for secondary insulation on motor applications with powder-coated stator cores. This was due to its very good insulation properties, mechanical robustness, and good bond strength to commonly used stator core materials. When the impending discontinuation of this product was announced, a multi-company task-force was assembled to work toward a solution that would provide equivalent or better performance.

Material Selection

The initial task of the task force was to identify and understand the technical properties of the 3M Scotchcast 5XXX products currently used by the industry to determine which products were impacted by 3M’s discontinuation. This exploration quickly determined that the primary impact to the space industry from the impending discontinuation was the Scotchcast 5555 family of electrical insulation.

Understanding the industry’s impacted products allowed a search into equivalent products to commence. This search involved known electrical insulation powder manufacturers as well as similar industries to epoxy resins such as adhesives and paints which may have electrical products in their portfolios but may not have marketed them into the Aerospace and Defense industry.

The result of this search produced six potential suppliers in the market (3M, PTI, Glyptal, SolEpoxy, AkzoNobel, and Sumitomo Bakelite). Upon further review of 3M’s published technical data sheets for Scotchcast 5555 against the corresponding physical performance characteristics of the potential supplier products, four possible products (Glyptal 1201, PTI 5133, SolEpoxy DK7-20H, and SolEpoxy DK7-0953) were selected to proceed forward with a Phase 1 initial screening.

Physical and performance properties considered during this paper technical data review included published information regarding: specific gravity, dielectric strength, cut through resistance, impact resistance, edge coverage, gel time, thermal shock, powder shelf life and UL approvals (important for some terrestrial applications). The reason for the selection of the initial candidates (which was based on published values from the datasheets) was as follows:

- PTI 5133: Good flexibility/impact resistance, some members of task force already familiar with this product, electro-static powder coating friendly
- SolEpoxy DK7-20H: Similar thickness and UL rating to 3M 5555. Good cut-through resistance (high temperature capability) and edge coverage.
- Glyptal: Potential simple application process, potentially could be applied with different thicknesses (since it is a liquid material unlike other candidates), good insulation resistance, good toughness and abrasion resistance

- SolEpoxy DK7-0953M: Good edge coverage, thinner coating (offers higher slot-fill potential), high cut-through resistance (high temperature capability), high impact resistance
- PTI 6500: New product from PTI, not much data yet, but advertising NASA outgassing compliance and higher temperature capability than PTI 5133. Added at last minute as replacement for PTI 5133 when it did not perform well in initial testing

Initial Screening Test Plan

Each candidate went through a test program consisting of an initial screening phase and a qualification phase, except for the PTI 6500 which was introduced for the final screening phase only. The tests performed in the initial screening phase were chosen due to both the importance of the tests for material qualification and because these tests could be performed more quickly and with less resources than the final screening tests. The initial screening phase was used to down-select to a reduced number of candidates which would then proceed into the final screening phase. Figure 2 shows the test flow, including specific tests per test phase.

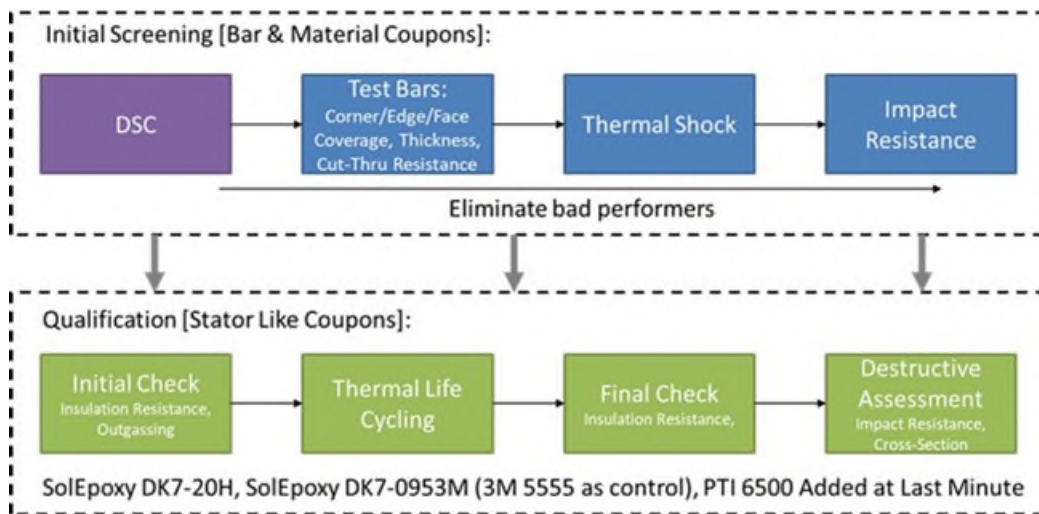


Figure 2: Initial Screening and Final Screening Test Plan Flow Chart

Raw Material Test Coupons

Raw material test coupons were thin sheets of the candidate materials both cured and uncured. Raw material coupons were used for Differential Scanning Calorimetry (DSC) analysis and Thermogravimetric analysis (TGA). See Table 1 for application and curing requirements used for each material tested.

Table 1: Candidate Materials Pre-Heat and Cure Requirements

Candidate Material	Form	Pre-Heat (°C)	Pre-Heat Time (min)	Dry Time (hr)	Cure Temp. (°C)	Cure Time (min)
3M Scotchcast 5555	Powder	188 (370 °F)	12	N/A	232 (450 °F)	20
SolEpoxy DK7 093M	Powder	177 (350 °F)	12	N/A	232 (450 °F)	20
SolEpoxy DK7 20H	Powder	182 (360 °F)	12	N/A	232 (450 °F)	20
PTI 5133	Powder	188 (370 °F)	12	N/A	232 (450 °F)	20
PTI 6500**	Powder	N/A	N/A	N/A	204 (400 °F)	10
Glyptal 1201	Liquid	N/A	N/A	≥72	177* (350 °F)	120*

*Temperature was profiled; 1 hour @ 65°C (150°F), 1 hour @ 121°C (250°F), 2 hours at 177°C (350°F)

**Not included in the initial screening tests as it was introduced after initial screening

Steel Test Bars

For the remainder of the initial screening phase, tests used A36 steel test bars coated with the candidate materials. Mild steel was chosen as the substrate for these tests because the material is a standard material for cut-through resistance testing, is easy to acquire quickly and has a relatively low cost. These factors allowed rapid testing of many different candidate materials for initial screening.

Surface preparation of the test bars was set to simulate typical surface finishes seen on motor stator laminations. Each bar contained two sets of faces, one set was grit-blasted to 1.5-2 μm (60-80 μin) rA (similar to abraded or oxidized laminations) and one set was ground to 0.4 μm (16 μin) rA (similar to as-received laminations)

All powder candidates were applied to the coupons via fluidized bed hot dip process. Glyptal 1201 was applied via thinned liquid dip process. Material was cured per the manufacturer's instructions, including any "ambient dry time" specified prior to the elevated temperature cure. See Table 1 for application and curing requirements for each material tested.

DSC and TGA Testing

Differential Scanning Calorimetry (DSC) analysis generates curves of heat flow through a sample versus time and temperature. These curves provide insight to changes in glass-transition temperature and thermal breakdown over a wide range of temperature. Thermogravimetric analysis (TGA) was used to determine mass loss and decomposition of the candidate materials. DSC and TGA analysis were used to assess the likelihood of candidate materials meeting the 200°C insulation rating.

DSC testing was performed on both powder and cured samples of each candidate material per ASTM E2041-13 using the Borchardt and Daniels (B&D) kinetics approach. All samples were run at 5°C per minute ramp rate from 20°C to 1000°C with a dry nitrogen purge for DSC and TGA testing.

Corner/Edge/Face Coverage, Thickness

The thickness on the faces and edges/corners was measured to a resolution of at least 2.5 μm (0.0001 in). The minimum and maximum thickness was recorded for each face 25 mm (1 in) from each end of the bar on all four sides using a Fischer FMP40 posi-tector. The minimum thickness in the "radial" direction radiating out from the corner was measured for each edge using a micrometer.

Dielectric Strength

Six test coupons of each coating material were evaluated for dielectric strength using a Vitrek V70 hipot tester. All 4 edges of each bar were tested on the middle 50-mm (2-in) section of the coated bars up to the maximum voltage of 11,000 V.

Cut-Thru Resistance

One test coupon of each coating material was tested for cut-thru resistance. Testing was done at two locations on each bar.

For the cut-thru resistance test, an un-insulated 18 AWG wire was wrapped around each bar with a 2.2-kg (1-lbf) weight hanging on the end of each wire. Testing started at 150°C (300°F) with 1 hour dwells. Chamber temperature was increased by 28°C (50°F) until all coupons failed or the maximum oven temperature was reached, 321°C (610°F).

Thermal Shock

Three test coupons of each coating material were tested for thermal shock. Samples underwent 10 thermal cycles from -80°C to +125°C, with a temperature tolerance of $\pm 5^\circ\text{C}$ and minimum dwell time of 2 hours. After cycling, samples were visually inspected for evidence of cracks, flakes and crazing at 10X magnification.

Impact Resistance

Impact resistance testing was performed using a Gardner IM-172 9.5-mm (3/8-in) impact tester with a 4.4-kg (2-lbf) weight. All three bars were tested: one bar post thermal shock testing, one bar post cut-thru resistance testing and one new cured bar. Seven heights were tested with a starting drop height at approximately 86 mm (3.4 in.) up to 206 mm (8.1 in) with 2 drops at each height. The drop set was performed on both the grit-blasted face and surface ground face of the coupons. Based on the performance, each impact zone was given a rating based on the criteria in Table 2.

Table 2: Impact Zone Evaluation Criteria

Rating	0	1	2	3
Description	Failure, delamination, chips removed from surface	Failure, delamination, all material intact	Partial failure, cracking, no delamination	Passing, indentation present but no cracking or delamination

Initial Screening Test Results

Based on the initial screening test results, the PTI 5133 and Glyptal 1201 coatings were eliminated from the test program. The PTI 5133 became very soft at a low temperature, failing the cut-through resistance below the desired 200°C insulation rating. It also performed very poorly in the impact resistance test after undergoing thermal shock. Per the DSC test results, the Glyptal 1201 was not fully cured after completing the manufacturer's recommended cure cycle. Therefore, a post-cure was developed (based on the DSC results) to ensure it would become fully cured. Unfortunately, after the post-cure was performed, the material failed almost every initial screening test, including dielectric strength. Although it probably would have performed better without the post-cure, it clearly would not have met the desired 200°C insulation rating since the post-cure was done at 176°C and ruined the mechanical properties of the material. Among the materials that continued forward to the final screening tests, the SolEpoxy DK7-0953M showed very promising results, significantly outperforming all of the other materials in the impact resistance test.

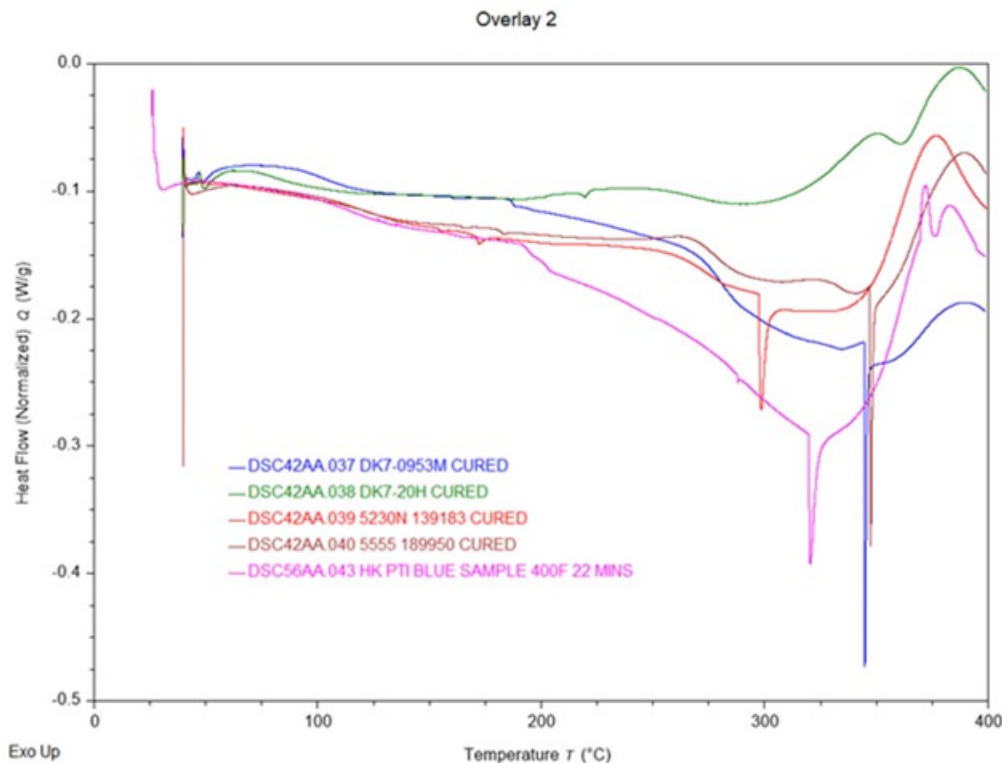


Figure 3: DSC Test Results for Cured Candidate Materials (Except Glyptal and PTI 5133)

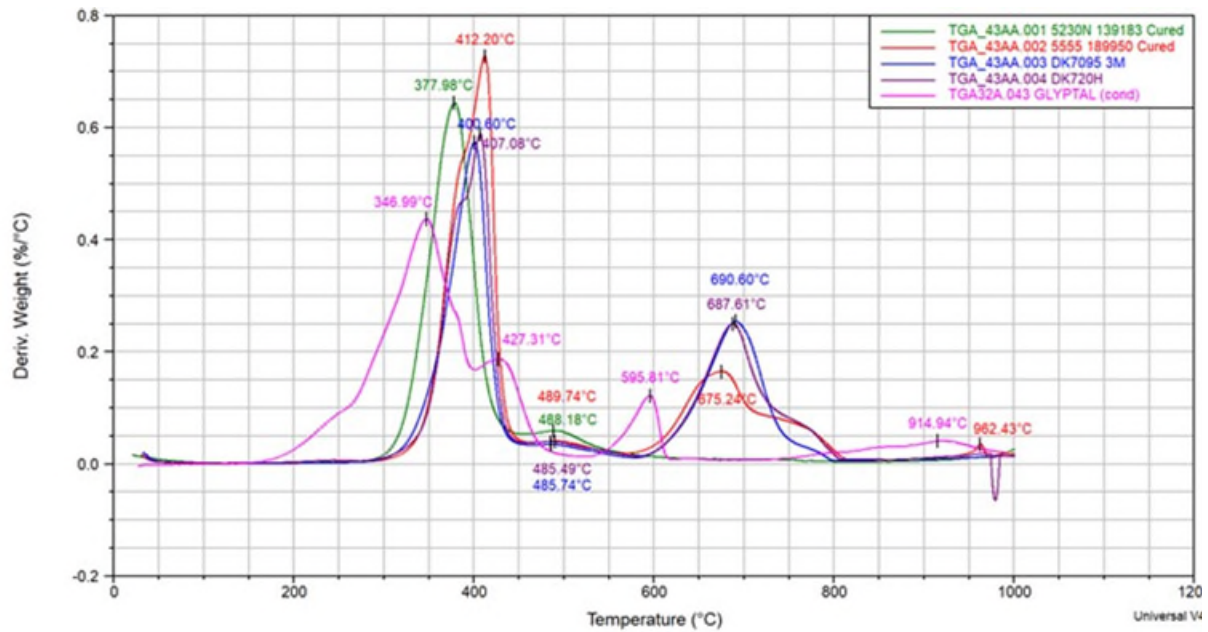


Figure 5: Differential TGA Results for Materials Tested Except PTI 6500

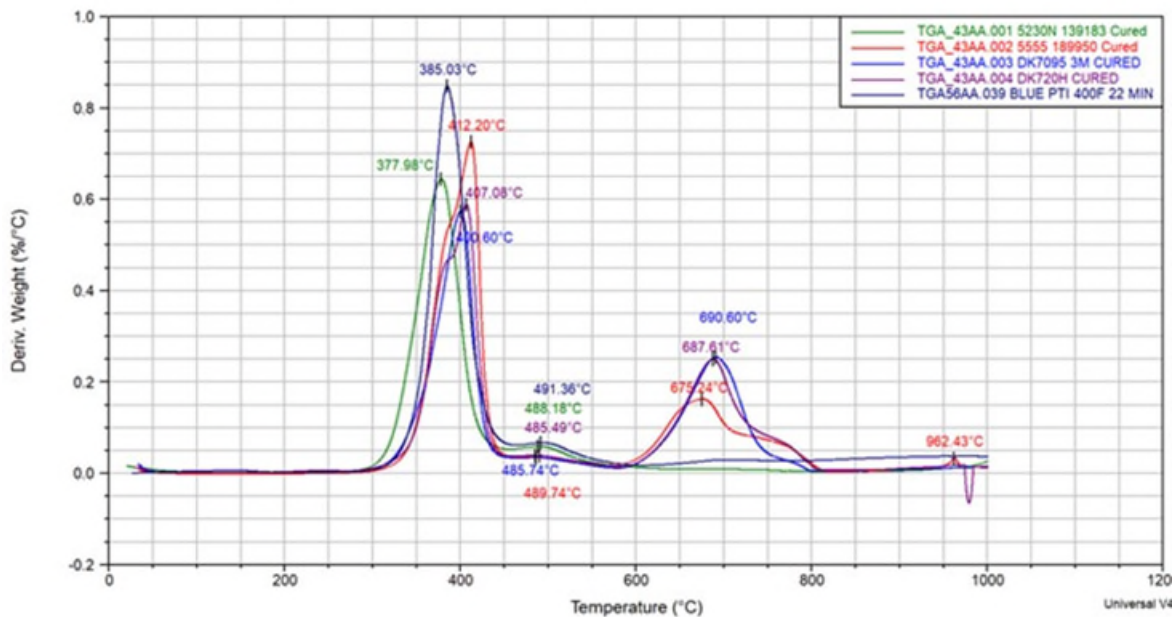


Figure 6: Differential TGA Analysis for Materials Tested (Except Glyptal)

Corner/Face/Edge Coverage

For initial screening, face thickness was measured for all initial samples: 3M 5555, SolEpoxy DK7-20H, SolEpoxy DK7-0953M, PTI 5133, and Glyptal 1201. Face thickness for the PTI 6500 was only measured on the final test bars, see the Final Screening Test Results section, Table 7 for these results. For the initial screening face thickness results, see Table 3. In terms of face thickness, the SolEpoxy DK7-20H and PTI 5133 showed the closest thickness to the 3M 5555. The SolEpoxy DK7-0953M and Glyptal 1201 were thinner than the 3M 5555, but it was decided that this would not be grounds to eliminate these materials outright, as a thinner coating that performs acceptably in the cut-through and insulation resistance tests is actually desirable, allowing for a higher possible slot-fill in a motor application.

Table 3: Initial Face Thickness Measurements

Candidate Material	Form	Face Thickness (um)
3M Scotchcast 5555	Powder	345 (.0136 in)
SolEpoxy DK7-0953M	Powder	193 (.0076 in)
SolEpoxy DK7-20H	Powder	269 (.0106 in)
PTI 5133	Powder	320 (.0126 in)
Glyptal 1201	Liquid	226 (.0089 in)

For initial screening, edge coverage was not measured for all samples. The intent was to assess edge coverage via the cut-through resistance test. Some edge-coverage data had been previously taken by one of the members of the working-group so this data was shared with the team and is included in Figure 7.

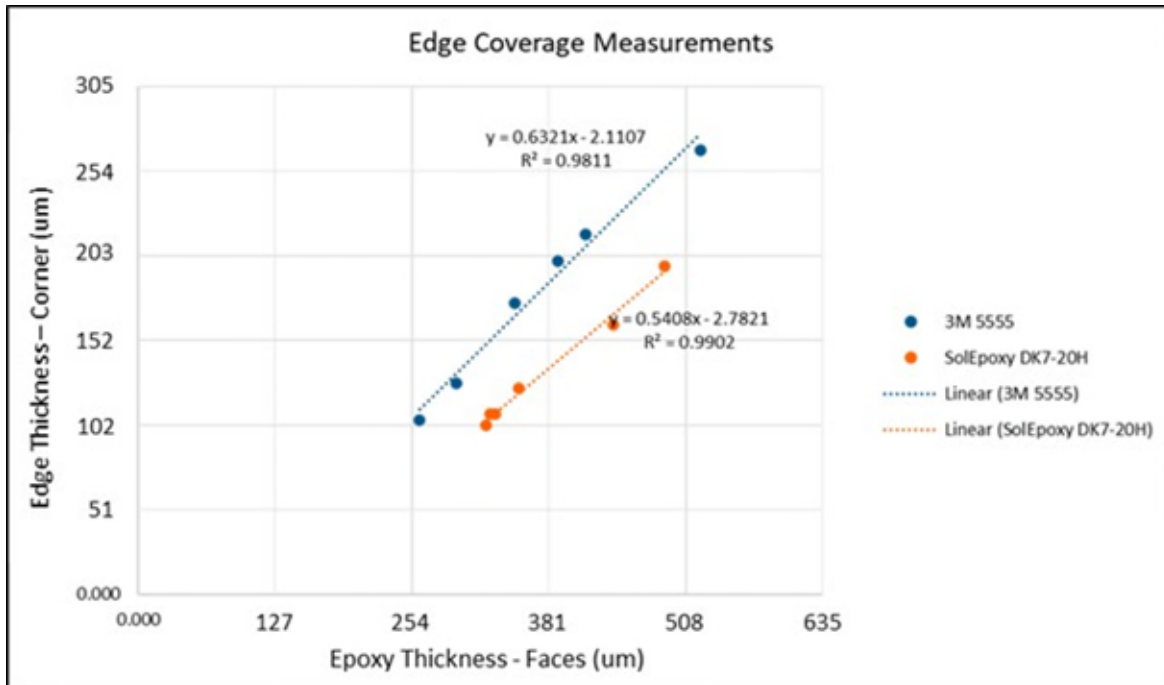


Figure 7: Edge Thickness vs Face Thickness for 3M 5555 and SolEpoxy DK7-20H

Dielectric Strength

The dielectric strength test results are shown in Table 4. In terms of kV.mm, the SolEpoxy 0953M performed the best, and in terms of overall breakdown voltage, the 3M 5555 performed the best. This test was the first indication that the Glyptal 1201 performance was adversely affected by the post-cure, as it did not show any dielectric strength in this test. Note that "Passing" in Table 4 means the measured breakdown voltage was greater than 11,000 volts. Tests were marked as "Failed" if the breakdown voltage was less than or equal to 11,000 volts. See Table 6 in the "Final Screening Test Results" section for the PTI 6500.

Table 4: Dielectric Strength Test Results

Candidate Material	Face Thickness	# Passing Samples	# Failing Samples	Lowest Failure	Dielectric Strength*
3M Scotchcast 5555	345 μm (.0136 in)	22	2	11,000V	63.7 kV/mm (1618 V/mil)
SolEpoxy DK7-0953M	193 μm (.0076 in)	4	20	8649V	89.6 kV/mm (2276 V/mil)
SolEpoxy DK7-20H	269 μm (.0106 in)	11	13	10,398V	77.2 kV/mm (1962 V/mil)
PTI 5133	320 μm (.0126 in)	21	3	10,830V	67.7 kV/mm (1719 V/mil)
Glyptal 1201	226 μm (.0089 in)	0	24	0.3V	N/A

Cut-Through Resistance

As shown in Table 5, All of the candidate materials except the Glyptal 1201 and PTI 5133 passed the cut-through resistance test. No further investigation was performed for the Glyptal 1201 since it also failed dielectric strength, most likely due to the post-cure. The failure of the PTI 5133 was unexpected so a follow-up test was performed. In the follow-up test, the cut-through test was performed at lower temperatures to see where the failure would occur. During this investigation it was found that the PTI 5133 material (cured) became soft at only 120°C (250°F). This was the primary reason for eliminating this material from the list of materials to undergo final screening. Figure 8 shows a photo of a passing cut-through coupon next to a failing coupon. For the PTI 6500, there was indication that the edges were thin and brittle at 343°C (650 °F). If the wire was not placed onto the edge with the utmost care, the edge would chip and the test would fail. After this occurred twice, extreme care was used in placing the wire and multiple passing results were achieved. When it was attempted to force a chip it took very little persuasion when done at 343°C (650 °F).

Following the Cut-through test, toughness of the coatings was manually checked at 200 C with a pick. This assessment was highly subjective, of course, but the results are included as they provided some insight. Glyptal was not tested. When ranked 1-5: PTI 6500 (1st), DK7-0953M (2nd), DK7-20H (3rd), 3M 5555 (4th), PTI 5133 (far behind 5th).

Table 5: Initial Cut-Through Resistance Test Results

Candidate Material	Face Thickness (samples)	Cut-through pass/fail
3M Scotchcast 5555	13.6	PASS
SolEpoxy DK7-0953M	7.6	PASS
SolEpoxy DK7-20H	10.6	PASS
PTI 5133	12.6	FAIL
Glyptal 1201	8.9	FAIL
PTI 6500*	12	PASS**

*Note: PTI 6500 coupons were tested after the final-screening phase

** Due to extremely thin edge coverage, slight differences in handling method when hanging the weight could cause the samples to pass or fail

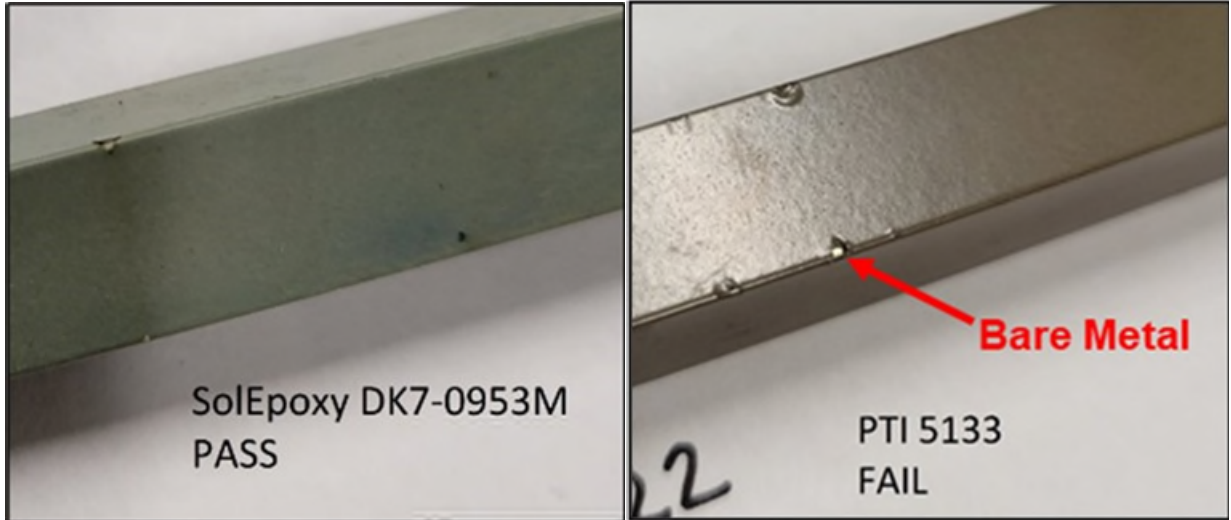


Figure 8: Passing Sample (SolEpoxy DK7-0953M) Next to a Failing Sample (PTI 5133)

Thermal Shock

All of the candidate materials performed well in the thermal shock test except the Glyptal 1201, which was the only material to develop cracks during the thermal cycling. Photos of all of the test coupons after thermal cycling are shown in Figure 9. PTI 6500 was subjected to the thermal endurance test but was not included in the thermal shock test.

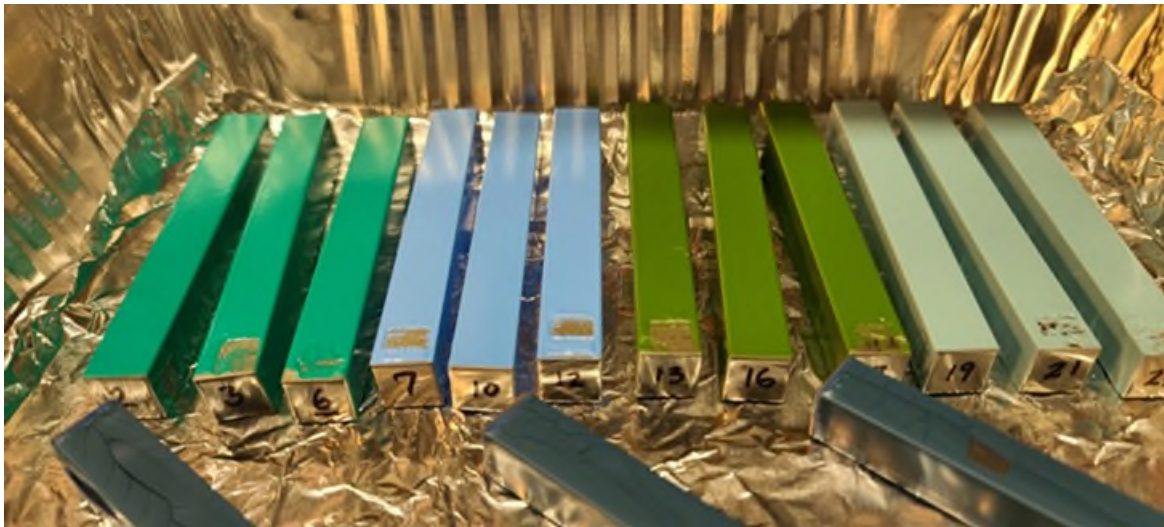


Figure 9: Test Coupons after Completing Thermal-Shock Testing. Left to Right: 3M 5555, SolEpoxy DK7-0953M, SolEpoxy DK7-20H, PTI 5133. Glyptal 1201 Coupons are in foreground.

Impact Resistance

Since the impact resistance tests were performed after the thermal-shock test, the test results include the effects of some thermal aging. One coupon for each material candidate was withheld from thermal-shock testing, so the results with and without thermal aging can be easily compared. The results of the impact resistance tests are shown in Table 5 and Figure 10. For impact resistance, the SolEpoxy DK7-0953M performed better than all of the other candidate materials by far. None of the materials showed any degradation in performance due to the thermal shock test except for the PTI 5133. The Glyptal performed very poorly, again most likely due to the post-cure. The cut-through resistance samples were also subjected to the impact resistance test. Interestingly, the high-temperature exposure of the cut-through test (324°C)

had no noticeable effect on the 3M 5555 and SolEpoxy DK7-0953M impact test results and improved the impact strength of the SolEpoxy DK7-20H. The impact strength of the PTI 5133 was degraded significantly by the high-temperature exposure during the cut-through resistance test. PTI 6500 was only subjected to impact resistance testing during the final screening tests. See Table 8 for the PTI 6500 impact test results.

Table 5: Impact Resistance Test Results (See Table 2 for Scoring Criteria)

Candidate Material	Face Thickness	ALL Results	Roughened Surface	Cure Only	Cut Through	Thermal Shock
3M Scotchcast 5555	13.6	17.3	21.3	16.5	24.0	15.7
SolEpoxy DK7-0953M	7.6	40.8	42.0	41.0	42.0	40.3
SolEpoxy DK7-20H	10.6	14.8	17.0	12.5	32.0	10.7
PTI 5133	12.6	23.0	29.0	29.0	0.0	26.7
Glyptal 1201	8.9	0.7	0.7	1.0	2.0	0.0



Figure 10: Impact Resistance Test Results, Ground Faces of Coupons.

Final Screening Test Plan

Following the downselect from the initial screening, flight-like coupons were fabricated using the coating materials SolEpoxy DK7-0953M, SolEpoxy DK7-20H, PTI 6500, and 3M 5555 as control. PTI 6500 was added at this point despite not being part of initial screening, as it was a new product from PTI and the team was interested in seeing how it would perform. Each coating material was applied to 12 mm x 12 mm x 100 mm (½ in x ½ in x 4 in) laminated test bars made from Hiperco-50 with Scotchcast 265 and M-19 silicon steel with Magna-Tack (material preparation given below). The test bars were then coated using a fluidized bed hot dip process followed by a cure cycle, with the exception of the PTI 6500, which was electrostatically applied by PTI. Three samples of each coating/substrate combination were prepared, for a total of 24 samples.

Test Coupons

Material processing requirements:

1. Hiperco-50 ASTM A801 Type 1 (0.36-mm [.014-in] thick laminates)
 - a. Annealed using vendor process compliant with ASTM A801.
 - b. After annealing, oxide coating applied by heating in air.
2. M19 Silicon Steel ASTM A677 Type 36F155 (0.36-mm [.01- in] thick laminates)
 - a. Annealed
 - b. ASTM A976 C5 core plate, AISI-C-5 core plate coating: Abraded for surface prep
3. Bond lamination stacks. Hiperco-50 stacks bonded with Scotch Cast 265 and. M19 stacks were bonded with Magna-Tack
4. Break edges to 0.13 to 0.25 mm (.005 to .010 in).
5. Solvent clean Hiperco-50 and Silicon Steel test bars and verify cleanliness. Repeat cleaning step if cleanliness is not sufficient.
6. Apply candidate material using fluidize bed hot dip with or without pre-heat of the substrate as required per the manufacturer instructions.
7. Cure material per manufacturer's instructions, including any "ambient dry time" specified prior to the elevated-temperature cure

Thermal Endurance Test

Thermal cycle testing was performed starting with 2 cycles to the survival temperatures followed by 20 cycles each to increasingly extreme temperatures or until failure (defined as any cracking). This proceeded per the following protocol:

- Perform 2 cycles to the survival temps of -80°C to +115°C. Open thermal chamber and inspect
- Bin 1: Perform 20 cycles from -44°C to +105°C. Open thermal chamber and inspect
- Bin 2: Perform 20 cycles from -54°C to +115°C. Open thermal chamber and inspect
- Bin 3: Perform 20 cycles from -64°C to +125°C. Open thermal chamber and inspect
- Bin 4: Perform 20 cycles from -74°C to +135°C. Open thermal chamber and inspect
- Bin 5: Perform 20 cycles from -84°C to +145°C. Open thermal chamber and inspect

At each inspection, all samples of a substrate/coating combination were removed if one sample of that combination had any cracks in it. Additionally, all samples of a given substrate were removed if any 3M 5555 sample of that substrate had any cracks. Inspection was done visually under a minimum of 5X magnification under a bright light source.

Insulation Resistance

Insulation resistance was measured per ASTM D149 using a Vitrek V70 hipot tester with a maximum voltage of 11,000 V after thermal cycling.

Impact Test

Impact testing was then performed on the samples after thermal cycling using the same procedure and equipment as in the initial screening tests.

Outgassing Measurement

Outgassing was measured via ASTM E595. The E595 test method determines the following properties:

- Total mass loss (TML): Total mass of material outgassed from a specimen that is maintained at a specified constant temperature and operating pressure for a specified time
- Collected volatile condensable materials (CVCM): The quantity of outgassed matter from a test specimen that condenses on a collector maintained at a specific constant temperature for a specified time
- Water vapor regain (WVR): The mass of the water vapor regained by the specimen after the optional reconditioning step

The outgassing test was performed for 24 hours at 125°C with a collector temperature of 25°C. Chamber pressure was maintained at or below 5×10^{-5} Torr. Three samples of each material were tested and empty sample “boats” were used as control coupons.

Final Screening Test Results

Thermal Endurance Test

On the Hiperco-50 substrate, the 3M 5555 coating performed the worst, developing severe cracks on one coupon after only being exposed to the survival cycles. Since the 3M 5555 coupons failed so early, it was decided to continue with the other Hiperco-50 test coupons. The remainder of the Hiperco-50 coupons were removed after bin two, when one each of the SolEpoxy coupons developed a very small crack on a corner. Note that the post-thermal impact resistance was of more interest than the development of small cracks, the small cracks were just used as an indicator that the coupons were starting to degrade. The PTI 6500 coupons did not develop any cracks

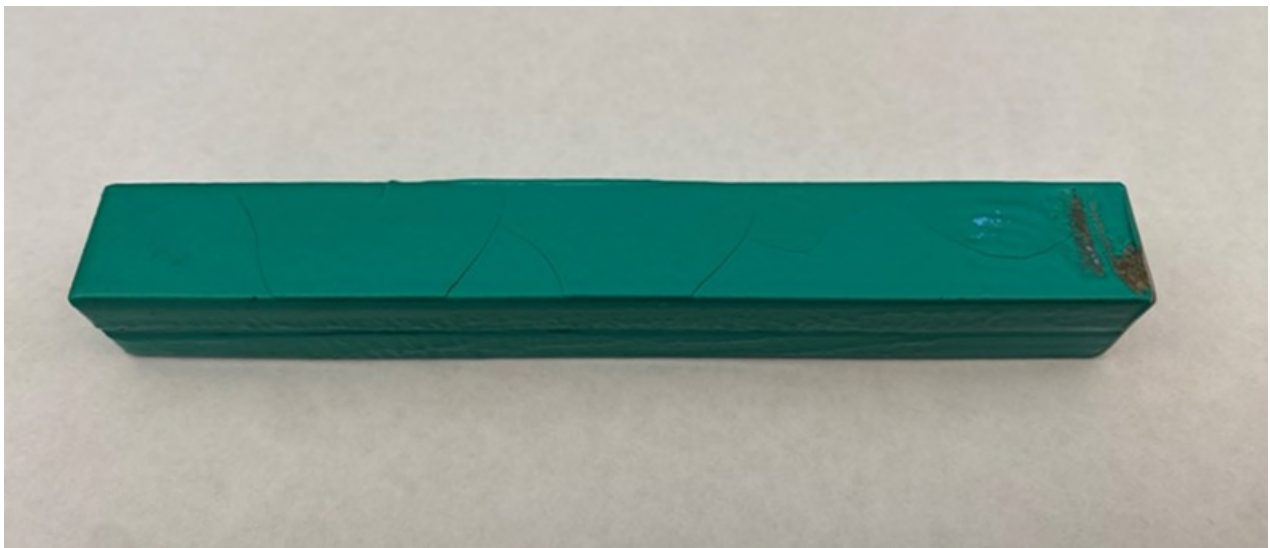


Figure 11: 3M 5555 on Hiperco-50 After Two Survival Cycles

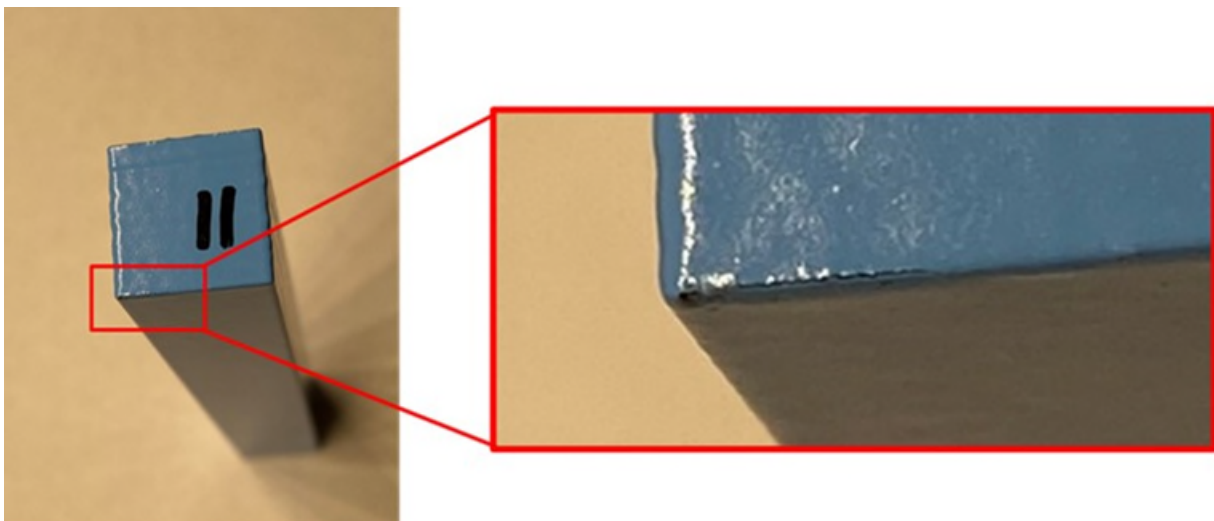


Figure 12: SolEpoxy DK7-0953M on Hiperco-50 After Thermal Cycling Bin 2

On the M19 substrate, neither the 3M 5555 nor the PTI 6500 developed any cracks, even after thermal cycle bin 5. One SolEpoxy DK7-20H coupon developed one small corner crack after thermal cycling bin 3, so the SolEpoxy DK7-20H coupons were removed from the chamber at this point. One SolEpoxy DK7-0953M coupon developed a small edge crack after thermal cycling bin 4, so the SolEpoxy DK7-0953M coupons were removed from the chamber at this time.

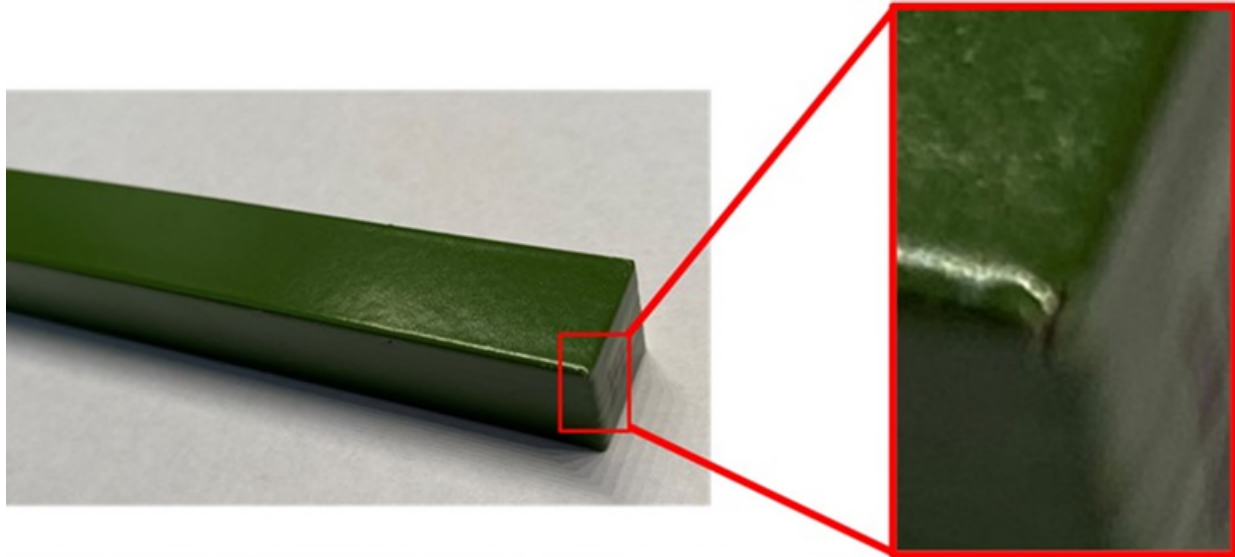


Figure 13: SolEpoxy DK7-20H on M19 After Thermal Cycling Bin 3

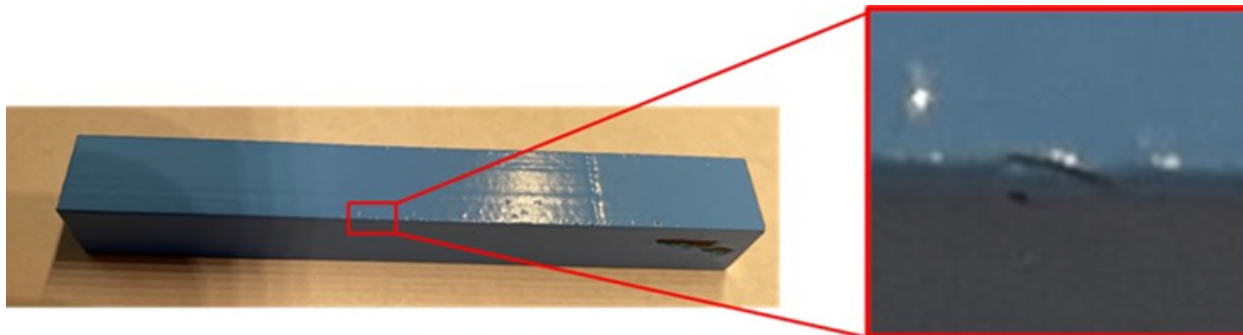


Figure 14: SolEpoxy DK7-0953M on M19 After Thermal Cycling Bin 4

Post-Thermal Insulation Resistance Test

The post-thermal face thickness and insulation resistance test results are shown in Table 6. It is interesting to note that the dielectric strength decreased and the difference between the highest and lowest values decreased. In this test, the SolEpoxy products performed the best, with the 3M 5555 and PTI 6500 showing similar test results.

Table 6: Post-Thermal Dielectric Test Results

Candidate Material	Face Thickness	Dielectric Strength
3M Scotchcast 5555	.381 ± .051 mm (.015 ± .002 in)	21.5 kV/mm (547 V/mil)
SolEpoxy DK7-0953M	.178 ± .025 mm (.007 ± .001 in)	28.9 kV/mm (734 V/mil)
SolEpoxy DK7-20H	.279 ± .025 mm (.011 ± .001 in)	29.4 kV/mm (748 V/mil)
PTI 6500	.305 ± .025 mm (.012 ± .001 in)	21.8 kV/mm (554 V/mil)

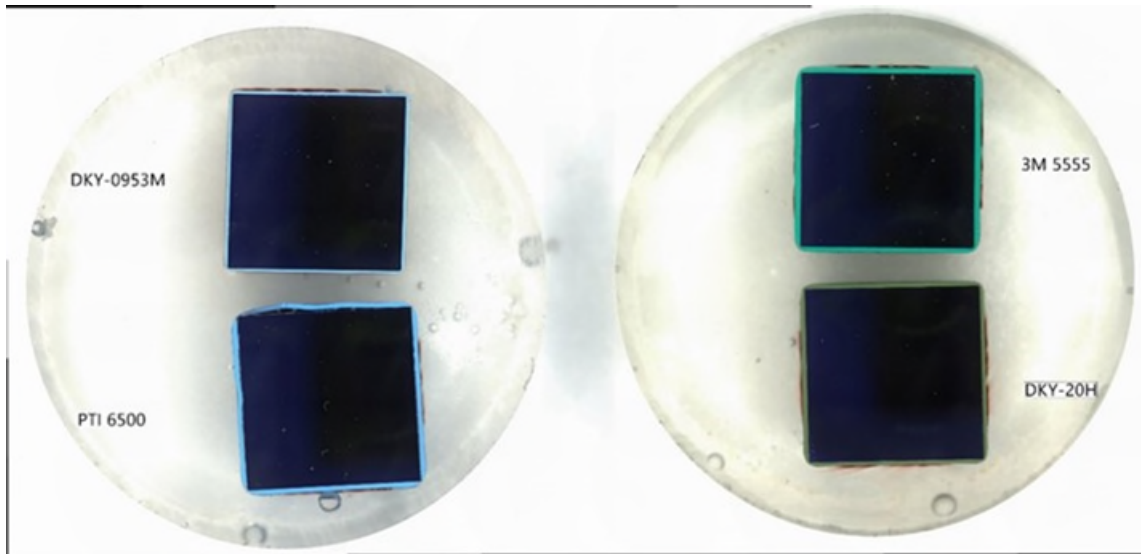


Figure 15: Face and Edge Thickness Cross-Sectioned Coupons

Edge Thickness – Cross-Sections

The edge-thickness results generally matched the expected values based on the initial screening data, except for the PTI-6500 coupons. As can be seen in Figures 15 and 16, the edge thickness for the PTI 6500 coupon was not very good, with a minimum of 0.025 mm (.001 in). It should be noted that the PTI coupons were coated using an electrostatic process, and the edge thickness both in the raw value and percentage of the face-thickness is out of family compared to the other materials. Additional PTI 6500 coupons were subsequently fabricated using a fluidize-bed dip process, with similar results. Based on the very thin edge coverage, PTI 6500 cannot be recommended at this time, despite its exceptional performance in other tests. See Table 7 for a summary of the edge thickness results.

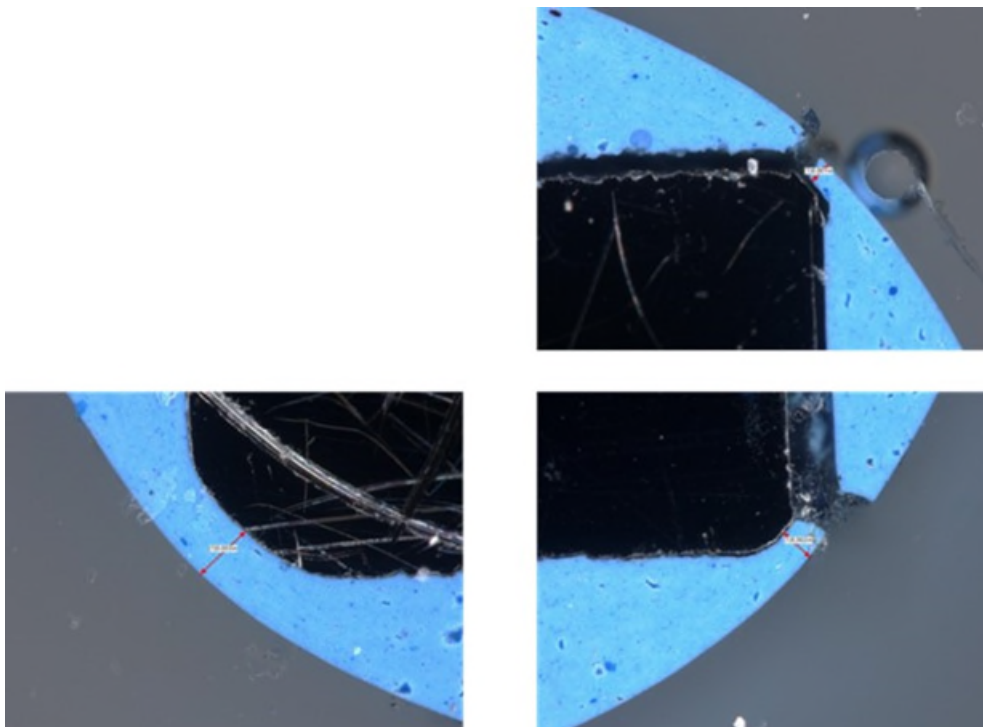


Figure 16: PTI 6500 Edge Thickness Measurement

Table 7: Edge Thickness Measurement Results

Candidate Material	Face Thickness	Edge Thickness
3M Scotchcast 5555	.381 ± .051 mm (.015 ± .002 in)	.178 - .228 mm (.007 - .009 in) 41 - 69%
SolEpoxy DK7-0953M	.178 ± .025 mm (.007 ± .001 in)	0.102 mm (.004 in) 50 - 67%
SolEpoxy DK7-20H	.279 ± .025 mm (.011 ± .001 in)	.102 - .127 mm (.004 - .005 in) 33 - 50%
PTI 6500	.305 ± .025 mm (.012 ± .001 in)	.025 - .076 mm (.001 - .003 in) 7.7 - 27%

Post-Thermal Impact Resistance Test

The post-thermal impact test results are shown in Table 8. The relative performance was similar to the initial screening results, except the 3M 5555 performed a little better and the SolEpoxy DK7-0953M performed a little worse. Some of the difference could be due to normal variation in workmanship, but it is also likely that the presence of Hiperco-50 as a substrate had an effect on the results. From general experience, Hiperco-50 is more difficult to bond to than the mild steel used for the initial screening bars. PTI 6500 performed amazingly well in this test, with not even a single chip in the coating.

Table 8: Post-Thermal Impact Resistance Test Results

Candidate Material	Average Score (Per Bar)	Comments
3M Scotchcast 5555	30	14 heights passed, 4 cracked, 10 failed
SolEpoxy DK7-0953M	36	18 heights passed, 8 cracked, 2 failed
SolEpoxy DK7-20H	21	3 heights passed, 8 cracked, 17 failed
PTI 6500	42	All 28 heights passed

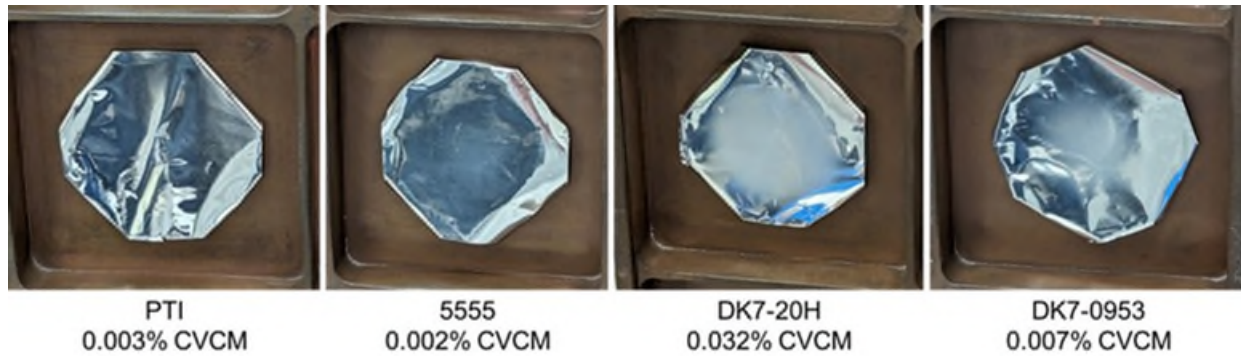
Outgassing

Table 9 and Figure 17 show the outgassing results for the materials tested. All of the materials tested met the traditional requirement for TML and CVCM of 1.0% or less and 0.10% or less, respectively. Most of the total mass lost was water vapor, as evidenced by the WVR values being close to the TML values. Some of the WVR values were higher than the TML values because the test was performed with an ambient relative humidity of 60% instead of the correct value of 50% per the ASTM spec. Per Figure 17, the collector foils showed some “haze” which is indicative of outgassed material condensing on adjacent surfaces. The SolEpoxy DK7-20H showed the most hazing and the PTI 6500 showed the least hazing. For motors fluidized with SolEpoxy DK7-20H or DK7-0953M used near optics, it is recommended to perform further characterization (including possibly testing of samples after a bake-out) prior to use.

Table 9: Outgassing Test Data

Material	%TML, average	%CVCM, average	%WVR, average
PTI	0.481 ± 0.016	0.003 ± 0.001	0.587 ± 0.013
5555	0.305 ± 0.010	0.002 ± 0.001	0.358 ± 0.008
DK7-20H	0.318 ± 0.012	0.032 ± 0.001	0.319 ± 0.010
DK7-0953	0.265 ± 0.002	0.007 ± 0.003	0.292 ± 0.002

Figure 17: Collector Foils After Completion of Outgassing Measurements



Conclusions

The results of the final screening tests were consistent with the initial screening test results, indicating that the initial screening did a good job of identifying good candidates to move forward to the final screening tests. With respect to the metrics listed for the tests presented here, the SolEpoxy DK7-0953M had one of the best balances in performance and the PTI 6500 performed very well in most tests. The extremely thin edge coverage observed for the PTI-6500 with both application methods used poses a significant risk of creating coil-to-stator core shorts in motor applications, unless mitigated via process changes/development. The detailed data is presented here and the reader can make their own judgement of which of the materials tested might be best for their application. It is strongly recommended that qualification testing of a flight-like article is performed prior to changing the stator secondary insulation material.

Acknowledgements

The authors would like to acknowledge the entire Fluidize Task-Force team, which over 2 years met regularly to discuss candidate materials, potential testing approaches, and test results. Every member dedicated a substantial amount of time and effort to this project and made meaningful contributions. Among the team members who are not authors, Howard Katzman (Aerospace Corporation) made a special contribution by performing all of the DSC and TGA tests, cross-sections, and facilitated the outgassing tests. Jeff Nagel (Windings Inc) also made a special contribution as he prepared all of the non-PTI coupons, performed all of the coating thickness, cut-through, dielectric strength and impact resistance measurements for the initial screening tests. The task-force members were (Listed in alphabetical company order): Aerospace Corporation: Don Denham, Howard Katzman; Lockheed Martin Space: Emmett Donnelley-Power, Kathryn Thomas, Jonathan Wood; Moog Inc: Robert Berning, Jenna Williams; Sierra Space: Jessica Hamm, Charlie Hodges, Jeff Moser, Jeff Mobley; Windings Inc: Jeff Nagel, Recarda Schmitz.

The authors would also like to acknowledge the companies involved with this effort. Each company contributed by funding a part of the effort, either through employee hours, direct cost, or both: Aerospace Corporation, Lockheed Martin Space, Moog Inc., Sierra Space, and Windings Inc.

Ti Beta-C Spring Development Testing for Low Cycle, Cold Deep Space Applications

Pavlina Karafillis * and Grady Lynch*

Abstract

Titanium springs are an attractive option compared to stainless steel springs due to their superior energy density. There is a lack of data for Titanium springs compared to their stainless counterparts, particularly at cold temperatures. To address potential performance risks of Titanium springs at cold temperatures on the Mars Sample Return Program, testing was performed. Mechanical cycling and life testing up to 3000 cycles were conducted at ambient temperatures and at -135°C. No strength loss, yielding, or rupture was observed at ambient or cold test temperatures. A stiffness increase of approximately 5.7% was observed between ambient and cold testing. Destructive microstructure evaluation of test and control springs demonstrated that alpha-enriched grain boundaries were present before and after testing. The alpha-enriched grain boundaries did not appear to function as crack initiation sites or cause any crack propagation as a result of the mechanical cycling. The processes utilized in Titanium helical compression spring fabrication were assessed to understand potential sources of alpha case and alpha-enriched grain boundary formation. From this assessment, a methodology for eliminating alpha-enriched grain boundaries is proposed.

Introduction

Stainless steel helical compression springs, particularly 300 series and 17-7 alloys, are commonly used in space mechanism applications. While not as common, Titanium springs are an attractive option due to their improved energy density, allowing for lower mass and improved packaging efficiency with equivalent performance. Ti 13V-11Cr-3Al springs were used in various aerospace applications throughout the 20th century but encountered significant challenges with production and fabrication. Ti 3Al-8V-6Cr-4Mo-4Zr, also known as Ti Beta-C, was developed in the 1960's as an easier-to-produce alternative to Ti 13V-11Cr-3Al. Since then, Ti Beta-C has been used in many aerospace applications, though little documentation exists for its usage at cold temperatures. A thorough literature survey was conducted but yielded no documented uses, test data, or material properties for Ti Beta-C at temperatures below -70°C. On the Sample Retrieval Lander Aeroshell, part of the Mars Sample Return mission, the protoflight cold temperature for the springs will be -135°C. To address this temperature gap, a development test campaign was carried out to exonerate three risks tied to Ti Beta-C helical compression spring usage at -135°C. First, the concern of reduced strength at cold was addressed by mechanical cycling at cold and ambient. Second, the concern of reduced performance due to fatigue at -135°C was addressed by a life testing up of 3000 cycles (over 100x expected total cycles) at -135°C. Lastly, the concern of crack initiation and growth at protoflight cold was addressed by microstructure analysis.

The testing described herein was designed to evaluate the performance of Ti Beta-C helical compression springs at -135°C and demonstrated that Ti Beta-C helical compression springs are acceptable for use in low cycle, cold deep space applications. Additionally, an investigation into alpha case formation and the associated crack initiation and growth risks was conducted, yielding a proposed method for effectively mitigating said risks.

Test Set Up

Test Overview

Three springs formed from Ti Beta-C per AMS4957, henceforth individually referred to as the Unit Under Test (UUT) and shown in Figure 1, were cycled. Each UUT is a nominally 254-mm (10-inch) long Ti Beta-

* Lockheed Martin Space, Littleton CO

C spring with a 10.64-mm (.419-inch) nominal wire diameter and a 78.64-mm (3.108-inch) nominal outer diameter. The UUT were not the same size and dimensions of the proposed flight springs but were brought to stress states matching the flight springs in order to conduct a representative test.



Figure 1. Titanium Spring

Each UUT was exposed to the test flow described in Figure 2. One control spring from the same lot as all the UUTs was sectioned to evaluate its microstructure.

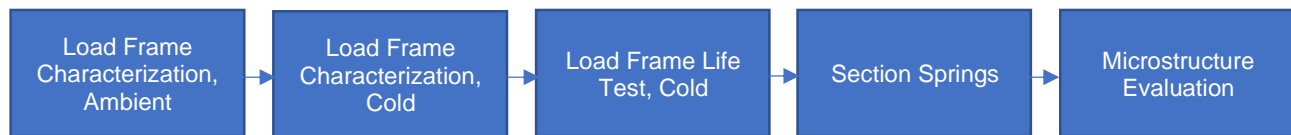


Figure 2. Test Flow

Load Frame Testing

Load frame testing was conducted at ambient and cold temperatures. As shown in Figure 3, the UUT was installed in custom 17-4PH fixturing and a CRES threaded rod. During all load frame testing, the UUT was loaded in compression, while the load frame maintained tension. All testing was completed on a 97860-N (22-kip) Load Cell and Load Frame from MTS Systems, calibrated to $\pm 1\%$ accuracy. Cold test temperatures were achieved using a Watlow Thermal Chamber and Temperature Controller and type E thermocouples, which can be seen in Figure 4. In the load frame, data was collected at about 100 Hz.

During load frame ambient characterization, the three UUTs were individually mechanically cycled five times at 22°C and 41% relative humidity. Mechanical cycling was executed between the free length of 248.9 mm (9.8 inches) and working height of 248.9 mm (6.2 inches) in a sine-wave profile with a maximum crosshead speed of approximately 127 mm/sec. Note that since an initial of compressive force of 90-130 N was maintained throughout the test, the spring was always slightly compressed, meaning it did not truly return to its free length on each cycle.

Following ambient characterization, each of the three UUTs were individually mechanically cycled five times at the cold temperature of -135°C to -145°C. The same crosshead speed as ambient testing was used. The Watlow temperature controller was set to a ramp rate of -5 degrees per minute to reach cold, and +5 degrees per minute to return to room temperature after the test. The test article dwelled at the set point temperature for 5 minutes prior to cycling.

Following cold characterization, each of the three UUTs were individually mechanically cycled 3000 times at the cold temperature of -135°C to -145°C. The previously noted crosshead speed and thermal chamber ramp rates and dwell times were used. For life testing, thermocouple 2 as shown in Figure 4 was omitted.

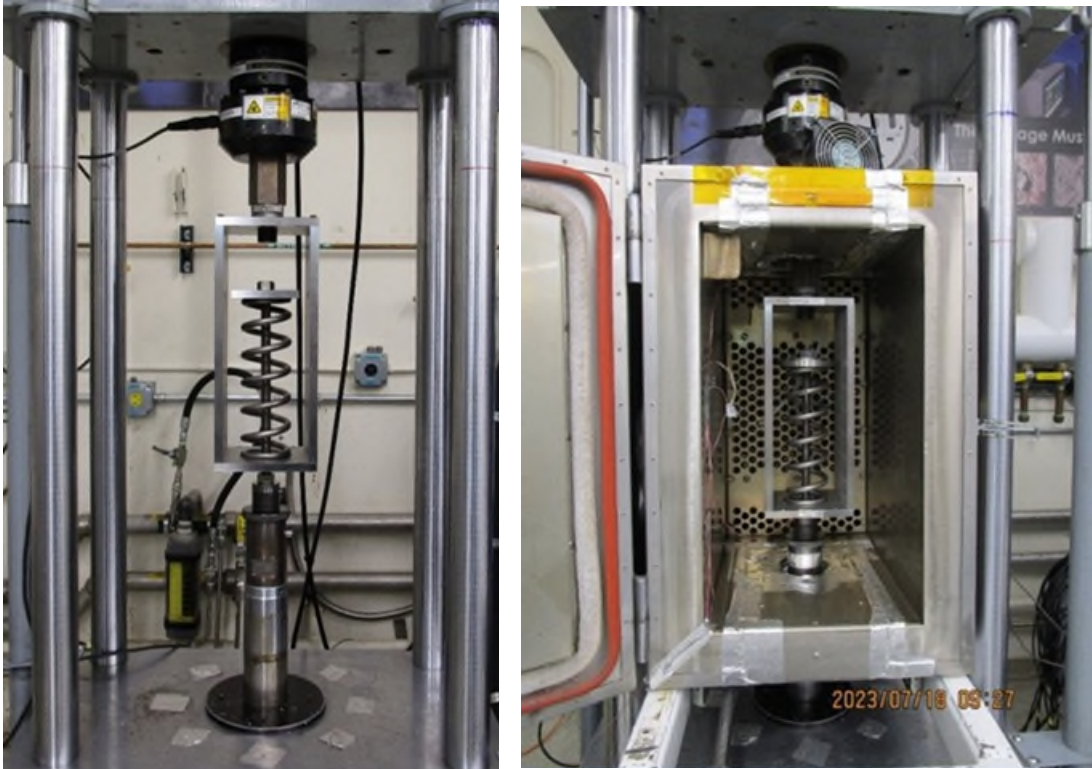


Figure 3. Load Frame Fixturing

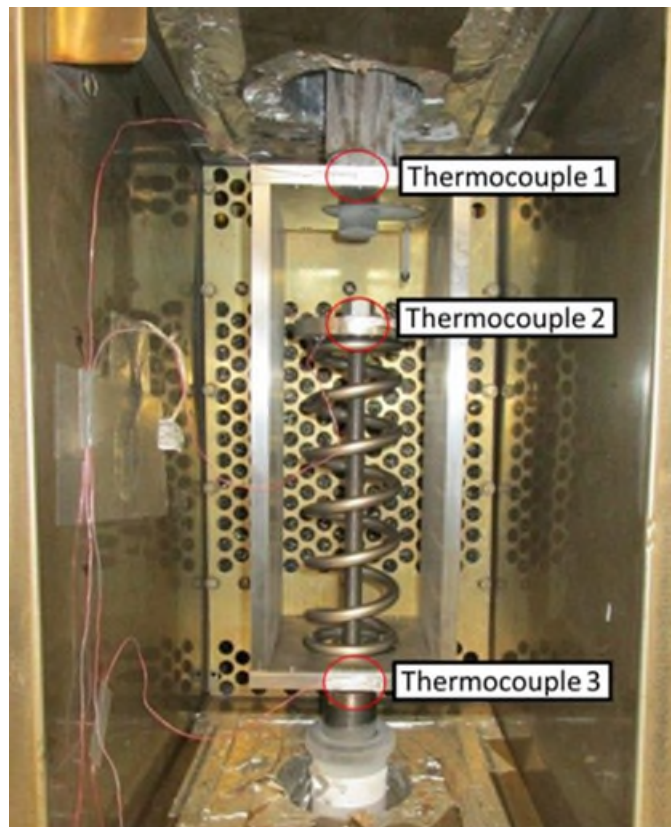


Figure 4. Thermocouple Placement

Microstructure Assessment

Following load frame testing, the three UUTs plus one control spring were each sectioned in three locations from the active coils. Microstructure evaluation was performed on each of the 12 sections using standard micro-sectioning techniques. This includes SiC abrasive paper, diamond polishing compounds, and AIO slurry. Then, the samples were etched to bring out the microstructure. Finally, the sections were imaged using a Zeiss Axio Observer Metallograph.

Test Results

Achieved Coil Stress

Table 1 summarizes the achieved max compression forces for each UUT during each test, as well as the corresponding maximum coil stress, using as nominal dimensions of the UUT. The maximum force achieved correlates to the maximum coil stress using Equation 1, where P is the maximum spring force, D is the mean spring diameter, d is the wire diameter, and K_s is the shear stress-correction factor. Assuming material properties per AMS4957 and a shear stress calculation per distortion Energy Theory, the allowable ultimate shear stress on this spring is at least 716.4 MPa (103.9 ksi).

$$\tau_{max} = K_s \frac{8*P*D}{\pi*d^3} \tag{1}$$

Table 1. Achieved Coil Stress Summary

Serial Number	Test	Max Force (N)	Max Coil Stress (MPa)	Ultimate Shear Stress (MPa)
SN02	Ambient Characterization	3126.3	495.3	716.4
SN03		3082.8	492.0	
SN04		3137.5	500.7	
SN02	Cold Characterization	3229.6	511.6	
SN03		3303.5	527.2	
SN04		3213.2	512.8	
SN02	Cold Life	3343.3	529.6	
SN03		3313.3	528.8	
SN04		3312.0	528.6	

Cold vs Ambient Performance Changes

As expected, the data across all tests are linear, with all datasets having best fit lines with R^2 values greater than 0.999. The consistency of the stiffness throughout the >3000 cycles demonstrates that no performance degradation was observed due to fatigue. As a detailed spot check, the spring stiffness derived from only first 100 cycles and the last 100 cycles of the life test were calculated to be within 87 mN/mm (<0.3%) of each other in all cases and R^2 remained greater than .999 in all cases. The y intercepts shown on the best fit lines reflect that the springs were preloaded to between 90 and 130 N and the initial position was zeroed out at this load prior to cycling. Not all the y intercepts of the best fit lines match the load at the zeroed position. This variation is attributed to the small but typical non-linearities in the first 5 mm of stroke of the spring, and measurement error.

Table 2 compares best fit spring stiffness values across ambient characterization, cold characterization, and cold life tests. There is a clear stiffness increase at cold temperatures compared to ambient, which agrees with the inverse correlation of temperature and Young’s Modulus presented in the Aerospace Structural Metals Handbook entry for Ti Beta-C, although, as previously mentioned, no explicit data exists for the temperature range of interest. The average magnitude of stiffness increase from ambient to cold was 5.7% and the cold spring stiffness was 1.4 N/mm (8 lbf/in) greater than ambient with 95% confidence. Equation 2 demonstrates that Young’s Modulus is directly proportional to spring stiffness. Accordingly, the

5.7% measured stiffness increase can be attributed to a corresponding 5.7% Young's Modulus increase under the cold test temperatures. Taking 104,110 MPa (15,100 ksi) as the value for Ti Beta-C Young's Modulus at ambient conditions, as is represented in the Aerospace Structural Metals Handbook, the calculated Young's Modulus at cold test temperatures is 110,047 MPa (15,961 ksi). In Equations 2 & 3, k is the spring constant, ν is Poisson's Ratio, D is the mean diameter, N_{ac} is the number of active coils, d is the wire diameter, and E is Young's Modulus.

$$k = \frac{d^4 * G}{8 * D^3 * N_{ac}}, G = \frac{E}{2(1+\nu)} \quad (2)$$

Solving for E:

$$E = k * \frac{16 * D^3 * N_{ac} * (1+\nu)}{d^4} \quad (3)$$

For all three springs tested, the spring stiffness observed during cold life testing was slightly higher than the spring stiffness observed during cold characterization testing. This was not expected because the measured temperature was within $\pm 5^\circ\text{C}$ between runs, and the life testing was not consistently colder than the characterization testing. For SN03 and SN04, the change between the two cold tests is negligible, and well within the $\pm 1\%$ calibration accuracy of the load cell. The spring stiffness change between cold tests for SN02 is notably higher than the other two springs, but still within the $\pm 1\%$ load cell calibration accuracy. Finally, the p-value for a two-tailed T-Test, between the stiffness of cold characterization testing and life testing is 0.49, indicating that there is no statistically significant difference between the two means. As the apparent stiffness changes between cold characterization and cold life testing are not statistically significant, and the application being investigated was not sensitive to variations less than $\pm 1\%$, root cause for slightly increased stiffness seen in test at extended cold was not identified.

Table 2. Ambient vs Cold Spring Stiffness

Serial Number	Ambient Char. Spring Stiffness	Cold Char. Spring Stiffness	Cold Life Spring Stiffness	Percent Change Between Ambient and Cold Life	Percentage Change Between Cold Ambient and Cold Life
	[N/mm]	[N/mm]	[N/mm]	%	%
SN02	32.204	33.720	34.167	6.1	1.3
SN03	32.046	33.873	33.910	5.8	0.1
SN04	31.802	33.361	33.457	5.2	0.3
Average	32.0	33.7	33.8	5.7	0.6
STD DEV	0.20	0.26	0.36	0.46	0.66
Max Delta	0.4	0.5	0.7	0.9	1.2
Variance	0.0	0.1	0.1	0.2	0.4

Spring Performance Summary

Figures 5 through 7 plot the force vs displacement data of all three UUTs at cold and ambient, with best fit lines. No strength loss, yielding, or rupture was observed during mechanical cycling at ambient or cold. This mechanical cycling addressed the concerns of reduced strength at cold, and reduced performance due to fatigue.

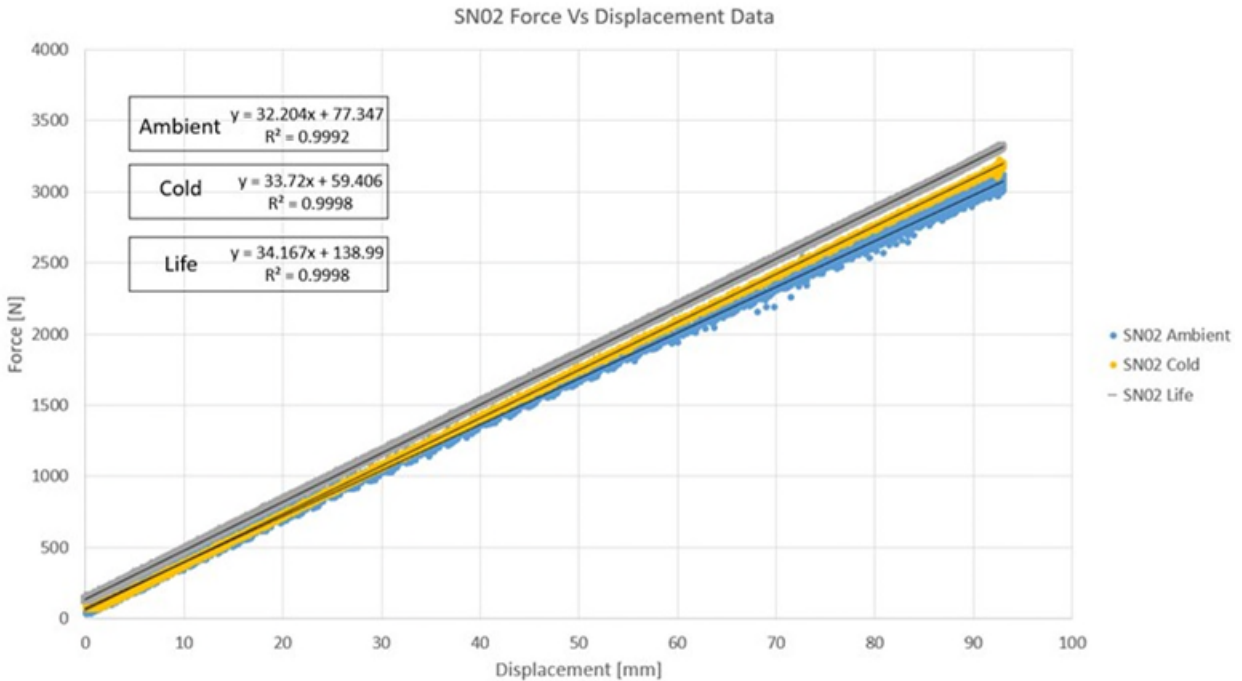


Figure 5. SN02 Force vs Displacement Overlay



Figure 6. SN03 Force vs Displacement Overlay

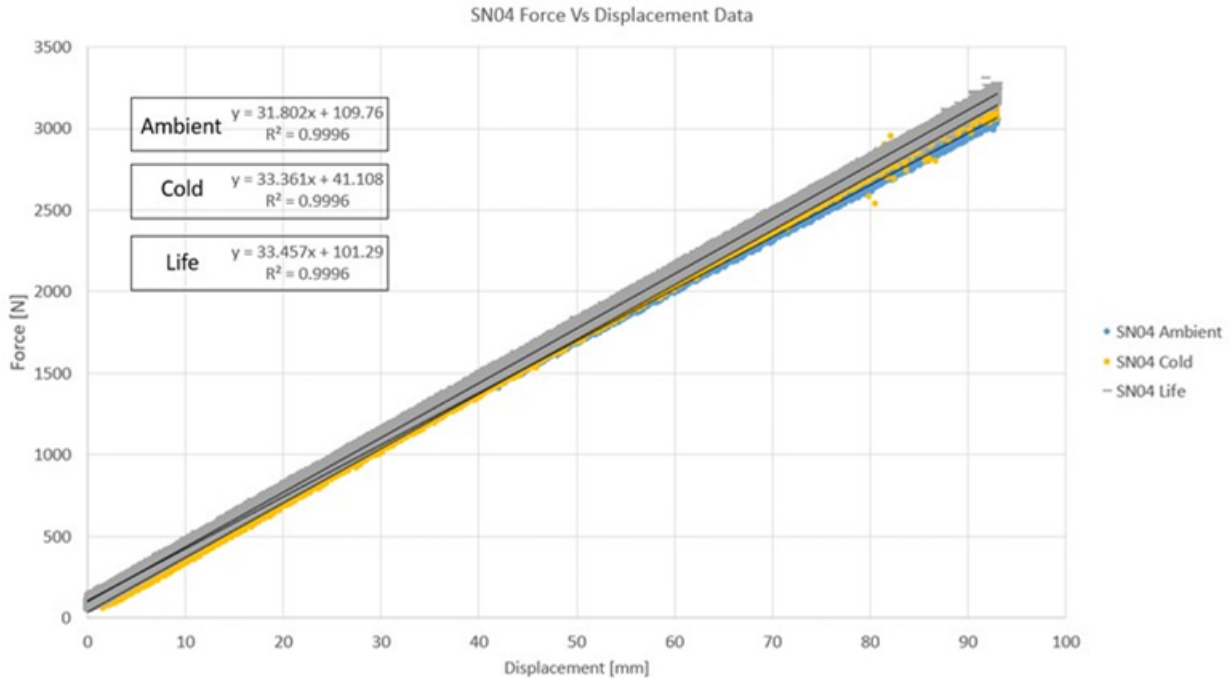


Figure 7. SN04 Force vs Displacement Overlay

Microstructure Evaluation

The overall microstructure was found to be consistent across all sampled springs. The primary finding from microstructure evaluation was the presence of alpha-enriched grain boundaries and small cracks on the outer edges all spring sections evaluated. The observed cracks are too small to be resolved during a level 3 dye penetrant inspection and are confirmed to have formed prior to the mechanical cycling testing, since the control spring exhibited the same cracking. See Figures 8 and 9 for observed alpha-enriched grain boundaries and micro cracks in a UUT and a control spring. The fact that the cracks on the mechanically cycled springs did not appear larger than those on the control spring suggests that the mechanical cycling at cold temperature did not cause crack growth. Moreover, the performance of the springs during characterization and life cycling suggests that even if flight springs had similar microcracking, the springs would still function as designed.

While the test results indicate that the springs would function as intended with alpha-enriched grain boundaries, their unexpected observation and known risks of cracking associated with alpha case prompted a deeper investigation into the formation mechanism for alpha case and the available options for removal of the alpha case and alpha-enriched grain boundaries.

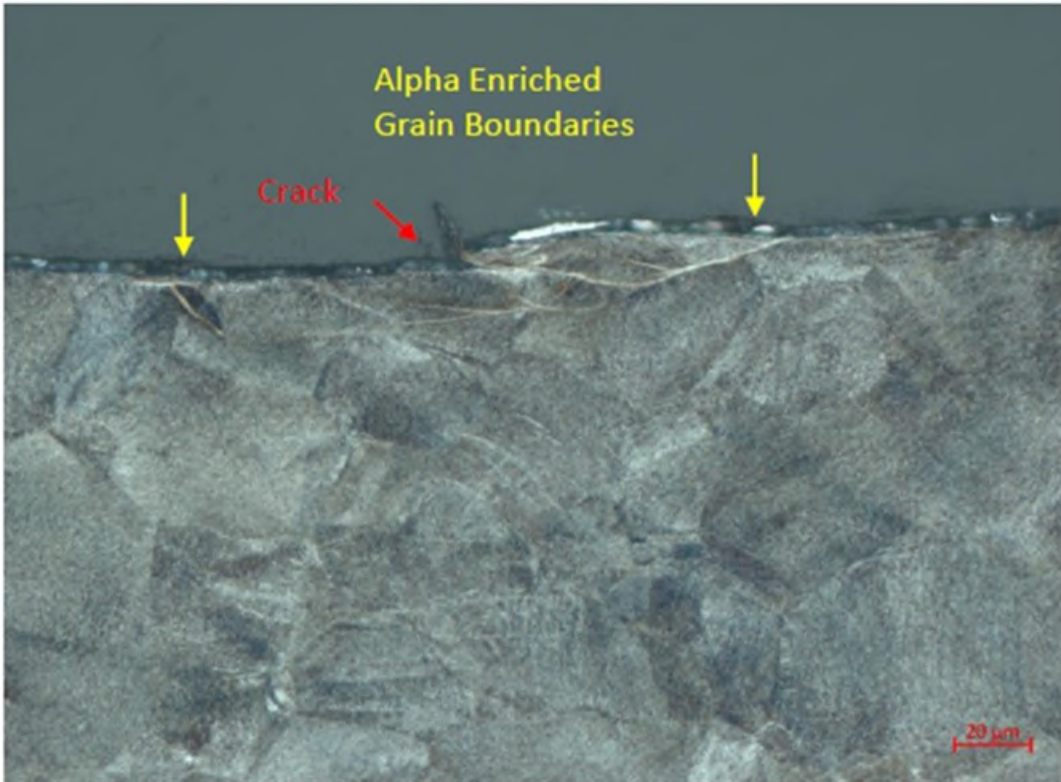


Figure 8. SN 02 Microstructure Evaluation (UUT)

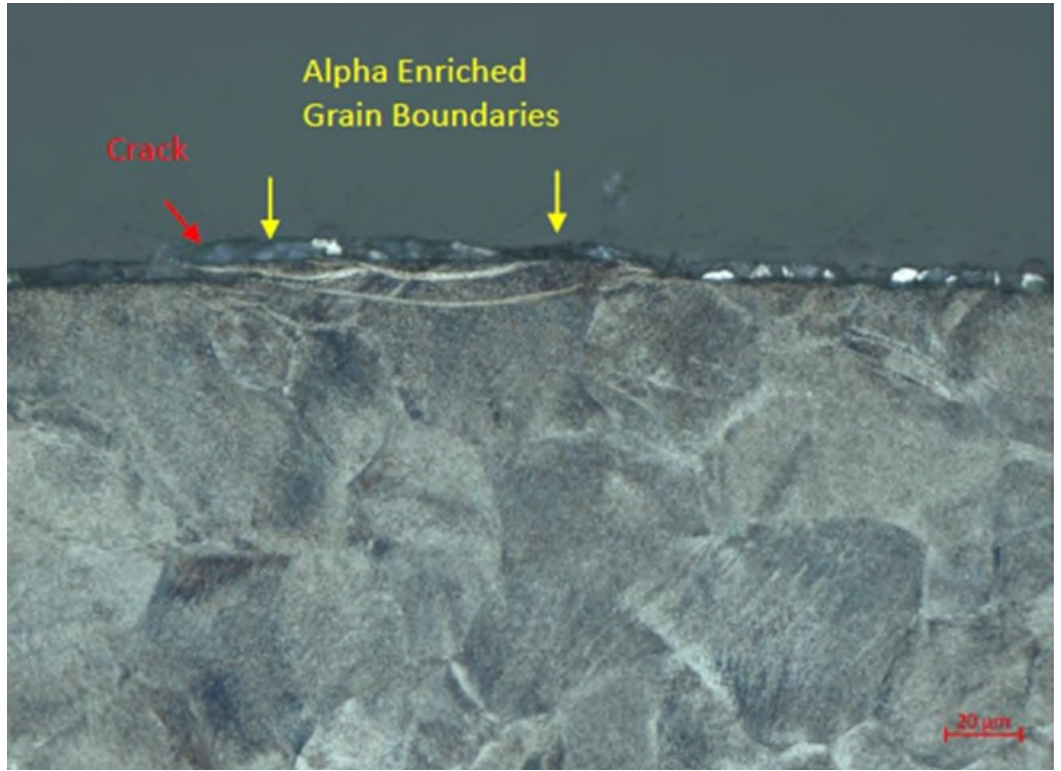
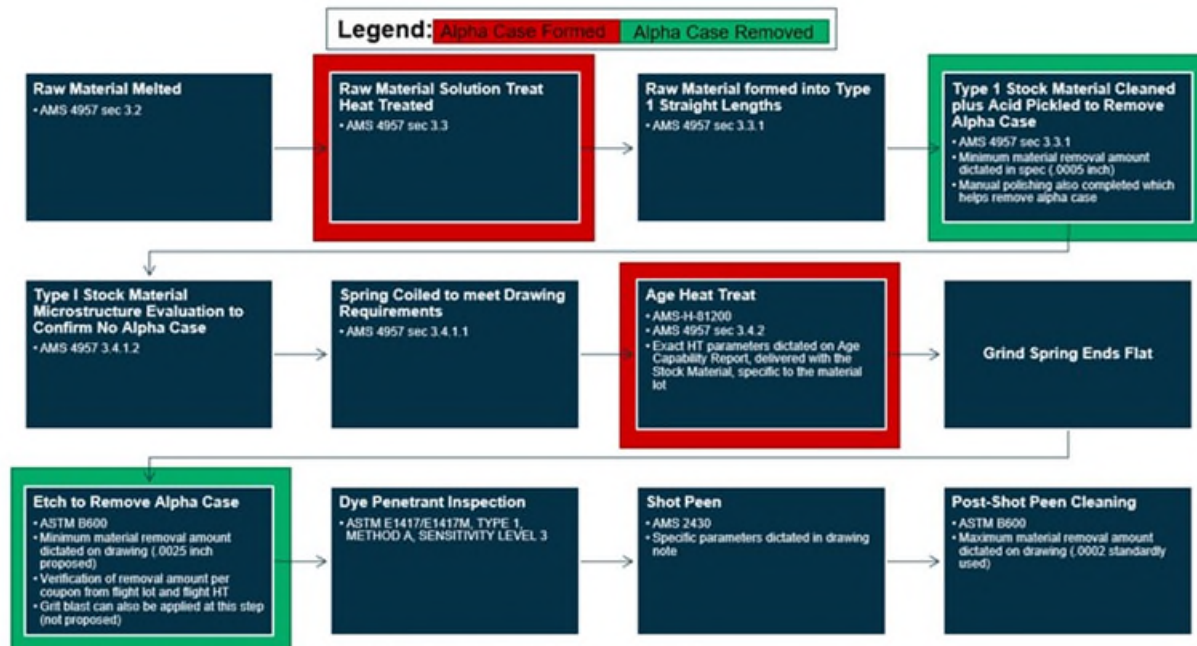


Figure 9. SN 05 Microstructure Evaluation (Control Spring)

Alpha Case Development and Crack Mitigation

After identifying alpha-enriched grain boundaries during UUT microstructure evaluation, an assessment of alpha case formation and mitigations during Titanium helical compression spring manufacture was conducted. Figure 10 summarizes the manufacturing process and highlights steps of interest where alpha-enriched grain boundaries form and are subsequently removed. Note that the term “alpha case” will be used to henceforth describe both alpha case and alpha-enriched grain boundaries. These two physical phenomena are similar and related, but not identical. Alpha case is the more generic term, while alpha-enriched grain boundaries specifically indicates that grain boundaries are enriched with alpha case.

As can be seen in Figure 10, alpha case is understood to form both during the initial raw material solution treat step and during the subsequent coiled spring age heat treat step. Alpha case formation and subsequent removal resulting from the initial raw material solution treat step is governed by AMS4957 and carried out by the raw material vendor. The subsequent age heat treat and alpha case removal step, which is controlled by the spring vendor or a subcontractor thereof is critical to the final state of alpha case on the part.



Note: Heat Treat is completed in non-inert environment

Figure 10. Ti Beta-C Spring Processing Steps

Alpha Case Formation

In order to understand the phenomenon of alpha case and how it forms on a Titanium part, it is instructive to review the Technical Datasheet for Ti-3Al-8V-6Cr-4Mo-4Zr published by Carpenter Technologies [1]. Carpenter Technologies explains that alpha case is a “brittle oxygen-stabilized alpha layer” of Titanium that forms on the exterior of the part during heat treat in a non-inert environment. While completing heat treat in an inert environment may decrease alpha case formation, it is typically financially advantageous to complete heat treat in a non-inert environment. Regardless of the heat treat environment, Carpenter advises that “it is very important to completely remove not only the surface scale, but the underlying layer of brittle alpha case as well” to preclude surface crack-induced failure. Moreover, “in [titanium] beta alloys, alpha case tends to penetrate the grain boundaries beneath the surface. Thus, the actual depth may be greater than is readily apparent, and the effective thickness may not be uniform.” Variable alpha case thickness was noted in the UUTs and control spring sampled.

Quantification of Alpha Case

Precise quantification of alpha case can be completed via sectioning and microstructure evaluation using a coupon of the same wire lot that undergoes the same heat treat process as fabricated springs, or with a spare sacrificial spring.

In lieu of sectioning and microstructure evaluation, a minimum material removal amount can be implemented that bounds expected alpha case formation depth. It is understood that the amount of alpha case developed and corresponding minimum material to be removed varies based on heat treat parameters of temperature and time, which inherently varies between material lots. AMS4957 dictates an acceptable range of temperature and time during which heat treatment may occur in order to achieve the required mechanical properties. Despite these variables, published data does exist for recommended material removal depth for Titanium Alloys based on heat treat temperature and time [2] [3]. Given the typical heat treat time of up to 10 hours at up to 593°C (1100F) and published data in [2] and [3], a removal value of 25.4 µm (.001 inch) is recommended for Titanium alloys. [3] All micro cracks identified in the control and UUTs were within 25.4 µm of the surface and would have been eliminated with an etching of 25.4 µm. However, the depth of the alpha case was seen to be as far as 48.3 µm in the springs sampled. No sources were found to explicitly call out Ti Beta-C in material removal tables, but [2] identifies that the alpha case depth may vary with alloy type, possibly explaining the deviation from published data seen. In order to bound the material removal completed in the manufacturing process of the sampled springs, a minimum material removal for Ti Beta-C springs of 63.5 µm (.0025 inch) is proposed in the post etch heat treat for Ti Beta-C springs for use on springs in this application. It is important to note that 63.5 µm is very small in comparison to wire diameter, as the UUT has a wire diameter of 10.64 mm (.419 inch), and the proposed application being assessed has a wire diameter of 12.7 mm (0.5 inch). Further work is recommended to assess if the etched amount should vary with the wire diameter.

Methods of Alpha Case Removal

The Carpenter Technologies tech data sheet [1] recommends that “Surface removal can be accomplished by mechanical methods such as grinding or machining, or by descaling (using molten salt or abrasive) followed by pickling in a nitric/hydrofluoric acid mixture”. At least two methods for alpha case removal currently employed in industry have been identified, abrasive grit blast and Hydrofluoric etch per ASTM B600 have been identified for alpha case removal. Vendor experience also indicates that shot peening after alpha case removal is a prudent step to further mitigate surface cracking risk. Further work is required to understand if one of these methods provides better results.

Verification of Alpha Case Removal

Similar to the question of determining how much alpha case is present, the most robust approach to verification of alpha case removal is via sectioning and microstructure evaluation, as is required following raw material solution treat heat treat per AMS4957. That said, it is often impractical to require coupon sectioning and microstructure evaluation in the middle of spring fabrication to verify complete alpha case removal. An acceptable alternative is to calculate material removal depth of 63.5 µm (.0025 inch) on a representative coupon via mass measurement pre- and post- alpha case removal operation. This approach works as-follows:

1. Prepare multiple representative coupons along with flight parts. Coupons must be from same material lot and must experience same age heat treat as flight parts.
2. Precisely measure mass of each coupon before alpha case removal operation (i.e. grit blast or etch)
3. Expose coupon to alpha case removal operation. Parameters for this operation must be identical to parameters used for flight parts.
4. Precisely measure mass of coupon after alpha case removal operation.
5. Use mass delta to calculate material removal depth over surface area of part

If desired, this mass measurement approach can be supplemented by final sectioning and microstructure evaluation of a sacrificial spring to develop additional confidence in complete alpha case removal. If alpha case is identified at this time and an additional etch is executed to remove it, the shot peen and later steps must be repeated for their impacts to take effect.

Conclusion

The successful test campaign conducted on Ti Beta-C helical compression springs demonstrates acceptable performance to temperatures as low as -135°C. The testing demonstrated a Ti Beta-C stiffness increase of 5.7% between ambient and cold test temperatures. The tested springs had residual alpha enriched grain boundaries and microcracking prior to testing yet still showed no signs of fatigue-induced failure or performance degradation, further supporting the conclusion that Ti Beta-C is appropriate for low cycle, cold space applications. While testing and microstructure analysis of UUT and control springs indicates that cycling up to 3000 cycles causes no identifiable increase in crack growth and crack initiation, the alpha case removal minimum depth of 63.5 µm (.0025 inch) and subsequent verification steps presented herein are believed to be sufficiently robust to effectively mitigate the risk of crack-induced failure for low cycle springs.

Acknowledgements

We would like to thank Julia Pimentel for all her work conducting testing on the load frame, and Curtis Ricotta for conducting the microstructure analysis. We would also like to thank Jeanne Eha for providing valuable material science input on the test formulation and when investigating the alpha enriched grain boundaries. Lastly, we would like to thank Mason Woish, Mike Knopp, and Don Lewis for their input into understanding and mitigating the alpha enriched grain boundaries. This testing was conducted by Lockheed Martin Space as part of contract number 1664478 with the Jet Propulsion Laboratory.

References

1. Carpenter Technologies Ti-3Al-8V-6Cr-4Mo-4Zr (Beta C™) Tech Data Sheet.
<https://www.carpentertechnology.com/hubfs/7407324/Material%20Safety%20Data%20Sheets/Ti%203Al-8V-6Cr-4Mo-4Zr.pdf>
2. Donachie, M. J. *Titanium: A Technical Guide – Second Edition*. ASM, ©2000.
3. AMS2801 Rev B

Lessons Learned in Building and Testing The Regolith and Ice Drill for Exploring New Terrain (TRIDENT)

Philip Chu*, Samuel Goldman*, Carter Fortuin*, Vincent Vendiola*, Helen Xu*, Jaqueline Stamboltsian*, Raymond Lin*, Anchal Jain*, Jack Wilson* and Kris Zacny*

Abstract

The Regolith and Ice Drill for Exploring New Terrain (TRIDENT) is a one-meter class drilling system that will operate on the Lunar surface as a part of the Polar Resources Ice Mining Experiment-1 (PRIME-1) and Volatiles Investigating Polar Exploration Rover (VIPER) missions. The PRIME-1 payload will explore the area outside of Shackleton crater onboard an Intuitive Machines Nova-C Lander (IM-2), while VIPER will be delivered to the Lunar surface onboard an Astrobotic Technology's Griffin Lander and investigate numerous Ice Stability Regions on Mons Mouton. Two nearly identical TRIDENT flight units have been built, and flight qualified. At the time of writing, one TRIDENT unit has been integrated with the VIPER rover, and has completed Comprehensive Performance Testing, while the other unit has been mechanically integrated to the IM-2 spacecraft panel, awaiting lander system-level integration and testing.

Introduction

The primary purpose of TRIDENT on the PRIME-1 and VIPER missions is to physically excavate regolith from the lunar subsurface and deliver it to the surface for remote sensing instruments to analyze. Regolith is captured in the drill flutes and deposited onto the surface in a cuttings pile. Sample excavation is performed in such a way as to preserve the volatiles in an uncontaminated state as much as practical, while maintaining stratigraphy. On VIPER, the Near InfraRed Volatiles Spectrometer System will characterize lunar surface composition, morphology, and thermophysical properties (Roush & Colaprete, 2021). The Mass Spectrometer Observing Lunar Operations (MSolo) will measure the concentration of ice and other volatiles in the extracted samples on PRIME-1 and VIPER (Aguilar-Ayala, 2023). Both instruments have their field of view aligned with the expected location of the cuttings pile. In addition to supporting remote sensing instruments, TRIDENT measures forces and displacements during operation to determine bulk physical properties of the regolith (King, 2024). This information will be used to understand the working environment and bound critical excavation parameters for future larger scale regolith mining equipment and processes. TRIDENT also includes a heater, and redundant temperature sensors inside the auger, which enables downhole measurement of regolith temperature, and potential assessment of thermal conductivity (Zacny & Chu, 2024). The two TRIDENT drills will accomplish a number of firsts, including the first robotic drilling systems deployed by the United States on the Moon and the first drilling systems deployed to the Lunar South Pole by any country.

TRIDENT has a number of subsystems which enable drilling and sample delivery to the surface, as shown in Figure 1. TRIDENT is designed with a rotary-percussive drill head which provides the ability to penetrate through ice-bearing regolith, and hard rock. The percussive system is able to actuate on an as-needed basis during drilling, providing 2 Joules per blow at up to 972 blows per minute. TRIDENT uses a 25.4-mm diameter auger with a tungsten carbide cutting bit and external helical flute structure to capture and transport regolith to the surface. The drill auger rotates at a speed of up to 120 RPM during operations. TRIDENT uses a deployment linear stage to move the drill footpad from the stowed position into preloaded contact with the Lunar surface, providing stability for drilling. After preloading the footpad, the rotary percussive drill head is actuated, and the drill Feed linear stage moves the drill string into the regolith using a feedback loop from actuator telemetry to adjust Rate of Penetration (ROP) and Weight on

* Honeybee Robotics, Altadena, CA

Bit (WOB). The right set of images in Figure 1 show the Footpad deployed to the surface, followed by the Feed linear stage extending the drill string to its maximum depth. Drilling is performed in short segments, known as “bites” (Zacny & Chu). Regolith is captured in the auger flutes during drilling, and after each bite segment, the auger is fully extracted from the borehole, and a passive spring-loaded brush is used to remove the regolith from the auger, allowing it to fall onto a sample delivery chute, followed by depositing in a cuttings pile for remote sensing instruments. Once regolith is cleared from the auger, another bite segment is collected, and the process repeats until the maximum depth of 100 cm is reached.

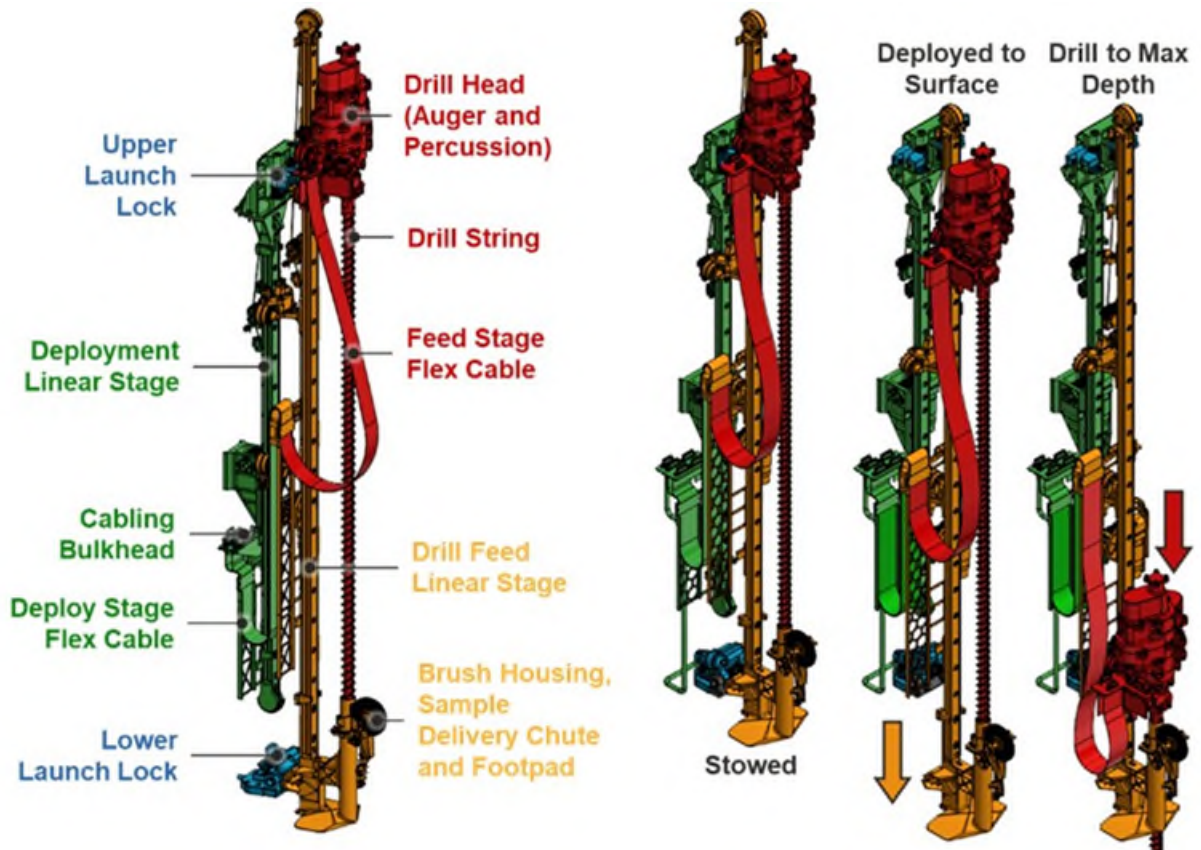


Figure 1. TRIDENT Mechanism Overview

Three total units of TRIDENT were constructed and tested. Two flight units were assembled, and flight qualified for PRIME-1 and VIPER, and an Engineering Unit was built to validate requirements associated with sample acquisition in Lunar simulants and environments so that cleanliness of the flight units could be maintained. The two flight TRIDENT units included two flight avionics systems which were significant efforts on their own, and a first-time development for Honeybee Robotics. These avionics systems provide power and control for the drill actuators, temperature sensors, and heaters. The two avionics systems also include onboard software which provides both low-level motor control and high-level logic to control TRIDENT operations. Dedicated ground software was also developed by Honeybee Robotics to enable TRIDENT engineers to control the drill in near real time from ground stations at NASA Kennedy Space Center (PRIME-1) and NASA Ames Research Center (VIPER). Avionics and software will not be discussed in this paper, but are worth mentioning, as they were both developed in parallel with the TRIDENT mechanism and form a fully functional flight qualified system.

Both TRIDENT flight mechanism units were environmentally tested, including sine vibration, random vibration, thermal vacuum cycling, self-induced shock testing, electromagnetic compatibility, and end-to-end integrated comprehensive performance testing. Prior to, and during a number of these tests, numerous issues were discovered, and the team had to perform detailed investigations to determine root

cause, impacts, and solutions to the problems. This paper will focus on lessons learned throughout the integration and testing of TRIDENT, as well as unique design features that can benefit the spacecraft mechanism community. An example of some of the issues that were encountered, and the lessons learned are as follows.



Figure 2. TRIDENT Flight Units for VIPER (Left) and PRIME-1 (Right)

Frangibolt Cup / Cone Design

TRIDENT uses a Frangibolt non-explosive actuator to initiate release of its Lower Launch Lock (LLL). The LLL consists of a pyramid-shaped cup and cone interface with a Frangibolt fastener passing through the middle of the connection. This cup and cone interface constrains the TRIDENT Footpad for launch. After landing on the Lunar surface, the Frangibolt actuator is initiated by heating a cylindrical shape memory alloy (SMA). This SMA expands, putting the Frangibolt fastener in tension, and eventually breaking the bolt at a specific location. Once the bolt is ruptured, a spring-loaded hinge mechanism swings the cone away from the cup, releasing the Footpad.

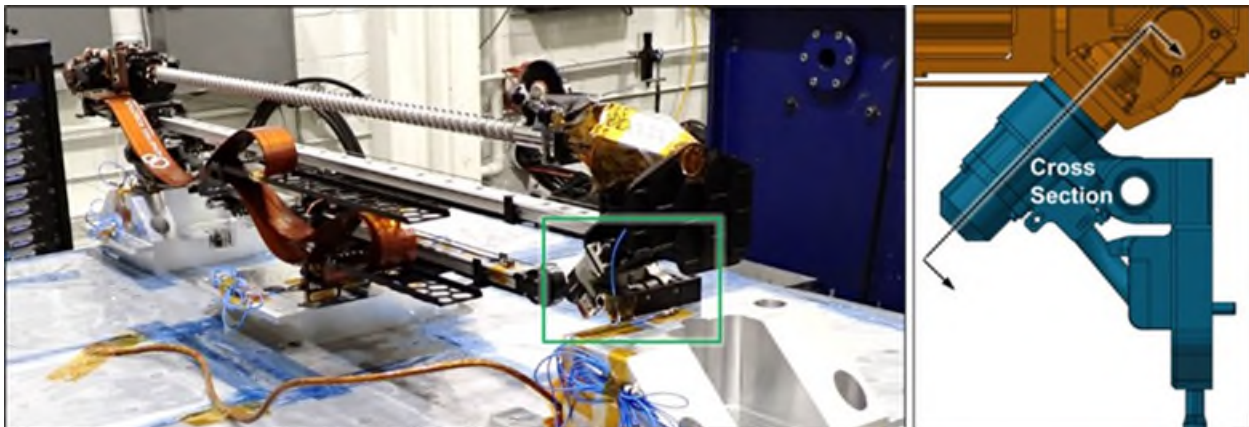


Figure 3. TRIDENT Lower Launch Lock Mechanism

A simplified cross section of the LLL Mechanism is shown in Figure 4, and the right image in Figure 3 illustrates the location and view direction of the cross section. The stack up of components eliminates any gaps between the head of the Frangibolt fastener, and the Frangibolt Nut. As shown, while eliminating gaps in the bolt path, this resulted in a slight gap between the parallel faces of the cup and cone interface.

During sine vibration testing on the VIPER TRIDENT flight unit, the Frangibolt fastener prematurely ruptured as the system was approaching peak acceleration in one test axis, releasing the Lower Launch Lock while under vibration. The test was immediately halted to protect the hardware, and the test campaign was paused while an investigation was performed. Initial reactions to the anomaly suggested that TRIDENT had been over-tested, however, upon reviewing the finite element model and accelerometer data, the estimated tensile load on the fastener was within expected structural limits. While this was being assessed, a parallel effort was initiated to investigate the way in which the bolt ruptured. Detailed photos under various lighting conditions were taken of the fastener fracture plane and communicated to fracture analysis Subject Matter Experts at the NASA Johnson Space Center to assess.

After reviewing the photos, the team concluded that the fastener had failed due to reverse bending (i.e., in-plane oscillation back and forth) as opposed to tension. Reverse bending causes cracks to propagate faster than uni-directional bending and can be seen in the fracture plane as semi-circular grooves with parallel striations (Figure 5). This suggested to the TRIDENT team that the cup and cone were “rocking” relative to one another during sine vibration. Figure 4 shows the direction of vibration during this test relative to the LLL cross section. The reverse bending evidence suggested that the slight gap on the outer perimeter of the cup / cone interface was the root cause of the anomaly. This issue was corrected on both TRIDENT units. The vibration test campaign was continued under the same loading conditions, and the Lower Launch Lock survived the remaining tests, and successfully released during follow-on comprehensive performance tests.

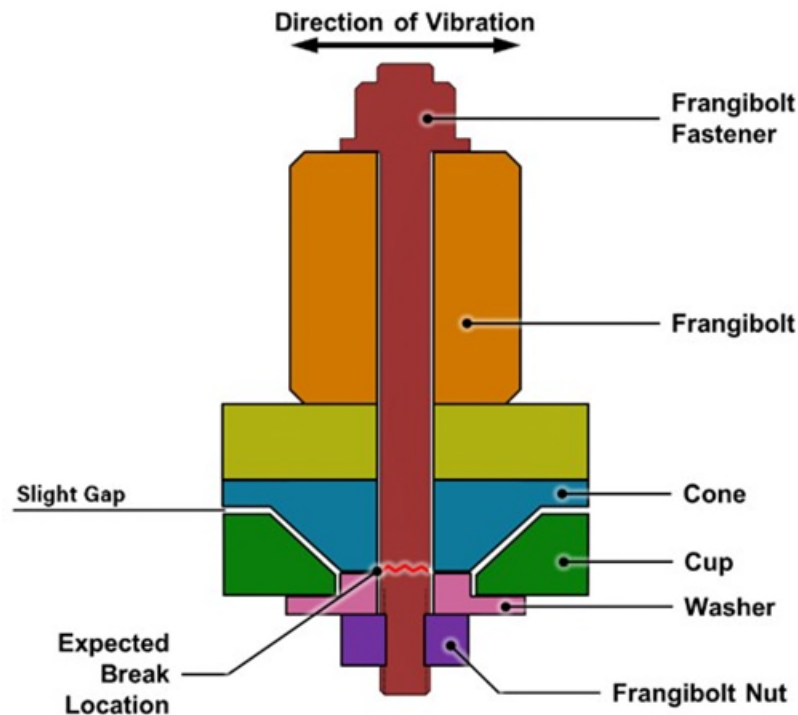


Figure 4. TRIDENT Simplified Lower Launch Lock Mechanism Cross Section (Not to Scale)

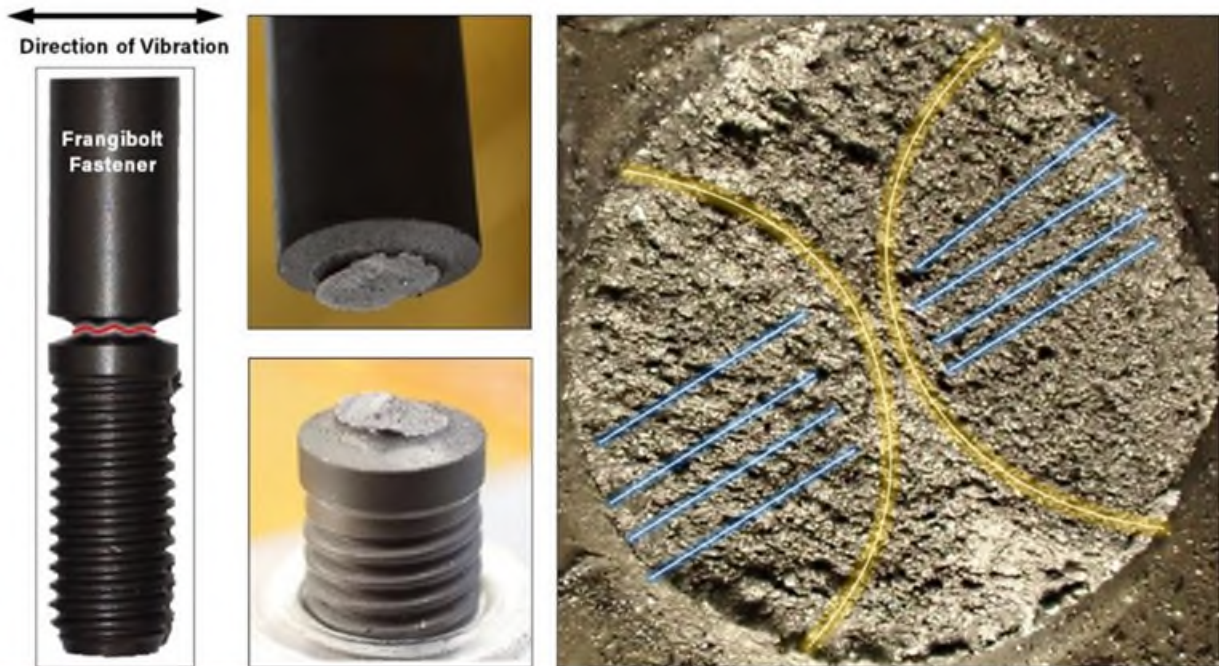


Figure 5. Frangibolt Fastener Fracture Analysis

The lesson learned is to minimize any gaps or compliance in the Frangibolt joint design, but do not allow the bolt itself to take moment loads, even with seemingly insignificant gaps between the cup and cone surfaces. Frangibolts are often used in a cup and cone configuration, where the cup and cone will react lateral loads. The Frangibolt bolt is not designed to take moment loads at the "necked down" region. Reverse bending fatigue, as well as load amplification due to the "heel-toe" effect will significantly reduce the strength capability of the joint and is also challenging to analyze due to the unknown material properties of the Frangibolt bolt in the necked down region.

Inappropriate Use of Needle Roller Bearings

The TRIDENT Upper Launch Lock (ULL) uses a unique method of releasing the Drill Head from its stowed position. Two torsion spring-loaded passive swing arms, each with pyramid-shaped cones, interface with corresponding cups on the Drill Head assembly, constraining it for launch. These swing arms are held in place using a cam roller mechanism connected to the TRIDENT Feed linear stage. Figure 6 illustrates the TRIDENT lower and upper launch lock release process, with the stowed for launch position shown in (1). After actuating the Frangibolt and releasing the LLL (2), the ULL is released by simultaneously actuating the Feed and Deploy linear stages in opposite directions at the same speed (3). The drill head cup and cone do not move relative to one another, but the cam roller mechanism slides away from the swing arms, eventually releasing them. Redundant torsion springs then pull the swing arms away from the Drill Head, unlocking it (4). The ULL cam roller mechanism uses two needle roller bearings mounted to the Feed linear stage (orange stage in Figure 6). These bearings hold the ULL swing arms in the locked position and are also highly loaded during launch vibration.

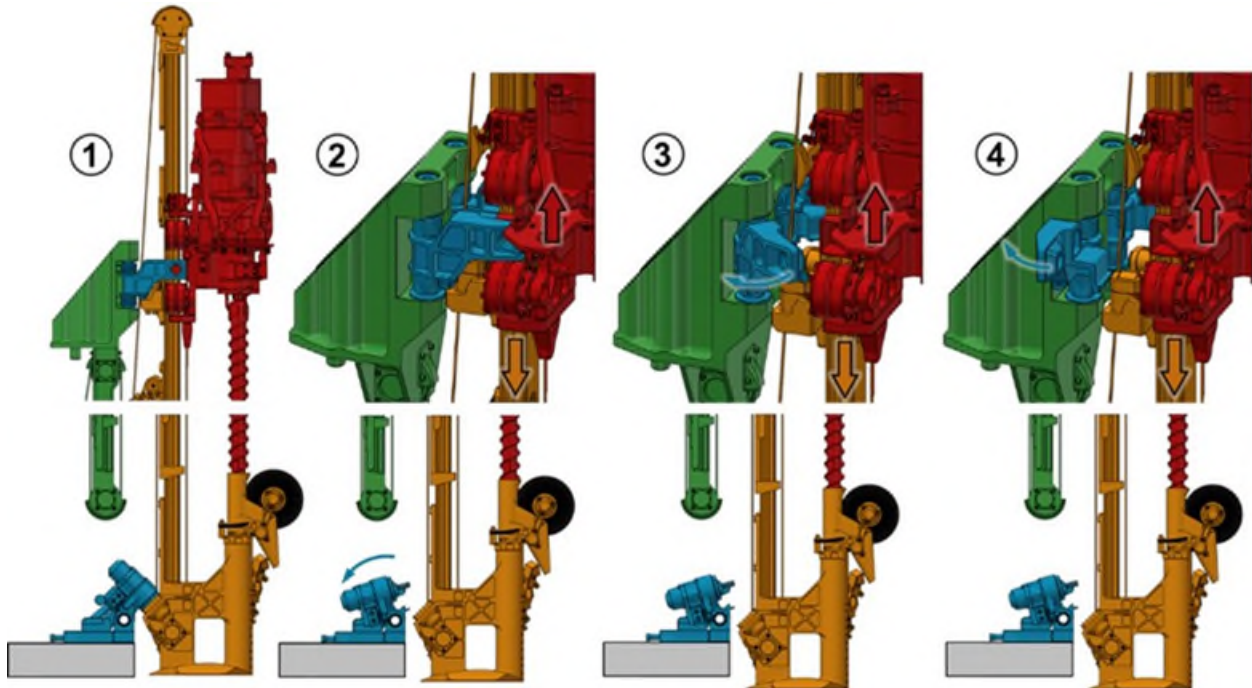


Figure 6. TRIDENT Launch Lock Release Process

After the Lower Launch Lock anomaly, TRIDENT was inspected in detail to search for any additional damage. It was found that the two needle roller bearings used in the ULL cam roller mechanism had experienced significant damage, and one of the bearings was completely fractured, as shown in Figure 7. These bearings react the full force of the drill head during launch. An investigation revealed that stress analysis of these bearings used appropriate loading conditions but compared the applied loads to the catalog dynamic load rating of the bearings. Acceptable margins were calculated for this load rating; however, this did not account for the fact that the bearing was mounted and implemented in an atypical manner. Needle Roller bearings are typically pressed or installed with a clearance fit into a bore, which provides support for the thin outer race of the bearing. In this configuration, small roller bearings of this size can support thousands of newtons of force. On TRIDENT, the ULL needle roller bearings were simply mounted on a shaft, with the outer race acting as a cam roller, holding the ULL swing arms in place. The lack of structural support on the thin outer race of the bearing caused one of the bearings to fracture due to the high vibration loads.

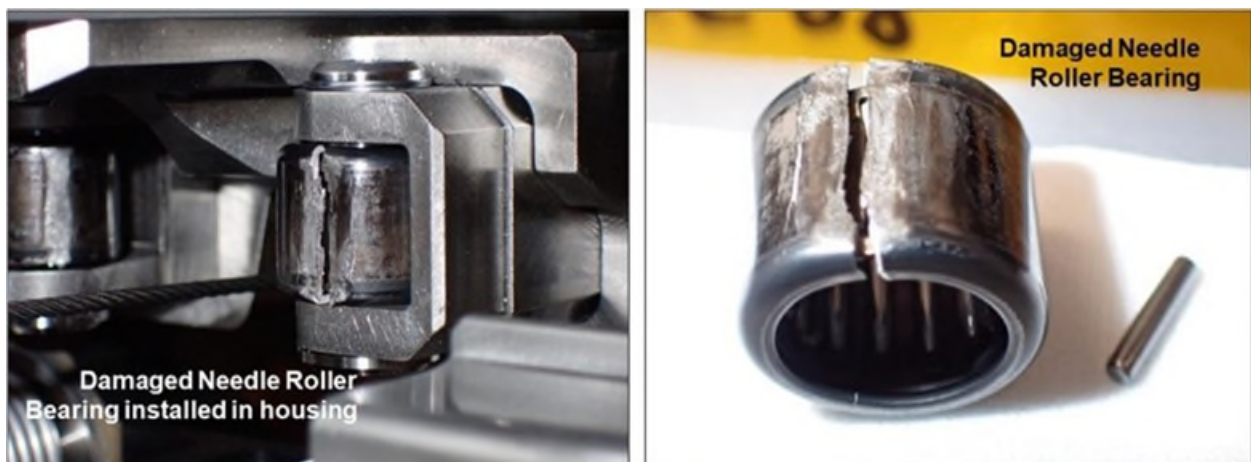


Figure 7. Upper Launch Lock Fractured Needle Roller Bearing

A number of needle roller bearings of the same size were subjected to load testing in the as-mounted configuration. A simple test stand was built to replicate the flight mounting method, and the bearings were subjected to a number of tests, including qualitative tests with a hand-held hammer, and repeated compressive loading at the catalog dynamic load rating of the bearing. The hand-held hammer test produced a large scale fracture after approximately 20 hammer blows, whereas the compression fixture test (Figure 8, left) produced a number of hair line cracks (Figure 8, right) after 24 load cycles at the catalog dynamic load rating. It is likely that the repeated loading during sine and random vibration testing caused hair line crack initiation, followed by larger scale fracturing from the thousands of repeated impacts throughout the vibration test campaign.

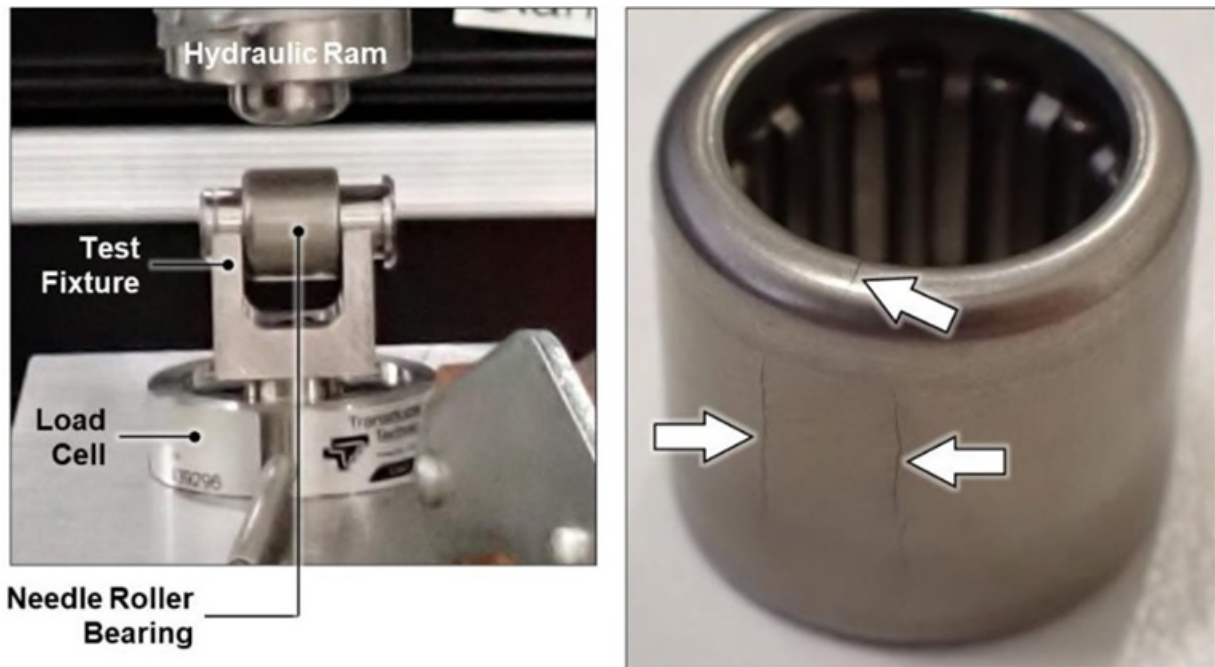


Figure 8. Needle Roller Bearing Load Test Fixture (Left). Hairline fractures in test bearing (Right).

The needle roller bearings were originally selected to reduce friction in the system when releasing the ULL. In practice, the Feed and Deploy actuators have significant force margin, and there is not much gain to using rolling bearings at this interface. The design was updated to not require these needle roller bearings, and follow-on vibration testing showed no issues with damage to the bushings or releasing of the ULL afterwards. It should be noted that the method of unlocking the Upper Launch Lock is robust to fracturing of the needle bearing. Even with the fractured needle bearing, the Upper Launch Lock was able to successfully release the swing arms and free the Drill Head from its stowed position.

The lesson learned is to be careful when applying catalog load limits to atypical bearing mounting situations. Any kind of thin-section bearing should not be used as a “cam” device in any mechanism that is highly loaded during operation, or launch environments, unless it is supported by a thicker-walled housing that can react that load. If this style of mounting is unavoidable, it is advisable to perform compression load testing of the bearing at the intended loads, particularly if those loads are close to catalog limits.

Surface Preparation for Bonding

TRIDENT utilizes a number of wire-wound Kapton film heaters throughout the mechanism to control the temperature of its actuators. Many heaters are mounted on curved surfaces, with the heaters initially hot-formed by the vendor to roughly match the shape of the surface. Each heater was applied to the corresponding surface using the following procedure.

1. Clean surfaces to be bonded with de-greasing solution.
2. Clean surfaces to be bonded with Isopropyl Alcohol using ultrasonic cleaning if possible.

3. Remove film covering Pressure Sensitive Adhesive (PSA)
4. Apply heater to surface and press firmly to allow PSA to make intimate contact with surface.
5. Place component in oven to cure PSA.
6. Stake perimeter of heater with epoxy in short beads, leaving gaps between beads for air to flow out.
7. Cure epoxy in oven and perform durometer check on coupon sample.

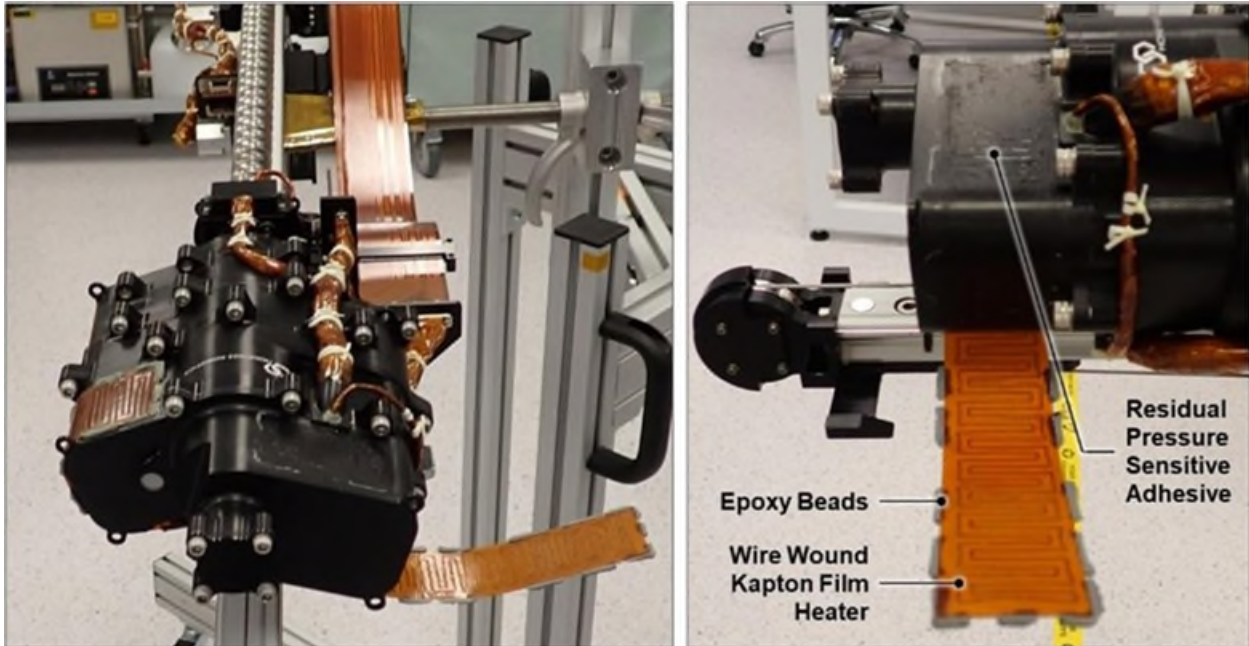


Figure 9. De-bonded Kapton Film Heater after TVAC

After completing one Thermal Vacuum (TVAC) cycle from +85°C to -135°C, the PRIME-1 TRIDENT drill was inspected and found to have multiple de-bonded Kapton film heaters on the Drill Head enclosure. An example of this de-bonding is shown in Figure 9. The pressure sensitive adhesive had completely separated, as well as many of the epoxy beads. The de-bonded portion of the heater had also mostly reverted back to its original flat shape prior to hot forming. Subject Matter Experts from NASA Kennedy Space Center were consulted on the root cause and recovery from this anomaly. It was determined that other than cleaning, no mechanical surface preparation had been performed on the anodized surfaces prior to heater application (e.g., scratching the surface or removing surface finish), and that this was the root cause of the heater de-bonding. Prior to TVAC, the heaters had survived sine and random vibration testing with no visible de-bonding. It is likely that differential thermal expansion between the aluminum housings and poorly bonded Kapton film heaters caused the separation during TVAC.

To recover from this anomaly, Subject Matter Experts were consulted, and an improved technique was implemented to first remove the existing heaters carefully, properly prepare surfaces for bonding, and attach heaters using thermally conductive epoxy, rather than PSA.

The improved heater installation technique was used on the two heaters on the drill head housing, which are both bonded to curved surfaces. Heaters on the Feed and Deploy actuators also exhibited a small amount of de-bonding after TVAC, however it was determined that removal and re-work of these heaters would introduce too much risk, due to significant harnessing re-build and resulting schedule impact if the heaters were damaged during removal. Since these heaters were installed on cylindrical actuator housings, they were mechanically reinforced with a number of wraps of lacing cord. Flat heaters mounted on the Lower Launch Lock housing also experienced issues with the perimeter staking, with a number of epoxy beads exhibiting cracks. For these flat heaters, the PSA seemed to still be intact. These heaters were removed and re-installed using the same technique.



Figure 10. Lower Launch Lock Heater Staking Issues

After reworking the heaters on both TRIDENT units, each mechanism successfully completed their respective thermal cycling campaigns, and were closely inspected afterwards. No further de-bonding or epoxy cracking issues were observed. The lesson learned is to always use proper surface preparation techniques prior to heater bonding. It is highly recommended to completely remove any surface coatings and expose the base metal (e.g., black anodize in this case). This should be planned for during design and procedure development. If possible, masking of heater bonding surfaces during plating processes should be considered, to minimize grinding and sanding work required after receiving parts. For aluminum, it is important to perform bonding of heaters as quickly as possible following coating removal and cleaning. This minimizes the formation of aluminum oxide, which creates a poor adhesive joint to the base metal. The technique and polymerics used in this system worked well for this application, although it should not be assumed that it will work for all applications. For example, extremely low temperature cryogenic applications may not benefit from this technique due to the difference in thermal expansion coefficient between the thermally conductive epoxy and the housing. In the case of wire-wound heaters mounted to curved surfaces, it is recommended that Pressure Sensitive Adhesive not be used for bonding, even with proper surface preparation technique. Foil-etched Kapton heaters are significantly more forgiving when conforming to curved surfaces and should be used if heater power requirements allow for it. While PSA was not tested on a properly prepared surface, wire-wound heaters are very difficult to hot form to perfectly match the shape of the curved surface. There will likely be residual gaps between the heater and the housing where the PSA does not come into good contact. Depending on the shape of the curved surface, it may be very difficult to clamp the heater and ensure even pressure during PSA application and curing.

Spring Cam Percussion Mechanism

TRIDENT uses a spring-loaded hammer and helical cam to create percussive impacts at the top of the drill string. The design was adopted from the Apollo Lunar Surface Drill (ALDS), with significant modifications to allow for operation under vacuum conditions, since the ALDS percussive system was enclosed in a nitrogen gas filled chamber. The percussive wave travels down the length of the drill string during drilling and creates an impact force at the tungsten carbide cutting bit, which helps to fracture and allow penetration into hard rocks such as basalt. As shown in Figure 11, the Percussive Cam Assembly consists of a helical cam system which is driven by a brushless DC actuator and supported by a pair of angular contact bearings. As the cam rotates, it raises the Percussive Follower Assembly, preloading it against the Percussive Spring. The Percussive Follower Assembly and Percussive Hammer are mounted to a commercial Ball Spline mechanism, which allows linear motion while constraining rotation of the shaft. When the Follower reaches the end of the Cam, it is suddenly released, allowing the potential energy in the spring to force the Percussive Hammer into the Drill String Anvil, initiating the percussive wave.

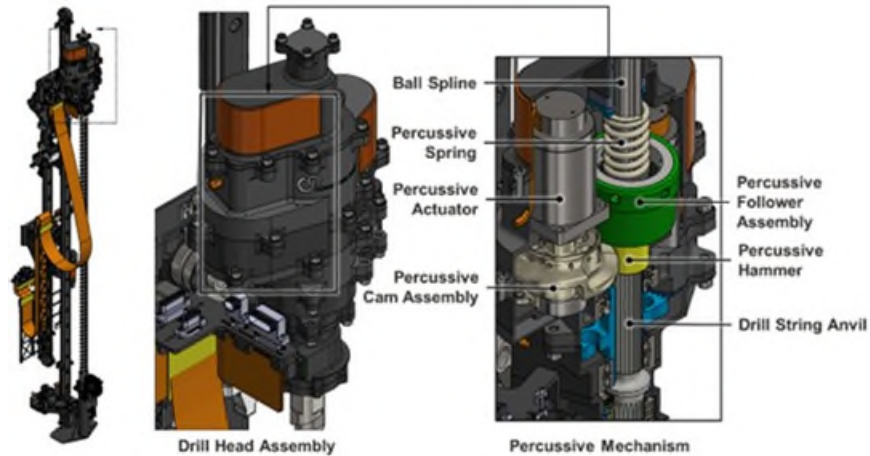


Figure 11. Percussion Mechanism Design

During drill mechanism TVAC, the TRIDENT percussion mechanism was actuated during an Abbreviated Performance Test at -70°C . During this test, the percussion mechanism was unable to function, with the actuator stalled at its maximum current limit. After the first occurrence of this issue while in TVAC, a number of tests were run during subsequent TVAC cycles to characterize the performance at periodic temperature intervals during the thermal ramp-up process. Attempts to actuate the percussion mechanism were performed at 10°C increments from -70°C to $+20^{\circ}\text{C}$. It was found that successful operation of the percussive mechanism only occurred at 0°C or warmer.

The team considered a number of possibilities as root cause for this issue, including the following.

- Increase in lubricant viscosity in Percussive Actuator gears and bearings
- Increase in lubricant viscosity in Percussive Cam Bearing
- Increase in lubricant viscosity on surface of Cam and Follower
- Increase in lubricant viscosity at Hammer Ball Spline
- Percussive Spring too stiff
- Thermal Expansion at Cam Bearing
- Thermal Expansion at Hammer Ball Spline

The system uses Braycote 601EF as a lubricant, which has a useful temperature range as low as -80°C . While Braycote is known to increase in viscosity as temperature decreases, the fact that the mechanism stalled at a temperature well above the useful lubricant temperature limit suggests that lubricant viscosity is not the primary contributor to the consistent stalling of the system below 0°C . It is also unlikely that thermal expansion of the angular contact pair (Cam Bearing) is a significant factor. Thermal expansion analysis had been performed on this bearing, and showed positive clearance between the bearing, shaft, and housing across the entire operational and survival temperature ranges. These bearings were lubricated using a 50/50 mix of Braycote 601EF grease, and Brayco 815Z oil (Herman & Davis, 2008) intended for highly loaded, long-life bearings. The Percussive Spring stiffness was measured at the component level, as well as during assembly of the drill head, and found to be in agreement with the intended spring rate. While spring material properties do change at extreme temperatures, it is unlikely that a reduction in temperature of $\sim 20^{\circ}\text{C}$ would result in a drastic change in spring stiffness.

While the exact root cause is still unknown and may be a combination of all of the previously discussed factors, it is suspected that the primary contributor is thermal expansion of the linear ball spline mechanism which supports the percussion hammer mechanism. This mechanism is likely causing the excessive friction in the system at reduced temperature. The commercial off the shelf ball spline comes with an outer race and a shaft with grooves for the balls to roll in. The commercial shaft was modified to allow for mounting of the Percussive Follower Assembly and Percussive Hammer. The shaft was also partially bored out to reduce mass.

During system-level analysis, it was assumed that the ball spline subassembly would thermally expand and contract at the same rate, since all components are stainless steel, so a detailed analysis was not performed to investigate the relative expansion of the spline, balls, and shaft. It is possible that slight differences in material properties between these components are causing just enough interference at reduced temperature to cause the consistent stalling of the percussive mechanism.

The lesson learned is to perform early breadboard testing to determine torque requirements at temperature for a helical cam-style mechanism, or any mechanical system where torque can vary widely across the rotational range. In addition, linear ball spline mechanisms should be carefully analyzed for thermal expansion, and tested early in the program if possible, particularly if using commercial off the shelf components. For the TRIDENT program, requirements for percussion actuator design were developed very early in the drill mechanism design phase, without any breadboard activities. These torque requirements were based on motor current data obtained from previous Engineering Test Unit percussion mechanisms in ambient conditions. Motor current was converted to torque using COTS motor catalog torque constants and used to define requirements for the Honeybee Robotics designed percussion actuator. Minimal effort was put into the implications of reduced temperature on increasing torque drag on the system, as this was thought to be a secondary effect on drag torque compared to the mechanical resistance of the helical cam spring mechanism itself. It is likely that some combination of thermal expansion and lubricant viscosity is providing just enough drag torque to prevent motion of the percussion assembly below 0°C. Lubricant exists in the cam bearings, ball spline, actuator bearings and gears, as well as on the surface of the cam and follower. If early breadboarding had been performed, it may have resulted in increased volume and mass being allocated to the Percussion actuator, allowing for a larger actuator with greater torque capacity at the desired speed. During mission operations, this will be mitigated by spending additional time warming the mechanism to operational temperature.

Conclusion

The Regolith and Ice Drill for Exploring New Terrain (TRIDENT) is a one-meter class drilling system that will operate on the Lunar surface as a part of the Polar Resources Ice Mining Experiment-1 (PRIME-1) and Volatiles Investigating Polar Exploration Rover (VIPER) missions. The primary purpose of TRIDENT on the PRIME-1 and VIPER missions is to physically excavate regolith from the lunar subsurface and deliver it to the surface for remote sensing instruments to analyze.

A number of issues were discovered during the assembly and testing of the two flight TRIDENT drill mechanisms, resulting in lessons learned that may be useful for future spacecraft mechanism designers. A seemingly insignificant gap between the faces of a launch lock cup and cone interface caused a Frangibolt fastener to prematurely rupture during a sine vibration test. This gap caused the Frangibolt fastener to be placed in reverse bending during the test, ultimately leading to fatigue failure. After eliminating this gap, subsequent vibration testing had no further issues. Frangibolts are very common release mechanisms used in the spacecraft mechanisms community, and care should be taken to minimize moment loading on Frangibolt fasteners.

Needle Roller Bearings used in a cam roller configuration fractured during vibration testing. These bearings are not meant to be highly loaded without first being pressed or installed into a housing for structural support. The thin outer race of the bearing fractured under repeated loading, despite having been designed to catalog dynamic load ratings. The needle roller bearings were replaced with bushings in the TRIDENT upper launch lock to eliminate this potential issue. Thin-section bearings should not be used as a “cam” device in any highly loaded mechanism unless it is supported by a thicker-walled housing that can react that load.

Kapton Film heaters applied to anodized coatings de-bonded during thermal cycling. This was due to lack of proper surface preparation, as well as applying heaters to curved surfaces using Pressure Sensitive Adhesive. It is highly recommended to completely remove any surface coatings and expose the base metal prior to bonding. This should be planned for during design and procedure development. In addition, Pressure Sensitive Adhesive is not recommended for wire-wound heaters bonded to curved surfaces, as

hot-forming of these heaters does not always perfectly match the contour of the bonding surface, resulting in gaps where the PSA is not in contact.

An early assumption of isothermal expansion of a commercial off the shelf ball spline mechanism may have primarily contributed to consistent stalling of the percussive mechanism at temperatures below 0°C. Early prototyping should be performed when designing any mechanism that has a highly variable torque profile over the stroke of the mechanism. Linear ball spline mechanisms should be carefully analyzed for thermal expansion and tested early in the program if possible.

Acknowledgements

TRIDENT is the result of numerous technology development efforts over the past two decades at Honeybee Robotics. Dozens of individuals have made significant contributions to the design, assembly, testing, and integration of TRIDENT for the PRIME-1 and VIPER missions. The authors would like to thank all of the TRIDENT program technicians, support staff, engineers, and management at Honeybee Robotics, as well as all PRIME-1 and VIPER personnel from NASA Kennedy Space Center (KSC), NASA Ames Research Center (ARC), NASA Glenn Research Center (GRC), and NASA Johnson Space Center (JSC) who have helped make TRIDENT a reality. The authors would specifically like to thank Jackie Quinn and Chris Johnson from NASA KSC, Julie Kleinhenz from NASA GRC, and Dan Andrews, Ryan Vaughan, and Brian Healy from NASA ARC for their technical and programmatic support of TRIDENT during its development.

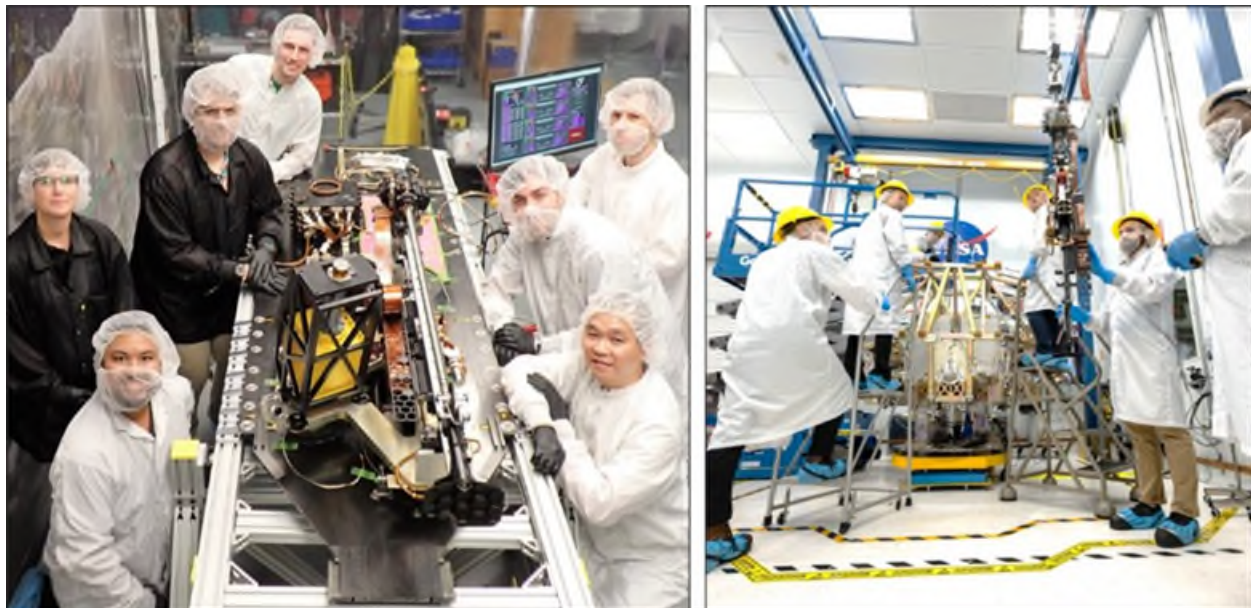


Figure 12. TRIDENT Integrated with Intuitive Machines Nova-C Panel (Left).
TRIDENT integration into VIPER Rover (Right)

References

1. Aguilar-Ayala, R. (2023). Mass Spectrometer Observing Lunar Operations (MSoLo). *71st ASMS Conference on Mass Spectrometry and Allied Topics*. Houston, TX.
2. Andrews, D. (2023). V I P E R: SYSTEMS INTEGRATION STATUS. *74th International Astronautical Congress (IAC)*. Baku, Azerbaijan.
3. Herman, J., & Davis, K. (2008). Evaluation of Perfluoropolyether Lubricant Lifetime in the High Stress and High Stress-Cycle Regime for Mars Applications. *39th Aerospace Mechanisms Symposium*. Marshall Space Flight Center.

4. King, I. (2024). A Technique For Using The TRIDENT Lunar Drill Footpad to Measure Modulus of Subgrade Reaction of Regolith on Upcoming South Pole Missions. *Lunar and Planetary Science Conference*. Houston, TX.
5. Kleinhenz, J., Paulsen, G., Zacny, K., & Smith, J. (2015). Impact of Drilling Operations on Lunar Volatiles Capture: Thermal Vacuum Tests. *SciTech 2015*. Kissimmee, FL .
6. Quinn, J. (2023). Polar Resources Ice Mining Experiment-1 (PRIME-1) NASA's First Polar Drilling and Volatiles Detection Mission. *Space Resources Roundtable XXIII Meeting* . Golden, CO .
7. Roush, T. L., & Colaprete, A. (2021). The Volatiles Investigating Polar Exploration Rover (VIPER) Near Infrared Volatile Spectrometer System. *Lunar and Planetary Science Conference*. Houston, TX.
8. Zacny, K., & Chu, P. (2021). TRIDENT Drill for VIPER and PRIME1 Missions to the Moon. *Lunar and Planetary Science Conference*. Houston, TX.
9. Zacny, K., & Chu, P. (2024). Development of TRIDENT Drill for Ice Mining on the Moon with NASA PRIME-1 and VIPER Missions. *ASCE Earth and Space*. Miami, FL.

Micro-Sampler: A Kilogram-Class Drill for Planetary Sampling and Powder Collection

Nicklaus Traeden*, Kathryn Bywaters*, Philippe Sarrazin**, Maite Diez**, Damien Hackett*, Gabriel Zwilinger*, Christian Sipe*, Peter Pulai* and Kris Zacny*

Abstract

Sampling on planetary surfaces is an integral part of mission operations, as samples can provide an insight into various geological and mineralogical characteristics and can ground truth data collected from orbit. The Micro-Sampler drill is a sub-kilogram sampling system capable of collecting precise amounts of powder from holes drilled in in-situ rocks, including saddleback basalt, and from unconsolidated materials such as loose sand. The system has gone through multiple design iterations, recently arriving at the TRL6 model. Various types of testing in baseline materials have been conducted along with wear testing and overburden testing. In this paper the mechanism design, testing results, and next steps are presented.

Introduction

Honeybee Robotics has developed and tested Micro-Sampler, a lightweight drill and sample collection system for investigating planetary surfaces. Micro-Sampler was designed as subsystem of a PICASSO project lead by Philippe Sarrazin at the Search for Extraterrestrial Intelligence (SETI) Institute to create a small instrument that could collect powder for X-ray diffraction (XRD) and X-ray fluorescence (XRF) analysis. The CheMin XRD/XRF instrument was deployed on Mars Science Laboratory (MSL) since 2012 and allows determination of sample mineral composition and relative mineral abundance [1]. CheMin as-designed is restricted to Flagship-class missions due to its size, mass, and power, as well as its reliance on a heavy and mechanically complex sample collection system. Miniaturization of the sampling systems allows deployment of XRD/XRF on smaller rovers (Mars Exploration Rover type) or other similar sized exploration architectures.

This paper will discuss the development and testing of the Micro-Sampler, detailing the drill architecture, powder funnel collection system, and sample release mechanism. Testing has been performed on a TRL4 model of the drill and a TRL6 build in a vacuum environment. Sections covering testing will detail the drilling results into various substrates including 105 MPa saddleback basalt, wear and lifetime testing into basalt, and characterization of overburden collection in the powder funnel design. Next steps will be discussed in the paper conclusion.



Figure 1. Image of the Micro-Sampler with items shown for scale. This assembly weighs 0.9 kg.

* Honeybee Robotics, Altadena, CA

** SETI Institute, Mountain View, CA

Micro-Sampler Drill Mechanisms

The Micro-Sampler is a rotary-percussive drill actuated by two brushless 28 V DC motors. One motor turns the drill string and drill bit, and the other motor actuates a lead screw to move the drill body along guide rails in the axis of the bit, or z-axis. Weight On Bit (WOB) is generated by loading the drill bit into a rock using the z-stage. An internal percussion dog clutch system is activated once there is enough WOB generated to compress an internal spring. This percussion provides a kinetic impact that travels down the drill string to break up the rock during drilling. A powder funnel collection system preloads against the cuttings pile generated during drilling to contain a precise amount of sample. This sample is released from the funnel by employing a fourbar mechanism actuated by the z-stage at the top of the lead screw's range of travel. The entire two actuator system is intended to be used on an end effector that can preload into the drill surface to counteract the WOB loads. External components are identified in Figure 2.

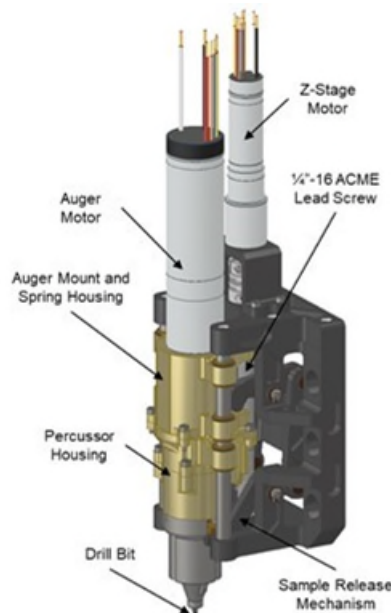


Figure 2. Micro-Sampler TRL6 CAD, detailing the major elements

Rotary Percussive Drill

The rotary drill system is driven by an axially mounted BLDC auger motor. This motor is coupled through a spline interface to a drill string that rotates with a drill bit. The drill bit is a 1/8-inch (approximately 3 mm) diameter commercial masonry bit. This size was derived from project requirements to be able to target small geological features such as a vein or nodule in a larger rock or outcrop without collecting large percentages of surrounding material. The drill body consists of a spring housing that doubles as the auger motor mount, and a percussor housing. This body is translated along guide rails using a lead screw driven by a second, smaller BLDC motor. Bronze bushings are located within the housings to provide lubricity on the guide rails and are match drilled as an assembly to avoid binding issues.

The Micro-Sampler utilizes a dog clutch system in conjunction with a Belleville spring stack to provide the percussive impact energy to break up the rock. This percussive system participates when the WOB is high enough to compress the percussion engagement spring, causing the two halves of the dog clutch to contact each other shown in Figure 3. These two elements have a matching lobe tooth profile that can be seen in Figure 3. An upper dog clutch element is held by the percussion housings and not allowed to rotate while the lower dog clutch is affixed to the drill string and rotates with the drill bit. As the drill string rotates the lobes of the dogs slide against each other and force the upper dog (shown in green in Figures 2 and 3) up, along with the entire percussion housing assembly, into a Belleville spring stack located in the spring housing. Fast rotation of the drill string allows a gap to form when the peaks of the lobes are cleared,

allowing the springs to discharge and push the percussion housing and upper dog clutch into the drill string and lower dog, creating an impact. This impact travels down the drill string, through the drill bit, and into the rock. This percussion continues while the weight on bit remains at the minimum threshold required. If not, the dog clutches return to their unloaded state, thus enabling rotary only drilling.

The percussor housing elements and the upper dog clutch form the percussive mass. The total energy per blow is dependent on the percussive mass, the Belleville stack spring rate, and the total axial displacement induced from the dog clutch, which varies depending on rotary speed and WOB. The spring stack was selected to provide enough impact energy to break up saddleback basalt. The spline profile in the motor coupler allows the drill string to move axially relative to the auger during WOB loading. Dog-bone elements on the spring housing engage with a lip feature on the percussion housing and keep the Belleville springs slightly preloaded. Multiple cam tooth profiles were investigated while performing design trades, and a symmetrical lobe was chosen for increased functionality over a more standard sawtooth design for the sample release.

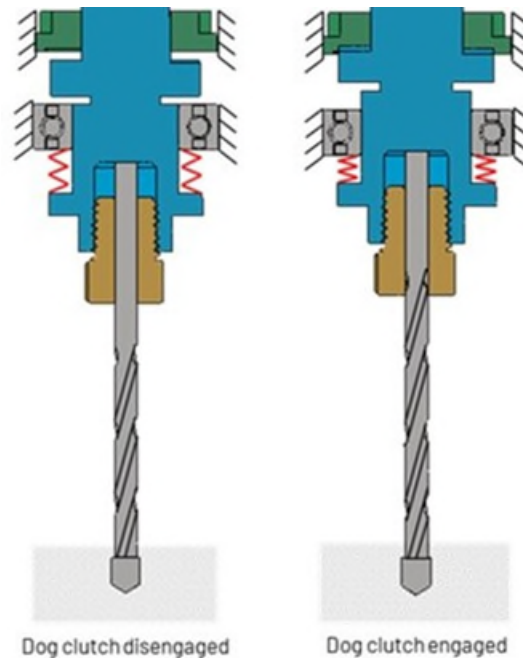


Figure 3. Section views of the percussive dog clutch mechanism.



Figure 4. (left) Sawtooth dog elements extracted from a commercial drill machine. (center) Image of the lobed dog clutch in the percussor housing. The dog element on the left rotates with the drill string shown in blue in the CAD section view (right). The upper dog (green) is constrained by the percussor housings (orange and red).

Powder Funnel Collection System

Sample collection and containment with the Micro-Sampler is achieved through the powder funnel collection system. This system consists of three elements that sit around the drill bit: the powder funnel, an engagement spring, and a mount element. During initial drilling the bit starts a hole and creates a cuttings pile on the surface of the rock. Further z motion from the drill preloads the powder funnel into the initial cuttings, and subsequent cuttings are forced up the auger flutes into the conical area around the drill bit, as shown in Figure 5. The narrow clearance between the shank of the drill bit and the lower ID of the powder funnel, in addition to the granular behavior of the cuttings, keeps sampled material in the funnel during drill motion to a deposition site. Counter rotation ribs allow the powder funnel to translate but keep it from catching on the spinning bit. The intended XRD / XRF analysis system is highly sensitive to overfill, so holes in the side of the funnel and an internal shelf have been added to the design to precisely control the volume of collected material. The Micro-Sampler can also use the powder funnel to collect unconsolidated material like sand or dust deposits. In these operations the drill processes into the unconsolidated area without rotating to a sufficient depth as to compress the powder funnel engagement spring. Then slow rotation of the drill will migrate existing particulate matter into the funnel, as demonstrated in Figure 6. Powder collection on slanted or natural surfaces is highly positionally dependent with the current design. Additionally, powder collection is rate dependent as moving too slow in hard materials will allow the powder to shake out of the funnel and cuttings pile during heavy percussion. Initial testing with the TRL4 and TRL6 drills used a semi-translucent 3D printed material to allow for easy inspection and troubleshooting. Vacuum testing replaced these test units with thin-walled aluminum versions with validation of fill being accomplished by watching for powder material falling out of the side holes. Future development of the powder funnel will allow for collection on more uneven surfaces and will investigate collection of more exotic materials.

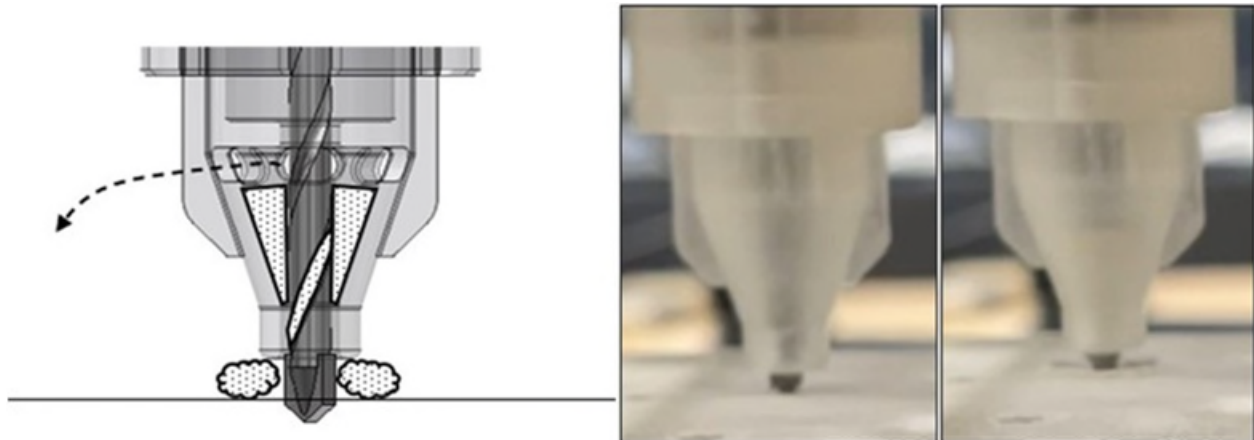


Figure 5. CAD diagram of TRL6 powder funnel operation (left). Powder fill before and after a TRL4 drill test into limestone (center and right).



Figure 6. Simulant collected from a vial of unconsolidated material (left). Powder collection is possible on natural surfaces, but current system design is positioning dependent (right).

Sample Release Mechanism

Once the Micro-Sampler has finished a drilling profile or collection of unconsolidated material, it is retracted from the hole and moved into position above a sample inlet port. It was determined through testing that simply running the drill in reverse was not sufficient to discharge the powder contained in the powder funnel. A brass thrust plate was added to the bottom of the drill in which a sufficient vertical load applied to its arms pushes through the drill string to engage the percussion dog clutch as shown in Figure 7. Percussive shocks coupled with reverse spin are highly effective at dropping all of the contained sample from the powder funnel. This behavior is why the symmetric lobe dog profile is preferable over a direction biased sawtooth profile. Activation of this force could be accomplished with drill motion into a static element above the drop point, but an internal solution was devised to avoid any load constraints or keep out zones that the instrument sensor area may have. A rapid prototype fourbar mechanism was implemented on the TRL4 drill that actuates the thrust plate into the percussion system at the top of z-stage travel, shown in Figure 7. A more robust fourbar was developed for the TRL 6 drill that saves volume by nesting around the z-stage, shown in Figure 8. A guide feature on the drill keeps the fourbar out of the way of the auger during drill operations. A gas puff discharge system was also designed to operate in microgravity environments such as asteroids.

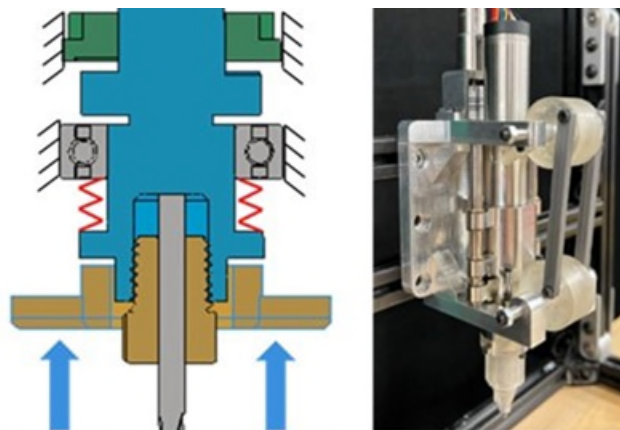


Figure 7. CAD section view depicting force action on thrust plate for percussor activation (left). TRL4 prototype fourbar mechanism to engage percussion during sample discharge (right).

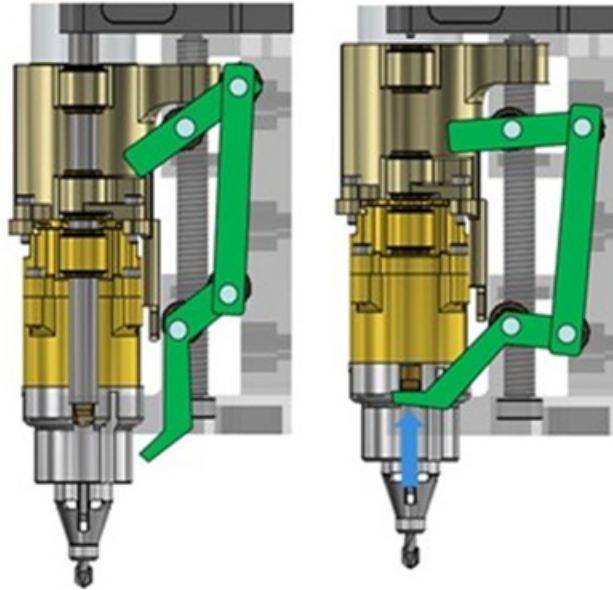


Figure 8. TRL6 sample release mechanism CAD with mechanism disengaged (Left), engaged (Right). Elements made transparent for clarity.

TRL4 Model Test Campaign

A test campaign for the TRL4 Micro-Sampler was conducted during 2022 and 2023. Initial baseline drilling tests were conducted with a variety of materials with different hardness values (Aircrete, Gypsum, Sandstone, Limestone, Concrete, and Saddleback Basalt). These different materials were selected to evaluate and document the baseline performance for the drilling system. One of the primary goals of these tests was to evaluate which auger velocities and z-stage feed rates were most efficient for each material. From this performance data, we aimed to evaluate the amount of auger power required to collect specific amounts of sample from each material. The system behavior for multiple materials can be seen in Figures 9 through 12. In each of the tests, the auger was commanded to its maximum value of 2000 RPM and the z-stage commanded to process downward at a constant rate. In each of the plots the mechanism behavior can be inferred from the auger motor current data in five main phases noted in Figure 9. The free spinning current can be seen initially as the drill is turned on before contacting the rock while the z-stage moves down at a constant rate. The current ramps up as the WOB is increased from the z-stage, increasing frictional forces on the bit. At slightly over 2 A it can be inferred that the percussion system has engaged, which has been correlated to audio taken during testing. The current readings during percussion appear to be very noisy and display high oscillations when drilling into hard rock at fast speeds, shown in Figure 10. When the z-travel stops at a predetermined point the auger current drops as the borehole is cleared until the drill is retracted from the hole. In soft materials or when moving at slow speeds the percussion system may not engage as rotary drilling is sufficient to evacuate a borehole enough to keep WOB below the percussion engagement load.

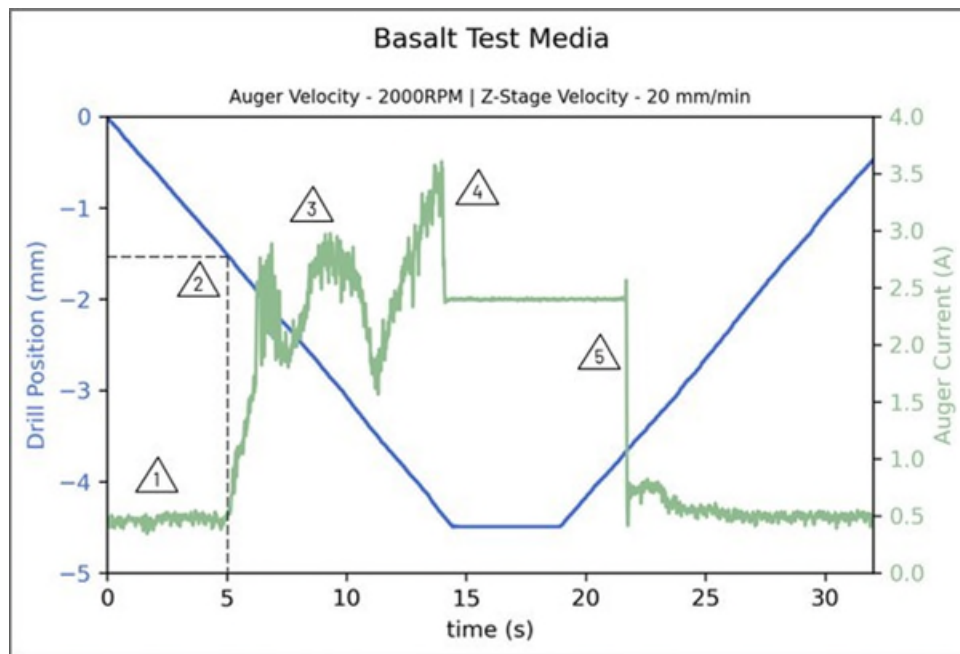


Figure 9. Plots of the TRL4 Micro-Sampler drilling into limestone (top) and non-vesicular saddleback basalt (bottom). 1) Auger spinning while z-stage is moving down at a constant rate before contact with rock. 2) Drill tip contacts the rock (~5s) and slowly increases preload to engage hammer mechanism. 3) Hammer mechanism engaged as drill cuts through rock. 4) Z stage stopped. Auger current drops as hammer spring unloads. Once hole is cleared current drops to no-load. 5) Auger is stopped and the drill is retracted from the hole. A faster z translation command into a harder material yields high oscillations in the motor current data as the percussor engages in waves and breaks up the rock.

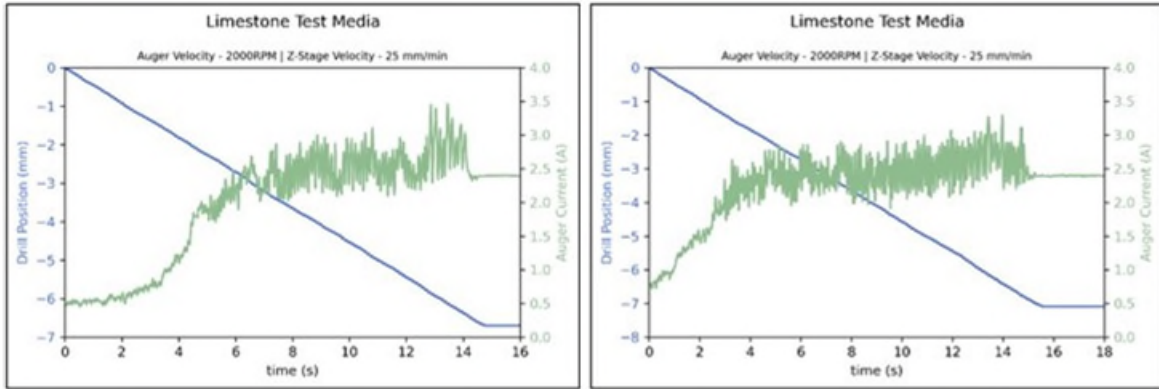


Figure 10. Drilling profile into limestone (left). Additional Drilling Profile (right).

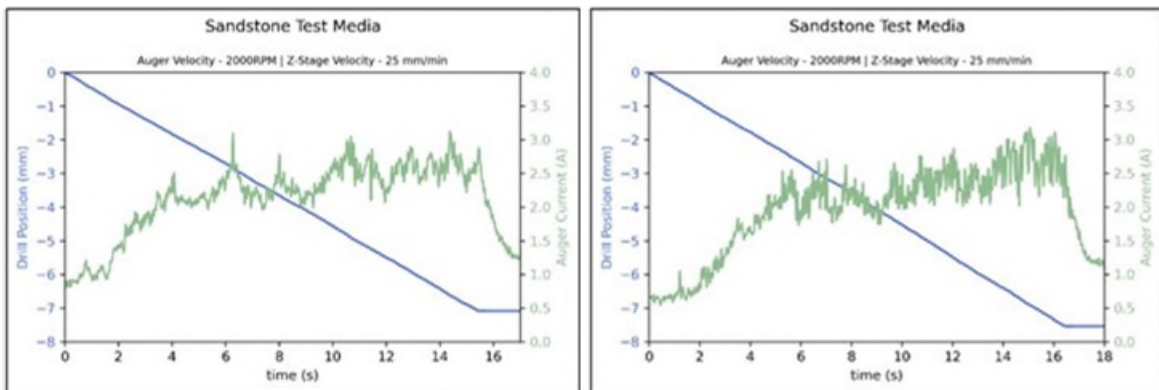


Figure 11. Drilling profile into sandstone (left). Additional Drilling Profile (right). Oscillatory behavior of the percussion system seen in the filtered data.

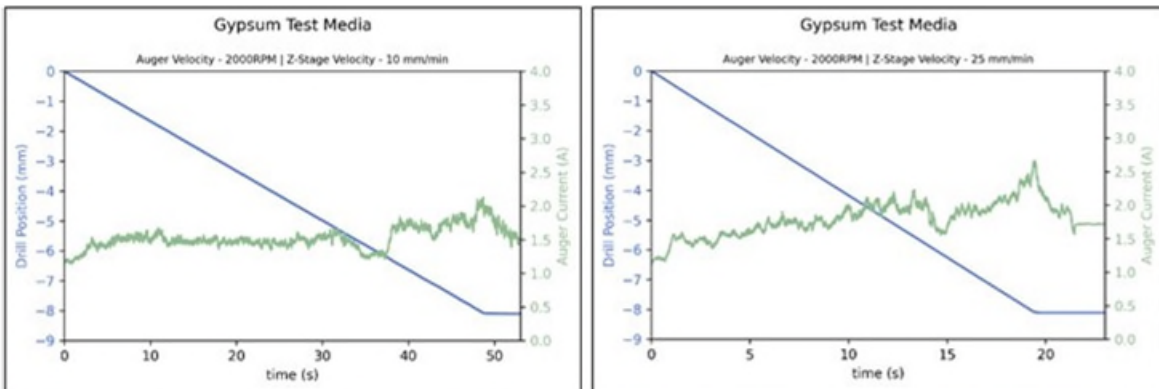


Figure 12. Drilling profile into gypsum (left). Additional drilling profile (right). Note the low current indicating the lack of engagement from the percussion system.

Several tests were run with each of the different materials to characterize the behavior and capabilities of the Micro-Sampler drill, and to test and evaluate different geometries of the powder funnel. The data received from these tests established the baseline efficiency combinations for the different materials and provided a foundation for the TRL-6 drill testing. Material collected from these drilling tests was collected and categorized for testing evaluation for the subsequent XRD / XRF system development.

Bit Wear Test Campaign

Through testing it was determined that the limiting factor for the Micro-Sampler drilling system is the drill bit. A wear campaign was conducted to evaluate the number of cycles the system can perform before the bit becomes dulled. We chose to test with our hardest material, saddleback basalt, to quantify bit life cycle using a worst-case scenario. These tests were run with an auger velocity of 2000 RPM and a z-stage velocity of 2 mm/min. The test campaign results showed that the drill can run a total of fifteen tests. Each of these tests aimed to drill down to a maximum depth before stalling. The first data point was a successful test to a depth of 15 mm, without any stalling from the auger motor. Following this, fourteen additional tests were carried out, where each of them stalled at varying depths. Each test and depth can be seen in the Fig. 8. System heat may have had an impact on subsequent drill tests. Bit life was monitored for all testing after the wear campaign and bits were replaced before they reached half of their linear drill life to ensure quality results in all future test data.

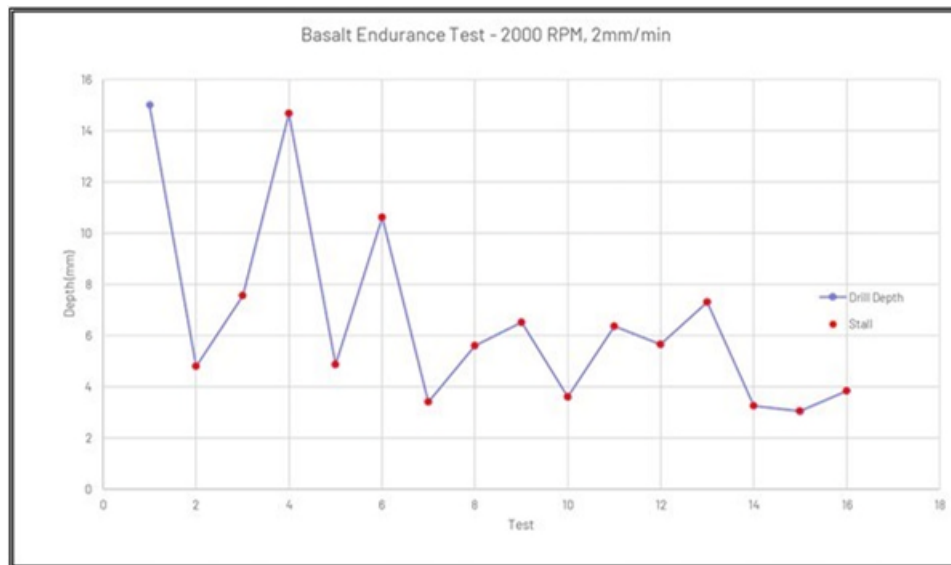


Figure 13. Drill Bit Endurance Testing

Overburden Testing

Following the initial benchtop and bit wear testing for the TRL-4 Micro-Sampler, we planned and conducted an overburden test campaign. On different planetary bodies, overburden can pose a problem for sampling and mining. Many Martian sampling targets have a weathered layer that is not of interest to planetary geologists. Collection of this layer may be minimized by altering the amount of protrusion of the base of the powder funnel. Given this background, an overburden test campaign was set-up that aimed to minimize overburden collection while maximizing sample collection. A test matrix showing the different configurations to be tested is shown in Figure 14. For overburden characterization it was vital that we could quantify how much of the overburden that we collected in our final sample.

Overburden Test Setup

To create our test media, we poured and formed a concrete block with a sloped overburden layer, which allowed us to test varying depths. The overburden layer consisted of self-leveling concrete doped with 20% iron powder (5 μ m). Initial characterization holes were drilled into the full overburden with no base concrete to quantify and validate the percentage of overburden collected with the powder funnel. Multiple tests were run and a baseline value percentage of 33% was quantified for the testing block. It is important to note that this baseline value is a bit higher than expected, as the percentage of the mixture (concrete leveler, water, and iron powder) had an iron percentage of 20%. We believe this discrepancy is due to reactions between all the different components along with the settling of the mixture.

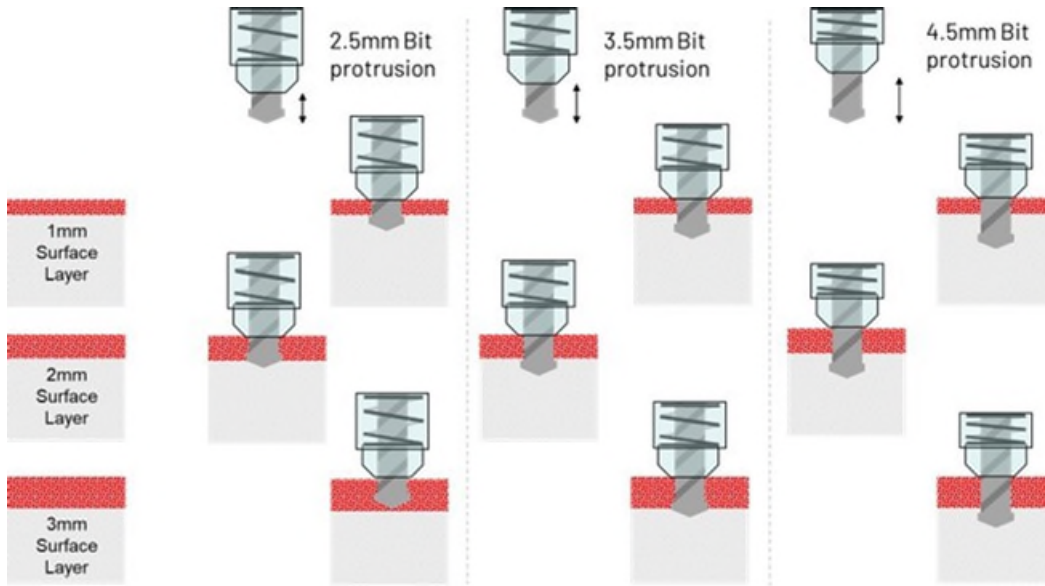


Figure 14. Chart showing varying levels of drill protrusion with respect to overburden thickness.



Figure 15. Different overburden layers shown on side profile of test media (left) and test media overhead view (right). The Micro-Sampler was used to drill holes and collect powder along the demarked lines. Controls were taken from the right side of the block, drilling only into overburden.

Overburden Sampling Analysis

Each overburden test is made up of three samples. Each test only yielded roughly 0.050 grams of material, so it became necessary to complete three tests to collect enough material for analysis. For analyzing the samples, they were first mixed with 99% IPA. Then, the mixture was put under an electromagnet separator. The rationale for the inclusion of the iron filings was to make it easily separable once mixed into an IPA solution. The separator assembly consisted of an 800 N electromagnet and a 667 N neodymium magnet. The magnets were aligned as shown in Figure 16, to attract iron. The electromagnet was pulsed to allow other collected sediments to fall out. Following iron collection, the iron samples were left out to dry and then were weighed out.

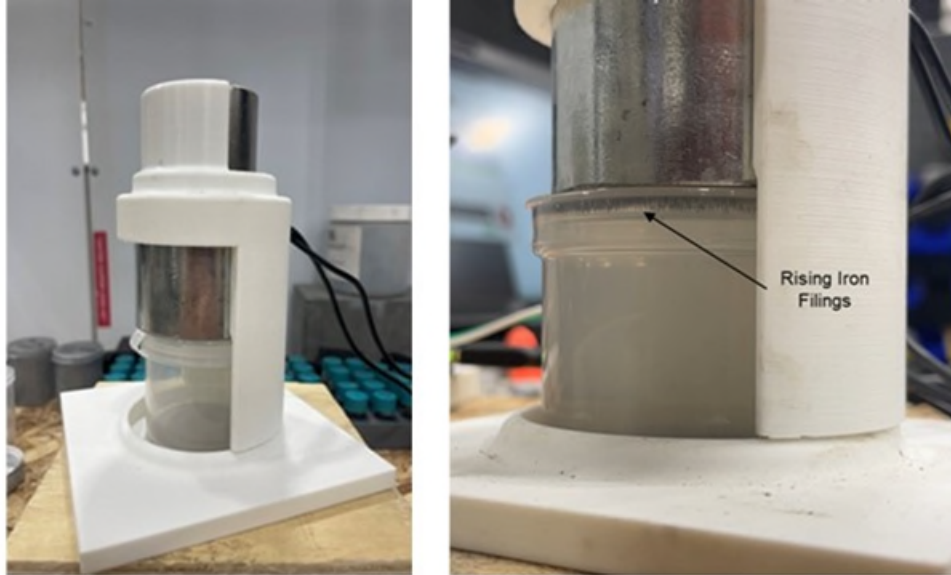


Figure 16. Magnetic separation system used for overburden testing.

The data was then analyzed and plotted to see if our measured percentage matched with that of what was predicted. Each data point on the graph is the culmination of three samples and the specified drill depth is averaged from each test. Upon analyzing the test data, a graph depicting the trend in predicted versus measured sample was generated and is shown in Fig. 17. Given the limited number of tests this data shows that the drill protrusion from the powder funnel can be designed to avoid collection of a weathered surface layer, or at least have a reasonable characterization of the quantity of overburden present in any sample. This can also be used to select material of a specified depth for sampling.

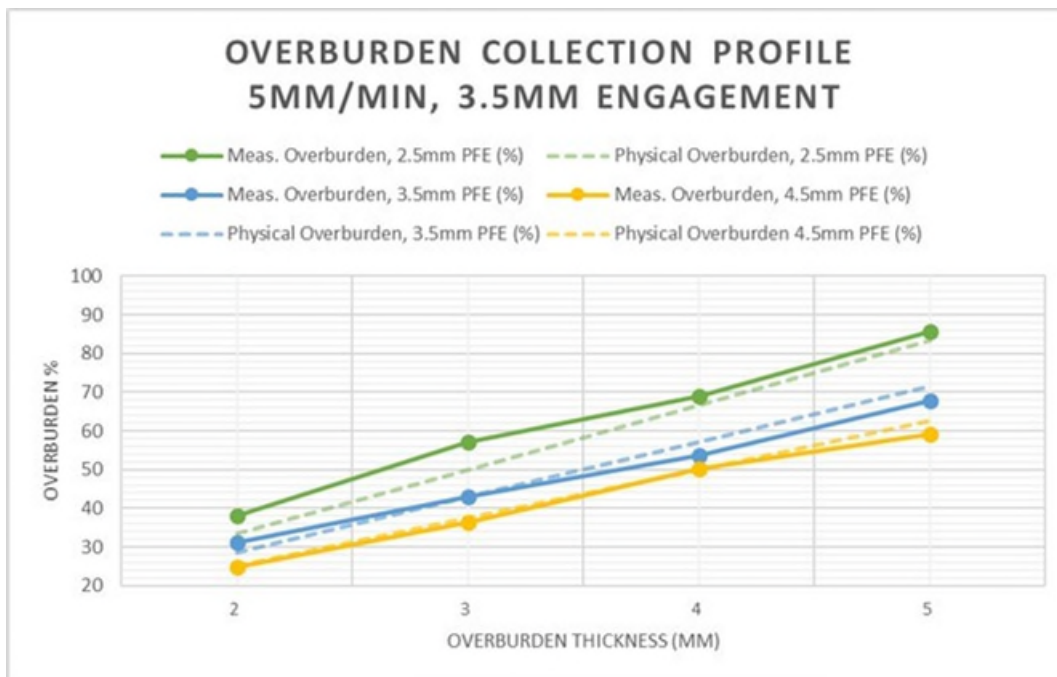


Figure 17. Graph depicting overburden percentage trend from samples collected during different drill protrusion tests.

Sample Collection Metrics

A baseline for sample collection was done to evaluate the general amount of sample collected with respect to drill depth. These tests were run with limestone and sandstone test medias at varying depths. The auger was run at a velocity of 2000 RPM and a z-stage rate of 50 mm/min and 20 mm/min respectively. The average amount of sample can be seen for both limestone and sandstone in Fig. 18.

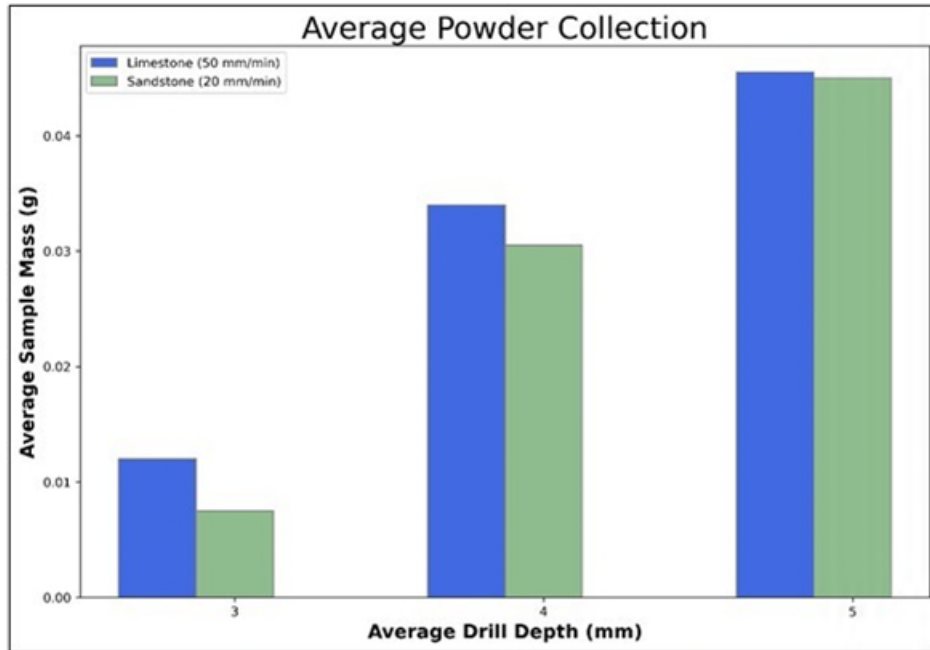


Figure 18. Average powder collection for limestone and sandstone sampling tests.

TRL6 Test Campaign

The latest version of the Micro-Sampler drilling system is the TRL6 prototype. The goal for the TRL6 prototype was to test in a vacuum environment with representative flight-forward materials. The housing elements of the drill body were machined from titanium and received titanium nitride surface treatment for abrasion resistance. The mount structure and powder release elements were machined from aluminum and type three anodized. Vacuum compatible Braycote grease is used in all bearing components in the TRL6 unit. Images of the TRL6 drill are shown in Figure 19. The total mass of the TRL6 Micro-Sampler is 0.9 kg.

Saddleback basalt, limestone, and sandstone were used to compare performance between the TRL4 and TRL6 drill models. Control experiments were done on a benchtop to validate TRL6 operation before drilling tests performed in a vacuum environment (~160 Pa or 1.2 torr). The graphs detailing performance compared to TRL4 performance are shown in Figures 20, 21, and 22. The basalt test was run at a more conservative z rate of 2 mm / min to monitor motor temperature while drilling in vacuum. A full end to end sampling and XRD / XRF analysis is scheduled before project conclusion.

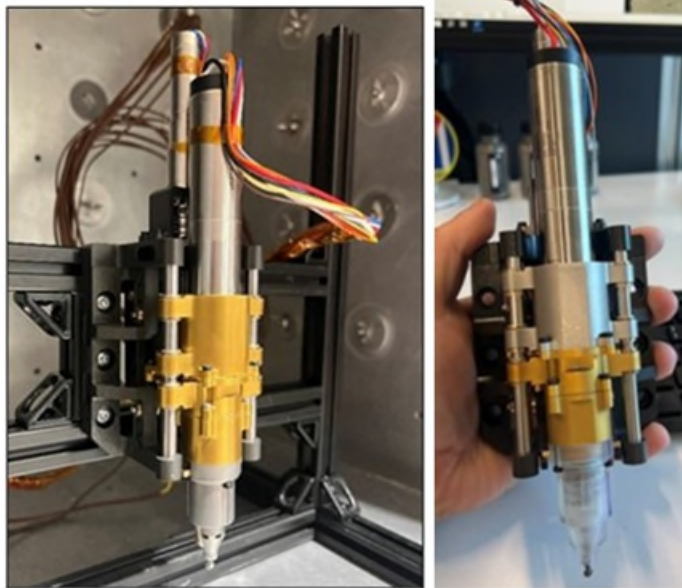


Figure 19. TRL6 Micro-Sampler set up in vacuum chamber (left). TRL6 drill held for scale (right).

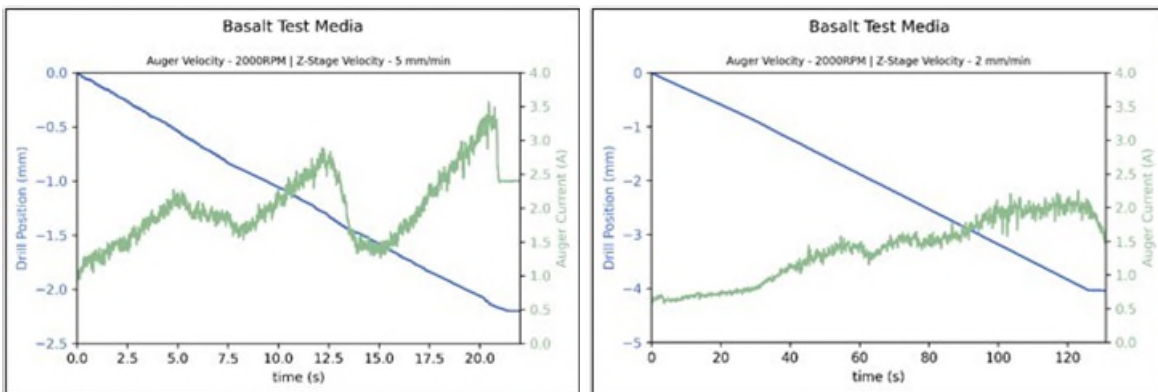


Figure 20. TRL4 test into saddleback basalt (left) and TRL6 vacuum test into saddleback basalt (right). Note the vacuum test was at a more conservative plunge rate.

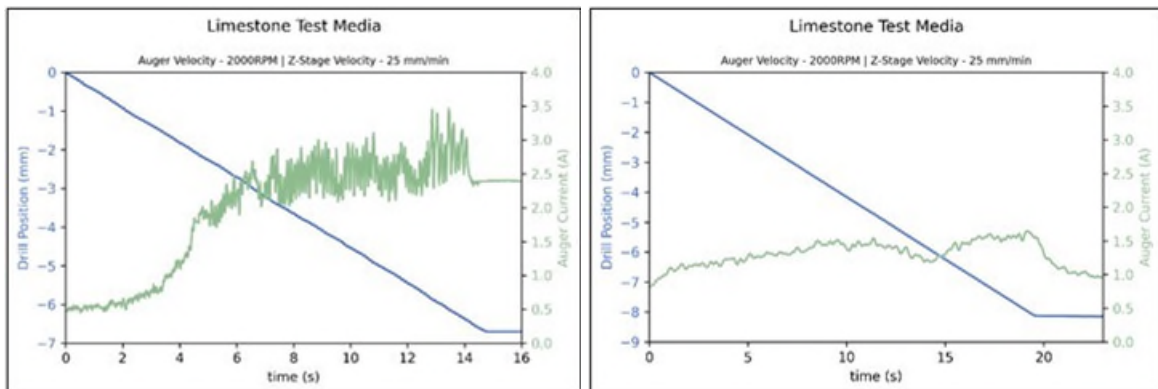


Figure 21. TRL4 test into limestone (left) and TRL6 vacuum test into limestone (right).

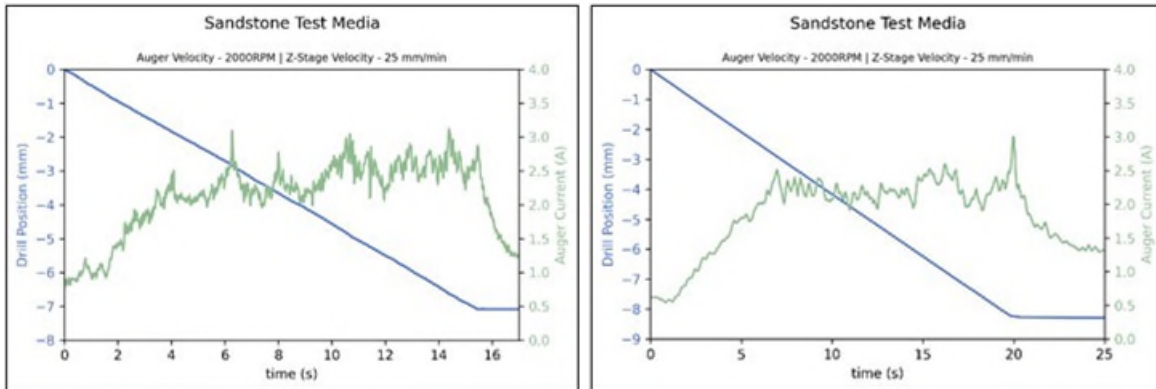


Figure 22. TRL4 test into sandstone (left) and TRL6 vacuum test into sandstone (right).

The TRL6 performance matches the TRL4 performance with respect to the different materials. On some materials (such as basalt and limestone), the TRL6 model performs better at the same parameters than the TRL4 model. This can clearly be seen with respect to the current drawn during the drilling profiles. Additionally, thermocouple data was monitored for the auger motor during operation. The auger motor nominally stays at 26°C while under vacuum and generally climbs to 29°C during drilling operations. The motor has spiked to close to 32°C during longer drilling operations (such as during the 2 mm/min profile for basalt) but is far below the motor’s maximum temperature rating.

Next Steps

A full end to end test of the drill system is scheduled before the project conclusion to deliver powder to an XRD / XRF system for analysis. Honeybee hopes to investigate improved powder funnel geometries to better collect material from natural surfaces and at odd angles. Additionally, Honeybee aims to investigate a bit change system or different bit cutter materials to extend the lifetime capability of the drill. Thermal and vibration testing may be warranted but we do not expect these to be major hurdles for this system. Temperature limits are set by the motor Hall sensors and the internal lubricants.

Acknowledgements

Honeybee Robotics has developed the Micro-Sampler in partnership with Philippe Sarrazin at The SETI Institute under subcontract for NASA’s PICASSO Grant 80NSSC20K1095 Titled: Micro-Sampling System for Mineralogical Instruments. This system is patent pending.

Conclusions

Micro-Sampler is a sub kilogram, TRL6 sample collection and delivery technology that can fundamentally change the sampling aspect of a high-level planetary exploration mission. The system can target small geologic features and can be designed to collect a precise amount of powdered material from a desired depth. Micro-Sampler’s capabilities along with the system mass, volume, and power open the door for lower class planetary science mission architectures to include mineralogy investigations.

References

1. Blake, D., Vaniman, D., Achilles, C. et al. Characterization and Calibration of the CheMin Mineralogical Instrument on Mars Science Laboratory. *Space Sci Rev* 170, 341–399 (2012). <https://doi.org/10.1007/s11214-012-9905-1>

Development of the DrACO Drill: A Rotary Percussive Drill for Cryogenic Operation

Grayson Adams*, Matthew Dottinger*, and Patrick Corrigan*

Abstract

The Drill for Acquisition of Complex Organics (DrACO) for the NASA Dragonfly program, developed at Honeybee Robotics in Altadena CA, is a rotary percussive drill designed for the collection of material from the surface of Titan. Various challenges relating to the development of the drill in an environment where heating can prove impractical are discussed. This paper presents challenges and recommendations relating to the design of dry lubed mechanism elements, particularly where conventional approaches to the use of dry lube are not feasible due to project constraints. Additionally, a novel design using thin film polymeric for a dust protection bellows is presented.

Introduction

The Dragonfly rotorcraft lander vehicle is a spacecraft designed to traverse the surface of Titan by powered flight, landing at different sites to collect and analyze local surface material. The vehicle consists of the primary spacecraft elements provided by Johns Hopkins APL, the DrACO sampling system provided by Honeybee Robotics, and various other systems and payloads. The Drill portion of DrACO sits on the exterior of the vehicle, exposed to the cold Titan atmosphere of ~ 94 K (-180°C). The DrACO drill consists of the Feed stage to provide axial motion of the drill head, the Spindle mechanism to rotate the drill bit, the Percussion mechanism to apply impact force to the back of the drill bit, and a flexible hose to connect the drill bit to the vehicle pneumatic suction system. Challenges in supplying and retaining the necessary amount of heat to support the use of wet lubricated motion elements drove the selection of dry film lubricant (DFL) for nearly all aspects of the mechanism that would normally use grease, with the exception of the drive actuators.

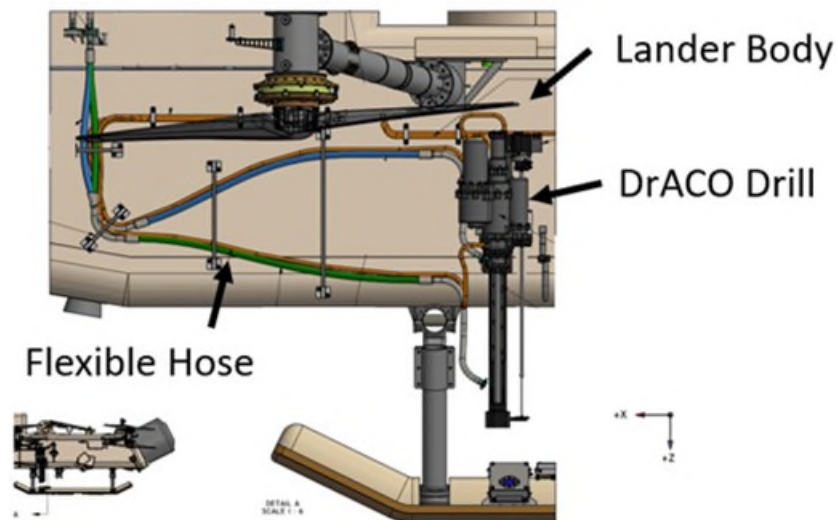


Figure 1. DrACO Drill shown on the side of the Dragonfly lander, external to the vehicle.

* Honeybee Robotics, Altadena, CA

While there are many moving parts within this system, the key challenges faced were with the Feed drive lead screw, Feed carriage rollers, Percussion support bearings, and Percussion helical cam and follower.

Feed Stage Mechanism

The Feed stage is a linear one degree of freedom (DOF) stage that moves the drill up and down, providing positioning and motive force for weight on bit (WOB) and retraction during drilling operations. The Feed is required to provide 150-N WOB (+Z) and 350-N (-Z) retraction force over a 160 mm stroke while subject to Titan conditions, most importantly a temperature of -180°C. Qualification life for the mechanism is defined as 200 bidirectional translations of the full stroke.

The Engineering Test Unit (ETU), similar to brassboard hardware, and Engineering Model 1 (EM1) were both built to these specifications. The ETU successfully completed life testing, while multiple problems were uncovered with EM1. An Engineering Model 2 (EM2), with a stroke of 300 mm for an alternate vehicle configuration, incorporates several lessons learned from the ETU and EM1 and is being built at the time of publishing this paper.

The ETU, EM1, and EM2 all have the same base design, consisting of a crossed roller carriage riding along a guide rail that constrains the carriage in 5 DOF. The carriage is driven by a kinematically constrained ACME leadscrew. The leadscrew is protected from dust with a pair of polymeric bellows and is connected through a gear pair to the drive actuator. All components, excluding the drive actuator, operate at -180°C and use DFL.

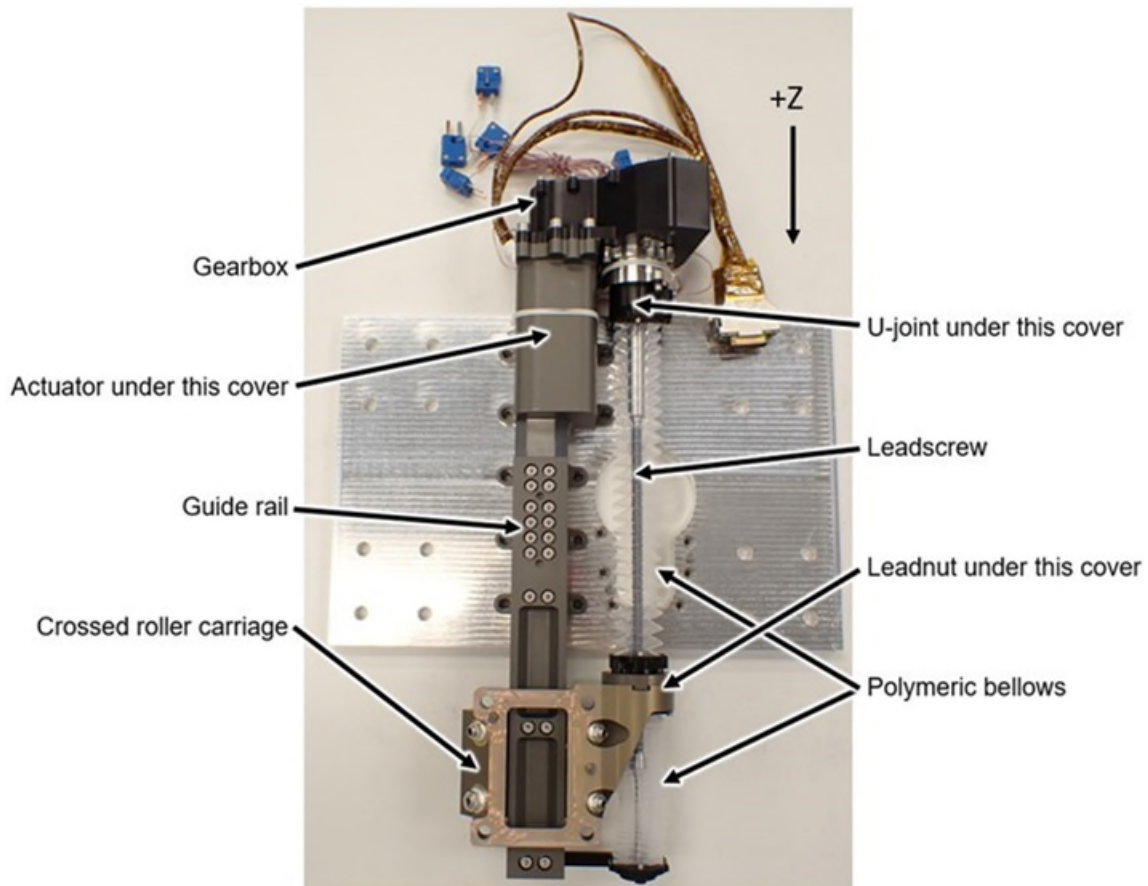


Figure 2. EM1 Feed stage mechanism.

Leadscrew Design

The leadscrew on the Feed stage uses a bonded DFL on the ACME threads of both the leadscrew and leadnut. A variety of different thread sizes, thread tolerance classes, part materials, and DFLs were tested between the ETU, EM1, and EM2 (Table 1).

Table 1. Leadscrew parameters for each build.

Parameter	ETU	EM1	EM2
Screw thread	1/4-16 ACME-2G	1/4-16 ACME-4C	5/16-14 ACME-4C
Nut thread	1/4-16 ACME-2G	1/4-16 ACME-4C	5/16-14 ACME-2G
Dry film lubricant	AS5272 Type II	iKote	AS5272 Type I
Screw Material	Nitronic 60 Level 3	Nitronic 60 Level 4	Nitronic 60 Level 4
Nut Material	C17200 TH04	C17200 TH04	Toughmet3 TX TS

The leadscrew is kinematically constrained to prevent excessive wear of the DFL and current increases at the ends of stroke caused by tolerance stackup in the mechanism. This is accomplished by connecting the output shaft to the top of the leadscrew with a universal joint (two rotational DOF) and constraining the nut with another two rotational DOF joint (spherical ball joint for ETU and EM1, universal joint style mount for EM2). The end of the leadscrew is left free.

EM1 testing showed that departures from a fully kinematic constraint condition of the leadscrew and leadnut may lead to extreme wear and premature failure when using DFL. Misalignment of the leadscrew and leadnut thread axes will cause the parts to settle into two or three edge contacts under load (Figure 4). These small contact patches quickly exceed the allowable stress of the DFL, causing it to fail in very few cycles. Once the DFL has failed, metal to metal contact at these small patches leads to rapid wear and potentially galling even with dissimilar metals, increasing drive torque.

Figure 3 shows the current telemetry for the first eight cycles of the EM1. Figure 5 shows the same screw after 15 bidirectional cycles at room temperature and -180°C at various operating/proof loads.

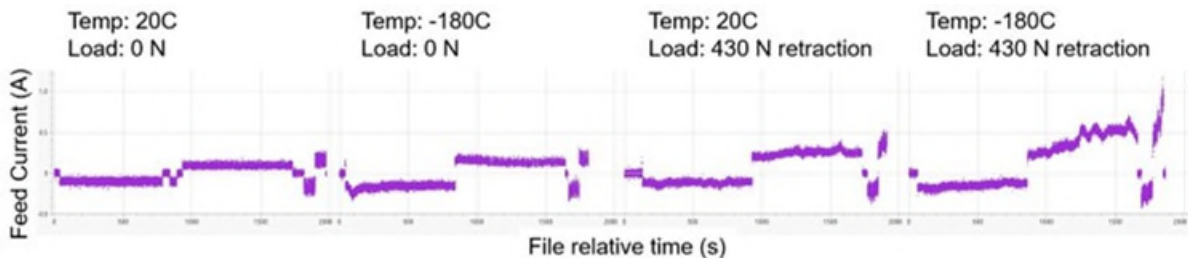


Figure 3. Current trace of first 8 cycles on EM1 leadscrew.

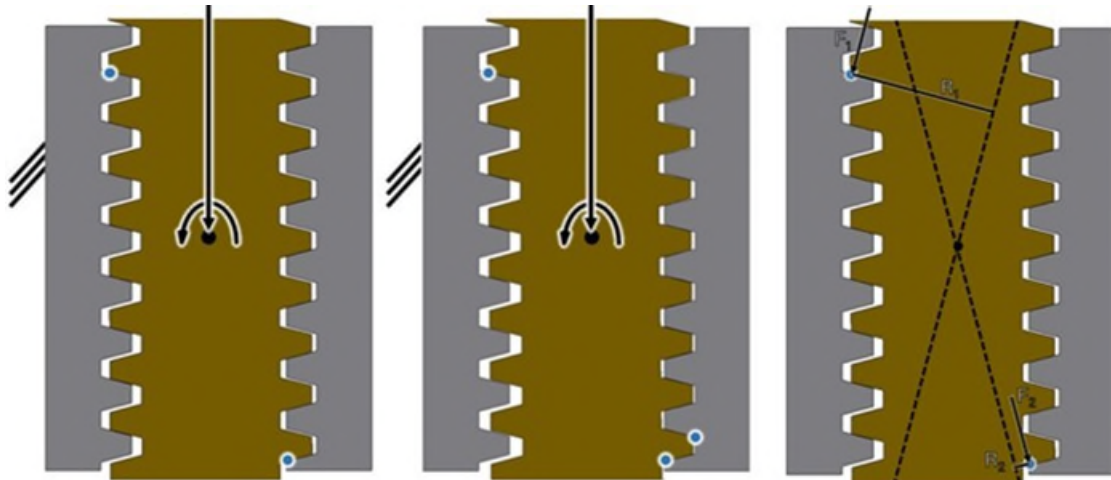


Figure 4. Cross sections of misaligned general-class ACME threads. In most cases, 2 edge contacts exist (left); at maximum misalignment, three edge contacts exist (center). Forces applied to the leadnut by a misaligned lead screw and their moment arm are the basis for determining gimbaling torque (right).

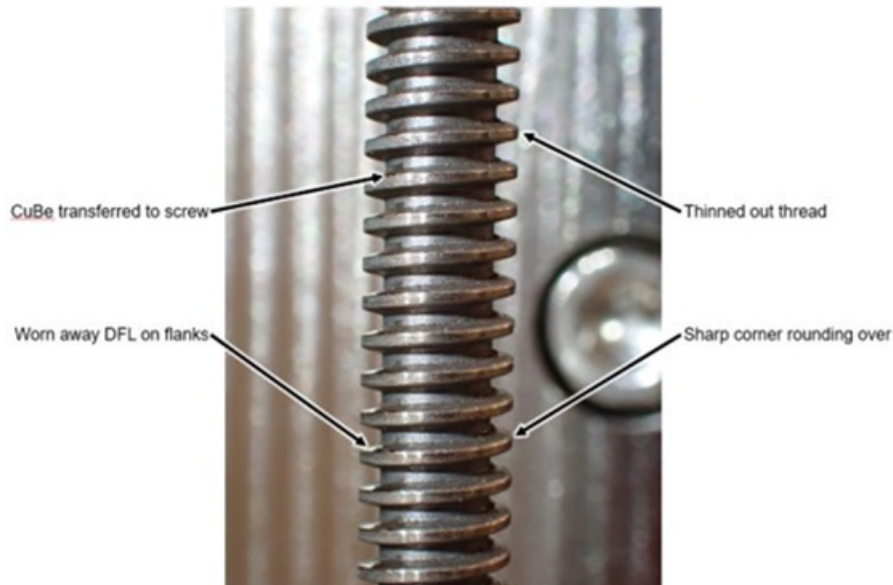


Figure 5. EM1 leadscrew after 15 cycles.

It was found that the cause of the misalignment between the EM1 leadscrew and nut was insufficient motion of the nut pivot due to high sensitivity to friction. This prevented the nut from gimbaling to self-align to the leadscrew as intended with the kinematic constraint. The EM1 leadnut is a relatively large spherical ball coated with DFL that sits in a PTFE-impregnated anodized aluminum pocket (Figure 6). After the failure, this joint was analyzed to compare the gimbaling moment provided by the pressure of the leadscrew on the leadnut threads to the resistive torque due to friction of the ball in its pocket. It was found that to gimbal the leadnut, a coefficient of friction (CoF) lower than 0.05 is required.

The ETU has a similar leadnut pivot, which requires a CoF lower than 0.06, but it did not experience the same failure as EM1 during testing to 2x life. This success is not fully understood currently. The specifications and suppliers for both the DFL and PTFE anodize were changed from ETU to EM1, and the ETU was not cleaned as thoroughly as the EM1, making it possible there was a large enough difference in tribological behavior to account for the success despite their similar geometry and fits.

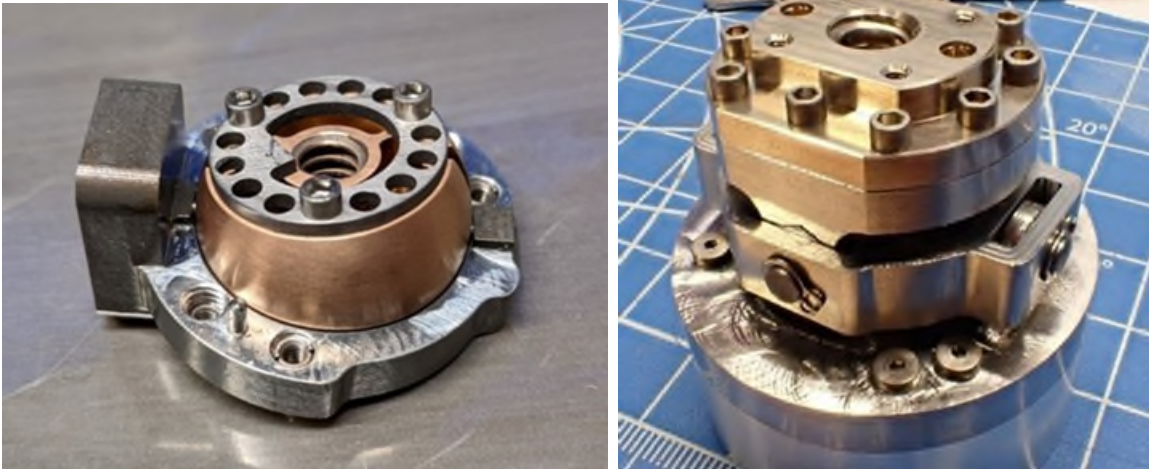


Figure 6. Comparison between ETU/EM1 style spherical joint (left) and EM2 style universal joint (right). ETU leadnut is shown before DFL in half of its mating pocket.

The EM2 was designed with small diameter pivots to decrease the resistive torque due to friction and the leadnut was lengthened to increase the provided gimbaling moment. By analysis, this joint requires a CoF lower than 1.04 to allow the leadnut to gimbal. While performing a run-in of the EM2 leadscrew and leadnut, no signs of wear or galling were observed where they were observed on EM1.

The analysis to determine whether a leadnut will gimbal can be summarized by a relationship: the gimbaling torque provided by the pressure of the leadscrew threads on the leadnut threads must be greater than the resistive moment due to friction of the pivot. While the resistive moment due to friction depends on the specific pivot design, the provided gimbaling torque can be calculated with the following technique. As shown in Figure 4 (left), when misaligned, the leadscrew typically contacts the leadnut in two places. The forces the leadscrew applies to the leadnut at these two locations can be seen on the right. These forces, acting through moment arms to the center of rotation of the leadnut, provide the gimbaling torque:

$$T_{gimbal} = F_1 R_1 - F_2 R_2 = \frac{P}{2 \cos \phi} (R_1 - R_2) \quad (1)$$

Where P is the axial load through the leadscrew and ϕ is the flank angle of the thread. Moment arms R_1 and R_2 can be calculated using the thread pitch, flank angle, and overall length of threads after accounting for manufacturing tolerances. Note that this calculation assumes the threads of both parts are rigid; deflection under load should be considered in borderline cases. For the Feed, the resistive torque due to friction is proportional to the leadscrew axial load P for both the spherical ball and universal joint style pivots, so gimbaling success is independent of the load applied.

Two types of error can cause misalignment between the leadscrew and leadnut threads. In the first type, the leadnut must progressively gimbal through a small angle over the entire stroke of the screw. This is caused by mismatched CTEs and tolerance stackup in the loop from the leadscrew through the mechanism and back to the leadnut. The second type of error is called "whirl," where the leadnut must gimbal through a repeating motion for each revolution of the leadscrew. A line extending along the thread axis of a whirling leadnut would trace a cone. Whirl can be measured as runout of the leadscrew. Its sources in the Feed mechanism are parallel misalignment between the input and output of the u-joint and straightness of the leadscrew. In the EM1 and EM2, the u-joint is shimmed to center to minimize whirl. Both types of error should be minimized to limit the amount of gimbaling the leadnut must do to maintain thread alignment. Special attention should be given to whirl as it increases the number of cycles on the pivot. As previously discussed, failure to gimbal with low friction leads to rapid lead screw failure.

Before applying DFL, the leadscrew and leadnut should be run in with each other. This process matches the flank angles of both parts, ensuring area contact of the threads. Run in should be performed with the same constraint scheme and operational loads as in the final mechanism to ensure parts wear into each other in the manner they will eventually be loaded. A leadscrew-leadnut pair that has not been run in prior to DFL application, even mounted on successfully gimballing pivots, can result in edge contacts and rapid wear out due to mismatched thread geometry.

A different problem was encountered while running in the EM2 leadscrew and leadnut. While loading the leadnut in the same direction that it was travelling, the leadnut would chatter and the free end of the leadscrew would vibrate. It is expected that this is caused by stick-slip occurring between the leadscrew and leadnut threads. This was solved for the run-in by using oil to reduce the difference between the static and kinetic CoFs and by installing a snubber on the free end of the leadscrew to damp any vibrations. While the snubber does over-constrain the leadscrew, in this application it was found this did not have a noticeable effect. The snubber is relatively far below the useable stroke of the leadscrew, allowing the long slender leadscrew to bend to accommodate the over-constraint. Araghi in "Friction-Induced Vibration in Lead Screw Systems" [1] provides techniques for predicting chatter by analysis and methods for eliminating chatter, including increasing damping of the leadscrew supports and using alternate control schemes.

Key conclusions from the ETU, EM1, and EM2 leadscrews include:

- Full area contact of threads is critical for leadscrew systems using DFL. Edge contacts will result in rapid failure of the DFL, extreme wear of the base materials, and infant mortality of the mechanism. Steps should be taken to ensure the thread flanks are well matched during fabrication by running-in the screw and nut together. Deflection under load, or use of elastic matching, should be considered.
- Misalignment of leadscrew and leadnut threads should be eliminated with low-friction pivots that kinematically constrain the system when using DFL and when oversizing of components is precluded by system requirements. The length of the leadnut should consider, among other factors like load distribution and wear rate, the gimballing torque required to overcome pivot friction. Sources of misalignment should be minimized, with emphasis on sources that cause whirl.
- Use of dissimilar metals, including ferrous and non-ferrous pairs, may not prevent galling if lubrication fails under high contact stresses caused by edge loading.
- Chatter can occur with poorly lubricated and lightly damped leadscrews that have large length to diameter ratios; small changes to the system stiffness, damping, or constraints may be enough to eliminate the chatter.

Polymeric Bellows

A polymeric bellows was developed to protect the Feed stage leadscrew from dust ingress. Polymers offer mass savings over metals for bellows construction but their use in compliant mechanisms for spaceflight and/or cryogenic applications has been limited due to embrittlement at temperatures below their glass transition temperatures. Crumpling has been demonstrated to be a viable method of compliant actuation for thin film polymers at cryogenic temperatures in compressible bladders for liquid hydrogen dispensation made from PET [3][4] and retractable contamination covers for spacecraft made from PVDF [5], but the non-deterministic nature of random crumpling limits cycle life.

A folding origami architecture was developed such that the film would undergo predictable and elastic deformation during repeated deployment and retraction. The fold pattern, known as an accordion fold, was selected over patterns that offer higher degrees of compressibility due its accommodation of independently varied inner and outer clearance diameters and ease of manufacturing at the scale of the application.

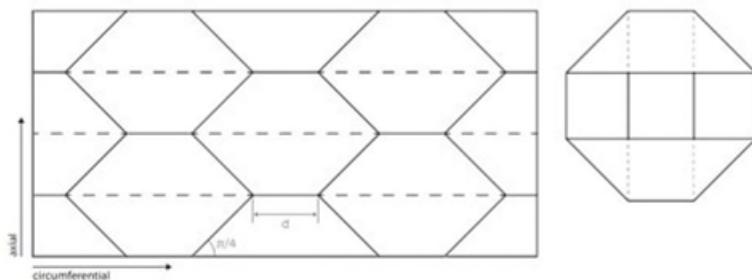


Figure 7. Accordion flat fold pattern (left) and folded cross section (right).

Three 4.5-cm tall, 4-cm OD sections of bellows were folded from 0.127 mm (5 mil) PET and cycled 1500 times (1 cycle = full compression followed by extension) while submerged in liquid nitrogen. No cracks were observed at folds or vertices, and no mass loss due to shedding was measured. Due to the bellows' line-of-sight directly over the sample site, a material change to a fluoropolymer was preferred. An identical bellows was folded from PVDF, but it exhibited high stiffness and fractured early during cycling. Tefzel (ETFE) was ultimately identified as having the most desirable combination of fluoridation, strength, and crease-ability.

The bellows is constructed from a flat sheet of 0.127 mm (5 mil) Tefzel ETFE film. The layout of the accordion fold pattern is creased into the sheet with a desktop CNC plotter and folded by hand. The seam is closed with ultrasonic spot welds along the length and secured with clamps at either end of the covered sections of lead screw.



Figure 8. Folding (left) and ultrasonically welding (right) of ETFE bellows.

Two articles participated in the successful life testing at -180°C of the ETU feed stage to 200x cycles. Cryogenic fatigue life testing was also performed on an EM test article submerged in liquid nitrogen to 2000x cycles. In both tests, isolated pinholes and/or small cracks appeared on some folds, but integrity and function of the bellows were maintained.

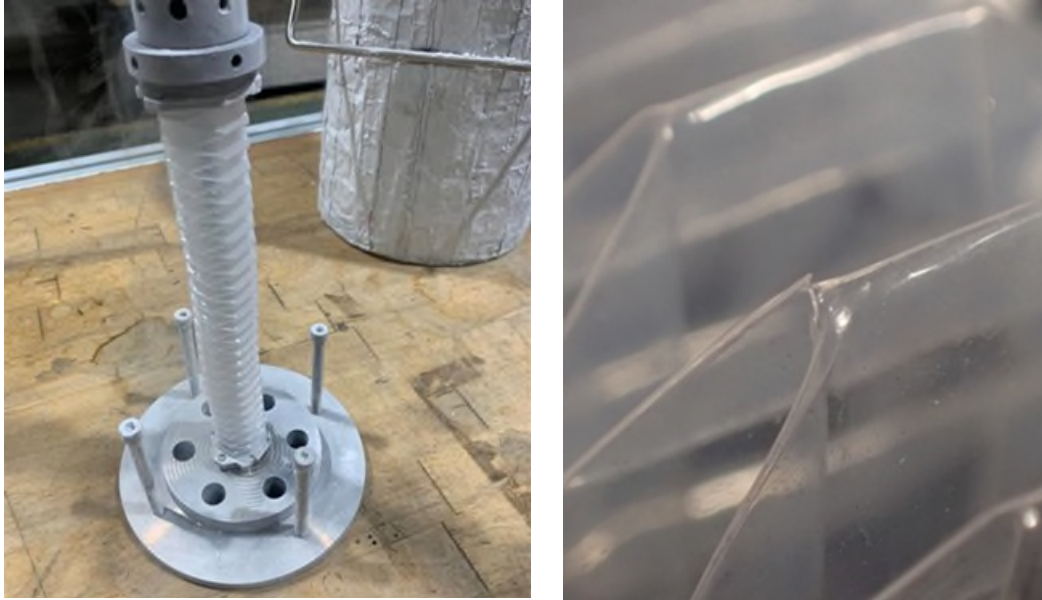


Figure 9. Cryogenic fatigue life test rig (left) and vertex fold crack (right). Cracks are isolated perforations that do not propagate or threaten integrity and function of bellows.

Key conclusions from development of the dust protection bellows include:

- Hermeticity is difficult to achieve with high aspect ratios. Thermo-vacuum-forming the bellows over a mandrel provides a method of forming the 3-dimensional shape with no seam to seal, but above a 3-4x L/D ratio, the method becomes non-viable due to thinning of the drawn film.
- The impact of scale on manufacturability should be considered during pattern selection. More compressible fold patterns had feature densities beyond what could be reasonably folded by hand at the scale of this application.
- Ultrasonic welding is effective for joining ETFE films when a hermetic joint is not required.
- Precision and consistency in forming are key to avoid pinhole cracks at vertices where stress can be concentrated.

Cam Rollers

The crossed roller carriage uses a set of studded crowned cam rollers coated with a sputtered DFL. The rollers feature a full complement of needle rollers; cross sections of the ETU and EM1/EM2 rollers can be seen in Figure 10. The ETU and EM1 each use 6 rollers while the EM2 uses 8 rollers for improved stiffness under vibration. These rollers ride in a crossed configuration in the V-groove shaped rail (Figure 11). The EM1 and EM2 use 3 and 5 eccentric rollers respectively to close clearances to the rail and account for manufacturing tolerances.

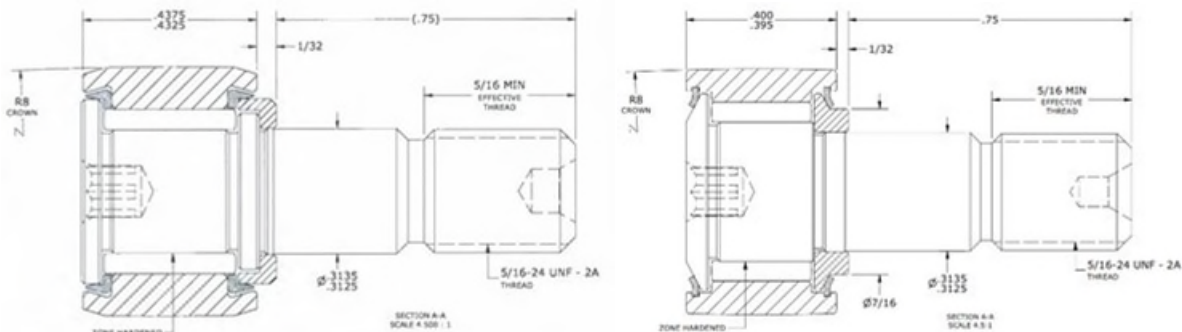


Figure 10. ETU roller (left) and EM1/EM2 roller (right).

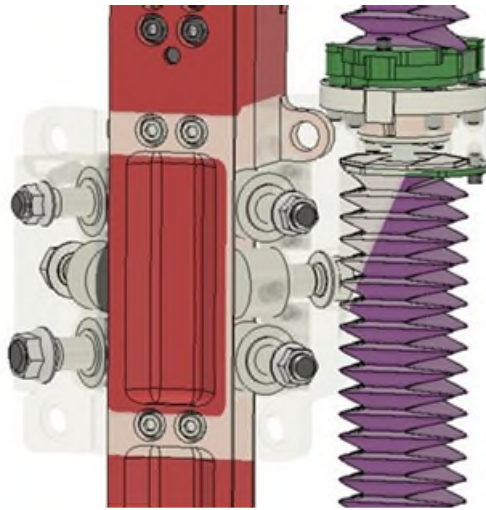


Figure 11. Cam rollers in crossed configuration on EM1 rail shown.

ETU testing of the Feed consisted of 1x life at -180°C under various loading conditions, then 1x life at ambient under various loading conditions with 60 minutes of cumulative dust exposure to wheat flour and silica dust. After 1x life at cold the rollers had low running torques, but after the dusty test, the rollers had running torques up to four times the initial running torque. Disassembly of the rollers revealed larger particulate than expected with normal DFL debris adhered to the rolling elements. SEM/EDS analysis showed that these debris had compositions consistent with a mixture of DFL debris, wheat flour, and silica dust, indicating dust had entered the rollers. The ETU roller nylon seals were slit to allow for thermal expansion, but this allowed dust incursion, resulting in dust combining with normal DFL debris and creating high shear strength particulate. The seals on the EM1 and EM2 rollers have a different design that does not require a slit, though dust exposure testing has not yet been performed.

The EM1 rollers experienced a second issue. After running for several cycles (~ 0.25 x life), the rollers were showing very high running torques, with some even locking up completely. Further investigation showed that this condition could be induced by rotating the roller while applying a cross-axis moment. The running torque increases until it reaches a plateau. Reversing the direction of motion instantly reduces the running torque back to its original value, after which it increases until it reaches another plateau.

It is believed that this behavior is due to the needles migrating through their axial clearance under a cross-axis moment load, caused by an axial load on the outer race. As the needles reach the end of their axial clearance, the tips of the needles contact and load against the flat perpendicular to the stud. As more needles load against the flat, the running torque of the bearing increases until all needles have contacted the flat. When reversing direction of motion, the needles migrate in the other direction until they all contact the opposite flat. Poor surface finish and high contact pressures between the needle tips and the flat cause the DFL to rapidly wear away, making this problem worse as the bearing ages. In this application, the use of a small rolling element maintains an overall advantage in reducing linear drag of the system compared to bushings. The system features large torque margins to compensate for this significant drag source.

Key conclusions from the ETU and EM1 cam rollers include:

- Dust entering rolling element bearings with sputtered DFLs can combine with DFL debris, creating a new debris mixture that is stronger in shear, posing a risk of increased running torques.
- Full complement needle cam rollers risk increased running torques mid-life due to migration of needles sliding on the end surfaces. This is particularly severe when DFL is used. Mechanism trades should account for either an increase in mass and volume to use a more robust rolling element, or an increase in force or torque margins required and a potential reduction in rolling element life.

Percussion Mechanism

The Percussion mechanism delivers a shock load to the rear of the floating drill bit to enable drilling of substrates with an unconfined compressive strength of at least 80 MPa while only requiring a nominal WOB under 100 N. The ETU, EM1, and EM2 percussion mechanism share the same basic mechanism architecture featured on the Apollo Lunar Surface Drill and by Honeybee Robotics for The Regolith and Ice Drill for Exploring New Terrain (TRIDENT). The system uses an actuator to rotate a helical cam which lifts a hammer against a coil spring before dropping it off the end of the ramp.

The follower rotation axis is roughly parallel to the cam axis, tilted by approximately four degrees to match the cam helix angle) and tracks via sliding rather than rolling contact with the cam. The DrACO cam spins at 810 rpm, lifting and dropping the follower and hammer once per revolution to deliver a percussion energy of 1.0 J at a frequency of 13.5 Hz. All mechanism components except for the actuator are dry film lubricated and operate at 94 K. Early development efforts sought to demonstrate functionality of DFL mechanism elements and identify cam and follower materials and geometries that would balance low friction torque throughout life with preservation of maximum spring deflection at end of life. Later development efforts focused on troubleshooting the three-bearing system that supports the cam.

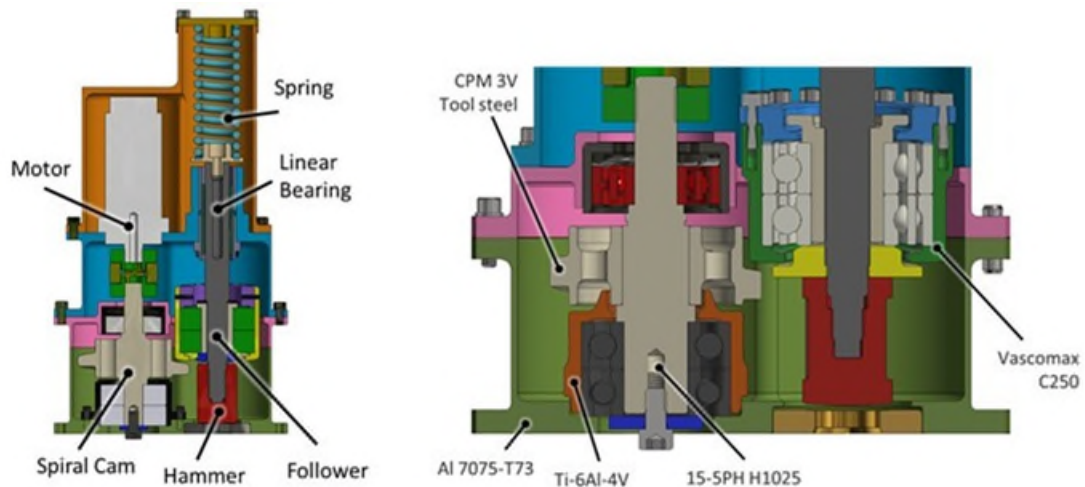


Figure 12. ETU Percuss Mechanism Cross Section.

Cam and Follower

Previous programs at HBR, including ICEBREAKER, THUPER, TRIDENT [6], and RANCOR, demonstrated good wear properties with ultra-high hardness steels – self-mated A2 tool steel at ambient conditions (ICEBREAKER, THUMPER), and Vascomax C350 (cam) and C250 (follower) at -70°C (TRIDENT). TRIDENT achieved a life of 2.4M cycles under ambient conditions with grease lubrication. RANCOR achieved a life of 50k cycles without grease before testing was suspended, but components showed very few signs of wear. For DrACO, a corrosion resistant steel with good ductility down to cryogenic temperatures and hardness approaching that of tool steels was sought. Coatings were initially avoided as TRIDENT testing showed that without grease, they would wear through in about 50k cycles. A series of tests was commissioned to identify a material pair and lubrication scheme capable of achieving 400k cycles (2x mission life) at -180°C with no heated elements beyond the motor.

V1.0 used Custom 465 for both the cam and follower, with an ion nitride case hardening to HRC 70 applied to the cam and a very thin layer of Braycote 600EF. This failed early at approximately 0.15x mission life. The mechanism failed by seizing after reaching actuator stall torque in 34k cycles. Severe galling of the cam and follower surfaces was observed. V1.1 and V1.2 testing used similar amounts of wet lubrication as TRIDENT on the cam and follower ramp surfaces. Braycote 602EF was used for V1.1 and Calcium Sulfonate with Teflon was used for V1.2. These reached 120k and 140k cycles, respectively, before

mechanism failure. Upon disassembly, observation indicated that the grease had frozen and subsequently shattered or sheared under load from the follower leaving bare wear surfaces. While not directly observed, it is thought that small amounts of grease remained on the follower which allowed operating to continue beyond where V1.0 failed.

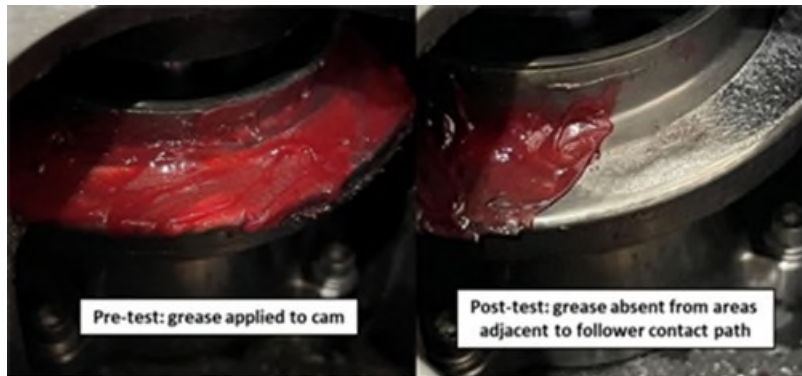


Figure 13. Grease from the V1.2 test, before and after operating at cryogenic temperature.

The lubricant failure in V1 demonstrated the ineffectiveness of grease as boundary-layer lubrication at -180°C and the incompatibility of self-mated Custom 465 H1000 in dry wear with ion-nitriding. For the V2 follower, Vascomax C250 was selected for its heritage on TRIDENT. Several materials known for their performance in relative sliding applications were tested for the cam against the Vascomax C250 follower at ambient temperatures in a dry nitrogen environment at the beginning of the V2 campaign. Beryllium copper showed high wear rates but no galling or unsteady operation at ambient temperature, quantified by a stable mean motor current draw through the test. However, at -180°C , the BeCu began to gall badly, leaving a very rough post-test finish, while still wearing at high rates. CPM 3V tool steel demonstrated the most favorable overall wear conditions and galling resistance at all temperatures.



Figure 14. Condition of cams of various materials at top of ramp (top) after 80k cycles against a Vascomax C250 follower (bottom).

The V2 mechanism ran to 400k cycles (2x mission life) at -180°C without stalling but failed to meet the mean current margin requirement. Disassembly and inspection of the mechanism revealed that the cam and follower duplex bearings exhibited very high intermittent friction torque consistent with raceway or rolling element damage.

Given the excellent wear performance of the CPM 3V cam and self-mated A2 from ICEBREAKER and THUMPER, a CPM 3V follower was used for the V3 testing. The follower geometry was revised to create a crowned contact patch on both the cam and follower, and the drop-off at the top of the V2 cam ramp was scalloped to match the radius of the follower. Improved FOD shielding was also incorporated into the bearing housings. The mechanism stalled after 176k cycles, and inspection revealed poor condition of the mated cam and follower wear surfaces.



Figure 15. Galled surfaces seen after testing self-mated CPM 3V tool steel.

The final round of ETU testing (V4) used the V2 materials, V3 geometries and mechanism improvements, and iKote solid film lubrication. The V4 cam and follower were successfully tested to 400k cycles (2x life) twice. Early life behavior of the cam and follower is characterized by a period of low friction torque followed by a sharp rise as the solid film lubricant is worn away at approximately 50k cycles. After 100k cycles, it is assumed that the cam and follower wear surfaces are stripped of all coatings and are wearing bare-metal against bare-metal. The CPM 3V cam and Vascomax C250 follower do not develop the runaway friction torque of self-mated CPM 3V or the excessive removal of material and resultant strike energy loss of the beryllium copper or Nitronic 60 cams.

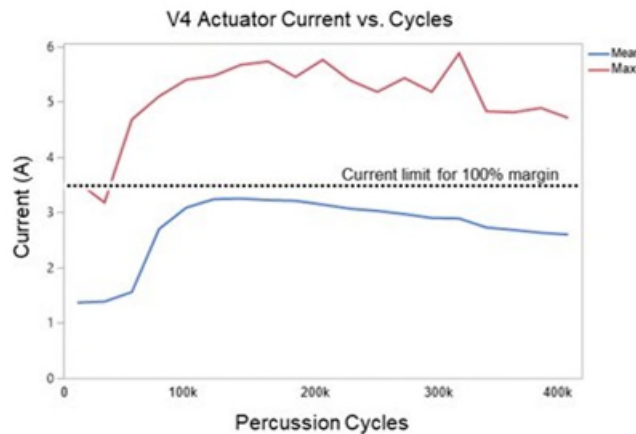


Figure 16. Telemetry from V3 life test, showing mean and max current over the course of the test.

Key conclusions from the cam and follower testing include:

- Tool steels, while not commonly used for spaceflight, should be considered for harsh sliding conditions. They were successfully demonstrated at cryogenic temperatures with high shock loads and no signs of brittle failure were observed, despite generally poor ductility at low temperatures.

- Testing the dry wear and galling conditions in a dry nitrogen environment at room temperature can lead to significantly different results than at cryogenic temperatures. Specifically, beryllium copper may perform poorly at cryogenic temperatures where it performs well at ambient temperatures.
- Where there is potential for dry lubrication failure, materials should be tested under unlubricated conditions to identify options that wear gracefully to prolong life. Testing under the planned flight conditions is critical as temperature, geometry, cleanliness, and many other factors may lead to unexpected results that cannot be extrapolated to other conditions.

Bearings

Rotating and translating components in the ETU Percuss Mechanism were supported by high precision COTS bearings. Modifications were made to the COTS bearings to adapt them for use in the mechanism at -180°C, with mixed results. A summary of the different bearing test configurations is shown in Table 2.

Hard-preloaded angular contact bearings were purchased at stock preloads or re-ground to custom preloads in a DF orientation for the cam duplex bearings and DB orientation for the follower bearings. High preloads were selected to increase bearing pair stiffness and ensure a mean Hertzian contact stress of at least 414 MPa (60 ksi) per ball at all times to prevent ball unloading and subsequent skidding. An upper bound on mean Hertzian contact stress of 1240 MPa (180 ksi) was also established for future design during V1 testing. The COTS linear bearing supporting the follower was not preloaded, while the trailer bearing used soft preload up to 180 ksi mean Hertzian stress. Steel balls in the linear bearing and the cam trailer bearing were substituted with silicon nitride balls. The bearings saw no signs of performance degradation over more than one million cycles. The hard preload of the cam and follower duplex pairs precluded the use of ceramic rolling elements due to the wide operating temperature and mismatched CTEs.

Factory wet lubricants were removed and replaced with HPS-2832 DFL (MoS₂-Sb₂O₃-Au) from Hohman Plating and iKote (graphite-doped MoS₂-Sb₂O₃-C) from AIM-MRO, formerly Tribologix. The iKote lubricant required burnishing with a formed Maple wooden dowel to prevent shedding large amounts of debris during the first few revolutions. Within the DF duplex set of bearings, debris generated in the upper bearing settled in the lower bearing, causing friction torque increases and additional heat generation during some tests. The iKote lubricant was also significantly thicker than the sputtered HPS-2832, increasing the unmounted bearing preload which was set in the unlubricated condition. Factory phenolic cages were replaced with cages manufactured from Durafilm TCGF-116 (Armalon), PGM-HT, and Vespel SP-3. Armalon and PGM-HT were desired for their ability to transfer unbonded PTFE lubricant to the raceways after solid film lubrication was worn away. The demonstrated outperformance of PTFE by MoS₂ as a lubricant in high-contact-stress applications [2] led to the initial selection of Armalon and PGM-HT, but Vespel SP-3 was later used due to PGM-HT material availability issues and its increased rate of lubricant transfer to the raceways.

Bearing Failure and Investigation

Varying degrees of success were achieved with all the described solid film lubricants, cage materials and preloads during the V1-4 ETU test campaigns. Chemistry and structure of solid film coatings used to lubricate rolling and sliding elements were not found to have an outsized impact on mechanism life when compared to one-another in all tests run, both successful and unsuccessful.

The custom bearings that were procured for the EM drill incorporated most of the design parameters that led to success in the ETU mechanism, except for raceway curvature. Several spare sets of EM cam and follower duplex bearings were installed into the ETU percussive mechanism and tested at -180°C. The cam bearings all failed early in life, and the mechanism and bearings were disassembled and inspected. Results from one of these tests are shown in Figure 17 and Figure 18. Follower bearings showed no signs of degradation or damage.

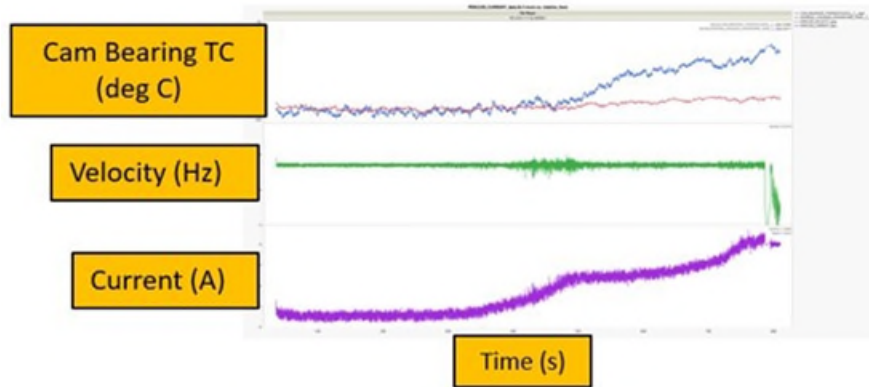


Figure 17. No-load testing after early failed V4.0 testing shows initially good performance, followed by bearing heating and motor drive current increases.

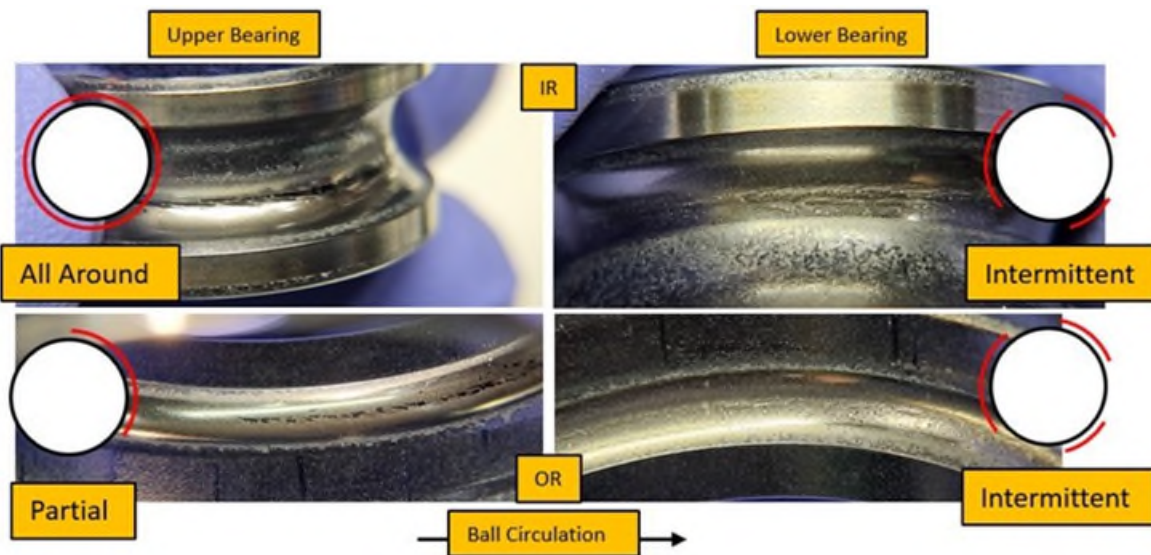


Figure 18. Upper duplex bearing (left) and lower bearing (right) visual inspection after no-load testing to failure.

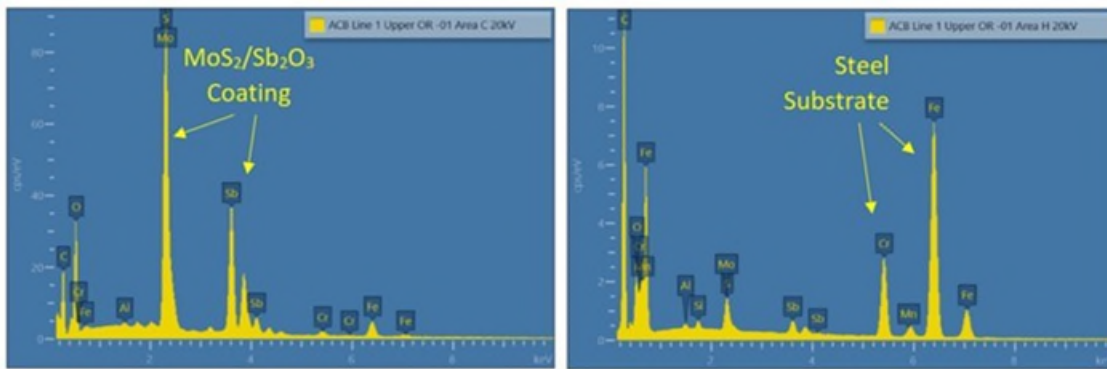


Figure 19. SEM analysis of raceways to determine presence, or lack, of remaining DFL.

Backscattered electron imaging was performed to assess the health of the raceways. A baseline survey of the fresh iKote coating adjacent to the raceways showed expected peaks of Mo and Sb, while the raceways had heavy carbon deposits and were almost entirely devoid of the Mo and Sb lubricating compounds.

Additional pairs of EM bearings were tested under the same conditions with HPS-2832 solid lubrication instead of the iKote, and Vespel SP-3 cages instead of the PGM-HT cages. Both subsequent tests failed at approximately the same point (12k-16k cycles) and exhibited the same visual condition of the raceways upon disassembly.

The high-heat-generation during operation, absence of any lubricative film within the ball tracks after failure, and the damage to the metallic raceway substrate consistent with galling/adhesive wear suggest a lubricant failure was responsible for the rise in friction torque and ultimate bearing failure. Both lubricants had seen significant testing during the ETU V1-4 tests in identical environments and similar or higher loading to the tests of the EM bearings in the ETU mechanism. Upon reexamination of design parameters of successful bearings against those of the failed EM bearings, raceway conformity was the only unquantified COTS bearing parameter of import. While it was expected that a tighter raceway conformity on both races rather than just one would reduce the operating stress and prolong the life, discussions with SMEs revealed that 52% curvature often leads to earlier bearing failure even with grease lubricant.

The root cause theory for the failed EM bearings is that tight raceway curvature applied to both races caused an unacceptable amount of friction and sliding within the bearing, destroying the DFL and heating the bearing quickly.

Table 2. ETU Percuss Cam Bearing Loading, Specification, and Configuration.

Requirement	ETU V1, V2	ETU V3	ETU V4	EM
Spring Energy	1.5J	1.5J	1J	1J
Unmounted preload	334-445 N (75-100 lb)	334-445 N (75-100 lb)	252 N (56 lb)	445 N (100 lb)
Inner raceway conformity (measured)	53.79%	53.79%	52.04%	52.17%
Outer raceway conformity (measured)	52.65%	52.65%	54.22%	52.35%
Bearing (race and ball) material	52100	52100	52100	440C
Cage material	Armalon	Vespel SP-3	Vespel SP-3	PGM-HT, Vespel SP-3
Lubrication	HPS-2832	HPS-2832	iKote	iKote, HPS-2832
Operating Cycles Demonstrated	>400k	>400k	>400k	<16k

Key conclusions from the rolling element testing include:

- Reducing operating stress by specifying tighter raceway curvature may reduce life in hard preloaded, dry lubricated, duplex bearings. Testing must be conducted to find an appropriate preload and raceway curvature. COTS bearing curvature may not be suitable for use with DFL even if all other properties besides curvature are the same between designs or manufacturers.
- Burnishing of dry lubricant may be required to reduce the total debris volume and minimize potential of debris embedding in the raceway and increasing running torque. Sputtered DFLs with co-sputtered additives do not usually require burnishing, have smaller impact on bearing hard preload, and offer promise even in applications with operating stresses approaching 200 ksi.
- Hybrid bearings with steel races and Si3N4 balls, operating under soft preload, fared significantly better than hard preloaded all-steel bearings with DFL.
- Matching cage material wear rates to bearing lubrication consumption rates is nearly impossible to predict and may involve trial and error in cage design and material selection with limited analytical approaches to cage design available.

Overall Conclusions

Many lessons were learned during the development of the DrACO drill when adapting previously successful wet lubricated designs to dry lubricated designs. Many aspects of the design that are inconsequential when using grease become critical with dry lubrication. Specific lessons learned are documented at the conclusion of each element section.

- DFL elements must be tested under the exact planned flight conditions, including temperature, loading, geometry, processing, and all interacting materials. Materials that are generally known to be better for the task could prove inappropriate if used differently from previously qualified efforts.
- Small changes to geometry can have an outsized impact on mechanism success when DFL is used, where they otherwise would be inconsequential in an oil or grease lubricated system. A thorough understanding of the contact and loading is required, and early testing of every configuration is highly recommended.
- Materials that will degrade gracefully when DFL wears out should be used to prevent catastrophic failure, due to the sensitivity of DFL to small geometry errors leading to edge loading.
- ETFE-film folded with origami techniques is a mass-effective solution for preventing bulk dust intrusion into mechanisms at cryogenic temperatures where hermetic sealing is not required.

Acknowledgments

The authors thank NASA GSFC and JHU APL for their continued support during this development. A special thanks to external reviewers Mark Balzer, Mike Dube, Claef Hakun, Jeff Lince, Ben Younes, Francis Dunne, and all the members of the DrACO team, past and present.

References

- [1] Araghi, O., "Friction-induced Vibration in Lead Screw Systems", UWSpace, <http://hdl.handle.net/10012/4404>, 2009.
- [2] Lince, J. R., "Solid Lubrication for Spacecraft Mechanisms", SMC-TR-97-12, 1997.
- [3] Pope, D. "Development of Cryogenic Positive Expulsion Bladders," NASA-CR-72115, 1968.
- [4] Wiederkamp, K. "Liquid Hydrogen Positive Expulsion Bladders," NASA-CR-72432, 1968.
- [5] Bonitz, R. G., et al., "NASA Mars 2007 Phoenix Lander Robotic Arm and Icy Soil Acquisition Device", *J. Geophys. Res.*, 113, E00A01, doi:10.1029/2007JE003030., 2008.
- [6] Paulsen, G. "The Regolith and Ice Drill for Exploration of New Terrains (TRIDENT); a One-Meter Drill for the Lunar Resource Prospector Mission", *Proceedings of the 44th Aerospace Mechanisms Symposium*, 2018.

Government Reference Design of the Vertical Solar Array Technology Demonstrator

Scott Belbin*, Carl Mills* and Ryan Chan*

Abstract

NASA Langley Research Center (LaRC) is developing and constructing a Government Reference Design (GRD) version of the Vertical Solar Array Technology (VSAT) Demonstrator for lunar surface applications. This paper provides an overview of the conceptual design effort and discusses the planned demonstrations of its associated mechanisms.

Introduction

With the upcoming robotic and human lunar surface exploration efforts, NASA seeks to provide a means of powering and recharging various assets on the lunar surface at the southern polar region. The VSAT Program is developing a system by which an array of photovoltaic cells can be elevated above shadowing caused by boulders, hills, mountains, and crater walls to provide near-continuous electrical power to those assets. The Program has awarded initial development contracts to three awardees to develop their concepts to at least TRL-6. Langley is simultaneously designing and building a GRD Concept Demonstrator to assist in mechanical deployment and stowing issue mitigations and to inform the various reviewers of the awardees' efforts in the upcoming down-selection of awardees for the next phase of the Program.

VSAT GRD Overview

Original Concept

VSAT Program advisor and AIAA Fellow Martin Mikulas provided the original concept of a deployable array system on a deployable mast to elevate the arrays (originally named Retractable Surface Array). Parameters included a minimum power capability of 10 kW and a minimum elevation of 10 m from the lunar surface to the bottom of the arrays. This yielded an estimated array size of 6 m x 6 m divided into two separate arrays on either side of a mast.

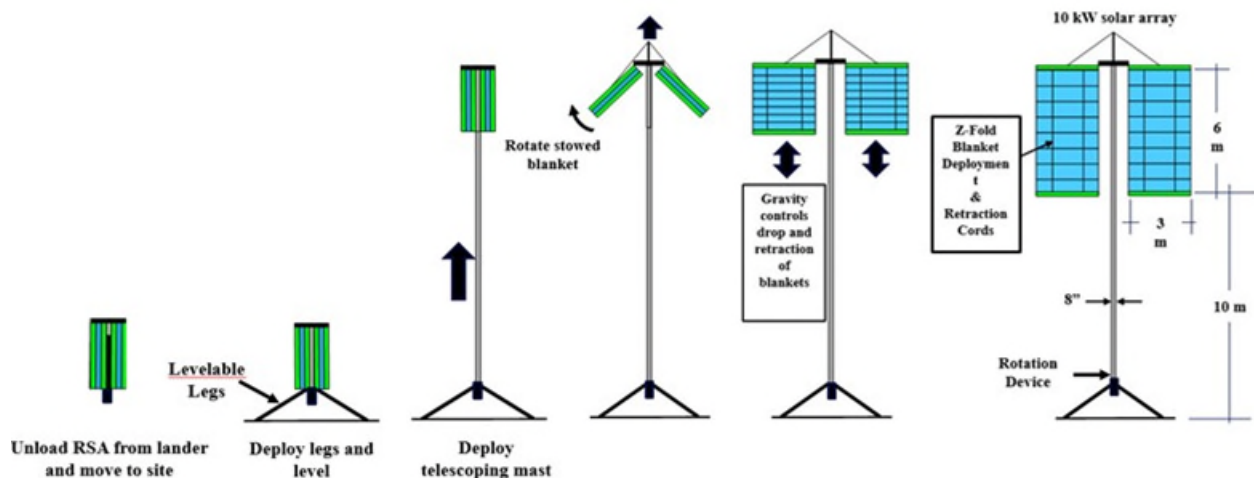


Figure 1. Original concept from Stowed State to Fully Deployed State

* NASA Langley Research Center

GDR Design

From this, preliminary designs of the various subsystems were developed, eventually evolving to a four-array package system to optimize volumetric packaging when stowed. Subsystems included a tripod base structure, gimbal for rotating the mast and making it plumb, deployable array housings, and deployable mock-arrays. This paper will discuss the decisions made in reaching this configuration along with the sizing of materials, mechanisms, and drivetrains, as well as lessons learned during the design and analysis phase, such as sizing gearmotors well in advance of final design and purchasing those gearmotors due to long lead times.

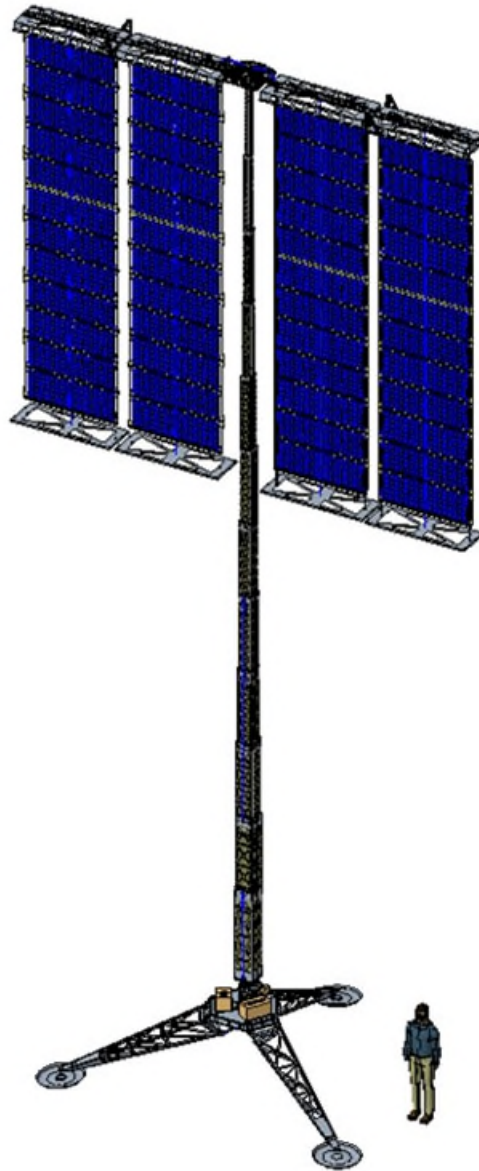


Figure 2. Four-Array Package GRD

Concept and Requirements

As originally presented by Martin Mikulas, a tall mast with two arrays on either side of the mast were shown with a series of images depicting deployment. To clear the shadowing of the local rims of craters and other lunar surface features, the arrays need to be elevated to a minimum of 10 m at their lowest extreme. The sizes of the arrays were determined by setting the goal of reaching 10 kilowatts of power available to end users.

Lunar Mission Requirements included:

- 36 m² solar array area
- 10 m from the lunar surface to the bottom of the arrays
- The ability to be off-loaded from the landing vehicle
- Accommodate local slope of no more than 15° at initial placement (pre-deployment)
- Autonomous mast verticality (plumbness)
- Autonomous deployment and retraction of the mast and arrays
- Transportability for relocation to other sites
- Survivability during the lunar night

This design of the GRD was to be flight-like, with all the features required to proceed to TRL-6 in parallel with the awardees. However, due to cost constraints COTS items were used whenever possible and the decision was made to focus on the deployment and stowage of the arrays, and not pursue actual solar panels or the surface interaction components. A truncated set of requirements was generated:

- 36 m² mock solar array area
- Minimal necessary clearance from the bottom of the arrays to the test cell floor (test cell ceiling height limits mast height)
- Accommodate local slope of no more than 15° at initial placement (pre-deployment)
- Autonomous mast verticality (plumbness)
- Autonomous deployment and retraction

Preliminary Design Iteration (Flight-like)

Referring to Mikulas' concept, major subassemblies were identified and include:

- Three axis gimbal
- Extendable/retractable mast with array support structure and lifting point.
- Two array packages
- Base with deployable legs and launch constraint features.

From the original concept, the estimated sizes of the array packages drove the retracted (stowed) mast height. With an array net width of 6 m, two 3 m width arrays would need to be housed with drives, with the housing needing to be slightly larger than 3 m.

Gimbal Design

The requirement of accommodating up to 15° of local terrain slope dictated the need for some means of making the mast plumb, that is, making the mast parallel to the gravity vector. Given the overall scale of the demonstrator, compactness of the gimbal was not a primary concern. Instead, control authority and stability of the demonstrator once fully deployed was of utmost importance. A concept for a 2-axis gimbal for use on a conceptual lunar crane had been initiated and was used as the basis for a larger version sized for the VSAT concept. As this early concept used high-force self-braking linear actuators to provide the needed stability for a tall structure in a gravity environment, larger COTS linear actuators of the same type were sized and selected. This larger version used ball screw linear actuators with worm drives and recirculating ball nuts driven via worm and worm gears using DC brushed motors, with the two linear actuators providing independent X axis and Y axis motion. To that, a rotating feature for Z axis motion was incorporated.

The gimbal consisted of three subassemblies; the base which had the X axis and the end pivot point for the X axis linear actuator, a cruciform middle subassembly which had the location for the trunnion for the ball-nut for the X axis linear actuator as well as the location for the trunnion for the ball-nut for the Y axis linear actuator. The third subassembly mounts to the Y axis of the cruciform subassembly and the location of the end pivot point of the Y axis linear actuator.

The new rotator feature for z-axis motion consisted of a central high-strength steel axle, two tapered roller bearings in a spool-shaped hub, and a lower and upper plate to which the mast is attached. It is driven by a right-angle gearbox, powered by a COTS gearmotor. The drive has a helical pinion gear driving a ring gear attached to the bottom of the rotator. This right-angle drive is attached to the upper subassembly of the gimbal. A slip ring assembly at the top of the gimbal below the rotator facilitates motor power and signal conductors such that continuous rotation would be allowable. This is in lieu of using a service loop, or an Omega shaped flat cable and rotating the mast $+180^\circ$ through zero to -180° . The slip ring has decks with each deck comprised of a rotor and stator. The rotor has concentric copper traces that align with spring loaded pins on the stator. The rotor is driven by the bottom of the rotating portion of the gimbal, with conductors passing through the rotator's bottom and top plates and out to the mast's side wall.

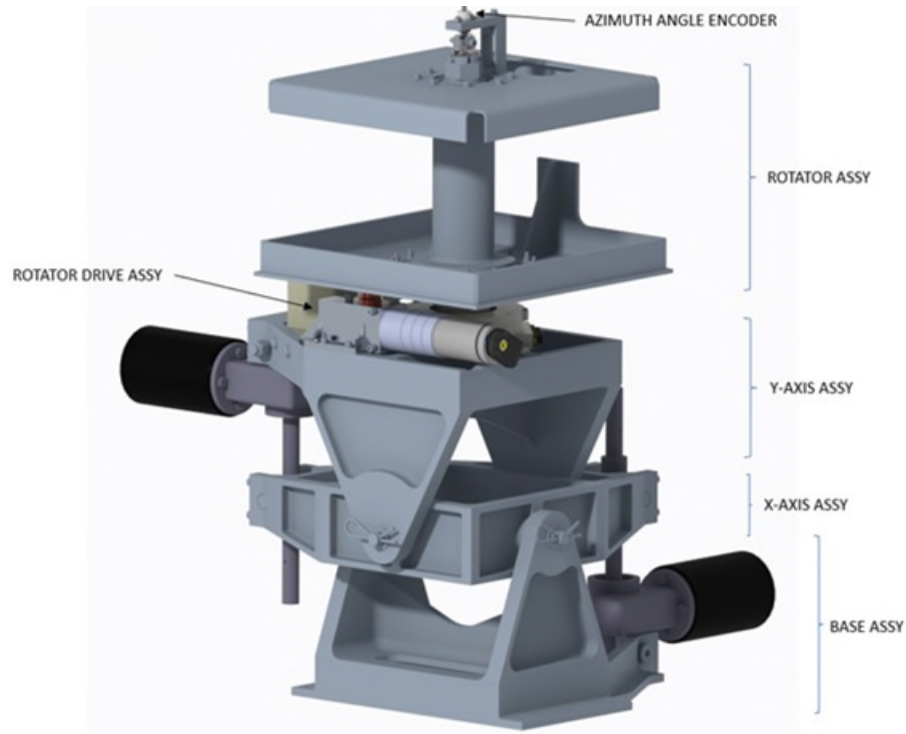


Figure 3. Gimbal Features, Rear

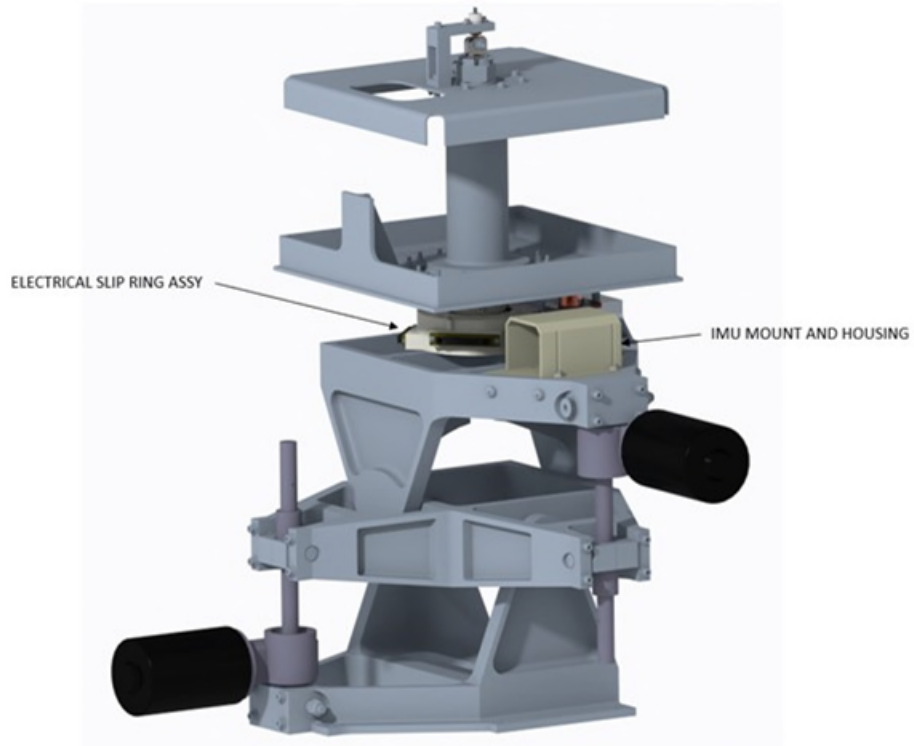


Figure 4. Gimbal Features, Front

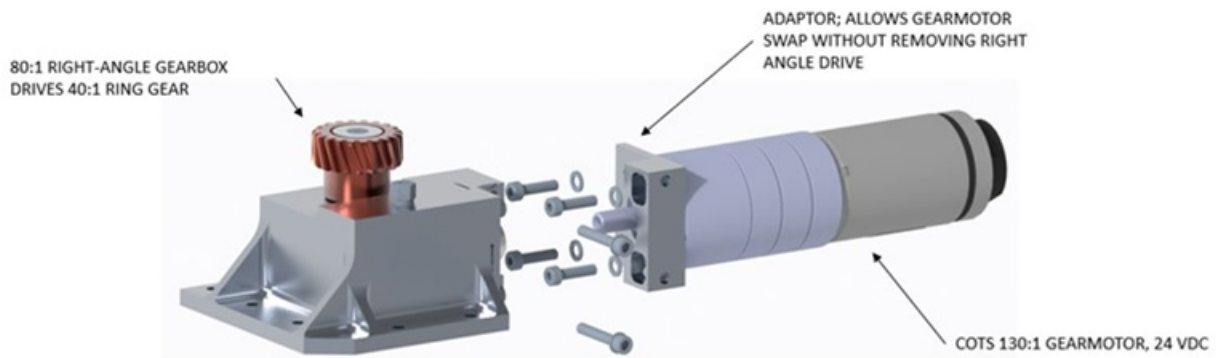


Figure 5. Rotator Drive Assembly

Mast Design

Being in a gravity environment, the mast requirements deviated from the typical booms used on spacecraft for their solar arrays. In addition to being stiff enough to prevent buckling in gravity, it must be retractable, which is a feature that few spaceborne booms have. It could also use gravity to retract instead of relying on a driving mechanism. The inspiration for the design came from terrestrial telescoping masts for light-towers and other portable industrial equipment. Those masts are driven by a winch mounted on the lowest segment (segment 1) which pulls segment 2 up. Segment 3 and the subsequent segments are each attached to the previous one via wire rope over a pulley at the top of each segment, bootstrapping all the segments up simultaneously.

For the telescopic mast segments, bespoke nesting box section extrusions were implemented in the CAD model, with the intent of procuring aluminum extrusions with the cross-sectional dimensions needed. These

extrusions would receive lightening features and wall-thinning to minimize mass. With two 3-meter arrays astride the mast and the gimbal at the bottom of the mast, initial sizing determined that the mast segments were limited to about 3 m in height. With a net deployed height of 16 m (6 m array height and 10 m clearance to the surface), it was determined that 6 segments would be needed.

The mast drive was designed using a worm and worm gear arrangement driven by a gearmotor, driving a wire rope drum. The mast drive is attached through the bottom of the first mast segment to the gimbal's rotator structure at the rotator assembly's base and upper plates.

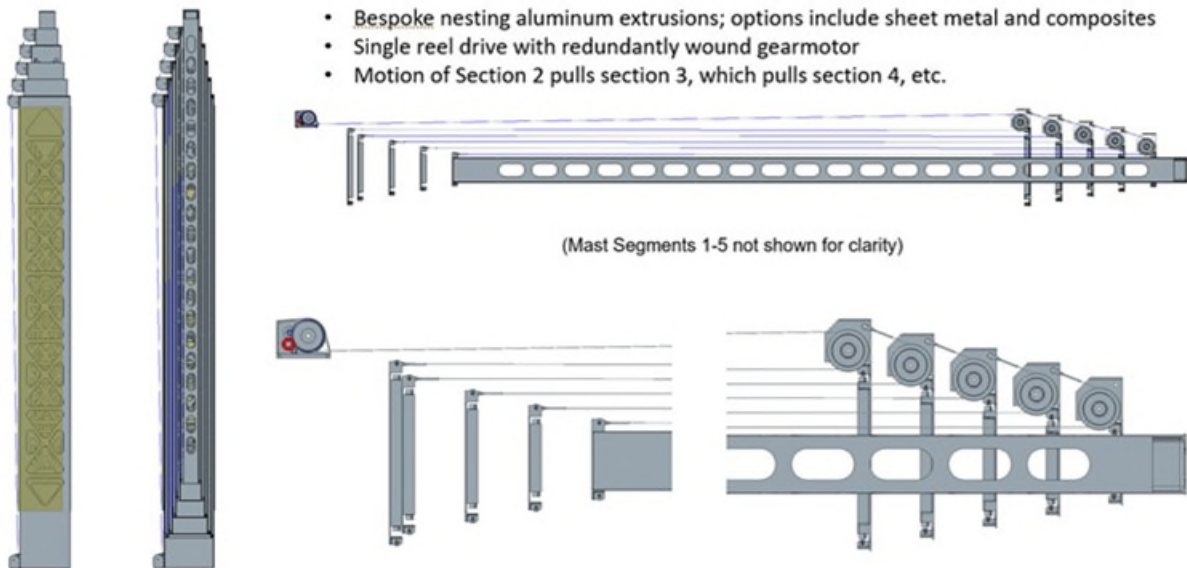


Figure 6. Six Segment Mast Details

A support structure was added to incorporate hinge points at the top of the mast for mounting array housings. This structure carried the two pulleys for the wire ropes that become taught when the mast is fully deployed, causing the array housings to fold upward to their deployed positions. It also incorporated the lifting point for the VSAT for off-loading from the landing vehicle and for relocating to alternate locations.

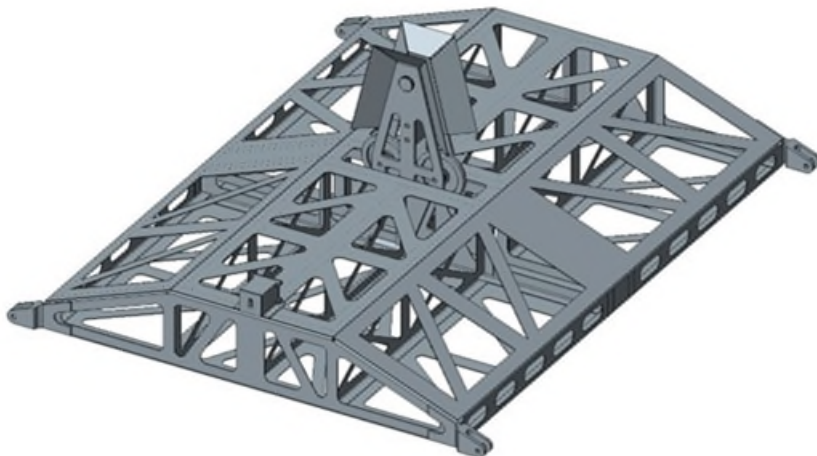


Figure 7. Array Support Assembly

Array and Array Housing Design

Array panels were sized at 3 m wide by .75 m high, with 8 panels per package. Being flat panels, they were arranged in a folding pattern with links at the top and bottom to attach to the housing and the housing closing panel, respectively.

Sheet metal housings were designed to keep regolith off the panels during landing and transport. Lightening cutouts were added to reduce mass, and Mylar film was to be used to cover the lightening cutouts. Hinged at their inboard ends and attached to the Array Support Assembly, the housing motion came from a single wire rope up through the mast that wyes into two ropes and becomes taught, pulling the housings to their positions normal to the mast. Relying on gravity, the array panels would then deploy via a dual drum winch atop the housings. The closing panels add weight to the arrays to assist deployment in lunar gravity.

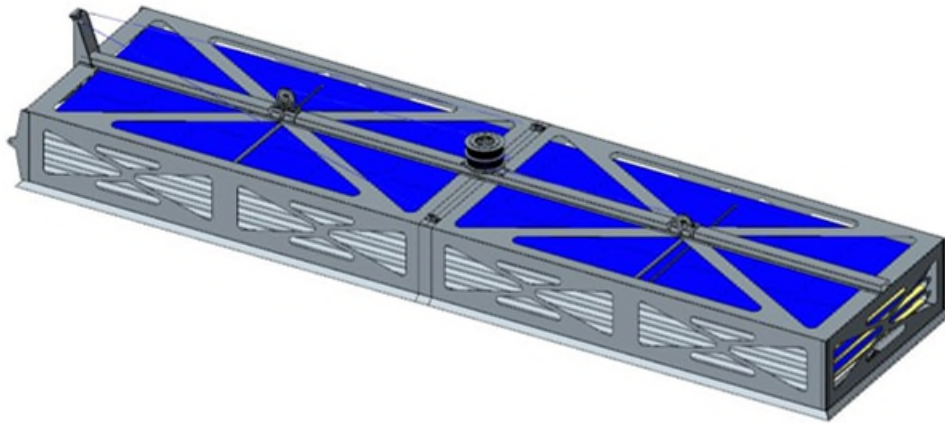


Figure 8. Three-Meter Array Package with Double Drum Rope Drive

The array panels are deployed via a drive with a double-wound drum for wire ropes that pass through the folded panels to the closing panels. The weight of the array panels and the closing panel cause the panels to descend as the ropes pay out. Unlike the CAD images, the panels do not unfold simultaneously, but rather, they stay folded near the bottom of the set with the uppermost panels unfolding first. Once the ropes deploy fully, the last of the panels move into their desired positions. The wire ropes are woven through in a manner that the panels cannot fold in the incorrect direction when retracting.

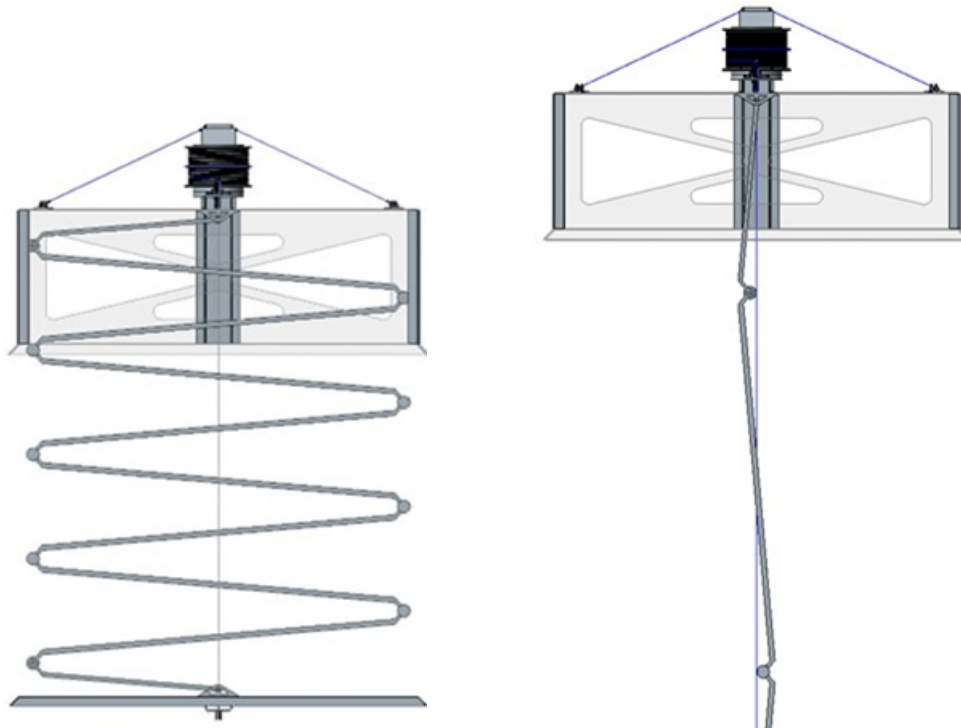


Figure 9. Array Panels Folding

Base Design

The base consists of a triangular platform with mounting points for the three legs with the gimbal mounted in the center. The legs retract upward and are stowed parallel to the mast. They are driven commonly via a single motor driving a triangular pivot with connecting rods to each leg.

Launch restraint components were designed and incorporated. These included a central pin with a ball-end that would be captured by an over-center hook latching mechanism and three cup-cones for constraining the VSAT. These same components could be incorporated into a transport vehicle for relocating the VSAT.

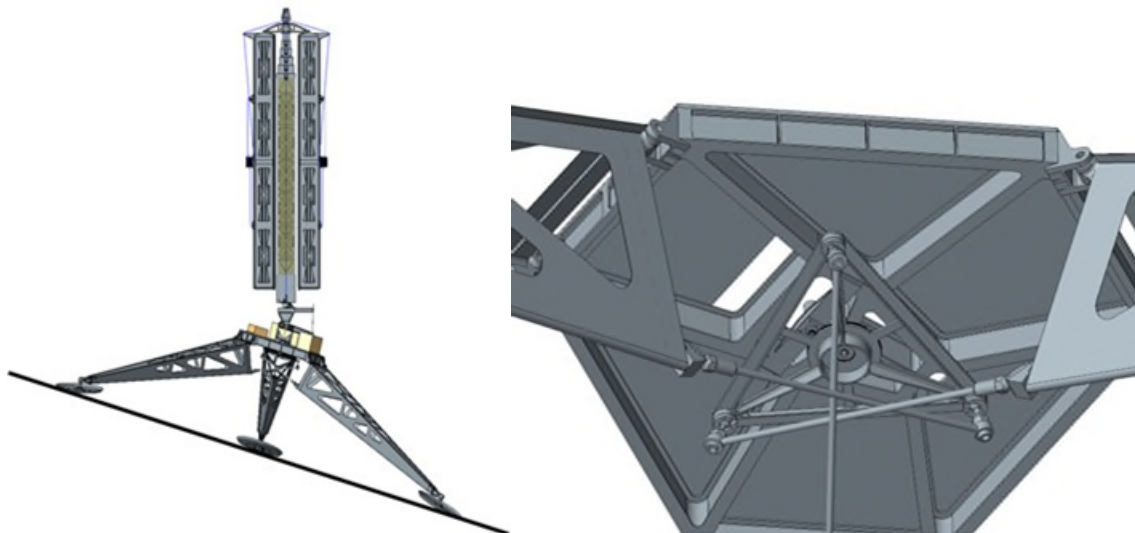


Figure 10. VSAT Base with 3 Leg Drive

Second Design Iteration

For the second pass at the overall design, it was decided to not proceed with the base and leg design since project management decided to not build a demonstrator of it. This allowed increased focus on the mast and array packages and their various drive mechanisms.

To reduce the overall volume and improve packaging of the stowed VSAT, the arrays were divided into two array sets per side yielding four 1.5 m wide arrays. With the array housing sizes reduced in stowed height, the mast's stowed height needed to be shortened as well, so the mast went from having six segments to twelve segments. While the added housings increased the stowed width of the stowed VSAT package, the net width did not exceed the base footprint and overall formed a better package volumetrically.

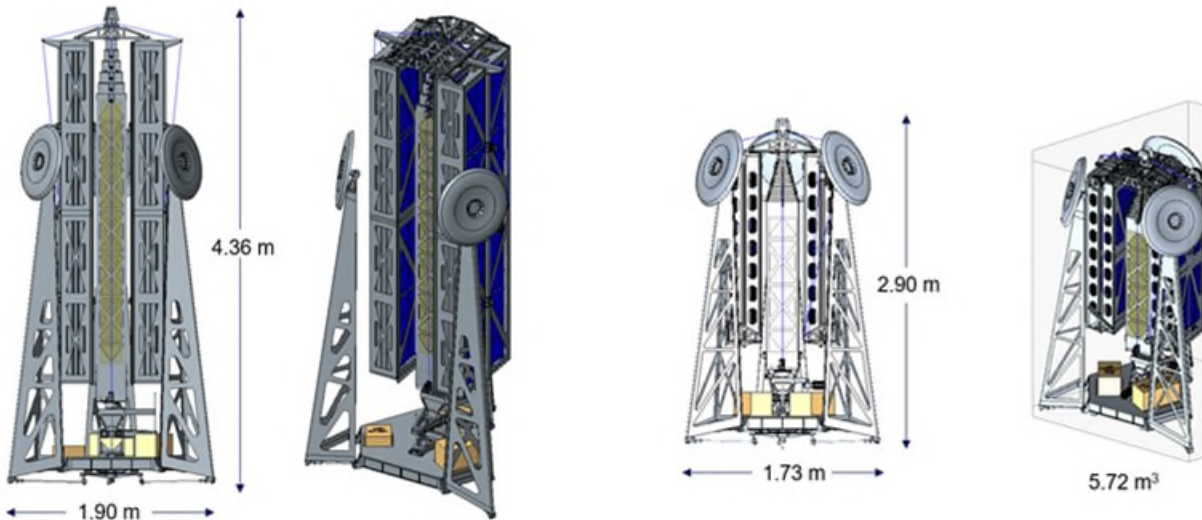


Figure 11. VSAT Iterations, Stowed Dimensions

Mast Second Iteration

Going from six to twelve mast segments wasn't necessarily difficult as the added segments were shorter versions of the original segments, with six additional smaller cross-section segments added. Efforts to purchase bespoke square telescopic extrusions proved to be excessively expensive for a concept demonstrator, so the design switched to formed sheet metal components riveted together to form the individual segments. Sealed bearings at the corners of each segment controlled the nesting of the segments and would provide smooth motion during extension and retraction. These bearings were placed in the corner of frames on each end of the nesting segments, with eight bearings per frame. These frames also provided locations for the wire rope pulleys at the segment tops and the rope anchor points at the segment bottoms. The thin walls of the segment sections were reinforced in the corners with doublers.

For the GRD build, a shorter seven segment version of the mast was built due to the constraints of the test chamber.

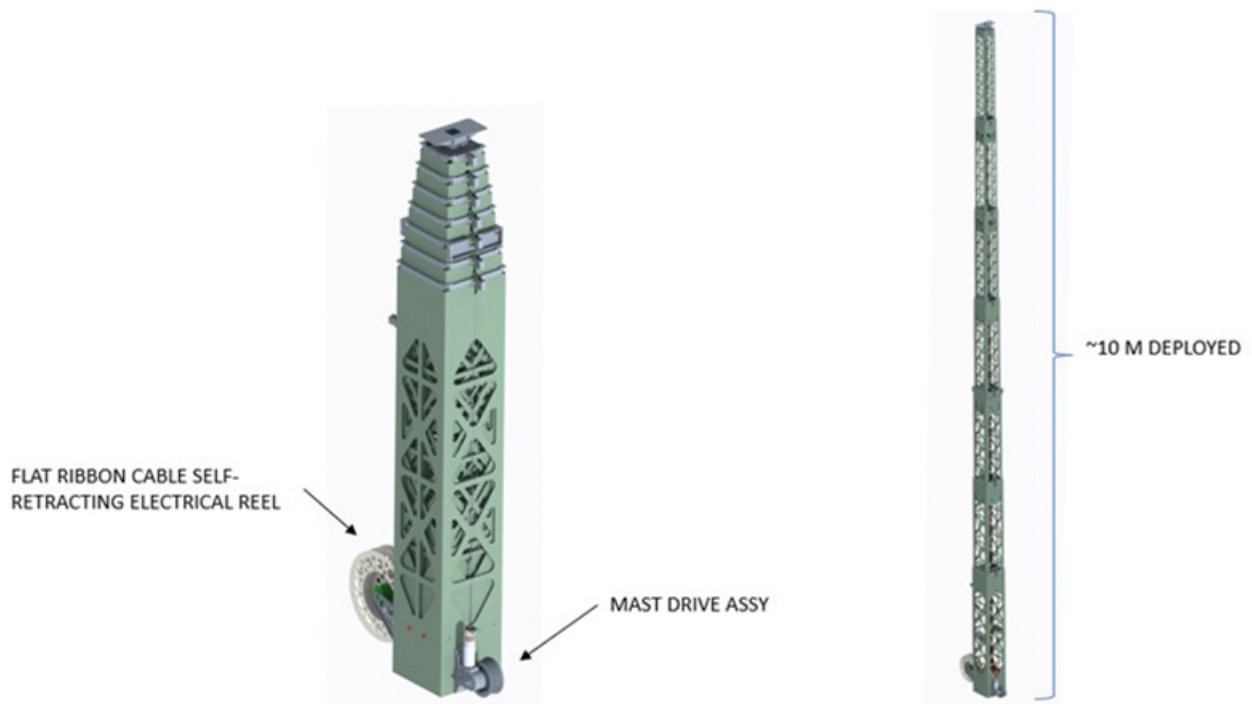


Figure 12. Revised 7 Segment Mast (GRD Build Version)

Wire ropes, drums, pulleys, and their terminations were designed and chosen per MIL-DTL-83420P, General Specification for Flexible Wire Rope for Aircraft Control. This document dictates safety factors, minimum radii, and breaking strengths of mil-spec wire rope. Drum winding management was handled via helical grooves in the drums, and the drums were designed for single wrap in their diameter and width. This eliminated the need for an active rope guiding fairlead.

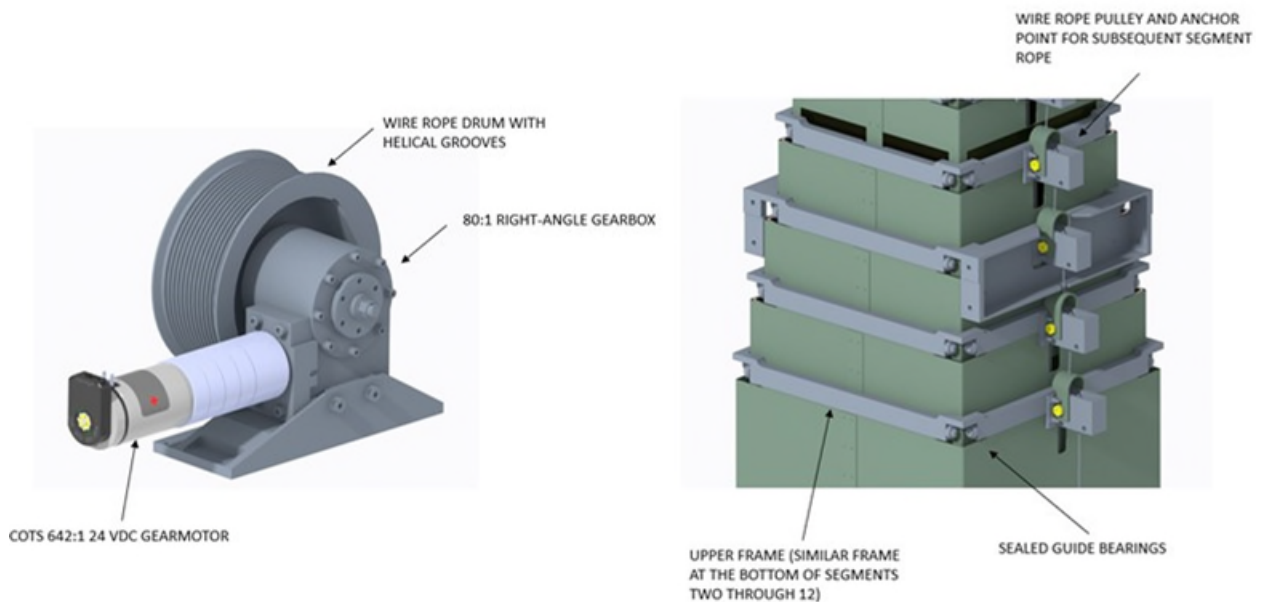


Figure 13. Segment Mast Wire Rope Drive and Guide Features

The Array Support assembly was redesigned in conjunction with the array packages to provide anchor points for new array housing drive ropes instead of the original taught rope pulleys. The estimate to build the sheet metal structure with machined fittings was deemed high, so a brief design study was performed exploring the use of bonded sandwich panels with machined fittings. The cost analysis was comparable to the sheet metal design, so the sheet metal design continued forward.

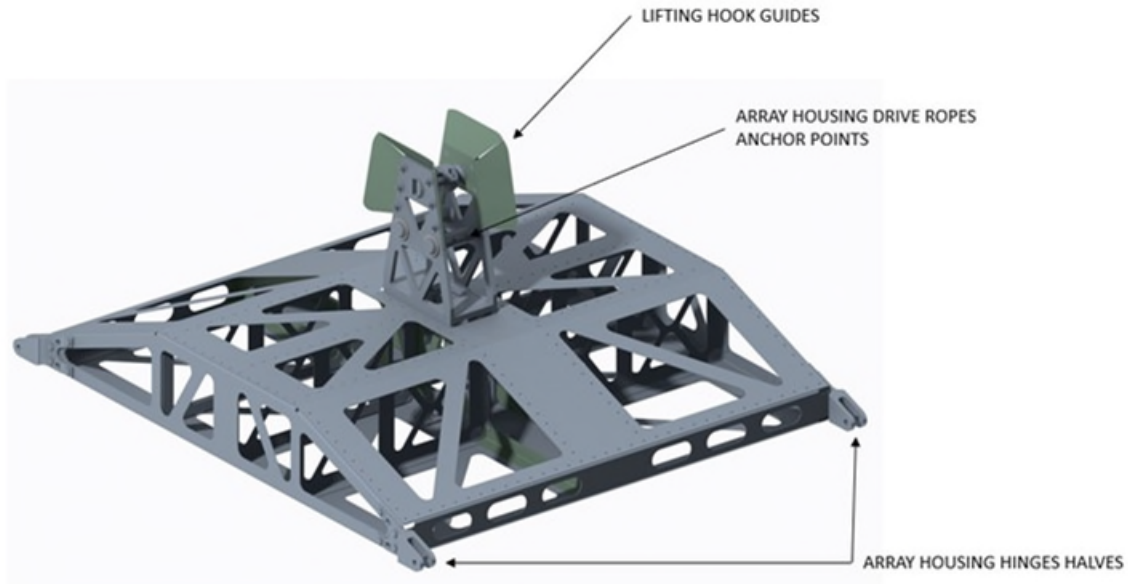


Figure 14. Revised Array Support Assembly

Array Packages Design, Second Iteration

Going from two array packages to four proved to be challenging. While the means of deploying the inboard housings via the single rope through the mast's core would work, unfolding the new outboard housings and having them return to their stowed positions would require a separate method. Instead, a common drivetrain for the inboard and outboard housings was developed that incorporated a drum for the inboard housing and two drums for the outboard housings. The driveline is operated via a right-angle worm drive powered by a COTS gearmotor, with the outboard housing drums attached to it. It in turn drives the inboard array housing through a planetary gear set with a ratio of 5:1. That reduction, along with the two different drum diameters, provide the 2:1 folding motion of the outboard array housing vs. the inboard array housing. That is, the inboard array must fold upward 90 degrees, and the outboard array housing must fold downward 180 degrees relative to the inboard array housing.

The inboard wire ropes are anchored to the Array Support Assembly and the outboard wire ropes are anchored at the outboard array housings distal ends. To prevent the wire rope crossing the inboard/outboard hinge-line, two “kickers” were added to the outboard housing to prevent a zero-angle-crossing rope geometry case. The heights of the kickers were set such that the wire rope tension did not exceed its working load capability.



Figure 15. Four Array Configuration at “Kicker” Contact Deployment Stage

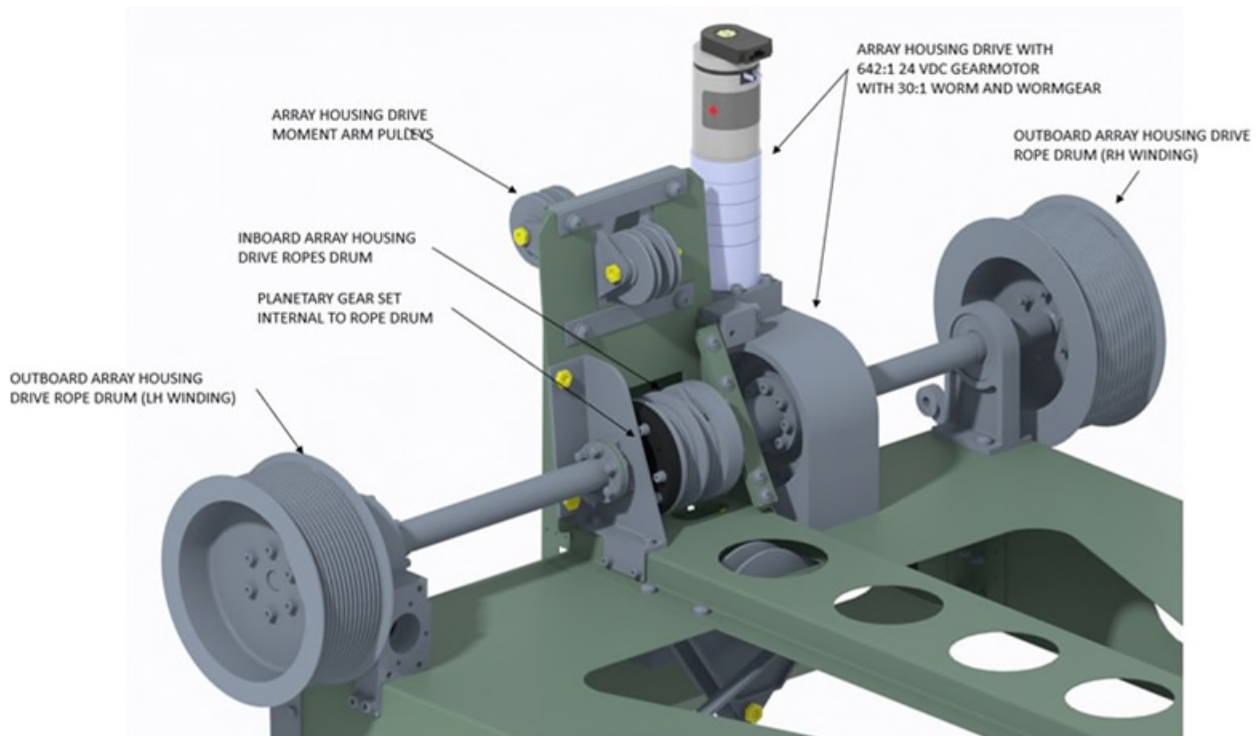


Figure 16. Array Housing Drivetrain

The array panel deployment method was changed to individual drivelines per package. This consisted of two array strap reels that unwind and wind nylon straps that lower and raise the arrays. These reels are on a common driveshaft driven by a right-angle gearbox and gearmotor. An adjustable clutch was added between the drive and the driveshaft to prevent stalling of the drive when the arrays are retracted. Strap length adjustment is provided by adjustable anchors on the bottom housing panels.

The mock array panel material was changed from thin aluminum to corrugated plastic panels to reduce mass, and instead of piano hinges, flexible tape was used for hinges. Only the first and last panels have bent aluminum sheet stiffeners to which the linkage pivot points are added.

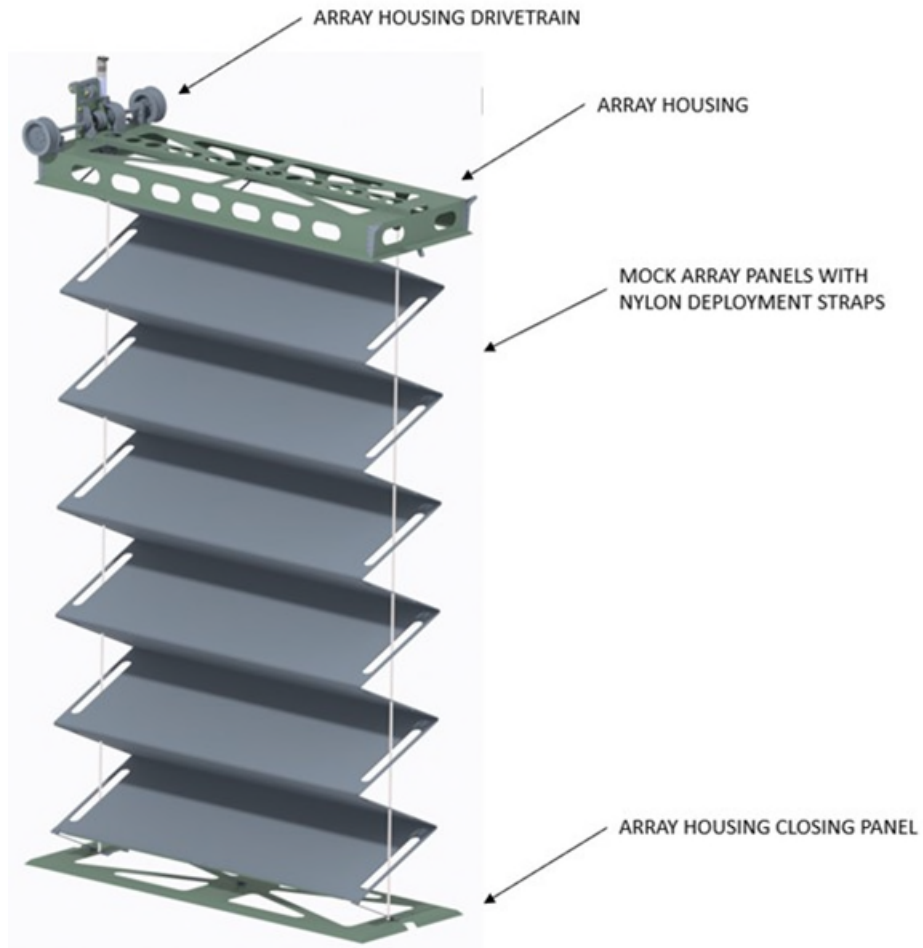


Figure 17. Inboard Array Package with Housing Drive

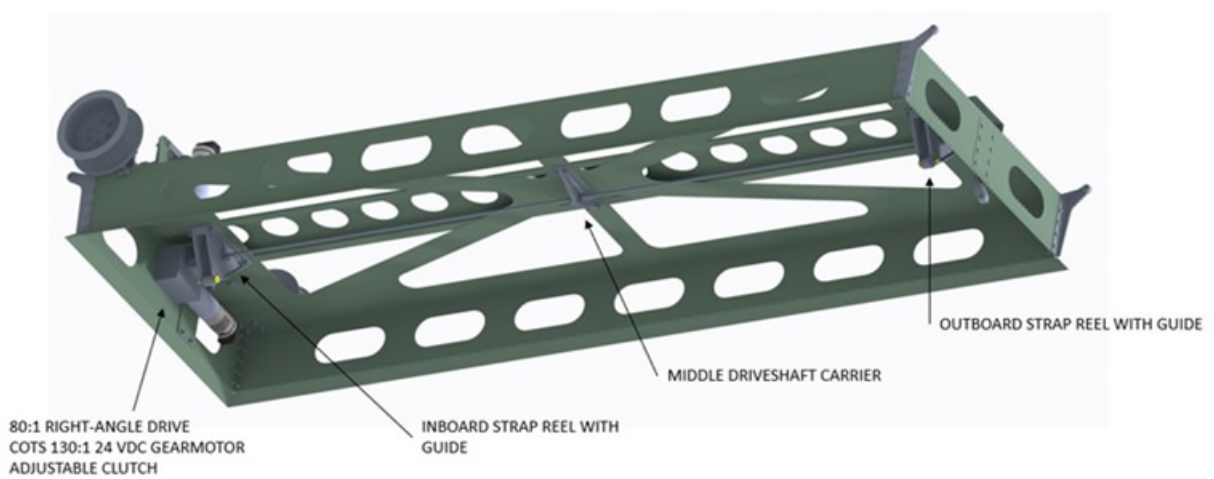


Figure 18. Array Panel Drivetrain

Control System

A SpeedGoat target machine serves as the main controller, taking both user and sensor input and generating analog control signals from this input. A motor driver takes these control signals and generates 24-volt PWM signals for the motors.

For the gimbal control, the SpeedGoat reads pitch and roll angle values from an inertial measurement unit (IMU) on the gimbal and feeds these angles into a proportional-integral-derivative (PID) loop. It then generates the control signals for the gimbal motors that will drive the mast to a desired angle. For the mast deployment control, the SpeedGoat reads sensor data from potentiometers and limit switches located at key points throughout the structure and uses this data to determine when to stop the mast, array housing and array panel deployment motors.

The user interacts with the control system by using a graphical user interface (GUI) running on a host machine connected to the SpeedGoat via an Ethernet connection. The user can set the desired gimbal angles and can start or stop the mast deployment. The user can also manually control each motor individually.

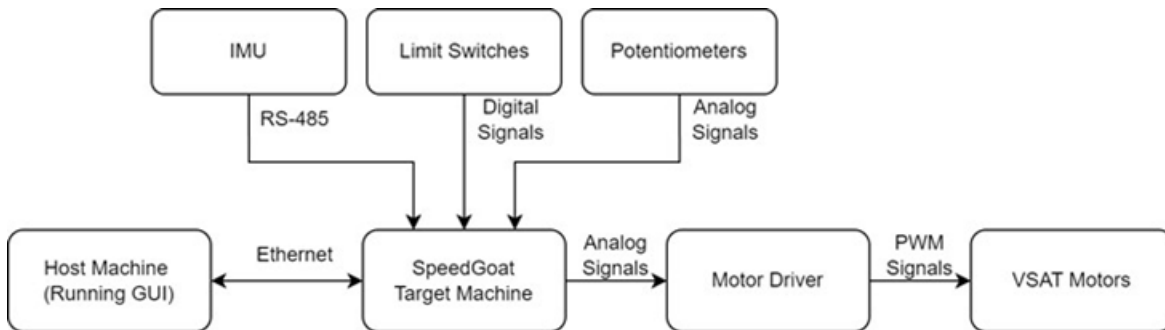


Figure 19. Diagram of the VSAT Control Setup

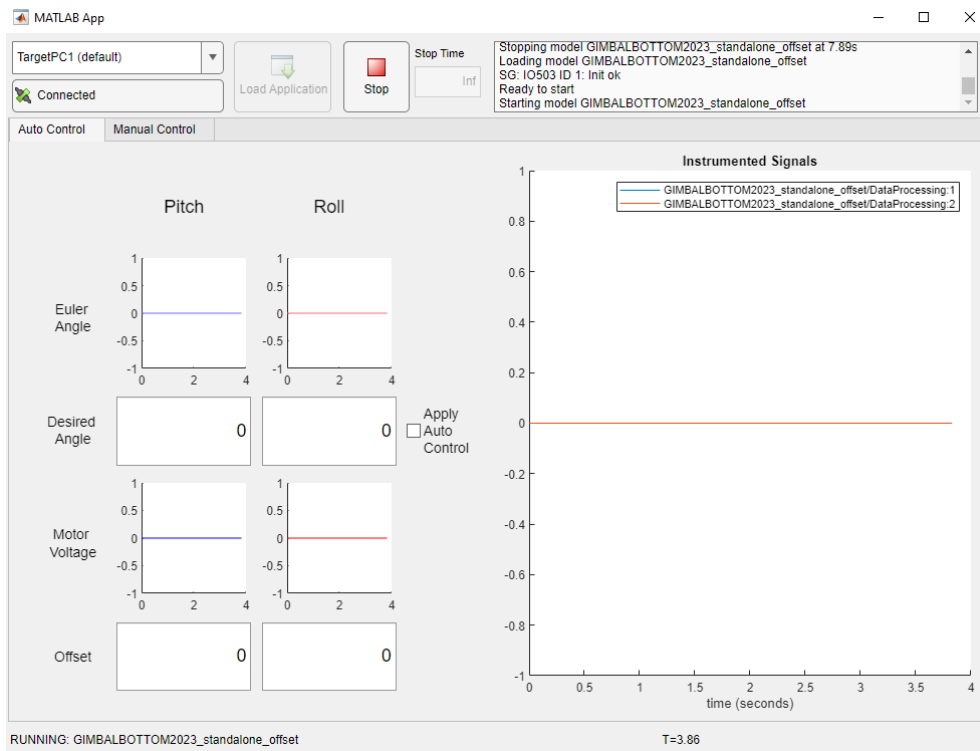


Figure 20. VSAT GUI

Conclusion

At the time of this writing, the VSAT GRD is undergoing assembly in a test cell in B1293B at Langley Research Center. All major components are complete or are near complete with revisions being made as assembly progresses. Wiring for the control system is partially complete and testing of the gimbal has been conducted successfully using a dummy mast with deadweight at the top to simulate the inertial properties of the VSAT in the stowed condition. The completed mast has been installed and the off-loader system is being installed.

Assembly and operational testing will be incremental with the assembly progress. As major components are installed, their operation will be tested. These steps include the following:

- IMU zeroing ensuring the mast is plumb
- Gimbal operation with the mast stowed to simulate mast up-righting
- Mast deployment and retraction/stowing
- Inboard array housings installations; deployment with the mast stowed (lower risk and allows for easier observation)
- Mast deployment with inboard arrays stowed
- Inboard array deployment and stowing
- Inboard array panel deployment and stowing
- Installation of the outboard arrays; deployment of inboard and outboard arrays with mast stowed
- Deployment of the mast with array housing deployment and stowing
- Deployment of outboard array panels

References

1. Mikulas, Martin M., et al., "Telescoping Solar Array Concept for Achieving High Packaging Efficiency." AIAA SciTech Forum, January 2015, <https://ntrs.nasa.gov/archive/nasa/casi.ntrs.nasa.gov/20150006022.pdf>
2. Pappa, Richard, et al., " Relocatable 10 kW Solar Array for Lunar South Pole Missions." *NASA/TM-20210011743*, March 2021.

Bearings for Extreme Environments – NiTi-Hf as a Premium Material for Miniature Radial Ball Bearings Intended for the use in Extreme Environments in Space and Healthcare Applications

Christoph Bayer*, Thomas Kreis* and David Nufer**

Abstract

Aerospace applications must survive one critical step before they start their operation in space, the launch; reports from space mechanism manufacturers indicate that many of them fail. Hence, the operation is done in a pre-damaged condition. At launch, a rocket subjects components, particular bearings, to high shock loads and random vibrations, which can result in damage and limited functionality or failure.

In cooperation with the NASA Glenn Research Center and the University of Akron, GRW developed a miniature ball bearing out of a highly specialized and exclusive alloy, which has three main advantages. One of them is its high static load capability; it can withstand high shock loads and random vibrations during a rocket takeoff, avoiding pre-damage and expensive repairs.

Results from this development have not been published. The status of the development is continuously reported to NASA Glenn Research Center and a few select customers who intend to perform application-oriented tests in the next development steps. This bearing type has flown to space on one occurrence; yet additional testing is required to finalize validation of the use of NiTi-Hf (Nickel-Titanium-Hafnium) miniature radial ball bearing in common space mechanism applications.

Introduction

The GRW project “Processing NiTi-Hf into Miniature-Ball-Bearings” aims to pave the way for the production of high precision miniature ball bearings in sizes down to 1.0 mm (0.039”) bore size from an alloy with promising characteristics. NiTi-Hf is a 60-Nickel-Titanium alloy with additionally added Hafnium. The processing of this alloy into ball bearings, as described in NASA’s LEW-18476-1 (USPTO 8,182,741) and related, is licensed by KAMAN with an Evaluation License. The background and the development of the specific material NiTi-Hf by NASA was stated and published before [1]. GRW, as a subsidiary of KAMAN Corporation, is a manufacturer of miniature ball bearings since 1942 and now takes the step to bring this alloy into a reliable serial production for ball bearings.

The project will result in anti-magnetic ball bearings with a significantly higher load capacity and corrosion stability compared to ball bearing steels currently in the market. In addition to some key facts about the alloy, these three major benefits of NiTi-Hf will be shown in the following sections.

Project Definition

60-Nickel-Titanium alloys as bearing steels have several advantages compared to common tool steels. They can be specifically designed for their use and therefore offer high hardness combined with a low modulus [3]. A little percentage of Hafnium is added for microstructural advantages, slowing down Ni_4Ti_3 growth rates of the alloy [3] and making the shape memory alloy a hardenable bearing steel with a hardness of above 56HRC.

* GRW, Rimpar, Germany (christoph.bayer@grw.de, thomas.kreis@grw.de)

** GRW, Bloomfield, CT (david.nufer@kaman.com)

As a powder metallurgical material, NiTi-Hf has a rather large grain size distribution with clearly visible grain structures, as seen on the left microstructure image of Figure 1. Therefore, compare the microstructure of NiTi-Hf, with grain sizes of up to 90 μm , to the grain structure of 440C, which is showing visible carbides that are only 40 μm in size (Figure 1). The special process of transforming this roughly structured material into a highly finished bearing surface is what makes these NiTi-Hf bearings special. With processes especially adapted to powder metallurgical materials and the manufacturing of titanium, GRW reaches surface qualities of common high-precision bearings made of 440C or 52100.

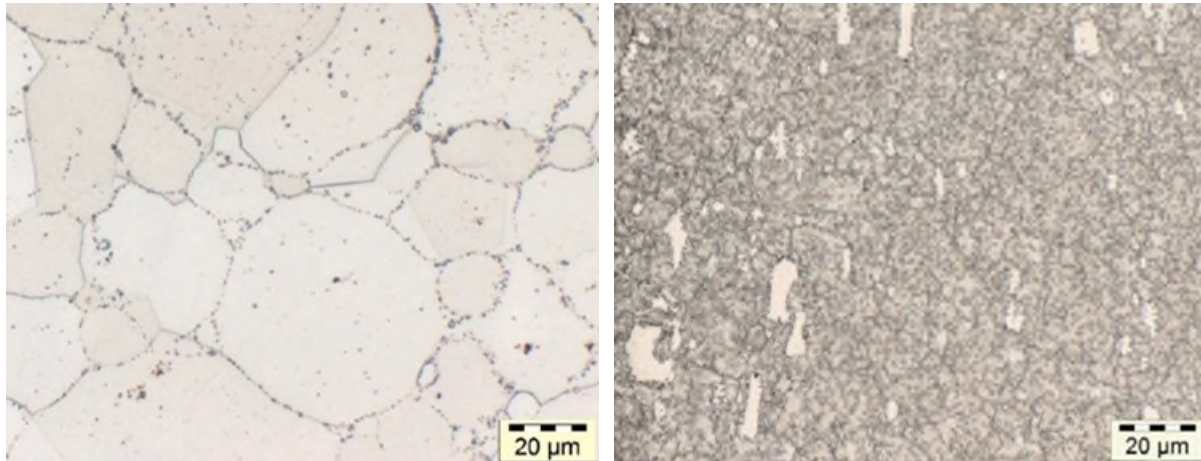


Figure 1: Microstructure images of NiTi-Hf and 440C compared after heat-treatment (Magnification 500:1)

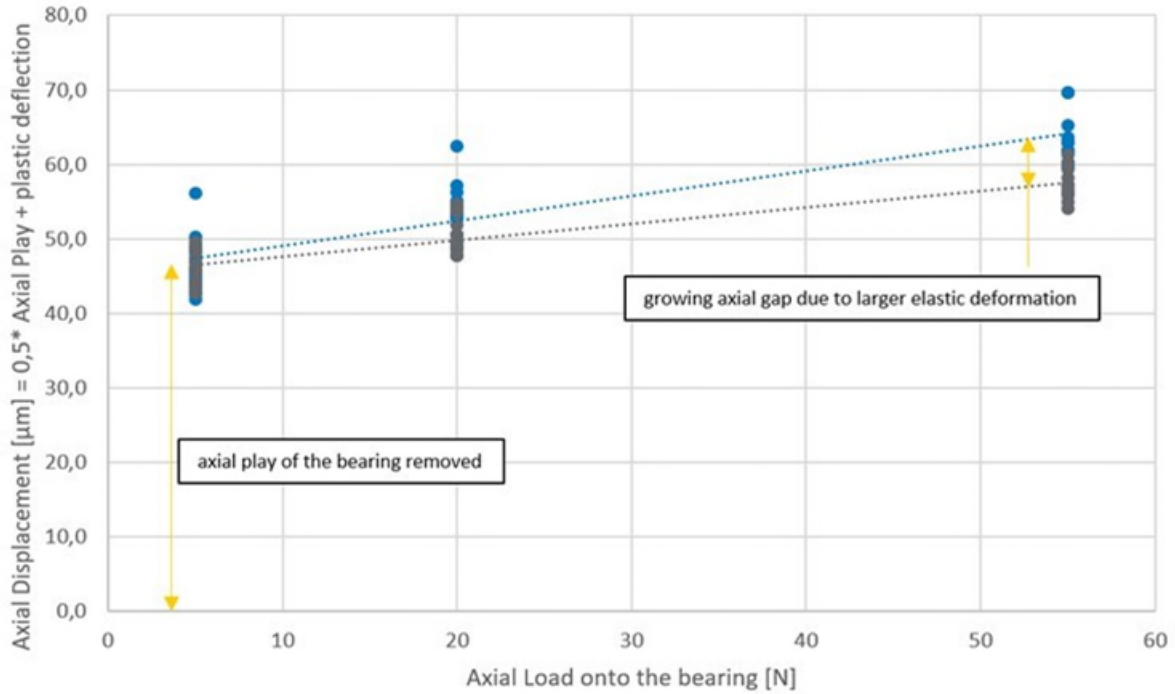
Table 1 shows the material properties of NiTi-Hf after the microstructure. In terms of density and thermal expansion, these properties are comparable to 440C, a widely used bearing steel.

Table 1: Material characteristics comparison [2]

Material properties	NiTi-Hf	Common bearing steel 440C
Density	6700 kg/m ³	7750 kg/m ³
Hardness	56 to 60 HRC	58 to 62 HRC
Young's Modulus	~95 GPa	~200 GPa
Maximum use temperature	400°C	200°C
Thermal expansion	~11.2 x 10 ⁻⁶ /°C	~10.0 x 10 ⁻⁶ /°C
Magnetism	Non	Magnetic
Corrosion resistance	Excellent	Marginal

The unique characteristic of NiTi-Hf is the combination of a high achievable hardness despite a low Young's modulus of only 95 GPa. This makes the material capable to convert high loads into elastic deformations and not creating excessively high stresses, which cause common bearings to fail. This difference in elastic deformation is shown in Figure 2 where the axial displacement of the bearing inner ring is measured over an increasing axial load on the inner ring. You can see the growing gap between a bearing made of common bearing steels (here, 440C) and a bearing made of NiTi-Hf.

Both geometrically identical bearings start with an axial displacement of roughly 45 microns at an axial load of 0.1 N. This is equivalent to half of the axial play of both bearings. Increasing the axial load onto the bearings inner ring, you can clearly measure higher axial displacement of NiTi-Hf bearings. This is because NiTi-Hf with the lower modulus is capable of transferring high loads into a higher elastic deformation, while 440C creates higher contact stresses with lower elastic deformation, as the static simulation in Figure 3 shows.



• NiTi-Hf (95GPa) • 440C (200GPa)

Figure 2: Measurement of the axial displacement of a bearing inner ring under increasing axial load on a NiTi-Hf bearing compared to a 440C bearing

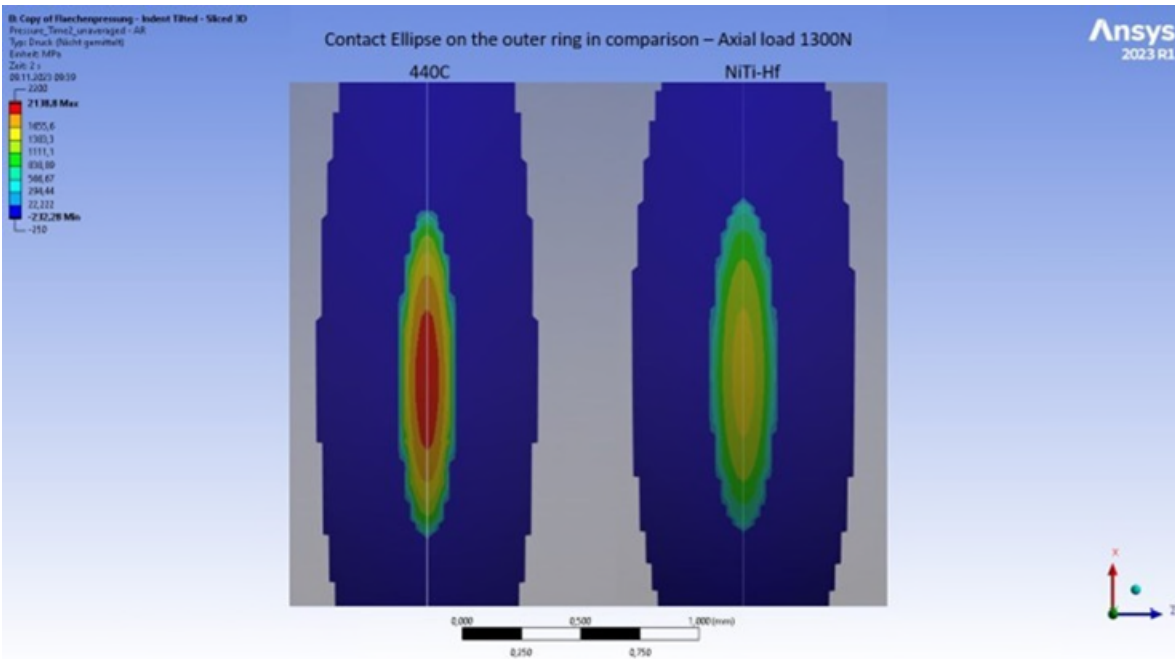


Figure 3: Simulation of the contact stresses in a NiTi-Hf bearing raceway under 1300N axial load, compared to a bearing raceway of 440C

Higher static load capacity

The current standard for bearings with the highest load capacity is 52100 bearing steel. GRW performs a test where the minimum load at which plastic deformation occurs first in the ball bearing is measured. Therefore, bearings are axially loaded in sequences of increasing load peaks. Between each sequence, we examine the bearings by noise measurement for plastic deformation in the form of ball indents on the raceway.

The first tests performed, as described, showed an improvement of NiTi-Hf bearing compared to 52100 of 200+%, as Figure 4 illustrates.

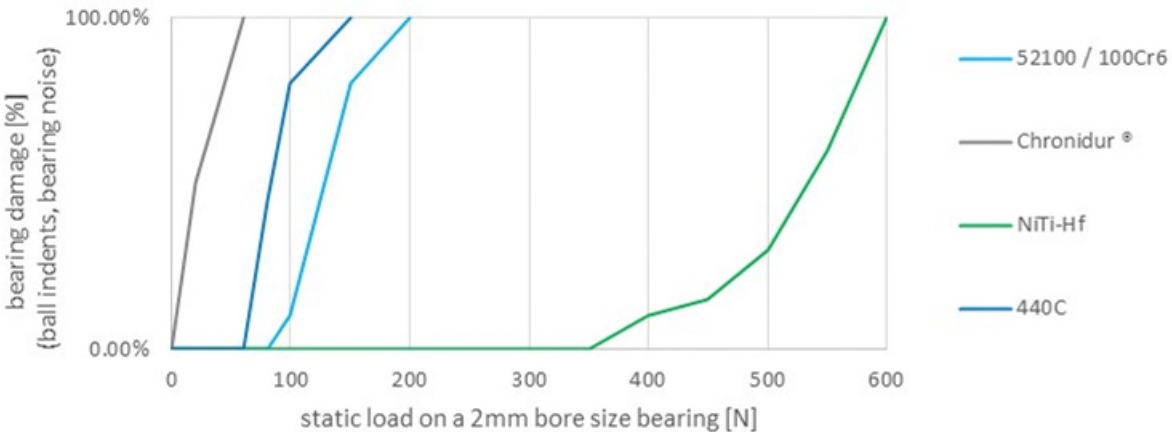


Figure 4: Load capability of bearing materials comparison

This improved load carrying capability can help the aerospace industry avoid common damages from launch loads and/or to miniaturize their bearings and therefore the application, or to increase their allowable payload on the bearings. All three possibilities can have a major impact for manufacturers of aerospace applications.

As an explanation for the shock load resistance, see the comparison of two radial ball bearing inner rings in Figure 5. Both bearings with an inner diameter of 2.00 mm were loaded with an axial load of 100 N. Where a common bearing material deforms plastically and the bearings raceway is damaged by ball indents (left figure, green area), NiTi-Hf material can withstand up to 6 times the load without plastic deformation.

A bearing pre-damaged with ball indents will result in increased starting/running torque, irregular running behavior and early failure.

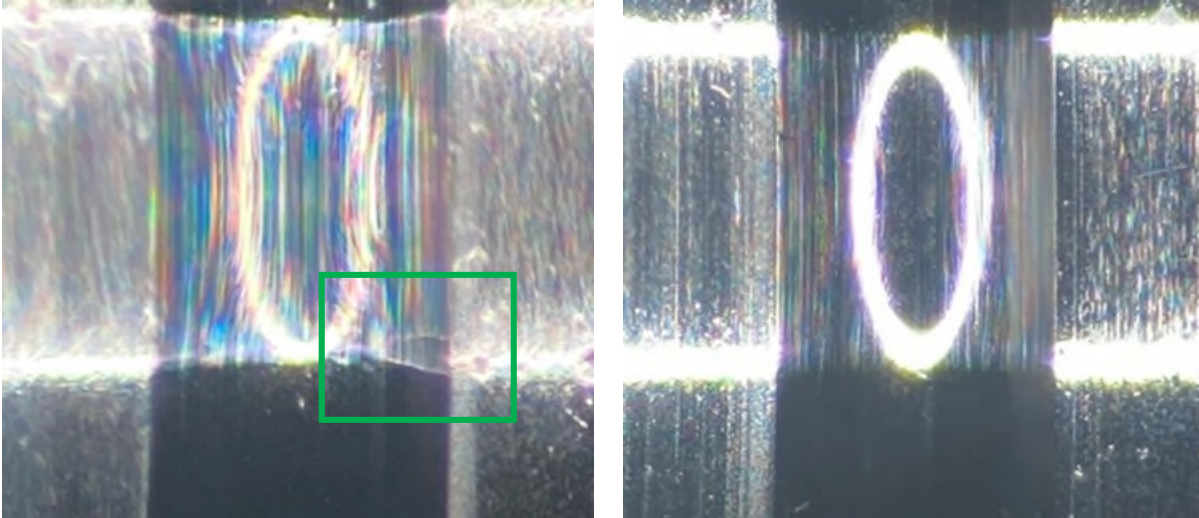


Figure 5: comparison of a common bearing raceway out of 440C material (left, ball indent) vs. a bearing raceway out of NiTi-Hf (right, no indent) after an axial load of 100N

Improved corrosion stability

In applications where high corrosion stability is essential due to aggressive media surrounding the bearing, customers currently use high-alloy, martensitic stainless steels, mainly Cronidur® 30 (X30CrMoN15-1) or 440C.

GRW uses the DIN EN ISO 9227 standardized, so-called Salt Spray Test in order to prove the corrosion resistance of bearing materials. Initial measurements showed that NiTi-Hf bearings are able to exceed the level of Cronidur® by more than 150%.

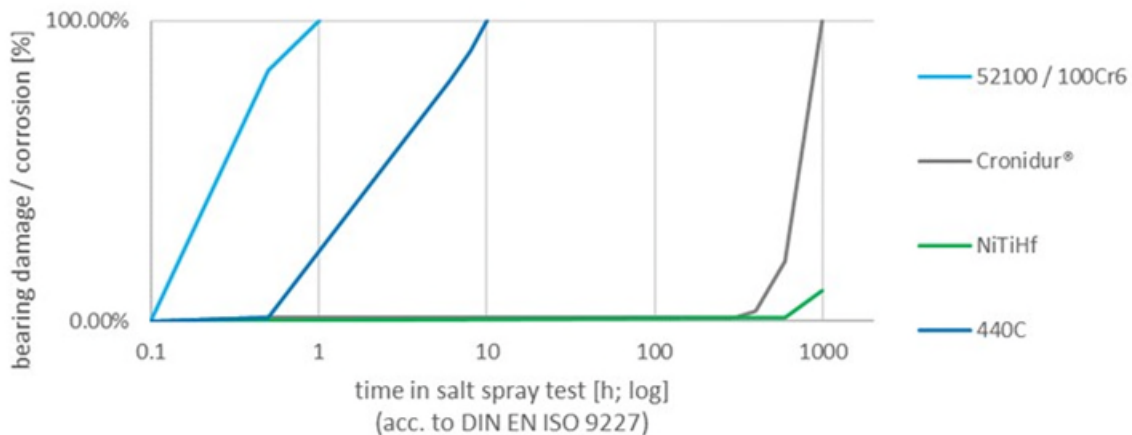


Figure 6: Corrosion stability of bearing materials

In addition to this highly corrosion-resistant bearing material's usefulness in aerospace applications, the medical industry will benefit greatly from this development. Surgical application specifically, which are faced with harsh environments and strong cleaning media during sterilization, are a likely ideal use-case. Most often, the subpar corrosion stability with today's bearing materials is the limiting factor in medical applications.

Anti-magnetism

In general, 60NiTi is an anti-magnetic shape memory alloy. With the addition of Hafnium, this alloy no longer counts among the shape memory alloys, yet keeps its anti-magnetic characteristics. Anti-magnetic ball

bearings are used in measurement technology or medical applications for example, where magnetic fields can influence the process in a negative way. Currently, customers have to resort to high-cost ceramic bearing materials to rectify this complication.

Conclusion

Uniting these three characteristics in one material, NiTi-Hf bearings can improve the performance in various fields of applications, specifically the critical aerospace and healthcare industries. The unique lessons learned during the subject presentation will be the initial performance of an innovative, production ball bearing steel and ways to optimize envelop dimensions by utilizing the benefits of NiTiHf radial ball bearings.

As this project is supported and managed in corporation with NASA Glenn Research Center, this project addresses at least two of the NASA Technology Taxonomy areas with:

- TX12.1.4 Materials for Extreme Environments” as a ball bearing with extreme static load capabilities.
- TX12.1.7 Special Materials” as a multi-functional material with anti-magnetic properties.

The Technology Readiness Level of this project can be rated at a seven. The current status of the work is, basically, Engineering Testing Complete. The internal engineering development processes at GRW have been completed; significant testing has been conducted but further application-specific testing, as well as supply chain optimization, are necessary before pilot production.

References

1. Christopher Dellacorte, L. E. (2014). *Launch Load Resistant Spacecraft Mechanism Bearings Made From NiTi Superelastic Intermetallic Materials*. NASA Goddard Space Flight Center: Aerospace Mechanisms Symposium.
2. Christopher Dellacorte, S. A. (2017). *Microstructural and Material Quality Effects on Rolling Contact Fatigue on Highly Elastic Intermetallic NiTi Ball Bearings*. NASA/TM-2017-219466.
3. Sean H. Mills, R. D. (2020). *Development of Nickel-Rich Nickel-Titanium-Hafnium Alloys for Tribological Applications*. ISSN 2199-384X: Springer.

Magnetic Fast Steering Mirrors for High Power Optical Communication

Etienne Betsch*, Gérald Aigouy*, Clément Cote*, Augustin Bedek*, Arnaud Barnique*, Nicolas Bourgeot*, Hugo Grardel*, Pierre Personnat*, Patrick Meneroud*, Théo Simon*, Marc Fournier*, Sylvain Chardon*, Frank Claeysen* and François Barillot *

Abstract

To cope with performances of Fine Pointing and Fast Steering mirror requirements for Space Optical Communication, CEDRAT TECHNOLOGIES (CTEC) is developing magnetic Fast Steering Mirror (M-FSM) family based on proprietary MICA™ flexure bearing magnetic actuator mechanism (Moving Iron Controllable Actuator), with embedded eddy current sensors (ECS).

FSM design is expected to be used for Optical Inter-Satellite Links in large-scale New Space constellations and is highly driven by mandatory cost efficiency for high-quantity recurrent production, while FSM design expected for Feeder-Link communication is driven instead by high-power laser requirements together with a high level of redundancy.

In this publication CTEC is presenting both the M-FSM45 and M-FSM-HPL designs and test results, respectively, for inter-satellites and feeder link optical communications.

Introduction

Starting from M-FSM62 former design heritage, CTEC has designed first the M-FSM45 dedicated to Giant constellations based on inter-satellites Communication, focusing on mandatory cost efficiency, with high repeatability of performances and reliability, while targeting no defect at customer integration over quantities beyond several thousands of units delivered in very short production time series.

After successful achievement of M-FSM45 Engineering Models design and testing, CTEC is proposing alternate M-FSM-HPL (High Power Laser) design dedicated to Feeder-link applications. The proposed design has been optimized for continuous laser power under vacuum, ranging from 40W to 80W, leading to SiC mirror design with very high reflectivity, and high conductivity. Together with the mirror heat conduction design optimization, a drastic improvement of the FSM heat sinking has been achieved, in order to maintain low equilibrium temperature on mirror surface, together with low thermal gradient, in order to cope with stringent wave front error (WFE) requirement. The FSM size has been increased in order to implement two redundant coils assemblies, each connectable to two separate drive electronics (redundant and nominal).

M-FSM45 and M-FSM-HPL Designs and Test Results

The angular stroke amplitude has been increased from $\pm 1.5^\circ$ on M-FSM45 to $\pm 2.5^\circ$ on M-FSM-HPL, together a new concept of eddy current position sensors, allowing redundancy. Additional end-stop devices have been implemented for the launch vibration and shock loads, successfully tested to 1.5-g²/Hz random vibration level at actuation resonance frequency and to 1000g SRS shock, avoiding any electrical launch locking device.

Starting from the very first former PYSCHÉ PAM30 flight project heritage for Deep Space Optical Communication, CTEC is developing FSM SiC mirror technology for both cost-efficient large-scale

* Cedrat Technologies, Meylan, France

constellations focusing on mirror cost optimization versus performance, and for Feeder-link high power Laser, focusing on very high reflectivity and high thermal conductivity.

The environmental test campaign for space qualification has been passed, which includes launch vibration and shock tests, thermal vacuum tests, high frequency accelerated lifetime fatigue tests, and closed loop position control tests based on advanced control achieved with LQG state feedback controller in order to reach the highest bandwidth possible at high stroke amplitude.

M-FSM45 Design Description

The M-FSM45 is a magnetic mechanism driving two tilt axes through a large angle. This FSM, which derives from M-FSM62 [4,5] is composed of the following parts:

- A magnetic circuit in soft magnetic composite material with 4 magnets and a moving part.
- 4 coils optimized to provide the best induction in the small volume with potting to dissipate the generated heat.
- An eddy current sensor device with aluminum targets embedded on the moving parts, and 4 sensing heads on a single PCB below.
- A moving part suspended on a flexure bearing ensuring high lifetime performances.
- A mirror fixed on a flexible baseplate limiting the integration deformations.

The magnetic design relies on forces due to tangential variable magnetic reluctance, which offers higher forces than Lorentz forces [6] and more linear forces than normal variable magnetic reluctance [7]. To ensure the FSM performance, magnetic calculations by FEA have been performed. The magnetic saturation, available torque, and parasitic forces were verified.

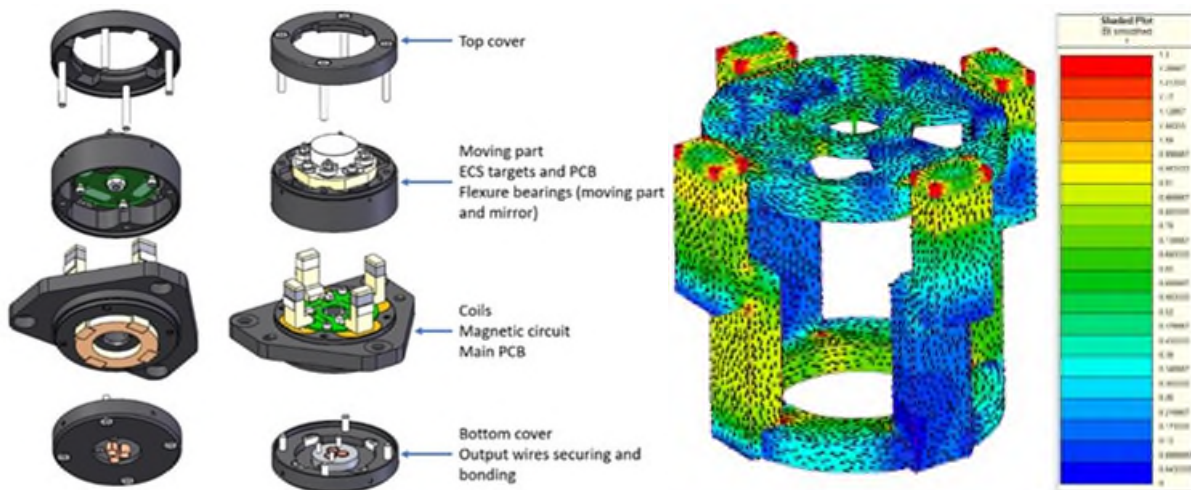


Figure 1: M-FSM cost efficient design concept (left) and magnetic circuit finite element modelling (right)

M-FSM45 Eddy Current Position Sensors (ECS)

To measure the mirror position and perform closed loop control, an eddy current sensor assembly is embedded in the mechanism. The sensor assembly is eased thanks to the design of a single PCB including the 4 sensing coils, taking advantage of the space qualification of PCB-ECS sensors [8]. This solution makes the M-FSM more compact, with an efficient one step assembly. The sensitivity has been optimized for the FSM stroke, making the sensor non-linearity acceptable for the application.

Mirror design

One of the main design constraints of an embedded optics mechanism is to keep the mirror surface deformation as low as possible to keep the induced optical wave front error within requirements. In this

case, a maximum of 40-nm rms RWE at 0° mirror surface flatness is the target (corresponding to a 20-nm rms optical surface flatness).

To ensure that the specification would be reached, CTEC used tools developed for previous space optical mechanisms projects. Specifically including evaluation of induced surface deformation caused by mechanical biases, thermal deformation as well as optimization of mirror shape and dimensions.

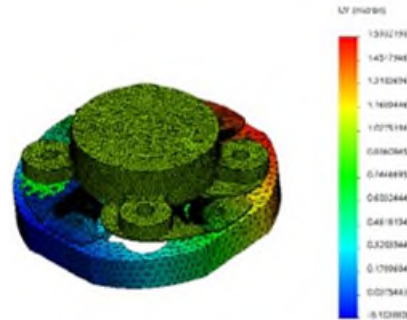


Figure 2: MFSM45 simulation (vertical displacement) for an integration simulation

The design optimization process included not only the mirror, but also an equally important part, the mirror support. The mirror support is the part ensuring the mechanical link between the actuators and the mirror. To greatly limit the mechanical deformation transmitted to the mirror from the mechanism distortions, CTEC developed a dedicated flexible mirror support.

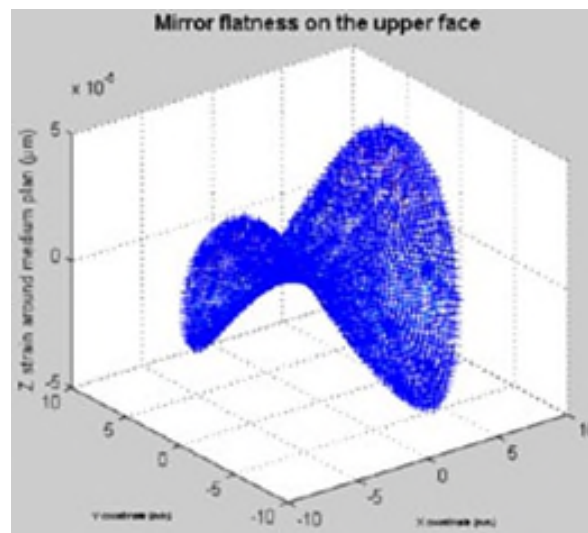


Figure 3: Simulated mirror deformation

For the MFSM45, a specific mirror and support design was developed. The design aimed at reducing the operational optical surface deformation, while keeping the assembly stiff enough to withstand (mechanical stress considerations) environmental conditions (temperature, vibrations) and mechanisms forces. The mirror deformation induced by the mechanism was targeted to be under 20nm rms RWE; the mirror manufacturer was requested to deliver a coated mirror under 20nm rms RWE (total RWE <40nm RMS).

Mirror procurement and verification

The mirrors were manufactured for the engineering models and optical verifications were performed. Figure 5 shows the mirrors RWE (reflected wave front error measured with Zygo interferometer at CTEC laboratory) and shows how after the mechanism assembly, the mirror surface flatness was controlled.



Figure 4: Free state mirror (left) and Mirrors RWE test after integration (right)

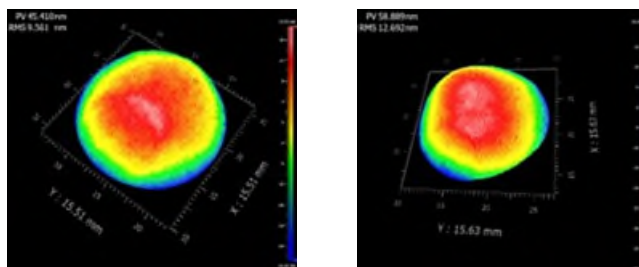


Figure 5: Mirrors RWE before integration (left) and after (right)

The optical verification indicates that the mirrors are compliant with important requirements in both free state and after integration.

Table 1: Mirror optical control results (specification: RWE < 40nm rms)

	M-FSM45
Mirror RWE before integration (nm rms)	10
Mirror RWE after integration (nm rms)	12.7

M-FSM45 Manufacturing and Assembly

The mechanism design has been optimized with the objective of reducing the assembly complexity and time, in order to achieve high-cost efficiency for very large quantity production. Specific tooling was designed for critical steps such as mirror integration, coils' potting, or moving part assembly into the magnetic circuit.

The magnetic parts were manufactured by industrial molding processes, dedicated to composite magnetic material featuring very low eddy currents. The geometrical tolerances were considered by design to sustain the worst-case air gaps in the torque calculation.

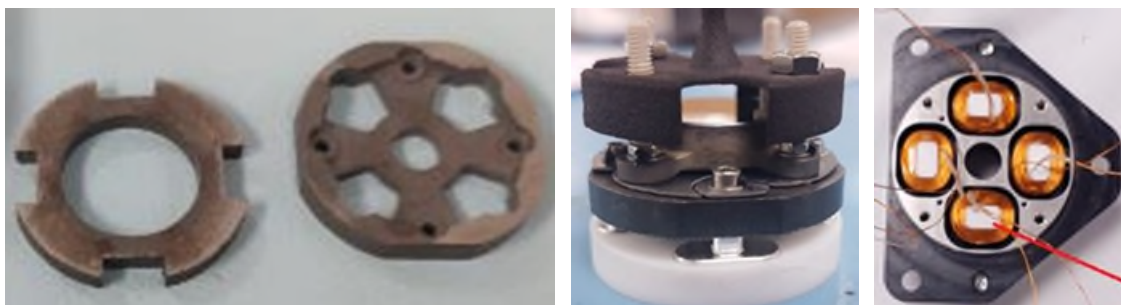


Figure 6: M-FSM SMC parts (left), tooling for mirror & moving part (center), and coils' assembly (right)



Figure 7: M-FSM45 Engineering Model N°1

MFSM45 tests main results

The M-FSM performance has been measured in open-loop to validate the available stroke, frequency, and coil values. As expected, the first resonance frequency is located around 100 Hz. The calculated coils parameters are validated through the impedance and inductance measurements.

The stroke measured shows that the M-FSM has a maximal stroke slightly lower than $\pm 1.5^\circ$ (± 25.8 mrad) for a ± 1 -A current input. The measurements have been performed with a large angle autocollimator allowing a single-angle low-frequency acquisition.

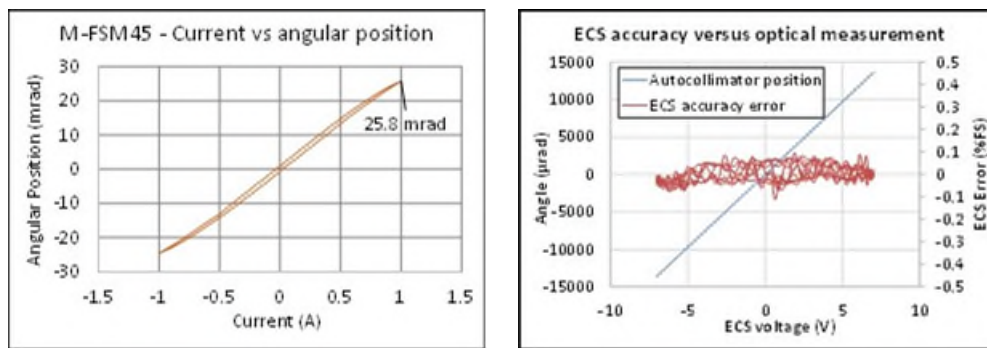


Figure 8: M-FSM45 stroke amplitude test (left) and ECS accuracy over full scale (right)

After complete assembly of the M-FSM45, the ECS position sensors' accuracy was measured compared to the optical measure of mirror position with an autocollimator facility. The accuracy error of ECS position sensors was in the range of $\pm 0.08\%$ of the ± 15 -mrad measurement full scale.

The frequency bandwidth test was achieved at ± 500 - μ rad position amplitude and has shown a -3dB frequency bandwidth up to 320 Hz on M-FSM45, which is considered a very good result.

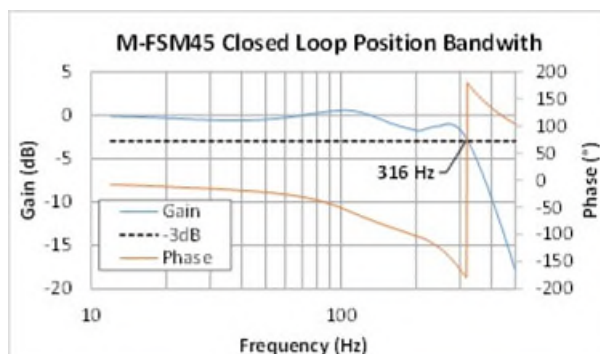


Figure 9: M-FSM45 Closed control bandwidth

M-FSM45-HPL Design Evolution

The M-FSM45-HPL is then derived from the M-FSM45 with some key points added to make it suitable for high-power Laser applications. The functioning principle stays the same with the magnetic circuit in soft magnetic composite material to remove the eddy current perturbations, 4 Coils (+ redundant channel) to generate the moving magnetic field, the eddy current sensor system with a new detection system, a moving part with optimized flexures bearings, and a mirror. As described in Figure 10, the coils will create a magnetic field that will couple with the permanent magnet effect to generate a torque on the moving iron.

As for the MFSM45, to hold the mirror on the moving part, a specific flexible element was designed to limit the impact of the screws tightening on the reflected wavefront error while keeping the mechanism resonances as high as possible.

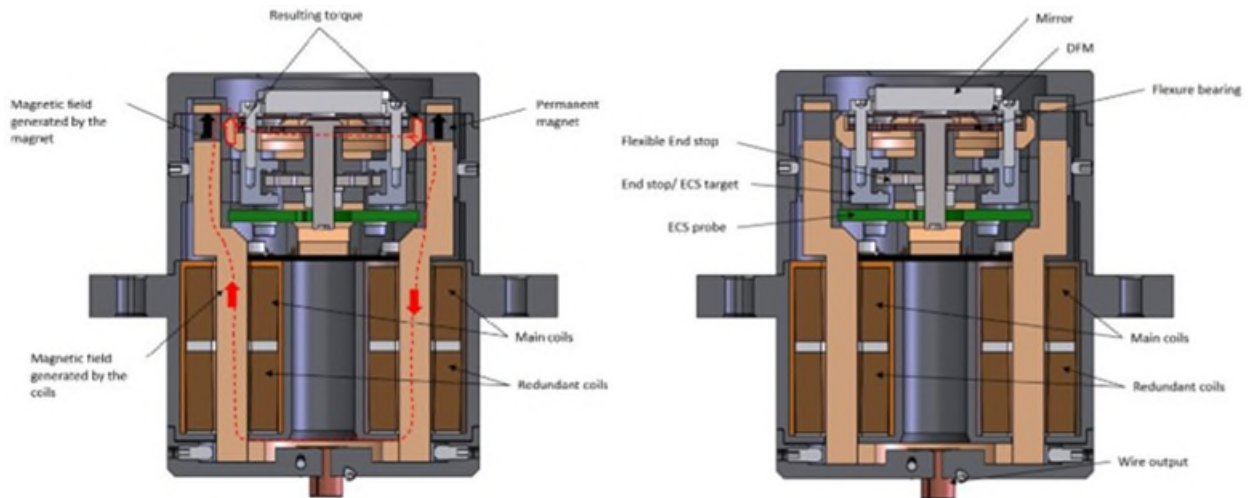


Figure 10 M-FSM45-HPL detailed view

The -3 dB bandwidth expected to be reached by the mechanism is higher than 500 Hz.

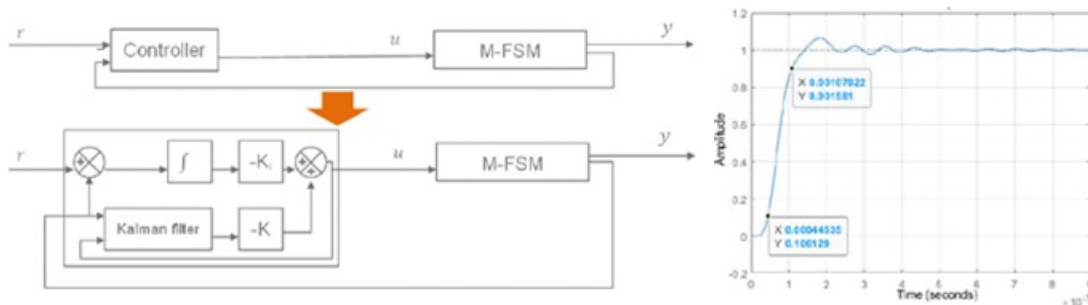


Figure 11. Closed loop bandwidth optimization with state feedback LQG controller

Angle increase

The mechanism has been reworked to optimize the available space inside the 45-mm diameter. Thanks to a magnetic redesign, the overall torque is increased, allowing an angle of $\pm 2.5^\circ$ while keeping the main resonance frequency higher than 80 Hz.

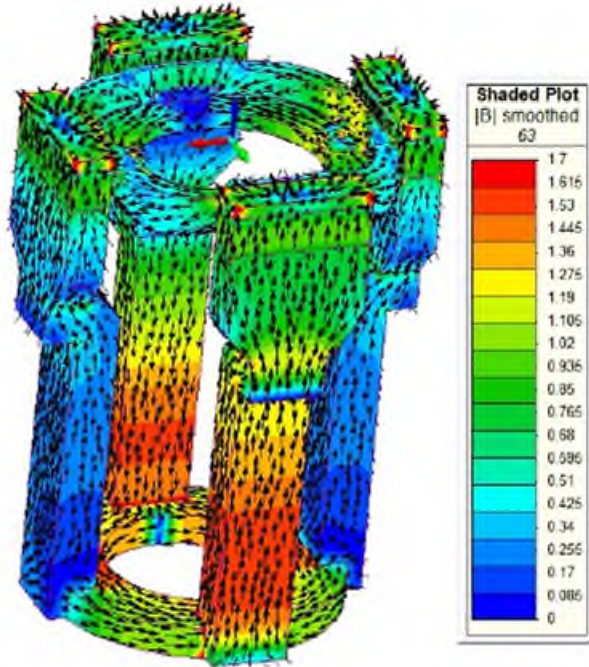


Figure 11 Magnetic field optimization

These magnetic performance improvements are also visible on the foreseen dissipated power. While the M-FSM45 reaches $\pm 1.5^\circ$ for a 4-W RMS power at low frequency, the M-FSM45-HPL performs a $\pm 2.5^\circ$ angle for a power lower than 0.7 W on the redundant channel worst case.

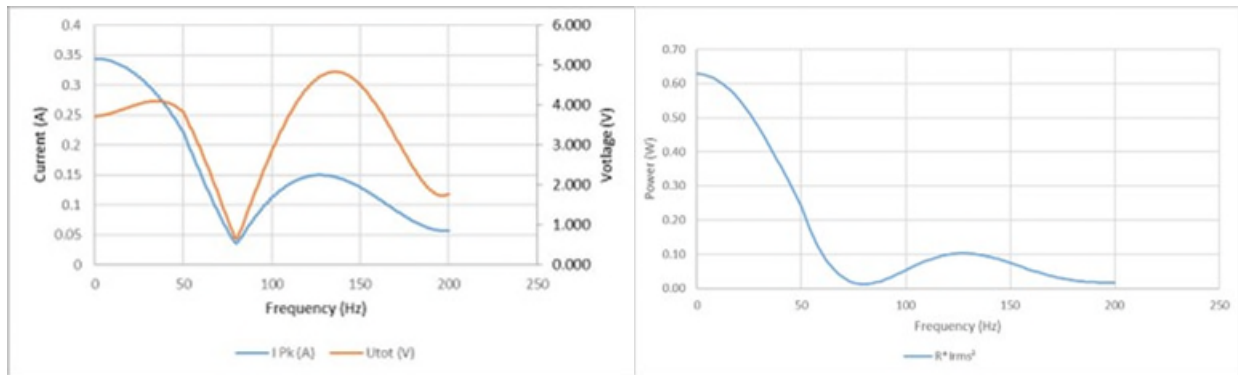


Figure 12 Calculated electrical performances of the M-FSM45-HPL

Thermal management

One of the key requirements of the mechanism is to be able to sustain a high-power laser up to 80 W. The mirror reflectivity is required to be higher than 99.5% to minimize the absorbed power by the mirror. The SiC mirror high thermal conductivity will allow a homogenous thermal distribution inside the mirror in order to reduce the laser effect on the reflected wavefront error. The flexure bearings are designed to dissipate as much heat as possible. Their material is chosen because of its good combination of high thermal conductivity and high yield strength. A stack of a few bearings is preferred instead of a single thicker one to adjust the global tilting stiffness and increase the heat exchange surface.

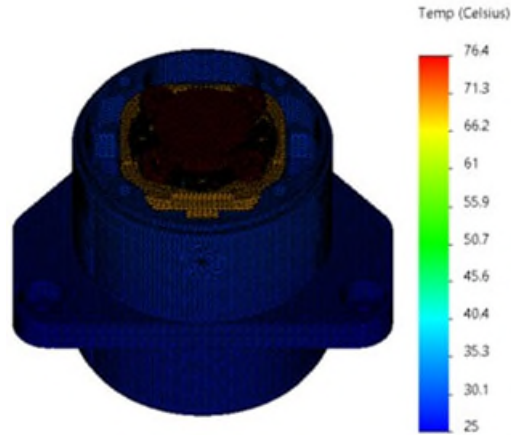


Figure 13 Thermal mapping for 80-W laser on the mirror

This design choices allow the mirror to stay under 80°C, which is foreseen to be the maximal temperature for the chosen mirror coating.

Redundancy integration

The redundancy management for this mechanism is mandatory as it needs to fulfill space flight requirements. The redundant coil system is added below the main coil channel inside the main coil casing, increasing the length of the mechanism. A cold redundancy solution is chosen here.

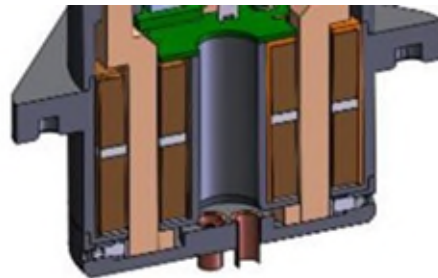


Figure 14 Redundant coil system

The ECS system is also reworked to include redundant functionality. To improve the mechanism linearity performance, a differential mode on a full axis is performed by software after the linearization of each probe individually. As each eddy current probe is independent with a single frequency detection strategy, the redundancy is ensured in case of a failure detection. The same mechanical design is used, with the probes on a single PCB to ease the integration.

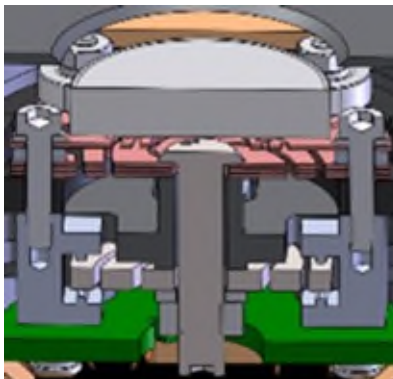


Figure 15 Eddy current sensors integration (PCB in green) and end-stop system

End-stop design

The M-FSM45-HPL is a mechanism with a moving part suspended on its flexure bearings. The high vibration level required for space launch environment is a difficult part of the design. Without additional elements, several notches would be required on the specified levels. The end-stop system designed for the mechanism (Figure 16) allows sustaining the full level of 1.5-g²/Hz random vibration at actuation resonance frequency and up to 1000g SRS shock.

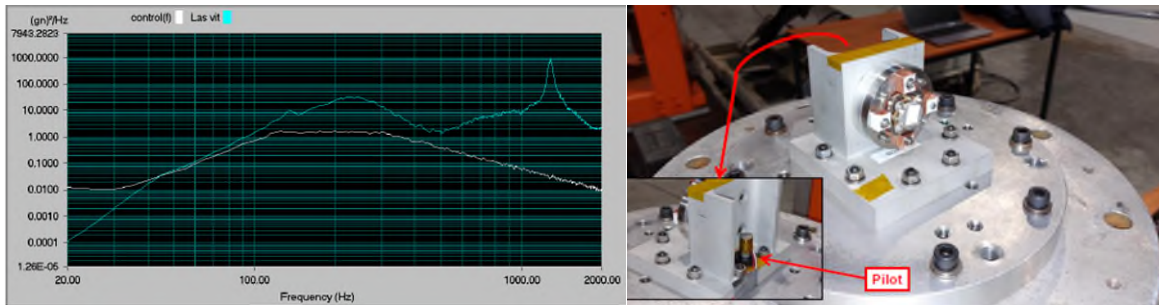


Figure 16 PSD input and system response (left), Shock test set-up (right)

A test campaign has been conducted on a mechanical breadboard with a representative moving part (Figure 18).

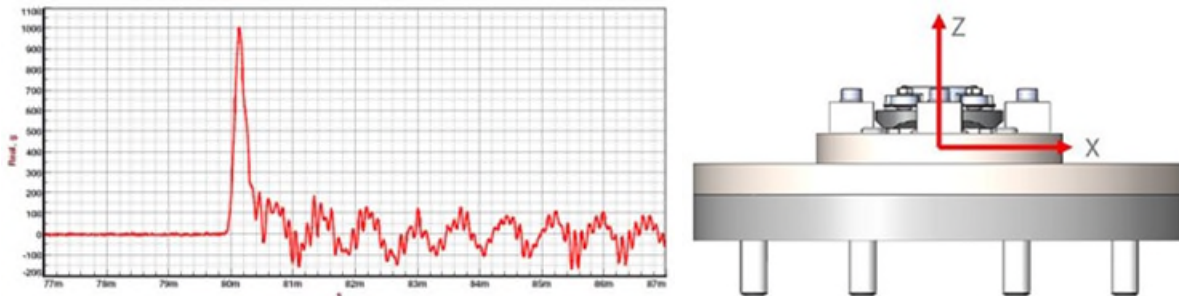


Figure 17 Shock test levels on the Z axis (left), Breadboard tested (right)

The health of the system is checked before and after the test campaign to validate the good behavior of the moving part and the flexure bearings. A particle pollution test has been conducted by Airbus Defence & Space under the CNES funded CO-OP program, leading to the conclusion that there is no risk of contamination for the mirror embedded in the mechanism.

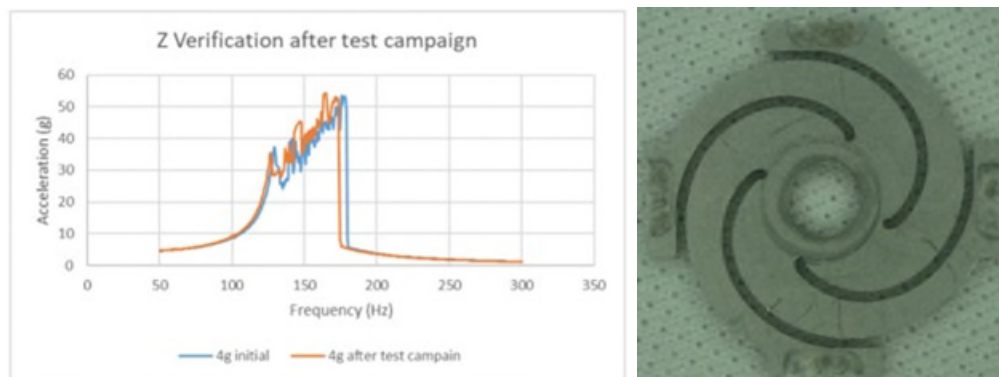


Figure 18 Health check sweeps (left), Post test visual inspection (right)

Manufacturing and assembly

The M-FSM45-HPL tooling has also been reworked to ease the global integration. Specific parts have been designed to allow a mobile part positioning with a high precision and good repeatability. The coil potting is also performed with a specific housing in order to avoid any leakage on critical parts.

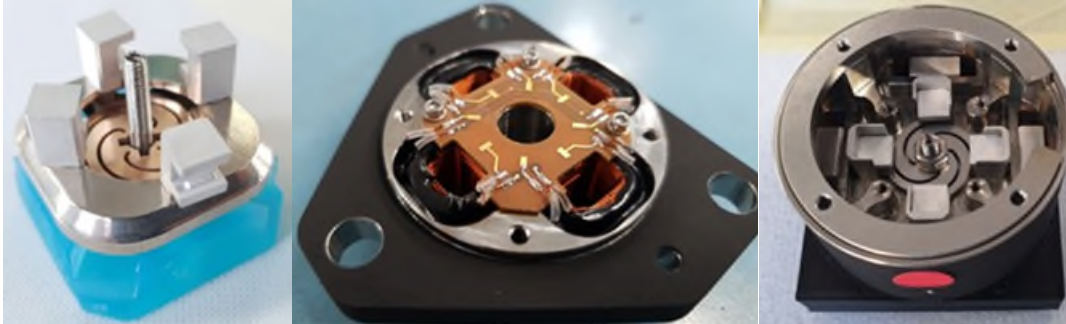


Figure 20 Tooling and assembly pictures

Performance summary

As a relevant summary the following table presents the difference of performance of both M-FSM versions.

	Tested on M-FSM45	Expected on M-FSM45-HPL
Mirror aperture	15 mm	16.2 mm
Housing Diameter	45 mm	45 mm
Height	35 mm	58 mm
Mass	195 g	370 g
Stroke amplitude	± 15 mrad	± 45 mrad
Resonance freq.	100 Hz	80 Hz
Rated voltage*	12 V	<7 V
Rated current*	0.5 A	<0.4 A

*for max angle low frequency (it may vary depending on the required angular profile)

Acknowledgement and Conclusion

These performances will be validated through a qualification test campaign that will be performed during 2024. All the key parameters will be checked through functional, environmental (thermal, vacuum) and lifetime tests. All this work was made possible through CO-OP funding via France Relance, with Airbus Defence & Space leading the project in collaboration with CNES.

References

1. G. Aigouy, A. Guignabert, E. Betsch, H. Grardel, P. Personnat, J.M Nwesaty, X. De-Lepine, A. Bedek, A. Baillus, N. Bourgeot, F. Claeysen, ICSO 2022 – « Piezoelectric and Magnetic Fast Steering Mirrors for Space Optical Communication ».
2. G. Aigouy, E. Betsch, A. Bedek, N. Bourgeot, A. Baillus, H. Grardel, P. Personnat, J.-M. Nwesaty, X. De Lepine, T. Maillard, F. Claeysen, AMS 2022 – « From PYSCHÉ PAM30 to Large Scale Free-Space Optical Communication ».
3. A. Guignabert, T. Maillard, F. Barillot, O. Sosnicki, F. Claeysen, AMS 2020 – « Point Ahead Mechanism for Deep Space Optical Communication, Development of a New Piezo-Based Fine Steering Mirror ».
4. F. Claeysen, Large-stroke Fast Steering Mirror for space Free-Space Optical communication, OPTRO 2020, n°0062, 28-30 Jan 2020
5. A. Guignabert, E. Betsch, G. Aigouy, Large stroke Fast Steering Mirror, Proc. ICSO, February 2021
6. W. Coppoolse, Dual-axis single-mirror mechanism for beam steering and stabilisation in optical inter satellite links, Proc ESMATS conf, 2003
7. Y. Long, Design of a Moving-magnet Electro magnetic Actuator for Fast Steering Mirror, J. of Magnetics, Vol. 19 (3), 2014
8. JC Barriere, Qualification of euclid-near infrared spectro-photometer cryomechanism, Proc. ESMATS 2017

Lessons Learned on Synchronization System Modelling for Solar Array Wing Deployment Predictions

Héloïse Boross* and Philipp Schmidheiny*

Abstract

A deep understanding of deployment behavior of a Solar Array Wing (SAW) is a necessity for in-orbit spacecraft operations, but also for an adequate and optimized sizing of the subsystems composing the SAW itself.

In general, the simulation of SAW deployment allows for design optimization and provides inputs to SAW mechanical analysis during early stages of projects. Additionally, by considering on-ground effects due to testing constraints separately (e.g., friction from SAW gravity offloading devices), an accurate prediction of the in-orbit behavior of the SAW deployment can be made by later-on removing these on-ground effects in the simulation [1].

However, the prediction of the deployment dynamics is a complex exercise due to the large number of parameters and their interdependencies which must be considered. Highest attention is to be paid towards the Synchronization System (being the core of the deployment dynamics) in order to generate reliable predictions.

In this research, we are presenting the different modelling approaches which we implemented for the simulation of our SAWs' Synchronization System. In addition, we are going through the hardware testing required to get the necessary input for our models. This testing spans from cable-level tests to flight model SAW level tests, via extensive testing on a breadboard wing, built specifically for the study of our Synchronization System.

Introduction

In order to support the development of SAWs within Beyond Gravity, a simulation tool predicting the SAW deployment behavior has been built using the Simscape Multibody toolbox within the MATLAB/Simulink framework. The different modelling approaches of the synchronization system presented in this paper are thus done using the same environment.

Lessons learned on collection of parameters from hardware as well as its implementation into the simulation are presented to show the different iterations which were required to achieve creating a baseline for deployments simulations reaching a reasonable accuracy level without overcomplications. It is to be kept in mind that the model in questions aims to give a general understanding of the deployment dynamics to help sizing the different systems of the SAW during its development.

Even though this paper focuses on the synchronization system, it is important to note that the model elaboration and correlation highlighted the importance of using input data obtained from SAW-level tests to generate and improve the core functions of our simulation framework driving the synchronization of the SAW, and not only to rely on mechanism behavior measured at component level. It is indeed one of the lessons learned.

* Beyond Gravity Switzerland, heloise.boross@beyondgravity.com,
philipp.schmidheiny@beyondgravity.com

Synchronization System Background

The synchronization system mechanism of Beyond Gravity is shown in Figure 1. It is composed of a set of pullies at each hinge-line and a pair of cables connecting the two hinge-lines. In general, the SAW deployment is powered by springs at each hinge-line and the whole wing is damped by an Eddy Current Damper (ECD) [2] situated at the root hinge. The cables used by Beyond Gravity for the synchronization system are made from braided Kevlar fibers. Despite the tests done with multiple cable types and parameters, all the results presented in this research focus on the parameters achieved with one cable type only, for simplicity reasons.



Figure 1. Synchronization System

The main pullies of the synchronization system are all made of aluminum while the rollers (name given to the small pullies redirecting the cables and maintaining them in positions) are made of stiff polymers.

Synchronization System Modelling

As the Synchronization cables in use are made from braided Kevlar fibers, several intrinsic parameters have an influence on the stiffness and damping behavior of the system, such as the braiding angle, overall cable length, and splice length of the cable. As these parameters may vary between projects, or even between two Synchronization Systems within one project, these parameters need to be accounted for in the modelling of the cables.

This is why multiple modelling approaches have been tried out and compared with each other. These methods could be categorized as: using only building blocks from the provided simulation framework, patching a custom synchronization system model into the framework, or even finding an in-between hybrid solution. They are described below along with their dedicated lessons learned.

Model A

The original idea was to keep the general SAW model as simple as possible. For this reason, the synchronization system was not modelled using rather complicated multibody objects, but the redistribution of torque between hinge-lines was driven by a mathematical function. At this initial state, only the hinges' angular difference to each other and thus cable elongation was used to calculate the cable force and thus resulting torque on the hinges. The cable is thus considered as a spring with a constant stiffness as can be seen on Figure 2.



Figure 2. Model A

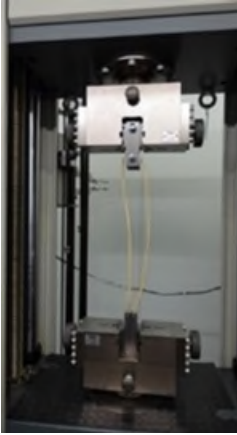


Figure 3. Cable during tensile testing

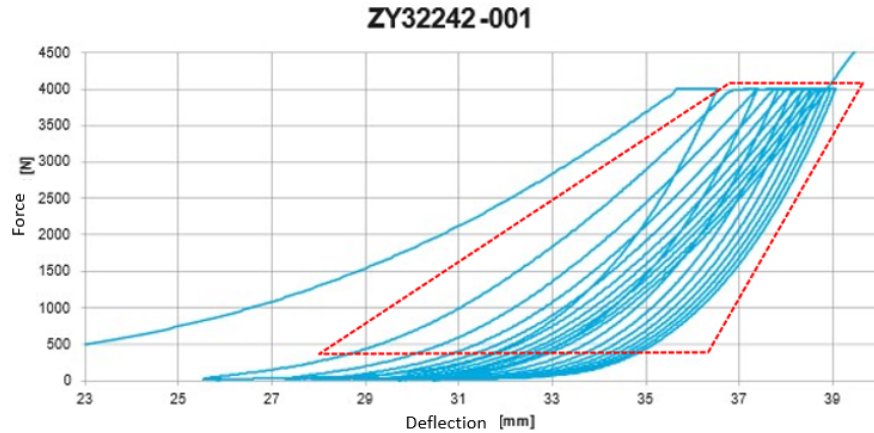


Figure 4. Plot of 10 tensioning cycles. The used data is highlighted by the red box. Only tensioning stiffness is used, not relaxation

To feed such model, the Kevlar cables are characterized under multiple cycles of tensioning as shown by Figure 3. The stiffness of the cable is then extracted from the linear portion of the tensile test results (see Figure 4). This was justified by the expected operating cable force range coming from the initial simulations. In order to better capture the variability of the cable, an average is done on the behavior observed during multiple cycles.

Initially it was expected that modelling the synchronization system between two hinges simply as a spring would be sufficient, with its constant stiffness corresponding to the theoretical synchronization cable stiffness. However, it eventually became clear that more complex modelling was required in order to accurately represent the complete system.

For example, linearized cable stiffness as measured during tensile tests cannot be used as-is for cable simulation as it doesn't encompass its actual non-linear behavior, especially apparent at low cable forces. During wing-level tests it has been discovered that the cables were working at a lower stiffness than anticipated, as the angle difference between hinges was measured to be larger than expected, at least for a part of the deployment. For this reason, Model B was implemented.

In addition, the stiffness of the cable is constantly evolving: the more tensioning cycles, the stiffer it becomes. The main reason for this is related to the realignment of fibers within the Kevlar braid. As this effect tends to reduce over the number of cycles, it has been decided to consider only the values starting from the second tensioning cycle. To be able to justify this omission, the step "cable integration into the SAW" had to be adapted. A pre-tensioning step has been added to the flow in addition to some recommendations on handling of these cables, to minimize disturbances in the fiber arrangement. The addition of this new step into the installation process also has the advantage of ensuring a bit more repeatability between multiple deployments on the same wing or between deployments of similar wings.

Model B

The second model extends the first one, but this time, the stiffness of the cable is modelled to be dependent on the elongation of the cable. This was expected to represent more closely the behavior observed during tensile testing of the single cable. This model is shown on Figure 5.



Figure 5. Model B

This model is fully based on the test results obtained at cable level on the tensile test bench. Only the implementation of the results in the simulation tool is modified. It can be seen on Figure 6 that results obtained show a completely different behavior in SAW deployment, especially during the initial dynamic motion of the outer panels. However, at this stage the simulated results were still quite far from observed behavior.

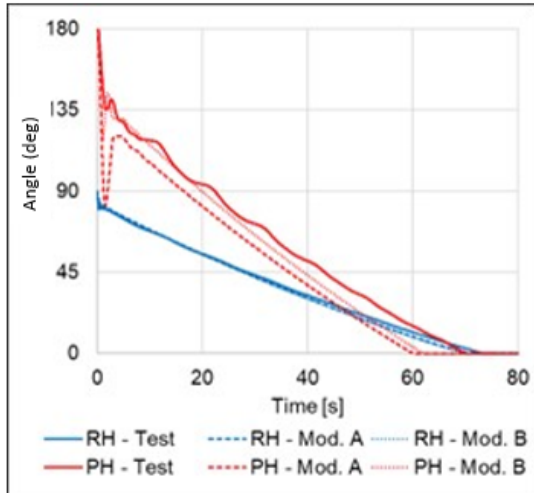


Figure 6. Plot with 3 lines: one for model A, one for model B and one for expected

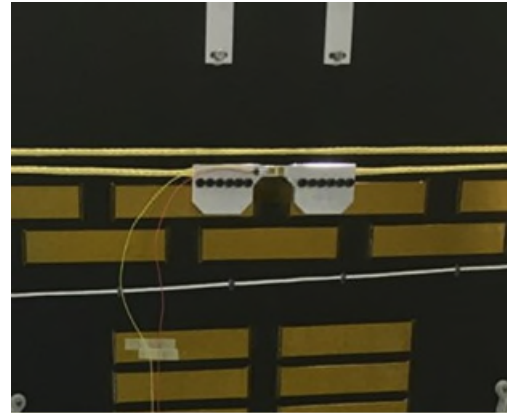


Figure 7. Cable force measurement on two-panel SAW SM

In order to verify that the assumptions on the cable working range were realistic, the actual cable force was measured on the cable itself during a deployment on a SAW structural model. The SAW used during the test was composed of two panels and the cable force measurement device attached can be seen in Figure 7. It has to be noted that this approach cannot be used on flight model hardware as the device clamps and therefore potentially damages the cable.

Implementing the cable stiffness as a function of cable elongation or cable tension was expected to be a more representative approach than the original implementation. However, this was found to not be entirely sufficient, as it became clear that the cables exhibit a non-negligible hysteresis, where energy is lost in the cable when force is applied to it, effectively making it a sort of damping element. One issue that arose at this stage was that the initial state of the installed cable with respect to the one during the tensile test is not known. This makes it difficult to achieve similar results between simulation and deployment if the initial parameters set-up in the simulation have a minor deviation from actual built-in values in the hardware.

Measuring the cable force directly on the SAW turned out to be less instructive than hoped. This method, being invasive, disturbed the synchronization system locally and thus the results could not be exploited to their full extent. As the cable force throughout the entire deployment is an important metric in order to compare it with the allowable loads of the hinges, it has been decided that future cable force estimates would be extracted from hinge angles measured via video analysis of deployment videos.

Model C

After observing the damping during panel oscillations during SAW deployments and the lack thereof during deployment simulations, it has been decided to model hysteresis in the mathematical representation of the Synchronization System to better represent this loss of energy and get more accurate results. The updated model is shown in Figure 8.

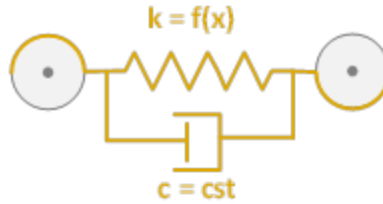


Figure 8. Model C

The damping was initially determined based on hysteresis of the data obtained during tensile test results. It has then also been estimated by analyzing deployment videos of a two-panel SAW developed at that time. All different losses in the Synchronization System are grouped into this one parameter instead of modelling all of them individually.

The loss of energy within the cable is assumed to be mainly coming from inner friction of the cable, more specifically from friction generated between the fibers composing the braid.

Furthermore, a change in cable behavior throughout multiple tensioning cycles on a tensile test bench was observed, which also showed that the deployment dynamics of a SAW will be significantly influenced not only by the initial state of the cable at its installation into the SAW, but also by the number of deployments already conducted with the SAW. This could be confirmed in tests conducted with the two different HERA SAWs, namely the protoflight model and flight model.

A further lesson learned during this process of cable characterization was therefore that an initial pre-stretching preparation of the cables before installation on the SAW could partially mitigate this variability between deployments.

This modeling approach provided good predictions after correlation with the two hinge-line SAW, however it turned out to lack scalability (i.e., adding more panels decreased the prediction accuracy).

Model D

As the mathematical cable model was starting to become more abstract and parameters could not easily be associated with physical characteristics, it was decided to change the approach by including in the model the components which were previously neglected such as the rollers and pulleys with their internal friction. This is illustrated by Figure 9.

The newly added components have been initially characterized at a breadboard level as can be seen on Figure 10. The friction of the rollers as well as their force transfer based on the contact angle of the cable on the roller has been measured. In parallel, deployment tests with a breadboard SAW have been conducted to gather deployment data of the complete synchronization system and not having it only as a sum of its contributors.

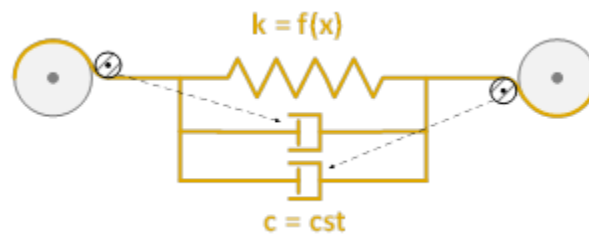


Figure 9. Model D

The breadboard SAW, as seen on Figure 11, is a wing with a flight representative synchronization system, hinges, and realistic mass, but with frames replacing the standard sandwich panels. This breadboard SAW can be adapted to different configurations, most notably the number of panels. A great feature of this breadboard is that it facilitates the understanding of the dynamics of one single Synchronization System, but then also the interactions of the various Synchronization Systems with each other. The use of a gravity offloading jig is required during deployments, and its influence was also accounted for in the deployment simulation.

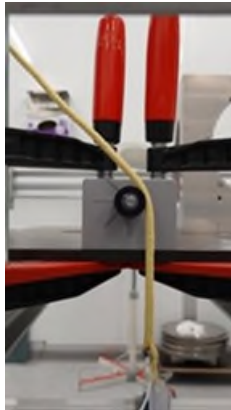


Figure 10. Roller friction test



Figure 11. Breadboard SAW for Synchronization Cable characterization (Yoke + 2 panel configuration)

The reason why a breadboard wing was built was the eventual realization that correlation of simulations using only component-level data as input with wing-level deployments proved to be exceedingly difficult. The breadboard enabled the acquisition of wing-level data and therefore a more direct correlation between simulations and deployment tests. From the roller friction test, it also became clear that cable is stressed differently on each side of the roller. This was not modelled up to this point, and it became clear that the rollers should no longer be neglected.

Model E

As the mathematical modelling approach described in the sections above was still failing to yield consistently accurate results and correlation was very difficult, it was finally decided to model the synchronization system fully within the multibody framework instead of the patchwork mathematical approach. This modelling approach now “physically” links two hinge-lines to each other, rather than distributing torque based on a mathematical function.

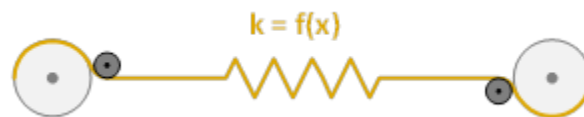


Figure 12. Model E

Deployment tests have been performed on multiple FM SAWs, e.g., on the HERA SAW built for the European Space Agency (see Figure 13). While this is useful for detailed correlation of the model, it however only allows less intrusive measurements and less flexibility in test configurations than the methods which can be used on the breadboard SAW. Figure 14 compares the simulation results with data obtained

via video analysis of two different deployments of the same wing. One can see non-negligible differences between two deployments, especially on the outer panels (called PH3 in the graph).

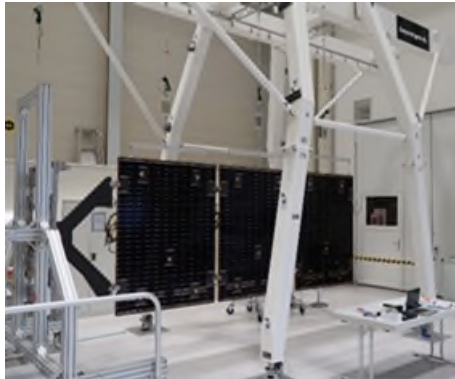


Figure 13. HERA SAW in mobile deployment rig

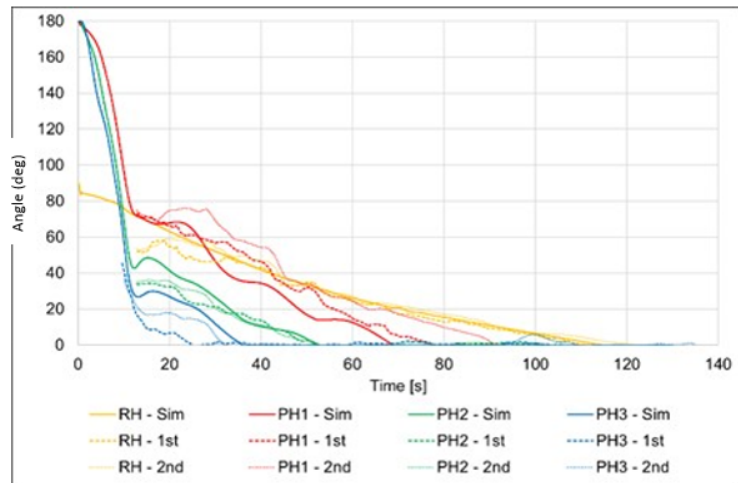


Figure 14. Plot of variation between Simulation (Model E) and two Deployments of same SAW

Comparing the cable approach in Model D and in the Model E, no clear conclusion could be reached on their accuracy. The reason for this is mainly the deployment behavior of a wing evolving over the number of deployments, and even more if two wings of the same type are compared, as shown in Figure 14.

Conclusion

During the investigation and comparison of each of the modelling approaches, lessons learned have been collected on both the testing and the use of the available test results. The driver for adding new parameters was mainly the increase of panels within a wing as prediction deviations grow with the number of panels. As the testing presented has only been performed at cleanroom conditions, the general deployment simulation model has also been correlated uniquely at these temperatures. Future work could be focusing on repeating this exercise in other conditions as each component of the synchronization system may have different reactions to environment changes. In general, one can say that the current accuracy reached by the last iterations of the models is very satisfactory in regard to the intrinsic variation in deployment behavior of the same wing when deployed multiple times. Thus, the simulation provides a reliable prediction helping the sizing of the different components of the synchronization system and assessing parameters such as overall deployment time and deployment envelope.

References

1. H. Boross, P. Schmidheiny (2023). *Modelling of Solar Array Wing Deployment Using a Hybrid Matlab/Simulink Approach and Correlation with Measured Wing Performances*. 20th European Space Mechanisms and Tribology Symposium, Warsaw, Poland.
<https://www.esmats.eu/esmatspapers/pastpapers/pdfs/2023/boross.pdf>
2. M. Hofer & M. Humphries (2009). *Development of an European Eddy Current Damper (Ecd-100)*. 13th European Space Mechanisms and Tribology Symposium, Vienna, Austria.
<https://www.esmats.eu/esmatspapers/pastpapers/pdfs/2009/hofer.pdf>

Testbed for Lunar Extreme Environment Wear Tolerant Applications

Valerie L. Wiesner*, Glen C. King*, Christopher S. Domack**, Brandon M. Widener**, Keith L. Gordon*
and Christopher J. Wohl†

Abstract

The abrasive dust from lunar regolith poses significant long-term durability and performance challenges to materials, vehicles, mechanisms and structures that will be used for the next generation of lunar exploration. The development of advanced materials, coatings and device technologies that can withstand these abrasive particles and extreme environmental conditions is critical. However, the lack of standardized and accessible methods for evaluating such materials and devices in a facsimile of the harsh lunar environment hinders progress in dust-tolerant technologies. To address this challenge, NASA Langley Research Center is creating an extreme environment testbed. This reconfigurable testbed will allow rapid, repeatable wear testing of material and candidate mechanisms under vacuum conditions, facilitating the development of critical materials technologies for lunar exploration. Preliminary results from exposing an actuating mechanism similar to a pin joint to lunar regolith simulant under high vacuum are reported.

Introduction

To ensure the success of long-duration, sustainable missions on the Moon's surface, it is imperative to develop materials and devices that can withstand the harsh lunar environment. Numerous environmental challenges threaten durability of space suits, roving vehicles, habitats and other critical technologies on extraterrestrial surfaces. Lunar dust, characterized by its fine particle size, rough surface morphology, and highly abrasive nature, poses a significant threat to the durability of components and vehicles [1]. Low lunar gravity free floating lunar dust particles are typically <100 micrometers (μm), capable of accumulating within cracks and crevices where cleaning tools cannot readily access [2]. These particles can erode, adhere to, or embed in surfaces and within confined device geometries, which increases the potential for premature failure of gears, bearings, interlocking systems, and other critical components. Abrasion and jamming of mechanisms with mating surfaces, such as gears and hinges, as a result of lunar dust incursion in space suits were noted during Apollo missions [3]. Soft goods such as outer-layer fabrics for space suits and flexible webbing for inflatable habitat structures are particularly sensitive to wear by dust [4]. Exposure to the vacuum of space with intense ultraviolet radiation and large temperature gradients results in degradation of materials and technologies [5] relevant for use on the Moon.

Maturation of technologies that can persist in extreme environments necessitates the ability to test and validate in such conditions. Developmental barriers to exposure of materials to space and lunar environments are being reduced due in part to commercialization of flight experiments. These include the Materials International Space Station Experiments (MISSE) [6] and the Commercial Lunar Payload Services (CLPS) initiative [7]. However, restrictions such as size, geometry and weight of specimens or the type of exposure (e.g., duration, static lunar surface), and access (e.g., long lead times, ride-along nature of experiments) limit testing in authentic, controlled environments. Accessible testing that simultaneously considers effects of abrasive regolith, vacuum, temperature and radiation for lunar technologies is an enormous market opportunity. A sustainable presence on the Moon via Artemis and a burgeoning lunar economy fostered by government, industry, and universities requires rapid, repeatable testing to advance concepts capable of persisting in the extreme lunar environment. The prime factors include atmospheric

* NASA Langley Research Center, Hampton, VA; Valerie.l.wiesner@nasa.gov

** Analytical Mechanics Associates, Inc., Hampton, VA

pressures down to 10^{-12} Torr, temperatures ranging from -20°C to 120°C , and ultraviolet solar particle-driven electrostatic charges.

To address this need, the Surveying Lunar Dust Influence on Device Efficacy (SLIDE) testbed is being developed as a reconfigurable platform to evaluate the wear performance of material and device candidates due to lunar dust simulant exposure (continuously or cyclically) under high vacuum. The goal of the SLIDE testbed is to identify and rapidly advance needed technologies from concept to device level. In parallel with testbed establishment activities, a pilot assessment of wear performance of a titanium alloy was conducted in the SLIDE testbed. The approach adopted in establishing the SLIDE testbed are outlined, and preliminary results are presented herein.

Materials and Methods

SLIDE Apparatus Configuration

The SLIDE apparatus consists of a stainless-steel vacuum chamber with multiple ports and feedthroughs, as shown in Figure 1(a). The diameter of the primary chamber door is 61 centimeters (cm) and sealed using nuts, bolts, and a copper gasket. The pumping system, consisting of a roughing pump and a single turbomolecular pump, is capable of base pressures down to approximately 10^{-6} Torr. The turbomolecular pump is mounted on a 90-degree bend attached to a gate valve to mitigate dust incursion into the pump. The initial pump-down occurs through the roughing pump only. A gate valve on the chamber is closed until the roughing pump drops the chamber pressure to 10^{-3} Torr level. The gate valve is then opened and the turbomolecular pump further drops the chamber pressure to 10^{-6} Torr level. The test mechanism onto which dust is deposited operates within a containment housing to minimize dust contamination within the chamber, as shown in see Figure 1(b). The approximate working volume is 86 cm (length) by 46 cm (width) by 51 cm (height).

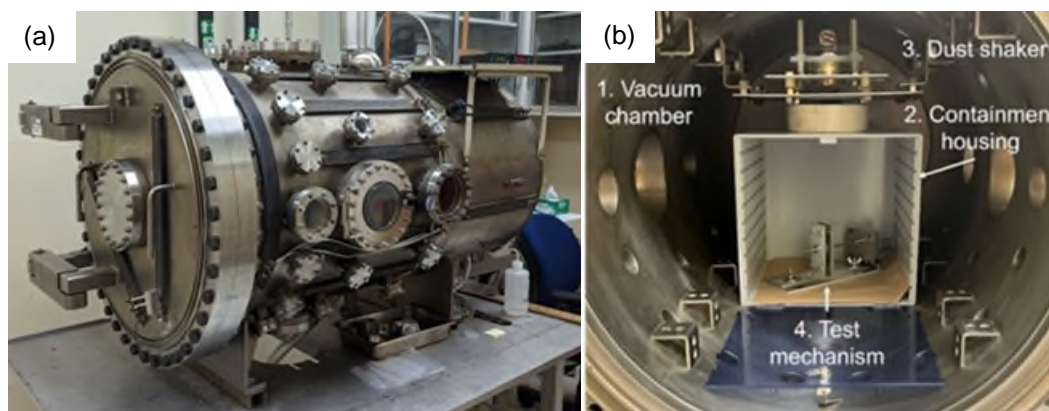


Figure 1. (a) Exterior and (b) interior images of SLIDE chamber²

Dust Shaker Device

Prior to use in the dust shaker device, the lunar dust simulant was passed through a stack of sieves with decreasing mesh opening sizes of $106\ \mu\text{m}$, $53\ \mu\text{m}$ and $45\ \mu\text{m}$ prior to testing to separate coarse particles from the fine particles. The fine particles (i.e., less than $45\ \mu\text{m}$ in diameter) were utilized in the experiment. Sieving prior to testing ensured that the dust simulant would pass freely through the dust shaker sieve with mesh opening of $106\ \mu\text{m}$ during testing.

A custom dust shaker device was fabricated to release controlled amounts of lunar dust simulant (LHS-1D, Exolith Lab, Oviedo, Florida¹) onto test articles within the SLIDE chamber. The shaker mechanism consisted of a sieve with stainless steel mesh (mesh opening of 106 μm) with an acrylic cover secured to a base plate using nylon bolts. The acrylic cover had a single vent hole with a diameter of 0.635 cm drilled into the top to minimize dust movement during the chamber evacuation process. The shaker base plate was supported by four rubber boots that surrounded nylon bolts attached to the chamber mounting plate. A rotating copper weight was affixed to a variable 24-V DC electric motor (maximum rotational rate of 5300 RPM) to induce a vibration on the base plate and sieve and dispense the lunar dust simulant, as shown in Figure 2.

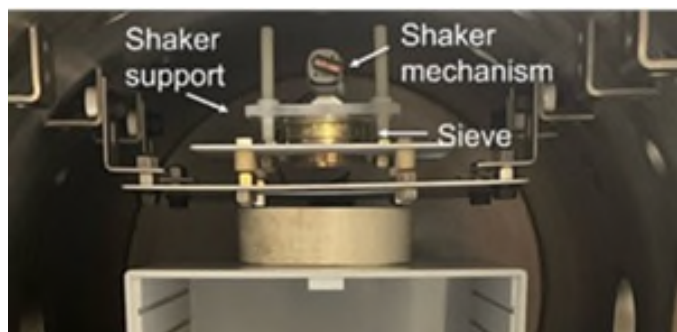


Figure 2. Dust Shaker Device

The deposition rate of lunar dust simulant at ambient pressure was determined through a series of dust shaker trials by powering the electric motor at 6 V and 24 V. A programmable 30-V power supply (KORAD KA3305P) was used. At the start of each trial, approximately 5 grams of lunar dust simulant was loaded into the sieve. The acrylic cover was placed onto the sieve and then secured onto the base plate of the dust shaker device. The distance from the bottom of the sieve through which simulant passed was situated approximately 33 cm from the collection surface below. The dust shaker device was then actuated for a discrete interval ranging from one minute to three minutes of continuous actuation. The dust simulant that passed through the 106- μm sieve was collected on an aluminum foil. The area over which the dust settled was measured to estimate areal coverage. The dust simulant that was collected was then weighed using a high-precision scale capable of measuring to 0.00001 g. The surface accumulation loading was averaged over three deposition cycles at each electric motor voltage level.

Pilot Assessment of Material Wear Performance

In order to evaluate the performance and efficacy of the SLIDE chamber, a test mechanism was fabricated to mimic the abrasive wear motion on material surfaces in a simplified pin-joint mechanism as shown in Figure 3. The mechanism design was influenced by the Lunar Surface Manipulation System [8] to replicate aspects of the two-body abrasive wear encountered by two dissimilar materials in a pin-joint-like configuration. Lunar dust simulant could be selectively introduced to enable capturing aspects of a three-body wear test. The drive shaft ran through a hole in the center of the active disc with diameter of 0.8 cm, and the test coupons had dimensions of 3.8 cm x 3.3 cm as shown in Figure 4. The active disc was secured to the shaft using two set screws, and the coupons were secured to their respective L-brackets that held them in place against the active disc. The L-brackets were then aligned and secured such that the test surface of the coupon was flush with the surface of the active disc. The drive shaft was then coupled to an electric drive motor that turned the active disc at a rate of 1.3 RPM. The assembled test mechanism apparatus was situated directly below the dust shaker device within the SLIDE chamber to ensure even dust deposition onto the active disc and test coupons during wear testing.

¹ Specific vendor and manufacturer names are used only to accurately describe the test hardware or software. The use of vendor and manufacturer names does not constitute an official endorsement, either expressed or implied, by the National Aeronautics and Space Administration nor does it imply that the specified equipment or software is the best available.

² All image credits to NASA

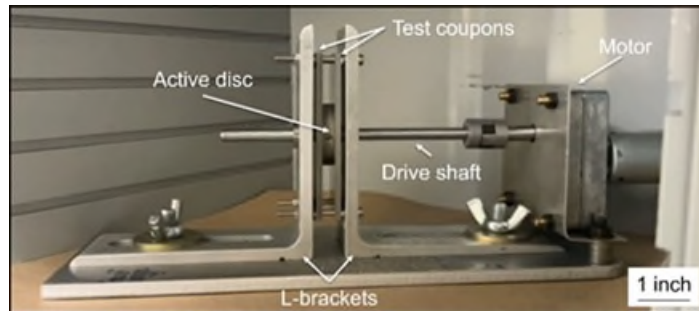


Figure 3. Pilot Test Mechanism

The test procedure involved initiating pump down of the vacuum chamber and waiting for approximately 15 minutes until a vacuum pressure of $<10^{-4}$ Torr was reached. The dust shaker and the electric motor that rotated the active plate were then powered to start a wear test. In the exploratory assessment of material wear, a test duration of 3 min was selected to simultaneously actuate both the dust shaker device using an electric motor supplied with 6 V and active plate rotation at 1.3 RPM after a vacuum pressure of 8.6×10^{-5} Torr was reached.

The materials used in the pilot assessment included an active disc of polytetrafluoroethylene (PTFE) or aluminum-6061 alloy (Al6061) and test coupons of titanium-aluminum-vanadium alloy (Ti-6Al-4V) (as shown in Figure 4). PTFE was selected as a more compliant material having a comparatively low coefficient of friction compared to Al6061 and Ti-6Al-4V [9], while Al6061 and Ti-6Al-4V were selected due to frequent use in aerospace applications [10]. The test coupons and active discs were polished using silicon carbide paper up to 1200 grit followed by polishing with an alumina colloidal suspension (median particle size $0.05 \mu\text{m}$) to ensure a consistent surface finish prior to testing. The test surface of each coupon that came in contact with the active plate was characterized using a FormFactor FRT Microprof 100 profilometer (Livermore, CA). Data was collected with $2.5 \mu\text{m}$ between data points and $12.5 \mu\text{m}$ between data lines to assess the surface of the test coupon before and after a test with or without flowing dust in the SLIDE chamber. Preliminary roughness parameters, such as average roughness, R_a , and root mean square roughness, R_q , were calculated using FormFactor FRT III analysis software to compare surface roughness for three regions approximately $1 \text{ mm} \times 1 \text{ mm}$ before and after wear testing. An F -test was performed to determine if the data sets possessed equal variances, which determined whether a t -test with equal variances (homoscedastic) or a t -test with unequal variances (heteroscedastic) was utilized. Then, a two-tailed t -test was used to ascertain statistical significance. Both F - and t -tests were calculated using the Microsoft Excel functions. Resultant p -values less than 0.05 indicated significant statistical difference.

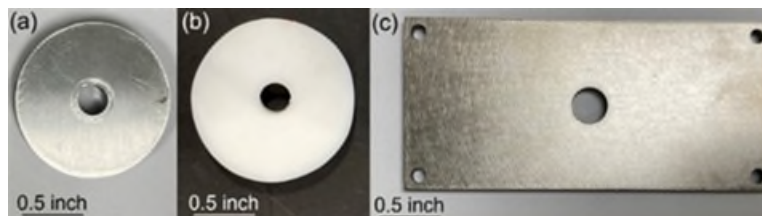


Figure 4. (a) Al6061 Active Disc, (b) PTFE Active Disc and (c) Ti-6Al-4V Test Coupon

Preliminary Results and Discussion

Surface Accumulation Loading of Dust via Dust Shaker Device

Preliminary surface dust accumulation loading results from both dust shaker trials are presented in Table 1. Lunar dust simulant was observed to deposit over a circular area with diameter of nominally 7.6 cm, which corresponded to the diameter of the dust shaker sieve through which lunar dust simulant passed. The average surface dust accumulation was determined to be $183.3 \text{ g/m}^2 \pm 68.9 \text{ g/m}^2$ after one minute of dust shaker motion at an electric motor drive voltage of 24 V. After three minutes of dust shaker motion at an

electric motor drive voltage of 6 V, the average surface dust accumulation was $141.8 \text{ g/m}^2 \pm 88.6 \text{ g/m}^2$. The large standard deviation in surface dust accumulation observed in the dust shaker device trials may be attributed to a number of variables, such as lunar dust simulant particle size distribution, that could influence the rate of particle deposition. Additional trials will be performed to assess and optimize the amount of dust deposited under different electric motor drive voltages and cycle conditions, including using lunar dust simulant pre-sieved to a finer mesh size and utilizing a sieve with small mesh size in the dust shaker device.

Though data from lunar surface operations are limited, surface accumulation loading for human-generated surface transported dust (particle size $<500 \text{ }\mu\text{m}$) has been reported as $<40 \text{ g/m}^2$ based on estimates from Apollo walking and rover video archives [2]. Thus, approximately 50 seconds or 15 seconds of dust shaker actuation at an electric motor drive voltage set at 6 V or 24 V, respectively, could achieve loadings comparable to those of human-generated surface transported dust relevant to lunar surface operations.

Table 1. Preliminary Surface Accumulation Loading Results from Dust Shaker Device Trials

Electric Motor Drive Voltage (V)	Surface Accumulation Loading (g/m^2)	Test Duration (min)
24	183.3 ± 68.9	1
6	141.8 ± 88.6	3

Results of Pilot Study on Assessment of Material Wear

Preliminary optical and profilometry results for a Ti-6Al-4V coupons tested in contact with an Al6061 active disc after wear testing with lunar dust simulant in vacuum are shown in Figure 5. The circular wear pattern was evident in optical and profilometry data of the coupon tested without and with lunar dust simulant compared with the pristine starting surface.

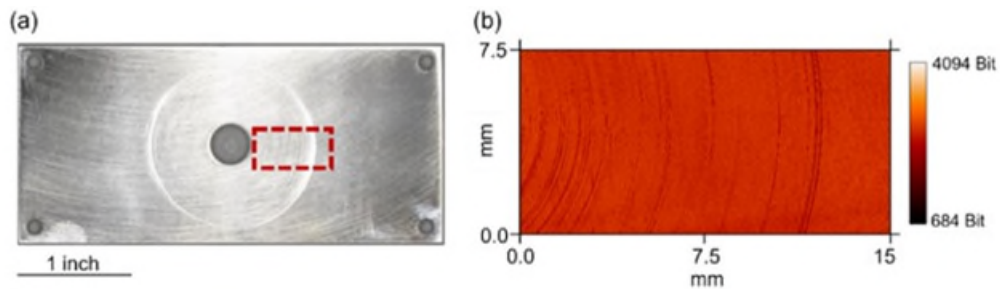


Figure 5. (a) Optical image of Ti-6Al-4V test coupon after SLIDE testing with lunar simulant exposure. The red rectangle corresponds to the region from which the profilometry intensity plot (b) was collected over wear path.

The wear test performed with the PTFE active disc without lunar dust simulant resulted in R_a and R_q values that were statistically similar to those of the as-polished surface prior to testing, suggesting that the wear interaction between the PTFE disc and Ti-6Al-4V coupon surface did not result in an appreciable change in surface roughness, as would be anticipated. In the case of wear testing with the Al6061 active disc and without lunar dust simulant, R_a and R_q parameters increased by approximately $0.003 \text{ }\mu\text{m}$ and $0.004 \text{ }\mu\text{m}$, respectively, both of which were statistically higher in comparison with R_a and R_q of the as-polished Ti-6Al-4V coupon surface.

Introducing a lunar dust simulant loading of $\sim 141.8 \text{ g/m}^2$, as determined during the pilot assessment, resulted in an increase in surface roughness parameters of the Ti-6Al-4V test coupon surface after the wear test with PTFE active disc. The change in surface parameters was a factor of two greater than for those measured for both the starting coupon and the coupon wear tested without lunar dust simulant. Similarly, the addition of lunar dust simulant during wear testing with the Al6061 active disc resulted in a nearly three-fold increase in R_a and R_q values. This statistically significant increase in surface roughness parameters suggested that the introduction of lunar dust simulant resulted in a higher degree of wear of the Ti-6Al-4V

surface than in wear tests without lunar dust simulant. Protective coatings could impart dust tolerance in certain applications [11]. These preliminary findings point to the importance of testing materials and devices with controlled dust exposure. These critical data will help ensure material and device performance in extreme environments, such as the lunar surface that is rife with dust and play a vital role in mission success.

Table 2. Summary of Selected Surface Roughness Parameters for Ti-6Al-4V Test Coupons before and after Wear Testing in SLIDE with or without Dust.

Test Coupon Material	Active Disc Material	Lunar Dust Simulant	R_a (μm)	R_q (μm)
Ti-6Al-4V	N/A (Control)	N/A	0.005 ± 0.001	0.006 ± 0.001
Ti-6Al-4V	PTFE	No	0.006 ± 0.001	0.007 ± 0.001
Ti-6Al-4V	PTFE	Yes	0.012 ± 0.003	0.014 ± 0.003
Ti-6Al-4V	Al6061	No	0.008 ± 0.001	0.010 ± 0.001
Ti-6Al-4V	Al6061	Yes	0.014 ± 0.002	0.019 ± 0.002

Summary and Continuing Efforts

In response to the need for evaluating material and device wear testing in the presence of lunar dust simulant under high vacuum conditions, the SLIDE testbed was developed to enable rapid advancement of critical technologies from conceptual stages to practical device implementation. The dust surface loadings that were achieved with the custom SLIDE dust shaker device varied from $141.8 \pm 88.6 \text{ g/m}^2$ for 3 min of actuation with an electric motor drive voltage setting of 6 V to $183.3 \text{ g/m}^2 \pm 68.9 \text{ g/m}^2$ for 1 min of actuation at 24 V, respectively, with lunar dust simulant particle sizes less than $45 \mu\text{m}$. Dust surface loadings could be tailored by adjusting the voltage supplied to the electric motor that actuated the dust shaker device and duration of actuation to achieve human-generated surface transported dust loadings relevant to lunar surface operations. Initial wear tests involving a Ti-6Al-4V coupon and a PTFE or Al6061 active disc were conducted within the SLIDE testbed under this apparatus' maximum achievable vacuum pressure with and without lunar dust simulant. Preliminary results revealed increased surface roughness of the Ti-6Al-4V coupons tested with dust compared to that of the coupons tested without dust exposure. The reconfigurable nature of the SLIDE platform allows for testing various materials, devices, and mechanism types under lunar dust simulant and reasonably high vacuum conditions. Compounding environmental effects, such as thermal gradients, cryogenic exposure, ultraviolet radiation, and electrostatic exposure, will be explored to test under such conditions. Testing will be tailored to incorporate aspects of other extraterrestrial environments, such as Mars, by utilizing Martian dust, regulating pressure and incorporating carbon dioxide. By testing in a combination of conditions, material and device concepts can be rapidly vetted and matured to end-use applications benefiting lunar and planetary exploration.

References

- Loftus, David J., Tranfield, Erin M., Rask, Jon C. and McCrossin, Clara, "The Chemical Reactivity of Lunar Dust Relevant to Human Exploration of the Moon," Planetary Science Division Decadal Survey white paper (2020).
- "Cross-Program Design Specification for Natural Environment (DSNE)," NASA Standard No. SLS-SPEC-159 Revision H (August 2020).
- McKay, David S., Heiken, Grant, Basu, Abhijit, Blanford, George, Simon, Steven and Reedy, Robert, Bevan M. French, and James Papike, "The Lunar Regolith," *Lunar Sourcebook* (1991), 285-356.
- Stubbs, Timothy J., Vondrak, Richard R. and Farrell, William M., "Impact of Dust on Lunar Exploration," *Dust in Planetary Systems*, (January 2007), 239-243.
- Stiegman, Albert E. and Liang, Ranty H., "Ultraviolet and Vacuum-ultraviolet Radiation Effects on Spacecraft Thermal Control Materials," *The Behavior of Systems in the Space Environment*. Dordrecht: Springer Netherlands, 1993.

6. deGroh, Kim K., Banks, Bruce A., Dever, Joyce A., Jaworske, Donald A., Miller, Sharon A., Sechkar, Edward A. and Panko, Scott R., "NASA Glenn Research Center's Materials International Space Station Experiments (MISSE 1-7)," *NASA Technical Memorandum*, no. 2008-215482 (2008).
7. Voosen, Paul, "NASA to Pay Private Space Companies for Moon Rides" *Science*, 362, no. 6417 (November 2018), 875-876.
8. Doggett, William R., King, Bruce D., Carno, Thomas and Dorsey, John T., "Design and Field Test of a Mass Efficient Crane for Lunar Payload Handling and Inspection: The Lunar Surface Manipulation System," *AIAA SPACE 2008 Conference & Exposition*, (September 2008), 7635-7647.
9. Zeng, Hongbo, *Polymer Adhesion, Friction, and Lubrication*, (2013).
10. Peters, Manfred, Kumpfert, Jörg, Ward, Charles H., and Leyens, Christoph, "Titanium alloys for aerospace applications." *Advanced Engineering Materials*, 5, no. 6 (2003), 419-427.
11. Wiesner, Valerie, L., Wohl, Christopher, J., King, Glen C., Gordon, Keith L., Das, Lopamudra and Hernandez, Jonathan J., "Protective Coatings for Lunar Dust Tolerance," *NASA Technical Memorandum*, no. 2023-0003195 (2023).

Development and Qualification of a New SADM for Small Satellites

Adrien Guignabert*, Flavien Deschaux*, Luc Herrero*, Etienne Magnin-Robert*
and Jean-Bernard Mondier**

Abstract

The SADM-200 (Solar Array Drive Mechanism for 200 W) is a new mechanism developed at Comat in order to provide solar array rotation and power transfer for small satellite applications. This mechanism is designed to be as compact as possible while providing a reliable angular positioning and electrical power transfer from the solar array to the satellite. Robust mechanical guidance and high-quality components selection allows an accurate positioning with low angular play while withstanding the tough mechanical and thermal environment faced during launch and in space. The development focused on keeping the cost as low as possible through the use of COTS (Commercial Off The Shelf) while maintaining a high quality requirement. This paper describes some aspects of the development and issues that were resolved.

Introduction

Following a growing demand for affordable off-the-shelf SADM for small satellite applications, Comat started the development of a new product with the help of the CNES, the French space agency. This paper presents the main development and risk reduction steps of this SADM-200 mechanism. The design started in 2020, the PDR was held in 2021 and the CDR was passed in 2022. Additional risk reduction tests were performed in 2023 and the qualification started in 2024 and is currently in progress, expected to be fully qualified in the second half of 2024. Six FM are being built for two already planned flight missions in 2025 and after.

Design and Development

The design resulted in the mechanism shown in Figure 1; this is the version without a cover.

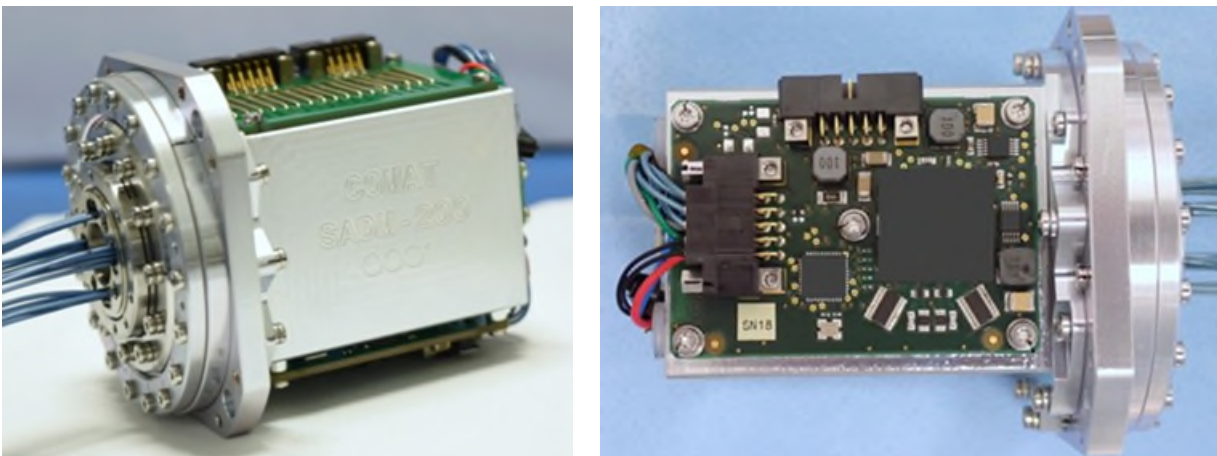


Figure 1: SADM-200 mechanism pictures

* Comat, Flourens, France

** CNES, Toulouse, France

A configuration with the addition of an external aluminum cover for additional mechanical and radiation protection for the electronics is also in development.

A Design Kept as Simple as Possible

The SADM-200 is built around 3 main components:

- **Slip-ring:** allow the power transfer from the solar array to the satellite while rotating, with unlimited rotation angle.
- **Gearhead motor:** drives a slow (up to 0.01 rad/s – 0.1 rpm in flight, 0.14 rad/s – 1.3 rpm in qualification) and relatively accurate rotation (<3° angular backlash).
- **Bearings:** ensure a smooth, low friction rotation.

Comat designed the SADM-200 embedded motor control PCB, benefitting from the development of the reaction wheel product line. Hence an important portion of the components (such as connectors or micro-controller) are reused, however, new embedded software was developed.

Main Requirements

The SADM-200 main characteristics are shown in Table 1.

Table 1: SADM-200 characteristics

Parameter	Value
Volume	Ø80, length 85 mm (cover-less version)
Mass	<0.465 kg
Operational Temperature (satellite interface)	-20 to +50°C
Non-Operational Temperature (satellite interface)	-40 to +60°C
Solar array Voltage	Up to 28 V
Solar array Current	7.14 A (through 7 pairs of power lines)
Supply voltage	10 to 18 V
Supply current	< 0.5 A
Dissipation	< 4 W
Range	Unlimited
Angular resolution	0,03° (per motor step)
Angular accuracy	<±3° (gearbox and reed switches)
Nominal speed	0.01 rad/s (0.1 rpm)
Qualified speed	0.14 rad/s (1.3 rpm)
Actuation torque	Up to 0.350 Nm
Holding torque (unpowered)	Irreversible motion (gearbox), <0.5 Nm
Lifetime	100,000 full turns (qualification target)
FIT	<124 @80°C (embedded electronic)

Reed Switches

Since the baseline mechanism does not include a position sensor for compactness reasons, two top-turns are positioned 180° apart in order to regularly be able to adjust the software position indication. The reed switches are magnetically activated, normally open devices. They close when the magnet fixed on the rotor passes nearby.

Regarding the magnet selection and design, past issues with NdFeB corrosion [1] and their higher sensitivity to temperature led us to select $\text{Sm}_2\text{Co}_{17}$ magnets. Although being less common on supplier shelves than NdFeB, their high resistance to temperature and corrosion-free material composition suited our needs. They also show high magnetic performances with typical remnant induction around 1.1T compared to 1.3T for NdFeB.

Reed signal flickering

The motor used is a two-phase stepper, supplied with a current-controlled driver. Owing to its compactness, the magnetic circuit is relatively thin and there is an important part of non-canalized magnetic field. Hence the two reed switches are impacted by the resultant motor magnetic field which overlaps the one generated by the switch's magnet placed on the rotor. The most notable consequence is a repetition of on/off toggles on the reed when the magnet is angularly closing in while the motor is activated, as shown in Figure 2 issued from measurement at nominal motor current and speed. This flickering should not be confused with the nominal bouncing behavior [2] that occurs at higher frequency and for a very short duration (a few ms) compared to the effect we are noticing (a few seconds, depending on rotation speed).

Based on the measurements (see Figure 2) with nominal current (360 mA), the reed can start to pull-in up to 5° before the final threshold angle (2° before in the figure), when the reed remains closed. Hence preventing accurate and repeatable position adjustment.

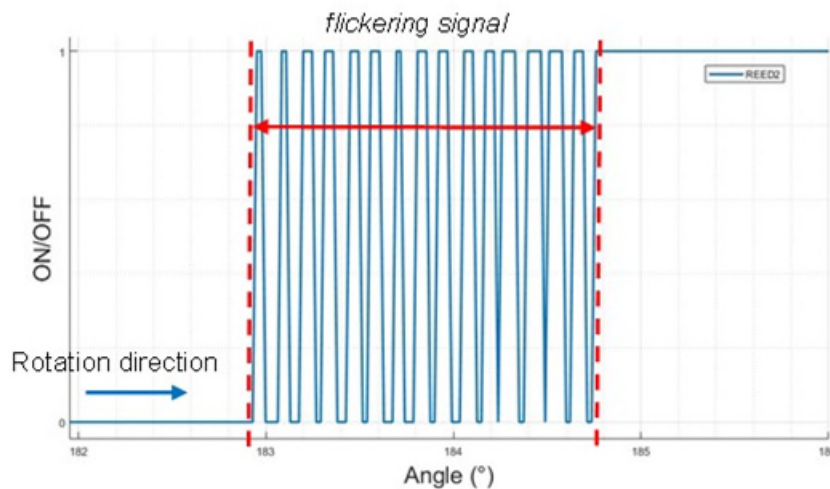


Figure 2: Reed signal measurement plots vs rotor angular position – magnet closing in and inducing flickering – raw, unfiltered signal

In addition, the motor influence regarding the reed flickering is further established by testing with different phase current values. The resulting number of reed activation per rotation is indicated in Figure 3.

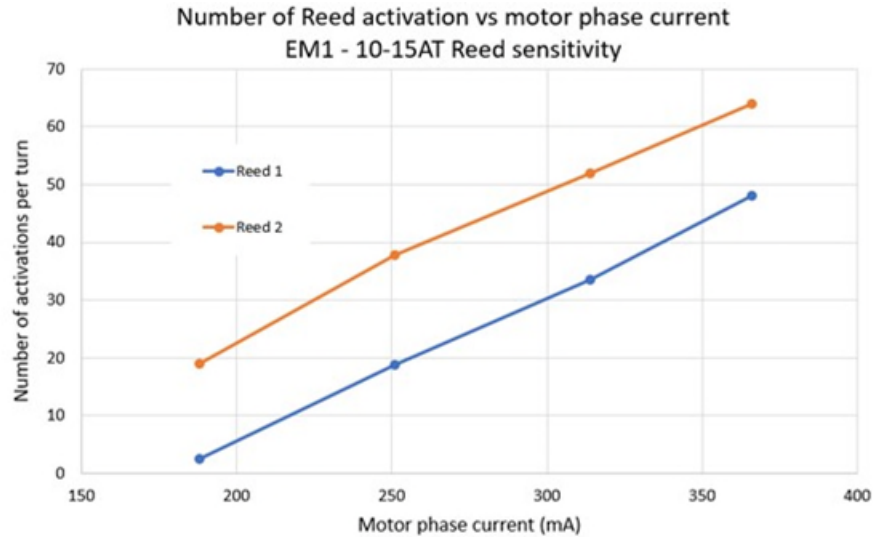


Figure 3: Number of reed activation per turn vs motor phase current

As expected, the higher the motor current is, the higher its external magnetic field is, hence inducing reed flickering at earlier angular positions and for a higher total number of activations. The higher number of reed n°2 is due to a lower magnet-induced field at its position (measurements performed) probably caused by a higher distance to the triggering magnet (within mechanical chain of dimensions tolerance). With a lower magnet-induced field at this location, the motor magnetic field then gets more relative impact on the reeds flickering range.

Mitigation options and selected solution

The reed activations number versus phase current relation is relatively linear and seems to reach 0 activations per turn at around 150 mA. Reducing motor current would then be an option to cancel the flickering effect, however, motorization margin would be affected. Magnetic shielding could also be possible to greatly reduce motor magnetic field but would add mass and require volume that is not easily available in this compact mechanism.

In the end, a software solution is preferred. Thanks to a built-in post-treatment algorithm, filtering out temporary reed's activations, these undesired activations are ignored and only one rising front per reed is considered. The final reed rising front positioning accuracy of the system is measured under 0.5° (3 sigma repeatability) which is well within the targeted 3° position uncertainty.

Impact on reed lifetime

The other impact of this flickering effect is that it increases the total number of activations during the mechanism entire lifetime. The required qualified number (qualification in progress) is 100,000 full revolutions, which is to be multiplied by the average number of reed activations per turn (50-60), leading to around 5 to 6 million. The reed supplier ensures a minimum number of 10 million activations for the lifetime, which then allows a maximum number of activations per turn of 100, covering the SADM-200 measured number with margin.

Mechanism Magnetic Moment

Initially designed without a defined magnetic moment target, later specified at 20 mAm^2 , the SADM-200 design specification was to use amagnetic materials. After the first EM was assembled and submitted to all tests, a magnetic moment measurement was performed in the dedicated CNES laboratory which locally cancels earth magnetic field (see Figure 4). Different SADM-200 operational configurations were tested, especially the modes: OFF, IDLE (embedded software switched on but motor off) and ON (motor activated at nominal speed and current).



Figure 4: Magnetic moment measurement on EM1 (CNES)

Magnetic Moment Measurement

The mechanism magnetic moment was measured slightly above 50 mAm² for the worst case, above the 20 mAm² target. Several angular positions were tested with the SADM-200 turned OFF and the measurements shows that the magnetic moment is turning along with the rotor, with an amplitude of 20 mAm² (see Figure 4).

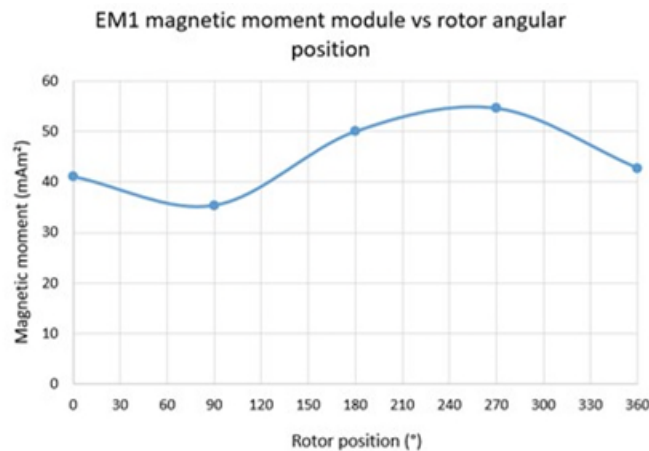


Figure 5: Variation of magnetic moment module during a full rotor revolution (motor OFF at each measurement step)

Magnetic moment sources identification and solution

This result indicates that some of the magnetic moment source is located within the rotor sub-assembly. The rotor parts were then checked and two potential culprits were found: the 440C from the bearing's rings and the 15-5PH stainless steel of the bearings preload nut. Extending to the stator parts, the same material was also used in and around the bearing assembly.

Both materials have a martensitic structure and known typical magnetic permeability up to 100 and remnant induction depending on the part history (especially during machining, vibration tests when the part is subjected to machine magnetic fields). The 440C is selected for obvious heritage reasons, no realistically usable alternative was identified. The 15-5PH was selected for its thermal properties (coefficient of thermal expansion) similar to the 440C (10 to 11 ppm/K), and large heritage within Comat past and current mechanisms.

The four parts of 15-5PH material were then updated to an austenitic non-magnetic 316L stainless steel in a design iteration to the final QM configuration. The qualification will include a new magnetic moment measurement with a value that should be noticeably reduced.

EM Test Results

The engineering model was subjected to many risk reduction tests including vibration, shock and thermal vacuum cycling. The thermal vacuum test allowed measurement of the self-heating behavior of the SADM-200, especially the motor and allow comparison with the model predictions and components temperature limits. At the maximum operational temperature of +50°C, motor overheating of +37°C was measured and a relative temperature offset with the temperature reference point (TRP) placed on the backside of the mechanism of near 30°C. Since there is no thermocouple on the motor (no available space), the TRP is the only thermal proxy for the motor temperature. Knowing the thermal offset at the maximum operating point then allowed us to indicate the maximum allowed temperature at the TRP in order to keep the motor temperature within its operational limits.

Qualification

The qualification sequence will follow a typical path of mechanical and thermal vacuum environments followed by a lifetime operational test under ultrahigh vacuum and thermal conditions. Regular functional tests will control the evolution of main performances throughout the qualification campaign.

The lifetime test will start with ground representative cycles (4000 full turns and 4000 ±30° sweeps). Then a total of 100,000 full rotations will be performed with a current of 1 A passing through the 14 power lines of the slip ring. An equivalent fraction of the total number of cycles will be performed at +50°C, -30°C and +20°C, in order to combine operational vacuum and temperature constraints. The test is performed at slightly higher speed (1.3 rpm compared to 0.1 rpm maximum flight speed) in order to keep its duration reasonable (57 days instead of 741 days, almost 2 years).

For the mechanical environments, based on our experience and the lessons learned [3], it was decided to perform impact-based shocks instead of controlled fall machines. The shock tests on the EM were performed with a fall machine and the levels exceeded the envelope target, without possible adjustments to keep it in control. Carefully adjusting the impact shock parameters will avoid the risk of over testing and better fit to the targeted shock response spectrum, especially in lower frequencies and limit the risk of jumping slip ring brushes or other failures. The shock tests are planned for April 2024 and so results are unfortunately not available at the time of this paper.

Conclusion & Acknowledgements

This paper focuses on two issues that were encountered during the development of the SADM-200. Due to the compact size of the mechanism, the reed switches are positioned close to the motor, causing a series of abnormal reed triggers when the magnet is closing in. This issue was solved by implementing a dedicated software filter. Regarding the excess magnetic moment, the mitigation option selected was to change the 15-5PH to an amagnetic 316L steel. The SADM-200 qualification is in progress and should hopefully validate the decisions made. The authors would like to thank CNES Toulouse and Comat teams for their support in this development.

References

1. Spanoudakis, Schwab. "Development challenges of utilizing a corner cube mechanism design with successful iasi flight heritage for the infrared sounder (irs) on mtg; recurrent mechanical design not correlated to recurrent development", *Proceedings of the 16th European Space Mechanisms and Tribology Symposium*, 2015.
2. Robroek, Kroon. "Reed: the manual", *Proceedings of the 20th European Space Mechanisms and Tribology Symposium*, 2023.
3. Wood, Pargett. "Solar Array Drive Assembly Qualification Lessons Learned" *Proceedings of the 44th Aerospace Mechanisms Symposium*, 2018, pp. 293-306.

Development of a Shape Memory Alloy Thermostat

Alai Lopez* and Kerri Cahoy†

Abstract

A shape memory alloy (SMA) thermostat is a passive device that functions by leveraging the high stroke of a two-way shape memory alloy (TWSMA) to open and close a circuit based on a preset temperature. SMA thermostats do not currently exist as commercially-off-the-shelf (COTS) or as custom components for space applications. SMA thermostats have the potential to be lower size and weight, improve reliability, operate at a wider temperature range, and offer a greater dead band compared to the current state of the art bimetallic disk (BMD) thermostats. The potential disadvantages over BMD thermostats are a slower response time, TWSMAs are not easily accessible to purchase in the market, and a lower temperature accuracy due to the hysteresis behavior of the TWSMA for applications that require the same ON/OFF temperature actuation. This paper focuses on the design, build, and test of an SMA thermostat prototype that successfully demonstrates functional feasibility for a given space application. The scope involves keeping the prototype low budget (<\$100), no size or mass constraints, no definition of the electrical or mechanical interfaces and no specific survivability or lifetime requirements.

Introduction

A thermostat is a sensor that receives a temperature stimulus and responds with a binary (True/False) electrical signal. They are commonly used in industry to safeguard components or systems from getting too cold or overheating. The goal is to develop a thermostat using an SMA. An SMA is an alloy generally composed of Nickel and Titanium, also dubbed NiTiNOL, that remembers/recovers its shape and size when heated to a specific transformation temperature, often referred to as a one-way SMA. A two-way SMA remembers two shapes; one when cold and one when hot without the need of an applied stress as shown in Figure 1. An SMA thermostat is a passive device that functions by leveraging the high stroke of a TWSMA to open and close a circuit based on a preset temperature. SMA thermostats do not currently exist as commercially-off-the-shelf (COTS) or as custom components for space applications. The authors did not find any previously published work during the literature review of an SMA component intended to function as a thermostat for space applications. The current state of the art space thermostats are bimetallic disk (BMD) thermostats. SMA thermostats have the potential to be lower size and weight due to the greater actuation energy compared with bimetallic disks [1]. Additionally, SMAs can improve reliability by increasing the acceptable tolerance range during manufacturing and assembly, which are known to be the main causes of dithering and “creepage” on BMD thermostats [2]. Other advantages include a wider temperature range from -114°C to 619°C [1] and a greater dead band, which reduces temperature swings and power consumption for applications with low temperature precision control. The potential disadvantages over BMD thermostats are a slower response time, TWSMAs are not easily accessible to purchase in the market, and a lower temperature accuracy due to the hysteresis behavior of the TWSMA for applications that require the same ON/OFF temperature actuation. This paper focuses on the design, build, and test of an SMA thermostat prototype that successfully demonstrates functional feasibility for a given space application. The thermostat is designed to regulate the temperature of a Li-ion battery pack flying in low earth orbit (LEO). This paper serves as a proof-of-concept for the use of an SMA as the main actuation mechanism in a thermostat. The scope of this prototype project is flexible to allow for wider design options over which to iterate during the development process. The scope involves keeping the prototype low budget (<\$100), no size or mass constraints, no definition of the electrical or mechanical interfaces and no specific survivability or lifetime requirements. The work is sensor-focused, and the prototype satisfies the functional

* MIT Lincoln Laboratory, Lexington, MA

† Massachusetts Institute of Technology, Cambridge, MA

requirements shown in Table 1. It is important to note that it will be passive device. Therefore, in contrast to other SMA applications, no additional power is required for thermostat operation, such as the use of a heater or electrical current to heat the SMA.

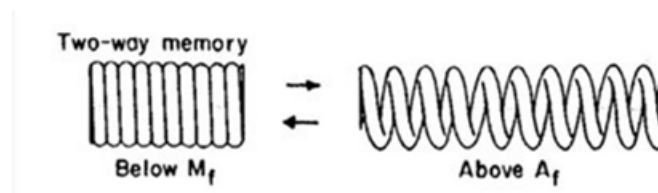


Figure 1. TWSMA spring phase transformation process, the martensite final (M_f) phase takes place in the cold state (spring contracts) while the austenite final (A_f) phase is in the hot state (spring extends) [3]

Table 1. Functional requirements of SMA thermostat [4]

No.	Name	Value	Rationale
1	Switch Close Temperature	5 C	Worst case lowest operating surface temperature of 18650 battery cells acquired from a battery market survey plus SMA tolerance
2	Max Switch Open Temperature (due to hysteresis)	50 C	Worst case highest operating surface temperature of 18650 battery cells acquired from a battery market survey for CubeSats
3	Switch Close Temp. Accuracy	+/- 10C	According to SMA temperature transformation tolerance provided by suppliers
4	Max. Switch Output	10VDC/3A	Max voltage supplied by EPS from market survey/ Max current handled by PCB boards from the AERO VISTA 6U CubeSat mission
5	Cycles to failure	>3000	Worst case, assuming a 90 min orbit with one actuation per orbit for a 6 month mission life

SMA Selection Process

During the design phase, while pursuing a market survey of COTS TWSMA springs, none were found. A couple of suppliers that advertised having COTS TWSMA springs did not respond to requests for information. Some provided a service of transforming a COTS SMA spring to TWSMA at a high cost (~\$1000) which was outside of the budget for this project. Fortunately, one of the suppliers called Kellogg's Research Laboratory (KRL) gained interest in the project and donated 30 uncharacterized scrap TWSMA springs. These springs were then quickly tested in a thermal chamber to identify springs that satisfied the criteria. The criteria are the following: Spring must have a displacement length < -0.41mm (-0.016 inches) when cooled between 15°C and -5°C and must recover that displacement when heated to a temperature <50°C. Springs were first heated to a temperature above 80°C to reset their shape. Then the springs were cooled to a temperature of 15°C, -5°C and heated to 50°C where their length was measured and recorded at each setpoint with a caliper. Out of 30 springs, one spring satisfied the criteria with a -4.83mm (-0.19 inch) displacement.

SMA Thermostat Design

The design of the SMA thermostat consists of a TWSMA spring that is sandwiched between two 3D-printed plates as shown in Figure 2. The bottom plate remains fixed, while the top plate moves with the spring by sliding on a linear rail or shoulder screw. Each plate holds two Pb-coated contacts that are connected to a 24 awg PTFE-insulated lead wire. When the thermostat is hot, the spring is extended, creating a gap between the contacts preventing current from passing between the wires (open circuit). When the thermostat is cooled, the spring contracts, reducing its length, displacing the plate downward due to gravity

and enabling both contacts to touch, thus closing the circuit. Although the force due to gravity cannot be relied upon to move the top plate in space, it was selected as our driving force in this prototype to ensure low degradation of the spring. The fully assembled prototype is shown at the bottom of Figure 2.

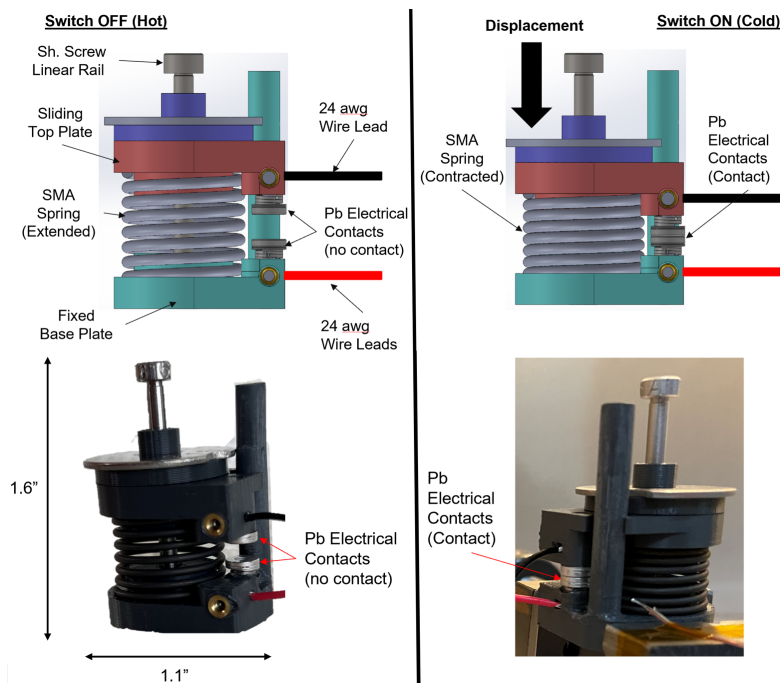


Figure 2. Design overview of the SMA thermostat with important components labeled; the thermostat is in the open-circuit and closed-circuit configuration on the left and right sides, respectively

Testing

The thermostat was tested inside of a thermal chamber (0.03-m cubed) for 11 days, equivalent to 260 thermal cycles. The data acquired from these cycles will be used to predict the performance of the thermostat at 3000 cycles. The test setup is shown in Figure 3. The bottom plate of the SMA thermostat was fixed via a vice and the entire assembly was placed on top of folded wipes that acted as vibration isolators. The wire leads were taped on the chamber wall at a location that minimized the force on the thermostat. A very low constant load was applied to the TWSMA spring (~ 0.12 N) to minimize degradation. An UNO R3 microcontroller, similar to the standard Arduino UNO, was used with a MAX6675 amplifier and an SD card reader as the data acquisition system (DAQ). Connected to the DAQ was a K-type thermocouple that was used to measure the ambient temperature very close to the spring. Additionally, the SMA thermostat is connected to the internal pull-up resistor input pin of the DAQ to measure the thermostat state. All measurements were recorded throughout the entire fatigue test at a 1Hz sample rate.

The thermal profile used was optimally selected to minimize time per cycle while ensuring correct measurements could be taken. The thermal profile as programmed in the chamber controller is shown in Figure 4a. Starting at a thermostat temperature of 50°C , the chamber starts by ramping down at a $5^{\circ}\text{C}/\text{min}$ rate and soaks for 7.5 minutes. This allows for the TWSMA spring to reach thermal equilibrium at $\sim 15^{\circ}\text{C}$. The chamber then ramps down again, but at a lower ramp rate of $1^{\circ}\text{C}/\text{min}$ to minimize the temperature lag of the TWSMA during the expected temperature range of actuation. As shown in Figure 4c, the maximum temperature lag computed at this temperature was $\sim 2^{\circ}\text{C}$ assuming a $25 \text{ W}/\text{m}^2\cdot\text{K}$ and worst-case NiTi properties [5]. The analysis also takes into account the actual ambient temperature of the TWSMA shown in Figure 4b. Finally, the chamber ramps up to 50°C at a rate of $5^{\circ}\text{C}/\text{min}$ and soaks for 7.5 minutes for the reasons already stated. No additional ramp rate of $1^{\circ}\text{C}/\text{min}$ was included in the ramp up because of the extra margin available for the closed actuation temperature requirement. The max temperature lag

computed between the TWSMA and the ambient temperature was 5°C. The total actual mean cycle duration was 55 minutes per cycle.

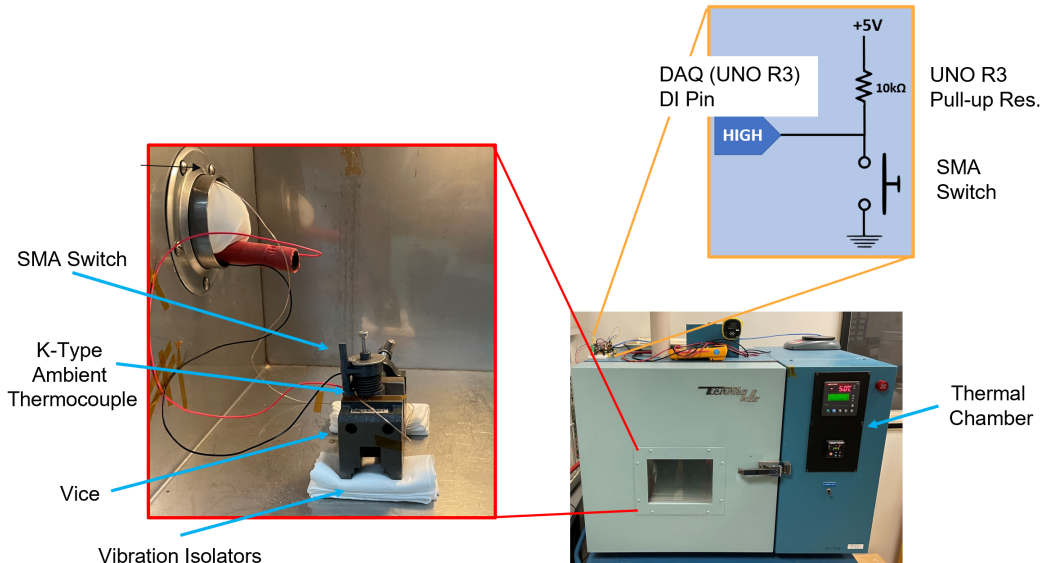


Figure 3. Thermal fatigue test setup

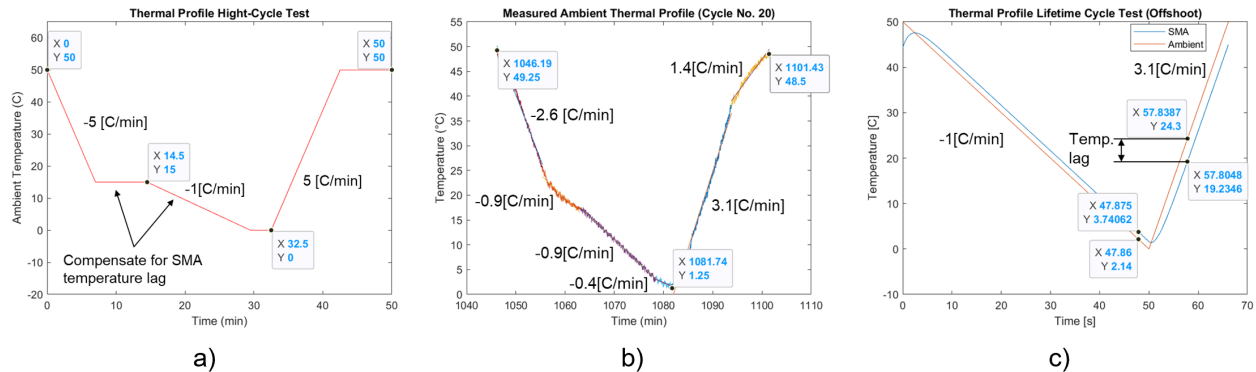


Figure 4. a) Thermal profile as programmed in the chamber b) Actual thermal profile measured by ambient thermocouple c) Temperature profile of TWSMA analytically computed taking into account a simplified version of the measured ambient temperature, 25 [W/m²*K] and worst-case NiTi properties [5].

Results

As discussed in the previous section, thermal fatigue testing was performed on the thermostat while measuring the signal state output and ambient temperature. A successful thermostat actuation is defined as a single signal output at the temperatures specified in the functional requirements 1 to 3 in Table 1. Signal peaks due to chatter that had a peak duration of <0.2 minutes were not taken into account and were removed from the plots in Figure 2. Out of 260 thermal cycles, results show a 100% success rate. An example of a successful actuation signal with respect to time and ambient temperature is shown in Figure 5a for cycle 259. As shown, the thermostat starts in the OFF state (open circuit) and turns ON (closes the circuit) at ~4°C until it is brought up to a temperature of ~20°C. A hysteresis behavior can be observed during thermal loading and unloading, which explains why the ON and OFF actuation temperatures are different. Figure 5b is a plot of 260 thermostat actuation cycles overlaid on top of each other as a function of ambient temperature. The thermostat ON and OFF temperatures are different due to hysteresis of the

TWSMA spring and therefore are labeled accordingly with brackets. An overview of the performance is shown in Table 2. Sensor accuracy degradation over cycle amount is shown in Figure 5c. The plot illustrates both ON and OFF temperatures and how they change as a function of time or cycle number. Linear regression trend lines of both ON and OFF behavior are overlaid in yellow and purple, respectively. The slope of 0.0001 is computed for both ON and OFF temperatures with a 3.3°C and 18.7°C y-offset, respectively. These results indicate a negligible degradation of sensor accuracy over 260 cycles.

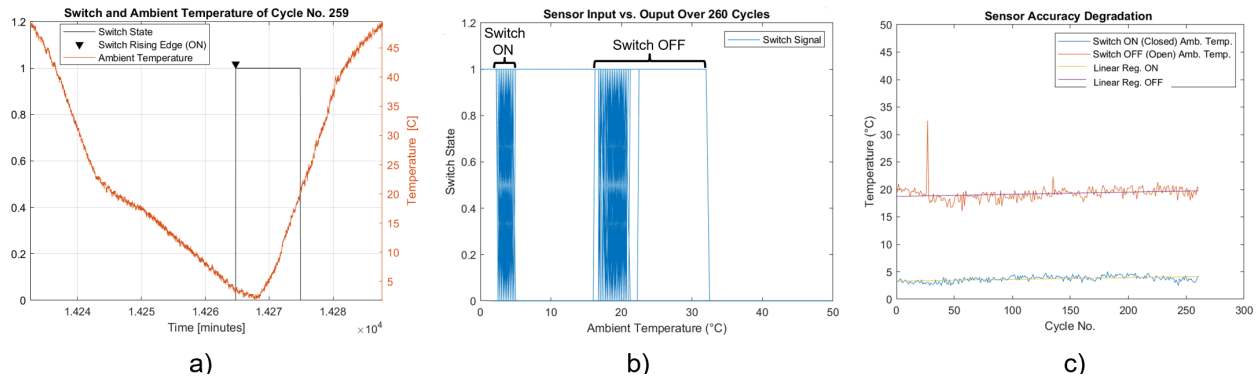


Figure 5. a) Thermostat signal overlaid on top of an ambient thermal profile. b) All thermostat signals overlaid with each other with respect to ambient temperature. c) Sensor accuracy degradation of both ON and OFF temperature with respect to cycles and a linear regression trendline overlaid.

Table 2: SMA Thermostat Performance

	ON Ambient Temp. [C]	OFF Ambient Temp. [C]
Min.	2.5	16
Max.	5	32.5
Mean.	3.7	19.2
Std. Dev.	0.5	1.2

In order to satisfy the thermostat output requirement (No. 4 of Table 1), the design of the SMA thermostat incorporated 24 awg PTFE wire and an ABS casing. According to MIL-STD-975, the derating criteria for a 24 awg PTFE wire operating at 70°C in vacuum is 3.3A, which satisfies our current output. The voltage limitation in the design is driven by the breakdown voltage of the material being used and wall thickness. Given a minimum wall thickness of 1mm and a minimum ABS breakdown voltage of 15.7 kV/mm, the max voltage output it can withstand without failure is 15.7kV. A direct comparison between functional requirements and results is shown in Table 3.

Lessons Learned

There were several lessons learned throughout the development of the SMA thermostat. The most important lessons were that COTS TWSMA actuators are scarce and difficult to find. One way to overcome this challenge is to do it yourself. Fortunately, there is vast amount of documentation to help tailor a standard OWSMA to fit your requirements through the use of laboratory equipment, such as [6]. For this effort, a total of 30 scrap TWSMA springs were donated by Kellogg's Research Laboratory. Additionally, there are no comprehensive testing standards to fully characterize an SMA, therefore a quick testing method to determine key thermomechanical parameters was developed and used to identify a TWSMA spring out of 30 scrap springs that satisfied our criteria. During testing of the thermostat, there were issues that occurred due to the contact resistance being too high and preventing a successful actuation. This problem was solved by changing the coating of the contacts to a more conductive coating (Pb) and increasing the contact

load. Finally, another problem observed during testing was signal chatter due to thermally induced motion causing the thermostat to be unstable in-between states. The most critical improvement proposed to eliminate signal chatter due to thermally induced motion is adding a magnetic pull-in force to future models.

Table 3: Status of functional SMA Thermostat requirements

Name	Req. Value	Actual Value	Status	Notes
Switch ON (Close) Temperature & Accuracy	5 +/- 10C	3 +/- 4C	Satisfied	Nominal value w/binary tolerances calculated from Table 2 taking into account DAQ (+/- 2C) and a worst-case temperature lag error (-2C)
Max Switch OFF (Open) Temperature (due to hysteresis)	50 C	35C	Satisfied	Worst-case max OFF temperature acquired from Table 2 and taking into account DAQ error (+2C).
Max. Switch Output	10VDC/3A	15 kV/3.3A	Satisfied	Max breakdown voltage for ABS material with a 1mm thickness; MIL-STD-975 current derating standard for 24awg PTFE
Cycles to failure	>3000	260 cycles	Satisfied (According to results)	No performance or physical degradation was shown over 260 cycles

Conclusion

NiTiInol materials have a shape memory effect that can be leveraged in sensors. SMA thermostats do not currently exist in the market and this paper has proven them to offer a passive control solution in thermal management for space applications. The goal to design, build and test an SMA thermostat designed to regulate the temperature of a Li-ion battery pack flying in LEO was successfully completed and all requirements were satisfied according to the results. Lessons learned throughout the process were discussed, most importantly a solution was proposed to eliminate signal chatter.

References

- [1] D. C. Lagoudas, Shape Memory Alloy Modeling for Engineering Applications, Springer, 2018.
- [2] W. C. Hu, "1978," American Institute of Aeronautics and Astronautics, New Orleans, An Investigation of Switching Behaviors of Bimetallic-Disk Thermostats.
- [3] L. Marioni, "Design and rapid prototyping of a SMA based actuator," ResearchGate, 2014.
- [4] V. Knap, "A Review of Battery Technology in CubeSats," *Energies*, 2020.
- [5] "Nitinol-technical-propertie," [Online]. Available: <https://matthey.com/products-and-markets/other-markets/medical-components/resource-library/nitinol-technical-properties>.
- [6] O. M. A. Taha, "EXPERIMENTAL STUDY ON TWO WAY SHAPE MEMORY EFFECT," *ARPN Journal of Engineering and Applied Sciences*, vol. 10, pp. 7847-7851, 2015.
- [7] D. G. Gilmore, Spacecraft Thermal Control Handbook, El Segundo, CA: The Aerospace Press, 2002.
- [8] J. O. Ruiz, "Design and Testing of a Low Cost Shape Memory Alloy (SMA) Heat Switch for CubeSats," JPL/Cal Poly SLO, 2017.

On the Internal Loading Distribution in a Radial Load Rolling Element Bearing

Mário C. Ricci*

Abstract

The external load of a rolling element bearing is transferred from one ring to the other through the rolling elements, and the device's stiffness, performance and life depend on the load distribution across the rolling elements, which is not uniform. The load distribution depends on the rings and rolling elements' materials, the internal geometry of the bearing, and the magnitude and direction of the external load. An internal parameter that has a strong influence is the radial clearance. Mitrović, Lasović *et al.*, derived load distribution factors for radial load ball bearings with positive and zero radial clearances, which are a measure of the rolling elements participation in the external radial load distribution. However, the factors derived by them aren't suitable for bearings with negative radial clearance (interference), since they are based on the calculation of active rolling elements, that is only valid for zero and positive radial clearance. In this work, the load distribution factors for the most loaded rolling element are obtained as functions of both relative radial clearance parameters: one with respect to elastic compression at the load line, $P_d/(2\delta_{\max})$, and the other with respect to the total relative displacement between the rings, $P_d/(2\delta)$; for a number of rolling elements in the bearing varying from 2 to 20 and for ball and cylindrical roller bearings, with positive, negative and zero radial clearances.

Introduction

A rolling element bearing is a device generally consisting of two concentric steel rings, where two grooves are machined: an inner groove is machined in the outer ring and an outer groove is machined in the inner ring. Rolling elements are placed between the grooves: cylindrical, conical or spherical rollers, or balls. A rolling element bearing provides load transmission between two structures, generally a shaft and housing, maintaining the relative position between the structures, but allowing 1 or 2 rotational and/or translational degrees of freedom. The external load of a rolling element bearing is transferred from one ring to the other through the rolling elements, and the device's stiffness, performance and life depend on the external load distribution across the rolling elements, which is not uniform. The load distribution depends on the rings and rolling elements' materials, the internal geometry of the bearing, and the magnitude and direction of the external load. An internal parameter that has a strong influence is the radial clearance.

Stribeck [1] was the pioneer to investigate the distribution of loads on the rolling elements of a radially loaded ball bearing and found that the *maximum* ball load could be derived by multiplying the *medium* load by 4.37 for zero internal clearance. This result is an approximation of the value found when considering an infinite number of balls, of infinitesimal diameter, symmetrically and evenly distributed in relation to the load line, which passes through the most loaded ball's center. This number came to be known as Stribeck's Number or Constant and, to account for nonzero diametrical clearance and other effects, Stribeck recommended rounding the Constant to 5.0.

Palmgren [2] stated that the theoretical value of Stribeck's Constant for roller bearings with zero internal clearance is 4.08 and suggested using Stribeck's recommended value of 5.0 for the Stribeck's Constant for either ball or roller bearings having typical clearance.

Ricci [3] showed how the Stribeck's Constants were found. It's also shown that the error when adopting the value 4.08 for a roller bearing Stribeck's Constant is 55.6 times greater than when adopting the value 4.37 for the ball bearing Stribeck's Constant.

Sjövall [4] proposed an integral method for load distribution calculation in bearings. The relationship between the load on the most loaded rolling element and the bearing loading was established using

* National Institute for Space Research, São José dos Campos, São Paulo State, Brazil

Sjövall's integrals. Houpert [5] improved Sjövall's integrals for multi-degree-of-freedom bearing system. A comprehensive mathematical model of bearings was developed by Harris [6]. The load zone was described by the load distribution factor, ϵ , and the contact stress-strain relationship between the ring and any rolling element was achieved. The load distribution can be obtained by continuous iteration procedure. However, studies have shown [7, 8] that the results obtained by the Harris method cannot rigorously satisfy the static balance, once that the problem of obtaining the load distribution in bearings with arbitrary radial clearance is to determine the number of rolling elements that participate in the transfer of the external radial load. Tomović [7, 8] considers two boundary positions of support of the inner ring and proposed a simple method to determine the number of rolling elements in the loading zone.

Research has shown that ball bearings should have slightly negative or zero internal clearance to maximize bearing life and reliability. However, zero or slightly negative clearance generates high contact stresses between raceways and balls [9, 10]. In addition, it increases bearing friction, which makes the bearing vulnerable to temperature rise. Therefore, a bearing with positive radial clearance is generally chosen to avoid such problems [11].

Xiaoli *et al.* [9] developed a mathematical model based on the Hertz elastic contact theory to determine the radial load distribution in ball bearings with positive, negative and zero clearance. Oswald *et al.* [10] investigated the effect of internal clearance on load distribution and fatigue life of radially loaded deep groove ball bearings. They found that life gradually decreases with increasing radial clearance's absolute value and is maximum under small negative radial clearance.

Mitrović [12] carried out an analytical study of the influence of radial internal clearance on the static load rating of ball bearings. To analyze the influence, a parameter was introduced: the load distribution factor, which is the ratio between the load on the most loaded ball and the external radial load. The ratio introduced in Eq. (3) of the Mitrović's paper is a function of the rolling elements' azimuth angles and the *relative radial clearance parameter with respect to the total relative displacement between rings*, $P_d/(2\delta)$, and measures the participation of the most loaded rolling element in the external radial load distribution. Lazović *et al.* [13] generalized the notion of load distribution factor introducing a slightly different load distribution factor, which is the ratio between the ball load component in the radial external load direction and the external radial load. They also introduced the definition of the *reduced* load distribution factor, which is the ratio between the ball load and the external radial load. The ratios that appear in Eqs. (13) and (16) of the Lazović *et al.*'s paper are functions of the rolling elements' azimuth angles and the *relative radial clearance parameter with respect to the elastic compression in the load line*, $P_d/(2\delta_{\max})$. They provided an overview of the load distribution of ball bearings with zero and positive radial clearance. However, the load distribution factors, as defined by both Mitrović and Lazović *et al.*, aren't suitable for bearings with some negative radial clearance. This is because the models don't allow negative radial clearance and also both use a parameter to define the load distribution factors, which represents the active rolling elements number, which actively participate in the transfer of the external radial load. However, such a parameter as defined is only valid for bearings, which have zero or positive radial clearance.

There are in the literature two definitions for *load distribution factor* with respect radially loaded rolling element bearings. One of them assumes that the load distribution can be given by a radial integral and the load distribution factor, ϵ , is defined as being the ratio between the load zone projected on the load line and the diameter [4, 5]. The second assumes that the load distribution satisfies the static equilibrium equation given by a sum of the discrete rolling elements' loads components in the radial external load direction. In this case, the load distribution factor is defined as the ratio between the rolling element's load component in the radial external load direction and the external radial load [12, 13].

In this work, the load distribution factors for the most loaded rolling element of a radial load rolling element bearing are derived in the same way as were done by Mitrović and Lazović *et al.* [13]. However, unlike Mitrović and Lazović *et al.*, here I address the load distribution factors as functions of both relative radial clearance parameters. One with respect to elastic compression at the load line, $P_d/(2\delta_{\max})$, and other with respect to the total relative displacement between the rings, $P_d/(2\delta)$. Here the radial clearance *sign* is also considered, and load distribution factors are also obtained for cylindrical roller bearings. Since the mechanical system can operate with positive, negative or null clearances, I presume that the introduction of the radial clearance sign in rolling element bearing models is a measure that makes them

improved. Recently, it has been discovered that increased life and performance without noise and vibrations is related to a small negative radial clearance, or preload [10]. Generally, a small positive clearance is used to avoid the effects of radial temperature gradients, which can even lock the shaft's motion with respect to the housing.

Radial Clearance, Maximum Hertzian Elastic Deflection and Total Relative Radial Rings Displacement

Assuming that z rolling elements are evenly spaced about a pitch circle, symmetrically distributed with respect to the radial load line, which passes through the center of the most loaded rolling element ($j = 1$), so, the radial clearance or interference, c_j , $j = 1, \dots, z$, at a given azimuth angle ψ_j , if the absolute diametric clearance $|P_d|$ is small compared to the radius of the tracks, can be expressed with adequate precision by

$$c_j = \begin{cases} \left(1 - \frac{|P_d|}{P_d} \cos \psi_j\right) \frac{P_d}{2} & \text{if } P_d \neq 0, \\ 0 & \text{if } P_d = 0. \end{cases} \quad (1)$$

If $P_d > 0$, on the load line where $\psi_1 = 0^\circ$, the clearance is zero; and where $\psi_j = 180^\circ$ the clearance is P_d . If $P_d < 0$ the clearance is zero at $\psi_j = 180^\circ$ and P_d (interference) at $\psi_1 = 0^\circ$.

The application of further load will cause elastic deformation of the rolling elements and elimination of clearance along a $2\psi_1$ arc. If the further elastic interference or compression in the load line is δ_{\max} the corresponding elastic compression δ_j of the ball or cylindrical roller bearings along a radius at an angle ψ_j to the load line is given by

$$\delta_j = \delta_{\max} \cos \psi_j - c_j, \quad (2)$$

which assumes that the rings are rigid.

Substituting (1) in (2), yields

$$\delta_j = \delta \cos \psi_j - \frac{P_d}{2}, \quad (3)$$

where

$$\delta \approx \delta_{\max} + \frac{|P_d|}{2} \quad (4)$$

represents the *total relative radial displacement* between inner and outer rings.

Ratio Between the Maximum Rolling Element Load and the Radial External Load

If P is a radial external load, then

$$P = \sum_{j=1}^z P_j \cos \psi_j, \quad (5)$$

where P_j , $j = 1, \dots, z$, are rolling elements' normal loads for rolling elements located at the azimuth angles ψ_j , with the portions of the sum referring to rolling elements, which don't participate in the load transfer, being assumed to be null.

Assuming that

$$P_j = k_n \delta_j^n, \quad j = 1, \dots, z, \quad (6)$$

where k_n is a load-deflection proportionality constant, $n = 3/2$ for ball bearings [1] and $n = 10/9$ for cylindrical roller bearings [2], then, dividing P_1 by Eq. (5), yields

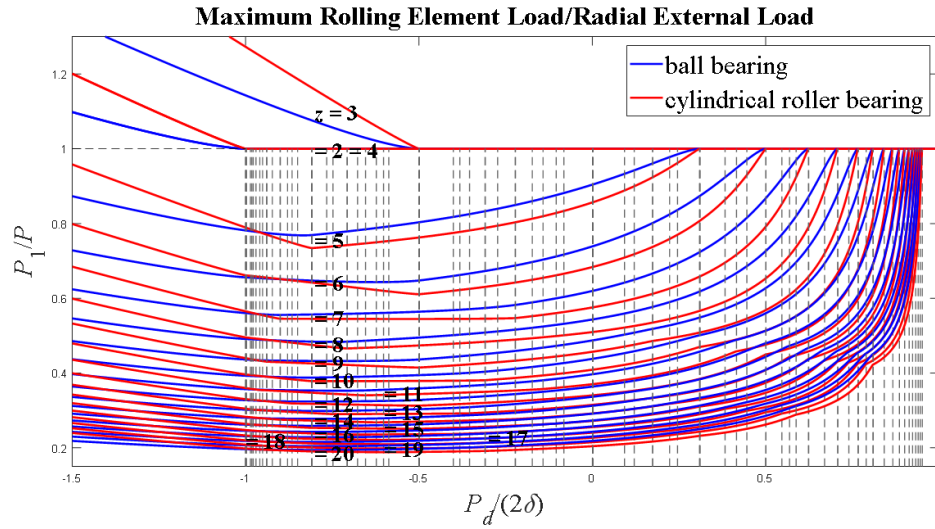
$$\frac{P_1}{P} = \frac{\left(1 - \frac{P_d}{2\delta}\right)^n}{\sum_{j=1}^z \left(\cos\psi_j - \frac{P_d}{2\delta}\right)^n \cos\psi_j} = \frac{\left(1 + \frac{|P_d|}{2\delta_{\max}} - \frac{P_d}{2\delta_{\max}}\right)^n}{\sum_{j=1}^z \left[\left(1 + \frac{|P_d|}{2\delta_{\max}}\right) \cos\psi_j - \frac{P_d}{2\delta_{\max}}\right]^n \cos\psi_j}, \quad (7)$$

which is a function of the rolling elements' azimuth angles and the *relative* radial clearance parameter. There are two relative radial clearance parameters. One of them is with respect to the total relative displacement between rings, δ , and the other is with respect to the further elastic interference or compression in the load line, δ_{\max} .

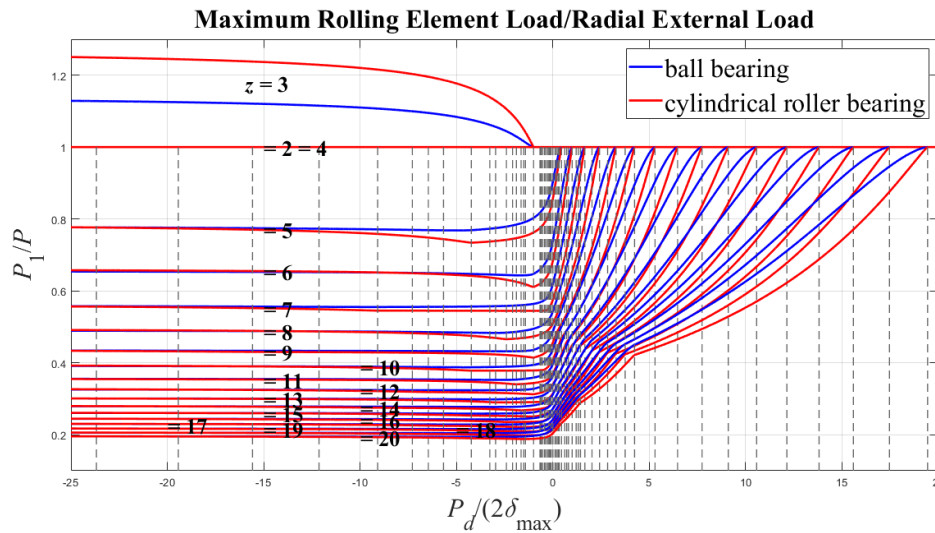
Numerical Results

Figure 1 shows the P_1/P ratios for ball and cylindrical roller bearings and some z values as $P_d/(2\delta)$ and $P_d/(2\delta_{\max})$ functions. If $P_d/(2\delta)$ or $P_d/(2\delta_{\max})$ increases, the P_1/P ratio values tend towards 1 and reach the value 1 sooner or later, depending on the number of rolling elements in the bearing. The greater the number, the later P_1/P ratio values reach the value 1. Note that the $P_d/(2\delta)$ parameter never reaches or exceeds the value 1, regardless of the number of rolling elements in the bearing. If this happened, it would mean that the relative displacement between the rings would be less than or equal to the radial clearance and, therefore, there would be no rolling element/race contact on any of the rolling elements. Unlike what it's observed for the $P_d/(2\delta)$ parameter, there is no theoretical superior boundary for the $P_d/(2\delta_{\max})$ parameter. Each rolling element added to the bearing expands the $P_d/(2\delta_{\max})$ range, in which P_1/P is less than 1. Note also that with increasing $P_d/(2\delta)$ or $P_d/(2\delta_{\max})$, when the P_1/P ratio reaches the value 1, it is reached for both ball and roller bearings with the same number of rolling elements, for a single $P_d/(2\delta)$ or $P_d/(2\delta_{\max})$ value. The numerous dashed vertical lines that appear in the figures, which are functions of the relative radial clearance parameters, indicate the parameters values at which there is a decrease, for the next odd number, in the active rolling elements number when the parameter increases, for *some* z value of rolling elements.

If $P_d/(2\delta) < -0.5$ or $P_d/(2\delta_{\max}) < -1$ and $z = 3$; or $P_d/(2\delta) < -1$ and $z = 2$ or 4 , the P_1/P ratio values computed for the cylindrical roller bearing are greater than the values computed for the ball bearing and in both cases, $P_1/P > 1$. This means that, for these $P_d/(2\delta)$ and $P_d/(2\delta_{\max})$ parameter ranges, and for these numbers of rolling elements in the bearing, the most loaded rolling element load is greater than the external radial load. Besides, for the same z value, the most loaded cylindrical roller transfers a greater portion of the external radial load than the most loaded ball. This is due to the fact that radial clearance is negative in these ranges; therefore, all rolling elements are under preload before the external radial load is applied. With the application of the external radial load, two rolling elements are released when $P_d = -\delta = -2\delta_{\max}$, $\delta, \delta_{\max} > 0$ for the bearing with three rolling elements. For the bearing with two or four rolling elements the release of the rolling element located at $\psi = 180^\circ$ occurs when $P_d = -2\delta$. If z is a multiple of four, the two rolling elements of the bearing located at $\psi = \pm 90^\circ$ never participate in the transfer of the external radial load. Therefore, for $z = 2$ and 4 the P_1/P ratio values are equal. If $P_d/(2\delta) \geq -0.5$ or $P_d/(2\delta_{\max}) \geq -1$ and $z = 3$; or $P_d/(2\delta) \geq -1$, $P_d/(2\delta_{\max})$ any, and $z = 2$ or 4 , $P_1/P = 1$ for both bearings, indicating that, as $P_d/(2\delta)$ or $P_d/(2\delta_{\max})$ increases from these values, all the external radial load is being transferred by a single rolling element, i.e., the rolling element whose number is $j = 1$.



(a)



(b)

Figure 1. P_1/P ratios for ball and cylindrical roller bearings and some z values as (a) $P_d/(2\delta)$ functions and as (b) $P_d/(2\delta_{max})$ functions

The P_1/P ratio values computed for the ball bearing are greater than the values computed for the cylindrical roller bearing, if $P_d/(2\delta_{max})$ is greater than a value, which can be between -29.5 up to -8.5 , depending on the number of rolling elements in the bearing, at least if the number of rolling elements is greater than or equal to five. Unlike what it's observed for the P_1/P ratio values as a $P_d/(2\delta)$ parameter function, the P_1/P ratio values as a $P_d/(2\delta_{max})$ parameter function vary little - it is almost a plateau, denoted more for ball bearings than roller bearings - for negative values of $P_d/(2\delta_{max})$ parameter and for any number of rolling elements in the bearing. For a given $z \geq 5$, increasing the $P_d/(2\delta_{max})$ parameter from zero causes the P_1/P ratio values to increase, from the characteristic plateau, for the given number of rolling elements, to the value 1.

Conclusion

A simple model was established to obtain the relationship between the radial clearance (which can be positive, negative or zero), the hertzian elastic deflection in the most loaded rolling element, and the relative displacement between the rings (considered rigid) when a radial load is applied in a rolling element bearing. Relationships between the most loaded rolling element load and the external radial load were obtained as functions of the $P_d/(2\delta)$ and $P_d/(2\delta_{\max})$ parameters, for the number of rolling elements in the bearing ranging from 2 to 20 and for ball and cylindrical roller bearings. Graphs were created for the P_i/P ratios, in which it's possible to compare the external radial load distribution performance of a cylindrical roller bearing with respect a ball bearing with the same number of rolling elements, and vice versa. Thus, theoretically, given an application and knowing the operating range of the $P_d/(2\delta)$ and/or $P_d/(2\delta_{\max})$ parameters, the use of these graphs allows choosing the most appropriate type of bearing, that is the type that provides the lowest P_i/P ratio value, which is an indicative of better distribution of the external radial load. Other factors, of course, must influence the choice of bearing type (ball or roller), such as friction, for example, but our objective here is to choose a type that provides a better load distribution.

References

1. Stribeck, R., Ball bearings for various loads. *Trans ASME* 29:420–463, 1907.
2. Palmgren, A., *Ball and roller bearing engineering*, SKF Industries Inc, Philadelphia, 1959.
3. Ricci M. C., On the Stribeck's numbers in radially loaded rolling element bearings, [doi://10.26678/ABCM.CREEM2022.CRE2022-0038](https://doi.org/10.26678/ABCM.CREEM2022.CRE2022-0038), 2022.
4. Sjövall H., The load distribution within ball and roller bearings under given external radial and axial load, *Tek Mek h*:9, 1933.
5. Houpert, L. A Uniform Analytical Approach for Ball and Roller Bearing, Proc. at the STLE/ASME Tribology Conf., San Francisco, ASME J. Tribol., 119, 1997, pp. 851–857.
6. Harris, T. A., *Rolling Bearing Analysis*, 4th ed., Wiley, New York, 2000.
7. Tomović, R., Calculation of the necessary level of external radial load for inner ring support on q rolling elements in a radial bearing with internal radial clearance. *International Journal of Mechanical Sciences* (60):23–33, 2012.
8. Tomović, R., Calculation of the boundary values of rolling bearing deflection in relation to the number of active rolling elements. *Mechanism and Machine Theory*, (47):74–88, 2012.
9. Xiaoli, R., Jia, Z., Ge, R., Calculation of radial load distribution on ball and roller bearings with positive, negative and zero clearance, *Int J Mech Sci*, 131–132:1–7, 2017. <https://doi.org/10.1016/j.ijmecsci.2017.06.042>
10. Oswald, F. B., Zaretsky, E. V., Poplawski, J. V., Effect of internal clearance on load distribution and life of radially loaded ball and roller bearings, *Tribol Trans*, 55:245–265, 2012. <https://doi.org/10.1080/10402004.2011.639050>
11. Sinha, R., Sahoo, V., Effect of relative movement between bearing races on load distribution on ball bearings, *SN Appl. Sci.* 2, 2100, 2020. <https://doi.org/10.1007/s42452-020-03833-5>
12. Mitrović, R., Analysis of the influence of internal radial clearance on the static load rating of the rolling bearing. *Facta Universitatis, Ser: Mech Eng* 2001;1(No 8):1039–1047.
13. Lazovic, T., Ristivojevic, M., Mitrovic, R. Mathematical model of load distribution in rolling bearing. *FME Trans* 36, 2008:189–196.

Programmable Lead Screw Actuated Self-Leveling Platform

Iok M. Wong*

Abstract

The Programmable Lead Screw Actuated Self-Leveling Platform (PLSASLP) was developed to provide a self-leveling and load-bearing foundation for payloads that need leveling of up to 15 degrees. Consequently, the PLSASLP can also provide a 30-degree conical field of view for precision pointing of instruments. PLSASLP is based on a simple, yet stable geometric model, where undesired motions are restricted to minimize hardware mass and complexity needed to keep the leveling base stable. Redundancy can also be implemented without changing the system architecture. Both system simplicity and configurability indicate the PLSASLP architecture is an effective, viable leveling and pointing solution for flight applications.

Introduction

The PLSASLP, shown in Figure 1, is designed to provide a self-leveling and load-bearing foundation required by various autonomously operated planetary surface robotic or deployable systems. The leveling platform was designed to withstand compressive and tensile loads resulting from applied static torque, while providing leveling capability in a scalable architecture that could support tall and heavy payloads.



Figure 1 - Programmable Lead Screw Actuated Self-Leveling Platform (PLSASLP) in standby position; detail on the right shows the PLSASLP tilted at 10 degrees. Prototype is complete and undergoing testing.

* NASA Langley Research Center, Hampton, VA

Targeted payload systems such as the 2.25-m reach Lightweight Surface Manipulation System with 35-kg tip mass handling capability (LSMS-L35) [1] and 16-m tall Vertical Solar Array Technology (VSAT) [2], have small foundational footprints and require electrical pass-through for power and data transfer at the base, where the leveling occurs. Self-leveling platforms, like most flight-hardware, also need to be lightweight, while providing redundancy to ensure system longevity for the duration of the mission and potentially beyond.

Initial System Capability Requirement

The primary and initial design requirement for the self-leveling platform is to level the supported payload from a slope of up to 15 degrees in any direction. 15-degree tilt tolerance is a requirement on many planetary landers to accommodate the uneven terrain conditions at the landing site. The leveling platform provides up to 20 degrees of peak tilt, at certain orientations, providing additional capability to accommodate unexpected events. The additional 5 degrees of tilt are redundancy reserved for critical use cases and should not be considered as part of the standard capability of the leveling platform.

A leveling platform driven electrically is desirable to accommodate operation at remote locations (on orbit or on a planetary surface). The leveling platform requires an inertial position input to perform self-leveling, which may come from external systems such as the payload mounted on the leveling platform, the lander the leveling platform is mounted to, or other forms of electronic perception systems, such as an inertial measurement unit (IMU). The leveling platform will use the input data to automatically level or point in the desired direction.

The leveling platform architecture is intended to be scalable. For the first implementation of the leveling platform architecture, the prototype was sized to support the LSMS-L35 prototype, which can generate up to 150 N•m of static torque at the base, from a maximum tip mass of 35 kg at full 2.25 m of reach. The leveling platform needs to passively withstand at least 900 N•m of static torque perpendicular to the mounting surface to provide a safety factor of six for where the LSMS-L35 prototype is mounted. The specific factor of safety is selected to match the safety factor of at least five for lifting devices, stated in Occupational Safety and Health Administration regulation 1926.753(e)(2) [3]. A safety factor of six ensures proper safety with additional margin to accommodate payloads that may experience unexpected load. The leveling platform, however, does not need to perform active leveling to counteract the 150 N•m of static torque load when the LSMS-L35 is being utilized at full system capacity. Payloads are expected to be leveled before deployment and operation. The leveling system should scale to meet the specific requirements of the targeted payload.

Precedent Research and Additional Design Recommendation

During the design process, precedent research was performed to identify and evaluate potential leveling solutions to meet the design requirements. The distinct leveling base architectures evaluated in the precedent research included:

1. Stewart platform [4]
2. Canfield joint [5]
3. Two rotary axes actuated joint (Gimbal, Heligimbal) [6]
4. Linear actuated two rotary axes joint (Stack Goniometer) [7]
5. Dome tilting platform (Only hand operated designs found) [8]

Each potential leveling solution was evaluated with realistic computer-aided design models or utilizing existing products, where both quantitative metrics and qualitative characteristics were compared. Hypothetical schematic level designs were used early in the study but were quickly found insufficient to provide adequate information needed to make a meaningful comparison between candidates. For example, some solutions are simple in theory, but to make a realistic implementation work with a targeted payload required overhead that negated the benefit of the proposed approach. Critical metrics such as mass, the

range of motion, footprint, and volume can also be difficult to estimate without a realistic implementation created for the targeted system. Furthermore, while all solutions considered in the precedent research could achieve the basic desired leveling function, some qualitative characteristics such as redundancy opportunities and kinematic behavior on the actual hardware, often deviated from the ideological model. Studies conducted with realistic hardware implementations helped identify undesirable behaviors to avoid and helped refine design features.

Based on lessons learned from the precedent research, two additional design recommendations were appended to help guide the design of the leveling platform. Unlike hard requirements, the recommendations were solely checks against features and behaviors that may impact the performance of a particular implementation on a case-to-case basis.

The first recommendation is to minimize lateral displacement caused by leveling or pointing operations. The payload being leveled should remain in place about the designated pivot point. As the study suggested, most leveling and pointing mechanisms will result in some degree of involuntary translational displacement (ITD) due to the geometric nature of the architecture. Lateral displacement often moves the payload out of the optimal load path, such as cantilevering the payload, which requires more structure to properly support the load of the payload. Base position shift can also affect the operation envelope of payload, which could be critical for certain missions. Additional degree of freedom (DOF) can be used to correct involuntary displacement but adds undesirable complexity to the leveling system.

The second recommendation is to avoid using rotary actuation to counteract static torque directly. Counteracting static torque with parallel rotary actuation generally requires larger, continuously powered actuators and brakes, which have significant negative impacts on the mass and energy consumption of the leveling and pointing system. Ideally, the platform will require no power to maintain position once set in place. Non-backdrivable lead screws, or worm gears are good candidates for maintaining position without power.

The leading leveling base architecture identified was the linear actuated Stewart Platform. Due to the parallel actuated nature of Stewart Platform, loads can be distributed among actuators more evenly, and the actuators did not need to accommodate the mass of actuators sitting on top of one another. In a parallel arrangement like the Stewart Platform, the full capacity of the linear actuators can be utilized to support the payload. The Stewart Platform, however, had one major drawback: six actuators are required for the platform, where only two actuators are really needed for a two DOF leveling or pointing platform. The investigation suggested the leveling platform should have a parallel actuated architecture, like the Stewart Platform, but with a minimum number of actuators to perform both leveling and pointing.

Mechanism Description of the PLSASLP

The PLSASLP achieves the specified leveling capability by using a set motor-powered solid zinc-plated alloy steel rod linear actuator, connected between the base platform and the motion platform as indicated in Figure 2. Three actuators were selected, as opposed to two, to provide redundancy. The actuators are located 120 degrees apart equidistant from each other and equal radial distance from the idealized center. The platform is leveled by differences in stroke length of the actuators. Each linear actuator is mounted onto the base platform with a one DOF rotary joint and mounted to the motion platform with a two DOF swivel joint to provide the necessary three DOF to move the motion platform for the leveling or pointing, as shown in Figure 2. Any two linear actuators can tilt the platform to achieve leveling or pointing, but the third linear actuator, when installed, can provide some redundancy, enhance leveling speed performance, and enable Z global translation for the platform. A fixed-length link may replace the third linear actuator, when redundancy is not required, as shown in Figure 2a.

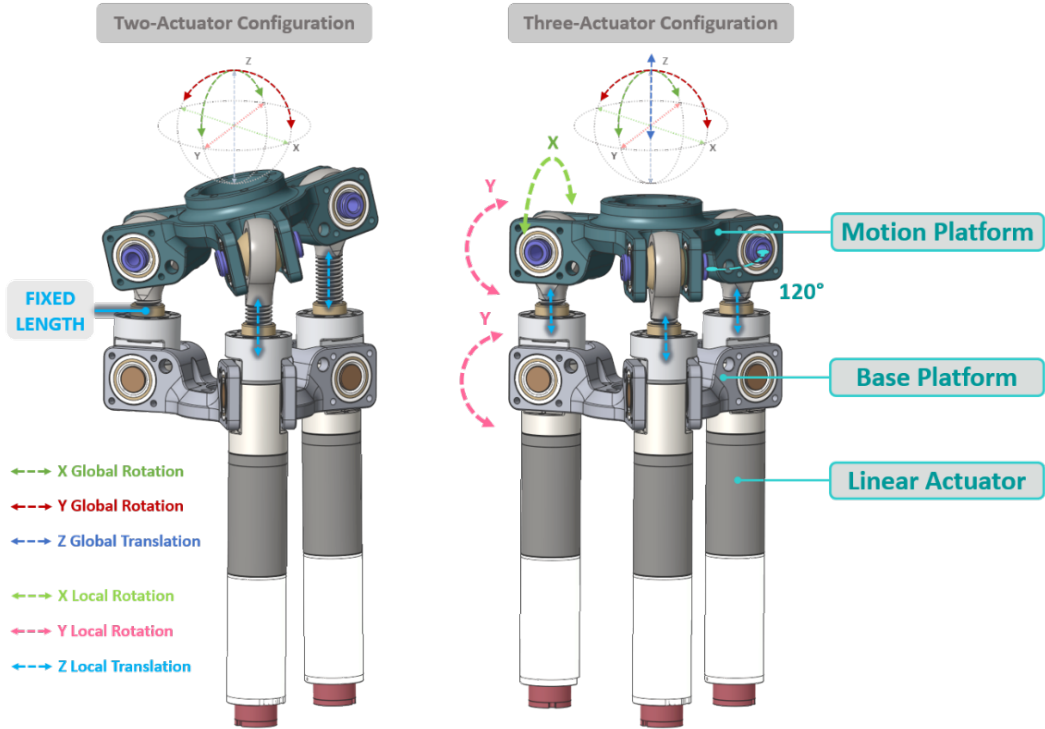


Figure 2 – Diagrams show the basic anatomy of the PLSASLP, and the corresponding global leveling motion resulted from the local linear moment powered by the linear actuators.

Motion wise, the PLSASLP can be simplified as two equilateral triangles, one staged on top of another, connected with variable links at each corner, as shown in Figure 3. One triangle is stationary, and the other triangle can only rotate about the roll (X) and pitch (Y) but cannot rotate about the yaw (Z) axis, as yaw (Z) rotation is restricted by the rotary joints at each corner on the stationary triangle. The rotary joints at each corner can only rotate toward the center of the stationary triangle. As a result, the mobile triangle can only be tilted with each corner staying on the plane bisecting the connected corners of the stationary triangle. The ratio between all variable links will determine in which direction and how much the mobile triangle will be tilted relative to the stationary triangle. Given the geometric constraint, the PLSASLP cannot fully eliminate ITD, but ITD is less than 0.75 mm at maximum tilt of 15 degrees, which will not significantly shift the load path or operational area of the targeted LSMS-L35 payload.

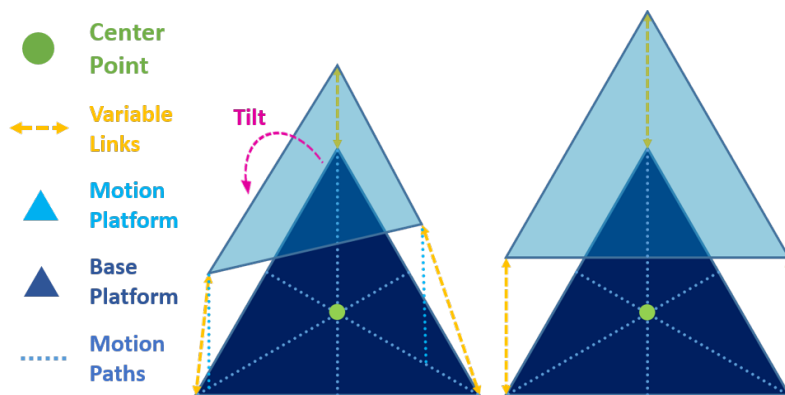


Figure 3 – Diagram shows the geometric principle PLSASLP is based on, which allows the tilting motion needed for the leveling and pointing, while restricting all other DOF to keep the platform stiff.

Prototype Specification and Features

The PLSASLP prototype can level a payload with the 15-degree slope. The PLSASLP prototype can also passively withstand more than 900 N•m static torque load acting perpendicularly to the mounting surface. There are three M10x1.25 mm lead screw swivel joints made of zinc-plated alloy steel, on the load bearing linear actuators supporting the payload. The linear actuators are evenly distributed, 120 degrees apart, 30.475 mm away from the center of the platform. While the tensile strength is not listed for the specific COTS lead screw swivel joint, the tensile strength is estimated based on similar M10x1.25 mm Hex-bolt made of the same material, rated at 965.266 N/mm² (140,000 psi) with 61.2-mm² tensile area. Each lead screw can provide 59,074.2 N of reacting force or about 1800 N•m of reacting torque at the worst position possible to counteract the 900 N•m specified static torque load.

Unlike passive load bearing, active leveling for an operating payload is not part of the requirements. Providing equally capable active leveling as the passive load bearing for the same load requirement would significantly increase the demand on the motors. In the worst-case scenario, only one linear actuator will be either pushing or pulling to level or point the payload. The active leveling capability limit is calculated below based on the conservative capability of a single linear actuator multiplied by the distance between actuator and the center of the motion base (30.475 mm).

Each linear actuator is powered by a 22-mm-diameter rotary motor-gearbox drive capable of up to 3.4 N•m of torque driving the M10x1.25 mm lead screw, assumed to have a 0.25 coefficient of friction for the worst-case scenario. The linear actuator load bearing assembly is estimated to be capable of 2325 N of pushing force based on lead screw equations (1) and (2) [9]

$$Torque(raise) = F * Dp / 2 * (L + u * \pi * Dp) / (\pi * Dp - u * L) \quad (1)$$

$$Torque(lower) = F * Dp / 2 * (L - u * \pi * Dp) / (\pi * Dp + u * L) \quad (2)$$

where F = Force, Dp = Pitch diameter, L = Lead (screw pitch), and u = Coefficient of Friction.

The PLSASLP prototype can perform active leveling to counteract up to 70.85 N•m of static torque generated by the payload.

The PLSASLP prototype has a small footprint that fits in a 108-mm-diameter circle with a total height of 192.3 mm (Within a 1761.64 cm³ cylindrical volume). The PLSASLP prototype measured only about 1.36 kg, which is mass efficient without much mass penalty to connect components together.

A utility pass-through corridor is located at the center of the PLSASLP prototype to allow electrical cable harnesses or other utilities to route from where the payload is mounted to the PLSASLP. The utility pass-through corridor is a critical feature needed by systems like the LSMS- L35, where external cable routing would significantly limit the system's range of motion.

Bolt mounting patterns are on both the base platform and the motion platform to provide mechanical connection between the PLSASLP and other systems. Primary mounting patterns surround the center utility pass-through corridor. Meanwhile, secondary mounting patterns are on the housing of each joint to allow loads to be transferred directly to the load-bearing lead screw powered by the flight-like motor.

Prototype Hardware Fabrication

Restricting unnecessary DOF, as in the geometric model in Figure 3, caused tight tolerance requirements. Significant misalignment on where the linear actuators are mounted would cause the leveling platform to lockup. Yet, high precision, tight tolerance, computer numerical control (CNC) manufactured processes are very expensive. As a cost saving measure to make the prototype feasible under budget constraints, the standard ±0.128 mm tolerance CNC manufacturing process was chosen to produce all the necessary custom parts. Critical alignment features housing the joint axes were then checked and fine-tuned in-house

to meet the tight tolerance design requirement. Both the motion platform and base platform are CNC parts with a unibody design to reduce part counts, while making the parts more structurally robust and stiff.

A lesson learned from early prototypes indicated that even the slightest misalignment between the two bearings where the rotary joint is mounted preloaded the joint, causing the joint to spring back to a neutral position following a move. The inconsistency of the joint movement can cause inaccurate sensor readings and added unnecessary load for the actuators to overcome. While most features are acceptable using the standard tolerance CNC manufacture process, critical features that affect the motion of the PLSASLP should be refined to ensure proper tolerancing and functionality of the PLSASLP.

Short lead time commercial off the shelf (COTS) parts were used whenever possible. Precision COTS bearings were used on the joints to keep the precise movement smooth and ensure the load can be distributed evenly to the load-bearing housing. The three linear actuators were powered by flight-like precision COTS motors with an integrated gearbox and encoder.

The linear drive screws used on the PLSASLP prototype were made in house to provide the optimal form factor and features needed to achieve the PLSASLP envisioned design. The linear drive screws, however, are not yet optimal for the intended application, as the construction was limited by need to integrate generic COTS components. Linear encoders were not integrated into the prototype, with the prototype relying on the motor encoder to predict the stroke length. Backlash is another issue found on the in-house linear actuator prototypes. While both the geometric architecture of the PLASALP and joints are both relatively stiff, backlash on the linear actuator can significantly reduce the stiffness of the platform and lead to undesirable chatter during operation.

To make the PLSASLP as reliable as possible, a custom-made linear actuator design with zero- or anti-backlash solid rod stroke actuation element is highly recommended for the production design to keep the PLASALP as stiff as possible. The solid rod stroke actuation element can make the integration of a linear encoder difficult, but a multi-turn absolute rotary encoder can be used to accurately predict the stroke length. An IMU can also be used to verify the position of the platform during operation.

Control and Sensor Implementation

PLSASLP is relatively simple in the realm of parallel robotics. However, common COTS robotic software like the Robot Operating System 2 (ROS2) [10] have significantly less ready-to-use support for parallel platforms than serial platforms. Custom inverse kinematics control software based on the geometric model, shown in Figure 3, needs to be developed or implemented into the existing framework to drive the PLSASLP.

Autonomous operation integration for performance and health monitoring is another challenging area when designing the PLSASLP. The IMU and position encoders for controlling the linear actuators are essential for the PLSASLP. Secondary perception sensors, such as joint encoders, or load cells on structure elements can provide more feedback for the control software to perform higher levels of autonomous health monitoring and precision control. As a development prototype, the PLSASLP is designed to allow a wide range of experimental sensors to be outfitted to test different sensor packages and control architectures for research purposes. However, overcrowding the design with sensor systems can make the leveling platform overly complicated, increase potential points of failure, and is not recommended for all applications.

Concluding Remarks

The PLSASLP architecture is designed to provide active leveling and pointing functionality with load bearing capability as a scalable system to support potentially tall and heavy planetary payloads. Precedent research with realistically implemented candidates was performed to investigate the viability of existing solutions for the targeted applications. Most of the candidates could meet all the essential requirements. However, potentially problematic behaviors, such as involuntary translational displacement was found among several

candidates, which would have negative unanticipated impacts on the intended application. Findings from the precedent research led to the design of PLSASLP.

Prototypes based on the PLSASLP architecture were made to further examine the concept for manufacturability, system performance, and operation robustness, while serving as a testbed for the LSMS-L35 system to support software control development. The precise, yet simple hardware architecture makes PLSASLP easy to implement, mass efficient and compact. The PLSASLP prototype meets the 15-degree leveling and 900 N•m of static torque load bearing requirement but has some minor ITD that does not significantly change the center of gravity and operation range for LSMS-35 operation. Overall, PLSASLP may be a feasible solution to perform leveling for payload up to 15 degrees or pointing with a 30-degree conical field of view. PLSASLP is currently patent pending.

References

- [1] Wong, Iok M., Cline, Julia E., "LSMS – L35, Miniature Crane for Payload Off-loading and Manipulation: Development, and Application.", AIAA ASCEND 2022, Las Vegas, Nevada, AIAA 2022-4237
- [2] Pappa, Richard, Taylor, Chuck, Warren, Jay, Chamberlain, Matt, Cook, Sarah, Belbin Scott, Lepsch, Roger, Tiffin, Dan, Doggett, William R., Mikulas, Martin, Wong, Iok, Blandino, Joseph, Blandino, Haste, Jerry, "Relocatable 10 kW Solar Array for Lunar South Pole Missions", NASA/TM-20210011743
- [3] Occupational Safety and Health Administration, Safety and Health Regulations for Construction, 1926 Subpart R, 1926.753, Hoisting and rigging.
- [4] Stewart D. "A Platform with Six Degrees of Freedom. Proceedings of the Institution of Mechanical Engineers." 1965
- [5] Short, Robert and Alan Hylton. "A Topological Kinematic Workspace Analysis of the Canfield Joint." 2018
- [6] Asadurian, Armond, "Design and Development of a Two-Axis Thruster Gimbal with Xenon Propellant Lines", 40th Aerospace Mechanisms Symposium 2010, Cocoa Beach, FL
- [7] High Precision DC Motor Goniometric Cradles - BGM200CC, Newport Corporation, Irvine, CA
- [8] Leofoto LB-60N / LB-65 / LB-75 / LB-75S Leveling Base with Butterfly Handle - LB-75, Leofoto USA, SKU: LB-75
- [9] Budynas, Richard G., Nisbett, J. Keith, (2011). *Shigley's Mechanical Engineering Design, Ninth Edition*. McGraw-Hill.
- [10] (2024). ROS2 Version 2 of the Robot Operating System (ROS) software stack. GitHub. <https://github.com/ros2>

Aerocapture Technology Demonstration Risk Reduction Activity

Scott Belbin* and Nicholas Vitullo*

Abstract

NASA Langley Research Center (LaRC) has developed and constructed a full-scale mockup of a trim tab mechanism for a steerable entry vehicle forebody to address the risks associated with a Technology Demonstration Mission (TDM) with respect to the mass and volume needed for such a system as compared to existing steering systems. This paper provides an overview of the conceptual design effort and the results of the risk reduction effort.

Introduction

Current state of the art steering of entry bodies includes jettisonable ballast systems, an example of which was used on the Mars Science Laboratory (MSL) which used a ballast system that accounted for 35% of the entry capsule [1]. Alternatively, the proposed Aerocapture TDM implements trim tabs that extend and retract to provide pitch and yaw control during descent through an atmosphere. Trim tabs have previously been discounted due to “large system weight and complexity” [2], but state of the art batteries and drive systems have decreased in mass such that a four trim tab system becomes feasible in the small entry body format (currently sized at 0.6 m diameter and 100 kg) used in this activity. This risk reduction effort advances the concept to the preliminary design phase with respect to sizing drives and batteries to ensure those components fit within the allowable volume of the entry body and have a net mass no greater than the current state of the art steering systems.

Risk Reduction Overview

Entry Body Volume Constraints, Component Sizing and Preliminary Design

Actuator Selection

Preliminary design used flight-like actuator mechanisms for initial placement. These were sized for the forces and rates required for deploying and retracting the trim tabs for the proposed demonstration. Once selected, the total amp hours required for driving the actuators during the demonstration period drove the size and number of batteries needed.

Actuator size considerations were based on preliminary load calculations and deployment timing requirements. Market research showed no off-the-shelf solutions were available, so several companies were contacted through a Request for Proposal (RFP). Only one company responded with a new design that would fit into the limited space available for the actuators in the overall design, providing the necessary linear force, stroke length and a compact design for flap deployment, and vehicle integration. Considerations for actuator placement within the forward shell included overall actuator stroke length, clearance with the cryogenic full tank and to provide mass as far forward in the forebody as possible. Actuator mounts and restraining elements were designed to nestle within the tight confines of the forebody, while taking assembly integration into consideration.

* NASA Langley Research Center

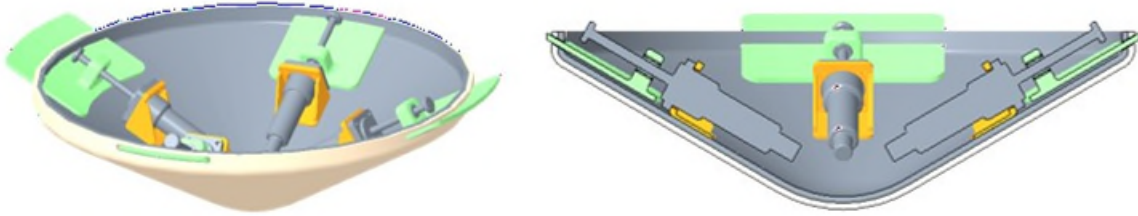


Figure 1. Preliminary Design using Flight-like Linear Actuators

With actuators selected, procurement of Engineering Development Units (EDUs) was solicited for this risk reduction effort. The solicitation requested new EDUs but allowed that existing or used actuators would be acceptable (if shown to be operable) due to the limited timeframe of this effort (about 11 months). Unfortunately, there were no responses from the responding vendor or any other due to the very short delivery period.

Mockup Final Design

To preserve schedule, a decision was made to substitute the flight-like actuators with commercial off-the-shelf (COTS) industrial linear actuators with the same mechanical characteristics. The mounting scheme for the actuators was modified to keep the actuators' lines of action in the same location. Batteries were nested in the forebody and play a dual role, primarily for flap actuators power and secondly, they provide additional mass in the forebody to assist in improving the vehicle's center of gravity.

COTS actuator characteristics included the following key parameters:

Actuator Physical Configuration:

Linear actuators are available in a wide variety of shapes due to the different methods of driving the threaded rod that provides the linear motion. Motors (or gearmotors) can be coaxial with the drive rod, as with the flight actuator originally selected, or parallel to the drive rod connected via spur gears, or at a right angle to the rod driving the rod via worm and worm gear. Market research failed to find a comparable coaxial actuator. Readily available right angle drive linear actuators were fitted to the CAD model successfully, but a source for one that met the speed requirement (discussed below) were not readily available. A parallel configuration actuator was located and successfully fitted to the CAD model, and it had the correct additional characteristics discussed in the following paragraphs.

Actuator Mass:

The COTS actuators selected weighed 1.63 kg (3.60 lbf) each, with a maximum force at 24 volts of 445 N (100 lbf). These are higher in mass than the flight units at 1.2 kg (2.64 lbf) but are well within the actuator mass allowable value for preliminary design of 1.8 kg (4 lbf) per actuator.

Actuator Force:

As the flaps move into the gas flowing over the forebody, the force on the flaps increases as the flaps proceed to their deployed limit, causing a rearward force on the rail system that guides the flaps. The force felt by an actuator is the force due to friction in the mechanism. For the flight design, we have identified the need for lubricated needle bearings to overcome the forces due to friction. Pressure differential is not considered as the rail system for flight would include an isolation cavity for the flap assembly to keep exterior gasses from entering the forebody. The selected actuators are rated for 445 N (100 lbf) at 24 VDC, well beyond the needs expected.

Actuator Speed:

With a no-load speed of 3.81 cm/sec (1.4 in/sec) at 24 VDC, and a rate of 3.18 cm/sec (1.25 in/sec) at full load of 445 N (100 lbf), the chosen actuators meet the deployment rate requirement of 2.54 cm/sec (1 in/sec) for flight.

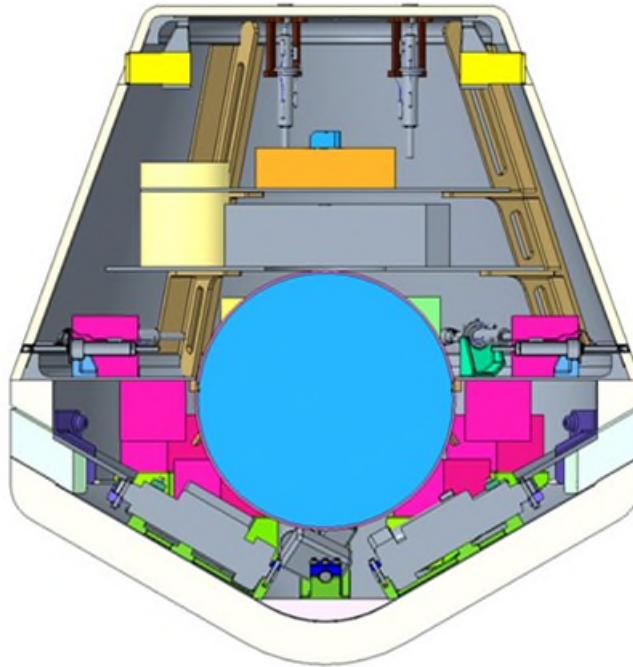


Figure 2. Actuators (gray) and Batteries (red) Clearance to Spherical Tank

Flight Flap Requirements and Preliminary Design

Flap sizing and locations were provided by the Principal Investigator and were used to generate the shape and locations of the flaps. Key characteristics for the preliminary design included:

- Dimensions are determined by aerodynamic considerations, and flight regime criteria, each radially offset 90° from each other with the flap sizes alternating.
 - Two measuring 20.32 cm (8.0 in) wide x 7.62 cm (3 in) long.
 - Two measuring 12.7 cm wide (5.0 in) and 7.62 cm (3 in) long, for a total of 4 flaps.
- Flap range of motion from flush with forebody to maximum deployment of 7.62 cm (3 in).
- Flaps are covered with TPS (Thermal Protection System) using the same thickness and grade as on the forebody.
- Flap deployment travel parallel with the cone angle of the vehicle's forebody.
- Flap movement guided internally by a rail system which keeps the flaps positioned properly during flap extension sequences.

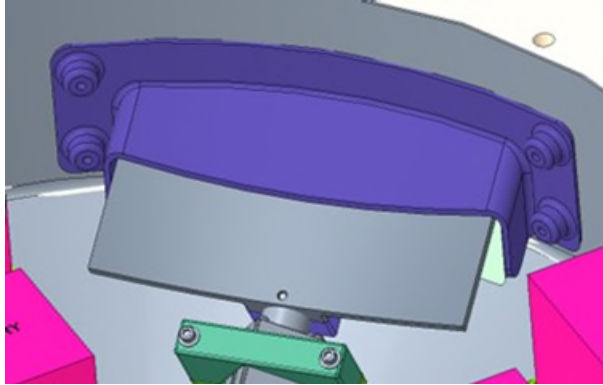


Figure 3. Flap Assembly and Guide Rail (Retracted)

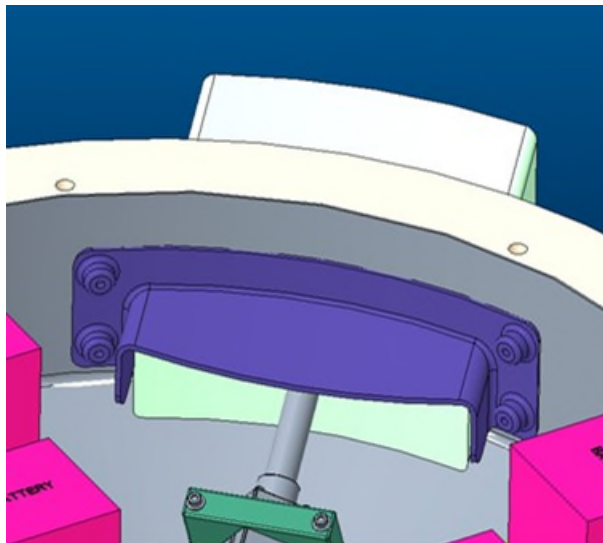


Figure 4. Flap Fully Extended

Preliminary design flap assemblies consist of a titanium carrier flap with flap-shaped TPS bonded to it. The carrier rides in a titanium rail system constraining the flap assembly during radial motion. The flap carrier also includes the actuator's flap connection, pinned to the end of the actuator's rod. The rail system is designed to be aligned axially with the actuator.

Actuator Mounting

Considerations for actuator placement within the forward shell included overall actuator stroke length, clearance with the cryogenic tank and to provide mass as far forward in the forebody as possible. Actuator mounts and restraining elements were designed to nestle within the tight confines of the forebody, while taking assembly integration into consideration. The mounts are contoured to fit the interior mold line (IML) of the forebody's titanium aeroshell liner, to which TPS is bonded.

Battery Placement Selection

Battery sizing and selection was conducted by the Electronic Systems Branch at LaRC. They took into consideration actuator power requirements, battery power output, durability, and reliability. Battery placements were incorporated in both the fore and aft body of the vehicle and were arranged with the intention of powering the electronic devices within their respective quadrant of the vehicle. Batteries within the forebody of the vehicle will power the actuators during the re-entry phase. The forebody battery

mounting bracket provides a mounting platform for the batteries as well as additional ballast mass in the forebody. A total of 8 batteries and 4 mounts are housed in the forebody.

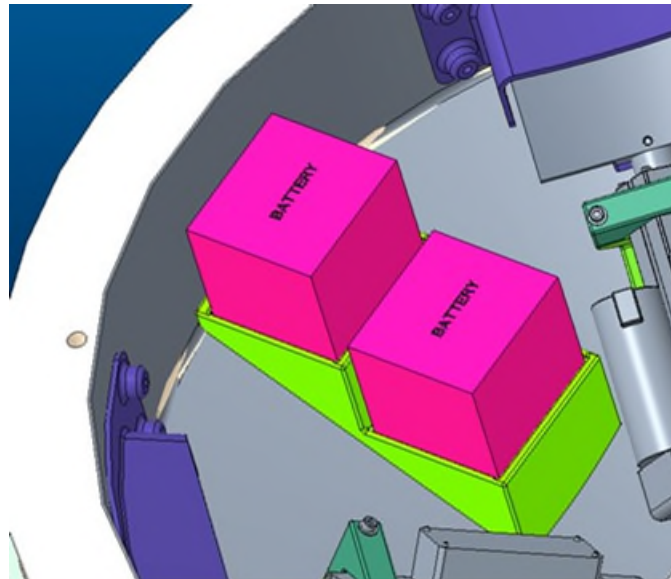


Figure 5. One of four battery installations

Mockup Fabrication and Assembly

With the preliminary design of the flaps and their actuators and batteries established, a mockup of the conceptual forebody with operational trim tabs was commissioned. The mockup was fabricated, assembled, and wired by LaRC technicians. Being a mockup, substitute materials were used including close-celled foam for the TPS on the forebody and trim tabs, fiberglass composite for the inner aeroshell liner, and printed polycarbonate for all other components. The industrial actuator mechanisms were mounted and test operated demonstrating extension and retraction.



Figure 6. Completed Mockup

Risk Reduction Results

This effort shows that the mass and volume of the flight-like actuator mechanisms and batteries meet the volumetric and mass constraints of the proposed TDM using COTS actuators with comparable physical and performance characteristics. Through this effort, a case can be made to proceed with the rest of the preliminary design for an Earth atmosphere flight demonstrator.

References

-
- [1] Edquist, Karl, et al., "Concepts for a Deployable Trim Tab on a Rigid Mars Aeroshell", NASA LARC Paper, December 2016
[2] Dutta, Soumyo, "Aerocapture Technology Demonstration Potential Risk Reduction Tasks", presented January 2022

Listening into the JUICE Deployments with the On-Board High-Accuracy Accelerometer

Ronan Le Letty*, Christian Erd*, Alessandro Atzei*, Massimiliano Pecora** and Luciano Less†

Abstract

On the 14th of April 2023, the JUICE spacecraft was successfully lifted into space by an Ariane 5 rocket from Guyana Space Centre in French Guyana. JUPITER ICY moons Explorer is an ESA science mission dedicated to the investigation of the Jupiter and its Galilean moons, and it will be the first spacecraft to orbit a moon of another planet beyond Earth.

The JUICE spacecraft includes many appendages and a High Accuracy Accelerometer (HAA), part of the 3GM instrument [1], which will investigate the gravity field of the Galilean moons. The HAA consists of three identical acceleration sensors (one per axis) and is inherited from the Bepi-Colombo ISA instrument. The HAA displays a high accuracy in the mg range at low frequency up to 3.5 Hz.

Deployment monitoring is generally achieved by using redundant microswitches. However, the microswitches were not redundant in some appendages and some microswitches failures were monitored on both Bepi-Colombo and Solar Orbiter. It was therefore decided to investigate if there was any possibility to use any other onboard sensor to get additional information relevant to the appendage's monitoring. The focus was put on the observability of the latch event (as the appendages will later have to face some orbit loads resulting from the Main Engine burns).

The paper addresses both analytically and experimentally with the flight data how the accelerometer could help confirm the correct deployment of some JUICE appendages. In some cases, the in-flight accelerometer data could be compared with the gyroscope signals.

The paper presents the flight data and shows how the accelerometer data helped confirm the deployments for the MAGBOOM [2] and the LP-PWI booms [3]. Unexpectedly, it also contributed to the Root Cause Analysis of the RIME deployment in-flight anomaly [4].

The JUICE Spacecraft

The JUICE spacecraft will provide a thorough investigation of the Jupiter system in all its complexity with emphasis on the three potentially ocean-bearing Galilean satellites, Ganymede, Europa and Callisto, and their potential habitability. The JUICE spacecraft carries the most powerful remote sensing, geophysical, and in situ payload complement ever flown to the outer Solar System (Figure 1). The payload consists of ten state-of-the-art instruments plus one experiment that uses the spacecraft telecommunication system with ground-based instruments. The payload includes :

- a deployable MAGBOOM, 10.6-meter long supporting five remote sensing units [2],
- four identical Langmuir probe booms [3],
- a deployable dipole low-frequency RIME radar antenna [4].

* ESA ESTEC, Noordwijk The Netherlands, Email: ronan.leletty@esa.int

** THALES Alenia Space Italia, Gorgonzola, Italy

† Sapienza University of Rome, Rome, Italy

Airbus Defense and Space oversaw the design, integration and test of the spacecraft. The deployment of the appendages are monitored by classical microswitches (with the exception of the RIME antenna, monitored by two cameras). All appendages were designed to be deployed as part of the Near-Earth commissioning phase.

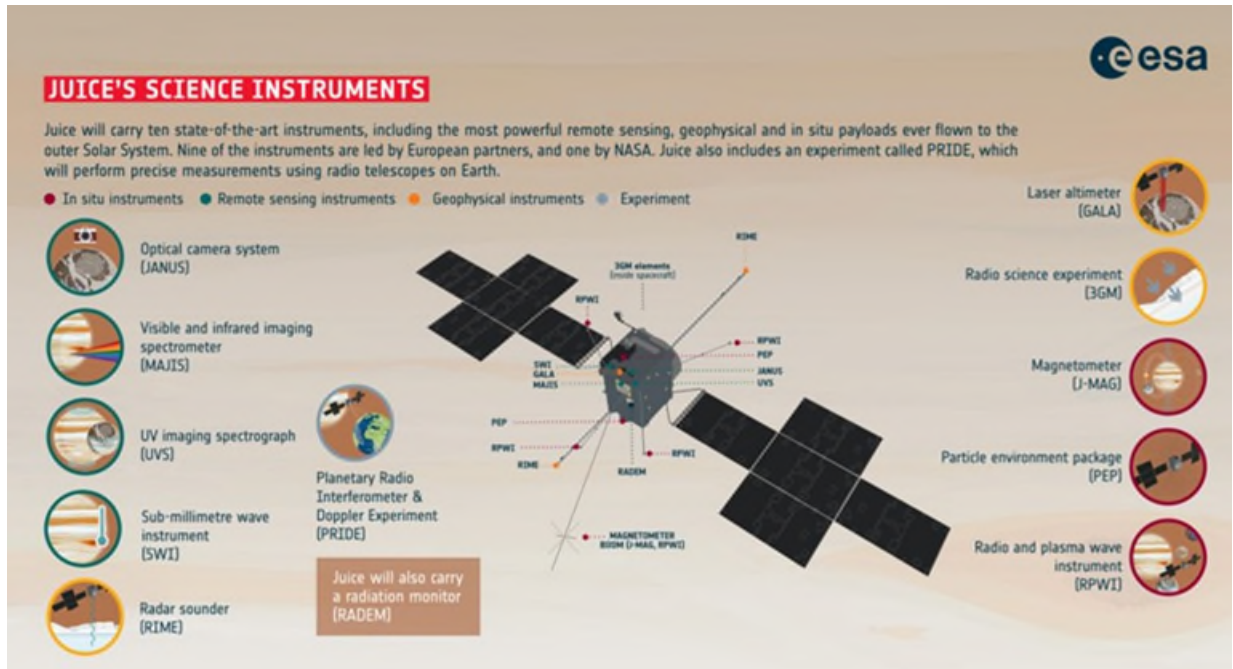


Figure 1: JUICE Spacecraft in deployed configuration

The High-Accuracy Accelerometer

The High Accuracy Accelerometer is part of the 3GM instrument, whose main science goals are the measurement of Ganymede, Callisto and Europa gravity fields, and probing the atmosphere of Jupiter by means of radio occultations. The gravity measurement can be affected by the spacecraft (S/C) sloshing and therefore an HAA has the ability to accurately measure the low frequency accelerations of the S/C along the 3 axis. The HAA is inherited from ISA (Italian Spring Accelerometer) on board the ESA Bepi-Colombo probe en-route to Mercury. It consists of three identical acceleration sensors, arranged along the 3 axes and its front-end electronic (Figure 2). The acceleration sensor is based on a suspended mass, whose motion is detected via capacitive coupling to a set of dedicated plates. The resonance frequency of the coupled system is 3.5 Hz. Therefore, the accelerometers can sense any acceleration below this frequency.

The HAA is located in the PX vault (protected from Jupiter's intense radiation field) and close to the S/C Inertial Measurement Unit, which includes three gyroscopes. The standard telemetry rate for the angular rate is 1 Hz and can be increased up to 8 Hz for troubleshooting.

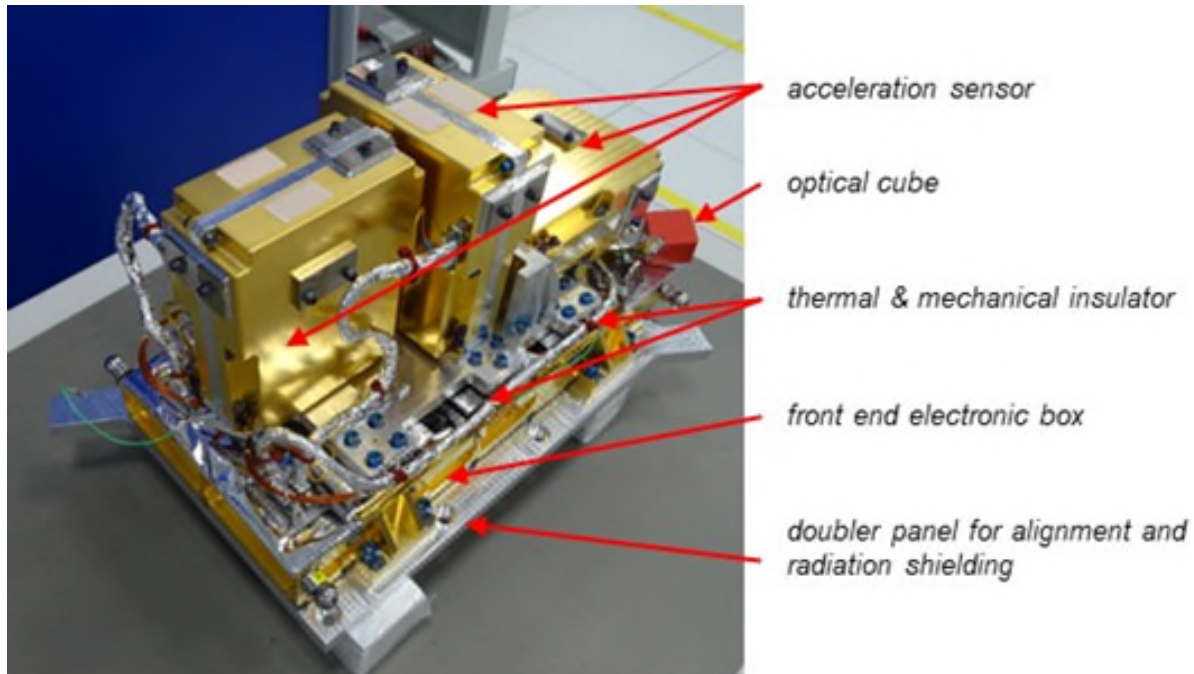


Figure 2: HAA Detector Unit (without external MLI)

The LP-PWI Booms' Deployment

The Langmuir Probe boom is a very lightweight two-segment 3-meter long deployable boom [3]. The combination of the four booms when deployed allows measuring the three-dimensional electrical field in the Jovian environment. The Langmuir Probe boom uses a single microswitch to monitor the effective latching of both the base hinge and the central hinge. The central hinge latches first (because it see a lighter inertia).

A multi-body model of this boom using MSC ADAMS was developed to evaluate the swept envelope during its deployment. The model also provides the shock at the S/C interface occurring at the end of the deployment. Since this spring-aided boom does not include any damper, the end-deployment shock is sizing the strength of the boom.

Analysis

To investigate if the HAA could detect the difference of torque behavior between a latch and a non-latched LP-PWI boom, the following assessment was performed (Figure 3):

1. Extraction on the S/C deployed configuration (full tank) of the transmissibility functions between the LP-PWI boom torques at base hinge and the three HAA sensors
2. Identification of an impulse filter corresponding to these transmissibility functions
3. Convolution of the computed transient torque functions (estimated from a multi-body model of the deployment) with the estimated impulse filters at the previous step; comparison of the estimated accelerations at HAA level with the functional performances of HAA, check the received signals with the HAA saturation threshold
4. Computation of the Fourier transform of the received signal on the three HAA channels

This study concluded that the HAA will be able to monitor the deployments; the 1st bending mode of the LP-PWI booms is estimated at 1.78 Hz and nicely fits in the HAA bandwidth. It was therefore decided to switch on this accelerometer quickly after launch and to monitor the appendages deployments with the accelerometer (in addition to the usual microswitches). In case the boom fail to latch, the 1st bending mode would not exist; the failure case shows the boom bouncing back several times.

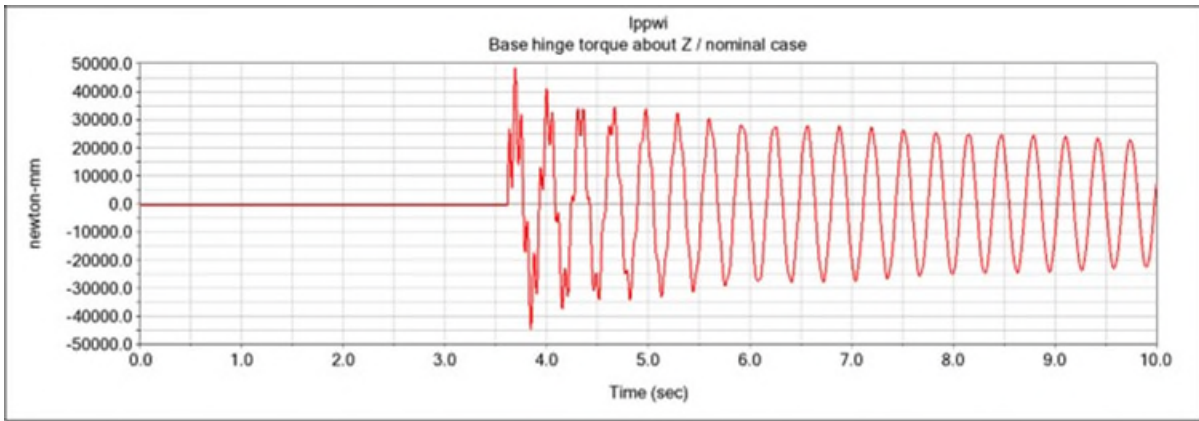


Figure 3a: LP-PWI analysis: transient torque during the deployment computed by MSC ADAMS multi-body simulation – nominal deployment

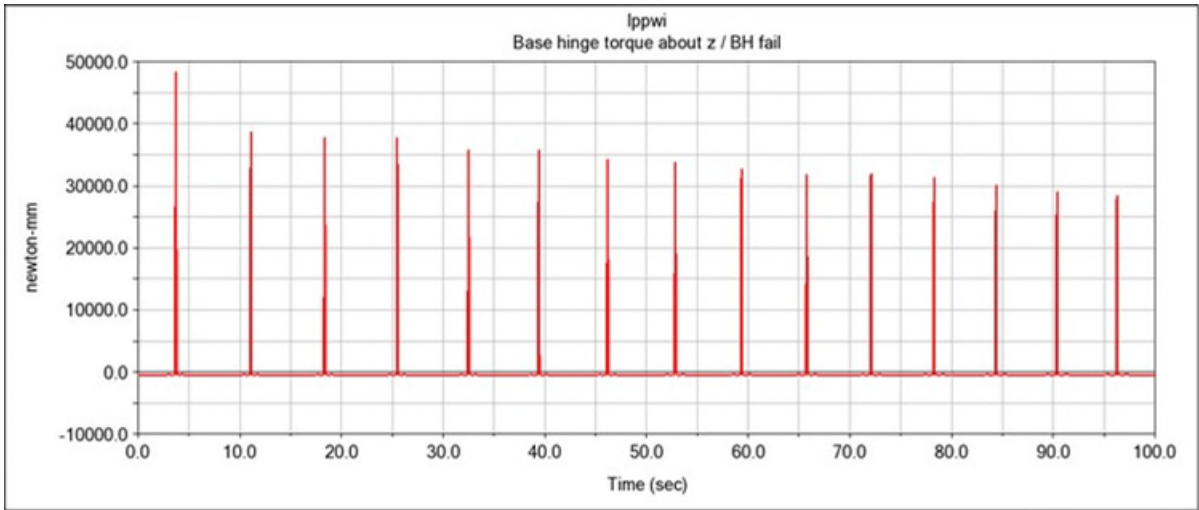


Figure 3b: LP-PWI analysis: transient torque for a failed latch at Base Hinge location

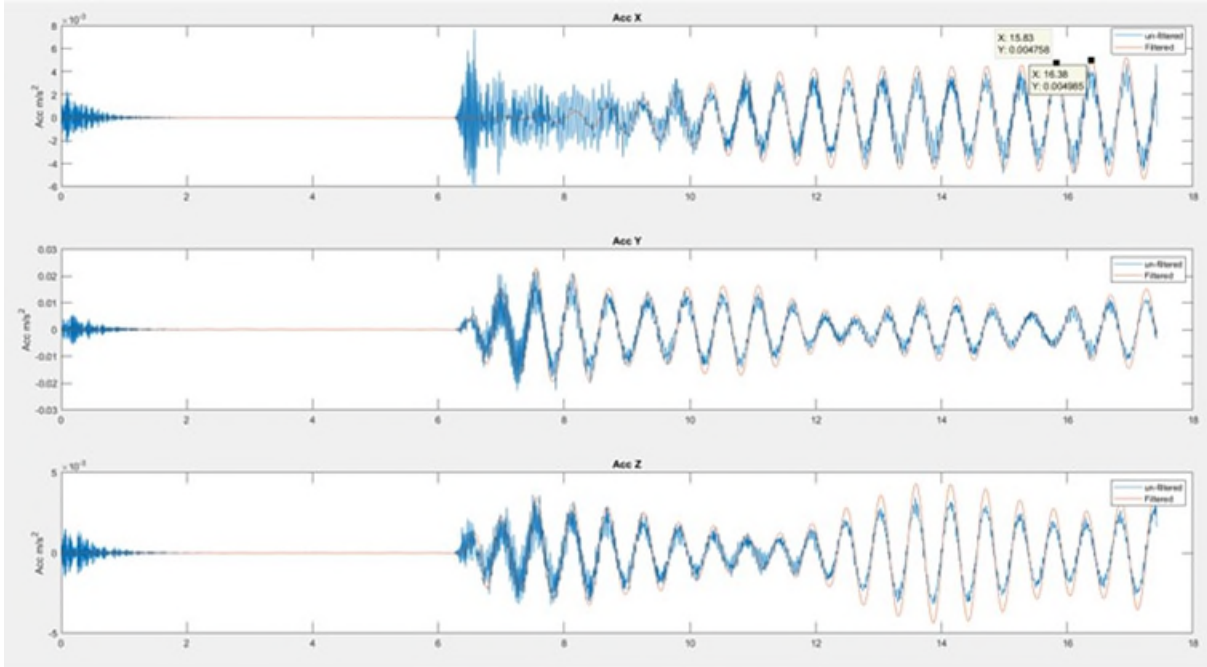


Figure 3c: LP-PWI analysis: computed time series at HAA location for a nominal deployment

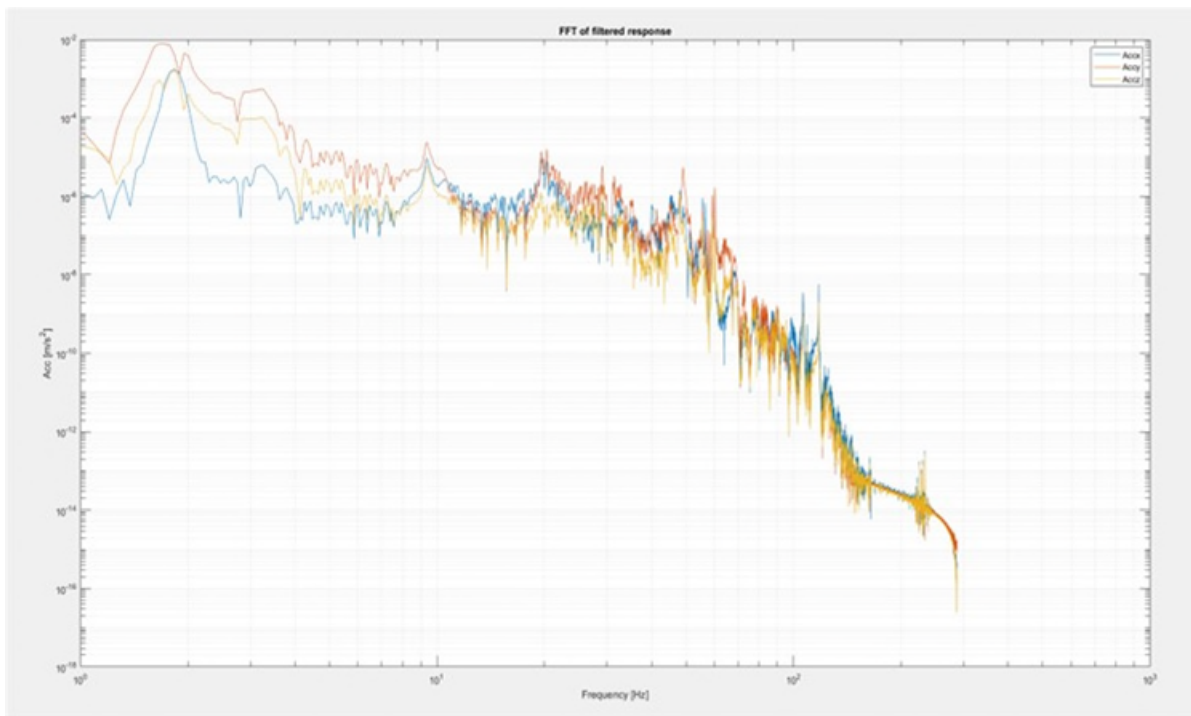


Figure 3d: LP-PWI analysis: Fourier transform of the HAA computed signals for the nominal behavior

On ground verification

Due to the fast nature of the LP-PWI boom's deployment, several gravity off-load approaches bring a significant drag effect on-ground (like helium balloons or a movable trolley) and could not be used. The supplier of the LP-PWI boom (Astronika (Poland)) developed a deployment table, which off-loads the boom via two ball transfer units (Figure 4). The main engineering resulting issue is that at spacecraft level this table needed to be brought up to 4.3 meters and properly aligned with respect to the gravity vector error

with an accuracy better than 0.1 deg in both axis thanks to a specially developed MGSE. The on-ground deployment tests at boom and the S/C level gave similar results, allowing verification of MLI clearances.

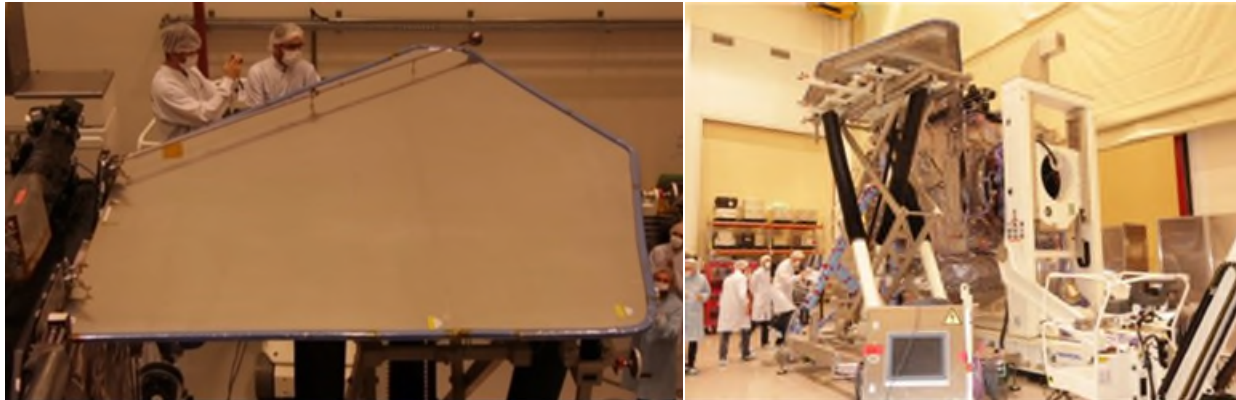


Figure 4: a) LP-PWI boom on the deployment table, b) deployment table close to the S/C

LP-PWI Deployment flight data

The four LP-PWI booms were deployed from May 22nd to 26th (one boom per day). The telemetries have shown a repeatable deployment behavior for all booms, despite a different thermal environment. Despite all microswitches working nominally, the HAA telemetries were received and compared to the predictions.

It can be seen that the estimated peak acceleration along the X axis was $6e-3 \text{ m/s}^2$, while the flight data give a peak value of $5e-3 \text{ m/s}^2$ (Figure 5). The Fourier transform of the flight HAA data gives a maximum value at 1.9 Hz, also close to the prediction. The spectrum is dominated by the low frequency Solar Array mode (especially the in-plane mode at 0.89 Hz), the 1st, 2nd bending modes of the MAGBOOM at 0.45 Hz and 3rd MAGBOOM mode at 2.6 Hz.

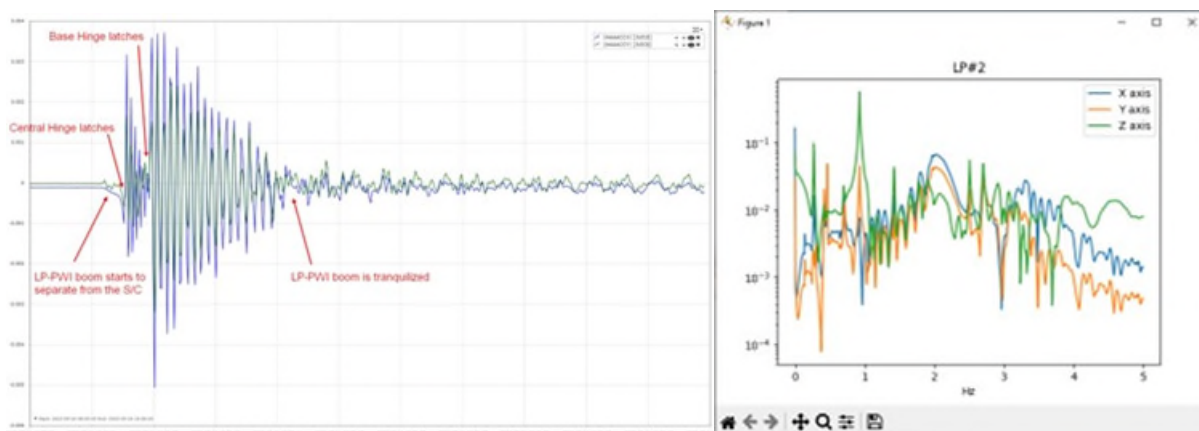


Figure 5: Example of in-flight data with interpretation: Langmuir Probe boom deployment read by HAA in m/s^2 : a) time data, b) Fourier transform

The MAGBOOM Deployment

Contrary to the Langmuir Probe booms, the JUICE (three segments, 10.6-meter long deployable) MAGBOOM is huge and features a synchronized deployment and redundant microswitches on its root hinge to monitor its deployment [2]. Its deployment was also modelled by the supplier SENER (Spain) with an MSC ADAMS model. The challenge was the size of the swept envelope. As such, it was not the focus of the HAA monitoring during the commissioning (it was expected that the HAA will be saturated), but the HAA telemetries were made anyway available.

On-ground verification

As this boom has a damper (speed regulator function), the helium balloons used as gravity off-load system have an acceptable level of drag (Figure 6) at low speed. This will be later confirmed by comparing the deployment time on ground with the deployment time in flight.



Figure 6 : Deployment of the MAGBOOM using helium balloons

Flight data

The MAGBOOM was successfully deployed on April 21st, 2023, For this deployment, the exchange of moment of inertia between the appendage and the S/C body is significant and the HAA data are very perceptive in revealing the S/C body rotation. Surprisingly, there was no obvious sign of the HAA saturation, especially during the hold down release mechanism (HDRM) firing.

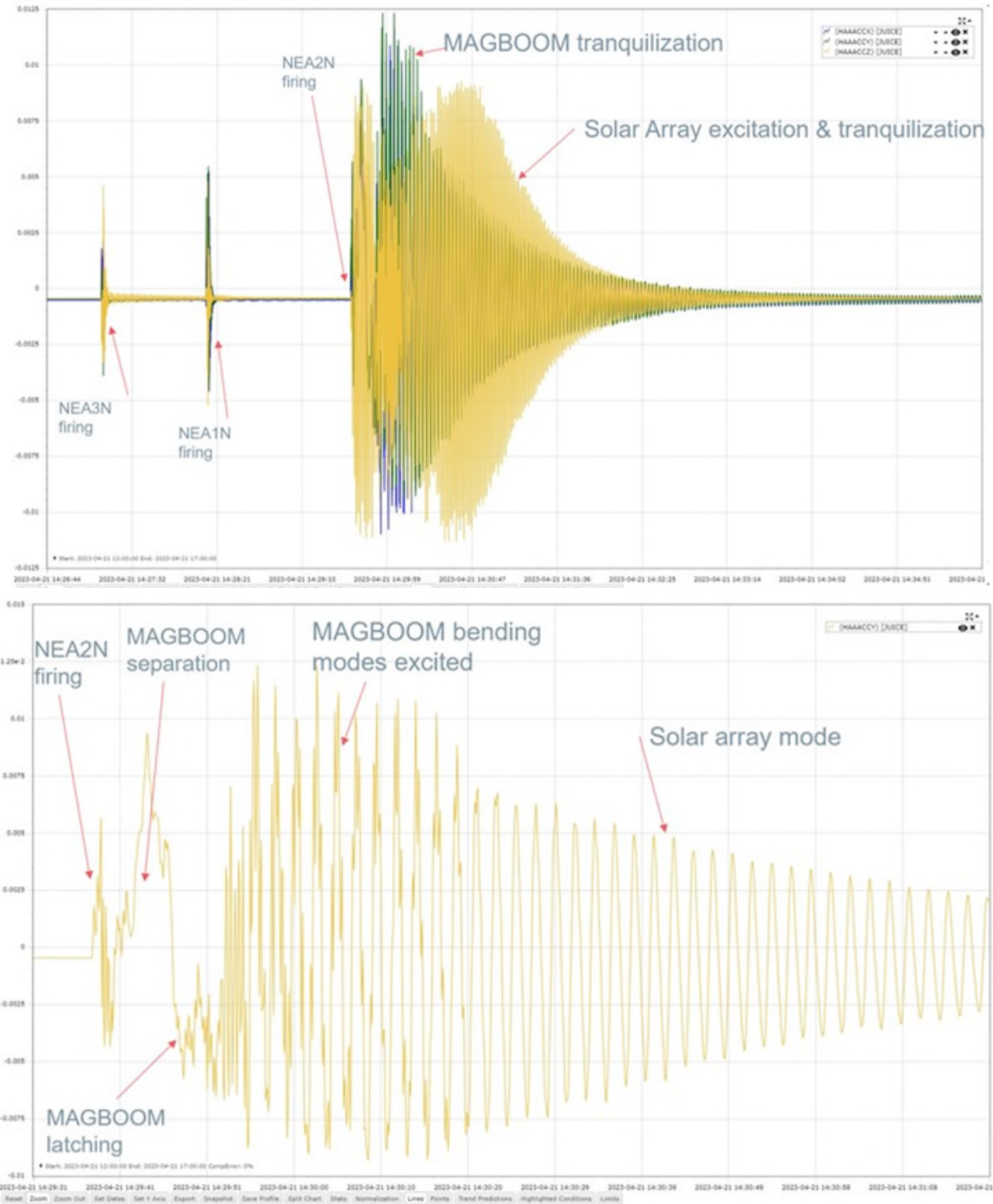


Figure 7: Example of in-flight data with interpretation: MAGBOOM deployment read by HAA (acceleration in m/s^2 as a function of time)

RIME Antenna Flight Data

It was initially not expected to use the HAA to monitor the deployment of the RIME dipole antenna, consisting of two identical monopoles (PX and MX) and developed by STI (Germany). An analysis was carried out before the launch to assess whether the HAA could contribute to the monitoring in a similar way as for the LP-PWI booms. As reported in [4], the deployment of this antenna did show an in-flight anomaly;

for this reason, all troubleshooting attempts were monitored with high frequency gyro and HAA data. There was no representative on-ground experimental data available, because such lightweight antenna is difficult to test on the ground; any gravity off-load system would provide a significant drag effect and drastically influence the dynamic behavior.

Analysis

An assessment was done with the MSC ADAMS multi-body model of the RIME antenna with a methodology similar to the one used for LP-PWI (Figure 8). It was concluded that it will be difficult to monitor the latching of the RIME antenna hinges by the HAA as the non-linear behavior of the RIME antenna was found difficult to model.

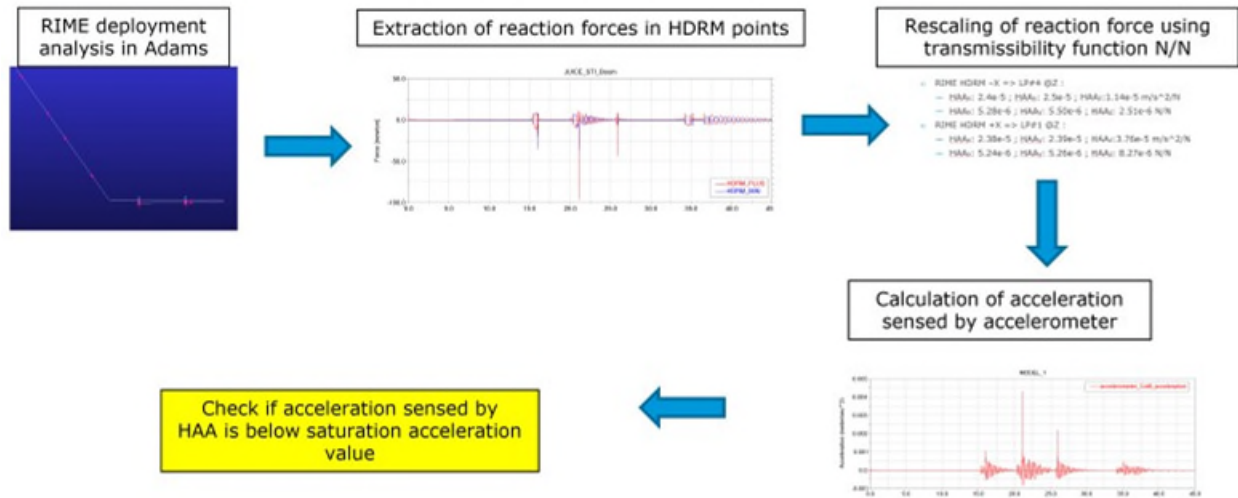


Figure 8 : Procedure used to estimate the HAA reading level during the RIME antenna deployment

Flight data

Due to the encountered in-flight anomaly [4] and for trouble-shooting purposes, all sensors were switched on with the highest possible sampling frequency during the successful release on May 12th, 2023. The gyroscope signals were monitoring at 8 Hz and gave the opportunity to compare them with the HAA signals (Figure 9).

The comparison between the accelerometer and the gyro data on the same event (the 2nd RIME monopole on the MX side) (Figure 9) shows:

- the initial HDRM shock is difficult to isolate, and overall, the HAA data are difficult to interpret (except the usual Solar Array modes being excited),
- the moment of inertia exchange between the antenna and the spacecraft is clearly visible on the Y-axis and Z-axis gyroscopes.

For this deployment, two monitoring cameras were available and key to understanding the in-flight deployment. It is interesting to note that the Z-axis gyroscope reveals a significant rotation of the spacecraft for the MX monopole (but not the PX monopole) and this can be attributed to this MX deployment that did not happen in the plane (Xs/c – Zs/c), as concluded by the analysis of the monitoring cameras [4].

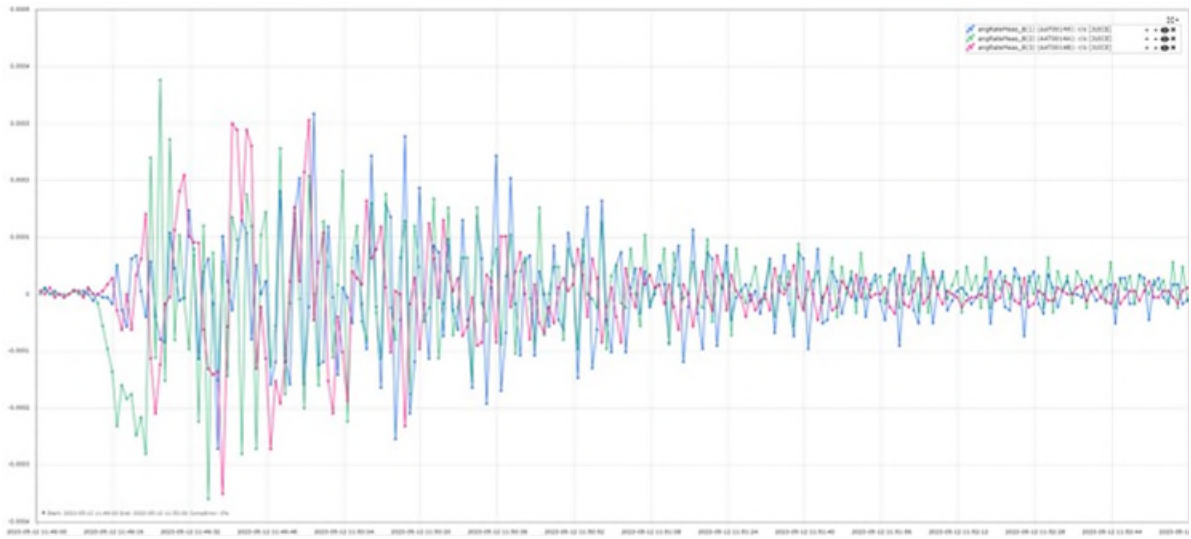


Figure 9a: RIME deployment a) PX monopole gyro data (in rad/s as a function of time)

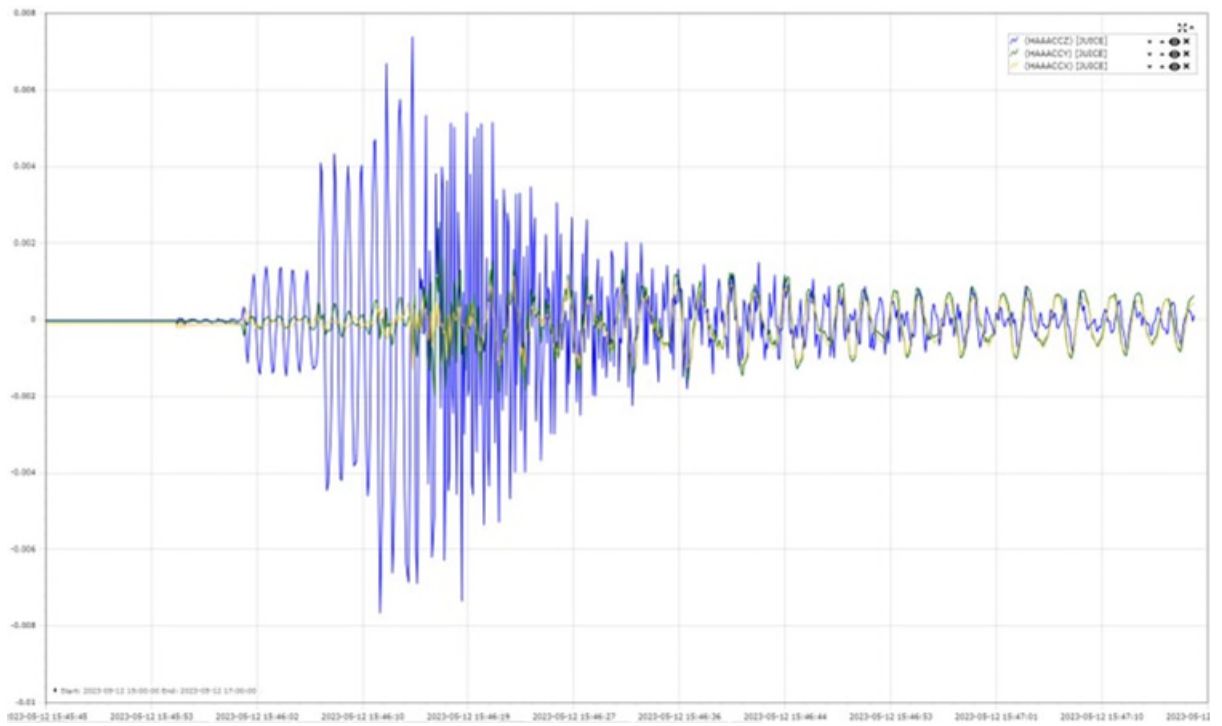


Figure 9b: MX monopole HAA data (in m/s² as a function of time)



Figure 9c: MX monopole gyro data (in rad/s as a function of time)

Conclusion and Recommendations

The in-flight accelerometer data show an excellent time resolution and a good agreement with the predictions for the lightweight LP-PWI booms' deployments. The successful latching can be confirmed by looking at the accelerometer data. It is noted as a lesson learned that the damping coming from the S/C structure and harness appears to be frequency dependant:

- much less than considered in the analysis at low frequency,
- higher than considered in high frequency (i.e., HDRM shocks).

In general, the HAA data have been found very useful in characterizing the low-frequency appendages modes during the commissioning of the AOCS subsystem. This is promising in view of the capability of HAA to monitor the tanks' sloshing during the JUICE science phase.

However, this good achievement on the LP-PWI booms' deployment (thanks to the 1st boom's mode in the HAA bandwidth) cannot be generalized to other appendages' deployments for several reasons:

- End-deployment shocks have only a well-defined signature for a fast deployment (i.e., excluding motorized and dampers),
- Appendage modes are largely mixed with other appendage modes, starting with the ones from the Solar Array wings. Identifying the modes may be tricky especially in a single event case of a deployment.

For these reasons, it remains recommended to include a redundant microswitch monitoring the latching event at the end of the deployment.

Acknowledgements

The authors would like to thank:

- the ESA ESTEC mechanisms team for their multi-body analysis,
- the Airbus structural analysis team for their computation of the transmissibility functions on the deployed S/C configuration,
- the Airbus AIT team for their efforts and dedication during the AIT campaign in Toulouse,
- the ESA ESOC operation team which managed to commission the HAA on day-2 after launch,
- the ESA ESAC team for the swift processing of the HAA in-flight data,
- the TAS-I HAA team for support during activities involving the HAA.

References

1. [1] P. Cappucio et al., "Callisto and Europa Gravity Measurements from JUICE 3GM Experiment Simulation", *The Planetary Science Journal*, 3:199, Aug. 2022
2. [2] A. Arce, D. Rodriguez, "Juice Magnetometer Boom Subsystem", ESMATS 2019 conference, Munich, 2019
3. [3] M. Borys et al., "LP-PWI Deployable Boom for the JUICE Mission – Innovative Features and Breadboard Model Development", ESMATS 2017 conference, Hatfield, 2017
4. [4] R. Le Letty et al., "The successful recovery of the JUICE RIME deployment anomaly", ESMATS 2023 conference, Warsaw, 2023.

Bricard Mechanism-Based Engulfing Gripper for Space Debris Removal

Abhijith Prakash*, Sankalp Vishnoi*, Sandeep R* and Biju Prasad B*

Abstract

Orbital debris consists of defunct human-made objects in space which create serious operational risks for critical space infrastructure. Presence of orbital debris leads to increased costs in spacecraft operations due to additional efforts in the form of satellite orbit raising or addition of shielding, or other methods, which are required to protect important space assets from eminent debris collisions. Some of these debris have been created as a result of astronauts dropping their tools while carrying out maintenance operations on space stations. Depending on the force/velocity conditions on the body just before being dropped, they can either get transferred to a different orbit or reenter into Earth's atmosphere. Loss of these items can be detrimental as it not only creates unwanted debris but also delays critical maintenance operations until the arrival of the next resupply mission. This paper aims to explore the feasibility of using an engulfing mechanism as the end-effector of a robotic arm attached to a space station for retrieving back such lost items for future space station endeavors. Focus is given to the design of the mechanism for engulfing end-effector, using a Bricard mechanism as a base unit. The gripper is designed to be actuated using a single rotary actuator to fully engulf the debris. The paper also covers the realization aspects of the engulfing gripper and using the same for a debris capture experiment/demonstration on the ground.

Introduction

Astronauts are required to routinely carry out extravehicular activities for maintenance of space stations. While carrying out such exercises, untethered tools and equipment can drift away leading to generation of unintentional space debris. This also leads to the loss of costly and critical tools which need to be replenished in subsequent resupply missions. As recently as November 2023, astronauts working on the ISS lost a tool bag worth \$100,000 which has now become space debris as shown in Figure 1.



Figure 1. Tool bag dropped by astronauts aboard ISS during extra-vehicular activity (Courtesy: NASA)

India is planning to deploy its indigenous space station officially called the Bharatiya Antariksha Station (BAS) by the year 2028. The space station will help to enhance India's presence in space and serve as a platform for performing scientific experiments in microgravity. In order to carry out the assembly and

* Vikram Sarabhai Space Centre, Thiruvananthapuram, India

maintenance operations of the station, a robotic arm is being developed. As a responsible space agency, the Indian Space Research Organization (ISRO) has initiated programs to avoid the creation of unintentional debris as well as mitigate existing debris of the small satellite class. The robotic arm along with a suitable gripper will be used to capture objects that have been accidentally dropped from the space station, thus preventing the unintentional creation of space debris.

Prior to implementing the system on BAS, the technology for free flying object capture will be demonstrated using the upper stage (PS4) of PSLV rocket. PS4 serves as a stabilized orbital platform (OP) with onboard power generation, to conduct short duration experiments (typically up to 6 months). The robotic arm along with the end-effector will be launched as an experiment on the OP. The technology associated with free-flying object capture will be demonstrated in two phases:

- Capture of a tethered object (of size less than 10 cm) using the specialized end-effector. The robotic arm with eye in hand configuration will autonomously track and capture the debris object.
- Capture of a freely floating debris object (of size less than 10 cm) using an engulfing end-effector as depicted in Figure 2. The object will be tracked and rendezvous operation will be carried out by OP. Subsequently when the object is in reach of the robotic arm, it will be captured.



Figure 2. Robotic arm with engulfing end-effector used for capturing freely floating debris object

As of 2023, there are approximately 35,000 trackable debris objects [2]. The trackability of such debris objects depends on size. Usually objects less than 10-cm range are nearly impossible to detect from ground-based tracking systems. Such small sized debris causes significant damage to operational satellites, when approaching at very high relative velocities. Current situational awareness systems cannot track the estimated 300,000 to 500,000 pieces of small sized debris, 1 to 10 cm in diameter. According to a NASA study on Orbital debris remediation [2] the most effective remediation methods to reduce risks to space assets are approaches for removing small debris and nudging large debris to avoid collisions. Demonstration of the debris capture experiment on the PS4 OP platform will provide confidence in utilizing the mechanism for capturing space debris smaller than 10 cm.

Since a majority of the debris 10 cm or smaller are completely non-cooperative, it would be appropriate to make use of an end-effector that does not require high precision to capture the object. An engulfing type end-effector is well suited for the debris capture operation. The engulfing envelope of the gripper is decided by the maximum size of the debris to be captured. Coupled with a robotic arm the engulfing gripper will be used for capturing multiple debris.

Engulfing Gripper Design

In order to construct a gripper which can engulf a debris object, it is necessary to construct a net of a solid figure. The net must be readily folded into a solid figure which can engulf the debris object. Platonic

polyhedra which include tetrahedron, hexahedron, octahedron, dodecahedron and icosahedron can be opened and folded back into the solid figure by rotating the faces (individual net segments) about axes which lie along the edges. It is concluded that from a volume efficiency and edge length perspective, the dodecahedron is the best polyhedron to choose for constructing an engulfing mechanism. Similar mechanisms have been proposed by Zhi Ern Teoh et. al. [3] for underwater capture of delicate marine organisms.

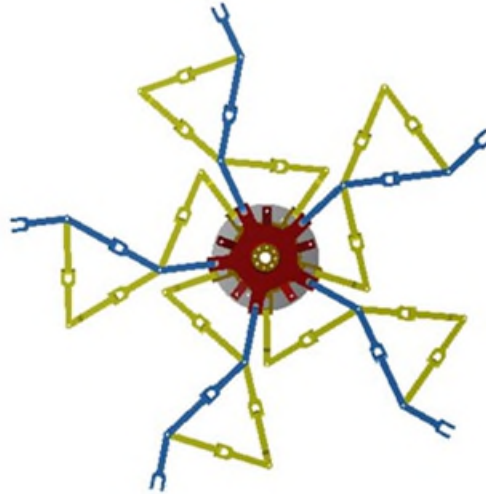


Figure 3. Skeleton structure of the engulfing gripper

Figure 3 shows the designed engulfing gripper based on the volume efficiency studies as discussed below. The minimum edge length required for engulfing a 1U class satellite (with 2x margin) with different platonic polyhedra is shown in Figure 4. It can be seen that for a given engulfing volume, a dodecahedron has the shortest edge length required. Figure 5 shows the volume engulfing efficiency of different platonic polyhedra. As the number of faces increases, volume efficiency of the polyhedra also increases. Considering both volume efficiency and the edge length as prime factors for selection of the mechanism, a dodecahedron stands out as the best polyhedra owing to the highest volume efficiency rise with the smallest edge length.

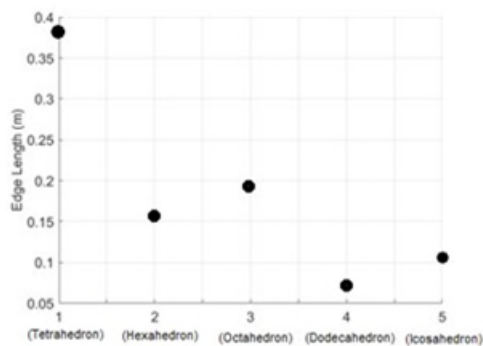


Figure 4. Edge Length of platonic polyhedra required for enclosing a 1U class debris effectively

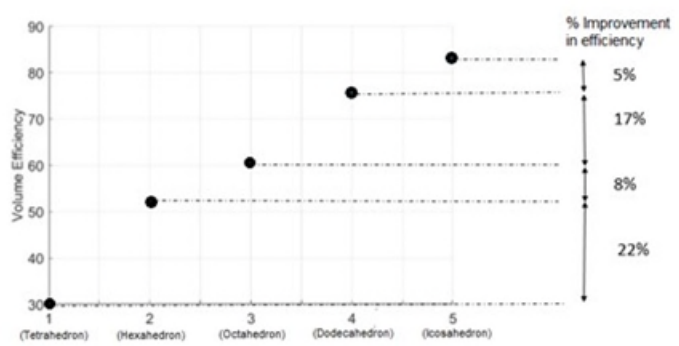


Figure 5. Volume Efficiency of platonic polyhedra

The engulfing mechanism consists of 5 arms (also referred to as 'leaf') that are actuated using a single actuator to open and close the engulfing envelope. Motion during actuation is achieved through the Bricard mechanism that connects the folding linkages to the actuator through a hinge as shown in Figure

6. A bricard mechanism acts as the fundamental unit for achieving the folding motion in the engulfing gripper. Figure 6b shows the arrangement of the Bricard mechanism as-implemented in the gripper.

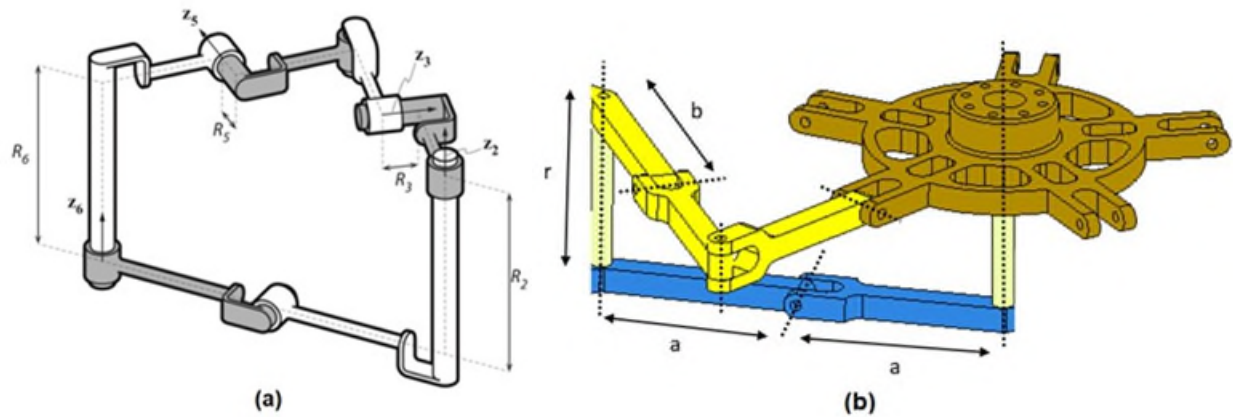


Figure 6. (a) Plane symmetric Bricard Mechanism, (b) Arrangement of Bricard Mechanism for engulfing gripper

The link lengths of the Bricard mechanism [3] as well as the link offsets determine the overall size of the engulfing gripper. The design parameters are selected as follows: 1) Link lengths selection is based on the capability of gripper to engulf and remedy debris of size up to 10 cm or a 1U class satellite with sufficient margin. 2) Link offsets are selected based on the overall external size of the engulfing gripper and associated mechanical advantage for the mechanism.

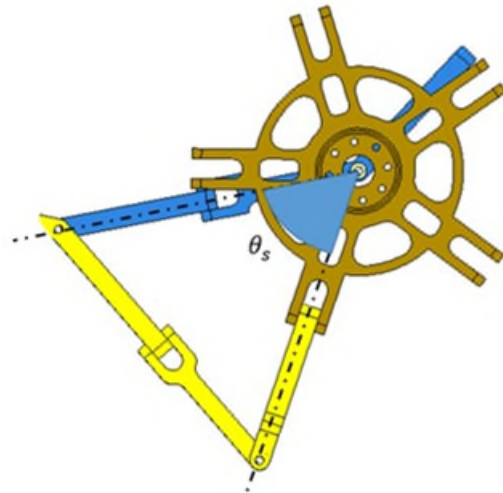


Figure 7. Kinematic arrangement of Bricard mechanism

The parameters associated with the design of the gripper are based on the selection of appropriate design parameters for the Bricard mechanism. The typical design parameters as shown in Figure 6 and Figure 7 are as follows:

- 1) a : Link length of the folding layer.
- 2) b : Link length of the driving layer.
- 3) θ_s : Starting Angle for the mechanism.
- 4) r : Joint axis offset

Calculation of the link lengths required is based on the internal volume of the engulfing gripper. The volume of a dodecahedron is given by:

$$V = \frac{(15+7 \cdot 5^{0.5})}{4} e^3 \quad (1)$$

Where e is the edge length of the pentagon forming the dodecahedron. The edge length e is determined based on the volume of the object being captured. To capture 1U class satellite debris with 2X volumetric margin, the edge length of the pentagon is calculated as:

$$e > 80\text{mm}$$

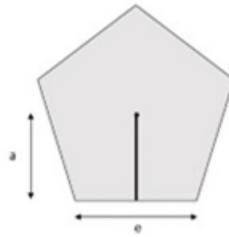


Figure 8. Link length and edge length relation

For a regular pentagon with $e > 80\text{ mm}$, link length (a) is found to be $a = 57\text{ mm}$ (Figure 8). For a plane symmetric Bricard mechanism the following relation between a , b and θ_s holds:

$$\frac{b}{a} = \frac{1}{2\cos(\theta_s)} \quad (2)$$

θ_s is chosen appropriately such that the realization of link lengths a and b is practically feasible. Therefore, to avoid non-terminating decimal places in the link lengths, the starting angle is chosen as $\theta_s = 60^\circ$. Therefore, $b = a = 57\text{ mm}$. The choice of link offset value r is based on the mechanical advantage to be achieved for the engulfing gripper. The mechanical advantage is also essential to size the rotary actuator and improve the overall performance of the gripper. A mechanical advantage study is therefore performed in ADAMS® with varying r . Figure 9 shows the variation of mechanical advantage at various link offsets in the range of $25\text{ mm} < r < 90\text{ mm}$, over the engulfing motion.

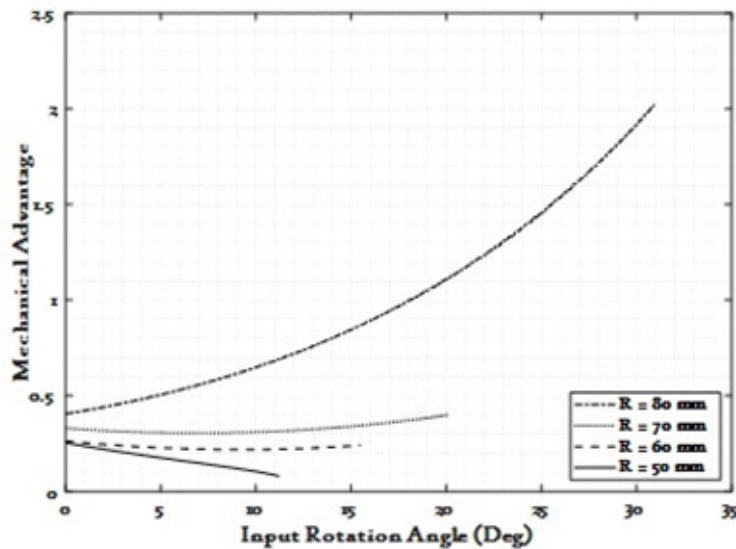


Figure 9. Mechanical Advantage Study

Table 1 shows the selected design parameters for the engulfing gripper.

Table 1. Design Parameters

Parameters	Value
a	57 mm
b	57 mm
r	80 mm
θ_s	60°

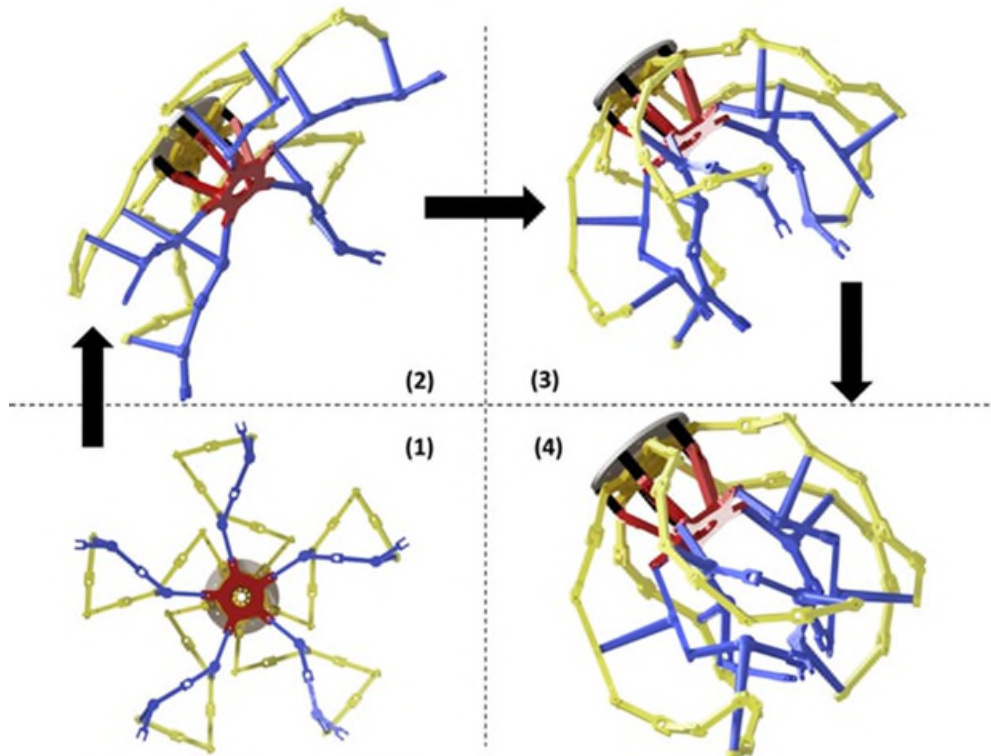


Figure 10. Folding sequence for the engulfing gripper

Hardware Implementation – Engulfing Gripper

The ground model of the engulfing gripper was realized through additive manufacturing using Acrylonitrile Butadiene Styrene (ABS). In total, there are 50 revolute joints connecting 42 links, actuated by a single motor in the engulfing gripper. Such a large number of revolute joints pose practical challenges such as controlling the joint tolerances to avoid bifurcation points in the mechanism. Dowel pins were used to assemble all the links for the joints. Tolerance control during the fabrication of the gripper was achieved using a high-resolution 3D printer. A dynamic simulation of the as-designed mechanism was carried out in ADAMS® to determine the actuation torque for the motor. The simulation results are validated with the experimentally obtained data in the realized hardware and are shown in Figure 11.

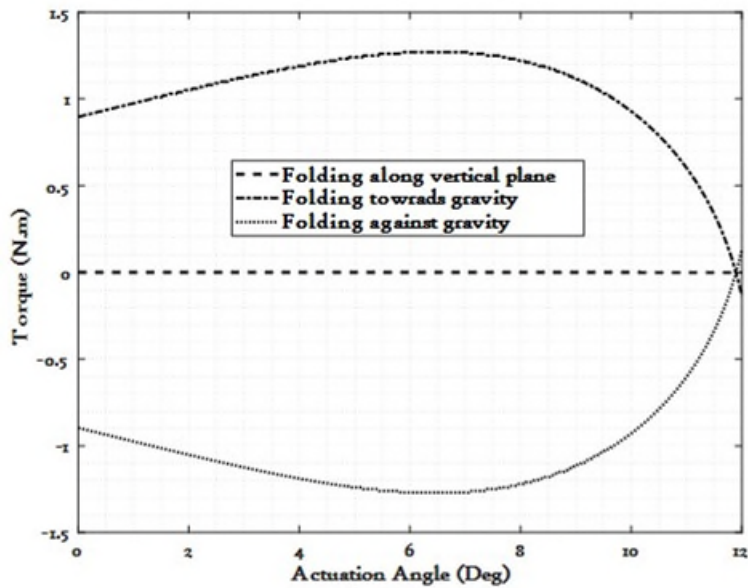


Figure 11. Actuator torque required for moving the actuated gripper

Debris Capture Experiment

In order to make sure that the engulfing gripper fully captures the debris, and to avoid escape of small sized debris from the gaps between the links of the fully actuated gripper, a net structure is used. The net structure is mounted on the inner layer of the engulfing mechanism as shown in the Figure 12.

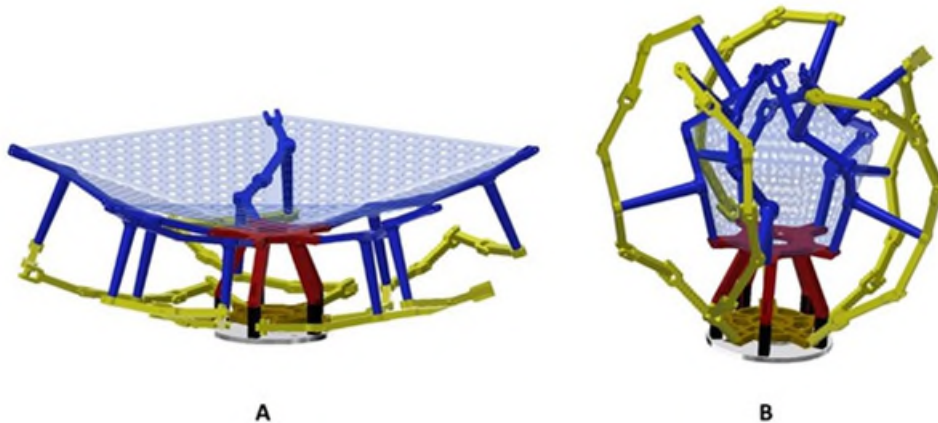


Figure 12. Engulfing gripper with net (A) fully open (B) fully closed

The engulfing gripper was tested and demonstrated on ground using an in-house developed robotic arm. Suitable mechanical interfaces on the engulfing gripper were provided in order to test the mechanism. The robotic arm has 5DoF with a reach of 880mm. The target object in the test setup was identified through image processing using a monocular camera attached to the base of the engulfing gripper. Figure 13 shows the robotic arm developed for the experiment.

The base joints of the robotic arm were configured using three identical smart actuators. These actuators included BLDC flat motors (MAXON® make) along with a harmonic gear drive for motion reduction. Both output and input side encoders were integrated to the actuators to negate the effects of joint backlash and

flexibility. The joint actuators were daisy-chained using the CAN-Bus communication protocol. The internal construction of the joint is shown in Figure 14.



Figure 13. Robotic arm with engulfing end-effector (A) Open condition (B) Closed condition

The three wrist joint actuators enabled the engulfing gripper to achieve any orientation in Cartesian space. Integrated actuators (DYNAMIXEL® make) were used to implement the wrist joints and were daisy-chained using RS-485 communication link.

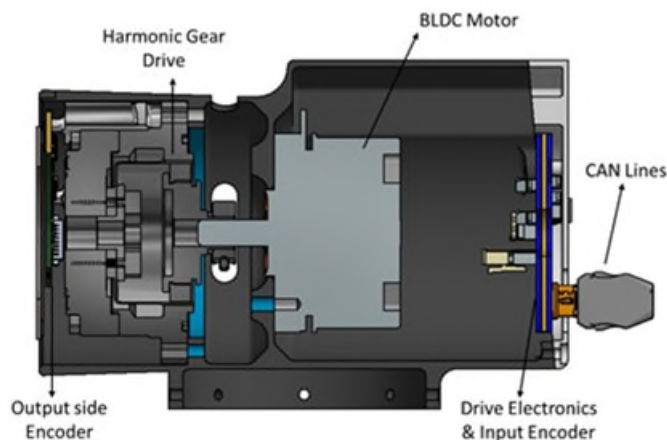


Figure 14. Internal Construction of Base Joint Actuator

Fiducial markers were attached to the target object debris. An RGB camera integrated to the base of the engulfing gripper was then used to track the marker using image processing. A typical Fiducial marker is shown in Figure 15. The image processing for visual servoing as well as control of the robotic arm was implemented on a Nvidia Jetson AGX Orin board. A typical workflow associated with the object capture is shown in Figure 16.



Figure 15. Fiducial marker attached to the object

After successful completion of ground testing, the end-effector will be deployed and tested in space on the PS4 Orbital Platform (OP) using a 2.4m long 5DoF robotic arm. There are several environmental

aspects that need to be considered while carrying out the debris capture experiment in-orbit. Since the mechanism is highly sensitive to tolerances, aspects including joint galling and thermal expansion/contraction of the joints have to be critically studied and evaluated on ground. Extensive environmental testing such as harmonic response, sine vibration, shock response, thermo-vacuum and humidity tests are planned to be carried out prior to deployment of the system in space.

The typical sequence of events executed during the debris capture experiment is given below:

- 1) **Robotic Arm Initialization and Health Check:** All the joints of the robotic arm are initialized on the command from the master controller. Various parameters from the joint motors, encoders and camera are analyzed in order to ensure the appropriate health of the robotic arm system. Once cleared, the robotic arm is then taken to a parking position (also referred to as scan state).
- 2) **Free Floating debris detection:** In the scan state, camera mounted at the end of the robotic arm tries to locate the free-floating debris using fiducial markers attached to it. This is achieved using the tag detection algorithm which returns the location and orientation of the debris in camera frame, which is then transformed back to the base frame of the robotic arm.
- 3) **Intercepting the located debris:** Once the debris is detected, the robotic arm is taken close to the debris through a suitable trajectory which minimizes interception time. The trajectory is updated continuously based on the free-floating debris location, to intercept it. Once the robotic arm reaches in the vicinity of the debris object, resolved rate motion control based tracking is used to precisely track and follow the moving object.
- 4) **Capturing the free-floating debris:** The engulfing gripper is then actuated to contain the free-floating debris inside it.
- 5) **Storing the captured debris:** The captured debris is then taken to a pre-determined location on-board. The engulfing gripper is opened and a magnetic latch is then used to dock the debris to the station and store it in a pre-planned location.

Figure 17 shows the capture phase of the experiment using engulfing gripper.

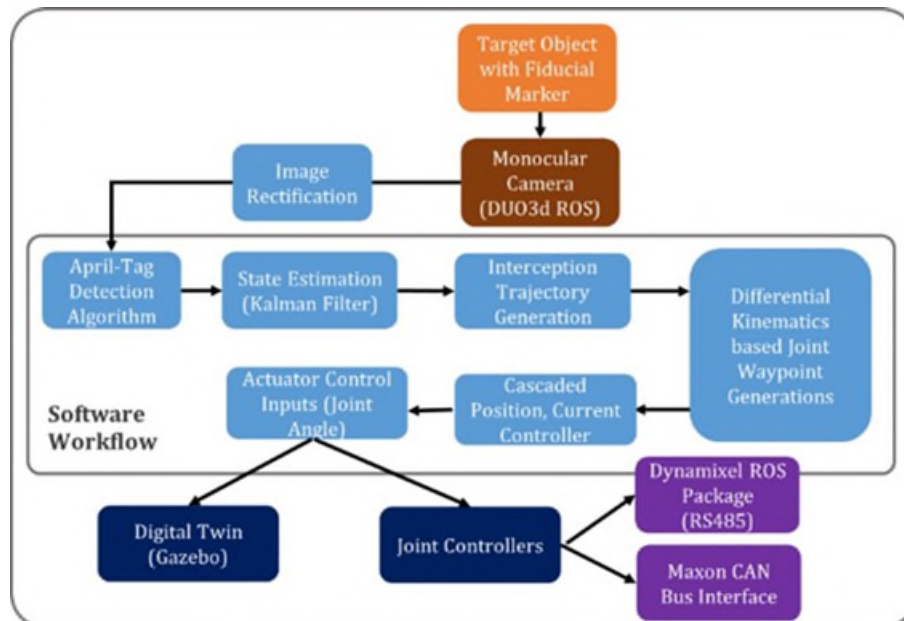


Figure 16. Software workflow developed for debris capture experiment

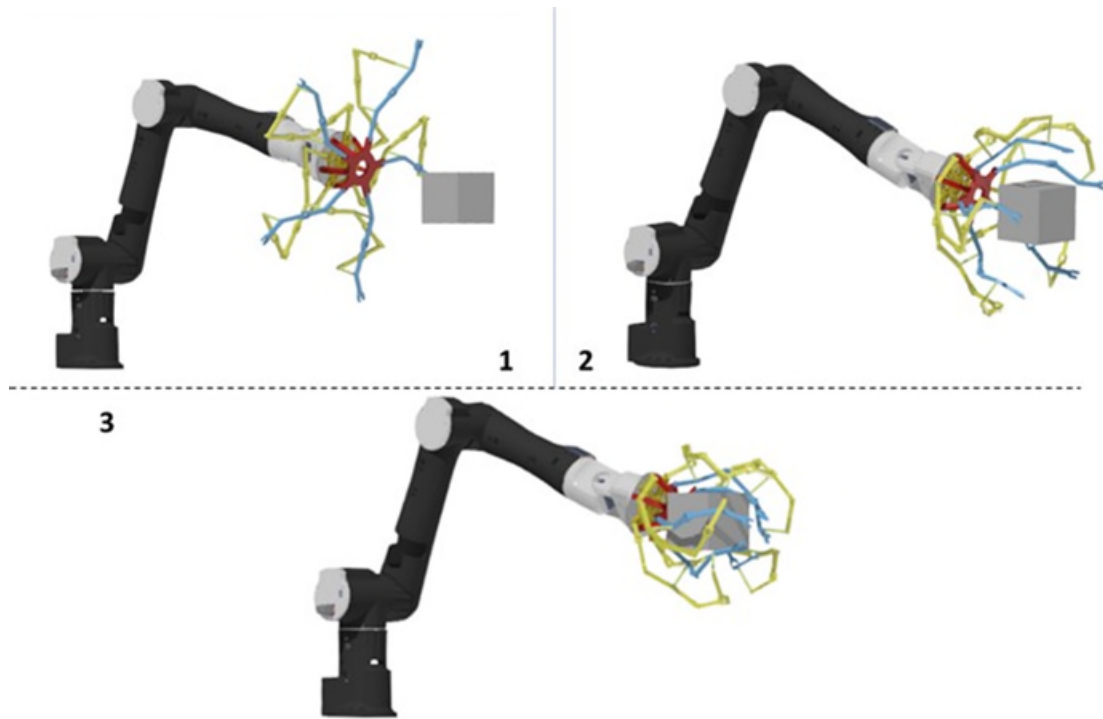


Figure 17. Capture sequence of the simulated debris using the engulfing gripper

Conclusion

With the efforts of the Indian Space Research Organization to establish its own space station, the requirement of a robotic arm capable of carrying out extra-vehicular activities is essential. The robotic arm with a suitable end-effector can be utilized for ensuring the sustainable operation of Bharatiya Antariksha Station (BAS) by preventing any unintentional creation of space debris. The ground testing of the engulfing end-effector shows good correlation with the simulation results. Ground tests were conducted with an object having a fiducial marker on it. It was tracked and captured using the engulfing gripper as the robotic arm end-effector. It is planned to conduct experiments to capture a free flying object on-board the PS4 Orbital Platform in a PSLV mission which will help validate the suitability of these systems for usage in the space environment. The engulfing gripper along with a net can be utilized for capturing smaller debris of size less than 1U size (10 cm cube) which cannot be tracked reliably from ground.

References

- 1) <https://www.nasa.gov/directorates/stmd/stmd-prizes-challenges-crowdsourcing-program/center-of-excellence-for-collaborative-innovation-coeci/coeci-news/nasa-seeks-solutions-to-detect-track-clean-up-small-space-debris/>
- 2) Thomas J. Colvin, John K. and Grace W. "Cost and Benefit Analysis of Orbital Debris Remediation", NASA Office of Technology, Policy and Strategy, March, 2023.
- 3) Zhi Ern Teoh et al., 2018, Rotary-actuated folding polyhedrons for midwater investigation of delicate marine organisms.
- 4) D. J. Kessler and B. G. Cour-Palais, "Collision frequency of artificial satellites: the creation of a debris belt," Journal of Geophysical Research: Space Physics, vol. 83, no. A6, pp. 2637–2646, 1978.
- 5) "Space debris by the numbers". ESA. 12 September 2023. Retrieved 21 October 2023.

DIABLO – Deployable Interlocking Actuated Bands for Linear Operations; Design, Development, Testing, and Applications

Vishnu Sanigepalli*, Robert Van Ness*, Brian Vogel* and Kris Zacny*

Abstract

Deployment mechanisms are widely used in the aerospace industry for their low mass and high packing efficiency. However, there remains a technology capability gap for deployment mechanisms that have high stiffness and strength for extraterrestrial surface applications such as drill stems and vertical masts. To fill this gap, we started developing a mechanism that emphasized high 20+:1 extension-stowage ratios, scalability to 100+ meter lengths, and survival in extreme thermal and dusty environments. This effort pioneered a new technology: DIABLO, Deployable Interlocking Actuated Bands for Linear Operations, a novel helical band actuator that wraps a self-interlocking band around the deployment axis to form a rigid tube that can be autonomously deployed and retracted with a motor. The deployed mast can be manufactured from traditional metals (steel, aluminum, etc.), composites, and even flexible printed circuits. We have demonstrated initial prototypes with a 45-mm diameter 3-meter height 304 SS configuration to serve as a drill stem for lunar pneumatic drills. This was later scaled to a 200-mm diameter 15-meter height vertical mast to deploy 10 kW of Solar Array at the lunar South Pole to generate power. This technology is currently enabling mission architectures that prove to be challenging with existing deployable technologies.

Introduction

Current aerospace deployment mechanisms such as Collapsible Tubular Mast, Coilable Boom, rollable composite masts, etc. have been used to deploy payloads in space such as solar panels, antennas, etc. Although these mechanisms are lightweight and have high deployment-to-stowage ratios, they struggle with load-bearing capabilities at large deployment lengths. To overcome these challenges, DIABLO deploys one self-interlocking high-strength element with a simple and robust rotary-linear drive mechanism. As the required design stroke is increased, the stowed band length is simply proportionally extended and can enable future deep drills or high lift applications. With its method of deployment and scalable geometry, this technology proves to be a highly competitive option for applications from small CubeSats to large 15-m+ deployable structures, as shown in Figure 1.



Figure 1. (left) DIABLO mechanism shown in stowed and deployed configuration with a diameter of 45 mm with a deployment length of 3 meters. (middle) DIABLO 200-mm diameter that can deploy up to 15 meters. (right) DIABLO 300-mm diameter that can carry 500-N payload on the tip.

* Honeybee Robotics, Altadena, CA

Requirements

The goal of developing DIABLO technology was to enable a capability for deployment mechanisms in extraterrestrial bodies (Moon, Mars, etc.) as well as low-gravity applications that can unlock new missions that are currently challenging with existing technologies. At the beginning of the program, the technology emphasized Key Performance Metrics, outlined in Table 1, to ensure that it can be tailored and integrated to various systems without a ground-up redevelopment of the mechanism.

Table 1: Key Performance Metrics that were set for DIABLO at the beginning of its development.

Key Performance Metrics	Requirement and Goals
Extension-to-Stowage Ratio	Low volume requirements for launch; 20+:1 ratio.
Material	Can be made from various materials such as metals, composites, plastic, etc.
Diameter/Lengths	Diameter and lengths are tailored specifically to the mechanism requirements. Smallest Diameter: 20 mm. Largest Diameter: <i>no limit</i> . Length: <i>no limit</i>
Moment Capability	Can take moment applied at the tip without additional offloading structure.
Multi-cycle Full Deployment/Retraction	Deploy and retract multiple times.
Deterministic	Deterministic deployment and retraction in any environment.
Low-cost Development	Easy to manufacture with conventional manufacturing techniques.
Regolith Ingress	Function with regolith exposure and ingress with minimal loss of performance; >100 cycles.

Mechanism and Concept of Operations Description

DIABLO consists of four main components, shown in Figure 2:

1. **Helical Drive Mechanism (HDM)** – driven by a brushless DC motor to assemble and deploy the boom using a helical track mechanism.
2. **Outer Roller Housing** – supports the boom during deployment and has a passive feeder to align the DIABLO bands into the HDM.
3. **DIABLO Bands** – flat sheets of bands with pre-installed rivets and spacers that helically overlap to create a deployed tubular structure. The rivet heads interlock with clearance holes in the band while the spacers on the opposite side of the band ride on the Helical Cam of the HDM to deploy.
4. **Storage Reel** - houses the bands in a spiral-like fashion for stowage and can rotate passively with the HDM or independently actuated with another motor for a deterministic band stowage.

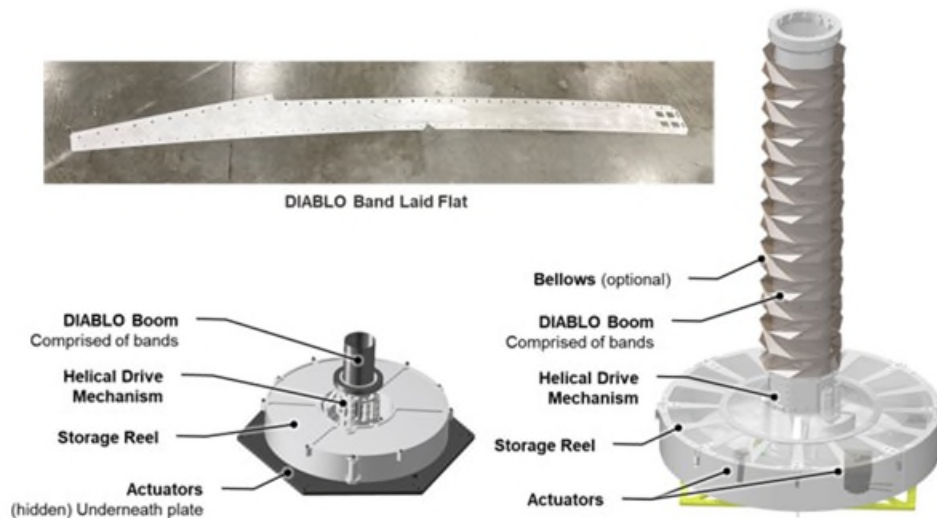


Figure 2. DIABLO component breakdown

Concept of Operations for Deployment and Retraction

To deploy, the BLDC motor rotates the HDM counterclockwise and the stowed DIABLO bands, stored in the Storage Reel, are drawn into the HDM and helically overlapped to create the boom, see Figure 3. The boom is driven upward as the HDM rotates and the process repeats for the full deployment length. For retraction, the HDM rotates in the opposite direction, and bands stow in a spiral geometry inside the Storage Reel. Sensors can be placed on the HDM to monitor for and prevent any potential misalignment.

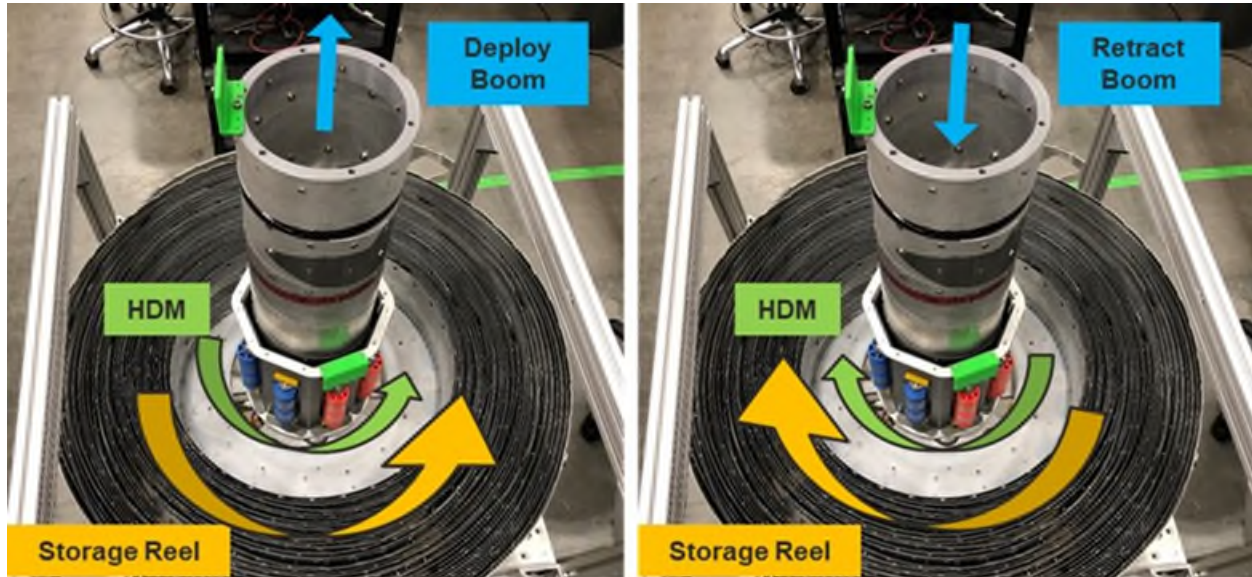


Figure 3. (left) Helical Drive Mechanism (HDM) deploys the bands that are stored in the Storage Reel into a circular boom. Reversing the rotation of HDM and Storage Reel retracts the boom.

Design and Manufacturing Considerations of DIABLO

Design of DIABLO Bands

The DIABLO bands are manufactured out of large sheet metal stock via conventional manufacturing techniques such as laser cutting, CNC milling, or chemical etching. The bands, when laid flat, form an arc to allow for the band to self-interlap without growing in diameter as it's helically deployed into a boom. The top of the band has clearance holes that interlock with the rivet head after deployment, and the bottom of the band has clearance holes for installation of the rivets and spacers before mechanism assembly.

Due to the limits of the manufacturing machine's workspace, the band design also had to accommodate the attachment of multiple band pieces together to form a large continuous band for the required deployment length. There are currently two methods that have been designed and tested for assembling the bands, shown in Figure 4. For thin sheet metal bands, less than 0.25 mm, the bands can be overlapped without a compromise in mechanism alignment during deployment and retraction. To attach the pieces, the bands have holes along the mid-plane that are riveted together permanently. For sheet metal bands that are greater than 0.25-mm thick, a supplemental doubler piece is used to attach the band pieces. The doubler is designed to provide continuous stiffness along the deployment axis without compromising the structural integrity.

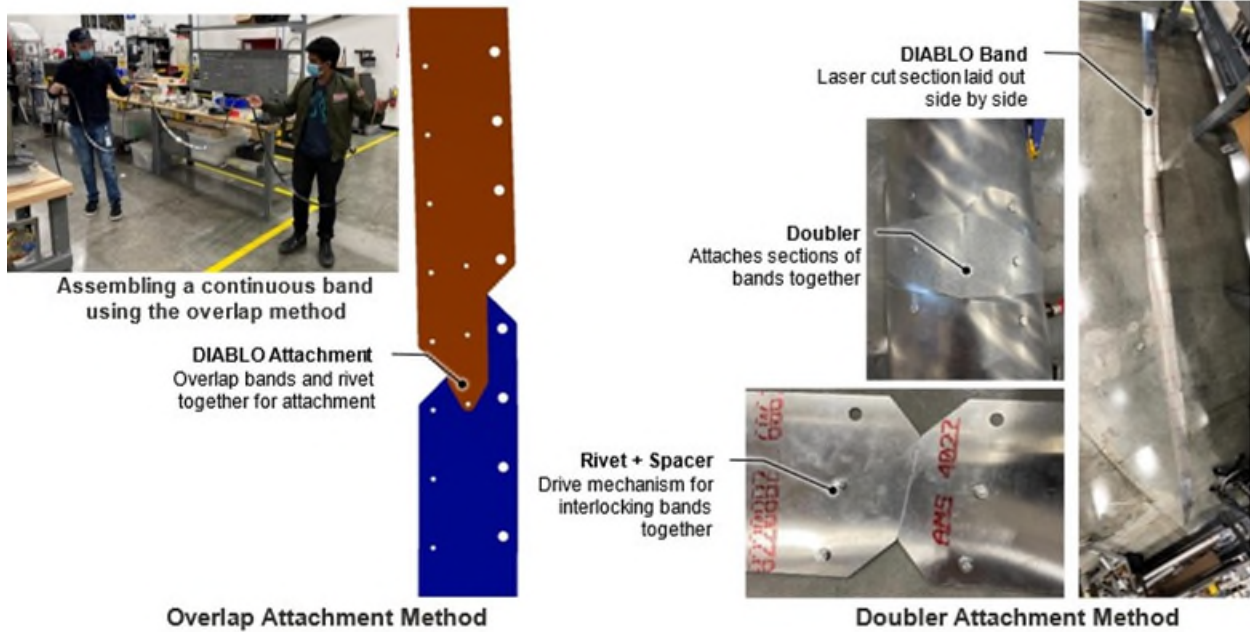


Figure 4. Two methods of attaching DIABLO band sections.

Helical Drive Mechanism (HDM) and Outer Roller Housing

DIABLO uses a Helical Drive Mechanism (HDM) to assemble and deploy the band. It is a radially outward-facing track comprised of 2 primary parts: a rotating screw-like Helical Cam and a fixed Slot Head. Deployment of the tube is performed by rotating the Helical Cam which pushes the deployed tube outward and drives the stowed band into the HDM shown in Figure 5. The band reacts with the track through the radially inward-facing pins that are riveted through the holes in the band. A second set of larger holes are laid over the radially outward-facing rivet heads as the band is deployed, interlocking and forming the circular boom. The interlocking interface is maintained by the geometry of the tube, preventing relative motion between the mating band sections. Retraction is performed by reversing the deployment operation. The Outer Roller Housing pushes the bands together to align the holes to the rivet heads. During retraction, it pulls the band section from the circular boom into a flat sheet for stowage.

The HDM is required to precisely align the bands, deploy the boom, and offload any external loads from the tip of the boom. To minimize any issues with differences in coefficient of thermal expansion (CTE) mismatch, the HDM and the bands are designed to be made of the same material.

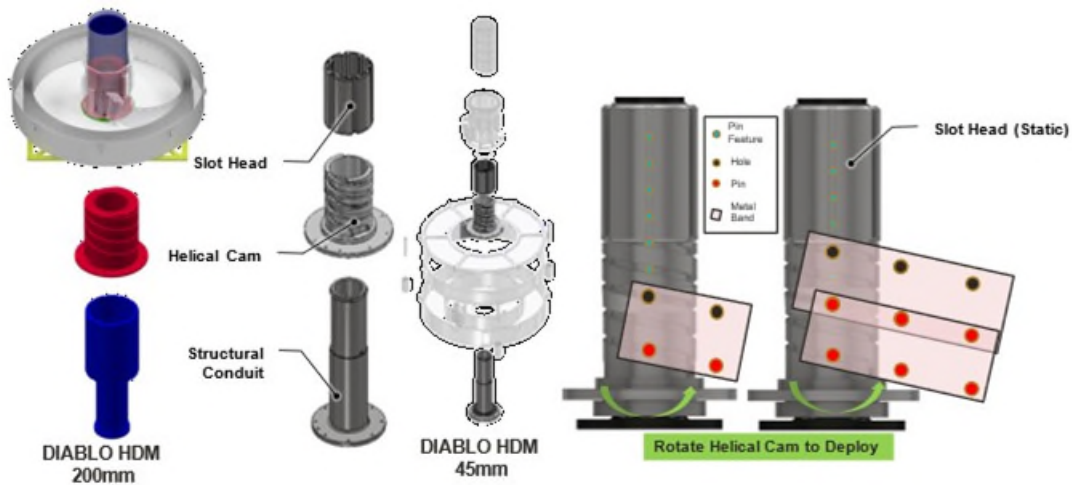


Figure 5. (left) Helical Drive Mechanism (HDM) 45 mm that drives and assembles the bands for deployment and retraction (right) HDM developed for 200-mm diameter DIABLO.

Bands and Storage Reel

The Storage Reel houses the bands in a spiral-like fashion before deployment and has an independent degree of freedom from the HDM, see Figure 6. Due to the difference in spiral geometry and the final boom diameter, the Storage Reel needs to rotate slower than the HDM. This can be done either passively or through another actuator. The DIABLO bands are stowed in a flat-spiral in the Storage Reel.

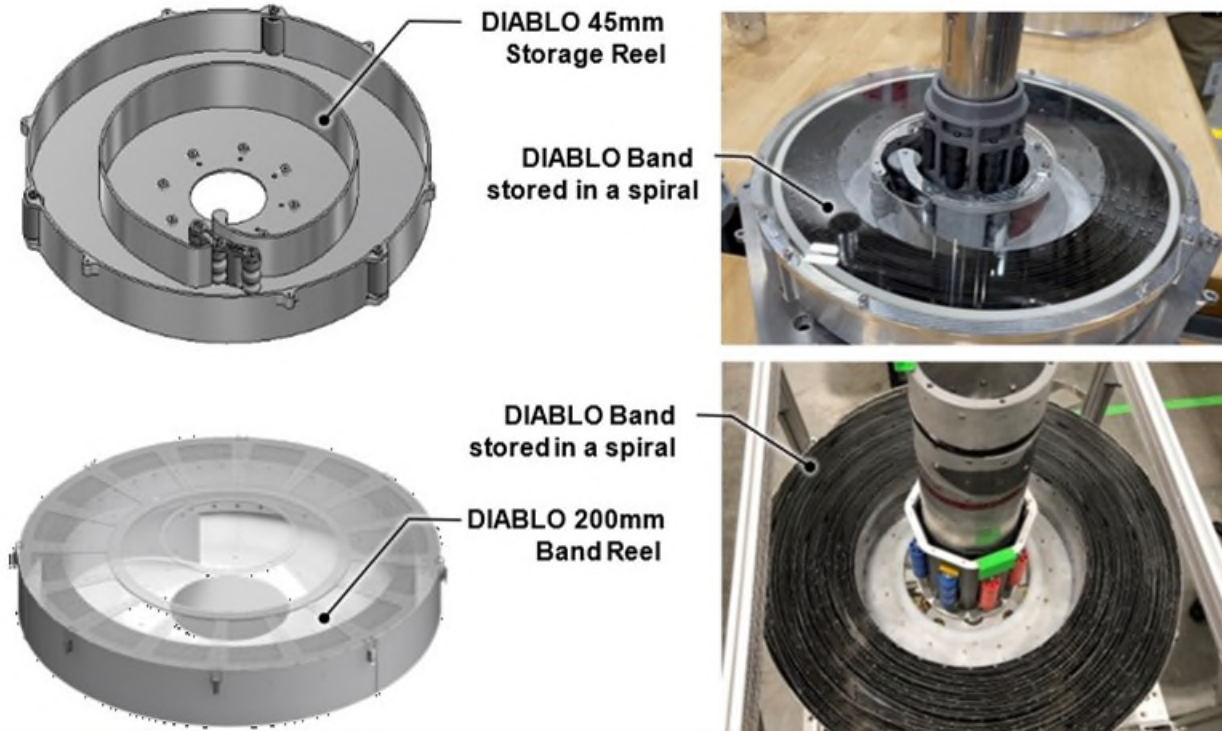


Figure 6. (top) Storage Reel with stowed bands (bottom) Storage Reel for larger 200 mm DIABLO

Other Notable Features of DIABLO

Since the inside diameters of both the boom and deployment system are open, DIABLO can accommodate deployment of harnessing cables and other utility connections directly through the mechanism. Harnessing can be stowed on a spool in the base for passive or active deployment. For example, Figure 7 shows a configuration with a ribbon cable and pneumatic tube that are passively deployed inside the boom to provide power, communication, and gas from the base-mounted electrical equipment to the end-effector. The DIABLO boom has the advantage of dual-purpose as it also serves as a conduit for the harness and shields it from external environments.

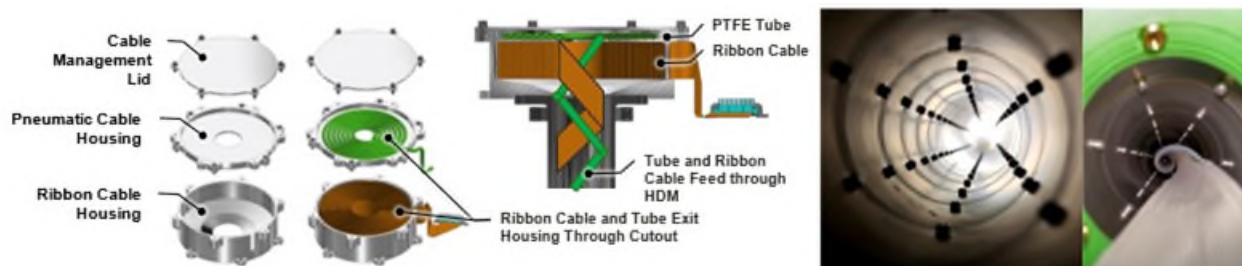


Figure 7: DIABLO allows for passive deployment of harness and pneumatic lines to the end effector to supply power or gas to the payload mounted at the tip.

Engineering Development Units and Testing

Development of DIABLO Bands

Development of the DIABLO technology was initiated by looking at the trade study for the boom and how it semi-permanently assembles and interlocks flat bands together. The designs varied from looking at various features such as the number of bands, type of drive mechanism, load transfer features, etc. The boom design was iterated 25+ times over 8 concepts (some are shown in Figure 8) while modifying geometry and key mechanism properties such as helical height, diameters, and interlocking features. The prototypes were made via Polyester Plastic/PETG 0.2-0.59 mm sheets and were manufactured in-house with a CO₂ laser cutter. The booms were initially hand-assembled but were later deployed with the HDM as it was being developed in parallel.

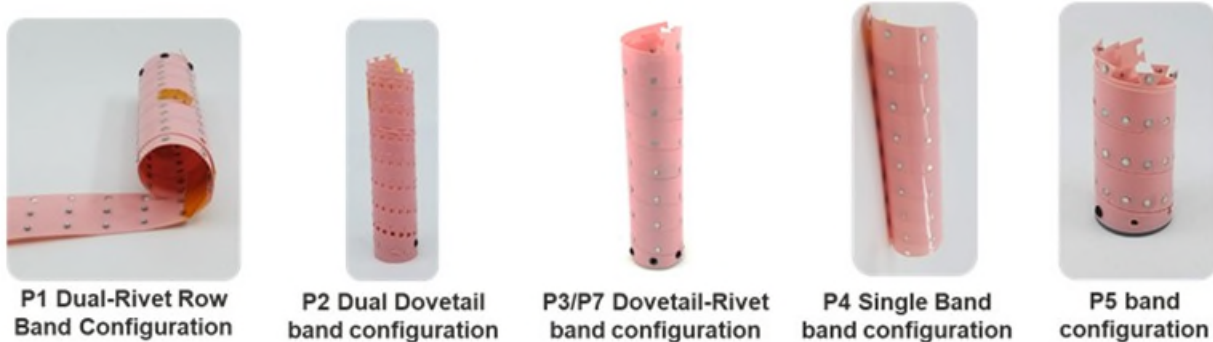


Figure 8. DIABLO early designs and prototypes. Band/boom designs were iterated for the final down selection with figures of merit such as complexity, manufacturability, and mass efficiency.

Due to the rapid iteration and tight schedule, the team utilized COTS components such as rivets and spacers with in-house rapid prototyping techniques such as 3D printers and laser cutters. Due to the limited precision capabilities of these techniques, it required us to calibrate the designs to overcome mechanism issues with misalignment and other challenges. While sending these components out for higher precision manufacturing may have mitigated some of these mechanical issues, it inspired the team to develop and integrate several features that dramatically improved the robustness and reliability of the mechanism, eliminating almost all prior misalignment cases observed during the early development phases. As a result, the mechanism can tolerate a wider range of band parameters and manufacturing tolerances.

Development of Helical Drive Mechanism and Storage Reel

The initial development of the HDM was made with ABS filament using fused deposition modeling printers to rapidly iterate the mechanism and its functionality. The design was eventually transitioned from the in-house prototypes to the out-sourced machined 304 SS components with tight tolerances and surface finishes. The tight-tolerance machined components enabled us to overcome the contact stress issues that have been seen with 3D-printed ABS. The evolution of the Helical Drive Mechanism, shown in Figure 9, highlights the increase in the fidelity of the design over the course of the development.

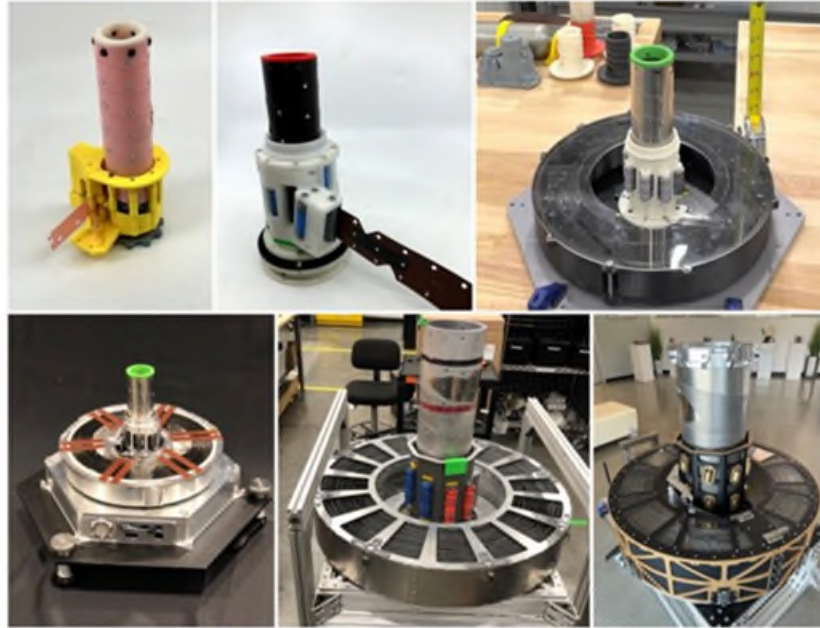


Figure 9. Development of the DIABLO with HDM and band technology over the course of the program

Assembly and Manufacturing Process Development

Rivet and Spacer Assembly

For the band assembly, the band is sandwiched with a rivet and a spacer on either side. An arbor press is used to deform the rivet core, which captures the spacer and permanently affixes them to the band, as shown in Figure 10. This process is repeated for each rivet and spacer along the length of the band. Pressure applied to the rivets is kept constant by replacing the lever of the press with a torque wrench. The process has been reliable across the thousands of rivets and spacers installed onto the band.

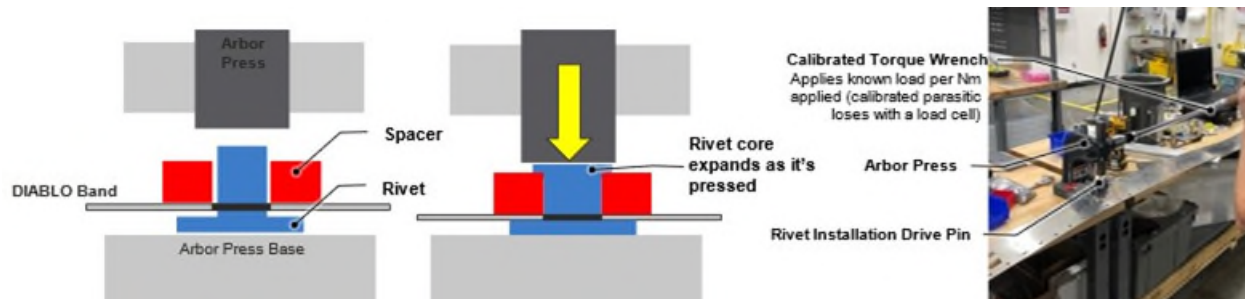


Figure 10. Attaching Spacers and Rivet to DIABLO Bands with custom GSE.

Rivet Metrology Ground Support Equipment (GSE)

During the early phases of development, COTS rivets were used to minimize manufacturing costs. However, the team found that the procured rivets had large variations in geometries that caused issues with deployment. Although tolerances in rivet head diameters were accounted for when sizing the hole diameter for the bands, the concentricity between the rivet shaft and rivet head was greater than expected. Some of the rivets, shown in Figure 11, highlight the outliers that caused issues during the early phases of development. To circumvent the issue, a Go and No-Go GSE metrology tool was designed and produced to determine if a rivet is within the anticipated tolerance spec. Each rivet was manually checked with this GSE tool one by one to ensure that the mechanism would not have alignment issues. More recently, custom high-precision rivets and spacers were designed and ordered in bulk to mitigate this issue, as the labor required to check each one of these rivets was no longer cost-effective. This also allowed the team to tailor the rivet features to the needs of the mechanism, such as the rivet head geometry.

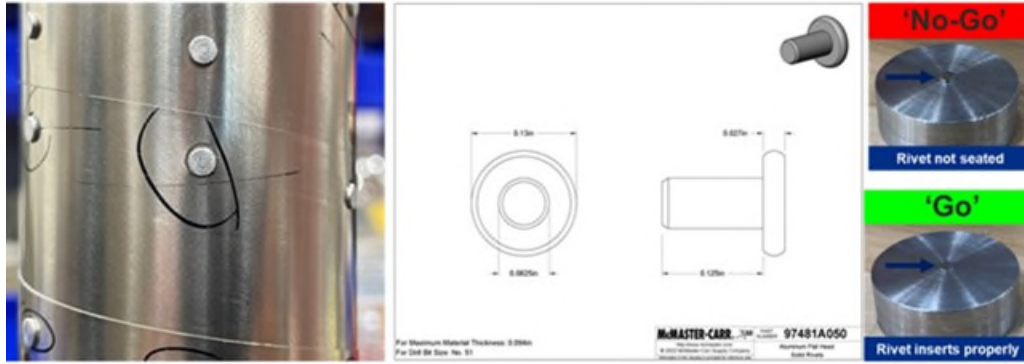


Figure 11. Non-concentric rivets that were causing issues with deployment reliability. A GSE was used to standardize the rivet tolerances by checking if the rivet is properly in the GSE machined features.

Characterization and Testing of DIABLO

Rivet Load Capability Testing

To better understand the capabilities and failure modes of the rivet and sheet metal bands, a single-plane shear test setup was used to quantify stress concentration factors. Two failure modes were identified and later modeled to understand the scaling factor for larger mechanisms, shown in Figure 12. The first type of failure occurs when the rivet shaft shears along the plane of the band. The second type of failure occurs due to the stress concentration between the rivet head and the clearance hole of the band. In this failure mode, the sheet metal band buckles locally and the rivet head is plastically deformed as well. The tests were done with 1100 Aluminum rivets and 304 SS bands.

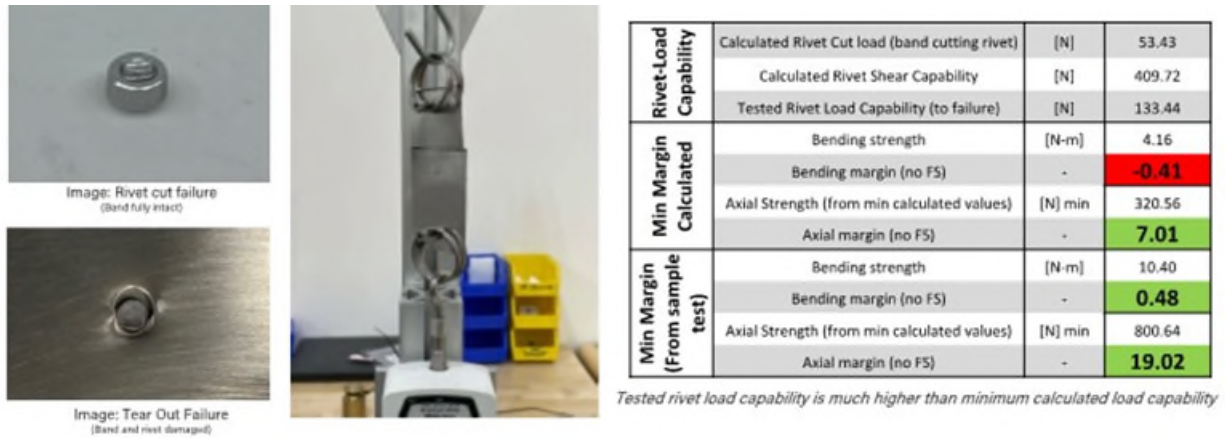


Figure 12. Rivet failure modes for DIABLO specific application through single shear tests

Buckling of DIABLO Bands during Stowage

The prototype, shown in Figure 13, has an acrylic cover for the team to visually understand how the bands stow and ensure that they are not binding. The initial prototypes and testing provided insight into the failure modes that can happen during retraction such as local band buckling. This primarily occurred during retraction with early development phase storage reels that were rotationally locked to the HDM. When the band stored in spiral geometry contacted the outer walls of the inside of the Storage Reel, friction would cause the band to deflect and begin to bind. The binding caused the tension to build up and buckle the band into the opposite direction, as shown in Figure 13. To mitigate this issue, PTFE tape was lined on the inside of the housing to reduce the friction that causes the bands to bind. This alleviated the issue at slow deployment speeds but did not help at higher speeds. This is likely since the band requires more time to slip past each other. To further mitigate the binding issues with the rotationally locked storage reel design, the team found success with a passive spinning outer hoop to reduce the friction build-up that caused the binding.

To eliminate the binding problems, later iterations of DIABLO use a second actuator for the Storage Reel to make the mechanism stowage more deterministic and increase the mechanism reliability. Since the spiral has a variable diameter, the rotation rate of the Storage Reel relative to the HDM is a function of deployed height, stowed band, and geometric variable of the spiral and deployed diameter. A feedforward control system is used to control the position between the HDM and Storage Reel to make sure that bands are properly stowed during deployment and retraction.



Figure 13. Band buckling failure more inside Storage Reel during retraction.

Load Testing

To characterize the payload carrying capacity for DIABLO, masses were placed on the tip of the boom to mock the loads from an instrument/payload. With a 45-mm OD and a 0.13-mm band thickness, payloads up to 50 N were demonstrated with deployment/retraction. Side/cantilever loads were applied with a force sensor to demonstrate the deflection of the mechanism shown in Figure 14. The deflection that is seen in the boom is a culmination of the clearance between the rivet head and the band hole, mechanical deflection, and the low stiffness of base mechanism (3D-printed ABS). The clearance/slop in the mechanism can be further reduced by switching from COTS rivets to custom higher precision rivets.

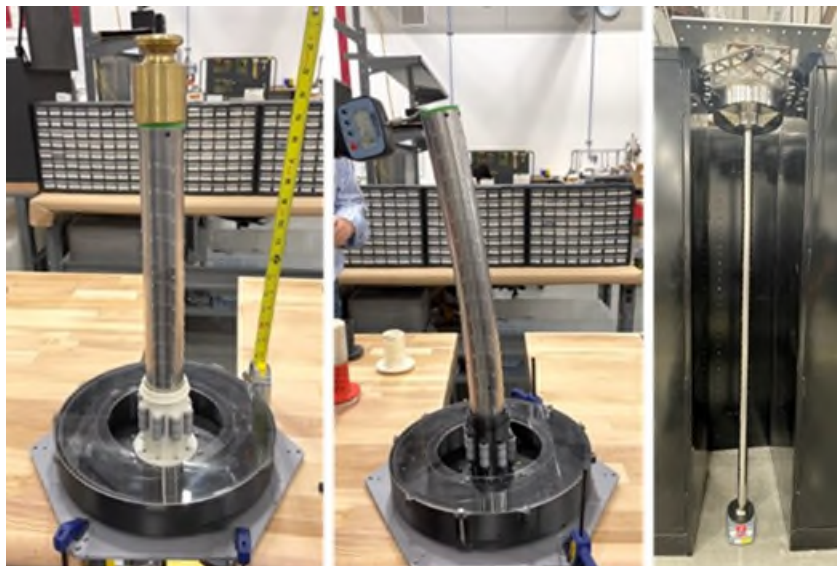


Figure 14. DIABLO undergoing tests with axial, lateral, and weight-on-bit loads.

Mechanical Slop and Deflection

During deployment, the mechanism requires sufficient clearance between the rivet head and the hole. This clearance allows for ease of deployment and reliability but also generates inherent slop in the mechanism. When deployed, the boom has slop deflection that does not require much minimal force for it to displace laterally and axially. However, after a certain amount of displacement, additional displacement is driven by external force and behaves like an ideal beam. This is tested on the horizontal 200-mm DIABLO, described in Figure 15, and has demonstrated mechanism phenomenon regions of mechanical slop and transition to behaving as an ideal beam.

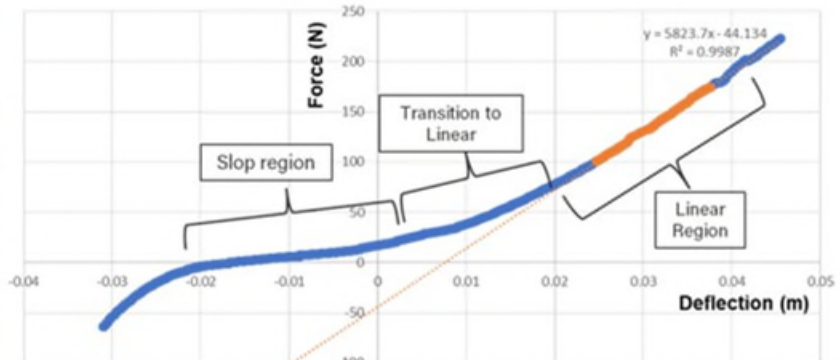


Figure 15. DIABLO boom demonstrating properties of mechanical slop and ideal beam. A lateral force is applied to the tip of the mast while the base is held static. It is swept across the deployment axis, where left is negative lateral deflection and right is positive lateral deflection.

Another source of the deflection was due to the tolerances and geometric shape of the rivets. The rivets were MIL-spec but had a fillet at the root which prevented the team from removing this slop without custom rivets. The holes in the bands had to clear the widest part of the rivet and when the band passes it and contacts the fillet, there is additional clearance that was not accounted for, as described in Figure 16. This additional diametrical clearance of 0.13 mm generated accounted slop that can only be fixed by removing the fillets. To fix these issues, custom machined rivets were procured to minimize the tolerance stack least material condition, largest hole diameter with the smallest rivet head diameter. This significantly improved the boom stiffness in both lateral and axial directions.

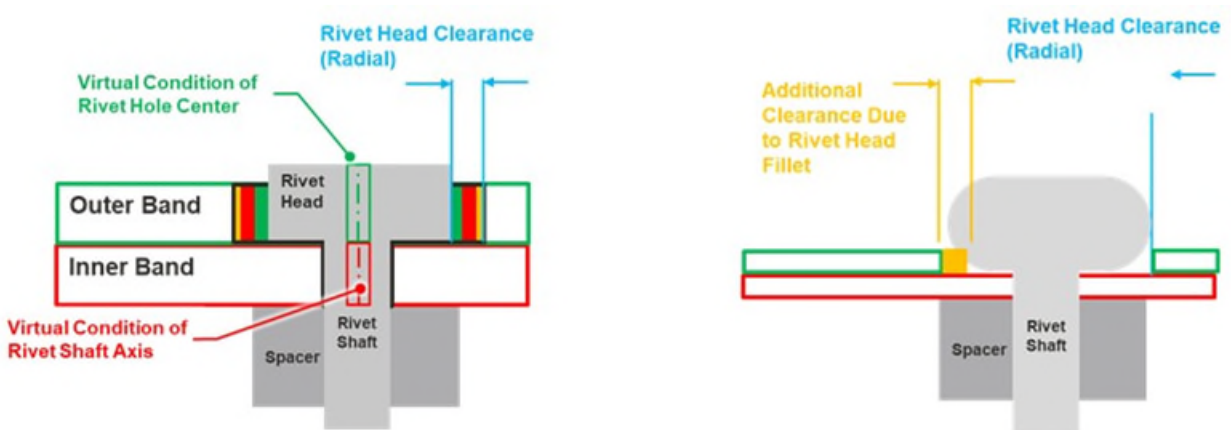


Figure 16. (left) Ideal square river interface and tolerance analysis. (right) Since the thickness of the band was much less than the fillet on the COTS rivet, it allowed for unaccounted mechanical slop.

This feature of fine-tuning the clearances between the rivet head and the hole is used to control the stiffness and can be advantageous for specific applications. For a deep drill system that has low weight-on-bit, low stiffness, and more clearance, a flexible boom can be used to steer against large boulders that can be impenetrable. On the other hand, a boom that deploys solar panels will require a higher stiffness to prevent dynamic movement due to seismic activity or thermal fluctuation due to eclipses.

Lubrication and Regolith Ingress

As the early prototypes were tailored for lunar applications, the lubrication strategy was a key factor in ensuring life cycle with the risk of regolith ingress. Since wet lubrication methods attract regolith particles and bind regolith particles, a spray-paint-based dry lube was used instead. As shown in Figure 17, lubrication was coated on the HDM before assembly. After cycling the mechanism and taking it apart, we noticed FOD that indicated that the dry lubrication strategy may require additional development work to survive a desired lifetime.

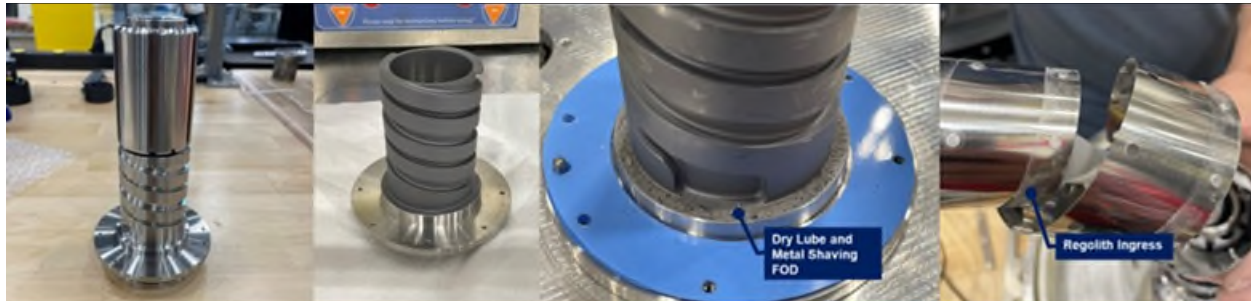


Figure 17. (left-right)(a) cleaned parts before applying dry lube (b) dry lube coating (c) after deployment, dry lube FOD found at the base of the Helical Cam (d) regolith ingress inside of DIABLO bands.

In later prototypes, PTFE-based lubrication was used to coat the HDM and the spacers that are on the ID of the band. The regolith ingress is still a risk and the vacuum chamber testing performed has highlighted that there is no significant reduction in performance. Other compartmentalized solutions such as origami bellows and felt-style seals have been proposed to create a barrier for the regolith for 100+ cycle missions.

DIABLO Test Campaigns

Testing DIABLO as a Drill Stem for Drilling Regolith Analog BP-1 in Vacuum

The 45-mm diameter DIABLO, made from 304 SS, was tested in a vacuum chamber with lunar regolith analog BP-1. DIABLO served as the boom for a pneumatic drill to bury a seismometer into the surface to help provide better attenuation for moon quakes. The test campaign was carried out in a vacuum chamber, shown in Figure 18, with a 2-meter regolith bucket bin filled with BP-1 that is vacuum compacted. The instrument is mounted on a force-torque sensor to monitor load and moments during the drilling process.



Figure 18. Regolith analog BP-1 used to test DIABLO-based pneumatic drill science instrument. A large regolith bin with a vibration motor is used to vibrate-compact the regolith.

The test campaign started with deploying DIABLO until the pneumatic drill head probes the surface while using motor current and load cells. After it reaches the surface, the pneumatic system turns on, flowing gas through the nozzle. Due to the expansion of gas in vacuum, the drill penetrates through compact regolith with minimal weight-on-bit (WOB). DIABLO has successfully deployed the seismometer at a target depth

of 0.6 meter, shown in Figure 19, while surviving vacuum and harsh regolith conditions. This resulted in a near TRL 6 end-to-end demonstration of a DIABLO integrated instrument, which resides in Honeybee's secured facility.

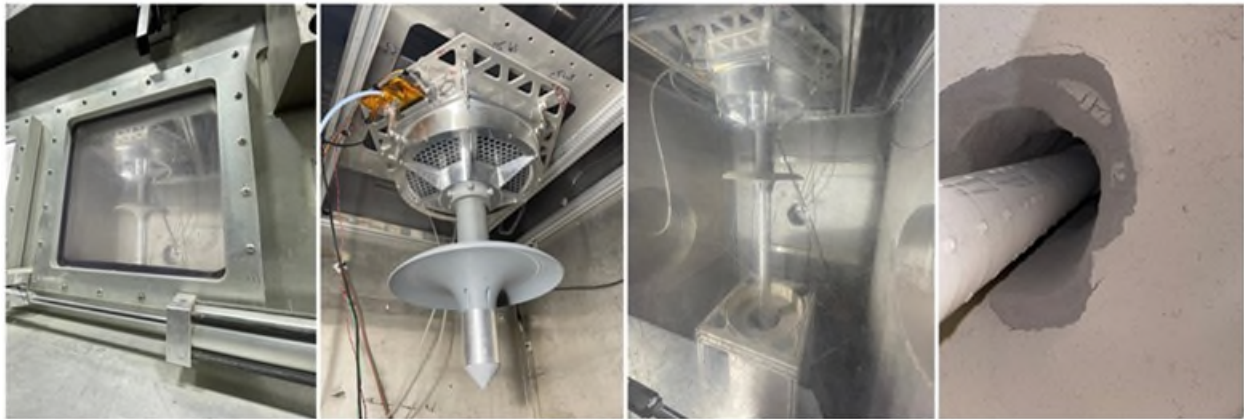


Figure 19. DIABLO-based drill instrument inside a vacuum chamber testing in lunar regolith analog, BP-1.

Testing DIABLO for a Mast for Deploying Solar Panel

DIABLO became a prime candidate for deploying a vertical mast for NASA's Vertical Solar Array Technology (VSAT) program and is a key technology for Honeybee's Lunar Array Mast and Power System (LAMPS) [4]. The system was scaled up to a 200-mm diameter and Aluminum 6061 was selected as the band material for the 15-meter vertical deployment, raising a large solar array payload in lunar gravity. The prior test data and lessons learned from previous mechanism development were used to inform critical scaling factors for this load case, such as diameter, materials, wall thickness, and tube geometry. It is designed to lift a 250+ kg payload above the lunar surface with a base that can self-level to accommodate variations in lunar terrain. Various factors such as mechanical slop, load, and thermal deflection were considered and modeled for the final specification requirements for this prototype.

LAMPS DIABLO, shown in Figure 20, was manufactured and assembled in-house for a deployment test in Honeybee's secured parking lot. For safety precautions, guy wires were used to control any additional loading from unanticipated high winds. The mechanism successfully deployed 15 meters off the ground and retracted completely without issue in under one hour. LAMPS DIABLO has demonstrated that this technology is scalable and can be utilized for lifting payloads off the lunar surface.

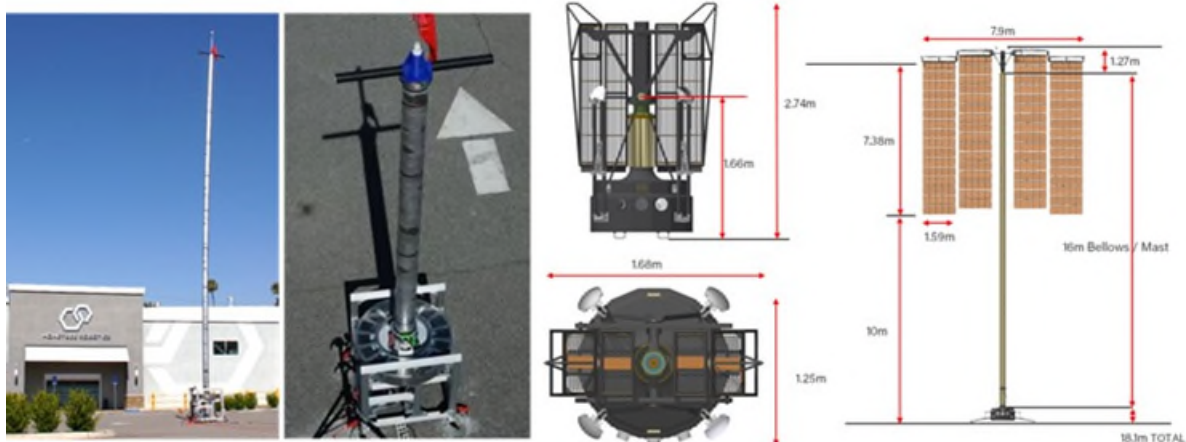


Figure 20. DIABLO 200-mm diameter deploying a 15-meter boom in secured facility parking lot.

DIABLO will be tested as part of Honeybee's LAMPS at the Johnson Space Center historic Chamber A to achieve TRL 6 in Summer 2024 [4]. This latest prototype has further increased lateral stiffness and buckling margins with updated band geometry and mechanism features. It was successfully demonstrated to lift

500 N of payload 15 meters off the surface. This includes a 300-mm diameter mast that satisfies the structural requirements involved in supporting the massive suspended 10-kW solar array, masthead structure, and supporting masthead avionics.

Upcoming Work and Evolution of Technology

DIABLO technology is going through extensive testing to demonstrate its capabilities in vacuum, cryogenic conditions, and harsh lunar regolith conditions for various form factors and materials. With more test campaigns, the team hopes to discover failure modes and build a better knowledge base to iterate and evolve the technology.

Weld DIABLO

Honeybee is exploring new technology developments such as weld DIABLO, where the DIABLO mast is welded as it's assembled for a single-time deployment, creating a permanent, rigid structure. This mitigates the mechanical slop deflection caused by the clearance between the rivet head and the adjacent hole. The weld is made across the seam that can either be spot welded or a continuous seam that runs helically along the length of the boom. Initial tests with Aluminum 6061-T6 have proven to be successful, demonstrating the feasibility of the welding technique for creating permanent structures for space and terrestrial applications.

flexDIABLO

The *flexDIABLO* is building up on DIABLO by manufacturing the bands with Flexible Printed Circuits where the power and signals are integrated into the bands. The novelty of making the DIABLO bands out of Flex Printed Circuits lies in using different copper weights and embedded structural material to tailor the boom's strength and stiffness based on the application, as shown in Figure 21. Ensuring that the flex cable and copper routing can survive the tight bend radius while maintaining its life margins in all environments will prove to be challenging. The design works with DIABLO's HDM and ensures that any power transmission/thermal environments prevent delamination of the flex cable. The *flexDIABLO* technology can be used in harsh environments applications that would prove to be difficult/complex with traditional mechanisms.

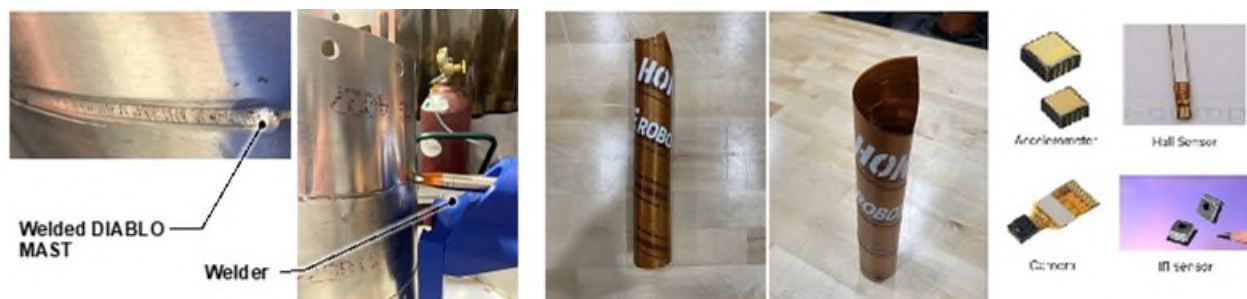


Figure 21: Weld DIABLO and flexDIABLO early concept development prototypes

Upcoming and Future Integrated Missions

DIABLO technology has become a key technology that is being utilized/investigated for various terrestrial, space, and lunar applications. Currently, DIABLO is integrated into a Development and Advancement of Lunar Instrumentation (DALI) funded seismic instrument, described in Figure 22, that uses a pneumatic drilling technology to bury a seismic sensor into lunar regolith. DIABLO technology has also proven to be scalable from a 45-mm OD to 300+ mm OD to carry heavier payloads for Vertical Solar Array Technology (VSAT) [1]. DIABLO will be extending a deployable solar array to generate 10 kW of power to support Artemis and future missions. It's also being investigated for Lunar Utility Navigation with Advanced Remote Sensing and Autonomous Beaming for Energy Redistribution (LUNARSABER) [2], to deploy 100+ meter towers on the Moon to provide critical lunar infrastructure and services under the LunA-10 program [3].

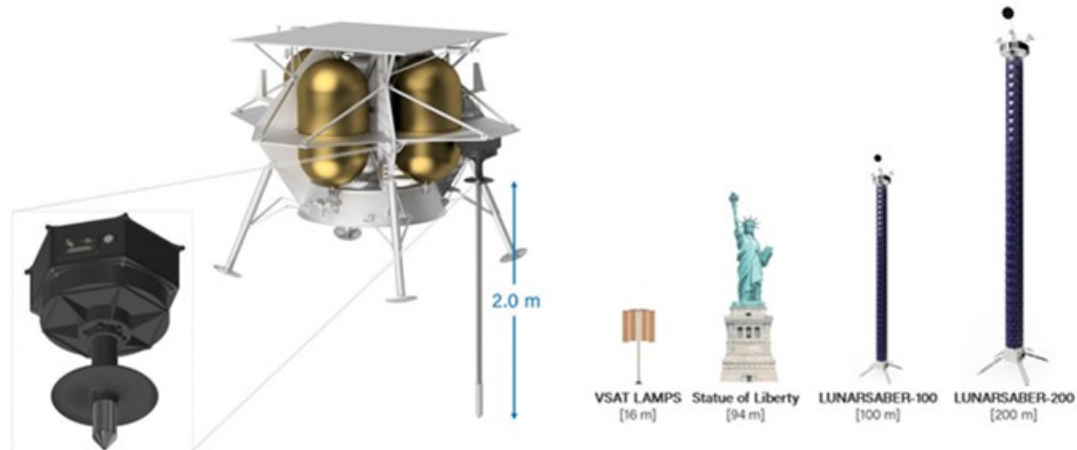


Figure 22. DIABLO Applications. (left) DALI Seismic instrument uses DIABLO drill/deploy seismic sensors into the lunar regolith. (right) DIABLO scaled to a 15-meter-tall mast for Vertical Solar Array Technologies (VSAT) and a 100+ meter-tall mast for LUNARSABER.

Conclusion

Having undergone a thorough technology development process and several complete mechanism builds and test campaigns, the DIABLO technology has achieved a high level of technical maturity and has demonstrated its versatility across a wide trade space. DIABLO represents a highly adaptable system that can meet form factor, material, structural, and extreme environmental requirements that were previously unattainable with compact linear deployment systems. Over the course of the development of this technology and mechanism, it has demonstrated unique performance characteristics, such as 80+:1 length-to-diameter ratios for masts, no limits on deployment-to-stowage height ratio, and high strength-to-mass performance. In its later stage of development, it is currently being investigated for its applications in upcoming CLPS missions for deploying science instruments and the NASA Game Changing Development’s LVSAT program for deploying solar panels at the lunar south pole. Upcoming studies are looking to scale the system for taller towers reaching up to 100+ meters tall to provide commercial services as a part of the lunar architecture. The technology is evolving to solve a wider range of challenges such as weld-DIABLO and *flexDIABLO* to address niche challenges in aerospace. DIABLO has established itself as a groundbreaking technology that is enabling new mission architectures and is set to change deployment mechanisms for space exploration.

Acknowledgments

This technology was developed by Honeybee Robotics, partially under the DALI contract with the University of Arizona and the LVSAT program under NASA Artemis. The authors would like to thank the many individuals who assisted and mentored during this technology development: Dara Sabahi, Gale Paulsen, Hop Bailey, Phil Morrison, Richard Margulieux, Peter Ngo, Dean Bergman, Bernice Yen, Lisa Thomas, Zachary Mank, Barry Goldstein, and Ray Crum.

References

- [1] “Vertical Solar Array Technology (VSAT).” Techport.nasa.gov, 2023, <https://techport.nasa.gov/view/116305>
- [2] Honeybee Robotics to Develop LUNARSABER for DARPA’s LunA-10 Program – Honeybee Robotics. www.honeybeerobotics.com/news-events/honeybee-robotics-to-develop-lunarsaber-for-darpas-luna-10-program/.
- [3] “A Framework for Optimized, Integrated Lunar Infrastructure” Darpa.mil, 2023, www.darpa.mil/news-events/2023-08-15.
- [4] Lunar Array Mast and Power System (LAMPS) for a Scalable Lunar Power Infrastructure. 17 Oct. 2023, <https://doi.org/10.2514/6.2023-4786>.

A Modular Ready-to-Use Active Gravity Offloading System

Frederik Doll*, Stefan Oechslein* and Benjamin Krolitzki*

Abstract

The modular active gravity offloading system (ZeroG) presented here for the first time, is a portable, modular standalone environment, capable of testing multi-stage deployment mechanisms, with three independent suspension points at the time of submission. Three more traverses are currently being integrated. The current system and its precursors have already been used for solar wing deployment testing and integration. An essential design feature resulting from lessons learned during the prototype stages is the integration of all functional components into the individual traverses. A significant advantage of this approach is relatively simple scalability by adding individual modules. To the authors' knowledge, the ZeroG-system presented here represents the most advanced fully operational offloading system currently available. Calibration and testing of a multi-panel solar generator deployment as well as for a generic deployable instrument boom with two full Carbon Fiber-Reinforced Polymer (CFRP) hinges are shown, covering full release kinematics from stowed to deployed. A standard procedure for characterizing gravity offloading devices (active as well as passive) is proposed.

Introduction

Even with big launch vehicles like Starship looming on the horizon, payload fairing volume remains a highly valued resource and a significant constraint for any spacecraft. Packing size of a spacecraft is usually reduced by folding extensions in varied ways. However, problems encountered during the deployment of stowed antennae, solar arrays, and instrument booms in orbit can lead to partial or complete mission failure [1]. One recent prominent example of a deployment anomaly is the Jupiter Icy Moons Explorer's Radar for Icy Moons Exploration (JUICE RIME) antenna, which remained stuck in a partly deployed state for several days before the European Space Agency (ESA) managed to achieve full deployment [2]. Given the critical importance of deployment systems for spacecraft functionality, significant emphasis is placed on testing these systems during the development phase. The fundamental approach of "test like you fly" [3] is constrained by the terrestrial test environment: While parameters such as vacuum conditions, solar radiation exposure, and cold temperatures can be effectively controlled, the replication of a gravity-free environment on Earth remains unattainable. To address this challenge, engineers typically use passive gravity offloading with strings, springs, or balloons in iterative testing loops that involve partial, stepwise deployment evaluations, along with simulation and approximation [4], [5].

Gravity Offloading Background

The limitations of passive gravity offloading strategies have been comprehensively highlighted elsewhere, emphasizing the need for an active gravity offloading environment [4]. The main limitation for passive gravity offloading systems being, that any suspension which does not actively follow the suspended test article (suspension with long cords from fixed points, from low-friction rail systems, from helium balloons...) will inevitably introduce forces that in turn interfere with the motion of the test article. This results in a distorted deployment trajectory and alters the force collective that acts upon the deployable during testing. Thus, the observed deployment mode will only partially reflect the situation in space. Consequently, active gravity offloading for deployment mechanism testing has been around as a concept for quite some time, with a

* CarboSpaceTech GmbH, Immenstaad, Germany; benjamin.krolitzki@carbospacetech.com

good and thorough overview over benefits and obstacles given by Fischer [4], and recently, some remarkable progress has been published [5].

While the basic requirements for a gravity offloading system are straightforward, translating them into a real test environment presents significant challenges. From the outset, our focus has been on providing a microgravity testbed environment, rather than interpreting the collected data. In terms of the actual testbed, published concepts tend to struggle with too little stiffness, too little speed, and too little range of motion. The most relevant systems are currently probably the Walking Anti-Gravity Machine (WAGM) and the Gravity Off-Load Follower (GOLF) [6], [5]; both feature a controlled Z-axis; however, z-control is not necessarily needed for deployment that is mostly in-plane (e.g. solar arrays). Despite the promising concepts and first results, current publications on gravity offloading stop short of a final conclusive, ready to use system, a gap we will try to bridge herein.

More Stiffness, Less Data: Lessons Learned during Concept & Development Phase and System Setup

The first functional prototype of our active gravity offloading system was constructed using leftover structural CFRP trusses from the breadboard phase of the EUCLID space telescope, providing rigidity with minimal mass. We opted for a parallel linkage mechanism, similar to a Selective Compliance Assembly Robot Arm (SCARA), which appeared to be an elegant solution due to its simplicity, featuring a single mounting point and rotational bearings. Implementing a controlled z-axis was achieved using a stationary winch and cable routed along one of the SCARA arms (Figure 1). However, target movement tracking via a camera system was challenging, as even at low resolution and a comparatively low frame rate of 120 fps, the data stream was too extensive to handle efficiently. Additionally, target recognition and image processing were prone to distractions, such as reflections, or, in one instance, too many engineers wearing white shirts in the room. Various mitigation approaches were attempted, including switching to infrared illumination, but with limited success. Moreover, the SCARA concept, comprising a series of cantilevered beams, proved demanding on the mechanical properties of the components, particularly the gear mechanisms and aluminum beam heads with bearings, but even the CFRP parts, which were found to be too soft for precise control with the SCARA arms extended to the full range of motion (approx. 3 m).

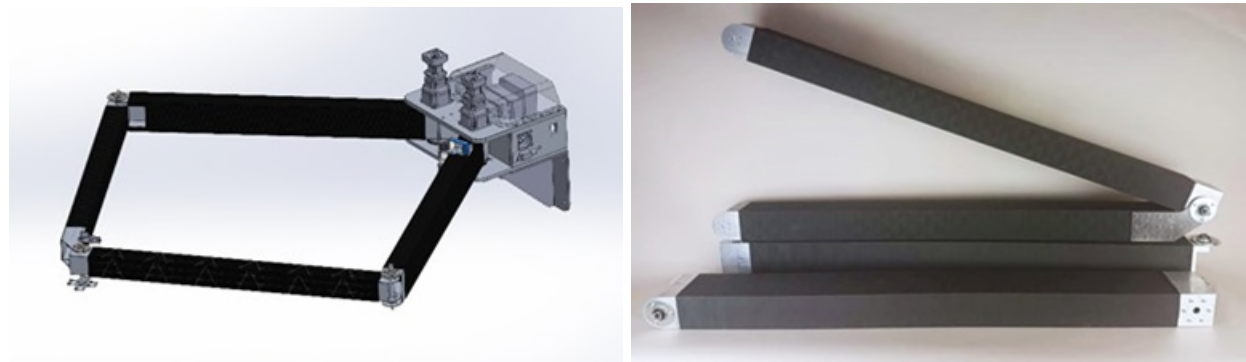


Figure 1: SCARA-gravity offloader design overview, the fully extended Range is about 3 m (left). SCARA-arms made from rectangular cross-section CFRP profiles with aluminum beam heads during manufacturing (right).

Consequently, despite the successful testing and the given potential for system expansion (i.e., multiple systems for multiple suspension points), we decided to pursue a mechanically less challenging variant with an x-y machine gantry. This decision involved sacrificing the elegant possibility of a controlled z-axis through a stationary winch, which was however deemed a minor limitation given that most deployments have defined planes or are cascaded, with pauses for system stabilization, between deployments on different planes (if any). The sensor concept was switched from camera target acquisition to line angle sensors, substantially reducing the amount of data processing. The mechanical stiffness of the machine

was greatly increased. The servo drives were replaced by linear motors. Sensor polling rate as well as control loop frequency were increased to 1000 Hz. However, the overall significant increase of the system bandwidth revealed another critical part of the system: the suspension cord that connects the test article to the machine. Besides suspending the article, the cord is also responsible for transmitting the positional information to the sensor. This transmission is limited by the eigenfrequency of the cord. Therefore, a cord with low eigenfrequency can limit the control bandwidth of the whole system. The eigenfrequency f_e of a cord under tension can be approximated by the formula for the first mode of string vibration (Eq. 1):

$$f_e = \frac{1}{2L} \sqrt{\frac{T}{\mu}} \quad (\text{Eq. 1})$$

L is the length of the cord, T the tension in the cord and μ the linear density of the cord (i.e., weight per length). Consequently, the tension in the cord is maximized by limiting the diameter. This approach is in turn limited by tensile strength of the material. The ratio of tensile strength to linear density must be high to achieve high eigenfrequency. Intentionally increasing tension seems counterintuitive, as this stands in contrast to the usual requirement of a high margin of safety (MOS) against rupture of the cord, but in this case, high eigenfrequency is essential for control bandwidth. Our solution was to perform proof loading of the installed cord to a margin of safety of 2.

For the chosen gantry configuration, unlike the SCARA, the motors for at least one axis now had to be moved with the system. Both the motors and the associated cable carriers lead to increased mass that had to be accelerated, and more friction. Still, high speeds and accelerations could be achieved with linear actuators on the x-axis. While manageable for the four independently controlled suspension points of the second prototype, this approach was nearing its viable limit (not least due to the sheer extent of necessary cable management).

Modularity is Key: Industrialization of the Concept

It soon became evident that the initial industrial application for such a system would be testing linear foldable solar arrays, with the benefit of active gravity compensation increasing with the complexity, i.e., the number of foldable elements. Since our goal was to provide a microgravity environment for large scale deployable mechanisms (preferably on-site at the customer's location), a modular system was the logical next step. With the requirement to facilitate the easy introduction of additional suspension points, the solution was to include all active elements in the individual traverses. To reduce weight and geometrical complexity, the cable chains were replaced by WiFi data links and conductive power rails to the control unit, and a friction wheel drive instead of a linear drive was chosen. Since translational speed requirements for the deployment of solar arrays were manageable and acceleration was limited by the suspension cord, the higher mass of the traverses limiting x-direction agility with friction wheel drive was considered an acceptable tradeoff. Due to availability of inhouse-manufacturing and the unmatched weight-to-stiffness ratio of carbon fiber, we stuck to this material for the traverses.

Think of the User Interface/Interaction Early On

Given the high level of functionality already achieved with our second prototype (stable, accurate, high speed, 4 suspension points), we were surprised by the mismatch of appraisal from potential users and the actual utilization rate of the provided testbed. The main reason was traced to usability issues: While the actual performance during testing and the acquired data was highly satisfying, the setup procedure and system operation was frankly quite cumbersome. Operation required continuous presence of a member of the development team, which meant this was no actual standalone system, let alone one that could sell as an industrial solution. Consequently, usability was emphasized during the development of the current, stable system early on.

One important improvement was to achieve easier mountability for the test article. While rapid exchange was not required, machine setup and remounting the test article should be feasible within one working day. Easy mounting of test article was initially lost along with the Z-winch in the transition from SCARA to the second (gantry) prototype, which was not beneficial for usability. With more suspension points, exact level alignment of all elements of the articulated test article becomes increasingly challenging. Thus, for fine adjustment of the elements, micro-winchers were introduced at each suspension point that were not included in the active closed loop but only used for the initial alignment of the full system.

Another improvement was the integration of remote-control functionalities. A handheld controller is used to switch system modes (inactive – handling mode - active testing - ...), with LED-strips on the traverses visually indicating the current mode. In active testing mode, the system exhibits high responsiveness, thus manipulation of the test article should be avoided during this mode, whereas during test article integration (handling mode), the system control is highly damped and speed is limited to provide a smooth and safe working environment. In addition, the LED-strips are assigned different colors to identify the traverses. The calibration procedure has been simplified to mass stabilization and sensor verification as described further down.

System Architecture and Calibration Challenges

To fulfil the goal of modularization, a decentralized system architecture with independent self-contained traverses was chosen. Each lightweight CFRP traverse contains a main controller board, which processes sensor inputs and runs the control loops depending on the chosen operation mode (integration or active offloading). See Figure 2.

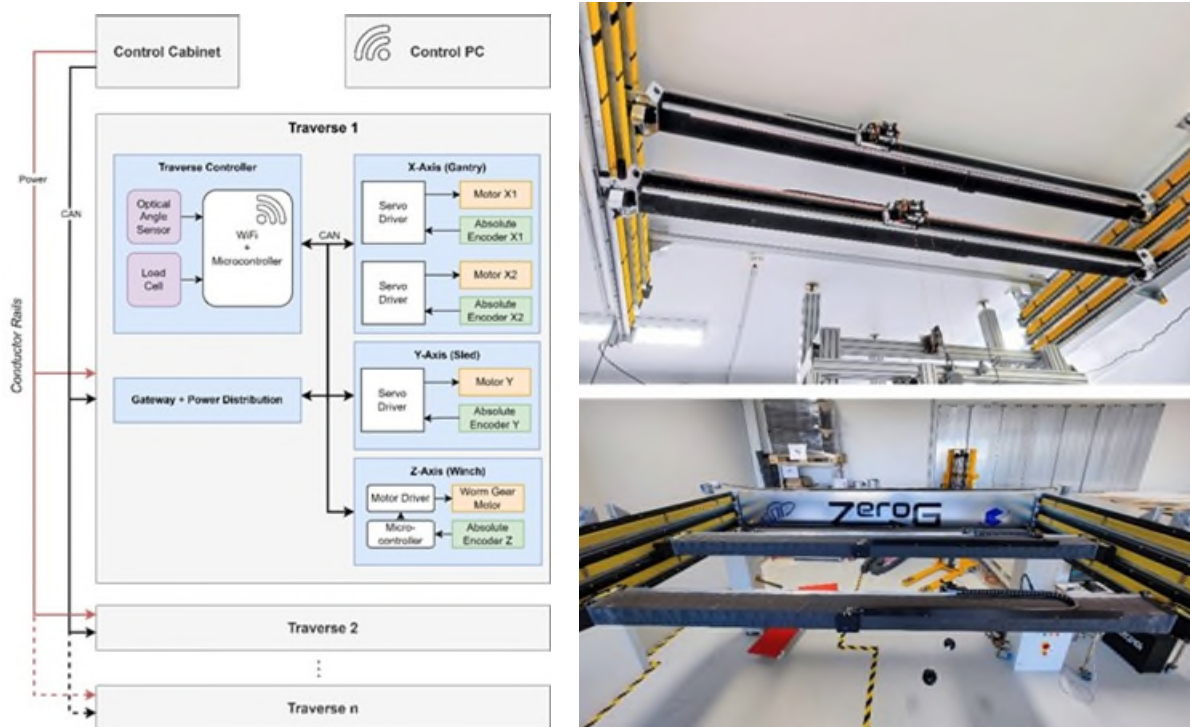


Figure 2: Modular system architecture with currently up to six traverses on three separate tracks (left). Right: Two traverses in operational condition visible. 2.40-m width covered by gantry, length modular up to 16 m with 30-mm stowed pitch.

Motor velocity setpoints are communicated via Controller Area Network (CAN) to the corresponding servo controllers. To avoid collisions with other traverses running on the same track, the current position and

velocity of each traverse is published on a dedicated CAN bus and evaluated in the control loops of the adjacent traverses. Brushless DC motors are used in combination with a friction wheel drive mechanism on all axes. Positioning accuracy is achieved using linear absolute encoders on each axis to eliminate remaining deviations due to wheel slip.

As noticed early on, the material of the suspension cords is crucial for system behavior. The initial first optimization strategy was aiming at high eigenfrequencies. However, it was observed during initial testing of the current setup that this approach is limited by another complication, which are the higher modes of the cord. These higher modes are extremely underdamped and feed back into the control loop, causing aliasing (higher frequency appearing as lower frequency). It was found that up to the 5th mode of a cord was visible in the signal. Given a first mode of 190 Hz this would equate to 950 Hz for the 5th mode. Since our sampling rate is 1000 Hz this would lead to the 5th mode being aliased to 50 Hz causing critical resonances in the servos. This essentially leads to an upper boundary of the eigenfrequency. From our testing we determined the eigenfrequency should be below 150 Hz. While different test articles may require some stiffness tuning, we settled on high-strength fishing cord for calibration, solar panel and generic instrument deployment.

For fine tuning of the offloading cords (z-axis), motorized micro-winches with self-retaining worm gears were developed and mounted at each suspension point (Figure 3). Additional passive springs (5.5 N/mm) mitigate any off-plane movements during deployment and compensate for remaining minimal inaccuracies of mounting (test article and system bed) for an unconstrained deployment.



Figure 3: Micro winch prototype during tension-loading test (left). Following validation of the prototype, a batch of micro-winches was manufactured and prepared for integration (right).

Calibration Procedure and Test Article Integration

During stabilization, the controller damps the oscillation of a suspended mass while keeping the original position (inputs=offloading line angle & position, output=velocity). As a result, the mass velocity and the offloading line angle will reach zero (Figure 4). This is used for zero-calibration of the system (Procedure 1, Figure 5). For the test mass, equilibrium is approximated within eight cycles. This method has the advantage of being unaffected by the non-linearity of the angle sensor as opposed to the commonly used approach of averaging multiple oscillations.



Figure 4: Several calibration masses were iterated. Despite the initial success with widely available rollerboards (left), we settled on the more standard ball of steel for calibration (right).

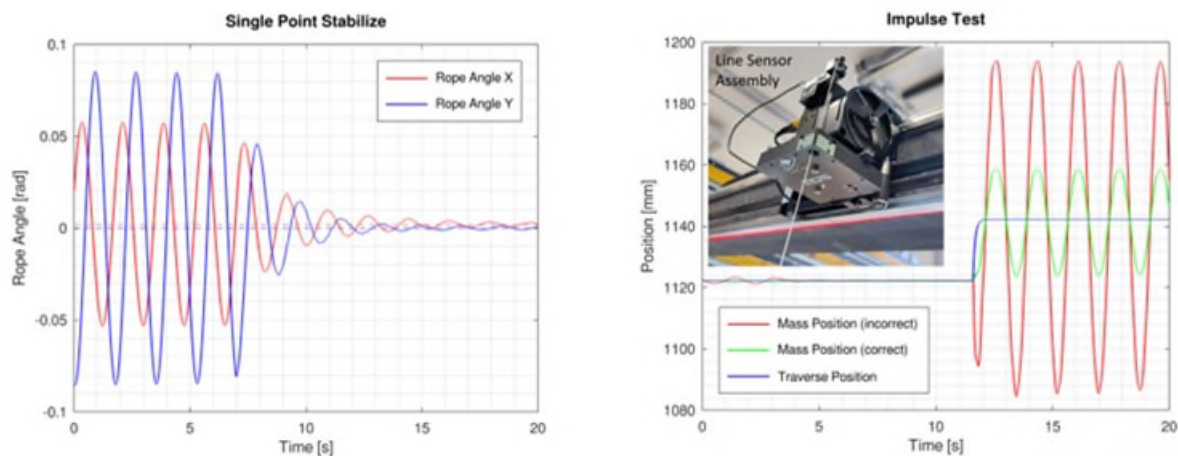


Figure 5: Single point stabilization. A free oscillating mass is suspended on an offloading line. Active damping the movement towards the original position (starting at 7.5 s) leads to decrease of amplitude (X&Y) of measured angle deviation from vertical over time (procedure 1). Right: Sensor proportionality verification is done by imposing a traverse position step onto a suspended mass with no external forces. Offloading line length is determined by the resulting eigenfrequency. Sensor proportionality is verified by comparing step length and resulting amplitude (procedure 2).

Following initial stabilization of the test mass, angle sensor proportionality is verified (procedure 2, Figure 5). Pendular motion of the test mass is induced by a defined position step in one axis. The observed frequency and amplitude are used to iterate the offloading line length and the test is repeated until the measured amplitude is within excitation step distance. After the system is stable and calibrated, the test article can be mounted on the suspension points.

After calibration, the test article (e.g., a solar array wing) is integrated into the offloader. The most straightforward approach was found to be hanging the individual components on the suspension points and mounting the hinge connections panel by panel while adjusting suspension cord length/tension in order to keep the force distribution constant. For this purpose, the micro winches proved to be essential. With the help of integrated force transducers, accurate leveling can be achieved by fine adjusting the suspension cord length (step length 0.025 mm). Passive springs mitigate any off-plane movements during deployment and compensate for remaining minimal inaccuracies of mounting (test article and system bed) for an unconstrained deployment. Sensor outputs are logged as force distribution over the suspension points during integration and deployment. The last preparation step is mounting the test article to the satellite simulator (in the case of solar wing deployment testing basically a sturdy vertical beam which keeps the wing root at its original position).

The system is then activated and remains active while folding the segments into the stowed position and then end-to-end deployment. While the system is active, data is constantly logged with a predefined sampling rate (up to 1000 Hz). A camera stream is recorded separately, and if necessary the log data and video may be synchronized in post processing using the LED status display. Easy data access has been found to drastically enhance the perception of usability, encouraging potential users to engage with the system.

How to Characterize and Validate an Active Gravity Offloading System?

While usability is something that we were able to approach in a straightforward manner, another related topic was less obvious: how can a gravity offloading system be characterized to give potential users a well-rounded picture of the system capabilities without going into detailed specifics?

There are already some ideas published. However, publications focus on “what do we know about our own system“, rather than what a user needs to know in order to decide if this system is applicable for their purpose. The core argument tends to be built on comparison to conventional offloading methods. However, we consider this sufficiently established, so we focus on a characterization that would allow for comparing our system to other approaches.

One common basic criterion is the maximum load that the system can support. Han et al. [6] determined this for the WAGM by actual proofloading of the inactive system with 711.7 N according to (customer) requirements and a subsequent damage assessment (none noted). A comparable test for our system was the piggyback-proofload-ride of one of our engineers (>75 kg equivalent to >735.8 N) on the traverse of the second prototype (Figure 6).

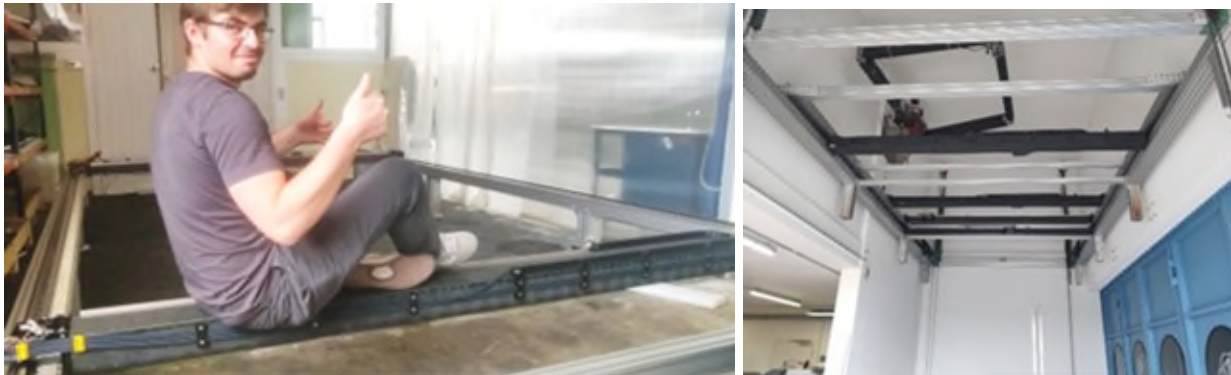


Figure 6: Proofloading of the gantry-prototype traverse (left). SCARA and gantry-prototype in their functional configuration (right).

Another easily accessible characteristic is speed and range in x, y and (if available) z directions. However, the actual max speed and max acceleration will depend on load, trajectory, and allowable error. Accordingly, the control error is actually the most important metric. Several approaches can be applied to describe the control error. A box test can be conducted, where the entire range of motion is covered. Alternatively, a typical trajectory can be defined and serve as a kinematic input for testing the offloader's ability to follow (Figure 7).

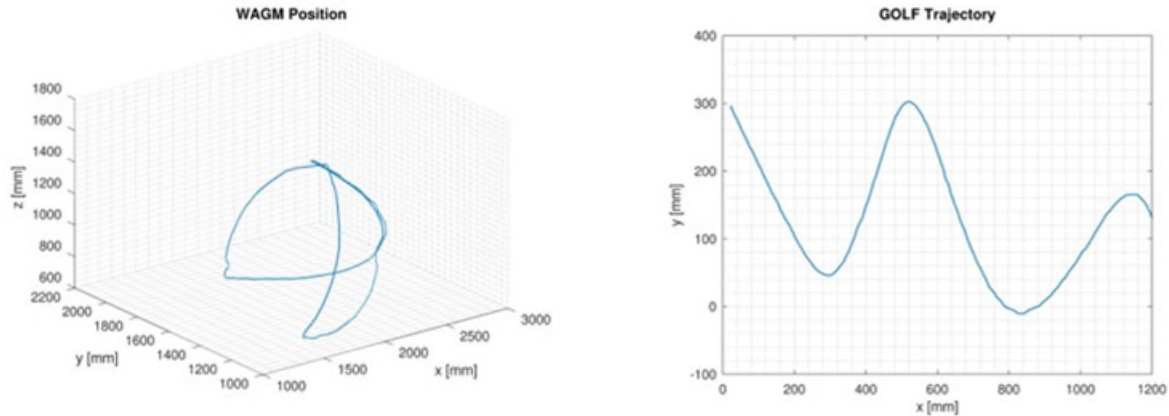


Figure 7: Box test trajectory as performed by Han et al. (WAGM, left). Right: Typical offload path trajectory-based characterization as proposed by Sullivan et al. for the GOLF-system. Data was extracted from the publications [6], [5].

Both approaches (box test and trajectory) provide information of higher-level system performance on a specific parameter range, either test-article specific (typical trajectory) or system specific (box test). We were looking for a more generalized system characterization and settled for a dynamic approach where a test mass is guided around a defined shape that provides challenging 90° trajectory turns – a square tracking test (SQTT or “Scotty”). The equipment for a basic test is very simple and can be 3D-printed (Figure 8). Guiding by hand is sufficient to cover a relevant range of speed, and because of its simplicity the test may be iterated several times to come to a conclusive result (Figure 9).

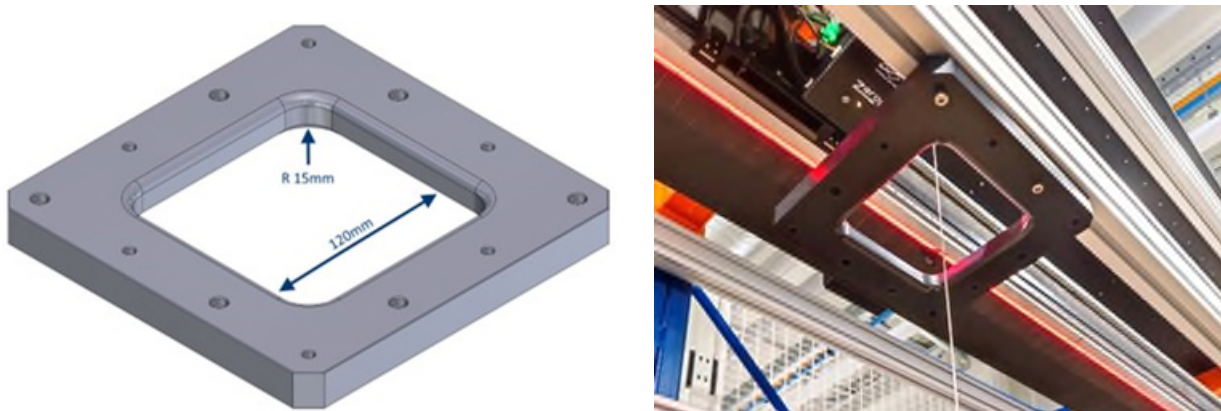


Figure 8: Proposed geometry for the SQTT test (left); 3D-plotted SQTT-frame mounted on the ZeroG with offloading cord visible in the center (right).

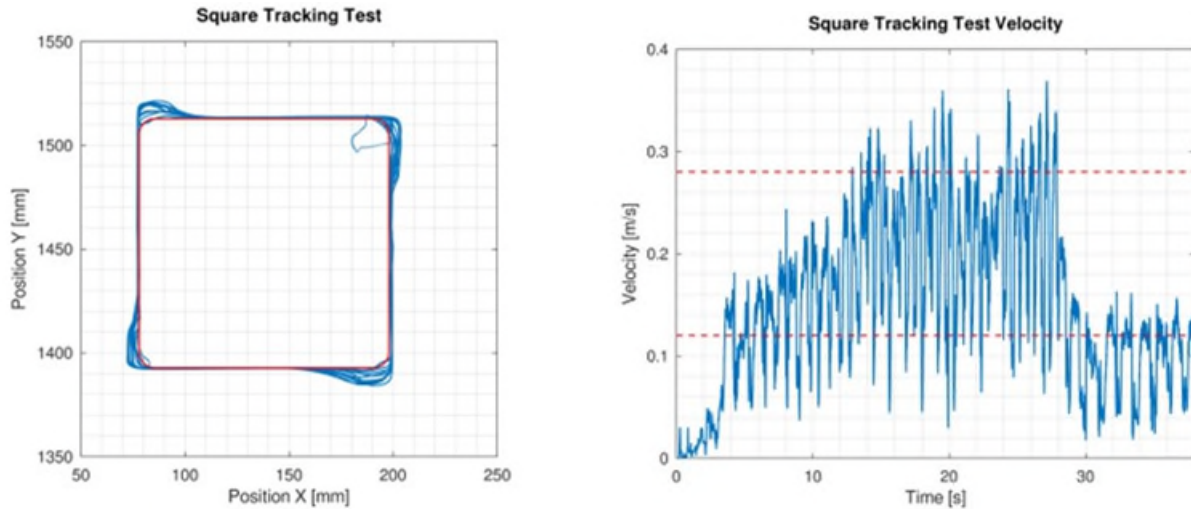


Figure 9: Proposed SQT; the velocities achieved by hand guiding along the trajectory defined by a pattern serve as a first approximation for estimating the system's response, the blue track representing the achieved trajectory and red the geometric pattern (left). The path velocity resulting from hand guiding shows negative peaks at the corners which correlate with the trajectory closer to the geometric pattern. The highest corner speeds of > 100 mm/s result in the envelope that represents the maximal deviation.

However, although the SQT offers a qualitative understanding of the system's capabilities, it lacks quantitative comparability. In order to use the SQT test to compare different gravity offloading systems, the geometrical offset of the trajectory and equally important force that results from said offset needs to be taken into account. In our setup (as in all systems using cords to suspend the test article below the offloading device) the resulting force depends on the length of the offloading cord (the z-distance between attachment points to the test article and the offloader). This will be further explored in the following deployment example.

Deployment testing examples

The ZeroG-device has been used in testing a variety of deployment mechanisms, most of which were deployable solar arrays except for one generic instrument boom with varying instrument payload mass at the tip. All shared the feature that deployment energy is stored in c-spring hinges, and thus show a characteristic "latching-kick", where the flattened c-spring bounces back to the original curved cross-section, which is particularly hard to integrate into passive gravity offloading concepts. Results from a two-sided, simultaneous deployment of two solar generator panels and deployment for one configuration of the generic instrument boom are shown.

For the symmetrical deployment of solar panels, half-circular trajectories with velocity (in the example, for the blue side) rising as a result of the stowed energy being transferred to kinetic energy over the process were recorded (Figure 10). Maximum velocity is reached during latching of the c-shaped metal hinges. The acceleration peak is accompanied by a sharp rise in error by a factor of 4 (to nearly 5 mrad, Figure 11).

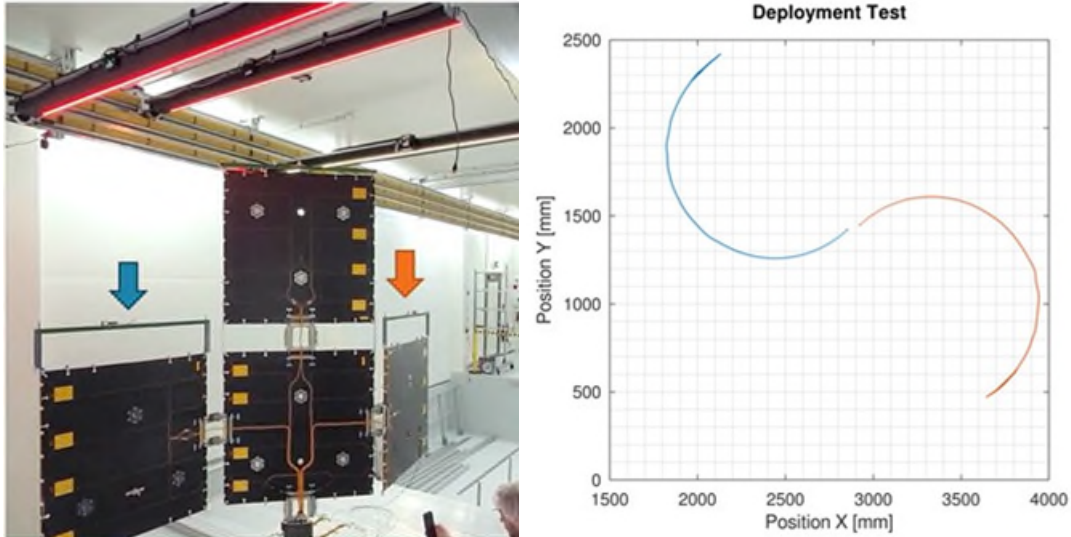


Figure 10: Deployment test for a multiple-panel solar array wing suspended on three offloading points (left picture). Right picture is the test article trajectory for left panel (blue) and right panel (red).

The tracing error from offloading cord angle can also be plotted as an impulse on the test article (direction and magnitude; Figure 11). The interpretation of this kind of diagram can help estimate the distortion of the free deployment that is imposed on the trajectory compared to a true zero-g environment. This could be used to limit the allowable impact of the system to a predefined impulse radius, which may even be defined with respect to time or deployment progress.

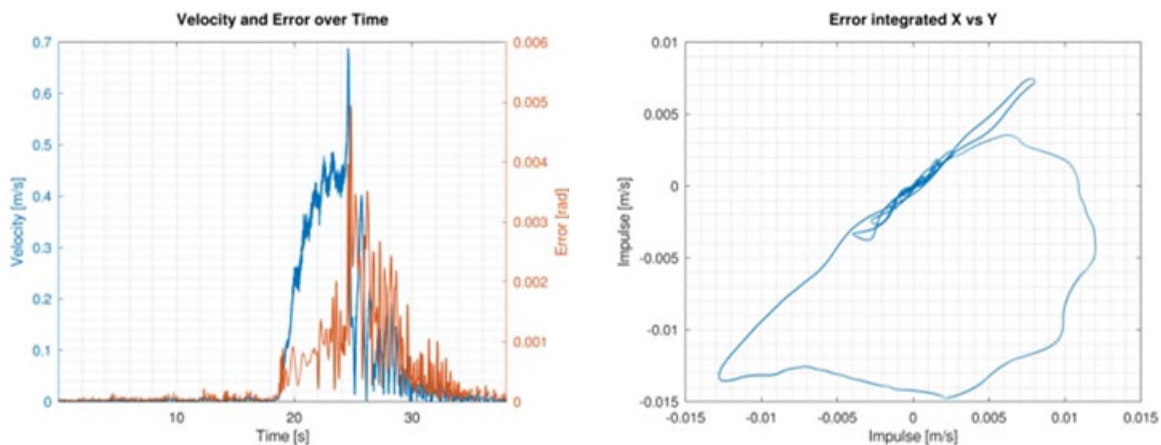


Figure 11: Velocity and error-plot over time, angular error peaking at latch-in close to 5 mrad (left). For small error angles, resulting acceleration equals the observed angle multiplied by gravity of Earth ($g = 9.81\text{m/s}^2$); i.e., 5 milli-g at latch-in. The error impulse can be derived from acceleration by integration. The integrated error is shown as a directional plot of impulse discrepancy induced by the gravity offloading system (right).

To explore further use cases for the ZeroG, a 1.8 m, 3-segmented boom with full-CFRP c-spring hinges similar to those used on the RIME instrument radar antenna of ESA's recently launched JUICE Mission was deployed, using the ZeroG system for gravity offloading. Results are shown here for a 0.3-kg instrument dummy at the boom tip (Figure 12, Figure 13).

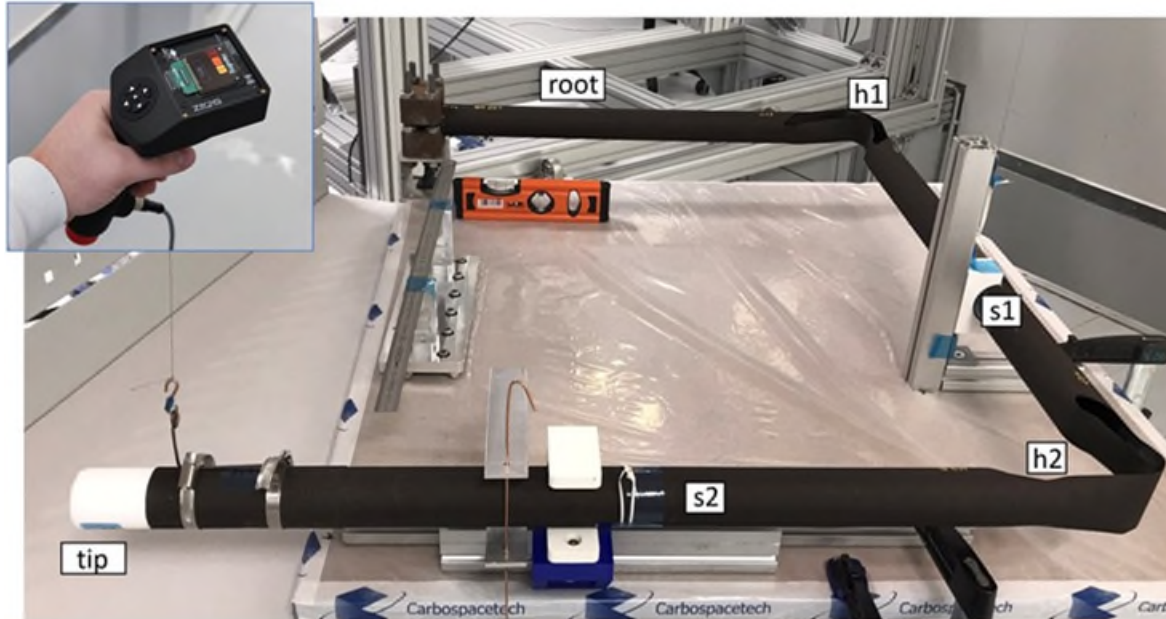


Figure 12: The handheld controller is used to move suspension points to the initial position for the generic instrument boom in the stowed configuration (hinges at 90°). The offloading lines are attached in the centers of gravity (cog) of segment 1 (s1) and segment 2 (s2). cog for s2 is close to the boom tip due to the instrument dummy mass.

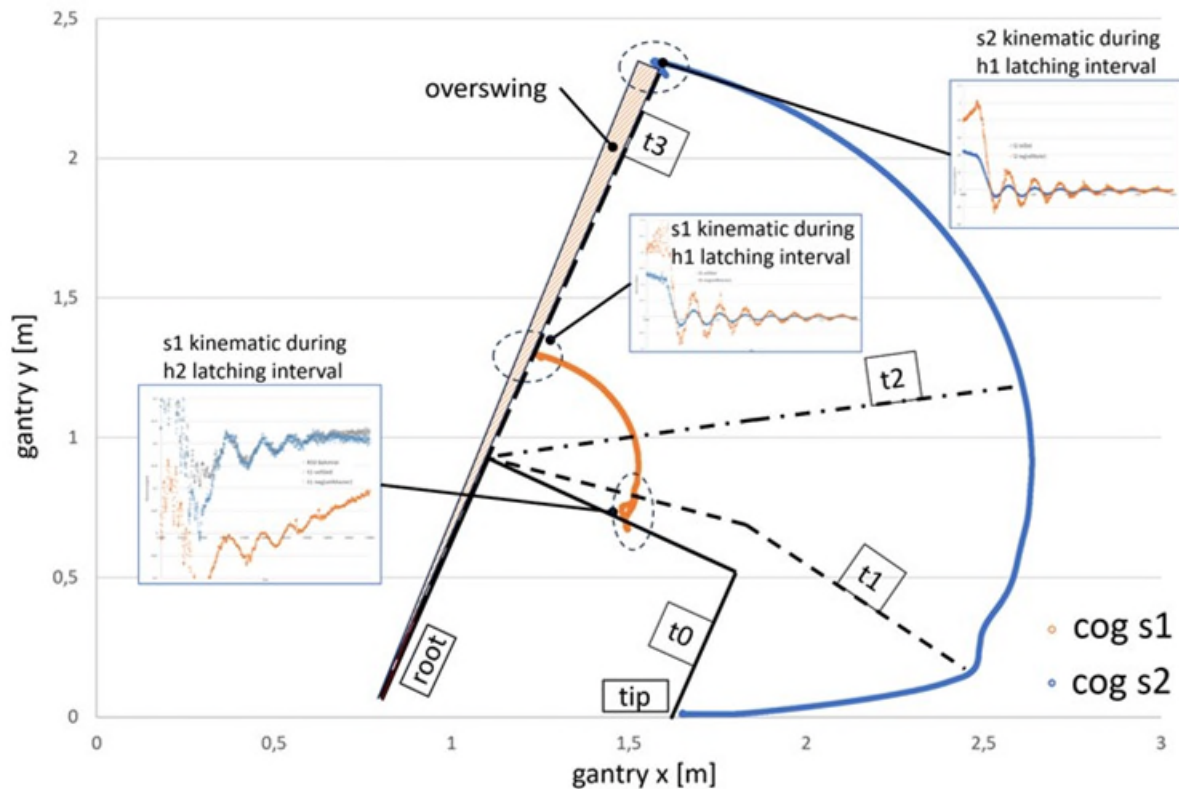


Figure 13: Deployment trajectory for instrument boom with 0.3-kg dummy mass at the tip with transient states t0 (release), t1 (both hinges deploying), t2 (outer hinge latched), t3 (both hinges latched, overswing oscillation fading).

Compared to the rather gradual deployment of the solar arrays tested so far, the instrument boom deployment was much more dynamic with a measured speed of up to 800 mm/s for the inner segment (Figure 14). Increased speed and acceleration during deployment and latching presented a challenge for the system, which manifested in elevated angular errors of up to 0.008 rad for steady state intervals of the trajectory and peaking at 0.027 rad during latching.

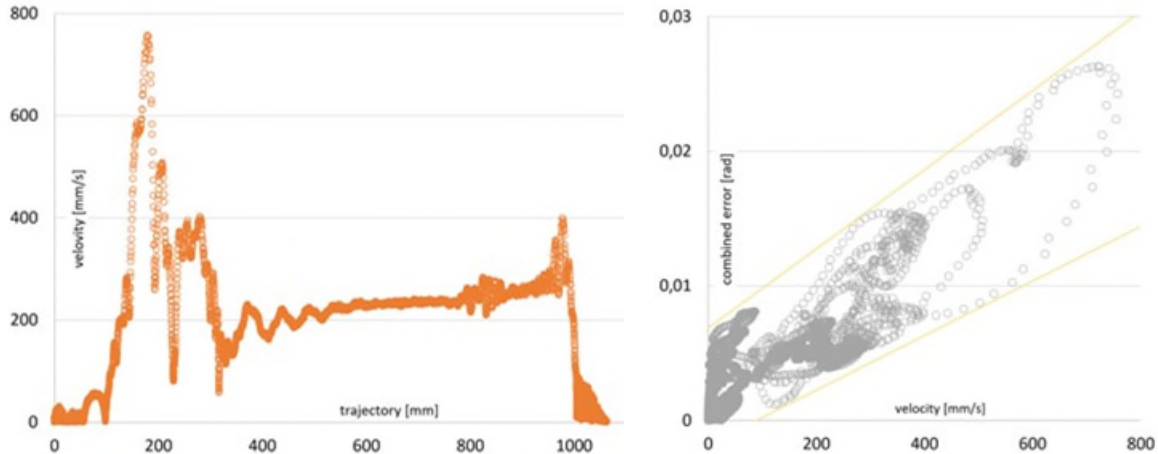


Figure 14: Velocity plotted along the trajectory for the inner segment s1. Latching of the hinges is clearly visible as two acceleration events at 200 mm and 1000 mm (left). Combined error (X and Y) correlates with velocity, with magnitude below 0.01 rad for the steady part of the movement and max error value of below 0.03 rad.

Nevertheless this was a successful first deployment of a multi-hinge instrument boom supported by active gravity offloading (something that would have been useful during the development of the JUICE RIME antenna). The capability to perform multi-hinge boom deployments using ZeroG opens new possibilities for exploring less frequently flown stowed-boom configurations (like the one shown in the example) with two 90-deg bent hinges.

Conclusion and Outlook

The ZeroG system has been developed well beyond the experimental stage. First applications in testing and integrating solar array wings and a two-hinged generic instrument boom made full use of the capability to support rapid deployment of multi-stage mechanisms. Mobility as a benefit of the modular layout is currently being field tested: One fully operational ZeroG-system (with 4 traverses & full range of 5.5 m x 2.4 m) has been built, set up, and calibrated at CarboSpaceTech (southern Germany) and was subsequently disassembled and shipped to the USA (Florida; Figure 15). At the time of submission, reassembly was still pending.



Figure 15: A modular ZeroG-system with four traverses is prepared for overseas shipping in one large box (left, ladder for scale). Right: With all Components neatly stacked, there would be room for another two traverses, allowing for six individual active gravity offloading suspension points at a stowed pitch of 30 mm.

One system with a full range of 16 m x 2.4 m remains at our facilities for further development and testing, with traverses 4, 5, 6 currently being integrated (Figure 16). A somewhat surprising effect of the overall usability noticeably freed up resources during verification testing, which inspired unscheduled rapid iteration of different conditions and parameters (e.g., variation of tip mass to simulate different boom instrument payload was impromptu integrated into the test). The system is fully validated for a payload range of 1 kg to 20 kg, and acceleration range of 1 m/s² to 10 m/s². Currently, those are preset limits and do not represent the full capabilities of the system. Payload capability was designed for a proof load of 100 kg, so the more prominent limitation is control bandwidth (response time, stability margins, actuator bandwidth, sensor bandwidth, control system design, etc.). All evaluations presented here were done from a practical perspective. Consequently, for the time being, an estimate for the trajectory velocity profile is required to assess if testing a specific deployable is possible without changing the control parameters or the suspension cord. To address this limitation, future work will include a comprehensive and detailed examination of the system with particular focus on the cord as a pivotal element within the control mechanism. Further software enhancements will expand the scope of the ZeroG-system to introducing external forces into a deployment to explore design margins or even emulate dynamic conditions (e.g., deployment on a rotating spacecraft and the accompanying Coriolis-forces). Emulation of external forces may also be used to create worst case situations for mechanism testing (e.g., acceleration to induce latching/overload failures, or application of opposing forces for torque margin analysis).



Figure 16: Latest version of the traverses with LED indicators visible running along the lower edge (left). Detail of a micro-winch with force sensor on the offloading cord (right).

References

- [1] A. Rivera and A. Stewart, "Study of Spacecraft Deployables Failures," in *Proceedings of the 19th European Space Mechanisms and Tribology Symposium ESMATS*, online, Sep. 2021.
- [2] R. Le Letty *et al.*, "The Successful Recovery of the JUICE RIME Antenna Deployment," in *Proceedings of the 20th European Space Mechanisms And Tribology Symposium ESMATS*, Warsaw (Poland), Sep. 2023.
- [3] J. D. White, "Test Like You Fly: Assessment and Implementation Process (commented presentation)." Space and Missile Systems Center, Air Force Space Command, Jan. 2010.
- [4] A. Fischer, "Gravity Compensation of Deployable Space Structures," Dissertation, University of Cambridge, Cambridge, 2000.
- [5] C. Sullivan, K. Gebhardt, C. Solis, T. Mitchell, and N. A. Pehrson, "Accurate Microgravity Simulation for Deployable Structures," in *AIAA SCITECH 2023 Forum*, National Harbor, MD & Online: American Institute of Aeronautics and Astronautics, Jan. 2023. doi: 10.2514/6.2023-1885.
- [6] O. Han, D. Kienholz, P. Janzen, and S. Kidney, "Gravity-Offloading System for Large-Displacement Ground Testing of Spacecraft Mechanisms," in *Proceedings of the 40th Aerospace Mechanisms Symposium*, May 2010.

Origami-Inspired, Re-Deployable, Compact Lunar Solar Array System

Alexander Gendell*

Abstract

NASA is returning humans to the Moon and establishing a long-term presence near the lunar South Pole via its Artemis missions. To accomplish this, a reliable, sustainable power source is required to support lunar habitats, rovers, and construction systems for future robotic and crewed missions. To provide this power, NASA issued a solicitation for vertical solar arrays that can autonomously deploy and retract for relocation as needed.

Introduction

Under a Phase I SBIR NASA project, Folditure began using its existing proprietary pyramid hinge technology to develop a new 10-kW Lunar Surface Solar Array: the Sunflake Solar Array (SSA) and Ultra Compact Tripod Tower (UCTT). Folditure is currently working on a Phase II SBIR NASA project for the 10-kW Array, aiming to bring the design to Technology Readiness Level 5.

With a subsequent Phase I SBIR NASA project for a larger 50-kW Lunar Surface Solar Array (the Sunflake XL), a new dimension to the scalability of the design was introduced. Together, these innovations provide unique, origami-inspired solutions for elevated lunar solar array systems.

Requirements

Both projects require lightweight, robust, re-deployable solutions that are supported on a stable base structure and can accommodate a terrain angle of up to 15 degrees. Because of potential terrain shadowing, the bottom of the array needs to be 10 m above the lunar surface. To capture the optimum and consistent power supply, the Array assembly is required to rotate 360 degrees, tracking the sun.

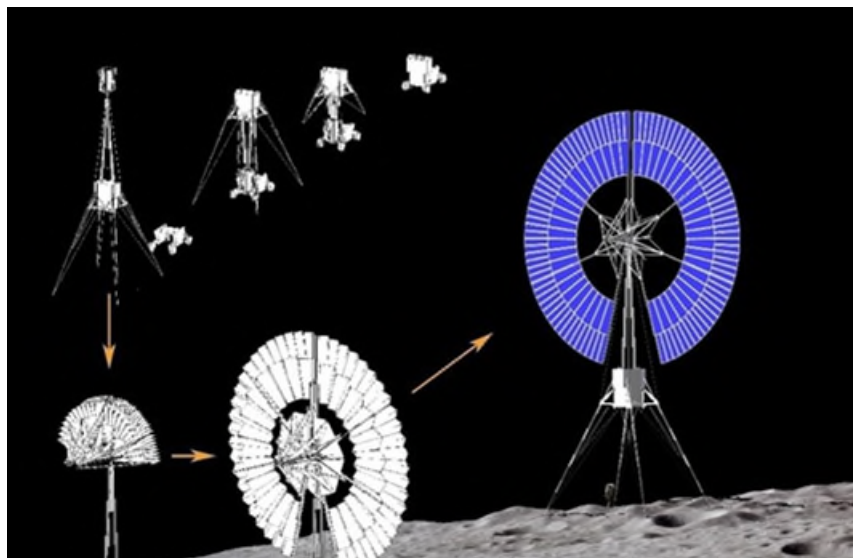


Figure 1. Rendering of 50kW Sunflake XL system

* Folditure, Hoboken NJ; alexander.gendell@folditure.com

Pyramid Hinge

The Pyramid Hinge is an origami-inspired, mechanical solution that allows flat panel-based designs to unfold into rigid 3-dimensional structures. The patented mechanism was originally developed for applications in foldable furniture, where torque to open and close the structure was applied by hand.

Pyramid Hinge Array

The Pyramid Hinge Array is a combination of Pyramid Hinge units that are deployed or retracted by a central motorized movement. In the Sunflake design shown below, a runner mechanism (R) pushes or pulls a pyramid angle lever (PA1).

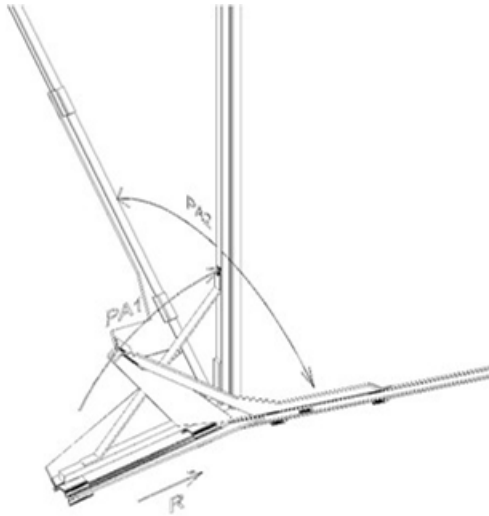


Figure 2. Single Pyramid Hinge Array segment shown opening

When approaching the open position, more force is exerted by the PA1 arm onto the PA2 angle, locking the array in place when fully open.

The three-dimensional “dead center” action of the opening geometry is a key feature of the Pyramid Hinge Array design. It assures that the array will always fully open and will easily retract.



Figure 3. Three-segment Pyramid Hinge Array shown opening

During project development, it was discovered that in certain conditions the same origami-based geometry can be implemented using thin linear structural members instead of lightweight flat panels. With this added versatility, the Pyramid Hinge Array can be designed with varying numbers of subdivisions. It also can be designed to have a fully open position that is less than 360 degrees.

XL Pyramid Hinge Array

In the new XL mechanism, a single linear motion in all directions powers the deployment and retraction of the entire array. The same runner assembly that opens the array radially also extends and retracts the XL solar panel support arms. In the current design, three levels of the extension arm support three levels of folded flexible Solar Array gores, which overlap when stowed. The current design enables a 175-m² array to have a stowed length of only 2.6 m.

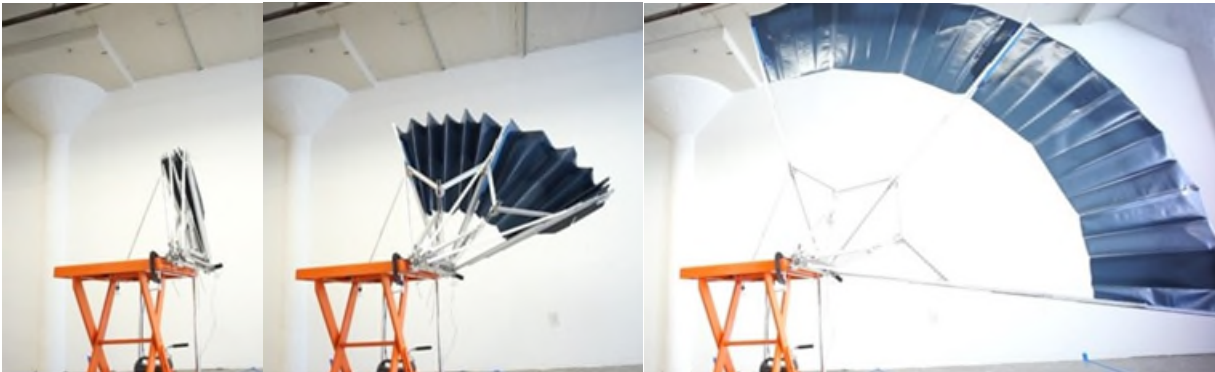


Figure 4. Prototype Sunflake XL array shown only with outer panel assembly

Number of Divisions, Runner Lever Assemblies, and “Dead Center” Action

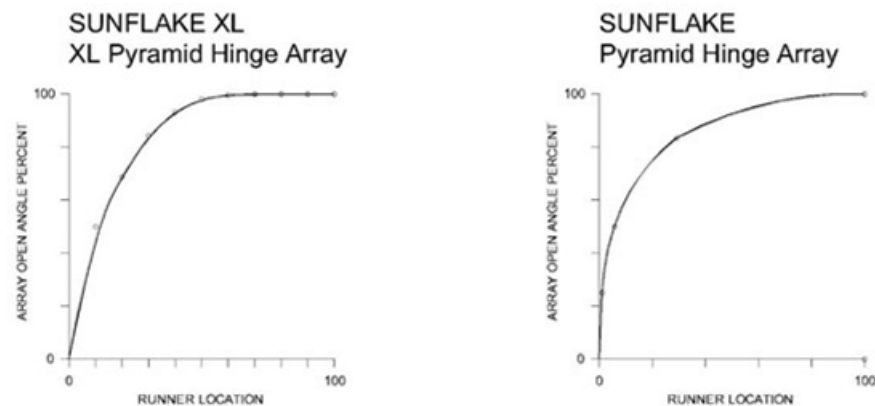


Figure 5. Runner movement and Array open percentage graphs

The Sunflake design has a fully open angle of 360 degrees with three pyramid hinge segments, making the PA angle (Figure 2) 120 degrees. The Sunflake XL has a fully open angle of 342 degrees with six pyramid hinge segments, making the PA angle 57 degrees.

The linear force applied to the runner assembly applies differently to the opening movement of the two designs. This is from the difference in PA angles, plus the different lever assembly designs. While enough force will always be available to lock the Pyramid Hinge Assembly in the fully open position, some initial force (other than the runner movement) might be needed to “pry” the array arms open a few degrees. This can be provided either by slight spring action, with lunar gravity (as in the case of the Sunflake Array design), or with a specially shaped runner mechanism that can pry the arms slightly open.

Overall Design and Deployment Sequence

The Sunflake/UCTT assembly was adapted to work with the Astrolab Lunar Rover, creating a comprehensive deployment, retraction, transportation, and storage solution. The flat, compact design enables four Sunflake/UCTT units to be transported and deployed by the rover.

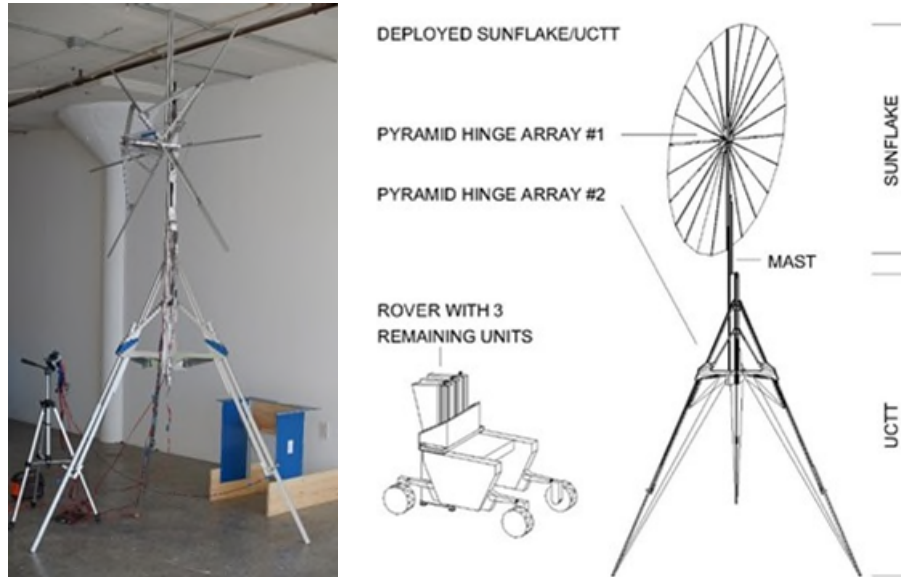


Figure 6. One-quarter scale prototype (left) Sunflake/UCTT components (right)

The UCTT was designed to provide a stable base for the Sunflake Array and allow space for the rover to maneuver underneath.

In the current design, four Sunflake/UCTT assemblies fit within a rack called the Sunflake Deployment System (SDS). The SDS is designed to meet the requirements of the Astrolab Rover front load payload. Because the rover can maintain a horizontal position on uneven terrain, the UCTT deploys vertically.

First, the mast lifts the UCTT above the rover, then it is deployed using a three-segment pyramid hinge array (similar to the Sunflake design). As it deploys, it positions three telescoping leg assemblies to a fixed angle, and the legs extend until they touch the terrain surface (Figure 7). The mast then moves in the opposite direction, lifting the Sunflake array out of the SDS assembly.



Figure 7. UCTT lifting (left) UCTT deploying (right)

Once the legs are deployed and the Sunflake clears the SDS and rover, the rover can move out of position. The Sunflake array continues lifting, opening once it clears the UCTT leg structure and reaches its deployed position (Figure 8).



Figure 8. Sunflake lifting (left) Sunflake deploying (right)

Mast Mechanism

A key component of this system is a robust, lightweight mast mechanism that can move in two directions. It moves in one direction to lift the UCTT, as shown in Figure 7, then it changes direction and lifts the Sunflake array, as shown in Figure 8. The novel gear and chain drive design, that helps the mast accomplish this, was implemented in the $\frac{1}{4}$ -scale prototype. Figure 9 shows part of the chain drive with the UCTT partially deployed.



Figure 9. Pyramid Hinge Array of UCTT opening leg structure

The larger $\frac{1}{2}$ -scale prototype creates a lighter, more scalable solution by using a mechanism that combines the chain drive with cables (Figure 10).



Figure 10. Five-component mast prototype

This new mast mechanism can have three or more linear components. While the driving chain is on the middle component in the current design of the ½-scale prototype, it can be positioned on any of the components. A great benefit of this mechanism is that the cable/harness can follow the same movement as the cable. The cable length is fixed, and there is no risk of stretching or entanglement.

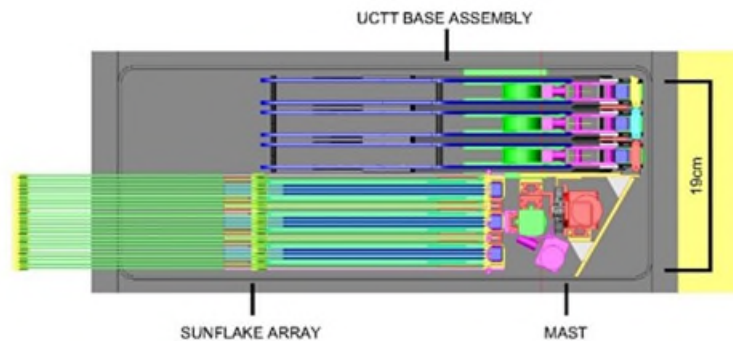


Figure 11. Stowed Sunflake/UCTT

Combining the Pyramid Hinge Array geometry with linear expanding structural members yields a compact, lightweight, and robust solution for providing solar power on the lunar surface. The current design performance is: 55.56-kW/m³ specific packing volume and 107.85-W/kg specific mass including all mechanical and electrical components. This exceeds NASA's requirements as stated in the solicitation.

Conclusion

The final Phase II SSA/UCTT design will have a 10-kilowatt capacity, and is engineered for deployment on the Moon with sun-tracking capability for optimal energy capture. When fully deployed, the structure will reach approximately 14 meters in height, including the mast.

Technology advantages over state of the art:

- The Sunflake Solar Array designs can easily be adapted for deployable arrays in microgravity and could be used on any mission that requires lightweight portable high-efficiency energy, including use on any form of human lander, future lunar outpost, or orbital station.
- The mast design is simple, robust and could be used at a much larger scale.
- Folditure's technology represents a shift in foldable solar array design, featuring compact folding and automated deployment, retraction, and re-deployment capabilities.
- The mechanisms are covered by existing and pending US patents.
- The technology can be manufactured using standard materials and manufacturing processes.

Acknowledgements

NASA SBIR contracts 80NSSC21C0199, 80NSSC22CA159, and 80NSSC23PB434 provided funding for the work. Special thanks to the team members, and NASA technical officers for their support.

Design and Testing of a Deployment Mechanism for NASA's 1,653-m² Solar Cruiser Sail

Zachary K. McConnel* and Mark S. Lake*

Abstract

NASA Marshall Space Flight Center (MSFC), in collaboration with Redwire and NeXolve, is advancing the design of a 1,653-tracm² Solar Sail System (SSS) for the Solar Cruiser mission. Since 2019, the program has been developing key components, including: the Sail Deployment Mechanism (SDM), high strain composite Triangular Rollable and Collapsible (TRAC) booms, and the ~ 413 m² thin film sail quadrants. In 2023 and 2024 validation testing was conducted to advance the SSS design to technology readiness level (TRL) 6 maturity. This testing demonstrated the challenges of using compliant mechanisms on such a large scale, and how the mechanism design and processes must be customized to enable the high strain composite structures to function properly. This paper describes the solutions the team found through the development and testing of a large-scale compliant structure which are necessary to support advanced mission concepts such as solar sailing missions.

Introduction

The SDM and TRAC booms [1], both developed and manufactured at Redwire in Longmont, Colorado, act as the deployment mechanism and support structure for the 1,653 m² Solar Cruiser solar sail (*Figure 1*), destined to orbit Lagrange point 1 and could support heliophysics studies along with other missions [2]. The TRAC booms are carbon fiber reinforced plastic (CFRP) with a laminate architecture referred to high strain composites. Redwire's Longmont facility (formerly Rocco) has specialized in high strain composite mechanisms for over a decade; each application comes with its challenges. For TRAC booms, these challenges come in the form of undesired buckling and delamination of the bonded edge during the stowing or deploying process. The latest laminate architecture designed for the Solar Cruiser mission proved to be resistant to both of these phenomena in early testing. After 4 years of development Redwire constructed the TRL 6 prototype to demonstrate the design's capability to survive environmental testing and deploy a full-scale sail quadrant.



Figure 1. Solar Cruiser TRL 6 prototype following single quadrant deployment testing.

* Redwire Space, Longmont, CO

Through two design/testing cycles, TRL 5 and TRL 6, the engineering team found and applied lessons learned to reach the results presented in this paper. This paper will primarily focus on the development of the mechanisms interfacing with the TRAC booms and the inherent challenges in testing compliant mechanisms for spacecraft on this large scale.

Background

Solar Sail Engineering Best Practices

The idea of solar sailing dates to the 1920's [3], but methods for engineering practical sail systems have only begun to emerge within the past 20 years. In 1999 the German Aerospace Center (DLR) proposed a now commonly accepted structural architecture for solar sails that includes four flexible booms co-rolled on a common reel and deployed in unison to tension four interconnected sail membrane quadrants [4]. This type of sail architecture was first flown in 2011 by NASA with the NanoSail-D mission [5].

At the 2016 Aerospace Mechanisms Symposium, engineers from NASA Marshall Spaceflight Center presented an 86 m² version of the 10 m² NanoSail-D2 sail system then under development for the planned NEA Scout mission [6]. That paper focused on the obstacles of scaling up the four-boom deployment mechanism to accommodate a larger deployed sail, and the lessons learned from a thorough development process. Design and flight-qualification of the NEA Scout system proved to require the development of approximately half a dozen prototypes to identify unforeseen problems, advance solutions, and build confidence in the final design product. The NEA Scout deployer utilized TRAC booms made of Elgiloy steel, which were prone to blooming and greater thermal deflection in comparison to composite alternatives. Meanwhile, Redwire developed a family of compact deployment mechanisms for high-strain composite booms [7] and advanced manufacturing and design best-practices for large-scale Triangular Rollable And Collapsible (TRAC) booms and their deployment mechanisms [8] to support NASA's quest for practical large-scale solar sail missions.

Challenges in Developing the Solar Cruiser Sail System

In 2020, A team led by NASA's Marshall Space Flight Center and including Redwire and NeXolve was funded to develop the Solar Cruiser mission to mature solar sail technology for future mission use in the 5–15-year timeframe [2]. The Solar Cruiser sail is the largest yet designed for flight with a 1,653 m², 2.5-micron thick sail membrane deployed by four 29.5-m composite TRAC booms (see *Figure 2*). In comparison to the 86 m² NEA Scout sail deployment mechanism, Solar Cruiser's deployment mechanism measures over ten times larger, while sharing many of the same engineering and development challenges (see *Figure 3*).

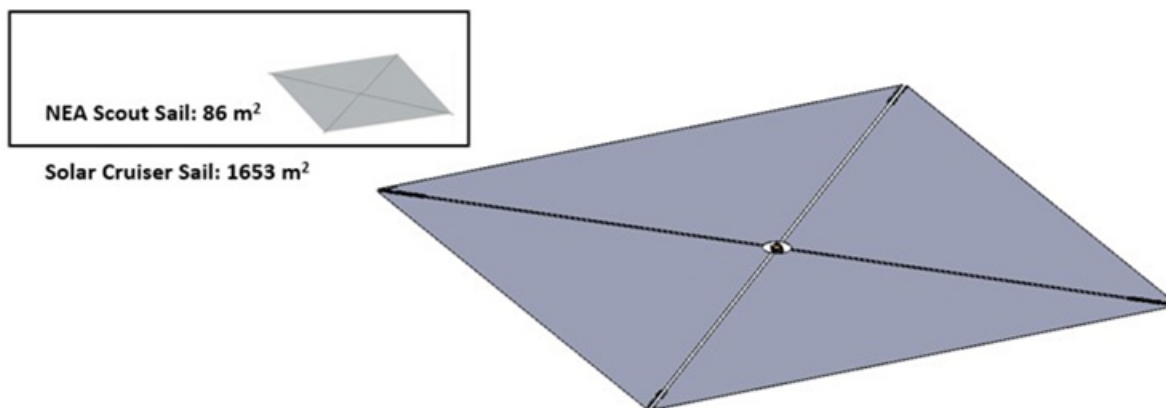


Figure 2. Solar Cruiser sail system compared with NEA Scout system, in deployed states.

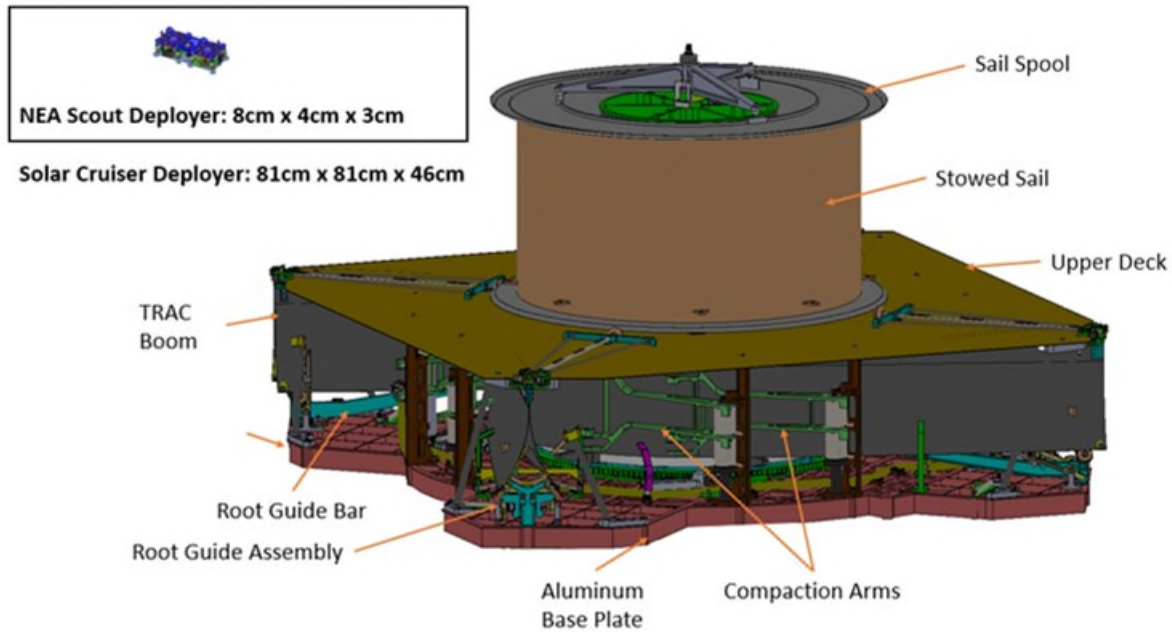


Figure 3. Solar Cruiser sail system compared with NEA Scout system in stowed states.

Scaling the sail deployment mechanism starts with scaling the deployed TRAC boom to accommodate longer length, higher stiffness, and increased stability requirements for the larger sail application. While attention must be given to structural scaling for deployed performance, equal attention must be given to ensuring the boom design provides adequate furling performance. Specifically, inner flange buckling of TRAC booms (see Figure 4) is a complex failure mechanism that can develop during boom furling and lead to packing inefficiencies and boom failure [8]. Inner flange buckling was a significant issue for both the NEA Scout sail deployment mechanism development [6] and the Solar Cruiser deployment mechanism development discussed here.

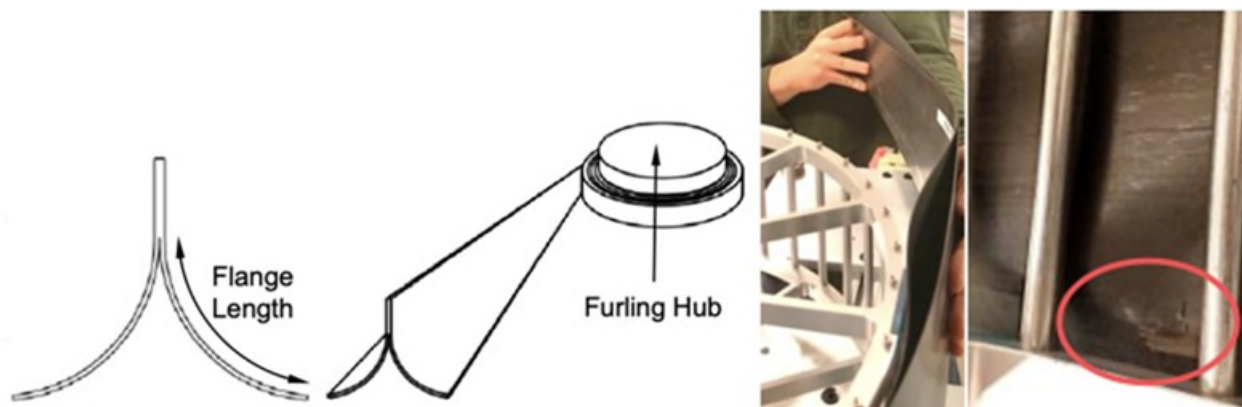


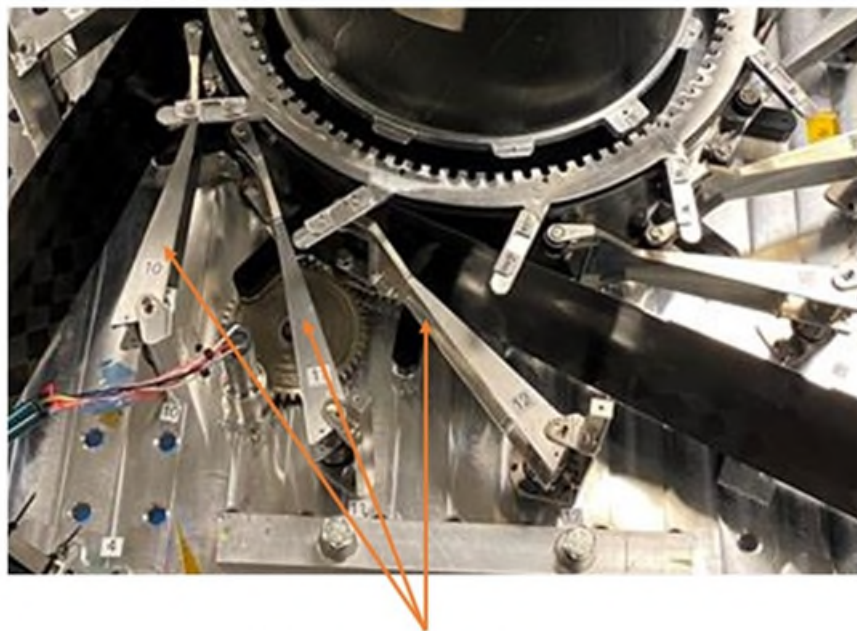
Figure 4. TRAC boom cross section (left), furling configuration (center-left), inner flange buckling mode (center-right), and material fracture failure mode enclosed in red circle (right).

Early during the Solar Cruiser program, an extensive engineering study was performed by Redwire to optimize the TRAC boom design to best-meet the packaging and deployed structural performance requirements of the mission [9]. This development program encompassed testing of a series of full-scale and sub-scale test articles in combination with an extensive finite element analysis effort to characterize packaging and deployed structural performance. In parallel with this effort, a series of EDUs were developed and tested for the system culminating in a first full-scale deployment test of an initial (TRL 5)

system including two TRAC booms and a single sail quadrant in 2022 [10] and a second full-scale deployment test of a flight-like (TRL 6) system in 2023-2024. The present paper summarizes lessons learned from this engineering development program.

Brassboard Prototype and TRL 5 Testing

The Brassboard prototype allowed for rapid testing and design iteration on the Solar Cruiser scale. The prototype allowed for functional testing of the mechanism while not meeting all flight requirements such as mass budget and thermal resilience. Full stowing efficiency, simply defined as a lack of inner flange buckles on multiple wrapped TRAC booms, was a goal for the new laminate architecture and Brassboard prototype. Notably, the design includes compaction arms and keys to contain the TRAC booms in their stowed wraps. The compaction arms have torsion springs which provide inward force through rollers to the stowed TRAC booms' outer circumference (see Figure 5). This compaction force prevents inner flange buckling during the furling and deploying processes.



Compaction Arms

Figure 5. Compaction arms on Brassboard prototype.

The keys are fixed to the top of the boom hub (see Figure 6), and interface with notches [11] cut into the web of the boom. The notches are cut early in the assembly process to allow for cleaning processes to take place. The deployment is driven by a single motor rotating the boom hub. The notches act as hard stops for the keys preventing blooming between wraps during deployment and driving the booms outward.

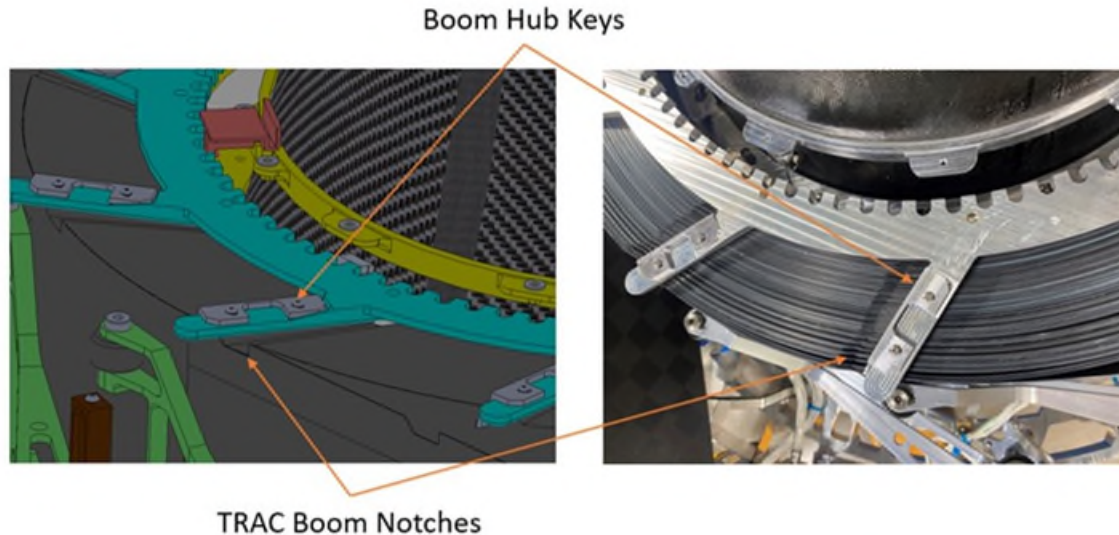


Figure 6. Keys and notches shown in the Solar Cruiser CAD (left) and actual prototype (right).

This brassboard prototype SDM was functionally tested in two forms: 1) with four subscale booms and 2) with two full length booms. Both tests yielded a better understanding of the capability of the sail deployment system and the behavior of the CP-1 sail material as it unfolds in ground testing. A detailed summary of these tests is included in “Test of a Full-Scale Quadrant for the 1,653 m² Solar Cruiser Sail” [10].

The first brassboard prototype test demonstrated that four 7.5-meter TRAC booms could be stowed effectively with no inner flange buckles or delamination and deploy four 1/16th scale area sail quadrants wrapped on a single hub simultaneously. During this test the booms were deployed above the sail quadrants to avoid any snagging on the notches as shown in Figure 7.

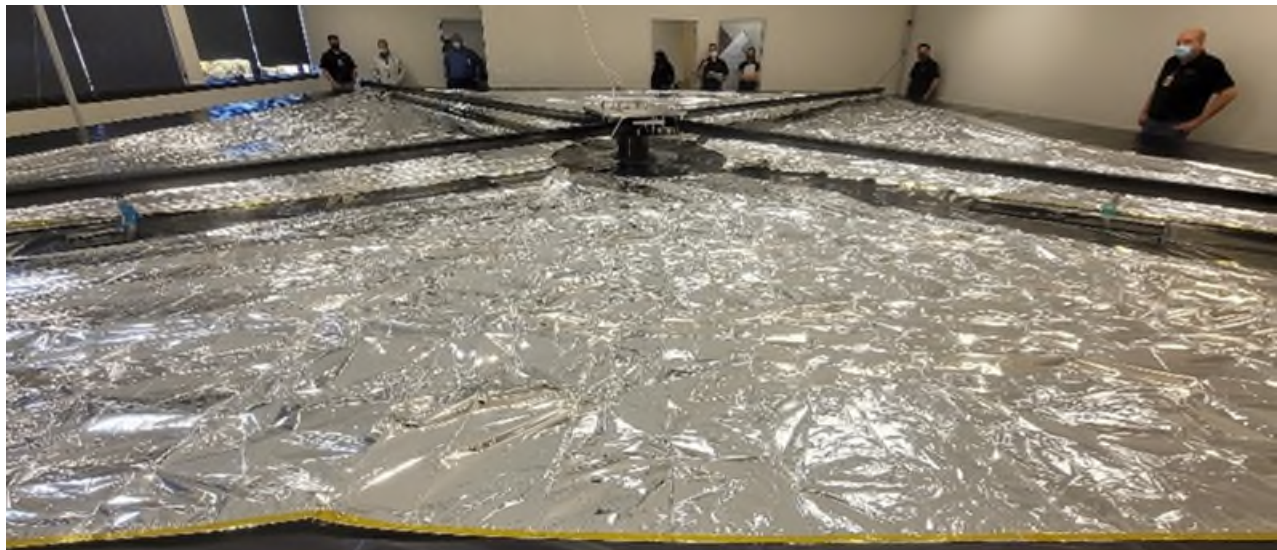


Figure 7. Brassboard Prototype deploying four quarter length booms and four 1/16th scale area sail quadrants.

The second brassboard prototype test demonstrated that two 30-meter TRAC booms could be stowed effectively with no inner flange buckles or delamination, and the SDM could deploy a full-scale sail quadrant as shown in Figure 8. During this test the sail quadrant was deployed below the booms and along a layer of anti-static film to minimize friction with the floor and un-realistic deployment resistance forces.

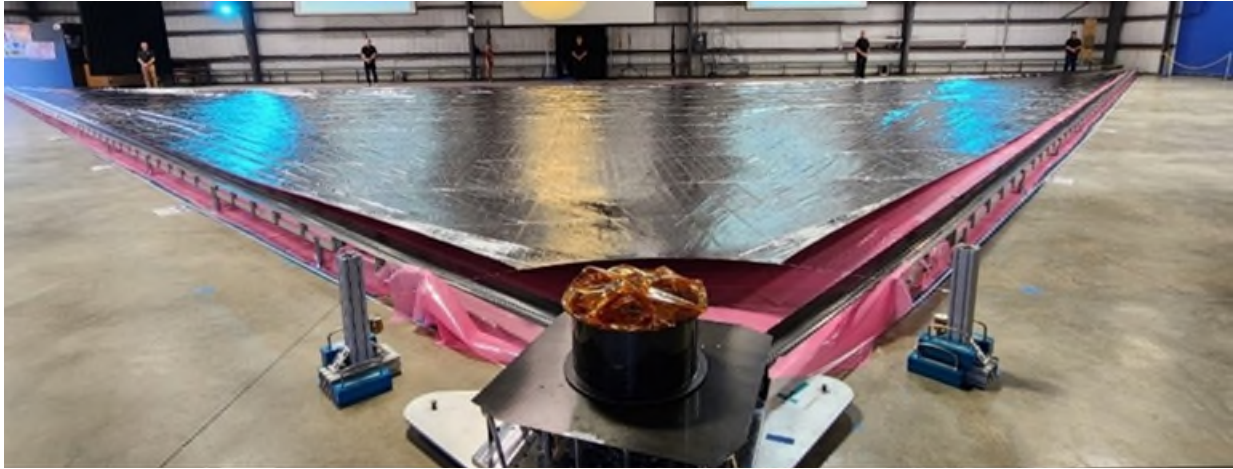


Figure 8. Brassboard prototype after deploying a single full scale sail quadrant with two full length booms.

Challenges with Ground Testing

Ground testing the Solar Cruiser deployment system in gravity presents many challenges, as the mechanism is designed to function in a microgravity environment. For the full-scale test, a single sail quadrant was deployed instead of the four quadrants in the flight design, to limit the cost and complexity. Finding a facility large enough to deploy a single quadrant was a challenge in early planning; much more difficult to find one for more quadrants. Access to the deployer and monitoring the sail for snagging were concerns for the deployment test, which were simplified by only deploying the single quadrant. The ground support equipment (GSE) roller and track assemblies supported the booms against the vertical and lateral loads experienced due to gravity and the absence of adjacent sail quadrants. The deployment area for the sail was covered in an anti-static low friction material to prevent snagging. The sail was deployed on the ground to allow for sail snag monitoring through relatively higher vantage points and to remove the cost of manufacturing a massive table surface.

In first assembly, two TRAC booms of the Brassboard deployer were supported by lower friction rollers than the GSE rollers used in the deployment test. This resulted in a newly observed phenomena known as notch migration. Due to the slightly greater tension put on the booms in this subsequent furling, the layers wrapped tighter on each other, shifting their relative notch locations. This only became an issue in the outer wraps which caused a slight interference between the key and notch. From this the team learned that the TRAC booms must be initially furling in the same loading conditions as future stowing procedures following deployment tests.

Solar Cruiser TRL 6 Prototype Assembly and Testing

To achieve a TRL 6 designation, the design team within Redwire built on the success of the Brassboard prototype, with a lightweighted design featuring flight materials and coatings. Solar sail performance requires a high area to mass ratio to achieve the necessary thrust performance. The updated design still used the same boom interfacing mechanisms developed on the Brassboard, with compaction arms, keys and notches. The TRL 6 prototype satisfied the flight configuration of four full length TRAC booms and only eight compaction arms for lightweighting. Once the assembly was complete, the solar sail system underwent vibration and thermal vacuum (TVAC) testing (see Figure 9). Intermittently throughout these tests, the launch restraints were released, and booms partially deployed to show functionality in environmental testing. Following these tests, a full-scale sail quadrant deployment test was performed, with two booms fully deployed outward and two spooled on GSE spools in January of 2024 (see Figure 1).

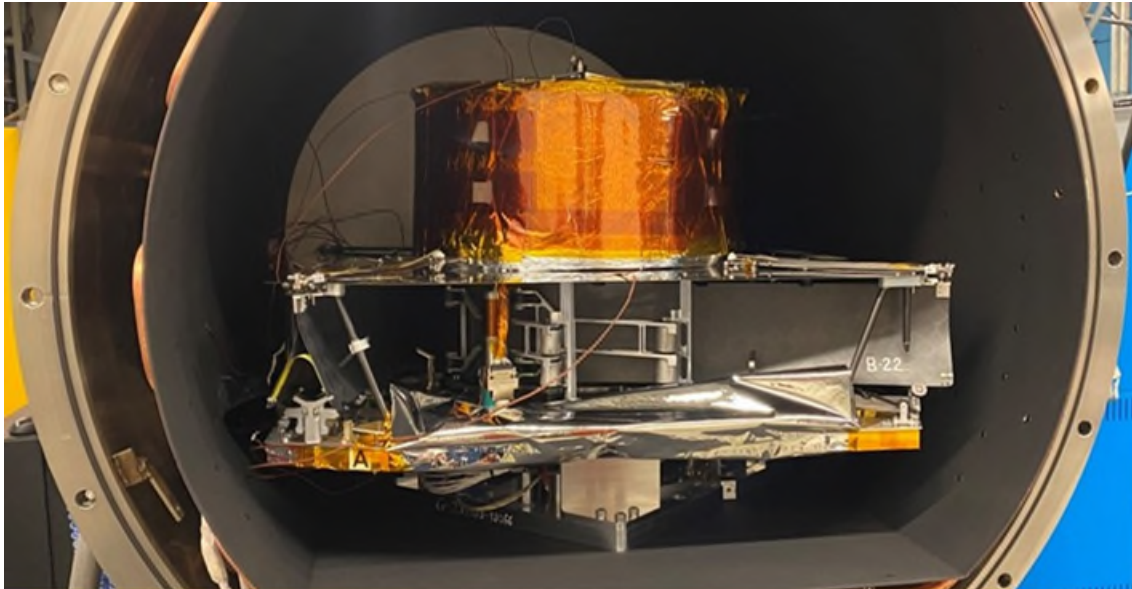


Figure 9. TRL 6 prototype in TVAC chamber before testing.

Complications Due to Inner Flange Buckling

Early in the assembly process, the four full-length TRAC booms must be stowed onto the deployer. This was foreseen to be challenging with the eight-compaction arm design, so four additional GSE compaction rollers were added to the system, which aided in the stowing process. After roughly a third of the boom length had been stowed, inner flange buckling began to occur. These buckles can be mitigated by manually applying pressure to the buckle location or reversing the motor direction; these mitigation strategies can also increase the buckle's amplitude or shift them farther in the wrap (see lefthand photo in Figure 10). The stowing process had been slowed down immensely, with buckles continuing to form until the end of stowing, increasing in frequency towards the outer wraps. Due to the successful furling of the booms on the Brassboard prototype, the inner flange buckling was not foreseen as an issue that would cause deployment failure on the TRL 6 prototype. As full stowing efficiency was not a project requirement, the project team agreed to accept inner flange buckling due to assembly timeline constraints. Therefore, notches were cut into the booms in this stowed configuration (see righthand photo in Figure 10).

Note that during testing a revised boom-stowage procedure was developed that completely eliminates the incidence of inner-flange buckling. This revised stowage procedure and implications for future work will be discussed later, but at this early juncture in the program a certain amount of inner flange buckling was accepted along with a degree of detrimental functional performance of the system due to the incidence of inner flange buckling. For example, the decreased stowing efficiency due to inner flange buckling was measured in roughly 1 cm asymmetrically added to the outer diameter of the stowed booms. The added diameter to the stowed booms on the hub caused an aluminum root guide bar positioned between the flanges of the TRAC boom, to bend outward beyond its intended travel. A small bearing on the end tip of the bar failed in early testing, breaking into pieces from the additional radial load in this deflected position. This bearing was repaired before final assembly, and not damaged again, but was an early indication to the importance of full stowing efficiency. The angle of the boom at its tangent point on the stowed wrap relative to the guide frame on the edge of the deployer changes as booms are furled onto the hub. The guide frame has rollers which provide downward force to the top web of the booms, the width of this roller is also based on the assumption of full stowing efficiency. Towards the end of the stowing process, the boom web tended to move to the side of the roller, due to the boom tangency angle changing beyond what was expected of the design. The assumption in design of full stowing efficiency led to these complications and has been noted as a potential tolerancing improvement on future designs.

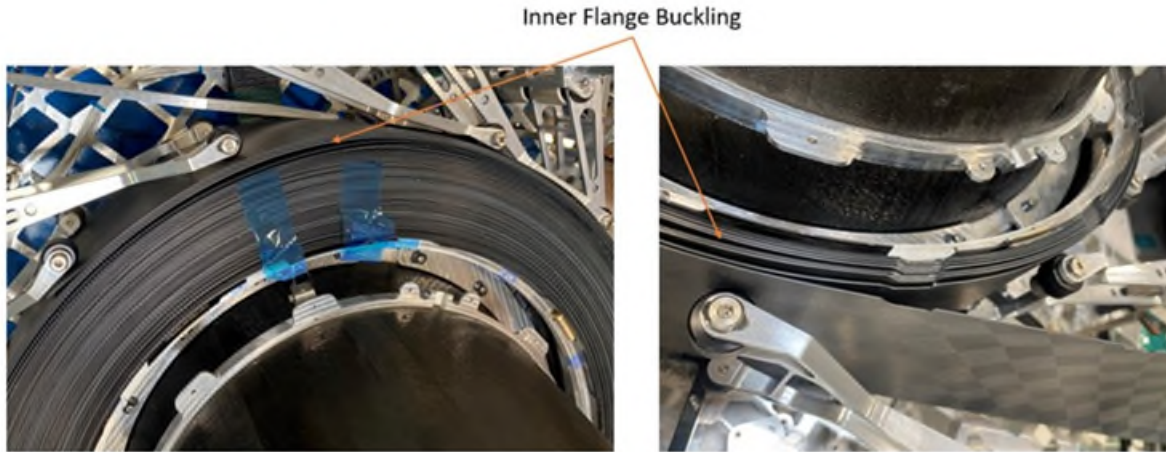


Figure 10. Inner flange buckling on TRL 6 prototype before (left) and after (right) notching process.

From the lessons learned on the Brassboard testing, the four full length TRAC booms were initially stowed on the same GSE intended for TRL 6 testing. This was intended to prevent the notch migration observed from changing boom support conditions. However, inner flange buckles form somewhat randomly during the stowing process, so there is no guarantee that boom notches will align properly after repeated deployment and stowage cycles. Indeed, variations in the formation of inner flange buckles were observed on the final deployment and stowage cycle for the SDM and the four TRAC booms prior to integration with the sail quadrant for final system deployment testing (see Figure 11). For this reason, a second notch cutting process was conducted in the final assembly steps leading up to testing of the complete system. Modifying these notches introduced foreign object debris (FOD) to the assembly, an acceptable level for ground testing but undesired for flight missions with contamination requirements. A second notch cutting processes would not be taken for a flight unit, however they were necessary to continue with planned ground testing.



Figure 11. Notch migration due to inner flange buckling, prior to second notch cutting process.

In the assembly process, a single deployed TRAC boom was measured and cut to the designated length. The other three booms were cut to length relative to points on the deployer, after a partial stowing procedure. The inner flange buckling was present in this process, resulting in the booms not fully stowing consistently in subsequent stows. A single boom would reach its fully stowed position while the other three remained slightly deployed to varied lengths. The greatest length being 1.3 cm from full stow, inhibiting launch restraint features in the system. To properly dock for vibration testing, the booms were manually pushed into position. This resulted in blooming of the outer wrap of the repositioned booms between compaction arm rollers. This blooming was shaken out in vibration testing, causing the booms to prematurely return to their not fully stowed states. In a flight configuration this would result in a premature tearing of the sail's launch restraint membrane.

Small design changes will be able to mitigate the complications mentioned above, however it is apparent that achieving TRAC boom furling without inner flange buckling is essential. Furthermore, it is essential to provide the time and attention to achieve full stowing efficiency before the booms are notched or cut to length. The decision to move forward with the assembly despite having inner flange buckles resulted in many unforeseen complications in the remainder of testing. At the time of this decision, it was unknown if the four TRAC booms could be stowed with full efficiency at the current scale. Following the successful deployment test, this uncertainty was reduced with the team accomplishing a full efficiency stow without inner flange buckles.

Post Test Stowing – Elimination of Inner Flange Buckles

Following the full-scale single quadrant deployment test of the TRL 6 prototype shown in *Figure 1*, the system was left in its deployed state for sail measurements to be taken. Once the sail was folded and removed, the team cautiously began the stowing process, knowing inner flange buckling was likely to occur. With careful attention, and moderate manual adjustments, the team was able to effectively stow the four full length booms on the sail deployment mechanism without any inner flange buckles. Some new techniques were utilized to adjust the height of the booms, deployer and GSE relative to one another. Even after a successful stow without inner flange buckles, the combined thickness of all the wrapped booms was 5.9 cm, where in the CAD it was represented with a thickness of 5.2 cm. This difference in thickness exemplifies an assumption of stowing efficiency that can be better accounted for in the deployer's design. As the notches were originally cut and recut with inner flange buckles present, the notches were misaligned. Improved processes, GSE and component level design modifications will improve the repeatability of stowing without inner flange buckles and improve the mechanism's resiliency to losses in stowing efficiency.

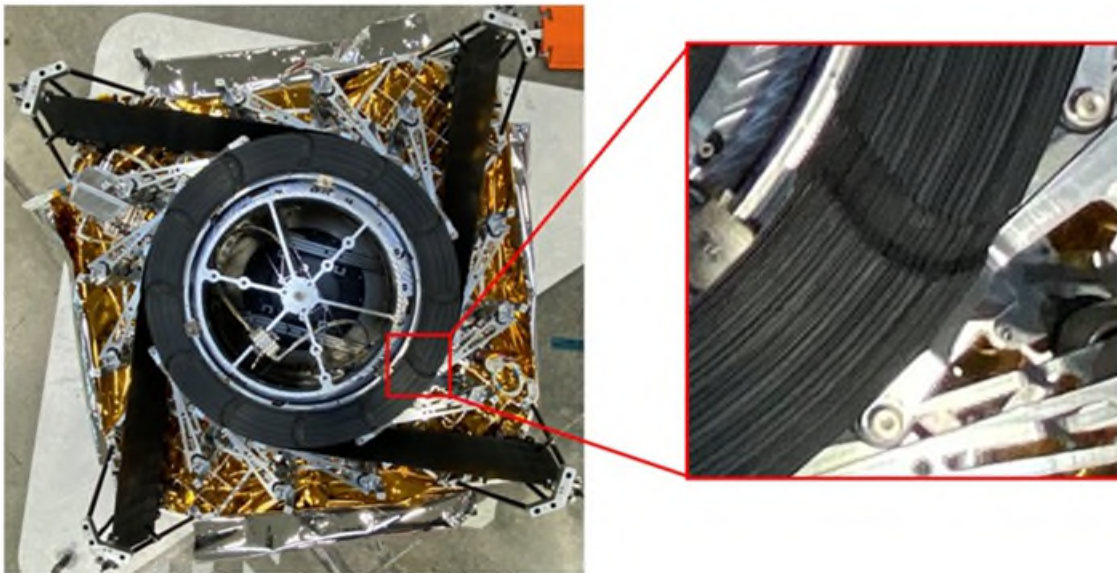


Figure 12. Successful full efficiency stowing with no inner flange buckling (left) and observation of the resulting migration of notches (right).

Conclusion

Through two design and testing cycles, TRL 5 and TRL 6, the engineering team at Redwire has been able to demonstrate the capabilities of the Solar Cruiser sail deployment mechanism, identifying challenges and finding solutions throughout. The design of the laminate architecture of the TRAC booms and interfacing mechanisms enabled a massive increase in scale of the solar sail deployer, when compared to previous flight designs. The success of the TRL 5 testing led to the flight capable design of the TRL 6 prototype, which came with the unexpected challenge of inner flange buckling. The loss in stowing efficiency coupled with a design assumption of full stowing efficiency, led to various losses in performance during testing. The engineering team's follow-on process improvements resulted in a full stow without inner flange buckles, validating the TRL 6 design and revealing design adjustments to enable a flight capable sail deployment mechanism.

Acknowledgements

The work herein was funded by NASA under Marshall Spaceflight Center contract 80MSFC21CA008. Thank you to team members from NASA, Redwire and NeXolve who made this technology development possible. Go Cruiser.

References

- [1] T. W. Murphy and J. Banik, "Triangular Rollable and Collapsible". United States of America Patent US 7,895,795 B1, 22 Oct. 2007.
- [2] L. Johnson and e. al, "The Solar Cruiser Mission: Demonstrating Lare Solar Sails for Deep Space Missions," December 2020. [Online]. [Accessed March 2023].
- [3] L. Friedman, Starsailing - Solar Sails and Interstellar Travel, New York: J. Wiley & Sons, 1988.
- [4] M. Leipold and et al, "ODISSEE - A Proposal for Demonstration of a Solar Sail in Earth Orbit," *Acta Astronautica*, vol. 45, no. 4, pp. 557-566, 1999.
- [5] D. Alhorn and e. al, "NanoSail-D: The Small Satellite That Could!," in *25th Annual AIAA/USU Conference on Small Satellites*, Logan, UT, 2011.
- [6] A. Sobey and et al, "Design and Development of NEA Scout Solar Sail Deployer Mechanism," in *43rd Aerospace Mechanisms Symposium*, Mountain View, CA, 2016.
- [7] B. Davis and M. Lake, "Development of Compact Mechanically Driven Systems for High Strain Composite Slit-tubes," in *43rd Aerospace Mechanisms Symposium*, Mountain View, CA, 2016.
- [8] K. Cox and K. Medina, "Scalability of Triangular Rollable and Collapsible Booms," in *AIAA Scitech 2019 Forum*, San Diego, CA, 2019.
- [9] L. Nguyen, "Solar Cruiser TRAC Boom Development," in *2023 AIAA SciTech Forum*, National Harbor, MD, 2023.
- [10] Z. McConnel and e. al., "Test of a Full-Scale Quadrant for the 1,700 m² Solar Cruiser Sail," in *6th International Symposium on Space Sailing (ISSS)*, New York, NY, 2023.
- [11] R. Taylor, D. Turse, L. G. Adams, M. Reavis and D. Richardson, "Slit Tube Locking Longeron". United States of America Patent US 8,863,369 B2, 20 Dec. 2011.

Advanced Composite Solar Sail System (ACS3): Mechanisms and Lessons Learned from a CubeSat Solar Sail Deployer

Nigel R. Schneider*, Gregory D. Dean*, Olive R. Stohlman*, Jerry E. Warren*, Juan M. Fernandez*,
W. Keats Wilkie* and Todd C. Denkins*

Abstract

This is an overview of the National Aeronautics and Space Administration (NASA) Advanced Composite Solar Sail System (ACS3) technology demonstration project mechanisms, their development, the testing they underwent, as well as the lessons learned in those activities. This overview includes an overall description of the primary deployment mechanisms and ground support equipment (GSE) needed for packaging the solar sail system.

Introduction

The ACS3 project is a technology demonstration mission utilizing 7-m rollable composite booms, provided by the Deployable Composite Boom (DCB) Project, to deploy an 81-m² reflective solar sail [1], the solar sail system shown in Figure 1. Critical elements of the spacecraft are shown in Figure 2. This project is a joint effort between NASA Langley Research Center and NASA Ames Research Center. The Sail Boom Subsystem (SBS) is the payload of the ACS3 spacecraft, a 12U CubeSat. The SBS uses several traditional mechanisms in combination to deploy the composite booms simultaneously with a solar sail on orbit in one smooth motion. These mechanisms were designed and tested over a 5-year period and were preceded by an earlier potential drop-in replacement design for the Near Earth Asteroid Scout (NEA Scout) mission utilizing the composite booms that was brought to a qualification level, but not selected for the final flight design of that mission [2]. Similar work at a lower technology readiness level (TRL) has been published by Deutsches Zentrum für Luft- und Raumfahrt (DLR, German Aerospace Center) [3].

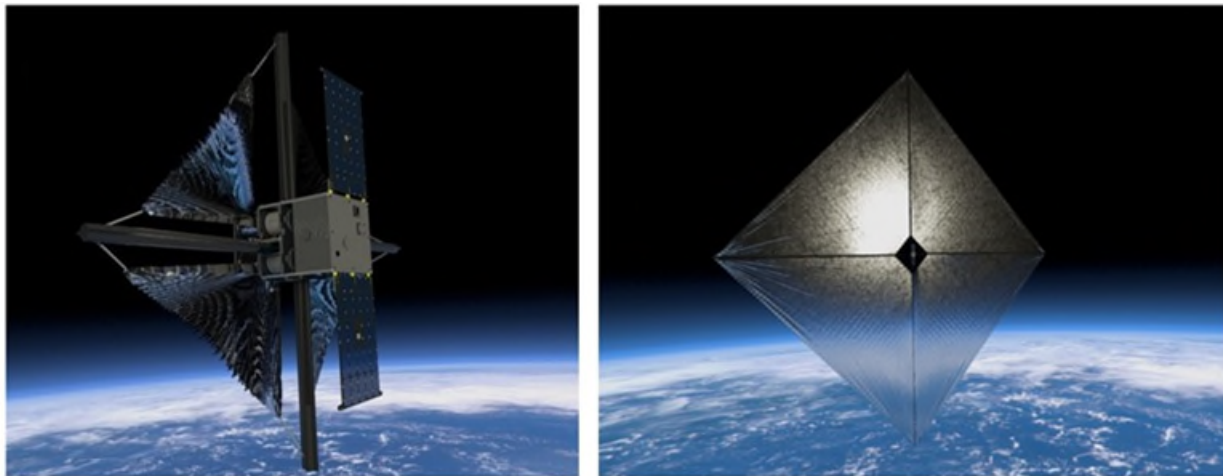


Figure 1: Artist's rendered image of the beginning of sail deployment (left) and fully deployed 81-m² sail (right).

* NASA Langley Research Center, Hampton, VA

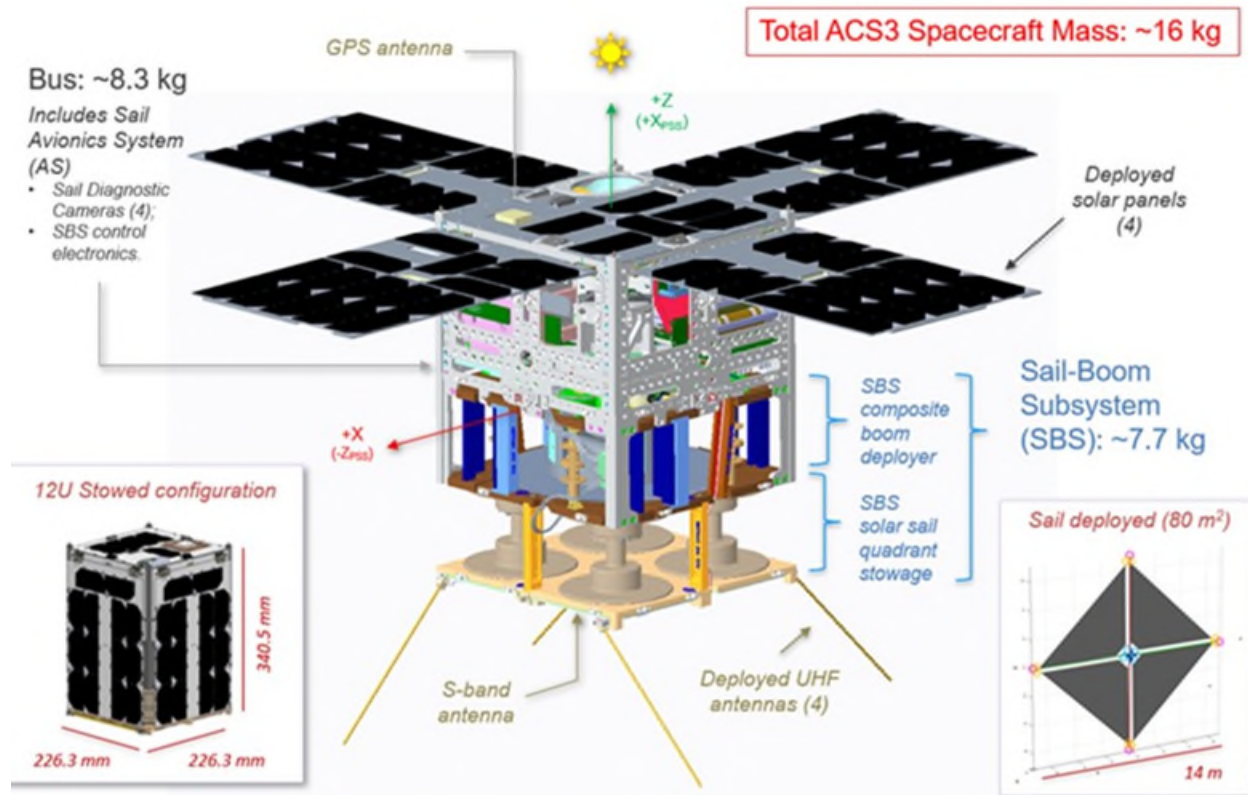


Figure 2: Essential elements of the bus of the ACS3 Spacecraft.

Solar sails are propelled by solar radiation pressure¹. Despite being massless, photons of light have momentum and energy. The photon imparts some of this momentum to the sail upon impact. The sail is reflective so that momentum is gained from the reflected light as well. By angling the sail relative to the sun, the resultant vector can be used to increase or slow the orbital velocity, raising or lowering the orbit. A common misconception is that solar sails gain thrust from solar wind, which is made up of the ejected electrons and protons. By the time these low mass particles reach Earth's orbit, the particle flux is low and they are relatively slow, making their contribution to changes in momentum negligible.

The ACS3 mission² is designed around the deployment and in-flight validation of lenticular composite booms, described by Fernandez [4], used to deploy and support a solar sail. The lenticular closed cross-section results in a low mass boom with good bending, torsional stiffness, and buckling capacity. This lenticular shape is set when the layered carbon fiber fabric reinforced epoxy prepreg is cured. The partially developed shape can be seen at the end of the stowed boom in Figure 3. The boom wall is only 2 layers thick per side, with dropped ply regions to reduce strain in storage. The thin/flexible walls of the boom enable the cross-section to be flattened, which in turn allows the booms to be tightly coiled on a hub.

There are complexities involved in deploying the booms in this state because the thin flattened cross-section can easily buckle and fold due to the low bending stiffness. This is especially while snaking around other parts in the SBS composite boom deployer, or simply "deployer", called out in Figure 2, as each change in direction offers a new chance for buckling to occur. Additionally, the internal strain energy of the boom coil pushes to expand to its straightened length and fully formed lenticular cross section. The combined effect can result in the booms failing to deploy by becoming internally bound up if not properly constrained, an effect commonly called blossoming [5]. The blossoming problem is exacerbated when the

¹ <https://www.planetary.org/articles/what-is-solar-sailing>

² <https://www.nasa.gov/smallspacecraft/what-is-ac3/>

CubeSat payload with continuous rails. The sail is also fixed to the tip of the booms, which means it is pulled out by the booms as they are pushed out of the SBS. This greatly simplifies the design over other systems that deploy the structure and then “hoist” the sail. However, with this simultaneous boom and membrane deployment, and the inability to retract the sail, deployment is in one direction only. If the booms were to be retracted, the un-tensioned sail becomes an unconstrained entanglement around the spacecraft.

The sail is made of polyethylene naphthalate (PEN, 2.5 μm) which is aluminized (Al 100-nm thick) on the sun-facing side to create a reflective surface and coated with chromium (Cr 15-nm thick) on the anti-sunward side for thermal management and to reduce degradation from atomic oxygen and solar particles. The two metallic sides are electrically shorted to prevent charged particle buildup on one side that could discharge to the opposite side, and electrically and mechanically grounded to their stowage spools. These spools then use a graphite brush to create a chassis ground to their respective spindles attached to the main structure. Stohlman et al [6] documented further details of the membrane. These spools also have a soft brake on them to prevent free spinning pre-deployment. The sail was constrained pre-deployment with a tab-and-slot belt made of polyimide.

Compared with previous versions, the final ACS3 mechanism improved the packaging efficiency, simplified fabrication and assembly processes, increased accuracy of the final boom hub deployed position, and reduced the time required to perform and cycle operational tests. This optimization and refinement were achieved by improvements in the deployment mechanisms and packaging solution, where most of the useful lessons have been learned. The total system addresses the combined needs of the project and results in a system that is not used elsewhere, largely due to the unique requirements of an ultra-low-volume and -mass solar sail system. The deployment mechanism was volume- and mass-constrained by the requirements of a CubeSat³ payload, leading to a drive to reduce the complexity and mass of the mechanical systems. Mass was of further critical importance to the overall mission due to the impact it would have on ability to demonstrate orbit raising of the solar sail.

Design History

NEA Scout was a mission beyond low earth orbit that would have approached and imaged asteroids to help determine their composition for future asteroid research missions. During the development of the NEA Scout mission, analysis showed that there were potential problems with their 6.8-m long metallic Triangular Rollable and Collapsible (TRAC) booms, where they could potentially twist, contort, and cause the sail to collapse in the anticipated thermal environment of that mission. While analyzing thermal management solutions for the existing design, the NEA Scout project supported an alternate design study of the lenticular composite booms being manufactured at NASA Langley Research Center [4]. This led to the development of a drop-in replacement prototype deployer that used the size and mass constraints of the metallic TRAC boom as a baseline. The size constraint meant a boom with a 45-mm flattened height needed to be developed. This Langley NEA Scout analogous prototype was successfully designed and tested [2]. The NEA Scout project ultimately chose to use the more mature baseline metallic TRAC boom design, with alterations to the sail membrane configuration for thermal control.

With a working prototype in hand, NASA chose to develop an independent low earth orbit (LEO) demonstration mission. This mission would have no scientific payload and would only further the Technology Readiness Level (TRL) of the composite booms and their deployer for potential future missions. This project was titled the Advanced Composite Solar Sail System and was approved with a two-year budget through the Small Spacecraft Technology program within the Space Technology Mission Directorate. Spacecraft payloads developed under this program are designed before bus providers, dispenser providers or launch providers are identified, which poses its own technical challenges.

The NEA Scout drop-in replacement was designed and built on an accelerated schedule, leading to several compromises. Necessary components were added on an ad hoc basis, with whatever hardware was minimally acceptable to fit within the volume. The 45-mm booms developed for that payload in the time

³ ISO 17770

frame allotted were of marginal strength. With the independence of a dedicated parallel technology development effort, the NASA DCB project⁴ and ACS3 project, these compromises could be addressed. The DCB Project was to focus on the design and manufacturing of the booms, and ACS3 would develop the hardware for the booms use on a solar sail mission.

The first modification was the development of larger cross-section and stiffer booms with a 65-mm flattened height. These booms were tested on the NEA Scout hardware, which was modified as necessary [7]. Several challenges became apparent quickly. Early estimates of boom packaging efficiency were done with individual 1-m long boom segments. These segments were wrapped tightly around rigid cores and the outer diameter measurement was extrapolated to a packaging efficiency for the total co-wound 7-m boom length. This is done by approximating the coil as an Archimedean Spiral of constant volume fraction. However, the 6U deployer had booms that were wound in pairs, and of longer length. During packaging, the engineers working by hand were unable to compress the booms as tightly, or maintain proper or consistent compression, especially over the whole duration of packaging. Total packaging efficiency varied based on the personnel carrying out the operation and from one packaging session to another. These combined effects resulted in a much larger outer diameter than anticipated.

Additionally, the inner diameter of the boom spool was too small. The strain placed on the boom by forcing to wrap it around a small diameter caused cracks to form and propagate at the root. The inner diameter grew through several iterations, which increased the outer diameter as well. This led to one of the first redesign efforts. The already delicate pieces of the Langley NEA Scout design were too fine to take the additional loads produced by the larger and stiffer 65-mm booms. There was also no room to move existing parts to where they now needed to be due to existing features. As such, a new design was started. Fastener sizes, shapes and lengths were consolidated, which allowed for the deployer to be refreshed and repackaged much more quickly between runs.

The outer diameter of the boom package was further increased by a decision to increase the sail area and boom length beyond the baseline requirement. The fully packaged 7-m 6U design exceeded the planform area allotted by the CubeSat standards. Additionally, the reaction wheels that could fit in the remaining volume allotted for the 6U bus could not guarantee control authority for pointing to handle the aerodynamic drag forces on a solar sail at the minimum planned altitude of 500 km. Because the project was to be a secondary payload on a launch of opportunity, there was a possibility but not a guarantee of a higher orbit.

It therefore became necessary to create a new design with a 12U size CubeSat form factor. This came with several technical challenges. It was possible to use four independent spools with one boom on each, in a mirror of the 6U design, or a single hub with the four booms co-coiled, which could allow for a larger spool diameter and potentially eliminate root cracking. In order to complete the redesign in as short a time as possible, it was decided to first mirror the 6U design. With a single boom per hub, rather than the 6U design's two booms, it was possible to increase the hubs' inner diameter while maintaining the same outer diameter. One additional difficulty with the 6U design was that the co-coiled tapes from two separate hubs were reeled onto a single tape spool during deployment. Minor differences in tape length, boom length, and packaging efficiency meant that the end of deployment did not happen at the same time for both hubs. However, since a pair of booms was on each hub, a pair of booms was guaranteed to be at the correct orientation, and the other to be close. Because it was based on the 6U design, the 12U 4-hub had four hubs, four tapes, and two tape spools. These two configurations are shown side by side in Figure 4. Minor differences in boom packaging efficiency now meant that only one boom would be sure to be in the correct position at the end of deployment. This can lead to two potentially serious problems. The first is that some of the booms could over-deploy and be pried off their respective hubs. The second is that some of the booms could under-deploy and their respective boom cross sections cannot fully open at the root, resulting in reduced structural integrity.

⁴ <https://www.nasa.gov/centers-and-facilities/langley/deployable-composite-booms-dcb/>

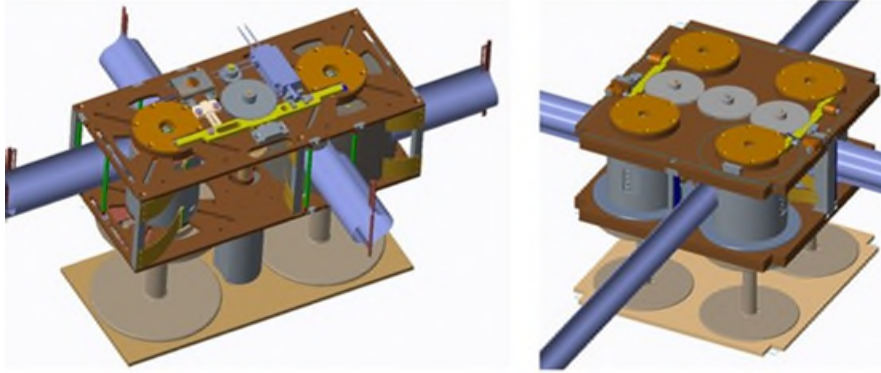


Figure 4: 6U configuration (left) vs. 12U 4-hub configuration (right)

This challenge was presented at a Technical Readiness Review before production of parts and final testing. Because the nature of this challenge could have resulted in the failure of the mission, it was the unanimous decision of the review board that the SBS should be redesigned to the monohub configuration, shown in Figure 3. The single large hub, in addition to reducing or eliminating coiling-strain-produced cracks, had all the boom roots fixed at known locations, which meant that the end of deployment would occur at the same time for all booms, regardless of packaging efficiency. There was still one steel tape per boom, so that each boom would always be constrained as much as possible to prevent blossoming. In testing, it was found that there were differences in the packaging efficiency of the steel tape being taken up onto their individual spools. This caused the tapes to lead and lag one another in cycles as the tapes were taken up. However, this never caused any problems with deployment.

The bus contract went out for bid while the 12U 4-hub design was still the baseline. From a mechanical perspective this meant that a significant portion of design had happened without guarantee of being able to find a bus that could achieve the requirements in the remaining volume, and the mechanical interface was undefined, but assumed to be a part of the continuous corner rails typical of CubeSats. There were few companies who made 12U buses at this time, fewer still who's business model was to sell a fully tested bus to be integrated, commissioned and flown by outside entities. Despite these challenges a functional bus was delivered and, with careful coordination of the interface control document the mechanical interface worked perfectly.

The CubeSat dispenser contract and launch provider contract did not go out for bid until the protoflight unit was in testing. There were several technical challenges because of this. The first was with procuring a dispenser. ACS3 does not have the typical continuous corner rails of a CubeSat due to the sail stowage area and the way the sail is joined to each boom. To create a continuous load path into the payload, the sail spool spindles were made structural, and a boss added to the end plate. This required the dispenser provider to custom modify the doors of their dispenser with corresponding load bearing locations. Furthermore, without a launch provider on contract up to this point, there was not a defined launch envelope or environment. This meant that the design needed to be more robust than was necessary, designed for as close to full General Environmental Verification Standard (GEVS) levels as possible. A contracted launch provider would have been able to provide reduced launch load data, and some dispensers provide attenuation. Once the launch provider was on contract, the launch was still unknown, as was the launch configuration. This meant that the altitude and inclination were unknown, which meant there were a wide range of potential thermal environments, including outside of the operational limits of some components.

Uncertainty in launch loads, dispenser orientation on the launch vehicle, and orbit parameters caused the mass of the SBS to be much higher than needed to survive the final launch loads as provided by the launch provider. This additional mass is detrimental to the performance of any propulsion system, but especially detrimental to the performance of a solar sail due to how small the resultant force of solar radiation pressure is. Future efforts could have more optimized mass characteristics if the launch environment can be detailed earlier.

Testing and Lessons Learned

Rapid Prototyping

One strategy for improving functionality and reducing mass was the use of additively manufactured parts in early prototypes of the SBS. Rapid prototyping allowed multiple design iterations to be tested before final production of a protoflight unit. Motor current data was recorded from the additively manufactured prototypes and compared between runs to find areas of improvement. Even the belt retaining the coiled sail went through several iterations, with several other intermediate retention methods of polyimide rapidly prototyped by cutting out on a laser computer numerical control (CNC) cutter. Testing these rapid prototype parts also revealed that some components from previous designs provided no observable benefit, and these were subsequently removed. Removing these components also resulted in the reduction of mass and complexity of the total system.

The prototype SBS was printed in primarily polylactide while some parts which were found to require additional strength were printed in polyetherimide. The final rapid prototype test configuration can be seen in Figure 5. Additive manufacturing was not without drawbacks, however. Some parts printed in plastic broke so frequently in testing that prototype metal components were made or commercial-off-the-shelf (COTS) parts purchased. This included the tape spools, which were particularly weak due to their cross-section and the direction of the print layers. Some parts that were cycled repeatedly needed to be reprinted because the threaded inserts wore out the parent material. When packaging the 7-m booms for the first time, strain in the bus plate holding the gears caused the plate to bend so much that gears began to slip. A replacement aluminum plate was procured from a CNC rapid prototyping service. This aluminum plate eliminated the flexure issues and allowed full scale testing until the protoflight hardware was delivered. The constant refinements of the model, primarily in plastic, and demonstration in testing, worked deceptively well, as there were problems on the first test run of the completed flight components that had not been anticipated, some of which persisted for the remainder of the project.

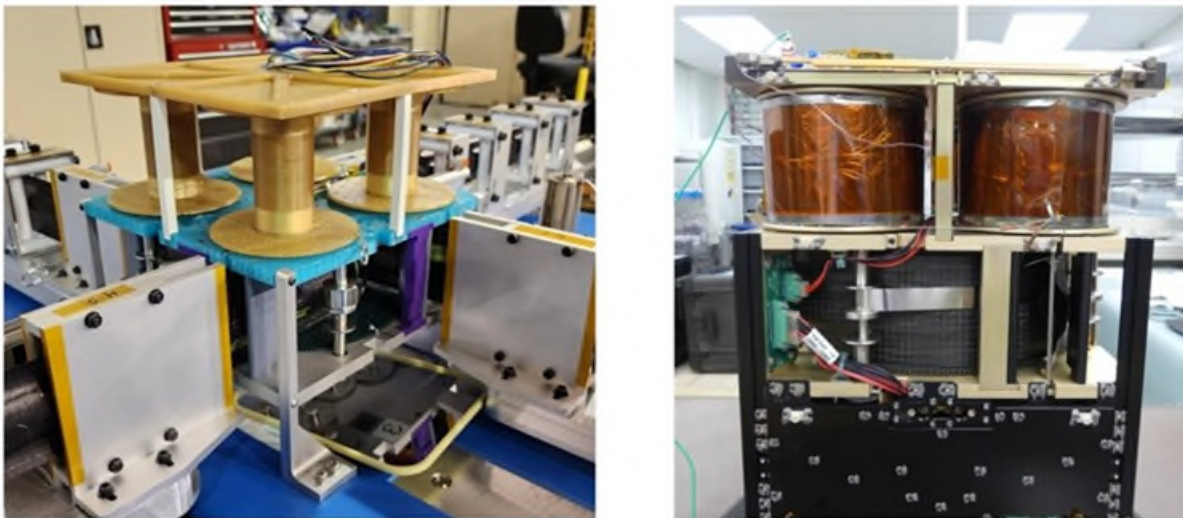


Figure 5: Final configuration of the plastic/metal rapid prototype test article (left), and the final assembly and packaging for flight (right)

Because of the number of parts that were printed, modified, and reprinted, press-in threaded inserts were used extensively for expediency in the plastic rapid prototyped parts. These press-in inserts did wear out the parent material faster through repeated cycling, and in some instances extra time was taken to use melt-in inserts to prolong the plastic components usability. None of the threaded inserts for plastic had locking features and given that the inserts were brass instead of steel, and the parent material was plastic instead of aluminum, no data was collected for running torque, only to refine the design and assembly procedure. Press in inserts are more likely to spin in place, and many of the final torque values had to be lowered for testing in plastic.

Transitioning to Metal Parts

There were several instances where the change to metal resulted in problems. The thread on the shoulder bolts for the idler gears, shown in Figure 3, did not have enough length to engage the locking feature of their respective insert. Because the view of the shoulder was obscured by the gear, the shoulder contacting the plate was thought to be the locking feature being engaged in the threaded insert. The bolt was torqued until it sheared off, and the threaded portion of the shoulder bolt needed to be extracted from the plate. The problem was identified to be twofold. First, was the mistaken thread engagement. The second was that the strength of the brass material was lower than stated from the supplier, resulting in the fastener shearing at a lower torque than anticipated once the shoulder contacted the plate. These shoulder bolts fell out of the range of sizes covered in their governing standard⁵ and were sourced from a bulk distribution center with unknown manufacturer due to repackaging. The brass, chosen for its lubricity and non-galling properties, was found to be of lower strength than indicated by the supplier. With this information the torque was recalculated, and the procedure was modified. Because the idler gears rotate alternately clockwise and counterclockwise for packaging and deployment, these shoulder bolts were already planned to be cross drilled and wire-tied to prevent backing out. From the same supplier, titanium nitride coated stainless shoulder bolts of the same size were also procured and tested. The titanium nitride coating should have resisted wear and prevented galling. This was also found to be substandard as the tested shoulder bolts of this type galled on the first run and were not used again.

Boom Hub Counter-torque

The 6U and 4-hub designs used clock springs to provide the counter torque to resist the self-deployment forces, which has been common to many of the boom deployment mechanisms to date. One of the potential benefits of a clock spring is the counter torque could be large enough to provide a way to repack the booms if the deployment motor were run backwards. However, these springs were COTS items that were not suited for the task in this design. The spring needed to fit within the volume of the hub, Figure 6, which limited the size of spring that could be used. The spring also needed to be preloaded a few turns. Most springs that met these initial requirements were already at or just beyond the limit of the maximum permissible number of turns per the manufacturer. Other design considerations for these springs are the OD of the spring coil, which is the ID of the housing, and the ID, which is the arbor the spring wraps around. As packaging efficiency increases, so does the number of revolutions. This meant that the springs were rotated well beyond the suggested maximum number of rotations. The springs were also dangerous to work with, where injuries were not uncommon installing the spring in the housing, preloading it, or releasing the preload during disassembly. The range of forces provided varied considerably even within a manufacturing lot, up to 20% according to the manufacturer. The number of rotations can be increased by linking the springs in series, and torque can be adjusted by linking the springs in parallel. However, due to the small size of these hubs, the cutouts for the roots of the booms, and the absolute rotation encoder at one end, there was no room to do this in these designs.

To save mass on the monohub design, the core of the hub was hollowed out. To provide structure between the two main plates, and a bearing running surface for the hub, a stationary cylindrical tube was placed at the center. This stationary element precluded the use of the earlier designs' clock-spring counter-torque method. However, something was necessary to resist the blossoming forces, and the boom axial loads generated while stretching the sail flat. Therefore, a simple friction brake was made utilizing a wave spring, shown in Figure 6. The wave spring bears against the flanges of the rotating hub, and a pocket in the main plates. If necessary, it would have been possible to shim the pocket to increase the normal force. This works in this application because deployment of the booms and sail is in one direction. This is because the sail spools also use a friction brake, but more so because the sail membrane cannot be refolded passively by simply rewinding the spool. However, a friction brake does not provide any ability to repack the booms, only to arrest movement. In this application, there is no way to furl and restow the sail, so there is no need, or possibility of retracting the booms. Additional critical elements and changes are shown side-by-side in Figure 6. The change to a stationary cylindrical tube also prevented the use of a shaft encoder. This was replaced by a pair of limit switches that acted in eight equidistant cam pockets on the flanges of the hub. The switches were located at 90 degrees to and co-witnessed one another.

⁵ ISO 7379

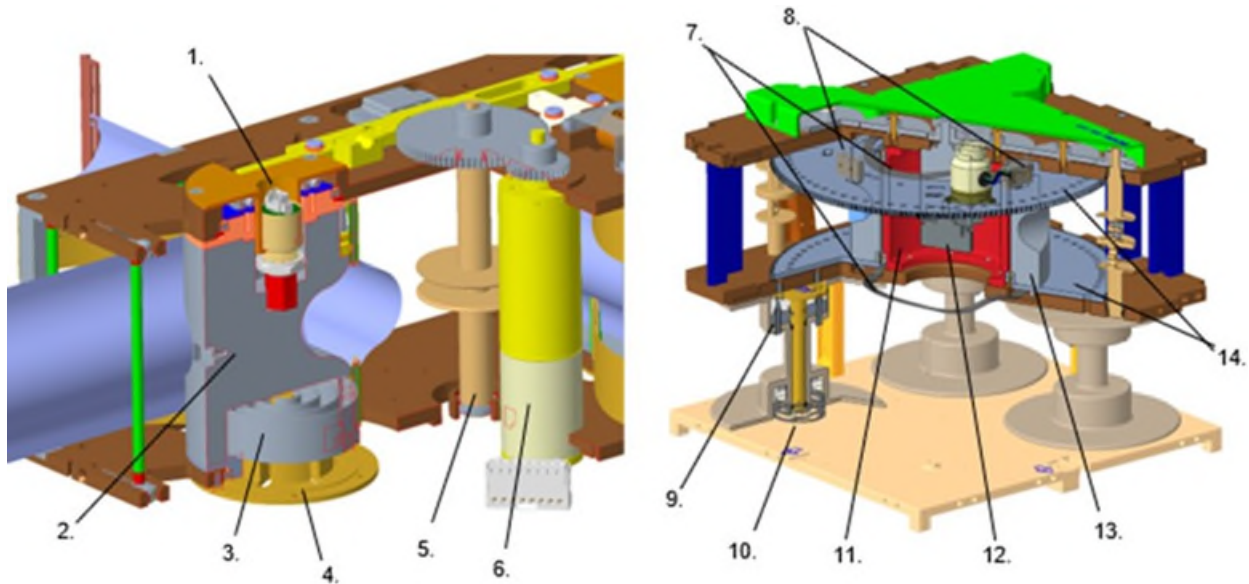


Figure 6: Side by side comparison of the 6U dual-hub (one shown for clarity) and 12U monohub configuration cross sections: 1) Shaft encoder; 2) Small diameter two-boom hub; 3) Clock spring; 4) Clock spring arbor; 5) Two-tape tape spool; 6) Brushless DC motor; 7) Wave spring brake for boom hub; 8) Limit switches acting as encoders; 9) Graphite grounding brush; 10) Wave spring brake for sail spool; 11) Stator (stationary hub support); 12) Brushless DC motor; 13) Four-boom hub; 14) Hub flanges

Tolerancing Issues

A series of problems with clearances and friction in the boom hub were discovered during early testing of the metal prototype unit. It was believed that this wave spring would also keep the hub adequately centered between the two main plates and running in plane. However, the wave springs did not properly pre-load the bearings, which had more play than usual to prevent binding in an unknown thermal environment. This meant that the flanges did not run parallel to the plates, nor in plane at the center of the plates. There are teeth on the rim edge of the hub flange to interface with the GSE, detailed in the next section. The flanges not running parallel caused the teeth at the rim of the flanges to scour the plates. This had not been noticed, nor was it a problem in the plastic prototypes due to a combination of the tolerance of the parts, the flexibility of the structure, and the soft material rubbing on soft material which left no mark. The increased rigidity and accuracy of the remaining features that had previously been plastic meant that the switches were not offset properly from the flanges, which were also not running true to their plane. In consequence, the lever arm of the switch dug into the soft aluminum, and one of the switches was also irreparably damaged. The pocket for the switches had been meant to be shimmed. However, because it had never been an issue with the plastic models, this detail had been forgotten at the time of the assembly of the protoflight unit. The wave spring brakes also scoured the surfaces of the soft aluminum on the main plates and the flanges of the hub. It had not been noticed that the crests of the wave spring had sharp corners that did not run in plane. It was also bearing against soft Iridite chemical conversion coating, which scratched easily.

These problems were solved with modifications to the existing protoflight hardware. The aluminum parts were skim cut to remove the worst of the scratches and the running surfaces had a hard anodization coating applied. Because the inserts had only been cycled once, the inserts were left in place and the holes were plugged. Several of the plugs failed and inserts were corroded by the electro-chemical process and needed to be replaced. The wave spring was hand worked to break the sharp edges, and on future assemblies was lightly lubricated. Delrin spacer plugs were added to the main plates in order to keep the flanges of the hub running in plane, and the switches were shimmed as necessary. Despite these improvements, it was common for one of the two switches to miss a count during a deployment. Due to vertical height constraints, optional lever arm extensions were left off that would have increased the active region and stroke of the

switch, increased the accuracy, and proper positioning of this longer lever arm may have eliminated the need for shimming. The switches could have also been oriented differently, into the axis of the rotating hub, a more rigid and precise dimension. The process used to mitigate these missed switch counts is discussed in the section Ground Support Equipment.

Fastener Retention

Helical inserts commonly get carried back out of the base material when fasteners are removed. Because of the large number of cycles of assembly and disassembly for repackaging the payload, the decision was made to use key locking inserts extensively from the onset. These key locking inserts were all made of A286. Some helical inserts were still used due to the wall thickness of the small components. These were made of A286, Nitronic 60, and 304 stainless steel (SS). The plan had been to replace all inserts before the final environmental and functional tests, which would be followed by the final repackaging for flight. However, once the parts were in hand, the fabrication cost of the parts and the lack of spare hardware became a serious concern to project management over the additional cost and risk associated with replacing the inserts. The M2 key locking insert with locking feature also fell outside of the governing standard for that part⁶ but could be procured through a reputable manufacturer of key locking inserts. Therefore, a test was performed to determine the life cycle of all inserts used in the project to ascertain the likelihood that any given insert would fall out of the acceptable running torque range of their associated standards and accepted practices. Ten samples of each insert were installed in an aluminum test plate, shown in Figure 7, and tested ten times each. Of these 60 total inserts: three M3 helical inserts (the only inserts made of 304 SS) did back out with the fastener on the first cycle; one M3 helical (Nitronic 60) had high, but within range, running torque and then damaged the threads of the test fastener after the first cycle rendering it unusable; and one M2 helical insert was found to be installed incorrectly and was not tested. None of these anomalies were corrected. These findings were noted when presenting the findings, and the data set for the affected inserts was simply reduced.

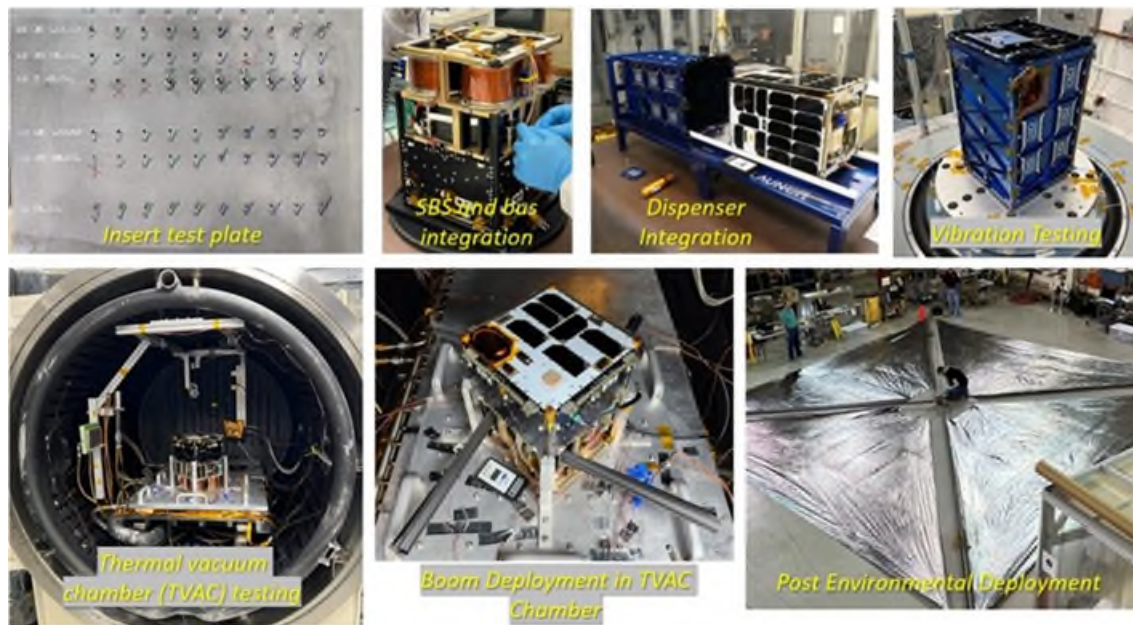


Figure 7: Insert testing, spacecraft integration, environmental- and post-environmental testing.

At this time, due to the time, cost and risk of damage of flight hardware associated with a full teardown and refurbishment of inserts across all parts, a management decision was made to not replace any of the inserts unless an insert became damaged and unable to perform. Based on the insert test performed, it was presumed that all of the inserts would be cycled more than the average number of times for the running torque of the locking feature to fall out of an acceptable range in the scheduled test campaign. Therefore,

⁶ NAS NA0147

alternate methods of retention were investigated. All fasteners were subsequently prepared with VC-3 thread doping compound. The fasteners were prepared before every assembly, so that the fasteners were always retained by the thread locking compound and final torque. In the end, all fastener heads, with the exception of the lock wired shoulder bolts, were also staked with epoxy at final assembly.

Flat-Sat Differences

It is beyond the scope of this paper to detail the specific differences between the flight hardware of the bus and the hardware provided as a flat-sat for deployer programming and con-ops testing. However, there were subtle differences in model numbers provided for key hardware that presented a project risk. During one test, an error that could not be reproduced on the flat-sat nearly caused damage to the flight hardware due to malfunction. It was only through preparedness and rehearsal for emergency stop procedures that the test was stopped with no damage to the hardware. Additionally, the previously detailed problem of switch count was difficult to reproduce on the flat-sat due to the hardware differences. This is believed to be in part due to the reduced complexity of the flat-sat.

Environmental Testing

Thermal and Vacuum testing (TVAC), shown in Figure 7, was complicated by the layer cake design and the circuitous path heat would need to travel to fully soak the spacecraft. However, because the first motions of deployment were to be done in TVAC at both a high and low temperature, it was necessary to have the spacecraft in an upright configuration on the platen in the chamber. A horizontal configuration would have increased the contact area with the platen but would not have allowed for the deployment of the booms in the TVAC environment. The minimal contact area was mitigated in part by having vertical rails, like those in a dispenser, that would touch the continuous corner rails of the spacecraft as much as possible to assist in transferring heat. It was necessary from a schedule and cost standpoint to operate in a reduced thermal environment and fewer cycles than typically recommended. Deployment of the first 30 cm of the booms at hot and cold (approximately 15 cm each) was performed successfully, with no noticeable increase in recorded motor current data as compared to ambient tests in atmosphere.

Ground Support Equipment

The design of the spacecraft GSE was primarily based on the difficulty of assembling the deployer and packaging the four 7-m booms. The packaging and handling of the booms was so physically demanding that the design became linked to the ground support equipment for packaging, which was designed around similar needs for reduction of complexity and man hours. The GSE for boom packaging became its own mechanism, as shown in Figure 8. Improved packaging, reducing the area required for packaging, and the reduction of personnel necessary is especially important for tentative future missions that could use similar composite booms of up to 30 m in length, resulting in a 1600 m² sail [8] [9].

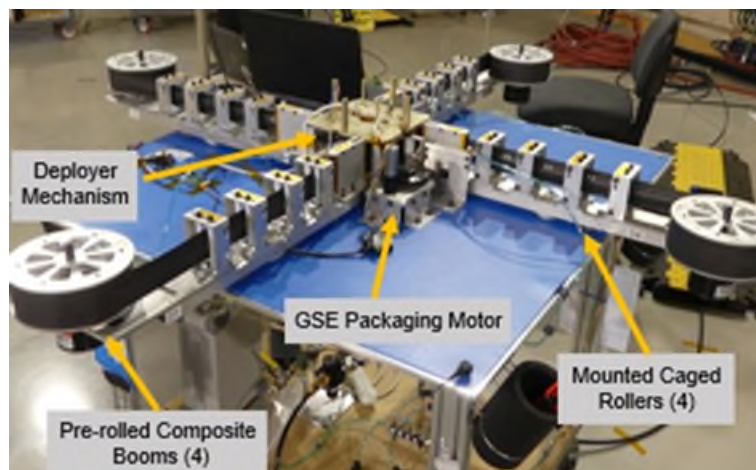


Figure 8: Boom packaging GSE at the beginning of the packaging operation.

Since the tape is reel-to-reel and not a complete belt, it is impossible to utilize the deployment motor to run the system backwards under its own power. Therefore, a GSE packaging motor is used to rotate the hub in the packaging direction. This packaging motor acts on the teeth on the edge of the boom hub flange. This was originally done with no power provided to the SBS deployment motor. This did mean that the deployment motor would need to be backdriven through its high reduction gearhead, which provided ample resistance to keep the steel tapes taut against the tightly coiled boom coil. The switches were powered and the switch counts for packaging were counted by a data acquisition system. The number of switch counts for packaging was then set in the bus software as the stop motor count to end deployment. Due to intermittent discrepancies between the switch counts, an additional method to co-witness would need to be devised.

The original boom packaging process required a large area because the booms were fully extended prior to packaging. Each boom was supported by two people, one at the free end and one at the mid span. Another person had to compress each boom to flatten it and push it tight onto the hub, while pulling it slightly, all to try to get a tight coil for improved packaging efficiency. It was also necessary to have one person running the GSE for packaging, and one person running the procedure and observing. In all, the original packaging process required 14-15 people. The four people at the midspan could be dismissed partway through packaging once enough of the boom was stowed. This still required a dozen people for a whole hour, and the additional four for half an hour, which made coordinating this effort difficult. The people supporting the free length of the boom were responsible for holding it at the same height for the whole time so that the booms would not rub excessively against the hub flanges. Despite the small mass of the booms, this is difficult and uncomfortable to maintain over an hour. The personnel responsible for compressing the boom to flat and pressing it into the hub experienced hand cramps and an unacceptable risk of carbon fiber splinters. Often, people would swap positions to gain some temporary relief from the strain of one position for the other. It was impossible to apply identical compressive forces among different individuals, or run to run, and packaging efficiency varied widely between tests.

The first major process improvement was to reduce the number of people required. The booms were directed through caged rollers which transitioned the booms from their lenticular deployed shape to their flattened cross-section. This reduced the number of people by four immediately and eliminated four of the most physically demanding positions along with their associated safety risk. The next improvement was to have the booms pre-rolled individually onto their own storage spools mounted to the end of the arms supporting the caged rollers. This eliminated the need for the eight people who would support the boom during the packaging process. These pre-rolled booms were mounted on magnetic hysteresis brakes, which provided even tension to all four booms. Additionally, the booms could be individually pre-rolled in advance of packaging into the ACS3 deployer. This process required only two to three people. The rollers were also adjusted to keep the boom flat, reducing the effort of the packaging motor required to package the booms. This also reduced the number of flattening to formed cross-section cycles of the booms, which are the single highest strain inducing event for the booms.

Finally, pneumatic linear actuators with rollers were added to compress the flattened boom to the hub. The pneumatic actuators were all linked through the same pressure manifold with a pressure release valve. This ensured that the compressive force on the booms at the hub was even and consistent throughout the packaging process. By making minor changes to the pressure and the torque of the magnetic hysteresis brake, the packaging efficiency was improved drastically and became very consistent between runs.

The torque required by the packaging motor increased through all these changes. There was a desire to keep the packaging speed low, taking approximately 20 minutes, so that the booms could be carefully observed. To achieve this low speed, the packaging motor had to be run slowly. A brief trial in running the deployment motor backwards during packaging so that the packaging motor did not have to back drive the high reduction planetary gear was attempted. This was done with the deployment motor at a lower relative speed than the packaging motor so that the tapes remained taut. However, there was a fundamental misunderstanding about how a brushless DC motor works when doing this. A brushless DC motor works on the Hall effect and requires a motor controller card to control speed by varying the duty cycle of each

coil at the time and position it can act. These controller cards are set for speed and will increase or decrease the duty cycle to achieve this speed, regardless of input. The deployment motor became more difficult to back drive with the coils energized and trying to achieve their target speed. However, it was necessary to power the deployment motor's Hall sensor circuit to record the number of motor rotations during packaging.

Brushless DC motors also have a minimum speed that they can be run at under load before they will start to stutter. This is due to the impulse during the duty cycle being too small to overcome the torque. The next impulse would be larger and exceed the speed setting, causing the next impulse to be short and not drive forward. It was possible to assist the motor by turning the hub by hand, however, that defeated the purpose of the GSE setup. A different motor should have been used for packaging, but one was not available. The speed was adjusted into a range where packaging was smooth but still slow enough to be acceptable.

It is difficult to track the incremental improvement of all the GSE modifications and their individual contributions. The initial metric for comparison was the number of switch counts and the measurement of the outer diameter. The measurement of the outer diameter was difficult to make precisely. In the 6U configuration structural features, as well as the boom tip end and steel tape, obstructed direct measurement, and the coiled boom was easily deformed by calipers due to its low packaging efficiency. Additionally, there were several changes to the inner diameter of the coil as the hub diameter was incrementally increased to reduce the stress on the stiffer booms, which was causing cracks to form and propagate. Once the design shifted to a 12U monohub, the inner diameter dimension became fixed. Furthermore, as the packaging efficiency improved, the coiled boom became less compliant and this outer diameter measurement became more consistent. The limit switch count became consistent to ± 1 . The clearest indicator of how consistent the packaging efficiency became was the highly repeatable number of motor revolutions achieved from run to run towards the end of the test campaign.

This repeatable motor Hall sensor count was achieved despite the high gear reduction of the planetary gearhead, the variable belt ratio, and the now minorly variable packaging efficiency. Therefore, motor count was selected to co-witness the switch counts to determine end of deployment final position. Motor count would get to the final rotation, the Hall sensor and switch count data compared to the numbers recorded during packaging, and if the switch count was determined to be accurate, the switches would determine final position. Fiducial marks were added in a regular repeating pattern for the first 650 mm of the boom root area, which can be seen by cameras on the bus. If the switch count recorded during deployment was found to be questionable, the motor hall sensor count could be used to get within the final anticipated range. Pictures from a nominal ground deployment could then be compared to returned images to confirm correct final position or drive forward more as necessary to complete deployment.

Conclusions and Remarks

COTS hardware and inserts can be found that fall outside the ranges covered by their usual governing standards that can be of good quality, depending on the source and quality of their manufacturer. This hardware scale is particularly important for CubeSats given their small nature, as well as the miniaturization of other parts for mass and volume savings in other form factors. Nitronic 60 inserts were noted to be of above average quality for repeatable and reliable use when multiple cycles were needed. A286 key locking inserts held up well over repeated cycles and did maintain good thread form for continued use as "free running" inserts after the locking feature becomes worn. However, all of these should be tested on a case-by-case basis since they may be non-standard parts. Additionally, none of the inserts installed in the flight article exhibited anomalous behavior shown in testing. Unifying the size and number of fasteners greatly reduced the complexity of assembly and improved the time necessary from a week to two days. The additively manufactured prototypes were invaluable but did not reveal all of the problems with the design, some of which caused damage to the flight unit.

The largest problem for the mechanism at the end of the project remained the limit switches. The very narrow active region of the switch plagued what should have been a reliable system. The limit switches should have faced into the axis of rotation. An optical encoder, or a shaft encoder working on a pinion gear in the teeth of the hub flanges, would have provided even greater positional accuracy.

Only one protoflight unit of the SBS was ever constructed. Because a portion of cost is in programming CNC machines, tooling, and fixturing, a second unit is often less expensive. With two units, one could have been an Engineering Development Unit (EDU) to go through a more extensive test campaign. Lessons learned could have been collected into single modifications of flight unit parts. A pristine flight unit could have been used for final verification testing and use on orbit. ACS3 also did not have an EDU bus, and while it did have similar components used in a flat sat configuration for testing of the control software for the payload, the dissimilarities were significant enough to cause problems in testing. Because of the protoflight nature of the ACS3 payload, the test campaign (shown in Figure 7) was more limited and was approached with great caution due to the lack of backup hardware. The cost of the slower and more thorough nature of testing with a protoflight unit would have been partially, if not completely, absorbed by the cost of duplicate EDU hardware. An EDU SBS combined with a full EDU bus would have provided a true-to-flight article for troubleshooting on-orbit problems on the ground, as well as a second chance at the cost of a new dispenser and launch in the event of an irreparable failure.

Removing as many people from the packaging process as possible improved repeatability, reduced cycle time for repackaging, and reduced labor costs significantly. This process also reduced the cumulative damage imparted to the thin-shell deformable booms generated during the packaging process. This solution for packaging the booms is scalable to much larger configurations. In contrast, the sail membrane packaging process remained an inefficient hand-folding procedure. Due to the delicate nature of the sail membrane, as well as the number and non-repeating shape of the folds [6], no mechanized assistance was able to be developed for ACS3. This resulted in the boom deployment being tested many more times than the sail membrane deployment.

References

- [1] W. K. Wilkie, J. M. Fernandez, O. R. Stohlman, N. R. Schneider, G. D. Dean, J. H. Kang, J. E. Warren, S. M. Cook, P. L. Brown and T. C. Denkins, "An Overview of the NASA Advanced Composite Solar Sail (ACS3) Technology Demonstration Project," in *AIAA Scitech*, Virtual, 2021.
- [2] J. M. Fernandez, G. K. Rose, C. J. Younger, G. D. Dean, J. E. Warren, O. R. Stohlman and W. K. Wilkie, "NASA's advanced solar sail propulsion system for low-cost deep space exploration and science missions that uses high performance rollable composite booms," in *International Symposium on Solar Sailing*, Kyoto, Japan, 2017.
- [3] M. Hillebrandt, S. Meyer, M. E. Zander and C. Hühne, "Deployment Testing of the De-Orbit Sail Flight Hardware," in *AIAA Spacecraft Structures Conference*, Kissimmee, Florida, 2015.
- [4] J. M. Fernandez, "Advanced Deployable Shell-Based Composite Booms for Small Satellite Structure Applications Including Solar Sails," in *International Symposium on Solar Sailing*, Kyoto, Japan, 2017.
- [5] A. Hoskin, A. Viquerat and G. S. Aglietti, "Tip Force during Blossoming of Coiled Deployable Booms," *International Journal of Solids and Structures*, pp. 58-69, 2017.
- [6] O. R. Stohlman, J. M. Fernandez, G. Dean, N. Schneider, J. H. Kang, R. Barfield, T. Herndon and P. Stokes, "Advances in Low-Cost Manufacturing and Folding of Solar Sail Membranes," in *AIAA Scitech*, Orlando, Florida, 2020.
- [7] J. M. Fernandez, G. K. Rose, O. R. Stohlman, C. J. Younger, G. D. Dean, J. E. Warren, J. H. Kang, R. G. Bryant and W. K. Wilkie, "An Advanced Composites-Based Solar Sail System for Interplanetary Small Satellite Missions," in *AIAA Scitech*, Kissimmee, Florida, 2018.
- [8] J. M. Fernandez and C. E. Volle, "Corrugated Rollable Tubular Booms," in *AIAA Scitech*, Virtual, 2021.
- [9] L. Nguyen, Z. McConnel, K. A. Medina and M. S. Lake, "Solar Cruiser TRAC Boom Development," in *AIAA SciTech*, National Harbor, MD, 2023.

Design and Test of the Orion Crew Module Launch Abort System Hatch

Jeff Heyne*, Aaron Larson*, Ryan Dardar*, Lance Lininger*, Evan Siracki* and Brian Emmett†

Abstract

The Orion spacecraft is part of NASA's Artemis program to establish a permanent human presence on the lunar surface and further enable future crewed missions to Mars. One of the key safety features of Orion is the Launch Abort System (LAS), which pulls the Orion Crew Module (CM) away in the event of a launch vehicle malfunction. It was necessary to design a LAS Hatch that allows for crew access to the CM during pad operations. This paper describes the background and evolution of the LAS Hatch design, the features used to address the crew safety requirements, the testing challenges in preparation for the Artemis crewed missions, and lessons learned.

Introduction

The Orion Launch Abort System, or LAS, is attached to the top of the Orion Crew Module (CM). It is designed to protect the NASA astronauts if a problem arises during launch by pulling the CM away from a failing rocket. Weighing approximately ~7,250 kg, the LAS can activate within milliseconds to pull the vehicle to safety and position the CM for a safe landing. The LAS is comprised of three solid propellant rocket motors: the abort motor, an attitude control motor, and a jettison motor. The Launch Abort System (LAS) Hatch is a structural / mechanical / pneumatic / electrical component that allows for ingress and egress through the LAS ogive fairing during nominal ground operations and pre-launch activities. It is also required to open quickly in emergency situations on the pad where the crew needs to exit in the event of a spacecraft or launch vehicle malfunction. The deployed LAS Hatch is shown on the spacecraft in Figure 1.

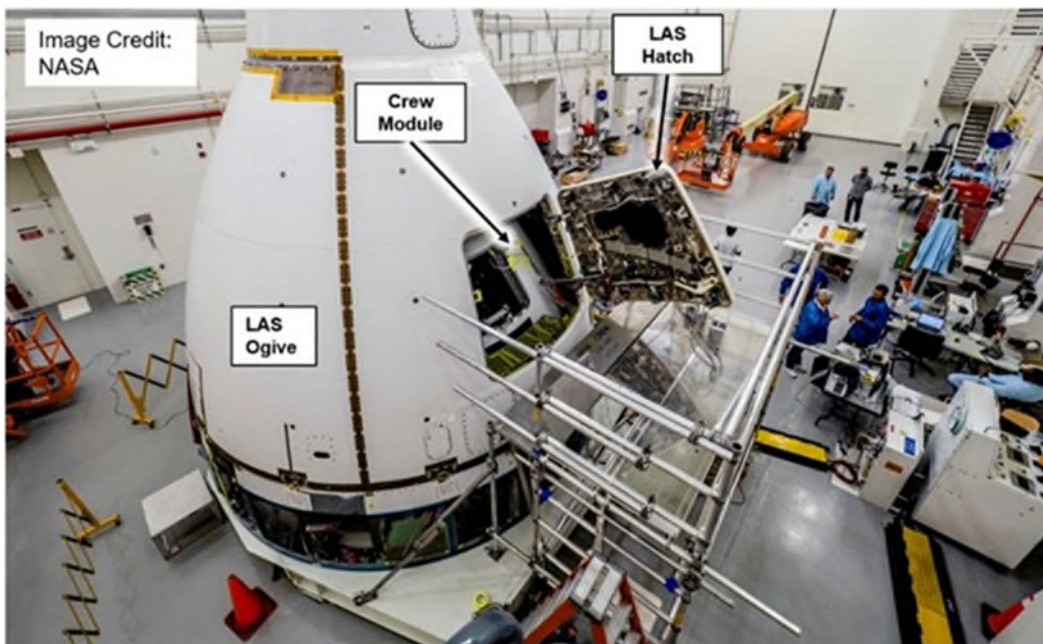


Figure 1. Orion LAS Hatch on the Ascent Abort 2 vehicle

* Lockheed Martin Space, Houston, TX and Littleton, CO

† NASA Langley Research Center, Hampton, VA

LAS Hatch Design Details

The LAS Hatch contains the following key components, reference Figure 2:

- Curved aluminum structural panel (conforming to the complex ogive shape of the LAS fairing)
- Window (aligned to the CM Hatch ~0.6 m away)
- 10 pneumatic latches used to compress the perimeter seal and retain the hatch to the LAS structure
- Pneumatic actuation system comprising solenoid valves, pressure transducers, check valves, batteries, a Composite Overwrapped Pressure Vessel (COPV), and steel tubing
- Perimeter weather and Electromagnetic Interference (EMI)/ Electromagnetic Compatibility (EMC) seal
- Deployment hinges (4-bar linkage design)
- Gate Release Assembly which initiates the emergency egress function (actuated by the opening CM Side Hatch)
- Bumper Assembly which the CM Side Hatch slides along to help open the LAS Hatch
- Tangential and radial hard stops which provide additional structural support
- Strut Assembly (pneumatic strut to help open the LAS Hatch)
- External Handle Assembly for opening the LAS Hatch from the exterior of the vehicle (for both nominal and emergency cases)
- Electrical system comprised of standalone batteries for emergency egress and sensors for crew situational awareness

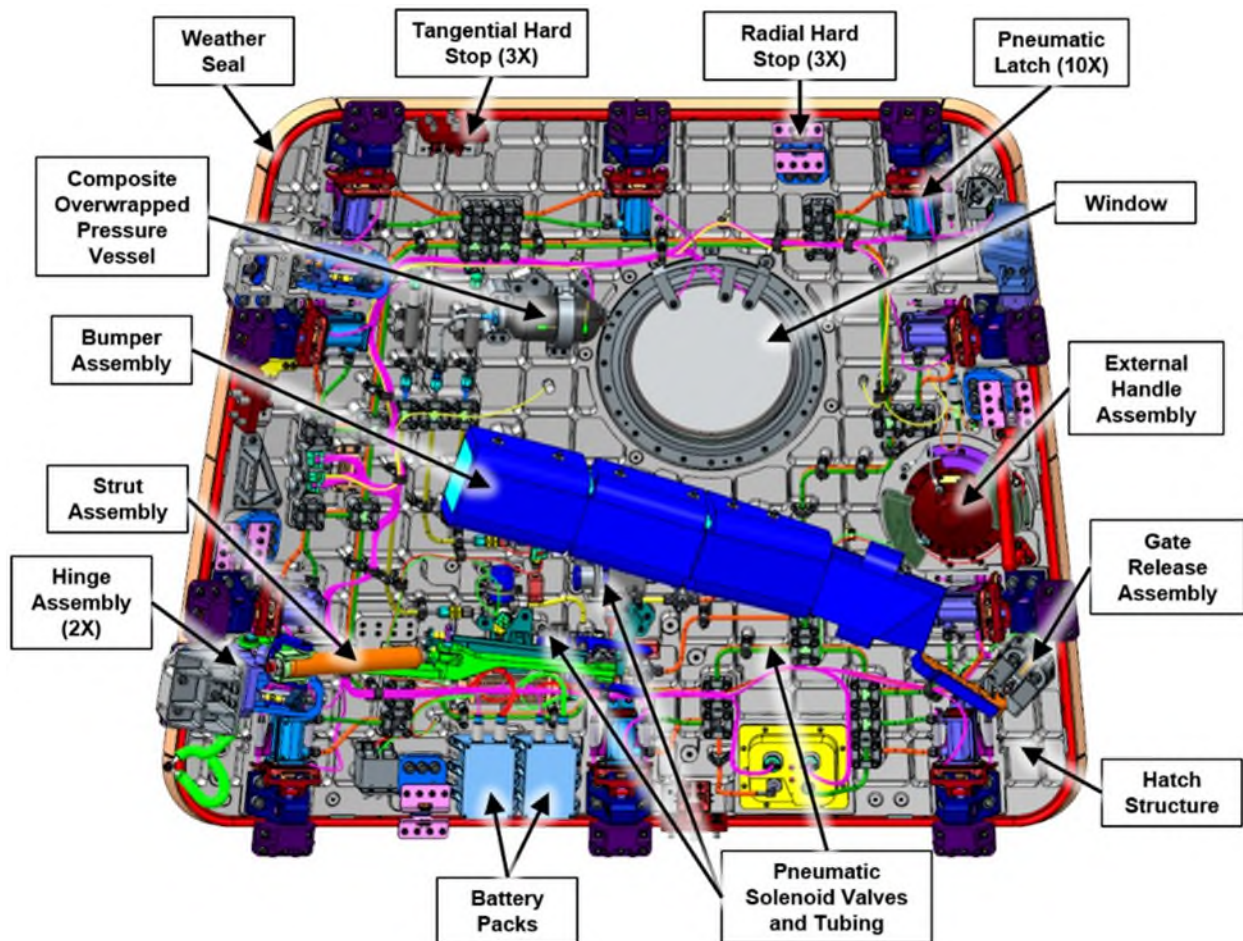


Figure 2. Orion LAS Hatch Overview (Interior View)

Emergency Operation Function

In the event of an emergency on the launch pad where the crew needs to exit the vehicle quickly, there are two scenarios:

1. Initiated by ground operations team: Ground team member pushes a button and turns the External Handle Assembly which actuates the pneumatic system to retract the latches, which then allows the ground team to pull open the hatch (aided by the pneumatic strut assembly).
2. Initiated by the flight crew (Figure 3): An astronaut will open the CM Side Hatch using either the manual gearbox system or an emergency pyro system. The Side Hatch is pushed open with its own pneumatic “counterbalance” strut, which then impacts the Gate Release Assembly on the LAS Hatch. The Gate Release Assembly actuates the LAS Hatch pneumatic system, unlatching the latches, which then allows the Side Hatch to push the LAS Hatch open as it slides along the bumper interface.

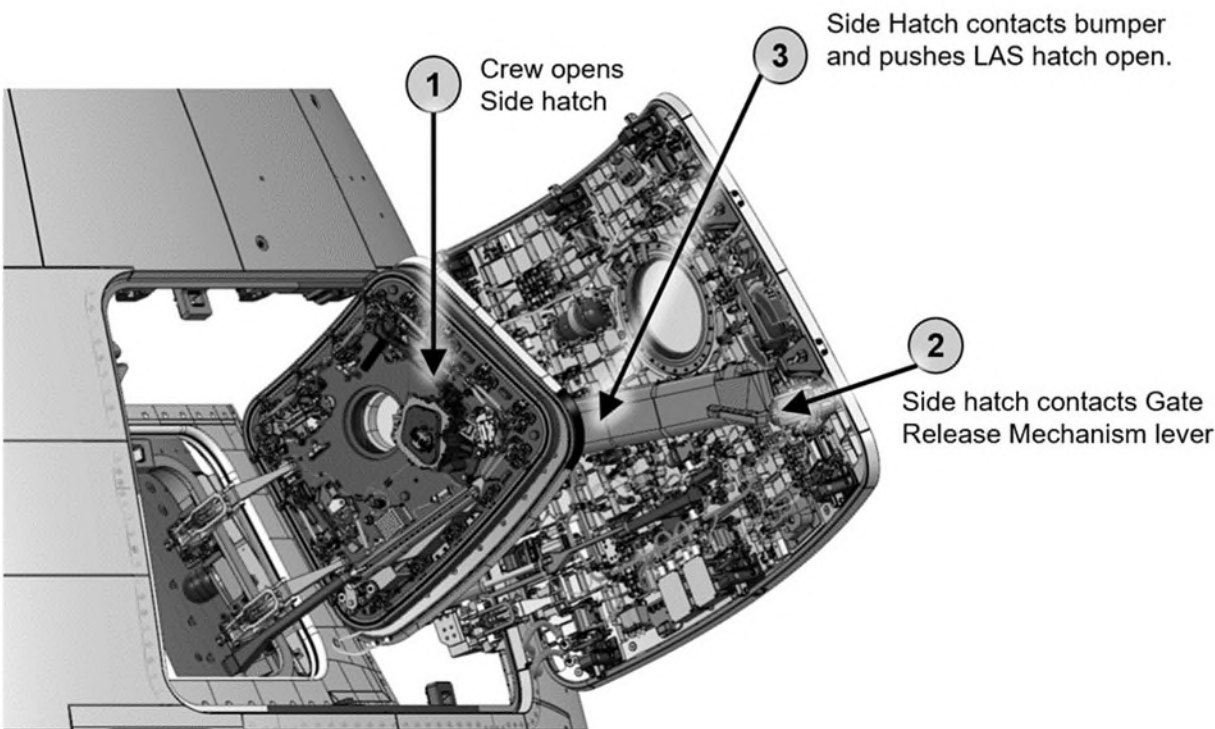


Figure 3. Orion Crew Module Side Hatch and LAS Hatch in Tandem

Design Development

The original pre-Preliminary Design Review (PDR) LAS Hatch design coming into 2014 was a similar design to the Crew Module Side Hatch, a mechanical design with mechanical latches, linkages, bell cranks, gearbox, mechanical release mechanisms, etc. The LAS team was tasked to pursue a less complicated and lower mass design to help reduce the already high mass of the LAS module. The mass of the LAS Hatch had a double impact on the overall LAS module mass (the mass of the hatch itself and the ballast mass opposite the LAS Hatch to maintain a center of gravity along the LAS module axis). The NASA Langley Research Center (LaRC) team developed a pneumatic design concept that simplified the hatch from the mechanical design by replacing the gearbox with an external pressure cart, linkages and bell cranks with pneumatic tubing, latches with pneumatic linear actuators, release mechanisms with electrical release technology, and many other changes. The pneumatic design was originally not looked upon favorably by the mechanisms team. It was a significantly different design from what had been worked and reviewed by the team since the Orion program started in 2006. The advantages of the design were very compelling, but the team would essentially have to restart the design process to implement the significant changes. The team decided to perform a trade study/Assessment of Alternatives (AoA) Analysis with an

agreed upon selection criteria (cost, schedule, risk, and mass) that would be weighted and scored using a software tool. The goal was to down select to a single design and then move one design forward to PDR.

NOTE: The original mechanical design used 15 latches (see Figure 4). To make a fair comparison, 4 designs were assessed: 15 latch mechanical baseline, 15 latch pneumatic, 10 latch mechanical, and 10 latch pneumatic. Preliminary analysis indicated that a 10 latch design was a feasible design alternative.

The AoA analysis was performed, and results presented to the Orion community: the 10-latch pneumatic design was the clear winner based on the agreed upon weighted criteria (see Figure 5). The next steps were to mature the details of the design and receive Orion program approval. The Orion community was originally very skeptical of the new pneumatic design, and several boards were needed to move the design towards acceptance. Some changes that were implemented were: Changing from pyro valves to solenoid valves for easier emergency egress turnaround, adding multiple strings of solenoid valves for redundancy (safety), adding pneumatic system updates to cover for unique scenarios such as failed valves, adding a suite of sensors to monitor the pneumatic system/latches/batteries (to provide situational awareness to the ground and flight crews), and adding batteries on the LAS Hatch directly for the case where the vehicle loses power. All of these changes were implemented, and the design approved.

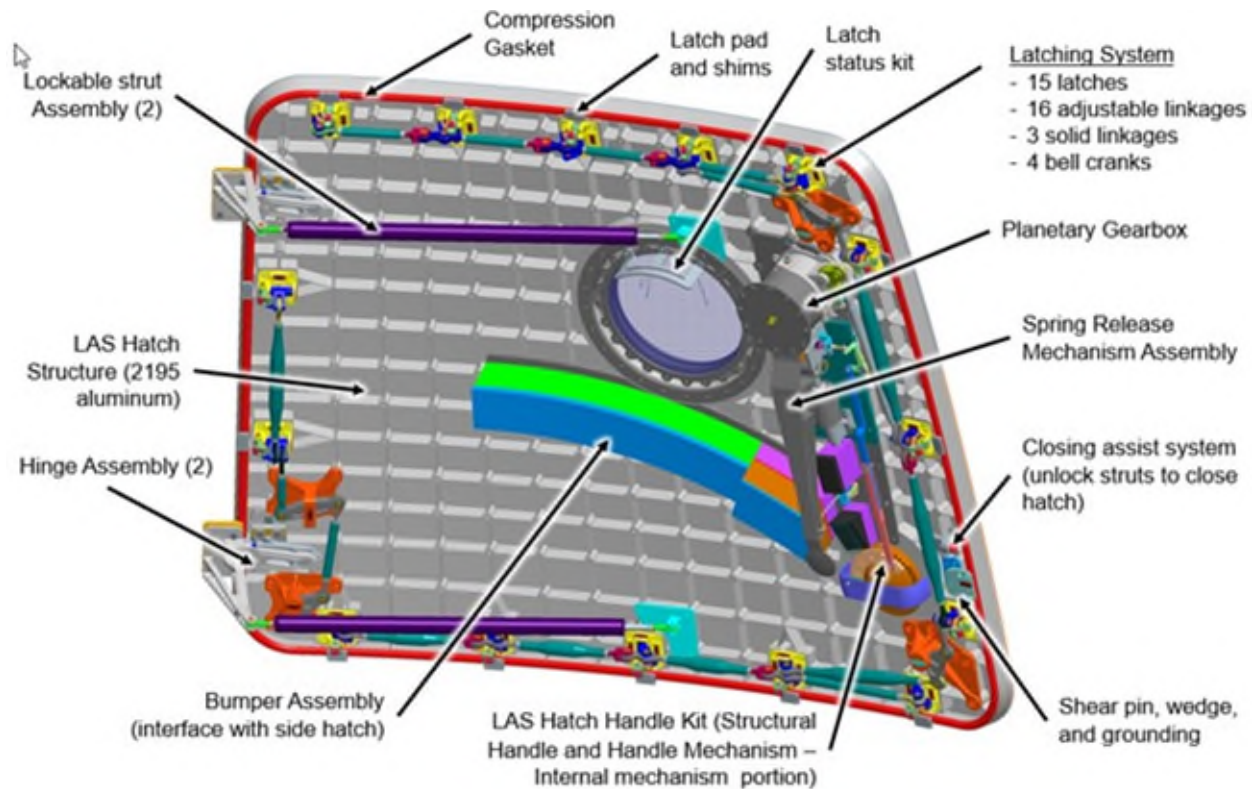


Figure 4. 15 Latch Mechanical LAS Hatch Baseline 2014

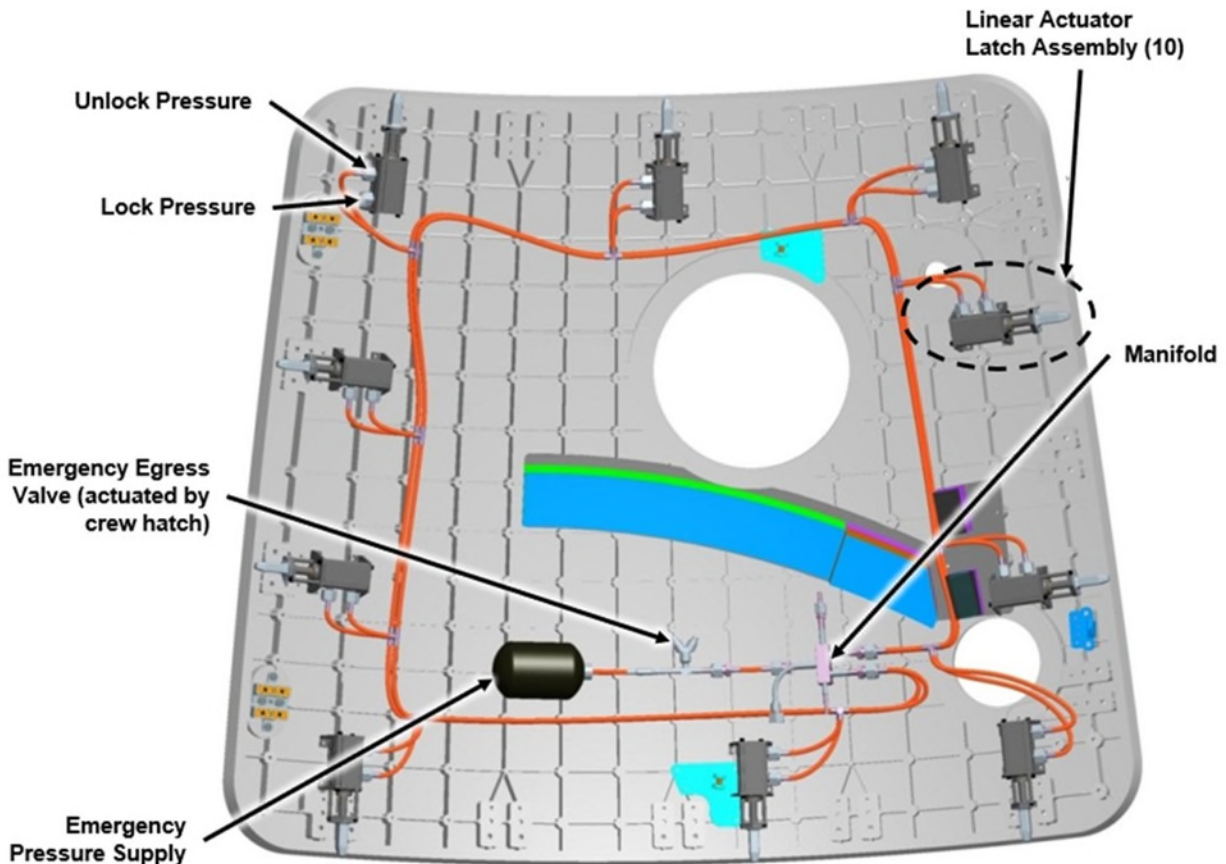


Figure 5. 10 Latch Pneumatic LAS Hatch Concept

Other design trade studies were completed such as:

- Use of venting valves to vent COPV after nominal launch to prevent inadvertent unlatching: Trade resulted in the use of two 2-way valves in series. Venting valves proved too difficult to control for launch sequence.
- Burst disks on closed latch volume: Trade resulted in leaving latch volume open to atmosphere.
- Multiple iterations of the sensor suite: Sensor suite optimized to provide ground and flight crew telemetry within channel allocations.
- Use of 3-way and 2-way solenoid valves: 3-way valve placed in series after the 2-way valve allows any leakage passing thru the 2-way and 3-way valve to vent thru the 3-way venting port. This ensures pressure does not enter unlatch volume.
- Addition of check valves: To prevent leakage into unlatch volume past the 3-way valve and to prevent pressure dump out of a failed to open 3-way valve in one of the valve Strings.
- Approval for adding fully functional LAS Hatch on the Ascent Abort 2 test.

Refer to Figure 6 for the Latch Pneumatic System.

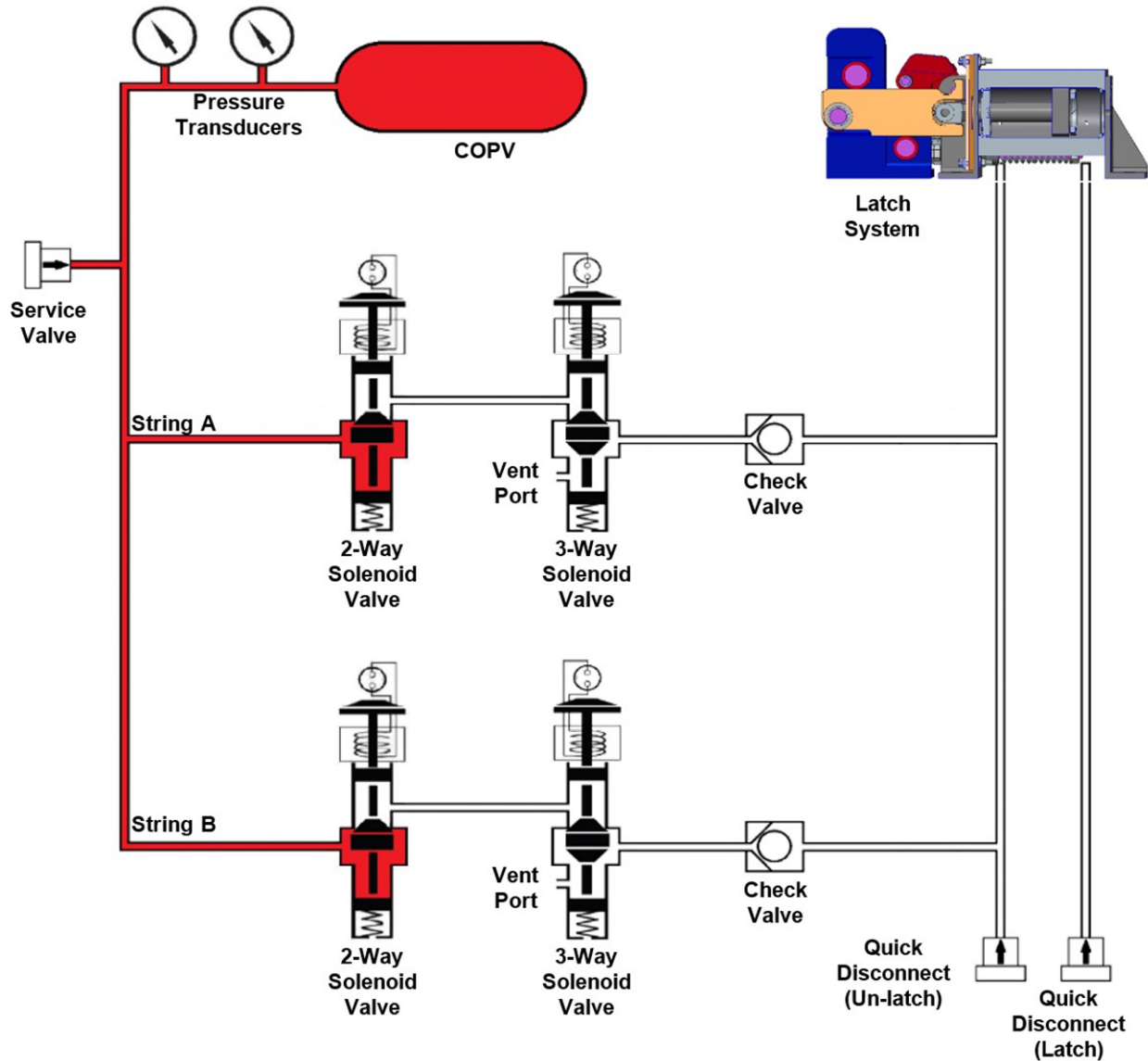


Figure 6. Latch Pneumatic System

Easy 5 (Docan Ltd.) simulating software was used to predict performance of the pneumatic system within the expected environments such as temperature changes. Using the Easy 5 software the simulation was able to predict all 10 pneumatic latch stroke distances and times. Iterations of the analysis consisted of altering tubing size, tubing length, valve configurations, pressure tank size and pressure limits, thermal effects on latch performance including pressure deltas, and predicted performance given various failure modes and redundant systems. Easy 5 simulation software aided in the final design solution of the pneumatic system to meet the latching performance requirements, such as time to unlatch the LAS Hatch in an emergency egress using worst case pressure changes due to thermal deltas and failure modes of redundant systems.

The initial pneumatic latch design used for the trade study with mechanical latches consisted of a pneumatic actuator, latch housing and the latch bolt. The actuator drove the latch bolt through the housing and into the receiving side of the LAS Hatch frame. Through multiple design iterations the design evolved to that shown in Figure 7.

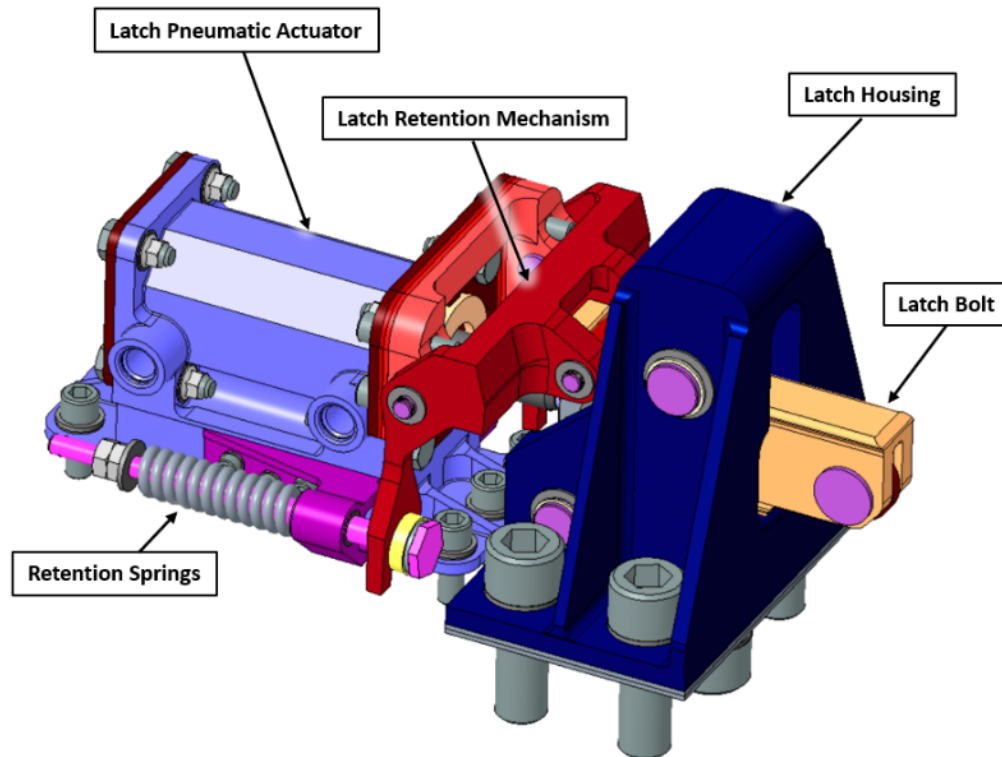


Figure 7. LAS Hatch Latch Mechanism

Due to the extreme acoustic environment created by the LAS rocket, several challenges had to be met including but not limited to:

- Ensuring latches remained latched during abort scenarios and random vibe environment
- Loads induced during abort sequence
- Hatch structure deflecting or “potato chipping” whereas the hatch structure would warp, creating large local deflections between hatch and frame
- Time for latches to unlatch in an emergency egress

The high acoustic levels generated large deflections between the hatch and the frame. Since the hatch is not required to maintain pressure before, during, or after flight (the seal between the hatch and frame is only for latch preload and electrical grounding requirements) the deflections were not a concern in terms of gapping. However, to reduce the overall loads within the hatch structure and reduce bending, the seal preload required would be an unattainable amount due to mass/stiffness. This required the design to have latches that retain the load in both directions. One direction is the hatch pushing outward against the Latch Ramp, compressing the seal further until the hatch bottoms out on frame bumpers (plastic strips along the frame such that the hatch does not contact metal to metal against the frame). The other direction is when the hatch pulls away from the frame. For this direction a receptacle was added on the frame limiting the amount of hatch deflection. Figure 8 shows a cross section of the actuator and latch which outlines the 2 different load paths and how they are resolved within the latch housing. As the latches are engaged the bolt rollers (shown as the red load path in Figure 8) allow the latch to move along the incline of the latch ramp, compressing the hatch seal and serving as the load path within the latch housing for direction 1. For

the reverse direction, the load path is resolved by hard stops located within the latch housing (shown as the yellow load path in Figure 8).

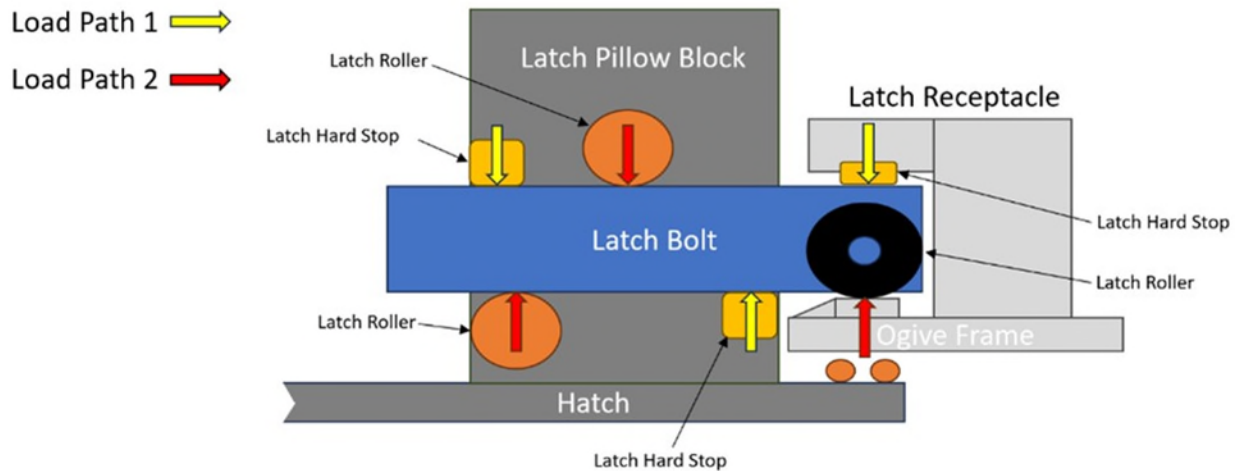


Figure 8. LAS Hatch Latch Mechanism Load Path Diagram

The pneumatic latches also provided a system that was not as affected by hatch structure deflections that a mechanical system would be. Since mechanical latches require linked mechanisms to operate a latch, those links are subject to hatch deflections that may alter latch over center positions, latching positions, as well as preload. The pneumatic latches are not dependent on mechanical links for latching.

The original plan for the linear actuator was to use a vendor supplied item or COTS hardware. The vendor chosen to make the actuators decided to back away from the project due to the environments and challenges of space hardware. This provided an opportunity to design a customized actuator that better suited the hatch interfaces, packaging constraints and performance which ultimately allowed for a much lighter and more efficient design.

The LAS Hatch pneumatic tubing system was designed as a lightweight solution to transfer energy and latch or unlatch the actuators, allowing the hatch to be “locked” or “unlocked”. The tubing system, as seen in Figure 9, can be broken down into four sub-systems: high-pressure weldment, solenoid valve weldment, low-pressure unlatch weldment and low-pressure latch weldment. The pneumatic actuators are connected to the low-pressure latch and unlatch weldments where they can be actuated using a pressure cart on the ground or an emergency supply of nitrogen gas stored within the high-pressure weldment on the hatch. During an emergency, the solenoid valves are energized through the external handle or gate release mechanisms, releasing the nitrogen and back driving the latches.

Within the high-pressure weldment, the bulk of the emergency nitrogen is stored within the COPV (composite overwrapped pressure vessel) tank. This tank is a standard COTS (Commercial Off The Shelf) item (similar to tanks used in paintball guns). It is designed to be leak-before-burst as a safety feature and is attached to the rest of the weldment through a custom fitting. The high-pressure weldment also includes two identical pressure transducers to measure the actual pressure within the weldment. The weldment is filled using a COTS Schrader valve threaded onto a custom manifold.

The high-pressure weldment is connected to the unlatch weldment through two identical solenoid valve weldments in parallel. This allows for redundancy if one of valve strings is stuck close or fails to energize. Each string is connected to an independent battery box which is mounted to the hatch and is decoupled from overall vehicle power. Within each solenoid valve string, there are two valves. The first valve is a 2-way solenoid and the second is a 3-way solenoid. This allows for accidental leakage past the first valve to be vented to atmosphere unless the valve string is intentionally energized. As part of the development test campaign, these valve strings were successfully tested in a partial abort environment where it was

confirmed that although there was leakage past the first valve, the second valve prevented gas leaking into the unlatching weldment.

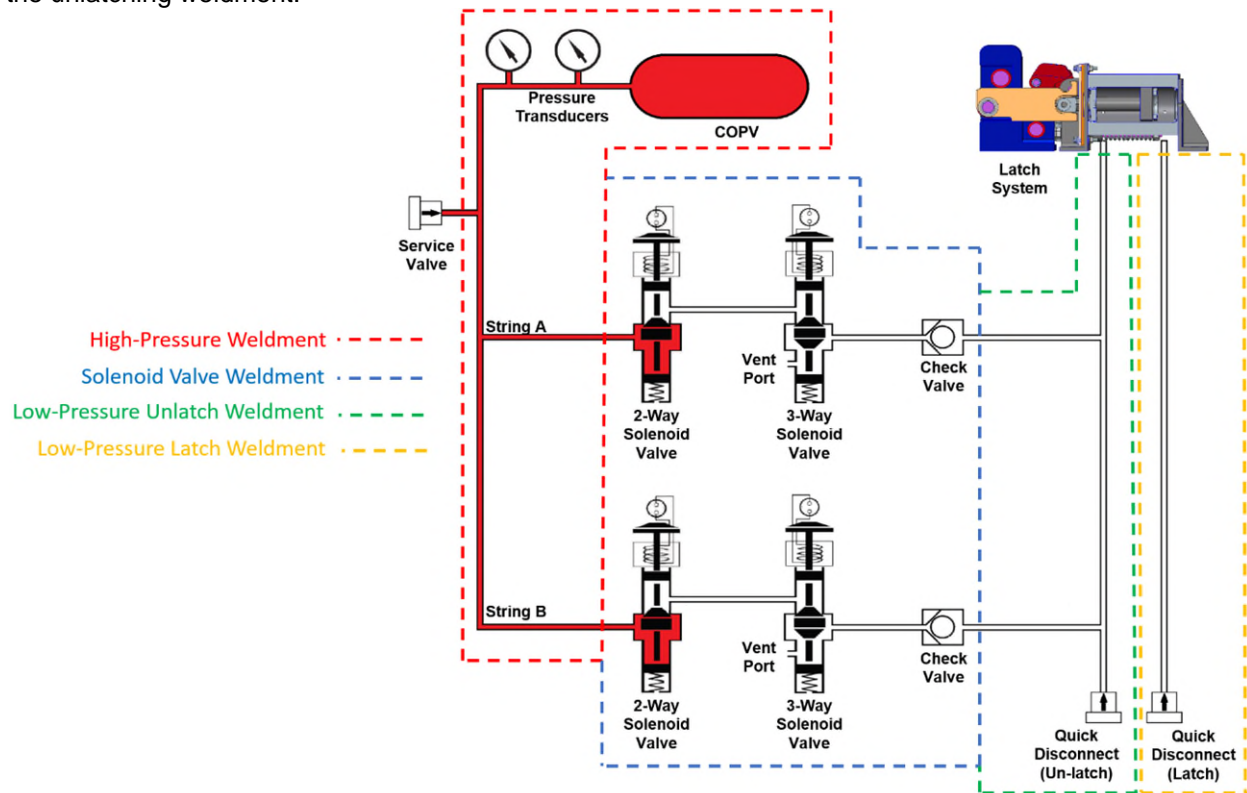


Figure 9. LAS Hatch Pneumatic Tubing System

Originally all the weldments were secured to custom clamps using COTS Teflon cushions and thick, pliable tape. The issue with this design was that it was impossible to simultaneously eliminate gaps while also prohibiting any side load from being induced during assembly. This problem was solved through the development of small injection holes within the clamps to allow for the injection of liquid Room Temperature Vulcanizing Silicone (RTV) between the clamps and tubing.

All tubing weldments are bent, fitted up and welded in-house at Lockheed Martin. To aid the tube assembly on the flight hatch, a weld tool was developed which uses the same flight interfaces but built to tighter tolerances. It also requires the use of the flight actuators which are serialized and installed in the same location on the weld tool as they are on the flight hatch. The weldments are fitted up on this tool prior to any welding and ensures that all the weldments can be assembled onto the flight hatch without issue. Each weldment is proof pressure and leak tested at the individual weldment level and again once they are integrated together on the flight hatch. During this testing it was discovered that the Swagelok fittings are very sensitive to orientation when re-swaging and led to multiple process changes throughout the assembly.

LAS Hatch Development Testing

The LAS Hatch is located directly below a LAS solid propellant rocket motor. When these rocket motors are activated, they provide a substantial acoustic environment for the LAS Hatch. A development unit was made along with LAS ogive test panels to be assembled and tested in NASA's Reverberant Acoustic Test Facility (RATF), see Figure 10. The test facility was not able to achieve the acoustic levels predicted however the data collected was used for model correlation which reduced risk for stress margins.

The EDU LAS Hatch used for the acoustic test at RATF was the same hatch and hardware used for the Ascent Abort-2 test (AA-2) shown in Figure 11.



Figure 10 (Left). EDU LAS Hatch installed into LAS Ogive test assembly at NASA's Reverberant Acoustic Test Facility (RATF)



Figure 11 (Right). Ascent Abort-2 test conducted on July 2nd, 2019, at Cape Canaveral SLC-46 launch site (Photo Credit: NASA/Tony Gray and Kevin O'Connell)

The purpose of the Orion Ascent Abort 2 (AA-2) Test Flight was to demonstrate a full up use of the Orion Launch Abort System (LAS). This test was accomplished by propelling a Crew Module simulator and flight LAS to an altitude of 9,450m, and a speed of roughly 357m/s, on a modified Peacekeeper first stage. During planning for the test, it was decided to fly the LAS Hatch Engineering Development Unit (EDU) as an Artemis I flight-like hatch. After the EDU was manufactured, the ongoing analysis showed the vibroacoustic loads continued to increase. These vibroacoustic loads are generated by the LAS Abort Motor firing above the hatch location. Upon review of the AA-2 loads, a decision was made to remove the pneumatic strut from the hatch during final closeout for flight due to negative stress margins on assembly (pneumatic gas strut assembly was later redesigned to handle abort loads). The rest of the EDU remained as designed. After launch, the LAS Hatch went through the flight and abort environments successfully. Upon completion of the test, the LAS descended from altitude and impacted the Atlantic Ocean, and then the seafloor in fifteen feet of water. A recovery crew was dispatched and discovered the LAS Hatch resting on the seafloor being guarded by a nurse shark. With cooperation from Lockheed Martin, NASA was able to recover the LAS Hatch (see Figure 12). The hatch was in good shape and still fully latched. This result provided significant confidence in the design of the LAS Hatch.



Figure 12. Orion AA-2 LAS Hatch Post AA-2 Launch

Tandem Test

To demonstrate the emergency egress capability of the Side and LAS Hatch, a test was performed using a flight like qual Side Hatch and the Artemis II LAS Hatch assembled in a fixture that represents the flight configuration. See Figure 13. After test set up was complete, a series of test cycles were conducted that reflect different emergency scenarios including:

- Side Hatch counterbalance set at different pressures to evaluate the deployment performance of both hatches
- Various openings using different flight and ground crew initiation.
- Employing a flight like equipped (Helmet and Gloves) Artemis II Astronaut that will be responsible for Side Hatch openings to perform various Side Hatch emergency and nominal openings.

Concerns going into the tandem testing revolved around the Side Hatch and LAS Hatch hinge capabilities. The hinges were designed to kinematically open normal to the hatches for a certain distance to minimize shear loading on hatch seals. After this predetermined distance, the hinges would then rotate the hatches as they are pushed outward. Since the hinges were designed with this kinematic motion, they are sensitive to the overall moment generated on the hatch due to the resultant load on each hatch such as counterbalance, gas strut, side hatch load on LAS Hatch during opening, etc. If the moment generated is high enough at certain kinematic positions of the hinges, then the hinges could bind or not be allowed to follow through with the kinematic motion. The kinematic location where the hinges were sensitive to the hatch moment was found to be near the hinge closed position. This is where the kinematic motion of the hinges transitioned from opening normal to the hatch to a motion of hatch translation and rotation. The hinges were fitted with strain gauges during the tandem test to monitor the induced loads within the links of the hinges. During LAS Hatch installation to ogive for Tandem testing it was also found that proper lubrication of the hinges is essential for proper operation. Lubrication on the hinges was initially called out to be applied sparingly to avoid contaminants on the neighboring LAS Hatch window. However, after several cycles of hatch openings, the hinges started to bind. After hinge disassembly, the hinge pins showed signs of galling. The lubrication notes for hinge assembly, as well as other mechanisms, were updated to remove the word “sparingly”, as well as specifying exactly where and how much lubrication to apply. The lubrication Braycote 601 was also replaced with Braycote 602. Braycote 602 includes Molybdenum disulfide which is a primary material for reducing or eliminating the possibility of galling.

The Tandem testing performed was successful. It was found that as long as the LAS Hatch Gas Strut provided enough force such that the LAS Hatch was pushed outward and past the sensitive kinematic position, then the load within the hinges remained within stress margins.



*Figure 13. Tandem Testing
(Left Picture – Hatches Closed)
(Right Picture – Hatches Open)*

Analysis Approach

The LAS Hatch analysis is performed to verify the numerous human rating requirements developed to ensure crew safety. Those requirements ensure the proper form, fit, and function of the hardware. The hardware is assessed against those requirements throughout the expected lifecycle. The definition of the “expected lifecycle” can be a challenging and iterative activity. In the case of the LAS Hatch, one critical event within the lifecycle is the abort event. This extreme set of environments proved challenging to find a mass optimized design and meet a stringent requirement set. The design complexity of the LAS Hatch required the development of Finite Element Model (FEM) math models. These FEMs are used to help derive environments and perform margin of safety assessments of failure modes. The FEM is an analytical representation of the structure that is used to predict the response when environments are applied to the model.

FEM results represent an approximation of the predicted response and should be verified by test methods. Figure 14 shows the hatch static load test performed to verify FEM results.

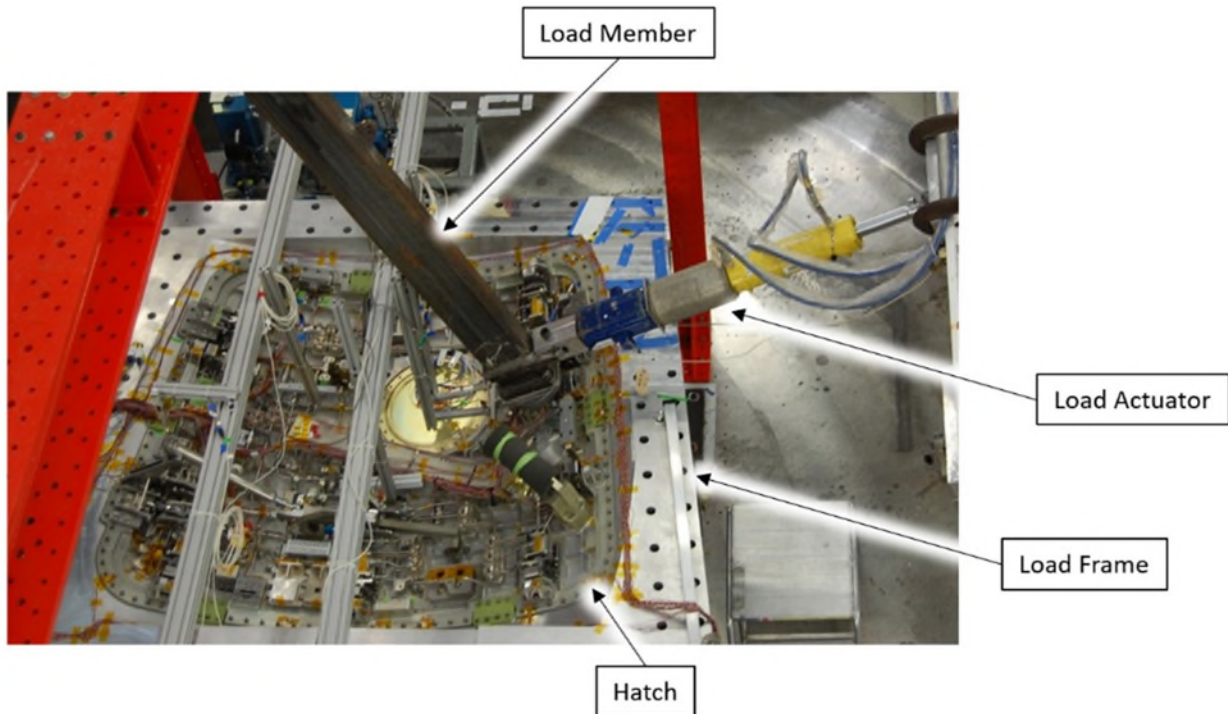


Figure 14. EDU LAS Hatch Static Load Test

In some cases, a coarse FEM is overly conservative and higher fidelity FEMs are required to meet mass critical design requirements while demonstrating positive margins of safety (MS).

During analysis, it was found that the extreme abort environment caused high deflections on the hatch structure inducing large loads. To counter these deflections, normal and tangential hard stops were added to the perimeter of the hatch. It was found, however, that due to the environment these hard stops did not reduce the loads to the extent expected. Rather, they created additional load paths that do not necessarily share the load. The normal and tangential hard stops were kept in the design since they did aid in reducing hatch structural load, even though the reduction was not as high as anticipated.

Through multiple iterations of structural analysis of the hatch and components installed onto the hatch it was found that, due to the high vibrate environment, the addition of mass to overcome of the induced loads would sometimes create a negative reinforcement loop where more mass created higher loads, which, in turn, required more mass and so forth. Therefore, alternative design approaches were sought to mitigate this loop such as hard stops to limit deflections and alternate materials to allow higher deflections.

Hinge Testing

The hinge design is a 4-bar linkage mechanism. When the hatch is in a closed position, the hinge hard stops engage and allow load to transfer between the hatch and frame.

Real-time monitoring of test data with strain gages, digital imagery correlations and actuator feedback data was required to protect the test article and correlate the analysis models. Great communication, trust and patience between the analyst and test team is required to maintain control of a 6 degrees of freedom system.

Statically testing this mechanism required weeks of trial and error, influence coefficient load cases and many adjustments to load/control systems to collect enough data to correlated FEM prediction models. Test campaigns of this duration and complexity require test discipline from the entire team. Despite the team's best efforts and good test discipline, repetitive activities can lead to human error. Approaching the end of the test campaign, a simple hydraulic value for the load jacks was configured incorrectly and resulted in an unexpected test failure of the article. The test campaign was considered successful because of the data collected; however, the failure was an important lesson related to test discipline. Figure 15 is the hinge in a closed position, ready to statically test.

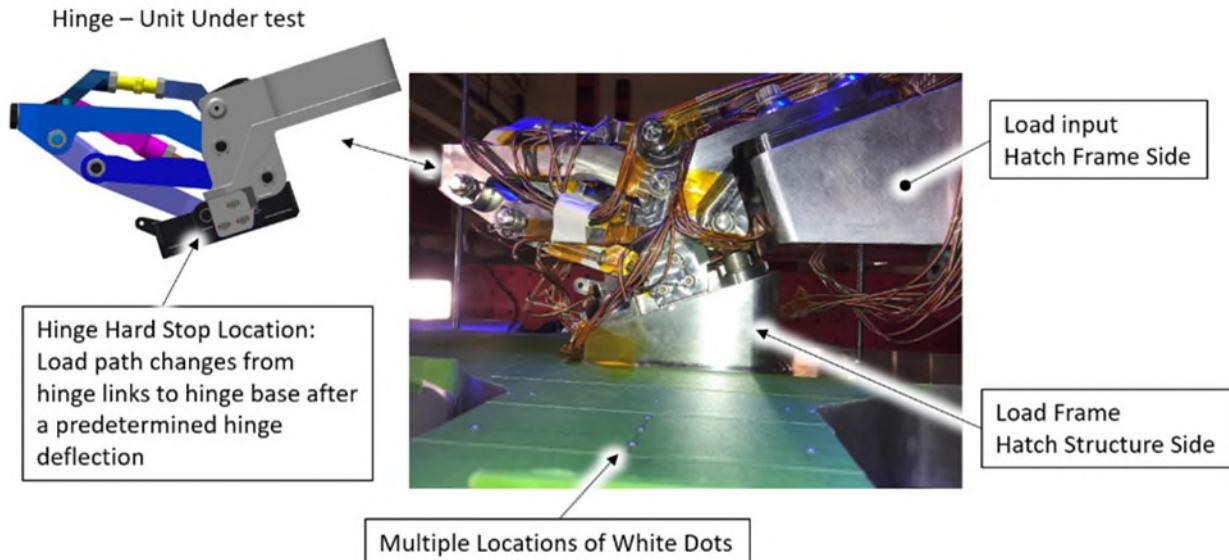


Figure 15. Hinge Static Load Test

Lessons Learned

- Test as early as you can: many issues found during testing were harder to overcome due to flight hardware already built to maintain schedule.
- The normal and tangential hard stops were added to the perimeter of the hatch to reduce hatch deflections, however due to such an extreme abort environment, the overall reduction in structural load was not as initially expected.
- The pneumatic latches provided a system that was less sensitive to hatch structure deflections than the original mechanical latch design.
- Testing found that if external spiral lock rings are not installed correctly, they can back out of the groove during a vibe environment. After external spiral lock rings were found to be backing out of the groove during a high vibe environment, an installation step was added for installing these rings where the outer diameter of the installed ring was measured and verified to be within tolerances. If they were out of tolerance, it could indicate one of the spirals may be seated improperly within the groove or other tolerances may not be met for proper installation.
- The use of COTS or vendor supplied items may look like the best option on paper but weighed against packaging, performance and reliability of a customized part, the COTS item may not be the best suited for the application. The LAS Hatch used COTS items such as solenoid valves and gas struts but designed the latch linear actuators in-house.
- Adding mass to take the high loads created a negative reinforcement loop where more mass created higher loads which required more mass and so forth...

Conclusion

The design and development of the LAS Hatch proved challenging due to the abort environment provided by the LAS rockets as well as providing a safe and reliable crew egress during on-pad emergencies. The pneumatic latches proved to be a lighter and more reliable system to the mechanical alternative. They also proved successful for timing requirements during Side Hatch/LAS Hatch emergency egress tandem testing. The LAS Hatch extreme environmental levels provided by the vehicle on pad, launch, in flight and possible abort activities provided challenging opportunities to develop test campaign approaches. The qual testing including Hinge Static load test and Tandem testing as well as the AA-2 abort flight test provided evidence of a safe and reliable LAS Hatch for future Artemis missions. This all culminated in the successful flight of the LAS hatch design on the Artemis I mission to the moon in November 2022 (Figure 16).



*Figure 16: Artemis 1 uncrewed test flight, November 16th, 2022, at Cape Canaveral launch site
Photo Credit: NASA/Keegan Barber*

Acknowledgements

- Lockheed Martin Orion Mechanisms team: John Lawlor, Mike Long, Ben Nesmith
- NASA Orion Mechanisms Team: Joseph Anderson, Brent Evernden

Precision Actuation in the Flight Design of the Roman-CGI Focus Control Mechanism (FCM)

Mineh Badalian*, Johnathan W. Carson* and Dalia Raafat*

Abstract

Piezo Electric Transducers (PZTs) are precision mechanisms used for single-axis translation by varying their input voltage. These devices can be powerful in applications where fine motion, in microns, is required. PZTs also have off-axis motion characteristics that affect their intended function of axial-only translation. These off-axis motions should be focused on when utilizing PZTs in mechanism design. This paper will discuss an application for PZTs as seen in the Focus Control Mechanism (FCM), a mechanism that lives inside of the Coronagraph Instrument (CGI) on the Nancy Grace Roman Space Telescope.

Introduction

The objective of the Coronagraph Instrument is to view planets in other planetary systems by decreasing the host star's glare [1]. In the Roman Space Telescope, CGI is located between the Spacecraft Bus and the Outer Barrel Assembly. The FCM is part of CGI and assembled on its optical bench, as seen in Figure 1.

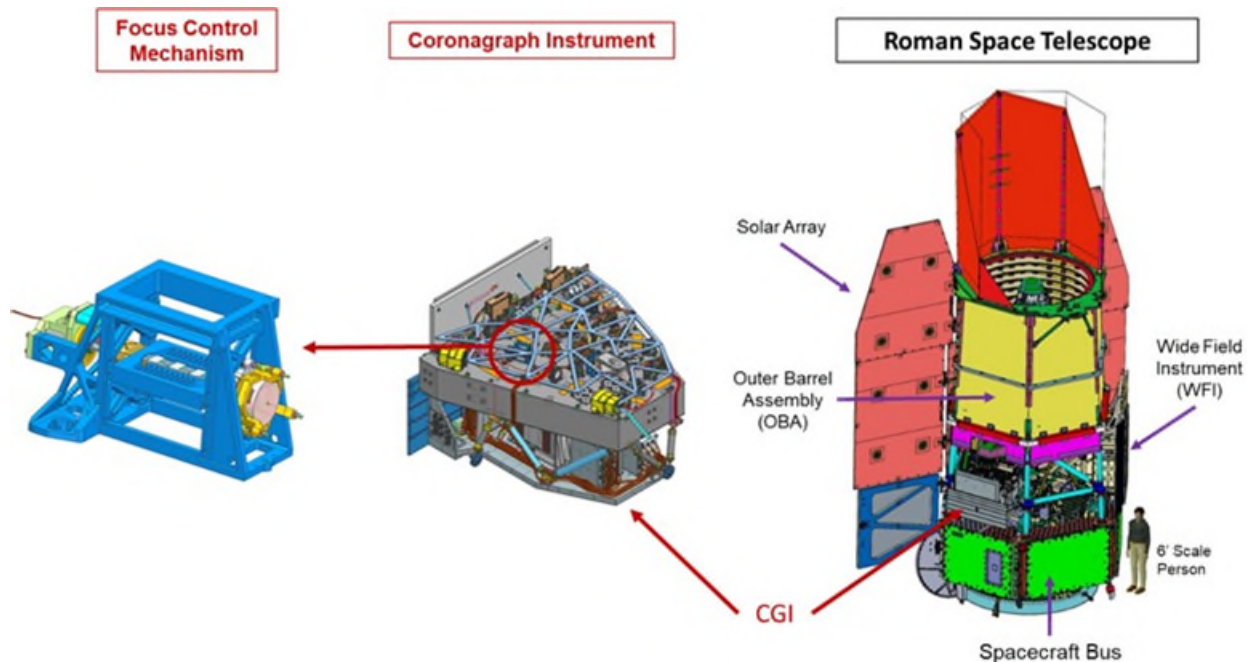


Figure 1. The Roman Space Telescope, the Coronagraph Instrument (CGI), and the Focus Control Mechanism (FCM)

In this instrument, the FCM consists of two stages that allow this mechanism to control the position of the Focus Control Mirror along a single axis: the Coarse Stage and the Fine Stage. In the Coarse Stage, a geared stepper motor drives a leadscrew which moves the carriage of the FCM for coarse operation. The

* Jet Propulsion Laboratory, Pasadena, CA; minehbadailan@gmail.com

motion of the carriage translates to motion of the Focus Control Mirror, which is attached to the opposite end of the FCM Frame. This stage is used infrequently to correct errors from ground to orbit shifts and static errors in masks and filters. The Fine Stage differs because it is used continuously during an observation to correct errors due to observatory thermal drift. A stack of three PZTs are bonded mechanically in series, and then bonded mechanically into the center of the flexured FCM frame carriage and preloaded to 600 N to keep them in compression during launch. Each device also has its own Strain Gauge for displacement feedback during operation. Increasing the input voltage to the stack of PZTs, causes displacement in the fine stage, which translates to movements in the Focus Control Mirror. The strain gauges on each PZT provide feedback on displacement. The position of the carriage remains fixed relative to the frame, and the flexures within the carriage bend to move the mirror. To put it into perspective, the Coarse Stage can provide 1.27 mm of stroke, while the Fine Stage can provide a maximum of 42 μm of stroke at worst case, with a requirement of 27 μm for the mission. This paper will dive deeper into the Fine Stage of this Mechanism. Figure 2 shows the Flight Model (FM) FCM assembly at the instrument level, with a breakdown of its stages and parts.

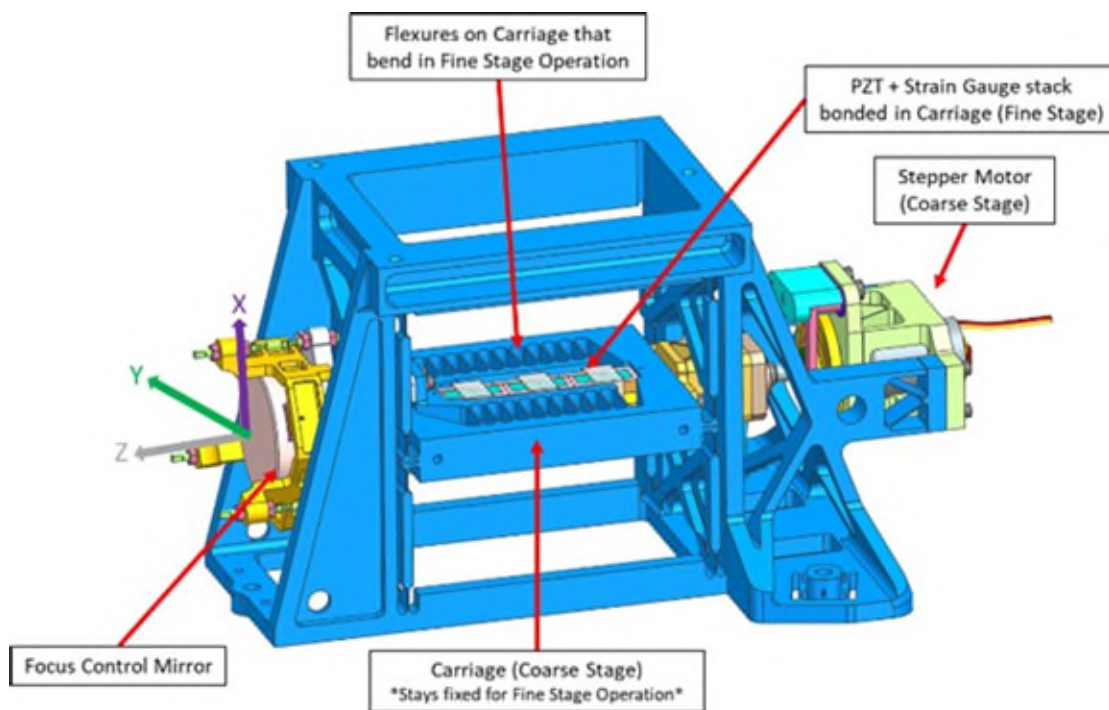


Figure 2. A model of the FCM, showing its various components and points of interest.

Requirements

The FCM Fine Stage has a crucial tip (or elevation) and tilt (or azimuth) crosstalk requirement. Tip is defined as rotation about the y-axis, tilt is defined as rotation about the x-axis, and piston is translation about the z-axis, as shown in Figure 2. This requirement is summarized in Table 1.

Table 1. Focus Control Mechanism Fine Stage Tip/Tilt Crosstalk requirement.

Stage	Requirement
Fine Stage Crosstalk	The RSS of the tip and tilt (rotations about Y and X axes in the FCM Optical CSYS) crosstalk of the FCM mirror interface over any 14 μm range of the fine stage travel of the FCM Mech shall not exceed 1.3 μrad .

The requirement asks for the Root-Sum-Square of the tip and tilt crosstalk over any 14 μm range of the full stroke of the mechanism, where the full stroke of the Fine Stage is 42 μm . Unfortunately, this requirement

was not met by the FCM assembly, causing an investigation and a need for rework. The EDU FCM exceeded the requirement by 1.9x, while the FM FCM exceeded the requirement by 3.7x. Prior to discussing the investigation and the results, it is important to dive deeper into PZTs and the design of the FCM Frame, with a focus on the fine stage flexures.

What are PZTs?

The piezoelectric effect in PZTs arises from its crystal structure, consisting of alternating layers of lead ions and oxygen ions. When subjected to mechanical stress, the asymmetry in the crystal lattice generates an electric field, leading to a polarization of the material. Conversely, when an electric field is applied, PZTs undergo mechanical deformation, making it an ideal material for transduction between mechanical and electrical energy [2]. Fine motion control is essential in various engineering applications requiring precise positioning, such as the optical system in the FCM. PZT-based actuators play a crucial role in achieving high-resolution motion control due to their fast response times, high precision, and displacement capabilities. PZTs operate based on the piezoelectric effect, wherein the application of an electric field induces mechanical deformation in the material. This deformation, typically in the form of expansion or contraction, results in motion. By controlling the magnitude and polarity of the applied voltage, precise control over the displacement of the actuator can be achieved. Moreover, PZT actuators exhibit low hysteresis behavior and excellent repeatability, making them suitable for fine motion control tasks requiring high accuracy [3].

FCM Frame Design

The frame of the FCM, housing the 600 N preloaded and bonded PZT stack, has several design and fabrication specifications that are important. Each side of the frame carriage has 10 flexure blades, a total of 20 flexure blades overall, that allow for fine stage motion. The nominal thickness of each flexure blade is 550 μm and deviations in thickness between any two of the 20 flexure blades shall not exceed 5 μm. Even more crucial are thickness deviations between two flexure blades that are symmetric on each side of the carriage. For example, in Figure 3, the variations in thickness between 1L and 1R shall not exceed 5 μm.

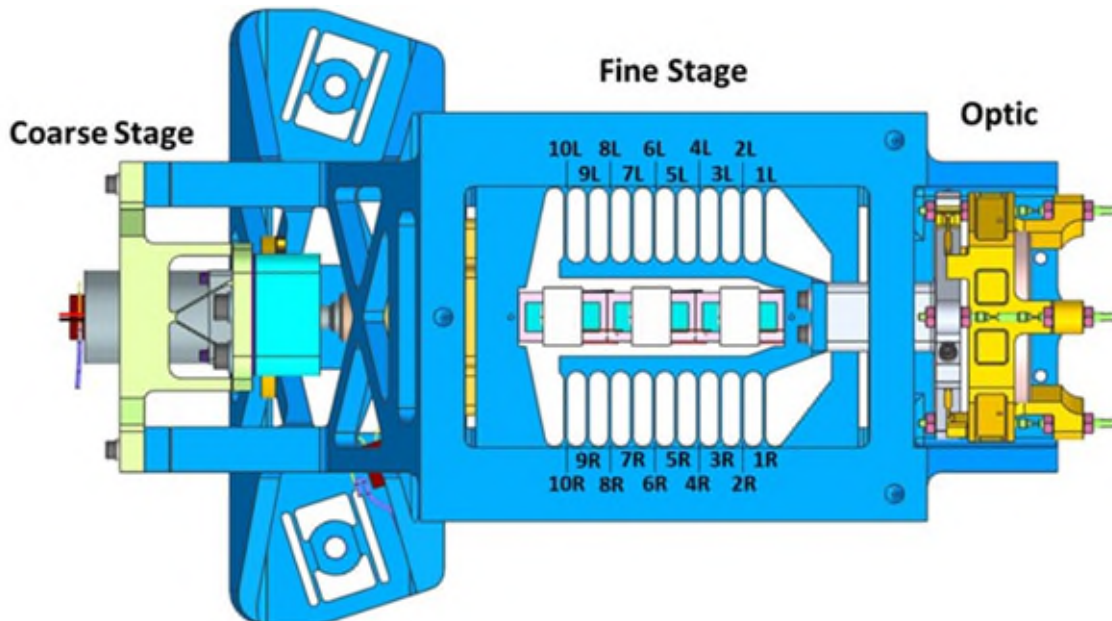


Figure 3. Top view of the Focus Control Mechanism, showing the frame’s fine stage flexure labeling scheme used for the tip and tilt crosstalk rework.

This insight into the fine stage flexure design requirements is important in understanding the investigation and the rework that brought the tip/tilt crosstalk of the FCM’s fine stage back into the required range.

Investigation

In the Fine Stage, the violation of the requirement had two possible sources to investigate. First were the differences in flexure blade thicknesses on each side of the carriage. Second and more importantly, the fine stage structure was sensitive to how the PZTs were aligned, in a stack to the frame, as well as to one another, with the highest sensitivity coming from y-axis misalignment. The motion characteristics of each individual PZT were different and were not tested prior to flight integration. A PZT motion characteristic test was performed during this investigation, which demonstrated that each PZT had its own tip and tilt characteristics and should have been tested prior to flight integration. This phenomenon of the unloaded PZTs was unknown previously and was a surprising discovery. If there was prior knowledge of the behavior, additional flexure elements would have been added to the design of the Fine Stage carriage to minimize the tip and tilt crosstalk violation.

Path Forward

A PZT motion characteristic test was performed with three Flight spare PZTs and three commercial off-the-shelf (COTS) mirrors to determine whether the transducers had their own tip and tilt characteristics. Each PZT was bonded to one COTS Mirror, and the test was performed on three separate PZT-Mirror assemblies by driving each PZT to its full range while measuring the tip and tilt. In this set of tests, the PZTs were not preloaded as they are in the FCM frame, and the stroke per PZT was $\sim 15\ \mu\text{m}$. This preload was in place for the FCM assembly because PZTs are brittle under tension, therefore, the preload was applied to ensure the PZTs stay in compression throughout the life of the mechanism. A preload was not necessary for this quick, low cycle, test. The transducers were initially cycled three times from 5 V to 95 V to counter the effects of hysteresis before being actuated from 5 V to 95 V in 5 V, 10 V, or 25 V increments, to mimic FM testing. Figure 4 shows this test setup with all three PZT-Mirror assemblies.

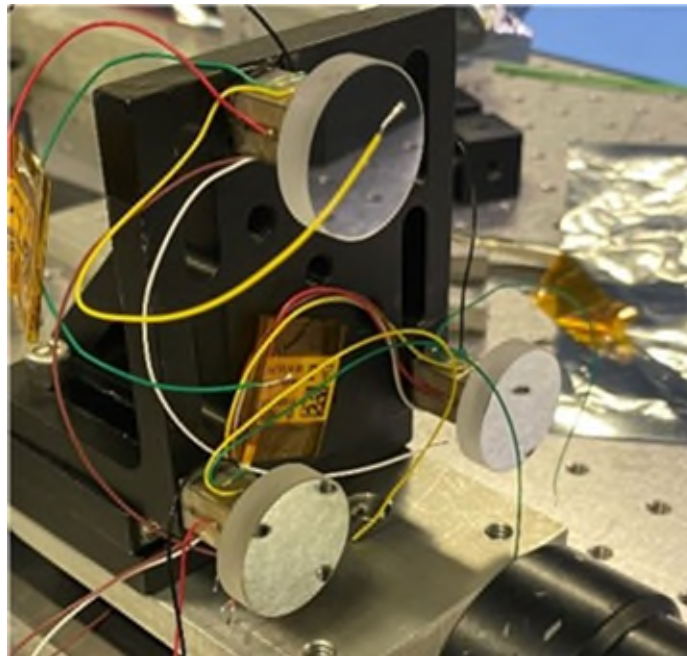


Figure 4. Configuration for the PZT Motion Characteristic Test

This test demonstrated that each PZT did have its own tip and tilt motion characteristics. Before bonding each PZT to the PZT stack and bonding the PZT stack to the FCM frame, a motion characteristic test should have been performed to account for this inherent nature of the transducers. The tip and tilt results for this PZT Motion Characteristic test are shown in Table 2.

Table 2. Tip and Tilt results from the PZT Motion Characteristic Test.

	Tilt (μrad)	Tip (μrad)
PZT 1	~68	~27
PZT 2	~90	~20
PZT 3	~58	~15

When this requirement violation was discovered, the Focus Control Mechanism was already in its assembled state (Figure 2) and a disassembly of the PZT stack would have introduced an unacceptable schedule hit, a repeat of the test campaign, and an increase in cost. As a result, another solution was needed to correct the discrepancy. The path forward for the fine stage tip/tilt crosstalk anomaly was to polish the flexure blades on each side of the carriage to compensate for the variation in tip and tilt, introduced by the motion characteristics of the PZTs. A closer look at the flexure blades of the FCM carriage through analysis guided the rework. An essential aspect of this rework included knowing which part of the flexure blade to polish and which flexure blade to focus on.

Analysis: FCM Fine Stage Motion

The FCM's Fine Stage structure was sensitive to how the PZTs were aligned, with the highest sensitivity in the y-axis (Figure 2) and through testing, the PZTs demonstrated their inherent motion characteristics. A combination from both these factors contributed to the large tilt (azimuth) discrepancy, and therefore, the overall fine stage tip/tilt crosstalk requirement violation. As the preloaded PZTs were actuated with an increased voltage input, the stack would bend under extension, causing elastic skewing of the frame, and rotation of the optics. This phenomenon is demonstrated in Figure 5.

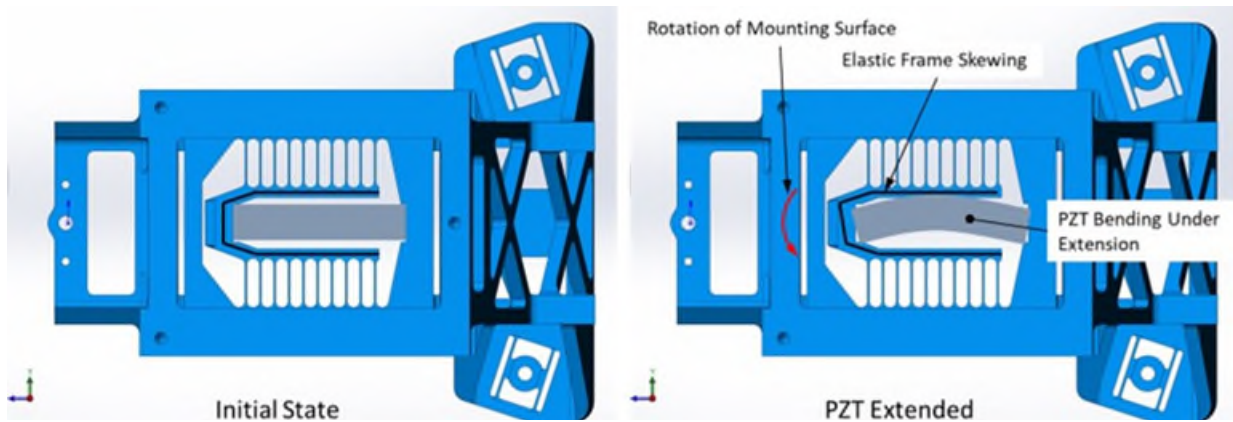


Figure 5. Effect of PZT Bending on FCM Fine Stage Motion

Finite Element Analysis (FEA) showed that tuning the first set of flexures, closest to the optic would have the largest effect on rotation. To recall, the differences in flexure blade thicknesses between one flexure and its symmetric counterpart contributed to the anomaly. Understanding the effects of differential spring stiffness across the carriage helped with the flexure tuning process. Differential forces acted on the flexures on each side of the carriage due to this stiffness variation, as shown in Figure 6.

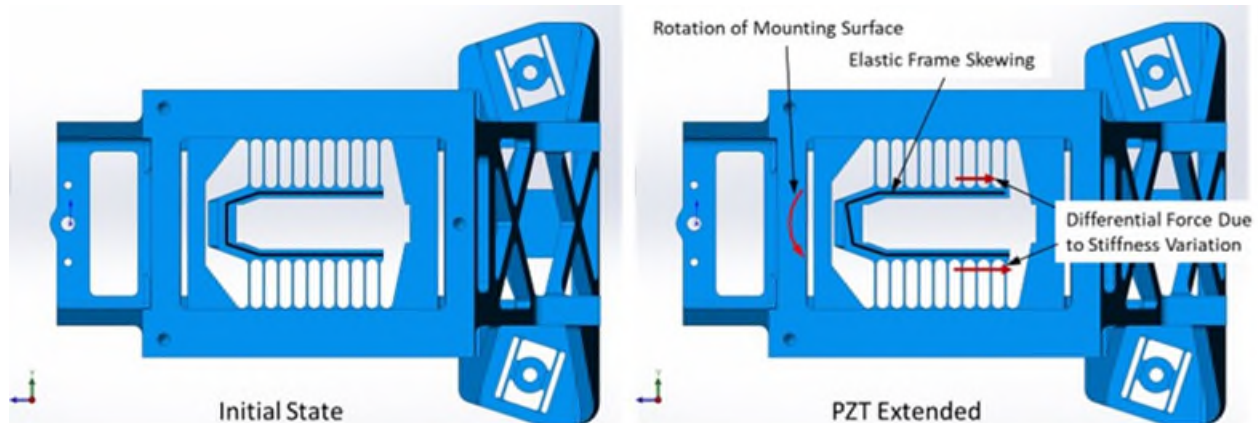


Figure 6. Effect of Differential Spring Stiffness on FCM Fine Stage Motion

Reducing the stiffness variation from side to side would bring the tip/tilt crosstalk into the specification range. During testing, if the tilt was negative, then the PZT stack was bending towards the right (“R” flexure side in Figure 3) under extension, and the stiffness of the left flexures (or “L” flexures in Figure 3) was higher. To bring this stiffness down, the left flexures needed to be tuned. With the same logic, if the tilt was positive, the PZT stack was bending towards the left under extension, and the stiffness of the right flexures was higher. To bring this stiffness down, the right flexures needed to be tuned.

Rework and Results

An autocollimator, an instrument used for taking high precision angle measurements, was used to measure the tip and tilt of the Fine Stage prior to tuning, between each tuning iteration, and after the final tuning operation. A custom emery board was used by bonding 18- μm aluminum oxide paper on a metal stick to tune the flexures in each iteration. This test setup is seen in Figure 7.

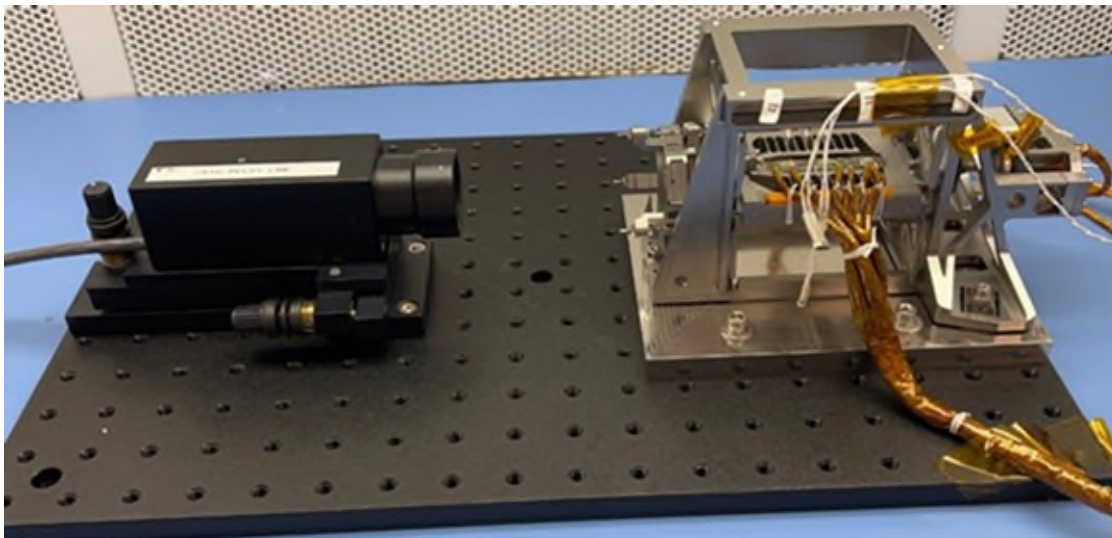


Figure 7. FCM Rework and Autocollimator test setup (The FCM EDU is shown).

Results Prior to Flexure Tuning

After each iteration, the RSS of the tip/tilt crosstalk was calculated per the requirement in Table 1. The plot in Figure 8 is the initial, pre-tuning measurement for the EDU FCM. The first three cycles are actuations of the PZT stack from 5 V to 95 V to counter any hysteresis effects, and the two cycles following are the actual measured cycles with voltage increments between the two extremes.

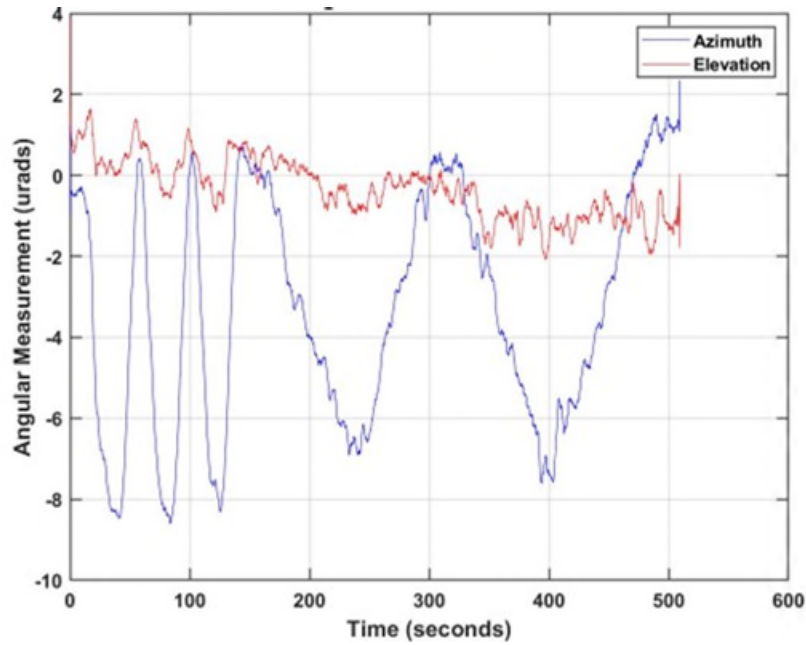


Figure 8. Tip (elevation) and Tilt (azimuth) measurements of FCM EDU Fine Stage pre-rework.

The azimuth in the FCM EDU showed a negative tilt, signaling that the L or left, front flexures (Figure 3) had to be tuned to bring the tip/tilt crosstalk into spec and reduce the stiffness on the left side of the carriage. Fine stage tuning was performed on flexures 3L to 5L. The opposite was true for the FCM FM unit, which is seen in the plot in Figure 9.

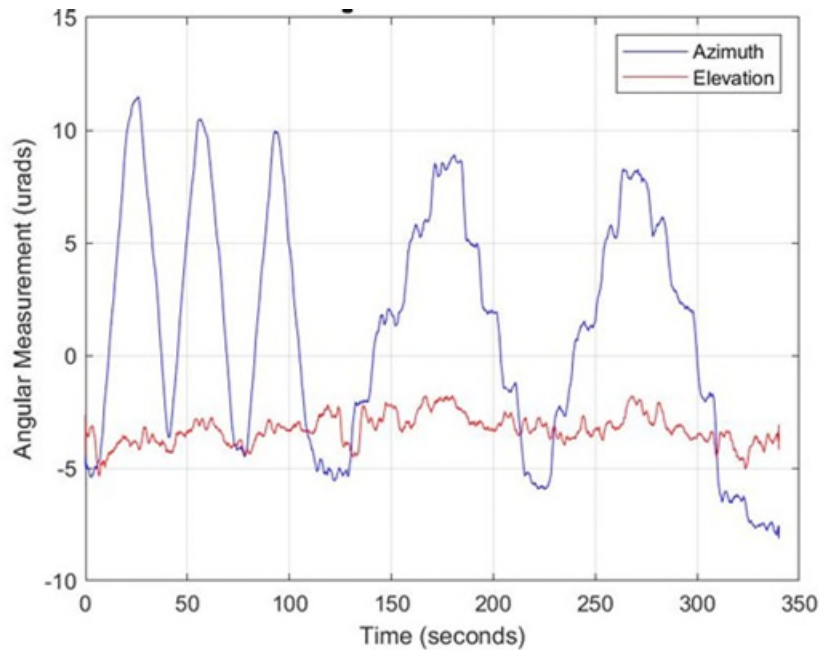


Figure 9. Tip (elevation) and Tilt (azimuth) measurements of FCM FM Fine Stage pre-rework.

The azimuth in the FCM FM unit showed a positive tilt, signaling that the R or right, front flexures (Figure 3) had to be tuned to bring the tip/tilt crosstalk into spec and reduce the stiffness on the right side of the carriage. Fine stage tuning was performed on flexures 1R to 5R with a focus on 1R to 3R. The

numerical values of the baseline tip and tilt measurements for the full stroke, and the RSS of the tip/tilt cross talk over any 14- μm range, are shown in Table 1.

Table 3. FM and EDU FCM Fine Stage Tip/Tilt Crosstalk results prior to rework.

FCM Unit	Stage	Tilt (μrad) – FULL STROKE	Tip (μrad) – FULL STROKE	RSS of Tip/Tilt Crosstalk (μrad) – over any 14 μm range
EDU	Fine	$-7.8 \mu\text{rad}$	$-1.7 \mu\text{rad}$	$2.5 \mu\text{rad}$
FM	Fine	$14.1 \mu\text{rad}$	$2 \mu\text{rad}$	$4.8 \mu\text{rad}$

Referencing the requirement in Table 1, both the FM and EDU FCM violated the Fine Stage tip/tilt crosstalk. The EDU FCM exceeded the requirement by 1.9x, while the FM FCM exceeded the requirement by 3.7x.

Tuning Process

As mentioned previously, the FCM EDU left fine stage flexure blades needed to be tuned to correct the error. Unfortunately, as seen in Figure 7, the PZT harness of the EDU interfered with the ability to tune the first set of flexures, therefore, flexures 3L through 5L were tuned to accommodate for this. The risk of breaking any of the PZT pigtail wires was alleviated with this strategy. The difference between an un-tuned flexure and a tuned flexure (4L) is shown in Figure 10.

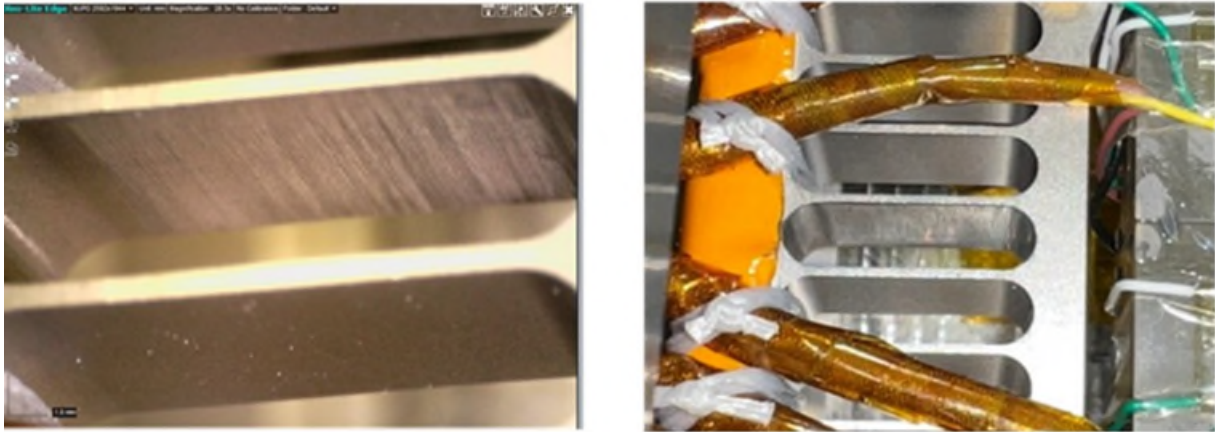


Figure 10. 1-mm scaled, fine-tuned flexure blade on the FCM EDU (left – top flexure blade), 1-mm un-tuned flexure blade on the FCM EDU (left – bottom flexure blade) and zoomed out image of the fine tuned and un-tuned flexure blades (right).

Striations from the aluminum oxide paper can be seen in the tuned flexure blade, as opposed to the un-tuned flexure blade. Each flexure blade was also polished with a finer aluminum oxide paper following the tuning to clean up the surfaces and reduce the surface friction.

The harnessing technique for the FM unit allowed for easier access to the first few flexures from the optic, 1R to 5R, with a focus on 1R to 3R. The reduction in flexure blade thickness prior to the rework and after the rework can be seen in Figure 11.

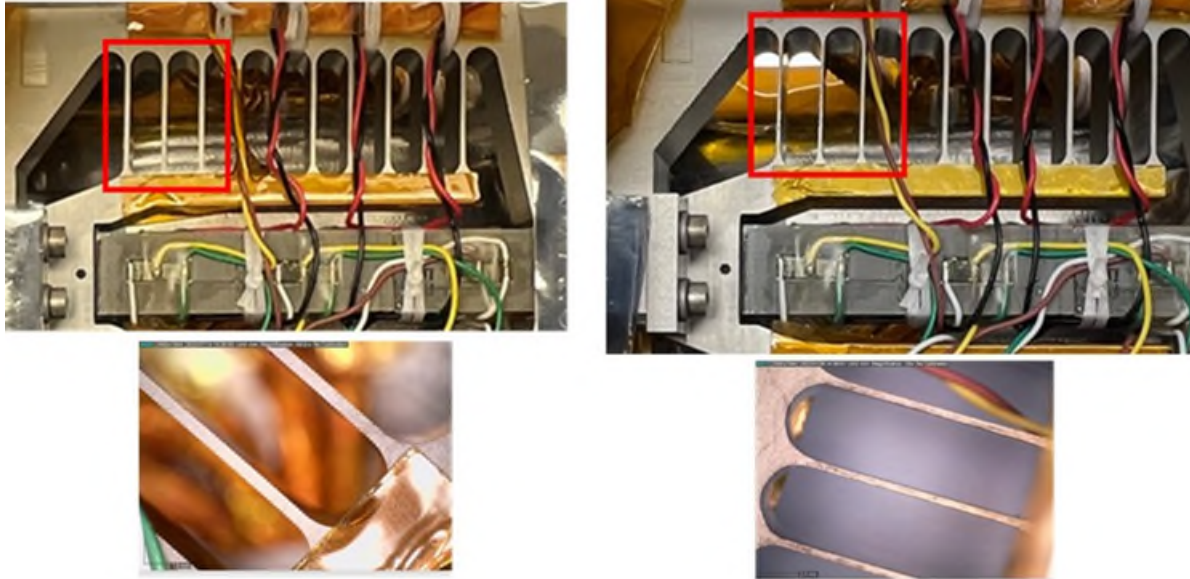


Figure 11. FCM FM pre-tuning flexures 1R to 3R (left images) and FCM FM post-tuning flexures 1R to 3R (right images).

Following the rework, flexure blade 1R had an average thickness of 0.47 mm and a ~0.07 mm reduction in thickness. Flexure 2R had an average thickness of 0.46 mm and a ~0.08 mm decrease in thickness. Flexure 3R had an average thickness of 0.47 mm and a ~0.07 mm reduction in thickness. All of these were measured relative to flexure 1L, an un-tuned flexure on the opposite side of the carriage. These results are summarized in Table 3.

Table 3. FM FCM flexure thickness post-rework (1R to 3R) with flexure 1L shown as reference.

Flexure Blade Number	Average Thickness (mm)	Change in Thickness (mm)
1R	0.4683	~0.0702
2R	0.4575	~0.081
3R	0.4712	~0.0673
1L (REF – not reworked)	0.5385	N/A

These measurements fell outside of the fine stage flexure design requirements because the deviations in thickness between any two of the 20 flexures did exceed 5 μm . However, this design requirement was set without the assumption of the PZT motion characteristics, errors in PZT bonding and PZT stack bonding to the frame. The functional requirement of the FCM in the ROMAN-CGI took precedence over the design requirement in the drawing, which was written to satisfy the tip and tilt crosstalk of the mechanism.

Final Tuning Results

The rework method to correct the Fine Stage tip and tilt crosstalk of the FCM was successful for both the FM unit and EDU. A rework of the EDU was performed prior to the FM unit to prove the success of the method and to reduce risk. The FM unit had a larger discrepancy against the requirement than the EDU initially, but both were corrected. Figure 12 shows the plot of the corrected FCM EDU.

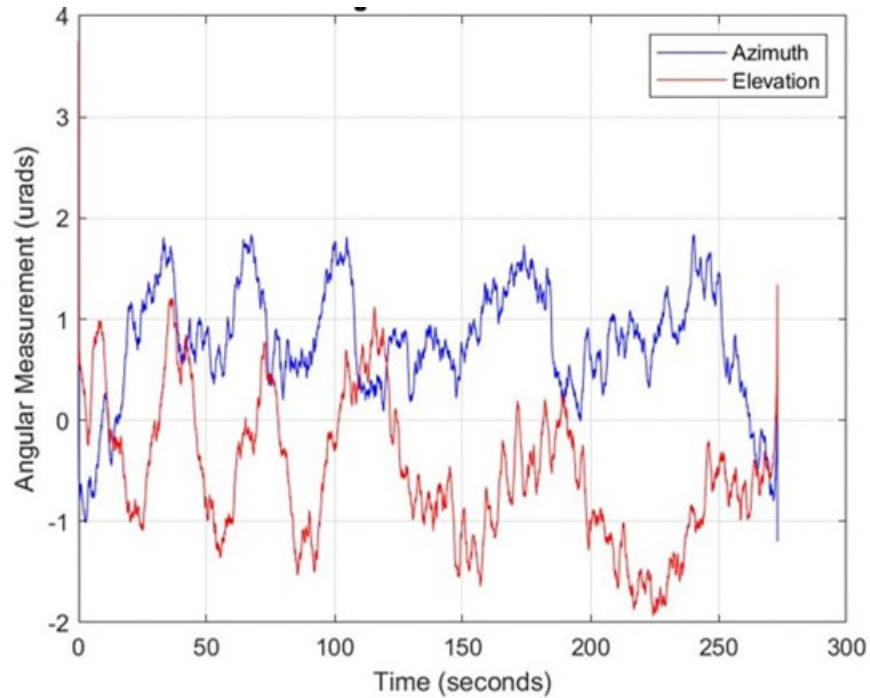


Figure 12. Tip (elevation) and Tilt (azimuth) measurements of FCM EDU Fine Stage post-rework.

The reduction in stiffness from the left side of the carriage, as the analysis showed, resolved the crosstalk issue in the Engineering Development Unit. The azimuth of the FM unit following the corrective action was reduced by almost 14x. There was a reduction of stiffness from the right side of the carriage as opposed to the left here. The plot for the FM unit, post rework, is shown in Figure 13.

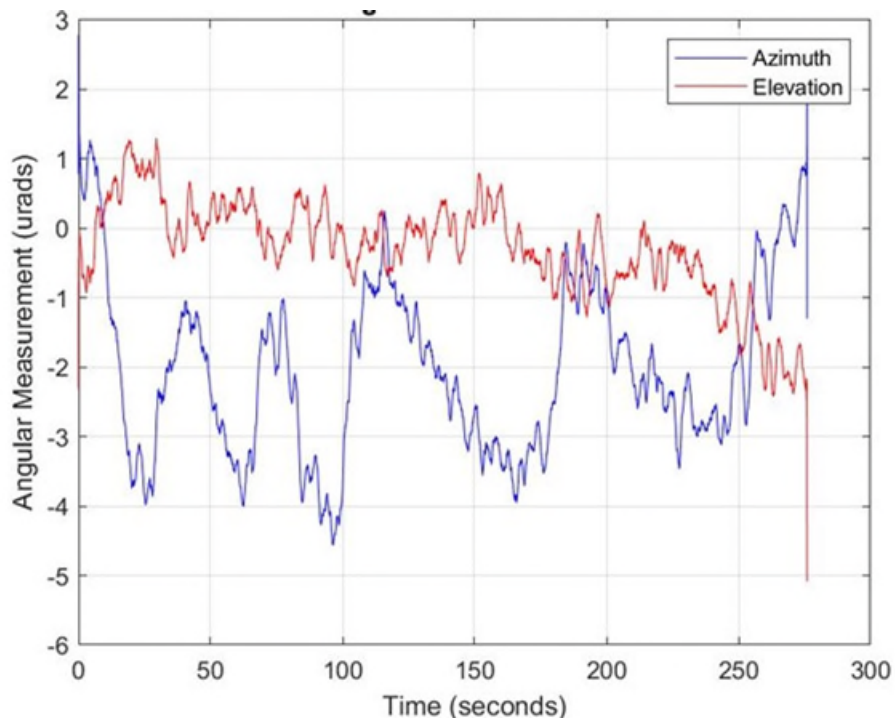


Figure 13. Tip (elevation) and Tilt (azimuth) measurements of FCM FM Fine Stage post-rework.

The full stroke tilt and tip of the EDU were measured as 1.5 μrad and 1.8 μrad , respectively, and the RSS of the tip and tilt crosstalk over any 14 μm range was 0.7 μrad . The full stroke tilt and tip of the FM unit were measured as 2.9 μrad and 1.3 μrad , respectively, and the RSS of the tip and tilt crosstalk over any 14 μm range was 1.1 μrad . These results are summarized in Table 4.

Table 4. FM and EDU FCM Fine and Coarse Stage Tip/Tilt Crosstalk results post-rework.

FCM Unit	Stage	Tilt (μrad) – FULL STROKE	Tip (μrad) – FULL STROKE	RSS of Tip/Tilt Crosstalk (μrad) – over any 14 μm range
EDU	Fine	1.5 μrad	1.8 μrad	0.7 μrad
FM	Fine	2.9 μrad	1.3 μrad	1.1 μrad

The rework proved to be successful, and both units satisfied the requirement of the Fine Stage tip and tilt crosstalk (Table 1).

Conclusion and Lessons Learned

The tip and tilt crosstalk requirement of the Focus Control Mechanism's Fine Stage were not met due to the off-axis motion characteristics of the Piezo Electric Transducers that affected their intended function of axial-only translation. To avoid repeating the test campaign, increasing the cost, and increasing the schedule, the correction had to be made without disassembling the stack of three PZTs from the FCM. The solution was to focus on the structure of the mechanism, understand the design intent of the flexures and PZT on the fine stage, and find a path forward. Fine tuning the flexures with iterations and testing the PZTs to accommodate their motion characteristics guided in resolving the tip and tilt crosstalk anomaly of the Fine Stage and bringing it back into its specifications.

There are several lessons learned from the FCM violating its Fine Stage tip and tilt crosstalk requirement, and the following design and assembly changes in the FCM could have prevented the anomaly and a need for a rework. When designing and assembling the FCM with the PZTs, it was crucial to take their alignment with one another and the surrounding structure into consideration. Tighter alignment control was necessary during assembly when the PZT stack was bonded together to avoid a violation from their intended function. Structures, especially those with flexures, are sensitive to how PZTs are aligned. These transducers have their own motion characteristics that contribute to alignment errors, and in the case of the FCM, tip and tilt alignment errors. Their individual motion characteristics should have been tested and incorporated into the design, especially for flight. Unfortunately, this tip and tilt of the unloaded PZTs was surprising and unknown to the team previously. If there was knowledge about this behavior, additional flexure elements would have been added to the design to minimize it, because a larger quantity of flexures would have reduced the stiffness variation from side to side and would bring the tip and tilt into the required range.

References

- [1] "Coronagraph - NASA Science," *science.nasa.gov*. <https://science.nasa.gov/mission/roman-space-telescope/coronagraph/>
- [2] Yi Chu Hsu, Chia Che Wu, Cheng Chun Lee, G. Z. Cao, and I. Y. Shen, "Demonstration and characterization of PZT thin-film sensors and actuators for meso- and micro-structures," *Sensors and Actuators A: Physical*, vol. 116, no. 3, pp. 369–377, Oct. 2004, doi: <https://doi.org/10.1016/j.sna.2004.05.024>.
- [3] S. Mohith, A. R. Upadhyaya, K. P. Navin, S. M. Kulkarni, and M. Rao, "Recent trends in piezoelectric actuators for precision motion and their applications: a review," *Smart Materials and Structures*, vol. 30, no. 1, p. 013002, Dec. 2020, doi: <https://doi.org/10.1088/1361-665x/abc6b9>.

The research described in this paper was performed by the Jet Propulsion Laboratory, California Institute of Technology, under contract with the National Aeronautics and Space Administration.

© 2024. California Institute of Technology. Government sponsorship acknowledged.

A Dust-Resilient Thermal Shutter Mechanism for Lunar Radiators

Andrew S. Gibson *, Olly Poyntz-Wright *, Angus Bishop *, Matthew Oldfield *, Angel Iglesias **, Fabrice Rottmeier **, Martin Humphries + and Philipp B Hager ++

Abstract

The design of an actively controlled lunar radiator must consider the effects of lunar dust on reliability and thermal performance, with protection offered to the radiator from dust obscuration being beneficial. The challenges to develop an active radiator have been undertaken, maximizing the range of operability across all possible lunar locations, with polar scenarios prioritized. Power limitations and the extreme temperature range (-150 to +120°C) have driven material and lubricant selection. Mechanism function and radiator performance are influenced by environmental conditions, including electrostatically charged regolith exposure, solar illumination, IR heating from the surface and landers or other man-made objects, as well as heat dissipation during the lunar night. An advanced breadboard lunar shutter design is described in detail, including a summary of lessons learned through validation of key mechanism elements via component testing of prototypes, analyses, and assembly of a breadboard. Overall design and heritage aspects are covered, including adaptations to achieve a dust-resilient device suitable for landers (Argonaut/EL3), rovers and long-duration lunar surface equipment/instruments. Results from component level derisking tests are presented, including sliding seal evaluation with regolith exposure, lifetime tests of axial polymeric seals and radial metallic bushings as well as cryogenic fatigue tests of polymeric flex-pivots.

Introduction

The Lunar Thermal Shutter (LTS) is a motorized, deployable cover intended for radiators mounted on lunar landers, rovers or other payloads or instrumentation used on the lunar surface. The primary functions are to provide a protective dust cover for the radiator thermal control surface and also to allow variation of the radiator performance by changing the surface area of the radiator exposed to the lunar radiative environment (which includes direct views to space). ESA requirements specify that the mounting of the shutter to the spacecraft or other platform is to be done independently from the radiator.

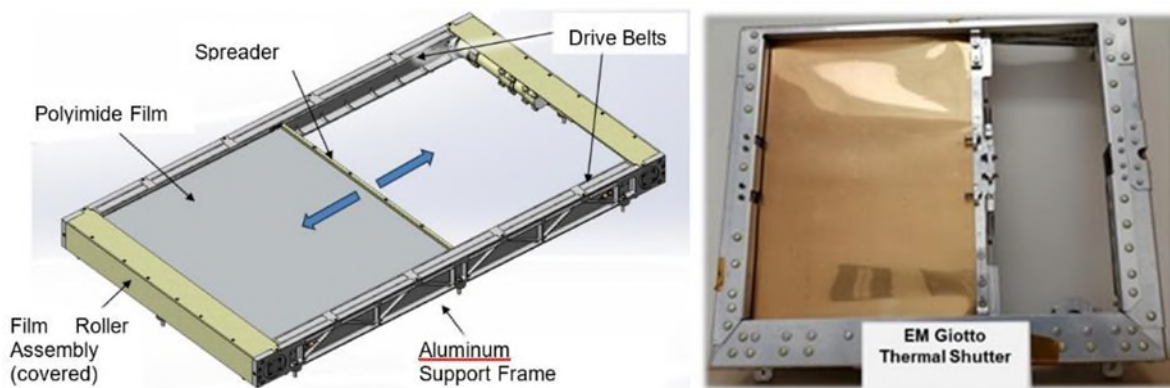


Figure 1. Left - Lunar Thermal Shutter CAD model showing spreader bar and film translation concept (external MLI covering omitted), Right - The Engineering Model Giotto Thermal Shutter [1]

* ESR Technology Limited, Warrington, UK; andrew.gibson@esrtechnology.com

** Almatech, Lausanne, Switzerland; angel.iglesias@almatech.ch

+ Spacemech Limited, Bristol, UK; martyehum52@gmail.com

++ European Space Agency (ESA/ESTEC), Noordwijk, The Netherlands; philipp.hager@esa.int

The shutter works by deploying an aluminized polyimide film (Kapton®) over the surface of the radiator. A roller, mounted at one end of the shutter structural frame, houses a spool of film that is rolled out and in front of the radiator surface, allowing it to control the amount of exposed radiator area with a view to space.

The film roller is wound/unwound by stainless steel belts driven by sprocket wheels attached to the roller assembly. As the spool unwinds, the film is also pulled by a spreader bar that joins the two belts. The metallic belt drive system features a sealed motor/gearbox design, having a magnetic coupling at the output. This approach is intended to be more dust-resilient, having large air gaps and a lightly loaded sliding seal to prevent bulk ingress of contamination. The drivetrain is significantly different from the heritage system, avoiding the use of bevel gear configurations in the linkage and adding a magnetic coupling.

The requirement to provide active control of the louver/shutter is driven not only by the wide temperature range on the surface, but also by the presence of lunar dust, providing the ability to regulate temperature of the payload with varying dust coverage. The shutter can be opened to expose the radiator fully, partially or closed whenever necessary to provide protection, i.e., potentially during the last part of the landing, the crossing of the terminator, local activities of humans, or during activities involving movement of rovers or robotic arms.

Assembly and testing of the full mechanism, targeting TRL 4, is planned for completion by mid-2024. The status of thermal vacuum testing will be provided including characterization of heat rejection and thermal controllability vs temperature. In addition, a low-vacuum dusty test of the assembly in a new UK-based facility at the University of Glasgow is planned following thermal vacuum characterization tests.

Background

Thermal shutter and louver devices have been enabling technologies for ESA's early space exploration missions, including Giotto (Figure 1), but also for American led missions including Viking, Mariner, Cassini and Magellan and others [1,2]. These devices provide high turn-down ratios for temperature regulation of critical radiator elements of spacecraft, where cold survival, mass and reliability are critical to mission feasibility and performance. The properties that were desirable for those missions will also be key for successful thermal control on the lunar surface, where the key difference will be to work in a harsh, dusty environment, which can affect heat rejection as well as mechanism reliability.

With many projects targeting a soft landing on the lunar surface and extended operations there, thermal control challenges associated with the lunar surface environment for longer durations have become apparent related to the European Argonaut/EL3 lander as a multi-mission platform (capability to deliver mass of ~2 tons to the lunar surface by 2030). ESA selected a technology development proposal led by ESR Technology to develop a thermal control mechanism based on heritage thermal shutters from the Giotto mission to be tailored for the lunar environment and scalable across a range of sizes to maximize reuse possibilities. The development program is being performed under ESA contract, having commenced in September 2021.

An early trade-off study was performed involving 2 scalable concepts, comparing thermal louver and shutter concepts. Working model prototypes were built (incl. ½ scale shutter and 3 vane louver) to demonstrate the feasibility of both. Key features of each are summarized:

- Louver: A multi-vane adjustable angle system, mounted on dust-resilient large angle flex-pivots, driven by a single actuator system with a novel drive linkage.
- Shutter: A spooled vacuum deposited aluminum (VDA) film to adjust the view factor of the radiator surface to space, pre-tensioned and driven by a single actuator with a magnetic coupling at output to drive metal belts.

The trade-off decision making was driven by results of early thermal modelling, with the shutter option favored vs the louver concept, showing fewer scenarios with net zero radiative capacity and with potentially lower mass and higher heat rejection. The shutter was deemed simpler, having a lower part count, with the

ability to protect more fully against contamination during radiation events or phases with high dust deposition, such as the passing of the day/night terminator, landing, or due to astronaut/rover/robotic activities. Shutter weaknesses were predicted for specific latitudes with the frame in vertical orientations [3] - addressed via an optional fixed baffle installed for these vertical cases, where a louvered mechanism/actuated baffle could be a preferred option for such cases. This baffle assembly is at a lower TRL, being outside the scope of the current contract.

Table 1. Summary of Key Requirements for the Dust-Resilient ‘Louvered’ Radiator

Parameter	Requirement Details / Values
Lifetime related Requirements	1 Earth year [goal of 2 years on lunar surface with 10,000 operation cycles (ECSS factored)], 30 krad radiation tolerance, 14 day lunar night survival implied
Thermo-Optical Properties (closed)	ϵ = IR emissivity < 0.20 (BOL) to 0.30 (EOL) α = UV absorptivity < 0.15 (EOL) to 0.25 (BOL)
Effective Radiator Properties (open)	ϵ = IR emissivity > 0.80, α = UV absorptivity < 0.20 (BOL) to 0.30 (EOL), Optical Solar Reflector or paint
Mass	Specific mass of < 9 kg/m ² + 0.5 kg/m ² harness = 2.05 kg (baseline size)
Scalability	Adaptable for radiator areas in the range of 0.06 to 2.0 m ²
Baseline dimensions (scalable –up/down)	Width x Length x Depth = 420 x 705 x 47 mm (shutter) = 360 x 600 mm (radiator)
Temperature Range	-150°C to +70°C (shutter operating) -150°C to +120°C (shutter survival), -223 to 120°C (surrounding surface)
Sine Vibration	15 g (17.1-100 Hz)
Random Vibration	0.25 g ² /Hz (16.7 G _{rms})
Shock	2 g at 10 Hz 2000g @ 2000-10000 Hz
Power	< 5W / m ² = 1.08 W (baseline geometry)
Controllability	±1°C controllability (closed loop stability)

Specific requirements assert that only one actuator sub-system may be employed, limiting redundancy options to the benefit of mass/complexity. Interfaces are tailorable for mounting to aid heat transfer from heat pipe or loop heat pipe transport systems, directly to payloads or electronic boxes, etc.

Overview of Shutter Functionality, Derived Requirements & Overview of Key Mechanism Elements

Requirements for the device are summarized as shown in Table 1. The goal of the design is to have the capability to function over the widest range of locations on the lunar surface, while the temperature range specified precludes only the most extreme (shadowed) locations. Requirements to operate on the lunar surface involve difficult to simulate conditions involving charged regolith expected to be deposited fairly regularly and greater rates when the unit is located near sites of activity on the surface. This necessitates the need for dust resilience and conductive links needed to bleed charge from the film and other parts.

The requirement to provide active control of the louver/shutter was mainly driven by the presence of dust on the lunar surface and being able to regulate temperature of the payload with varying dust coverage. It was considered relevant to be able to actively open or close the louver/shutter whenever necessary, i.e.,

potentially during the last part of the landing, the crossing of the terminator, local activities of humans, or the movement of rovers or robotic arms.

Belt Drive and Wheel Sprocket Systems with Flex-Pivot Tensioning

The belts are driven by a motorized sprocket wheel at the opposite end of the aluminum frame. This drive wheel is attached to a stepper motor and gearhead and is driven through a non-contact magnetic coupling. When the film is deployed, the tension is maintained through a flexible element within the roller assembly. This ensures the film is deployed and recoiled in a repeatable and consistent way.

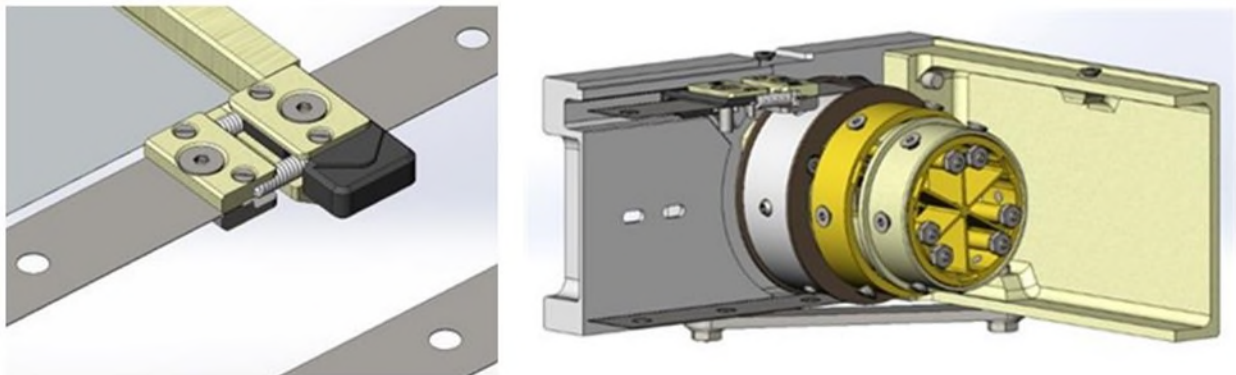


Figure 2. Spreader bar sliders and belt tensioning springs (left) and sprocket/flexure sub-assembly (right)

Flexible pivots for Roller Support and Roller Preloading

To ensure the film wraps tightly around the spool, a positive, deterministic film tension must be maintained throughout actuation. The tension in the film when fully deployed is set during assembly by deflecting the flex pivots and measuring the tension using a force gauge. As the film is retracted to expose the radiator, the thickness of film on the spool increases, and thus the radius where the film joins the spool increases. If the film is to remain taught throughout deployment, the spool must rotate relative to the wheels as the film is wound. This leads to a change in the angle of the flex pivots, and thus a change in the film tension.

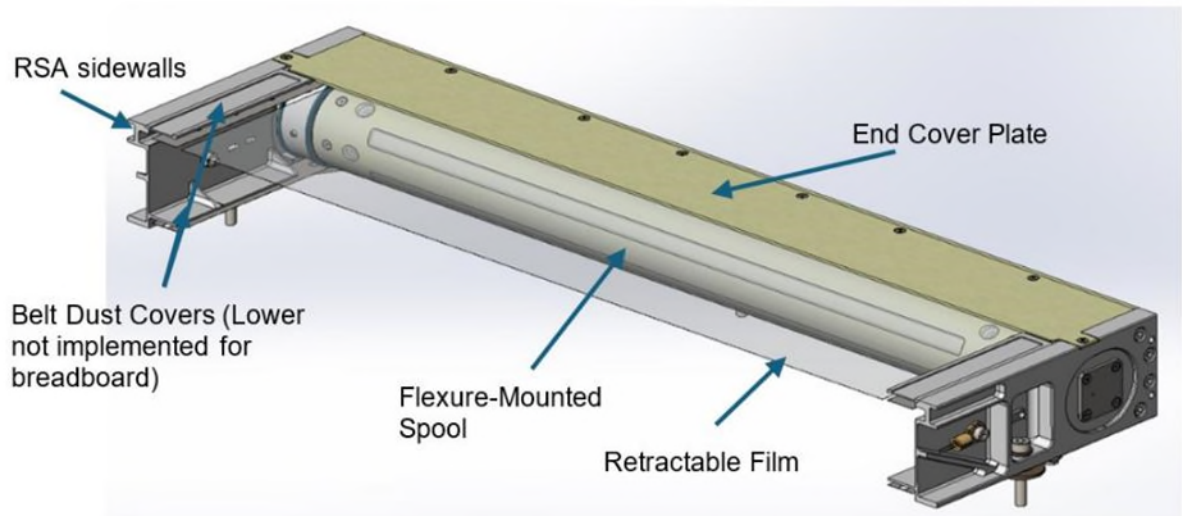


Figure 3. Roller tube film support sub-assembly

This was modelled by assuming the film forms an Archimedes spiral as it wraps around the spool, which is a useful approximation since it is a continuous function. By calculating the arc length of this spiral as a function of the wrap, the angle through which the roller must turn to entrain a given length of film can be found. Subtracting this from the angle through which the sprocket has turned gives the relative deflection angle of the flex pivots. The angle of the flex pivots, together with their spring rate and the varying spool

radius, allows the film tension to be calculated. This is illustrated in Figure 4. The minimum on this curve indicates where the radius of the film leaving the spool is exactly equal to the radius of the sprocket. The choice of flex pivots for the spring element between the sprocket wheels and spool was driven by their dust resilience. While clock springs and bearing surfaces may have provided a lower spring rate and thus a more consistent film tension, these would have required additional tribological surfaces and accompanying dust seals. With the flex pivot design, there are no tribological components required to maintain concentricity and no geometry where sub- ~ 0.5 mm particles could cause a seizure of the spool relative to the sprocket wheels.

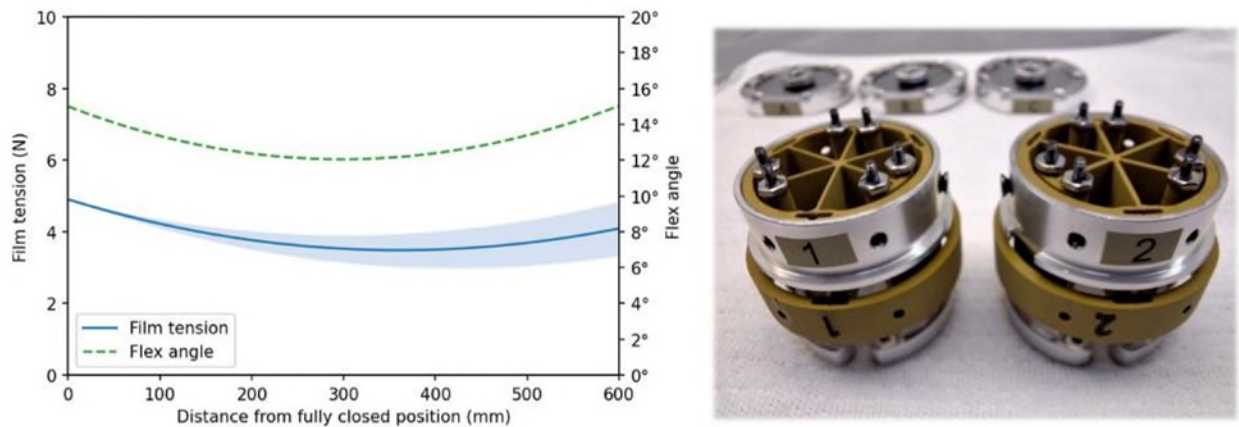


Figure 4. Left - Typical Roller Film tension and flex angle variation over actuation cycle (left) assuming tension is set in the 0-mm position (shows uncertainty bands for ± 0.05 -mm variation of as-machined spool diameter), dual flex pivot assembly (right) made by waterjet cutting, breadboard sub-assemblies.

Drive System with Planetary Gearhead and Magnetic Coupling Output

The drive system has been developed to meet ESA European Cooperation for Space Standardization (ECSS) requirements for torque margin in relevant environments, including on-ground with 1-g gravity (vacuum) or in vacuum under lunar gravity and incorporation of dust protection features as safeguards against this aspect of the lunar environment.



Figure 5. Magnetic coupling design and drive sub-system 'in-progress' images: Actuator test-fit with magnetic coupling inner (left), non-redundant actuator mounted in sealed housing (center), motor in sealed housing with drive wheel spigot (right)

The magnetic coupling provides torque transmission from gearhead to one wheel. The design has been optimized for this application to be mass efficient, within the specifications of actuator output stiffness and peak torque output. The deflection of the coupling is within 2 deg for expected nominal actuator operation and maximum torque transmission is approximately 1 N-m. Magnet material was selected as SmCo for consistent performance over temperature with an FeCo soft magnetic return ring and carrier used to improve the specific performance of the assembly. The magnetic coupling adds 60 g of mass to the assembly and introduces benefits including a soft launch preload and overdrive clutch (gearbox protection).

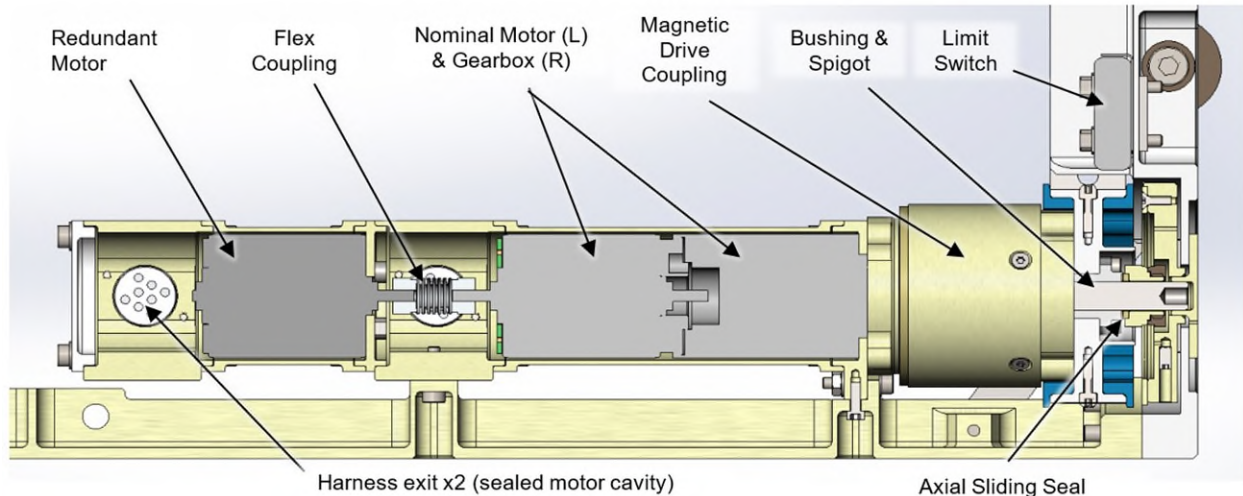


Figure 6. Actuator Drive Train (with optional redundant motor)

End Stop Limit Switches

The unit is fitted with heritage Honeywell 11HM1 switches with the JS-151 roller attachment at the end of travel in each direction, where the spreader bar triggers the roller. Redundant switches are possible as an option but not baselined given that step counting is the baseline for position knowledge, with the end stops as a secondary verification/calibration check. The effect of different shutter positions on the radiator temperature will be evaluated in the breadboard test campaign. While redundancy of intermediate position knowledge is not available, position knowledge can be reset at the end of travel.

Tribological Design Overview

Notably, the use of large-angle flex pivot technology patented by Almatech (with support from Spacemech) has limited the number of tribological contacts from the outset. These flexures ensure that the movement required for tensioning of the film on the roller will be extremely resilient to dust. This leaves the following essential tribological elements of the mechanism, consisting of:

- Motor and gearhead (quantity 1, where a redundant motor is optional)
- Sliders at ends of spreader bar (quantity 1)
- Corner support bushings (quantity 4)
- Belt to wheel sprocket interfaces (quantity 4, including 6 timing pins each and flat contacts)

Motor and Gearhead Tribology

The motor and gearhead bearings and gears have been manufactured with solid lubricant MoS₂-202 sputtered by the European Space Tribology Lab, with the intent to provide a maximum temperature range of operation without the limitation ((as is common) to heat prior to operation. This enables compliance with the ~1 W power requirement and provides maximum logistical simplicity for use across future missions. Notably, this actuator has previously been developed to TRL 6 by Almatech under ESA funding for a liquid lubricated configuration [4], while it has not been life tested for this application. The requirement on motor lifetime is seen to be challenging, with a factored demand of 7.2 million motor revolutions, but it is noted that the current program will only provide an initial derisking involving a total of approximately 30% of the intended worst-case factored lifetime. This is noted as a residual risk for future work, being deemed a lower priority in comparison with other tribological aspects being verified in this activity, as agreed with ESA.

Spreader Bar Sliders

A composite material based on Polyetheretherketone (PEEK), with a carbon filler and tribo-additives has been selected for the sliders, which are lightly loaded, flat contacts (notionally). This material has a low CTE below 30 ppm/°C and was verified to perform well in a pin-on-disc tribometer trial between -80°C and 80°C,

demonstrating relatively consistent and low friction coefficient in both air and vacuum, with reasonable wear rates considering the carbon content. A small amount of wear product can be expected, which will be evaluated for acceptability at the end of test.

Corner Wheel Bushing Supports and Spigots

The wheel bushings are designed in X65Cr13 stainless steel running against spigots made of medium alloyed tool steel, both coated with sputtered MoS₂-202 deposited by ESTL. Originally, a bronze material with reduced lead content (<4% in line with transitional Restriction of Hazardous Substances (RoHC) guidance) was trialed, running against a Kolsterised® 300 series stainless steel spigot (for CTE match). This material was evaluated in the component prototype tests and was not successful, lasting on the order of a few hundred rotations. The MoS₂ coating rapidly degraded along the single line contact of the spigot. More information is provided in the prototype derisk section below. Changing the bushing to stainless steel allowed the internal diameter of the bushing to be coated with MoS₂, providing some additional resupply/recirculation of the lubricant. Additionally, the use of harder surfaces and changes to the geometry (removal of sharp edges) limited debris generation, as was seen to accelerate wear in earlier testing with bronze bushings.

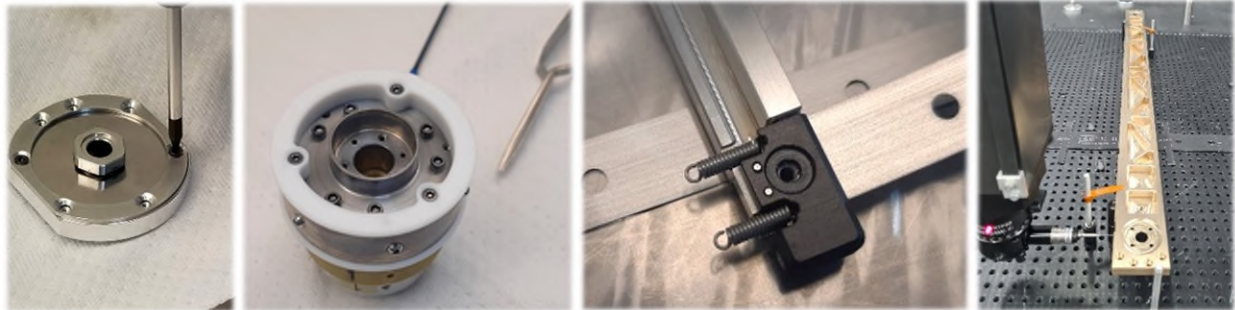


Figure 7. Breadboard Component Photos: Diaphragm spring pack (left), sprocket wheel/flex assembly (center left), spreader bar slider (center right), sidewall structure in final inspection (right)

Sliding Seals for Bushing and Magnetic Coupling protection

The axial bushing and magnetic coupling both employ lightly loaded polymeric seals to prevent significant ingress of regolith from affecting functionality. These seals are closely controlled to maintain preload of a few Newtons on bushing seals and a lighter preload on the larger magnetic coupling seal (being less sensitive with large air gaps). The sliding seal material is a composite with PolyTetraFluoroEthylene (PTFE) additive, selected from the ESTL test database having been tested in pin-on-disc tests and shown to have one of the lowest rates of wear debris generation measured, with relatively consistent friction in air and vacuum ($\mu = 0.1$ to 0.25). The geometry of the coupling seal was optimized following early dusty test trials described below.

Belts and Wheel Sprockets

The wheel hubs are made from RSA aluminum for mass savings and CTE matched to belts and will be coated with silver as a baseline (not included for breadboard). Drive pins were upgraded to PH 15-5 alloy for greater resilience versus carbon steel used in early trials. Belts are made from high yield 301 stainless steel (consistent with heritage from a previous boom mechanism) with laser cut hole patterns.

Risk Reduction by Prototype Validation

Three significant prototype initiatives were undertaken to derisk the design, two of which were tribologically focused and one focused on a fatigue check of the polymeric flexures at cryogenic temperatures.

Dusty Testing of Sliding Seals in Ambient conditions

Dust susceptibility tests were performed to examine the resilience and effectiveness of the sealing elements within the actuation train to prevent the ingress of dust. A key part of the test was to verify the selection of the preload within the sealing elements as well as the functioning of the seal geometry on the spigot and the magnetic coupling seal. The tests were intended to provide confidence in the ability of critical components to withstand exposure to lunar dust; the test methodology is not consistent however with allowing conclusions to be drawn on the spatial distribution of dusty material.

The dust test rig consisted of representative elements of the magnetic coupling and stub axle assembly, with a measurement of the combined resistive torque elements of the magnetic seal and the stub axle bushing and seal. The overall test setup is shown in Figure 8, which made use of several 3D-printed parts and a Commercial off-the-shelf (COTS) idler bearing assembly. Dust injection was done with Exolith LHS-1D simulant, to aim at a specific region with a flexible nozzle, with the sample released by means of a charged sample container vented into the chamber using a timed solenoid device. Torques were measured using a Kistler torque transducer by rotating the assembly in each direction for 4 revs; the reported torque value is calculated by halving the difference between the torques in each direction.

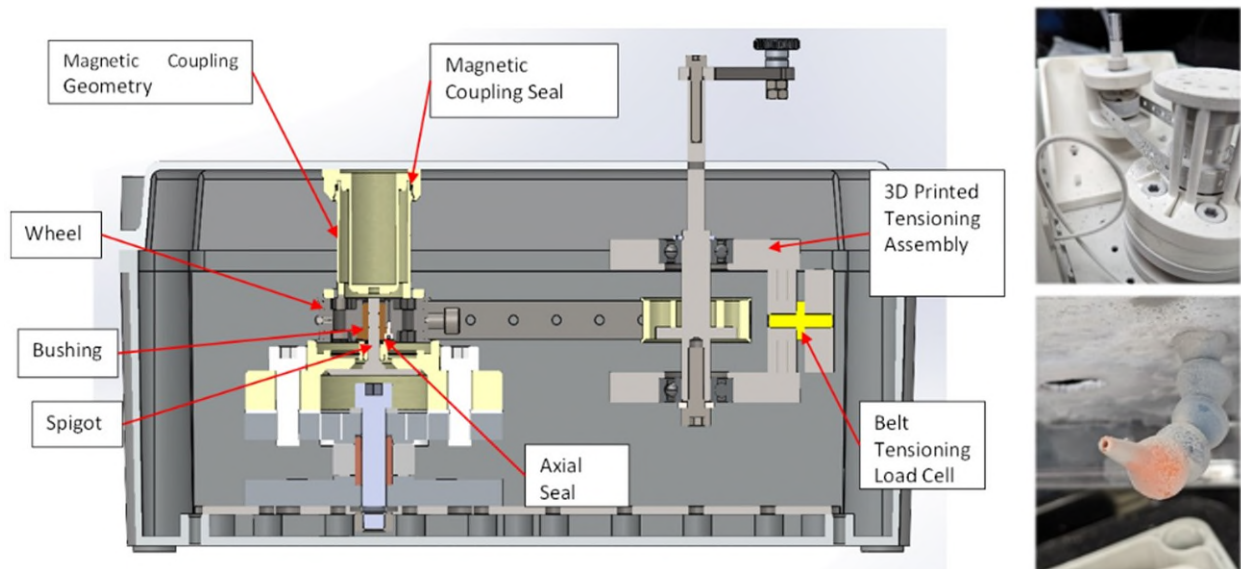


Figure 8. Ambient Dusty Test Setup with hand-cranked belt drive: CAD section view (left), view with cover removed (upper right), dust injection port (lower right)

Torque was seen to rise initially but stabilized at levels just less than double the pre-dust torque indicating some impact from the regolith interacting with seals and possibly belt to wheel interactions, but it stabilized relatively quickly following the initial increase. This indicates some room for improvement in the seals (Figure 9), though it was deemed to be a 'worst-case' test with very fine simulant in high quantity.

Bushing and Seal Prototype Lifetime Testing

Not only are the bushings required to maintain alignment and handle loads transmitted through the wheels, but these sliding contacts also need to be able to bleed charge from any significant build-up of electrostatic effects of floating elements.

A combined prototype activity was devised with the intention to validate both axial seals and radial bushings, with monitoring of radial bushing conductivity throughout. As circumstances progressed, the activities ended up with separate validations of each. An initial lack of success with a bronze bushing design being short-lived through several trials (see Figure 10), was combined with the successful verification of the associated axial seal test. This was then continued to validate the lifetime of the axial seal on its own. Despite significant debris generated internally, the soft polymeric seals continued to function and remained intact. After the bronze bushing configuration was abandoned, the axial seals were allowed to resume testing (radial load reduced) and completed prototype life-testing in vacuum.

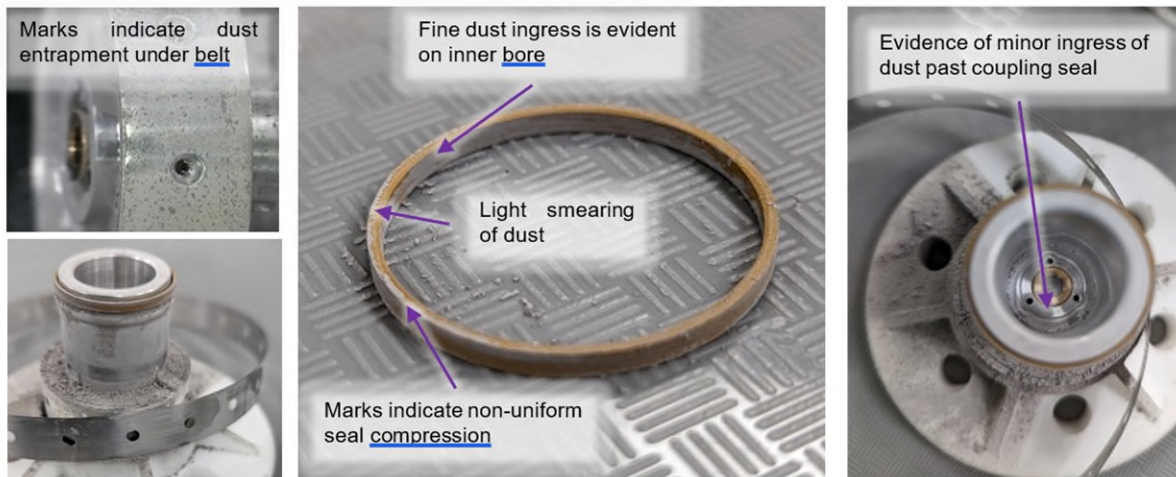


Figure 9. Dusty Test Post-Test Inspection Key Findings indicating non-ideal coupling seal function with extreme exposure to LHS-1D Exolith highland simulant (axial seals were fully successful to limit ingress)

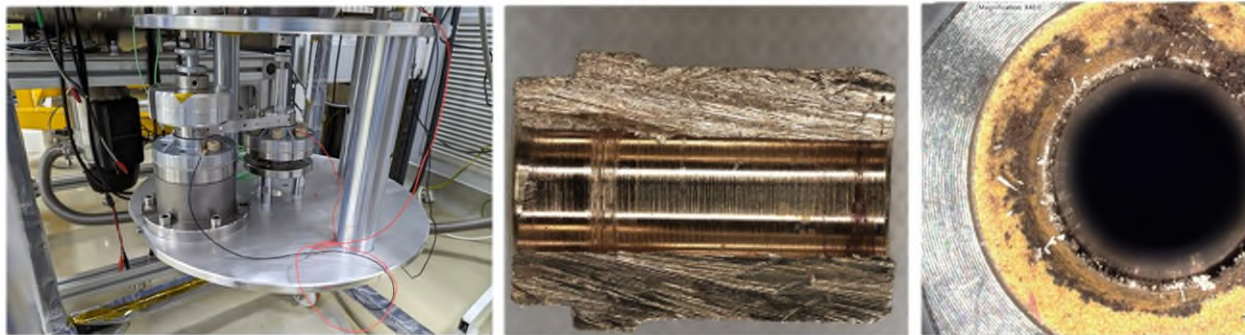


Figure 10. Vacuum test rig for bushing and axial seal evaluation (left), early bronze bushing failure (center), axial seal after 10,000 revs in air (right) with some bronze debris embedded at inner interface

In parallel, the bushing design was modified to use harder contact materials, based on an insightful study of vacuum bushings by the US Air Force [5] which described a similar, successful configuration using hardened stainless materials and sputtered MoS₂. The original design was far too dependent on the line contact with the spigot, where the MoS₂ wore away after some hundreds of rotations exposing the hardened spigot (via Kolsterising®) to run against bare bronze (with inadequate lead content to form a lubricating film) only to be worn quickly, generating significant debris. The reconfigured bushing and spigot were initially tested in air for over 8,000 revolutions followed by 19,000 in vacuum. With a 50% rise in torque observed after 14,000 cycles in vacuum, it was determined that the initial in air running had been excessive.

While the test was not intended to run so long in air, a setup error for the test led to the findings for extended run-in in air, as summarized in Figure 11. The effect of a long run-in in air demonstrates a steady increase

in running torque, indicative of increased MoS₂ wear whilst the MoS₂ is known to perform less ideally in a moist environment so is not in itself surprising.

The findings emphasized the need to set a clear allocation on ground operations to avoid impacting the remaining in-vacuum lifetime and so that subsequent tests could be performed and account for a reasonable budget for in-air operation. This was set and agreed with the client to be based on 15 mechanism actuation cycles in air, where further ground testing could be performed in air or N₂ with much reduced impact. This allocation will be reviewed again ahead of qualification activities, where any inputs from potential users would be welcomed.

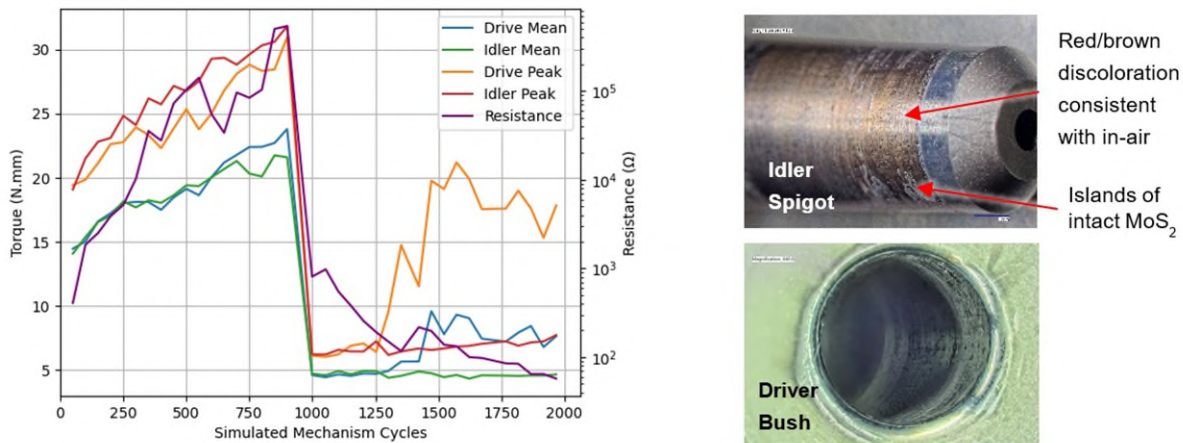


Figure 11. Preliminary Testing of Bushing/Seal Friction Torque with significant in-air run-in with reconfigured hardened steel bush and spigots with sputtered MoS₂-202 (multiply cycles x 10 for revolutions)

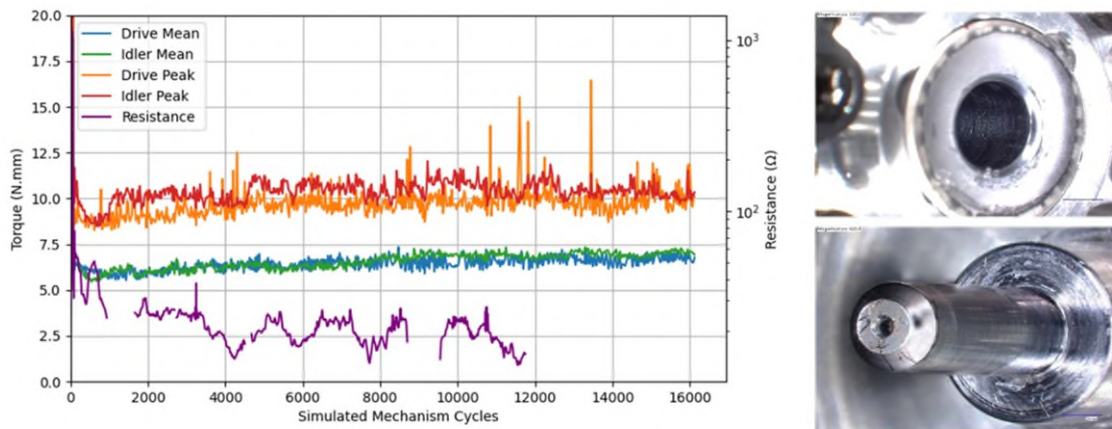


Figure 12. Left - Final prototype life testing of bushing/seal friction torque and conductance over 100,000 revolutions with hardened steel bushings and spigots with sputtered MoS₂-202, Right - Final condition of spigot and bushing following life-test prototype completion (seals used were PTFE)

The bushings both demonstrated some minor surface pitting, and the spigots showed evidence of some MoS₂ degradation on the running surface. MoS₂ was still present in the bushing and on the surface of the spigots. This is indicative of an end-of-life condition for the contact.

Cryogenic Prototype Testing of Polymeric Flexures for Fatigue Resilience

The idea of relying on stressed polymer flexures down to the cold survival temperature of -150°C seems at first questionable, as most plastics would be highly brittle at these temperatures. However, extensive manufacturer data for the grade of Polyamide-imide used suggested that this was in fact feasible. To validate this assumption, a simple rig was designed which would allow the torque across the flexure to be

measured at both at room temperature and at -150°C . This temperature was achieved by cooling a fixture at one end with LN_2 and allowing the opposite end to interact convectively with the surrounding atmosphere of dry nitrogen.

An extract of the torque data from the room temperature tests is shown in Figure 13. The material clearly exhibits some viscoelastic behavior, with decay in torque magnitude over time. This behavior was distinct from charge amplifier drift, which was expected while using a piezoelectric transducer. In the mechanism, the flexures will be deflected at a much slower rate, such that any transient effects are expected to be negligible. The ‘steady state’ torque was measured and compared for a range of deflection angles to fully characterize the pivot over its operating range, showing reasonable correlation with Finite Element Analysis.

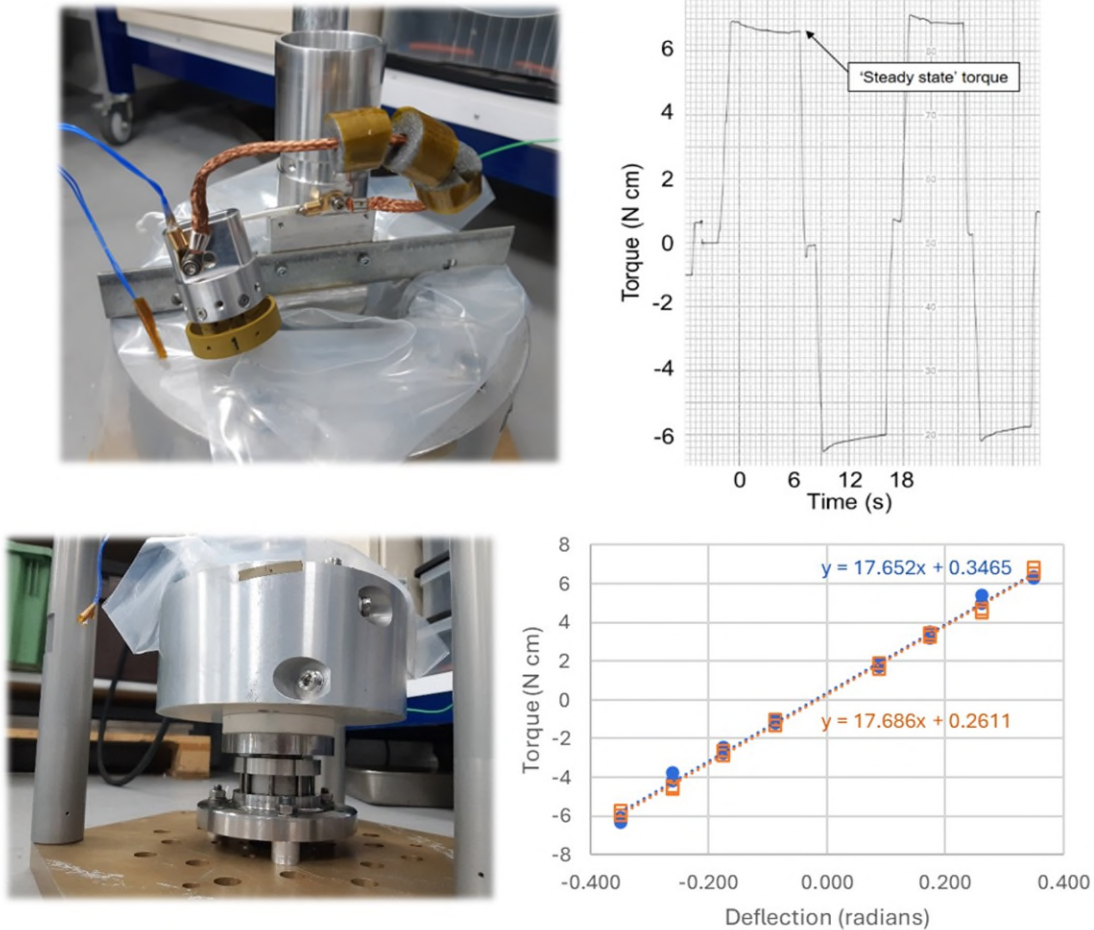


Figure 13. Cryogenic flexure test setup and results – Top Left: Flexure mounted in the large central tube, cooled via the bath at the base filled with LN_2 , Top right: Torque data, showing viscoelastic behavior of the flex pivot, Bottom left: LN_2 bath mounting to Kistler Load Cell, Bottom Right: Torsional stiffness relationship checked for stability at two points during test.

These tests were repeated at -150°C with the pivot surviving over 300 cycles over its normal operating angles, with stiffness increasing at cold (factor of ~ 2.2). These cycles, together with over 1700 cycles at room temperature, demonstrated survival after $>20\%$ of the required lifetime. A post-test inspection confirmed no signs of damage or wear and validated these parts for use in the full mechanism build.

Structural and Thermal Considerations

A detailed thermal analysis of the LTS was performed by Almatech, considering the potential use cases of the LTS for a wide range of landing sites across the lunar surface from equator to poles. Analyses performed assumed the shutter frame external surfaces to be wrapped in MLI. For the purposes of modelling, a 10-layer blanket was assumed with a Beta-cloth external layer, although not a critical parameter and expected to be mission specific. Due to the proximity of moving parts (belts and film), MLI was only applied to external surfaces, leaving a view factor to the inside of the frame at acute angles of incidence.

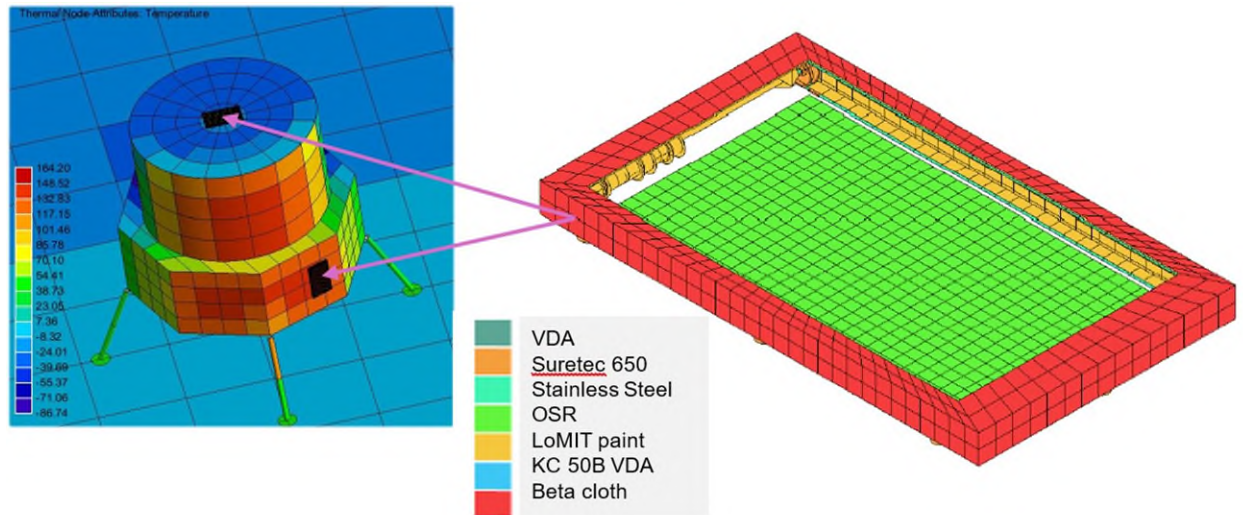


Figure 14. Thermal Case Description showing thermo-optical materials used in modeling and horizontal and vertical positioning of the shutter on the ESA generic Argonaut lander model (rover case not depicted)

With the potential for solar loading, lunar IR or albedo heat flux, the thermal finish of the inside of the frame is an important consideration. To achieve a design that is as insensitive to these heat fluxes as possible, a low emissivity (ϵ) and low absorptivity (α) surface finish is desirable, where a ratio of $\alpha/\epsilon < 0.5$ is preferred to avoid a net heating effect. As part of this program of work, thermo-optical properties of Lo/MIT paint and a thin layer of Keronite[®] are being evaluated. The breadboard model has not been coated with these finishes along with a reference chromate coating, while the results of the thermo-optical testing on sample coupons will inform the final design choices for future iterations, where correlation modeling will be used to evaluate the effect of changes from the chromate coating on the breadboard to each of these options.

In summary, the thermal analysis predicted that the mechanical parts of the shutter would all remain within acceptable temperature limits. Estimates for the shutter thermal performance in terms of turndown ratio ranged from around a factor of 10 in the vertical orientation up to a factor of 30 for horizontal cases, in line with expectations. The thermal environment and associated temperature predictions confirmed the wide operational and non-operational temperatures that are required from the LTS with gradient predictions to be cross-checked in test.

With MoS₂ lubricant employed and materials selected to withstand the thermal environment, the main impact of the wide temperature range relates to thermo-elastic issues and the relative geometric changes in materials with different thermal expansion coefficients within the shutter. A key aspect here is maintaining the tension within the drive belts across the temperature range. If perfectly matched CTEs were possible for the drive belts and the structure and gradients limited, the belt tension would be invariant with temperature. Commonly used structural Al alloys (6000 series) have a CTE ~ 7 ppm/ $^{\circ}$ C greater than the stainless steel belts; their use would result in near total loss of tension in the coldest cases and greatly increased tension in the warmest; both of which could render the mechanism undriveable. Therefore, a material was sought with a thermal expansion coefficient closely matched to that of stainless steel. The

alloy selected was RSA-4062-T6, a proprietary alloy manufactured by RSP with a CTE that is within 0.1 ppm/°C of the stainless belts, resulting in a predicted belt tension variation of less than 0.5 N from the room temperature value.

This breadboard program seeks to verify the functionality of the LTS mechanism and to characterize the potential thermal performance in terms of heat rejection control. To demonstrate this, a custom test facility has been developed that will subject the LTS to the thermal extremes for functional testing and will also provide a representative radiative environment to gauge the effectiveness of the device as a thermal control device. For functional testing the shutter temperature is driven by heaters to above ambient temperature and utilizes a cryocooler and thermal straps for below ambient tests.

Thermal Straps can be configured to cool target or shutter interface (or both)

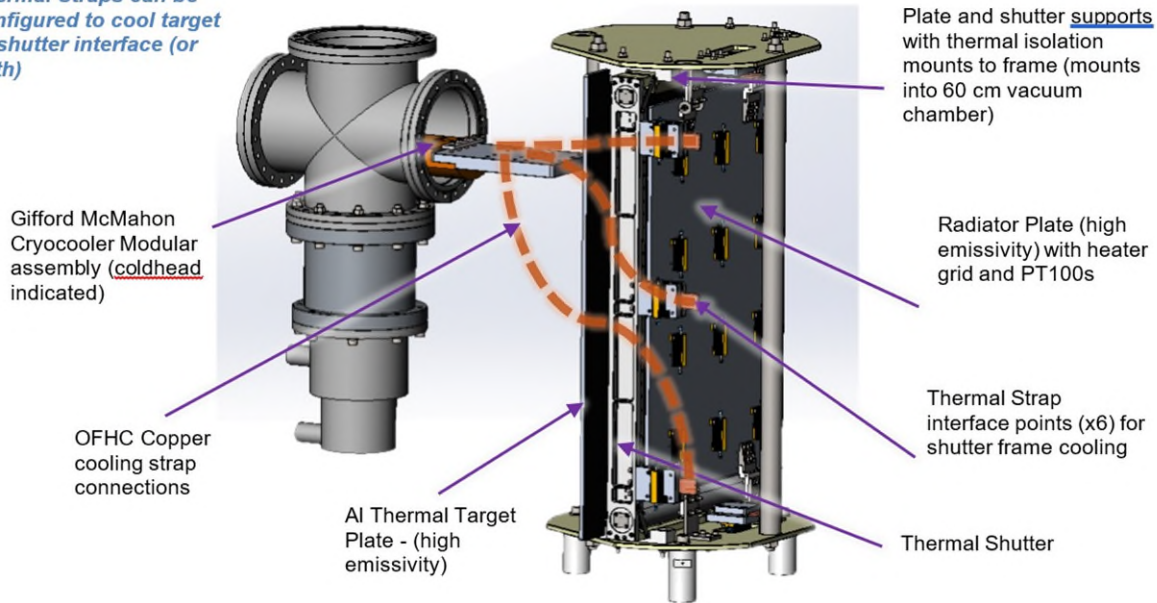


Figure 15. Thermal Vacuum Characterization Setup (60-cm diameter chamber not shown)

To assess the thermal control aspects, the shutter frame is centered around a high emissivity radiator panel, intended to be representative of a lunar lander radiator. Positioned immediately in front of the shutter is a cold target that mimics the cold radiative environment of space. This arrangement allows for the radiator to be maintained at fixed temperature whilst the power required to heat it is measured by the facility; the variance in heater power for different shutter positions will establish how much heat is being radiated to the cold target. This will allow an initial estimate of the turndown ratio the shutter could provide.

A structural analysis was also performed by Almatech to evaluate modal behavior, stresses, and loads within the shutter during launch. Some higher stressed components were found but no significant issues were identified, with adjustments made to reduce stresses. The final analysis confirmed that the expected loads on the motor and gearbox assembly were consistent with the levels already achieved during the actuator level qualification tests. Analyses also confirmed the selection of displacement limiting snubbing surfaces within the mechanism.

Lessons Learned from Prototyping and Recent Build Activities

A significant number of lessons have been learned through the design, analysis, prototyping and build activities to date, noting that the next few months of testing will undoubtedly result in further lessons learned. To date the following lessons were most notable, where the results stress the value of early, environmentally representative tests were helpful to quickly illuminate design flaws and material related issues. Errors made in testing can sometimes produce some very interesting results, in this case results were very insightful for understanding of the tribological limitations. In this case, the importance of assigning allocations for ambient testing of solid lubricated parts was emphasized early enough to plan and communicate adequately with the client.

The axial seal material, chosen for its low wear rate, was proven to be a solid choice, confirmed by testing at ambient (air & vacuum) with no issues reported. This material showed very little degradation through prototype life tests, with minimal wear products, though non-zero. This experience also highlighted the value of the ESTL database of pin-on-disc studies for tribo-material selection for new applications. Though undesirable, the bronze debris generated in early prototype testing was embedded near the inner diameter of the seals, but caused no significant issues, indicating significant resilience to the presence of debris.

The control of light preloads on axial seals has not been a trivial matter. Precise control was enabled for prototype testing with the use of fixed masses working under gravity, but to realize this in all orientations with respect to gravity in the mechanism has been more difficult. The diaphragm approach taken with steel diaphragms is an elegant solution but has resulted in a spring system with a low range of operation, of less than 300 μm which does not allow for much tolerance variation due to individual parts and necessitates some iteration in the build. The approach taken to use an uninterrupted diaphragm (no spirals etc.) was applied because of the need to block ingress of dust into the wheel system, but the solution is somewhat over-constrained. An alternative solution with a titanium diaphragm or a soft wave-washer and a polymer membrane will be considered in the future to relax tolerances.

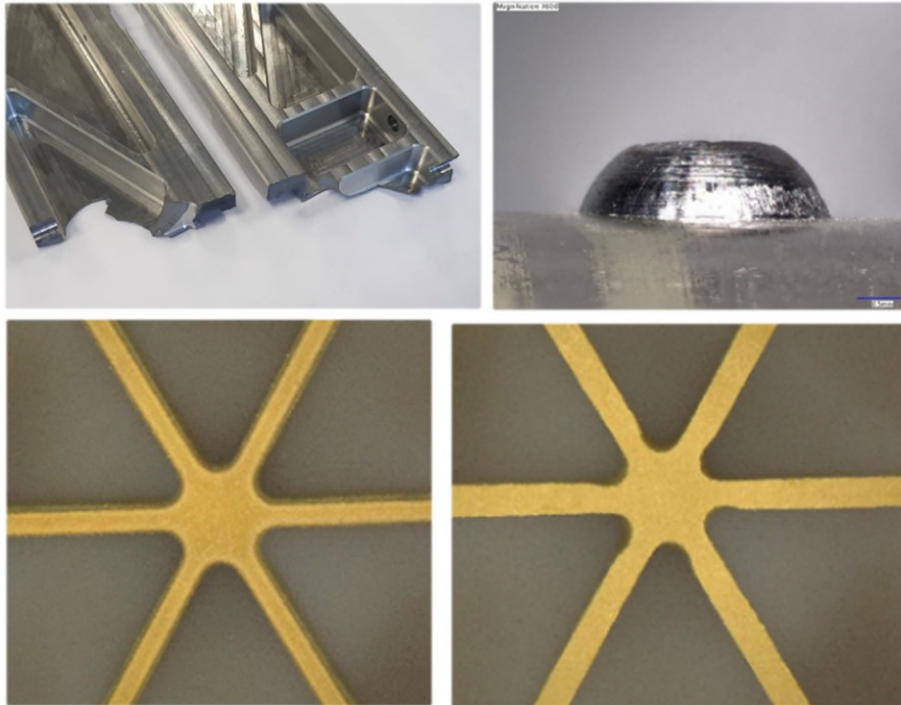


Figure 16. Materials Lessons - Brittle fracture of DISPAL S260 frame (top left), prototype timing screw wear of Ni plated carbon steel (top right), geometry variation at entry/exit of waterjet features (lower)

Early dust testing and bushing lifetime tests highlighted the sensitivity of the timing pin height and radius, identifying a non-conformance that had been missed at incoming inspection. Following this issue, tolerances were refined and adjusted to limit such issues in the future. The nickel-plated carbon steel was also deemed not hard enough based on wear observed in prototype tests, opting to change to PH 15-5 stainless. Refer to Figure 16 showing evidence of wear on this low-cost plated prototype part.

Waterjet cutting was used to manufacture the PAI flex pivot components. This allowed cutting of fairly precise flexure beams to achieve reasonable control of relative motion between parts. However, a closer inspection (as shown in Figure 16) revealed that where the water jet entered the parts, edges were clean, while opposite side edges were uneven. A draft angle was present, with the parts thicker on the jet exit side. Around the thin webs (which act as torsion springs), thickness variations of about $\pm 15\%$ were observed. It was also noted that the flat PAI stock had a $\sim 1\text{mm}$ outer layer with a darker color than the bulk material (a product of the annealing process). While datasheets suggested this layer had the same mechanical properties as the bulk material, it proved to be harder and difficult to waterjet cut and so was milled from both sides before cutting. The worst-case effects on stresses will require some further consideration, to establish appropriate controls prior to qualification.

A substitute material used for the breadboard frame, aimed at reducing cost and schedule, while maintaining realistic CTE effects, was problematic. DISPAL S260 was selected to have a representative CTE (within $0.5\text{ ppm}/^\circ\text{C}$) of the baseline alloy (RSA 4062-T6) but resulted in machining difficulties. While the materials have a similar composition featuring high silicon content, the DISPAL was considerably more brittle, with elongation of about 0.5% vs 2.5% for the baseline RSA material. Two failures of parts occurred near to completion of machining deep pockets in the sidewall parts. One part was made successfully, given several stress relief cycles, while the mirror image part was never completed, despite procuring additional material and near identical geometry. As a compromise, one breadboard wall was made from a bronze alloy with a similar CTE, accepting a mass difference for this build. In addition to brittle behavior, symmetric pocket design (on either side of the wall) would have been beneficial to balance stresses, or to opt for Electrical Discharge Machining to avoid stress accumulation.

Early prototyping work allowed for rapid validation of magnetic concepts. Producing custom magnets and soft magnetic materials requires a good relationship with a magnet vendor, but when this is in place model validation can be inexpensive and fast. Use of early motorisation margin targets as design requirements, with envelope limitations applied, produced a good set of constraints for iteration. Stiffness, peak torque, size, mass, and ease of assembly are competing requirements, but automated analysis and processing helped, and the results provided confidence that solutions were feasible.

The timing/wide scope of a proposed fluorinated product ban in the EU, which emerged at the commencement of the program, poses potential issues going forward that will require consideration. Prior awareness might have affected material selections and could require considerable additional testing in the future.

Conclusions

The design of a lunar thermal shutter has been significantly advanced and derisked to overcome various environmental and lifetime challenges posed, including for wide thermal limits and a dusty lunar environment, such that it can be expected to be suitable for a wide range of payload/lander/rover applications. A full test campaign is planned to be completed in the upcoming months to further verify the capability of the full mechanism design to operate in these environments.

Extensive component testing has been performed to verify the suitability of the bushing and seal technologies, in terms of lifetime and conductivity to bleed charge from the assembly. Axial seals showed the required durability to protect from lunar dust and to meet the required lifetime but will require testing in higher fidelity lunar simulation environments to be able to declare them fully resilient and compatible with electrostatic challenges for a range of missions. The program of work has also proven the potential for long

lifetimes of dust-resilient polymeric flex pivots for small angle oscillations, operating to cryogenic temperatures. Further it has been demonstrated that the electrical connection through sliding metallic bushings, with sputtered MoS₂ lubrication, can be maintained consistently throughout the required lifetime, with relatively low resistance maintained and trending lower throughout the lifetime.

Clearly, further adaptations may be required to enhance dust resilience of the mechanism following upcoming evaluations in dusty low vacuum testing, where lessons learned with this technology for radiators should be transferrable to other lunar applications involving solar panels, which share a similar susceptibility to dust. The device can also be considered for use as solar habitat solar blinds, particularly given scalability and relative ease of adaptation to different platforms. The importance of this type of thermal control in various lunar surface applications, with dust protection incorporated to ensure reliable operation, should not be underestimated. However, the design will require further work to mitigate the effects of lunar regolith in increasingly realistic environmental tests, to ensure the effectiveness for the future success of landers, rovers and other payload performances in more extreme environments and to survive the lunar night.

References

1. Felici, F., Brouwer, G.F., "The Giotto Thermal Control Shutter," *13th ICES Proceedings*, San Francisco (1983), 337-344.
2. Gilmore, D. G., *Spacecraft Thermal Control Handbook: Volume 1: Fundamental Technologies*, 2nd Edition, Chapter 9 (Louvers), El Segundo, California, AIAA - Aerospace Press ©2002.
3. Gibson, A.S., Bailes-Brown, D. et al, "[Design of an Actively Shuttered Dust-Resilient Radiator for Lunar Applications](#)", 52nd ICES, Calgary, Canada, ICES-2023-448 (2023).
4. Hayoz, S., Blecha, L., Liberatoscioli, S., Rottmeier, F. et al, "[Miniaturised Stepper Motor for Space Applications](#)", 19th European Space Mechanisms and Tribology Symposium (2021).
5. Rachel S. Colbert, Luis A. Alvarez, Matthew A. Hamilton, et al, "Edges, clearances, and wear: Little things that make big differences in bushing friction", *Wear* 268 (2010) 41-49.

An Introduction to Flexure Design

Johnathan W. Carson* and Gary Y. Wang*

Abstract / Introduction

Flexures have become more and more common in aerospace mechanisms. I was first introduced to them shortly after I started working at JPL in January of 1992 and have continued to use and advocate for them ever since. While flexures have seen a continued increase in usage, many engineers, while having heard of them, don't truly understand them, or how to go about designing them. This paper is intended to introduce the novice flexure designer to the many uses, design considerations, and fabrication options for flexures along with presenting many example designs to inspire creativity and innovation in budding flexure designers.

What are Flexures?

Flexures are best described as “compliant structure”. While they share many of the same attributes as springs, they differ in that flexures are part of the primary structure of an object or device. Flexures are often integral to a device whereas springs are mechanically captured in place. While springs may be in the load path, they share that load path with additional structure. A simple example which illustrates the difference between springs and flexures is the Jeep (the iconic American 4-wheel drive vehicle) suspension. Older Jeeps use leaf springs while newer Jeeps have coil springs. They both have solid, straight axles with springs to cushion the ride, but the new Jeeps with coils have trailing arms and track bars (4-bar linkages) to locate and attach the axle to the frame. If the springs were removed from this arrangement, the axle would still be connected to the vehicle and it could probably still be driven, though it may not be a pleasant ride. The older Jeep uses leaf springs to provide the suspension as well as attach and position the axle to the vehicle. The leaf springs are primary structure in this case, and if they are removed, then the axle is no longer attached to the Jeep.



Figure 1. My grandfather's vintage sheep shears. This was made from a single sheet of steel which was cut, bent, and folded as needed to produce the blades, handles, and flexure.

Metallic flexures have been around for hundreds of years, likely since shortly after people started forging steel and discovered its flexible properties. Two examples over 200 years old that immediately come to mind are the leaf spring type suspension for the bench seat on a horse drawn wagon and the hand-operated sheep shear (Figure 1).

* Jet Propulsion Laboratory, California Institute of Technology, Pasadena, CA;
Jonathan.w.carson@jpl.nasa.gov

It wasn't until around the late 1950s or early 1960s however that flexures started to see use in aerospace structures and mechanisms. Since then, they have gained popularity and have continued to see more and more usage in the aerospace industry. This is at least partially due to more recent enabling technology such as computer-aided design (CAD) and finite element analysis (FEA) along with improved manufacturing methods and processes, like the development of Electrical Discharge Machining (EDM) techniques. [1]

While flexures can certainly be made by conventional manufacturing techniques, and a great many have been, the development of the wire EDM process drastically changed the world of flexure design. Its small kerf, high precision, and ability to cut thin blades allows for very small, intricate, and integrated flexure designs (where the flexure, the mounting structure, and the moving component are all implemented as a single part) that are simply not possible with conventional machining. The compact brake mechanism shown in Figure 2 is a good example of a device that could not be reasonably made through a process other than wire EDM. The evolving additive manufacturing (3D printing) technology promises to advance the possibilities of flexure design even further. Metallic 3D printing allows the design of overlapping and interweaving flexure elements and even changing material throughout the length of the flexure blade to tailor the design properties.

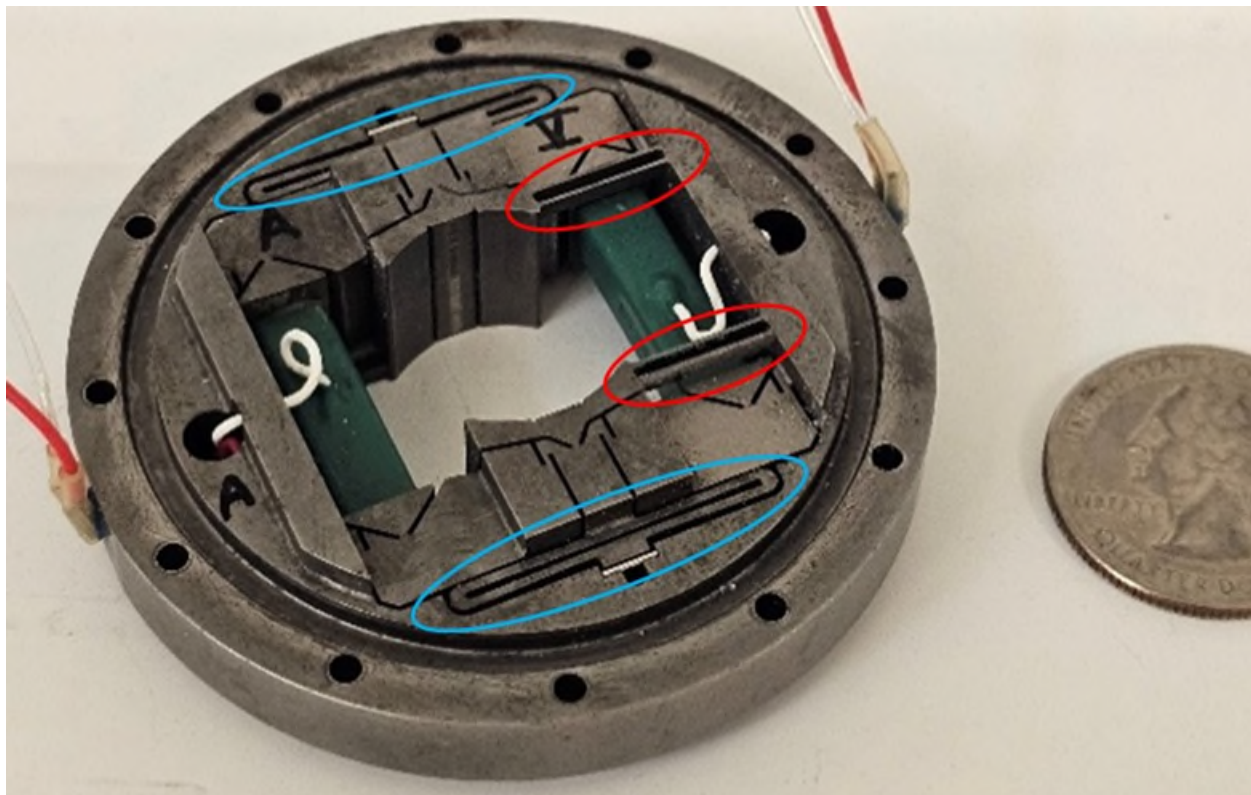


Figure 2. A piezo electric transducer (PZT) actuated brake mechanism for a coaxial rotor (not shown). Note the out of plane “tangent bars” (circled in red) which stabilize the brake shoes. The many short flexures here function like pivots. The large “racetrack” flexure blades (circled in blue) function as integral springs to preload the brake shoes against the rotor. Note the light-colored shim material inserted outboard of these springs to generate the preload.

Why flexures?

Flexures offer some very attractive features for the hardware designer. Flexures can be incorporated in mechanisms with moving joints as pivots and sliders, enabling rotation and translation without wearing parts or stiction. They are also quite useful in providing semi-kinematic mounts and allowing for relatively large

CTE mismatches or thermal gradients between parts. Because of their low cross-sectional area and long conductive path, flexures also provide good thermal isolation while still maintaining robust structural support. Along with other design elements, they can even be used to provide highly repeatable separation joints in precision devices. They are frictionless, require no lubrication, and exhibit little to no hysteresis. They can even be designed to provide infinite life with no wear or loss over time.

Flexures are typically used for linear or rotary motion, where a bending beam is employed. While less common, torsional flexures can also be designed and used. Flexure motions can be very small, highly precise, and repeatable (sub nanometer), or quite large while still providing smooth, predictable motion. Flexures are commonly coupled with high precision actuators, like PZTs, to provide preload, precise guided motion, and small output strokes. These arrangements are commonly found in opto-mechanical devices and typically range in stroke from sub nanometer to tens of microns. When coupled with actuators like voice coils or lead screws, flexure motion can range from a few microns to several millimeters, and even larger for bigger devices. Of course, these large motions require large flexures and the volume to accommodate them.

Fundamental Flexure Types

There are four different fundamental types of flexures, as illustrated in Figure 3. They are the wire, toroidal, blade, and notch (though they may be referred to by other names as well). It is important to comprehend the different degrees of freedom (DoF) that each of these fundamental flexure types constrain and why one type may be better suited to a specific application than another. Once these basics are fully understood, these fundamental types can be arranged and combined to design a flexure system (typically two or more in parallel, series, or a hybrid of both parallel and serial flexures) that meets the application's needs.

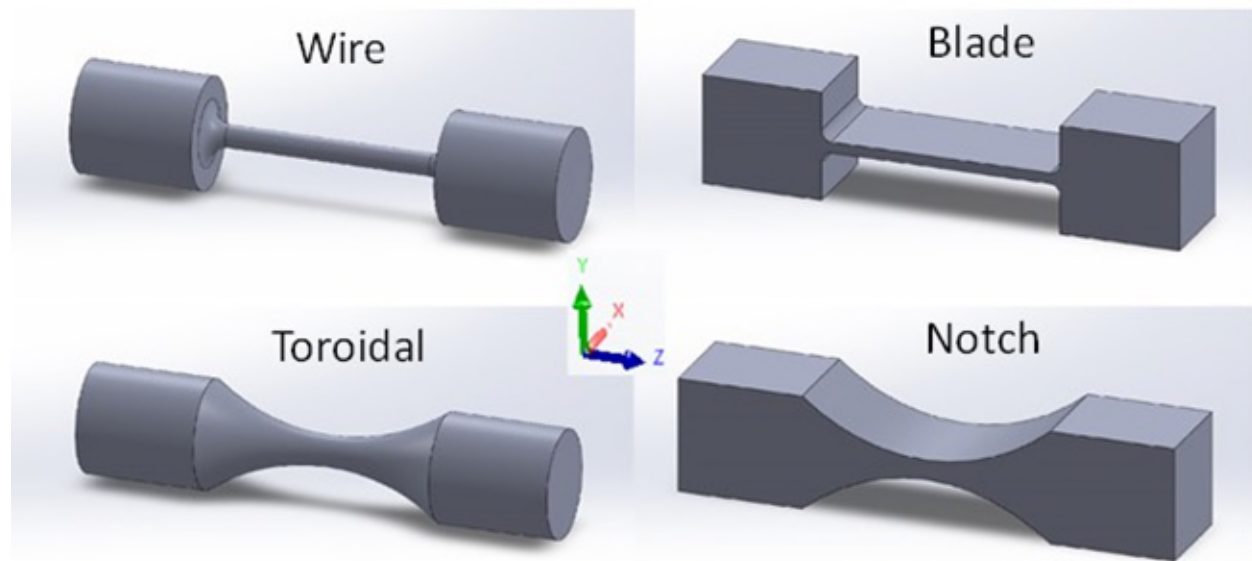


Figure 3. The Four Fundamental Flexure Types

The wire flexure only constrains 1 DoF, translation along its length (the Z axis in the figure). It is compliant in the other 5 DoFs, lateral translation (along the X and Y axes) and bending about all three axes. Because of the long, spindly nature of this type of flexure blade, it is typically loaded primarily in tension as its buckling strength is relatively low.

The toroidal flexure is like the Wire type, but because of its geometry, it can take much higher compressive loads than a similarly sized Wire flexure. The toroidal also constrains an additional two degrees of freedom for a total of 3 DoF, translation along all three axes. The toroidal flexure remains compliant in bending about

all three axes, just like the wire flexure. A common usage for the toroidal type of flexure is at the ends of struts or linear actuators where it is undesirable to translate moment loads. Sometimes both the wire and toroidal flexures are referred to as “pin” flexures.

The blade flexure (sometimes referred to as a leaf flexure) is arguably the most common type and is usually what people envision when discussing flexures. The blade flexure constrains 3 DoF, translation along the X and Z axes and rotation about the Y axis. It is compliant in translation along the Y axis and bending about the X and Z axes. This type of flexure is a good choice when long stroke is required, and the compressive loading is low.

Like the toroidal flexure, the notch flexure offers increased buckling load capability over the blade flexure and constrains an additional two degrees of freedom for a total of 5 DoF, everything but rotation about the X axis. The notch flexure can often save the day when compressive loads are high.

Initial Design

When designing a flexure, several questions must be answered. Which degrees of freedom need to be constrained, and which need to be free? Is a pivot type of flexure needed or a translation type? What is the required stroke, load magnitude, direction, and stiffness? Consideration of these questions will help guide the selection of which basic type of flexure to start with and how the flexure needs to be arranged. The following example assumes this information is known and that a simple cantilevered blade flexure is needed to provide linear motion, but the process is very similar for pivots or flexures that are fixed at one end and fully guided at the other (see Figures 5 and 6 for examples of this arrangement).



Figure 4. An example of multiple flexure blades in series to provide long stroke in a compact envelope. Note the integrated hard stop/load shunt. These linkages allowed 1 mm of linear motion and were used in an over-centering mechanism to provide reliable function without the need for adjustment. A small amount of discoloration can be seen because of excessive heat generated during the wire EDM process.

When sizing a flexure blade, there are three main parameters to work with: blade thickness, length, and width. Keep in mind that the length and thickness parameters are usually interdependent as well. For example, while the stress in a blade is primarily governed by its thickness, increasing the length of the blade reduces the amount of bending required, thus reducing the stress.

With the required displacement known, typically it is best to start a flexure design by determining the amount of length available. Don't be afraid to get creative here. Maximize the length if needed by curving the flexible element to fully occupy the available space. Flexure blades can also be stacked in series to provide more displacement in a compact volume, as shown in Figure 4.

$$K = \frac{E \cdot b \cdot t^3}{4 \cdot l^3} \quad (1)$$

Where:

K = stiffness

E = Young's modulus

b = width of the blade flexure

t = thickness of the blade flexure

l = length of the blade flexure

Once the working length of the flexure blade has been determined, pick a blade width that fits in the design volume and a reasonable blade thickness, then calculate the resulting stiffness and stress in the blade at the maximum required stroke. This can easily be done by hand at this stage, but if a CAD program is being used to design the flexure, it may be just as easy to utilize the finite element analysis (FEA) tool in the CAD software (or even a stand-alone FEA tool), if one is available. A linear analysis is sufficient for small deflections or for providing a "first look" at flexures with larger deflections, but a non-linear analysis is recommended to give more accurate stress and stroke prediction for large deflections, especially if the flexure is fixed at one end and fully guided at the other (see Figures 5 and 6). This requires the flexure blade to form an "S" shape when deformed, which results in a change in length. To accommodate this, either the flexure blade needs to stretch, or the surrounding structure needs to deform inward (toward the flexure).

The process of initially sizing a flexure requires iteration to close in on a design that meets the stroke and stiffness requirements within a reasonable stress level. Don't get discouraged if the final design is not found right away. Change either the blade length or thickness (it's best to only change one parameter at a time, at least at first) and try again. Sometimes a design will close quickly, with only a few iterations, while other times it may feel like this process will go on forever. If a combination that works cannot be found, consider another flexure design configuration, and try again.

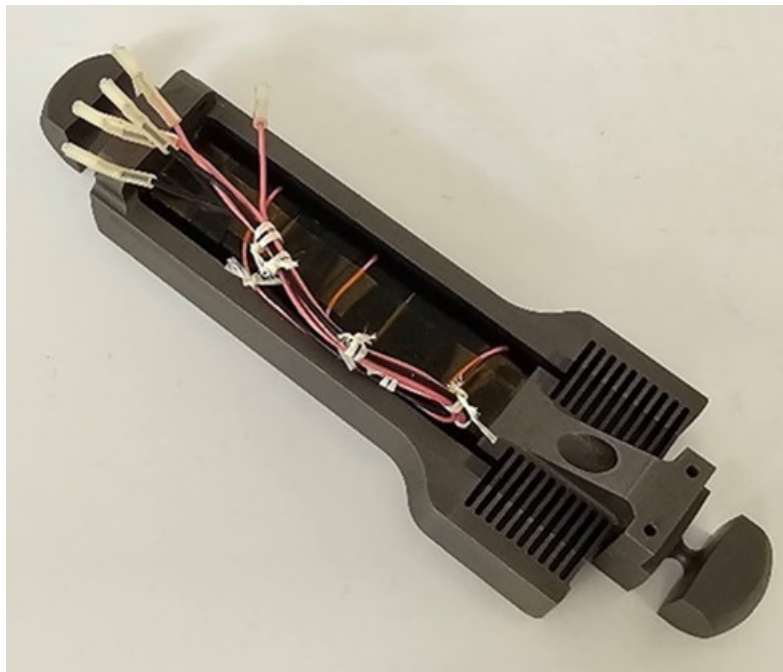


Figure 5. A PZT actuated strut with multiple parallel flexure blades. Note the toroidal flexures at the ends to reduce moment loads.

Once a flexure design is found that nearly meets the needs, the stiffness and force capability can be further refined by varying the width of the blade. Changing the width of the flexure linearly changes the load capability without impacting the stress in the flexure blade. This makes “fine tuning” a flexure relatively easy, however there are limits. For example, the width required may become too large for the packaging constraints. There are also limits in manufacturing, as the risk of deformations such as “cupping” (where the material bends or cups to form a concave surface on one side), increase as the blade width increases. (How wide a flexure blade can be machined to depends on many factors. It is best to work with a manufacturing engineer or machinist if in doubt.) If width limits are encountered, multiple blades may be arranged in parallel to provide the values needed. This approach is often employed for flexures requiring high force and relatively long stroke (where long blades are needed). See Figures 5 and 6 for examples of this parallel beam approach.

There are other design considerations to keep in mind as well. For example, flexures are sensitive to geometric tolerances. Since the thickness and length are cubic functions, the flexure stiffness is very sensitive to these dimensions. Typically, most flexures are long enough that standard tolerances are not a big concern, but they can be a factor for very short flexures. However, the blade thickness is often thin enough though that close attention must be paid to the part tolerances. Again, use of the wire EDM process is of real benefit here because of its precision. The flexure shown in Figure 6 was used in an optical instrument that required nearly perfect linear motion (no tip/tilt). The thickness tolerance of these blades was a real concern, even with wire EDM. In this case, extra blades were used to help minimize the impact of blade thickness variation. The thought was that the error would average out over the larger number of flexure blades and minimize the impact.

Another design element that requires consideration are stress concentrations at the root of the flexure, as this can be critical to cycle life. When there is a sudden change in stiffness, a highly localized stress region exists, but a generous fillet will reduce this stress concentration effect. A stress concentration factor is defined as the ratio between the maximum stress and the nominal stress. The book “Peterson’s Stress Concentration Factors” [2] goes into detail on how to determine and utilize the stress concentration factor, however it’s good practice to make these fillets as large as reasonable. A larger fillet radius will only help reduce the stress at the root of the blade. There are limitations here though, as the fillet should not be made so large as to significantly impact the active length of the flexure blade.

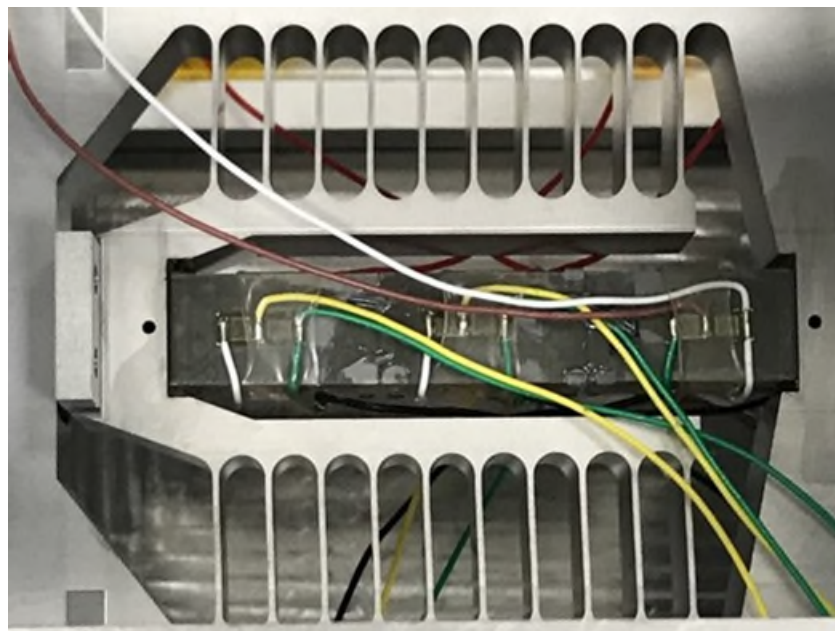


Figure 6. An example of multiple parallel blades used in an optical instrument to ensure precise linear motion.

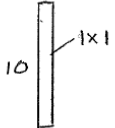
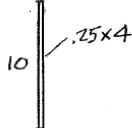
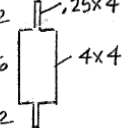
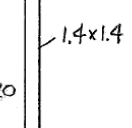
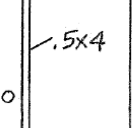
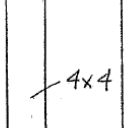
For flexures that will be loaded in compression, buckling is a critical concern. When calculating the critical buckling load for flexures, there are two important considerations to keep in mind. First, if the flexure is going through large deformations, then nonlinear buckling analysis needs to be performed. Second, if the flexure is deformed due to installation, misalignment, or functional requirements prior to the external load being applied, then the buckling analysis needs to include the deformed shape, as the critical buckling load will be drastically reduced.

If buckling is an issue, there are a few tricks that can help. One approach is to simply make the blade longer. While this may be counterintuitive, the longer flexure blade allows it to be made thicker, which helps reduce buckling. This trade doesn't always work, but it's worth trying. Another option that usually works well is to design the flexure such that the bending elements are only at the ends of the beam with a long solid section in the middle. Since most of the bending occurs at the ends of a deflecting beam, use this to your advantage. The table in Figure 7 compares these different approaches and their relative differences in stiffness and buckling strength.

Like in any good structure design, the load lines in a flexure system are important and must be managed. When designing flexures, it is critical that the load line runs down the center of the flexure blade to avoid applying moment loads. If not, the flexure will bend and move in unexpected and unwanted ways and will also be much more likely to buckle. This is especially important when designing flexure bipods for semi-kinematic mounts where they are the primary structure and under axial load. If the load line is eccentric to the flexures, the moment that is generated will significantly reduce the buckling capability of the flexures.

Fatigue is also a critical design consideration for flexures. As a rule of thumb, flexures should be designed to stay below the material's endurance limit to achieve infinite life. For spaceflight applications, NASA-STD-5001 requires a minimum service life factor of four be applied to the cycle life for fatigue assessments. This can generally be achieved by limiting the flexure's alternating stress to stay below 20% of the material yield strength. Many factors can affect the material's endurance limit though, so it's best to test the flexure design. These factors, known as a set of Marin factors, are clearly described in Shigley's "Mechanical Engineering Design" [3] and should be well understood when testing is not practical. When a flexure is subjected to random vibration excitations, the Palmgren-Miner linear damage rule, along with a fatigue life (S-N) curve, is often used to estimate the total fatigue damage for the applied stress levels and cycles. The details of how Miner's rule works can be found in "Metal Fatigue Analysis Handbook" by Yung-Li Lee, Hong-Tae Kang [4].

Flexure Comparison

Dimensions						
Strength	1	1	1	2	2	1
Axial Stiffness	1	1	2.29	1	1	2.00
Lateral Stiffness	1	.063	.080	.50	.063	.016
Axial Stiffness / Lateral Stiffness	1	16	29	2	16	125
Buckling Strength	1	.063	1.56	1	.125	1.56
Lateral Deflection for Given Stress	1	4	3.14	2.83	8	7.80
Energy Storage	1	1	.79	4	4	.97

D. Moore 9/8/2004

Figure 7. Flexure Comparison Table generated by Don Moore, an expert in flexible structures and opto-mechanical design at NASA's Jet Propulsion Laboratory. (The dimensionless numbers in this table are for relative comparisons between the flexure options shown.)

Fabrication

When designing flexures, it is important to keep in mind how they will be fabricated as this often will influence many parameters of the overall design. Flexures can be made by many different manufacturing processes. Some common methods are milling, laser cutting, abrasive water jet cutting, etching, wire and plunge EDM, and cutting or stamping blades then bonding, clamping, or welding them in place. Each of these various methods has different design restrictions like material type, blade thickness, cutting depth, and spacing between blades, just to name a few.

Flexures used in aerospace and precision mechanisms are often made using the wire EDM process. The development of this type of machining was a complete game changer for flexures and opened a whole new world of design opportunities. For very small or densely packed flexures, wire EDM is often the only practical way to go. Wire EDM machines can reliably cut most materials using a 0.15 mm (.006 in) diameter wire (which yields a kerf of about 0.20 mm to 0.25 mm (.008 in to .010 in) and hold tolerances of ± 0.18 mm (± 0.005 in). (Wires as small as 20 μ m (.0008 in) in diameter can be used and tolerances as small as ± 5 μ m (± 0.0002 in) can be held under certain circumstances using the latest machines.) This small kerf and ability to hold tight tolerances allows for very intricate and compact designs. The EDM process also allows production of very thin blades because, unlike conventional milling, no significant side forces are exerted on the material during the cutting process. Just how thin a blade can be cut is dependent on many factors, but generally a flexure width to thickness ratio of 50:1 can be easily cut in most common flexure materials with the wire EDM process. This is a good starting point but be aware that this thickness to width ratio can

be pushed much further under ideal conditions, as shown in Figure 8. Work closely with a machinist or manufacturing engineer to determine what may be possible for a particular application.

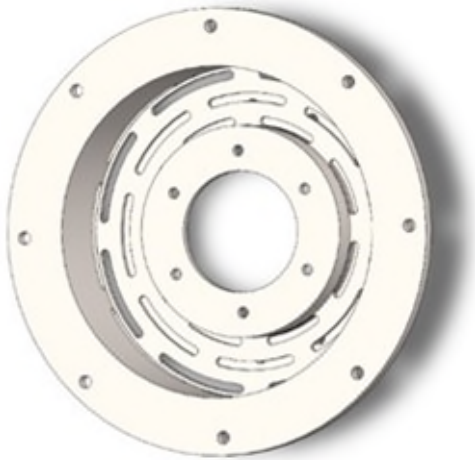


Figure 8. A simple diaphragm flexure designed to be machined conventionally on a lathe and a mill.



Figure 9. My very first flexure design. Versions of this diaphragm flexure design were cut by wire EDM and by milling.

While the wire does offer a lot of advantages for machining flexures, there are a few limitations. This process does require full access to both sides of the cut because the wire must pass through the material in a straight line (similar to a band saw blade). Because the cut is made using an electric arc, the EDM process can only be used on electrically conductive materials. Also, while the EDM machine can cut the hardened condition of metals just as easily as the annealed condition, the temperature of the electric arc is 10,000 degrees C. This heat is managed by flowing de-ionized water around the wire and through the cut, but it can locally affect the temper of the material. This is called the heat affected zone (often referred to as the HAZ) and it can extend as much as 0.38 mm (.015 in) into the material when using older EDM machines. When using modern wire EDM machines however, the HAZ is significantly reduced, approaching a near zero depth under ideal conditions.

If there is only access to one side of the part being machined, the plunge EDM process may be utilized. An electrode must first be machined, which is then used to burn the part. This electrode is slowly eroded through use, so the cut dimensions can change during the manufacturing process. This often requires the use of multiple electrodes and cutting passes. The plunge EDM process offers many of the same advantages as wire EDM, but it is used less frequently than the wire due to the added cost and time of making the electrodes. Still, this process can be very helpful when machining access is limited.

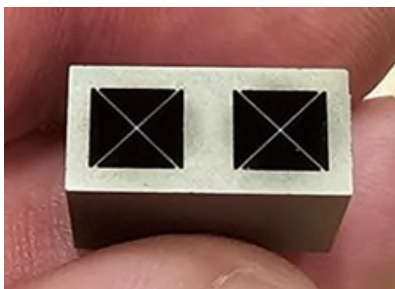


Figure 10. The blades in this steel block are 12.7-mm (.5-in) wide and only 0.05-mm (.002-in) thick, a width to thickness ratio of 250:1.

Another area that needs to be considered when using EDM is the recast layer. The recast layer is a thin layer that develops on the cut surface during the EDM process as the metal is melted by the electric arc. Most of this molten metal is flushed away, but a few particles end up getting redeposited on the parent material where it fuses to the surface. The presence of this thin metal layer on the flexures tends to generate micro-cracks when the flexures are stressed. These micro-cracks induce stress concentrations and can greatly reduce the flexure fatigue life. Hence, it is essential to remove the recast layer on all flight flexures, highly stressed flexures, or any flexure system that needs to provide a high cycle life or high reliability.

The recast layer can be removed through abrasion if sufficient access is available, but it is typically removed by chemical etching. Regardless of the method used, this is something that must be planned for as it adds cost and lead time to the machining process. A thickness allowance must be added to the flexure to account for the material being removed by abrasion or chemical etching. Newer wire EDM machines and processes are capable of making cuts with very little recast layer formation. This reduces the amount of material that needs to be removed and I would even consider forgoing the recast removal process completely on non-critical flexures with low cycle life (i.e., non-flight, lab test only applications where a flexure failure would not damage critical hardware or impact schedule).



Figure 11. The Free Flex Pivot flexure from Riverhawk (originally designed by Bendix)

Besides the EDM process, many other options exist for machining and manufacturing flexures. Take for example the Free Flex Pivot flexure (Figure 11) originally developed by Bendix in the early '60s. This flexure consists of blades cut from flat stock and then welded to cylindrical sections to provide rotary motion. [5] Similarly, flexures can be made by cutting or even stamping blades from material such as shim stock and then clamping or even bonding them into place. If the blade geometry allows, conventional milling can be utilized as well. Plenty of flexures have been made this way. The water jet method of machining can be very attractive for flexures that don't require high precision or fine surface finish. The relatively low cost of this process makes it a good choice for demonstration models or prototypes. The rough surface left from this process can cause issues similar to the recast layer discussed above, therefore it should not be considered for critical flexures (flight use, high stress, high cycle life, etc.).

The flexure design depicted in Figure 12 is made by clamping high strength steel to aluminum mounts using simple bolts and doubler plates. This allows the use of very high strength (2413 MPa (350 ksi)) flexure blades with a very lightweight system. In addition to the mass savings over an all-steel design, this approach is very simple to machine and assemble, resulting in a quick, low-cost solution. This is a great option for prototyping and test fixtures. One potential issue to be aware of with this design is the possibility of the blades slipping under high loading conditions.

Metallic additive manufacturing promises to open new flexure design options just like the development of wire EDM. Being able to print flexure blades allows the creation of geometry that cannot be machined in any way. Imagine interlaced flexure blades, multiple out of plane blades, blades that transition from one material to another along the length of the blade, and many other exciting possibilities!

Regardless of the type of machining used, precision flexures will often require rough cutting, then stress relieving, followed by final machining. Sometimes multiple stress relieving steps are required. Flexures will also often require some post processing, such as the previously mentioned recast removal or shot peening, which may also be used to relieve internal stresses and reduce crack propagation.

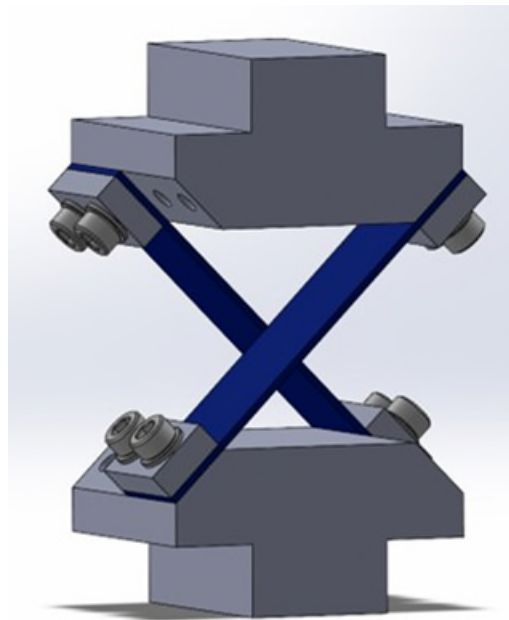


Figure 12. A Simple Cross Blade Flexure. This flexure is designed to be made by cutting hardened steel shim stock and clamping them to aluminum bases.

Materials

Flexures can be made from all sorts of materials, especially if the stress and life cycle count is low. Titanium 6Al-4V is very often used because of its light weight, high strength, and favorable endurance limit, but flexures have been made from 7075 aluminum, copper-beryllium, G-10 fiberglass, various plastics, and steels, just to name a few. In general, if the material is a good choice for a spring, it will work well for a flexure.

When selecting a material for flexures, it generally needs to be strong yet flexible, which means the material needs to have a high young's modulus to yield strength ratio. Other material properties that may need to be considered, depending on the application, are thermal diffusivity, coefficient of thermal expansion (CTE), and density when the flexures need to satisfy both thermal and dynamic environment requirements.

Center Shift

One of the disadvantages of pivot flexures is center shift. When these types of flexures are rotated, the blades are deformed in an "S" shape. Since the length of the blade does not stretch, the pivot point is forced to move away from the initial center. The amount of this shift in the center point is directly proportional to the rotation angle of the flexure.

This center shift phenomenon can be minimized by constraining the flexure blades such that they are forced to stretch. (See Figure 13 for an example.) This design approach can virtually eliminate center shift, but because the beam stretch increases the stress significantly, the stiffness is increased considerably as well, and the achievable angular displacement is much lower. Additional flexure elements can be added to reduce the blade stretch, thus increasing angular displacement, but at a cost of reduced translational stiffness. This may result in lateral motion of the center point though, especially when subjected to lateral loads.

Integral Travel Limits

When possible, it is recommended to incorporate travel limits into your flexure designs. This is especially true of small flexures with thin blades that can easily be deformed by hand. The travel limits should be sized to prevent the flexure material from yielding. Typically, these limits are set just slightly beyond the necessary travel, but sometimes in small flexures the size of the kerf is significantly larger than what is needed for the travel requirements. Also be aware that while these travel limits may help protect the flexures, they do not protect the rest of the structure. Once the travel limit is reached, the load is now reacted directly into the structure. Make sure to analyze for this and design appropriately.

Inflection Point

When flexure blades pass through their inflection point (the zero-stress position) when changing direction, a small non-linearity may be observed. This may also be referred to as “snap through”. This is typically not a problem for less sensitive devices with large ranges of motion, but it is likely to be an issue for highly sensitive mechanisms which are controlled to nanometers. Optical mechanisms that utilize flexures often restrict their motion to one direction only and limit the range of travel such that the flexure does not reach its inflection point. This also has the added benefit of eliminating stress reversal in the flexure, which will increase the cycle life.



Figure 13. A pivot flexure with minimized center shift and integral travel limits.

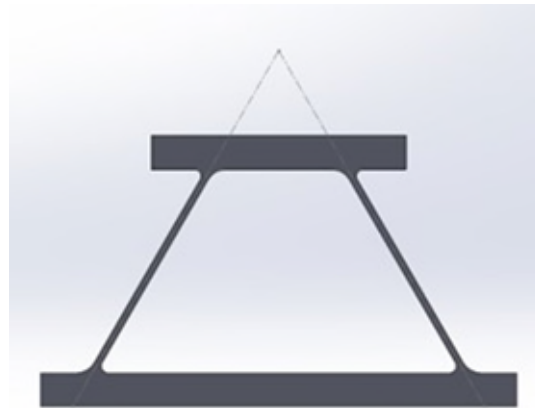


Figure 14. This Virtual Center Flexure pivots about the origin point (where the load lines intersect).

Miscellaneous Tips and Tricks

Sometimes it is desirable to add damping to a flexure. This can be achieved several ways. One method is to simply bond some viscoelastic material to the surface of the flexure blades. This approach provides some damping, but it is much more effective to utilize constrained layer damping. Returning to the leaf spring flexure example from the beginning of this paper, placing flexure blades in contact with each other and constraining them such that they are forced to move together provides damping. This approach also results in some stiction and particle generation from the blades scrubbing against each other, neither of which are desirable for precision mechanisms. However, if a layer of viscoelastic film is bonded between those same blades, good damping is obtained without the stiction or scrubbing.

A pair of blade flexures can be used to mount an object. If those blades are angled and used like a bi-pod mount, the supported object will pivot about the point where those two blades intersect. This can be used to the flexure designers benefit by making virtual pivot points where desired. Unlike when using bearings or pins, the pivot point does not need to be contained within the structure's envelope. By using flexures, this pivot point can be projected well outside the structure. This little trick is illustrated in Figure 14. Let's say a sensor with X thickness must be pivoted about its front surface. By attaching this sensor to the bipod flexure shown in the figure with the flexure centerlines crossing X distance from the mounting surface, this desired virtual pivot point can be achieved without having any structure protruding past the mounting surface. This sort of arrangement is still subject to the center shift phenomenon discussed earlier.

A flexure's stiffness is only as good as its base. When designing any type of flexure, pay attention to how it is secured or attached. A thick, stiff flexure blade that is attached to a soft base may not give the strength or stiffness expected. The same is true when modeling or calculating the flexure blade stress, stiffness, and stroke. Make certain that the base is accurately represented in the analysis.



Figure 15. An example of a flat spring that followed a similar design process as a flexure. This part is about 25 mm in diameter.

The item shown in Figure 15 is not truly a flexure by our definition but a flat spring. It is included here because, while this type of spring is less efficient than a common helical compression spring, it can be very advantageous for certain designs due to its packaging options. This type of spring is designed using the same process, analysis, and design considerations as a flexure.

Be cautious when designing stiff housings that contain flexure blades that are fixed at one end and fully guided at the other. As stated previously, this type of configuration requires the blades to stretch, which increases stress and reduces stroke. When this sort of flexure design is needed though, adding a small perpendicular flexure blade at the end of the main blade (as shown in Figure 16) will reduce the stress and increase the stroke with only a small reduction in the overall stiffness.

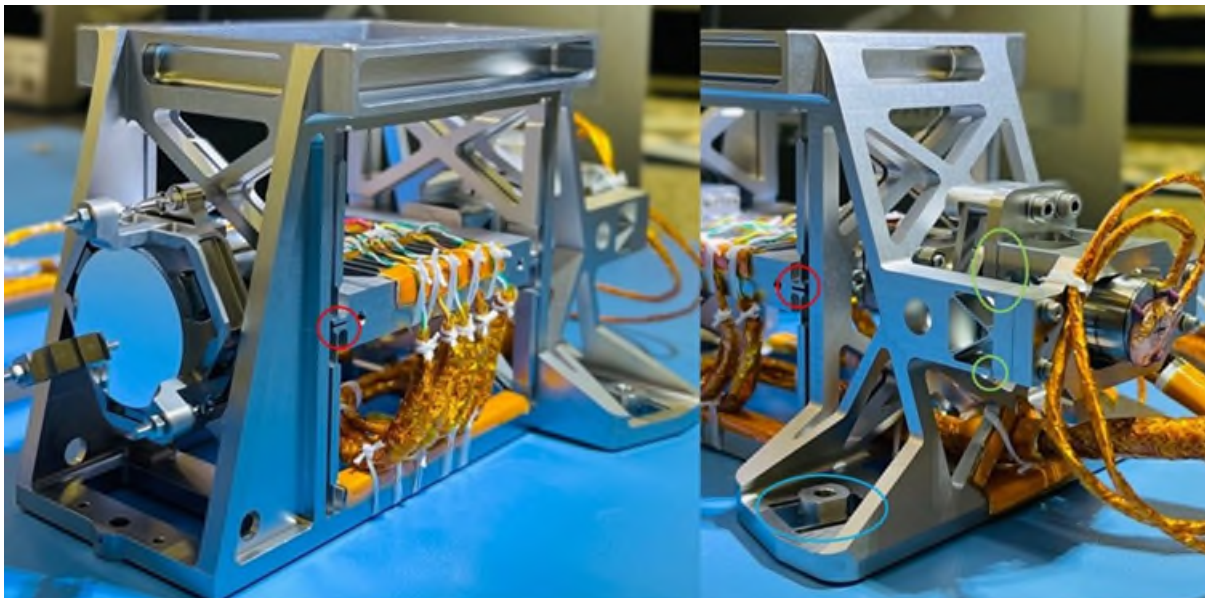


Figure 16. The Focus Control Mechanism for the Coronagraph Instrument contains many different flexure elements. Note the small flexures at the inner ends of the main flexures (circled in red). These small blades significantly reduced the stress in the main flexures and allowed a larger stroke. The small gaps circled in green serve as travel limits for the motor mount flexures. The "H" shaped flexures circled in blue allow for thermal expansion

The remaining pictures are provided to inspire ideas and possible solutions to flexure design problems. These are all flight designs developed for various missions and demonstrate some unique approaches to flexure design.



Figure 17. A flexured rod that makes up part of a precision mount assembly commonly used at JPL on opto-mechanical devices. It is referred to as a “Moore Mount” after its originator, Don Moore. These were machined using an end mill.

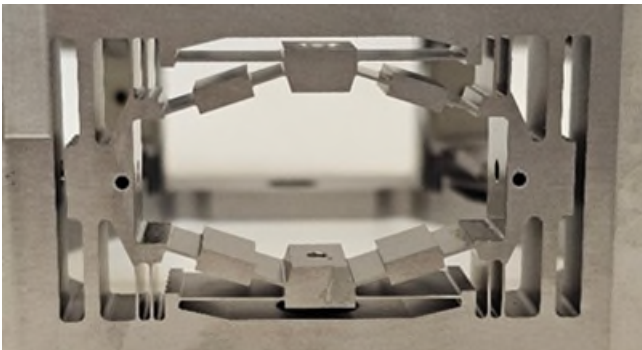


Figure 18. A “scissor jack” flexure arrangement demonstrating many of the design concepts discussed. This is part of an opto-mechanical mechanism originally designed for a space interferometer. It was wired out of a single piece of titanium. The flexure arrangement shown is approximately 50-mm wide.

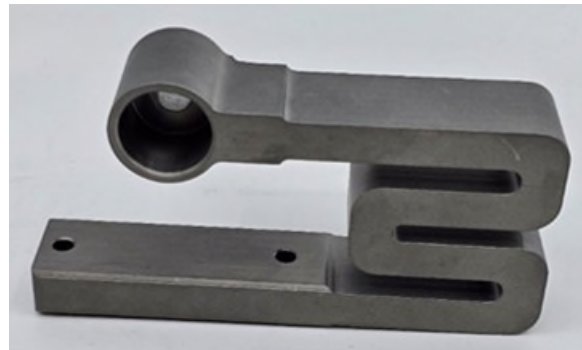


Figure 19. A simple cantilevered flexure design that is “folded” to gain more length in the volume allowed. This was designed to be used for the Mars Sample Return containment vessel.



Figure 20. Three different Mars rover wheels, all using flexures to provide a simple suspension.

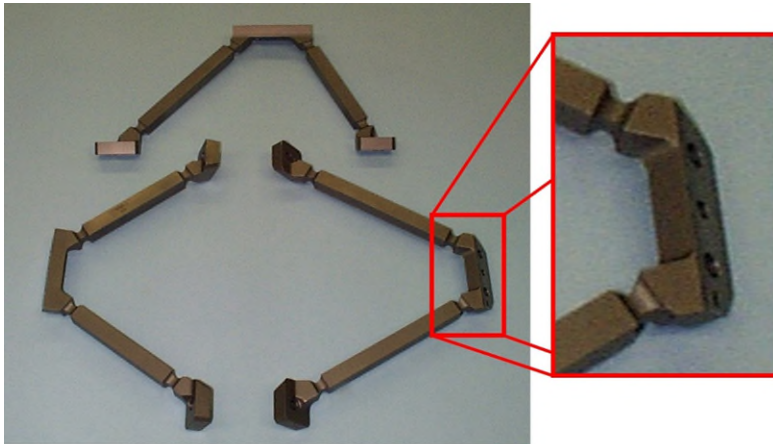


Figure 21. Flexured mounting bipods designed to mount a laser assembly to the Microwave Limb Sounder THz instrument optical bench. These were machined conventionally from Ti 6Al-4v. Note the hybrid notch/toroidal flexures.



Figure 22. A flexured rod guide. The extremely low cycle requirement allowed the use of aluminum 7075 for this part.

Conclusion

There is often a need to add compliance to modern aerospace structures and mechanisms. This is often particularly needed for opto-mechanical devices, high precision mechanisms, and even designs needing materials with different coefficients of thermal expansion and will experience a wide temperature excursion. Having a solid understanding of the fundamental flexure types and their characteristics is essential. The basic concepts and design considerations presented in this paper were meant to provide guidance during the process of developing flexure-based solutions to meet challenging design requirements, but this is just the beginning. I sincerely hope that this paper, along with the additional references listed, has inspired the reader to continue investigating the nuances and challenges of flexure design and the many variants that exist. The constant improvements in fabrication and the budding potential of additive manufacturing promise to open new possibilities and design options for the creative flexure designer.

Acknowledgements

I wish to take a moment to thank the numerous people who took the time to review this paper and provide feedback on it. Your efforts have greatly improved the quality of this document and I am grateful for it. I would also like to thank Don Moore, one of JPL's great opto-mechanical design engineers and flexure guru, for taking me under his wing when I started at JPL so many years ago. Don was a great mentor and a true friend! He was the person who introduced me to flexures, and so many other engineering topics that I never learned in school. Much of what I know about flexures and mechanical design came from Don. Finally, I would like to thank Don Sevilla, another legendary JPL mechanical engineer, for inspiring me over the years to be a better engineer and for encouraging me to write this paper. If it wasn't for his numerous initial suggestions and feedback, it would never have gotten off the ground. Thank you for giving me the push that I needed.

References

1. Herzl, G., "Mechanical Suspensions for Space Applications", 3rd Aerospace Mechanisms Symposium (1968)
2. Pilkey, D. F., Pilkey, W. D., Bi, Z. (2020) *Peterson's Stress Concentration Factors* (4th ed.), Wiley
3. Budynas, R., Nisbett, K. (2019) *Shigley's Mechanical Engineering Design* (11th ed.), McGraw Hill

4. Lee, Y., Barkey, M., Kang, H. (2011) *Metal Fatigue Analysis Handbook: Practical Problem-solving Techniques for Computer-aided Engineering* (1st ed.), Butterworth-Heinemann
5. Seelig, F., 1968, "Flexural Pivots for Space Applications", 3rd Aerospace Mechanisms Symposium
6. Free Flex Pivots. (n.d.) *Frictionless pivot bearings & custom engineered bearings*.
<https://www.flexpivots.com/>
7. Bal-Tec. (n.d.). *Bal-Tec – Flexural Encyclopedia*.
https://www.precisionballs.com/Flexural_Encyclopedia.php
8. Advanced Techniques in Aerospace Manufacturing from Makino, www.radical-departures.net/articles/advances-in-edm-for-aerospace/
9. Thelen, Michael P., Moore, Donald M., "The Mechanical Design of a Kinematic Mount for the Mid Infrared Instrument Focal Plane Module on the James Webb Space Telescope", 2009 IEEE Aerospace Conference (March 7, 2009)
10. Dudik, Matthew, Moore, Donald, "Alignment Stage for a Cryogenic Dilatometer", NASA Tech Briefs (September 1, 2005)
11. Anderson, Eric H., Moore, Donald M., Fanson, James L., Ealey, Mark A., "Development of an active truss element for control of precision structures", *Optical Engineering*, Volume: 29 (November 1, 1990)

The research described in this paper was performed by the Jet Propulsion Laboratory, California Institute of Technology, under contract with the National Aeronautics and Space Administration.

© 2024. California Institute of Technology. Government sponsorship acknowledged.

Design and Test of Retention Mechanism to Apply Direction-Dependent Axial Force to Mars Returnable Sample Tube Assemblies

Jay R. Marion *

Abstract

This paper describes a compact, high force, fully reversible 2-way latching mechanism intended to interact with hardware currently on Mars. Details of the mechanism and a wire-wound joint design are presented alongside preliminary test results and lessons learned. A hardware-rich, iterative design approach has informed the design, which has potential applications for future high-reliability aerospace latch mechanisms.

Mars Sample Return Background

Mars Sample Return (MSR) plans to return up to 30 Martian rock samples in a multi-mission campaign. Samples are currently being acquired and processed on Mars by the Perseverance rover as a key objective of the Mars 2020 (M2020) mission. The samples are sealed inside Returnable Sample Tube Assemblies (RSTAs) for eventual handoff to the Sample Return Lander (SRL). Under the current architecture, the SRL will contain a robotic arm to install the RSTAs into the Orbiting Sample (OS). The OS is the payload on the Mars Launch System which would be injected into Mars orbit for pickup and Earth return by a future mission. The OS is designed to withstand a planned ballistic Earth landing at end of mission.

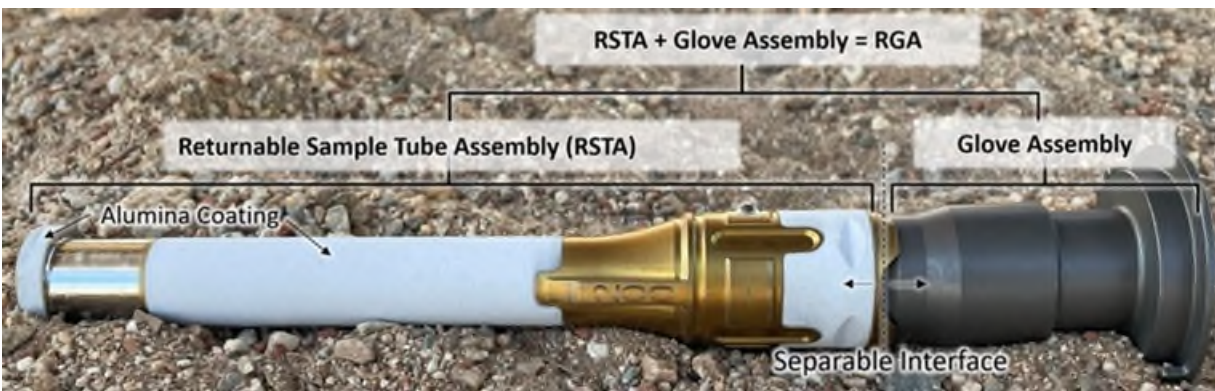


Figure 1. A Returnable Sample Tube (RSTA) and Glove Assembly in the connected RGA configuration.

Returnable Sample Tube Assembly Background

The RSTA external geometry was primarily driven by the sample acquisition and handling functions required by M2020. Many of these geometric features challenge robotic installation by the SRL; the RSTA contains eccentric regions, a rotational hardstop, steps, and small chamfered edges. Adding to these robotic challenges, a high roughness alumina coating was applied to regions of the RSTA exterior to keep sample temperatures within requirements during the planned sample caching operations. Prior to caching, the RSTA is robotically manipulated onboard M2020 via a “Glove Assembly”, which was originally designed to limit contamination of RSTAs in the Adaptive Caching System. Early MSR architectures envisioned that the M2020 handling system would disconnect the Glove Assembly from the RSTA prior to caching and / or handoff to SRL. However, the Glove Assemblies serve as engineering adapters, and provide a friendlier

* Jet Propulsion Laboratory, California Institute of Technology, Pasadena, CA

© 2024. California Institute of Technology. Government Sponsorship acknowledged.

Proceedings of the 47th Aerospace Mechanisms Symposium, NASA Langley Research Center, May 15-17, 2024

robotic interface by which future missions can manipulate the RSTA. For this reason, the MSR campaign determined in early 2022 that M2020 would instead handoff and cache the RSTA with Glove Assemblies attached.

RSTA Insertion Concept of Operations

In the current MSR architecture, the RSTA + Glove Assembly (RGA) is inserted into one of 30 sleeve mechanisms inside the OS by the robotic arm. Successful insertion is verified by resolving robotic sensor data to determine the RGA has reached the axial hardstop at end of travel. Once RGA insertion is verified, the robotic arm preloads the RGA into the sleeve hardstop, to unload the Glove to RSTA ball locks. Next, the sleeve must guarantee deterministic handoff of an RSTA from the robotic arm to the OS by providing a minimum reaction force, such that the Glove can be separated and discarded. The Gloves have no scientific value, and there is insufficient volume in the OS to return them to Earth. After Glove separation, the sleeve mechanism must passively seat the RSTA against the sleeve axial hardstop, with no free play, to provide clearance for OS lid installation.

During a fault where the Glove fails to separate from the RSTA, the sleeve must also permit the extraction of the faulty RGA, within the axial force capability of the robotic arm. The sleeve must guarantee retention of the RGA / RSTA below a repeatable threshold force, above which the RGA or RSTA must be released. This retention force limit dually permits the extraction of a malfunctioning RGA by the robotic arm, and for release of RSTAs into energy dissipating crushable during ballistic Earth impact.

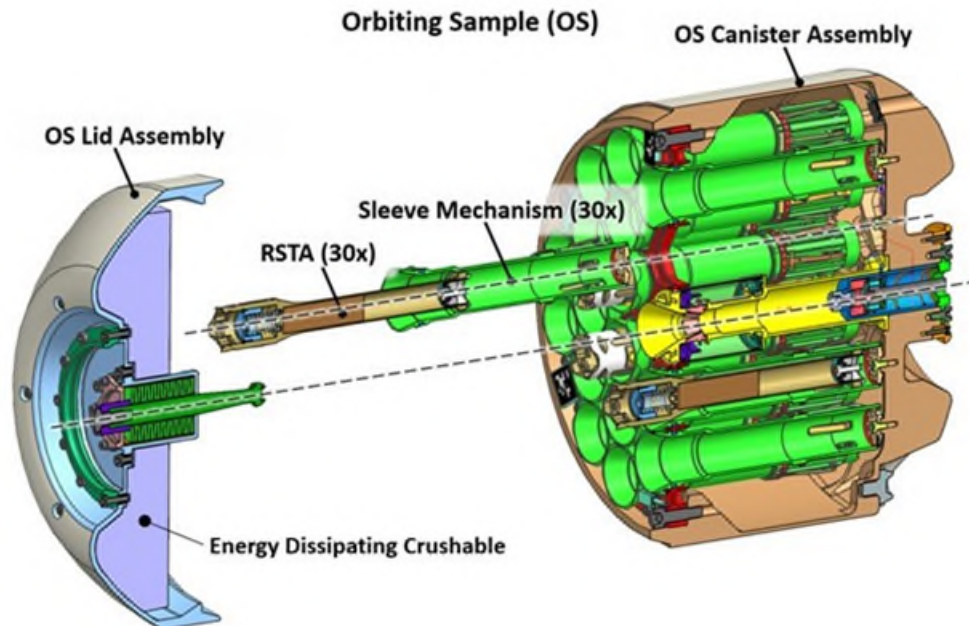


Figure 2. Orbiting Sample (OS) component overview.

Orbital Sample Sleeve Mechanism Key Functions and Constraints

The sleeve mechanism has the following key functions, listed in order of mission operations:

1. Provide mechanical guidance for the RSTA during installation into the OS with the robotic arm
2. Provide passive axial seating force to the RSTA to guarantee successful installation and mechanical clearance during OS lid installation
3. Provide axial compressive reaction force to robotic arm for ball lock unloading of Glove from RSTA
4. Provide axial tensile reaction force to guarantee separation of nominal Glove by robotic arm

5. Allow extraction of RGA by robotic arm during stuck glove contingency
6. Release RSTA into crushable material during ballistic Earth impact

The above functions must be performed across a wide temperature range (-120°C to +80°C), in the presence of Mars dust particles, without any externally powered elements, and must be re-usable and self-resetting through mission lifecycle. The mechanism must operate within a challenging annular volume (ID Ø19 mm, OD Ø 31 mm) and limited mass budget.

Sleeve Mechanism Implementation

Design Overview

A mechanism was developed that applies a direction-dependent axial force to the RSTA as it is translated by the robotic arm. A set of rotating pawls interact with the RSTA and are angularly displaced in opposite directions during RSTA insertion and extraction (Figure 3). A single flat spring energizes each pawl via two unique cam surfaces, with each cam surface separately tuned for insertion or extraction of the RSTA. The resulting RSTA axial force profile demonstrates low (35 N) insertion forces, and reliable retention at a higher force (130 N) across a wide range of friction coefficients, dust environments, and temperatures.

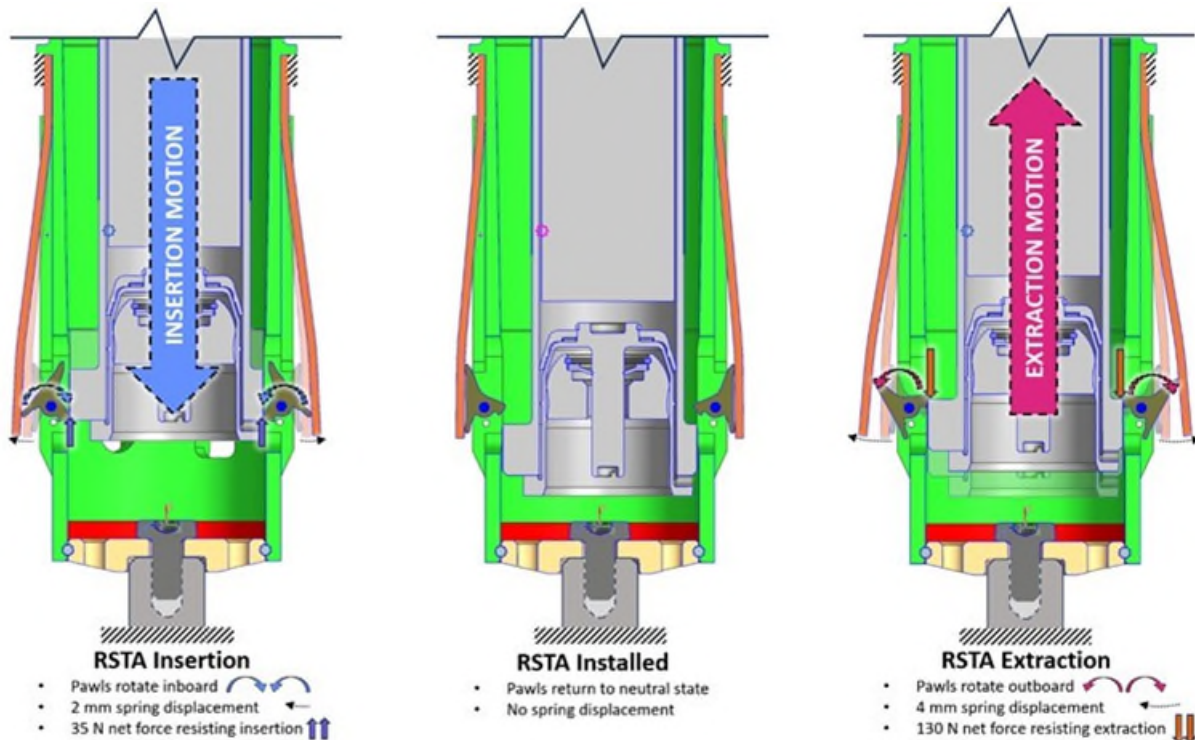


Figure 3. Section view of sleeve mechanism motion during RSTA insertion and extraction.

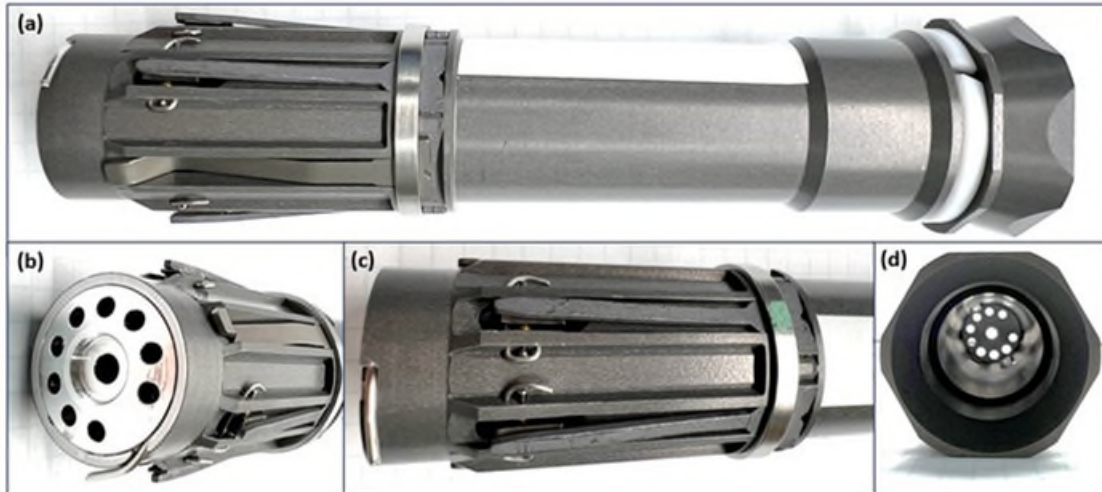


Figure 4. Prototype sleeve mechanism photos. (b) Detail view of sleeve endcap. (c) Detail view of pawl springs and shrink ring. (d) View looking down entry cone where RGA is installed.

Mechanism Design Drivers

Initial prototypes of the mechanism used a ramped leaf spring flexure that directly slid across the surfaces of the RSTA bearing race (Figure 5). The RSTA installation is required to be clocking agnostic, so the bearing race was initially selected for mechanism interaction. It provides a minimum mechanism engagement depth of 1.3 mm in the most eccentric clocking orientation of the RSTA. The initial insertion and extraction forces were satisfactory, but quickly deteriorated as the alumina coating of the RSTA wore down the sliding surfaces and drove up the sliding friction. It was evident that a new approach that was less friction sensitive was required in order to meet the requirements for cycle count, and to accommodate the high coefficient of friction associated with the alumina coating on the RSTA.

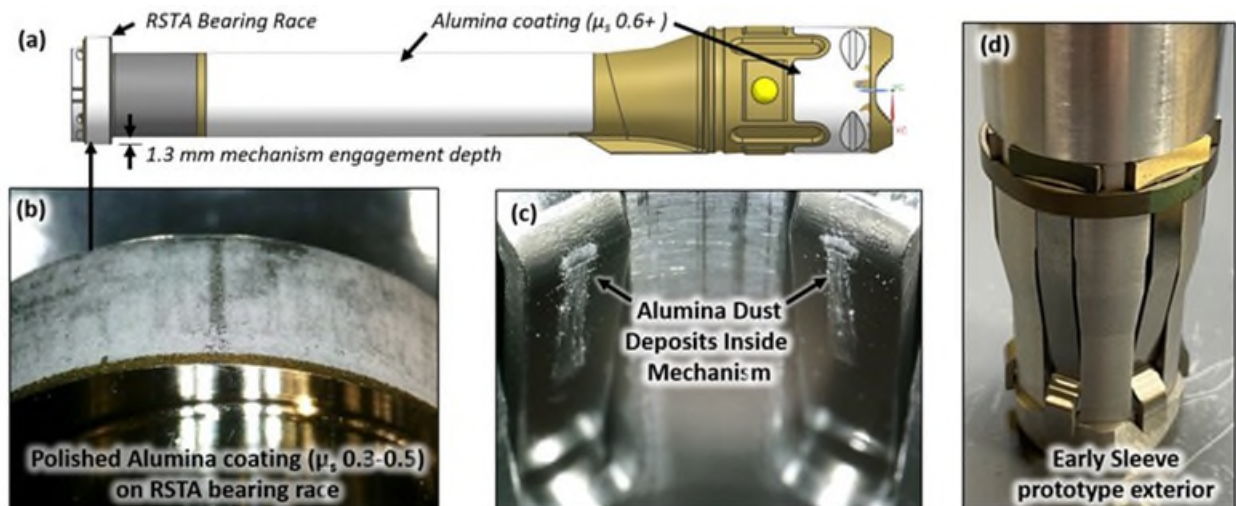


Figure 5. Alumina coating applied to the RSTA (a, b) challenged the viability of the initial dual-ramped leaf spring retention mechanism (c, d). The design shown was retired as it was too friction sensitive.

Due to the robotic challenges associated with inserting the irregularly shaped geometry of the RSTA into the sleeve, significant force is allocated to the misalignment loads that are generated during robotic installation. This reduces the total robotic force available for the sleeve mechanism to activate during insertion, as illustrated in Figure 6. During extraction, the force requirements for the sleeve mechanism are driven by both the worst-case separation loads between the Glove and RSTA, and the requirement to

remove the RGA in the event of a stuck glove. These factors result in force requirements on the sleeve mechanism that are different for RGA insertion (Figure 6a) and extraction (Figure 6b). A direction-dependent passive mechanism solution is needed to meet the system level requirements.

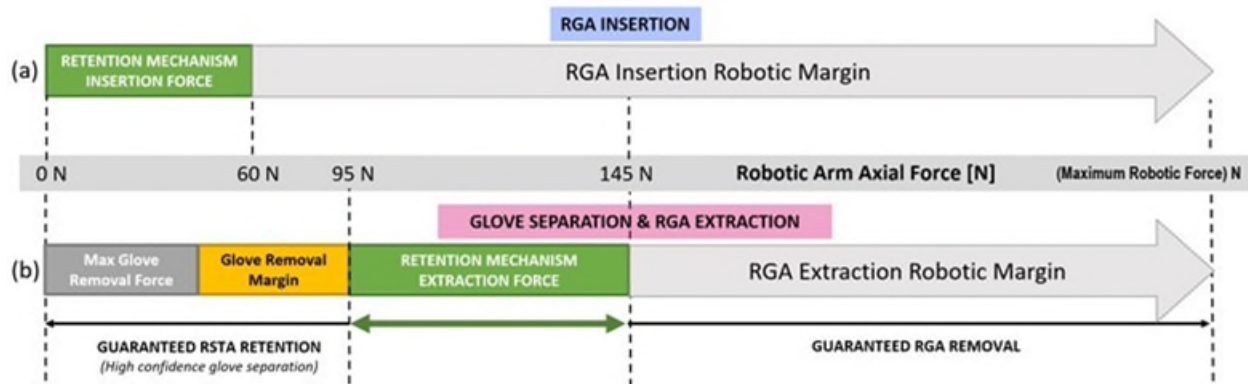


Figure 6. Graphic representation of different RGA insertion (a) and RGA extraction (b) axial force windows. Mechanism axial force is required to be direction-dependent.

To achieve the direction dependent function, a “rocker” design was conceived where a pawl would rotate in opposite directions depending on the direction of travel of the RSTA. To address the self-resetting constraint, the potential energy of the system is at the lowest level when the pawl is in a neutral state with no RSTA in the sleeve. Pawl displacement by the RSTA in either direction increases the potential energy in the system. When the RSTA is no longer in contact with the pawls, the potential energy is released as the pawls rotate back into the neutral state. At this point, the sleeve is ready to receive an RGA again.

During RGA insertion, the effective length of the pawl leaf spring in bending is longer, and the pawl enforced displacement of the spring is shorter. During RGA extraction, the effective bending length is shorter, with greater enforced displacement. This configuration takes advantage of both the length (L) and displacement (δ) terms of the cantilevered beam force calculation shown in equation (1). The load P applied by the leaf spring to the pawl results in a significantly increased pawl rotational stiffness during RGA extraction than during RGA insertion. This difference in pawl rotational stiffness results in a lower axial RGA installation force, with a higher extraction force.

$$P_{beam} = \frac{3EI\delta_{max}}{L^3} \quad (1)$$

The pawl tooth geometry also allows the mechanism to be less sensitive to the high friction alumina coatings on the RSTA. The peak force events for both insertion and extraction occur while the pawl is in the “flip zone” – this is defined as the region where the pawl tooth rotates over the leading or trailing edges of the RSTA bearing race, as shown in Figure 7. In these “flip zones”, the normal force generated between the RSTA and pawl are largely aligned with the robotic insertion axis. Critically, the leading and trailing edges of the bearing race are also free of alumina coating. In the “slide zones”, only the friction force developed between the pawl and alumina coating on the RSTA contributes to the robotic axial force. This allows significantly higher ($\mu > 0.8$) friction coefficients to be tolerated before the extraction and insertion forces of the “slide zone” exceed the peaks observed in the “flip zone”. The RSTA axial force vs. position signature of a typical sleeve assembly is shown in Figure 8.

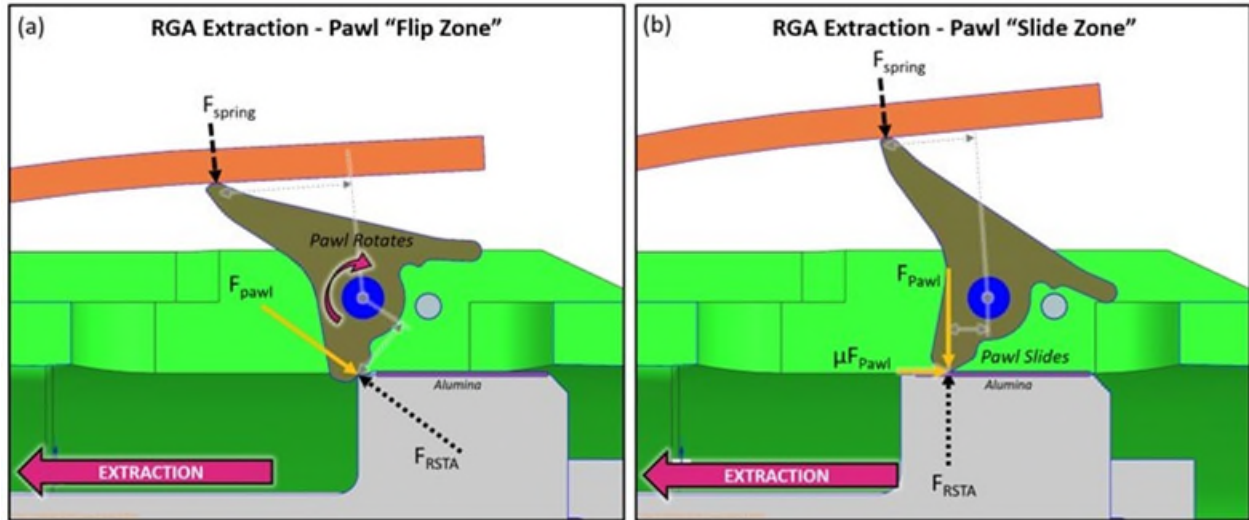


Figure 7. Comparison of pawl to RSTA forces during "Flip Zone" (a) and "Slide Zone" (b).

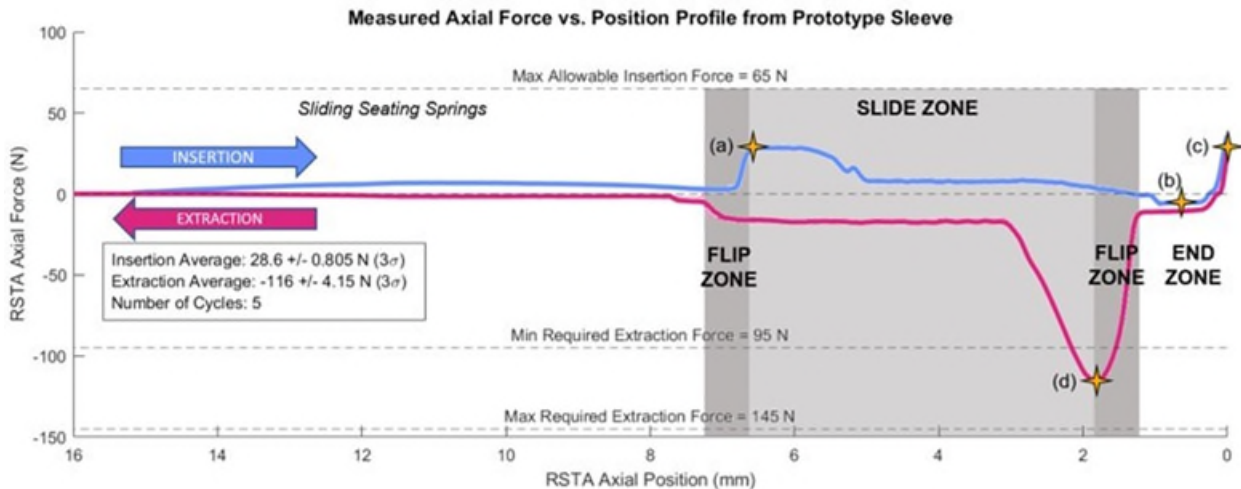


Figure 8. Plot of axial force vs. RGA axial position of insertion and extraction from a sleeve. Note the force signature associated with the flip and slide zones, and the peak force events (a) and (d) that occur in the flip zones. These peak forces are used to evaluate compliance with requirements. The anti-backlash function of the seating springs is seen by the negative force at (b), while (c) represents robotic preloading against the axial hardstop. This extraction force trace, and others presented in this paper, represents removal of a stuck-glove RGA.

Sleeve Mechanism Component Design

Pawls are made of a precipitation hardened stainless steel selected for maximum hardness. During initial prototyping, unhardened pawls quickly wore where they contacted the alumina coated RSTA. Mechanism function was compromised after only a few cycles. The pawl tip geometry was modified and the material was changed to allow hardening to levels closer to the alumina coating hardness. This change significantly increased the number of cycles the over which the mechanism meets extraction force requirements.

The pawls rotate on 1-mm diameter pivot pins fabricated from cold worked Nitronic 60 material. The pins have a sputtered MoS2 dry film lubricant applied. The pivot pins are axially retained in the sleeve structure by a 0.6-mm diameter wireform that is bent over each pin end during assembly. The wireform additionally provides a hardstop function, preventing the pawl from over-rotating and entering a non-recoverable state.

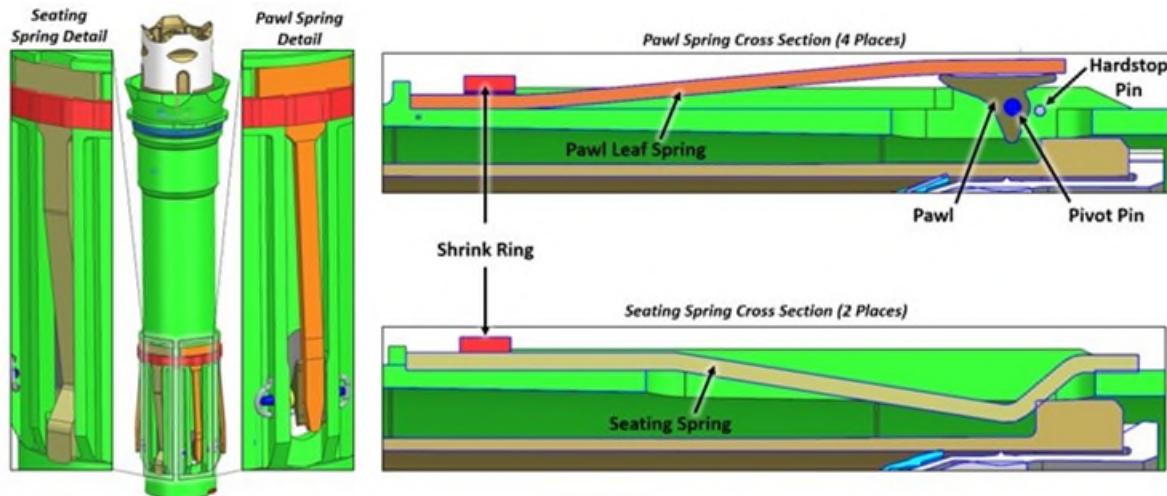


Figure 9. Nomenclature and section view of sleeve mechanism components.

There are 4 pawl springs formed from 1 mm thick sheet metal which apply force to the pawls as they are rotated by the RSTA. Dry film lubricant is applied to the contact surfaces where the pawl slides against the spring to improve mechanism life and force repeatability.

The second cantilever spring design, called the seating spring, is used to remove RSTA-sleeve backlash. Because the RSTA must travel beyond the pawls in order for them to latch over the bearing race, there is a small amount of backlash in the installed state. This backlash was undesirable for many reasons. Primarily, it would result in the RSTAs being installed into a position with a large axial uncertainty. Any number of protruding RSTA could interfere with subsequent robotic OS lid installation, which would be a mission-ending failure. If the lid were able to be installed, axial rattle of the RSTA within the OS poses a risk to the Mars Ascent Vehicle's orbital trajectory due to energy dissipation. To remove the backlash and address these risks, two seating springs are mounted to the sleeve that directly interact with the RSTA bearing race. A shallow lead-in contact angle provides relatively low insertion force, while a steeper lead-out angle pushes the inserted RSTA into its axial hardstop.

All six cantilevered springs are retained within a t-shaped recess in the sleeve structure. The cantilever fixed end is realized by installing a heat-shrinkable shape memory alloy ring over the springs. After shrinking during the installation procedure, the ring constrains one edge of the t-slot recess and applies a clamping force to each spring. See Figure 9 for detailed views of the shrink ring geometry.

Sleeve Structural Design

The primary structure of sleeve provides mechanical guidance for the robotic installation of the RGA. It also defines the boundary conditions of the installed RSTA during return to Earth. The pre-existing geometry of the RSTA, coupled with a requirement to be clocking agnostic for robotic installation, largely defined the inner profile of the sleeve structure early in the development process.

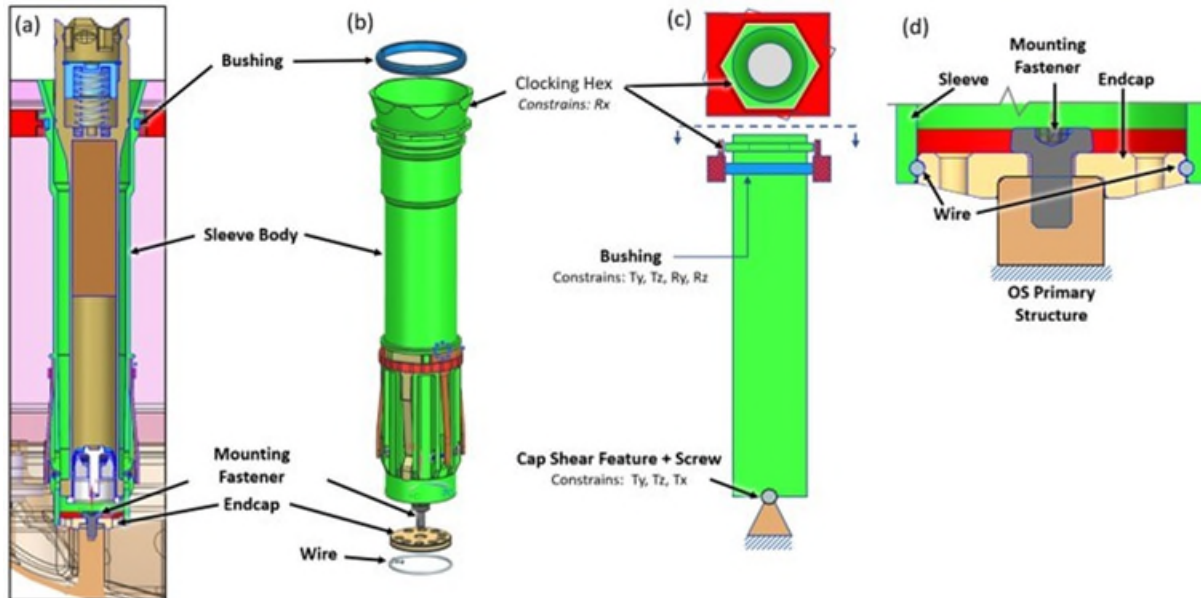


Figure 10(a). Sleeve mounting shown in context of OS primary structure. (b) Sleeve structure exploded view. (c) Sleeve kinematic mounting diagram. The sleeve endcap behaves like spherical joint (over a small range of motion), while the bushing allows for axial and radial CTE mismatch with respect to the OS primary structure. (d) Cross-section of endcap wound-wire joint and sleeve mounting fastener.

The external geometry of the sleeve interfaces to the OS structure: Early in the development process, a two-piece sleeve structure was chosen, which features a sleeve and separate endcap component fastened together to form the overall structure. The two-piece design allows for significant manufacturing tolerance improvement along the entire 120 mm long RSTA-interfacing internal profile, since the profile can be supported and machined from either end during lathe turning. After assembling the sleeve body and endcap, the completed sleeve mechanism is bolted to the OS structure with one fastener installed through the endcap. At the entrance end the sleeve body, a compliant bushing allows for radial and axial expansion of the sleeve body with respect to the OS structure. The relative coefficient of thermal expansion (CTE) difference between the OS primary structure (titanium) and the sleeve structure (aluminum) largely drove the kinematic mounting strategy shown in Figure 10(c).

Initial sleeve mechanism prototypes featured an endcap that was threaded into the inner diameter of the sleeve body. The threaded connection required significant axial length to have reliable thread engagement and structural capability. There were also concerns about secondary locking for the threaded endcap connection. Due to the single fastener mounting strategy, any radial misalignment between the endcap shear feature and the bushing would cause the mounting fastener to be put in bending. A more compliant connection that could accommodate manufacturing tolerances was needed.

In place of the threaded endcap design, a circumferentially wound wire joint was implemented. In this concept, an annular groove with a circular cross-section is machined into the inner diameter of the sleeve body. A corresponding groove is machined into the outer diameter of the endcap. During assembly, a length of corrosion resistant wire is inserted into a radial hole in the endcap. Using dedicated tooling, the endcap is then rotated counterclockwise, drawing the wire into the channel formed by the two grooves in the endcap and sleeve. As the wire is drawn around the joint circumference, the endcap is secured to the sleeve.

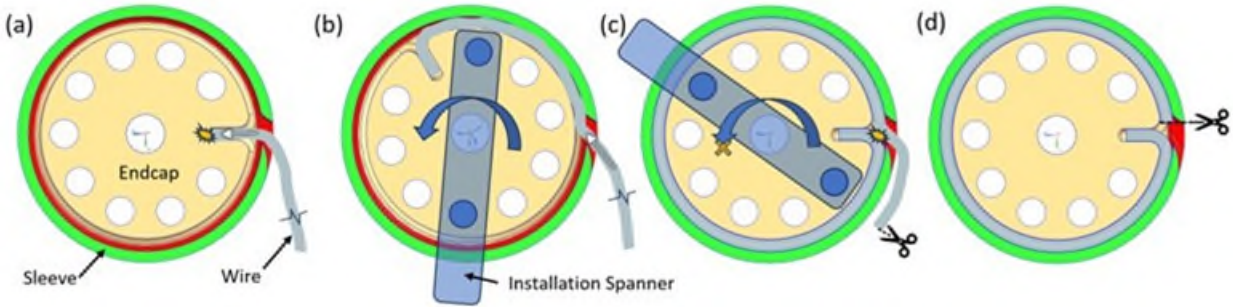


Figure 11. Section views of wire-wound endcap joint at various stages of assembly. (a) Initial installation of wire through sleeve installation slot into endcap retaining hole. (b) Endcap is rotated counterclockwise, drawing wire into channel. (c) Wire is drawn completely around circumferential channel and self-interferes. External wire pigtail remains for endcap removal. (d) Wire is cut and pulled into joint for irreversible configuration.

A short length of wire is left extending from the channel to permit disassembly at any point. Using pliers to pull on the wire end, while applying removal torque to the endcap, it is possible to disassemble caps from the sleeves for inspection or re-work purposes. Prior to flight, this extra length of wire can be cut, and the wire end can be further wound into the channel. As this point, it is impossible to unwind the wire from the joint, and the endcap and sleeve become an inseparable assembly.

Testing has demonstrated that the wound-wire endcap has similar axial capability to the previous threaded connection, but with many other advantages. Because the wire joint is not preloaded, there is a small amount of radial and angular float between the sleeve and endcap. This is advantageous for the OS design, where the float is used to accommodate manufacturing tolerances in the OS structure and to prevent bending in the mounting fastener. The ability of the joint to float within bounded limits with a large axial force capability and inseparable connection make it potentially appealing for other applications.

Table 1. Performance comparison of OS wire-wound sleeve endcap joint vs. threaded alternative

Endcap Joint Type	Joint Thickness	Assembled Joint Float		Axial Force Capability
		Axial	Angular	
Wire-wound Ø 19.1 mm	2.2 mm	0.013 mm	±0.5 deg	2500 N (yield) 4400 N (ultimate)
Threaded MJ20 x 1.0	3.0 mm (Including 1 full thread, with thread relief and flange)	None		3900 N (Ultimate)

Mechanism Test Performance

Ambient Testing

Initial prototypes were tested on a benchtop force-displacement load frame. The sleeve was mounted in flight-like interfaces to the stationary end of the frame. The RSTA was mounted via a misalignment coupling to ensure no cross-moment misalignment loads were realized between the RSTA and sleeve. This ensured the test results only addressed the axial force contributions from the sleeve mechanism.

The ambient test configuration is used to perform functional checkout testing on every sleeve mechanism immediately following assembly. During checkout testing, the RSTA is inserted into the sleeve, preloaded into the axial hardstop, then extracted from the mechanism. This cycle is repeated five times, and the average performance is evaluated. The checkout testing confirms that the RSTA insertion force falls below the requirement threshold of 65 N, and that the extraction force falls between 95 – 145 N. During checkouts,

the retention force can be tuned by replacing the pawl springs with narrower (softer) or wider (stiffer) versions. By adjusting the width of the cantilever springs only, the design can accommodate adjustments of $\pm 60\%$ from the nominal extraction force value. In practice, the required spring width is determined once, and a single lot of sleeve hardware can be assembled with the same width of springs. The retention force variation in hardware lots built to date with the same spring width is only $\pm 3\%$.

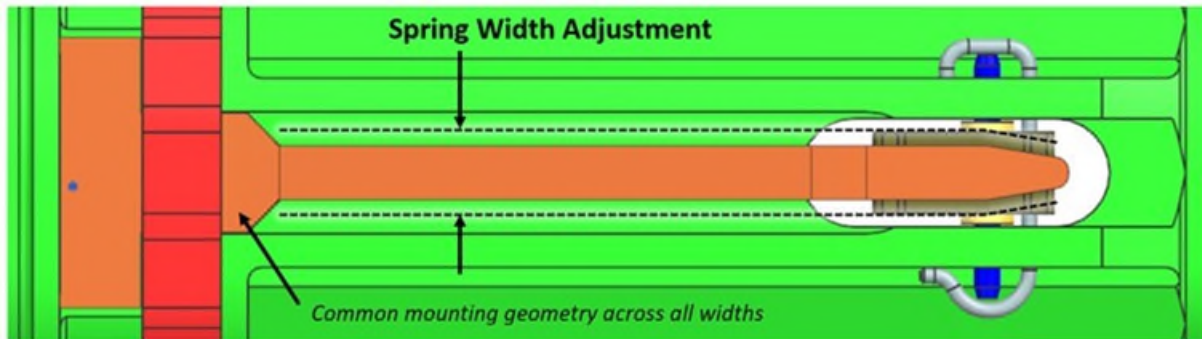


Figure 12. Spring width adjustment dimension of the leaf springs allows for tuning of peak mechanism insertion and extraction forces.

Ambient insertion and extraction tests produced the force displacement curve shown previously in Figure 8. The insertion and extraction force signatures are highly repeatable, and have features that the robotic arm will be able to interpret during operation.

Checkout testing was also repeated with dirt-covered RSTAs to learn more about the mechanism behavior when exposed to potential Mars particles. Initial tests at room temperature were promising; the mechanism still operated within force requirements and did not suffer any jamming. Future testing will be performed with dirt-covered RSTA installed in a Mars atmosphere, pressure, and temperature environment.

Thermal Testing

The sleeve mechanism operational qualification temperature range is -120°C to $+80^{\circ}\text{C}$. A risk reduction test was performed using a force-displacement frame with an attached thermal chamber. A flight spare RSTA was inserted into and extracted from a sleeve mechanism with flight-like geometry and surface coatings. The chamber was cooled with liquid nitrogen, and condensation on the hardware was managed with additional nitrogen purge, pre-test bakeout, and desiccant inside the chamber.

The thermal tests revealed two major findings that are being incorporated into the latest design. The first finding was a CTE-induced over center condition at the cold limit, where the pawls over-rotated and jammed against the bearing race of the RSTA. This condition allowed for the RSTA to be inserted, but not extracted, at the cold limit temperatures. The pawl geometry was revised to eliminate the possibility of the over-center condition, and the tests were repeated successfully with multiple sleeve serial numbers. The results of the testing with revised pawl geometry are presented in Figure 13.

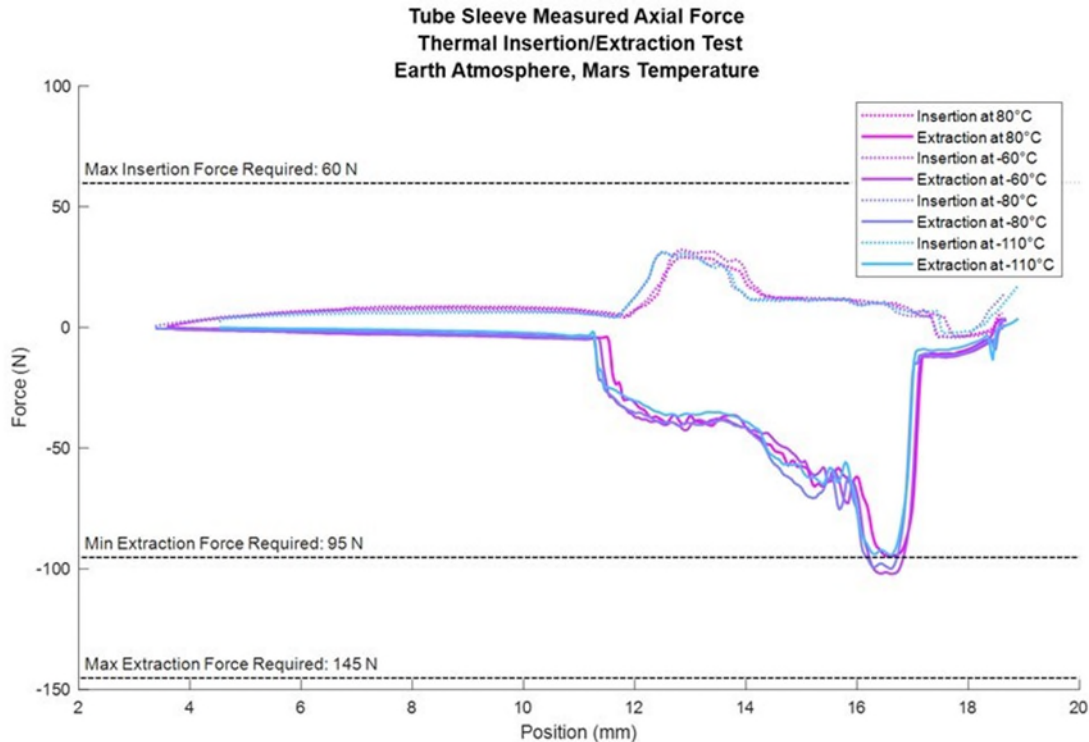


Figure 13. Force vs. displacement curves for RGA insertion and extraction in +80°C to -110°C for a sleeve with revised pawl geometry. Note that the extraction force is tightly grouped near the minimum force requirement. In the future, a wider set of pawl springs would be installed to shift the extraction force peak into the middle of the required range for this pawl geometry.

With the cause of the over-center jamming failure addressed, another limitation of the design at limit cold became evident. The shape memory alloy ring that retains the leaf springs starts to undergo a material phase change at around -100°C, where it recovers up to 0.75% strain. This recovery effectively expands the ID of the ring, and reduces the clamp force applied to the six cantilever springs. The CTE difference between the ring and aluminum sleeve structure further reduces the clamping force as temperature decreases. At -120°C, a sharp reduction of mechanism retention force is observed as the shrink ring diameter is effectively gapped by 0.25 mm from the cantilever springs. The cantilever springs are still retained in their mounting recesses, but their fixed boundary condition is relaxed, and the pawls no longer exert the same forces on the RSTA during operation. Fortunately for the design, the strain recovery of the phase change is fully reversible, and full ring clamping force is restored when the temperature is increased to -50°C [1].

Hardware revisions are in work that allow the cantilever spring mounting end to elastically follow the shrink ring as it expands at limit cold. This should reduce, but not fully eliminate, the retention force reduction at limit cold. In parallel, the thermal requirements continue to mature and are trending warmer, which may allow this risk to be retired without a design change.

Impact Testing

The OS design must accommodate a ballistic Earth landing at the end of mission. During impact landing, the RSTAs are released from the sleeve mechanism into energy dissipating crushable lattice. The lattice is an additively manufactured structure, with properties tuned to keep the RSTA within established peak acceleration and shock response limits. The impact behavior of the crushable lattice is complex, and not discussed in this paper.

The behavior of the sleeve mechanism during impact, along with the crushable performance, was evaluated in a series of impact tests (Figure 15). Instrumented RSTAs with triaxial shock accelerometers mounted internally were installed in sleeve mechanisms. The sleeves were mounted above crushable lattice material within a larger impactor test vehicle. The impactor was accelerated downward at JPL's Impact Test Stand into a gravel bed (Figure 14). Impact velocities of approximately 45 m/s produced transient accelerations of approximately 1200 G, which bounded the expected worst-case Earth landing loads.

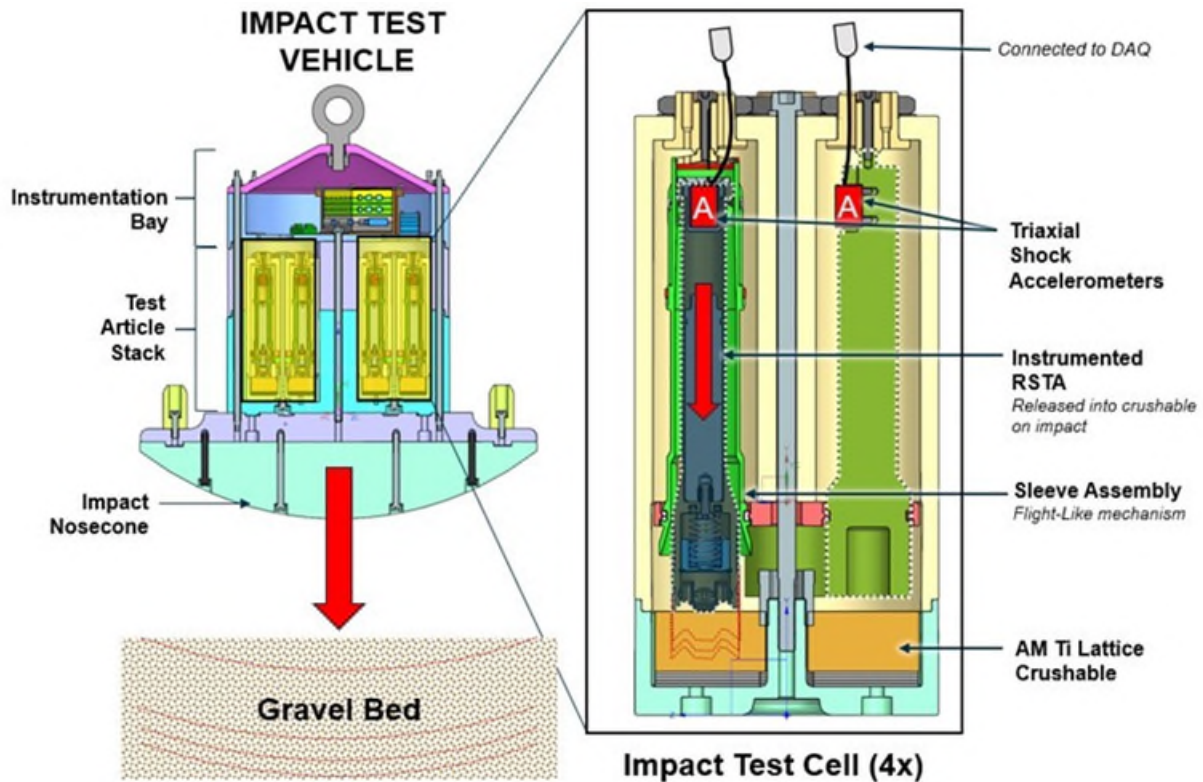


Figure 14. Overview of reusable impact test vehicle used to simulate Earth landing environments at JPL.

During Earth landing, the sleeve mechanism must reliably release the RSTA into the crushable lattice, without overloading the RSTA bearing race. The sleeve mechanism must not be damaged during impact in a way that could cause damage to the RSTA. The motive force for release into crushable is the inertial loading of the RSTA caused by the impact event. The contribution of the retention mechanism to the overall impact response of the RSTA was also a concern. A series of 12 impact tests were conducted. Control sleeves with no retention mechanism were included in each to drop to compare the resulting RSTA response.

A sample of relevant results are shown in Figure 16. The transient axial accelerations are processed into the frequency domain to better evaluate the results. The retention mechanism is responsible for increased RSTA response above 7 kHz when compared with the control sleeves. Despite the increased shock associated with the RSTA rapidly extracting from the sleeve mechanism, the response falls well within the RSTA shock qualification levels.



Figure 15. High speed photographs of test vehicle containing sleeves, RSTAs, and crushable lattice impacting the gravel bed.

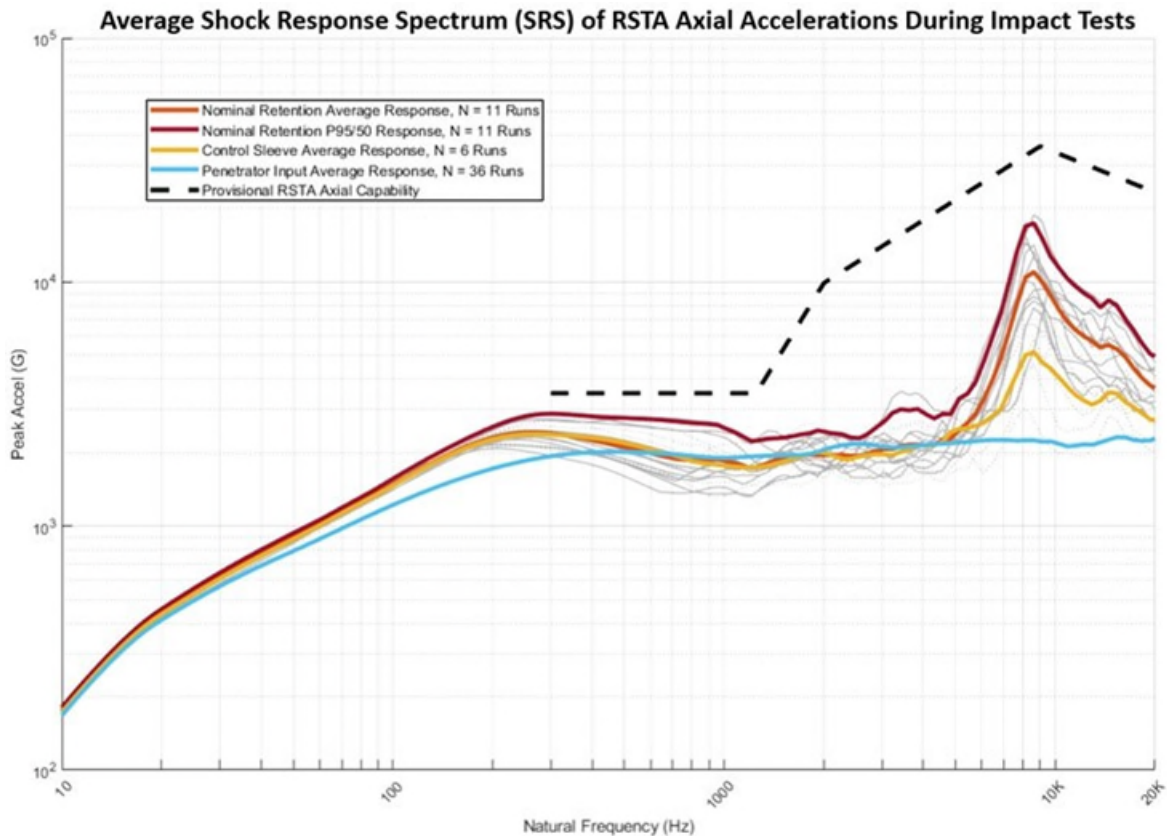


Figure 16. Shock Response Spectrum of RSTA during impact testing at JPL Impact Test Stand. The data shown was collected from a set of impact tests, performed at the same impact velocity, with the same crushable lattice type under test. The blue line shows the frequency response of the vehicle as it impacts the gravel bed. The yellow line shows the response of an RSTA supported in a sleeve without any retention mechanism. The orange line shows the response of an RSTA with retention mechanisms. The increased response magnitude due to the retention mechanism is clearly visible, but the levels fall within the black dashed line denoting the provisional axial capability of the RSTA seals.

Beyond the valuable acceleration data collected, the impact tests conducted were an excellent stress-test of the mechanism durability. Individual sleeve mechanisms were built, impacted, inspected, and re-impacted up to 12 times at the time of publishing this paper. All sleeves subjected to impact testing still meet their checkout acceptance requirements at the conclusion of testing.

Impact testing early in the development process has enabled continuous design improvements. During initial impact testing in 2022, pawl over-rotation was observed, where the pawls would rotate into a non-

resettable state during impact. This was not an expected outcome by the pre-test analysis. It was undesirable from a mission reliability perspective to have the mechanism be able to enter a state where an RSTA is unable to be inserted or extracted from the sleeve. As a result of this early impact test, a hardstop was added to the design that utilized the existing pivot pin retention wire. Since incorporating the hardstop, no pawl over-rotation has been observed during subsequent impact tests.

Future Testing

Prior to project CDR, the team has plans to perform mechanism testing at Mars temperature and pressure, in both clean and dusty hardware configurations. As testbed maturity increases, the team will be able to incorporate robotic misalignment forces and moments as the RSTA is installed in the sleeve mechanism.

Potential Applications

The direction dependent function of the sleeve mechanism has numerous potential applications in aerospace mechanisms. The cantilever spring and pawl can generate significant direction-dependent forces in a small volume compared to other options. The design discussed in this paper could be adapted to apply detent force on an extending strut or boom deployment. The pawl could interact with a rotating gear or axle to apply direction-dependent holding torque passively, without the use of large torsion springs. In human spaceflight applications, the latching concept could be adapted to hold workpieces securely during flight, but permit easy re-stowing by crew after use.

The endcap fastening method described in this paper can also be applied to a number of structural applications. Any design where hollow cylindrical struts are connected to end fittings could adapt this joining strategy. A clear candidate is for monopods or struts where small angular compliance is required, but the capability of a conventional spherical rod end is not needed. The wire shape and groove size could be adapted to withstand significant axial loads, while allowing for axial rotation between the end cap and strut element.

Challenges and Lessons Learned

Detailed Lessons Learned

Where practical, the sleeve development has prioritized early prototypes and risk-reduction testing over detailed analytical models. Many elements of the design, such as the pawl profile and seating spring contact profiles, were developed first with rudimentary hand calculation models, and then iterated to their current design with low-cost testbeds. Stereolithographic additive manufacturing (SLA) was extensively used to iterate the sleeve geometry without costly machined prototypes. An early prototype with an SLA sleeve body, metallic pawls, commercially available pins, and flat, non-formed sheet metal springs was shown to meet force requirements with a flight-like RSTA.

Shape memory alloy (SMA) fastening systems in the form of contracting rings, expanding pins, and other shapes should be implemented cautiously. The details of the fastener alloy and temperature-dependent phase changes should be understood and compared against the expected thermal environment for a given application. It may be possible to mitigate the effects of near-cryogenic strain recovery in SMA fasteners by careful selection of joint materials with low CTE, and tuning the stiffness of the substrate to allow increased elastic following of the SMA as it undergoes strain recovery.

The RSTA exterior surfaces utilize aluminum oxide (alumina) as a thermal coating. Use of alumina as a thermal coating should be carefully evaluated in applications where coated surfaces may need to slide against other surfaces. The high hardness and abrasive properties of alumina make for a challenging tribological pairing with most typical aerospace materials and coatings. Engineers considering alumina coatings should address the risk of abrasive grit migration into critical mechanism surfaces, especially in microgravity environments.

Looking to the Future of MSR and Beyond

The sleeve mechanism was developed to interact reliably with hardware already on the surface of Mars. When the RSTAs were developed, the details of how they would be robotically installed into the future OS design were not fully understood. As a result, the OS sleeve mechanism design must be responsive to high-friction alumina coatings, eccentric features, and challenging geometries present on the RSTA.

Working to a fixed interface on another planet poses its own challenges, and unique opportunities. A hardware-rich development strategy replaced what is usually a protracted process of co-engineering interfaces. This approach required close collaboration with RSTA engineers of past and present, as well as challenging some of the assumptions about the existing hardware design.

Early in the development process, the OS engineering team was provided a limited number of Mars 2020 flight spare, full-fidelity unsealed sample tubes from the MSR campaign. The flight spare RSTA was tested with the earlier sleeve prototype, and fundamental issues with the previous design were immediately evident. The alumina coatings on the RSTA surfaces were damaged by the initial design, which steadily increased friction coefficients and rendered the required robotic force windows unrealistically narrow. The design presented in this paper is a direct consequence of going back to the drawing board after testing with a full-fidelity twin of the interfacing hardware.

As the aerospace community undertakes increasingly larger scale, multi-mission, multi-decade, multi-national engineering campaigns such as MSR, the value of a hardware-centric development process should be recognized. Only so much information can be captured by even the best interface drawings, and personnel turnover should be expected, not an unplanned exception, when planning for long duration development schedules. There is no substitute for an ample supply of high-fidelity flight spare hardware to inform future mission development.

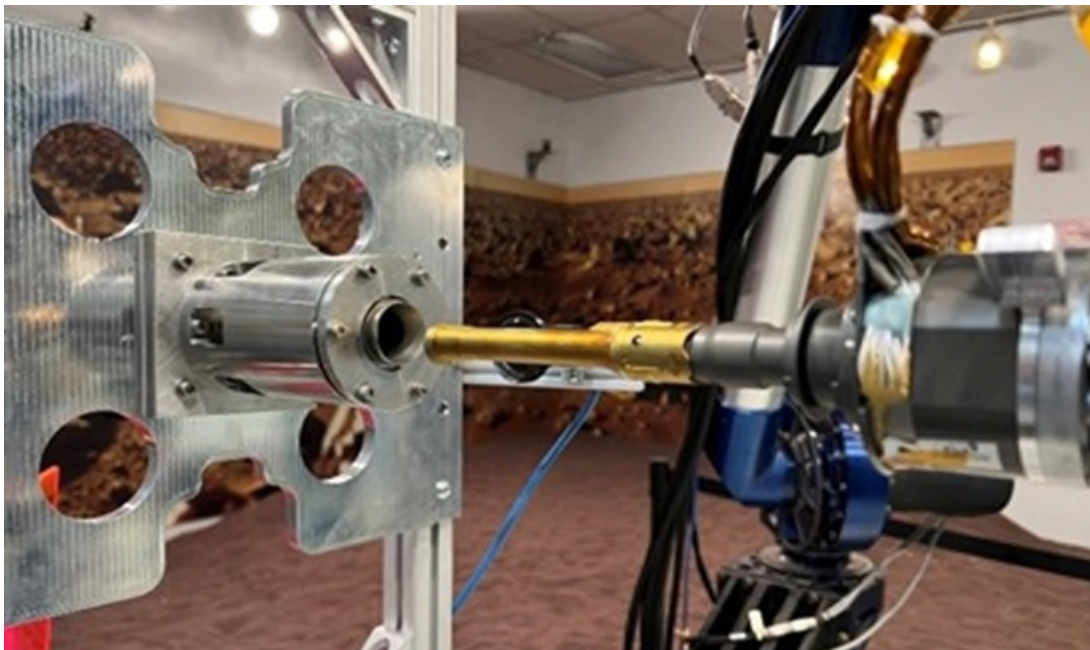


Figure 17. RGA insertion and glove separation testing with a sleeve mechanism and robotic arm.

References and Acknowledgments

1. Intrinsic Devices, Inc. 2022. "Shape Memory Alloy Fasteners." San Francisco.
https://www.intrinsicdevices.com/Shape_Memory_Alloy_Fasteners.pdf.

This research was carried out at the Jet Propulsion Laboratory, California Institute of Technology, under a contract with the National Aeronautics and Space Administration (80NM0018D0004). The decision to implement Mars Sample Return will not be finalized until NASA's completion of the National Environmental Policy Act (NEPA) process. This document is being made available for information purposes only.

Tough Precision Piezoelectric Motors for Space Applications

Francois Barillot*, Jocelyn Rebufa*, Etienne Betsch*, Jolan Gauthier*, Alexandre Pagès*
and Nabil Bencheikh*

Abstract

This paper presents several piezoelectric motors from Cedrat Technologies (CTec) that can be used in hard environments such as those found in space applications. These motors have been designed starting from CTec's proven space technologies. However, they may have been designed for a different field of applications. A consequence is that they can fulfill even harder requirements than those usually found in space actuators.

The first motor is BSMA which has been designed for the space instrument IASI-NG onboard METOP-SG. Results from the 8 delivered flight models are presented. Then several original precision actuators are presented, along with key experimental results. A specific focus is placed on the requirements fulfilled by these mechanisms, such as thermal, mechanical and radiative environments, which can significantly exceed the usual space requirements.

Introduction

Many applications, and more specifically space and instrumentation projects, show needs for a stable sub-micrometer positioning actuator combined with large stroke. They are typically needed to adjust the position of sensitive instruments after launch during initialization or throughout flight life to accommodate aging and other long term variations.

A common requirement is also that, as long periods can be expected between position changes, the actuator should preserve its position in a passive way (i.e., not powered) once the adequate position has been achieved. This characteristic is a key feature for all the motors presented below.

Piezoelectric motors can cover such needs of fine positioning with long stroke and locking at rest. They are widely available for high precision in quiet environments, typically thermally stabilized clean rooms for the semiconductor industry. On the other side, space is a very demanding environment either due to launch vibration or for radiation once in flight. These conditions are obviously not friendly for high-precision piezoelectric motors.

BSMA is a new piezoelectric motor that has been successfully developed by Cedrat Technologies (CTec) to fly inside IASI-NG space instrument onboard Metop-SG. This paper first presents the latest results from the production of the flight models. In addition to BSMA, CTec has succeeded with providing piezoelectric motors for others applications that also face harsh environmental conditions in the fields of defense, industrial, scientific, and nuclear. This paper presents several of these motors with their respective characteristics.

Beam Steering Mechanism for IASI-NG

Motor presentation and general requirements

A major piezoelectric motor for space, called BSMA, is onboard the new IASI-NG instrument developed by AIRBUS DS for CNES. The IASI-NG instrument is one of the key payloads on board METOP-SG which is a new EUMETSAT meteorological satellite for Europe. This linear piezo motor offers a 40-nm resolution

* Cedrat Technologies, Meylan, France, actuator@cedrat-tec.com

and maintains its fine position over weeks, thus allowing a very fine tuning of the IASI-NG instrument while in flight.

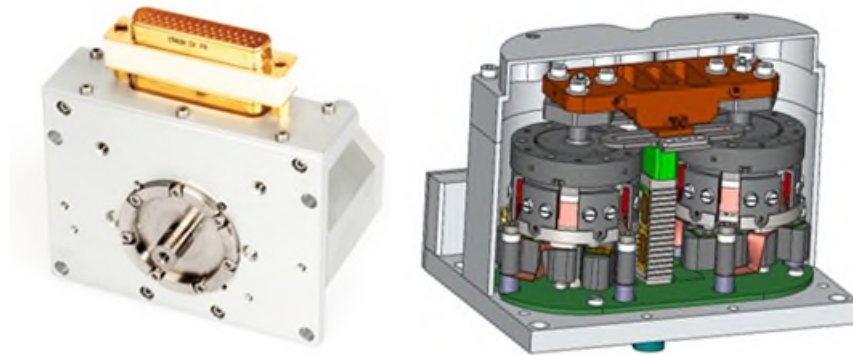


Figure 1. BSMA Engineering Model with connector saver and CAD cut view

The major requirements for the BSMA are:

- Movement: 45-nm resolution step motion over a $\pm 40 \mu\text{m}$ range with up to 20-N force
- Launch: withstand launch including up to 50-N force on output shaft
- Unpowered position stability:
 - 0.15 μm over 24h/1K stability
 - 0.30 μm over 6 months
 - 1.4 μm long term
- Driver capability:
 - Piezo: Max voltage 120 V, Max current 0.1 A
 - Mag: Max voltage 50 V, Max current 0.3 A
- Cold redundancy

In order to meet the requirements, the BSMA motor is based on a combination of a differential screw and an inchworm rotating motor patented by CTec. The major specificity is that the clamp is driven by an electromagnetic actuator that allows large displacement. Details of the internals and on the development have been presented during former ESMATS [1] and AMS [2] symposiums.

One Engineering Model, one Qual Model and eight flight model BSMA's have been built and delivered to ADS. Because of the cold redundancy requirements, each actuator has two inchworm piezoelectric motors, hence a total of 20 motors. It must be noted that this successful work has been possible thanks to an excellent collaboration with ADS Toulouse and CNES.

Assembly and fine adjustment of key elements

During design, a key element was the balance between clamp stroke and clamp force. On one hand, a maximum force is needed to ensure the proper transmission of the piezoelectric stage torque to the rotor. On the other hand, sufficient clamp stroke is required to ensure the proper release of every clamp tooth and ensure that no transmission occurs when the piezoelectric stage returns to its base position.

Optimizing the rotor integration alignment is then a key factor to ensure the motor works but also generates sufficient driving torque. During the Breadboard and initial Engineering Model phase, this was found to be a key issue and rotor adjustment was frequently failing. For Engineering Model and following models, adjustment screws were then added to allow fine tuning of the rotors during assembly. The alignment was finally achieved through first a methodical integration under a 3D CMM to ensure the proper alignment when stacking the various elements. Once this was done, a clever yet simple procedure, which includes some driving of the clamps, was found that allowed to check and finely adjust the center of the rotor.

During design, a second element of concern was the adjustment of the end-stops. The stops prevent the rotors from exceeding their rotation range which would ultimately endanger the differential screw. The key

issue is that the rotor rotation range is several turns. The end-stops positioning needs then to be very precise in order to catch the proper turn.

This issue was anticipated when designing the end stops. A specific yet simple tooling was added that would allow the operator to position the end stops before locking them in position. Another specific concern during parts design was to anticipate and take every simple opportunity to reduce sensitivity to friction. The concern was to minimize random micromovements that occur when tightening the screws that would lock parts in place.

Although minor adjustments had to be made versus the initially foreseen procedure, assembly and adjustment of the end-stops was finally found to be rather easy.

BSMA is a very delicate mechanism to assemble and many issues were faced with first Engineering Model. However, these issues were finally solved and the assembly process is found to be reliable.

Clamp torque margin acceptance test

In order to verify the proper behavior of the BSMA's, the clamp torque margin was verified with every model. The test principle is to underpower the clamp until the motor is unable to move anymore. To accept an actuator, the minimal ratio between the nominal current and the minimal driving current is set to 3 (in order to reflect ECSS requirements).

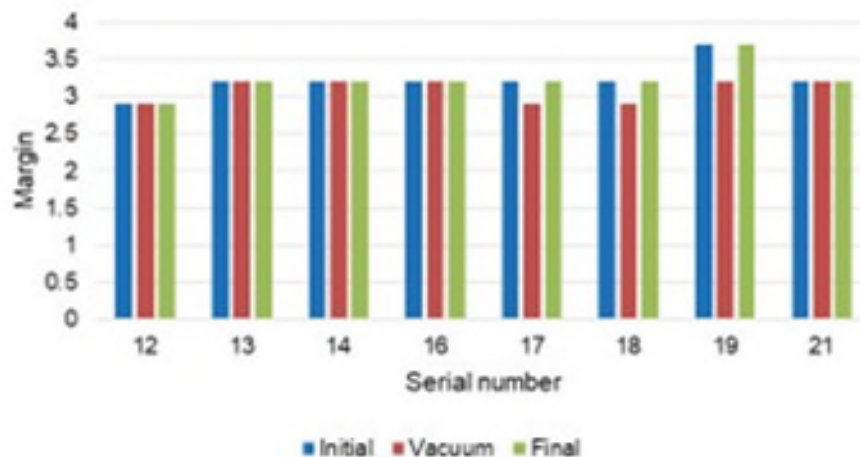


Figure 2. Measured clamp margins

Figure 2 shows the minimum measured margins between nominal and redundant clamp at various steps of the acceptance tests. The 2.9 margin results were accepted as they were due to test constraints; the margin was verified with steps of 0.3, hence either 2.9, 3.2, 3.5, ... The effective threshold is then expected to be better than what is visible on this graph. This proves the repeatability of the clamps behavior, including between air and vacuum.

Step size acceptance test

Step size has been found to be a revealing property for piezoelectric inchworm motors. Its value as well as its stability is a good indicator for the assembly quality and more generally of the motor good health. For BSMA, the measurement is a little more difficult because the steps are 40 nm and being very small, parasitic behaviors can mix in the measurement (test bench relaxation, dynamic thermal expansion, ...).

Figure 3 shows a typical improvement that can be achieved when re-assembling a BSMA that was not properly adjusted.

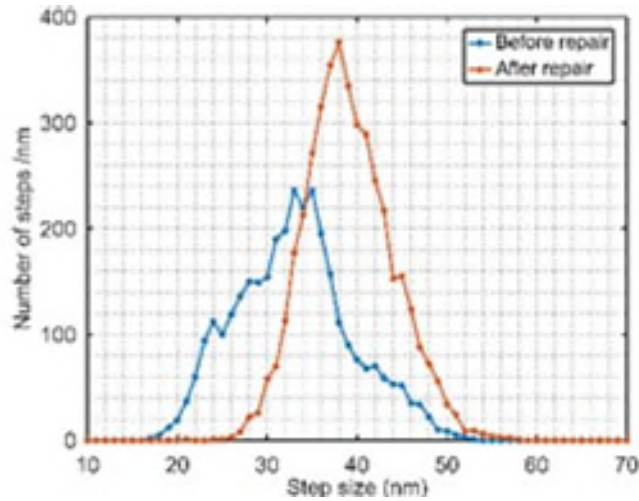


Figure 3. Step distribution for a motor before and after re-adjustment.

However, it was found that for all 10 models that were built (20 motors), step sizes showed a stable behavior, both for average size and dispersion. Figure 4 shows the average step size for some flight models.

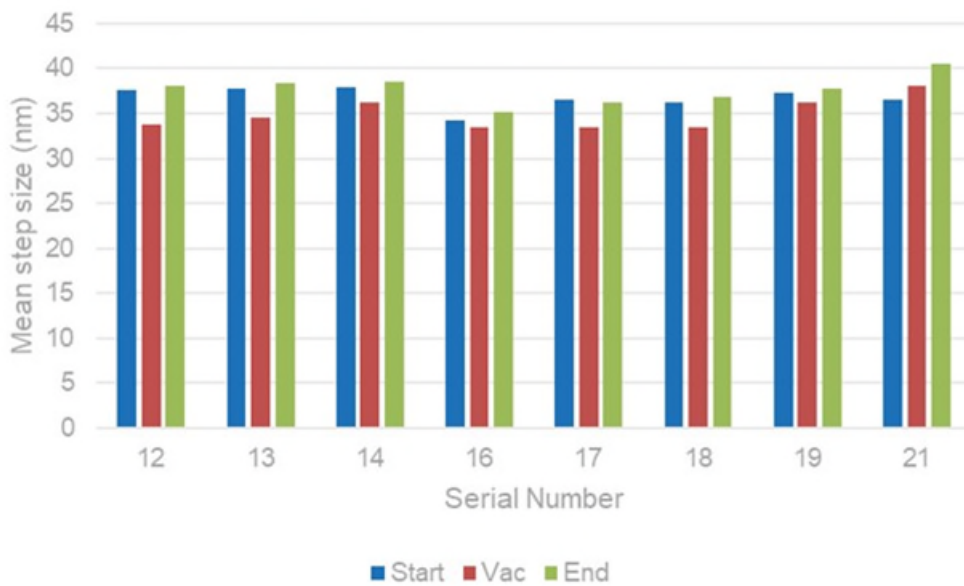


Figure 4. : Mean step size measurements

Lesson learned

A major lesson learned is that it is the simplest solution, most of the time, that offers the best results. Therefore, it is usually worth it to start with simple solutions and update them in the simplest way when problems are found. Meanwhile, anticipation of problems (especially during design but not only), has one include simple details to parts or procedures that can be game changers during assembly and integration. This was found to be especially true for very fine positioning operations such as those needed within BSMA assembly.

AUDACITY Motor

A High-force Piezoelectric Inchworm motor

The AUDACITY motor is a large piezoelectric motor of Inchworm type [3]. It has been designed and tested during a project funded UE and targeting aeronautic applications. This motor has great potential for space applications as it is relying on materials that are used within space-qualified motors or mechanisms, such as BSMA (onboard IASI-NG) or Midas (onboard Rosetta). This especially true for the friction materials, which is key element for inchworms.

In practice, the clamp is designed to support a 500-N sliding force without slippage at room temperature. Combined with a 150- μm driving actuator, this achieves a 15-mm stroke with a $\sim 10\text{-mm/s}$ speed under maximum load.



Figure 5. AUDACITY Inchworm motor

Tribological tests

The friction materials selection is a key element of the AUDACITY inchworm actuator. The pair chosen provides a high friction coefficient as well as limited wear. It is important to note that slippage is very limited when using the inchworm principle as the clamp is released before moving it versus the friction surface.

The high friction coefficient is needed to minimize the forces in the clamp as well as contact pressures when it is locked. A complete and detailed study has been performed by the AUDACITY partner UNIROMA, and thanks to a dedicated test bench codesigned between UNIROMA and CTec, the most suitable materials have been embedded in the actuator.

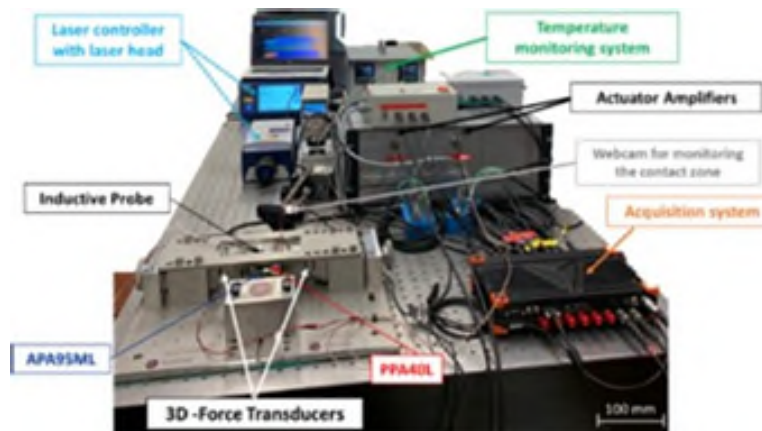


Figure 6. Main instrumentation and sensors embedded in the setup

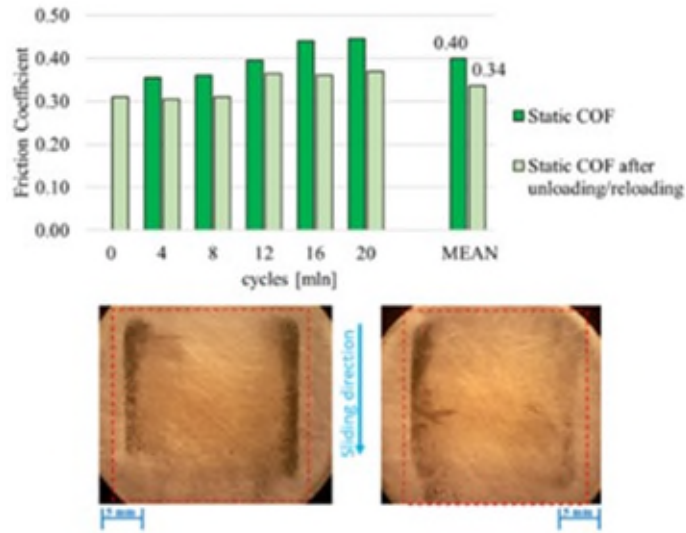


Figure 7. Friction coefficients and Microscope images of the worn surfaces after 20106 sliding cycles

The friction coefficient measured with the bench is suitable and stable enough for the application, and the inspection performed after the test campaign shows a good behavior with less than 1 mg of measured mass loss and a homogenous wear on the friction pads.

Performance tests at -55°C and +71°C

Operating piezoelectric motors over large temperature ranges is challenging as deformation from thermal expansion becomes larger than the piezoelectric effect. This is true for most types of piezoelectric motors whose performance decrease with temperature and even fail below -20°C [4]). For Audacity, the motor uses a new clamp which can accommodate >100K temperature variations thanks to the addition of thermal compensation.

The motor has been tested in a thermal chamber by CSEM under constant load from -55°C up to +71°C. The motor was operated versus a preloaded spring and therefore test load increased over the 14-mm travel. The 350-N load is achieved at mid position.

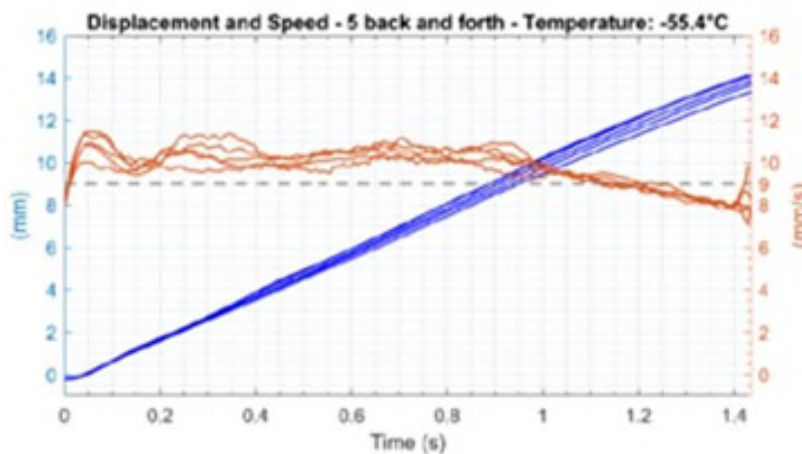


Figure 8. Speed and step size at -55°C @ 350 N

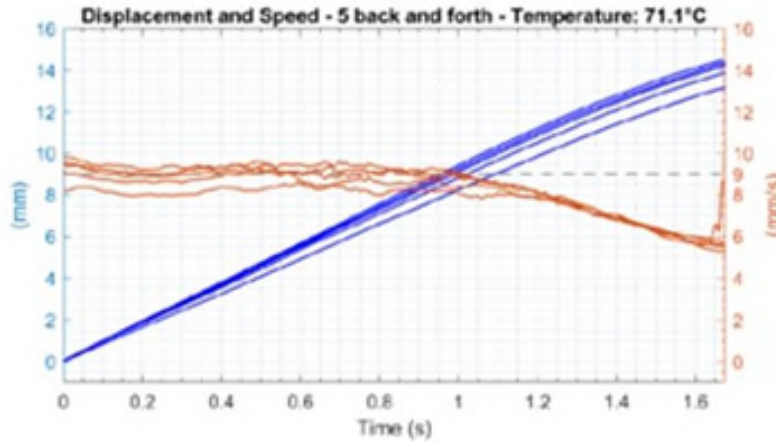


Figure 9. Speed and step size at +71°C @ 350 N

The resulting speed variation is limited when operated at -55°C. On the other side, the speed variation is much more significant when the motor is operated close to its maximum temperature (+71°C). Due to remaining thermal mismatch, the clamp is nearing its slipping threshold and motor speed falls significantly when the force exceeds 350 N.

Conclusion

Thanks to thermal expansion compensation, this rather large inchworm (~2 kg unoptimized) has proven its capability to provide 350 N over a large temperature range (-55°C/+71°C). This type of motor could prove useful to move or deform active optics and to move large mirrors in ground telescopes.

Performance	Value
Stall force	500 N (room) 350 N (op. temp.)
Max weight	< 2 kg
Stroke	15 mm
Speed	> 9 mm/s
Expected lifetime	130000 cycles (>3.5 km)
Op. temperature	-55 to +71°C

Based on some of the knowledge acquired with Audacity motor, Cedrat Technology is now working for ESA on several nonmagnetic high-force inchworm piezoelectric motors. These motors are targeting various needs for the future Laser Interferometer Space Antenna (LISA) mission.

RSPA XS Micromotor

Inertial piezoelectric motors

An alternative class to Inchworm piezoelectric motor is the inertial motors. They are simplified compared to inchworm actuators as they rely on a passive (instead of active) clamp. Only one driving electronic channel is required. The drawback is that higher currents are required to generate the inertial forces needed to achieve clamp slippage.

Based on this principle, Cedrat Technologies is building inertial motors using amplified actuators. Larger pulse amplitudes can then be achieved, allowing longer pulses and less current. This eases the requirements on the electronic driver compared to direct piezoelectric actuators.

Also in regards to amplified actuators, this patented principle is intrinsically better suited for small motors where current is very significantly reduced due to downscaling. It has to be noted that piezoelectric principle is usually becoming increasingly interesting over magnetic forces when size is reduced.

RSPA 30uXS micro-motor

A typical example of such a robust miniature piezoelectric motor is the SPA25uXS. The piezoelectric ceramic is as small as $2 \times 2 \times 5 \text{ mm}^3$. This allows building a complete piezoelectric motor in a volume as small as $20 \times 17 \times 6 \text{ mm}^3$.

The motor generates roughly 500 mN·mm which is much more than electromagnetic motors of comparable size while offering a much simpler construction. A key characteristic for this motor is the electrical pulse characteristic. Thanks to the amplification, driving pulse duration can be extended to 0.2 ms for a 100 V leap, thus only requiring a maximum 60 mA.

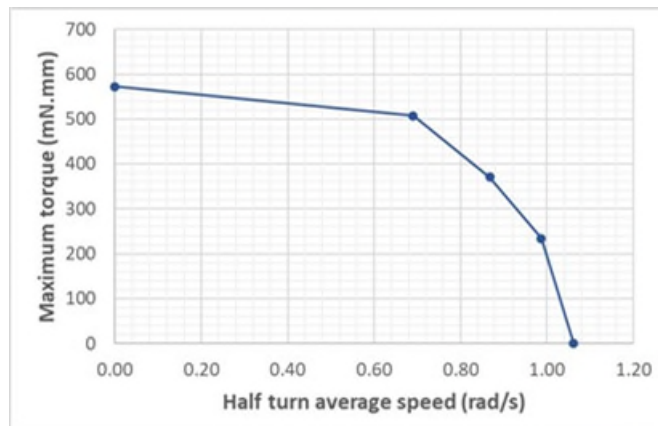
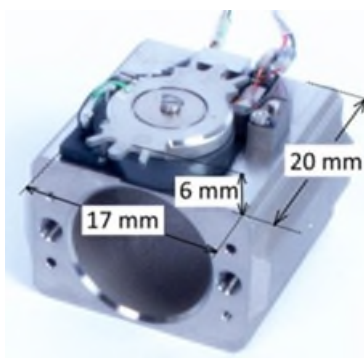


Figure 10. RSPA 30uXS performance, driver 0-100V 60mA

Extreme shock tests

The motor is designed for a special application that requires extreme shock capability. In addition to rather conventional 20g RMS random vibrations, nine 500 g shocks were applied on all six directions. The motor showed no significant change of performance throughout the test campaign.

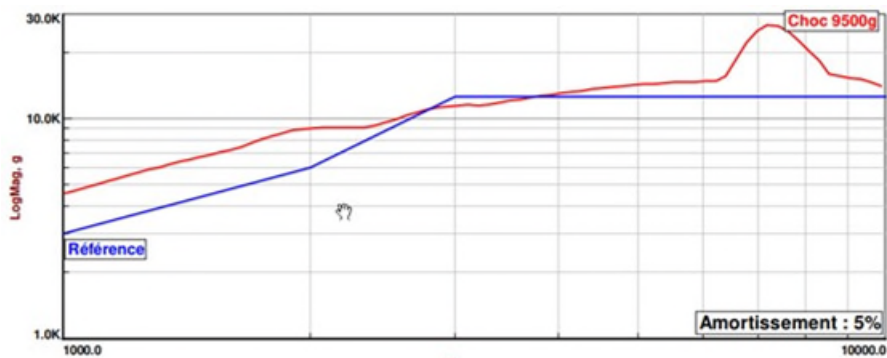


Figure 11. SRS profile measured during one of the shock tests.

The only minor issue during the shock test campaign was the failure of two glue dots. These dots are used to secure the path on to the frame for the wire that provides electrical power to the piezoelectric ceramic. In practice, this had no impact on motor powering and therefore functionality remained unaffected.

It must be noted that the shock levels were limited by the test bench capability. The expectation is that the motor would have passed significantly higher levels.

Temperature

The RSPA has been measured over -45°C to $+120^{\circ}\text{C}$. As expected, speed changes with temperature and shows a maximum close to 40°C . This is due to the optimal combination of the preload (which decreases with temperature due to thermal expansion mismatch) and temperature (which decreases piezoelectric effect when going to lower temperatures).

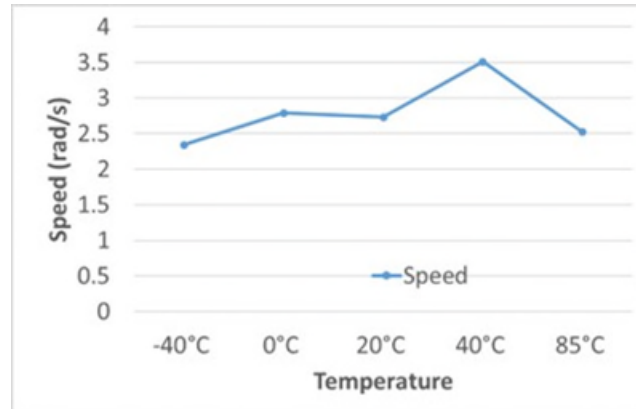


Figure 12. : RSPA speed vs temperature

However, it is important to note that, as long as the motor rotates, the generated torque does not change significantly with SPA motors. This advantage was measured by ESTL during a test campaign [5] where a linear SPA motor showed stable force generation (less than 25% decrease) from 0°C down to -180°C (90K).

RSPA SM Motor for ITER

Introduction

Another larger RSPA motor [3] is currently being designed and tested to be used within the Tokamak of the ITER project. This motor is much larger ($50 \times 35 \times 50 \text{ mm}^3$) and is expected to deliver roughly 1.5 N and therefore a torque of 25 N-mm for track of $\text{Ø}35 \text{ mm}$.

As can be expected, this motor is fully non-magnetic: it is designed to avoid disturbances of the high intensity field of 3.5T that surrounds it. Similar to space, the motor is operated in vacuum. This work is partially funded by European Commission including F4E.

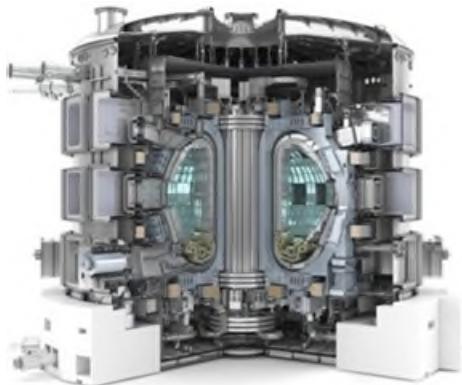


Figure 13. View of ITER Tokamak

Radiation test

A key requirement for equipment used in the vicinity of the Tokamak is their ability to support high radiation levels. In order to validate the RSPA piezoelectric actuators, several amplified actuators have been built and exposed for 3500 hours at rates of roughly 300 Gy/h (or 30 kRad/hour). The resulting TID (Total Ionizing Dose) was a little more than 1 MGray or 100000 kRad. It is true that the radiation profile is not the same as what can be expected in space but this remains relevant to demonstrate.

Figure 14 (left) shows photos of a standard amplified actuator. Due to the radiation, the powering wire insulation (which is PTFE) is badly damaged and sections have even turned to dust. For Figure 14 (right), the ceramic was upgraded with Kapton wires. This is the usual practice for actuators delivered for space projects.



*Figure 14. Pictures of two amplified actuators after exposure to 100 000 kRad
left is using PTFE wire, right is Kapton wire*

Several ceramics suppliers were tested during that campaign. The major conclusion is that, for all tested actuators, no degradation was measured aside from the wires. Actuators remained fully functional with no significant variation of behavior such as their stroke or resonance frequencies. PTFE wires were badly damaged whereas ECS- compliant Kapton wires showed no degradation. This result proves the common practice at CTec to replace the standard PTFE wires with Kapton ones for mechanisms submitted to high levels of radiation.

Lifetime test at high temperatures

Another important test for this application was to perform a lifetime test at 70°C in vacuum. Due to the unusual high temperature, a specific friction pair was selected for the application. A dedicated test bench was built and operated. The test bench includes unbalance masses which make the motor operate with varying torque conditions.

During the 1-month test, the motor achieved ~200k revolutions with an average speed of 6 rpm and a cumulated distance of 20 km. The removed material at the friction interface was estimated at 40 µm which is quite acceptable for the application. This result demonstrates the capability for RSPA motors to be operated over long distances.

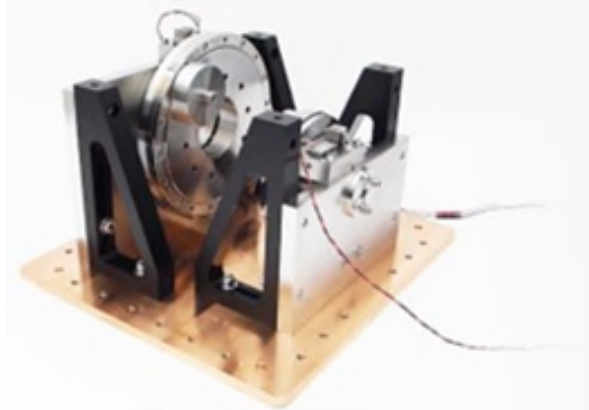


Figure 15. RSPA lifetime test bench

Conclusion

The RSPA motor for the Tokamak has been verified for several major characteristics of RSPA piezoelectric motors. The first characteristic is that piezoelectric ceramics and overall piezoelectric ceramics have the capability to withstand large radiation doses. In addition, a lifetime test was done with a new friction material pair and the wear of the friction track over a 20 km displacement was measured.

SPA-FSM : 3 Axis RX, RY, TZ Piezoelectric Motor

Motor principle and harsh operating conditions

Three specific small (approx. $5 \times 8 \times 13 \text{ mm}^3$) MSPA35XS piezoelectric motors [6] are assembled in a 120° pattern surrounding a $\text{Ø}20\text{-mm}$ moving element. The three SPA are driven independently, thus allowing a 3 degrees of freedom movement of the moving element: RX, RY and TZ.

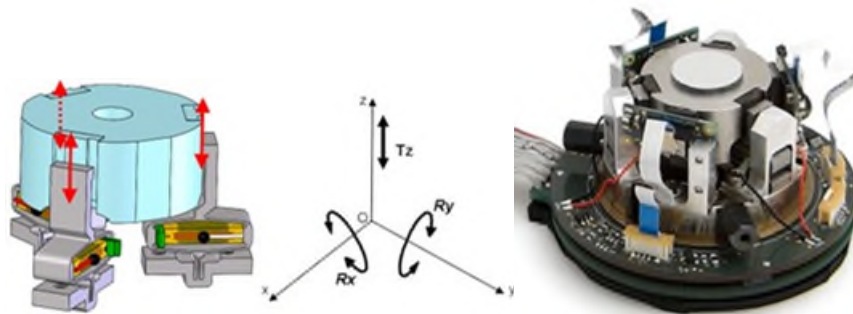


Figure 16. View of FSM-SPA and its principle

The present configuration is optimized for TZ displacement. In practice, the achievable strokes are $\pm 2.5 \text{ mm}$ for TZ and $\pm 75 \text{ mrad}$ for both RX and RY axis.

At the origin, this 3 DOF mechanism has been designed to replace another micro-mechanism that suffered regular failure. The cause is a very close liquid nitrogen blow which at times can spread on the mechanism. Due to the cryogenic capability of SPA motors [4], the SPA-FSM actuator easily supports this event without loss of performance.

Position measurement

Position is measured using 3 COTS low-cost high-resolution magnetic linear encoders placed in a similar 120° pattern (i.e., similarly to the actuators). These sensors offer a resolution below $1 \mu\text{m}$ and stroke is only limited by the magnetic track target length.

An interesting feature of these sensors that has been validated with this mechanism is their ability to measure the position even if the target is not moving in a very straight manner, which is an implicit requirement for this multi-axis actuator. Using the sensor feedback, it is possible to measure the position with a $\sim 1\text{-}\mu\text{m}$ resolution for TZ and $\sim 50\ \mu\text{rad}$ for tilt. Alternative contactless sensors (however more expensive) would allow better performance.

Mixed closed loop control

Based on the sensor feedback, a multi-axis closed-loop control is implemented that mixes pulses to make steps as well as fine positioning mode. The resulting performance is that the mechanism is able to move close to the final position with steps and then achieve a fine positioning. The movement resolution is then mainly limited by the electronic SNR. In practice, TZ resolution is on the order of 1 nm and tilting resolution is 0.1 μrad .

Serial production and reliability

Close to 200 SAP-FSM actuators have been produced and delivered over the last 6 years. They are being used by customers for lab equipment to automate measurement and allow high duty cycles. Over the last six years no issues were identified with the core functionality (i.e., 3 axis movement and closed loop positioning).

This result proves that, although the contact conditions may vary significantly in a random way (because of the tilt movement), the performance of the motor remains stable over time and meets operational requirements.



Figure 17. View of SPA-FSM batch

Conclusion

The 3 axis SPA-FSM is currently produced and delivered for a ground application. This mechanism is based on the same actuators and materials as the RSPA XS (presented in above section) which has proven its capability to support hard environment conditions.

It also must be noted that SPA-FSM construction shows major similarities with a much larger breadboard that is currently being built and tested at CTec for ESA. This motor has already passed initial room temperature tests and will be tested in cryogenic conditions in the near future.

Conclusion

Several piezoelectric motors that support hard operating conditions are presented in this paper. It must be reminded that all of these motors are based on the same key materials (piezo ceramic, friction materials...) as other mechanisms from CTec which already have a flying space heritage [7,8].

Some of these hardened motors, that may not be fully space compliant at this time, could be upgraded to meet complete space requirements.

References

1. Barillot F. & al., "Beam Splitter Mechanism Actuator for IASI-NG", Proc. 18th ESMATS, 2019
2. Barillot F., Nanometric positioning with IASI-NG 's Beam Splitter Mechanism Actuator, AMS 45th Aerospace Mechanisms Symposium, Houston Texas USA, 13-15 may 2020
3. E. Betsch, et al High power density Piezo motors for critical environments – ACTUATOR 2022 29-30 June Germany Mannheim – ISBN 978-3-8007-5894-4 © VDE VERLAG GMBH · Berlin · Offenbach
4. Buttery M. & Watters R. & Roberts E. "Piezo-electric linear actuators in vacuum", Proc. 14th ESMATS, 2011
5. C. Belly & Buttery M. & Claeysen F., "Thermal vacuum behaviour of a stepping piezo actuator", Proc. 14th ESMATS, 2011
6. F. Barillot, Improvement of MSPA Module of Stepping Piezo Actuator CEDRAT TECHNOLOGIES, Conference Actuator, Bremen Germany, 25-27 June 2018 – Proceedings A3.8 p121
7. P. Guay et al Piezo Qualification for Space Applications, Proc Actuator 2002, Ed. Messe Bremen (G), June 2002, pp 284-287.
8. <https://cedrat-technologies.com/applications/space-and-new-space/>

VenSpec-H Filter Wheel Mechanism Breadboard Development and Test

Gerhard S. Székely^{*}, Robert Eberli^{*}, Marco Grossmann^{*}, Samuel Tenisch^{*},
Hans-Peter Gröbelbauer[†], Florian Wirz[†], Pascal Seiler[†], Paola Kögl[‡], Stefan Kögl[‡],
Paul J. Tackley[§], Taras Gerya[§], Ann-Carine Vandaele^{**} and Eddy Neefs^{**}

Abstract

ESA's upcoming Venus orbiter EnVision aims to provide a comprehensive understanding of the planet's evolution. Building on the success of Venus Express, it will map Venus's surface with unprecedented detail, enhancing insights into its geological evolution. One of the instruments – VenSpec-H – is focusing on the lower atmosphere and clouds and will analyze volcanic plumes, complementing surface and subsurface observations. The results are foreseen to support the research teams of BIRA-IASB under Instrument Lead (IL) Dr. Ir. Ann Carine Vandaele [1,2] and ETH Zürich under Profs. Paul Tackley and Taras Gerya [3,4] – Co-ILs of the VenSpec-H Instrument – in understanding commonalities and differences between the planetary evolutions of Venus and Earth. This spectrometer uses an echelle grating to diffract uniform light for detailed compositional analysis. The spectrometer section is preceded by a band selection based on a combination of a filter wheel and a fixed horizontal double stripe filter.

This paper focusses on the unconventional approach of developing the Filter Wheel Mechanism (FWM) by the HSLU in Phase B1 and gives insight on the building and testing of an elegant breadboard that is currently undergoing a full test campaign at the facilities of FHNW. The development is part of the Swiss contribution to VenSpec-H, led by ETH and managed by KOEGL Space.

Introduction

Background

EnVision is the fifth medium-class mission of the European Space Agency (ESA) and scheduled for launch in the early 2030s with the aim of characterizing the internal dynamics, surface features, and atmospheric dynamics of Venus. This mission will delve into the intricate interplay between Venus's interior, surface, and atmosphere. Central to EnVision's scientific apparatus are two radar instruments: a synthetic aperture radar provided by NASA, designed to penetrate Venus's thick atmosphere and capture high-resolution surface images, and a ground-penetrating radar sounder tasked with mapping the subsurface structure. In addition to radar capabilities, EnVision is equipped with spectrometers tailored for analyzing the chemical composition of Venus's atmosphere and surface. These instruments serve to detect shifts in elemental abundance, potentially indicative of ongoing volcanic activity. Furthermore, EnVision encompasses a radio science experiment aimed at probing Venus's internal structure and gravitational field.

The spectrometer suite aboard EnVision comprises three distinct channels: VenSpec-M, VenSpec-H, and VenSpec-U, accompanied by a common Central Control Unit. Notably, each channel provides independent optics to accommodate diverse imaging concepts and wavelength ranges.

* Lucerne University of Applied Sciences and Arts, Switzerland

† University of Applied Sciences and Arts Northwestern Switzerland

‡ KOEGL Space GmbH, Switzerland

§ ETH Zürich, Switzerland

** Royal Belgian Institute for Space Aeronomy, Belgium

VenSpec-H (Venus Spectrometer with High resolution) Overview

VenSpec-H is one of the channels in the spectrometer suite. It is designed to monitor minor species within Venus's lower atmosphere on the night side and above the clouds on the day side. This instrument plays a major role in characterizing volcanic plumes and other phenomena influencing gas exchange between Venus's surface and atmosphere. VenSpec-H's focus on volcanic and cloud-forming gases aims to uncover composition anomalies potentially linked to volcanic activity, complementing observations from VenSAR and VenSpec-M focused on surface and subsurface features.

During nighttime operations, VenSpec-H will survey the near-surface atmosphere (0 – 20 km) and the atmosphere beneath the cloud layer (20 – 45 km), while daytime observations will focus on the composition of the atmosphere above the cloud deck (65 – 80 km). To achieve the primary scientific goals, VenSpec-H utilizes four highly specific narrow spectral bands tailored for atmospheric probing. Notably, Band #2 is further divided into Band #2a and Band #2b, a distinction that will be elaborated upon later. Bands #1, #2, and #3 are particularly instrumental for penetrating the cloud layer during nighttime observations, known as the spectral night windows of Venus. Further details regarding the scientific objectives of VenSpec-H and the entire VenSpec suite can be found in [5] and [6].

The overall instrument functional diagram and a 3D image is shown in Figures 1 and 2. After passing a shutter, the incoming light is filtered by optical filters located on a filter wheel, enters a filter slit assembly followed by an echelle grating spectrometer, and finally is received by the detector.

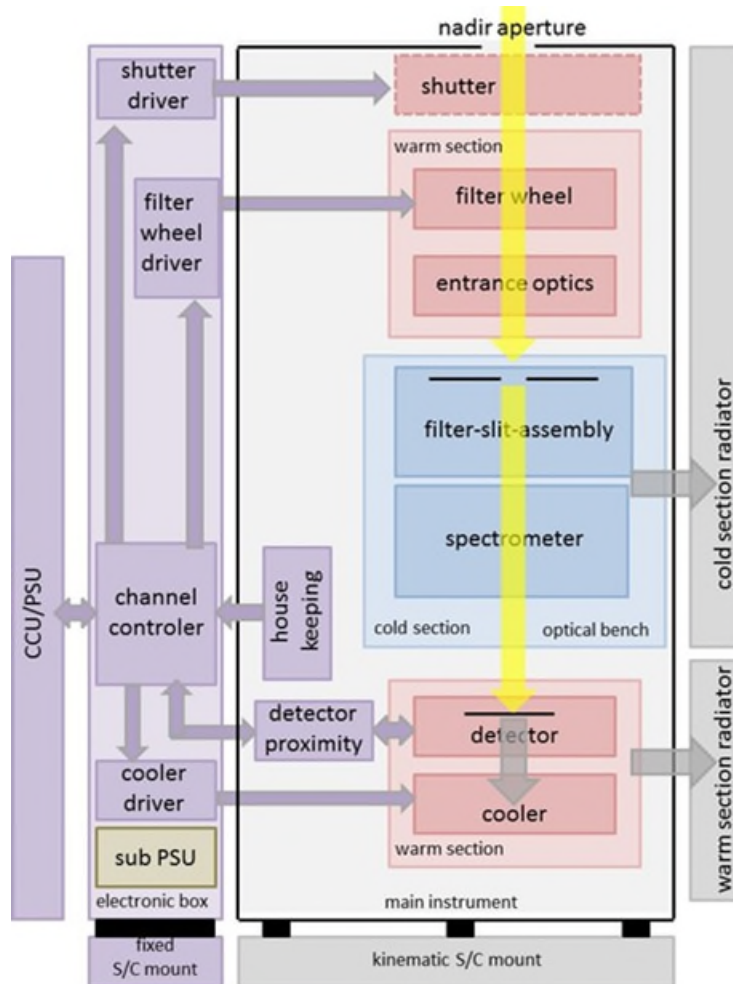


Figure 1. VenSpec-H Instrument Functional Diagram

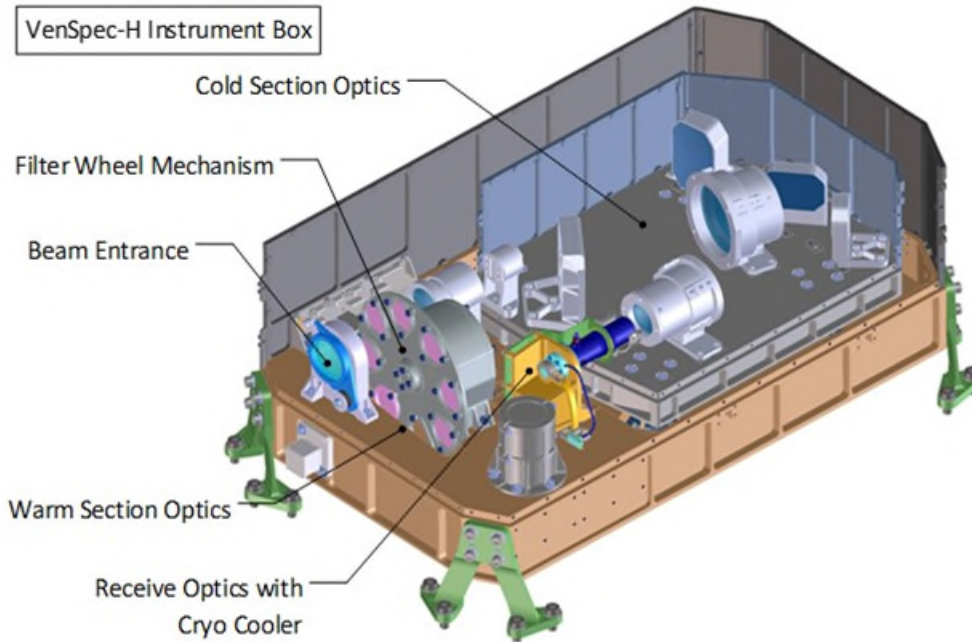


Figure 2. VenSpec-H Instrument Box Overview

Filter Wheel Mechanism (FWM)

The main functions of the FWM can be summarized as follows:

- hold in place optical filters located on a wheel;
- rotate the filter wheel and place each of the filters in the optical path following a dedicated observation strategy;
- survive all environmental conditions throughout the complete lifetime of the mission.

An overview of the filter wheel mechanism is given in Figure 3. It provides space for 6 filters, and two positions used for calibration (one fully closed, one fully open)

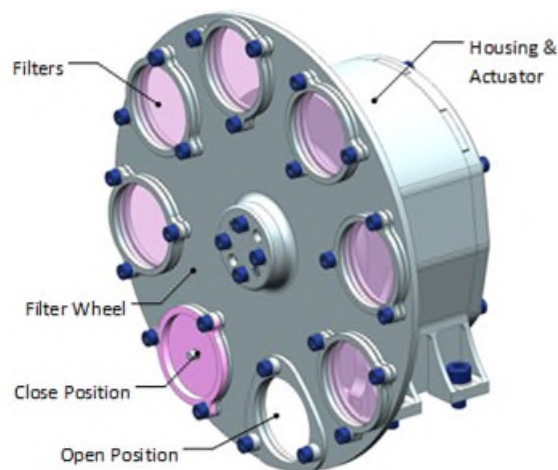


Figure 3. FWM overview

This paper focuses on the development of the filter wheel mechanism. In particular it provides insight in the development, building and testing of an elegant breadboard with the focus on de-risking the overall VenSpec-H instrument box development.

Unconventional Development Approach

Challenges

After a high-level phase A study, the need of a Filter Wheel Mechanism became clear to fulfil the mission objectives of the VenSpec-H instrument that shall use an observation sequence with multiple spectral bands in both the day and the night of Venus. However, several requirements were not yet frozen or available, as the satellite architecture was not yet defined.

In addition, the following key challenges were identified:

- the FWM operates very close to sensitive optics and solid lubrication is required;
- with a nominal operational life of 4 earth years and the required functional pattern, a total of ~2 million revolutions need to be demonstrated;
- high repeatability of the filter re-positioning is required (0.1°);
- the spectrometer section operates at cold (-45°C) temperature in Venus orbit. Hence the heat dissipation (and power consumption) of elements close to this optical bench, like the FWM, has to be minimized;
- some optical parameters as well as the number of filters and their exact position were still evolving;
- the launch loads needed to be estimated on experience and evolved over the development time;
- the predecessor of the instrument did not include a filter wheel hence the TRL of the initial concept for the FWM was considered very low (TRL<4).

All this was identified as a significant risk for the VenSpec-H instrument box development, for which all major components had to be brought to a TRL of 5-6 within 1.5 years after Phase B1 Kick-Off.

Swiss Team for the VenSpec-H FWM

To mitigate risks associated with the development of the mechanism, a specialized consortium was involved as part of the Swiss VenSpec-H contribution:

- Professors from universities of applied sciences (UAS) in Switzerland bring extensive industrial experience to the table. In addition, these UAS possess advanced manufacturing and testing facilities, enabling rapid prototyping, construction, and evaluation.
- Expertise and equipment for space mechanisms is available across several institutions. For instance, within the VenSpec-H project:
 - At HSLU the core space mechanism expertise is located along with sophisticated design and manufacturing capabilities.
 - FHNW houses state-of-the-art environmental testing laboratories for space instruments, equipped for vibration, shock, and thermal vacuum testing
- While universities of applied sciences primarily prioritize education, they are typically not specialized for full-scale space instrument development. As a result, they often encounter constraints in resources necessary for comprehensive space project management and product assurance. Therefore, these essential resources were sourced from a specialized company.

Based on this, the FWM work has been implemented as shown in Figure 4. To work in such a consortium, the members need to rely on each other, be willing to share knowledge between each other and in particular speak the same “language” and share their tools and templates. In case of the VenSpec-H FWM this worked very well including the collaboration with BIRA and ESTEC. Many potential obstacles could be solved on the way in the regular meetings without many formalisms.

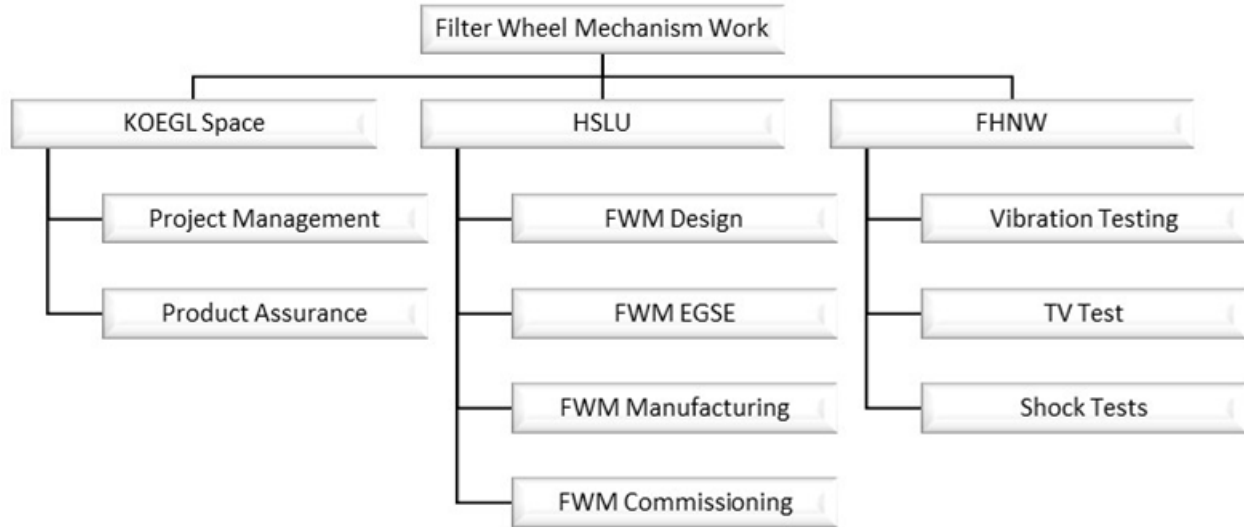


Figure 4. FWM work distribution

Technical Development approach for the VenSpec-H FWM

To meet the technical requirements and challenges, it was decided to reduce the design complexity to the absolute necessary. At minimum a physical architecture is required as depicted in Figure 5.

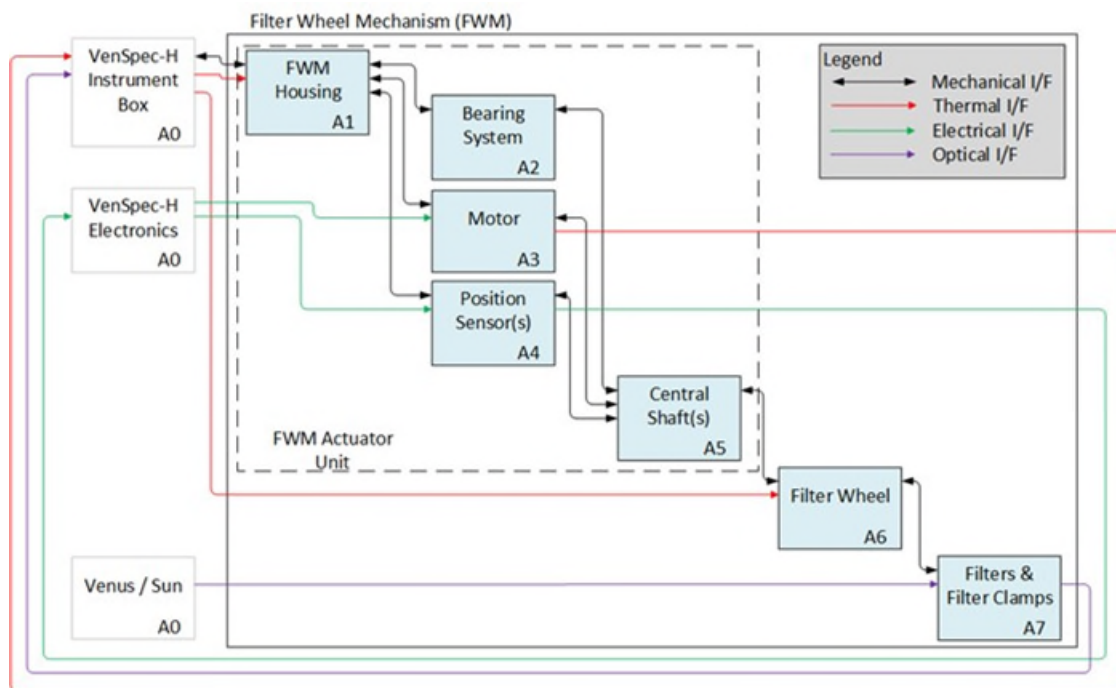


Figure 5. FWM minimal physical architecture

The concept relies on the following technical paradigms:

- to reduce tribological issues to a minimum, a direct drive is foreseen, where the filter wheel as well as the motor are sitting on the same axis and supported by a single bearing pair (i.e., no gearbox is present);
- as the bearings shall be solid lubricated and the number of changes high, the wear shall be minimized by low wear distance and as low a preload as possible;

- to avoid the need of launch locks and to allow minimal heat dissipation by the motor, a stepper motor is selected;
- the sensor concept shall be as simple as possible;
- if possible avoid the implementation of launch locks.

Bearing configuration selection

Two options were identified for the bearing configuration selection (Figure 6). Option a) relies on a simple duplex back-to-back bearing configuration whereas b) is a classical configuration with bearings being further apart. Option a) was selected, as it allows for simple pre-load setting and characterization at the bearing manufacturer, hence reducing integration time and the need for special integration devices. However, to minimize the required preload of the bearings as well as the bearing diameter to optimize lifetime, for option a) the CoG of the rotating parts (filter wheel, shaft, motor and sensor) is required to be placed as close as possible to the center of the bearing pair.

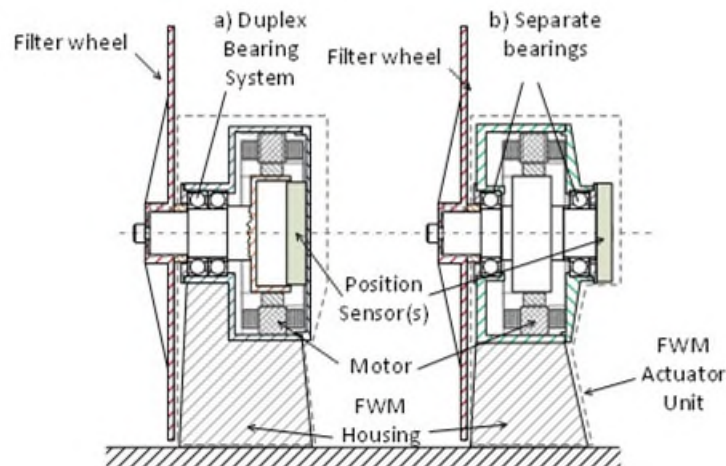


Figure 6. Bearing concept options

Motor concept

A stepper motor solution is foreseen, where the detent torque of the motor is sufficient to stop filter wheel rotation during launch. A major resulting derived requirement is to balance the filter wheel statically and dynamically about the rotation axis. In addition, the motor current shall be switched off during observations at stable positions of the stepper motor. Hence, a motor with a high number of steps is required, which also leads to a relatively large diameter.

Sensor concept

During the first months of the project, an absolute rotary sensor was implemented. However, the final sensor selection needed to be left open until the control concept was clear. Therefore, the decision was taken to put the sensor at a location where minimal design change would be required later in the project, i.e., at the rear of the mechanism.

Procurement challenge

The prime technical risk identified during the first weeks of the project was the performance of the bearing system. Therefore, it was decided to build as fast as possible a breadboard and perform a mission-compatible life test. The challenge was to have representative hardware ready within approximately one year, although many things, such as launch load environment and temperatures were still unclear.

The approach that was taken was rather unconventional. Based on some inputs from [1] and the experience of the first author, axial, radial and bending loads were defined for the bearing pair using simple calculations. In addition, a thorough calculus was performed with the highest possible changing speeds of known stepper

motors, taking into account the expected number of filter changes and thus obtaining the total number of bearing revolutions over lifetime. Furthermore, preliminary thermal calculations defined the expected operational temperature range. After applying the typical margins, various bearing suppliers were contacted to see if they would have a solution readily available with lowest possible lead time. At this stage, the detailed design had not been started. Once a viable solution was available, design was further matured with this option included, and procurement was initiated already. For risk mitigation purposes, in addition to the solid lubricated bearings – with still longer lead time – a set of oil lubricated bearings was procured with a short lead time to be used during commissioning of the drive electronics without risking the degradation of the solid lubricated version.

A similar approach was taken with the motor procurement. Here, a frameless configuration was needed which considerably reduced the choices. During discussions with potential providers, a solution was found to use a readily available motor with some geometric out-of-tolerances that were not acceptable for their originally intended use. As also here the design and manufacturing were not yet started, the out-of-tolerance issues were dealt with by the design and an appropriate integration jig.

As for the sensor, for the breadboard it was decided to use the one with lowest possible lead time that was suitable for TV testing and could be made available for space later on.

Breadboard Filter (breadboard) Wheel Design

The concept being so reduced and to avoid discussions on representativity of upcoming tests, the originally planned simple breadboard design evolved into a full-scale almost-final design as shown in Figure 7. The design builds on the Concept a) from Figure 6.

The fused silica filters are placed in recesses of an aluminum wheel. In order not to overload the glass by the clamping forces from the screws, the load is distributed by a special aluminum clamp ring that is preloaded by an optimized, ring-shaped leaf spring made from titanium. For the required close position an aluminum plate of the same diameter as the filters is foreseen with an adapted thickness. The open position will be equipped with a mass compensator ring for static and dynamic balancing of the wheel.

The filter wheel is mounted onto the directly driven shaft. It can be dismounted for integration purposes without disassembly of the actuator part. The shaft system is carried by a duplex bearing pair in back-to-back configuration from ADR. Stainless steel is used for races and balls, the cages are PGM HT, the lubricant is sputtered MoS₂. To be able to operate the breadboard outside a vacuum chamber, the breadboard is equipped with a fitting for purging with dry N₂.

The drive is facilitated by a 1°/step stepper motor from SAFRAN/SAGEM. To reduce micro-vibration, the motor will be driven in micro-stepping mode. The filters are located at stable positions of the motor when the driver electronics is in idle mode. This allows a reduced power consumption during observations and thus minimizes dissipation into a demanding cavity. To allow as many observation cycles as possible, the rotation speed of the motor is set to 80°/s. Due to the relatively high torque of the motor, the start-up acceleration phase is comparably short, the wheel reacts almost instantly. The procured motor eccentricity issue of the stator is solved by allowing radial adjustment of its titanium holding structure – that is needed anyways to match the CTE of the stator – into the housing structure. The alignment is performed using a simple self-centering clamping type solution with the bearing seats being the reference.

For the breadboard, a resolver was designed and installed. Nevertheless, after the breadboard was built, it was identified that the feedback loop on the foreseen drive electronics will need to drive the FWM in open loop to reach the necessary speeds and thus for the flight units the resolver will be replaced by redundant reference Hall sensors.

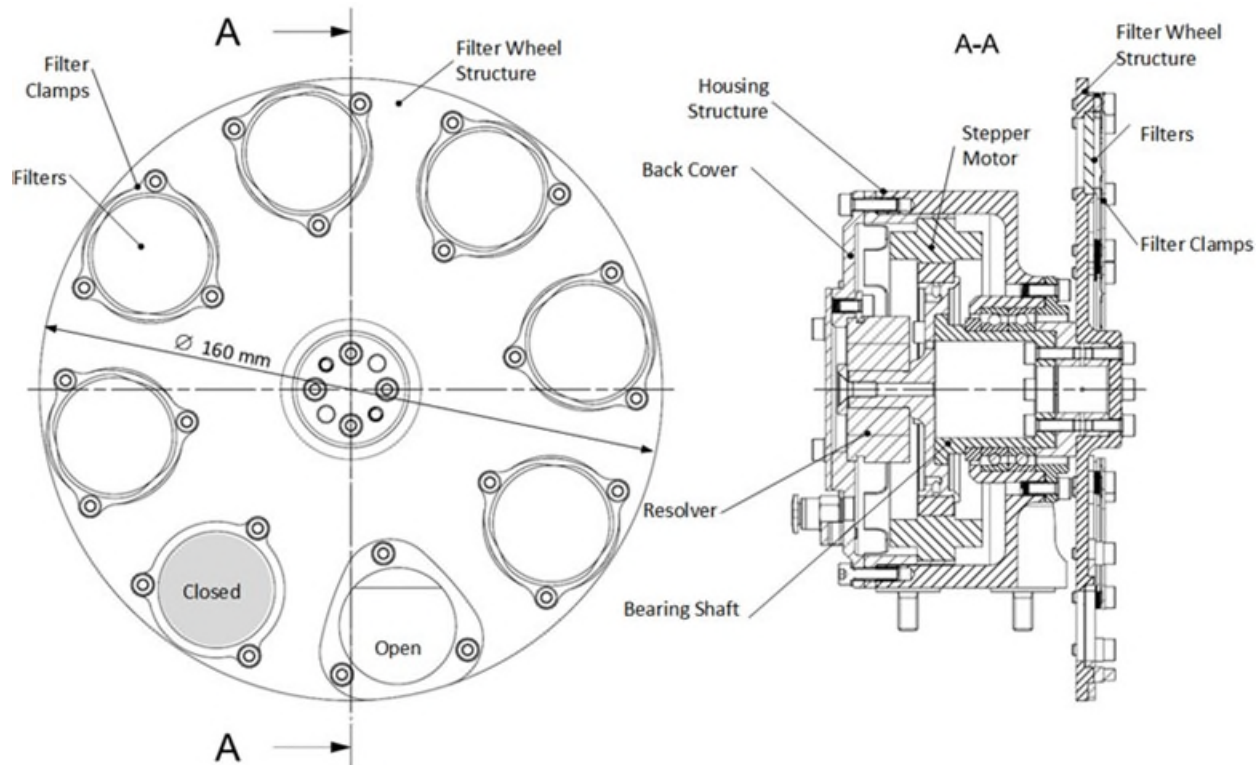


Figure 7. FWM breadboard design overview

The structural materials are similar to the foreseen flight design and structurally and dynamically fully representative. However, some compromises needed to be made to keep the tight schedule. For example, AL 7075 T6 was quickly at hand although we recommend using AL 7075 T7351 for flight. The bearings and the motor are fully flight representative.

To be representative in all aspects of a bearing life test including pre-conditioning by vibration loads and thermal cycling, a full set of mechanism, structural and thermo-elastic analyses was performed showing the required margins.

The major differences from the current perspective between the breadboard and the later flight design are the mentioned sensors, some material adaptations, the final coatings, and some installation and referencing items.

The mass of the breadboard including the cables and bolts is 1.3 kg with a filter wheel mass of ~0.2 kg.

Lessons Learned from Assembly and Commissioning

With the mentioned procurement mitigations, parts and components came in timely. The oil-lubricated bearings were very handy for exercising the integration of the FWM. Also, this “lubricated” version was very useful to setup the EGSE. However, the building of the breadboard helped to identify and solve two issues, as described in the following sections.

Changing Dummy Filters

The original purpose of the breadboard was to de-risk potential lifetime issues with the bearings. In this context the design of the wheel itself aimed at being a representative mass and inertia dummy. For fast

procurement purposes filter dummies were planned to be made of aluminum with representative mass. The clamp design was foreseen for the next phase of the project.

While the items were in production, we came up with the idea to replace the aluminum dummies with glass billets from the same material as intended for the flight filters. Due to out-of-tolerances of the thickness of the glasses, they were cracked at the surface after clamping at the edge and torquing the screws.

As a consequence, the filter mounting was completely revised and structurally analyzed. This resulted in a design and build of an elegant and light clamping system of the filters. New undamaged glasses were mounted in the adapted clamping system, confident now that the mechanical launch loads could be survived.

Using Off-the-Shelf Drive Electronics

Flight electronics being still in the design phase, a temporary flexible control system was required, where we could adapt the mechanism settings easily. Instead of building an EGSE from scratch, it was decided to buy an off-the-shelf stepper motor driver that could be commanded using an USB interface and that allowed controlling the motor both in closed and open loop. Besides the motor driver, the controller also required a transducer unit for the resolver control and A/D conversion of the read values. The setup is shown in Figure 8.

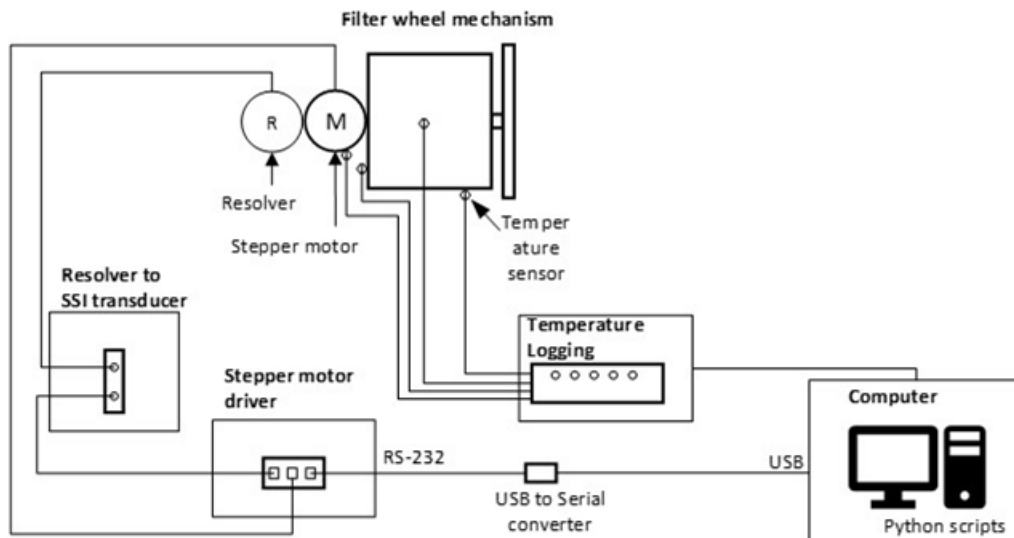


Figure 8. EGSE Setup

Being able to exercise with the FWM breadboard with oil bearings turned out to be most useful. After a number of iterations in setting up the controller, still a number of issues remained:

- The flight electronics will drive the FWM in open loop using micro-stepping and will switch off motor power at the filter positions. When using this philosophy with the temporary controller randomly at different filter locations the current switch-off leads to hiccups in the wheel movement. Later tests of the FWM with a flight electronics breadboard that became available did not show any hiccups.
- The resolver was kept in the system and was intended to be used as a passive measurement device for the positioning error during tests. It turned out that the transducer/resolver had quite a large error compared to the requirements. This was diagnosed with a completely stopped and unpowered motor.

The micro-stepping with the controller worked properly and was tuned to the same value as foreseen for the flight electronics. A way was found to incrementally reduce the maximal drive current of the motor by Python scripts running on the EGSE computer. It allowed to slowly reduce and ultimately find the minimum startup current at the instant step loss was detected with the resolver.

The lesson learned and recommendation is that with the same effort a better FWM controller could be implemented from scratch including all functionalities needed.

Life Testing the FWM Breadboard

In Figure 9 the FWM breadboard is shown as used for functional tests, mounted on the shaker for X-Axis vibration tests and in the TV chamber. It shall be mentioned that it includes 8 glass dummies representing the filters.



Figure 9. FWM breadboard as used for functional, vibration and TV & life testing

A major issue with breadboard life tests is the question about representativity. To minimize discussions on this topic, a full flight-standard qualification level test program was set up and agreed with ESA, as shown in Figure 10.

The program started with the commissioning and tuning of the FWM breadboard with the oiled bearings together with the EGSE, then changing the configuration to the solid lubricant version, followed by initial functional tests, a full vibration test campaign, a full thermal cycling campaign in vacuum and finally the life test sequence. As the shock test levels were not yet clarified and shock was deemed more detrimental for the optical elements than the bearings, it was decided to perform the shock tests after the life test sequence.

At the end of the test campaign the breadboard will be stripped down, thoroughly examined and refurbished with the oil lubricated bearings and integrated in a breadboard of the VenSpec-H Instrument box for further micro-vibration testing.

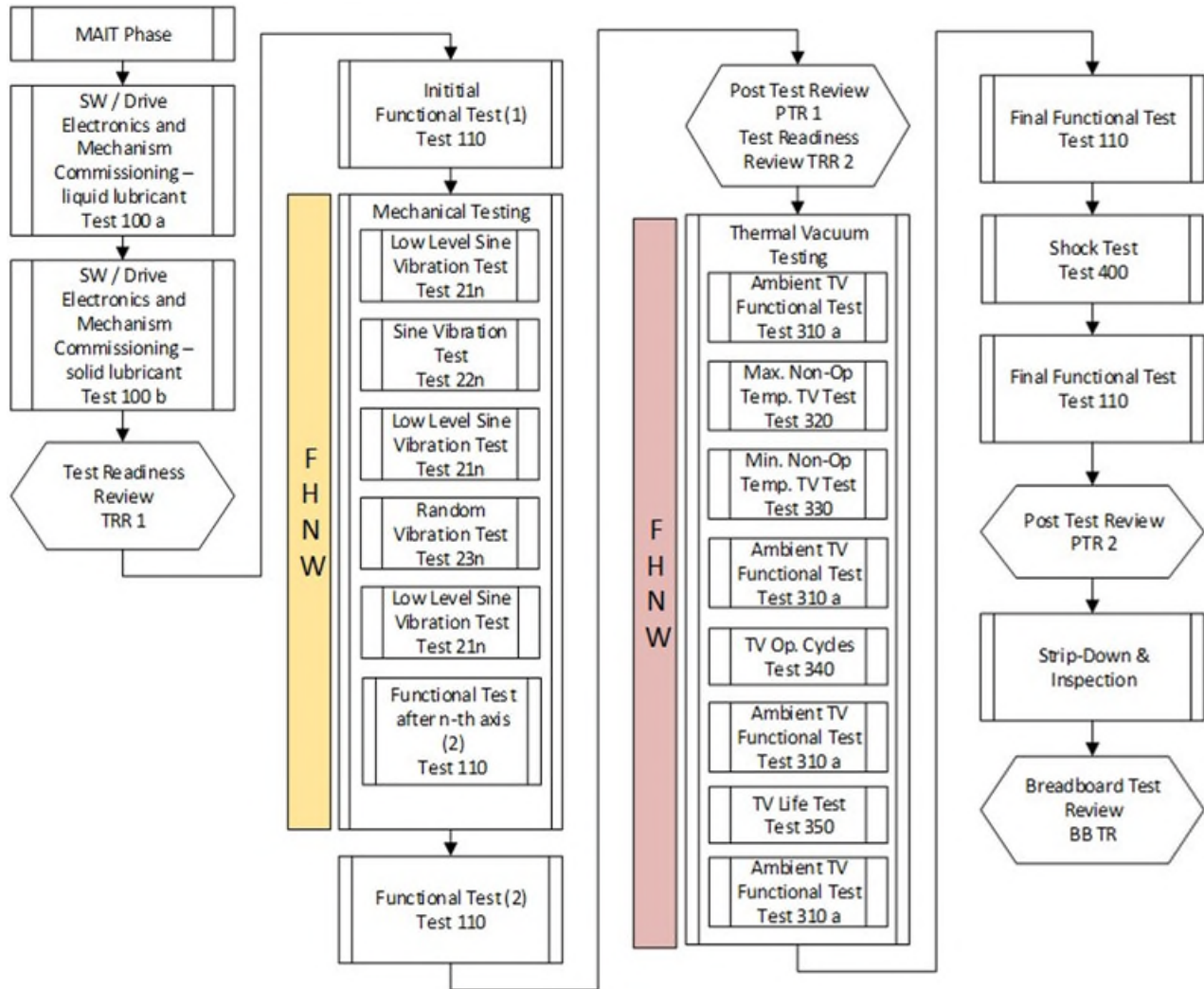


Figure 10. FWM BB Test Program

Functional Test Program

The functional test sequence was fully automated and controlled by a Python script. It consists of the following sequence as also depicted in Figure 11:

- (1) driving two revolutions (720°) forwards and backwards at nominal current (0.18 A)
- (2) driving two day cycles at nominal current (0.18 A)
- (3) driving two night cycles at nominal current (0.18 A)
- (4) driving two revolutions (720°) forwards and backwards at reduced current (0.06 A)
- (5) performing the repeatability test movement
- (6) performing the minimum startup current measurement starting from each filter position

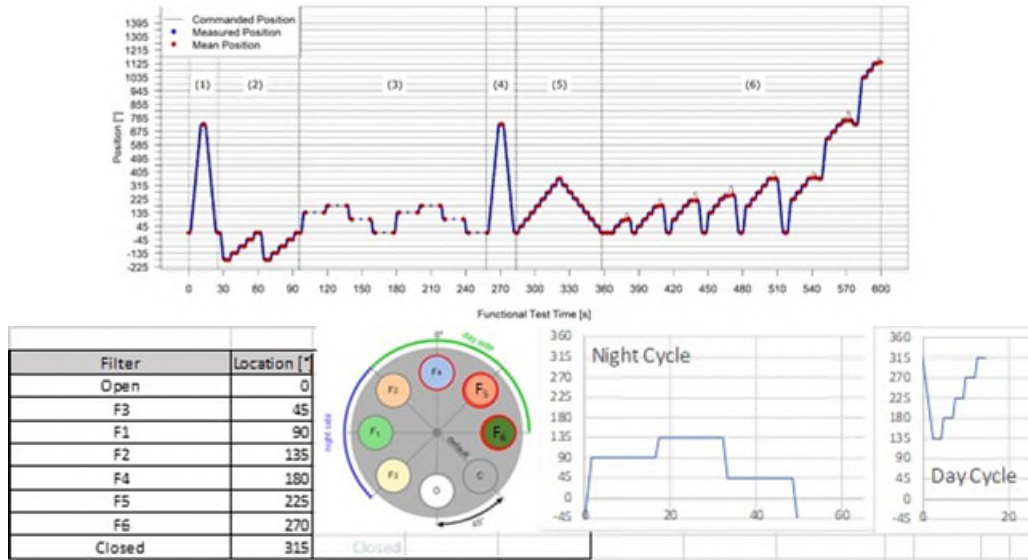


Figure 11. FWM BB functional test sequence

Vibration Test Levels

The most demanding test levels are the random vibration levels reaching peak values ($3 \cdot g_{rms}$) of 85.3 g. They are derived from [7] and cross-checked with preliminary analyses of the VenSpec-H instrument box. During testing, the damping levels were relatively low, hence some notching was applied in regions where the instrument box provided high attenuation. Also, cross-coupling on the base was noticed, as actually expected. The applied and measured values are shown in Figure 12 for the x-axis test – which was most severe.

Visual inspection after vibration did not reveal any damage on the structural parts nor on the dummy glass filters. The functional tests revealed a slightly increased start-up current, but still in the acceptable range.

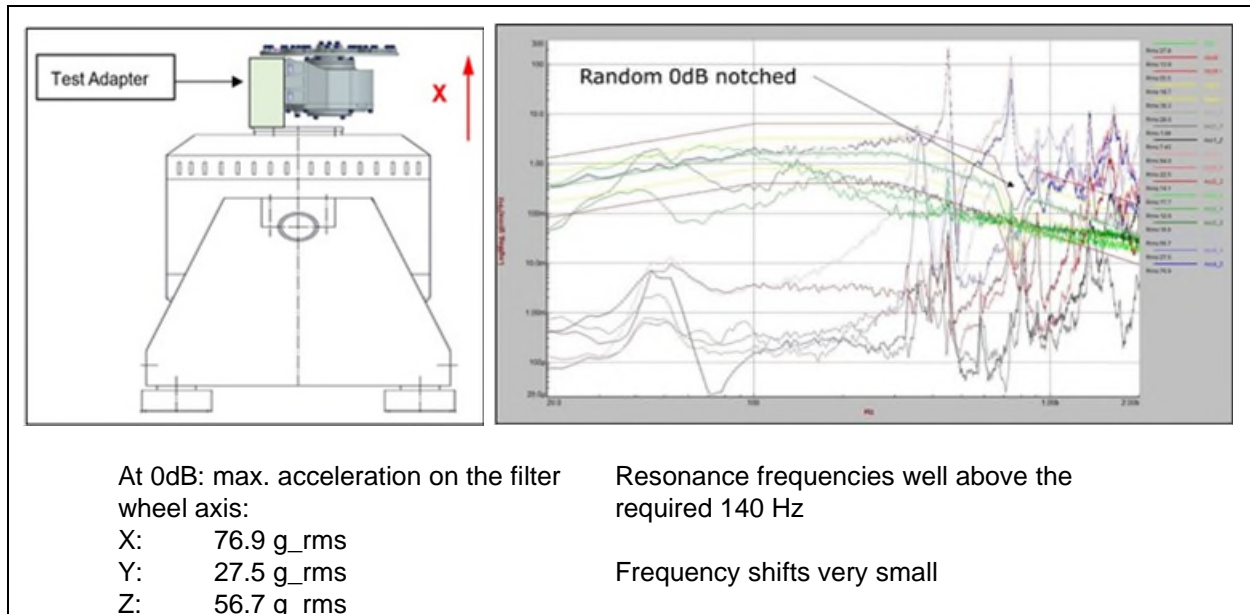


Figure 12. FWM BB Vibration test in x-direction of the FWM

TV and Life Test Levels

The testing temperature ranges for the FWM have been derived from specifications and thermal analyses of the VenSpec-H instrument box:

- Non-Operational: -50°C to + 70°C 3-hr dwell time
- Operational Qualification Thermal Cycling: -25°C to +25 °C 3-hr dwell time
- During Life Test -15°C to +15 °C 24-hr dwell time

During each operational test (both Thermal Cycling and Life Test) the FWM rotates half the time continuously forward and half the time backwards. At the end of the dwell time, the functional tests are repeated with the adaptation that at hot temperatures the daytime sequence is performed and at cold the nighttime sequence.

Based on the mission duration, the observation time and the shown measurement sequence a total number of 1.4 million revolutions is expected during the mission. In addition, an absolute maximum of 50000 revolutions is estimated during ground testing. From this, the life test duration including margin sums up to 1.9 million revolutions in total.

At the time of the submission of this paper the FWM performed 1.24 million revolutions. The evolution of the minimum start-up current is shown in Figure 13.

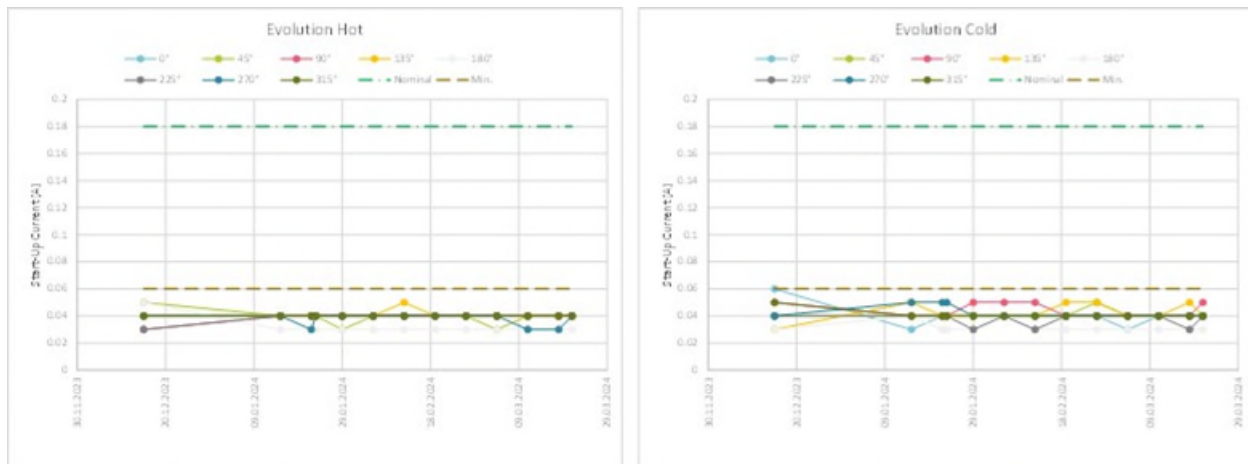


Figure 13. FWM BB Minimum Start-Up Current evolution

It can be seen that, except for fluctuations well inside the measurement accuracy range of the electronics, the values are very stable.

Conclusions

An elegant breadboard of the FWM for VenSpec-H has been built and is undergoing an extensive test campaign. The development approach followed and implemented by a consortium of universities of applied sciences showed much flexibility allowing for quick adaptations and improvements during an early phase of this space project. Another notable advantage is that this endeavor facilitated the training of aspiring engineers for the space industry through their involvement at the UAS.

Acknowledgements

This work is financed by a PRODEX contract with ESA / Swiss Space Office. Special thanks are due to Dr. Ronan Le Letty from ESA for the good collaboration and fruitful discussions during the bi-weekly teleconferences.

References

1. C. Wilson, et al. (in revision) Possible Effects of Volcanic Eruptions on the Modern Atmosphere of Venus, *Space Science Reviews*
2. E. Neefs, A. C. Vandaele, R. De Cock, J. Erwin, S. Robert, I. R. Thomas, S. Berkenbosch, L. Jacobs, P. Bogaert, B. Beeckman, A. Brassine, N. Messios, E. De Donder, D. Bolsée, N. Pereira; P. Tackley, T. Gerya; S. Kögl; P. Kögl; H.-P. Gröbelbauer, F. Wirz; G. Székely; N. Eaton; E. Roibás-Millán, I. Torralbo, H. Rubio-Arnaldo, J. M. Alvarez, D. Navajas Ortega; L. De Vos, R. Sørensen, W. Moelans, A. Algoedt, M. Blau; D. Stam; E. Renotte; P. Klinkenberg; B. Borguet; S. Thomas; M. Vervaeke; H. Thienpont; J. M. Castro, J. Jimenez (in preparation), VenSpec-H spectrometer on the ESA EnVision mission: Design, modeling and analysis
3. J. Tian, P. J. Tackley and D. L. Lourenco (2023) The Tectonics and Volcanism of Venus: New Modes Facilitated by Realistic Crustal Rheology and Intrusive Magmatism, *Icarus*.
<https://doi.org/10.1016/j.icarus.2023.115539>
4. A. J. P. Gülcher, T.V. Gerya, L.G.J. Montési, and J. Munch, (2020) Corona structures driven by plume- lithosphere interactions and evidence for ongoing plume activity on Venus. *Nature Geoscience*, vol. 13, pp. 547-554, DOI: 10.1038/s41561-020-0606-1
5. J. Helbert, A.-C. Vandaele, E. Marcq, S. Robert, C. Ryan, G. Guignan, Y. Rosas-Ortiz, E. Neefs, I. R. Thomas, G. Arnold, G. Peter, T. Widemann, L. Lara, "The VenSpec suite on the ESA EnVision mission to Venus", *Proceedings of SPIE 11128: Infrared Remote Sensing and Instrumentation XXVII*, 9 September 2019, San Diego, USA (DOI: 10.1117/12.2529248).
6. E. Neefs et al., (planned issue 2024) VenSpec-H spectrometer on the ESA EnVision mission: Design, modeling, analysis, *Acta Astronautica*, (under review)
7. ECSS-E-HB-32-26A, *Spacecraft mechanical loads analysis handbook*

Development of an Advanced 2-Axis Electrical Propulsion Pointing Mechanism

Paul Janu*, Daniel Ruckser*, Jarmila Suhajdova*, Zoran Ignjatov* and Mario Toso**

Abstract

The **Advanced Electrical Propulsion Pointing Mechanism 2-Axis** (APPMAX2), developed by Beyond Gravity Austria GmbH (BGA) is a novel mechanism for medium thrusters of 5-kW size (mass range 10 kg to 15 kg) with minimum pointing range of half cone $\pm 15^\circ$ ($\pm 15^\circ$ around X-axis and up to $\pm 27^\circ$ around Y-axis) which focuses on reduction of higher-level effort and risk at customer level.

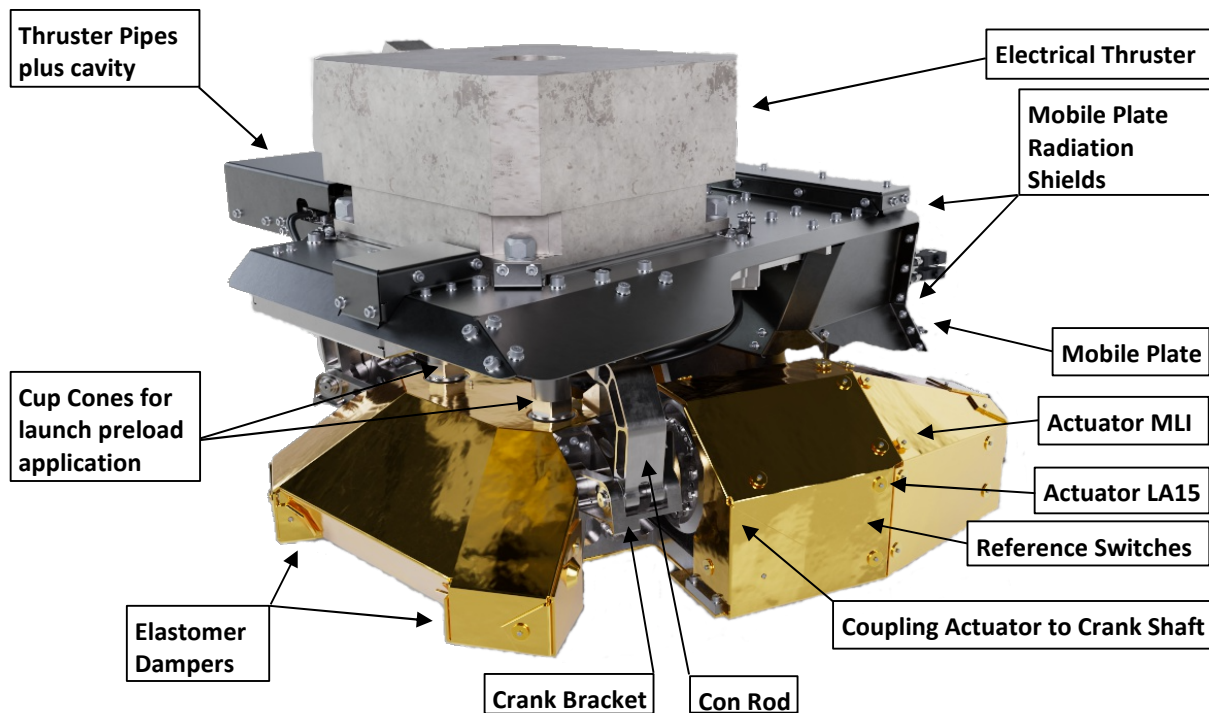


Figure 1. APPMAX2 Mechanism Overview – Deployed Configuration

This paper focuses on the BGA APPMAX2 which provides 2-axis thrust vector control in a compact mechanism size, hence without any boom-like structures. For applications with the need of even higher pointing angles and/or the need of higher distance of the thrusters to the spacecraft the BGA APPMAX3 is used which is equipped with 3 actuators and 2 long booms (not presented here).

* Beyond Gravity, Austria; paul.janu@beyondgravity.com, daniel.ruckser@beyondgravity.com, jarmila.suhajdova@beyondgravity.com, zoran.ignjatov@beyondgravity.com

** ESA/ESTeC, Noordwijk, The Netherlands

Introduction

For many years Electric Propulsion Pointing Mechanisms were developed following typical design principles:

- A thruster mounted on a Mobile Platform supported in the launch case by a Hold Down and Release Mechanism (HDRM) pre-loaded by a low shock release device.
- Actuators positioned around the HDRM directly in the main load path.

These mechanisms typically have the disadvantage that the release devices need physical access, often they even need to be dismantled and reset apart from the mechanism. The release devices produce shocks at release, need dedicated harness and electrical units producing the fire current impulse.

The actuators are normally attached directly via their output shafts to the moving structures. This design produces bending loads in the actuator output bearings at dynamic load cases and under on ground pointing with the 1 g effect on the thruster and mobile platform. Failure cases resulting from uncontrolled load introduction in the output bearings due to mishandling during on ground commissioning are a high risk for reduced in-orbit lifetime.

The thermal control of movable actuators (positioned between mobile platform / thruster and the stationary assembly) is complicated - it needs to be performed only via radiation because the actuator bearings have low thermal conductivity. Thermal gradient across actuator main bearings also is a limiting element and has to be taken into account in classic mechanism designs.

There are applications which omit a HDRM by using a mass-balanced design (no mass eccentricity) in combination with unpowered holding torque of actuators and high actuator gear inertia at higher frequency, but such solutions provide low stability / robustness when mounted on the spacecraft where rocking modes are often dominating. This problem cannot be solved only by a mass-balanced design.

Key Improvements with BGA's APPMAX2

The APPMAX2 mechanism does not require a dedicated launch lock device.

The mechanism is kept highly pre-loaded by its rotary actuators: launch-lock is done by the actuators pulling the mobile plate to the base frame with a force > 6000 N.

Its inherent launch-lock can be remotely operated without need of refurbishment -> very easy to use and robust against errors.

The APPMAX2 provides high resistance against acceleration loads in all directions plus resilience against all kinds of rocking modes when mounted to the spacecraft.

The mechanism concept allows to build subassemblies in parallel, improves the production sequence, thus reducing cost. Moreover, refurbishing or repair in case of any discovery during final acceptance is simplified.



Figure 2. APPMAX2 in highly pre-loaded Launch Configuration (shown with Thruster Mass Dummy)

Consequently, locking into launch configuration can be performed without access to the mechanism just by operating the rotary actuators until electrical switches provide the signal that the pre-loaded configuration is reached. This increases reliability (no potential failure of an additional launch-lock device) and significantly reduces AIT effort for the customer.

The mechanism provides high mechanical robustness by separation of the actuators from the main load path just keeping them in the torsional load path. The bending load path is routed over self-lubricating polymer sliding bearings (high load capability, low volume) which can be loaded higher than classic ball bearings and allow much higher 1g on ground loads as well as load introduction caused by mishandling. This design highly reduces the risk of overloading the actuator output bearings. The remaining mechanical gaps inside the polymer sliding bearings are compensated by an internal pre-loading structure inside the mechanism that works as a compliant spring element.

Both actuators are mounted on the mechanism base frame which is thermally enclosed in MLI and therefore is at moderate temperature levels similar to the spacecraft. The metallic base frame structure allows long operation of the thermally well-connected actuators with negligible heating of the base frame.

The actuators mounted on the base frame allow short harness distances and simple protection capability by metallic shields and MLI against X-ray radiation, micrometeorites, and sun radiation.

The mechanism uses an elastomer damping concept which has longstanding space heritage at BGA. Having elastomer damping elements with damping capability of 25% this solution provides an overall amplification in the main modes of <4. In addition, the damper stiffness can be well accommodated to avoid coupling with critical thruster local modes.

The elastomer damping concept reduces the thruster input loads significantly because of the damping effect of the high mass (mechanism ~14 kg with thruster ~12 kg) with one significantly well-damped main mode. The elastomer dampers can be replaced by stiff structural parts if damping is not required.

No zero-g device is needed for on-ground commissioning, even if the thruster is mounted. The APPMAX2 can be operated and can remain unpowered in any configuration with respect to the gravity direction. Therefore, no extra volume on the spacecraft must be allocated for zero-g envelope, and no zero-g device has to be mounted on the mechanism during testing by the customer again saving cost and AIT effort.

The mechanism uses the BGA in-house developed high magnetic detent torque rotary actuator LA15, the BGA low-cost actuator solution: it is fully developed, engineered, built and assembled in house. Accommodation to application needs can be performed with respect to the required torque, required voltage and required power for actuator heaters.



Figure 3. LA15 High Detent Torque Actuator from BGA

The LA15 consists of a hybrid stepper motor, a small planet gear set which is followed by an output (large) planetary gear stage and high load main ball bearings.

It has the following key characteristics:

- Delivered Output Torque: 15 Nm at the gear's output shaft, considering ECSS motorization rules
- Unpowered Detent Torque (purely magnetic contribution): 13 Nm at the gear's output shaft (already considering an ECSS uncertainty factor of 1.1). The measured detent torque with internal friction of the components is >21 Nm at ambient
- Step Size: 0.008 deg
- Total Backlash: less than ± 0.2 deg at load conditions
- Nominal Step Rate: 1 Hz up to 20 Hz (full steps)
- External Loads: combined load cases are assessed on a case-by-case basis
- Dynamic Loads:
 - Designed for quasistatic acceleration load of 90g (qualification)
 - Designed for quasistatic loads on the output shaft of
 - Axial Force: up to 350 N
 - Radial Force: up to 600 N
 - Bending Torque: up to 50 Nm
 - Mass: 1450 g
 - The actuator is equipped with temperature sensors and heaters which can be accommodated to the mission needs
 - Temperature Range:
 - Maximum Operational Temperature Range: -40°C to $+120^{\circ}\text{C}$
 - Winding Temperature (operational) up to 130°C
 - Design Operational Temperature Range: -30°C to $+110^{\circ}\text{C}$
 - Maximum Non-Operational Temperature Range: -100°C to $+130^{\circ}\text{C}$
- The LA15 has been fully qualified in the frame of a self-standing component-level qualification campaign (90 g sine, 30 gRMS random, 1000 gSRS shock, 3500 output revolutions operated in life representative motion profile in TVAC) and has seen a full higher-level qualification inside the APPMAX2 mechanism

Mechanism Performances

Pointing Range

Nominal pointing range: $\pm 15^\circ$ half cone as stated in the figures below.

Maximum pointing range: much higher compared to the nominal pointing range resulting in $\pm 15^\circ$ around X-axis (alpha) and $\pm 27^\circ$ around Y-axis (beta).

Pointing Accuracy

Absolute accuracy is better than $\pm 0.15^\circ$ over the nominal pointing range.

Relative accuracy (repeatability of a target position) is better than $\pm 0.05^\circ$ over the nominal pointing range.

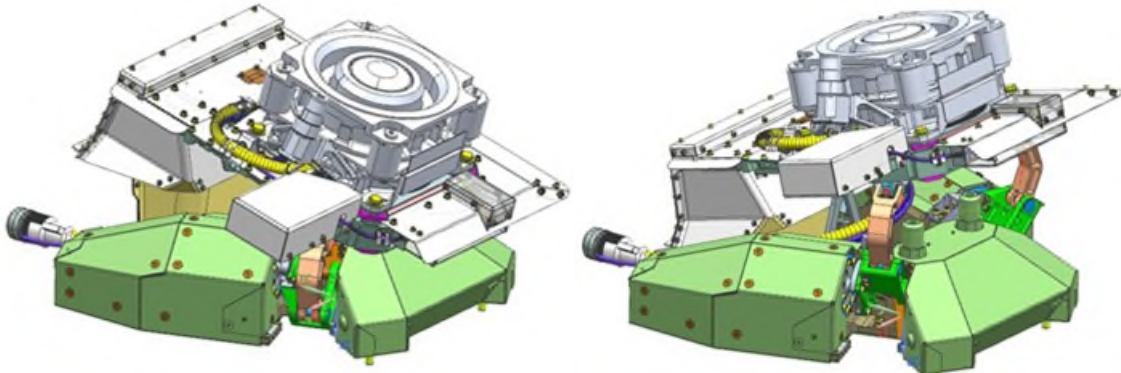


Figure 4. Pointing around X-axis $-15^\circ/0^\circ$ and $+15^\circ/0^\circ$

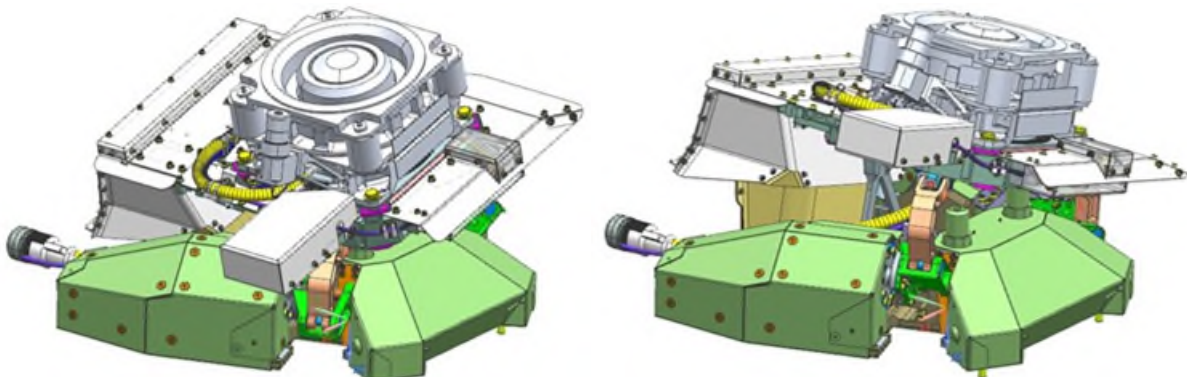


Figure 5. Pointing around Y-axis $0^\circ/-15^\circ$ and $0^\circ/15^\circ$

The mechanism is here and following presented with the PPS[®]5000 thruster from Safran Space Propulsion, being the thruster used for the first customer projects. Different thrusters can be implemented by changing the interface on the mobile plate.

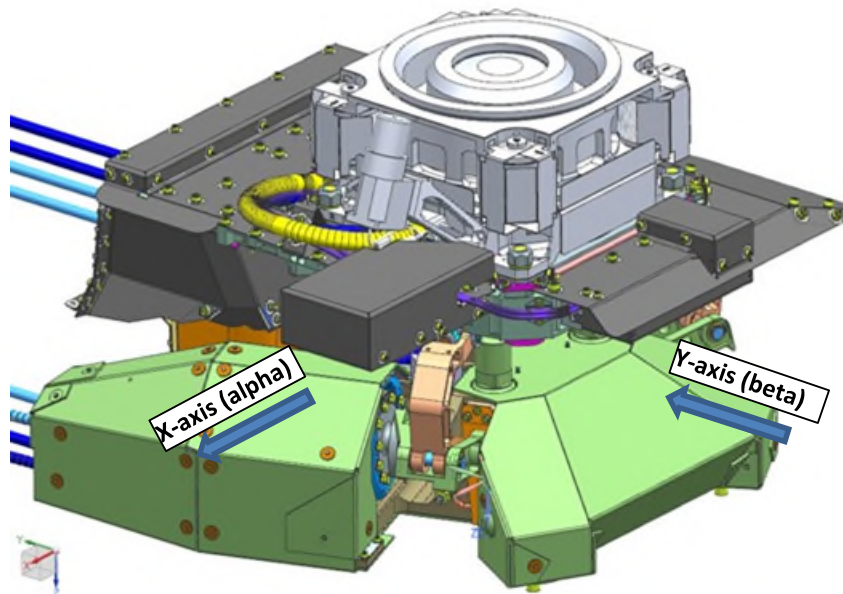
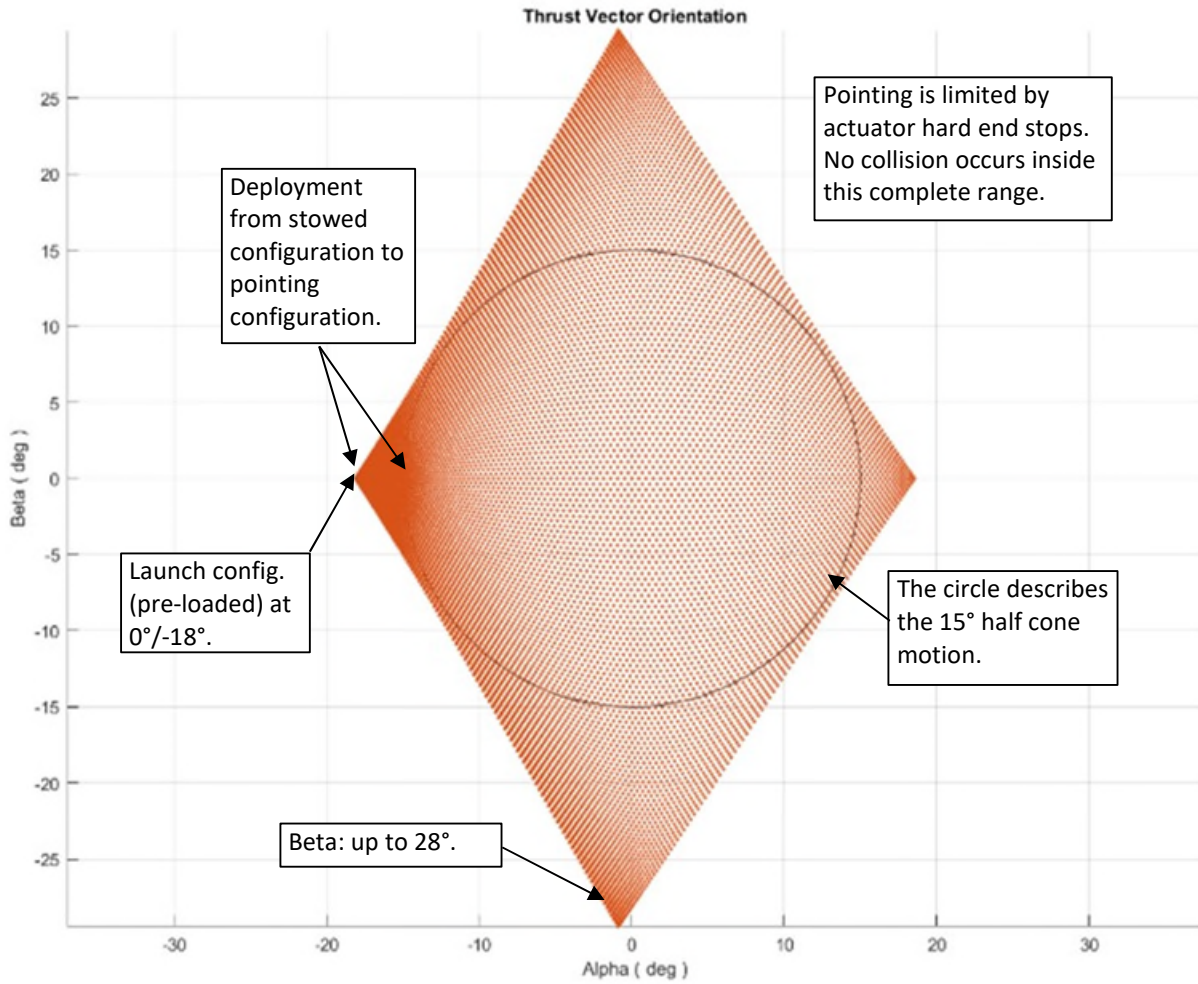


Figure 6. APPMAX2 in Horizontal Configuration – Rotation Axis Naming Convention

Pointing Look-Up Table

Pointing is performed using the mechanism dedicated look-up table covering direct and inverse kinematics. The look-up table is part of the logbook of each mechanism.

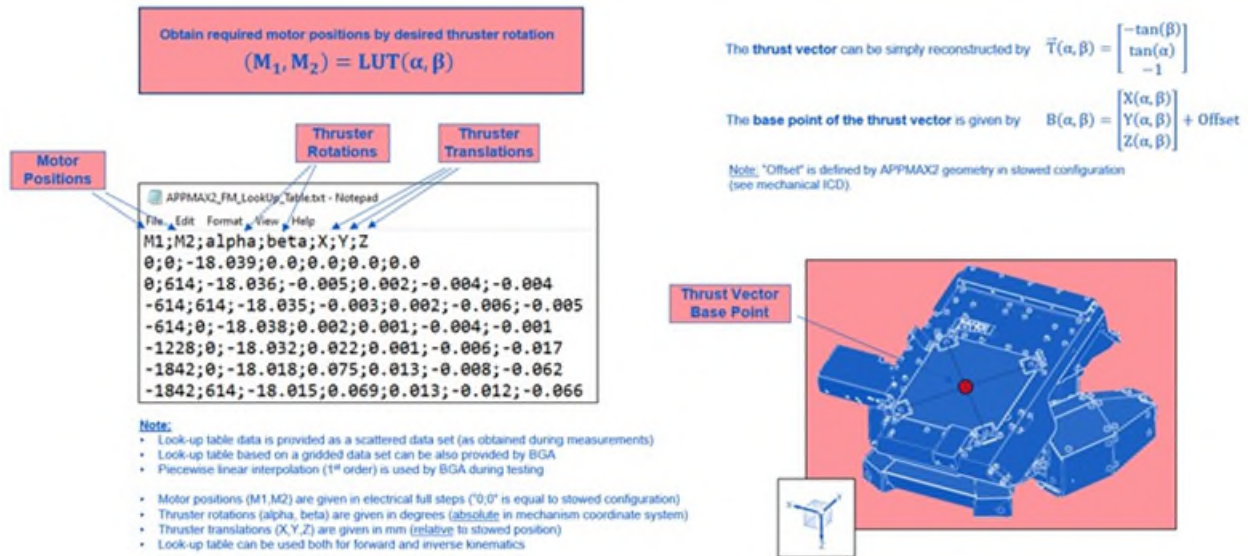


Figure 7. APPMAX2 Control via Look-Up Table

Vibration Performance

Because of the use of damping elements, the mechanism provides an overall amplification of only $Q < 4$. Figures 8 and 9 show the in-plane random test results. Figure 8 is the random input and Figure 9 is the random response. X-axis and Y-axis are nearly identical. Out of plane is similar at stiffness 2x higher than in-plane.

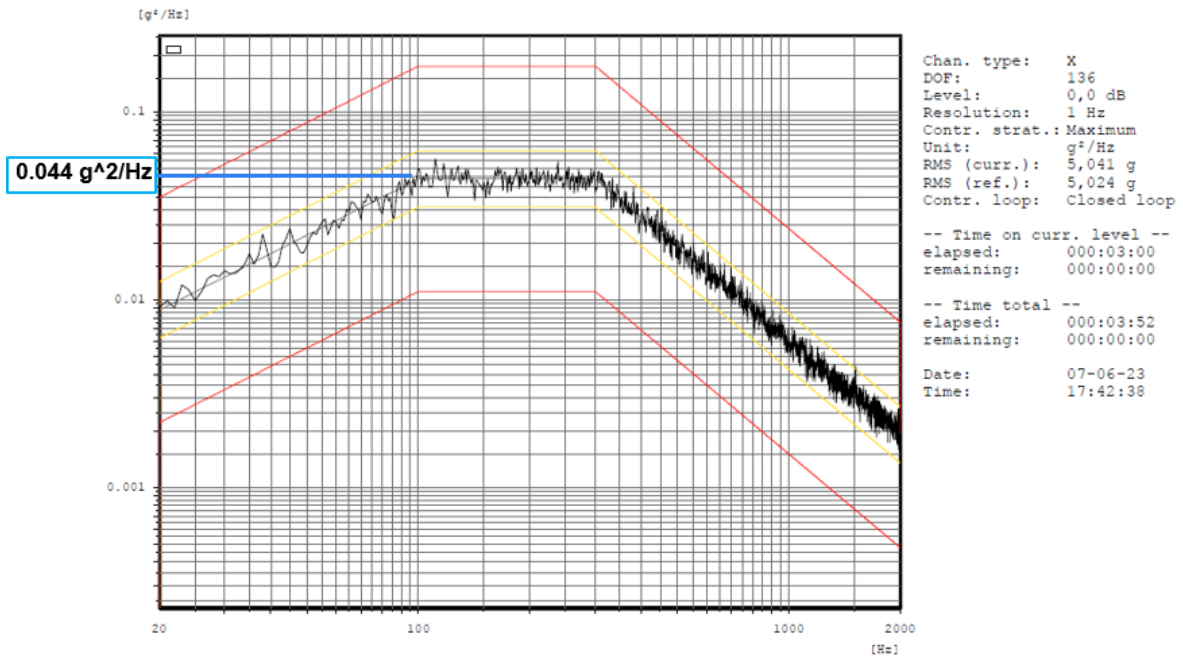


Figure 8. APPMAX2 Random Input Spectrum during In-Plane Testing

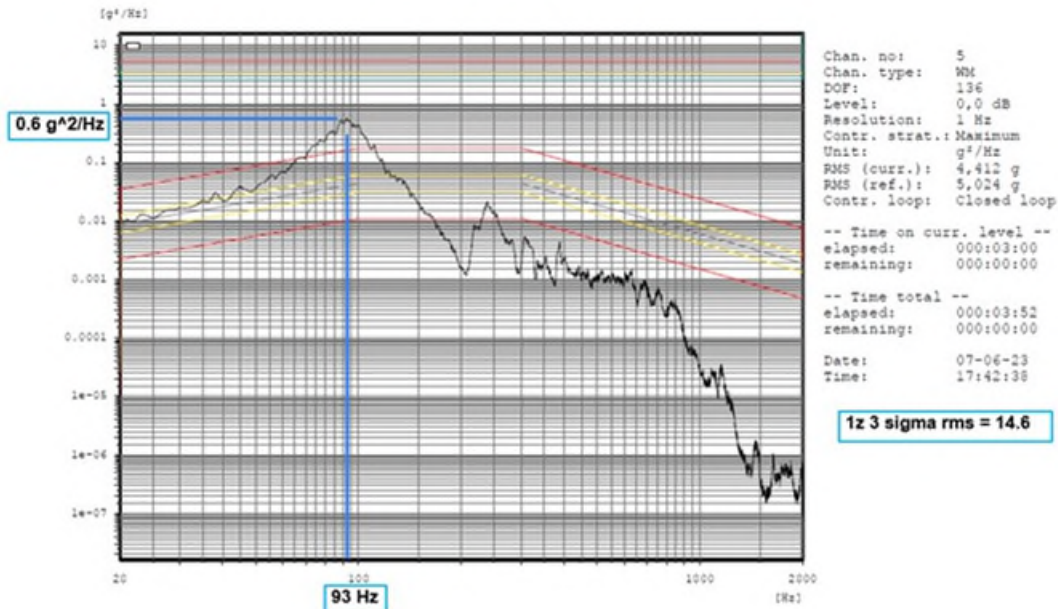


Figure 9. APPMAX2 Random Response Spectrum during In-Plane Testing

Shock Performance

Low shock inputs into the thruster is a major requirement for each EP mechanism. In plane shock attenuation: in Figure 10 the shock input into the mechanism is shown in acceleration direction Y. In Figure 11 the shock response at the thruster is shown. The shock input at the thruster is more than a magnitude lower than the shock input at the mechanism spacecraft interface. The out of plane shock attenuation is very similar.

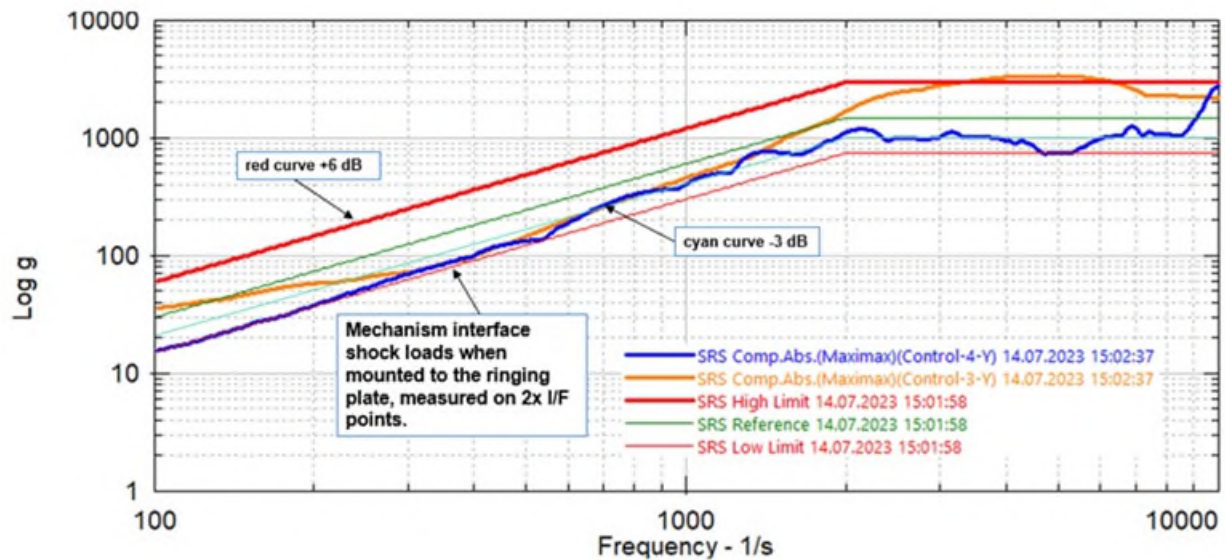


Figure 10. APPMAX2 Shock Input Spectrum during In-Plane Testing

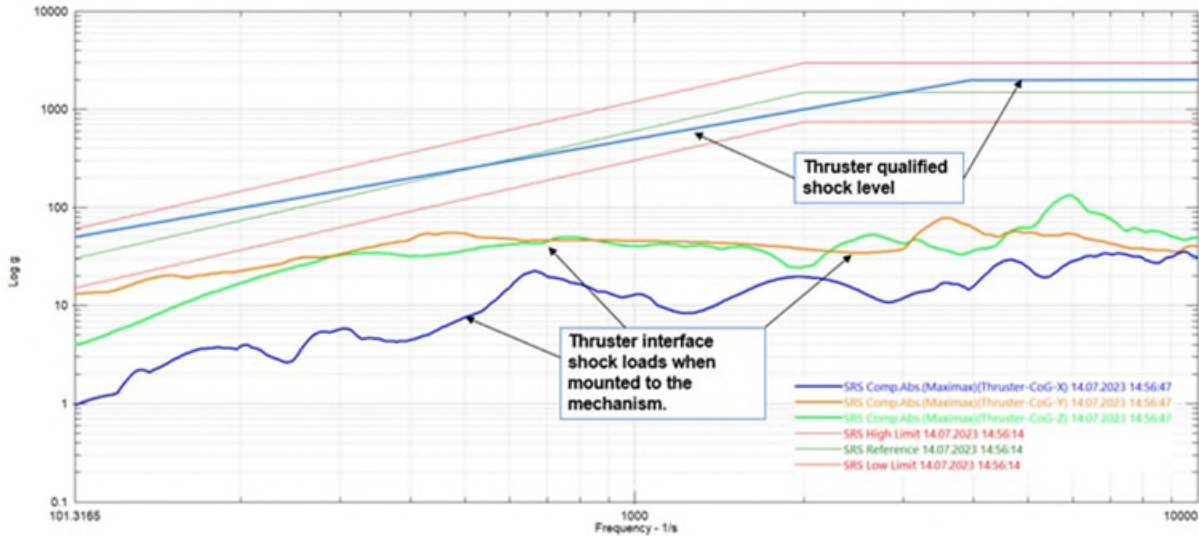


Figure 11. APPMAX2 Shock Response Spectrum during In-Plane Testing

The mechanism has no dedicated release device and the release from highly pre-loaded configuration to deployed configuration is performed very slowly by operation of the actuators. No shock is generated during the deployment operation.

Micrometeorite Protection

Micrometeorite protection for the Xenon piping is essential for high reliability because the Xenon supplies for the thrusters are not redundant.

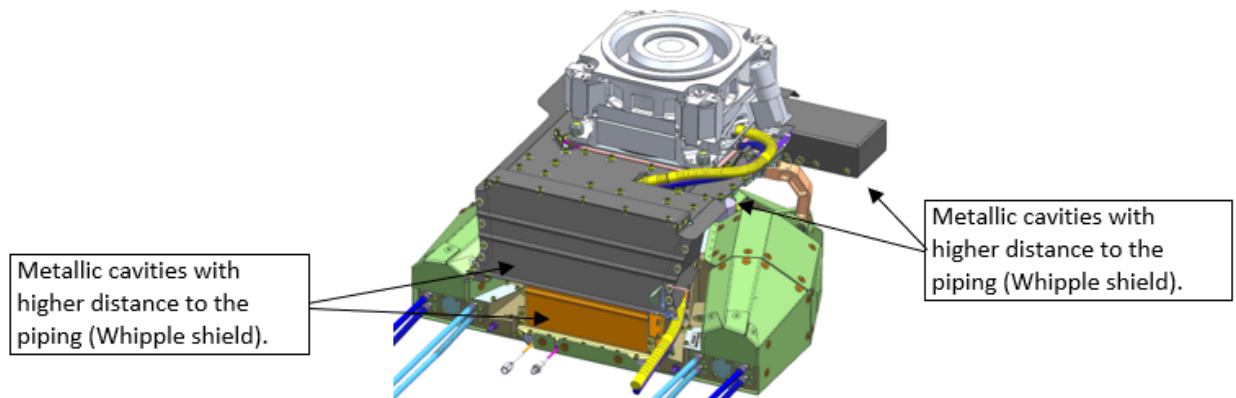


Figure 12. Micrometeorite Protection for the Xenon Piping

On Ground Operation

The APPMAX2 on ground operation capability was widely tested with dedicated dummy masses (including additional 50% mass margin to the nominal thruster mass). No gravity compensation device is needed. No collisions occur in the complete pointing range even at highest gravity impact. Pointing with a heavy dummy mass (1.5 g) is still possible with an absolute accuracy of up to $\pm 0.4^\circ$ in all directions.

Thermal Performance

The mechanism is equipped with radiation shields which emit dissipation power of the thruster to deep space. This thruster cooling effect is important because most thrusters are only qualified on thruster level neglecting shading of the spacecraft and increase of solar power through coupling from large OSR or MLI spacecraft surfaces (double sun effects). This would result in overheating of the thruster if it is not cooled by the mechanism in addition.

Both rotary actuators are mounted to the base frame with high thermal mass. The base frame is well protected by thermal Multi-Layer Insulation (MLI) protection. Being one of the leading spacecraft MLI suppliers worldwide, these blankets are produced by BGA in-house.

Reliability

The mechanism provides a reliability of >0.999 for 15 years GEO application. It is highly redundant and fully ECSS compliant.

Qualification Approach

Dedicated breadboard test programs were performed in the early phase of the project.

Structural and Functional Model

A Structural and Functional Model (SFM) for the mechanism was designed, analyzed and tested. This model is similar to the later built EQM but was equipped with rotary actuator dummies. These actuator dummies could be operated by hand and allowed measurement of the resistive torque during operation. No elastomer dampers were used for this model. The SFM was used for verification of the resistive torque during pointing and was also subjected to a vibration and shock testing campaign for its undamped configuration.

Piping Breadboard

A representative pipe routing for function, vibration and shock testing with dynamic test set-up was established. This set-up allowed verification of resistive torque, verification of structural integrity for the dynamic loads and verification of the life profile.

Thruster Harness Breadboard

A representative function test set-up of the thruster harness was built to quantify the resistive torque of the movable harnesses at ambient, hot and cold temperature. This also allowed measurement of thermal radiation capability of the braided thruster harness (emission to the chamber walls). Mechanical life testing with high margins to the baseline specification was performed.

Hinge Line Breadboard

The refurbished SFM was equipped with non-flight actuators and flight-representative sliding bearings. The sliding bearings were procured with minimum and maximum gaps in radial directions. A dedicated function and life testing campaign was performed at ambient and in TVAC.

Flight representative high-level mechanism testing was started from here on.

Engineering Model

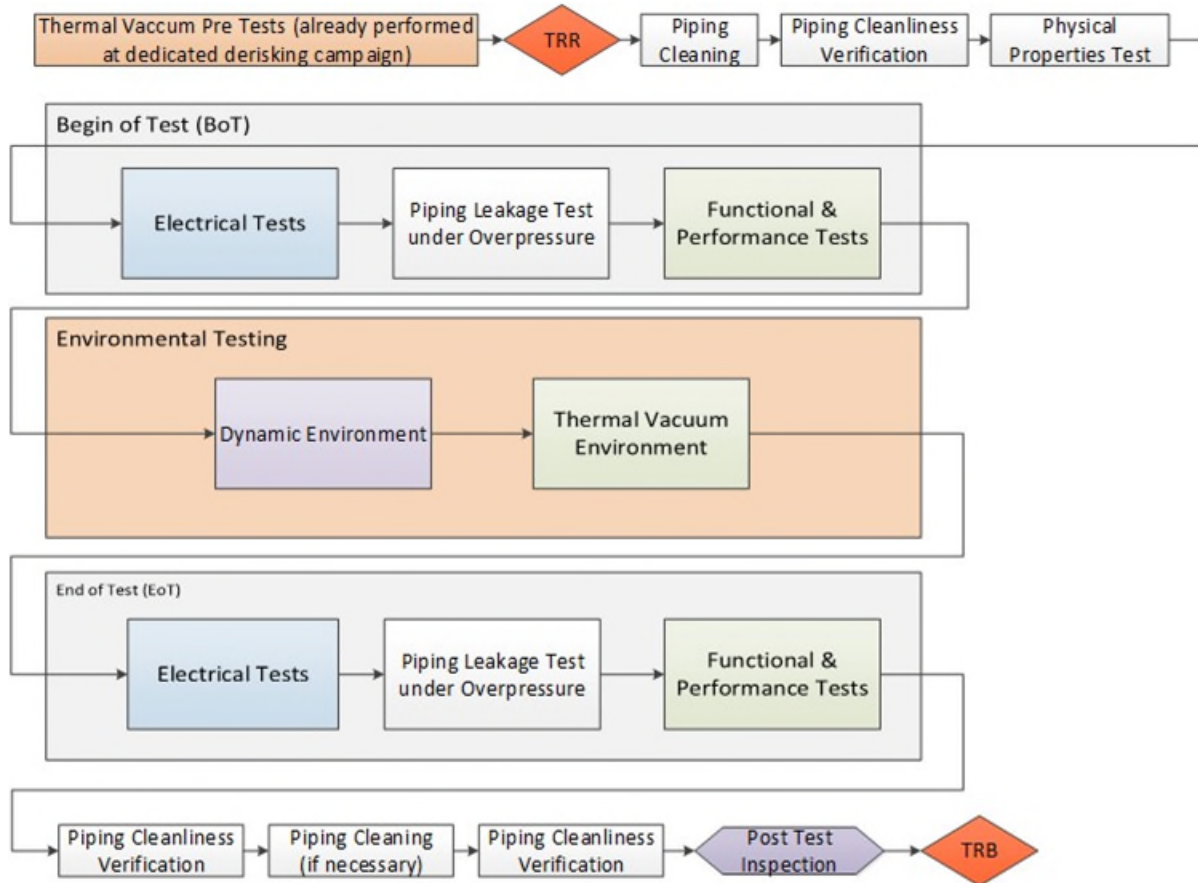
An Engineering Model (EM) of the APPMAX2 was used for optimization of the mechanism function. It was equipped with baseline LA15 rotary actuator and optional lightweight SA15 rotary actuator (both from BGA). An extensive test campaign was performed on this model. This EM was also used for a combined vibration test with a model representative to flight model PPS®5000 thruster from Safran Space Propulsion at BGA premises.

Engineering Qualification Model

After the EM test campaign, the mechanism was refurbished to an Engineering Qualification Model (EQM). With this EQM a complete qualification test campaign was performed.

EQM qualification test campaign

A complete qualification test campaign was performed for the EQM of the APPMAX2.



For the FMs similar campaigns are performed except for shock test and mechanical life test.



Figure 13. Vibration, TVAC, and Pipe Overpressure He Leakage Testing



Figure 14. Pointing Performance Test Setup at BGA (shown for X direction)

Status of the APPMAX2 Development

The mechanism was originally qualified for an ESA mission and is qualified via PFM approach for other customer specific missions. The first Flight Models have already been delivered and currently the series production of APPMAX2 mechanisms for different customers in Europe and US is ramping up.

Scalability of the APPMAX2 Mechanism

Since its birth, scaling down and scaling up of the mechanism for smaller and bigger thrusters ranging from 1 kg to 55 kg was embedded in the APPMAX2 concept philosophy. This APPMAX2 family extension approach allowed for maximizing the reusability of the internal return on experience while limiting the additional non-recurring financial effort.

The smallest member in the family, the APPMAX2-XS, is designed for thrusters between 1 kg and 2 kg. An engineering model of this mechanism has already been developed for a potential application.

The biggest APPMAX2 family member is currently the APPMAX2-H dedicated for a 55-kg plasma thruster. This mechanism is in active development and a structural model was already produced and tested successfully. Two flight models will be built for the lunar gateway mission.

For thrusters between 2 kg and 8 kg there is the APPMAX2-S as an intermediate concept, to date available as a CAD model.

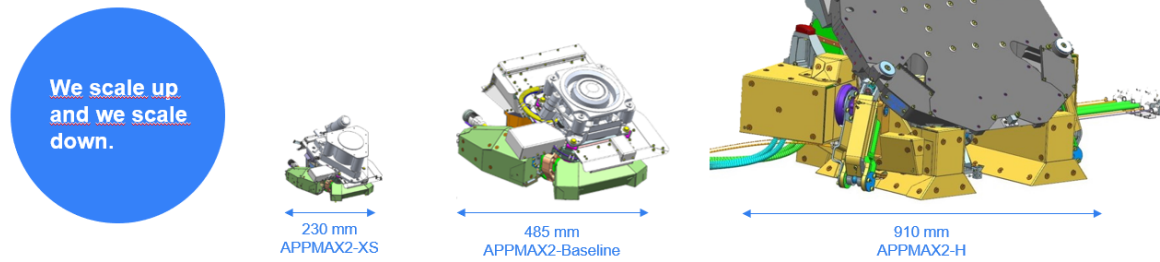
For thrusters between 15 kg and 30 kg the APPMAX2-L shall be used, which is currently also available as a CAD model.

All family members can be adapted to smaller or bigger pointing ranges, depending on customer needs. The maximum achievable pointing ranges are $\pm 28^\circ$ around X-axis (alpha) and $\pm 45^\circ$ around Y-axis (beta).

Mechanisms which require even higher pointing ranges and operational versatility shall be based on BGAs APPMAX3, a modular 3-axis boom product line, which can be supplied as a compact 2-axis version or as a deployable 3-axis configuration with pointing ranges up to $\pm 120^\circ$. A customized configuration of the APPMAX3 is contracted for several models and the first flight set will be delivered mid 2025 for launch end of 2025 or early 2026.

The APPMAX2 Family

beyond gravity



	APPMAX2-XS	APPMAX2-S	APPMAX2-Baseline	APPMAX2-L	APPMAX2-H
Thruster Mass	1.3 kg e.g. SPT50	max. 5 kg	8-15 kg e.g. PPS85000, SPT140	max. 30 kg	50 kg
APPMAX2 Mass	Ca. 2 kg	8.4 kg	14.9 kg	19.2 kg	29.5 kg
Main Dimensions LxWxH	170x150x95	344x342x199	486x484x281	493x593x385	493x765x497
Actuator	Nemo&PG		LA15		SA15
HDRM		none (locking by Actuators)		Heritage EPPM HDRM 2x Burnwire Release Actuator	
Development Status	TRL4 bread board built	conceptual design	TRL8 multiple FMs ordered	conceptual design	CDR status FMs ordered

The APPMAX2 can cover a wide series of applications supporting a broad spectrum of thrusters and mission profiles.

APPMAX2 Drive Electronics

The APPMAX2 mechanism can be directly provided with BGAs Core Drive Electronics (CODE), see Figure 15. BGA provides an end-to-end system which is tested and delivered together. The CODE is qualified and to a customer delivered together with APPMAX2 flight models to be launched end of 2024.

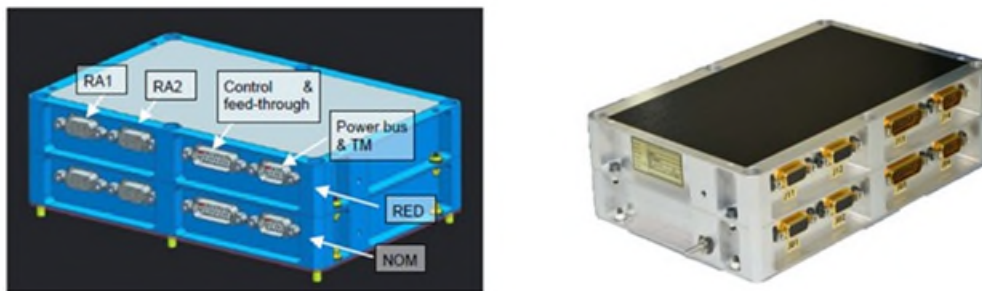


Figure 15. APPMAX2 BGA Core Drive Electronics (CODE)

The datasheet of the control unit is accessible on the BGA home page https://www.beyondgravity.com/sites/default/files/media_document/2023-11/BG-CODE.pdf

If customer drive electronics shall be used, the APPMAX2 electrical parameters (rotary actuator coil resistance, heater resistance) can simply be adjusted to the customer needs.

Lessons Learned from this Development

Reliability is by far the most important requirement for EP mechanisms and allows no compromises.

A simple and robust mechanism concept leads to significant improvements both during BGA's assembly and testing as well as during customer commissioning.

The use of BGA's in-house built rotary actuators enables short lead times and easy modification to customer needs.

Supply chain issues during Covid 19 pandemic could be effectively mitigated by BGA due to extensive use of in-house components and infrastructure.

Engineering feedback by ESA and other higher-level customers highly improved the product quality and reliability.

End to end testing of APPMAX2 and a real PPS®5000 thruster - supported by Safran Space Propulsion - enabled to test real load cases in both dynamic and thermal vacuum environment and to optimize the effort for thruster integration.

Conclusion

The **A**dvanced **E**lectrical **P**ropulsion **P**ointing **M**echanism **2-A**xis (APPMAX2) was successfully developed and qualified by BGA for 10-kg to 15-kg electric thrusters. The first sets of higher number of ordered APPMAX2 are already delivered, two of them scheduled for launch in 2024.

The tested mechanism's performance is fully in line with both the predictions and market needs.

Development of scaled modular versions of the APPMAX2 are ongoing successfully to establish a comprehensive EP mechanism family.

Acknowledgement

We would like to express our sincere thanks and appreciation for the strong support received from the ESA ARTES team and the Aeronautics and Space Agency (ALR) team of the Austrian Research Promotion Agency (FFG) for this APPMAX development and throughout our EP-mechanism developments.

MPCV SADA for ARTEMIS Program

A Story of Increasing Demands and Continuous Improvement

Josef Zemann^{*}, Paul Joachim Schüngel^{*} and Matthias Schmalbach^{*}

Abstract

As part of the European Service Modul (ESM) industrial team, Beyond Gravity (former RUAG Space) is responsible for the Solar Array Drive Assembly (SADA). This paper deals with the development of the SADA and particularly, with the development of the Solar Array Drive Mechanism (SADM). Special focus is the experience on brake development, Harmonic Drive lubrication and development of a stronger inner axis motor that was necessary due to increased customer demands.

Introduction

In the early 2000s NASA focused on having a crew vehicle serving both for crew transport to ISS as well as to support planned manned Lunar and Martian missions. Consequently, there was a demand for a Multi-Purpose Crew Vehicle (MPCV). A cooperation with the European Space Agency (ESA) was established. NASA, with their industrial partner Lockheed Martin, is overall responsible for the spacecraft as such, and for the Crew Module (CM), the manned part. ESA, with their industrial partner Airbus, is responsible for the European Service Module (ESM), providing supplies and propulsion.

Evolution of the need scenarios of the MPCV turned it into a crew transport vehicle in the NASA Artemis Program, now under the name "Orion Spacecraft". The Artemis program focuses on going back to the moon and beyond. Beyond Gravity Switzerland (formerly RUAG Space Switzerland) is responsible for the Solar Array Drive Assembly (SADA) of the ESM. Each ESM has four Solar Array Wings (SAW). So, a complete SADA set consists of four Solar Array Drive Mechanisms (SADM), two Solar Array Drive Electronics (SADE) each driving two SADMs, and the interconnecting Solar Array Drive Harness. When starting the program, the idea was to develop and qualify one SADA (one SADM QM and one SADE QM), and, once qualified, the SADA flight hardware for all Artemis missions would be fully recurring items. In this paper the fully qualified MPCV SADM MkI (ESM1-3) with flight heritage is presented. The follow-on development, resulting in 'MkII' SADM that serves ESM4+ increased technical needs, is mentioned as well. The MkII development, including exhaustive breadboard testing, is finished and CDR is passed. Achievement of MM performance under TV conditions is confirmed on the flight model identical Engineering Model. QM assembly is completed and the MkII QM test campaign is started.

Description of MPCV SADM

Beyond Gravity has served the international satellite market with a broad portfolio for solar array mechanisms for LEO, GEO and deep space missions for decades. Common to these applications is that for driving the SAW mainly the internal friction must be overpowered. In contradiction to that, under Artemis orbital scenarios, the Orion SAWs are exposed to high accelerations due to Trans Lunar Injection (TLI) and Trans Earth Injection (TEI) maneuvers. These accelerations induce very high bending loads to the mechanism. In addition, the SAW must be protected from thruster plumes. For that, a dedicated tilting capability is required that, together with flight operational needs, results in the design concept of a two-axis SADM.

^{*} Beyond Gravity, Zürich, Switzerland

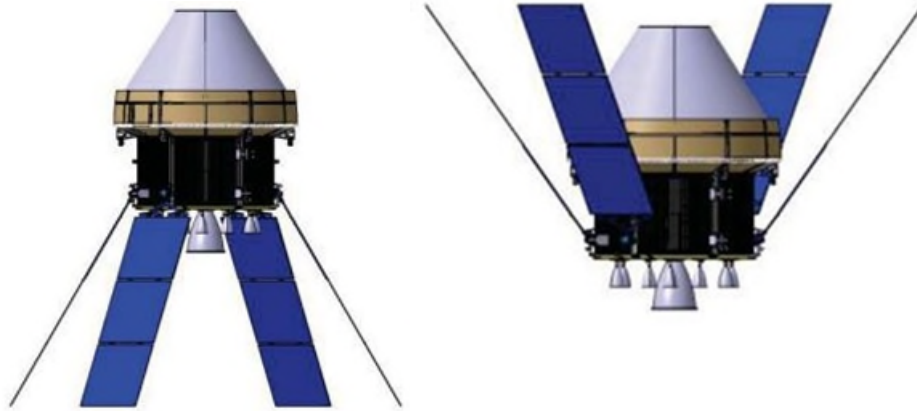


Figure 1. Orion TLI (left) and TEI SAW Configuration

Several concepts were developed, and a number of breadboards built to test critical functions.

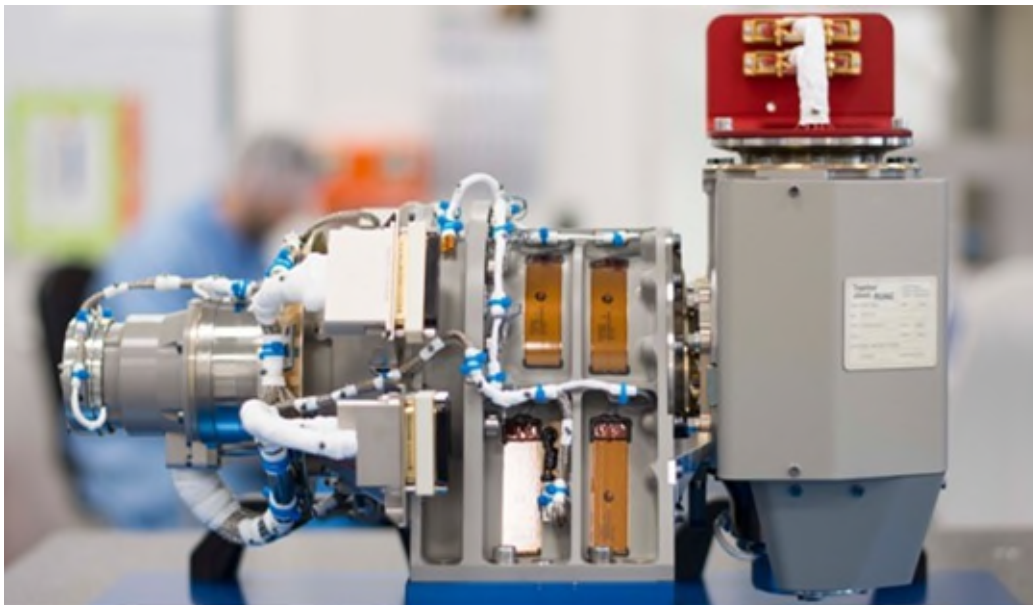


Figure 2. Orion SADM for Artemis 2 Mission

The Outer axis (OA) seen on the right-hand side of Figure 2 has its heritage from a standard SADM allowing continuous rotation under moderate loading. The power from the solar cells and signals are transferred by a dedicated brushed slipping.

The inner axis (IA) allows a limited tilting motion. To reduce noise and losses a twist cartridge is used for electrical transfer. Although a strong stepper motor is implemented on the IA, this is not sufficient to transfer the high bending loads (torques on this axis) seen in TLI and TEI. Therefore, a dedicated mechanical brake is implemented to the IA.

The positions of OA and IA are monitored by potentiometers. Heaters are implemented so that the fluid lubricants are kept at a moderate temperature level reducing the resistive friction in cold environment. All electrical components of the mechanism are fully redundant.

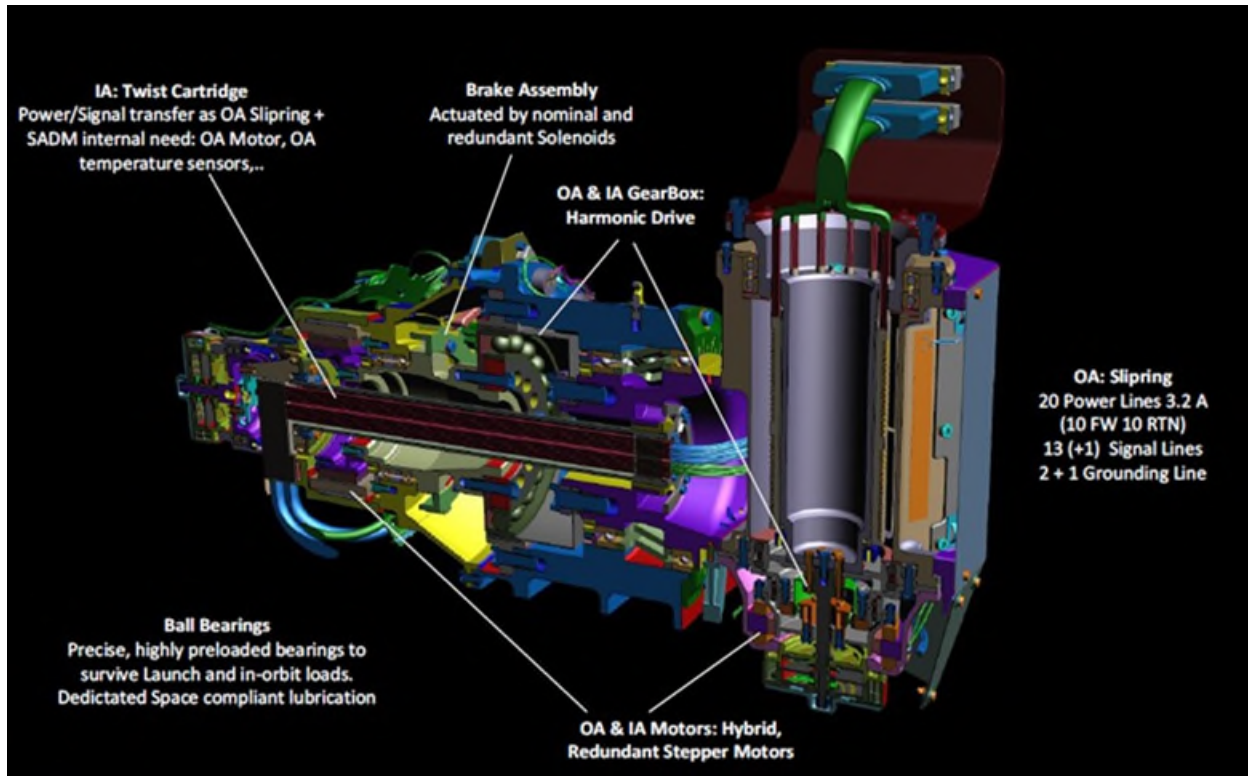


Figure 3. Cross-section MkII SADM (For Artemis 4 mission)

The SADM “ESM1” that has been qualified participated in the Artemis maiden flight in the frame of successful Artemis 1 mission end of 2022 during the unmanned Orion flight demonstration with orbiting the moon. SADAs for ESM2 and ESM3 are fully acceptance tested and delivered and will serve Artemis 2 (orbiting moon with Astronauts) in 2025 and Artemis 3 planning a landing on the moon. Already SADM for ESM2 and ESM3 saw some small modifications like an improved thermal concept.

The main development challenge was the significantly increased IA driving torque demand compared to the initial concept phase of the Artemis mission (more than a factor 3 increased). Starting with Artemis4/ESM4 the demands exceeded the design capabilities so that a design update including a completely new qualification test campaign was seen necessary. This now is under the designation ‘MkII’ (Mark2).

Key Performance Parameters (MkII) Considering Required Margins

- Fully Redundant Design
- OA: Speed up to 2°/s, operational 1.2°/s, with high load 12 Nm @ 0.1°/s
- IA: Speed up to 1°/s, operational 110 Nm @ 0.6°/s; Powered hold 220 Nm
- Holding with engaged Brake > 1200 Nm
- 10 FWD 10 RTN Powerlines, up to 3.2 A
- OA Continuous Rotation
- IA ±65° tilting capability
- SADM Mass 20 kg
- Designed to serve ISS and Lunar missions

Evolution of Demands

When entering MkI PDR, the overall design, specifically the definition of the LLI like motors and gearboxes was assumed to be defined. By that, specifically also the outer envelope got frozen which obviously limited the freedom for later improvements.

Axis Drive capability

Motor margins verification for inner and outer axis were in MkI determined based on NASA-STD-5017. The outer axis was initially required to drive a load <2 Nm as it was aligned with the SAW centerline. For ESM3 the demands increased and drivability for low speeds up to 12 Nm was demonstrated. For Mk2, full MM compliance to 12 Nm was required for slow motion. This represents a performance increase by a factor of 6 compared to the initial design assumptions. For Inner Axis, the demand from MkI to MkII increased from driving an external load $T < 40 \text{ Nm}$ to $T > 100 \text{ Nm}$.

Getting compliant to the increased motorization demand was done by improving the SADE (micro stepping) and higher power (obviously limited by dissipation limitations), as presented below in more detail for MkII a design update for the IA axis actuator units was unavoidable. A certain relaxation was given by the permission to use NASA-STD-5017A by which the margins for the specified external loads were possible to be reduced from $K = 2$ to $K = 1.5$.

Brake

In the initial project phase, simple acceleration loads were assumed to act. By that only a unidirectional brake to transfer the maximum loads was assumed necessary. The brake development including Bread Board (BB) models was already well advanced. However, by more detailed investigations on spacecraft level, the demand for having the possibility to block the SAW in vicinity to the CM was stated which led to a development of a bi-directional brake. Focus was put on safe locking and latching, with a specific sequence defined for release operations. A launch lock was built in as well.

The brake has sensors for fully disengaged and engaged position while some intermediate states (on the Bump, see Figure 6) are possible for MkI design with unsatisfactory monitoring. This was demanded to be eliminated in MkII.

Mechanical & Fatigue Loads

Some external load evolutions were communicated, specifically by the planned update of the upper stage of the SLS from iCPS to EUS the bending loads increased. Fatigue loads were underestimated at the beginning of the project, specifically for MkII, with remarkable loads coming from crew exercises. It was not possible to do an assessment by covering load spectra but a very detailed analysis was necessary. In addition to that, a lot of critical components require a detailed non-destructive inspection (NDI) (ultrasonic, special reference samples needed to be produced).

Loaded TV Life Testing

For MkI, the external loads were low enough so that the TV life test was accepted to be done against the internal loads (only). Because of increased MkII loads this was no longer seen possible and a dedicated IA TV chamber with high load capability was necessary to be built. This enables also now parallel testing of IA and OA in TV.

Main Development Steps MkI (ESM1-3)

The early development phase was driven by the need to get a common understanding on the requirements and associated design solutions.

Separable Inner to Outer Axis Interface

Due to the high loads to be transferred from SAW IF to the spacecraft, it was foreseen to have an OA housing that is directly supported by massive ball bearings in the IA Housing.

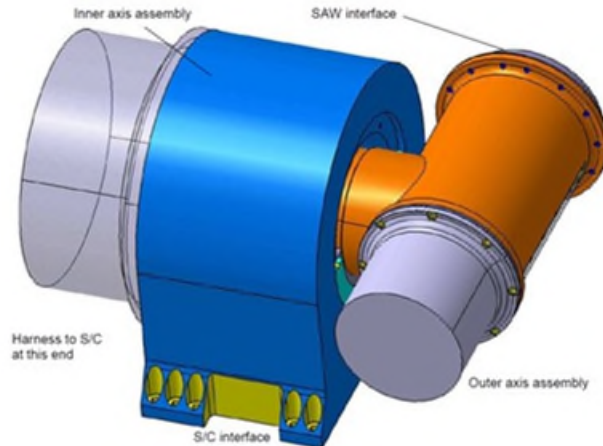


Figure 4. Mkl PDR Design

The disadvantage of this design was faced when detailing the verification approach: MM determination with applied loads under TV conditions were required to be determined. Specifically, by the fact that the OA needs to demonstrate continuous rotation no practicable approach was found.

The solution to solve this problem was to update the design to have a separable interface between IA and OA. This enhances modularity and allows to test the IA and OA for itself under TV conditions. The TV chamber has a dedicated mechanical feed through and on the outer side torsional loads can be applied (see the wheel with cable in Figure 5).



Figure 5. MPCV TV Chamber with Mechanical Feed-Through

By this approach for the FMs, the acceptance approach was defined that deviates a little bit from the usual approach:

- First TV test including loaded MM determination on axis level.
- 'Marriage' IA and OA
- Vibration test as acceptance and workmanship test

The QM qualification testing then continued with static load and shock test. This is followed by SADM level TV and TV Life test considering that the dominating Mkl loads for life testing come from internal resistance (specifically internal HD friction) and not so much from external loads.

Development and finding Inner Axis Brake

As already highlighted, during TLI and TEI powered flight events, bending loads >1000 Nm are introduced into the mechanism. These loads are much too high to be held by a powered motor. The overall operational demand is even more to hold these loads in a failure mode, meaning main (or redundant) SADE is unpowered. So, after significant trade-off for concepts and actuators, a dedicated mechanical form fit brake was developed with a tooth wheel and a brake lever that engages between the teeth. A nominal and a redundant solenoid can drive the lever out of engaged into disengaged position. Torsional springs are available that, in unpowered mode, rotate the brake lever back into engaged position. The force-to-distance characteristic shows a strong nonlinear behavior. So, in MkI every other tooth of the brake wheel was formed as a “bump” that allowed, using a special SADE implemented automated disengagement sequence, to mechanically raise the lever towards the solenoid and so reduce significantly the power needed to disengage the brake.

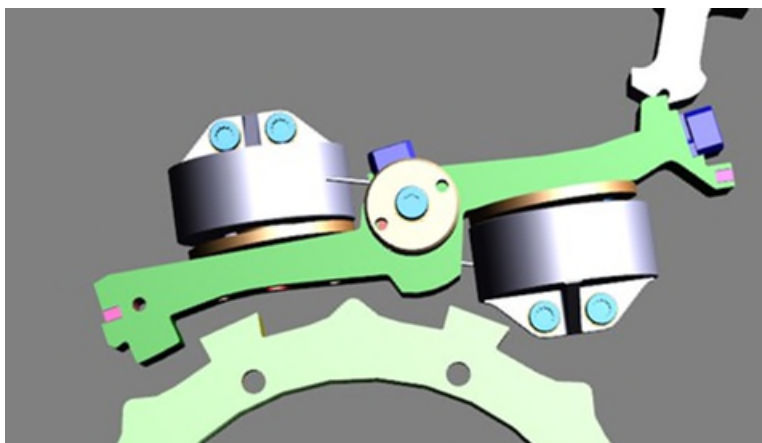


Figure 6. MkI IA Brake

In the initial mission phase, the SAW is stowed and fixed by a dedicated hold down and release mechanisms. High vibrational loads are introduced into the mechanism. To avoid over-constraints by a potential additional torsional constraint by the SADM, in the mechanism a dedicated launch lock lever (far right in Figure 6) is introduced that fixes the brake lever close to the fully disengaged position. Once the solenoid is powered for the first time, the brake lever is driven out of the locked position and the launch lock lever moves, spring driven, in its parking position where it stays till end of the mission.

During qualification testing, the unfortunate event of an undesired launch lock release was observed during dynamic testing. The spring preloads were confirmed to be correct and also the friction assumptions were not seen as the root cause. It is highlighted that the brake lever and the launch-lock lever see a dedicated CoG balancing process as part of the assembly to ensure with fine tuning of counterweights that the CoG is close to the rotational axis.

A detailed simulation with ADAMS multi-body dynamic analysis software establishing a very detailed brake model finally revealed the root cause: The play between the lever axis and the bushes was too large. In a dedicated BB model with narrowed tolerance, the brake stayed closed under the dynamic loads. The ADAMS simulation, however, showed that micro-sliding is unavoidable. This is not covered by NASA-STD-5017(A). As an alternative, instead of MM with SF=2, it was demonstrated that the brake stays closed under qualification load +6 dB.

Design Update MkI (ESM1-3) to MkII (ESM4+)

Development of a new Strong Stepper Motor for MkII Inner Axis

The holding and driving torque demands increased significantly from MkI to MkII (driving torque factor 2.5 higher). So, a new, stronger actuator including a new stepper motor needed to be developed. The design constraints were given by:

- Sensitive components as the brake should not be modified in their overall size.
- Length of actuator unchanged by SADM limited clearance
- Diameter increase limited by SADM clearance and interface to brake sub-assembly which should remain unchanged in its overall design
- Limitation in power consumption and specifically power dissipation to be considered.

The main modification compared to MkI were:

- Stator diameter increased by 30%
- Step size increased from 1° to $\sim 1.5^\circ$ (by that Harmonic-drive gear ratio changed, see dedicated chapter)
- Stator laminated design (possible by change of supplier)

The initially developed design (internally named Bread Board 1 BB1) showed satisfactory results at the maximum needed speed of ~ 25 RPM. When testing in detail, a significant torque break-down at low speeds was observed (see Figure 8). This was identified as result of the very high detent torque of 1 Nm which is 60% of the pullout torque at the lowest operational current.

The situation was analyzed in detail and the solution was found to build an almost identical motor (Bread Boards 2 BB2) with identical stator, but rotor teeth number slightly enlarged. With that the detent averaged out and dropped by almost a factor of ten while keeping an acceptable pullout performance over the complete operational speed range.

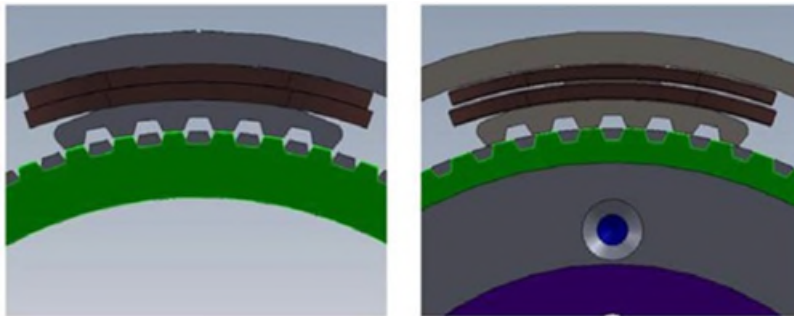


Figure 7. Comparison BB1 to BB2 motor Pole Design

With this design stable performance was achieved and the torque degradation at low speed was eliminated.

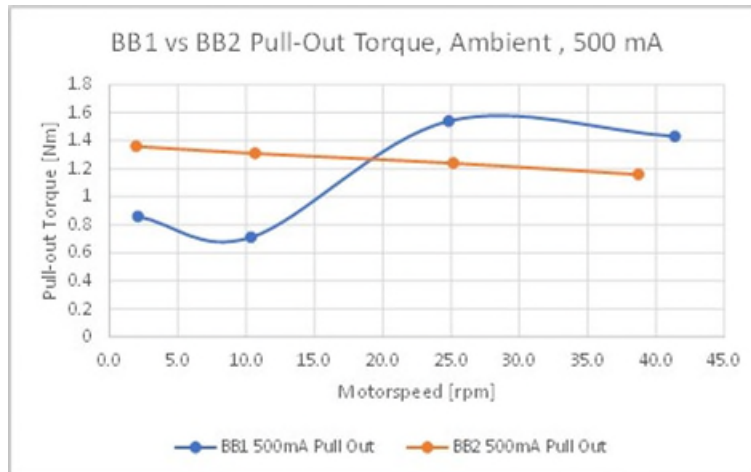


Figure 8. pullout Torque BB1 to BB2 motor

Lubrication Concept Change Mkl to MkII

A change from MAP-based lubrication to PFPE-based lubrication was implemented to achieve lower friction torque in cold conditions. This effect can be seen well from comparing OA HD test results.

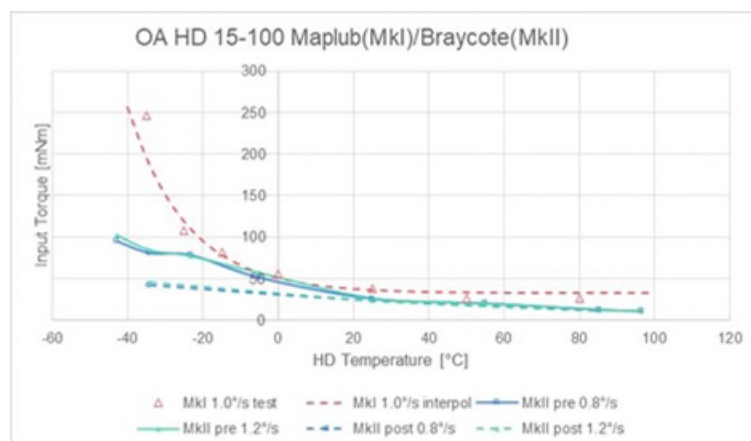


Figure 9. Comparison Internal Torque Mkl to MkII OA HD

It is well seen that for low temperatures there is a significant friction increase of the Maplub-lubricated HD. Interesting to see that after life test the friction is even lower than before. This indicates the benefits of a run-in process.

The lubricant amount was gently adapted, also under the consideration that the creep barrier concept worked well in Mkl. The first IA BB TV life test failed by too high lubricant consumption in the geared section. This was seen because of the known lower life-load capability of Braycote compared to Maplub. In a second attempt, an overall lubricant volumetric scaling recommended by specialists from a comparable successful test with smaller HD gears was done. This resulted in a successful OA loaded life test. However, from the wave generator bearing, flooding was observed by QM/FM integration. In contradiction to the gear tribological interface, this bearing was identified as not life critical respectively covered by other tests. Here, scaling in relation to the wetted area instead of scaling to volume was found to be the better approach. Finally, an optimized, well-balanced concept was found.

Increased Fatigue Spectra Requirements

The specified fatigue spectra evolved over time, specifically for MkII moderate load levels but high number of load cycles were introduced to cover crew exercises. For structural parts it was possible to cover fatigue by analysis (and appropriate inspection). The IA Gearbox was seen as a critical part and analytically difficult to cover. Although the overall geometrical design remained the same, the gear ratio was increased by more than 50% from MkI to MkII. For this range, little experience from the supplier was available. So, a dedicated fatigue load test on an (blocked = mechanical brake engaged) IA gearbox was executed. The low number of highest load cycles (>2000 Nm for BB testing) were applied using a dedicated static load test set-up. For the high number of low-load-cycles, a dedicated test was performed using a shaker and a mass-carrying cantilever. The CoG of the mass was adjustable and so 3 load levels with different number of cycles were tested. The test was successfully completed. Almost no signs of wear were seen on the gears.

SADE Upgrade

MkII has a new drive electronics. The main change is the update in the drive concept from voltage control full step to power control micro-step. For OA powered holding, a hot redundant powering concept is now available. The MkII SADE is also more flexible in “late” parameter changes (parameters are no longer stored hard coded in FPGA but stored in EEPROM).

Obsolescence Removal and Small Improvements

Due to the long-lasting development phase of the MPCV/Artemis program, obsolescence issues were encountered. These were resolved in “MkII”. An example is the surface treatment Alodine 1200S, which is no longer allowed by REACH restrictions and is replaced with SurTec. Findings and lesson learned from MkI were implemented as a further improved EMC hardness.

Conclusion

Beyond Gravity contributes to the Artemis program by providing the SADA Assembly for the ESM for more than 10 years and continues to do so. ESM1 SADA was successfully flown in Artemis I, ESM2/3 SADAs are delivered and under integration into the spacecraft. For ESM4+ increased demands were considered by a general design update, mainly affecting IA actuator assembly. Running a completely new qualification test campaign for MkII was unavoidable but had the advantage of considering lessons learned in MkI and as well to remove obsolescences.

The extensive MkII BB phase is completed with a lot of interesting findings, CDR passed and the QM test campaign, based on the experience from MkI, is started.

Lessons Learned during SADM/SADA Development

- Not specifically new but confirmed: Use of PTFE-based lubrication (Fomblin Z25 Oil/Braycote) has significant advantages in cold; insufficient lubricant amount leads relatively fast degradation and must be avoided.
- Scaling of lubrication amount from successfully tested gears assemblies to comparable gears assemblies with overall larger dimensions is not straight forward. A volumetric approach (3rd power of scale factor) can lead to inappropriate amount of lubricant with risk of flooding, specifically for bearings. In addition, for evaporation analysis based on Langmuir formulas and extrapolating spiral orbit tribometer consumption test results, it is wise to make a crosscheck with “rule of the thumb rules” for lubricant volume and lubricant film thickness.
- In MkI, no flight equivalent SADM Engineering Model was foreseen to be built. Unplanned tests (for example in case of NCs) and specifically tests with SADE could so be done only on QM or, even worse, with FMs. For MkII, a dedicated flight model equivalent SADM Engineering Model is built.
- The expectation of having developed a recurring product in such a complex project was not very realistic. This is already given by the fact of obsolescence of some components, given the project has up to now been running for ~12 years, and is worsened by the hesitation of the customer for procuring all 9 SADAs for Artemis 1 to 9 in one batch. This is also a consequence of increasing customer demands over time.

- The effort for achievement of getting compliance to fatigue requirements was underestimated.
- During Mkl FM testing, on first sight a pre/post shift in the low level sine signature after HL Random was seen. A detailed investigation reveals that there was no shift but only a change of damping behavior between two modes. It turned out that for such complex mechanism it is better to use low level random signatures for health verification (see dedicated ESMATS paper)

The contract was carried out under MPCV program and founded by European Space Agency. Beyond Gravity wants to thank all Institutional and Industrial partners enabling this development. In specific for the technical team: Xavier Vo, Emmanuel Gogibus and Mohamed-Ali Ben-Akez from Airbus, Sandro Patti from ESA and Ed Lewandowski from NASA.

Disclaimer: The information presented in the paper reflects the actual project status, having passed many reviews between Beyond Gravity and the customers. The abstract is, however, not officially approved by the European Space Agency.

List of Abbreviations

An exhaustive list of Artemis/Orion program specific abbreviations can be found in the NASA Orion Reference Guide. Here some specific abbreviations used in this paper:

HD	Harmonic Drive
IA / OA	Inner Axis /Outer Axis
MM	Motor Margin
SADA/M/E	Solar Array Drive Assembly / Mechanism / Electronics
SAW	Solar Array Wing

References

1. National Aeronautics and Space Administration "Orion Reference Guide"
<https://www.nasa.gov/reference/orion-spacecraft/>
2. Kathleen Schubert, NASA Glenn Research Center et al. "The Multi-purpose Crew Vehicle European Service Module: a European Contribution to Human Exploration" *AIAA-2013-5477*
3. National Aeronautics and Space Administration "NASA's Lunar Exploration Program Overview September 2020" *NP-2020-05-2853-HQ*
4. Rajagopal, K. R., Singh, b., Singh, B.P. "Optimal Tooth-Geometry for Specific Performance Requirements of a Hybrid Stepper Motor" *IEEE Transactions on Magnetics, Vol. 39, No. 5*
5. Palladino M., Murer J., Didierjean S., Gaillard L. "Life Prediction of Fluid Lubricated Space bearings: A Case Study" *14th European Space Mechanisms & Tribology Symposium – ESMATS 2011*
6. Gaillard, L. et al, "FeF3 Catalytic Influence on PFPE Lubricant's Lifetime under Loaded Conditions", *Proc. 41st AMS Jet Prop. Lab., 2012*
- 7.. S Schulke, M., Jansson M. et al "Performance and Life of Harmonic Drives for Space Application" *ESMATS 2019*
8. J. Zemann, J., Bolognini, A., S. Battige, S. Sgobbo, R. and Patti, S. "The Importance of Low Level Random Search in Space Mechanisms" *ESMATS 2023*

Development and Qualification of an Electrical Thruster Two Axis Pointing Mechanism

Richard Horth*, Stéphane St-André*, Xavier Marcotte*, Marc-André Verreault* and Etienne Desrosiers*

Abstract

A two axis 5 kW class electrical thruster holding and pointing mechanism has been developed and qualified in the context of a “GSTP Element 2: Make” contract in partnership with the European Space Agency (ESA). This paper presents the design and qualification of the Thruster Pointing Mechanism (TPM) used to hold and point the electrical thruster. This electrically redundant TPM includes actuators, drive trains, position sensors, thermal control system, Xenon piping and cable management systems. It is based on the fine pointing mechanism patents US 9172128B2 [1] and EP 2 608 313 B1 [2]. The novelty of the system is that the payload (thruster) is held in such a way that it precludes the use of hold down and release mechanisms or snubbers, greatly reducing its mass and volume and increasing its reliability.

Introduction

With the advent of electrical thrusters, the need for pointing them to account for spacecraft center of gravity changes has arisen. Since MDA has developed many different antenna pointing mechanisms, it was in a good position to design one for electrical thrusters. This paper describes the design of the mechanism, the problems encountered during qualification and the modifications implemented to correct them.

TPM Design Overview

The TPM is presented in Fig. 1. It can point the payload at any orientation within a half cone of 15 degrees, extendable if required to 22 degrees.

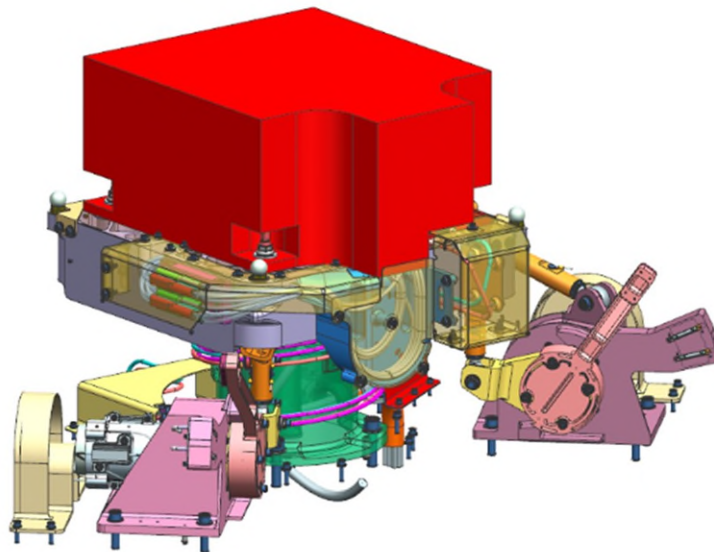


Figure 1: Thruster Pointing Mechanism

* MDA, QC, Canada

It contains a mobile plate on which the thruster (or other payload) is mounted. The mobile plate sits on a central spherical bearing to constrain the three translation degrees of freedom. The two driven rotations are actuated by Rotary Actuators (RAs). Each RA contains a stepper motor that drives a one stage planetary gear stage that drives a Harmonic Drive. The RA output bearing is thin section cross roller bearing to react the axial, radial and bending moments. The RAs rotate a crank that imparts rotation to the payload through a connecting rod. The final rotational degree of freedom is constrained using an anti-rotation bar.

Major Design Challenges

During the design phase, the following major design challenges were identified.

1. Isolating the mechanisms from the very hot temperature of the thruster.
2. Heating the thruster to the appropriate temperature.
3. High electrical power transfer through the gimbal.
4. Routing of the piping and the harness to minimize exposure to radiation, temperature excursion and Micro Meteorite Orbital Debris (MMOD) impact while keeping full flexibility on the mechanism pointing range.
5. Holding and pointing a 12 kg thruster

Isolation of Hot Thruster

The mobile plate has a thruster attached to it. The thruster can dissipate up to 1000 W. The mobile plate has to manage that heat to control the thruster temperature and to limit exposure to the mechanisms underneath. Heat conduction is minimized by the low thermal conductivity of the titanium thruster base and the insertion of a 75 μm thick sheet of Kapton coated with Vapor Deposited Aluminum facing the thruster. Any heat that gets by the above is radiated out sideways by the use of clear sulfuric anodized aluminum radiators on all sides.

Heating of Thruster Prior to Start

The thruster must be above a certain temperature prior to start. Thirty-five Watts of heaters arranged in redundant pairs are installed under the mobile plate to achieve this. The temperature is monitored using 3 RTD sensors.

High Current Mobile Harness

A 5 kW thruster requires a lot of voltage/current. The configuration implemented here requires sixteen 1 mm^2 (approx. 17 AWG) double insulated wires which bundled together form a 20 mm OD cable bundle. The routing of the dynamic part of the harness is shown in Fig. 2.

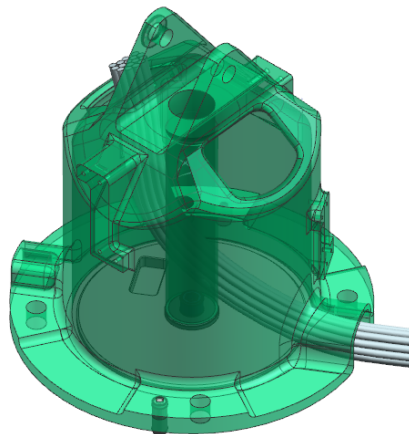


Figure 2. Mobile Harness

As can be seen, the cable bundle is routed through the pedestal to limit temperature exposure and to protect it from MMOD and radiation. The bundle is clamped at the fixed end on the baseplate and the mobile end on the mobile plate. In between, each wire is free to move which reduces the composite stiffness of the mobile portion of the bundle. The bundle is routed such that it interfaces with the mobile plate as close as possible to the spherical bearing to minimize the translations of its mobile portion. The routing of the harness' flexible portion is designed to reduce friction with adjacent surfaces. Inner surfaces of the pedestal are coated with a low friction surface finish to protect the harness from friction wear.

Mobile Gas Piping

The electrical thruster requires two separate gas pipes, one for its anode and one for its cathode. They are both type 304 stainless steel tube of OD 3.17 mm and wall thickness of 0.508 mm. Fig. 3 shows the piping routing around the pedestal with the clamping arrangement. The challenge was to find the balance between stiffness and flexibility. The tube shall be long enough to reduce the stress induced by the enforced displacement from the thruster support plate tilt and minimize the tilting resistive torque on the mobile plate. These tubes could not be excessively long though in order to minimize the pressure drop.

The solutions chosen were:

- a) to fix the piping on the mobile plate as close as possible to the main spherical bearing to minimize translations at that point,
- b) to minimize the diameter of the coil,
- c) to link both coils with plastic brackets to avoid contact between coils, protect the tubes from the vibration environment and have a uniform behavior of both tubes.

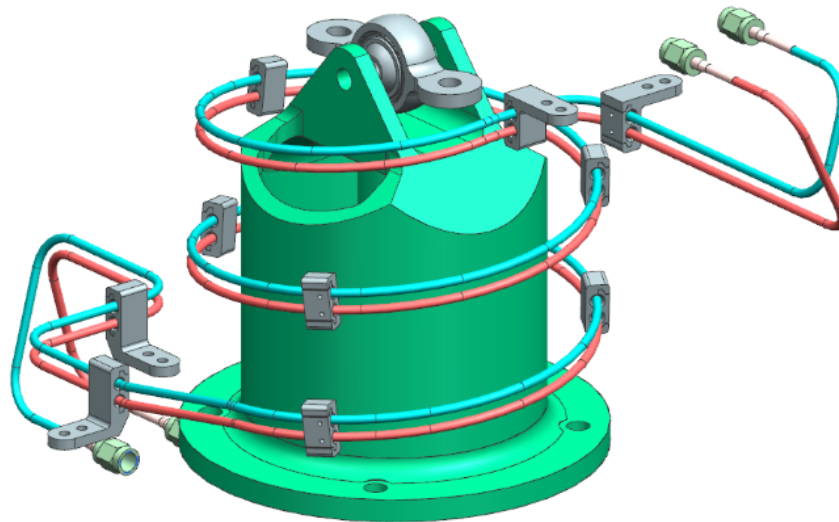


Figure 3. Mobile Gas Piping

Holding and Pointing a 12 kg Thruster

The use of the design of the Fine Pointing Mechanism patents [1] [2] was critical to obtain a system that was competitive in terms of volume, mass, reliability and simplicity of use. The design is such that the center of gravity of the payload is as close as possible to the main spherical bearing holding it. This means that during vibration, very little loads are transferred to the rotary actuators. Additionally, in the stowed configuration, the crank arms are in line with the connecting rods meaning that any remaining launch loads are not converted to torques on the RAs. These features enable holding this 12 kg payload without the use of hold down and release mechanisms, simplifying the use and improving reliability. Finally, the design holds the payload as low as possible to the base minimizing the volume of the system.

Development Plan

The full development took approx. 2 years from May 2021 to May 2023.

The components that needed development and qualification were:

- Mobile piping
- Mobile harness
- Spherical bearings
- Thruster plate with thermal hardware

For the mobile piping and harness, several Bread Boards (BB) were manufactured, vibrated and life tested in ambient conditions to determine their capacity to perform the mechanical life. These tests permitted fast iterations of the mobile harness and piping designs. These initial BBs were mechanical cycled through full range of travel. This permitted to fail fast and tweak the design for each new iteration. After we knew that the design could take the mechanical life, the next step was to constrain it in the stowed condition such that it could survive launch loads.

Finally, a full up TPM was qualified. The qualification model TPM is shown in Fig. 4.

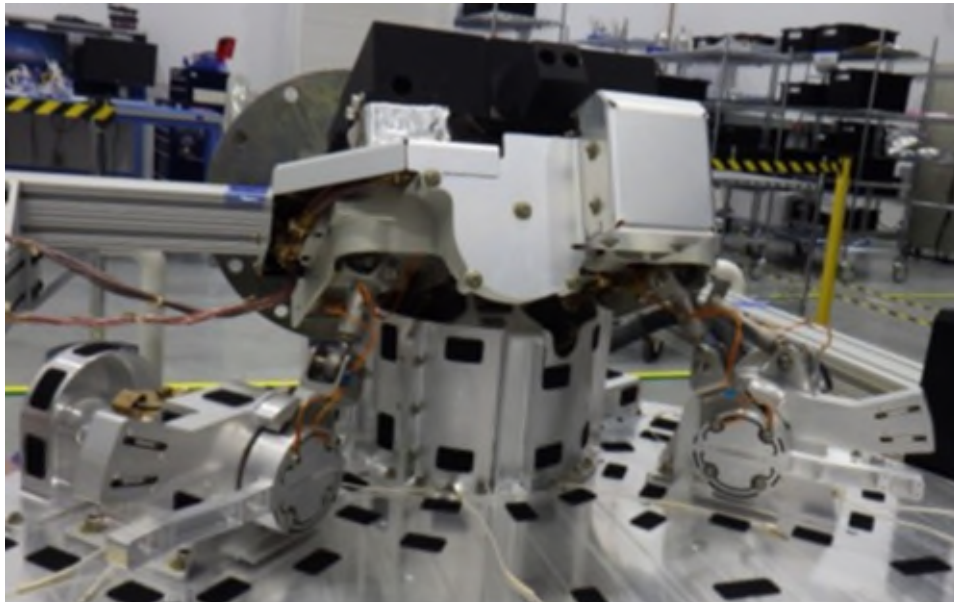


Figure 4. Qualification Model TPM

Test Problems and Lessons Learned

This section will review test problems and the associated design improvements and lessons learned. Fracture of a major component during vibration testing and its cause, corrective and preventive actions. How to hold high power mobile electrical cabling through the launch environment. How to hold mobile gas piping through the launch environment

Fracture of a Major Component During Vibration

During qualification level random vibration in the Z direction, a Titanium bolt broke. Fig. 5 shows the location of the bolt in the TPM.

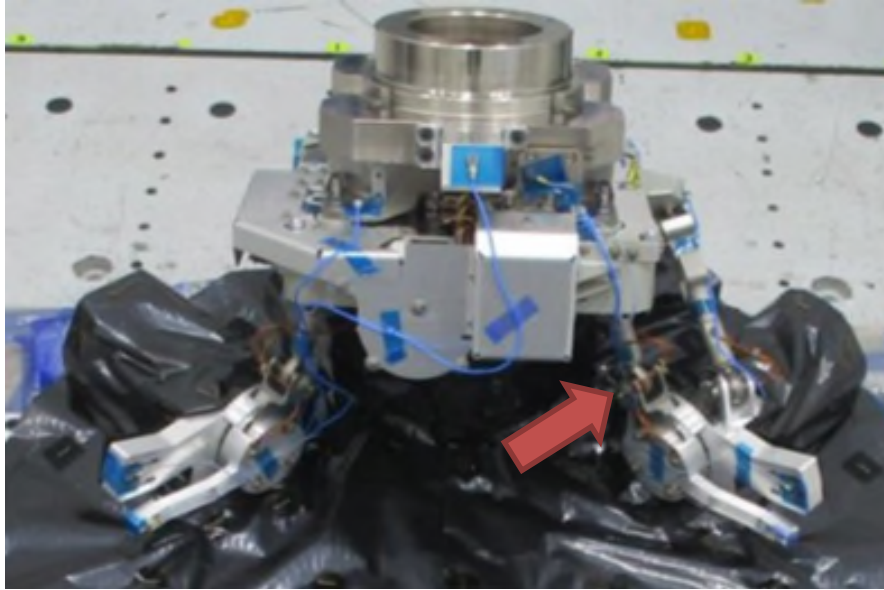


Figure 5. Location of Broken Bolt on TPM

Fig. 6 shows the bolt in question. Note that in Fig. 6, the left-hand spacer is missing.

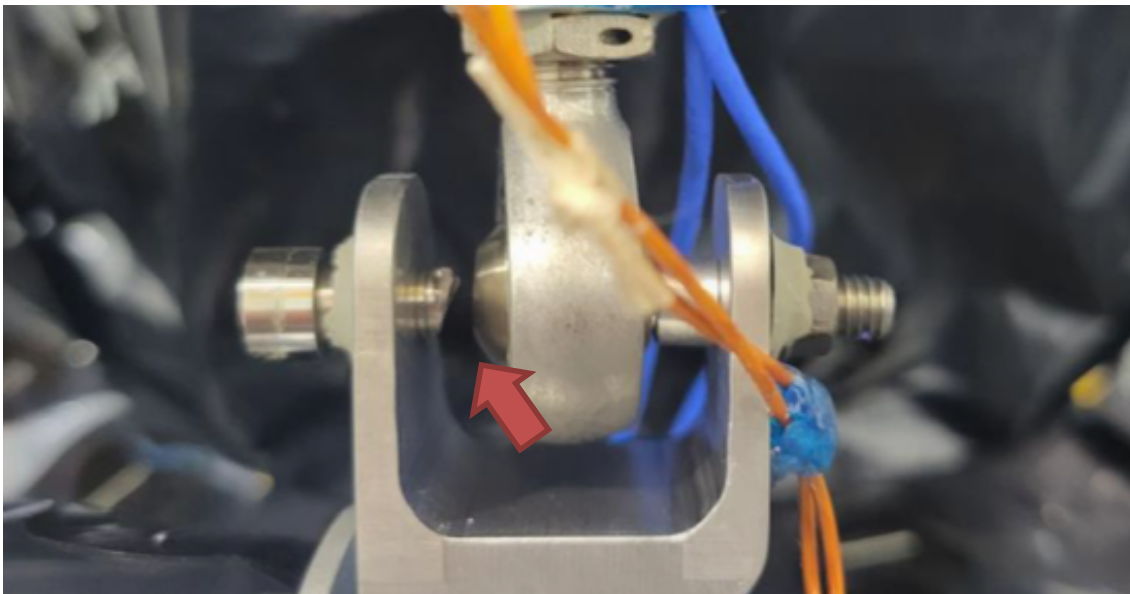


Figure 6. Broken Bolt

Cause of Failure:

Two separate causes were found.

1. A chamfer around the through hole of the ball of the spherical bearing was not on the drawing. This chamfer reduced the contact area between the ball and the two spacers on either side of the ball. The spacers yielded and the axial preload in the bolt was lost. Without the spacers participating in reacting the bending moments in the bolts, they no longer had positive margins and failed.
2. The spherical bearings developed some radial gaps which caused non linear behavior that was difficult to predict.

Corrective Actions:

1. The spacer size was increased to take into account the chamfer in the balls and reduce their stress. Fig. 7 shows the larger spacer.
2. The random vibration notching plan was updated to better define the notched profiles and protect the mechanism in case cross axis modes are excited during vibration.

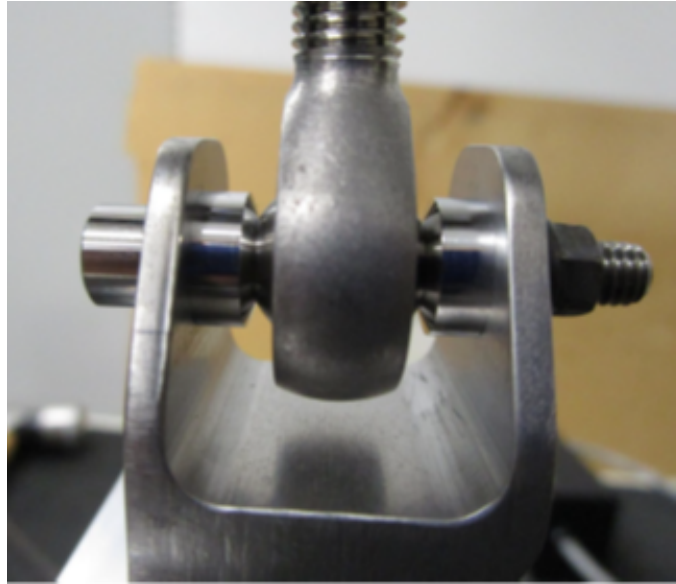


Figure 7. New Design

Lesson Learned:

Beware of small contact surfaces on parts. The effects of chamfers and internal radii are often missed in analysis.

Problems with Mobile Power Harness During Vibration

The thruster power cable bundle is provided by the thruster and therefore cannot be changed. Each of the 16 wires in that bundle has a jacket that contains silicone and as such is very tacky. This is not an ideal jacket for a mobile harness as rubbing between tacky wire jackets causes significant resistive torque and rapidly causes wear and debris. The final solution was to limit the motion of the mobile harness as much as possible by clamping it on the mobile plate as close as possible to the main spherical bearing. This configuration was tested on a BB prior to implementing it on flight equipment. Fig. 8 shows the third BB with the harness and piping installed and ready for vibration testing.



Figure 8. Third Harness and Piping BB

Problems with Holding the Piping During Vibration

One of the design challenges is to sufficiently hold down the gas piping during launch vibration while permitting it to be flexible enough to meet pointing travel and not impart too much resistive torque to the rotary actuators. Several breadboards were manufactured to come up with the current design. These BBs were first vibrated and then life tested through an accelerated life test. It is only on the third attempt that a satisfactory performance was achieved.

Lessons learned during testing:

1. Since there are two tubes through the mobile portion, their relative positions have to be well maintained to prevent inter tube chatter.
2. The tubes have to be permitted to move but their motion has to be controlled during vibration. Some sections of the tube are snubbed in the stowed configuration and some sections are permitted to impact plastic bumpers during vibration.

Conclusion

MDA has designed, manufactured and qualification tested an electric Thruster Pointing Mechanism that manages high temperatures, MMOD and radiation. Several flight units have now been manufactured and delivered. Problems were encountered during breadboard and qualification testing. They were resolved and the lessons learned during these activities were presented.

References

1. Horth, R.O., Godin, M.A. "Antenna Pointing System". US Patent Office (2015).
2. Horth, R.O., Godin, M.A. "Antenna Pointing System". EU Patent Office (2019).

Dry-Film Lubricated Ball Bearing Tests for High-Speed, Moderate-to-Long Life, Cryogenic Operation

Robert Wei*, Gale Paulsen*, Andrew Bocklund*, Nate Jensen*, Zach Begland* and Tim Newbold*

Abstract

A recent technology development effort at Honeybee Robotics aimed to achieve a successful dry-film lubricated (DFL) bearing configuration for a high-speed, moderate-to-long life, cryogenic application. The bearing test articles utilized a pair of soft-preloaded 7201-size (32-mm/12-mm OD/ID) angular-contact ball bearings and spun up to 14000 rpm in a 94 K (-179°C), GN₂ environment. Honeybee Robotics experimented with several different configurations of dry-film bearing cage materials, cage geometries, and raceway coatings.

One test configuration, which utilized a PGM-HT (PTFE glass-filled molybdenum disulfide, high-temp) cage material, survived to 60 hr and 38,000,000 revolutions[†] without experiencing any adverse performance trends or instances of dry cage instability – the primary failure mode for all other test units. This success seems to represent a novel data point in DFL bearing technology by sustaining higher speeds (10-14 krpm, or 120000-168000 dN, where dN = Bore ID [mm] x [rpm]) for cycles exceeding 10M.

However, four subsequent attempts failed to replicate this successful test and all exhibited similar patterns of bearing health degradation and early cage instability (~2M to 7M cycles). This paper discusses lessons learned from this effort and evidence for causes of successful and unsuccessful tests.

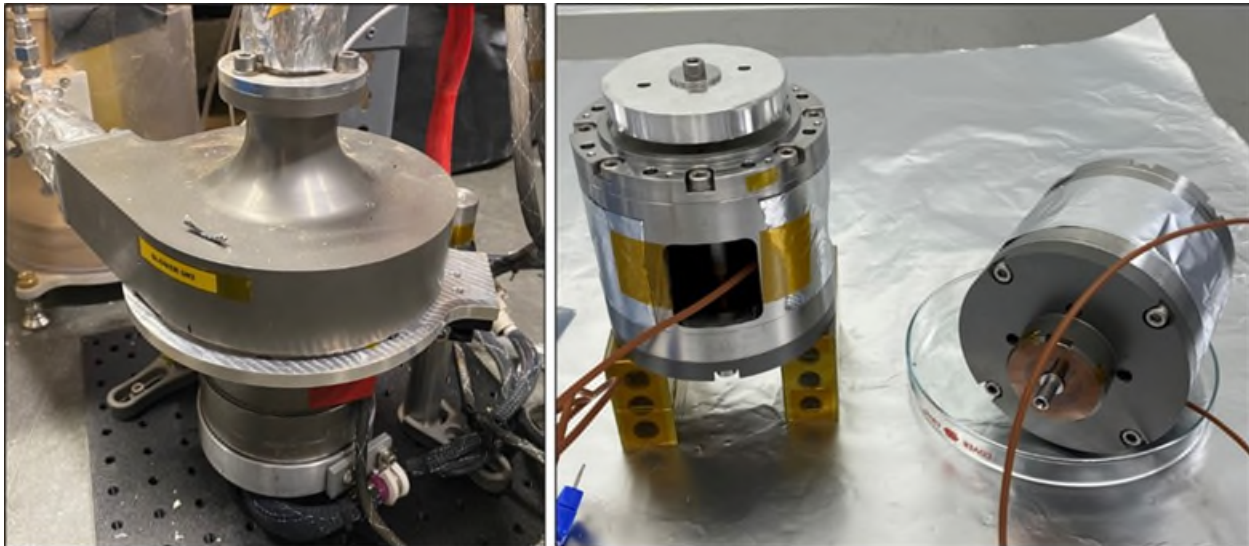


Figure 1: (Left) Barber Nichols BNHP-35G Prototype Blower, SN2;
(Right) Bearing Test Articles SN1A and SN2A after assembly

* Honeybee Robotics, Altadena, CA

† Note – Honeybee's main success criteria was reaching a cycle count that was driven by the project's mission requirements. This means, unfortunately, successful bearings were not tested to failure, but it is reasonable to assume that the eventual failure mode for this test would be related to excessive wear of the PGM-HT cage.

Introduction

The Dragonfly rotorcraft lander vehicle is a spacecraft designed to traverse the surface of Titan by powered flight, landing at different sites to collect and analyze local surface material. The vehicle consists of the primary spacecraft elements provided by Johns Hopkins APL, the DrAMS instrument provided by NASA GSFC, and the DrACO sampling system provided by Honeybee Robotics, as well as additional payloads.

The Pneumatic Transport System, one of four DrACO subsystems, relies on a blower mounted externally on the Dragonfly lander to provide pneumatic suction for material sampling on Titan. Operating in Titan's 1.45-atm, ~94K (-180°C) ambient environment presented an opportunity to explore development of dry-film lubricated (DFL) bearings, since DFL bearings are capable of withstanding cryogenic temperatures without the need for heaters or insulation.

Honeybee has few endeavors into the field of DFL bearings. Notable examples include the 460°C Venus motor and DrACO's Sample Acquisition Drill that sits adjacent to the blower on the outside of the Dragonfly Lander. However, the blower bearings life and speed requirements (24M revolutions, 14 krpm) present a unique challenge.

For blower bearing testing, four functionally identical test articles that approximated the notional blower's geometry were assembled. They underwent run-in and vibration testing before experimentation focused on different cage materials, geometries, and DFL raceway coatings. In total, eight DFL bearing configurations were tested, with only one, labeled "SN2A," proving successful.

Subsequent attempts to replicate SN2A's success failed due to dry-cage instability, suggesting sensitivity to design or environmental factors. Despite failures implicating bearing misalignment or cage design, successful testing exonerated potential causes like thermal gradients or raceway coating depletion.

These findings underscore the complexities of DFL bearing technology, with both successful and unsuccessful tests providing valuable insights for future developments.

Design – Description of Test Articles and Test Rig

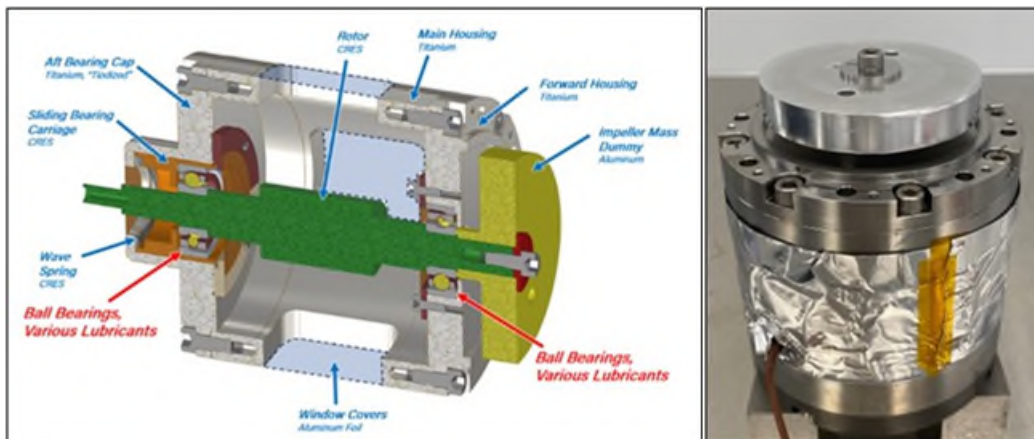


Figure 2: (Left) Labeled cross-section of the bearing test article, with common components labeled blue, and (Right) Photo of assembled bearing test article

Various bearing configurations were tested using a standardized test article design. Key components common to all configurations included a titanium housing, 15-5PH CRES rotor, aluminum flywheel, and a 17-4 CRES "Sliding Bearing Carriage" with an L/D ratio facilitating axial translation. The aft bearing remained fixed within the sliding carriage, while the forward bearing's outer race was clamped with an aluminum plate.

The assembled rotor shaft, flywheel, and fasteners were balanced to 25 krpm and balance grade 3.5 per ISO 1940-1 standards. Bearings, arranged face-to-face on the rotor shaft, were soft preloaded to 89±10 N (~20 lbf) using a wave spring, with preload verification conducted through force-displacement measurements. This soft-preloaded design was favored for its lighter preloads, lower contact stresses, and reduced sensitivity to thermal gradients and differential thermal expansion across operating temperatures (ΔT 's > 200).

Operating primarily under axial spring preload, the bearings experienced a maximum mean hertzian contact stress (mmhcs) of 758 MPa (110 ksi) and a peak stress of 1141 MPa (165 ksi). In recent tests, a lower preload of 67 N (15 lbf) was used, resulting in 648 MPa (~94 ksi) mmhcs. Highest non-operating loads are driven by the 14.1 G_{rms} random vibration environment, where a snubber was used to protect the bearings from excessive displacement.

Table 1: Ball bearing design stresses common to both test articles

Operating Condition	Nominal Spring Preload	Max External Load	Max Mean Hertzian Contact Stress	Notes
Non-Operational, MMC, Launch, 20°C, Axial Direction	89 N (20 lbf)	(From Test Data) 613 N (138 lbf)	1310 MPa (190 ksi)	All balls unloaded. No ellipse truncation.
Non-Operational, MMC, Launch, 20°C, Radial Direction		(From Analysis) 236 N (53 lbf)	1241 MPa (180 ksi)	5 of 9 balls unloaded. No ellipse truncation.
Operational, MMC (20°C)		(From Gas Flow) 4.5 N (1 lbf)	696 MPa (101 ksi)	
Operational, MMC (-190°C)		(From Gas Flow) 4.5 N (1 lbf)	758 MPa (110 ksi)	

Table 2: (Reference) Ball bearing parameters common to both test articles

Bearing Parameter	Characteristic
Original Stock P/N	GRW SV7201CEP4TAXULL001/CP1P2
Bearing Type	25-degree Angular Contact, outer race relieved
Static Capacity	3571 N (803 lbf) (catalog value based on metal balls)
Dynamic Capacity	7318 (1645 lbf) (catalog value based on metal balls)
Speed Limit	66000 RPM (catalog value based on metal balls, grease)
Material – Races	Cronidur 30 (X30CrMoN15-1)
Material – Ball	Si ₃ N ₄ (Replacing original X65Cr13 balls)
Outer Diameter	32 mm, +0, -6 μm
Inner Diameter	12 mm, +0, -4 μm
Width	10 mm, +0, -40 μm
Ball Size	5.953 mm ±0.025 μm (15/64" ±1 μin)
Balls per Bearing	9
Raceway Curvature	52% to 52.5% (As inspected)
Radial Play	0.045 mm (0.0018")
Axial Play	0.201 mm (0.0079")
Tolerance	P4 (ABEC-7)
Ball Grade	Grade 5

*All values nominal or catalog values unless otherwise noted

The bearings are made from COTS GRW 7201-size, 25-degree angular contact bearings and subsequently re-balled, re-caged, and re-lubricated based on the desired test configuration. A summary of the tested bearing configurations is shown in Table 3. A total of four bearing test articles were machined, labeled SN1 through SN4, with different serial number suffixes indicating distinct bearing configurations.

Table 3: Table of test article configurations & overall outcome in chronological order from left to right

Design Parameter	Test Article Configuration Serial Numbers							
	SN1	SN2	SN1A	SN2A	SN4A	SN2B	SN3C	SN1B
Cage Material	¹ Armalon	¹ Armalon	⁵ Vespel SP-3	⁴ JPM PGM-HT	⁴ JPM PGM-HT	⁴ JPM PGM-HT	⁴ JPM PGM-HT	⁴ JPM PGM-HT
Raceway Lubricant	² Microseal 200-1	³ HPS 2832	² Microseal 200-1 (Brg1) ³ HPS 2832 (Brg2)	² Microseal 200-1 (Brg1) ³ HPS 2832 (Brg2)	³ HPS 2832	³ HPS 2832	³ HPS 2832	³ HPS 2832
Cage Geometry	NES Cage PN 7201-3001	NES Cage PN 7201-3001	NES Cage PN 7201-3001	NES Cage PN 7201-3001	NES Cage PN 7201-3001	NES Cage PN 7201-3001	HBR Cage 32027998 "Hole-slot-hole"	HBR Cage 32027543 "GRW COTS Geometry"
Spring Preload [lbf]	20	20	20	20	20	20	15	15
Overall Outcome	Cage instability, cage fracture	Cage instability, cage fracture	Cage instability, test aborted	Successful test to 38M cycles. No indications.	Cage instability, test aborted	Cage instability, test aborted	Cage instability, test aborted	Cage instability, test aborted

1. American Durafilm TCGF-116 Teflon-Coated Glass Fiber, a.k.a. "Armalon"
2. E/M Coatings Microseal 200-1 (Impingement-applied MoS₂ DFL, 1.3 - 2 μm)
3. Hohman Plating HPS 2832 (Sputtered MoS₂ + Sb₂O₃ + Au, 0.2 - 1 μm)
4. PTFE Glass-filled Molybdenum Disulfide, High-Temperature made by JPM of Mississippi
5. DuPont Vespel Polyimide SP-3, 15% MoS₂ Filled

Bearing fits and tolerances conformed to design guidelines per NASA-SP-8048, Liquid Rocket Engine Turbopump Bearings, with exception of misalignment angle, which was not achieved in these bearing test articles.

The test rig refers to the assembly which houses and spins the bearing test articles while measuring their drag torque. The rig consists of a torque sensor attached to the test article's housing, a drive motor that spins the test article's rotor through a shaft coupler, and a structural housing. Speed, temperature, and torque telemetry were recorded for each test.

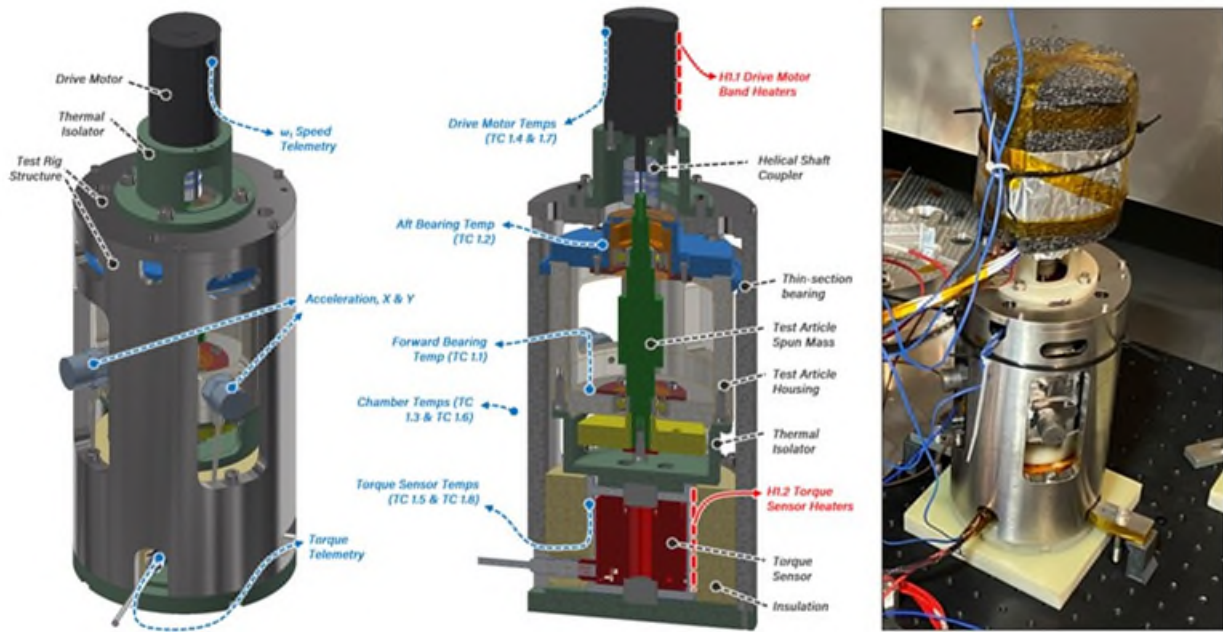


Figure 3: Bearing Test Rig with (left) labeled external components, (Center) labeled cross-section with the test article mounted inside, and (Right) a photo of the test rig in testing configuration

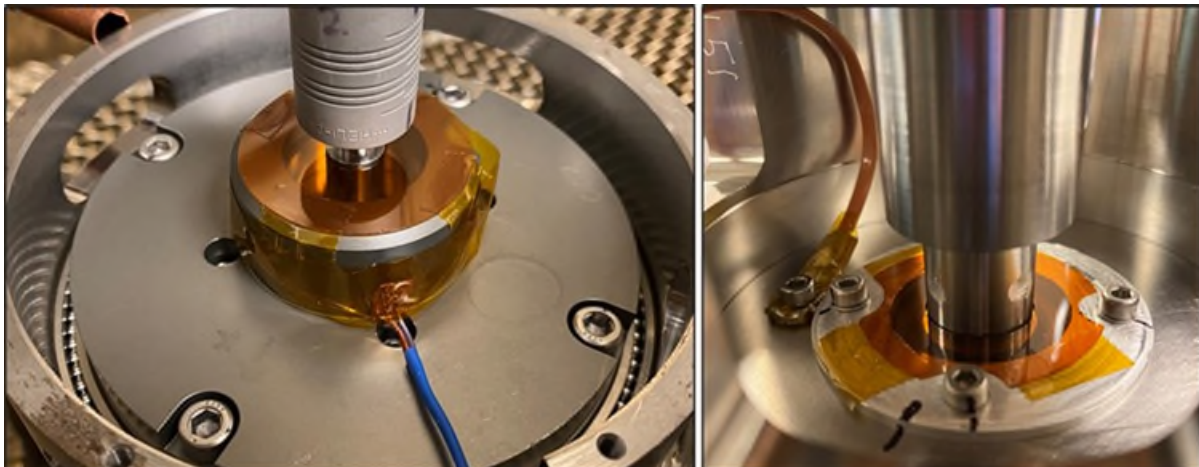


Figure 4: Post-Life testing images for SN2A of (Left) aft bearing thermocouple mounted to structure; (Right) forward bearing thermocouple bolted housing cap

Test Operating Specifications

The bearings' operating environment is driven by Titan's 1.45-atm, -180°C, and 95% GN₂ atmosphere. Due to feasibility constraints, tests were conducted at ambient pressure in a 100% GN₂ environment.

The required bearing cycles, speeds, and start/stops were defined by DrACO operating's requirements. These evolved slightly over the course of testing to observe test-as-you-fly principles, but overall, the target number of bearing revolutions representing 2x mission life was ~24M cycles. The primary operating speed was 10000 rpm, with 5-10% of cycles spent at 14000 rpm. Run-ins were performed at both room-temp and in cryogenic operating conditions, depending on whether the cage geometry enabled safe room-temperature operation. Exposure to a 14.1 G_{rms} random vibration environment for two minutes per axis was performed on a schedule-permitting basis, but this pre-conditioning step did not seem to affect test outcomes.

Table 4: (Reference) High-level list of bearing life testing parameters

Test Parameter	Room Temp. Cycles			Low-Temp. Cycles		
Atmosphere	>99% N ₂ (RH < 5%), ambient pressure (14.2 - 14.7 psia)					
Test Temperature	25 ±5°C			-180 ±5°C		
Start Stops	-			100		
Operating Point 1 *incl. run-in <10 krpm	10000 rpm	35 min	280000 revs*	10000 rpm	2200 min (36.7 hr)	21.6M revs*
Operating Point 2	N/A			14000 rpm	108 min	1.51M revs

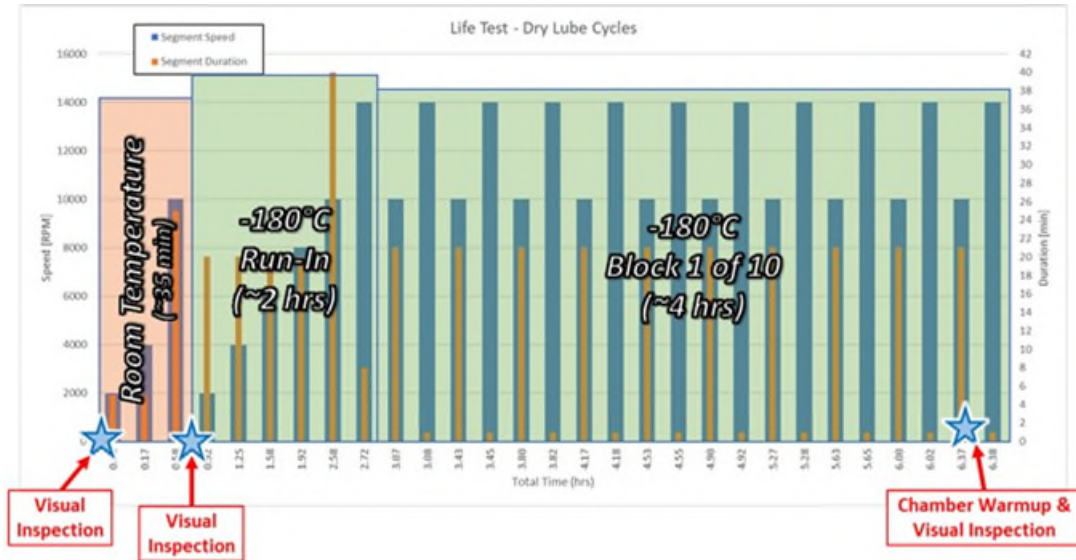


Figure 5: Example of a bearing speed/duration/start-stop schedule depicting a room temp. and low temp run-in, and low temp operation

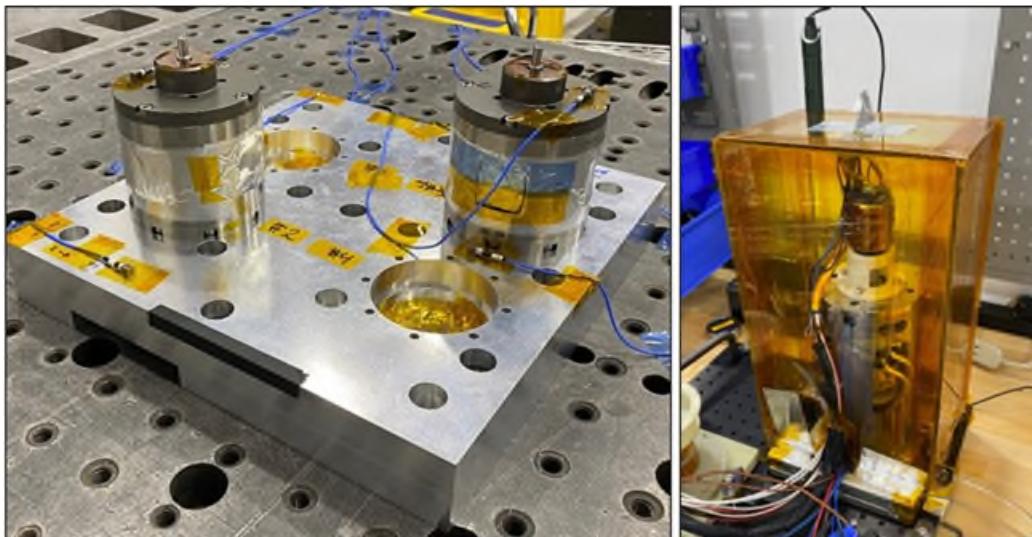


Figure 6: (Left) Bearing test articles mounted to vibration fixture; (right) bearing test rig in N₂-purged box for room-temperature run-in

Test Results - Summary

A high-level summary of tested bearing configurations and respective outcomes is shown in Table 5. The “performance” rows are intended to provide qualitative insight for when bearings began to exhibit off-nominal behavior, based on personal observation. More emphasis will be placed on the PGH-HT cage configurations – the other cage materials seemed inappropriate for this application.

Table 5: Table of test article initial serial number configurations.

Design Parameter	Test Article Configuration Serial Numbers							
	SN1	SN2	SN1A	SN2A	SN4A	SN2B	SN3C	SN1B
Cage Material	Armalon	Armalon	Vespel SP-3	JPM PGM-HT	JPM PGM-HT	JPM PGM-HT	JPM PGM-HT	JPM PGM-HT
Raceway Lubricant	Microseal 200-1	HPS 2832	Microseal 200-1 (Brg1) HPS 2832 (Brg2)	Microseal 200-1 (Brg1) HPS 2832 (Brg2)	HPS 2832	HPS 2832	HPS 2832	HPS 2832
Cage Geometry	NES Cage PN 7201-3001	NES Cage PN 7201-3001	NES Cage PN 7201-3001	NES Cage PN 7201-3001	NES Cage PN 7201-3001	NES Cage PN 7201-3001	HBR Cage 32027998 “Hole-slot-hole”	HBR Cage 32027543 “GRW COTS Geometry”
Spring Preload [lbf]	20	20	20	20	20	20	15	15
Pre-Conditioning								
RT Run-in	yes	yes	yes	yes	yes	no	no	no
LT Run-in	no	no	yes	yes	yes	yes	yes	yes
Random Vibe	yes	yes	yes	yes	yes	no	no	no
Performance								
<i>First indication of raceway lubricant loss</i>	Not tracked	Not tracked	1.4M revs	N/A	2.4M revs	2.0M revs	1.8M revs	1.6M revs
<i>First high-drag upset event</i>	Not tracked	Not tracked	2.1M revs	N/A	4.4M revs	1.3M revs	N/A	5.8M revs
<i>Onset of persistent instability</i>	Not tracked	Not tracked	2.3M revs	N/A	4.6M revs	2.4M revs	2.5M revs	6.4M revs
<i>Test abort (arbitrary determination)</i>	28M revs (2x life)	28M revs (2x life)	3.4M revs	38M revs (3x life)	4.6M revs	2.5 M revs	4.2M revs	6.9M revs
Overall Outcome	Cage instability, cage fracture	Cage instability, cage fracture	Cage instability, test aborted	Successful. No adverse indications.	Cage instability, test aborted	Cage instability, test aborted	Cage instability, test aborted	Cage instability, test aborted
Fwd Cage Health	Fractured	Fractured	High Wear Debris	No Issue	Excessive Debris	-	-	-
Aft Cage Health	Wear Debris	Frayed Cage	No Issue	Some wear debris	No Issue	-	-	-

Test Results – SN1, SN2: Armalon Cages

The first two bearings with Armalon cages both experienced cage instability almost immediately, exhibiting high drag torques (>50 mN-m (7 in-ozf) at 10 krpm) and bearing ΔT 's >50°C. Despite this, the bearings were operated for 28M cycles and revealed significant wear debris and cage fractures upon disassembly and inspection (an expected outcome of running unstably for prolonged periods of time).

For both test articles, the forward bearing cage was in much better condition than that of the aft bearing. This pattern reappears in subsequent tests with different bearing cages, indicating a potential design issue. A low temperature run-in was not performed for these bearings, and very high initial operating temperatures were observed. After these tests, a run-in was always performed in the target operating environment.

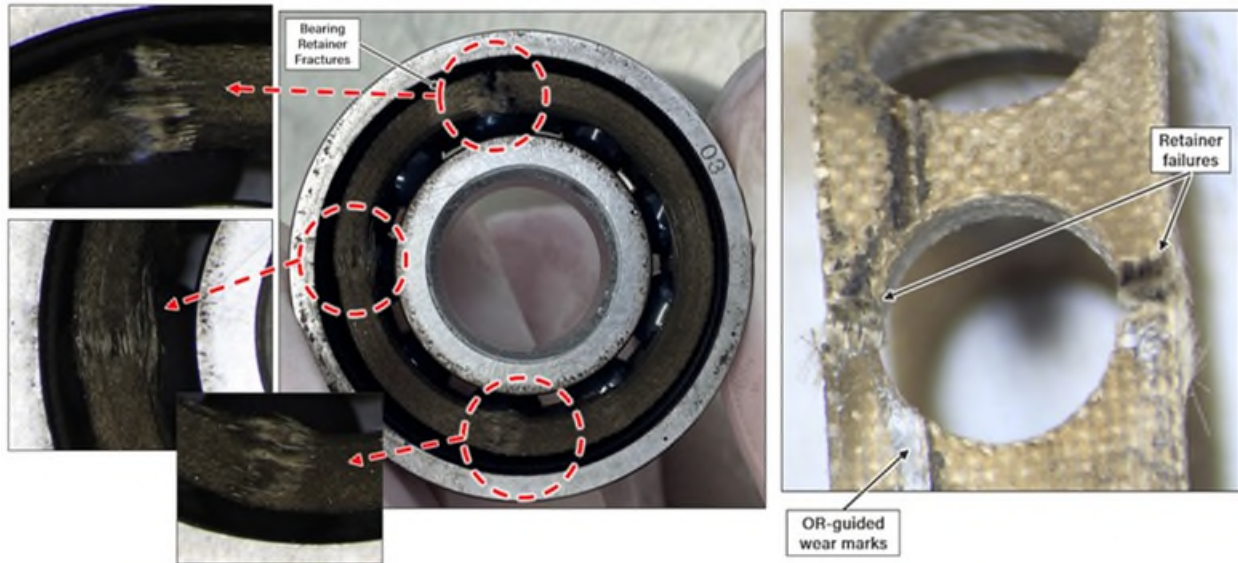


Figure 7: Armalon retainer damage after extended unstable operation

Test Results – SN1A (Vespel SP-3) & SN2A (PGM-HT)

Armalon proved ineffective in maintaining adequate lubrication for our application. Subsequent cages were machined from sacrificially-wearing, self-lubricating composite materials designed to replenish lubricant via wear particles containing dry-film lubricant generated during ball-to-retainer contact. Candidate materials included Salox M, Rulon E, and Rulon AMR, with the final choices of PGM-HT and Vespel SP-3 based on recommendations from Michael Dube of NASA NESC and research by Michael Buttery from ESTL^[4], which also endorsed PGM-HT.

Test article SN1A utilized Vespel SP-3 cages, a polyimide material containing 15% fill of molybdenum disulfide. Vespel SP-3 is used in spacecraft bearing cages for its dimensional stability across a wide temperature range and vacuum lubricity. However, this cage material exhibited instability within 10% of the target mission life, prompting a test abort. Inspection afterwards revealed excessive particulate debris generation.

Test article SN2A used a retainer made from PGM-HT, a randomly oriented, glass-fiber reinforced, PTFE sheet containing molybdenum disulfide and manufactured by JPM in Mississippi. SN2A exhibited highly consistent behavior and low drag torques (<1 in-ozf) throughout its life test and beyond, over 3x the required mission life, or 38M revolutions.

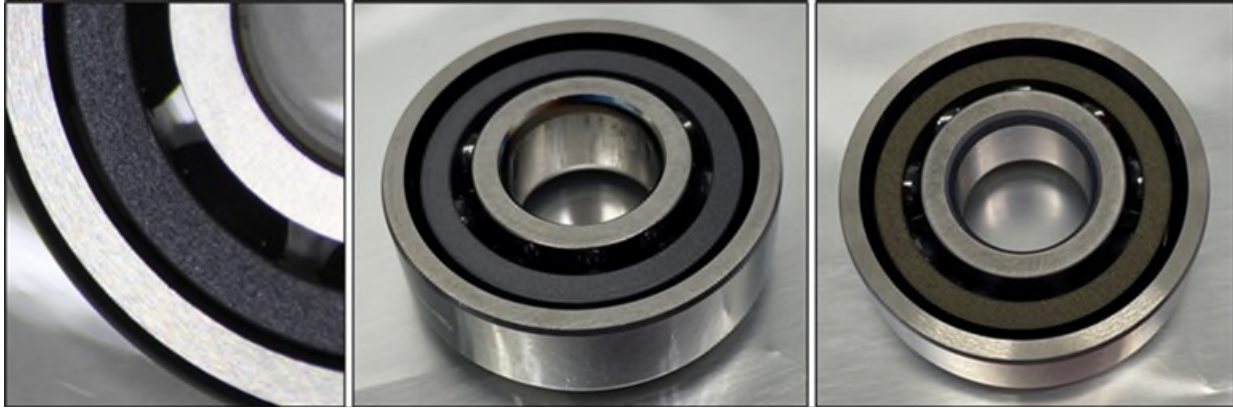


Figure 8: (Left) Microscope image of PGM-HT cage; (Center) Bearing with PGM-HT cage (grey-blue); (Right) Bearing with Vespel SP-3 cage (brown)

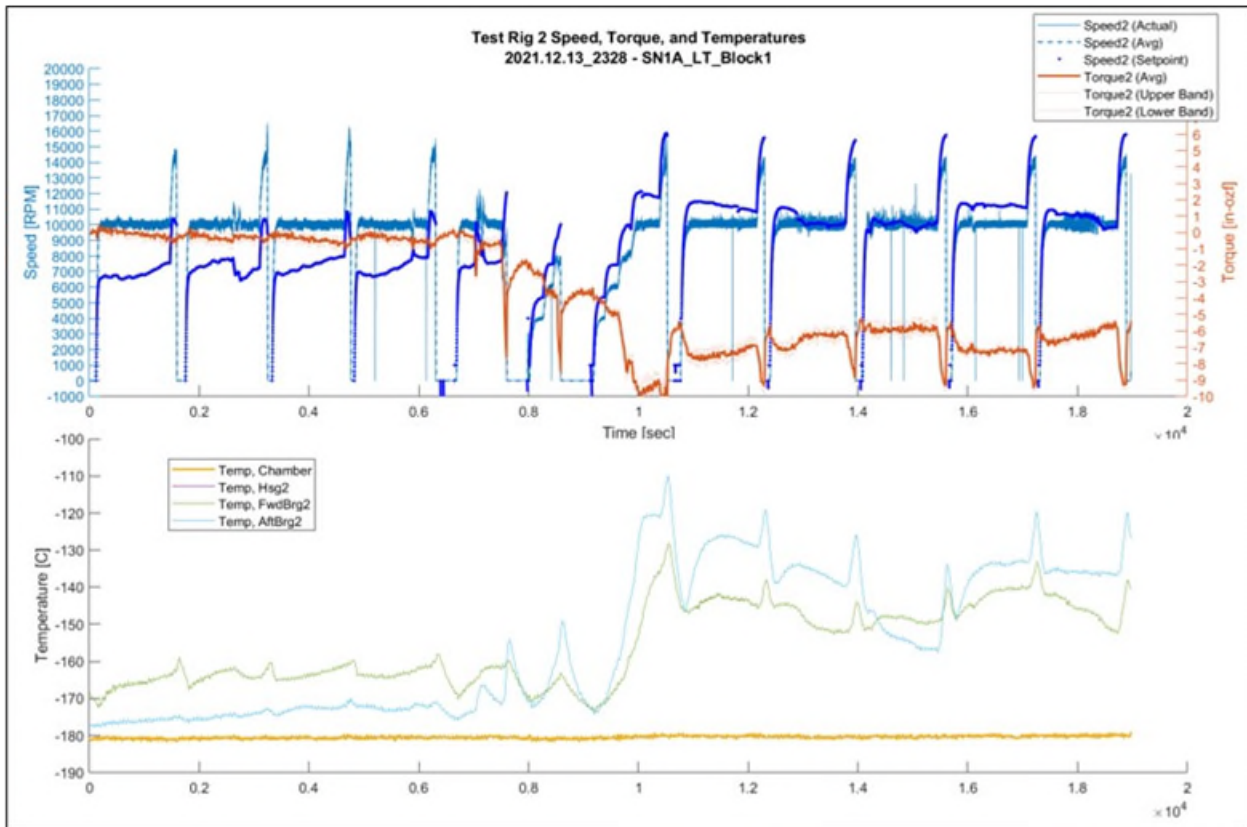


Figure 9: SN1A -180°C Life Testing, Block 1 of 10. (Top half) Note how motor power, tracked with the dark blue line, gradually-increases. Torque (orange line) increases as well in the negative direction. (Lower half) Bearing temperatures, shown in blue and green, spike after SN1A's transition to persistent instability

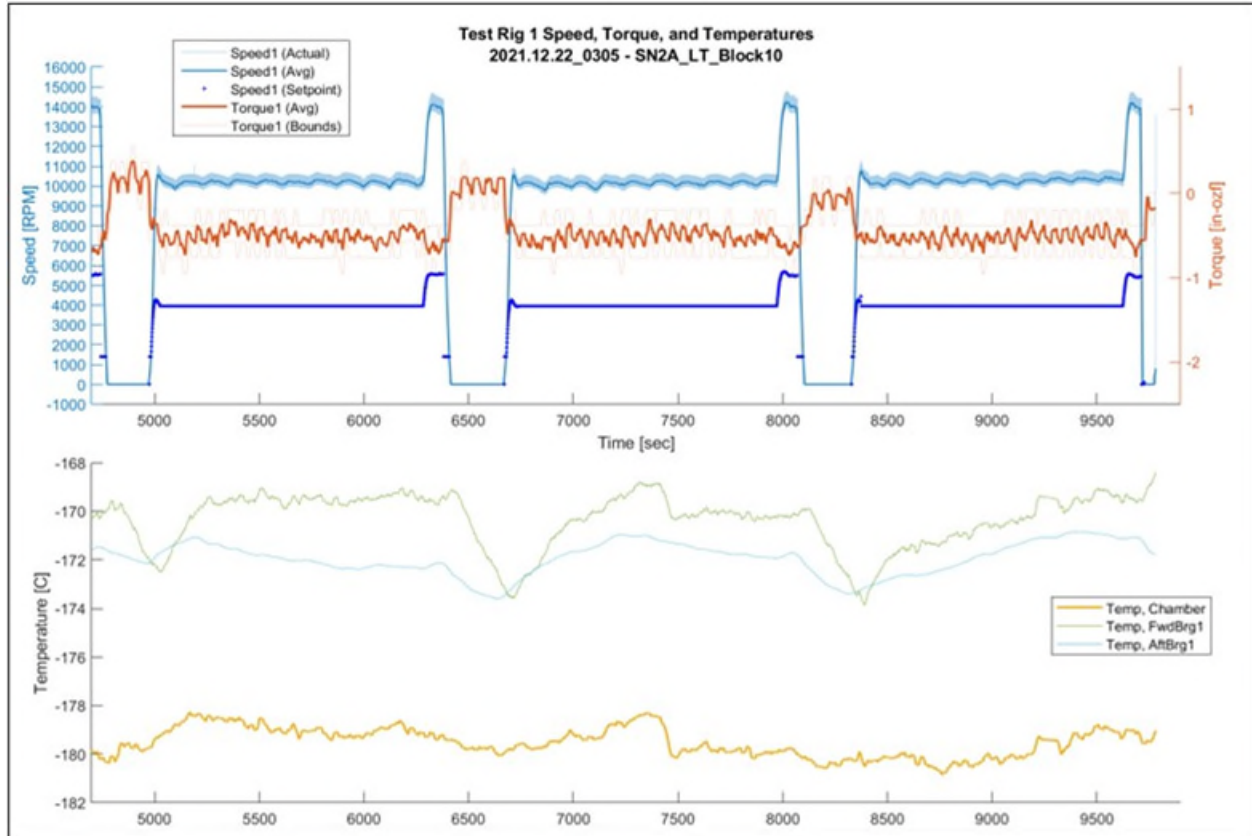


Figure 10: SN2A -180°C Life Testing, Zoom-in on Blocks 10.8 Through 10.10 (Final hours before achieving 2x Life). Note the consistency of the telemetry.

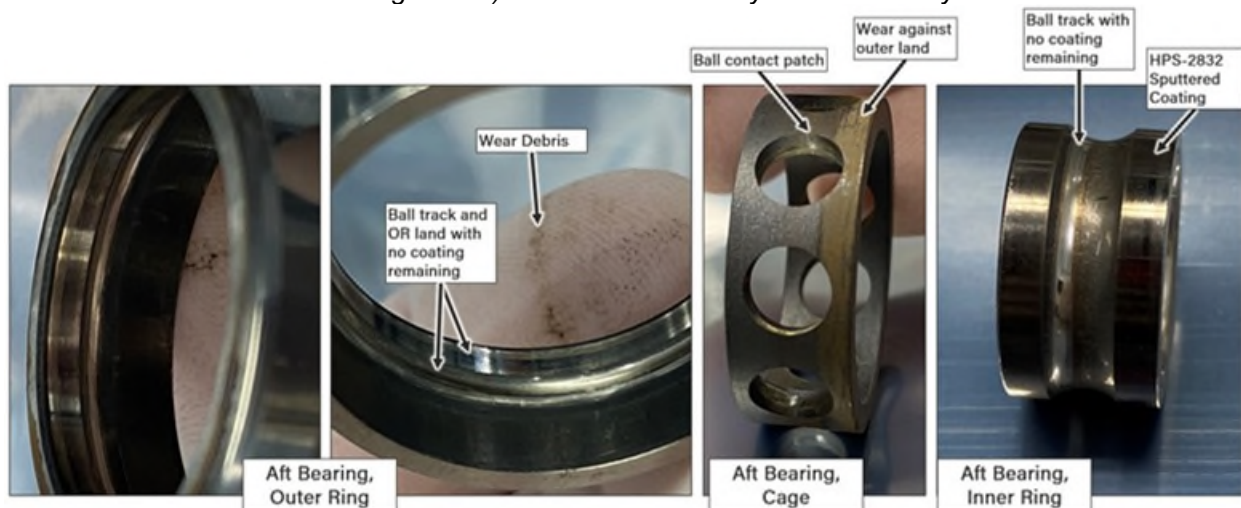


Figure 11: Photographs of Test Article SN2A's disassembled DFL bearings with PGM-HT cages after a successful life test

Test Results –Attempts to Replicate Successful PGM-HT Test; New Cage Designs for Improved Stability

Immediately following the successful test of SN2A, the same test configuration was re-tested twice. However, both tests were aborted due to presence of cage instability within the first 20% of target life. This implies sensitivity to some aspect of the design which was not understood.

A fault tree conditionally implicated several items, among which included improper cage design. Up to this point, all the bearings featured a ball-piloted cage design, but a land-guided cage design, among other suggestions, was recommended for improving cage stability. Two new bearing cages were tested, that satisfied additional criteria based on recommended dry-film bearing cage clearances:

- (M. Balzer, P. Ward) Ball pocket clearance should be 20-30% larger than guiding land clearance to ensure cage is land-piloted
- (Gibson, NASA/TP-2019-220549) Ball pocket clearance should be 2.5-3.5% of the ball diameter
- (NASA-SP-8048) Guiding land clearance should be at least 0.3% of the guiding land diameter

Parameter	Unit	GRW 7201 Value	NES Cage for HBR ETU (Baseline, P/N 7201-3001)			Custom Cage #1 (GRW COTS Cage Geometry) 32027543			Custom Cage #4 (Max Cage OD, Hole-slot-hole) 0.63 mm slot width 32027998		
			NOMINAL	MIN	MAX	NOMINAL	MIN	MAX	NOMINAL	MIN	MAX
LOW TEMPERATURE											
GRW Bearing - OR Land Dia	mm	26.156									
GRW Bearing - IR Land Dia	mm	17.770									
Pitch Diameter	mm	21.963									
Ball Diameter	mm	5.949									
Cage OD	mm	(Radial CTE)	25.52	-0.050	0.050	25.62	-0.059	0.059	25.78	-0.059	0.059
Cage ID	mm	(Radial CTE)	20.72	-0.050	0.050	20.37	-0.059	0.059	20.57	-0.059	0.059
Cage Thickness	mm		2.399			2.624			2.608		
Cage Width	mm	(Axial CTE)	8.68	-0.100	0.100	8.68	-0.098	0.098	8.68	-0.098	0.098
Ball Pocket Diameter	mm	(Axial CTE)	6.08	-0.050	0.050	6.26	-0.059	0.059	6.41	-0.059	0.059
Slot Length (Circumferential)	mm	(Axial CTE)	0.00			0.00			0.39		
Ball to Ball-Pocket Clearance (Diametral)	mm		0.135	0.085	0.185	0.310	0.251	0.369	0.459	0.401	0.518
OR Guiding Land Clearance	mm		0.637	0.587	0.687	0.537	0.477	0.596	0.372	0.312	0.431
IR Land Clearance	mm		2.951			2.600			2.798		
Cage Design Conditions:											
[1] Ball-pocket clearance / piloting circumferential clearance = +20% to +30%			-79%	-88%	-68%	-42%	-58%	-23%	129%	84%	192%
[2] Ball pocket clearance should be 2.5% to 3.5% of ball diameter			2.3%	1.4%	3.1%	5.2%	4.2%	6.2%	7.7%	6.7%	8.7%
[3] Guiding land clearance should be at least 0.3% of guiding land diameter			2.4%	2.2%	2.6%	2.1%	1.8%	2.3%	1.4%	1.2%	1.6%
Non-guiding land clearance should be at least 2x guiding land clearance			4.6			4.8			7.5		
Pitch diameter within Cage OD/ID?			Yes			Yes			Yes		

Figure 12: Comparison of new cage geometries vs original cage geometry (NES 7201-3001) taking into account CTE and -180°C operating temperatures.



Figure 13: Images showing new bearings with HPS-2832 coating on raceways, and a custom PGM-HT cage with a hole-slot-hole ball pocket configuration prior to assembly

These new cages were tested in test articles designated SN3C and SN1B. As before, both test articles also encountered instability and aborted within the first ~25% of life, which does not represent a significant improvement.

Analysis – Patterns of Degradation

In the dry-film bearing tests, a consistent failure pattern emerged, typically beginning with gradual degradation in torque and current telemetry. This was followed by intermittent "high-drag" upsets or torque anomalies that increased in frequency. Eventually, the bearings experienced persistent, irrecoverable cage instability. The initial degradation in performance may stem from raceway lubricant depletion, as bearings tend to run smoothly for the first ~1.5 million revolutions regardless of cage design or material. Subsequently, there may be a period of steady state operation before sudden torque anomalies occur.

SN2A's successful test did not exhibit increases in torque after initial run-in or sudden torque anomalies. However, the appearance of high-torque anomalies typically indicates that persistent, irrecoverable instability will arise within the next 1 million cycles (<2 hr)

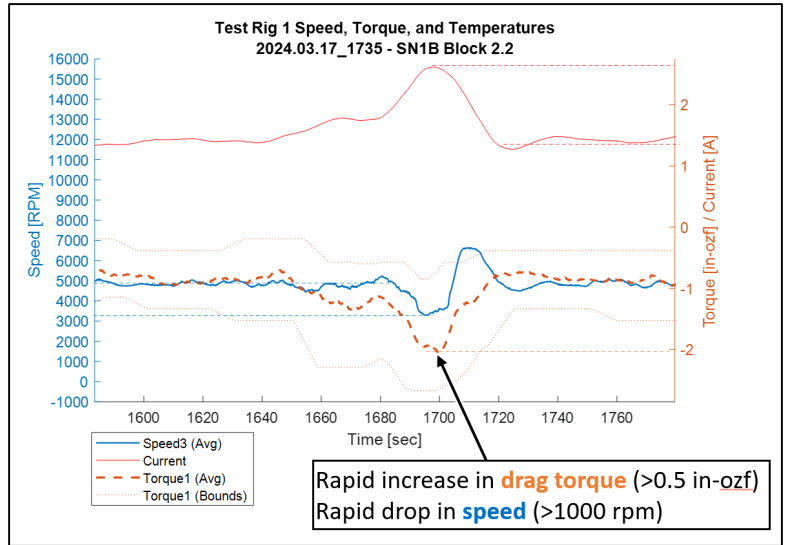


Figure 14: Example of a torque anomaly for Test Article SN1B. Note the increase in torque, decrease in speed, and increase in compensatory current. Eventually, the bearings will operate persistently within this regime, indicated generally by high current, speed v

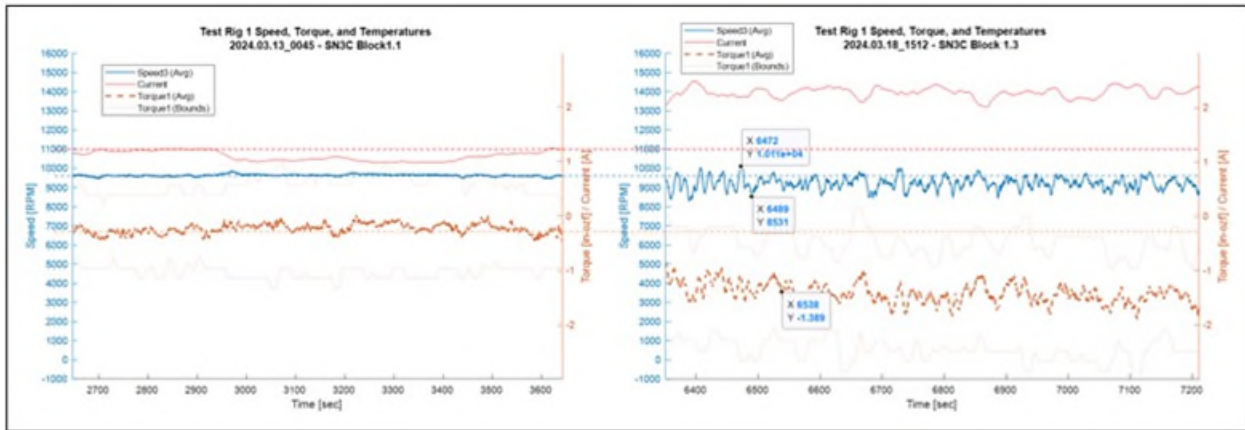


Figure 15: Telemetry for Test Article SN3C comparing (Left) flat, steady torques, currents, and speed at the beginning of life, vs (Right) doubling of current, drag torque, and speed variations around ± 1000 rpm

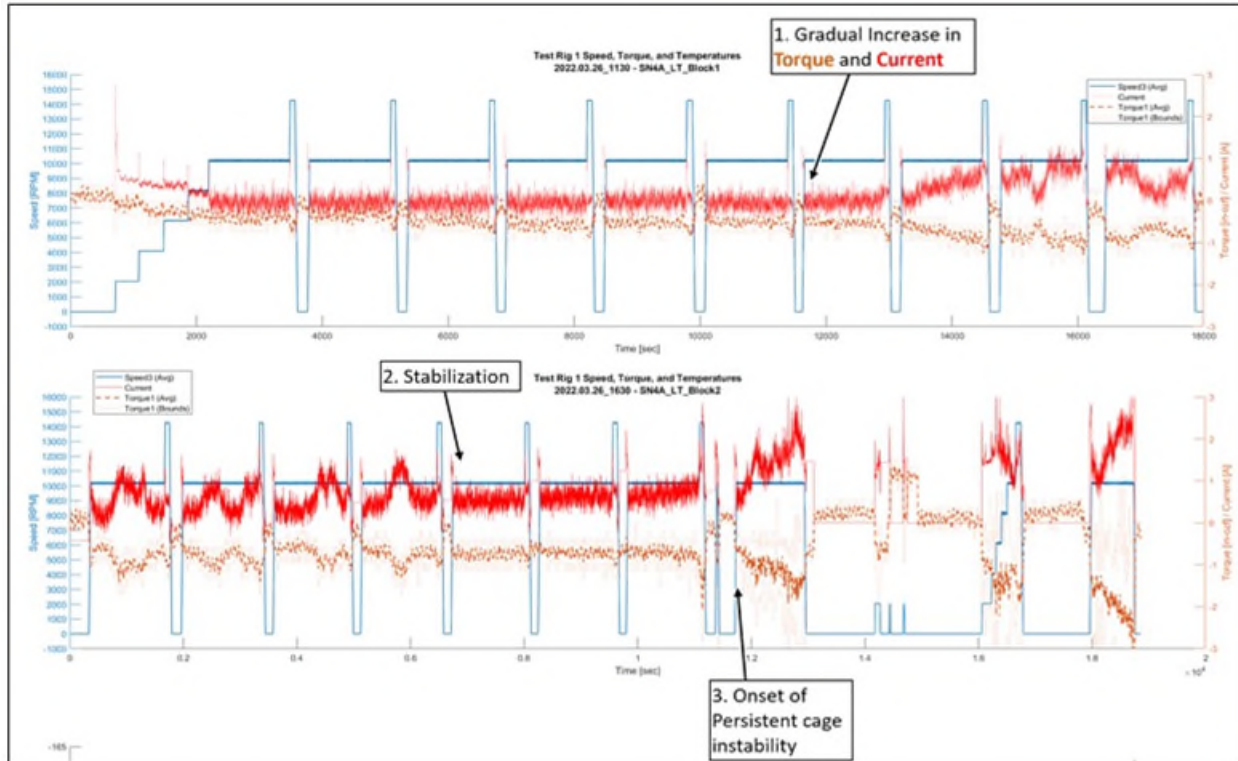


Figure 16: Torque, Speed, and Current telemetry for Test Article SN4A, showing progressive degradation from (Top) the first 10% of the life test, to (Bottom) the second 10% of the life test, which was aborted prior to completion.

Conclusions and Future Work

Common issues for bearing cages in unidirectional motion include cage hang-up and cage instability^[1]. Hang-ups are characterized by high torque throughout bearing rotation, rough running, excessive temperature rise, and rapid cage failure. Hang-ups can occur due to ball speed variation[‡], which is caused by misalignment, ball size variation, and forces that keep balls in contact with the raceway, preventing them from moving freely such as thrust loads or high-speed centrifugal loads.

Cage instability, on the other hand, involves excessive motion of the cage leading to damaging collisions with other components in the bearing system[‡]. Symptoms include increased friction torque, temperature, and noise from high frequency excitation of the cage. However, unlike cage windup, instability usually gets worse as the cage wears.

While the design contains risk factors for both issues, the bearings seem to exhibit symptoms of instability, because the bearings become progressively worse over time, accelerometer measurements indicate high frequency content at frequencies >2000 Hz and audible noises consistent with instability have been observed.

The failures from testing previously successful bearing configurations suggests sensitivity to the design of the test article. Cage designs with near zero stability margin will be highly sensitive to any change. Furthermore, the *similarity* of the failure patterns between different cage designs and configurations may indicate a common flaw between test articles, agnostic of the bearings being tested. Prior to additional testing, two possible areas to address are identified:

[‡] Balzer, Mark, Mar 2024

1. Cage guidance: All cages were outer race guided, which had a relieved land, instead of guided using a non-relieved land. Per Munro[1], “the ultimate decision on the running land is based on which race is relieved,” and it would make sense to test inner-race guidance, which provides a symmetric piloting surface for the cage.
2. Cage clearances: the DFL bearing’s lubricant consumption at the ball-pocket interface must be equal to the consumption at the ball-to-race interface, and this double-transfer equilibrium is difficult to predict and balance[§]. The successful cage design could have been borderline sufficient, but subsequent cage designs, which all had *larger* ball pocket clearances, could have been inadequate.

Future iterations could also consider other potential changes:

- Lower raceway conformity (e.g., 57% instead of 52%), which generates a smaller contact patch, less sliding friction, and a decrease in overall drag and rate of lubricant consumption^[2]
 - o Lower conformity may also improve tolerance to dry-lubricant debris buildup
- The test article’s “aft” bearing interface, which was not clamped inside the “sliding carriage”, seemed to degrade more quickly than the forward bearing and may be worth revisiting.

Lessons Learned

1. Dry-lubricated bearings can be highly sensitive to tolerances, as evidenced by the fact that only one of three “identical” test configurations successfully passed.
2. The ball retainer in a DFL bearing is critical, and because dry cage instability is difficult to predict analytically or root cause, determining optimal cage design can be iterative. Be prepared with several different cage designs and/or materials, which enable quick iteration.
3. Raceway coating is not as important as cage geometry/material.
 - a. Thin MoS₂ coatings applied to bearing races and/or balls wear away quickly and are not necessary for DFL bearings using a self-lubricating cage, but coatings can provide lower run-in friction while ball pocket contact patches wear-in on the cage^[4].

Acknowledgments

The authors thank external reviewers such as Mark Balzer (JPL), Mike Dube (NESC), Stu Loewenthal, Dino Christopoulos, Ron Hayes, and the members of the DrACO team for their expert guidance and support.

References

1. Munro, G. J., et al., The Impact of Cage Design on Ball Bearing Torque Behavior, ESTL/ESA SP-653, 2007
2. Loewenthal, Stuart H. “Two Gimbal Bearing Case Studies: Some Lessons Learned.” 22nd Aerospace Mechanisms Symposium, NASA, 1 May 1988.
3. Buttery, Michael, et al., Modern Self-Lubricated Composites for Space Applications: PGM-HT & Sintimid 15M, ESTL, 14th ESMATS, 2011

[§] Christopoulos, Dino, July 6, 2022

Cold Welding under Space and Launch Conditions

Roland Holzbauer^{*}, Andreas Merstallinger^{*}, Lionel Gaillard^{**} and Nathan Bamsey^{**}

Abstract

A common failure mode seen during the testing and operation of spacecraft is termed 'cold welding' ('contact welding', 'adhesion', 'sticking' or 'stiction'). Cold welding is a solid-state welding process in which joining takes place without fusion or heating at the interface of the two parts to be welded. This effect mainly concerns metal-to-metal contacts. Contacting parts may stick together and their separation forces might be higher than expected – e.g., at hold-down-and-release mechanism. This paper presents risks of cold welding in design and material selection, basic rules, and how to overcome the risk of cold welding in space mechanisms.

Introduction

Cold welding was first recognized as a general materials phenomenon in the 1940s. It was then discovered that two clean, flat surfaces of metal might strongly adhere if brought into contact in vacuum. This effect is seen mainly in metal-metal-contacts, but also with the addition of vibration (fretting [2]). Cold welding is a significant issue that spacecraft engineers need to consider.



Figure 1. Galileo spacecraft (photo credits: Courtesy NASA/JPL-Caltech.)

In 1991, the Galileo spacecraft (Figure 1) high-gain antenna failed to fully deploy due to cold welding issues. Investigations showed that three ribs of the umbrella-shaped antenna were cold welded in the folded configuration. Vibrations during transport and lift-off caused damage on the coating that exposed bare metal-metal contacts. It was concluded that the wear rate of the coating used is higher in air than in vacuum and was already worn out when it was needed [1].

^{*} Aerospace & Advanced Composites, Austria, roland.holzbauer@aac-research.at

^{**} European Space Agency, Noordwijk, The Netherlands

Bending of wire harnesses in vacuum may lead to cold welding of single wires of a wire strand – see Figure 2. Cold welded wires lead to increased stiffness of the harness and needs to be considered in the motorization margin of the mechanism. On the other hand, cold welded wires may also lead to the breaking of wires, which lead to electrical overload of the harness.

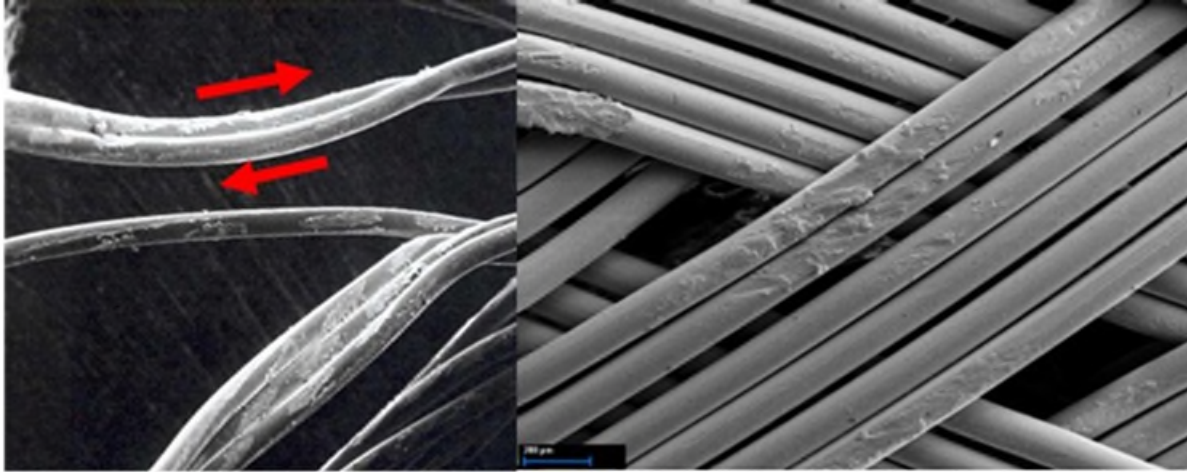


Figure 2. stranded wires with typical signs of cold welding (photo credits: AAC)

Another reported mechanism failure due to cold welding is shown in Figure 3. This picture illustrates how the anchor (Y-piece), manufactured from a magnesium alloy, has cold welded against one of the end stops (labelled C in Figure 3), which is also made of a similar magnesium alloy. All corrosion protection coatings on these alloy parts have been “knocked” away due to several hundreds of thousands of impacts to leave bare metallic contacting points. The photograph shows the sister mechanism after ground-based tests performed under vacuum in order to assess the in-orbit anomaly. In technical terms, the adhesion forces were greater than the separation forces available from the spring in this mechanism moving the anchor to the center position.

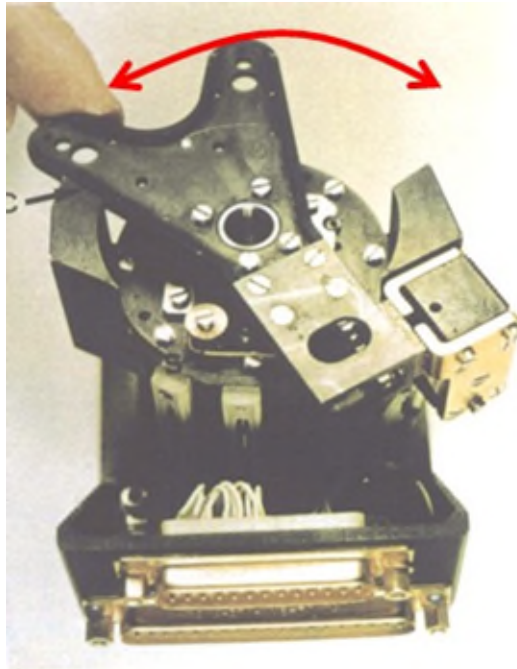


Figure 3. Anchor with cold welding at end stop (picture taken from [4])

Typical mechanism prone to cold welding

In general, metal – metal contacts on a spacecraft are at a high risk of cold welding. These are namely: HDRM (Hold Down and Release Mechanism), stranded wires, mechanical end stops, gear toothing, bearings, slippers and many more.

Cold Welding vs. Galling

Cold welding is a process where two clean, flat surfaces of metal strongly adhere if brought into contact while in a vacuum without fusion or heating at the interface. [4] The term “cold welding” was agreed between ESA and AAC in early 1995 when setting up a test method to measure adhesion forces after impact (without lateral motion, to explain the failure described above). Second reason was to keep publications on this effect traceable, as the term “adhesion” is dominated by “adhesion of coatings to their substrates”.

Physically spoken, this effect is only of technical relevance between two metals and even then, only if both surfaces are clean enough to enable direct contact between two metal atoms (without any oxides in between). Then even a static contact can cause adhesion, but at levels being much too low to be of technical relevance [4]. Levels increase under impact and fretting. This situation appears only in vacuum (space) if surface layers (natural or artificial) are removed. On the ground, the effect gets only visible when tightening austenitic screws too strongly or in the process of friction welding. Although, in rotation welding, friction is used to heat up both partners and the weld is established by a vertical push after stop of rotation. It shall also refer to the test method where the vertical separation force is measured (STM-279). Often indirect assessments need to be done, e.g., metallographic analysis after shaker tests (in air) or bread board tests (in vacuum) thereby analyzing the microstructure (see Figure 4). The presence of grain fining / mechanical alloying of the subsurface region is then used to state that risk of cold welding is evident. And here we overlap with galling.

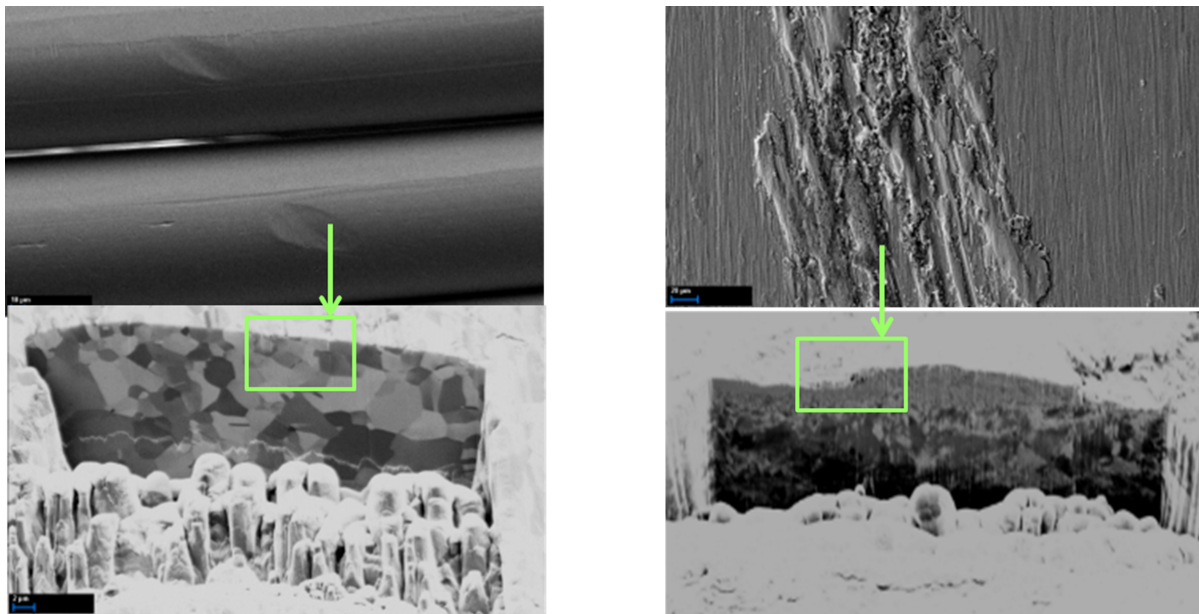


Figure 4. Left: Subsurface with unchanged microstructure (negligible risk of cold welding “static”) Right: Severe subsurface damages (cold welding very likely) overlapping with galling (photo credits: AAC)

Galling is a process of adhesive wear between sliding surfaces. The outgrowth from the adhesive bonds between two rubbing metals are the criterion to decide if galling occurred. [5]

Those definitions of cold welding and galling indicate that both processes are not mutually exclusive. The broadly defined notions of galling and cold welding between two metal surfaces overlap in many instances, moreover as only lateral motions (fretting) are causing technically relevant adhesion forces. A joint between two metallic surfaces might be the result of both cold welding and galling. This paper does not exclusively differ whether the process of adhesion is due to galling or cold welding but put its emphasis on the risks for space mechanisms due to joining between metals and gives basic recommendations to avoid those. In the following, the joint between two metallic surfaces is referred to as cold welding without making a distinction as to whether it was exclusively cold welding or galling.

Cold Welding Measurement with Pin on Disc under Fretting

All further presented data, results and conclusions are based on tests with a tribometer which consists of a vertically moveable pin with a spherical contact area and a fixed flat body (disc) – see Figure 5. The pin is fixed to a pushrod which is suspended by plate springs. Through a bellow, the pushrod goes through an electromagnet which applies the load. Unloading is realized by a spring mounted outside the vacuum chamber. The loading and adhesion forces are measured by piezo transducer mounted directly below the disc in vacuum. The vacuum chamber is pumped by an ion getter pump to ensure vibration free measurements. Fretting tests can be performed down to typically 10^{-5} Pa. Fretting movement is introduced via a piezo actuator for a stroke of $50\ \mu\text{m}$. (For the following neither static nor impact conditions are included.)

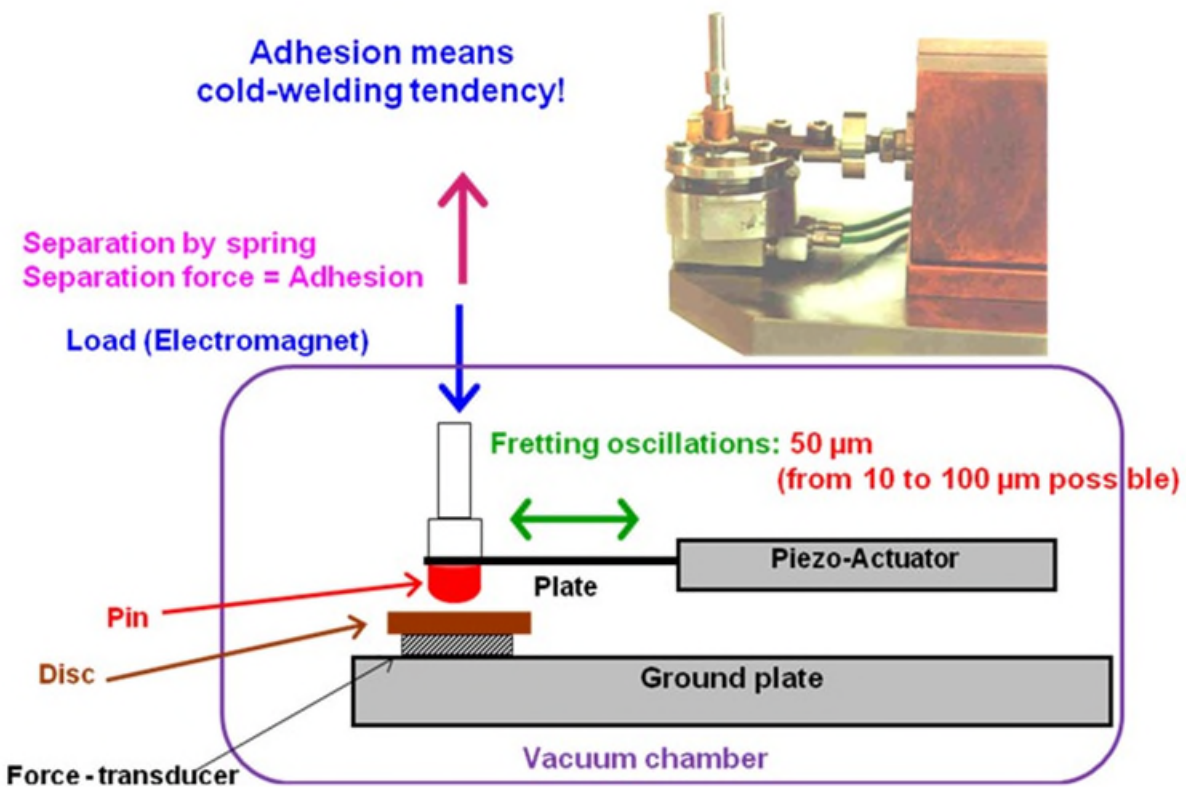


Figure 5. Scheme of fretting facility (photo credits: AAC)

One loading-unloading-sequence is called a “cycle” and consists of contact loading, holding the load level (‘static load’) for a definite time (‘holding duration’), fretting and unloading with measurement of the separation force, i.e., adhesion force. After a ‘resting time’ the next cycle starts with loading. This contact between a spherical pin and a flat disc is made for several thousand times thereby simulating the lifetime

of applications. The term adhesion force refers to the force necessary to open the contact in vertical direction.

A typical outcome of the test device is shown in Figure 6: The adhesion force of 17-7 PH steel coated with MoS₂ versus Ti6Al4V in vacuum (loaded with 60% of the elastic limit, 210 Hz for 10 seconds per cycle). The MoS₂ layer failed in vacuum after 40 cycles (~84000 lateral micromotions) – then the pure metals were in contact and adhesion starting from 100 mN up to 6000 mN is measured.

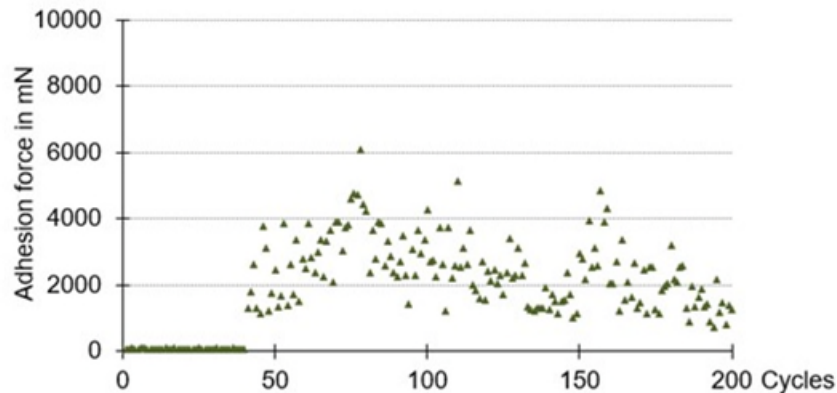


Figure 6. Adhesion of 17-7 PH steel coated with MoS₂ versus Ti6Al4V in vacuum over fretting cycles (1 cycle = 2100 motions)

Cold Welding - Critical Environments

In general, no cold welding in ambient pressure is found. Depending on the material combination under test, adhesion is observed at environmental pressure of 1 Pa and below. At higher ambient pressure, new oxide layers are formed between the materials which inhibit cold welding, i.e., re-oxidation is quicker than the fretting frequency. Therefore, mainly two different situations are considered to be the main points of risk:

1. Cold welding with regular space operation might occur between two metal-metal contacts due to impact (see failure above) or vibration. Any coating or surface treatment including initial oxide layers (in case no coating was applied) might be worn or damaged after some time. It shall be kept in mind, that any removed coating like the protection coating on the end stops of the anchor mechanism (Figure 3) or MoS₂ exposes bare, oxide free metal surface which is very likely to cold weld at next closure.

It is essential to know the wear rate and/or durability of the used coating to determine the safe functionality of the mechanism. See as example Figure 3, where the coating was worn before the nominal end of life was reached.

2. Cold welding in launch situation might be found in any space mechanism with metal-metal contact. During launch (including terrestrial transportation / ground testing), mechanisms are likely to be exposed to a high level of vibration which might damage or abrade coatings and surface treatments already in air. This can lead to a reduced lifetime for the regular space operation as experienced at the Galileo spacecraft. Figure 7 shows the comparison of 17-7 PH steel coated with MoS₂ versus Ti6Al4V tested in vacuum only (Figure 7 left graph) and tested under launch conditions (Figure 7 right graph). It is found that the MoS₂ coating is damaged during launch and the lifetime for the regular operation (in vacuum) is shortened by a factor of >3.

Another example of failure is shown in Figure 8, where Ti6Al4V vs itself is tested under launch conditions. The left graph in Figure 8 shows the combo with MoS₂ coating on both surfaces, which

fails already in air after 3 cycles. The friction coefficient indicates the failure of the MoS₂ coating and in air adhesion is measured, as the abraded coating exposes pure metal – metal contact. In comparison, with the same material combination without MoS₂ (Figure 8 right graph) the coated combo performs even worse due to the increased adhesion in air because the abraded coating preserved pure metal – metal contact at the point of failure. In technical terms, this mechanism might have failed already during ground testing. (It may be noted that adhesion force after this single peak again decreases. This is due to the presence of oxygen, but it would not have avoided the failure of the mechanism if the adhesion force of this single event exceeded the separation force of the opening device.)

It is essential to consider the stresses of prelaunch environment onto the space mechanism. Coatings and surface treatments may have different wear behavior in the laboratory environment compared to vacuum environment (e.g., as experienced at the Galileo mission).

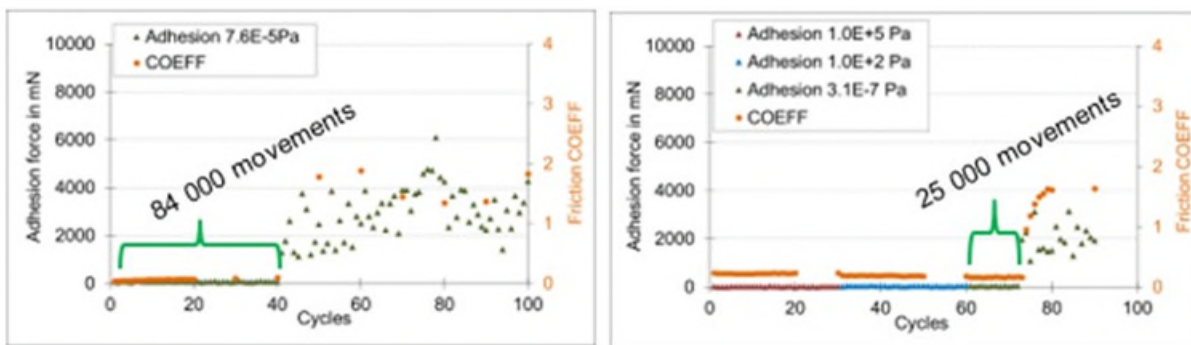


Figure 7. MoS₂ coating as cold welding inhibitor in vacuum (left) and under launch conditions (right)

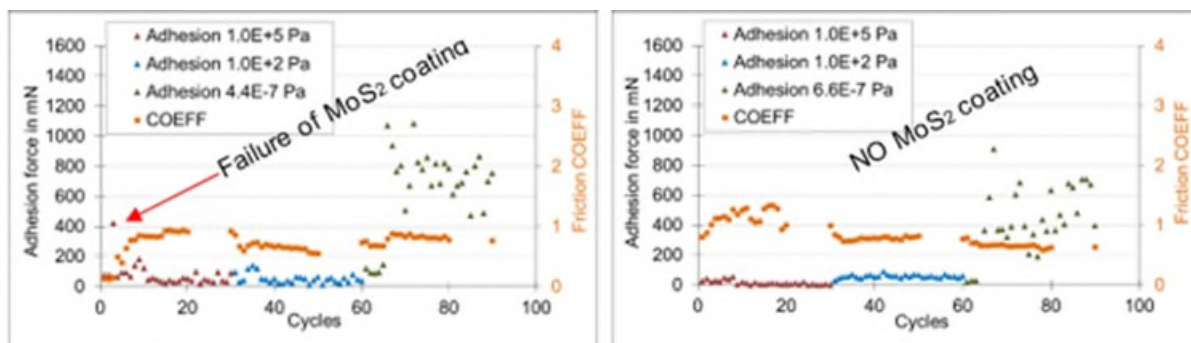


Figure 8. Launch conditions of Ti6Al4V vs. itself with (left) and without (right) MoS₂

Minimize Risk of Cold Welding

Here are some recommendations to minimize the danger of cold welding in space mechanisms:

- Cold welding can only occur in metal-metal-contacts. Avoid metallic contacts if possible. If metallic contacts cannot be avoided, there has to be some other form of cold welding prevention.
 - The maximum adhesion force in fretting between two metals in contact differ in a wide range. Adhesion forces between tungsten vs. tungsten and molybdenum vs. molybdenum stay well below 500 mN. Silver vs. silver, copper vs. copper, 17-7PH vs. 17-7PH and many more show adhesion forces far higher than 12000 mN (which is the maximum measurement range of the used test facility). In those tests the load force was in the range of few newtons!

- A very common mistake is the assumption that two dissimilar metals are unlikely to cold weld. As an example, AISI440C hardened vs itself has adhesion forces up to 2700 mN but AISI440C hardened vs Ti6Al4V has adhesion forces of up to 5500 mN – even higher than against itself. Dissimilar metal combinations do not prevent cold welding!
- Grease is a good cold welding inhibitor. However, using grease in metallic contacts suffers from two limitations, which need to be considered:
 - Grease tends to outgas in vacuum. This needs to be considered or evaluated for each space mechanism separately as any optics close to that mechanism might suffer from redeposition of the outgassing grease.
 - Using grease in separable contacts leads to slightly increased adhesion due to “grease stiction”. Grease minimizes the friction force but increases the separation force (perpendicular to the sliding surface) this is more a “suction” than cold welding or galling.
- Non-metallic contacts are not known to join. Sometimes washers from non-metallic material might be an option to avoid cold welding (e.g., PEEK, Kapton, Vespel, Terasint, CFK, GFK)
 - In contrast to metals, polymers and ceramics cannot form a cold weld (from their physical nature). However, mechanical properties limit their range of application. It seems difficult to use non-metallic materials in HDRM applications for instance, as typically high loads rule out polymers and brittleness limits ceramics.
 - A compromise is seen in polymeric coatings. But for them life has to be critically assessed.
 - Like greases, many polymeric materials (including their coatings) suffer from outgassing in vacuum which needs to be considered and evaluated for each space mechanism.
- If metal-metal contact cannot be avoided, coating of the contact areas is essential. There are some rules of thumb to follow:
 - The advice “a lot helps a lot” seems easy but should be considered as follows: Coat, if possible, both surfaces – if one coating fails, there is still the other coating which might save your mechanism. If feasible, apply several coatings on each other – layerize. Consider that coatings are not always well defined in thickness and might lead to challenges when a tight fit is needed. As shown in Figure 8 left picture, this advice has some limitations as well.
 - Pure “on top coatings” (e.g., PVD-coatings) tend to flake off under harsh conditions – see Figure 9. Especially for softer materials, the “eggshell” effect can be seen. Prefer surface treatments that increase the subsurface strength and form an interlayer between surface and bulk material.

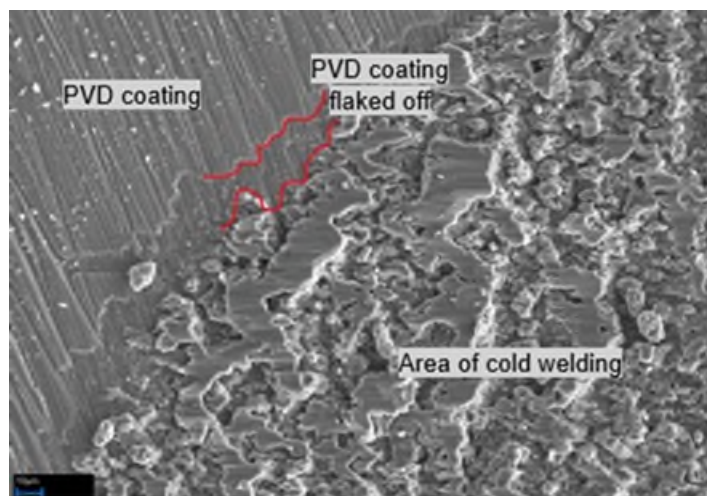


Figure 9. PVD coating flaking off

- The source of coating / surface treatment is important and needs to be evaluated carefully. Most suppliers of coatings / surface treatments use their own recipe. Interact with your supplier and perform verification tests with the same recipe from the same supplier as your flight hardware.
- Some coatings are prone to degrade under ambient environments like humid air. Consider the whole environmental cycle of your space mechanism to avoid early damage of the selected coating.
- Finally, for a certain combination the adhesion forces measured by the presented method enable derivation of a worst case approximation for separable contact surfaces [4]. This value can be rated versus the available opening forces, e.g., by springs.

Conclusions

Whether “cold welding” or “galling”, metal – metal contacts are risky to a joint in space mechanisms. There are known failures from space missions due to increased adhesion and therefore, metal – metal contacts need to be treated carefully. Damage of any surface treatment in prelaunch or launch conditions need to be considered. There are several workarounds to avoid direct metal – metal contacts like usage of grease, usage of non-metallic parts, or coatings. Talking about coatings, some considerations on the type of coating, wear rate per environment and bonding to the surface need to be evaluated carefully.

Tracking the potential danger of adhesion between metal – metal contacts in space mechanisms at an early stage is recommended to adapt the design and avoid cold welding in space (see Figure 10).

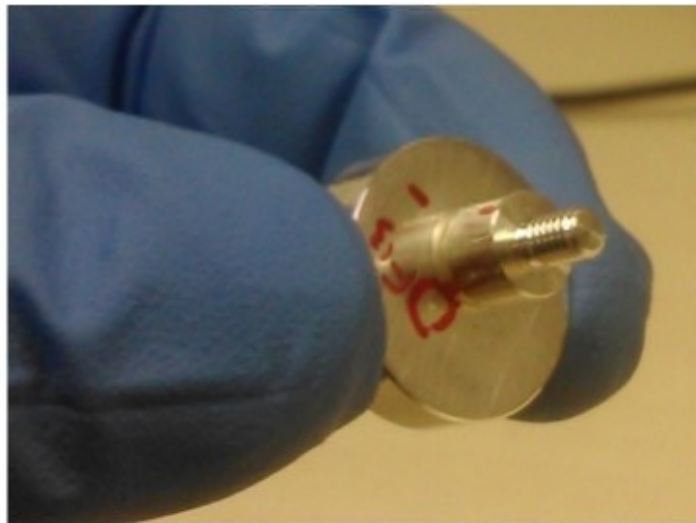


Figure 10. Cold welded pin to disc (silver vs silver)

References

1. Johnson M. R. (1994) "The Galileo High Gain Antenna Deployment Anomaly." *28th Aerospace Mechanisms Symposium*,
2. Merstallinger A., B. Dunn B., Semerad E., "COLD WELDING DUE TO IMPACT AND FRETTING UNDER HIGH VACUUM", Proc. ISMSE 9th, Noordwijk/NL, ESA/ESTEC, June 2003.
3. Merstallinger A., Holzbauer R., Bamsey N. (2021). "Cold Welding in Hold Down Points of Space Mechanisms Due to Fretting When Omitting Grease", *Lubricants* 2021, 9(8):72. <https://doi.org/10.3390/lubricants9080072>
4. Merstallinger A., Semerad E., Dunn B. D. (2009). "Assessment of Cold Welding between Separable Contact Surfaces due to Impact and Fretting under Vacuum", ESA STM-279
5. Budinski K., Budinski S. (2015). "Interpretation of galling tests", *Wear Volumes 332-233* 2015

Qualification of RHEOLUBE 3000-3Pb for the BABAR-ERI Chopper Mechanism

Darren Erickson* and Bob Hoffman**

Abstract

BABAR-ERI is an Earth-imaging radiometer, currently under development as a 12U “cubesat”. This instrument includes two imaging telescopes, detectors, and a Chopper Mechanism which modulates the light entering the telescopes. The Chopper Mechanism includes a rotating disk, supported by a pair of angular contact bearings, and actuated by a brushless DC motor. The disk rotates at a constant rate of 228 rpm and has a lifetime requirement of 720 million revolutions. Lubrication analysis indicated that our “heritage” lubricants would cause the mechanism to operate in the boundary lubrication regime. Moreover, lubricant breakdown was highly likely, leading to the eventual failure of the mechanism.

It was theorized that the high lifetime requirement could be achieved if the mechanism was operated in the elastohydrodynamic (EHD) lubrication regime. To achieve this, RHEOLUBE 3000-3Pb, a high-viscosity grease from NYE lubricants, was investigated. Fluid film thickness analysis showed that this grease results in a film thickness ratio of $\lambda = 3$, indicating the onset of EHD. Bearing torque testing was performed to experimentally verify operation in EHD, but unfortunately the results were inconclusive. However, life testing is currently underway, and after 520 million revolutions, the bearings show no signs of degradation. Based on the lubrication analysis and life testing, RHEOLUBE 3000-3Pb appears to be an enabling technology for the BABAR-ERI Chopper Mechanism.

The BABAR-ERI Instrument

BABAR-ERI is an Earth-imaging radiometer, currently under development with funding from NASA’s Earth Science Technology Office. This optical/infrared instrument uses two telescopes to measure the reflected and re-radiated energy leaving Earth’s atmosphere over a broad wavelength range from 300 nm – 100 μm . The energy is focused onto novel detectors that employ vertically aligned carbon nanotubes to absorb >99.8% of the incident radiation over the entire bandpass. These detectors are designed by the National Institute of Standards and Technology in cooperation with the Laboratory for Atmospheric and Space Physics (LASP) [1, 2]. By miniaturizing a number of key technologies, the BABAR-ERI instrument is designed to fit within the volume of a 12U cubesat, as shown in Figure 1.

The broadband radiation measurements made by BABAR-ERI are critical for understanding the Earth radiation budget (ERB). When combined with atmospheric and terrestrial properties derived from spectral imagers, the BABAR-ERI observations will also enhance and accelerate physical process-level understanding of clouds, ERB quantities and surface temperature, or “cloud feedbacks”. BABAR-ERI’s “cloud-resolving”, 1-km, spatial footprint ensures that clear- and cloudy-sky ERB quantities can be accurately established, which is key to improving our understanding of climate variability and change by reducing the uncertainties in cloud feedbacks [3, 4].

* Laboratory for Atmospheric and Space Physics, University of Colorado Boulder, Boulder CO

** NYE Lubricants, Inc. (Member of the FUCHS Group), Fairhaven, MA

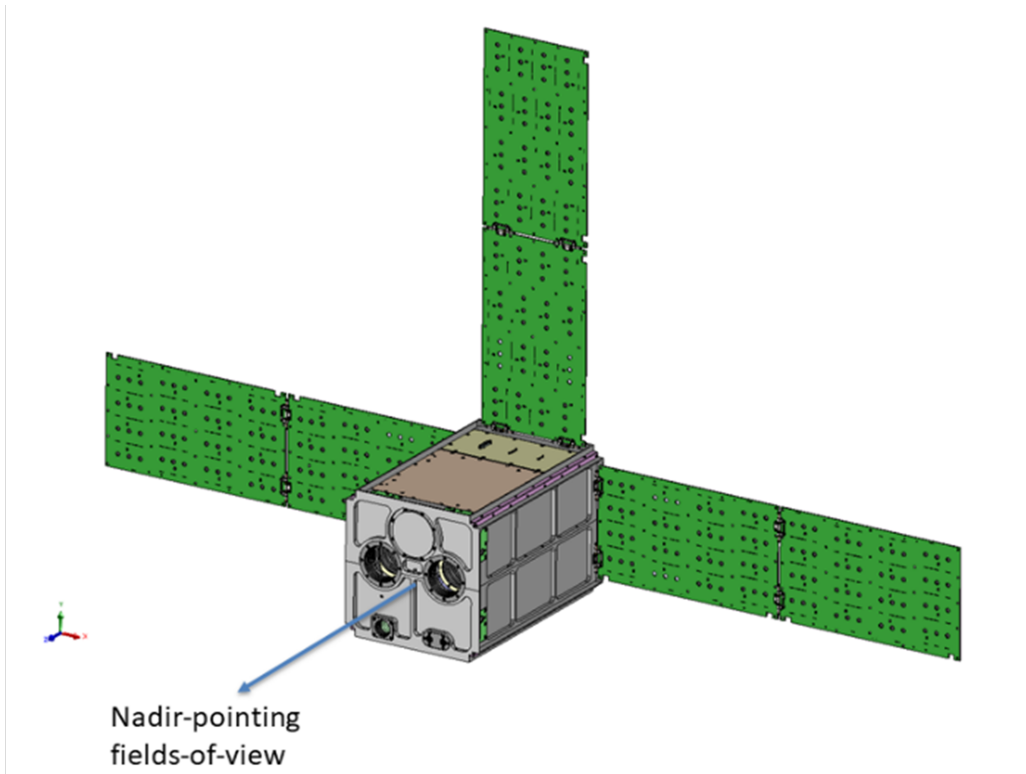


Figure 1: BABAR-ERI instrument inside a Nadir-pointing, 12U cubesat with three deployable solar panels

Chopper Mechanism

In order to make on-orbit calibrations, the two telescopes are optically chopped with a mechanism that opens/closes each aperture at 7.6 Hz (Figure 2). The Chopper Mechanism is a simple wheel with two open and two closed quadrants, attached to a shaft and supported by a duplex pair of angular contact bearings in back-to-back configuration. The wheel rotates at a constant rate of 228 rpm, using a 3-phase Brushless DC (BLDC) motor and optical encoder (Figure 3).

The mechanism operates at approximately 20°C, with an on-orbit lifetime requirement of 2.5 years. After adding an additional 1.2x factor of safety to account for ground testing, and a 2x factor safety for life testing per GSFC-STD-7000 (GEVS) [3], the required design life of the mechanism is almost 720 million revolutions. The mechanism driving requirements are summarized in Table 1.

Table 1: Mechanism driving requirements

Driving Requirements	
Rotational velocity	228 rpm
Max mass	0.5 kg
Distance between telescope axes	116.8 mm (4.6 in)
Max wheel diameter	117.8 mm (7.0 in)
Operating temperature	20 ± 5°C
Quasi-static limit load	30 g
Random vibrate level	10.0 g _{rms} (acceptance) 14.1 g _{rms} (qualification)
Lifetime	2.5 years on-orbit, 720 million revolutions

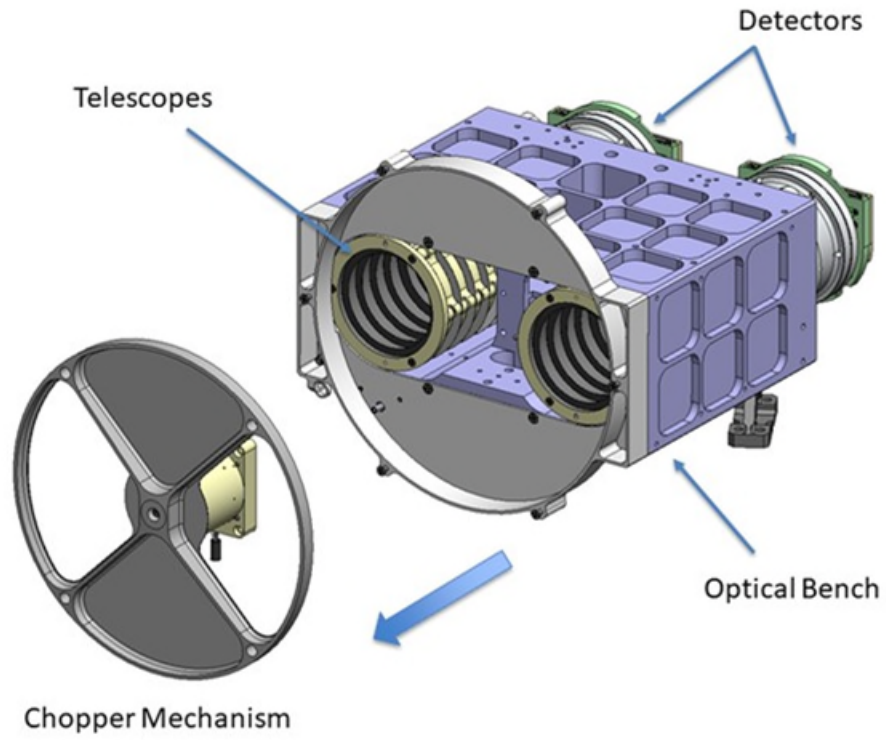


Figure 2: Chopper Mechanism and BABAR-ERI optical system

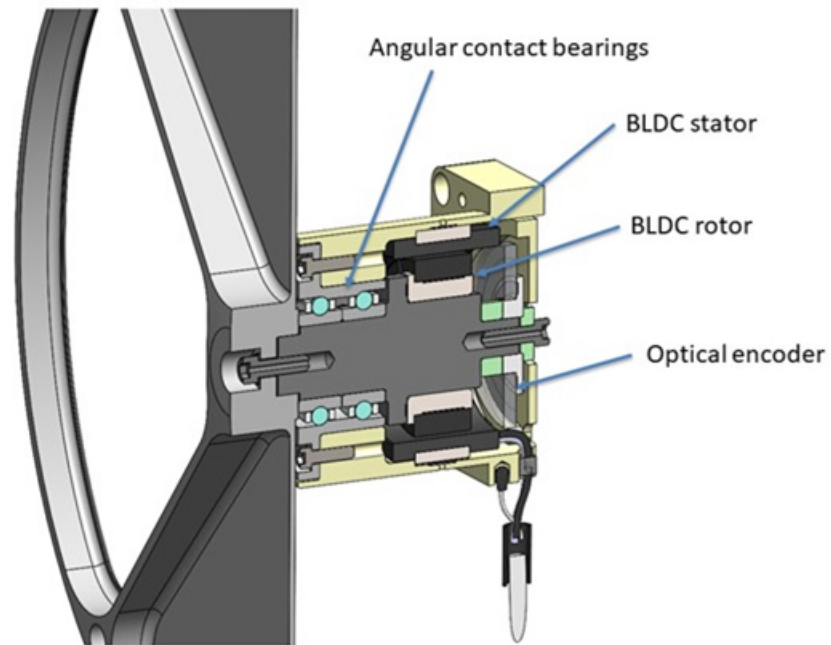
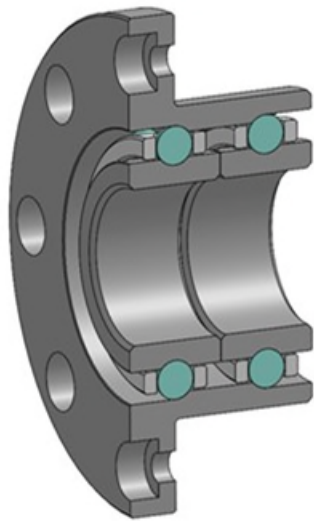


Figure 3: Chopper Mechanism section view

Bearing Design and Lubrication

To meet the requirements of this mechanism, a custom bearing was specified and procured from CEROBEAR GmbH (Figure 4). This bearing is a duplex angular-contact bearing in back-to-back configuration, with a 29-N (6.5-lb) axial preload. This preload was chosen to prevent gapping between the balls and races under our worst-case axial launch vibration accelerations. This preload results in a mean Hertzian contact stress of 807 MPa (117 ksi) at the inner ring contact ellipse.



Bearing Specification	
Outer diameter	25.4 mm (1.0 in)
Inner diameter	12.7 mm (0.5 in)
Width	16.26 mm (0.64 in)
Ball diameter	3.175 mm (0.125 in)
Contact angle	15°
Preload	29 N (6.5 lb)
Race curvature	0.54
Tolerance class	ABEC 7
Materials:	
Rings	AISI 440 C stainless steel
Balls	Si3N4 (silicon nitride)
Cage	PEEK

Figure 4: Bearing design and specification

Given the high lifetime requirement of this mechanism (720 million revolutions), Ball-Pass Analysis was used to calculate the lubricant Cumulative Degradation Factor (CDF) for this bearing according to the method outlined in [6, 7]. This calculation is assumed to be valid for bearings operating in the boundary lubrication regime. At LASP, we typically use conservative CDF limits of: 2e12 (ball pass-psi) for Perfluoropolyether (PFPE) lubricants and 20e12 (ball pass-psi) for Multiply Alkylated Cyclopentane (MAC) lubricants. This Ball-Pass Analysis indicated that the Chopper Mechanism has a CDF of 580e12, which is 290x higher than the CDF limit for PFPE and 29x higher than the CDF limit for MAC lubricants. This result indicates that the Chopper Mechanism is unlikely to achieve its lifetime requirement due to lubricant breakdown if operated in the boundary regime.

To verify our assumptions, the lubricant film thickness ratio was calculated using the method outlined by Hamrock and Dowson [8] and includes the starvation correction factors proposed by Zaretsky [9]. Our standard lubricants were used in this calculation, including Castrol Braycote 601EF (a PFPE grease) and NYE RHEOLUBE 2004 (a MAC grease). Both yielded a film thickness ratio (λ -ratio) of approximately $\lambda = 1$ at our operating temperature, which implies that the mechanism would indeed be operating in the boundary/mixed lubrication regime [10].

So, we ask ourselves: if Ball-Pass Analysis predicts bearing failure due to lubricant breakdown, how is it that some mechanisms, such as reaction wheels, can achieve lifetimes that are orders of magnitude higher than the Chopper Mechanism? We believe the answer is that they typically operate in the elastohydrodynamic (EHD) lubrication regime rather than the boundary regime. In the EHD regime, friction, wear and subsequent surface damage are minimized [7].

In order to achieve EHD, the film thickness ratio must be increased to $\lambda \sim 3$, by either increasing the mechanism speed, decreasing the contact stress within the bearing, or increasing the lubricant viscosity. Given our other design constraints, using a high viscosity lubricant was seen as the only available option.

RHEOLUBE 3000-3Pb Grease

RHEOLUBE 3000-3Pb is a high-viscosity MAC grease developed by NYE Lubricants, based on Synthetic Oil 3001A. It is formulated for use in aerospace and vacuum environments and is fortified with antioxidants and anti-wear additives. It is especially well suited for use in the BABAR-ERI Chopper Mechanism because its kinematic viscosity at 20°C is 20x higher than LASP's "heritage" lubricants: RHEOLUBE 2004, and Braycote 601EF.

Some useful properties of RHEOLUBE 3000-3Pb are shown in Table 2 below. Additional information is also available through the NYE Lubricants website. Viscosity data was extrapolated over a wide temperature range using the method outlined in ASTM D341-20. This data is plotted in Figure 5 for Synthetic Oil 3001A, as well as Synthetic Oil 1001A, 2001A and Brayco 815Z, for comparison. It is believed that the viscosity data for these base oils is also representative of their corresponding greases.

Table 2: RHEOLUBE 3000-3Pb properties

Property	Typical Value	Test Method
Kinematic viscosity ** @ 40°C @ 100°C	2082 mm ² /s 202 mm ² /s	
Viscosity index **	227	ASTM D-2270
Density	0.89 g/cm ³	
NLGI Grade	2	ASTM D1403
Oil Separation (24h @ 100°C)	0.09%	ASTM D6184
Outgassing	(TBD)	ASTM E-595
Vapor pressure @ 150°C @ 100°C @ 75°C @ 25°C (calculated)	2.9e-10 MPa 7.9e-11 MPa 5.2e-11 MPa 1.0e-11 MPa	(NYE internal procedure)

** data measured using Synthetic Oil 3001A, but is believed to be representative of RHEOLUBE 3000-3Pb grease

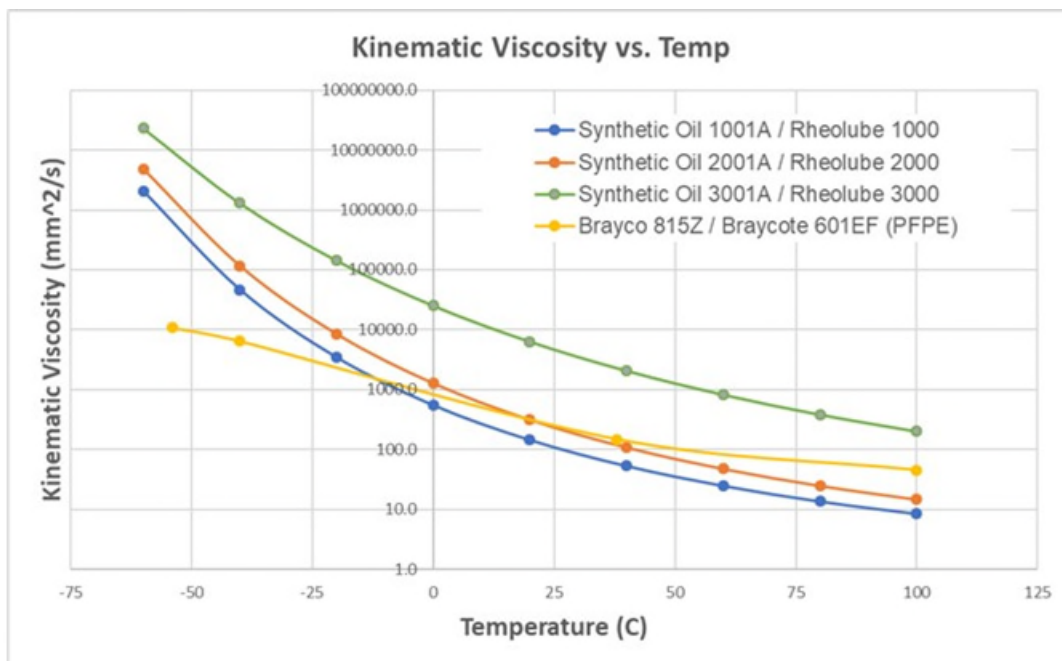


Figure 5: Comparison of kinematic viscosity vs. temperature for selected lubricants

Film Thickness Modeling

Fluid film thickness calculations were repeated, using the viscosity data for RHEOLUBE 3000-3Pb shown in Figure 5. The results are plotted as λ -ratio vs. temperature at the bearing inner and outer ring in Figure 6. At our nominal operating temperature of 20°C, the film thickness ratios are $\lambda = 3$ at the inner ring and $\lambda = 3.7$ at the outer ring, indicating that the bearing is operating near the onset of the EHD lubrication regime. Although we'd prefer to operate *fully* within the EHD regime ($\lambda \gg 3$), the constraints placed on our bearing design and operational speed prevent this. Overall, these results indicate a significant improvement over the use of medium-viscosity lubricants such as RHEOLUBE 2004 or Braycote 601EF, which result in boundary lubrication regime ($\lambda \sim 1$).

In summary, the high viscosity of RHEOLUBE 3000-3Pb enables the mechanism to operate near the onset of the EHD lubrication regime, even at low speeds which would normally result in boundary lubrication. By operating at/near EHD, we expect to be able to meet the high cycle-life requirement which would otherwise be unobtainable.

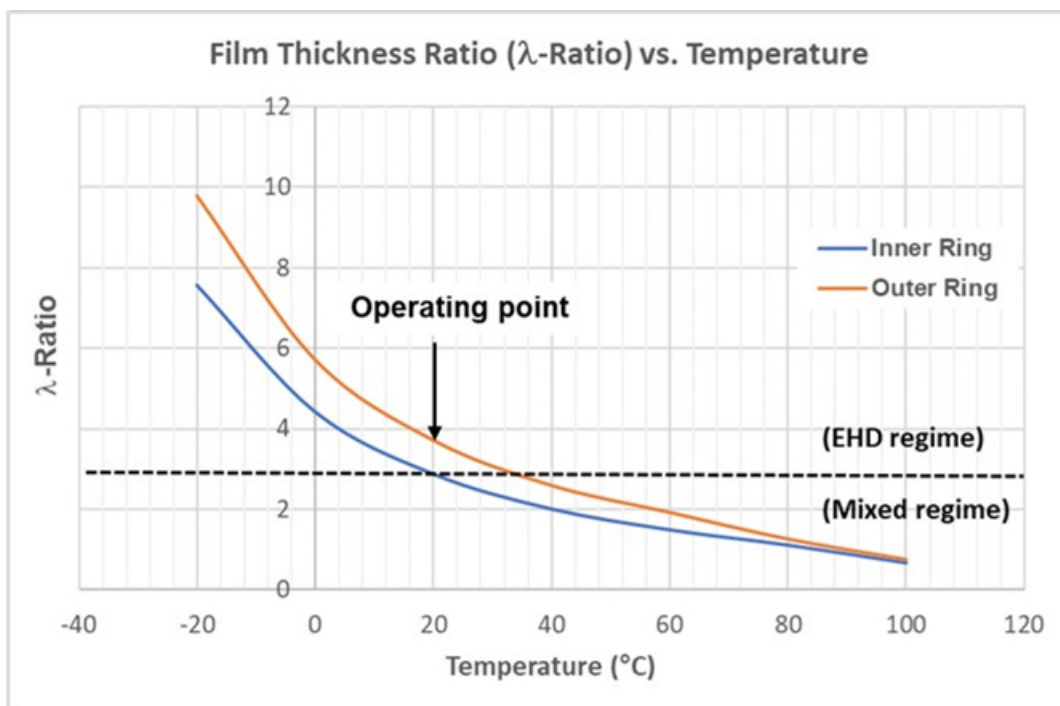


Figure 6: Calculated film thickness ratio for RHEOLUBE 3000-3Pb

Bearing Torque Tests

Bearings were procured from the vendor unlubricated, so that the grease could be applied at LASP. For our initial tests, the volume of grease added to each bearing was equivalent to 30% of the internal free volume of the bearing (Figure 7). This volume was carefully controlled by weighing the bearing before and after lubrication and using the density to calculate the volume. After a low-speed run-in to evenly distribute the grease, it was observed that a significant quantity of grease had been pushed out of the ball track and was deposited near the outer surface of the cage. For subsequent tests, we decided to reduce the grease fill to 15% of the free volume. Bearings with reduced fill percentage showed less grease migration, with most of the lubricant remaining near the ball track. Reduced grease volume is not a concern for our application since NyeBar barrier film is used to limit oil migration (creep), and our relatively low operating temperature limits evaporative loss.

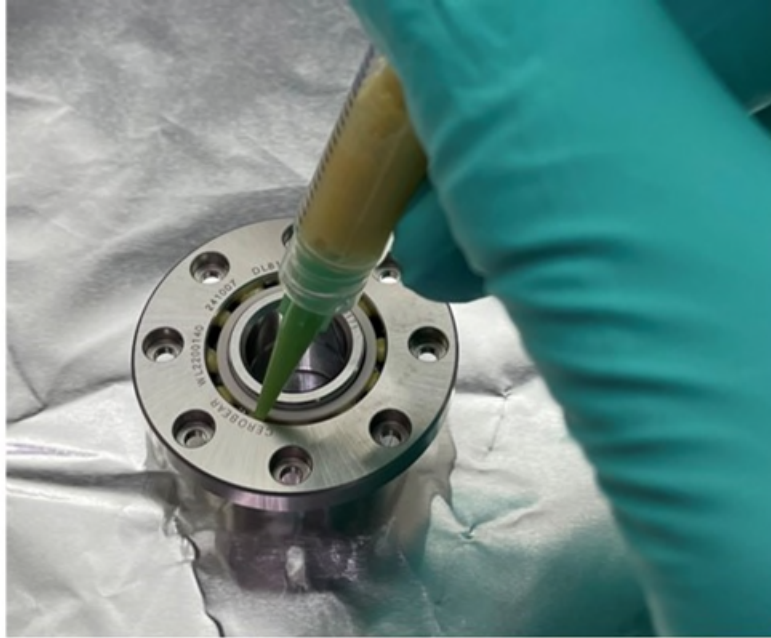


Figure 7: Injection of grease into a bearing

After lubrication, the bearings were placed on a torque testing fixture. This fixture uses a brushed DC motor under closed-loop control to rotate the shaft of our mechanism at a set speed. The outer housing of the Chopper Mechanism was attached to a static torque transducer which subsequently measured the reaction torque due to friction in the bearing. This facility was used to measure the bearing friction at our nominal operating speed of 228 rpm, as well as measure the torque vs. speed characteristics of the bearing from 20 – 400 rpm.

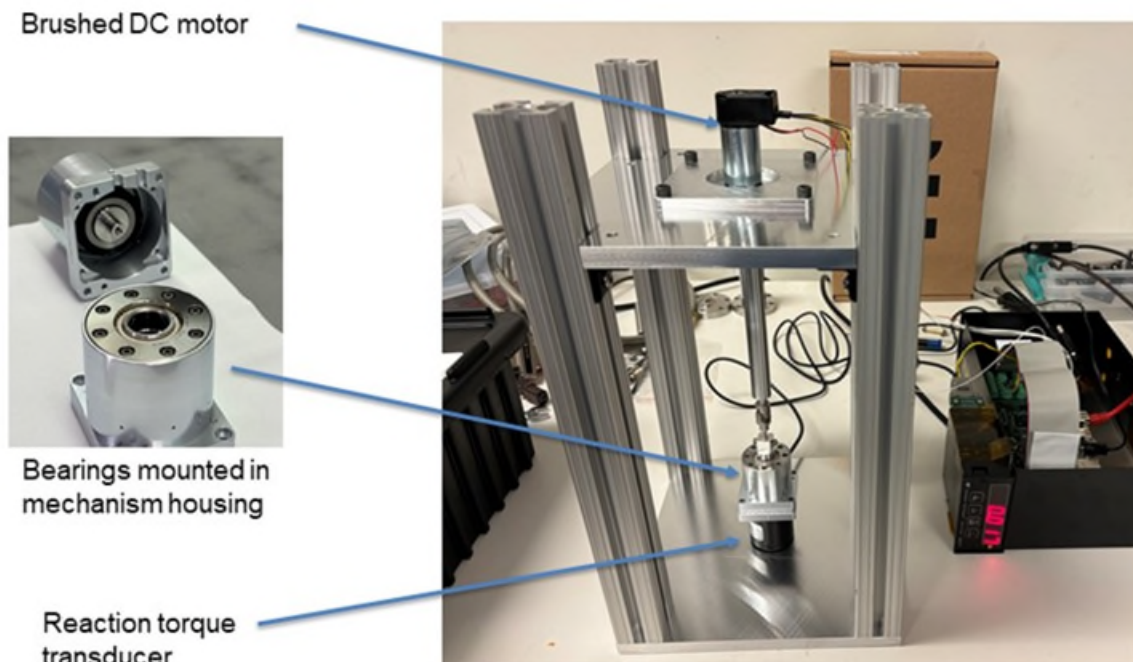


Figure 8: Bearing torque test fixture

Torque vs. Time

Tests were conducted to measure the bearing friction torque at the nominal operating speed of 228 rpm, and a typical plot is shown in Figure 9. These tests indicated a “bi-modal” behavior, where the measured torque alternated between a “low state” (often 4.6 mNm, or 0.65 oz-in), to a “high state” (often 5.6 mNm, or 0.8 oz-in). These jumps were often correlated with a visual change in the motion of the cage. During normal operation, the cage showed a slight eccentricity as it rotated, due to the clearance between the inner ring and the cage (which was inner-ring piloted). Additionally, the cage also exhibited several modes of cage instability, including: a “piston” motion where it would translate along the rotation axis, and a “tip/tilt” motion where it would rotate about axes normal to the rotation axis. The jumps in measured torque were often accompanied by a visual change in the cage motion (for example, from quiescent operation to a mode where the cage translated along the rotation axis). It is believed that the high viscosity lubricant may be contributing to increased levels of cage instability, as described in [11].

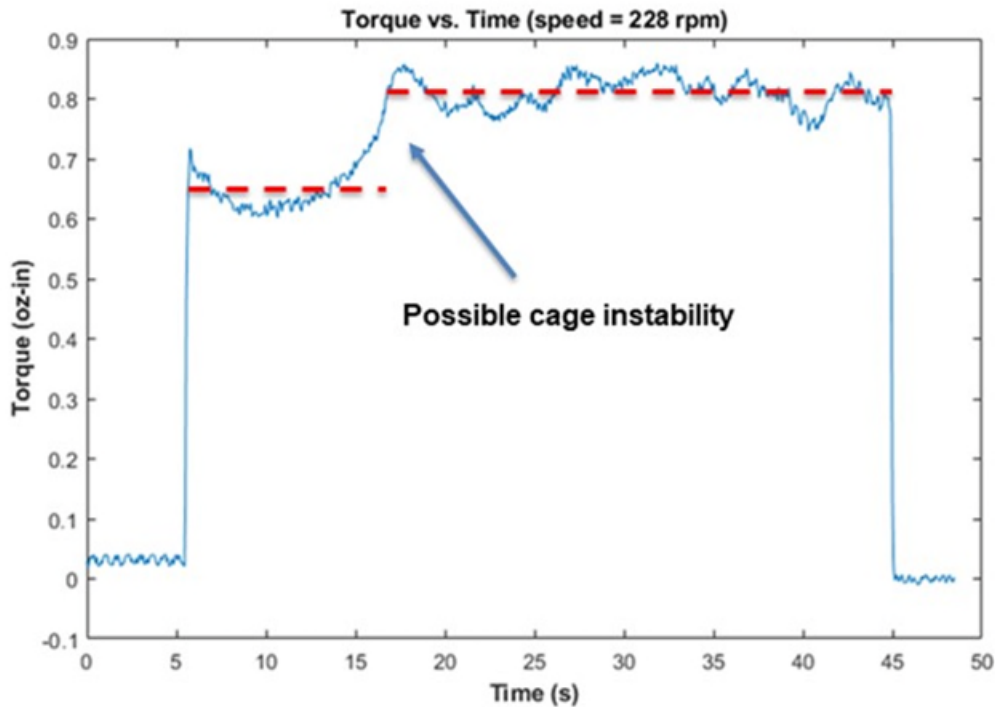


Figure 9: Measured friction torque at 228 rpm

Torque vs. Speed

Torque vs. speed measurements were obtained over the range from 20 – 400 rpm, which spans the boundary, mixed and EHD lubrication regimes. The goal was to experimentally verify that the bearings were entering EHD at 228 rpm, by observing a reduction in the friction torque as predicted by the Stribeck-Hersey curve [10]. Figure 10 shows data taken from 10 consecutive tests of the same bearing (left) as well as the mean and standard deviation of these tests (right). The data is generally noisy, and some measurements exhibit the bi-modal response discussed above. There is also no clear indication of a reduction in friction torque, and thus no conclusions can be made about where the EHD lubrication regime begins. After consulting with experts at NASA, they indicated that we were unlikely to see evidence of a transition to EHD in this kind of test, and that we should rely on the numerical modeling in this case.

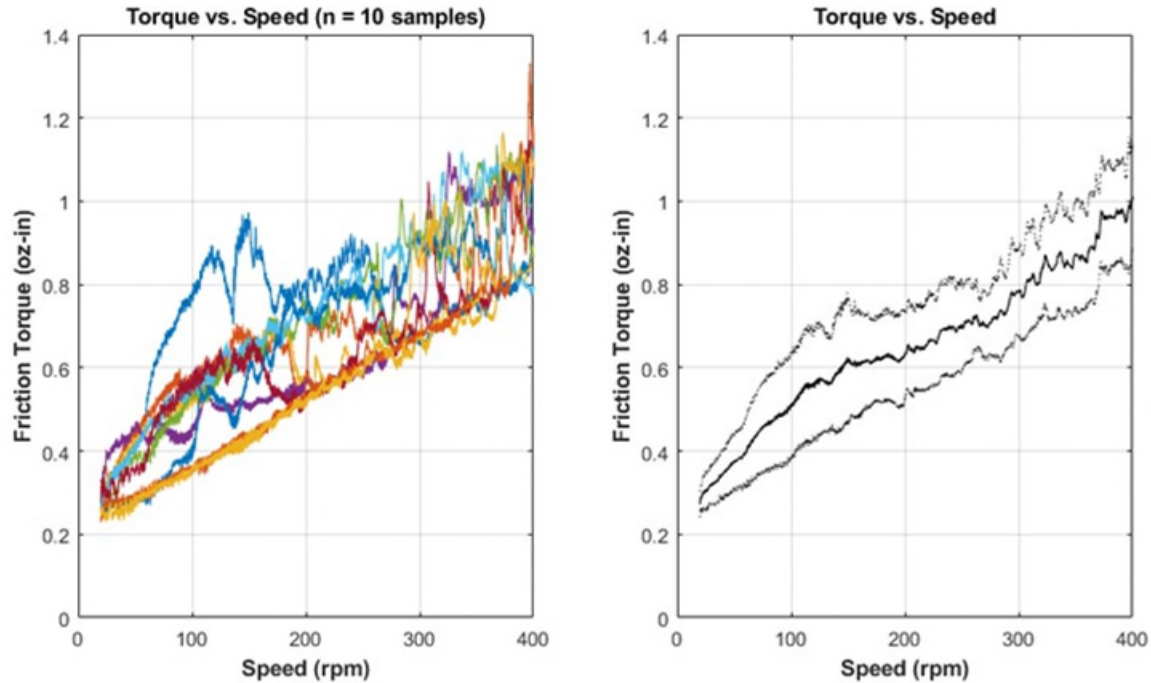


Figure 10: (left) Torque vs. speed measurements from 10 consecutive tests, (right) Mean and ± 1 standard deviation of 10 consecutive tests

Mechanism Life Testing

A flight-like Life Test Unit (LTU) of the Chopper Mechanism has been built and is currently undergoing life testing. The LTU has received a 3-axis vibration test, followed by Thermal-Vacuum (TVAC) tests, including thermal cycles between its hot and cold survival limits. After TVAC, the test unit was transferred to an ambient temperature vacuum chamber where it is currently operating. At the time of writing this paper, it has accumulated 520 million of its planned 720 million cycles and is expected to complete its full life test by May 2024. During operation, the closed-loop motor torque is constantly measured and trended to look for any sign of increased friction or bearing degradation. To date, no anomalous trends have been observed.

In order to meet schedule, budget and facilities constraints, the life test has been accelerated by operating the mechanism at 6x its normal speed (i.e., now 1368 rpm). This decision was made to reduce the total duration of the test from 6 years, to 1 year. Careful consideration was paid before deciding to accelerate the test. Lubricant film thickness analysis indicates that accelerating the test results in the λ -ratio increasing from $\lambda = 3$ at 228 rpm to $\lambda = 5$ at 1368 rpm. Since $\lambda = 3$ is at/near the onset of the EHD regime, it was felt that the mechanism was not undergoing a significant change in lubrication regime by running faster. Although not ideal, it is felt that the benefits of accelerating the test from 6 year to 1 outweigh the risks of an anomalous result.

Conclusions

An optical Chopper Mechanism has been built to fulfill the needs of the BABAR-ERI mission. This mechanism included a disk, supported by a pair of angular contact bearings, rotating at 228 rpm. The most challenging requirement of the mechanism was its lifetime of 720 million revolutions. Ball-Pass Analysis indicated that the lubricants commonly used at LASP (RHEOLUBE 2004 and Braycote 601EF) would have a high likelihood of breakdown, resulting in mechanism failure. This analysis was supported by the fact that the mechanism would be operating in the boundary lubrication regime using the lubricants noted above.

Given the history of other mechanisms, such as reaction wheels, it was theorized that the Chopper Mechanism could achieve its lifetime requirement if it were operating in the EHD lubrication regime. The most feasible way of achieving EHD in this mechanism was to employ a high-viscosity grease, such as NYE RHEOLUBE 3000-3Pb. This grease is based on Synthetic Oil 3001A, a Multiply Alkylated Cyclopentane (MAC) fluid. Lubricant film thickness calculations were performed, indicating a λ -ratio of $\lambda = 3$ at the nominal operating temperature of 20°C. These results show that the mechanism should be operating at or near the onset of EHD using the high viscosity grease.

Experimental torque measurements were made in an attempt to verify operation in the EHD regime. Unfortunately, the torque data was noisy and exhibited additional signatures which made it difficult to interpret. Certainly, there was no clear indication of a transition to EHD, as predicted by the Stribeck-Hersey curve. Despite this, a Life Test Unit was built and is currently undergoing an accelerated life test. This test has completed 520 million of its required 720 million cycles and is on track to finish by May 2024. To date, the test has not shown any signs of bearing degradation or increased friction.

Lessons Learned

A number of valuable lessons have been learned throughout this investigation, including:

- Use caution when relying on “heritage” mechanism designs. Subtle changes to lifetime requirements, or operational parameters such as speed, can dramatically change the bearing and lubrication requirements.
- Lubricant analysis, such as Ball-Pass Analysis or film thickness calculations are a critical part of any mechanism design and should not be overlooked.
- It is very difficult to experimentally determine the onset of the EHD lubrication regime. If this determination is important to a design, the engineer may have to rely on numerical modeling alone.

Acknowledgements

The authors would like to sincerely thank the NASA Earth Science Technology Office for providing funding for the BABAR-ERI project, and for supporting this work. Additional thanks go to NYE Lubricants for generously providing grease and oil samples, as well as invaluable engineering data.

We’d also like to thank Mike Dube (Technical Fellow, NASA-NESC) and Joe Schepis (Chief Engineer, Mechatronics and Robotics Branch, NASA-GSFC) for sharing their fluid film thickness calculations with us, and for taking the time to discuss the results of our torque testing. Your help over the years on this project, and others, is deeply appreciated.

And finally, thanks to Zach Castleman (Mechanical Engineer, LASP) for suggesting an elegant solution to this design challenge, and for sharing with me his significant knowledge of space mechanisms, bearings and lubrication.

References

1. Stephens, M., Yung, C., Tomlin, N., Harber, D., Straatsma, C., Dan, A., Freire Antunes, E., Pilewskie, P., Coddington, O., Lehman, J. "Extremely broadband calibrated bolometers and microbolometer arrays for Earth radiation budget measurements," *Proc. SPIE 12234, Infrared Sensors, Devices, and Applications XII*, 1223403 (30 September 2022)
2. Yung, C., Tomlin, N., Straatsma, C., Rutkowski, J., Richard, E., Harber, D., Lehman, J., Stephens, M., "BABAR: black array of broadband absolute radiometers for far infrared sensing," *Proc. SPIE 10980, Image Sensing Technologies: Materials, Devices, Systems, and Applications VI*, 109800F (13 May 2019)
3. Coddington, O., et al., "The BABAR-ERI Instrument: Benefits, applicability, and readiness for Earth Science", *Earth Science Technology Forum*, Pasadena, CA, June 20-22, 2023.
4. Coddington, O. et al., "The BABAR-ERI Instrument: An Innovative Solution for Imaging Broadband Radiation at High Spatial Resolution", *AMS Annual Meeting*, Baltimore, MD., Jan 28- Feb 1, 2024.
5. GSFC-STD-7000B, "General Environmental Verification Standard (GEVS) for GSFC Flight Programs and Projects" 2021.
6. Braza, J., Jansen, M., Jones, W. "Lubricated Bearing Lifetimes of a Multiply Alkylated Cyclopentane and a Linear Perfluoropolyether Fluid in Oscillatory Motion at Elevated Temperatures in Ultrahigh Vacuum." *12th European Space Mechanisms and Tribology Symposium*, 2007.
7. Jones, W., Jansen, M. "Lubrication for Space Applications." *NASA/CR-2005-213424*, 2005.
8. Hamrock, B., Dowson, D. "Isothermal Elastohydrodynamic Lubrication of Point Contacts, II – Ellipticity Parameter Results" *NASA Technical Note D-8166*, Lewis Research Center, 1976
9. Zaretsky, E., Bearing Elastohydrodynamic Lubrication: A Complex Calculation Made Simple" *NASA Technical Memorandum TM-102575*, Lewis Research Center, 1990.
10. Space Tribology Handbook, 5th Ed. (v2), 2013
11. Fusaro, R., Khonsari, M. "Liquid Lubrication for Space Applications" *NASA Technical Memorandum TM-105198*, Lewis Research Center, 1992

Development of Strain Wave Gearing lubrication for the Steering Unit for the Manned Pressurized Rover

Jun'ichi Kurogi^{*}, Yoshihide Kiyosawa^{*}, Masaru Kobayashi^{*}, Takuya Akasaka^{*}
Hiroyuki Toyoda^{**}, Shoichi Shono^{**},
Shingo Obara⁺, Koji Matsumoto⁺ and Nobuo Kenmochi⁺

Abstract

There is development underway to use Strain Wave Gearing (SWG) as a reduction gear for the steering unit of the manned pressurized rover. SWG has been used in various space equipment in the past, including the Apollo LRV, but its applications are sometimes limited by the lifespan of lubrication. This paper describes the research done to extend the life of SWG by using dry lubrication and powder, and the results that were achieved.

Introduction

The steering unit of the manned pressurized rover, which is necessary for manned exploration activities on the lunar surface, is an important functional component of the rover that must operate in a harsh space environment (vacuum, -170 to 120°C). To achieve the compact size, light weight, and low power consumption required for the steering unit, a dry lubricant was applied to the gear. This would eliminate the need for a heater, which was previously required when using grease at low temperatures, and would ensure output (efficiency) at low temperatures. Furthermore, testing was focused on the low operating temperature of -60°C, which is the limit of the test equipment. The performance evaluations were conducted over a range of -60°C to +100°C.

Steering Unit

The steering unit that was evaluated is responsible for steering the wheels of the manned pressurized rover, as shown in Figure 1. SWG was selected as the reducer to be used in the steering unit (Figure 2). The reason for selecting SWG are its frequent use/heritage in space applications, it is inherently lightweight and compact and it offers high reduction ratios that allow a smaller motor to be used, resulting in lower weight and lower power consumption. In this case, in order to achieve even an even higher reduction ratio, a two-stage architecture with a planetary gear pre-stage was adopted. The overall size was minimized by making the planetary gear a part of the wave generator (hereinafter referred to as W/G). Table 1 shows the specifications of the reducer (the structure of the two-stage gearhead will be described later).

Next, we will discuss the expected load torque while driving. Conventionally, in space applications, due to the difficulty of lubrication in a vacuum, the design load is significantly lower than the rated specifications for use on the ground. However, in this case, there are severe restrictions on the mass and size of the steering unit as well as power requirements. Thus by using dry lubrication, the heater can be eliminated, reducing the size while also satisfying durability requirements even under extremely high load torque conditions compared to conventional space applications. The steering unit was developed with this goal in mind.

^{*} Harmonic Drive Systems, Inc, Japan

^{**} Toyota Motor Corporation, Japan

⁺ Japan Exploration Agency, Japan

This development aimed to achieve long life in a thermal vacuum using a dry lubrication. This is a difficult requirement for a SWG operating under high load conditions (close to the rated torque of the gear), and has little known precedence for space applications.

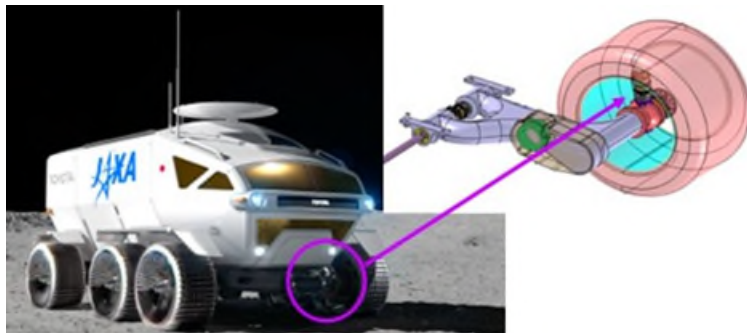


Figure 1. Position of Steering Unit

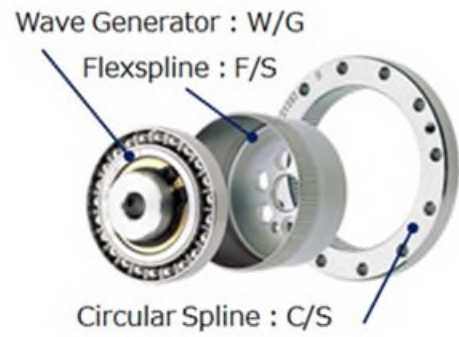


Figure 2. SWG components

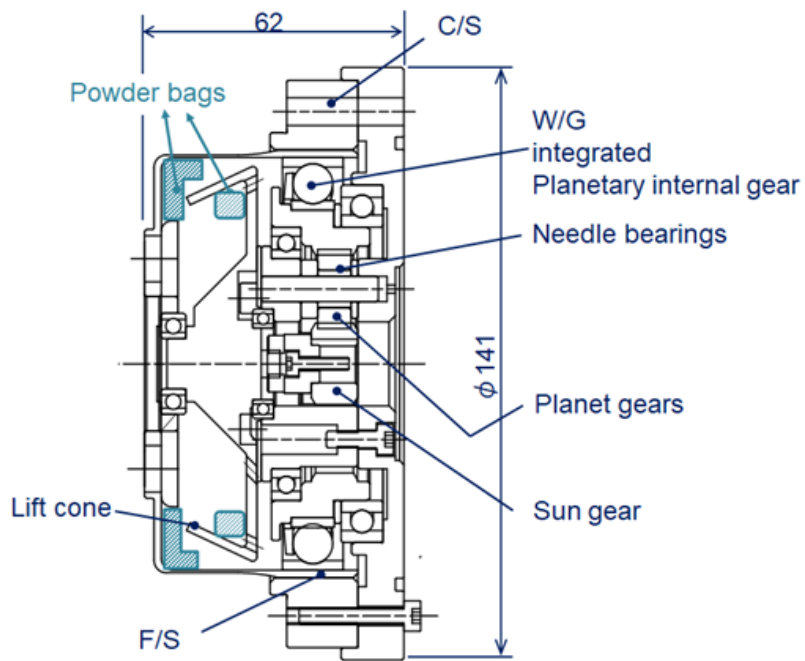


Figure 3. Structure of SWG

Table 1. Specification of SWG

Reduction Ratio	1/300 (two-stage reduction) 1St Stage : Planetary Gear 1/3 2nd Stage : SWG 1/100
Rated Torque	265 N·m
Repeated Peak Torque	568 N·m
Material of component parts	Mainly stainless steel Some bearing steel, resin and ceramic balls (Si_3N_4)
Loaded conditions during driving	Average Loaded Torque : 179 N·m Maximum Loaded Torque : 500 N·m

Lubrication Specifications and Test Unit

When using grease as a lubricant in the space environment, a heater is usually used at low temperatures near or below the pour point. However, assuming a mission with a travel distance of 10,000 km, we aimed to save energy by reducing power consumption and weight, and investigated the effects of applying dry lubricants.

It is known that dry lubricant used with a SWG has a short lifespan because after the dry lubricant wears out, abrasive wear will continue unless lubricant is supplied to the contact parts [1]. Therefore, the use of dry lubricant with SWG has been very limited.

To address this issue, in addition to treating the SWG with a dry lubricant coating, MoS_2 powder was used as the lubricant introduced to the contacting parts. However, if a large amount of MoS_2 powder enters the bearing all at once, it may lock up, so the powder must be supplied little by little. As a mechanism for supplying the appropriate amount of MoS_2 powder, a bag (powder bag) containing MoS_2 powder was used inside the SWG (see Figure 4). This powder bag is made of coarse PTFE cloth and formed into a bag shape using PTFE thread. Its purpose is to discharge MoS_2 powder little by little and supply it to the contacting areas. In addition, a part called a lift cone (see Figure 4) rotates in synchronization with the motor shaft, and the ejected powder collides with this lift cone, which prevents large amounts of MoS_2 from suddenly entering the bearing and contacting parts even under vacuum. The device is designed to supply MoS_2 powder to the parts. By using these measures, we aimed to extend the life of SWG with dry lubrication. Furthermore, to prevent the MoS_2 powder discharged from the powder bag from flowing out of the steering unit, PTFE felt is placed on the sliding part as a seal.

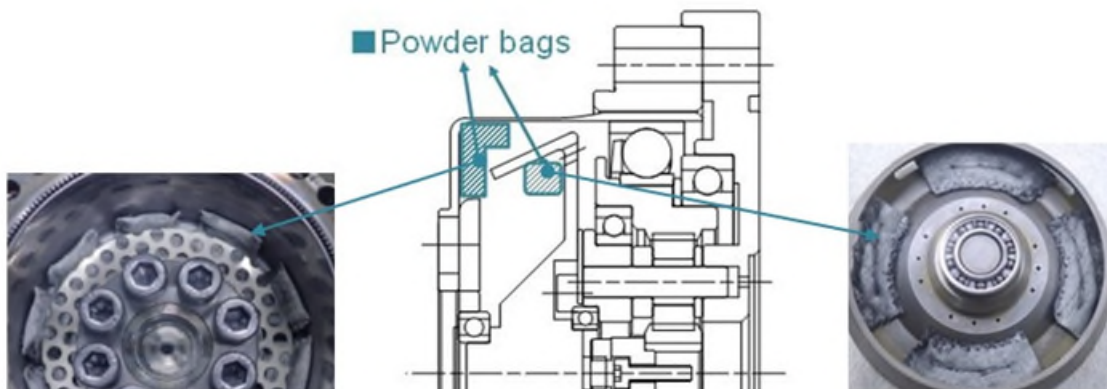


Figure 4. Powder Bags Mounting Position

For comparison, a test SWG with grease lubrication was prepared. The grease used was Spacelube MU (Kyodo Yushi Co., Ltd.), which has a hydrocarbon-based multi-alkylated cyclopentane (MAC) oil as its base oil. The specifications of both lubricants are shown below.

1. Solid lubrication specification

- Tooth surface and sliding part surface: MoS₂ shot peening
- W/G: MoS₂ shot peening for the raceway, Si₃N₄ for the ball, and PAI material for the retainer.
- Support bearing: Replaced the ball with Si₃N₄ and the retainer with PAI material.
- Pre-treatment of MoS₂ is carried out on the planetary needle.
- Aging was performed to transfer MoS₂ powder to the contact area before testing.

2. Grease lubrication specifications

- Grease name: Space Lube MU (Kyodo Yushi Co., Ltd.)
- Amount applied: Approx. 12g [2] *Calculated by volume ratio from literature
- Application location: Each contact area (see Figure 5)
- No lift cone used

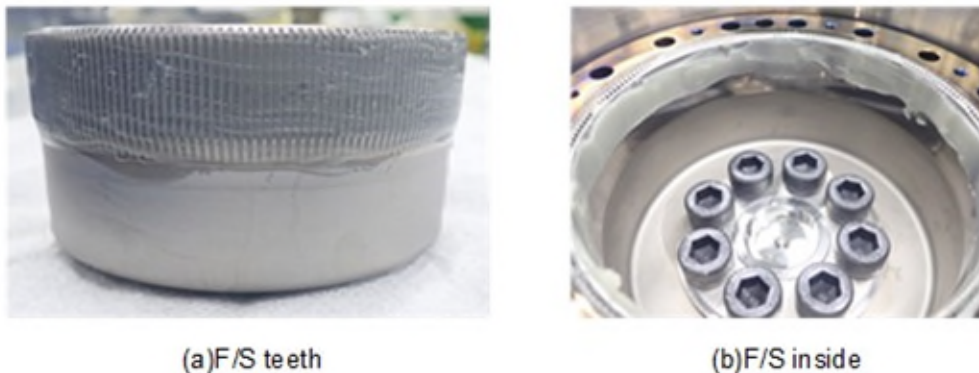


Figure 5. Specimen Lubricated with Grease (Before Assembly)

Test Conditions

The test conditions are shown in Table 2 for the environmental temperature, Tables 3 and 4 for the operating conditions, and Table 5 for the test items.

The test environment temperature was set as normal temperature, low temperature, and high temperature. Test time percentages were 20%, 50%, and 30%, respectively. The low temperature was set at -60°C (the maximum capacity of the equipment) for the dry lubrication test specification, and -40°C for the grease lubrication test specification, the lower limit of the grease operating temperature. In addition, the high temperature was set at 100°C for the dry lubrication test specification in consideration of the tempering temperature of the bearing steel used in some components, and 80°C for the grease lubrication test specification, which is the standard operating temperature range for general vacuum liquid lubricants (see Table 2).

The operating conditions are performance guaranteed durability*¹ and function guaranteed durability*², respectively, including rough road driving conditions (described as "bad road driving" in the table), normal driving conditions (described as "normal driving" in the table), and maximum operating conditions. The load mode (described as "maximum load" in the table) was set. Tables 3 and 4 show each operating condition.

*¹ Performance guaranteed durability refers to the number of operations while maintaining performance.

*² Function guaranteed durability refers to the number of operations after the performance guaranteed durability regardless of the performance.

Table 5 summarizes the tests performed based on the above conditions. Tests were conducted in order from the top of the table, and the total test time was 631.8 hours. Evaluations were made by measuring performance at the beginning, during, and after each test. The performance measurement items are as follows.

1. Efficiency: Measured efficiency at input speeds of 150, 600, and 1500 RPM and load torque up to 500 N·m in CW and CCW.
2. No Load Running Torque (NLRT): Measure the input torque at an input rotation speed of 1500 RPM in CW and CCW.
3. Temperature: Measure the temperature of the base, test unit, and housing using the base-plate temperature of the vacuum chamber as the environmental temperature.
4. Lost motion (LM): With the input fixed, a light load is applied to the output shaft and the amount of twist is measured.
5. Torsional rigidity: With the input fixed, a load of up to $\pm 500\text{N} \cdot \text{m}$ is applied to the output shaft and the stiffness is measured.

Table 2. Test environment temperature

Durability type	Environment	Temperature setting	
		Solid	Grease
Performance Guarantee	Normal	20°C	20°C
	Low	-60°C	-40°C
	High	100°C	80°C
Functional Guarantee	Normal	20°C	20°C
	Low	-60°C	-40°C
	High	100°C	80°C

*Table 3. Operating condition: Performance Guarantee Durability^{*1}*

Driving Mode	Operating conditions
Bad road driving	Operating angle : ± 4 deg Output torque : $\pm 23.9 \sim 170$ N·m
Normal driving	Operating angle : $\pm 3 \sim 15$ deg Output torque : 33.5 N·m
Maximum load	Operating angle : ± 15 deg Output torque : 500 N·m

*Table 4. Operating condition: Functional Guarantee Durability^{*2}*

Driving Mode	Operating conditions
Bad road driving	Operating angle : 0 deg Output torque : 108 N·m
Normal driving	Operating angle : $\pm 3 \sim 15$ deg Output torque : 33.5 N·m
Maximum load	Operating angle : ± 15 deg Output torque : 500 N·m

Table 5. Summary of test items (Total test time : 631.8h)

Durability type	Environment	Mode		
		Bad road	Normal	Maximum Load
Performance Guarantee (428.1h)	Normal	72.0h	→ 11.3h	→ 2.3h
	Low	180.0h	→ 28.3h	→ 5.8h
	High	108.0h	→ 17.0h	→ 3.5h
Functional Guarantee (203.7h)	Normal	8.3h	→ 36.8h	→ 2.3h
	Low	0.0h	→ 91.9h	→ 5.8h
	High	0.0h	→ 55.1h	→ 3.5h

Test Equipment

The test apparatus consisted of a housing with the test unit inside a vacuum chamber, a motor for input and a direct drive motor for load outside the vacuum chamber. The test apparatus is shown in Figure 6, and its installation is shown in Figure 7 and 8.

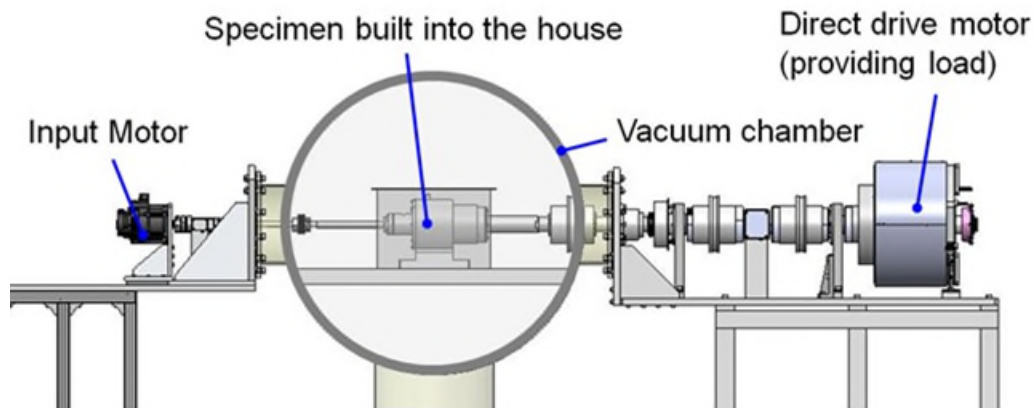


Figure 6. Configuration of the test equipment



Figure 7. Test equipment (output side)

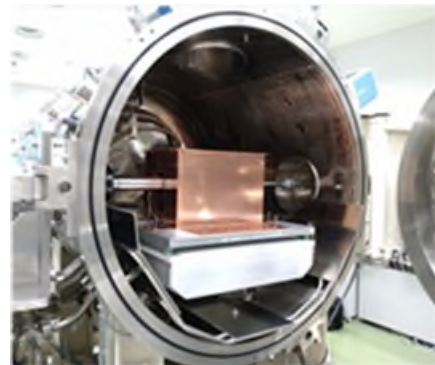


Figure 8. Specimen enclosed in copper plate

Test Results

Durability Test and Performance Measurement

The solid lubrication specimen completed the performance guarantee test and was stopped when the running torque and temperature increased after the normal running mode at room temperature in the

functional guarantee test. The elapsed time was 473.2 hours. The grease-lubricated specimen completed the entire run (631.8 h).

Figure 9 (a) and (b) show the changes in efficiency vs. temperature over the life of the test. The horizontal axis shows the elapsed time, and the vertical axis shows the efficiency and temperature of the test unit.

It can be seen that the efficiency of the dry lubricated test unit was less affected by temperature than the grease lubricated test unit (the red arrow in each figure represents the change in efficiency), and the dry lubricated test unit maintained a high level of efficiency up to 425 h of elapsed time.

The dry lubricated test unit showed a decrease in efficiency (from 79.0 to 54.2%), an increase in running torque, and a rise in temperature after the maximum load mode (elapsed time 428h) at the performance guarantee high temperature. However, since the performance guarantee, which was the initial target, was met, it was decided to continue the test until the reduction gear was damaged, and the test was shifted to the function guarantee normal temperature and continued. After the assumed normal running condition at the guaranteed function temperature (473.2 h), the running torque and temperature increased and an abnormal noise was observed, so the test was stopped to investigate.

In comparison, the grease-lubricated test unit completed the entire process (631.8 h). It should be noted that although the low temperature was set to -40°C , which is warmer than the condition of the dry lubrication test unit, the efficiency at the start of the low temperature test was low (37% at the performance guarantee and 36.5% at the function guarantee) and the running torque was high, and the efficiency improved as the temperature increased after the machine started running. The results showed that the characteristics of grease lubrication, which are affected by temperature, were well represented.

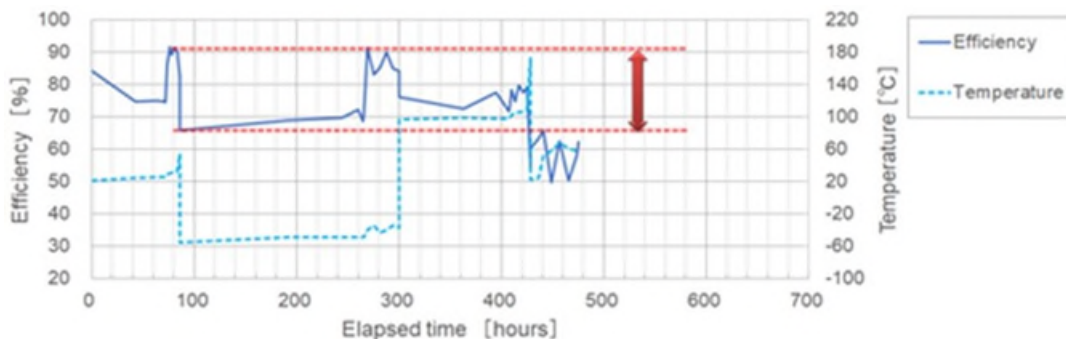


Figure 9(a). Elapsed time and efficiency - Solid lubrication -

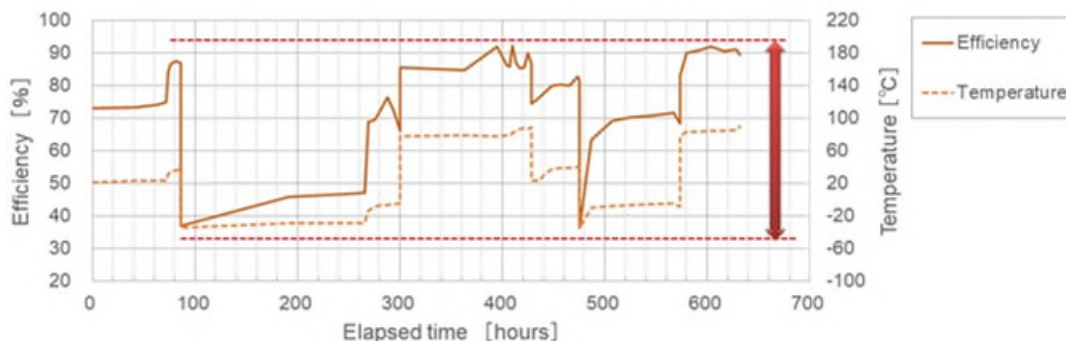


Figure 9(b). Elapsed time and efficiency - Grease lubrication -

Investigation of the Test Units

It was found that both test units were exposed to a common defect of the test equipment. The problem was radial play of the input shaft, which transmits the motor rotation from outside the vacuum chamber. This

radial play was found to be due to wear of the bearing track on the motor side of the bearing that supports the input shaft in the housing, shown in Figure 10.

Table 6 shows the parts of the planetary gear and Table 7 shows the parts of the SWG. In the dry lubrication test unit, the fixing bolt of the sun gear was found to be loose, and slight wear was observed on the tooth flanks of the planetary section at the tooth tips. The needle bearing surfaces were rough and worn. In contrast, in the grease-lubricated test unit, although oil content remained, wear on the tooth flanks was more advanced than in the dry-lubricated version. However, the needle bearings were not worn.

Next, the condition of the powder bag used for the dry lubrication specification was examined (see Figure 11). The powder was found to be discharged into the F/S cup, and the amount was measured and found to be almost exclusively from the powder bag attached to the lift cone (see Figure 12). The MoS₂ powder that had been discharged from the bag had an iron powder concentration of 10% by weight and was therefore believed to contain wear debris.

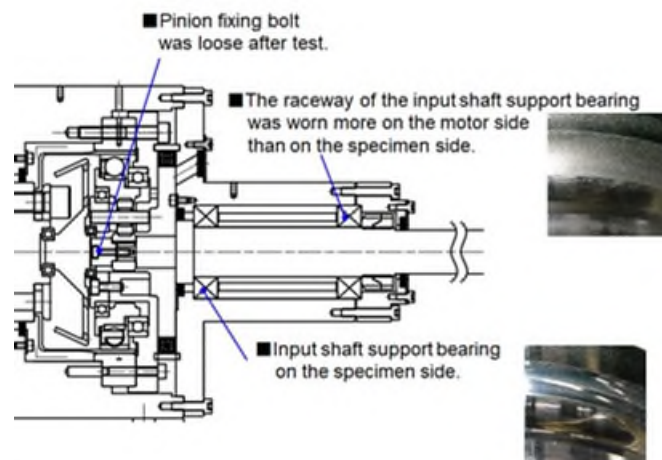


Figure 10. Input shaft support bearing failure

Table 6. Condition of planetary gear parts

Parts Name	Item	Lubrication specifications		Parts Name	Item	Lubrication specifications	
		Solid	Grease			Solid	Grease
Pinion	Tooth surface			Internal Gear	Tooth surface		
	Tooth profile				Tooth profile		
Planetary Gear	Tooth surface			Note (about Gears)	<ul style="list-style-type: none"> • rough surface • wear on the tip of teeth • MoS₂ transfer remains 	<ul style="list-style-type: none"> • wear on the tip of teeth • Oil residue 	
	Tooth profile			Needle bearing	Surface		
				NOTE	<ul style="list-style-type: none"> • rough surface • wear 	<ul style="list-style-type: none"> • no wear 	

Table 7. Condition of SWG parts





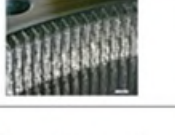



Parts	Item	Lubrication specifications		Parts	Item	Lubrication specifications	
		Solid	Grease			Solid	Grease
W/G	Outer ring circumference			F/S	Tooth surface		
	NOTE	<ul style="list-style-type: none"> MoS₂ powder cohesion and transfer remain Wear marks due to entrapment and adhesive wear Smoothly pulled out of F/S during disassembly 	<ul style="list-style-type: none"> Grease had turned to black Grease had less Oil Adhesive wear Hard to get out of F/S during disassembly 	C/S	Tooth surface		
F/S	Internal condition			NOTE (about tooth surface)		• wear due to entrapment and adhesive wear	• wear due to entrapment
	NOTE	<ul style="list-style-type: none"> MoS₂ powder cohesion and transfer remain surcumferencial scratch adhesion wear 	<ul style="list-style-type: none"> adhesin wear scratching due to adhesion when pulling out WG 				



Figure 11. Inside view of F/S



Figure 12. Powder bags attached to the lift cone

Conclusions

Based on the results of the investigation, the cause of this failure is believed to be the misalignment of the input shaft due to wear of the input shaft support bearing on the equipment side. In particular, the fixing bolt of the sun gear was loose in the dry lubrication test unit. This is believed to be due to the effect of the sun gear pivoting movement (precessional movement) caused by the tilt of the input shaft. This precession also occurred in the grease test unit, and as with dry lubrication, it is assumed that the running torque increased due to wear on the planetary gear and internal gear tooth flanks and the intrusion of wear particles into various parts. Countermeasures include increasing the size of the support bearing and extending the distance between the support bearings.

It is noteworthy that the W/G was smoothly disengaged despite the fact that abrasive wear was observed at the mating area between the W/G and F/S bore in the dry lubrication test unit as shown in Table 7. Normally, when abrasive wear occurs, it is difficult to remove the W/G from the F/S (as was the case with the grease-lubricated test unit), and scratches are created (see Table 7), but in the dry-lubricated test unit, the aggregation and transfer of MoS₂ powder were observed in the contacting area between the W/G and F/S, suggesting that the contacting area was lubricated even though abrasive wear occurred due to the effect of the MoS₂ powder. It is believed that the MoS₂ powder was effective in lubricating the mating parts even though abrasive wear occurred.

The performance was improved after shifting from rough road running to normal running and was a common observation with both test units. This may be due to the fact that the input rotational speed was higher and

the operating angle was larger under normal running conditions than under rough road running conditions, which resulted in more lubricant being applied to the contacting areas. Future testing will be conducted under more realistic driving conditions, including rough road, normal, and maximum load.

As a comparison between dry lubrication and grease lubrication, Figure 13 shows the temperature of the test unit on the horizontal axis and the efficiency on the vertical axis. The test results show that the dry-lubricated test unit (blue data) is less temperature- and speed-dependent than the grease-lubricated test unit (orange data).

A graph comparing the results of this test with past vacuum environment tests [1] [2] of SWG is shown in Figure 14. The horizontal axis shows the ratio of the rated torque to the average load torque during the test, and the vertical axis shows the total number of W/G revolutions. The black data shows the results of overseas tests using dry lubrication and the orange data shows the results of domestic tests using grease lubrication, with the dry lubricated test unit shown in light blue and the grease lubricated test unit shown in dark blue. The dry lubricated test unit was useful for longer periods than conventional dry lubrication, and the results were on the same level as grease lubrication, even under high loads.

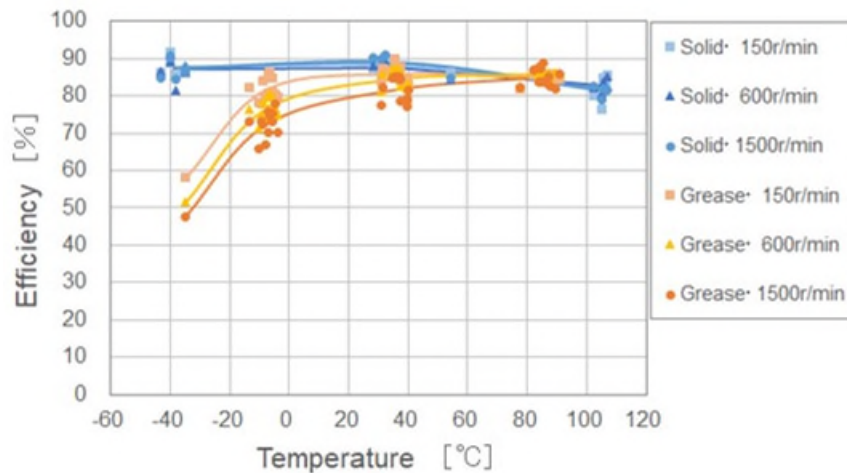


Figure 13. Temperature and Efficiency ($T = 500N \cdot m$)

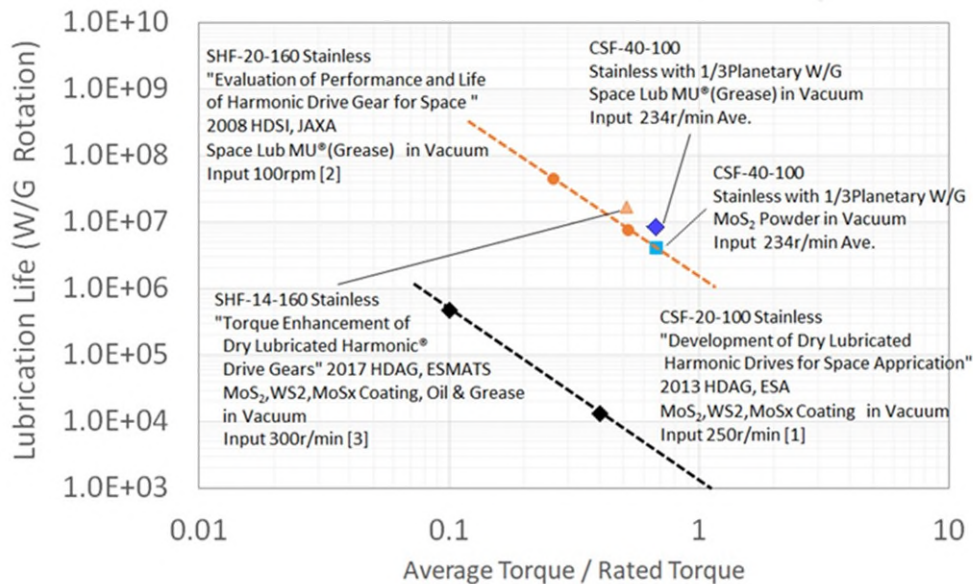


Figure 14. Rated torque ratio and lubrication life [1] [2]

Next Phase

The use of MoS₂ powder in the dry lubrication process for the SWG dramatically improved the lifetime despite testing in the high-load range, achieving the performance guarantee endurance goal. In addition, the results showed that low power consumption can be achieved because of the gear's high efficiency at low temperatures.

The use of MoS₂ powder for lubrication shown in this test is still in the trial-and-error stage, and we are currently verifying the effects of vibration during launch, the amount of MoS₂ powder ejected from the bag, the particle size of the MoS₂ powder, and the optimum coarseness of the powder bag. The following are some of the items currently in-work.



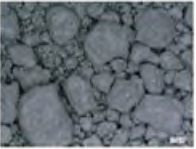






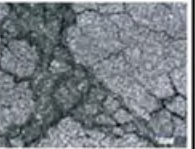
Vibration test

There is a possibility that MoS₂ powder may coagulate depending on the particle size. The results of a simple vibration test are shown in Table 8. It is desirable that the particle size is small consistent with the clearance of the parts needing lubrication, but it was found that small particles are more prone to coagulate due to the vibration than large particles. The coagulation was not resolved even after vacuum was drawn in this state. From this result, it was determined that the powder could coagulate during launch or storage, potentially reducing the amount discharged from the bag during usage. In the future, we will confirm how the state of the powder in the bag is affected by the vibration during launch. At the same time, the discharge from the bag will be evaluated.

Vertical shaft test

The steering actuator is actually installed with the rotation axis of the SWG vertical. In order to confirm the effect of this orientation on powder lubrication, the test apparatus shown in Figures 15 and 16 has been prepared and tests have been started. The latest information will be reported at the time of the presentation.

Table 8. Simple vibration test (magnification x50)

Particle Diameter	Initial	Movement			
		Horizontal Swing (by hand)	Vertical Swing (by hand)	Supersonic wave 28kHz	Supersonic wave 45kHz
2 μm					
20 μm					
Note		Particle size 2 μm is ball-shaped.	Particle size 2 μm is ball-shaped.	Particle size 2 μm is ball-shaped. X 59G m/s Y 39G m/s Z 27G m/s	Particle size 2 μm is ball-shaped. X 59G m/s Y 71G m/s Z 49G m/s

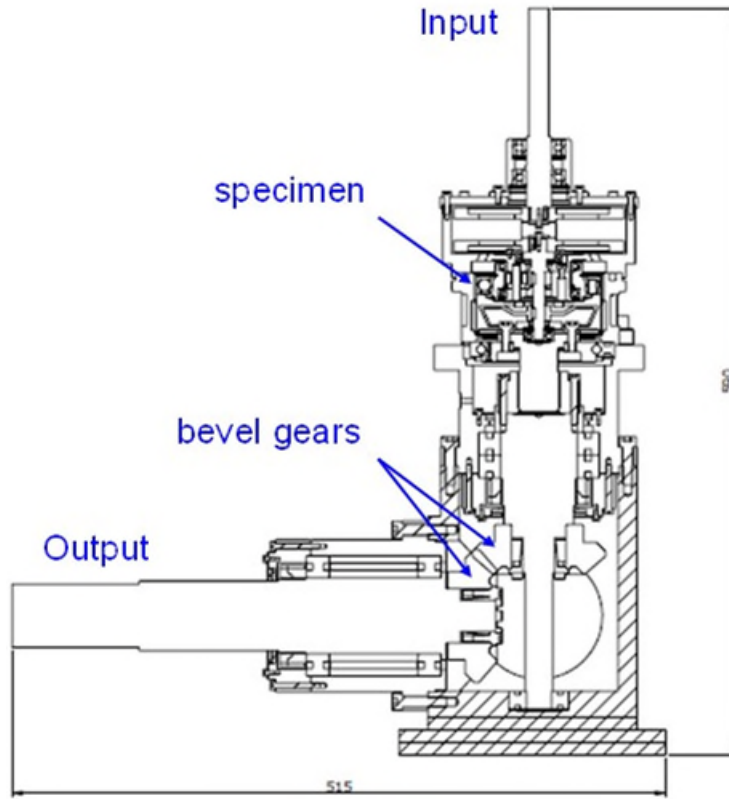


Figure 15. Vertical Shaft Test Cross-Section

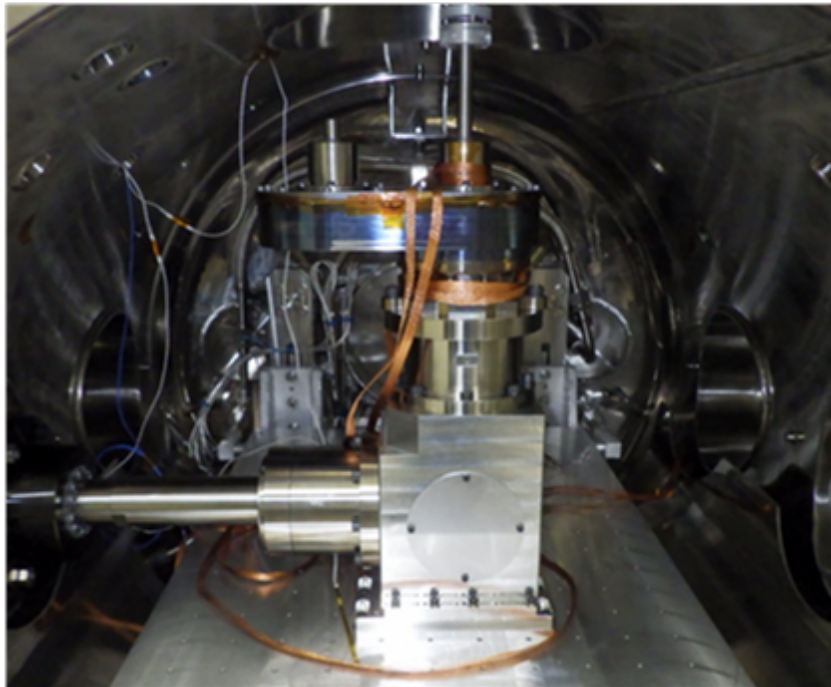


Figure 16. Vertical Shaft Test Photo

References

1. Markus Jansson, Hans Koenen, Jose-Luis Viviente, Adam Tvaruzka, Andreas Merstallinger : Development of Dry Lubricated Harmonic Drives for Space Applications, pp. 7,2013.
2. Hiroshi Miyaba, Shingo Obara, Mineo Suzuki and Keiji Ueura : Evaluation of Performance and Life of Harmonic Drive Gear for Space Use, pp. 52-53,2008.
3. Markus Jansson, Dr. Hans Koenen, Robert Nöbauer , Gottfried Dallhammer, Grazyna Mozdzen, Andreas Merstallinger : TORQUE ENHANCEMENT OF DRY LUBRICATED HARMONIC® DRIVE GEARS, pp.7,2017

On the Potential of Orthoborate Ionic Liquids to Meet Lubrication Challenges in Space Mechanisms

Román de la Presilla*, Oleg N. Antzutkin** and Sergei Glavatskih+

Abstract

An exploration of new space lubricant architectures is motivated by the lack of diversity of heritage space lubricants, their known limitations, increasingly demanding mission objectives, and the emergence of new regulations. In this study, we have benchmarked a non-halogenated orthoborate ionic liquid (IL) lubricant formulation against two space heritage commercial fluids based on multiply alkylated cyclopentane (MAC) and perfluoropolyether (PFPE) using a simple vacuum pin-on-disk test performed at three temperatures (40, 100 and 140°C). The study encompasses friction data, detailed wear quantification, high-quality surface digitalization, and mass spectrometer analysis of gases generated during tribological tests. The results reveal that each one of the different lubricant chemistries is conducive to a drastically different level, and character, of friction and wear behavior. The non-halogenated orthoborate IL formulation shows extraordinary surface protection compared to the heritage fluids in boundary lubrication, with average wear volume reductions in excess of an order of magnitude. This indicates a promising potential to expand the operating conditions of mechanisms before detectable wear occurs. Further research is needed to comprehensively verify and validate the usability of specific IL formulations for space lubrication; however, these results suggest that such efforts should be undertaken.

Introduction

Commercial formulations of vacuum-compatible lubricants are limited in diversity. They are mainly drawn from two chemical families: perfluoropolyethers (PFPEs) and multiply alkylated cyclopentanes (MACs). Both families have an ample track record of space mechanism qualifications, and their limitations are known. One shared limitation is that their underlying chemical nature hinders their ability to provide lubricity and prevent wear in the boundary lubrication regime. This lubrication regime is invariably encountered in many space-bound machine components that operate under scarce fluid lubrication or at low speeds [1], such as bearings undergoing oscillatory motions in gimbals [2], where there is no significant build-up of a hydrodynamic film that may separate the surfaces.

In such boundary conditions, PFPEs react with the steel interfaces and create metallic fluorides that act, in situ, as a boundary film [3]. These fluorides attack and decompose PFPE molecules, establishing a catalytic reaction [4] which negatively impacts their effective lubricant life [5]. Mitigating strategies usually involve passivation of the steel surfaces, using branched Y-type instead of linear Z-type PFPE, and setting a low ceiling on the contact pressures the lubricant can withstand. Additionally, PFPEs and their associated solvents are threatened by growing environmental concerns and the advent of new legislation, which may restrict or fully ban their production and use [6]. MACs, on the other hand, are synthetic hydrocarbons. As such, they are neither aggressively reacting with the steel surfaces nor inherently lubricious [7]. MAC lubricity can be improved with the use of additives [8], but this usually implies a penalty in vapor pressure [1] and requires the careful consideration of additive solubility, volatility, and eventual depletion. Such palliative measures mitigate these boundary lubrication issues without directly addressing the bulk chemistry of the lubricant. Their value lies in that incremental progress is obtained

* KTH Royal Institute of Technology, Stockholm, Sweden

** Luleå University of Technology, Luleå, Sweden

+ University of New South Wales, Sydney, Australia and Ghent University, Ghent, Belgium

with bounded uncertainty, but leaps in progress are likely to require the uprooting of the underlying source of the limitations.

The effectiveness of boundary lubrication relies on thin boundary films, formed on the lubricated surfaces through complex physicochemical processes governed by the lubricant molecules and their interactions with the surfaces. The lubricant design process thus relies on the availability of a wide range of molecular building blocks that allow for the design/selection of species that can readily adsorb at the surfaces and, if conditions are harsh enough, have degradation pathways that result in the moderated production of beneficial compounds. Ionic liquids (ILs) significantly expand the range of available species. A vast diversity of cations and anions and their combinations are possible [9]. ILs have several properties essential in lubrication. Some of them provide outstanding boundary lubrication performance [10–13]. ILs have also been shown to have low evaporation in vacuum [14, 15], low radiation sensitivity [16], electrical conductivity [17], as well as large operating temperature windows [18]. These attributes make ionic liquid design a promising avenue for developing the next generation of space lubricant solutions. Studies on ILs as space lubricants have already materialized promising results [14, 15, 19–22]. However, the chemical diversity of ILs poses as much of a tractability challenge as it does an opportunity. In general, most of the tribological IL research pertains to halogenated ILs. Halogen-containing anions are highly reactive to moisture. They can undergo hydrolysis, leading to the formation of hydrogen fluoride and other corrosive byproducts through tribochemical reactions, and compromising the integrity of the lubricated surfaces [9]. Another issue with halogens is the inherent risk of the formation of dangerous substances like hydrofluoric acid. They are also susceptible to the emergence of the same kind of regulations that threaten PFPEs. In the present study, we have benchmarked a non-halogenated orthoborate IL lubricant formulation against two space heritage liquids: one based on multiply alkylated cyclopentane (MAC) and another on perfluoropolyether (PFPE). The presence of boron in lubricants is known to enhance tribological performance [23]. The benchmarking encompasses friction data, detailed wear quantification, high-quality surface digitalization, and mass spectrometer analysis of gases generated during vacuum tribological tests. This investigation was carried out to probe whether the remarkable boundary lubrication performance previously demonstrated for non-halogenated orthoborate ILs [10–13] translates into a vacuum environment.

Materials and Methods

Lubricants

The ionic liquid formulation evaluated in this work consists of a blend of non-halogenated orthoborate ionic liquids. The reference heritage fluids are a linear perfluoropolyether (Fomblin Z25) and a multiply alkylated cyclopentane (Pennzane NYE 2001). These reference fluids are in common use as space oils and are used as provided by the manufacturers.

Test procedure

Experiments were conducted on a pin-on-disc tribometer at Aerospace and Advanced Composites GmbH in Wiener Neustadt, Austria. The tribometer was placed in a vacuum chamber that enabled ambient pressure reduction to less than 10^{-5} mbar throughout the tests. Steel balls (AISI 52100, 6-mm diameter, $R_a < 0.02 \mu\text{m}$) were used as pins. Bearing washer rings (WS81106) were used as discs (AISI 52100, $R_a \approx 0.06 \mu\text{m}$). Tests were carried out at a constant normal load of 15 N (1.1 GPa mean pressure), sliding speed of 0.2 m/s for 1750 meters, and temperatures of 40, 100, and 140°C. 20 μl of the lubricant samples were distributed around the raceway of the disc before the start of each experiment. Outgassing processes during the tests were analyzed using online mass spectroscopy in selected experiments. Surfaces were analyzed using a confocal laser scanning microscope (LEXT OLS5100), which allows for the direct measurement of the wear volume.

Results

Figure 1 shows a summary of the tribological results. Overall, and regardless of temperature, the MAC oil provides comparatively high and unsteady friction. The PFPE experiences a surprisingly steep decay

from the starting friction towards a very low friction coefficient (≈ 0.05). The orthoborate formulation yields a steady friction coefficient which consistently remains in the vicinity of 0.1. Increases in temperature worsen the MAC lubricant friction response at the onset of the test. The steepness of the friction decay with the PFPE is noticeably increased with temperature. For the orthoborate formulation, the temperature increase does not drastically affect the friction coefficient.

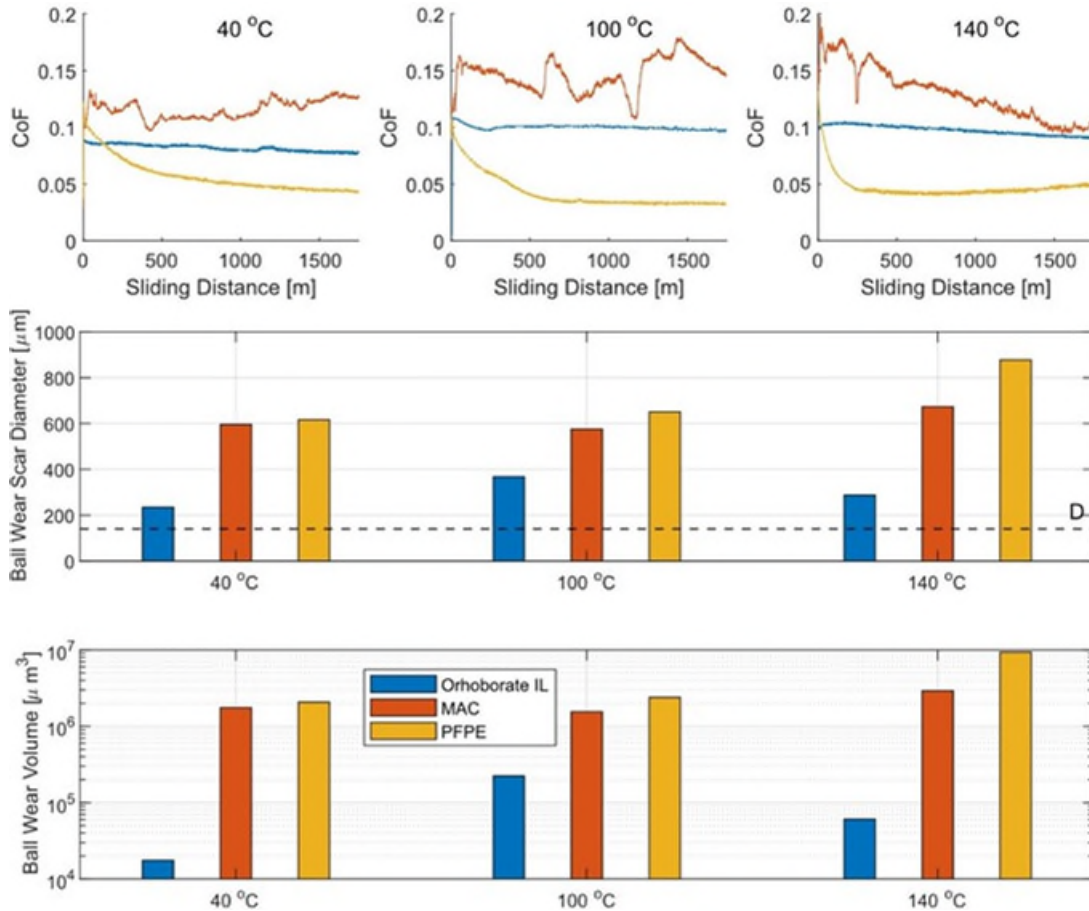


Figure 1: Friction and wear data for pin-on-disc tests at three temperature levels. The lubricants are IL blend (Blue), MAC (Red), and PFPE (Yellow). Coefficient of friction (CoF) as a function of sliding distance, wear scar diameters of the balls with dashed line D corresponding to the original Hertzian contact diameter for reference, and measured wear volumes.

Wear measurements (Figure 1) reveal that, regardless of the temperature level, the PFPE results in the largest wear volumes, followed in decreasing order by the MAC and then the orthoborate formulation. The differences between the orthoborate formulation and the reference liquids is large enough to necessitate the use of a logarithmic scale. For the PFPE, wear is aggravated with increasing temperature. The MAC only experiences a significant increase in wear at 140°C. The measured wear with orthoborate formulation increases with temperature at the 100°C level, but again decreases at 140°C. Notice that the wear scar diameter is not necessarily an accurate indicator of wear volume. Using the wear scar diameter to estimate volume tends to result in overestimation. Such overestimates would range from 4.5% to 180% in this data, with errors increasing at small wear volumes, where the effect of elastic recovery is more pronounced. Figure 2 shows images of the ball specimen wear scars. The images are presented with a common scaling to immediately communicate the discrepancy in the magnitude of material loss between the reference liquids and the orthoborate formulation. There is significant diversity in the character of the wear processes between the different lubricants. Detailed images of the experiments conducted at 100°C

(Figure 3) reveal that distinct material interactions between the sliding surfaces occur depending on the lubricant chemistry. A mirror finish of the ball is obtained with PFPE (Figure 3 - top row), where dotted products of a dark coloration appear to be causing visible scratches to the surface. The severity and scale of this scratching worsens at 140°C (Figure 2 - top right). Adhesive smearing and plowing characterize the MAC (Figure 3 - mid row), and the orthoborate formulation results in the deposition of dark and blue products at the contact patch (Figure 3 - bottom row).

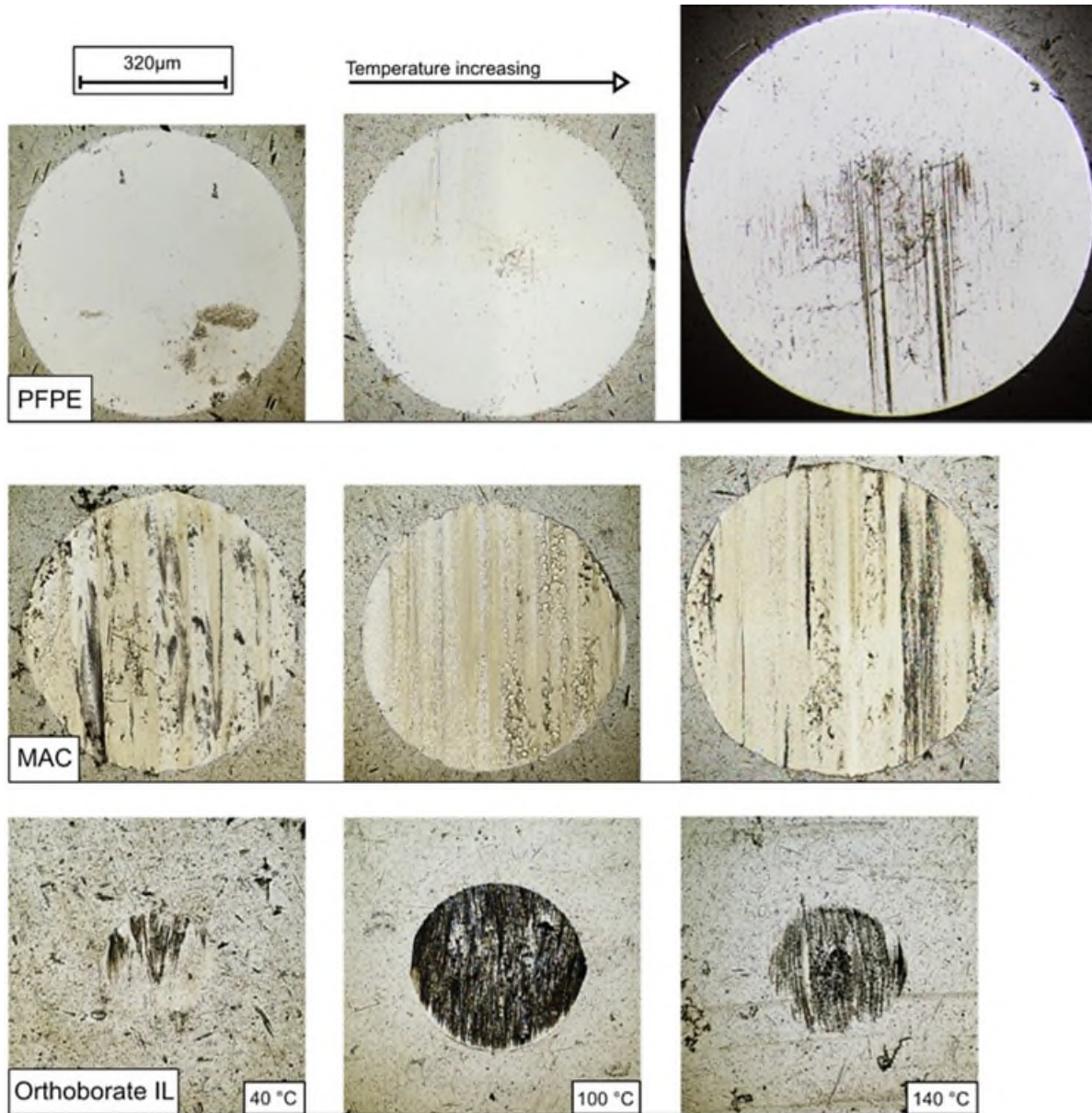


Figure 2: Representative ball specimen wear images for all lubricants at 40, 100 and 140°C.

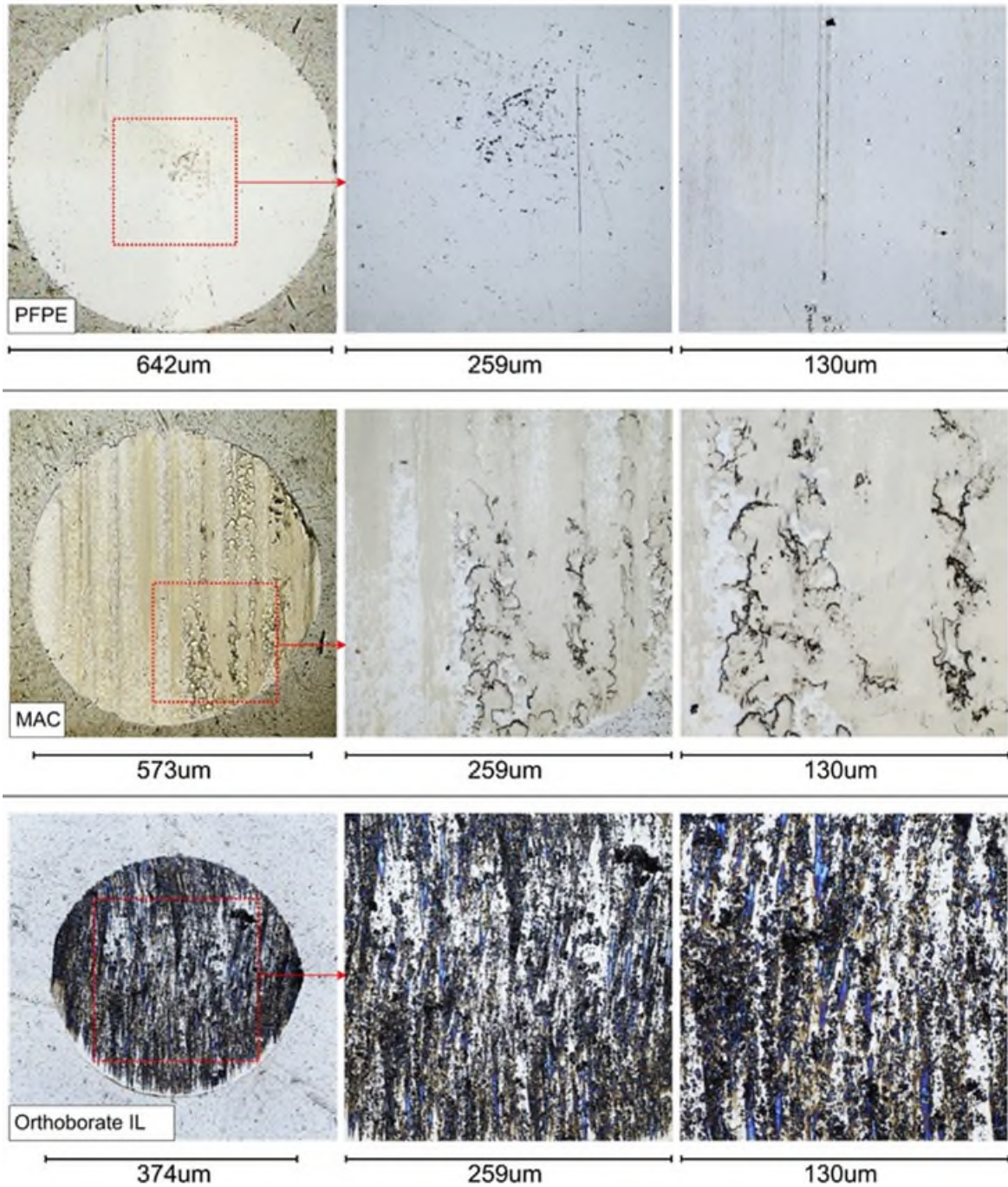


Figure 3: Detailed ball specimen wear at 100°C for PFPE, MAC and the orthoborate IL formulation.

Closer inspection of the orthoborate experiments at 40°C (Figure 4 - top row) indicates that the conditions are not causing the totality of the contact patch to be covered in deposited materials, with only traces of discolored material at the inlet of the contact. Topographical data (Figure 4 - Top right) shows that these dark deposits correspond to areas of increased wear depth. At 100°C the contact area of the ball is almost fully covered in dark patches and some blue products (Figure 4 - middle row). At 140°C the contact area of the ball is sparsely covered in similar dark patches (Figure 4 - bottom row).

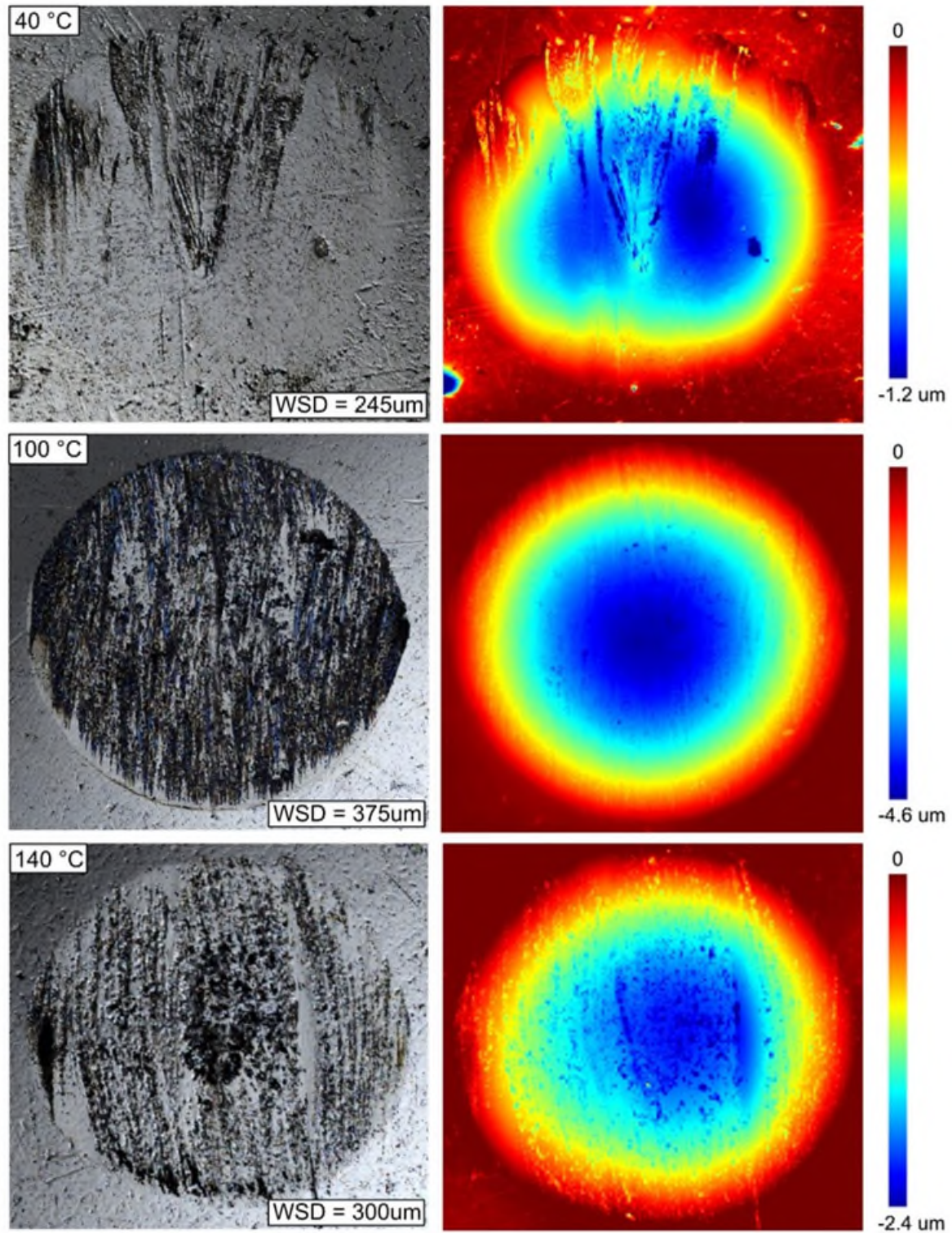


Figure 4: Ball specimen. Detailed wear scar diameter (WSD) images for the orthoborate formulation. Colormaps for the height have been corrected by removing the spherical geometry of the specimen via interpolation and subtraction.

Examination of the flat surfaces (Figure 5) shows that, with MAC, similar damages occur in the flat surface as they do in the ball at every temperature. PFPE resulted in mild abrasion of the track but not nearly substantial enough to do away with the manufactured surface features. Additionally, the surface has a patchy covering of a shimmering light blue material accompanied by brown products. For the PFPE, at 140°C, there is an additional presence of brown products towards the periphery of the contact track, resembling degradation products that have been observed in PFPE lubricated bearings [1]. The orthoborate IL formulation does not display any sign of surface alterations in the flat at 40 and 140°C, but the experiment at 100°C shows sparsely packed patches of material deposits.

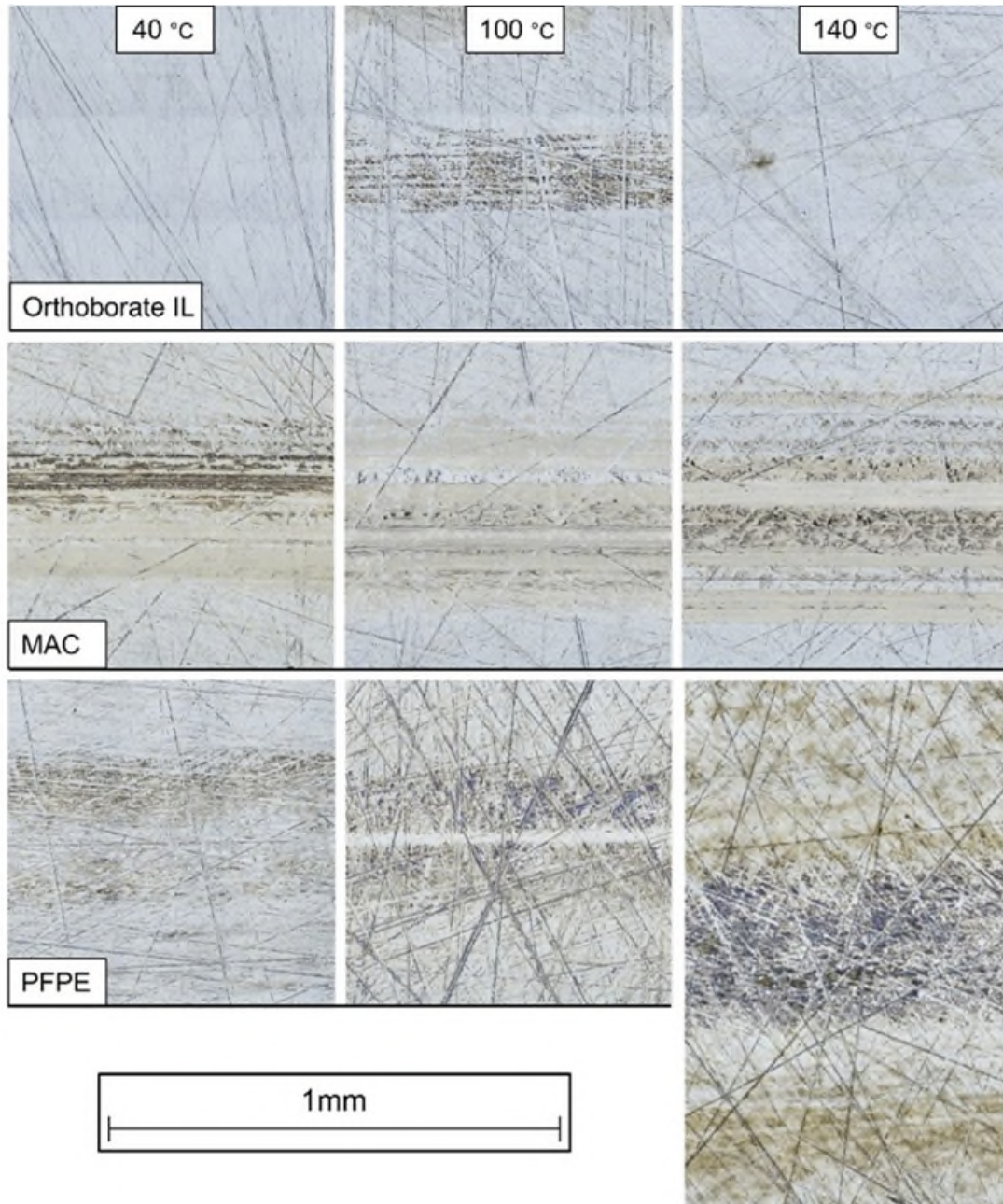


Figure 5: Flat specimen wear tracks.

Figure 6 shows the evolution of the residual gas analysis (RGA) data as a function of elapsed time in the test. Prominent early peaks at 18 and 28 are water and nitrogen respectively, decaying as the vacuum is improved. Consistent peaks emerging as a product of the tribological process were not detected for any of the tested lubricants.

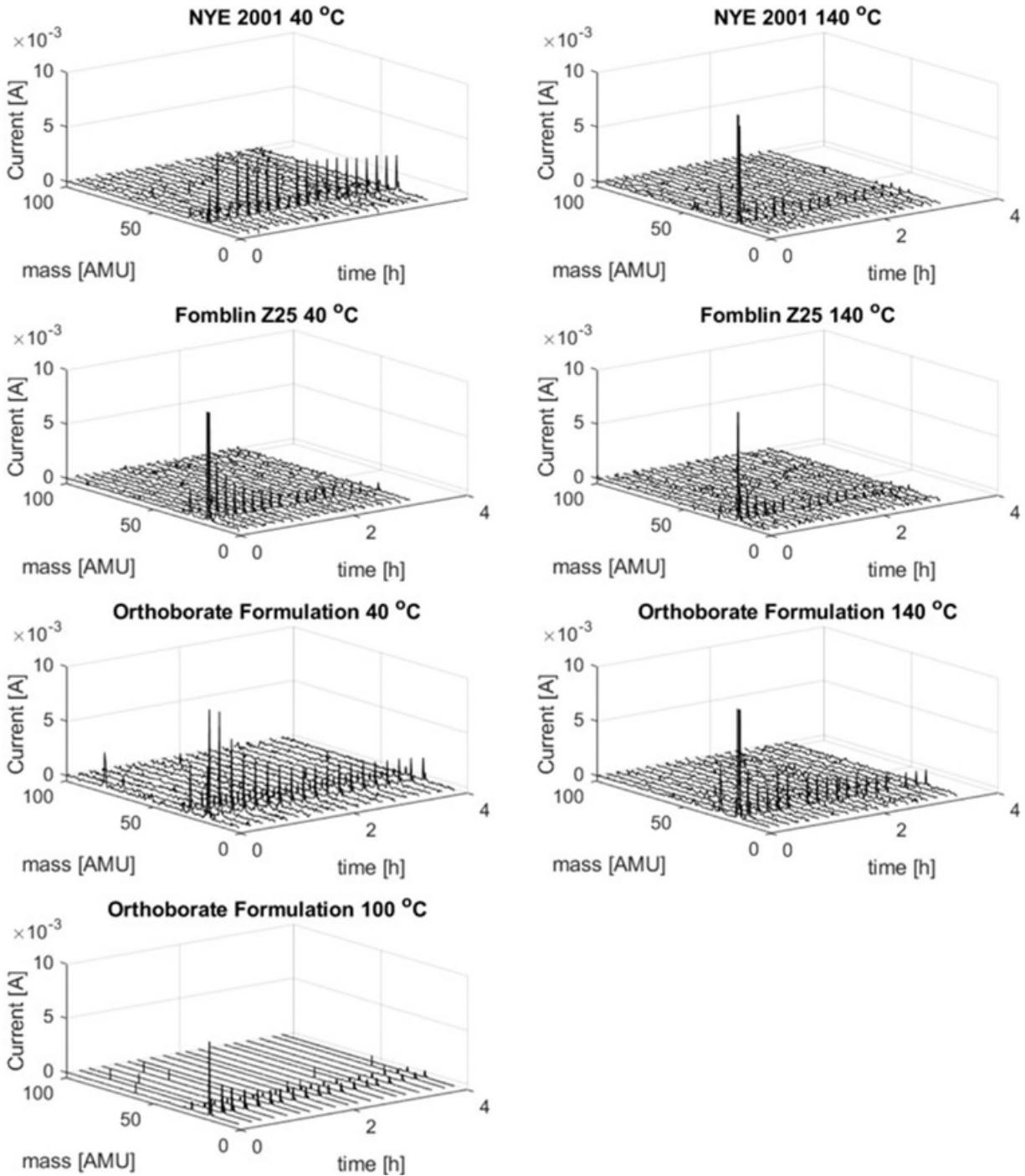


Figure 6: Residual gas analysis (RGA) for selected experiments.

Discussion

Each of the lubricants resulted in remarkably distinct tribological phenomena. The MAC is unable to sustain a stable friction coefficient in these conditions, despite being a fully formulated product that contains additives to improve its boundary lubrication properties. The wear scars of both the ball and the flat display adhesive smearing and plowing, indicating strong metal-to-metal interactions which, in turn, demonstrate the lack of a coherent and robust boundary film. The high friction peaks at the start of the test and the seizure-like morphology of the wear scars are reminiscent of previous work [7, 22]. The PFPE does provide very low friction, yet it does so at the expense of a substantial penalty in wear which, in appearance, resembles a chemical-mechanical polishing process. This polishing phenomenon is not unique to this work. It has been imaged before [7] and described as a "metallic luster" [22]. The extent of the PFPE wear at the higher temperature level is such that the contact pressure can be estimated to have dropped by about an order of magnitude by the end of the test. Care should be taken when comparing such results because the integrity of the contact conditions has been altered to such an extent that the mere comparison of CoF can be misleading, since two different contacts at vastly different pressures may be evaluated. The observed limitations of heritage fluids in terms of boundary lubrication properties are substantial and correspond to those reported in previous work for MAC [7, 8, 22] and PFPE [1, 3–5].

In contrast, the orthoborate formulation results in a steady friction coefficient which is consistently near 0.1 and major reductions in wear volume, regardless of temperature level. Comparison of ball wear volume measurements reveal that the orthoborate yielded wear reductions of roughly 100x at 40°C, 10x at 100°C, and 150x at 140°C when compared to the PFPE reference. Analogous comparison for the MAC results in 85x, 7x, and 48x, respectively. Examining the surfaces reveals the deposition and buildup of a tribologically generated film, particularly evident at 100°C. Previous research with orthoborate ILs has shown that these liquids have remarkable boundary lubrication properties in an air atmosphere [10–13] and it appears that the lubrication mechanisms involved are not compromised by the vacuum environment. Furthermore, these lubrication properties can be tuned by altering the anion [11] and cation architectures [10]. The lubrication mechanisms of these ILs have been attributed to their ability to strongly adsorb as a self-assembled layer at the surfaces, and, if conditions are harsh enough, they can decompose and form protective sacrificial films. The breakdown of the anion is critical for the formation of such films [10, 11] and its tribochemical breakdown sensitivity can be modified by altering both the core structure of the anion, as well as its peripheral features [11]. This offers a vast degree of flexibility in design of the lubricant and its properties, even when dealing exclusively in orthoborate formulations and especially when considering that blending of different ILs also adds further design freedom. Two strategic points emerge from the previous considerations: First, since the ionic liquid bulk is the surface-active component of the lubricant, it represents a lubrication strategy that is, in principle, not susceptible to end of life by additive depletion. Second, since the sensitivity to tribochemical breakdown in the presence of steel surfaces can be moderated by modifying the ionic liquid architecture, runaway chemically assisted wear of the surfaces can be avoided, as it was avoided in this study.

The reduction in wear for the orthoborate IL formulation as the temperature increased from 100 to 140°C is an interesting phenomenon that requires further experimentation to explain. The lower viscosity afforded by the higher temperature may ease the displaced lubricant in returning to the contact track before the next revolution occurs. Increased surface activity of the IL formulation could also be a factor.

There is a lack of consistent emerging peaks in the residual gas analysis (RGA) as the test progressed. Considering the visual evidence of degradation products that are present at the wear scars for all lubricants, it may be related to the range of the instrument, which is not registering heavier species, or its signal-to-noise ratio in conjunction with the duration of the test, and other outgassing products in the vacuum chamber, which may have precluded detection. Nevertheless, it does indicate that the none of the lubricants appear to be outgassing significantly during the test.

Boundary lubrication properties are not the sole parameter by which a lubricant formulation should be evaluated. Vapor pressure, outgassing, viscosity index, pour point, and many other considerations must be leveraged according to the demands of the application. The field of space tribology has evolved and adapted to these limitations of boundary lubrication performance. Nevertheless, it is an aspect where available fluid lubricant technology is lacking and in which progress has the potential to significantly expand the operation envelopes of space mechanisms while still meeting stringent wear and friction criteria during qualification.

Conclusions

- Distinct boundary lubrication mechanisms of MAC, PFPE and an orthoborate IL blend were observed.
- The orthoborate ionic liquid formulation provides steady and low friction ($\text{CoF} \approx 0.09 - 0.1$) and the lowest wear in boundary lubrication, regardless of temperature. This formulation resulted in wear volume reductions of over 88 times when compared to the PFPE lubricant reference, and over 47 times less than the MAC reference, when averaging across all temperatures evaluated.
- Optical evidence of sacrificial tribofilm deposition was obtained for the orthoborate ionic liquid formulation. These results indicate that the sacrificial boundary lubrication mechanism exhibited by the orthoborate formulation in harsh tribological conditions can indeed be translated into a vacuum environment.
- MAC formulation is not inherently lubricious. It displays high and unsteady friction caused by plowing and adhesive effects.
- PFPE resulted in an aggressive polishing wear mechanism, which provided low friction at the cost of high wear rates.
- PFPE showed substantial increases in wear with increasing temperature, which hints towards temperature accelerated chemical reactions that are driving the wear process.
- Ionic liquids are versatile in the cation and anion architecture and pairings, but more importantly, additional design freedom can be achieved by mixing different ionic liquids to enhance performance flexibility.
- Further research addressing other properties of orthoborate ILs that are relevant to the lubrication of space mechanisms will be conducted.

Acknowledgements

The Swedish Foundation for Strategic Research (project EM16-0013), the Knut and Alice Wallenberg Foundation (project KAW2012.0078), and the Swedish Research Council (projects 2022-04819, 2018-05017, and 2013-5171) are gratefully acknowledged for financial support. The Research Initiative on Sustainable Industry and Society (IRIS) is also acknowledged for providing funding for the acquisition of the confocal laser-scanning microscope employed to produce the surface images presented in this work.

References

- [1] E. Roberts, Space tribology: its role in spacecraft mechanisms, *Journal of Physics D: Applied Physics* 45 (50) (2012) 503001.
- [2] R. de la Presilla, S. Wandel, M. Stammer, M. Grebe, G. Poll, S. Glavatskih, Oscillating rolling element bearings: A review of tribotesting and analysis approaches, *Tribology International* (2023) 108805.
- [3] S. Mori, W. Morales, Tribological reactions of perfluoroalkyl polyether oils with stainless steel under ultrahigh vacuum conditions at room temperature, *Wear* 132 (1) (1989) 111–121.
- [4] D. J. Carré, Perfluoropolyalkylether oil degradation: inference of fef3 formation on steel surfaces under boundary conditions, *ASLE transactions* 29 (2) (1986) 121–125.
- [5] M. Buttery, L. Gaillard, S. Rajala, E. Roberts, T. Rohr, A. Merstallinger, Fomblin z25: A new method for its degradation assessment & proposal for safe operation in space, *Proc. 15th ESMATS* (2013).
- [6] T. Thomas, A. Malek, J. Arokianathar, E. Haddad, J. Matthew, Global regulations around pfas: The past, the present and the future, *International Chemical Regulatory & Law Review (ICRL)* 6 (1) (2023).
- [7] M. Masuko, H. Mizuno, A. Suzuki, S. Obara, A. Sasaki, Lubrication performance of multialkylatedcyclopentane oils for sliding friction of steel under vacuum condition, *Journal of Synthetic Lubrication* 24 (4) (2007) 217–226.
- [8] S. C. Peterangelo, L. Gschwender, C. E. Snyder Jr, W. R. Jones Jr, Q. Nguyen, M. J. Jansen, Improved additives for multiply alkylated cyclopentane-based lubricants, *Journal of Synthetic Lubrication* 25 (1) (2008) 31–41.
- [9] M. Cai, Q. Yu, W. Liu, F. Zhou, Ionic liquid lubricants: When chemistry meets tribology, *Chemical Society Reviews* 49 (21) (2020) 7753–7818.
- [10] P. Rohlmann, J. J. Black, S. Watanabe, J. Leckner, M. R. Shimpi, M. W. Rutland, J. B. Harper, S. Glavatskih, Tribochemistry of imidazolium and phosphonium bis(oxalato)borate ionic liquids: Understanding the differences, *Tribology International* 181 (2023) 108263.
- [11] B. Munavirov, J. J. Black, F. U. Shah, J. Leckner, M. W. Rutland, J. B. Harper, S. Glavatskih, The effect of anion architecture on the lubrication chemistry of phosphonium orthoborate ionic liquids, *Scientific Reports* 11 (1) (2021) 1–16.
- [12] P. Rohlmann, S. Watanabe, M. R. Shimpi, J. Leckner, M. W. Rutland, J. B. Harper, S. Glavatskih, Boundary lubricity of phosphonium bisoxalatoborate ionic liquids, *Tribology International* 161 (2021) 107075.
- [13] R. de la Presilla, J. Leckner, S. Glavatskih, Grease lubricity in the fretting contact: Are ionic liquids the solution?, *Tribology International* 185 (2023) 108509.
- [14] N. Dörr, A. Merstallinger, R. Holzbauer, V. Pejaković, J. Brenner, L. Pisarova, J. Stelzl, M. Frauscher, Five-stage selection procedure of ionic liquids for lubrication of steel–steel contacts in space mechanisms, *Tribology Letters* 67 (2019) 1–18.
- [15] K. W. Street Jr, W. Morales, V. R. Koch, D. J. Valco, R. M. Richard, N. Hanks, Evaluation of vapor pressure and ultra-high vacuum tribological properties of ionic liquids, *Tribology Transactions* 54 (6) (2011) 911–919.

- [16] X. Fan, L. Wang, Highly conductive ionic liquids toward high-performance space-lubricating greases, *ACS Applied Materials & Interfaces* 6 (16) (2014) 14660–14671.
- [17] A. B. Reddy, F. U. Shah, J. Leckner, M. W. Rutland, S. Glavatskih, Ionic liquids enhance electrical conductivity of greases: an impedance spectroscopy study, *Colloids and Surfaces A: Physicochemical and Engineering Aspects* 683 (2024) 132875.
- [18] K. Kobayashi, A. Suzuki, Y. Fujinami, T. Nogi, S. Obara, M. Masuko, Lubrication performance of ionic liquids as lubricants for space mechanisms under high vacuum and low temperature, *Tribology Online* 10 (2) (2015) 138–146.
- [19] M. Buttery, M. Hampson, A. Kent, C. Allegranza, B. Park, Development of advanced lubricants for space mechanisms based on ionic liquids, in: *Proceedings of the European Space Mechanisms and Tribology Symposium*, (2017).
- [20] V. Totolin, M. Conte, E. Berriozábal, F. Pagano, I. Minami, N. Dörr, J. Brenner, A. Igartua, Tribological investigations of ionic liquids in ultra-high vacuum environment, *Lubrication Science* 26 (7-8) (2014) 514–524.
- [21] T. Okaniwa, M. Hayama, The application of ionic liquids into space lubricants, in: *Proceedings of the 15th European Space Mechanisms and Tribology Symposium*, Noordwijk, The Netherlands, 2013, pp. 25–27.
- [22] A. Suzuki, Y. Shinka, M. Masuko, Tribological characteristics of imidazolium-based room temperature ionic liquids under high vacuum, *Tribology Letters* 27 (2007) 307–313.
- [23] F. U. Shah, S. Glavatskih, O. N. Antzutkin, Boron in tribology: From borates to ionic liquids, *Tribology Letters* 51 (3) (2013) 281–301.

Design and Test of Bearings used in Electromechanical Systems Operating under High Vibration Environments

Kyle Gotthelf*, Javier Becerra* and Andrew Maurer*

Introduction

High-power-density battery and motor technologies continue to expand the use of electromechanical actuators into aerospace applications previously reserved for hydraulic systems. Among other applications, high-power electromechanical Thrust Vector Control (TVC) systems now trade favorably for certain launch vehicles and upper-stage vehicle systems. TVC application requirements have significant implications for the design of related ball/lead screw and thrust bearing subsystems.

Electromechanical Thrust Vector Control systems experience unique environments relative to other space mechanisms – specifically they operate in close proximity to pyroshock devices, during highly dynamic engine firings ($>60 \text{ g}_{\text{rms}}$), and with challenging radiative and conductive thermal boundary conditions (due to both nearby cryogenic fuels and combustion events). In this paper we report on the unique considerations required to make a TVC thrust bearing design close, in particular the impact of the vibratory conditions on the drag torque of the rotating assembly.

Initial Design and Analysis

Spaceflight mechanism bearing analysis is typically characterized by two regimes: high non-operational loading during launch followed by low to moderate loading during operation. In contrast, TVC systems experience high nonoperational loads during launch, followed by high (or even *higher*) *operational* loads and thermal extremes after separation (for second stage vehicles). This presents a unique challenge to the design wherein common simplifying assumptions may no longer be valid.

One such assumption is the thrust bearing drag. Compared to a solar array or antenna position mechanism, the operational load and velocity of a TVC system are extremely high. This causes the drag of the primary thrust bearing to constitute a much more significant fraction of the system power relative to other orbital mechanisms. Key questions in this design phase include:

- Are common assumptions for the scaling of variable losses (e.g., friction) valid under extreme vibratory conditions?
- Can viscous losses associated with common lubricants (e.g., Braycote) be tolerated at temperatures below -50°C ?
- Given the above, is there a bearing preload scheme which maintains preload under high operational and dynamic loading, while also accommodating extreme survival temperature ranges?

As is typical, the first analysis iteration was performed for PDR using ANSYS to analyze the vibration environment and Orbis to analyze the bearing maximum mean hertzian contact stress, truncation, life, and drag torque. In such an analysis, the bearing loads come from operation loads (pushing and pulling on the engine), vibration reaction forces created inside the actuator from the given vibration PSD boundary condition, and thermal loading due to CTE mismatch. Applying these forces cumulatively to the thrust bearings showed very high drag torques due to coulomb and viscous drag torques. Therefore, various tests were performed to validate the analysis.

* Honeybee Robotics, Longmont, CO

In addition, torque margin analysis was proving difficult to pass given the wide temperature range (approximately -80°C to 120°C) and the unknown effects of vibration loading on the system. Various best practices were deployed for this challenging application:

- Steel bearing sleeves to isolate bearings from the aluminum housing and prevent excessive or insufficient preload due to CTE
- Tight bearing fits to reduce tolerance stack ups within the actuator
- Limiting viscous drag by controlling lubricant quantities

Still, drag torque predictions based on actuation load combined with random vibration loads were found to be infeasibly large. Thus, a test campaign was commissioned as it remained unclear as to whether the bearing drag torque during vibratory and actuation loads were appropriately margined.

Variable/frictional losses are afforded significant Factors-of-Safety in sources such as NASA-STD-5017, however it remained an open question whether bearing preloads (set via precision-ground bearing pairs) and vibration loads (per an environment set by specification) should properly be booked as Known or Variable loads in operational cases. Furthermore, Honeybee’s standard practice conservatively assumes that *desirable* frictional torques (e.g., in friction brakes) must drop to zero under vibratory conditions, however such an assumption is clearly not conservative for the drag torque of an operating bearing system. Thus, we sought to determine the degree to which vibratory loading increased or decreased the bearing drag for a highly preloaded and highly dynamically loaded bearing set.

During the design and analysis phase, the bearings were optimized to minimize coulomb drag torque while still maintaining proper allowables for bearing max mean hertzian contact stress and no truncation. The stress and truncation results are also evaluated under worst-case bearing tolerances (raceway curvature, preload, and contact angle) and thermal extremes plus thermal gradients. It was found that increasing raceway curvature makes the largest impact on coulomb drag torque but also has a huge impact on increased contact stress. Therefore, the outer race has a much higher curvature than the inner race which not only balances the hertzian contact stress between the inner and outer race but allows drag torque to be reduced. A higher raceway curvature also helps reduce stiffness, which reduces reaction loads from vibration analysis. A larger contact angle also helps with drag torque but had a negative impact on bearing truncation and allowable deflections. Low contact angles were also desired to minimize bearing moment stiffness which results in lower moment load reactions due to vibration loading. Bearing preload was also minimized to reduce drag torque but had its limitations to avoid dramatic ball offloading and bearing contact stress. This results in the key bearing parameters shown in Table 1.

Table 1. Key Bearing Parameters

Description	Value	Units
Free Contact Angle	15	Degrees
Inner Race Curvature	52	Percent
Outer Race Curvature	56	Percent
Un-Mounted Preload	2670	Newtons

Ball offloading was a concern in the initial design phase, so this is also something to keep an eye on during the testing and post-test inspections. The Orbis analysis shows that the ball will offload in both axial and radial vibration directions. This will result in unknown load conditions not predicted by Orbis when the balls recontact the raceway in a highly dynamic loading. Things to look for include excess torque spikes and ball or raceway damage or brinelling.

A specifically designed test article was prepared to allow exploration of these factors on flight hardware, as shown in Figure 1.

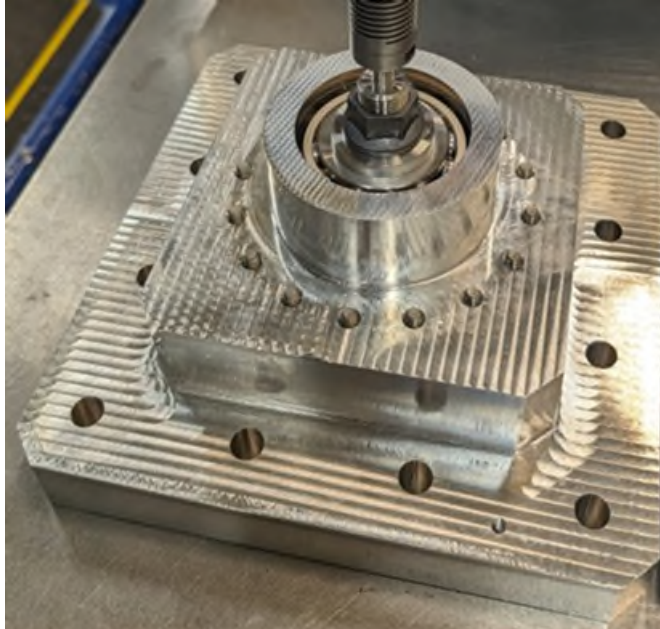


Figure 1. Test Article with Flight Bearings

Structural Analysis

To inform the drag torque estimates before vibration testing, a structural analysis model was created for the test article and bearing loads were extracted for the various random vibration profiles. Beam loads were also provided to calculate crucial fastener margins such as joint slip and joint separation. ANSYS 2022 R2 was used to perform the analysis.

The analysis model included key geometry that can be seen in Figure 2. Bearing race geometry was not modelled, but rather the bearing was modelled as a joint connection with Multi-Point Constraint formulation and stiffness coefficients from Orbis which can be seen in Table 2. These stiffness values were iterated on several times using the extracted bearing loads of each run until the values converged within 10%. Note that the bushing connection has a local coordinate system that differs from the model coordinate system, with the X and Y axis being the radial direction of the bushing and the Z axis being the axial direction.

After performing typical model checks the modal analysis was run from 0.00 to 3000.00 Hz with a fixed support applied to the calculated pressure cones on the housing. This can be seen in Figure 3. The modal analysis resulted in four (4) distinct modes; Table 3 shows the frequencies, mass participation and brief description of the mode shape.

Lastly, a random vibration analysis was run on the model for both the in (X axis GCS) and through plane (Y axis GCS) direction. The same profile was used for both analysis and a total of eight (8) analysis were run at various levels. Two analyses were done at full levels (64.41 g_{rms}), two at -3 dB (45.60 g_{rms}), two at -6 dB (32.28 g_{rms}) and two at -12 dB (16.18 g_{rms}).

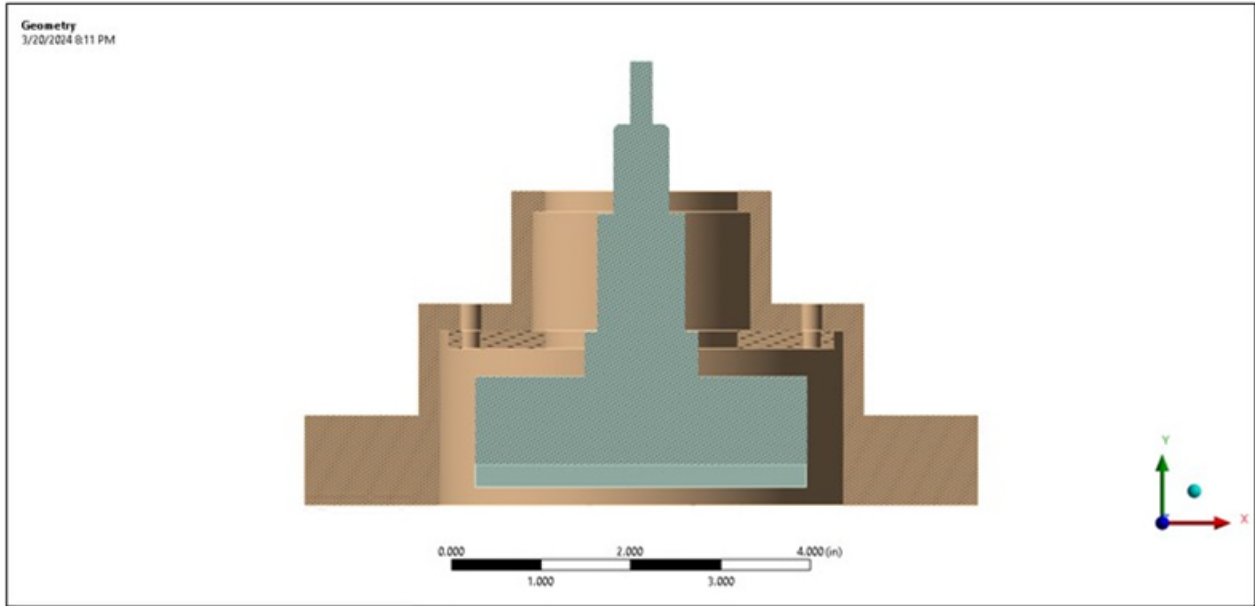


Figure 2. ANSYS Model – Final Test Setup with Flight Bearings

Table 2. Bearing Stiffness Inputs

Direction	Stiffness Coefficient
Kx (radial)	6.36e8 (N/m)
Ky (radial)	7.04e8 (N/m)
Kz (axial)	2.64e8 (N/m)
Kxx (radial)	2.17e5 (N-m/rad)
Kyy (radial)	1.97e5 (N-m/rad)
Kzz (axial)	0.11 (N-m/rad)

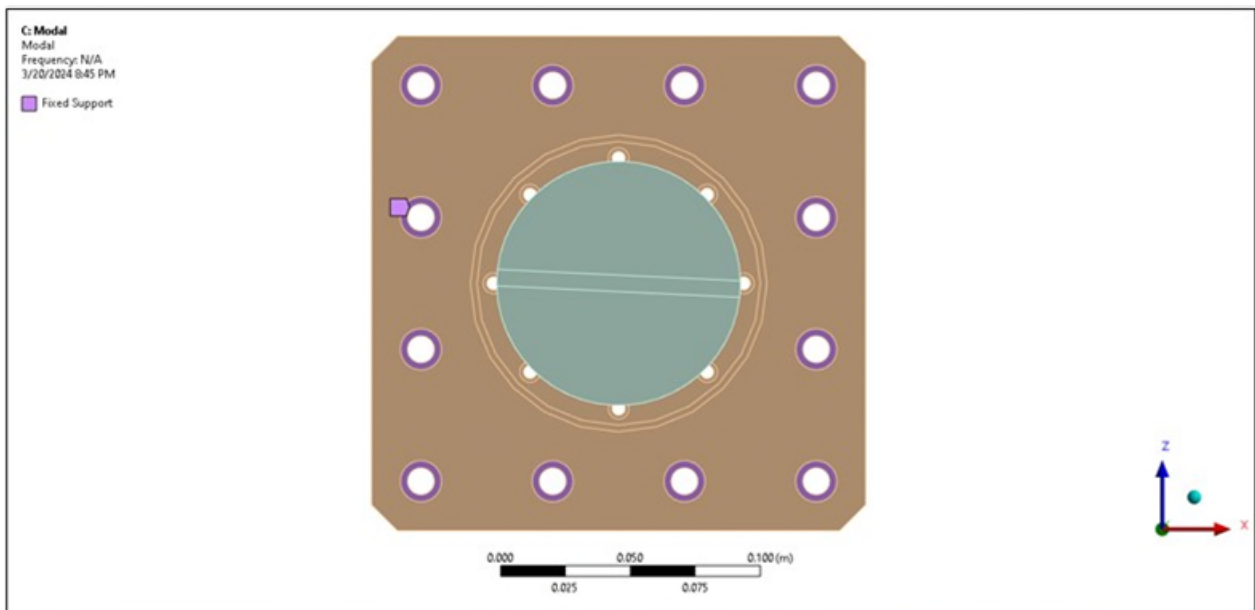


Figure 3. Bearing Housing Pressure Cones

Table 3. Resulting Fundamental Frequencies and Mass Participation

Mode	Freq. (Hz.)	X Dir.	Y Dir.	Z Dir.	Rot. X	Rot. Y	Rot Z.	Description
1	1.17	0.00%	0.00%	0.0%	0.00%	3.94%	0.00%	Shaft spinning about Y axis (GCS)
2	821.16	14.65%	0.00%	0.00%	0.00%	0.00%	14.08%	Shaft bending about X axis (GCS)
3	848.93	0.00%	0.00%	14.54%	14.13%	0.00%	0.00%	Shaft bending about Z axis (GCS)
4	1529.40	24.98%	0.00%	0.00%	0.00%	0.00%	0.00%	Shaft pumping in/out about Y axis (GCS)

Development Testing

Thrust Bearing Vibe Test details are shown below, which are intended to confirm the predicted bearing coulomb drag torque vs actual drag torque during vibration environments. This Initial Test was performed very early on (before the final flight bearing design was complete) in order to get preliminary results to reduce risk. Further testing is performed on the flight bearings which is detailed later. Note that the initial test has a smaller dummy mass which is sized for the smaller bearings used compared to the final test using flight bearings:

Initial Testing (see Figure 4 and Table 4):

1. Input shaft fitting to allow measurement of bearing drag (by hand with a torque watch) while under vibratory conditions
2. GEVS vibe input (Qualification) was used for the test (due to facility limitations, and desire for comparison with lower/typical vibration environments)
3. High misalignment constant velocity coupling was used to isolate vibrations from the measurement tool
4. Bearing housing with DB angular contact bearings and ID-mounted dummy mass to provide inertial loading

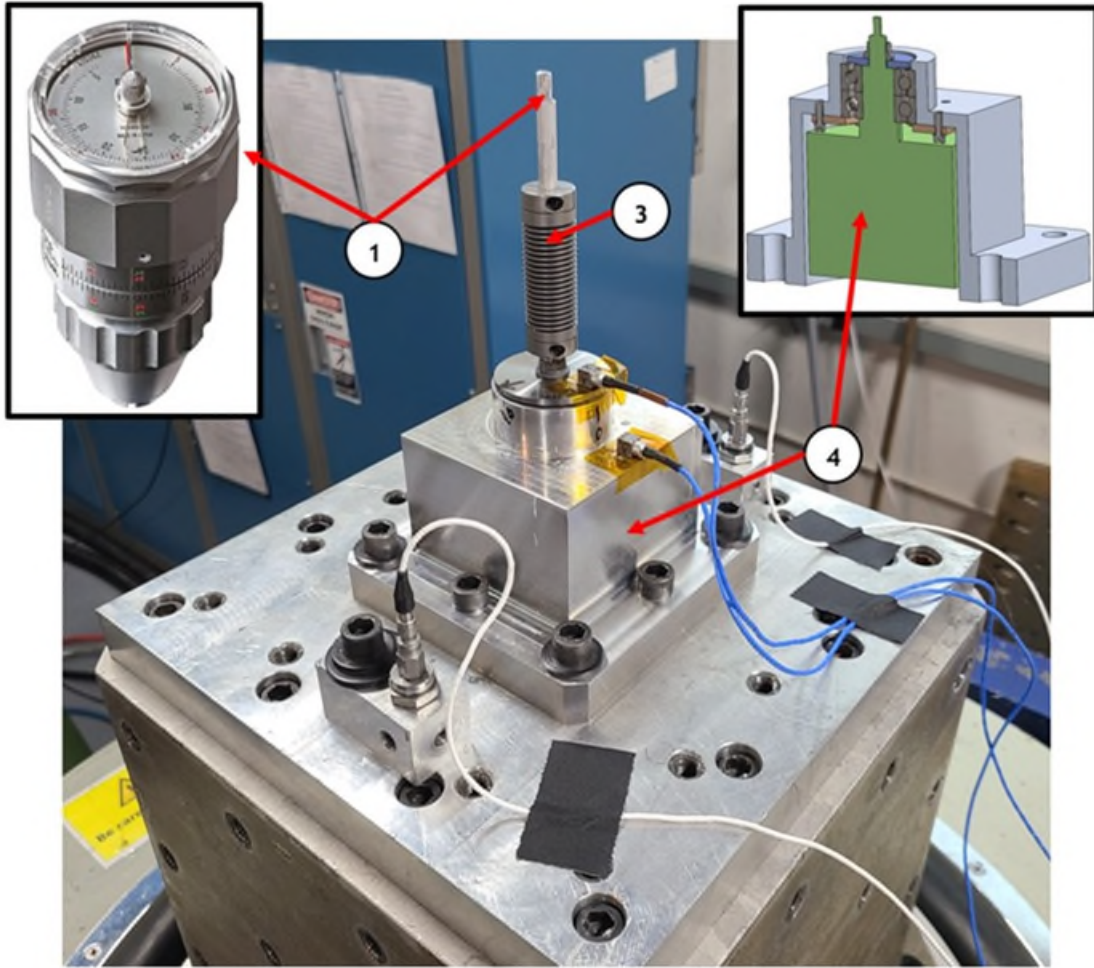


Figure 4. Initial Test Setup – Smaller, Non-Flight Bearings

Table 4. GEVS Vibration Input

Generalized Random Vibration Test Levels
Components (ELV)
22.7-kg (50-lb) or less

Frequency (Hz)	ASD Level (g^2/Hz)	
	Qualification	Acceptance
20	0.026	0.013
20-50	+6 dB/oct	+6 dB/oct
50-800	0.16	0.08
800-2000	-6 dB/oct	-6 dB/oct
2000	0.026	0.013
Overall	14.1 G_{rms}	10.0 G_{rms}

Thrust bearing vbe test results are shown in Table 5.

Table 5: Initial Test Results

	Description	Value	Units
Bearing Drag Predictions from Orbis	No load (preload only)	7.1	mNm
	1s dynamic/vibe loads	110	mNm
	3s dynamic/vibe loads	520	mNm
Measured Bearing Drag	No load (preload only)	28	mNm
	Dynamic/vibe loads	14	mNm

These test results demanded further investigation in order to correct several concerns with the initial test:

- Actual flight vibration environment is significantly higher than GEVS (64.4 g_{rms} vs 14.4 g_{rms})
- The analog torque watch suffered from some vibratory motion during the test, making the true drag value difficult to discern
- Only one vibratory level/environment was tested, leaving the *trend* of drag torque reduction vs vibration level unknown

The revised test plan was as follows:

Final Testing (see Figure 5):

1. Digital torque watch to capture drag torque with a higher sample rate and reduce human error
2. Higher vibe input of 64.4 g_{rms} was used for the test (per flight spec, proprietary profile not shown), and data was taken in ~11.5 g_{rms} increments
3. Same coupling as used in the Initial Test
4. Different fixture as used in the Initial Test, but sized to accommodate larger bearings and increased loading without causing rapid unscheduled disassembly

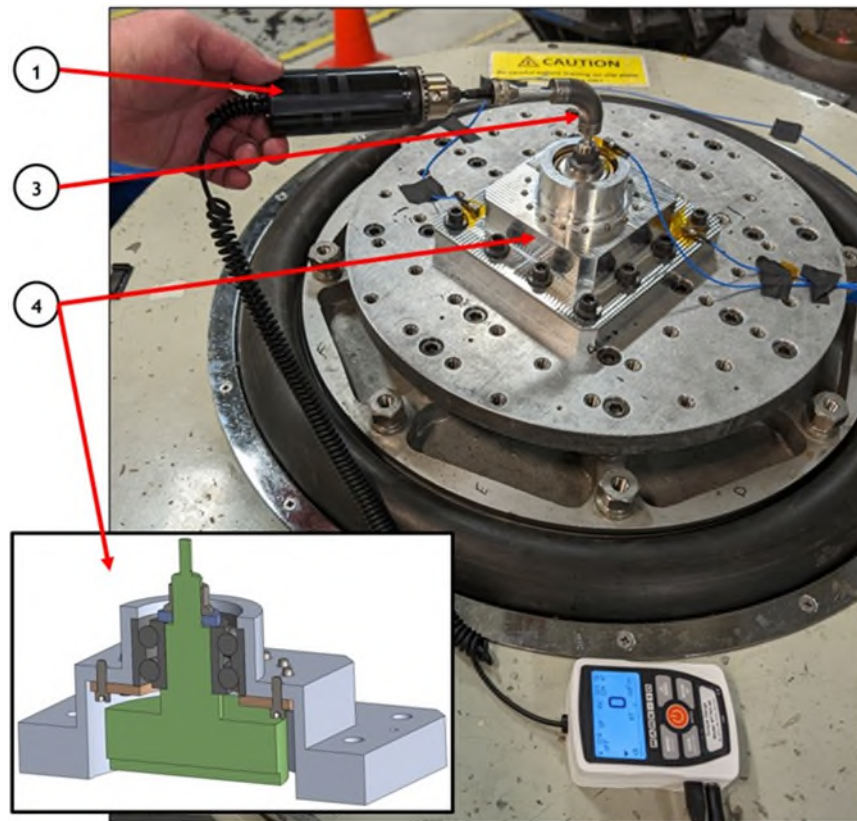


Figure 5. Final Test Setup - Axial

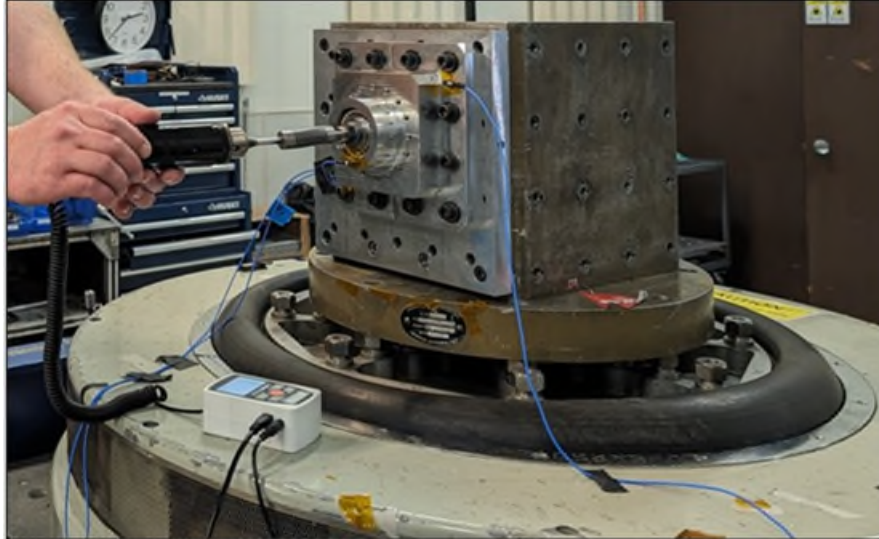


Figure 6. Final Test Setup - Radial

The test was run at qual flight PSD inputs which was slowly ramped up from zero dB to just under full level (57.6 g_{rms} was the max level due to shaker capabilities). The test would stabilize incrementally during the ramp up to obtain torque measurements by hand. Torque data was only collected up to $\sim 32 g_{rms}$ for safety concerns and the misalignment coupler failed. Examples of the test data is shown in Figure 7. The unstable torque reading was due to operating the digital torque watch (sampling rate of 250 Hz) by hand for simplicity as the test is only looking for gross trends and not precise measurements. The bearing was rotated 360 degrees CW and then 360 degrees CCW to obtain torque data.

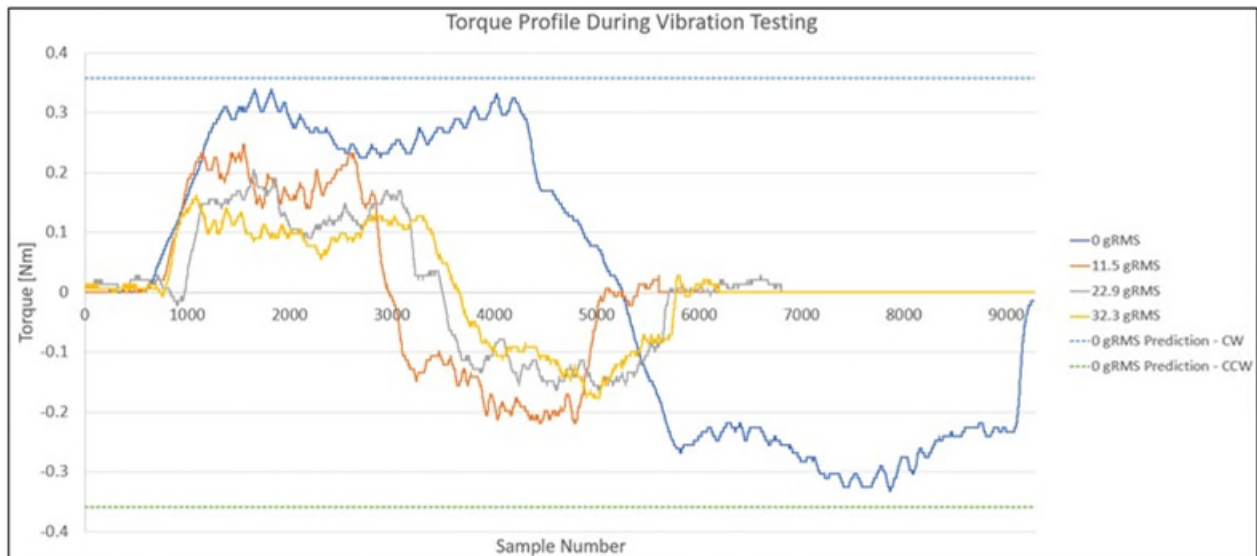


Figure 7. Measured Torque Data from Vibration Testing¹

These results are also shown in Figure 8 where a general trend is seen showing that drag torque decreases as vibration levels increase. This is distinct from the Orbis predictions which show a steep upward trend

¹ Note that during 0 g_{rms} test the CW to CCW transition occurred near sample 5000. During the 11.5-32.3 g_{rms} tests the transition occurred sooner, near sample 3000, because the operator was afraid of the vibration table and rotated the bearing faster in order to limit the total duration. In all cases the bearing rate was slow enough (< 5 RPM) that the measured result effectively represents only Coulomb drag without a significant viscous component.

under combined loading. The measured drag torque can be extrapolated to compare to predictions at max vibration inputs (>60 g_{rms}) to ensure there will be no issues on the flight mechanism torque margin calculations. This results in higher predicted torque margins based on collected test data. The predicted drag torque under bearing preload only (0 g_{rms}) was in-line with measurements which validates Orbis predictions while the system is not experiencing vibration environments.

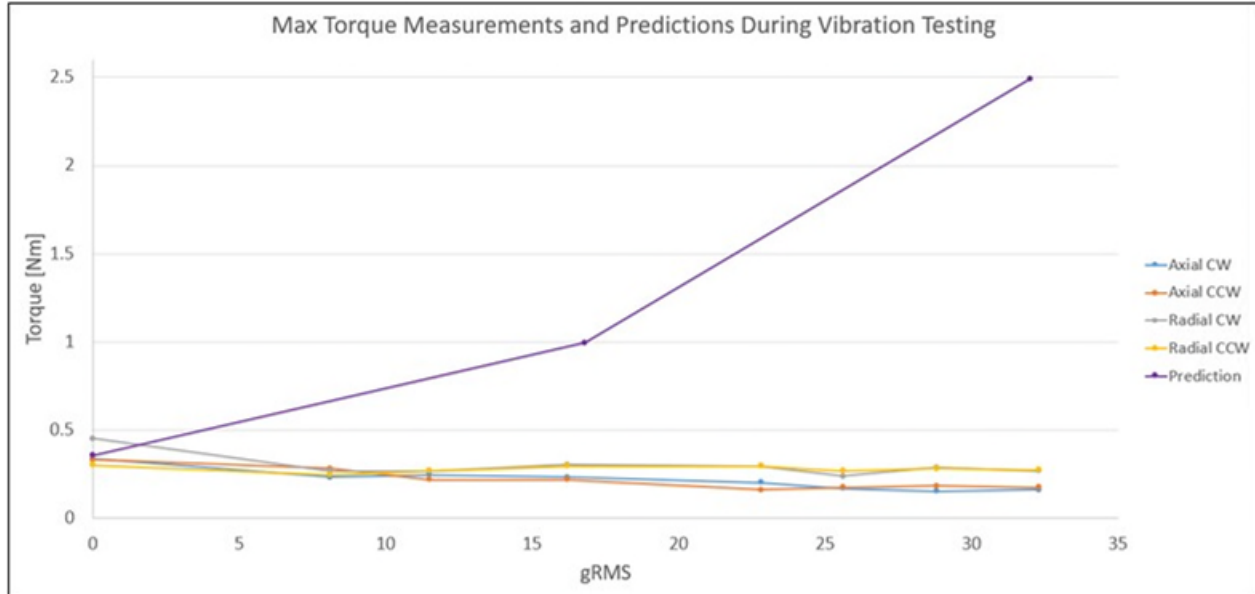


Figure 8. Max Measured Torque Data and Predicted Torque over Varied Vibration Levels

The bearings were inspected for ball offloading concerns post testing with an optical microscope and high magnification images using a Keyence digital microscope. No torque spikes could be detected when rotating the bearing by hand or with a torque watch, but inspections were performed to ensure there is no damage or brinelling.

Figure 9 shows the bearings post vibration testing and before the grease was removed – both balls and races appeared in good condition and free from damage. Figures 10 and 11 show some level of marking to the outer races once the grease was removed. This is explained by the bearing analysis prediction that the contact angle will change from 8.9 degrees to 27 degrees during vibratory loads: these markings correspond to this large change in contact angle (the markings are in the axial direction). Optical profile measurements could not find any discernable material displacement; thus, we conclude these are superficial “polishing” marks and not brinelling or subsurface shear damage.



Figure 9. Bearing Cage and Balls Post Vibration Testing



Figure 10. Bearing Outer Raceway at 50x Magnification

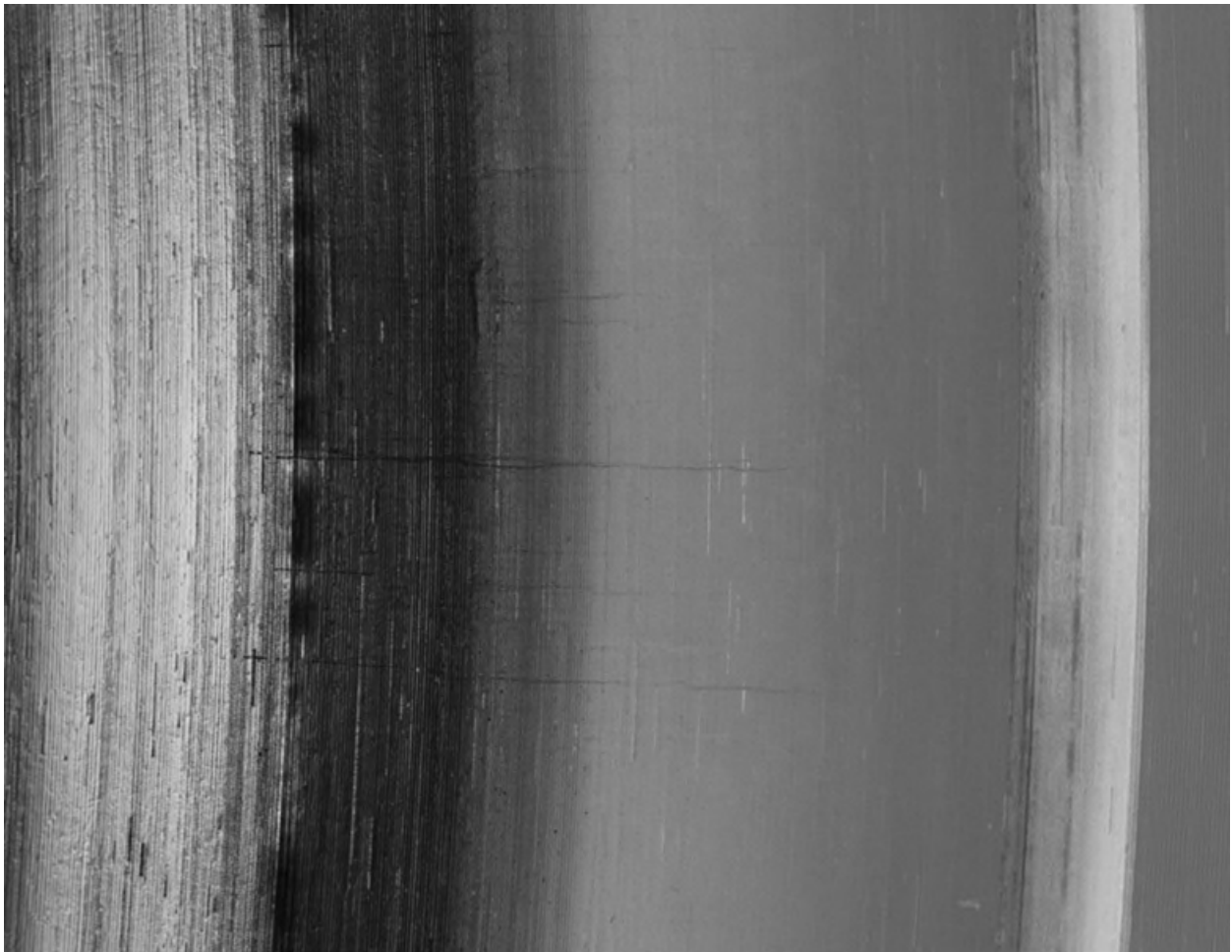


Figure 11. Bearing Raceway at 50x Magnification Post Digital Processing

Lessons Learned

- Torque testing under vibratory conditions is challenging and should be conducted with electronic measurement equipment/sensors. *However*, the simple apparatus shown here was effective for the task.
- Spare non-flight bearings used in the Initial Test were needed to reduce risk early on in the program but data collection with flight articles and to flight loads proved more informative.
- Predicted coulomb drag using reaction loads from combined operational and vibration environments is not accurate; the actual drag torque during vibration is, in all cases, lower than the 0 g_{rms} case and did not increase with dynamic loads as analyzed.
- Ball offloading showed no adverse effects to the bearings and therefore would be tolerated in the flight assembly and performance life of the mission.

Conclusion

Based on this analysis and testing, conventionally predicted drag torques due to preload, operational loads, and random vibration loading are not accurate for highly preloaded bearings operating in high vibration environments. We conclude that this is due to the random loading direction changes happening over very short time durations. The bearing contact stress analysis still accounts for vibration, actuation, and thermal loads whereas the drag torque only accounts for actuation and thermal loads.

Development and Qualification of an Extreme Mechanical Life Antenna Pointing Mechanism, Part of the Inter Satellite Link on an ESA Mission Spacecraft

Richard Horth*, Stéphane St-André*, Nicolas Sturkenboom* and William Dumberry*

Abstract

An ESA mission funded by the European Union requires inter satellite links. Each antenna has to perform 14 million communication periods during the 15 year spacecraft on orbit life. These communication periods contain a high speed slew phase for target acquisition and a slow speed track phase for communication. These movements have a cumulated steering range of 900E6 degrees including ECSS margins. A special gimbal joint and drive system containing a cable cassette, an RF rotary joint and the Rotary Actuator (RA) was developed. The RA consists of a resolver, a redundant discrete permanent magnet brushless motor, a planetary gearhead and an anti-backlash bull gear stage. It is driven using Field Oriented Control to maximise efficiency and life. The TVAC qualification life test was completed in April 2023. The paper presents the problems, lessons learned and difficulties encountered during qualification testing.

Introduction

Inter satellite links are becoming increasingly popular. For some missions, the performance of the gimbals pointing the antennas is very challenging. In the present case, the antenna has to repoint itself anywhere within a hemisphere 14 million times during its 15 year life. The repointing is also very dynamic because it has to occur within 6 seconds. The paper describes the design of the mechanism, the problems encountered during qualification and the modifications implemented to correct them.

Rotary Actuator Design Overview

The Rotary Actuator (RA) is presented in Fig. 1.



Figure 1. Extreme Life RA

It contains a redundant Variable Reluctance Resolver (VRR). The resolver is used for the commutation of the motor and for position and speed inputs to the servo. A three phase, four pole redundant motor is

* MDA, QC, Canada

mounted on the same shaft. The motor shaft feeds the mechanical power through a 2 stage planetary gearbox. Finally, a radially preloaded, zero backlash spur gear stage provides mechanical power to the output. The complete Motor Gear Head (MGH) is on a suspension to preload the final gear mesh. A bracket holding an elastomer damping bumper holds the motor in place during dynamic environments. The purpose of the final stage is to reduce the planetary backlash to acceptable levels. The output of the RA uses a thin section cross roller bearing to react the axial, radial and bending loads.

Life Extending Design Characteristics

The previous largest mechanical travel life qualified by MDA was 70E6 output degrees for an inter-satellite link on a LEO constellation mission. This mission required an RA that could travel over 900E6 and perform 14.9E6 reversals. Because of the extreme demands of this mission, several variations were implemented in order to maximise the mechanical life. They are listed below.

1. The motor is controlled using Field Oriented Control (FOC) in an attempt to have the motor shaft rotate as smoothly as possible to maximise the life of the pinion of the first stage planetary.
2. The complete gear train was oversized to minimise the gear mesh contact stresses and maximise the lubricant life.
3. The gear ratio was minimised (within an acceptable mass) to reduce the number of revolutions of the motor pinion and bearings. The life test requirement still requires 280 Million revolutions of the motor shaft to pass.
4. The use of alternate lubricants everywhere instead of PFPEs.
5. Heating the RA to above 0°C to ensure that the lubricant remains fluid enough to replenish the working surfaces as required.

Life Test Acceleration

Since the mission RAs are in continuous operation for 15 years, it is out of the question to design a life test that duplicates the mission. Several discussions were held with the customer chain in order to set the parameters of an accelerated life test. The originally agreed test plan included 3 identical test units named RA1, 2 and 3. The unit and their purpose are detailed below:

RA1: Will be subjected to full environments, static load, qualification level vibration and shock, thermal and vacuum. It will perform the main part of its travel at high speed regime and 10% of the mechanical cycles at low speed regime to perform the remaining travel to prove that the unit can perform the total travel but not the total number of reversals.

RA2: Will also be subjected to full environments. It will perform the totality of the mechanical cycles at low speed regime to have the correct amount of reversals and to show that with transition Stribeck numbers (lubrication regime), the unit will pass.

RA3: This unit is the “fail fast” unit to uncover major design flaws as fast as possible. It simply consists of an ambient test where a RA is hooked up to and offset mass and run at full speed. The offset mass is rotating along a horizontal axis so when the mass is going up, it simulates the acceleration phase of the rally profile and when the mass is going down, it simulated the deceleration phase of the rally profile. The system includes a belt drive with a 4:1 ratio to be able to simulate the correct number of acceleration/deceleration phases without running the RA too fast. Fig. 2 shows the set up.

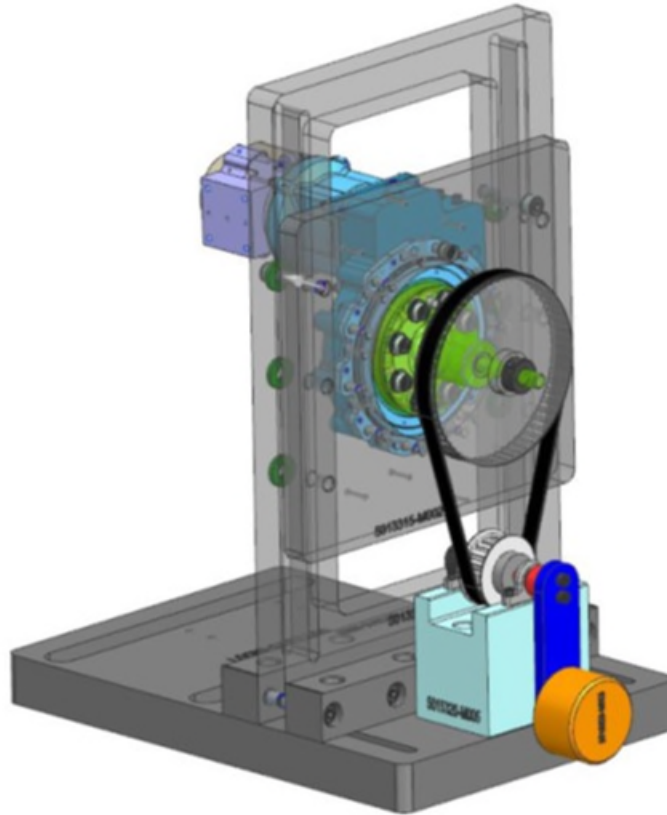


Figure 2. RA3 Life Test Set Up

Problems and Solutions

Several problems were encountered which caused the team to re-design portions of the RA and re-think the original qualification test plan. They are presented below.

Problem no. 1: Variable Reluctance Resolver Inaccuracy

During initial testing, it was discovered that the VRR caused discontinuities in the Resolver to Digital Converter output causing large accelerations/decelerations of the motor shaft which is opposition to achieving an extreme mechanical life for the RA. Several solutions were implemented to overcome this problem.

1. MDA worked with the supplier to improve the variable reluctance resolver performance and agreed to a pass/fail criteria that consisted of the maximum slope of the error between the motor shaft true position and the resolver reported position.
2. A sinusoidal correction curve was implemented in the controller to compensate for the remaining resolver error.

For the life test to proceed with the original resolver, it was decided to run the motor completely open loop using sinusoidal currents. The logic is that in open loop, the motors detent would cause some motor shaft acceleration/deceleration which the flight servo would correct for providing some margin on the life test.

The lesson learned is that when procuring a new component from a supplier, surprises are to be expected. It takes some time and a lot of communication for the supplier and the user to agree on a nomenclature and understand what performance is really required.

Problem no. 2: Structural Failure

During vibration testing, the screws holding the bracket that supports the motor came loose. Failure investigation revealed that the interface was seeing higher loads than anticipated. The design was strengthened by enlarging the screw size and increasing their number. Fig. 3 shows the original and redesigned RAs side by side for comparison.

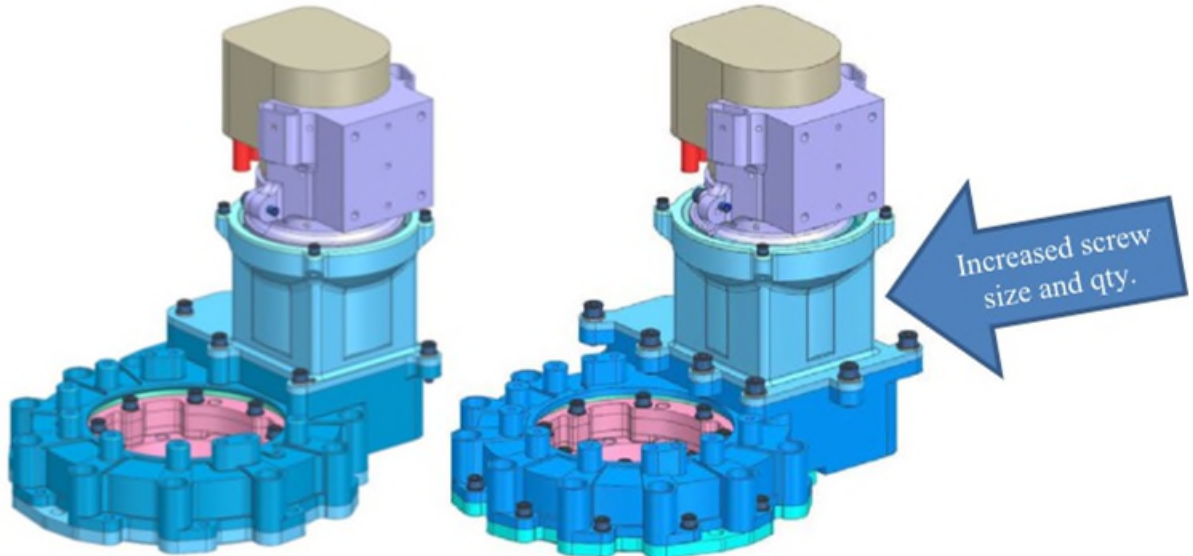


Figure 3. Original and Final RA Structural Design

The redesign required remanufacturing critical components which would take significant time. In order to retire life test risk as early as possible, it was decided to proceed with life testing with the original structural design. The justification being that the structural redesign did not affect the drive train. The cause of the design flaw was an incorrect stiffness used at the damping bumper interface, which was based on a previous program where the MGH had a smaller mass due to the lack of a resolver. The addition of the resolver on the back side of the motor added significant load on the holding bracket.

The lesson learned is that when analysing a heritage design for re-use on a new program, even if the proposal assumed build to print, the impacts of all changes have to be thoroughly analysed.

Problem no. 3: Increased Friction

At about 55 % through travel life, the QM RA2 experienced failures on unpowered holding torque and threshold voltage at cold while passing all other performance tests. Investigation revealed that a portion of the extra resistance was caused by a worn out TVAC ferro fluidic coupling. The coupling was changed and an intermediate performance test plateau was set at 0 °C to see at which temperature the RA started exhibiting higher resistance. After a while, the RA performance came back into family and continued until the end of test. Since this life test was a large step out from MDAs heritage life tests, it was expected that some rotating Ground Support Equipment (GSE) would fail during life. In order to reduce the down time caused by these GSE failures, spares of all rotating equipment were procured in advance.

Problem no. 4: RA1 Failure After 32% of Travel Life

In order to qualify the structural design changes that were corrective actions for problem no.2, it was agreed that a structurally stronger RA would go through all vibration and shock and would then start life testing until the first qual unit completed its second life test. RA1 was repurposed for this activity. Unfortunately, that RA failed after 32% of mechanical life. During a cold plateau, the current suddenly spiked until stall. Fig. 4 shows the current variation as a function of time during the failure.

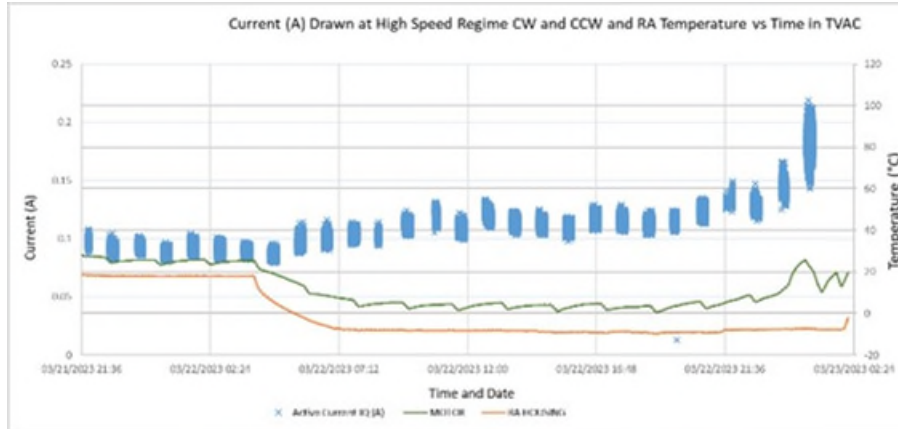


Figure 4. Gradual Current Increase During Failure

The RA was disassembled to determine the location of the failure in hope that it would help find the cause. The failure was traced down to the first stage planetary. Due to lubricant failure, a portion of a planet tooth cold welded in the root between two motor pinion (sun) teeth. Every time that tooth portion came into contact with a planet tooth, it crushed the planet tooth and caused more debris. Fig. 5 shows the motor pinion with an intertooth root filled with a planet tooth.

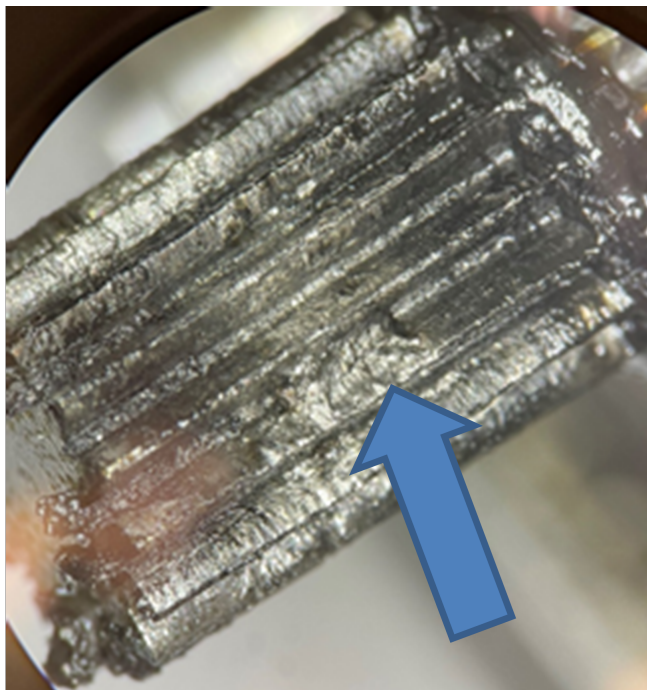


Figure 5. Failed Planetary Sun of RA1

The problem now became finding what caused the lubricant failure. Analysis shows that the contact stress at that mesh is benign during worst case loading. After several investigation steps, it was found that the Electronic Ground Support Equipment (EGSE) for RA1 sent a large current ripple to the motor. The motor shaft experienced large accelerations/decelerations due to this current ripple. This erratic motion caused the motor pinion teeth to chatter which caused the failure.

The design of the EGSE is such that the RA primary and redundant channels are multiplexed to a single controller. During green runs prior to closing the TVAC chamber door, only one RA channel was hooked up and everything ran smoothly. During automated life testing in TVAC, both primary and redundant

channels were mated to the EGSE. In that configuration, the currents sent to the motor were much noisier. As can be seen in Fig. 6, the currents even cross zero, which means that the motor shaft was actually braking at that frequency causing tooth chatter between the first stage sun and its planets. This was found to be the cause of RA1 life test failure.

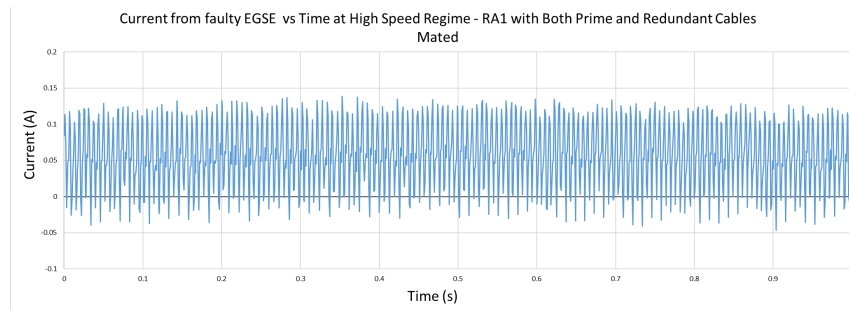


Figure 6. Faulty EGSE Current Ripple Sent to RA1

The lesson learned is that all electrical configurations have to be checked during green runs prior to closing the TVAC chamber door.

Problem no. 5: Damage to 3rd Stage Gear Teeth

After performing the high speed test campaign of RA1 and the low speed test campaign that was originally intended for RA2 for a total of 903E6 output degrees travelled and 20E6 reversals, the unit passed all functional tests at hot, cold and ambient for what seemed to be a successful life qualification. The 3rd stage gear train of RA2 was disassembled and inspected. Damage was found on the teeth on both mating gears of that stage. The damage did not prevent the RA from passing all performance tests at the end of life. The damage pattern indicated that the rotation axes of both gears was not parallel. Fig. 7 shows the damage on the MGH output pinion. Similar damage was found on the mating bull gear.



Figure 7. Damage to Last Stage Gear Mesh

After review of the design, it was concluded that there were too many stacked up tolerances to guaranty proper parallelism. The corrective action is to inspect each unit and shim the MGH mounting flange in order to correct for out of parallelism errors.

The lesson learned is that with extreme life requirements and relatively wide gear teeth to minimise contact stress, the parallelism between rotation axes of mating gears becomes critical.

Qualification Status

In summary, as of June 2023, MDA had to update its initial qualification test plan with the following:

- QM RA #2 went through a successful life test in open loop
- QM RA #1 passed all its structural tests, TVAC operational cycling, but failed during its closed loop life test due to an EGSE issue.
- QM RA #3 (Bench Test) was cancelled since QM RA #2 went through its full test campaign successfully.

MDA is currently in discussion with the customer chain to confirm that the above qualification test campaign is sufficient to validate full qualification of the RA for the ESA mission.

Conclusion

MDA has designed, manufactured and qualification life tested a rotary actuator that has 13 times the travel life of the previous MDA designed long life rotary actuator. Several problems were encountered which caused the design team and customer chain to work together to continuously update the qualification test plan to obtain a successful outcome.

Acknowledgment

MDA wants to acknowledge that this contract was carried under a program funded by the European Union and led by the European Space Agency as a procurement agent. Moreover, MDA wants to thank TESAT, Airbus and ESA for their support in the development of this Extreme Life Rotary Actuator.

This document has been produced under funding of the European Union. The views expressed herein can in no way be taken to reflect the official opinion of the European Union and/or ESA